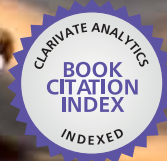




IntechOpen

Progress and Developments in Ionic Liquids

Edited by Scott Handy



WEB OF SCIENCE™

PROGRESS AND DEVELOPMENTS IN IONIC LIQUIDS

Edited by **Scott Handy**

Progress and Developments in Ionic Liquids

<http://dx.doi.org/10.5772/62621>

Edited by Scott Handy

Contributors

Qingshan Liu, Lin Mou, Qige Zheng, Quan Xia, Michiaki Matsumoto, Pius Dore Ola, Fabrice Mutelet, El Shaimaa Abumandour, Dominique Alonso, Hu Yu Lin, Yen-Ho Chu, Yi-Pin Chang, Qibo Zhang, Anna Koziróg, Agnieszka Wysocka-Robak, Viorel Cîrcu, Yoshiro Kaneko, Pannuru Venkatesu, Awanish Kumar, Meena Bisht, Indrani Jha, Masoud Mokhtary, Mohamed Ibrahim Abdul Mutalib, Ouahid Ben Ghanem, Takaya Sato, Toshio Kamijo, Hiroyuki Arafune, Takashi Morinaga, Kazue Kurihara, Muhammad Moniruzzaman, Hamayoun Mahmood, Suzana Yusup, Hazizan Md Akil, Saiful Zubairi, Zetty Shafiqah Othman, Nur Hasyareeda Hassan, Lavinia Lupa, Petru Negrea, Adriana Popa, Gloria Villora, Mercedes G. Montalbán, Mar Collado-González, F. Guillermo Díaz-Baños, Sudha J Devaki, Renjith Sasi, Takahiro Takekiyo, Lenore Dai, Stella Nickerson, Elizabeth Nofen, Denzil Frost, Xingli Zou, Xionggang Lu, Xueliang Xie, Luca Magagnin, Roberto Bernasconi, Gabriele Panzeri, Alessandra Accogli, Francesco Liberale, Luca Nobili, Masahiko Matsumiya, Abdul Kariem Arof, Siti Nor Farhana Yusuf, Attila Gollei

© The Editor(s) and the Author(s) 2017

The moral rights of the and the author(s) have been asserted.

All rights to the book as a whole are reserved by INTECH. The book as a whole (compilation) cannot be reproduced, distributed or used for commercial or non-commercial purposes without INTECH's written permission.

Enquiries concerning the use of the book should be directed to INTECH rights and permissions department (permissions@intechopen.com).

Violations are liable to prosecution under the governing Copyright Law.



Individual chapters of this publication are distributed under the terms of the Creative Commons Attribution 3.0 Unported License which permits commercial use, distribution and reproduction of the individual chapters, provided the original author(s) and source publication are appropriately acknowledged. If so indicated, certain images may not be included under the Creative Commons license. In such cases users will need to obtain permission from the license holder to reproduce the material. More details and guidelines concerning content reuse and adaptation can be found at <http://www.intechopen.com/copyright-policy.html>.

Notice

Statements and opinions expressed in the chapters are those of the individual contributors and not necessarily those of the editors or publisher. No responsibility is accepted for the accuracy of information contained in the published chapters. The publisher assumes no responsibility for any damage or injury to persons or property arising out of the use of any materials, instructions, methods or ideas contained in the book.

First published in Croatia, 2017 by INTECH d.o.o.

eBook (PDF) Published by IN TECH d.o.o.

Place and year of publication of eBook (PDF): Rijeka, 2019.

IntechOpen is the global imprint of IN TECH d.o.o.

Printed in Croatia

Legal deposit, Croatia: National and University Library in Zagreb

Additional hard and PDF copies can be obtained from orders@intechopen.com

Progress and Developments in Ionic Liquids

Edited by Scott Handy

p. cm.

Print ISBN 978-953-51-2901-1

Online ISBN 978-953-51-2902-8

eBook (PDF) ISBN 978-953-51-4108-2

We are IntechOpen, the world's leading publisher of Open Access books Built by scientists, for scientists

3,500+

Open access books available

111,000+

International authors and editors

115M+

Downloads

151

Countries delivered to

Our authors are among the
Top 1%

most cited scientists

12.2%

Contributors from top 500 universities



WEB OF SCIENCE™

Selection of our books indexed in the Book Citation Index
in Web of Science™ Core Collection (BKCI)

Interested in publishing with us?
Contact book.department@intechopen.com

Numbers displayed above are based on latest data collected.
For more information visit www.intechopen.com



Meet the editor



Scott Handy is currently the interim associate dean of the College of Graduate Studies at Middle Tennessee State University and professor of Chemistry. He received his PhD degree in Chemistry from Indiana University under the direction of Professor Paul Grieco. After an NIH postdoctoral fellowship at Stanford University in the research group of Professor Paul

Wender, Handy began his independent career at Binghamton University, before moving to Middle Tennessee State University. His research interests include the use of nontraditional solvents (ionic liquids and deep eutectic solvents) in organic synthesis and the synthesis and study of bioactive natural product derivatives (most recently aurones).

Contents

Preface XIII

Section 1 Applications 1

Chapter 1 **Are Ionic Liquids Suitable as New Components in Working Mixtures for Absorption Heat Transformers? 3**
El-Shaimaa Abumandour, Fabrice Mutelet and Dominique Alonso

Chapter 2 **Gas Sensing Ionic Liquids on Quartz Crystal Microbalance 35**
Yi-Pin Chang and Yen-Ho Chu

Chapter 3 **Application of Ionic Liquids in Paper Properties and Preservation 51**
Koziróg Anna and Wysocka-Robak Agnieszka

Section 2 Biological 73

Chapter 4 **The Role of Ionic Liquids in Protein Folding/Unfolding Studies 75**
Awanish Kumar, Meena Bisht, Indrani Jha and Pannuru Venkatesu

Chapter 5 **Ionic Liquid-Induced Unique Structural Transitions of Proteins 97**
Takahiro Takekiyo and Yukihiro Yoshimura

Chapter 6 **Green Composites from Ionic Liquid-Assisted Processing of Sustainable Resources: A Brief Overview 117**
Hamayoun Mahmood, Muhammad Moniruzzaman, Suzana Yusup and Hazizan Md. Akil

Section 3 Electrochemistry 133

Chapter 7 **Ionic Liquids as Electrodeposition Additives and Corrosion Inhibitors 135**

Zhang Qibo and Hua Yixin

Chapter 8 **Ionic Liquid Enhancement of Polymer Electrolyte Conductivity and their Effects on the Performance of Electrochemical Devices 157**

Siti Nor Farhana Yusuf, Rosiyah Yahya and Abdul Kariem Arof

Chapter 9 **Recent Advances in Electrocatalytic Applications of Ionic Liquids 185**

Yu Lin Hu

Chapter 10 **Purification of Rare Earth Amide Salts by Hydrometallurgy and Electrodeposition of Rare Earth Metals Using Ionic Liquids 213**

Masahiko Matsumiya

Chapter 11 **Electrodeposition from Deep Eutectic Solvents 235**

R. Bernasconi, G. Panzeri, A. Accogli, F. Liberale, L. Nobili and L. Magagnin

Chapter 12 **Electrodeposition of Zn, Cu, and Zn-Cu Alloys from Deep Eutectic Solvents 263**

Xingli Zou, Xionggang Lu and Xueliang Xie

Section 4 Liquid Crystals 283

Chapter 13 **Ionic Liquid Crystals Based on Pyridinium Salts 285**

Viorel Cîrcu

Chapter 14 **Ionic Liquids/Ionic Liquid Crystals for Safe and Sustainable Energy Storage Systems 313**

Sudha J. Devaki and Renjith Sasi

Section 5 Physical Properties 337

Chapter 15 **Predicting Density and Refractive Index of Ionic Liquids 339**

Mercedes G. Montalbán, Mar Collado-González, F. Guillermo Díaz-Baños and Gloria Villora

- Chapter 16 **Thermodynamic Properties of Ionic Liquids 369**
Liu Qingshan, Mou Lin, Zheng Qige and Xia Quan
- Chapter 17 **Behavior of Ionic Liquids Under Nanoconfinement Greatly Affects Actual Friction 413**
Toshio Kamijo, Hiroyuki Arafune, Takashi Morinaga, Takaya Sato and Kazue Kurihara
- Chapter 18 **Ecotoxicity of Ionic Liquids Towards *Vibrio fischeri*: Experimental and QSAR Studies 429**
Mohamed Ibrahim Abdul Mutalib and Ouahid Ben Ghanem
- Chapter 19 **Dielectric Characteristics of Ionic Liquids and Usage in Advanced Energy Storage Cells 451**
Attila Gölle
- Section 6 Separations 475**
- Chapter 20 **Ionic Liquids in Multiphase Systems 477**
Stella Nickerson, Elizabeth Nofen, Denzil Frost and Lenore L. Dai
- Chapter 21 **Imidazolium-Based Ionic Liquid Binary Solvent System as an Extraction Medium in Enhancing the Rotenone Yield Extracted from *Derris elliptica* Roots 495**
Zetty Shafiqah Othman, Nur Hasyareeda Hassan and Saiful Irwan Zubairi
- Chapter 22 **Use of Ionic Liquids in Solid-Liquid Separation Processes 517**
Lavinia Lupa, Petru Negrea and Adriana Popa
- Chapter 23 **Supported Ionic Liquid Membranes for Metal Separation 539**
Pius Dore Ola and Michiaki Matsumoto
- Section 7 Supported Ionic Liquids 557**
- Chapter 24 **Ionic Liquids Immobilized on Magnetic Nanoparticles 559**
Masoud Mokhtary
- Chapter 25 **Preparation of Ionic Liquids Containing Siloxane Frameworks 579**
Yoshiro Kaneko, Akiyuki Harada, Takuya Kubo and Takuhiro Ishii

Preface

The area of room temperature ionic liquids (RTILs) continues to grow and expand at a rapid pace. While the number of truly new RTILs reported has definitely slowed (with perhaps the exception of the newer subfamily of deep eutectic solvents), that has been more than replaced by efforts exploring their application in a wide range of areas. In this volume, several recent areas of effort are reported and reviewed, with the goal of encouraging further diversification of effort. Indeed, some of these chapters clearly demonstrate that the applications of RTILs are only limited by the imagination and that they certainly have potential benefits to offer to almost any area of science and technology.

That said, this volume begins with some highly unusual areas of application, featuring a chapter on the use of RTILs in gas-sensing quartz crystal microbalances (Yen-Ho), as working mixtures for absorption heat transformers (Fabrice), and, quite interestingly, as modifiers for paper preservation and strengthening (Anna).

From there, a number of chapters feature different aspects of applications in the biological arena. While it has been known for some time that RTILs can be useful solvents for enzymatic reactions, these chapters expand this scope to include studies of the role of RTILs in protein folding and unfolding (Pannuru), structural transitions induced by RTILs (Takahira), and the use of RTILs for processing of various biomaterial-derived green composites (Nuhammad).

Another frequently reported area of application for RTILs is in electrochemistry. Understandably, much of this effort has been directed in the area of electrodeposition and purification and with considerable opportunity for realistic application. In this respect, electrodeposition from deep eutectic solvents is covered (Luca), electrodeposition of zinc and copper (Xingli) and electrodeposition of corrosion inhibitors (Qibo), polymer electrolyte conductivity enhancements (Mariem), rare earth metal purifications (Masahiko), and electrocatalytic applications (Hu).

A somewhat related area is that of liquid crystal technology. RTILs are an interesting border region between conventional crystals and conventional liquids and, as such, have been studied with considerable interest. A chapter discussing pyridinium-based RTILs (Viorel) and one discussing energy storage applications (Sudha) are included.

For as long as people have studied RTILs, there has been a recognition of the importance of predicting the properties and behaviors of new, unreported RTILs. While much has been reported in this respect, it is far from a solved problem. Recent efforts on a variety of topics found in this volume include predicting density and refractive index of RTILs (Gloria), the correlation between dielectric properties and RTIL usage in energy storage systems (Attila),

determination of thermodynamic properties of RTILS (Qingshan), the connection between friction and the nanospace behavior of RTILs (Takaya), and the very important determination of RTIL toxicity using *Vibrio fischeri* (Ibrahim).

The use of RTILs in various types of separations continues to grow as well. In addition to the earlier chapter on the electrochemical purification of rare earth metals, the use of RTILs as membranes for metal separation (Michiaki), in solid/liquid separations (Lavinia), as multiphase systems (Lenore), and as extraction media (Saiful) is presented.

Finally, two interesting chapters focused on supported RTILs (important due to the high cost of most RTILs and thus the economic drive for recycling) are included: siloxane-based system (Tyoshiro) and magnetic nanoparticle-immobilized systems as catalysts (Masoud).

In short, the potential for RTILs continues to be as endless and unlimited as the proposed number of RTILs. While they may not be reaching the market for commercial applications as quickly as hoped, their future remains as exciting as ever. I hope that you enjoy this volume as much as I have and that it serves to inspire your creativity and imagination.

Prof. Scott Handy
Middle Tennessee State University
USA

Applications

Are Ionic Liquids Suitable as New Components in Working Mixtures for Absorption Heat Transformers?

El-Shaimaa Abumandour, Fabrice Mutelet and
Dominique Alonso

Additional information is available at the end of the chapter

<http://dx.doi.org/10.5772/65756>

Abstract

The working mixture almost exclusively used to operate absorption heat transformers (AHT) is $\{H_2O + LiBr\}$ ($\{H_2O + NH_3\}$ can also be used). Unfortunately, both working pairs present some drawbacks: corrosivity, toxicity, crystallization or high working pressure. Ionic liquids (ILs) possess very interesting properties (thermal stability, possible miscibility with water, negligible vapor pressure) that make them good candidates to be used as absorbents in AHT. This paper aims at providing an overview of available thermodynamic data concerning $\{H_2O + IL\}$ mixtures that could be used to operate an AHT.

Keywords: absorption heat pump, waste heat, ionic liquids, absorption heat transformers, thermodynamic properties, coefficient of performance

1. Introduction

Most of the industrial and domestic activities require large amounts of thermal energy to generate steam or heat by burning fossil fuel. After being used and degraded, low temperature heat is released to the environment as low grade waste heat. Large quantities of low temperature thermal waste heat streams from many industrial facilities such as power plants are discharged as thermal pollutants to the air and to the water at temperatures ranging from 60 to 100°C on a daily basis [1].

Among heat-driven devices are the absorption cycles. They can be divided into three classes: absorption heat pump (AHP), absorption chiller (AC), and absorption heat transformer (AHT). Absorption cycles become of great interest since electrical energy is replaced with low grade or waste heat allowing both primary energy savings and energetic efficiency improvements [2]. Consequently, absorption cycles enhance the atmospheric conditions by reducing the

emissions of greenhouse gases. Environmental impacts of absorption cycles can even be reduced by the adoption of environmental friendly working mixtures [3, 4].

One of the key points to the performance of an absorption cycle is the working fluid used. Nowadays, the most used binary systems in the absorption heat cycle are {water + lithium bromide ($\text{H}_2\text{O} + \text{LiBr}$)} and {ammonia + water ($\text{NH}_3 + \text{H}_2\text{O}$)}. The aqueous solution of LiBr is the most successful working mixture in absorption cycles and widely spread all over the world [2, 3]. Nevertheless, LiBr aqueous solution has some main drawbacks as follows:

- Absorption heat pumps cannot operate at an evaporation temperature below 0°C because of the use of water as a refrigerant, which makes it unusable for subfreezing refrigeration or heating/domestic hot water (DHW) supplementation in cold regions. Crystallization of $\{\text{H}_2\text{O} + \text{LiBr}\}$ at high concentrations is a common problem. High vacuum conditions should be preserved in the system for suitable operation of the $\{\text{H}_2\text{O} + \text{LiBr}\}$ system; otherwise, the performance of the absorption cycle would be greatly reduced [5]. $\{\text{H}_2\text{O} + \text{LiBr}\}$ is corrosive to metals [2–6].
- $\{\text{NH}_3 + \text{H}_2\text{O}\}$ requires high working pressure and ammonia is toxic.

Due to these disadvantages, which have not been solved properly, the absorption technology has known a very limited expansion [7, 8]. That is why heat pump and absorption chiller technologies suffer from lack of suitable working pairs. Hence, searching for new beneficial and reliable binary systems (to overcome these technical limitations) has become of great importance lately.

Limited numbers of critical reviews have been published in the literature on the subject of absorption technologies. In 2001, Srihirin et al. [6] reviewed different configurations and types of absorption refrigeration cycles and working pairs. Performance development and enhancement of absorption cycles were evaluated. They concluded that double-stage absorption refrigeration cycle based on $\{\text{H}_2\text{O} + \text{LiBr}\}$ has the highest coefficient of performance (COP) if compared to other systems in the market. In addition, they stated that multistage absorption cycles have a promising future.

In 2012, Sun et al. [3] have shown that $\{\text{H}_2\text{O} + \text{LiBr}\}$ and $\{\text{NH}_3 + \text{H}_2\text{O}\}$ mixtures can be improved by the use of additives. They also stated that working pairs dedicated to specific applications such as solar or geothermal energy should use hydrofluorocarbons (HFCs) as a refrigerant.

Ionic liquids (ILs) are environmentally friendly solvents, which have attracted considerable attention recently. Ionic liquids are salts in liquid state having melting point below some arbitrary temperature, such as 100°C (373 K). These solvents consist of ions (an asymmetric, large organic cation, and organic or inorganic anion). A great advantage of ILs is that their physical properties such as melting points, density, and hydrophobicity can be adjusted to design different types of ILs that can be used for various applications.

It is now well established that ILs exhibit interesting physicochemical properties allowing their use for various industrial applications [1–10].

ILs could be used as alternative working mixtures in absorption heat pump cycles. Hence, the possibility to have ionic liquids with a low melting point (lower than the temperature of the

cold heat source of absorption heat pumps) allows overcoming the crystallization problem of the {water + LiBr} solution that can occur under some conditions [2]. Moreover, aqueous solution of ionic liquids seems to be less corrosive than the {water + LiBr} solutions. Finally, many ionic liquids show a high miscibility with water, which is a recommended refrigerant for absorption cycles (high latent heat, low viscosity, nontoxic, etc.). Consequently, the analysis of binary systems composed of {ILs + water} for this application has to be explored [10].

Few papers were published concerning working fluids containing ILs and a refrigerant such as NH_3 , water, ethanol, or halogenated hydrocarbon series. Although many working fluids are proposed in the literature, there is not a complete review with comparison of their properties and performances. Studies mainly focus on the evaluation of $\{\text{H}_2\text{O} + \text{IL}\}$ systems for their potential use in absorption heat cycles [11, 12]. Khamooshi et al. [2] studied the performance of different working fluids containing ILs and different types of refrigerants in order to define the most suitable binary system. The coefficient of performance obtained on binary systems $\{\text{H}_2\text{O} + \text{ILs}\}$ in absorption cooling cycle is lower than $\{\text{H}_2\text{O} + \text{LiBr}\}$. Nevertheless, the COP of these systems is higher than 0.7.

In 2014, Zheng et al. [13] presented a compilation of thermodynamic properties of binary systems containing $\{\text{H}_2\text{O}$ or NH_3 or HFCs or alcohols + ILs}. The simulation of IL working fluids for single effect absorption cooling cycles showed that several binary systems have a real potential.

Publications concerning the development of working fluids and absorption cycles almost exclusively focus on air conditioning and refrigeration. It seems that no previous review has comprehensively summarized the studies and applications of absorption heat transformers using $\{\text{H}_2\text{O} + \text{ILs}\}$ as the working fluid. Recently, IoLiTec has developed working mixtures composed of $\{\text{H}_2\text{O}$ or $\text{NH}_3 + \text{ILs}\}$ for absorption cycles and filled the first patent application in this field in 2004, which is now owned by BASF. Meanwhile, other companies, such as DuPont and Degussa, are interested in using ILs in absorption cycles. This ensures the great potential of ILs in this application. Encouraging the use of ILs in this technology in combination with upgrading industrial and other waste heat could enhance the conservation of fossil fuels and hence decrease the emissions of greenhouse gases [14].

This work mainly focuses on the study of binary systems $\{\text{H}_2\text{O} + \text{ILs}\}$ in absorption heat transformers. The first part of the paper briefly describes the absorption cycle. Then, the thermodynamic and physical properties of the binary systems $\{\text{H}_2\text{O} + \text{IL}\}$ are summarized and the influences of the IL structure on these properties are presented. In this section, results found in the literature about the performance of absorption cycles using $\{\text{H}_2\text{O} + \text{IL}\}$ as working mixtures are also presented. The last section of this paper is devoted to the calculation of the coefficient of performance of an AHT operated with each binary system $\{\text{H}_2\text{O} + \text{IL}\}$.

2. Absorption heat cycles

Absorption cycles perform heat exchange between several heat sources or sinks. In the simplest case, there are three heat reservoirs characterized by their relative temperature level (high, medium, and low) as shown in **Figure 1**.

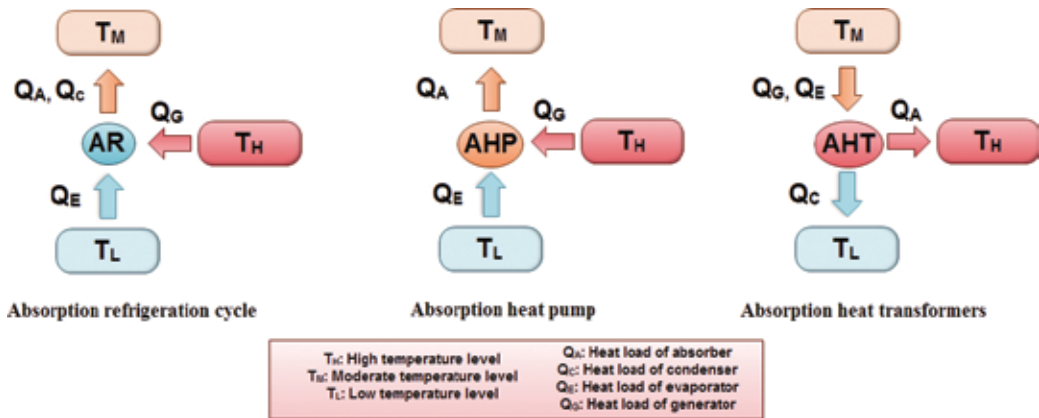


Figure 1. Simple absorption cycle.

Absorption systems can operate according to different modes differing by the nature of the driving heat and by the desired useful effect. These modes are as follows:

- Refrigerator: The driving heat is provided to the absorption cycle by a high temperature heat source. The low temperature source also provides heat to the cycle producing the cooling effect (useful effect). Heat is released to the medium temperature heat sink (generally the environment).
- Heat pump: As well as in a refrigerator, the cycle is driven by the heat provided by the high temperature source. The cycle also receives heat from the low temperature source. The useful heat is released to the medium temperature sink (generally a building or process that requires to be heated).
- Absorption heat transformer: Compared to both previous modes, sink and sources are reversed. The driving heat is a medium temperature heat (generally a waste heat). The upgraded useful heat is rejected to the high temperature sink and degraded heat is rejected to the low temperature sink (generally the environment).

Absorption cycles are composed of five main components: evaporator, condenser, generator, absorber, and solution heat exchanger (economizer) (Figure 2). They generally use a binary working mixture composed of a low boiling component called the refrigerant and a high boiling component called the absorbent.

In an absorption heat transformer (Figure 3), the driving heat (medium temperature waste heat) is provided to the mixture of an absorbent and a refrigerant (weak solution) in the generator at a low pressure producing two streams: a pure refrigerant vapor stream and a liquid mixture stream (strong solution).

This vapor is condensed in the condenser releasing heat to the low temperature heat sink. The condensate is increased to high pressure through a pump and vaporized in the evaporator, thanks to medium temperature heat. The strong solution passes through a pump to high pressure and is sent to the absorber where it absorbs the vapor produced in the evaporator.

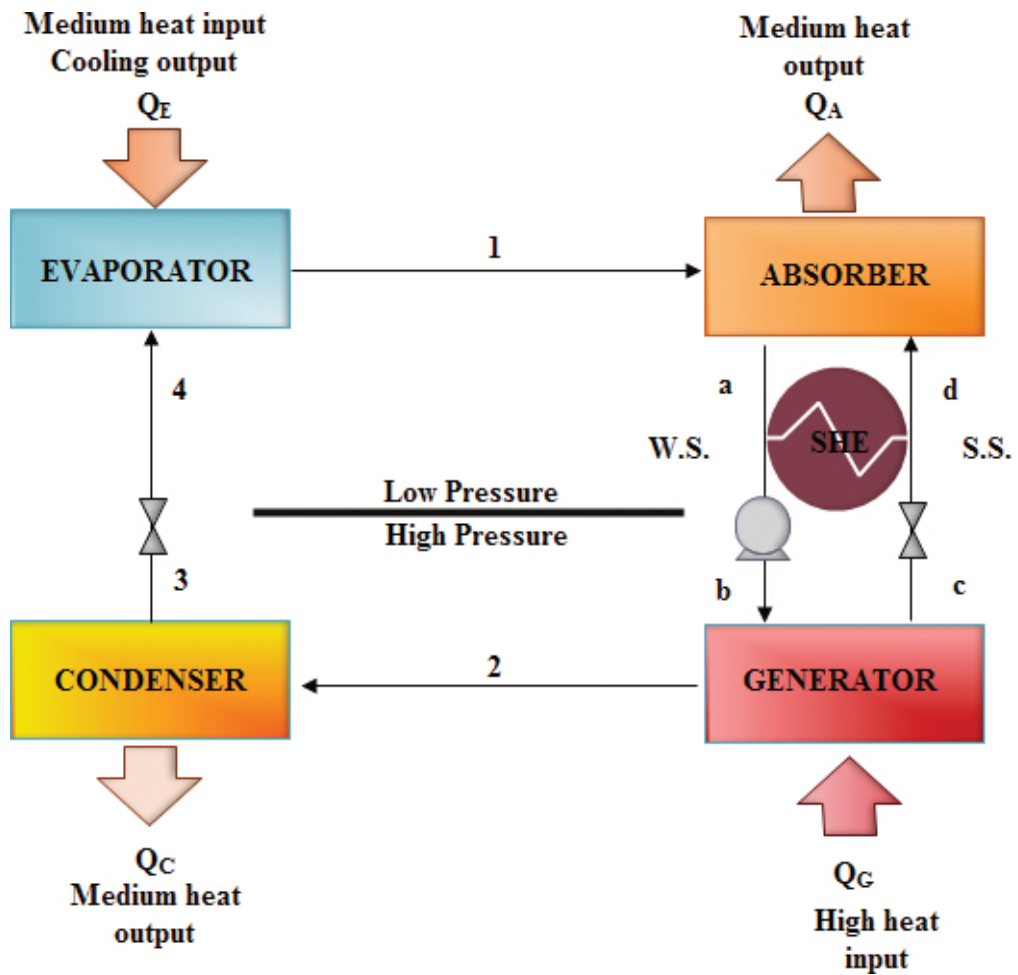


Figure 2. Schematic diagram of an absorption refrigeration cycle; A: absorber, C: condenser, E: evaporator, G: generator, SHE: heat exchanger.

This operation releases high temperature useful heat. The resulting weak solution is throttled through a valve and sent back to the generator. The solution heat exchanger allows preheating the strong solution entering the absorber by exchange with the weak solution leaving the absorber [15]. In refrigeration or heat pump absorption cycles (**Figure 2**), pressure levels are reversed (high pressure in the generator and in the condenser and low in the evaporator and the absorber), high temperature heat is provided to the generator, low temperature heat is provided to the evaporator and medium temperature heat is rejected at the condenser and absorber.

The working mixture properties will directly affect the absorption cycle performance. The following criteria can be followed to properly choose a working mixture [3]:

- i. The presence of absorbent in the refrigerant must increase as high as possible the boiling point of the solution.

- ii. In order to reduce refrigerant flow rate, its vaporization latent heat has to be as high as possible.
- i. In order to reduce exchange areas, pressure decreases and more generally the size and cost of equipment, viscosity of the solutions have to be the lowest as possible whereas thermal conductivity and diffusion coefficient have to be the highest as possible.
- ii. Components of the working mixture should not be too expensive.
- iii. Components of the mixtures should be noncorrosive and nontoxic.
- iv. The environmental impact of the working mixture should be the lowest as possible, especially in terms of GWP and ODP.

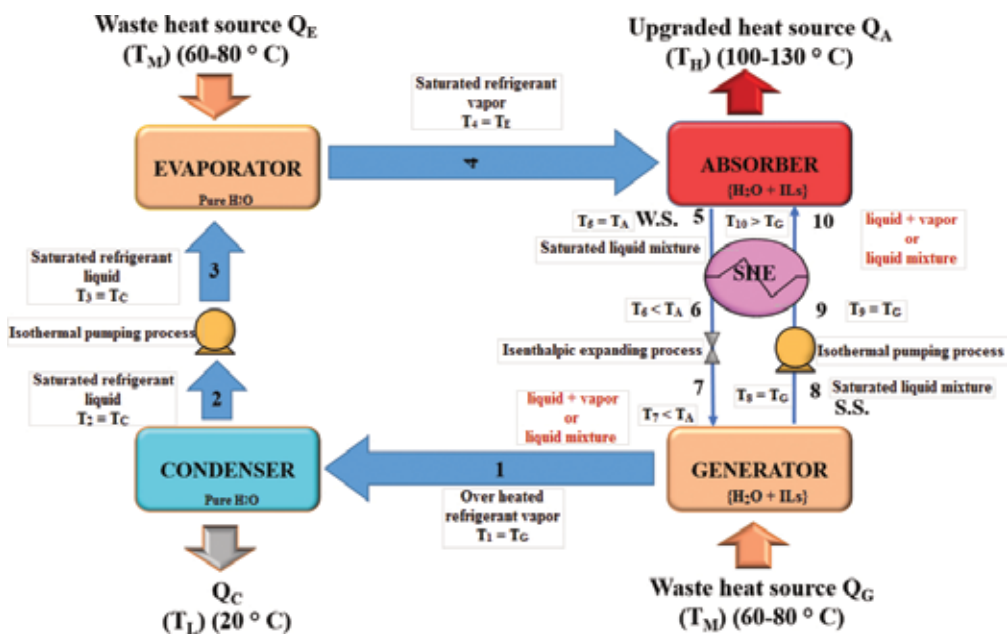


Figure 3. Schematic diagram of an absorption heat transformer; A: absorber, C: condenser, E: evaporator, G: generator, SHE: heat exchanger, P1 and P2: pump, v: valve.

To assess the energetic performance level of an absorption cycle, a criterion was defined: the coefficient of performance. Its expression depends on the kind of absorption cycle (refrigeration, heat pump, or AHT). Nevertheless, it is possible to define it as the ratio of the useful heat flow exchanged to the costly heat flow consumed [1]. For example, in a refrigeration cycle the expression of COP becomes [7–16]:

$$\text{COP} = \frac{\text{Low temperature heat flow exchanged at the evaporator}}{\text{High temperature heat flow provided at the generator} + \text{Mechanical pumping power}} \quad (1)$$

For an absorption heat transformer the COP expression is [8]

$$\text{COP} = \frac{\text{H. temp. heat flow exchanged at the absorber}}{\text{M. temp. heat flows exchanged at the generator and evaporator} + \text{Mechanical pumping power}} \quad (2)$$

3. Working fluids containing {water + ILs} for absorption cycles

Water can be considered as a green refrigerant, nontoxic, having high latent heat and excellent thermal characteristics. ILs used in the working fluids {H₂O + ILs} have to be hygroscopic and stable in aqueous solution. Numerous articles have studied the behavior of ILs with water, but there is still a lack of thermodynamic data for such mixtures.

3.1. {H₂O + ILs} binary systems in the literature

Recently, the performances of binary mixtures {H₂O + IL} have been evaluated as alternative binary systems in the absorption cycle [16–18, 19]. Numerous articles present thermodynamic studies of binary systems containing water and IL. **Table 1** lists the most studied ILs in the literature and the thermophysical properties available. Alkylsulfate- and alkylphosphate-based ILs are well known, and their performance in working fluids {H₂O + IL} was evaluated in different absorption cycles [7–26].

The binary systems {H₂O + dialkylimidazolium alkylphosphate}, 1-dimethylimidazolium dimethylphosphate, and 1-ethyl-3-methylimidazolium dimethylphosphate were extensively studied in numerous papers, where not only the data of vapor-liquid equilibria (VLE) but also density, viscosity, heat capacity, and excess enthalpy are available [7–25, 27–29]. These data make it possible to simulate the performance of these binary mixtures as working fluids in the absorption refrigeration cycle [7–25, 27, 30]. The simulation results show that the cycle performance of both systems is lower but close to the value obtained with the conventional working pair {H₂O + LiBr}. Yokozeki and Shiflett [31] also examined the feasibility of different binary systems {H₂O + IL} in an absorption cooling cycle and they found out that the best system is {H₂O + [EMIM][DMP]}.

The performance of {H₂O + LiBr} is still higher with a COP of 0.78 and a solution flow rate 53% smaller than [EMIM][DMP]. Nevertheless, the use of {H₂O + [DMIM][DMP]} as the working fluid enables to work in a large range of temperatures and to stop crystallization and corrosion caused by {H₂O + LiBr}. Several papers were focused on the measurements of thermodynamic properties of the binary system {H₂O + [EMIM][EtSO₄]} [16–25, 27, 30, 32], {H₂O + [EMIM][Ac]} [33, 34], or {H₂O + [HOEtMIM][Cl]} [35]. Even if these systems have some interesting properties such as low density and heat capacity or strong negative deviations from Raoult's law, no simulation of the performance of these working fluids in an AHT was presented.

4. Thermodynamic properties of {H₂O + IL}

The knowledge of thermodynamic properties, phase behavior, and safety/environmental hazards of {H₂O + IL} is required for the evaluation of this system in an AHT. The following section presents the behavior of ILs in the presence of water and the influence of their structure on thermodynamic properties.

ILs	Refrigerant	VLE measuring methods	Thermo. Para.	References
1,3-dimethylimidazolium chloride [DMIM][Cl]	Water	B. P. method	ρ	[57]
1,3-dimethylimidazolium dimethylphosphate [DMIM][DMP]	Water	B. P. method	C_p, ρ, H^E	[7, 24, 28–30]
1-(2-hydroxyethyl)-3-methylimidazolium chloride [HOEtMIM][Cl]	Water	B. P. method	VLE, C_p, ρ	[35]
1-(2-hydroxyethyl)-3-methylimidazolium trifluoroacetate [HOEtMIM][TFA]	Water	Fischer Labodest apparatus (model)	VLE data, H^E	[16]
1-ethyl-3-methylimidazolium tetrafluoroborate [EMIM][BF ₄]	Water	Static method	ρ	[63]
1-ethyl-3-methylimidazolium dimethylphosphate [EMIM][DMP]	Water	B. P. method	C_p, ρ, H^E , viscosity	[8, 22, 25–27, 30]
1-ethyl-3-methylimidazolium bis-(trifluoromethylsulfonyl)imide [EMIM][Tf ₂ N] or [(CF ₃ SO ₂) ₂ N]	Water	Static method	VLE data	[28]
1-ethyl-3-methylimidazolium acetate [EMIM][Ac]	Water	Dynamic method	C_p, ρ , viscosity	[33, 34]
1-ethyl-3-methylimidazolium ethyl sulfate [EMIM][EtSO ₄]	Water	B. P. method and static method and Fischer Labodest apparatus	C_p, ρ, H^E , viscosity	[26, 28, 29, 31–45, 47–55]
1-ethyl-3-methylimidazolium diethyl phosphate [EMIM][DEP]	Water	Circulation still	VLE data, H^E	[16–37]
1-ethyl-3-methylimidazolium trifluoromethanesulfonate [EMIM][TFO] [Triflate]	Water	Static method and Fischer Labodest apparatus	C_p, ρ, H^E	[56]
1-ethyl-3-methylimidazolium trifluoroacetate [EMIM][TFA]	Water	Fischer Labodest apparatus	C_p, ρ, H^E	[51]
1-ethyl-3-methylimidazolium methanesulfonate [EMIM][MeSO ₃]	Water		H^E	[16]
1-butyl-3-methylimidazolium tetrafluoroborate [BMIM][BF ₄]	Water	B.P. method & Static method	C_p, ρ, H^E , viscosity	[57]
1-butyl-3-methylimidazolium trifluoromethanesulfonate [BMIM][CF ₃ SO ₃] [TFO][triflate]	Water	Isobaric microbulliometer	C_p, ρ, H^E	[39–45, 47–56]
1-butyl-3-methylimidazolium methanesulfonate [BMIM][C ₁ SO ₃]	Water	Isobaric microbulliometer	VLE data	[39]
1-butyl-3-methylimidazolium chloride [BMIM][Cl]	Water	Labodest apparatus	VLE data	[34, 35, 37–39]
1-butyl-3-methylimidazolium bromide [BMIM][Br]	Water	B. P. method & Isobaric microbulliometer	VLE data	[39]
1-butyl-3-methylimidazolium acetate [BMIM][Ac]	Water	Isobaric microbulliometer, static method	VLE data	[34, 35, 37–39]
1-butyl-3-methylimidazolium trifluoroacetate [BMIM][CF ₃ CO ₂]	Water	Isobaric microbulliometer	VLE data	[39]

ILs	Refrigerant	VLE measuring methods	Thermo. Para.	References
1-butyl-3-methylimidazolium thiocyanate [BMIM][SCN]	Water	Isobaric microebulliometer, static method	VLE data	[39]
1-butyl-3-methylimidazolium tosylate [BMIM][TOS]	Water	Isobaric microebulliometer	VLE data	[39]
1-butyl-3-methylimidazolium methylsulfate [BMIM][MeSO ₄]	Water	Labodest app.	C _p , ρ, H ^E	[56]
1-butyl-3-methylimidazolium dibutyl phosphate [BMIM][DBP]	Water	Ebulliometric method	VLE data	[36]
diethylmethylammonium methanesulfonate ([DEMA][OMs])	Water	Dynamic method	VLE data	[27]
1-hexyl-3-methylimidazolium tetrafluoroborate [HMIM][BF ₄]	Water		ρ	[63]

Table 1. Thermodynamic parameters of different binary systems composed of {water + ILs}.

4.1. Thermodynamic models for the representation of a binary system {H₂O + IL}

A large number of thermodynamic models have been used to represent the phase diagrams of binary systems {H₂O + IL}. Some groups show that the NRTL model can be successfully used to represent thermodynamic properties of systems containing ILs [7–25, 27–29, 32–37]. Avezizou et al. [38] also used the UNIFAC model to describe the phase equilibria of solvent/ionic liquid systems. While the ionic liquids were based on an imidazolium cation and a hexafluorophosphate anion, water was considered to be the refrigerant. Two new main groups, the imidazolium and the hexafluorophosphate groups, were introduced in UNIFAC. SAFT-type equation of state was also used to represent mixtures containing ILs. This equation is a good tool to evaluate the density of pure ILs, solute activity coefficients but also VLE or LLE of binary or ternary mixtures {solute 1 + solute 2 + IL} [39, 40]. Cubic equations of state such as Peng-Robinson (PR) and Soave-Redlich-Kwong (SRK) were also used to represent quite accurate VLE, bubble point data or critical points of systems containing ionic liquids, gases, and/or liquids [31, 33–35, 37–45].

4.2. Experimental thermodynamic data of {H₂O + IL}

4.2.1. Vapor-liquid equilibrium (VLE)

The experimental techniques used for VLE measurements are a boiling point technique [16–25, 30, 35, 37, 38, 46], static apparatus [32], and a quasi-static ebulliometer method [37]. The boiling point technique is the most appropriate to study mixtures containing ILs. Most of the articles related to VLE measurements concerning the binary systems {H₂O + IL} are listed in **Table 1**.

Activity coefficient can be calculated from VLE data. This parameter illustrating the deviation from ideality of the mixture can be used to investigate the interaction between H₂O and ILs and the hydrophilicity of the IL [16–39]. Preferentially, ILs used in AHT might be hydrophilic

and completely water soluble. Therefore, good working pairs are those presenting a highly negative deviation from Raoult's law [47].

Most binary systems {water + ILs} present activity coefficients lower than unity. The deviation from Raoult's law of {H₂O + IL} is proportional to the IL content [17–19, 23–33, 36]. With respect to the anion, Ficke [16] has shown that the γ values decrease according to: [(CF₃SO₂)₂N]⁻ > [BF₄]⁻ > [EtSO₄]⁻ > [lactate]⁻ > [CH₃SO₄]⁻ > [glycolate]⁻ > [(CH₃)₂PO₄]⁻.

It is important to note that dialkylimidazolium [(CF₃SO₂)₂N] with water present a miscibility gap [28]. The ability of IL to increase the water boiling temperature can be estimated using a simple relationship based on solvation model's parameters such the hydrogen-bond basicity [48].

Studies on water sorption by imidazolium-based ILs with anions [Cl]⁻, [BF₄]⁻, [Br]⁻, [Tf₂N]⁻, and [PF₆]⁻ show that ILs with the shorter alkyl chain length lead to the highest water sorption capacity [7, 25–37]. Moreover, it was found that imidazolium cation is more efficient than pyridinium cation [49]. Cao et al. [49] also studied the anion effect on water sorption for nine ILs with [BMIM]⁺ cation and they found that ILs followed this trend [Ac]⁻ > [Cl]⁻ > [Br]⁻ > [TFA]⁻ > [NO₃]⁻ > [TFO]⁻ > [BF₄]⁻ > [Tf₂N]⁻ > [CHO]⁻ > [PF₆]⁻. The nature of the IL anion plays an important role on the boiling temperatures and its impact is as follows: [CF₃SO₃]⁻ < [SCN]⁻ < [CF₃CO₂]⁻ < [TOS]⁻ < [Br]⁻ < [C₁SO₃]⁻ < [C₁CO₂]⁻ [39]. This work shows clearly that the observed trend is related to the anion and to its capacity to interact with water. Other research groups confirmed that anion has an essential rule that aiming to lower the vapor pressure of water H₂O [25, 27, 30, 32, 33]. Seiler et al. [50] have shown that some ILs such as acetate and chloride-based ionic liquids are not suitable for absorptions cycles due to their insufficient stability and/or too high corrosion rates.

All VLE of binary systems {H₂O + IL} found in the literature have been correlated using the NRTL model. The average relative deviations on activity coefficient and pressure obtained using the NRTL model range between 0.01 and 3.5%. Deviations of the 35 investigated systems are within $\pm 13\%$.

4.2.2. Heat capacity

Heat capacity evaluates the heat storage capacity of a fluid [51]. Only one theoretical model based on an artificial neural network is proposed in the literature to predict the heat capacity of binary systems containing ILs [52]. This approach gives good estimate of C_p of mixtures containing ILs with an average absolute relative deviation of about 1.60%.

In general, heat capacity is expressed using a temperature- and composition-dependent polynomial equation [35]:

$$C_p = \sum_{i=0}^3 (A_i + B_i T) x m_2^i \quad (3)$$

where C_p is the mass heat capacity in kJ kg⁻¹ K⁻¹, A_i and B_i are adjustable parameters, T is the absolute temperature in K, and $x m_2$ is the mass fraction of ILs. We have correlated all heat capacity

data of {H₂O + ILs} published in the literature using Eq. (3). The mass excess heat capacity, C_p^E can be calculated from the heat capacities of the mixture and that of the pure compounds:

$$C_p^E = C_p - \sum x_{mi} \cdot C_{p,i} \quad (4)$$

where C_p is the mass heat capacity in kJ kg⁻¹ K⁻¹ of the mixture, $C_{p,i}$ is the mass heat capacity of the pure compound and x_{mi} is its mass fraction.

The low mass heat capacity values of the binary systems {H₂O + ILs} lead to reduce power consumption, beneficial to heat transfer and improves the COP in the absorption cycle [7, 26, 28, 29, 31, 33–45, 47–55].

4.2.3. Excess enthalpy (H^E)

H^E is a key parameter for the simulation of the performance of AHT and it also gives an insight into the interactions between the molecules. Few H^E data for binary systems {H₂O + ILs} can be found in the literature. This leads to make the hypothesis that H^E is equaled to zero in simulation.

Garcia-Miaja et al. [56] measured H^E for different binary mixtures containing triflate or alkylsulfate or [BMPyr]-based ILs. All collected data show that the sign of H^E is mainly related to the nature of the anion [56].

Kurnia and Coutinho [10] reviewed the behavior of H^E for binary systems composed of {H₂O + ILs}. They found that the conductor-like screening model for real system (COSMO-RS) is a successful estimating method to predict the behavior of the interaction between water and ILs. It is obvious from the literature [10–16] that the positive (endothermic) H^E of the binary system mainly depends on the hydrogen bonding, water molecules, and hydrophobicity. Weak interaction between the water-IL binary system causes water to use the energy of the system to rearrange their molecules and the process turn to be endothermic and the reverse occurs in the case of the exothermic process. Ficke [16] stated that with the increase of the alkyl chain length the hydrophobicity increases hence decreasing the negativity of H^E .

H^E data found in the literature are regressed using Redlich-Kister polynomials [25]:

$$H^E = x_{m1}x_{m2} \sum_{i=1}^n A_i x_{m2}^i \quad (5)$$

where H^E is the excess enthalpy in kJ kg⁻¹, A_i is the adjustable parameter, and x_{m_i} is the mass fraction of species i ($i = 1, 2$).

We used Eq. (5) to regress all H^E data found in the literature.

4.2.4. Density

Density is an important property because its knowledge is necessary to evaluate the pumping cost in a process. The density of pure ILs roughly ranges between 1.1 and 1.6 g cm⁻³. The density of an IL depends on the type of anion and cation, but the key parameter is the anion. Hydrophobicity of ILs has also an important effect on the density of binary mixtures {H₂O + IL}. The hydrophobicity of a dialkylimidazolium-based IL increases with an increase of the

alkyl chain length [26, 31, 33–35, 37–45, 47–57]. Consequently, the density of such ILs decreases with the increase of the alkyl chain length.

An increase in water content or temperature causes a decrease in the density in most of the binary systems studied. Hence, physical properties of ILs can be adjusted to fulfill the needs of applications for hydrophilic ILs by adding water or changing the temperature [57].

The density data for the 19 investigated binary systems were fitted [35] using Eq. (6).

$$\rho = \sum_{i=0}^3 (a_i + b_i T) x_2^i \quad (6)$$

where ρ is the density of the solution in g cm^{-3} , T is the absolute temperature in K, x_2^i is the molar fraction of the ILs, and a_i and b_i are adjustable parameters.

Excess molar volume (V^E) is an important parameter for the process design while it gives information on the nonideality of the working fluid. In the case of binary mixtures $\{\text{H}_2\text{O} + \text{IL}\}$, the sign of excess molar volumes is related to the structure of the IL (anion, cation, and alkyl chain length) [26, 31, 33–35, 37–45, 47–56, 58, 59]. Generally, the anion imposes the sign of V^E . Hydrophobic anions ($[\text{BF}_4]$, $[\text{SCN}]$, and $[\text{CF}_3\text{SO}_4]$) leading to repulsive interactions with water have positive excess molar volumes. Strong IL- H_2O interactions observed with anions containing oxygen atoms lead to negative V^E [26, 46, 60]. Gonzalez et al. [61] stated that V^E behavior for their investigated binary systems according to the cation type has the following trend: imidazolium $V^E >$ pyridinium $V^E \approx$ pyrrolidinium V^E . A full description of excess molar volumes of binary mixtures containing $\{\text{H}_2\text{O} + \text{IL}\}$ can be found in the recent review of Bahadur et al. [62].

4.2.5. Viscosity

It is well known that pure ILs have higher viscosity than other solvents such as water, methanol, and ethanol [26]. This may enlarge the AHT size (exchange area) and increase the power required for the pumping process [63]. Nevertheless, various publications [26, 31, 33–35, 37–67] stated that viscosity of ILs sharply decreases when temperature increases and/or ILs are mixed with water. Taking into account that AHT has a high generator and absorber temperature (between 80 and 150°C), the viscosity of the $\{\text{H}_2\text{O} + \text{ILs}\}$ should not be a limitation for their use as absorbents in AHT [36]. The viscosity of $\{\text{H}_2\text{O} + \text{ILs}\}$ binary systems decreases because of the weak interaction between the IL anion and cation so the mobility of ions increases and the viscosity decreases [67]. It was noticed that fluorinated anions have lower viscosity than other anions such as alkylsulfates [64].

4.2.6. Thermal decomposition

Thermal decomposition could possibly be one of the most important properties to measure during the initial screening of an IL, especially for the operating temperatures of the processes related to this work. Most of the decomposition temperatures of ILs are measured using weight loss thermogravimetric (TGA) experiments and selected data are given in **Table 2**.

Nevertheless, it must be kept in mind that data taken from TGA will not serve to determine the maximum temperature limit for working without decomposition of the IL because this technique overestimates the decomposition temperature [68–70]. The experimental procedure proposed by Seiler et al. [50] based on a long-time thermal decomposition analysis seems to be more appropriate.

The decomposition temperatures of ionic liquids containing the [TF₂N] anion are higher than others [16–45, 47–50, 53, 54]. Ficke [16] and Seiler et al. [50] have shown that the decomposition temperature of [EMIM]⁺-based ILs ranges between 178°C and 388°C (**Table 2**). The decomposition temperature mainly depends on two structural parameters: the nature of the anion and the alkyl chain length [46, 50–52, 55–71]. Ficke et al. [55] found that [EMIM][EtSO₄] reacts with water to give [EMIM][HSO₄] and ethanol. Another negative effect of using ILs is their hydrolysis [72]. Kinetic of hydrolysis is governed by the pH and the temperature of system [73, 74]. [TOS]⁻, [DMP]⁻, [BF₄]⁻, and [PF₆]⁻-based ILs are known to be unstable in the presence of water under specific conditions [75].

IL	Decomposition temperature (°C)	References
[EMIM][TFA]	178	[16]
[EMIM][EtSO ₄]	355	[16]
[EMIM][HSO ₄]	359	[16]
[EMIM][MeSO ₄]	362	[16]
[EMIM][TFO]	388	[16]
[EMIM][MeSO ₃]	335	[16]
[EMIM][SCN]	281	[16]
[EMIM][DEP]	273	[16]
[EMIM][PF ₆]	375–348.29	[15]
[EMIM][BF ₄]	412–393	[4]
[OHEMIM][TFA]	187	[16]
[P ₂₄₄₄][DEP]	314	[16]

Table 2. Decomposition temperature for miscible ILs.

5. Coefficient of performance (COP)

5.1. Simulation of the AHT cycle performance

This work focuses on single effect absorption heat transformers (AHT). The simulations used to evaluate the performance of the AHT were performed with the following assumptions [7–9, 16–76]:

- i. Steady-state operation;
- ii. Negligible heat loss;

- iii. Pressure drops not taken into account;
- iv. Outlets of the generator and the absorber are liquids at their bubble point;
- v. Liquid and vapor at the outlet of the condenser and the evaporator are saturated;
- vi. Enthalpy of the fluid is conserved through the throttling valve;
- vii. Minimum temperature difference between strong and weak solutions equal 5°C in the heat exchanger;
- viii. Pumping mechanical power is neglected compared to heat flow exchanged.

The steady-state simulation of such a process is achieved by solving mass and energy balance equations.

The generator can be described by the overall and ionic liquid mass balance and heat balance equations:

$$\dot{m}_7 - \dot{m}_1 - \dot{m}_8 = 0 \quad (7)$$

$$\dot{m}_7 x_7^m = \dot{m}_8 x_8^m \quad (8)$$

$$Q_G + \dot{m}_7 h_7 - \dot{m}_8 h_8 - \dot{m}_1 h_1 = 0 \quad (9)$$

The strong solution at the outlet of the generator is a saturated liquid,

$$p_8 = p(T_8, x_8^m) \quad (10)$$

where $T_8 = T_1 = T_G$ and $p_8 = P_1 = p_G = p_c$

The condenser can be described by

$$\dot{m}_1 = \dot{m}_2 = \dot{m}_3 = 1 \text{ kg} \cdot \text{s}^{-1} \quad (11)$$

$$\dot{m}_1 h_1 - \dot{m}_2 h_2 - Q_c = 0 \quad (12)$$

For state point 2 (saturated liquid water at the condenser outlet), we have:

$$p_2 = p_c = p^s(T_c) \quad (13)$$

In the case of the evaporator:

$$\dot{m}_3 = \dot{m}_4 \quad (14)$$

$$\dot{m}_4 h_4 - \dot{m}_3 h_3 - Q_E = 0 \quad (15)$$

Vapor is saturated at the outlet of the evaporator, so for point 4, we have:

$$p_4 = p_E = p^s(T_E) \quad (16)$$

Balance equations for the absorber give:

$$\dot{m}_4 + \dot{m}_{10} - \dot{m}_5 = 0 \quad (17)$$

$$\dot{m}_5 x_5^m = \dot{m}_{10} x_{10}^m \quad (18)$$

$$\dot{m}_4 h_4 + \dot{m}_{10} h_{10} - \dot{m}_5 h_5 - Q_A = 0 \quad (19)$$

State point 5 is described by Eq. (20)

$$p_5 = p(T_5, x_5^m) \quad (20)$$

where $T_5 = T_A$ and $p_5 = p_A = p_E$

Then, the heat exchanger is characterized by the minimal temperature approach between hot and cold streams:

$$T_5(\text{hotinlet}) - T_{10}(\text{hotoutlet}) = 5K \quad (21)$$

Heat balance on the solution heat exchanger can be written:

$$\dot{m}_5 h_5 + \dot{m}_9 h_9 - \dot{m}_6 h_6 - \dot{m}_{10} h_{10} = 0 \quad (22)$$

where \dot{m}_i , h_i , x_i^m ($i=1, 2, 3, \dots, 10$) are, respectively, the mass flow rate (kg s^{-1}), specific enthalpy (kJ kg^{-1}), and the mass fraction of an absorbent (IL) of each stream. $p^s(T)$ is the saturated vapor pressure of H_2O at temperature T and $p(T, x)$ is the saturation pressure of the $\{\text{H}_2\text{O} + \text{ILs}\}$ solution at temperature T with an ionic mole fraction x . They are obtained by the following relations [25]:

$$p(T, x) = x_2 \gamma_2 p_1^s(T) \quad (23)$$

$$p^s(T) = \exp\left(\frac{73.649 - 7258.2/T - 7.3037 \cdot \ln(T) + 4.1653 \cdot 10^{-6} \cdot (T^2)}{1000}\right) \quad (24)$$

with p is the total pressure, x_2 , γ_2 and p_1^s is the IL mole fraction in the liquid phase, ionic liquid activity coefficient for the liquid phase, and saturated vapor pressure of the refrigerant, respectively.

Usually, when simulating an absorption heat transformer, the temperature level of the waste heat source is known (the medium-temperature level) as well as the temperature of the environment that is used as cold heat sink (the low-temperature level). The objective temperature level of the upgraded heat is also an input in this problem (the high-temperature level). Hence, temperatures T_G , T_E , T_C and T_A of the generator, the evaporator, the condenser, and the absorber, respectively, are known and taken as independent variables in the present research.

The enthalpy of a liquid mixture is expressed as follows:

$$h = x_1^m h_1 + x_2^m h_2 + \Delta_{\text{mix}} h \quad (25)$$

with

$$h_1 = h_{ref} + \frac{1}{\rho_{1,liq,T_{ref}}} * (p - p_{ref}) + \int_{T_{ref}}^T C_{p,1} dT \quad (26)$$

$$h_2 = h_{ref} + \frac{1}{\rho_{2,liq,T_{ref}}} * (p - p_{ref}) + \int_{T_{ref}}^T C_{p,2} dT \quad (27)$$

where h_1 and h_2 are the enthalpy of pure liquid H₂O and IL, x_1^m and x_2^m are the mass fraction of H₂O and IL, respectively, $\Delta_{mix}h$ is mixing enthalpy of the system, which can be sometimes neglected. $C_{p,1}$ and $C_{p,2}$ are the heat capacity of H₂O and IL, respectively. The reference state for enthalpy calculations is defined T_{ref} , h_{ref} , and p_{ref} , respectively, its temperature, enthalpy, and pressure. These parameters are chosen arbitrarily as being:

$$h_{ref} = 0$$

$$T_{ref} = 273.15 \text{ K}$$

$$p_{ref} = 101.325 \text{ kPa}$$

$\rho_{1,liq,T_{ref}}$ and $\rho_{2,liq,T_{ref}}$ are the densities of pure liquid water and pure IL at reference temperature and pressure, respectively.

The performance of the AHT is evaluated through different criteria. The main one is the coefficient of performance. Its expression is given in Eq. (2) as the ratio of useful heat flow produced at the absorber to the waste heat flows provided to the generator and to the evaporator (pumping work is neglected).

Among other meaningful criteria, Δx^m is the difference between ionic liquid mass fractions in the strong and weak solutions.

$$\Delta x^m = x_8^m - x_5^m = x_s^m - x_w^m \quad (28)$$

If COP is used to represent the quantitative aspect of heat upgrading, the gross temperature lift Δt , which is the temperature level difference between the upgraded heat and the waste heat, provides a qualitative performance criterion. It is defined as follows:

$$\Delta t = T_A - T_E \quad (29)$$

Another important criterion is the solution circulation ratio f , which is defined as the ratio of the strong solution mass flow rate to the vapor mass flow rate:

$$f = \frac{\dot{m}_7}{\dot{m}_1 = \frac{x_s^m}{(x_s^m - x_w^m)}} \quad (30)$$

This criterion allows knowing if the use of one working mixture leads or not to high solution flow rate which is linked to the capital cost (cost of the required working mixture and pumps) and operating costs (pumping energy cost). Observed values of f for the {H₂O + LiBr} and {H₂O + NH₃} systems are generally low (typically around 10 [2–16]).

Another criterion to assess system compactness is the available heat output per unit mass of refrigerant, q (kJ kg⁻¹):

$$q = \frac{Q_A}{\dot{m}_1} \quad (31)$$

5.2. COP for the absorption refrigeration cycle

The performance of {H₂O + ILs} as working fluids was mainly evaluated for the absorption refrigeration cycle. Zhang and Hu [27] estimated the COP of an absorption chiller using {water + [EMIM][DMP]} and {H₂O + LiBr} mixtures under the same operating conditions. {H₂O + [EMIM][DMP]} leads to a value of COP higher than 0.7 that is lower than that obtained with {H₂O + LiBr}.

Under precise conditions, Kim et al. [63] found that the COP value for a {H₂O + [EMIM][BF₄]}-based refrigeration cycle can reach 0.91, this good performance is linked to the suitable compatibility of water with [EMIM][BF₄] and to the excellent intrinsic properties of water as a refrigerant.

The {H₂O + [DMIM][DMP]} mixture has been studied by Dong et al. [7] and was compared to {H₂O + LiBr} in a single-effect absorption refrigeration configuration. The ionic liquid-based working mixture leads to close performance to those obtained with the conventional mixture. Nevertheless, {H₂O + [DMIM][DMP]} presents the advantage to allow a wider temperature working range as well as avoiding corrosion and crystallization problems.

5.3. Absorption heat transformer

A VBA dedicated calculation code has been developed to evaluate the performance of {H₂O + IL} mixture as a working fluid in an absorption heat transformer (**Figures 4 and 5**).

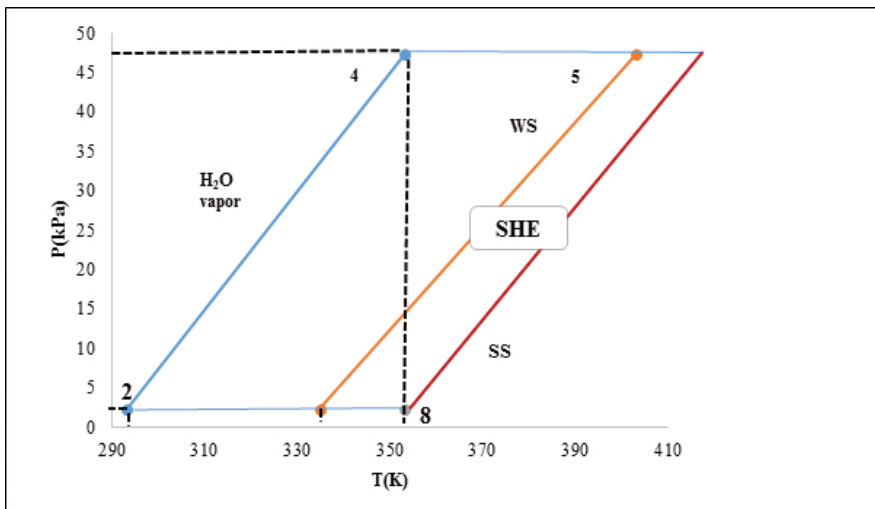


Figure 4. Thermodynamic cycle in absorption heat transformer (AHT).

Simulation results for both {H₂O + IL} mixtures and conventional fluids as working fluids in AHT are presented in **Table 3**.

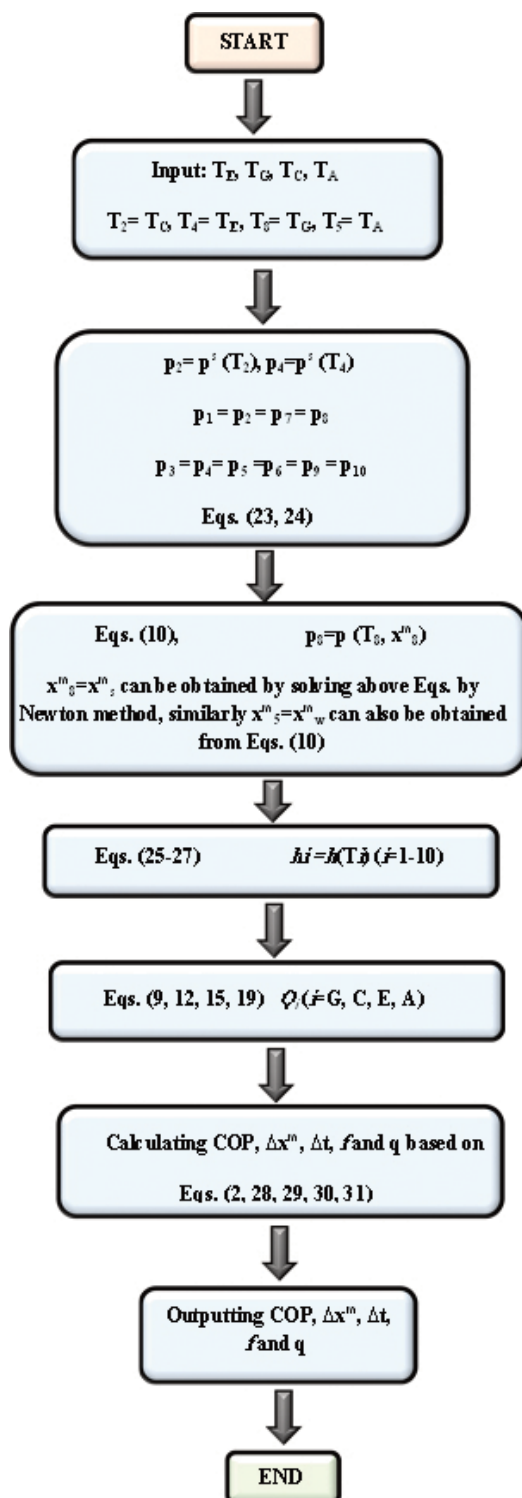


Figure 5. Flowchart for COP simulation.

Refrigerant	Absorbent	COP		x_s^m	Δx^m	f
		T (°C)	T _C	T _E	T _G	T _A
		35	90		90	130
Water	LiBr ^{1*}	0.50	0.64		0.07	11.00
TFE	E181 ^{2*}	0.42	0.90		0.10	9.00
Water	[EMIM][DMP] ^{3*}	0.48	Not mentioned		Not mentioned	Not mentioned
Water	[DMIM][DMP]	0.45	0.92		0.09	10.01
Water	[EMIM][DMP]	0.44	0.92		0.08	11.26
Water	[EMIM][DEP]	0.44	0.92		0.07	13.54
Water	[EMIM][AC]	0.44	0.87		0.08	10.54
Water	[HOEtMIM][Cl]	0.45	0.94		0.10	9.88
Water	[EMIM][EtSO ₄]	0.41	0.97		0.03	38.21
Water	[EMIM][Triflate]	0.42	0.99		0.02	41.34
Water	[EMIM][TFA]	0.44	0.97		0.05	19.70
Water	[DEMA][Oms]	0.44	0.95		0.08	12.63
Water	[BMIM][Triflate]	0.36	0.99		0.01	71.56
Water	[BMIM][BF ₄]	0.43	0.97		0.04	25.01
		25	80		80	130
Water	LiBr ^{4**}	0.48	Not mentioned		Not mentioned	9.51
Water	[DMIM][DMP]	0.43	0.93		0.06	15.92
Water	[EMIM][DMP]	0.41	0.93		0.05	19.52
Water	[EMIM][DEP]	0.42	0.92		0.04	21.06
Water	[EMIM][AC]	0.43	0.87		0.05	17.98
Water	[HOEtMIM][Cl]	0.43	0.95		0.06	15.58
Water	[EMIM][EtSO ₄]	0.14	0.97		0.01	172.47
Water	[EMIM][Triflate]	0.38	0.99		0.01	69.49
Water	[EMIM][TFA]	0.42	0.97		0.03	31.99
Water	[DEMA][Oms]	0.43	0.96		0.05	21.07
Water	[BMIM][Triflate]	0.27	0.99		0.01	140.50
Water	[BMIM][BF ₄]	0.40	0.97		0.02	43.60
		20	80		80	130
Water	[DMIM][DMP]	0.44	0.94		0.07	12.90
Water	[EMIM][DMP]	0.42	0.94		0.06	15.09
Water	[EMIM][AC]	0.43	0.89		0.06	14.16
Water	[EMIM][DEP]	0.43	0.88		0.93	17.71
Water	[HOEtMIM][Cl]	0.43	0.96		0.07	13.14
Water	[EMIM][EtSO ₄]	0.35	0.98		0.01	74.48

Refrigerant	Absorbent	COP	x_s^m	Δx^m	f
	T (°C)	T_C	T_E	T_G	T_A
Water	[EMIM][Triflate]	0.39	0.99	0.02	60.08
Water	[EMIM][TFA]	0.42	0.98	0.04	26.58
Water	[DEMA][Oms]	0.43	0.97	0.06	17.30
Water	[BMIM][Triflate]	0.32	0.99	0.01	108.71
Water	[BMIM][BF ₄]	0.41	0.98	0.03	34.96

* Data found in the literature [8].** Data found in the literature [60].

Table 3. Calculated COP of {H₂O + ILs} binary systems for single-effect absorption heat transformer cycle.

In this work, evaporating temperature T_E , condensing temperature T_C , absorbing temperature T_A , and generator temperature T_G are set to 80°C, 20°C, 130°C, and 80°C, respectively (**Figures 6** and **7** and **Table 3**).

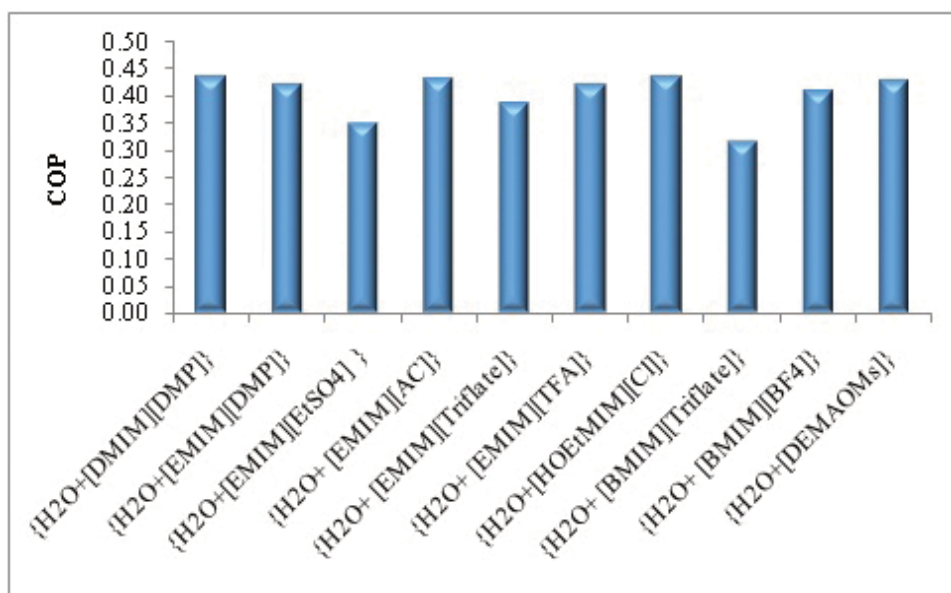


Figure 6. Calculated COP of binary systems {water + ILs} presented.

The NRTL model, C_p , H^E , and density correlation parameters that were regressed by the authors and used for the simulations. The resulting calculated COP values for 12 binary systems are shown in **Table 3**.

The influence of the working temperature levels on the COP is shown in **Figures 8–10**.

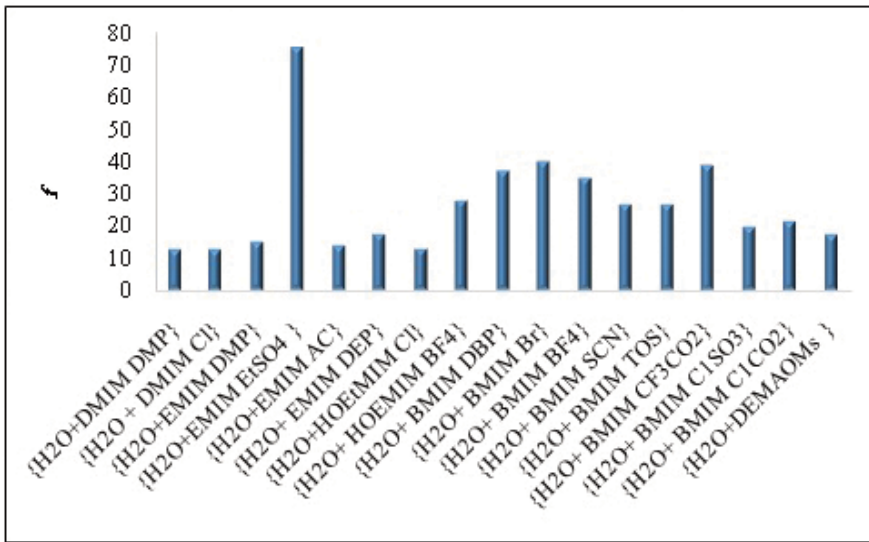


Figure 7. Circulation ratio f of binary systems {water + ILs} presented.

Figure 8 shows that an increase in the condenser temperature leads to a decrease in the COP. This behavior is due to the fact that the low pressure level evolves the same way as the condenser temperature. Hence, when the condenser temperature increases, the strong solution ionic liquid fraction will decrease and f increases. For the investigated working pairs, the COP remains unchanged for T_C lower than 30°C. The COP sharply decreases especially for {H₂O + LiBr}, {H₂O + [BMIM][MeSO₄]}, {H₂O + [BMIM][Triflate]}, and {H₂O + [EMIM][EtSO₄]}. when T_C is higher than 30°C.

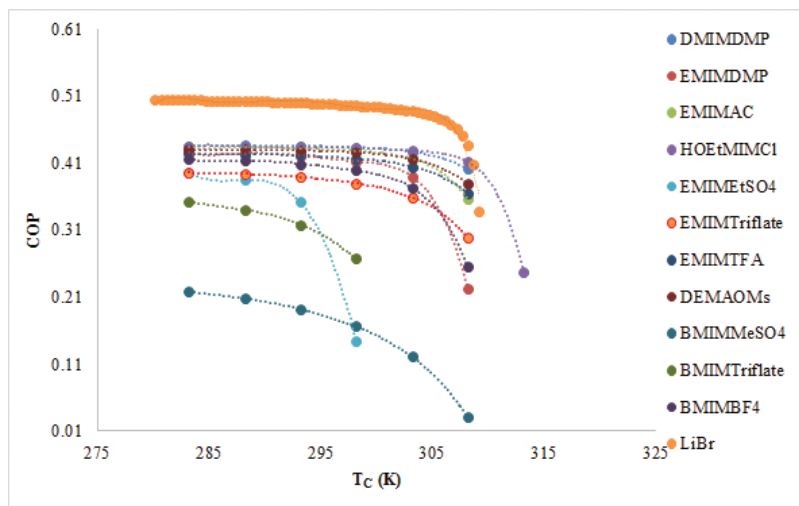


Figure 8. COP of binary systems {water + ILs} versus (T_C) T_L for single-effect absorption heat transformer cycle.

Figure 9 shows that an increase of T_E or T_G leads to an increase of the COP. In fact, the high pressure level of AHT depends on the evaporator temperature. Increasing T_E (or T_G) leads to a decrease of the weak solution concentration by decreasing the flow ratio. The lower flow ratio results in a higher heat flow released during absorption and consequently in a higher COP. **Figure 9** shows that the evolution of the COP values versus the generator temperature is quite similar to $\{H_2O + IL\}$ for all binary systems studied in this work. The evolution of COP values with T_G firstly increases, then stabilizes and finally decreases. When T_G approaches its minimal value, f tends to reach infinity and so it requires the generation of heat. Consequently, the COP of the cycle tends toward zero. With the increase of generator temperature, f decreases, COP sharply increases and then smoothens.

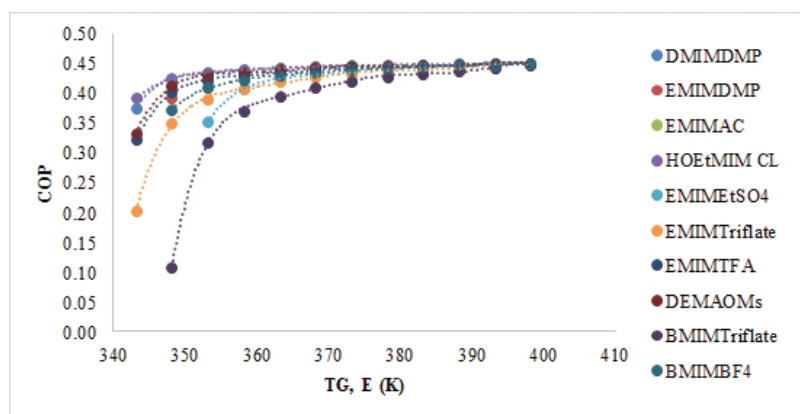


Figure 9. COP of binary systems $\{water + ILs\}$ versus $(T_G, E) T_M$ for single-effect absorption heat transformer cycle.

It can be seen from **Figure 10** that the COP of an AHT decreases at different rates depending on the working mixture when absorber temperature (T_A) increases. This behavior can be explained in **Figure 11** that illustrates the ionic liquid mass fraction variation of the weak solution x_w^m with T_A .

A decrease of x_w^m means that the less refrigerant has been absorbed and consequently less heat is released at the absorber, which leads to lower the COP. The same behavior was observed by Zhang and Hu [8]. **Figure 10** shows that the COP of all the binary systems $\{H_2O + IL\}$ as well as $\{H_2O + LiBr\}$ is basically unchanged when the gross temperature lift is lower than $45^\circ C$. Upon increasing the gross temperature lift more than $45^\circ C$, the COP of $\{H_2O + LiBr\}$ and $\{H_2O + ILs\}$ sharply decreases.

The available heat output per unit mass of refrigerant (q) for the studied binary systems was calculated and compared with Zhang and Hu [8] data under the same conditions. It was found that q for $\{H_2O + [DMIM][DMP]\}$ is 2029 kJ kg^{-1} and for $\{H_2O + [HOEtMIM][Cl]\}$ is less than 2026 kJ kg^{-1} . For the other binary systems, q ranges between 2012 and 1527 kJ kg^{-1} (**Table 4**).

These values must be compared with those obtained for $\{H_2O + LiBr\}$: 2466 kJ kg^{-1} and 311 kJ kg^{-1} for $\{TFE + E181\}$. Hence, to produce the same amount of useful heat, the refrigerant flow rate is lower when using water-based mixtures (water latent heat of vaporization is much higher than that of E181).

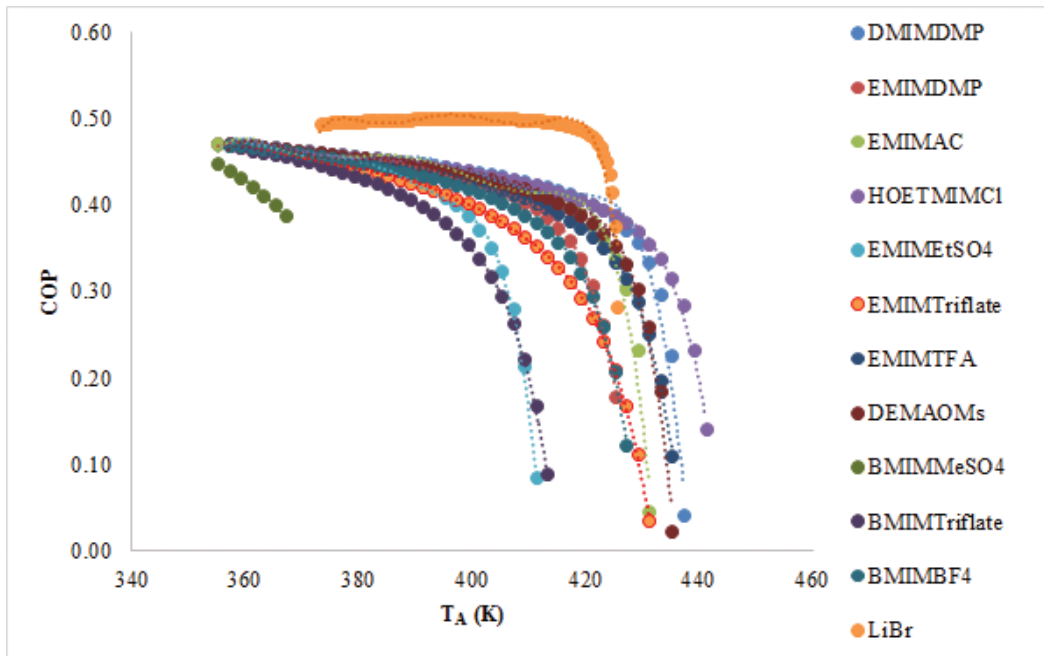


Figure 10. COP of binary systems (water + ILs) versus $(T_A) T_H$ for single-effect absorption heat transformer cycle.

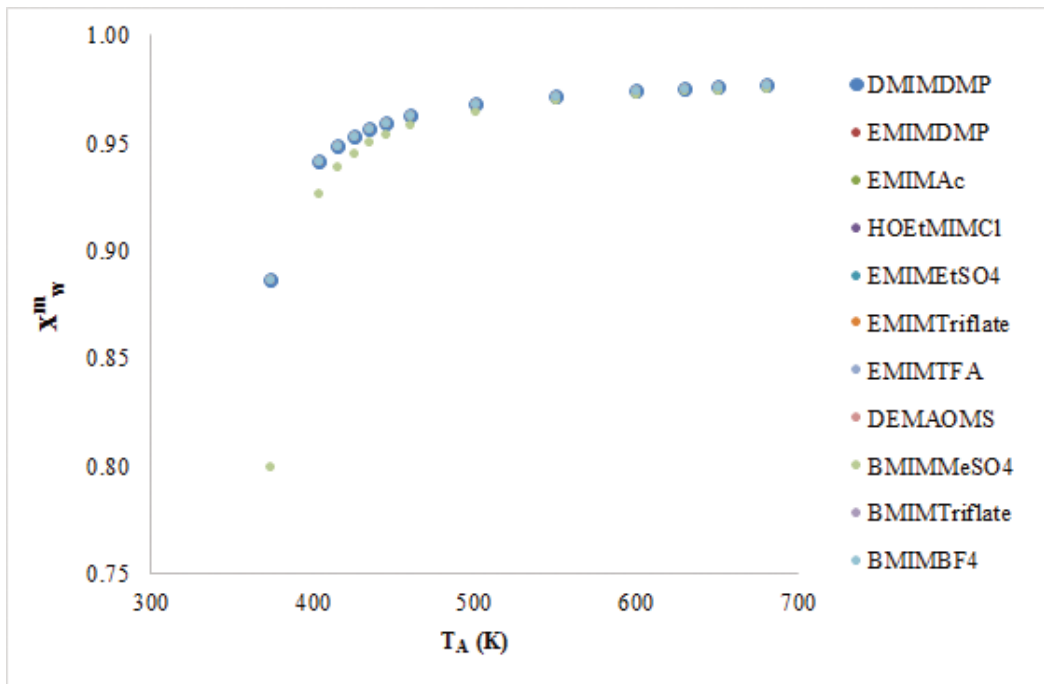


Figure 11. Effect of $(T_A) T_H$ on x_w^m .

T_C	T_G	T_E	T_A
20	80	80	130

Binary system	q (kJ kg ⁻¹)	Binary system	q (kJ kg ⁻¹)
{H ₂ O + [DMIM][DMP]}	1982.31	{H ₂ O + [EMIM][TFA]}	1871.63
{H ₂ O + [EMIM][DMP]}	1867.90	{H ₂ O + [HOEtMIM][Cl]}	1974.05
{H ₂ O + [EMIM][EtSO ₄]}	1391.97	{H ₂ O + [BMIM][Triflate]}	1198.78
{H ₂ O + [EMIM][Ac]}	1953.77	{H ₂ O + [BMIM][BF ₄]}	1777.21
{H ₂ O + [EMIM][Triflate]}	1636.28	{H ₂ O + [DEMA][OMS]}	1932.00

Table 4. The available heat output per unit mass of refrigerant (q) for AHT cycle.

The concentration (mass fraction) of ILs in the strong solution is exceeding 0.9 for most of the binary systems studied, and is only 0.64 for {H₂O + LiBr} (**Table 3**). This behavior is not in favor of ionic liquid-based working mixtures and will particularly lead to increased pumping costs.

Simulation results show that for {H₂O + [DMIM][DMP]}, {H₂O + [HOEtMIM][Cl]}, {H₂O + [EMIM][Ac]}, {H₂O + [EMIM][TFA]}, and {H₂O + [DEMA][OMS]} mixtures, COP values are close to, but lower than, that obtained working with {H₂O + LiBr}. Nevertheless, these slightly low performances of ionic liquid-based mixtures can be counterbalanced by the ability to reach higher gross temperature lifts and to potentially avoid corrosion issues.

Simulations for evaporator temperature T_E , condenser temperature T_C , absorber temperature T_A , and generator temperature T_G are set to 80, 20, 130, and 80 °C, respectively, which shows that the COP values for the studied binary systems have the following behavior:

[DMIM][DMP] > [HOEtMIM][Cl] > [EMIM][Ac] > [DEMA][OMS] > [EMIM][TFA] > [EMIM][DMP] > [BMIM][BF₄] > [EMIM][Triflate] > [EMIM][EtSO₄] > [BMIM][Triflate]. We can conclude that ionic liquids with a short-alkyl chain lead to higher COP values and a lower circulation ratio f .

Simulations indicate that binary systems {H₂O + acetate or chloride-based ILs} have high COP. Nonetheless, these families of ILs are not sufficiently stable and they present high corrosion rates [50]. It was noticed that binary system composed of {H₂O + [BMIM][MeSO₄]}. Its largest observed Δt is about 40 K and the lowest is 30 K. Simulation of the binary system consisting of {H₂O + [BMIM][MeSO₄]}. is not promising due to low solubility of IL in water or to stability of the IL [16].

Thirty-three binary systems out of 39 are found to have only VLE data available, the literature lacking other thermodynamic properties. Using NRTL, the VLE data of these 33 binary systems were correlated, and f was determined. Simulations for these binary systems performed with evaporator temperature T_E , condenser temperature T_C , absorber temperature T_A , and generator temperature T_G are set to 80°C, 20°C, 130°C, and 80°C, respectively. Simulation results showed that there are promising binary systems exhibiting low f values such as [BMIM][C₁SO₃], [BMIM][I], [BMPyr][DCA], which are 19.892, 16.958, and 17.247, respectively.

In the light of these results, it would be highly recommended to further investigate these binary systems.

6. Conclusion

A large number of binary mixtures {H₂O + ILs} have been identified to be used in absorption heat transformers. The resulting performances of these new working fluids were evaluated for single-effect absorption heat transformer cycles.

Ionic liquid-based working mixtures lead to slightly low COP than the classical {H₂O + LiBr} mixture and larger circulation ratios. Nevertheless, the possibility to find ILs that are significantly less corrosive than LiBr is a condition for reliable operation and a moderate investment cost. Moreover, many ILs are totally miscible with water which avoid crystallization problems.

It must be kept in mind that thermal and chemical stability of {H₂O + IL} mixtures have to be assessed in order to prove their practical use for industrial applications.

Author details

El-Shaimaa Abumandour, Fabrice Mutelet* and Dominique Alonso

*Address all correspondence to: fabrice.mutelet@univ-lorraine.fr

Laboratoire Réactions et Génie des Procédés (CNRS UMR 7274), Ecole Nationale Supérieure des Industries Chimiques, Université de Lorraine, Nancy, France

References

- [1] Horuz I, Kurt B. Absorption heat transformers and an industrial application. *Renewable Energy*. 2010;**35**:2175–81. DOI: 10.1016/j.renene.2010.02.025
- [2] Khamooshi M, Parham K, Atikol U. Overview of ionic liquids used as working fluids in absorption cycles. *Advances in Mechanical Engineering*. 2013;**2013**:1–7. DOI: [org/10.1155/2013/620592](http://dx.doi.org/10.1155/2013/620592)
- [3] Sun J, Fu L, Zhang S. A review of working fluids of absorption cycles. *Renewable and Sustainable Energy Reviews*. 2012;**16**:1899–1906. DOI: 10.1016/j.rser.2012.01.011
- [4] Schaefer LA. Single pressure absorption heat pump analysis [thesis]. Georgia: Georgia Institute of Technology; 2000.
- [5] Wu W, Wang B, Shi W, Li X. An overview of ammonia-based absorption chillers and heat pumps. *Renewable and Sustainable Energy Reviews*. 2014;**31**:681–707. DOI: [org/10.1016/j.rser.2013.12.021](http://dx.doi.org/10.1016/j.rser.2013.12.021)

- [6] Srikihrin P, Aphornratana S, Chungpaibulpatana S. A review of absorption refrigeration technologies. *Renewable and Sustainable Energy Reviews*. 2001;**5**:343–372. DOI: 10.1016/S1364-0321(01)00003-X
- [7] Dong L, Zheng D, Nie N, Li Y. Performance prediction of absorption refrigeration cycle based on the measurements of vapor pressure and heat capacity of {H₂O + [DMIM][DMP]} system. *Applied Energy*. 2012;**98**:326–332. DOI: org/10.1016/j.apenergy.2012.03.044
- [8] Zhang X, Hu D. Performance analysis of the single-stage absorption heat transformer using a new working pair composed of ionic liquid and water. *Applied Thermal Engineering*. 2012;**37**:129–135. DOI: 10.1016/j.applthermaleng.2011.11.006
- [9] De Lucas A, Donate M, Molero C, Villasenor J, Rodríguez JF. Performance evaluation and simulation of a new absorbent for an absorption refrigeration system. *International Journal of Refrigeration*. 2004;**27**:324–330. DOI: 10.1016/j.ijrefrig.2003.12.008
- [10] Kurnia KA, Coutinho Joao AP. Overview of the excess enthalpies of the binary mixtures composed of molecular solvents and ionic liquids and their modeling using COSMO-RS. *Industrial & Engineering Chemistry Research* 2013;**52**:13862–13874. DOI: 10.1021/ie4017682
- [11] Kim S, Patel N, Kohl PA. Performance simulation of ionic liquid and hydrofluorocarbon working fluids for an absorption refrigeration system. *Industrial & Engineering Chemistry Research* 2013;**52**:6329–6335. DOI: 10.1021/ie400261g
- [12] Kim S, Kim YJ, Joshi YK, Fedorov AG, Kohl PA. Absorption heat pump/refrigeration system utilizing ionic liquid and hydrofluorocarbon refrigerants. *Journal of Electronic Packaging*. 2012;**134**:031009–9. DOI: 10.1115/1.4007111
- [13] Zheng D, Dong L, Huang W, Wu X, Nie N. A review of imidazolium ionic liquids research and development towards working pair of absorption cycle. *Renewable and Sustainable Energy Reviews*. 2014;**37**:47–68. DOI: 10.1016/j.rser.2014.04.046
- [14] Iolitec. Product, N. *Ionic Liquids Today*. 2011;**1**:1–11.
- [15] Liang S, Chen W, Cheng K, Guo Y, Gui X. The Latent Application of Ionic Liquids in Absorption Refrigeration. In: Prof. Scott Handy, editors. *Applications of Ionic Liquids in Science and Technology*, Croatia. InTech; 2011. 494 p. DOI: 10.5772/23953
- [16] Ficke LE. Thermodynamic properties of imidazolium and phosphonium based ionic liquid mixtures with water or carbon dioxide [thesis]. Notre Dame: Graduate School of the University of Notre Dame; 2010.
- [17] Nakanishi T, Furukawa T, Sato N. Industrial high-temperature heat pump. *Hitachi Zosen Technical Review* . 1981;**42**:7–12.
- [18] Kim S, Kohl PA. Analysis of [hmim][PF₆] and [hmim][Tf₂N] ionic liquids as absorbents for an absorption refrigeration system. *International Journal of Refrigeration*. 2014;**48**:105–113. DOI: 10.1016/j.ijrefrig.2014.09.003

- [19] Merkel N, Weber C, Faust M, Schaber K. Influence of anion and cation on the vapor pressure of binary mixtures of water plus ionic liquid and on the thermal stability of the ionic liquid. *Fluid Phase Equilibria*. 2015;**394**:29–37. DOI: [org/10.1016/j.fluid.2015.03.00](https://doi.org/10.1016/j.fluid.2015.03.00)
- [20] Wu W, Wang B, Shi W, Li X. Absorption heating technologies: A review and perspective. *Applied Energy*. 2014;**130**:51–71. DOI: [org/10.1016/j.apenergy.2014.05.027](https://doi.org/10.1016/j.apenergy.2014.05.027)
- [21] Grossman G. Absorption heat transformer for process heat generation from solar ponds. *ASHRAE Transactions*. 1991;**97**:420–427.
- [22] Ikeuchi M, Yumikura T, Ozaki E, Yamanaka G. Design and performance of a high-temperature-boost absorption heat pump. *ASHRAE Transactions*. 1985;**91**:2081–94.
- [23] Zawadzki M, Krolikowska M, Lipinski P. Physicochemical and thermodynamic characterization of N-alkyl-N-methylpyrrolidinium bromides and its aqueous solutions. *Thermochimica Acta*. 2014;**589**:148–157. DOI: [10.1016/j.tca.2014.05.028](https://doi.org/10.1016/j.tca.2014.05.028)
- [24] Merkel NC, Romich C, Bernewitz R, Kunemund H, Gleiß M, Sauer S, Schubert TJS, Guthausen G, Schaber K. Thermophysical properties of the binary mixture of water + diethylmethylammonium trifluoromethanesulfonate and the ternary mixture of water + diethylmethylammonium trifluoromethanesulfonate + diethylmethylammonium methanesulfonate. *Journal of Chemical & Engineering Data*. 2014;**59**:560–570. DOI: [org/10.1021/je400097](https://doi.org/10.1021/je400097)
- [25] Ren J, Zhao Z, Zhang X. Vapor pressures, excess enthalpies, and specific heat capacities of the binary working pairs containing the ionic liquid 1-ethyl-3-methylimidazolium dimethylphosphate. *Journal of Chemical Thermodynamics*. 2011;**43**:576–583. DOI: [10.1016/j.jct.2010.11.014](https://doi.org/10.1016/j.jct.2010.11.014)
- [26] Gong Y, Shen C, Lu Y, Meng H, Li CX. Viscosity and density measurements for six binary mixtures of water (methanol or ethanol) with an ionic liquid ([BMIM][DMP] or [EMIM][DMP]) at atmospheric pressure in the temperature range of (293.15 to 333.15). *Journal of Chemical & Engineering Data*. 2012;**57**: 33–39. DOI: [org/10.1021/je200600](https://doi.org/10.1021/je200600)
- [27] Zhang X, Hu D. Performance simulation of the absorption chiller using water and ionic liquid 1-ethyl-3-methylimidazolium dimethylphosphate as the working pair. *Applied Thermal Engineering*. 2011;**31**:3316–21. DOI: [10.1016/j.applthermaleng.2011.06.011](https://doi.org/10.1016/j.applthermaleng.2011.06.011)
- [28] Kato R, Gmehling J. Measurement and correlation of vapor–liquid equilibria of binary systems containing the ionic liquids [EMIM][(CF₃SO₂)₂N], [BMIM][(CF₃SO₂)₂N], [MMIM][(CH₃)₂PO₄] and oxygenated organic compounds respectively water. *Fluid Phase Equilibria*. 2005;**231**:38–43. DOI: [10.1016/j.fluid.2005.01.00](https://doi.org/10.1016/j.fluid.2005.01.00)
- [29] Wang J, Wang D, Li Z, Zhang F. Vapor pressure measurement and correlation or prediction for water, 1-propanol, 2-propanol, and their binary mixtures with [MMIM][DMP] ionic liquid. *Journal of Chemical & Engineering Data*. 2010;**55**:4872–4877. DOI: [10.1021/je100483d](https://doi.org/10.1021/je100483d)

- [30] Wang JF, Li CX, Wang ZH, Li ZJ, Jiang YB. Vapor pressure measurement for water, methanol, ethanol, and their binary mixtures in the presence of an ionic liquid 1-ethyl-3-methylimidazolium dimethylphosphate. *Fluid Phase Equilibria*. 2007;**255**:186–192. DOI: 10.1016/j.fluid.2007.04.010
- [31] Yokozeki A, Shiflett MB. Water solubility in ionic liquids and application to absorption cycles. *Industrial & Engineering Chemistry Research*. 2010;**49**:9496–9503. DOI: 10.1021/ie1011432
- [32] Zuo G, Zhao Z, Yan S, Zhang X. Thermodynamic properties of a new working pair: 1-ethyl-3-methylimidazolium ethylsulfate and water. *Chemical Engineering Journal*. 2010;**156**:613–617. DOI: 10.1016/j.cej.2009.06.020
- [33] Romich C, Merkel NC, Valbonesi A, Schaber K, Sauer S, Schubert TJS. Thermodynamic properties of binary mixtures of water and room temperature ionic liquids: vapor pressure, heat capacities, densities and viscosities of water + 1-ethyl-3-methylimidazolium acetate and water + diethylmethylammonium methane sulfonate. *Journal of Chemical & Engineering Data*. 2012;**57**:2258–2264. DOI: org/10.1021/je300132
- [34] Fendt S, Padmanabhan S, Blanch HW, Prausnitz JM. Viscosities of acetate or chloride-based ionic liquids and some of their mixtures with water or other common solvents. *Journal of Chemical & Engineering Data*. 2011;**56**:31–34. DOI: 10.1021/je1007235
- [35] Nie N, Zheng D, Dong L, Li Y. Thermodynamic properties of the water + 1-(2-hydroxyethyl)-3-methylimidazolium chloride system. *Journal of Chemical & Engineering Data*. 2012;**57**:3598–3603. DOI: org/10.1021/je3007953
- [36] He Z, Zhao Z, Zhang X, Feng H. Thermodynamic properties of new heat pump working pairs: 1, 3-dimethylimidazolium dimethylphosphate and water, ethanol and methanol. *Fluid Phase Equilibria*. 2010;**298**:83–91. DOI: 10.1016/j.fluid.2010.07.00
- [37] Zhao J, Jiang XC, Li CX, Wang ZH. Vapor pressure measurement for binary and ternary systems containing a phosphoric ionic liquid. *Fluid Phase Equilibria*. 2006;**247**:190–198. DOI: 10.1016/j.fluid.2006.07.00
- [38] Alevizou EI, Pappa GD, Voutsas EC. Prediction of phase equilibrium in mixtures containing ionic liquids using UNIFAC. *Fluid Phase Equilibria*. 2009;**284**:99–105. DOI: 10.1016/j.fluid.2009.06.01
- [39] Passos H, Khan I, Mutelet F, Oliveira MB, Carvalho PJ, Santos LMN BF, Held C, Sadowski G, Freire MG, Coutinho JAP. Vapor-liquid equilibria of water + alkylimidazolium-based ionic liquids: measurements and perturbed-chain statistical associating fluid theory modeling. *Industrial & Engineering Chemistry Research*. 2014;**53**:3737–48. DOI: org/10.1021/ie4041093
- [40] Llovel F, Valente E, Vilaseca O, Vega LF. Modeling complex associating mixtures with [Cn-mim][Tf2N] ionic liquids: predictions from the Soft-SAFT equation. *Journal of Physical Chemistry B*. 2011;**115**:4387–4398. DOI: org/10.1021/jp112315b

- [41] Chen Y, Mutelet F, Jaubert JN. Experimental measurement and modeling of phase diagrams of binary systems encountered in the gasoline desulfurization process using ionic liquids. *Journal of Chemical & Engineering Data*. 2014;**59**:603–612. DOI: [org/10.1021/jc400510](https://doi.org/10.1021/jc400510)
- [42] Nann A, Held C, Sadowski G. Liquid-liquid equilibria of 1-butanol/water/IL systems. *Industrial & Engineering Chemistry Research*. 2013;**52**:18472–18481. DOI: [org/10.1021/ie403246](https://doi.org/10.1021/ie403246)
- [43] Shariati A, Peters CJ. High-pressure phase behavior of systems with ionic liquids: measurements and modeling of the binary system fluoroform+1-ethyl-3-methylimidazolium hexafluorophosphate. *Journal of Supercritical Fluids*. 2003;**25**:109–117. DOI: [10.1016/S0896-8446\(02\)00160-2](https://doi.org/10.1016/S0896-8446(02)00160-2)
- [44] Carvalho PJ, Alvarez VH, Machado JJB, Pauly J, Daridon JL, Marrucho IM, Aznar M, Coutinho JAP. High pressure phase behavior of carbon dioxide in 1-alkyl-3-methylimidazolium bis(trifluoromethylsulfonyl) imide ionic liquids. *Journal of Supercritical Fluids*. 2009;**48**:99–107. DOI: [10.1016/j.supflu.2008.10.01](https://doi.org/10.1016/j.supflu.2008.10.01)
- [45] Ren W, Scurto AM. Phase equilibria of imidazolium ionic liquids and the refrigerant gas, 1, 1, 1, 2-tetrafluoroethane (R-134a). *Fluid Phase Equilibria*. 2009;**286**:1–7. DOI: [10.1016/j.fluid.2009.07.007](https://doi.org/10.1016/j.fluid.2009.07.007)
- [46] Seddon KR, Stark A, Torres MJ. Influence of chloride, water, and organic solvents on the physical properties of ionic liquids. *Pure and Applied Chemistry*. 2000;**72**:2275–87. DOI: [10.1351/pac200072122275](https://doi.org/10.1351/pac200072122275)
- [47] Morrissey AJ, O'Donnell JP. Endothermic solutions and their application in absorption heat pumps. *Chemical Engineering Research and Design*. 1986;**64**:404–406.
- [48] Lungwitz R, Spange S. A hydrogen bond accepting (HBA) scale for anions, including room temperature ionic liquids. *New Journal of Chemistry*. 2008;**32**:392–394. DOI: [10.1039/b714629a](https://doi.org/10.1039/b714629a)
- [49] Cao YY, Chen Y, Lu L, Xue ZM, Mu TC. Water sorption in functionalized ionic liquids: kinetics and intermolecular interactions. *Industrial & Engineering Chemistry Research* 2013;**52**:2073–83. DOI: [org/10.1021/ie302850z](https://doi.org/10.1021/ie302850z)
- [50] Seiler M, Kühn A, Ziegler F, Wang X. Sustainable cooling strategies using new chemical system solutions. *Industrial & Engineering Chemistry Research*. 2013;**52**:16519–16546. DOI: [org/10.1021/ie401297u](https://doi.org/10.1021/ie401297u)
- [51] Hu HC, Soriano AN, Leron RB, Li MH. Molar heat capacity of four aqueous ionic liquid mixtures. *Thermochimica Acta*. 2011;**519**:44–49. DOI: [10.1016/j.tca.2011.02.027](https://doi.org/10.1016/j.tca.2011.02.027)
- [52] Lashkarbolooki M, Hezave AZ, Ayatollahi S. Artificial neural network as an applicable tool to predict the binary heat capacity of mixtures containing ionic liquids. *Fluid Phase Equilibria*. 2012;**324**:102–107. DOI: [10.1016/j.fluid.2012.03.015](https://doi.org/10.1016/j.fluid.2012.03.015)
- [53] Carvalho PJ, Alvarez VH, Marrucho IM, Aznar M, Coutinho JAP. High carbon dioxide solubilities in trihexyl tetradecylphosphonium-based ionic liquids. *Journal of Supercritical Fluids*. 2010;**52**:258–265. DOI: [10.1016/j.supflu.2010.02.00](https://doi.org/10.1016/j.supflu.2010.02.00)

- [54] Carvalho PJ, Alvarez VH, Marrucho IM, Aznar M, Coutinho JAP. High pressure phase behavior of carbon dioxide in 1-butyl-3-methylimidazolium bis (trifluoromethylsulfonyl) imide and 1-butyl-3-methylimidazolium dicyanamide ionic liquids. *Journal of Supercritical Fluids*. 2009;**50**:105–111. DOI: 10.1016/j.supflu.2009.05.00
- [55] Ficke LE, Rodriguez H, Brennecke JF. Heat capacities and excess enthalpies of 1-ethyl-3-methylimidazolium-based ionic liquids and water. *Journal of Chemical & Engineering Data*. 2008;**53**:2112–2119. DOI: 10.1021/je800248w
- [56] Garcia-Miaja G, Troncoso J, Romani L. Excess enthalpy, density, and heat capacity for binary systems of alkylimidazolium-based ionic liquids + water. *Journal of Chemical Thermodynamics*. 2009;**41**:161–166. DOI: 10.1016/j.jct.2008.10.002
- [57] Dong L, Zheng DX, Wei Z, Wu XH. Synthesis of 1,3-dimethylimidazolium chloride and volumetric property investigations of its aqueous solution. *International Journal of Thermophysics*. 2009;**30**:1480–1490. DOI: 10.1007/s10765-009-0651-x
- [58] Lehmann J, Rausch MH, Leipertz A, Froba AP. Densities and excess molar volumes for binary mixtures of ionic liquid 1-ethyl-3-methylimidazolium ethylsulfate with solvents. *Journal of Chemical & Engineering Data*. 2010;**55**:4068–4074. DOI: 10.1021/je1002237
- [59] Vercher E, Orchilles AV, Miguel PJ, Martinez-Andreu A. Volumetric and ultrasonic studies of 1-ethyl-3-methylimidazolium trifluoromethanesulfonate ionic liquid with methanol, ethanol, 1-propanol, and water at several temperatures. *Journal of Chemical & Engineering Data*. 2007;**52**:1468–1482. DOI: 10.1021/je7001804
- [60] Chakrabarty D, Chakraborty A, Seth D, Sarkar N. Effect of water, methanol, and acetonitrile on solvent relaxation and rotational relaxation of coumarin 153 in neat 1-hexyl-3-methylimidazolium hexafluorophosphate. *Journal of Physical Chemistry A*. 2005;**109**:1764–1769. DOI: 10.1021/jp0460339
- [61] Gonzalez EJ, Dominguez A, Macedo EA. Physical and excess properties of eight binary mixtures containing water and ionic liquids. *Journal of Chemical & Engineering Data*. 2012;**57**:2165–2176. DOI: org/10.1021/je201334p
- [62] Bahadur I, Letcher TM, Singh S, Redhi GG, Venkatesu P, Ramjugernath D. Excess molar volumes of binary mixtures (an ionic liquid + water): A review. *Journal of Chemical Thermodynamics*. 2015;**82**:34–46. DOI: org/10.1016/j.jct.2014.10.003
- [63] Kim YJ, Kim S, Joshi YK, Fedorov AG, Kohl PA. Thermodynamic analysis of an absorption refrigeration system with ionic-liquid/refrigerant mixture as a working fluid. *Energy*. 2012;**44**:1005–1016. DOI: 10.1016/j.energy.2012.04.048
- [64] Rodriguez H, Brennecke JF. Temperature and composition dependence of the density and viscosity of binary mixtures of water + ionic liquid. *Journal of Chemical & Engineering Data*. 2006;**51**:2145–2155. DOI: 10.1021/je0602824

- [65] Pandey S, Fletcher KA, Baker SN, Baker GA. Correlation between the fluorescent response of microfluidity probes and the water content and viscosity of ionic liquid and water mixtures. *Analyst*. 2004;**129**:569–573. DOI: 10.1039/B402145M
- [66] Rebelo LPN, Najdanovic-Visak V, Visak ZP, Da Ponte MN, Szydłowski J, Cerdeirina CA, Troncoso J, Romani L, Esperanca JMSS, Guedes HJR, De Sousa HC. A detailed thermodynamic analysis of [C4mim][BF4] + water as a case study to model ionic liquid aqueous solutions. *Green Chemistry*. 2004;**6**:369–381. DOI: 10.1039/B400374H
- [67] Ayou DS, Curras MR, Salavera D, Garcia J, Bruno JC, Coronas A. Performance analysis of absorption heat transformer cycles using ionic liquids based on imidazolium cation as absorbents with 2, 2, 2-trifluoroethanol as refrigerant. *Energy Conversion and Management*. 2014;**84**:512–523. DOI: 10.1016/j.enconman.2014.04.077
- [68] Wooster TJ, Johanson KM, Fraser KJ, MacFarlane DR, Scott JL. Thermal degradation of cyano containing ionic liquids. *Green Chemistry*. 2006;**8**:691–696. DOI: 10.1039/B606395K
- [69] Ngo HL, LeCompte K, Hargens L, McEwen AB. Ngo HL, LeCompte K, Hargens L, McEwen AB. Thermal properties of imidazolium ionic liquids. *Thermochimica Acta*. 2000;**357–358**:97–102. DOI: 10.1016/S0040-6031(00)00373-7
- [70] Baranyai KJ, Deacon GB, Mac FDR, Pringle JM, Scott JL. Thermal degradation of ionic liquids at elevated temperatures. *Australian Journal of Chemistry*. 2004;**57**:145–147. DOI: 10.1071/CH03221
- [71] Huangfu L, Wu X, Guo K, Ding N. Heat characteristics research of a water-soluble ionic liquid as absorption workers. *Chinese Journal of Analytical Chemistry*. 2011;**50**:39–44.
- [72] Freire MG, Neves CMSS, Marrucho IM, Coutinho JAP, Fernandes A M. Hydrolysis of tetrafluoroborate and hexafluorophosphate counter ions in imidazolium-based ionic liquids. *Journal of Physical Chemistry A*. 2010;**114**:3744–3749. DOI: 10.1021/jp903292n
- [73] Islam MM, Ohsako T. Roles of ion pairing on electroreduction of dioxygen in imidazolium-cation-based room-temperature ionic liquid. *Journal of Physical Chemistry C*. 2008;**112**:1269–1275. DOI: 10.1021/jp7096185
- [74] Swatloski RP, Holbrey JD, Memon SB, Caldwell GA, Caldwell KA, Rogers RD. Swatloski RP, Holbrey JD, Memon SB, Caldwell GA, Caldwell KA, Rogers RD. Using *Caenorhabditis elegans* to probe toxicity of 1-alkyl-3-methylimidazolium chloride based ionic liquids. *Chemical Communication*. 2004;**6**:668–669. DOI: 10.1039/B316491H
- [75] Uerdingen M, Treber C, Balsler M, Schmitt G, Werner Ch. Corrosion behavior of ionic liquids. *Green Chemistry*. 2005;**7**:321–325. DOI: 10.1039/B419320M
- [76] Parham K, Khamooshi M, Tematio DBK, Yari M, Atikol U. Absorption heat transformers—A comprehensive review. *Renewable and Sustainable Energy Reviews*. 2014;**34**:430–452. DOI: [org/10.1016/j.rser.2014.03.036](http://dx.doi.org/10.1016/j.rser.2014.03.036)

Gas Sensing Ionic Liquids on Quartz Crystal Microbalance

Yi-Pin Chang and Yen-Ho Chu

Additional information is available at the end of the chapter

<http://dx.doi.org/10.5772/65793>

Abstract

Recent advances in “designer solvents” have facilitated the development of ultrasensitive gas sensing ionic liquids (SILs) based on quartz crystal microbalance (QCM) that can real-time detect and discriminate volatile molecules. The amalgamation of tailored-made SILs and label-free QCM resulted in a new class of qualitative and semi-quantitative gas sensing device, which represents a model system of electronic nose. Because a myriad of human-made or naturally occurring volatile organic compounds (VOCs) are of great interest in many areas, several functional SILs have been designed to detect gaseous aldehyde, ketone, amine and azide molecules chemoselectively in our laboratory. The versatility of this platform lies in the selective capture of volatile compounds by thin-coated reactive SILs on QCM at room temperature. Notably, the detection limit of the prototype system can be as low as single-digit parts-per-billion. This chapter briefly introduces some conventional gas sensing approaches and collates recent research results in the integration of SILs and QCM and finally gives an account of the state-of-the-art gas sensing technology.

Keywords: chemoselective gas sensing, ionic liquid, label-free detection, quartz crystal microbalance and volatile organic compound

1. Introduction

Real-time detection and monitoring of naturally occurring or human-made volatile compounds are of paramount importance in many areas such as (1) disease diagnosis (e.g., breath VOCs); (2) manufacturing industry (e.g., flammable and toxic gases); (3) environmental protection (e.g., automobile emissions and greenhouse gases); (4) indoor air quality monitoring (e.g., asphyxiant and hazardous gases); (5) homeland security (e.g., chemical and biological warfare agents). Mammalian olfaction has been used as tools in many settings to detect or measure

volatile molecules in drinks, food, perfumes as well as explosives and illegal drugs. Perfumers, flavorists and sniffer dogs are trained professionals and experts in aroma; however, they cannot work 24/7 and their sensory can be extremely subjective, regardless of other factors such as sensitivity, toxicity and when sites are beyond reach. Inspired by the mammalian olfactory system, artificial olfaction or electronic noses have been developed to precisely analyze smells or odorants [1]. In this chapter, the development of chemoselective SIL-based QCM gas analysis system for the detection of VOCs in our laboratory is described. **Figure 1** illustrates the side-by-side comparison of the human olfactory system and the SIL on QCM gas sensing system.

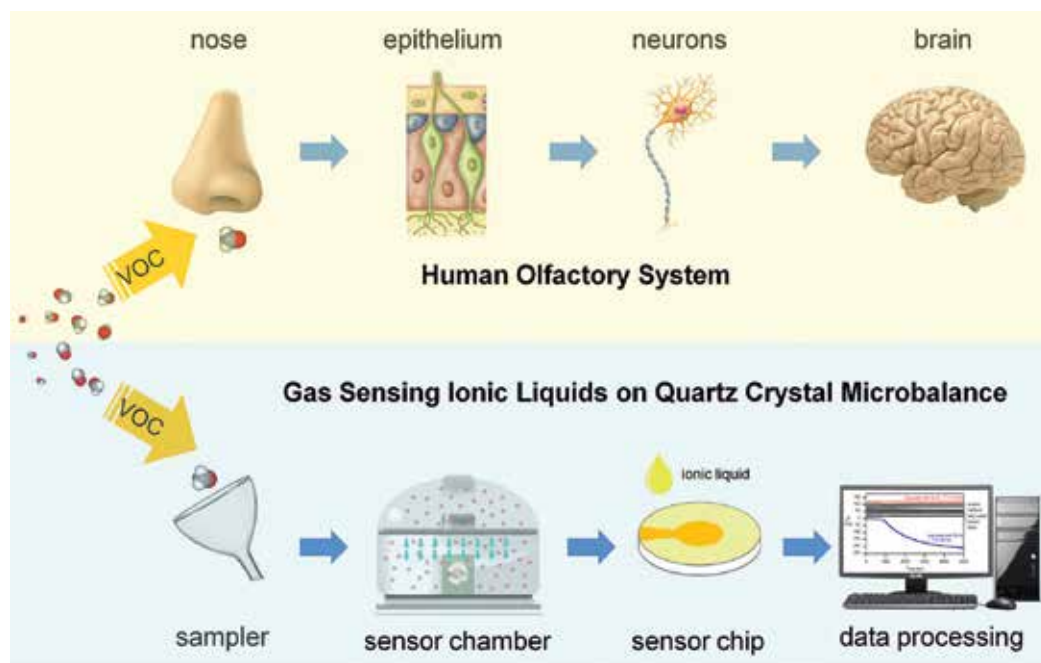


Figure 1. Side-by-side comparison of the human olfactory system and the SIL on QCM gas sensing system.

Gas is one of the fundamental states of matter that is considered between the liquid and plasma states. Unlike other states of matter, what distinguishes gas from liquid and solid is the distinct separation of the individual gas molecules, which makes them travel fast and freely, and is usually invisible to the human naked eyes. A pure gas can be composed of single atoms (e.g., noble gas), one type of atom (e.g., oxygen), or organic molecules made from a combination of atoms (e.g., acetone). The question is how to selectively detect and precisely measure a single gas out of a mixture of other gases? In the human olfactory system, volatile compounds are inhaled into nasal cavity and then diffuse through mucus to epithelium receptor cells. The peripheral system then senses the external stimulus and the central system encodes it as an electric signal in neurons, where all signals are integrated and processed in the brain to give us the sense of a smell. The design of a gas sensing device is similar to human

olfaction, in which the sensing material plays a pivotal role in the recognition or capture of volatile molecules. The gas sample passes through the sensor chip and induces physical or chemical changes in the sensing material, which are transduced into electrical signals or patterns and then processed by a computer system. The sensing material should be sensitive enough to recognize the presence of target gas, which is the counterpart of the peripheral system in the human olfactory system. The first event of molecular recognition underscores the importance of sensing material that sensitivity and selectivity are inherited in the gas sensing system.

Ionic liquids are room-temperature molten salts that have been increasingly used in electrochemical devices, such as batteries, fuel cells and biosensors. Their intrinsic unique physiochemical properties by design have facilitated the birth of a variety of novel sensing technologies in recent years. Zhang et al. [2] reported fabrication of polymeric ionic liquid/graphene nanocomposite for glucose oxidase immobilization and direct electrochemistry. Liu et al. described a hydrophobic ionic liquid was used as an entrapping agent to facilitate the electron transfer of horseradish peroxidase on a glassy carbon electrode [3]. Ratel et al. developed imidazolium-based ionic liquid self-assembled monolayers for binding streptavidin to promote affinity biosensing [4]. Abdelhamid et al. designed UV-light absorbing ionic liquid matrices for matrix-assisted laser desorption/ionization mass spectrometry (MS) [5]. Arkan et al. demonstrated an impedimetric immunosensor based on a gold nanoparticle/multiwall carbon nanotube-ionic liquid electrode for the determination of human epidermal growth factor receptor 2 [6]. As shown above, the scope of the applications of ionic liquid-based sensors is abundant, but its use in gas sensing is in the ascendant.

Conventional gas sensing methods can be generally categorized into conductivity sensors (e.g., metal-oxide semiconductors and conducting organic polymers), piezoelectric sensors (e.g., quartz crystal microbalance (QCM) and surface acoustic waves (SAW) and spectroscopic instruments. These gas sensing systems require a set of reactive materials that recognize gaseous molecules and transduce the volatile compounds into electrical signals. A number of nanomaterials have been developed for gas sensing, such as field effect transistors (FETs) based on single-walled carbon nanotubes (CNTs) [7, 8]. The design of sensing materials generally utilizes the "lock-and-key" method, which has theoretical high sensitivity and selectivity. In some cases, it may not be practical for the analysis of complex samples due to the fact that most sensing materials exhibit some cross-reactivity to structurally similar compounds. In addition, higher selectivity may come at the price of irreversibility, lengthy recovery times, memory effects and lower sensitivity (detection limits down to hundreds part-per billion).

QCM is a highly sensitive instrument that measures the mass difference per unit area by recording the change in resonant frequency of a build-in quartz crystal [9]. The transduced signal (ΔF) represents the measured frequency change (Hz), which is based on a physical phenomenon called the converse piezoelectric effect. Piezoelectricity is generated on opposite surfaces of a crystalline material upon mechanical deformation (e.g., pressure or torsion) of the crystal along a given direction. Among the many types of crystals exhibit piezoelectricity, quartz exceptionally possesses the desired chemical, electrical, mechanical and thermal

properties and is thus used as the crystal in QCM systems. In order to make the best use of QCM, exquisite design on the chip is needed to functionalize the electrode with a variety of surface chemistries and modifications for molecular recognition [10]. Our laboratory has a long-standing interest in QCM, where a 9-MHz QCM apparatus was used to develop the integrated system equipped with ionic liquids tailored for reaction-based gas sensing. This chapter will give a brief introduction on current gas sensing technologies and latest advances in the field of gas SILs based on QCM.

2. Gas sensing methods

2.1. Spectroscopic gas sensors

Spectroscopic instruments are mainly based on absorption and emission spectrometry. The principal of absorption spectrometry is the Beer Lambert law that differential optical absorption spectroscopy, Raman light detection and ranging, tunable diode laser absorption spectroscopy, and so on, have been developed. One of the most commonly used on-site methods for continuous monitoring of airborne VOCs is differential optical absorption spectroscopy [11]. It has the advantages of fast response time and low limit of detection, but also has the disadvantage of optical interference from oxygen, ozone, and several hydrocarbons. The theory of emission spectrometry is that excited atoms emit photons and then return to its ground state that laser-induced breakdown spectroscopy is one example. Interestingly, Fourier transform infrared spectroscopy can be used in either absorption or emission spectrometry such as non-dispersive infrared and quantum-cascade lasers gas sensors for the latter [12].

Analytical instruments have been utilized for gas detection such as mass spectrometry (MS) and gas chromatography (GC). Mass spectrometry via direct injection is frequently used for the detection of VOCs. To enhance the sensitivity required for the identification of trace levels of VOCs, tandem mass analysis is typically employed. Ions of a particular mass to charge ratio are selected first and then subject to the next stage for further fragmentation. The fragmented daughter ions are analyzed without interference of large amount of unrelated parent fragments and thus beneficial for the detection of trace gases in complex mixtures. For example, Proton-transfer reaction mass spectrometry (PTR-MS) is among the techniques that have been used extensively for on-line analysis of VOCs [13]. The PTR-MS technique offers rapid and accurate measurement of VOCs with a very low limit of detection. However, isomeric and isobaric compounds are not able to be separated and measured individually by PTR-MS instruments. On the other hand, gas chromatography (GC) in conjunction with flame ionization detection, mass spectrometry or photoionization has been utilized for VOC detection such as in the food industry [14]. GC is used for analyte separation, while the coupled detector is for the measurement of separated analyte. These GC-related methods normally utilize batch detection that involves analyte sampling, transportation, pre-concentration and finally separation via chromatography before data analysis. These methods are useful for trace VOC detection, but they are time- and labor-consuming. In addition, the concentration detected

from such analysis is the average or accumulated level rather than spatial variations over the sampling time period.

2.2. Conductivity gas sensors

Metal-oxide (SnO_2 , CuO , Cr_2O_3 , V_2O_5 , WO_3 and TiO_2) semiconductors are one of the most common sensing materials due to its low cost and good sensitivity [15, 16]. The principle of detection is through redox reactions between the oxide surface and the target gas, where the electronic variation on the oxide surface is transduced into an electrical resistance variation. Depending on the transducer, the difference of resistance can be determined by the change of capacitance, mass, optical characteristics, reaction energy or work function. Metal oxides have been used to detect combustible, oxidizing, or reducing gases such as carbon monoxide, hydrogen, liquid petroleum gas, methane and nitrogen oxide [17]. Despite the fact that some metal-oxide semiconductors have good sensitivity, they may also suffer from poor response linearity and selectivity due to the interference of other gases. In addition, most metal-oxide gas sensors require high operating temperature (up to 500 °C) to reach the optimal reaction temperature for the target gas [18]. The sensing material has to be preheated to enhance the adsorption of gas molecules on the sensing surface, which has limited the application of metal-oxide gas sensors. Another major issue is the long recovery time that may make it unpractical for the development of electronic noses. In general, metal-oxide gas sensors exhibit drastically greater sensitivity to inorganic gases and a few VOCs such as ethanol and formaldehyde. However, it has been demonstrated that the indiscriminate response of methyl, ethyl, isopropyl and butyl alcohols on SnO_2 films, which reflects the major challenges in gas sensing using metal-oxide semiconductor devices, that is, selectivity and response time. In addition, many other VOCs that result in health problems are not able to be detected by metal-oxide gas sensors effectively [19].

On the contrary, conducting polymer-based gas sensors are frequently used to detect a wide range of gases such as VOCs, aromatic volatiles and halogenated compounds. The organic gas sensing polymer composite may be spray-, spin-, or dip-coated onto the sensor, which typically has two electrodes that are fabricated on an insulating polymer. Upon exposure to a gas, the physical properties of the insulating substrate changes due to the absorption of volatile molecules. The signal transduction mechanism can be described by London dispersion, dipole/induced dipole interactions, dipole/dipole interactions and hydrogen bonds, in which responses are normally measured as the relative differential resistance. Polyaniline, polypyrrole, polythiophene and their derivatives are typical organic conducting polymers that have been investigated for gas sensing, in which doping process is required to increase conductivity by redox reactions or protonation [20]. Polymer-based gas sensors have several advantages for gas detection, including high sensitivity and short response time. Moreover, while operation temperatures of metal-oxide gas sensors are usually more demanding, polymer-based sensors operate at room temperature. However, polymer composites are also sensitive to temperature fluctuations that may result in variation of sensor responses and thus output errors in the system.

2.3. Piezoelectric sensors

A general piezoelectric gas sensor is composed of a substrate of quartz that is cut at a crystalline angle to support a pressure- or mass-sensitive material that is coated on the quartz surface. QCM and surface acoustic wave (SAW) devices are two typical microbalance sensors that the former employs a bulk acoustic wave sensor while the latter uses a surface acoustic wave sensor. Sensing materials such as non-conducting polymers can be coated on QCM and SAW sensors to detect the analytes of interest. When the sensing material adsorbs specific molecules, the mass of the coated material increases and causes the acoustic waves to travel slower. The piezoelectric quartz converts acoustic waves to electric signals. This subtle change in mass can be detected by the sensor microelectronics once the acoustic wave is converted to an electric signal. The signal response varies in physisorption and chemisorptions. A few materials such as carbon nanotubes [21], ionic liquids [22] and molecular imprinted polymers [23] have been used to coat on QCM and have enabled the detection of a variety of pollutants and the sensing of VOCs. Temperature and humidity control are the major issues for accurate detection, as the resonant frequency is affected by those factors in this type of gas sensors. Therefore, modifications in coating materials have been the focus to improve the sensitivity and specificity in gas sensing. Some commercial QCM sensor systems are available for moisture and inorganic gas detection, but the detection for VOCs is rare and sensitivity is typically in the range of 10–103 ppm, which is not good enough for trace level detection [24].

3. Gas sensing ionic liquids and quartz crystal microbalance

3.1. Ionic liquids for gas sensing

A sensor array using room-temperature ionic liquids as sensing materials and a QCM as a transducer was developed for the detection of ethanol, dichloromethane, benzene and heptane at ambient and elevated temperatures [25]. These ionic liquids responded proportionately and reversibly to the volatile compounds at room and elevated temperatures but deviated from this linear relationship at high concentrations for the highly volatile dichloromethane. The different response intensity of the gas sensor to the volatile compounds depends on the solubilities of organic vapors in ionic liquids and interactions between each organic vapor and ionic liquid. In addition, the study of a diverse set of ionic liquid showed structural differences resulted in selective responses. Consequently, a sensor array of ionic liquids is promising to effectively differentiate different volatile compounds in pattern recognition in room or high temperatures. A room-temperature ionic liquid has also been developed for the sensing of ammonia gas. The work function responses of the cast films with and without IL were analyzed by “stepwise” changes of ammonia gas concentration from 0.5 to 694 ppm in air. The camphorsulfonic acid-doped polyaniline layers showed enhanced sensitivities, lower detection limits and shorter response times. Experimental evidence suggested that polyaniline forms a charge-transfer complex with imidazolium cation [26]. The first use of ionic liquid-doped electrospun nanofibrous materials as highly responsive fluorescence quenching-based optical CO₂ sensors was reported. The sensor slides have high sensitivities due

to the high surface area-to-volume ratio of the nanofibrous membrane structures. The preliminary results showed that the sensitivities of electrospun nanofibrous membranes to detect CO_2 are 24- to 120-fold higher than those of the thin film-based sensors. The response times of the sensing reagents were short, and the signal changes were also fully reversible. In addition, the stability of the employed matrix materials was excellent as there was no significant drift in signal intensity after stored in the ambient air for months [27]. The effects of conductive polymer oxidation states and structures on the design and development of ionic liquid/conductive polymer composite films for gas sensing have also been systematically characterized. Polyvinyl ferrocene films were tested for their sensing properties (e.g., sensitivity, selectivity, response time, linearity, and dynamic range against various gas analytes such as dichloromethane, ethanol, natural gas, methane, formaldehyde and benzene) utilizing QCM. The highest sensitivity film immobilized with ionic liquids allowed the development of a ionic liquid composite-based sensor array to analyze complex mixtures utilizing structural differences and the extent of intermolecular interactions [28]. An electrochemical ethylene sensor was reported by employing a thin layer of ionic liquid as electrolyte. Ionic liquids served as an alternative electrolyte for many electrochemical gas sensors generally relied on a strongly acidic electrolyte. A detection limit of 760 ppb and a linear response up to 10 ppm were achieved in this work [29]. Next, an ionic liquid-mediated electrochemiluminescent sensor for the detection of sulfur dioxide has been developed. The portable system is based on the strong quenching effect of SO_2 on the electrochemiluminescent of the coreactant system in the ionic liquid film. This proposed SO_2 electrochemiluminescent sensor can be operated at room temperature and shows high selectivity, good reproducibility and long-term stability in a dry atmosphere [30]. A room temperature ionic liquid was used as a solvent for the detection of highly toxic methylamine and hydrogen chloride on Pt screen-printed electrodes. The achieved limit of detections were lower than the current Occupational Safety and Health Administration Permissible Exposure Limit, suggesting that Pt screen-printed electrodes can successfully be combined with ionic liquids as cheap alternatives for amperometric gas sensing [31]. Most recently, a gas sensing approach based on differential capacitance of electrified ionic liquid electrode interfaces in the presence and absence of adsorbed gas molecules was developed. The observed change of differential capacitance has a local maximum at a certain potential that is unique for each type of gas, and is concentration-dependent. Characterization of SO_2 detection was completed at ppb levels with less than 1.8% signal from other interfering species (i.e., CO_2 , O_2 , NO_2 , NO , SO_2 , H_2O , H_2 and cyclohexane, tested at the same concentration as SO_2) [32]. The aforementioned studies pave the way of utilizing ionic liquids for the development of gas sensing devices.

3.2. Reaction-based gas sensing ionic liquids on QCM

A new series of reaction-based SIL gas analysis system on QCM have been continuously developed in our laboratory. This SIL-on-QCM chip system not only is a cost-effective approach but also shows a great potential to detect a wide range of VOCs with high efficiency and specificity. In combination, the tunable chemical reactivity, negligible volatility, and good thermal stability of ionic liquids with high sensitivity of QCM sensor chips make this integrated platform highly attractive for chemoselective gas sensing. The negligible vapor pressure of ionic

liquids ensures that the sensors do not “dry out” on QCM chips and show free of leakage and the loss of loading during the measurement. As illustrated in **Figure 2**, when gases rapidly diffuse into the SIL thin film on QCM chips and specific chemical reactions for selective gases in ionic liquids occur under appropriate experimental conditions. The mass changes on QCM chips during the chemical reactions of a gas analyte and the tailored ionic liquid are readily obtained and ultimately transduced to generate an analytical signal. The thin coatings (200–300 nm thickness) of ionic liquids on the surface of the QCM chip (9 MHz) are achieved by depositing the diluted methanol containing SILs. The used SIL layer on QCM chip could be easily washed away by methanol and further replaced with a new SIL. This regeneratable SIL-on-QCM chip system can be performed at room temperature, and dried ambient air is used as carrier gas.

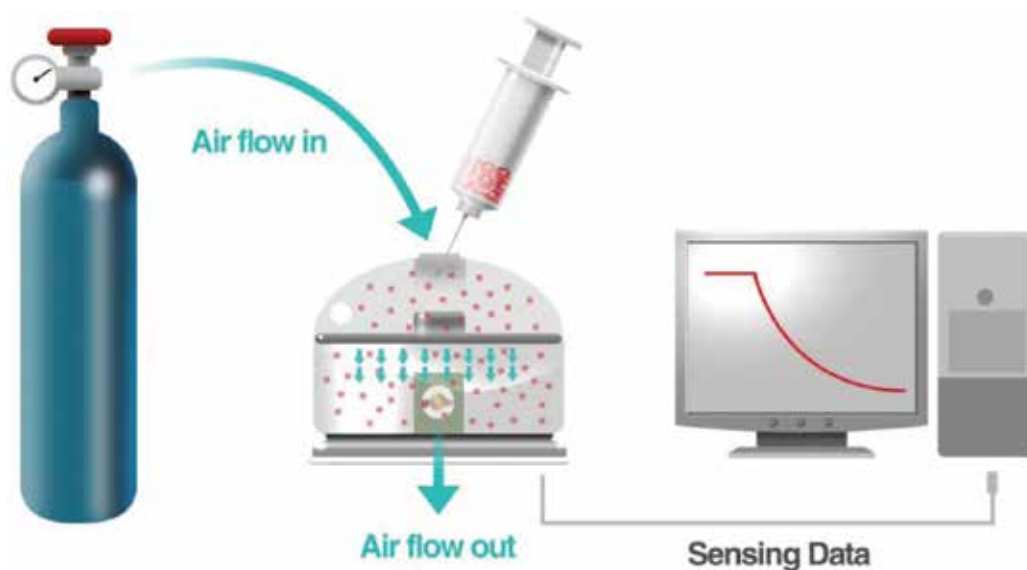


Figure 2. Schematic representation of a SIL-on-QCM gas analysis system for reaction-based gas sensing.

As shown in **Figure 3**, a series of chemoselective SILs for the detections of aldehyde, ketone, amine and azide gases have been prepared. This section is intended as a comprehensive update to our previous and recent works on the developments of SILs. **SIL 1** was first synthesized for the detection of aldehyde and ketone gases [33]. Interestingly, the results showed that **SIL 1** was more sensitive and selective to capturing aldehyde than ketone gases. To improve the sensitivity of ketone gas sensing, **SIL 2** was synthesized subsequently [34]. As the sensing reactions take place, **SIL 1** and **SIL 2** formed imine and hydrazone adducts with aldehydes and ketones, respectively (**Figure 4**). **SIL 1** displayed a similar reaction rate to aliphatic and aromatic aldehydes while **SIL 2** reacted efficiently with acyclic and cyclic ketone gases. It is noted that the irreversible nature of the frequency drops from QCM

measurements of aldehyde and ketone sensing by both SILs suggesting a non-equilibrium formation of Schiff bases. Notably, this SIL-on-QCM chip system was totally insensitive to common VOCs such as methanol, ethanol, ethyl acetate, hexane and most importantly, moisture (water) ($\Delta F \sim 0$ Hz); that is, any water present in the gas stream would not be in any direct competition with target gases. The results of sensing aldehyde and ketone sensing prompted us to synthesize **SIL 3** for the detection of amine gases. The chemical reaction between **SIL 3** and amine gases was based on the transimination reaction. Although the model amine gas (propylamine) was detectable at low concentration (28.5 ppb), the minimal QCM response (~ 0.5 Hz) and seemingly reversible in its signal were noticed. From a quick search of the literature, we realized that Lewis acids could notably facilitate the transimination reaction as well as imine and hydrazone forming reactions in conventional molecular solvents. We found that **SIL 3** with 1 mol% hint of $\text{Sc}(\text{OTf})_3$ could catalyze the transimination reaction to produce the largest and irreversible QCM response ($\Delta F = 20$ Hz). The sensitivity of detection was also significantly improved about 11.4-fold for the model amine gas (28.5 ppb \rightarrow 2.5 ppb). Remarkably, even the smallest molecular weight amine gas, ammonia, the detection limit could be achieved approximately 3.9 ppb ($\Delta F \sim 1.0$ Hz). With this in mind, we could expect to develop an ultrasensitive SIL for detection of ketone gases. Indeed, **SIL 2** with 2 mol% of $\text{Sc}(\text{OTf})_3$ also could promote hydrazone formation and produce twofold increase and irreversible QCM response. With the addition of metal triflate, the detecting sensitivity of **SIL 2** was significantly down to 0.6 ppb for cyclohexanone and 1.1 ppb for acetone, respectively. Surprisingly, even the masked ketone gases such as 2,2-dimethoxypropane was also detectable at a level of 34 ppb.

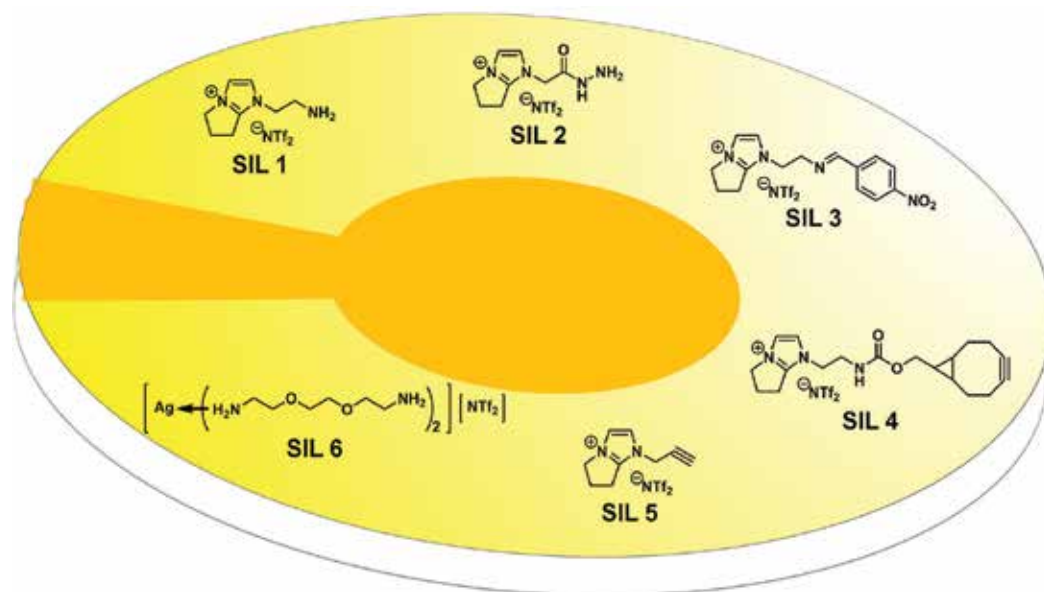


Figure 3. Chemical structures of SIL 1-6.

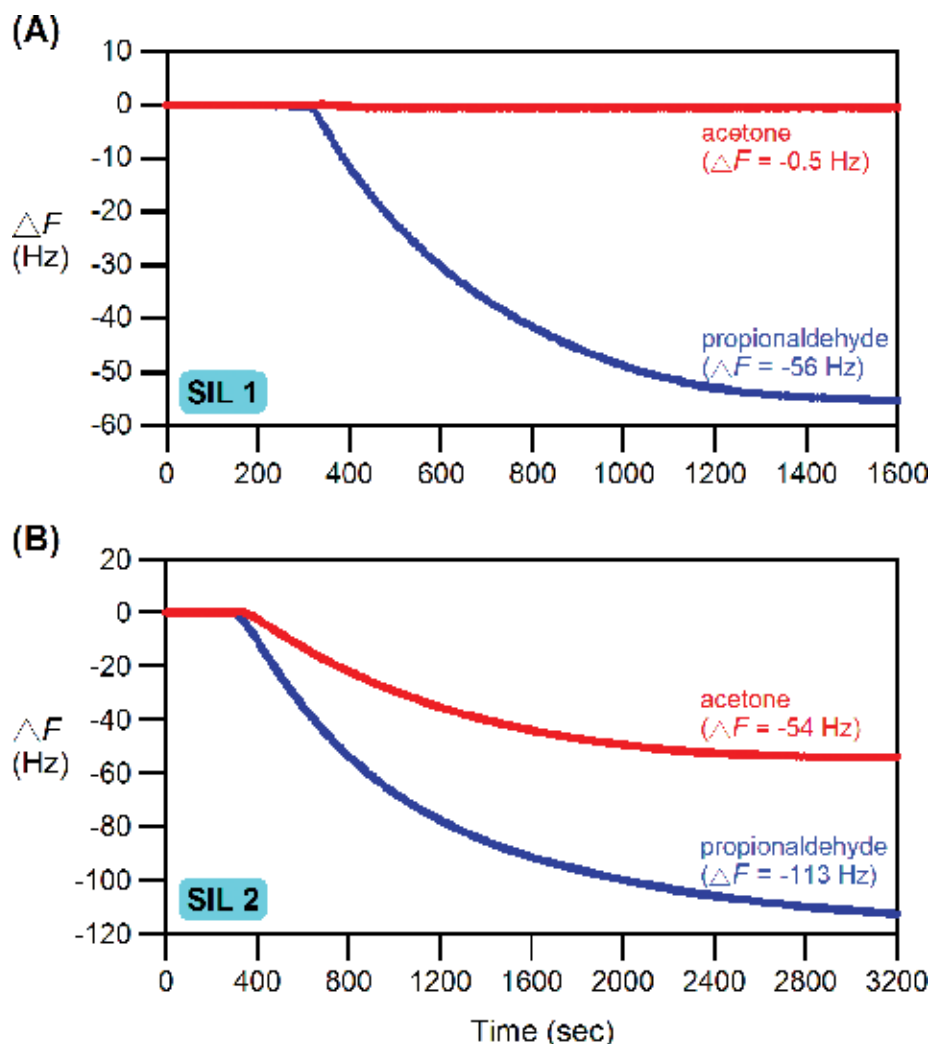


Figure 4. Chemoselective detection of acetone and propionaldehyde gases (98 ppb each) of identical molecular weight (C_3H_6O) by 9 MHz QCM thin coated with (A) SIL 1 and (B) SIL 2 (3.3 nL each, 300 nm thickness). Air was used as the carrier gas with a flow rate of 3 mL/min, and gas samples were injected at 300 s. The resonance frequency drop (ΔF) is the QCM response on the quartz chip surface.

Next, on the basis of the recent advances in click chemistry, the Huisgen 1, 3-dipolar azide and alkyne [3+2] cycloaddition, we synthesized SIL 4 and 5 for the chemoselective detection of organic azide gases [35]. Compared to the unstrained SIL 5, we can expect that the strained SIL 4 should possess much greater enhancement in reactivity toward organic azides. Indeed, SIL 4 showed high sensitivities toward both aliphatic and aryl azide gases, but SIL 5 was totally inert toward azide gas sensing (Figure 5). Among all azide gases investigated, the sensitivity of detection was 5 ppb for benzyl azide and 35 ppb for butyl azide, respectively. It is noted that the reactivity order of benzyl azides > phenyl azides > allyl azides toward SIL 4 could be understood by the reported activation energy [36]. In addition, SIL 4

could be applied to detect azide gases with dual functional groups such as 2-azioethyl amine. Most remarkably, **SIL 4**, which carries a reactive alkyne dienophile group, can also readily capture cyclopentadiene gas at low ppb (65.5 ppb) through the Diels-Alder [4+2] cycloaddition reaction [35]. Namely, **SIL 4**-based upon cycloaddition reactions is well-suited to detect both azide and diene gases with a high sensitivity.

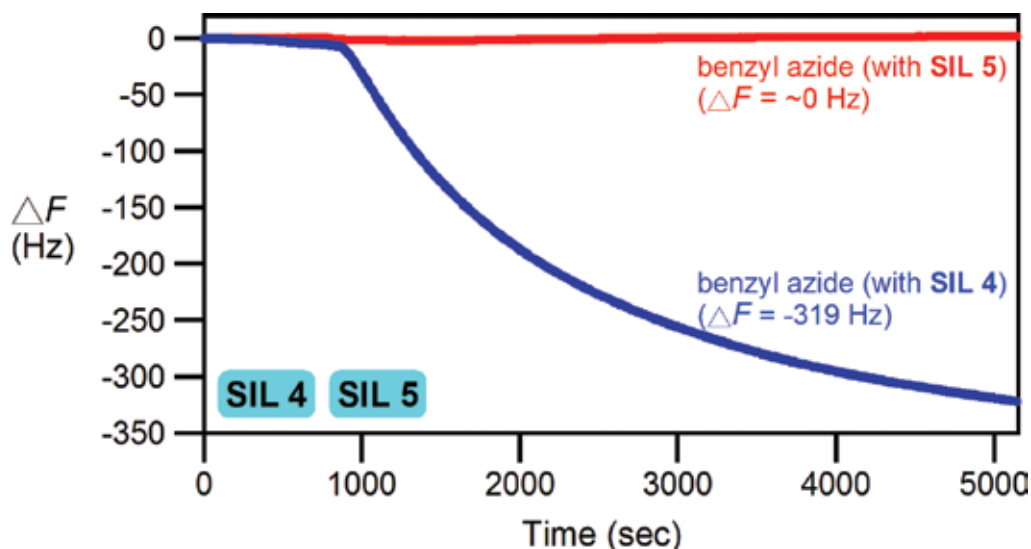


Figure 5. Chemoselective detection of benzyl azide gas (146 ppb) by 9 MHz QCM thin coated with **SIL 4** and **SIL 5** (3.3 nL each, 300 nm thickness). Nitrogen was used as the carrier gas with a flow rate of 3 ml/min, and gas samples were injected at 1000 s. The resonance frequency drop (ΔF) is the QCM response on the quartz chip surface.

Recently, transition metal-containing ionic liquids have received significant research attention. Due to the strong affinities between transition metal ions and neutral alkylamines, transition metal-containing ionic liquids can be easily prepared under convenient reaction conditions (e.g., aqueous solution and room temperature) with high efficiency. Furthermore, there is no tedious organic synthesis steps involved but only simply sample mixing followed by straightforward extraction workups. Thus, we synthesized a new transition metal-containing ionic liquids, **SIL 6**, for detecting exclusive for aldehyde gases from an inexpensive and commercially available alkylamine, 1, 2-bis(2-aminoethoxy)ethane as the ligand for silver (I) [37]. Unlike the synthesis of imidazolium-based **SIL 1** that required four synthetic steps with a low yield (37%), the preparation of **SIL 6** could be achieved by only straightforward mixing of silver and amine reagents with a moderate high yield (66%). **SIL 6** was totally insensitive to the ketone gases. Notably, with the same concentration of model aldehyde gas (propionaldehyde, 100 ppb), **SIL 6** displayed a stronger QCM response ($\Delta F = -40$ Hz) than **SIL 1** ($\Delta F = -19$ Hz) (**Figure 6**). Despite silver ionic liquids having the apparent but inherent drawback that they are less stable toward light, they process many advantages such as only minute amounts of SILs (10–15 nL per quartz chip) are consumed. In addition, no chemical immobilization on quartz chips is needed, plus they can be readily regenerated by simply

washing them away. Finally, the SIL platform developed in this work is highly chemoselective (SIL 1 and SIL 6: specific to aldehyde, SIL 2: sensitive to ketone, SIL 3: specific to amine, and SIL 4: selective to azide gases, respectively) with superior gas reactivity for SIL 6 than the imidazolium-based SIL 1 and, most significantly, totally insensitive to moisture.

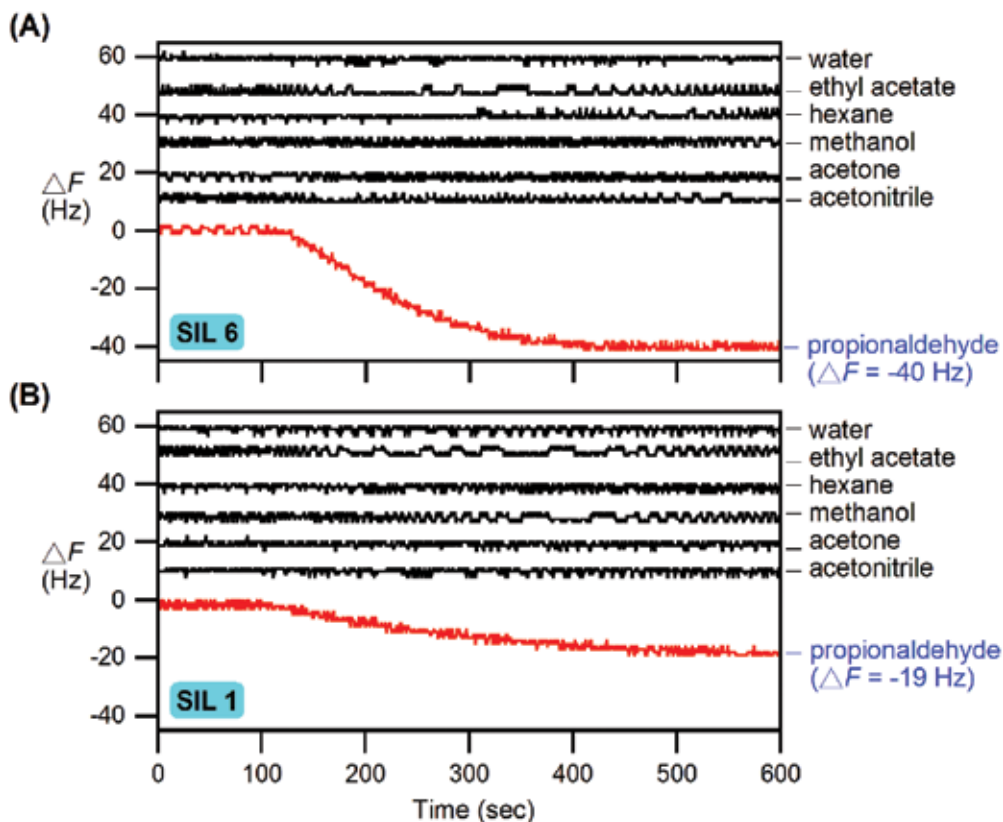


Figure 6. Chemoselective detection of water, ethyl acetate, hexane, methanol, acetone, acetonitrile and propionaldehyde gases (100 ppb each) all by a multichannel QCM thin coated with (A) SIL 6 and (B) SIL 1 (33 nmol each, 200–300 nm thickness). The QCM sensograms for water, ethyl acetate, hexane, methanol, acetone and acetonitrile gases were vertically shifted (10 Hz in between) for clarity. Nitrogen was used as the carrier gas with a flow rate of 3 mL/min, and gaseous samples were injected at 100 s. The resonance frequency drop (ΔF , in Hz) is the QCM response on the quartz chip surface.

4. Conclusion

Ionic liquids are commonly defined as molten organic salts, which have been used in analytical sciences and biosensing technologies by harnessing the transformation in chemical structure and hence fine-tuning their physicochemical properties. A myriad of assays can be performed in ionic liquids and a plethora of composite materials based on carbon nanotubes, graphene, graphite, metal nanomaterials, polymers and sol-gels have demonstrated their usefulness in biosensors. However, there are few examples of gas sensors exploiting

the properties of ionic liquid. Gas sensing systems based on different principles have been developed for real-time detection of human-made or naturally occurring VOCs including QCM. In light of the potential problems of many gas sensors, the electromechanical device, QCM represents an excellent platform if sensitive, selective and versatile sensing materials were available. To this end, we have developed a series of ultrasensitive SILs that are capable of detecting VOCs selectively. SILs on QCM detect VOCs by sensing normally neglect changes in weight on a nanogram level. Target analytes are captured by SILs and the accumulated weights are transduced into frequency shifts on QCM. An integrated multi-channel system could be crafted to efficiently detect and optimally exploit the advantages of various SILs for various VOCs sensing simultaneously. We thus anticipate the design of a pattern recognition library of chemical sensor arrays in the future. Finally, the ultimate goal would be SILs on QCM electronic nose system to “smell” as good as mammalian olfaction or better.

Acknowledgments

We thank Jerry Lo and Dr. I-Nan Chang of the ANT Technology Co. for longstanding support and assistance. This work was supported in part by a grant (MOST103-2113-M-194-002-MY3) from the Ministry of Science and Technology of Taiwan, Republic of China.

Author details

Yi-Pin Chang¹ and Yen-Ho Chu^{2*}

*Address all correspondence to: cheyhc@ccu.edu.tw

1 The Forsyth Institute, Cambridge, MA, USA

2 Department of Chemistry and Biochemistry, National Chung Cheng University, Minhsiung, Chiayi, Taiwan, ROC

References

- [1] Gutierrez J, Horrillo MC. Advances in artificial olfaction: sensors and applications. *Talanta*. 2014;124:95-105.
- [2] Zhang Q, Wu S, Zhang L, Lu J, Verproot F, Liu Y, et al. Fabrication of polymeric ionic liquid/graphene nanocomposite for glucose oxidase immobilization and direct electrochemistry. *Biosens Bioelectron*. 2011;26(5):2632-7.
- [3] Liu X, Feng H, Zhang J, Zhao R, Liu X, Wong DK. Hydrogen peroxide detection at a horseradish peroxidase biosensor with a Au nanoparticle-dotted titanate nanotube hydrophobic ionic liquid scaffold. *Biosens Bioelectron*. 2012;32(1):188-94.

- [4] Ratel M, Provencher-Girard A, Zhao SS, Breault-Turcot J, Labrecque-Carbonneau J, Branca M, et al. Imidazolium-based ionic liquid surfaces for biosensing. *Anal Chem.* 2013;85(12):5770-7.
- [5] Abdelhamid HN, Khan MS, Wu HF. Design, characterization and applications of new ionic liquid matrices for multifunctional analysis of biomolecules: a novel strategy for pathogenic bacteria biosensing. *Anal Chim Acta.* 2014;823:51-60.
- [6] Arkan E, Saber R, Karimi Z, Shamsipur M. A novel antibody-antigen based impedimetric immunosensor for low level detection of HER2 in serum samples of breast cancer patients via modification of a gold nanoparticles decorated multiwall carbon nanotube-ionic liquid electrode. *Anal Chim Acta.* 2015;874:66-74.
- [7] Paska Y, Haick H. Interactive effect of hysteresis and surface chemistry on gated silicon nanowire gas sensors. *ACS Appl Mater Interfaces.* 2012;4(5):2604-17.
- [8] Wu WQ, Feng HL, Rao HS, Xu YF, Kuang DB, Su CY. Maximizing omnidirectional light harvesting in metal oxide hyperbranched array architectures. *Nat Commun.* 2014;5:3968.
- [9] Fang J, Ren C, Zhu T, Wang K, Jiang Z, Ma Y. Comparison of the different responses of surface plasmon resonance and quartz crystal microbalance techniques at solid-liquid interfaces under various experimental conditions. *Analyst.* 2015;140(4):1323-36.
- [10] Cheng CI, Chang YP, Chu YH. Biomolecular interactions and tools for their recognition: focus on the quartz crystal microbalance and its diverse surface chemistries and applications. *Chem Soc Rev.* 2012;41(5):1947-71.
- [11] Parsons MT, Sydoryk I, Lim A, McIntyre TJ, Tulip J, Jager W, et al. Real-time monitoring of benzene, toluene, and p-xylene in a photoreaction chamber with a tunable mid-infrared laser and ultraviolet differential optical absorption spectroscopy. *Appl Opt.* 2011;50(4):A90-9.
- [12] Siciliani de Cumis M, Viciani S, Borri S, Patimisco P, Sampaolo A, Scamarcio G, et al. Widely-tunable mid-infrared fiber-coupled quartz-enhanced photoacoustic sensor for environmental monitoring. *Opt Express.* 2014;22(23):28222-31.
- [13] Ting VJ, Romano A, Soukoulis C, Silcock P, Bremer PJ, Cappellin L, et al. Investigating the in-vitro and in-vivo flavour release from 21 fresh-cut apples. *Food Chem.* 2016;212:543-51.
- [14] Duong S, Strobel N, Buddhadasa S, Stockham K, Auldism M, Wales B, et al. Rapid measurement of phytosterols in fortified food using gas chromatography with flame ionization detection. *Food Chem.* 2016;211:570-6.
- [15] Fine GF, Cavanagh LM, Afonja A, Binions R. Metal oxide semi-conductor gas sensors in environmental monitoring. *Sensors (Basel).* 2010;10(6):5469-502.
- [16] Wales DJ, Grand J, Ting VP, Burke RD, Edler KJ, Bowen CR, et al. Gas sensing using porous materials for automotive applications. *Chem Soc Rev.* 2015;44(13):4290-321.
- [17] Batzill M, Diebold U. Surface studies of gas sensing metal oxides. *Phys Chem Chem Phys.* 2007;9(19):2307-18.

- [18] Sanchez JB, Berger F. Towards a hybrid micro-device allowing the selective detection of hydrogen fluoride vapours in a complex mixture. *Talanta*. 2009;80(1):385-9.
- [19] Liu X, Cheng S, Liu H, Hu S, Zhang D, Ning H. A survey on gas sensing technology. *Sensors (Basel)*. 2012;12(7):9635-65.
- [20] Kaushik A, Kumar R, Jayant RD, Nair M. Nanostructured gas sensors for health care: an overview. *J Pers Nanomed*. 2015;1(1):10-23.
- [21] Yunusa Z, Hamidon MN, Ismail A, Mohd Isa M, Yaacob MH, Rahmanian S, et al. Development of a hydrogen gas sensor using a double SAW resonator system at room temperature. *Sensors (Basel)*. 2015;15(3):4749-65.
- [22] Kubersky P, Altsmid J, Hamacek A, Nespurek S, Zmeskal O. An electrochemical NO(2) sensor based on ionic liquid: influence of the morphology of the polymer electrolyte on sensor sensitivity. *Sensors (Basel)*. 2015;15(11):28421-34.
- [23] Jha SK, Hayashi K. A quick responding quartz crystal microbalance sensor array based on molecular imprinted polyacrylic acids coating for selective identification of aldehydes in body odor. *Talanta*. 2015;134:105-19.
- [24] Si P, Mortensen J, Komolov A, Denborg J, Moller PJ. Polymer coated quartz crystal microbalance sensors for detection of volatile organic compounds in gas mixtures. *Anal Chim Acta*. 2007;597(2):223-30.
- [25] Jin X, Yu L, Garcia D, Ren RX, Zeng X. Ionic liquid high-temperature gas sensor array. *Anal Chem*. 2006;78(19):6980-9.
- [26] Saheb A, Josowicz M, Janata J. Chemically sensitive field-effect transistor with polyaniline-ionic liquid composite gate. *Anal Chem*. 2008;80(11):4214-9.
- [27] Aydogdu S, Ertekin K, Suslu A, Ozdemir M, Celik E, Cocen U. Optical CO₂ sensing with ionic liquid doped electrospun nanofibers. *J Fluoresc*. 2011;21(2):607-13.
- [28] Hou KY, Rehman A, Zeng X. Study of ionic liquid immobilization on polyvinyl ferrocene substrates for gas sensor arrays. *Langmuir*. 2011;27(8):5136-46.
- [29] Zevenbergen MA, Wouters D, Dam VA, Brongersma SH, Crego-Calama M. Electrochemical sensing of ethylene employing a thin ionic-liquid layer. *Anal Chem*. 2011;83(16):6300-7.
- [30] Chen L, Zhang Y, Ren S, Huang D, Zhou C, Chi Y, et al. An ionic liquid-mediated electrochemiluminescent sensor for the detection of sulfur dioxide at the ppb level. *Analyst*. 2013;138(22):7006-11.
- [31] Murugappan K, Silvester DS. Sensors for highly toxic gases: methylamine and hydrogen chloride detection at low concentrations in an ionic liquid on Pt screen printed electrodes. *Sensors (Basel)*. 2015;15(10):26866-76.
- [32] Wang Z, Guo M, Mu X, Sen S, Insley T, Mason AJ, et al. Highly sensitive capacitive gas sensing at ionic liquid-electrode interfaces. *Anal Chem*. 2016;88(3):1959-64.

- [33] Tseng MC, Chu YH. Chemoselective gas sensing ionic liquids. *Chem Commun (Camb)*. 2010;46(17):2983-5.
- [34] Liu YL, Tseng MC, Chu YH. Sensing ionic liquids for chemoselective detection of acyclic and cyclic ketone gases. *Chem Commun (Camb)*. 2013;49(25):2560-2.
- [35] Tseng MC, Chu YH. Reaction-based azide gas sensing with tailored ionic liquids measured by quartz crystal microbalance. *Anal Chem*. 2014;86(4):1949-52.
- [36] Garcia-Hartjes JD, J.; Wennekes, T.; van Delft, F. L.; Zuilhof, H. Electronic effects versus distortion energies during strain-promoted alkyne-azide cycloadditions: a theoretical tool to predict reaction kinetics. *Eur J Org Chem*. 2013;18:3712–20.
- [37] Li HY, Hsu TH, Chen CY, Tseng MC, Chu YH. Exploring silver ionic liquids for reaction-based gas sensing on a quartz crystal microbalance. *Analyst*. 2015;140(18):6245-9.

Application of Ionic Liquids in Paper Properties and Preservation

Koziróg Anna and Wysocka-Robak Agnieszka

Additional information is available at the end of the chapter

<http://dx.doi.org/10.5772/65860>

Abstract

For centuries, paper has been an important medium of information. Currently, the basic risk to the paper collection is “acidic paper” and the action of enzymes secreted by microorganisms on them. In order to ‘prolong life’ of these materials, in recent years, various chemical compounds have been used. In this chapter, ionic liquids (IL) are explored as substances for deacidification of paper and its conservation, including antifungal activity. The use of these substances in the manufacturing of paper is possible, but the ingredients play an important role. Imidazolium IL cause an increase in the pH (deacidification) of historical papers and do not cause worsening of their strength properties, but these compound can cause a colour change. Benzalkonium DL-lactate and didecyldimethylammonium DL-lactate and derivatives of 1,2,4-triazole are used as effective inhibitors of growth of moulds on paper. The best antifungal activity in these ionic liquids is observed in the paper pine at a concentration of 5% and weakest in the samples from the pulp after chemical-thermomechanical treatment. New paper impregnated with ionic liquids is characterised by an increase in tear resistance, reduction of breaking length and a favourable influence on the paper colour.

Keywords: ionic liquids, paper deacidification, antifungal activity, paper properties

1. Introduction

Since the time of its invention, paper has been an essential carrier of historical, cultural, economic and scientific information. However, for the past several decades, paper has been facing competition with electronic media. Nevertheless, the majority of human knowledge and artworks of an inestimable historical value are recorded on paper.

Until the nineteenth century, paper was manufactured by craftwork in an alkaline environment, using pulped rags with highly polymerised cellulose. The increasing demand for paper was the reason for its production on an industrial scale, using wood fibres, commenced in the nineteenth century. Paper obtained in this manner is characterised by a lower degree of polymerisation and acidic pH (pH = 4.5–5.5), which additionally increases the rate of cellulose depolymerisation. This process is also assisted by microorganisms, in particular, moulds producing cellulolytic enzymes. All these factors adversely affect the durability and quality of the paper, resulting in reduced ageing resistance [1, 2].

In recent years, paper manufacturers have replaced the applied technologies with acid-free methods. However, the problem of accumulated vast collections of acidic paper in archives and libraries remains. Due to the extent of this problem, many million tonnes of paper collections are to be protected. Intensive measures are being taken on a global scale to preserve our heritage. A range of methods has been developed for deacidification on a large scale and for the partial preservation of the archive collections, but none of the methods devised thus far meet the expectations.

The factors causing paper degradation can generally be divided into endogenous—acidity, metal ions and lignin; and exogenous—UV radiation, humidity, pollutants and microorganisms. As previously mentioned, moulds dominate among the latter. Additionally, the quality of paper materials can be deteriorated by bacteria; however, bacteria, as compared with moulds, require more humidity for growth. Environmental conditions typically present in libraries, archives and museums are more suitable for the growth of moulds than bacteria.

Various chemical compounds are used in order to prevent the above-described factors from creating favourable conditions for paper degradation. They are paper disinfection, deacidification and coating. The substances used during the processes should provide a good chemical stability and ensure cost efficiency. They cannot be toxic to humans and the environment. Also, the effect on the material is important as it cannot undergo any negative changes. As antimicrobial agents, they should be characterised by a wide spectrum of action at low concentrations and in a short period of time [3, 4].

While selecting an agent for paper protection in the broad sense, one must bear in mind that the agent must possess marketing authorisation. Regulation (EU) No. 528/2012 of the European Parliament and of the Council of 22 May 2012, concerning the making available in the market and use of biocidal products has been in force since 1 September, 2013 [5].

In recent years, attention has been paid to chemical compounds generally known as ionic liquids (ILs), many of which show promising properties with the potential for use in the paper industry [6]. These are chemically, electrochemically and thermally stable compounds, which do not decompose at high temperatures. Due to low volatility, they are also recognised as environmentally sound. Moreover, they are characterised by incombustibility, antimicrobial activity or pH buffering capability [6–10].

2. Ionic liquids as neutralisers of acid paper

The reason for paper instability can be sought in two improvements that were introduced in the nineteenth century: a new method of paper sizing and a change in raw material. Paper sizing, necessary to obtain a writable surface, was improved by means of an adhesive added to the pulp before forming a paper sheet or band. Sizing with a resin adhesive added to the pulp required an additive such as aluminium sulphate as a coagulating agent. In an aqueous environment, the compound undergoes hydrolysis; as a result, sulphuric acid is produced, leading to an acidic reaction of the paper-pulp-water suspension. In addition, this causes continuous cellulose depolymerisation in the finished product. With the development of wood-based method of manufacturing, the quality of the manufactured paper product began to worsen compared to that of the paper that was until then manufactured using long, fibrous rag pulp. One of the problems faced today is disintegration of pages in books and documents that were printed in the nineteenth and twentieth century; however, the incoming flow of such materials to libraries and archives was fortunately stopped by new, less expensive and acid-free methods of paper manufacturing, which developed towards the end of the twentieth century [11–14].

The internal factor causing deterioration of paper properties with time is its chemical composition, and the factors are:

- type of the fibrous pulp used to produce paper (wood or wood-less pulp, fibre length, degree of polymerisation, cellulose content, lignin content)
- ancillary agents used during paper production (the amount of aluminium sulphate as an additive for paper sizing in pulp with resin adhesives should not exceed 5% in terms of the input mass of fibrous raw materials)

Symptoms of paper ageing mostly include yellowing and structure weakening (brittleness), resulting in some extreme cases in a complete lack of mechanical resistance. Paper ageing is a very complex process, because of the non-homogeneous composition of this fine material. According to the recent research, paper degradation and ageing are believed to mostly attribute to autocatalytic reactions of acid hydrolysis and oxidation, i.e. processes accelerated by protons and active oxides, respectively [12, 15–21].

During acid hydrolysis, cellulose chains are torn apart into smaller pieces, which results in the following two phenomena:

- shorter average chain length, and as such—reduced paper tearing resistance;
- on both ends of the torn polymer chain, there are active groups which easily attach to the adjacent cellulose chains resulting in improved structural cross-linking, which enhances structural stiffness and the paper becomes brittle.

Cut cellulose fragments may also undergo oxidation to form carboxylic acids, such as formic acid and acetic acid. These organic acids reduce paper pH and accelerate acidic hydrolysis reactions, providing fuel to other reactions and causing autocatalytic degradation in paper.

Acidic hydrolysis is one of the most dangerous degradation reactions, which happens in libraries and archives worldwide [20–24].

There are millions of materials printed on unstable paper lying in libraries, archives and museums. In order to save and protect them from damage and disintegration into pieces, some methods have been developed which slow down cellulose degradation, namely deacidification, which involves introduction of excess alkali into the paper structure to prevent decomposition—the so-called alkaline reserve. In addition, to extend paper lifetime, objects undergoing deacidification are protected from acid-forming air components, and deacidification is combined with reinforcement of partially degraded paper (filling up material losses, patching, lamination) [12].

Features of a perfect deacidification method [11, 25] are as follows:

- it should be effective, ensuring that the deacidification substance can penetrate into the book or document;
- paper deacidification should take place within the entire thickness;
- it should leave permanent alkaline reserve in the paper to provide pH close to 8.5;
- it should not adversely affect any material in the book (paper, adhesives, printing inks, writing inks, illustration paints, leather and leather-like elements);
- it should not cause any formation of deposits on the surface left after deacidification;
- it should not cause any permanently unpleasant odour;
- it should be suitable for deacidification of any object regardless of the type of paper, its format and the degree of degradation;
- it should not leave any visible or sensible sign after the treatment;
- applied deacidification agents cannot sensitise paper to light or be allergic for humans;
- it should not adversely affect the environment;
- it should be efficient in use, inexpensive and available at the site where the collections at risk are stored;
- the deacidification agent should not promote flammability, hygroscopicity or paper susceptibility to microorganisms; and
- it should result in paper purification and strengthening.

There are many deacidification methods in the world; however, none of them can meet all of the mentioned requirements simultaneously. The application of ionic liquids in paper preservation increases great hopes. The discussed group of compounds appears to be promising in terms of their ability to change acidic pH of the paper as well as disinfection (removal of microorganisms) and disinsectisation (removal of insects and rodents).

The presented tests verified whether the selected ionic liquids had a deacidification effect on 'acidic paper', whether they could change pH from acidic ($\text{pH} < 7$) to alkaline ($\text{pH} > 7$).

For test purposes, paper materials from old books were used (designated as A1 and A2 in the following text, **Table 1**). While selecting the materials for tests, the following criteria were applied: age of the book—publication year before 1970, i.e. age > 45 years; pH < 7 and the raw material composition—different content values of groundwood and cellulosic pulp.

Paper	Age	pH [-]	Fibrous composition
A1	48	2.83 ± 0.16	30% cellulose pulp and 70% groundwood
A2	56	4.75 ± 0.27	100% cellulose pulp

Table 1. Samples' fibrous composition and pH.

Solutions of the tested ionic liquids were prepared by dilution of 50% alcoholic solutions of ionic liquids using an appropriate amount of isopropyl alcohol (IPA).

The paper samples were impregnated using two methods. The first one was carried out on petri dishes for the liquids [C₄mim] [Bt] (1-butyl-3-methylimidazolium benzotriazol) and [C₄mim] [Tr] (1-butyl-3-methylimidazolium 1,2,4-triazolate). The ionic liquid was applied on the paper with a pipette (**Table 2**). Then, the paper was put aside for 24 h. As this method failed to be effective for the liquid [DDA][DL-lactate] and the impregnation was not complete, another impregnation method was employed using a closed container instead of a petri dish (**Table 3**). These samples were also put aside for 24 h (the container provided constant temperature and relative humidity during impregnation). After 24 h of impregnation, the samples were transferred onto petri dishes for another 24 h to remove the solvent (IPA) that evaporated naturally. This procedure enabled to obtain paper samples impregnated only with ionic liquids.

Ionic liquids	Paper			
	A1		A2	
	G [g/m ²]	Z [cm ³ /g]	G [g/m ²]	Z [cm ³ /g]
[C ₄ mim] [Bt] and [C ₄ mim] [Tr]	60	0.50	120	0.25
	60	1.50	120	0.75
	60	2.50	120	1.25
	60	3.50	120	1.75
	60	4.00	120	2.00

Note: G, paper grammage, g/m²; Z, consumption of ionic liquid solutions per 1 g impregnated paper.

Table 2. The consumption of ionic liquid solutions per 1 g impregnated paper (petri dish).

Ionic liquids	Paper			
	A1		A2	
	G [g/m ²]	Z [ml/g]	G [g/m ²]	Z [ml/g]
[DDA] [DL-lactate]	60	5.00	120	2.50
	60	6.00	120	3.00
	60	7.00	120	3.50
	60	8.00	120	4.00
	60	9.00	120	4.50

Note: G, paper grammage, g/m²; Z, consumption of ionic liquid solutions per 1 g impregnated paper.

Table 3. The consumption of ionic liquid solutions per 1 g impregnated paper (closed container).

After impregnation of the A1 and A2 paper samples, the pH values were changed using the ionic liquids [C₄mim] [Bt] and [C₄mim] [Tr] at concentrations of 1–8%, and the solutions [DDA] [DL-lactate] (didecyldimethylammonium DL-lactate) at concentrations of 10–20%, as presented in **Table 4**.

Concentration of the solution %	Paper A1			Paper A2		
	pH 24 h after impregnation			pH 24 h after impregnation		
	[C ₄ mim] [Bt]	[C ₄ mim] [Tr]	[DDA] [DL-lactate]	[C ₄ mim] [Bt]	[C ₄ mim] [Tr]	[DDA] [DL-lactate]
1	4.96	4.39	–	5.99	5.66	–
3	7.55	5.76	–	7.24	7.59	–
5	7.56	7.93	–	8.09	7.83	–
7	9.01	8.02	–	8.45	7.92	–
8	9.60	8.13	–	9.22	7.98	–
10	–	–	4.05	–	–	4.61
12	–	–	4.11	–	–	4.60
14	–	–	4.14	–	–	4.62
16	–	–	4.16	–	–	4.65
18	–	–	4.24	–	–	4.68
20	–	–	4.34	–	–	4.59

Table 4. pH values of samples after impregnation of solutions of [C₄mim] [Bt]; [C₄mim] [Tr] and [DDA][DL-lactate].

Based on the results of A1 and A2 paper impregnation, it was found that the ionic liquid [C₄mim] [Bt] showed high capability of deacidification of acidic paper. In the case of both A1 and A2 paper samples, the 3% solution of the compound used for impregnation increased pH of the objects undergoing deacidification to more than 7, from 2.83 (A1 paper) and 4.85 (A2 paper), respectively. Moreover, it was observed that the increase in the concentration of the [C₄mim] [Bt] solution resulted in a noticeable rise in paper pH after impregnation. The

liquid [C₄mim] [Tr] proved to be a slightly less effective in deacidification. As a result of impregnation of the A1 and A2 paper samples with this liquid at 5% concentration, their pH values increased to more than 7. However, when [C₄mim] [Tr] at a concentration over 5% was used, pH of the A1 and A2 samples after implementation practically did not change and remained to be approximately 8.

Different results were obtained for [DDA] [DL- lactate], which was applied at a concentration of 10–20%, increasing pH of the A1 paper after impregnation from 2.83 to 4.05–4.34, respectively. For the A2 paper, its pH after impregnation practically did not change. For both the A1 and A2 papers, the pH value after impregnation remained at a practically constant level, independently of the applied concentration of the ionic liquid solution.

Due to the fact that neutralisation of acid paper should not leave any visible or detectable sign, once the treatment was completed, the effect of the ionic liquids on colouring substances as well as appearance and odour of the paper were checked.

Paper impregnated with solutions of the ionic liquids [C₄mim] [Bt] and [C₄mim] [Tr] was not affected in terms of print, odour and texture—no textural changes were noticed in the paper. Paper was not deformed either (no creasing or rolling occurred). Unfortunately, the liquids reduced non-transparency of the paper during impregnation; however, once the solvent evaporated, transparency was restored to the initial state. In addition, printing inks from illustrations spilled out and dyed the paper. While observing the paper after impregnation in a closed container, however, it was found that [DDA] [DL-lactate] did not damage the print and the paper experienced no deformation during impregnation. As an effect of the solution of the liquid discussed above, the impregnated paper permanently lost its non-transparency.

Based on the results, it was concluded that, among the tested ionic liquids, [C₄mim] [Tr] and [C₄mim] [Bt] turned out to be effective in paper deacidification. The compounds changed paper pH to alkaline when solutions at a concentration exceeding 3% were used.

Paper deacidification is just preventive because paper degradation can be only stopped, not reversed. Unfortunately, basic deacidification methods fail to meet all the parameters which determine whether the method is effective or not. Nevertheless, ionic liquids create a new perspective in this area.

3. Effect of ionic liquids on paper properties

The application of chemical compounds to paper is only possible provided its original parameters can be maintained. Any change in properties of this organic material can contribute, for instance, to quality deterioration of particularly valuable antique works created on paper. Therefore, the effect of ionic liquids on selected optical and strength properties of the material was checked. For this purpose, hand sheets made of bleached pine pulp, recycled pulp and CTMP were used. The pine pulp beating was carried out in a valley beater according to ISO 5264-1:1979 [26]. Paper test sheets of approximately 70 g/m² were made under

laboratory conditions using the Rapid-Köthen apparatus in accordance with ISO 5269-2:2004 [27]. The test sheets were conditioned in accordance with ISO 187:1990(E) [28].

Then, the prepared paper was treated with ionic liquids: benzalkonium nitrate [BA][NO₃]; benzalkonium [BA][DL-lactate] and didecylodimethylammonium DL-lactate at a concentration of 3% and 8%. The paper samples underwent impregnation on petri dishes by analogy to the deacidification process.

3.1. Paper impregnation with ionic liquids versus paper brightness

Paper brightness is determined as a percentage ratio of the light reflected from the paper surface to the diffused light reflected from the surface of the masterpiece, the brightness of which is assumed to be 100%. Brightness was determined using SpectroEye supplied by GretagMacbeth, in accordance with ISO 11475:2004 [29].

Figure 1 shows a small increase in paper brightness as the effect of ionic liquids. In case of the pine pulp paper, lactates proved to be the most effective, although the effect depended on their concentration.

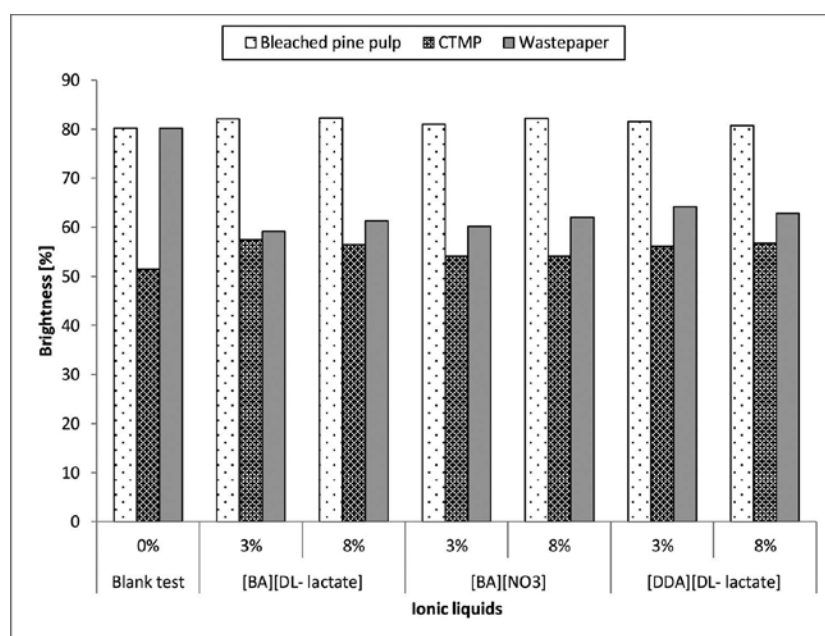


Figure 1. The brightness of paper impregnated with ionic liquids vs. blank test.

For [BA][DL-lactate], the highest brightness was obtained when the concentration was 8%, and for [DDA][DL-lactate]—a lower concentration was effective. The CTMP paper showed a regular increase in brightness as a result of each of the three applied compounds. In turn, the recycled paper obtained the highest increase in the parameter when [DDA][DL-lactate] was used.

3.2. Change in paper opacity after impregnation with ionic liquids

Paper opacity is an important performance parameter of publishing and packaging paper materials; it determines the resistance of paper against light penetration. This parameter is reciprocal to visible light penetration. It characterises non-transparent paper as completely impenetrable to visible light. The parameter was determined according to ISO 2471:2008 [30].

It is required that printing papers should feature the highest possible opacity because this enhances print legibility and aesthetics. Opacity of all tested papers—bleached pine pulp, CTMP and wastepaper—which were impregnated with ionic liquids, remains at a similar level (Table 5). A small 3–5% increase in opacity was observed for the pine pulp paper for all three tested compounds.

Ionic liquid	Concentration	Opacity [%]		
		Bleached pine pulp	CTMP	Wastepaper
Blank test	–	81.3	98.9	77.1
[BA][DL-lactate]	3%	84.8	99.1	100.0
	8%	84.3	99.4	99.2
[BA][NO ₃]	3%	84.6	99.3	100.0
	8%	84.3	97.9	99.1
[DDA][DL-lactate]	3%	84.5	98.2	98.6
	8%	86.4	98.4	98.6

Table 5. The opacity tested papers.

3.3. Effect of paper impregnation with ionic liquids on breaking length

Another very important paper parameter is its breaking length. It should be emphasised that this parameter is not measured but it is calculated from tensile force at break, according to ISO1924-1:1992 [31]. Nevertheless, in papermaking field, the breaking length, not the tensile force, is used as one of the key parameters for characterising end-use properties of paper. Breaking length is generally used in the paper trade to characterise the inherent strength of paper. The breaking length is the paper strip length at which the sample would break by its own weight, if suspended vertically from one end. It affords an excellent basis for comparing the strength of papers made from different furnishes and having different basis weight.

All the three ionic liquids—benzalkonium nitrate [BA][NO₃]; benzalkonium lactate [BA][DL-lactate] and didecyldimethylammonium DL-lactate [DDA][DL-lactate]—reduced breaking length, compared to non-impregnated samples (Figure 2). Also, concentrations of the compounds play a significant role. As the concentration rises, breaking length of the paper sample decreases.

However, it must be emphasised that the average breaking length of publishing paper materials reaches approximately 2000 m, and hence impregnation with 3% compounds does

not disqualify any paper, except CTMP. While soaking with ionic liquids, the material structure was slackened, so that breaking length measurement could not be taken.

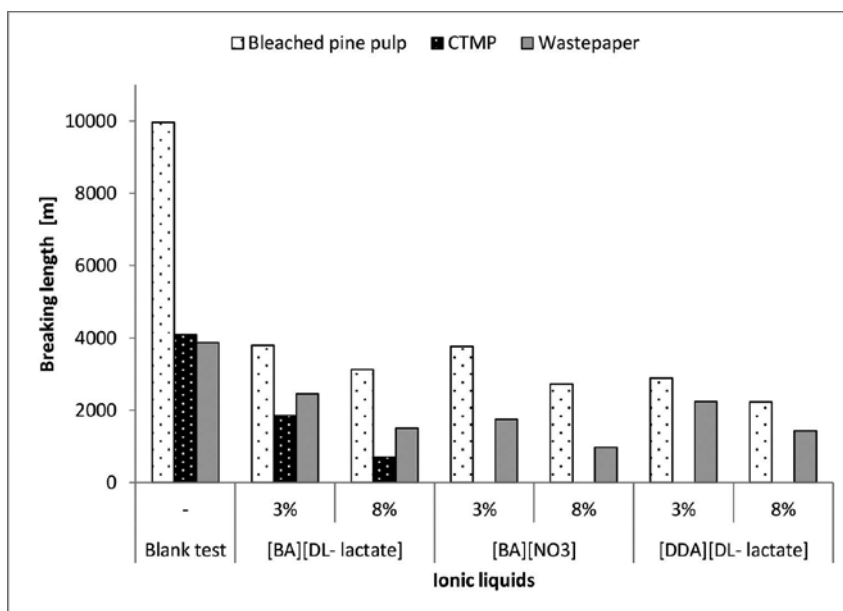


Figure 2. The breaking length of paper impregnated with ionic liquids vs. blank test.

3.4. Changes in tear resistance of the paper impregnated with ionic liquids

Tear resistance is the force required to tear a notched paper sample. This property depends on the length of fibres and their longitudinal or transversal arrangement. The result of tear resistance after application of ionic liquids on the paper samples was determined according to ISO 1974:1990 [32] as presented in Figure 3.

By the effect of [BA][NO₃], tear resistance of pine and wastepaper pulp (impregnation with a 3% solution) increases; for CTMP, compared with samples without ionic liquids, the value decreases. Tear resistance of the pine pulp paper, impregnated with [BA][DL-lactate] at a higher concentration, is also higher, compared to the non-impregnated paper. For the wastepaper pulp, it was found that tear resistance increased as concentrations of all three ionic liquids decreased.

3.5. Summary

Benzalkonium nitrate [BA][NO₃]; benzalkonium lactate [BA][DL-lactate] and didecyldimethylammonium DL-lactate [DDA][DL-lactate], as representatives of ionic liquids, showed a beneficial effect on paper optical properties. Depending on the ionic liquid concentration, paper brightness changes; higher concentration results in higher brightness. Also, raw material

composition of the tested papers plays a significant role. The highest brightness was encountered in the case of the pine pulp paper, whereas the highest opacity was observed for the CTMP paper. The paper samples impregnated with ionic liquids were characterised by worse static properties; however, dynamic strength properties were improved.

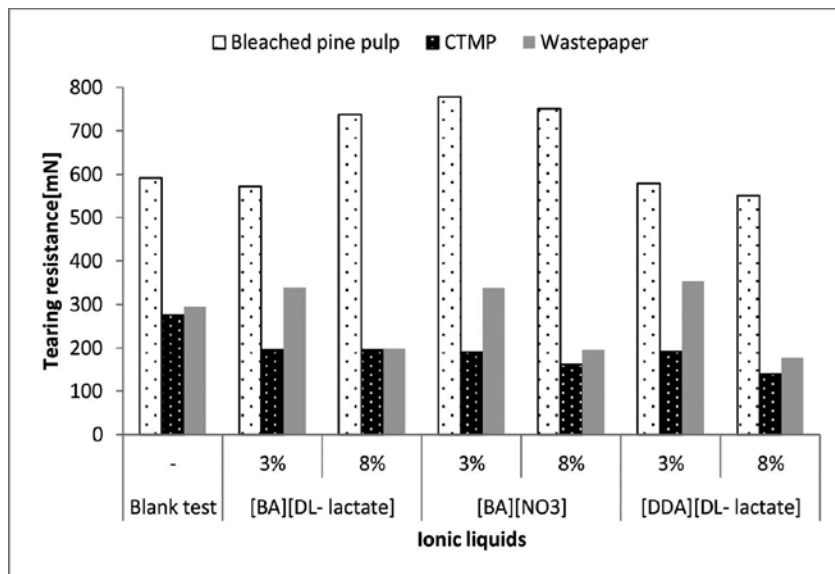


Figure 3. The tearing resistance of paper impregnated with ionic liquids vs. blank test.

The ionic liquids used in the research cause a high reduction in breaking length, which clearly depends on the concentration. Higher concentrations result in lower breaking length. It may be supposed that the change in this property by the effect of ionic liquids results from slackening of the structure and breaking bonds between fibres, which reduces paper strength.

In the case of paper impregnated with ionic liquids, an increase in tear resistance was observed. The best results were obtained for the pine pulp paper samples impregnated with [BA][NO₃].

4. Application of ionic liquids in protecting paper from the growth of microorganisms

Paper is an easily biodegradable material. It is particularly susceptible to microbiological decomposition as its main component—cellulose—is a polymer decomposed by many microorganisms, among which moulds are the most active group. They participate in oxygenic paper decomposition through the production of extracellular cellulases. Initially, moulds from the *Aspergillus*, *Penicillium*, *Trichoderma* and *Fusarium* genera, which require a less humid substrate, take part in the process. As the source of nutrients, they use components present in paper and, simultaneously, they prepare the substrate for other fungi—*Alternaria*, *Chaetomi-*

um and *Stachybotrys*—which, in turn, require higher humidity, but are capable of hydrolysis of resistant cellulose fibres. Cellulose decomposition can completely disqualify finished paper products since the degree of cellulose polymerisation is decreased by the activity of cellulolytic enzymes. An impairment of structure of the cellulosic fibre results in its reduced strength, and hence in the complete decomposition [33–35]. However, one must bear in mind that there are plenty of various types of paper in the world, and not every type is susceptible to microorganisms to the same extent. Paper biodegradation is affected by technological parameters of the material, the manufacturing process and environmental factors [36–38].

In recent years, biocides have been used more and more often and to a greater extent. They are used not only for disinfection, but also for finishing processes in cellulosic materials, and thus the latter may become less susceptible to the destructive action of microorganisms. Also, antimicrobial agents are used to protect different paper forms (books, photographs, paintings) stored in libraries, archives and museums [2, 15, 36, 39].

The aim of the presented study is to determine the antifungal activity of ionic liquids which, once added, protect paper from the growth of moulds.

4.1. Minimal concentrations of ionic liquids inhibiting the growth of moulds

Two of basic parameters determined during the control of the antimicrobial activity of various chemical compounds or mixtures are minimal inhibitory concentration (MIC) and minimal bactericidal/fungicidal concentration (MBC/MFC). The former describes the lowest compound concentration that inhibits the growth of microorganisms in the sample. Values of the latter parameter—MBC/MFC—refer to the lowest concentration of the antimicrobial agents required to reduce the viability of 99% microorganisms. In research on the antimicrobial activity of ionic liquids, these two parameters are determined most frequently, as reported in references [8, 10, 40–43]. Primary research methods used to determine MIC/MBC/MFC values include dilution tests and agar diffusion tests [10, 44].

To date, most of the research has focused on bacteria and yeast, while the biodegradation of paper is most frequently caused by moulds. For that reason, in course of authors' own research [45], the effect of the following ionic liquids on moulds was verified: benzalkonium DL-lactate [BA][DL-lactate], didecyldimethylammonium DL-lactate [DDA][DL-lactate], benzalkonium nitrate [BA][NO₃], 1-butyl-3-methylimidazolium benzotriazole [C₄mim][Bt], 1-dodecyl-3-methylimidazolium benzotriazole [C₁₂mim][Bt], and 1-butyl-3-methylimidazolium 1,2,4-triazolate [C₄mim][Tr].

Based on the results, it has been concluded that there are three compounds inhibiting the growth of moulds at concentration up to 100 ppm: lactates and nitrates (Table 6). Among them, the best antimicrobial properties were demonstrated by [DDA][DL-lactate], the MIC values of which were in the range of 19.5–78.2 ppm. Within the group of imidazole-based ionic liquids, the lowest MIC values were obtained for 1-dodecyl-3-methylimidazolium benzotriazole, which was effective at 30- to 60-fold lower concentrations compared to two other compounds—[C₄mim][Bt] and [C₄mim][Tr].

Ionic liquids	Mould strains				
	<i>A. niger</i> ATCC 16404	<i>A. terreus</i> ATCC 10020	<i>A. versicolor</i> ATCC 9577	<i>P. aurantiogriseum</i> ATCC 18382	<i>P. chrysogenum</i> ATCC 60739
I GROUP					
[BA] [DC-lactate]	78.2	39.1	39.1	78.2	78.2
[DDA] [DC-lactate]	78.2	39.1	39.1	39.1	19.5
[BA][NO ₃]	156.3	39.1	39.1	78.2	39.1
II GROUP					
[C ₁₂ mim][Bt]	107.9	107.9	107.9	215.8	107.9
[C ₄ mim][Bt]	3439.5	3439.5	3439.5	6879	6879
[C ₄ mim][Tr]	6145	6145	6145	>6145	6145

Table 6. Value of minimal inhibitory concentration [ppm] [45].

Taking the strains of the investigated moulds into account, it was *Aspergillus niger* that was found least susceptible to the action of ionic liquids in Group 1. For imidazoline ionic liquids in Group 2, the highest MIC values were recorded for two strains of the genus *Penicillium*.

The ionic liquids used in the research show good antifungal activity, but their effectiveness essentially depend on the molecular structure. The lowest MIC values were obtained for didecyldimethylammonium DL-lactate and 1-dodecyl-3-methylimidazolium benzotriazole. These are compounds, the structures of which contain long alkyl chains responsible for the antimicrobial activity of the compounds. The results are confirmed by the work conducted by Dembereinyamba et al., who managed to determine MIC values of quaternary 1-alkyl-3-methylimidazolium compounds against bacteria, yeasts and algae. The lowest values were obtained for compounds containing 12–14 carbon atoms in the alkyl chain. The relationship between MIC and the length of the alkyl chain in ionic liquids was also repeatedly as proven by Refs. [9, 41]. Overall, it was found that the highest antimicrobial activity across all the groups of ionic liquids is obtained for the compounds with an alkyl chain substituent of 12 carbon atoms on the cation.

4.2. Evaluation of the antifungal activity of paper modified with ionic liquids

A series of testing methods have been developed for the evaluation of antimicrobial properties of paper; the differences lie in the intended use of the tested paper materials, time of exposure to microorganisms, and their physical properties. Selecting adequate microorganisms, depending on the chosen testing method is also an important element of the tests.

The methods to evaluate the bioactive effect on paper products can be divided into quantitative and qualitative. They are described in various standards developed by, for instance, ASTM International (ASTM E723, ASTM E875, ASTM E1839, ASTM D2020) and the Technical Association of the Pulp and Paper Industry (TAPPI T449, TAPPI T487) [4]. For paper testing,

the standards developed by the Association of Textile, Apparel & Materials Professionals (AATCC 100, AATCC 147) are followed as well.

4.2.1. Antifungal activity of paper: qualitative method

The qualitative methods are used to determine the bioactivity of paper materials containing biocides and make it possible to evaluate the bacteriostatic and fungistatic properties. The methods essentially consist in placing a paper sample on an agar substrate with cultivated microorganisms with the appropriate density of inoculum. If the tested paper shows antimicrobial properties, a zone where the growth of microorganisms under the sample and around it has been inhibited, will be present. The usual good effect of the biostatic action of paper for this method is indicated by the lack of growth of microorganisms in the sample.

In course of authors' own research [35], paper samples were soaked with four of the most effective ionic liquids: benzalkonium DL-lactate [BA][DL-lactate], didecyldimethylammonium DL-lactate [DDA][DL-lactate], benzalkonium nitrate [BA][NO₃] and 1-dodecyl-3-methylimidazolium benzotriazole [C₁₂mim] [Bt]—at concentration of 3% and 5%. Next, the spore suspension (10⁶ conidia/mL) was placed on petri dishes containing malt extract agar (Merck). Prepared paper stripes with ionic liquids were then placed there one by one. The dishes were incubated at 28°C for 24–72 h. Once the experiment was completed, the efficiency of ionic liquids action on the paper against the moulds was evaluated. The growth of microorganisms between the medium and the tested sample was checked for this purpose. In addition, the inhibition zones around the sample relative to the reference sample without ionic liquids were determined. The results are presented in **Table 7**.

It was found that the ionic liquids in the paper at concentration of 3% do not show potent antifungal properties against the tested species. A very good antifungal activity relative to the studied strains was not obtained until compounds at concentration of 5% were used. The best antifungal activity among the four biocides was demonstrated by 1-dodecyl-3-methylimidazolium benzotriazole. For the *Aspergillus terreus* strain—the most sensitive one among the studied strains—growth inhibition zones on pine paper are more than 4-fold higher compared with the *Aspergillus niger* strain. The tested microorganisms can be ordered according to their decreasing sensitivity as follows: *Aspergillus niger* > *Penicillium aurantiogriseum* > *Penicillium chrysogenum* > *Aspergillus versicolor* > *Aspergillus terreus*.

Taking the type of paper into account, the largest inhibition zones were observed for pine paper, whereas the smallest for CTMP paper. CTMP paper, obtained using cellulosic mass after chemical-thermo-mechanical treatment with the tested compounds at concentration of 3%, showed limited antimicrobial activity against *A. niger* and *P.aurantiogriseum*. For pine paper, the growth inhibition zones of the mentioned strains were twice as large compared with the CTMP paper.

The interpretation of the results in qualitative methods is based on an analysis of the growth inhibition zone, which can indicate not only high antimicrobial activity of the tested paper materials, but also the weak binding of the biocide with the surface of the material in question. Also in the TAPPI T487 test, the evaluation of paper resistance to moulds involves

macroscopic observation. Despite the fact that they are less labour consuming, qualitative methods should not be the final tests aimed to obtain result at the antimicrobial evaluation of selected materials.

Mould strains	Kind of paper	Kind of ionic liquid							
		[BA] [DL-lactate]		[DDA] [DL-lactate]		[BA][NO ₃]		[C ₁₂ mim] [Bt]	
		3	5	3	5	3	5	3	5
<i>A. niger</i> ATCC 16404	Bleached pine pulp	1	2	3	5	3	4	1	2
	Wastepaper	1	2	2	3	2	3	1	2
	CTMP	0	2	0	2	0	2	0	1
<i>A. terreus</i> ATCC 10020	Bleached pine pulp	6	9	4	6	8	10	13	16
	Wastepaper	6	8	5	6	7	9	12	14
	CTMP	4	6	3	4	5	7	10	10
<i>A. versicolor</i> ATCC 9577	Bleached pine pulp	7	10	4	6	10	11	5	7
	Wastepaper	7	8	4	5	7	9	5	8
	CTMP	4	7	3	5	7	10	2	4
<i>P. aurantiogriseum</i> ATCC 18382	Bleached pine pulp	3	4	4	4	3	5	5	6
	Wastepaper	1	3	3	3	4	4	3	4
	CTMP	0	3	0	2	2	3	2	3
<i>P. chrysogenum</i> ATCC 60739	Bleached pine pulp	4	5	3	4	5	6	4	6
	Wastepaper	4	5	2	3	4	5	4	5
	CTMP	3	4	2	3	3	5	3	4

Table 7. Growth inhibition zones [mm] observed for moulds under the influence of ionic liquids contained in paper samples [35].

4.2.2. Antifungal activity of paper: quantitative method

In the next stage of the study, the changed amount of conidia on paper samples with ionic liquids within 24 h was determined. For the test purposes, *A. niger* was selected as a strain which is least susceptible to ionic liquids, and the CTMP paper and pine BKP paper containing benzalkonium DL-lactate [BA][DL-lactate], didecylodimethylammonium DL-lactate [DDA][DL-lactate], benzalkonium nitrate [BA][NO₃] at concentrations of 3 and 5% were used. Papers without biocide constituted reference samples. On each paper sample, 0.1 mL

of conidia suspension (10^7 conidia/mL) was placed in petri dishes. The dishes with the samples were incubated for 24 h at 28°C and the relative humidity RH of 80%. After 0, 3, 6, 12 and 24 h, the samples were shaken in a saline solution with a neutraliser in order to leach microorganisms from the test material. Next, the suspension was diluted and transferred onto petri dishes and the MEA (Merck) medium was poured them. The dishes were incubated at 28°C, RH 80%, for 72 h. Taking the dilutions into account, it was possible to calculate the conidia that survived on the paper surface. The results were presented as log conidia per paper cm^2 in **Figures 4** and **5**.

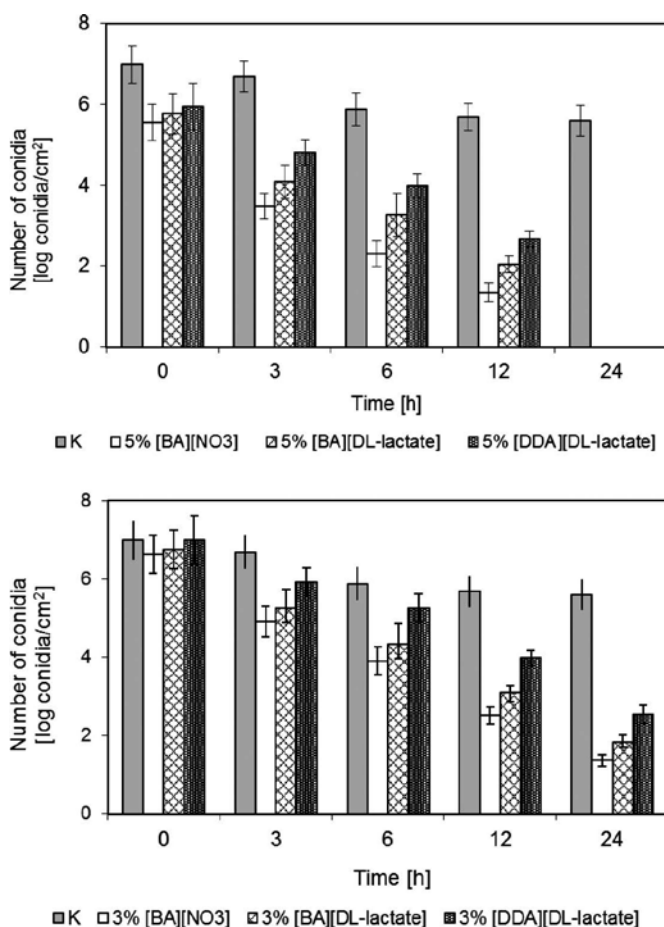


Figure 4. Changes the number of conidia on the surface of the tested paper stripes with CTMP modified with ionic liquids. Concentration of ionic liquids in the samples: (a) 5% and (b) 3% [35].

Active conidia (see **Figure 4**) were still observed after 24 h on the paper made of CTMP pulp with an addition of each of the three ionic liquids at concentration of 3%. This number decreased by more than 5 log in samples with benzalkonium nitrate and didecyltrimethylammonium DL-lactate. On paper materials modified with didecyltrimethylammonium, DL-

lactate amount of conidia was reduced by 4.5 log and equalled 2.5 log. The reduction of the number of conidia by 4–5 log as the disinfecting effect is high. However, even conidia at such a low concentration (10^2 conidia/sample) in paper with higher humidity can develop into mycelium and cause material destruction. For this reason, ionic liquids were added to other samples in an amount of 5%.

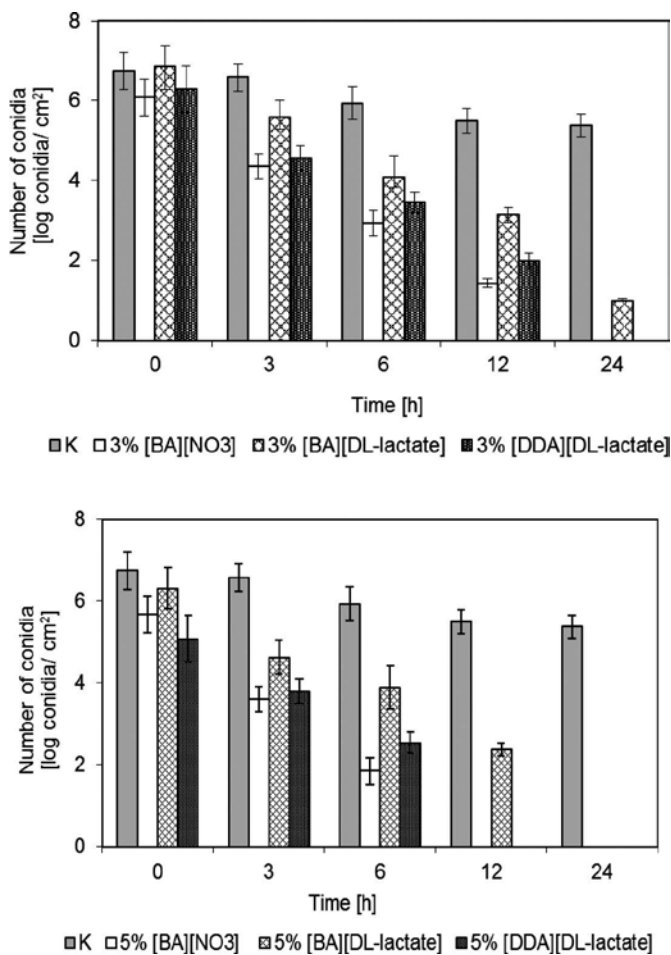


Figure 5. Changes the number of conidia on the surface of the tested paper stripes (pine bleached kraft pulp) modified with ionic liquids. Concentration of ionic liquids in the samples: (a) 3% and (b) 5% [35].

A higher concentration proved to be much more effective. After 24 h, no presence of conidia was found on any paper, except the reference sample (the one without biocide).

The ionic liquids in the pine BKP paper were more reactive compared to the CTMP paper; the same conclusion was drawn during the already presented qualitative tests. For paper materials with 3% [BA][NO₃] or [DDA][DL-lactate], no growth of conidia was observed after 24 h. An exception was presented by [BA][DL-lactate], for which the number of conidia decreased by 6

log compared with the initial concentration, but active forms were still present. The increase in concentration by 2% contributed to a quicker reduction of conidia. After 24 h, no growth of moulds was recorded on any tested paper. As soon as after 12 h, the reduction of active conidia amounted to 100% for the samples with [BA][NO₃] and [DDA][DL-lactate]. The number of spores within the period reached 2.4 log for paper materials with the additive of [BA][DL-lactate].

5. Conclusion

In recent years, ionic liquid have enjoyed more and more interest, both in research and in practical applications. Their various aspects are discussed, such as antimicrobial properties [8, 10, 42, 46] used in histopathologic diagnostics [47], in paper protection [6] and in wood preservation [48]. In the presented research, ionic liquids were used as an additive to paper to neutralise acid paper and as antifungal compounds. Ionic liquids create an alternative to currently used compounds; a great number of combinations (10^{18}) due to their ionic structure is the reason why this type of liquids seems to be an almost inexhaustible resource. Thus, newer and newer compounds with improved properties can be designed, and such compounds can be applied for purposes of paper protection, too.

Acknowledgements

The study was supported by KBN grant 'The research of paper conservation with the use of ionic liquids' N N209 199238.

Author details

Koziróg Anna^{1*} and Wysocka-Robak Agnieszka²

*Address all correspondence to: anna.kozirog@p.lodz.pl

1 Institute of Fermentation Technology and Microbiology, Faculty of Biotechnology and Food Sciences, Lodz University of Technology, Lodz, Poland

2 Institute of Papermaking and Printing, Lodz University of Technology, Lodz, Poland

References

- [1] Wandelt P, The evolution of graphic paper over the centuries and their durability. *Paper Industry Review*. 2010; 9: 21–44 (in Polish).
- [2] Sequeira S, Cabrita EJ, Macedo MF. Antifungals on paper conservation: An overview. *International Biodeterioration and Biodegradation*. 2012; 74: 67–86. DOI:10.1016/j.ibiod.2012.07.011
- [3] Paulus W, editor. *Directory of microbicides for the protection of materials – A Handbook*. 1st ed. Kluwer Academic Publishers; Dordrecht, The Netherlands; 2004. 787 p. DOI: 10.1007/1-4020-2818-0
- [4] Rossmore HW, editor. *Handbook of biocide and preservative use*. 1st ed. Springer, Netherlands; 1995. 425 p. DOI:10.1007/978-94-011-1354-0
- [5] Regulation (EU) no 528/2012 of the European Parliament and of the Council of 22 May 2012 concerning the making available on the market and use of biocidal products. *Official Journal of the European Union L 167/1*, 27.6.2012.
- [6] Przybysz K, Drzewińska E, Stanisławska A, Wysocka-Robak A, Cieniecka-Rosłankiewicz A, Foksowicz-Flaczyk J, Pernak J. Ionic liquids and paper. *Industrial & Engineering Chemistry Research*. 2005; 44(13): 4599–4604. DOI: 10.1021/ie0402315
- [7] Holbrey JD, Seddon KR. Ionic liquids. *Clean Products and Processes*. 1999; 1(4): 223–236. DOI:10.1007/s100980050036
- [8] Demberelnyamba D, Kim K, Choi S, Park S, Lee H, Kim C, Yoo I. Synthesis and antimicrobial properties of imidazolium and pyrrolidinium salts. *Bioorganic & Medicinal Chemistry*. 2004; 12: 853–857. DOI:10.1016/j.bmc.2004.01.003
- [9] Pernak J, Śmiglak M, Griffin ST, Hough WL, Wilson TB, Pernak A, Zabielska-Matejuk J, Fojutkowski A, Kita K, Rogres RD. Long alkyl chain quaternary ammonium-based ionic liquids and potential applications. *Green Chemistry*. 2006; 8: 798–806. DOI: 10.1039/B604353D
- [10] Gilmore BF. Antimicrobial Ionic Liquides. In: Kokorin A, editor. *Ionic Liquides: Application and Perspectives*. 1st ed. InTech; Rijeka, Croatia; 2011.p. 587–604. DOI: 10.5772/13861
- [11] Baty JW, Maitland CL, Minter W, Hubbe MA, Jordan-Mowery SK. Deacidification for the conservation and preservation of paper-based works: A review. *BioResources*. 2010; 5: 1955–2023.
- [12] Łojewski T. Acidic paper. Chemical disaster in libraries. *Paper Industry Review*. 2004; 60: 200–201(in Polish).

- [13] Przybysz K, editor. The technology of pulp and paper. Vol. 2. Paper technology. 2nd ed. WSiP; Warsaw, Poland; 1997. 278p. (in Polish)
- [14] Garlick KA. Brief review of the history of sizing and resizing practices. The Book and Paper Group Annual 5, 1986 [Internet]. 2011. Available form: <http://www.cool.conservaion-us.org/coolaic/sg/bpg/annual/v05/bp05-11.html> [Accessed: 2016-06-30].
- [15] Zervos S, Alexopoulou I. Paper conservation methods: A literature review. Cellulose. 2015; 22: 2859–2897. DOI: 10.1007/s10570-015-0699-7
- [16] Steven R, Middleton SR, Scallan AM, Zou X, Page DH. A method for the deacidification of papers and books. Tappi Journal. 1996; 79: 187–195.
- [17] Zyska B. Permanence of paper in Polish books of the period 1900-1994. Restaurator. 1996; 17: 214–228. DOI: 10.1515/rest.1996.17.4.214
- [18] Podsiadło H, Baranowska A. Natural and artificial aging paper. Paper Industry Review. 2006; 62: 215–218. (in Polish).
- [19] Ahn K, Rosenau T, Potthast A. The influence of alkaline reserve on the aging behavior of book papers. Cellulose. 2013; 20: 1989–2001. DOI: 10.1007/s10570-013-9978-3
- [20] Bukovsky V. The influence of light on aging of newsprint paper. Restaurator. 2008; 21: 55–76. DOI: 10.1515/REST.2000.55
- [21] Łojewska J, Miśkowiec P, Łojewski T, Proniewicz LM. Cellulose oxidative and hydrolytic degradation: In situ FTIR approach. Polymer Degradation and Stability. 2005; 88: 512–520. DOI:10.1016/j.polymdegradstab.2004.12.012
- [22] Havlínová B, Katšćák S, Petrovičová M, Maková A, Brezová V. A study of mechanical properties of papers exposed to various methods of accelerated ageing. Part I. The effect of heat and humidity on original wood-pulp papers. Journal of Cultural Heritage. 2009; 10: 222–231. DOI:10.1016/j.culher.2008.07.009
- [23] Polovká M, Polovková J, Vizárova K, Kirschnerová S, Bieliková L, Vrška M. The application of FTIR spectroscopy on characterization of paper samples, modified by Bookkeeper process. Vibrational Spectroscopy. 2006; 41: 112–117. DOI:10.1016/j.vibspec.2006.01.010
- [24] Lattuati-Derieux A, Bonnassies-Termes S, Lavédrine B. Characterization of compounds emitted during natural and artificial ageing of a book. Use of headspace-solid-phase microextraction/gas chromatography/mass spectrometry. Journal of Cultural Heritage. 2006; 7: 123–133. DOI:10.1016/j.culher.2006.02.004
- [25] Kačík F, Kačíková D, Jablonský M, Katušćák S. Cellulose degradation in newsprint paper ageing. Polymer Degradation and Stability. 2009; 94: 1509–1514. DOI:10.1016/j.polymdegradstab.2009.04.033
- [26] ISO 5264/1-1979 (E) Pulps—Laboratory beating—Part 1: Valley beater method.

- [27] ISO 5269-2:2004 (E) Pulps — Preparation of laboratory sheets for physical testing — Part 2: Rapid-Köthen method.
- [28] ISO 187:1990 (E) Paper, board and pulps—Standard atmosphere for conditioning and testing and procedure for monitoring the atmosphere and conditioning of samples.
- [29] ISO 11475:2004 (E) Paper and board—Determination of CIE whiteness, D65/10 degrees (outdoor daylight).
- [30] ISO 2471:2008 (E) Paper and board—Determination of opacity (paper backing)—Diffuse reflectance method.
- [31] ISO 1924-1:1992 (E) Paper and board—Determination of tensile properties—Part 1: Constant rate of loading method (20 mm/min).
- [32] ISO 1974:1990 (E) Paper—Determination of tearing resistance (Elmendorf method).
- [33] Zyska B. Fungi isolated from library materials: A review of the literature. *International Biodeterioration and Biodegradation*. 1997; 40: 43–51. DOI:10.1016/S0964-8305(97)00061-9
- [34] Stobińska H, Zyska B. Paper – production, products of paper, materials in library collections. In: Zyska B, Żakowska Z. editors. *Microbiology of materials*. 1st ed. Publisher Lodz University of Technology; Lodz, Poland; 2005. p. 137–180 (in Polish)
- [35] Koziróg A, Wysocka-Robak A, Przybysz K. Antifungal activity of paper modified with ionic liquids. *Fibres & Textiles in Eastern Europe*. 2015;4(23): 134–137. DOI: 10.5604/12303666.1152745
- [36] Fabbri AA, Ricelli A, Brasini S, Fanelli C. Effect of different antifungals on the control of paper biodeterioration caused by fungi. *International Biodeterioration and Biodegradation*. 1997; 39: 61–65. DOI:10.1016/S0964-8305(97)00001-2
- [37] Pinzari F, Pasquariello G, De Mico A. Biodeterioration of paper: A SEM study of fungal spoilage reproduced under controlled conditions. *Macromolecular Symposia*. 2006; 238: 57–66. DOI:10.1002/masy.200650609
- [38] Araujo Reis-Menezes A, Gambale W, Giudice MC, Shirakawa MA. Accelerated testing of mold growth on traditional and recycled book paper. *International Biodeterioration and Biodegradation*. 2011; 65: 423–428. DOI:10.1016/j.ibiod.2011.01.006
- [39] Neves ER, Schäfer, Philips A, Canejo J, Macedo MF. Antifungal effect of different methyl and propyl paraben mixtures on the treatment of paper biodeterioration. *International Biodeterioration and Biodegradation*. 2009; 63: 267–272. DOI:10.1016/j.ibiod.2008.07.011
- [40] Pernak J, Sobaszkiewicz K, Mirska I. Anti-microbial activities of ionic liquids. *Green Chemistry*. 2003; 5: 52–56. DOI: 10.1039/b207543c

- [41] Pernak J, Chwała P. Synthesis and anti-microbial activities of choline-like quaternary ammonium chlorides. *European Journal of Medicinal Chemistry*. 2003; 38: 1035–1042. DOI:10.1016/j.ejmech.2003.09.004
- [42] Busetti A, Crawford DE, Earle MJ, Gilea MA, Gilmore BF, Gorman SP, Lavery G, Lowry AF, McLaughlin M, Seddon KR. Antimicrobial and antibiofilm activities of 1-alkylquinolinium bromide ionic liquids. *Green Chemistry*. 2010; 12: 420–425. DOI: 10.1039/B919872E
- [43] Iwai N, Nakayama K, Kitazume T. Antibacterial activities of imidazolium, pyrrolidinium and piperidinium salts. *Bioorganic & Medicinal Chemistry Letters*. 2011; 21: 1728–1730. DOI:10.1016/j.bmcl.2011.01.081
- [44] Brycki B, Kowalczyk I, Koziróg A. Synthesis, molecular structure, spectral properties and antifungal activity of polymethylene- α,ω -bis(*N,N*-dimethyl-*N*-dodecyloammonium bromides). *Molecules*. 2011; 16: 319–335. DOI:10.3390/molecules16010319
- [45] Koziróg A, Wysocka-Robak A., Przybysz K, Michalczyk A, Walkiewicz F. Imidazolium azolates. Antifungal activity and the ability to use in papermaking. *Chemical Industry*. 2013; 92: 1618–1620.
- [46] Carson L, Chau PKW, Earle MJ, MA, Gilmore BF, Gorman SP, McCann MT, Seddon KR. Antibiofilm activities of 1-alkyl-3-methylimidazolium chloride ionic liquids. *Green Chemistry*. 2009; 11: 492–497. DOI: 10.1039/b821842k
- [47] Pernak A, Iwanik K, Majewski P, Grzymisławski M, Pernak J. Ionic liquids as an alternative to formalin in histopathological diagnosis. *Acta Histochemica*. 2005; 107: 149–156. DOI: 10.1016/j.acthis.2005.02.003
- [48] Zabielska-Matejuk J, Urbanik E, Pernak J. New bis-quaternary ammonium and bis-imidazolium chloride wood preservatives. *Holzforschung*. 2004; 58: 292–299. DOI: 10.1515/HF.2004.045

Biological

The Role of Ionic Liquids in Protein Folding/Unfolding Studies

Awanish Kumar, Meena Bisht, Indrani Jha and
Pannuru Venkatesu

Additional information is available at the end of the chapter

<http://dx.doi.org/10.5772/65924>

Abstract

Ionic liquids (ILs) have emerged as novel solvent medium for several biotechnological processes *in vitro*. The use of ILs starts from protein extraction to catalysis to folding/unfolding studies. ILs are becoming the most favorite non-aqueous medium for protein studies due to their unique ionic combinations (cation + anion) and tunable physical properties. In this context, several research results have been published that use of pure or aqueous IL solutions as stabilizer for proteins. Hence, herein, in this chapter, we present a collection of research work that focuses on the importance of ILs (and their mixture) in protein stabilities. In addition, we have also reviewed the unique properties of ILs as counteracting solvents for cold-induced denaturation and also their refolding properties. This report will definitely generate a new understanding for the ILs, their importance and applicability in protein folding studies.

Keywords: ionic liquids (ILs), proteins, stability, biocompatibility, counteraction

1. Overview of the structure and importance of ILs

In recent years, various solvents have been used for numerous processes in academia and industries. Nevertheless, because of new environmental regulations, the challenges of using non-harmful solvents have prompted a great development of innovative products [1, 2]. In this regard, ionic liquids (ILs) emerged as new and novel class of solvents that are now considered to reduce both economic and environmental pollution [2–4]. The term ILs describe a popular class of organic salts that melt below $\sim 100^{\circ}\text{C}$ and have an appreciable liquid range [1–4]. IL is entirely composed of positive and negative ions [5, 6]. ILs typically consist of organic nitrogen-containing heterocyclic cations and inorganic anions [7]. Historically, the organic compound

that is now considered as the first IL is ethylammonium nitrate ($[\text{C}_2\text{H}_5\text{NH}_3][\text{NO}_3]$, EAN) and was prepared by Paul Walden in 1914 and has a melting point of 12°C [8]. After a long gap, the major studies of room temperature molten salts of pyridinium halides with aluminum chloride (AlCl_3) were made in the 1940s by a group led by Frank Hurley and Tom Weir at Rice University [9]. Later, alkyimidazolium salts (C_nmim)⁺ were also reported in the early 1980s [10]. An excellent short history of the birth of ILs, which covers the crucial moments of this area, is presented by John S. Wilkes [11].

In its initial revolutionary stage, ILs were vastly considered in analytical chemistry based on their unique and tunable physical properties. Since then, synthesis of a large number of multifunctional ILs has been a prime interest for synthetic chemists [12, 13]. In this context, varieties of task-specific ILs have been synthesized and the advantages of their physical properties have been reported in an open literature [14]. Common ILs include ammonium, phosphonium, sulfonium, guanidinium, pyridinium, imidazolium and pyrrolidinium cations. The most common anions are chloride, bromide, tetrafluoroborate, hexafluorophosphate, trifluoromethanesulfonyl, bis(trifluoromethanesulfonyl)imide, dicyanamide and alkyl sulfate anions. These ILs have some unique properties such as negligible vapor pressure, good thermal stability, tunable viscosity and miscibility with water, a wide electrochemical window, high conductivity and high heat capacity [15–17]. These physical properties make IL a promising material in numerous fields, for example, their use in electrochemical devices and replacements for several organic reactions [18, 19]. Gordon [20], Parvulescu and Hardacre [21] and Crowhurst et al. [22] pointed out that there is an obvious advantage in performing many reactions in ILs due to the improvement in reaction activity, selectivity and yield. An in-depth literature survey reveals that there tremendously exist a large number of scholarly articles as well as elegant reviews that explicitly elucidate the various scientific applications of ILs [23–45].

2. Classification of ILs

ILs are composed solely of ions and their bulk and interfacial behavior is complex, governed by Coulombic, van der Waals, dipole-dipole, hydrogen-bonding and solvophobic forces [22, 46]. When an IL is formed by mixing a strong acid with a strong base, the proton is generally assumed to be located very strongly on the base. In this situation, the IL is most likely composed entirely of ions; however, ion complexation and aggregate formation may also occur [47]. A majority of the ILs with various combinations of the cation as well as the anions have been classified as protic ILs (PILs) and aprotic ILs (APILs) based on their respective physical properties to protonate/deprotonate in aqueous media [48]. The reason for this distinction is that PILs are volatile by their nature because the acidic proton can be abstracted by the basic anion at ambient temperature. The acid-base equilibrium for the abstraction reaction allows the formation of neutral molecular species that readily evaporate [49].

The potential environmental impact of PILs is expected to be smaller than the impact of APILs, due to their simpler structure. These PILs can be easily produced through the combination of a Brønsted base and a Brønsted acid [36]. A comparison with the APILs reveals that PILs often have higher conductivities and fluidities than the APILs. On the other hand, in PILs, the sizes

of the ions are small and they also tend to melt at lower temperatures than their APIL analogs. The obvious difference of the PILs compared with APILs is the reversible hydrogen transfer between the acid and the base [50, 51]. This implies that for PILs where the transfer is weak, the properties are closer to the corresponding binary liquid, whereas the aprotic ILs keep their ionic character until decomposition [52].

3. Toxicity in ILs and its environmental impact

ILs in green chemistry mean that it should be applied to all the aspects of the product life cycle that begins from its invention to the disposal. Broadly speaking, it should be recycled easily from the environment [53]. Tremendous amount of recent research has focused on the physical properties of ILs and more recently relationship and cross-linking between the chemical properties, the toxicity and biological properties of ILs have been one of the most highly debated topics in this field [31, 54]. Pham et al. have reviewed the toxic effect of ILs on the environment and biological systems in a comprehensive way [55]. It was shown that with increasing hydrophobicity of the cation, the IL gets more toxic [56]. Literature reveals that increased alkyl chain length in the cation of ILs showed higher toxicities on biological systems [57].

4. Protein stability in the presence of ILs

The advantages of using ILs in enzymatic biocatalysis, as compared to volatile organic compounds (VOCs), are the enhancement in the solubility of substrates or products without inactivation of the enzymes, high conversion rates and high activity and stability [35, 53]. These unique properties of ILs make them very attractive nonaqueous solvents for protein stability studies. It is revealed from various studies that physicochemical properties of ILs can play a pivotal role in altering the structure, stability and activity of proteins/enzymes [44]. Moreover, ILs offer new possibilities of application of solvent engineering to enzymatic reactions. Biocatalysis with ILs as reaction medium was first showed in the beginning of 2000 [58–60]. Review on ILs as cosolvents in aqueous biocatalytic reactions reveals that these ILs help to dissolve nonpolar substrates while avoiding enzyme inactivation like water-miscible organic solvents, as dimethyl sulfoxide (DMSO) or acetonitrile [61]. During the last decade, ILs have increased their attention as reaction media for enzymes in aqueous media with some remarkable results [62, 63].

In the present situation, the stability of proteins in ILs has been an area for active research because of their biological and pharmaceutical applications. The first report on the protein stability in the presence of ILs came in the year 2000 by Summers and Flowers [64]. Later, in 2004, Iborra and coworkers [65] studied the stabilizing ability of 1-ethyl-3-methylimidazolium bis[(trifluoromethyl)sulfonyl]imide [Emim][NTf₂] on α -chymotrypsin (CT) and the stability of CT in this IL was compared with water, 3 M sorbitol and 1-propanol. Subsequently, lots of works have been reported on the stability of various proteins in various ILs. Among all the solvents, the IL was found to be a strong stabilizer for CT structure than with other solvent

media [65]. Studies carried out by various groups using CT suggest that the physical properties of ILs such as polarity and hydrophobicity play a major role in their stabilizing behavior toward CT [18, 52, 53]. Among various families of ILs, ammonium-based ILs are identified to display their wide range application in biochemical processes [44].

Many key studies related to ammonium-based IL interactions with lysozyme have been carried out, focusing on the role of these ILs. A study by Summers and Flowers [64] on lysozyme showed that ethylammonium nitrate (EAN) stabilized the lysozyme against irreversible thermal denaturation. Byrne et al. [66] reported the thermal refolding as well as extended period stabilization of lysozyme with concentration >200 mg/mL. To achieve the refolded fraction of the protein, EAN was used. Triethylammonium methanesulfonate [TEA][MS] was able to refold 97% of thermally denatured lysozyme [66]. Mann et al. [67] observed that ammonium-based ILs such as ethylammonium formate (EAF), propylammonium formate (PAF), 2-methoxyethylammonium formate (MOEAF) and ethanolammonium formate (EtAF) not only acted as good stabilizers for the lysozyme native structure but also protected the protein against thermal unfolding. Ammonium-based ILs such as EAN, triethylammonium triflate (TEATF) and triethylammonium mesylate (TEAMS) were observed to be acting as solvents for solubilizing the aggregates (amyloids) of denatured lysozyme structure. Interestingly, after solubilization in the ILs, the activity of aggregated lysozyme was observed to reappear up to 80% in the presence of EAN and more than 50% in the rest of the ILs [68]. Many studies, related to the role of ammonium-based ILs on lysozyme, suggest the role of ammonium family ILs as a refolding additive, fibrillizing agent, precipitating agent, additives for protein crystallization, prevention of aggregation and renaturing agent, as well as stabilizers against thermal unfolding [66–70]. Also, based on the above experimental results, EAN can be termed as a refolding additive, from the thermally as well as chemically denatured lysozyme. Furthermore, talking particularly about the cations having various hydrogen bond donor sites result in more effective coordination to the protein, thereby stabilizing the biomolecule structure in a more efficient manner. The stability of lysozyme in imidazolium-based ILs is an interesting aspect that helps us to understand the interactions that are responsible for stabilizing/destabilizing the protein structure in various ILs. The thermal stability of lysozyme crystals was obtained using imidazolium-based ILs such as 1-butyl-3-methylimidazolium tetrafluoroborate ([Bmim][BF₄]), 1-butyl-3-methylimidazolium chloride ([Bmim][Cl]), 1-butyl-3-methylimidazolium bromide ([Bmim][Br]) and 1,3-dimethylimidazolium iodine([Mmim][I]), as additives during lysozyme crystallization [71].

The stability of lysozyme in imidazolium-based IL is observed to vary with the concentrations of the IL. In this regard, Takekiyo et al. [72] observed the structural change of lysozyme in aqueous 1-butyl-3-methylimidazolium nitrate ([Bmim][NO₃]) solutions by using Fourier transform infrared (FTIR), circular dichroism (CD) spectra and small-angle X-ray scattering (SAXS) methods. The results illustrated that the structure of the protein significantly varied with changes in the structure and concentration of the ILs. In the first view, the authors observed that the increase in the [Bmim][NO₃] concentration completely disrupted the tertiary structure of lysozyme at 5 M of IL. Lange et al. [73] reported that the imidazolium-based ILs can also be considered as refolding agents. They tested the refolding of lysozyme in the set of imidazolium ILs, [Emim]⁺, [Bmim]⁺ and [Hexmim]⁺ cations with a fixed anion Cl⁻.

Interestingly, the stability of lysozyme in imidazolium-based ILs was observed to decrease significantly as the alkyl chain of the ILs increased from ethyl to butyl to hexyl. However, all ILs acted as refolding enhancers for the completely denatured lysozyme structure.

Interestingly, experimental results reveal that the partitioning of bovine serum albumin (BSA) is predominated by the hydrophobic interactions between the protein and imidazolium cation of the ILs in the aqueous system, which can be improved or modulated by changing the cation chain length of the ILs or modifying the surface of the BSA [74, 75]. The study indicated that the secondary structure of BSA was stabilized at low IL concentration (<3 mM) and the protein was denatured at higher IL concentration (>3 mM) [76]. Rawat and Bohidar [77, 78] reported that the interaction between imidazolium-based ILs and BSA is obviously dependent on the concentrations of the ILs. They observed that the BSA retained the secondary structure at low concentrations of 1-octyl-3-methylimidazolium chloride ([C₈mim][Cl]) of 0–0.2% w/v. Moving above this concentration range, the BSA structure was denatured significantly that is most likely caused due to intercalation of alkyl chain of the imidazolium cation of [C₈mim][Cl] IL into the hydrophobic interior of the protein [77].

5. Structure and stability of some other proteins in different ILs

In the earlier sections, the protein stabilization studies of most commonly used proteins have been delineated. Even though, the literature is still scattered, which deals with the stability of proteins in the presence of ILs. Hence, in this section, we have tried together all these research reports [79–114] under the same roof, so that it is easily available to the readers and also to expose its importance to the scientific world. An overview of the literature reveals stability studies of proteins such as amyloglucosidase [79], thyroglobulin [79], glutamate dehydrogenase [79], lactate dehydrogenase [79], glucose dehydrogenase [80], formate dehydrogenase [94], glycosidase (α and β) [81], monellin [82], β -galactosidase [83], glucose oxidase [106], lactate oxidase [109], oxidoreductases [107], subtilisin Carlsberg [84], Amano protease P6 [85], pepsin [86], papain [87, 100] esterases from *Bacillus subtilis* and *Bacillus stearothermophilus* [87], *Penicillium expansum* lipase [88], mushroom tyrosinase [88], chloroperoxidase [89], porcine pancreatic lipase [91], α -helical protein Im7 [92], pepsin [93], adenosine deaminase [95], α -amylases [96], xylanase II (GH11 enzyme, from *Trichoderma longibrachiatum* [97], lactoferrin [99], α -synuclein [101, 103], ribonuclease A [102], casein [104, 105], epoxide hydrolase [110], avidin [111], Abeta [1–40] peptide [112], zein [113] and firefly luciferase (*Photinus pyralis* luciferase) in the ILs. Among them some of the proteins have been stabilized [79–91], while some other proteins have shown to be destabilized in the presence of ILs [92–97].

Apart from the studies related to protein folding/unfolding, there are other research articles which have recognized the use of ILs as two-phase systems which are used for protein preservation, protein separation, purification, partitioning of proteins and many more purposes. For example, the extraction efficiency of papain was increased to 98.3% in the biphasic mixtures containing ILs [100]. On the other hand, Ebrahimi et al. [114] delineated the activity and stability of *P. pyralis* luciferase in two tetramethylguanidine-based [TMG][Lac] and [TMG][Pro]. The authors found that the luciferase activity increased up to 0.25 M of [TMG][Lac]

conversely the activity diminished in the presence of similar concentrations of [TMG][Pro]. Further, thermal stability studies show more stability of luciferase only in the presence of [TMG][Lac], whereas thermal stability was not improved in [TMG][Pro] [114]. Similar effects were observed in the stability of insulin in the presence of a set of imidazolium-based ILs such as [Bmim][Cl], [Bmim][Br], 1-butyl-3-methylimidazolium thiocyanate ([Bmim][SCN]), 1-butyl-3-methylimidazolium hydrogen sulfate ([Bmim][HSO₄]), 1-butyl-3-methylimidazolium acetate ([Bmim][CH₃COO]) and 1-butyl-3-methylimidazolium iodide ([Bmim][I]) [115]. The experimental findings reveal that [Bmim][Br] and [Bmim][Cl] ILs stabilized the native state of insulin, while the rest of the [Bmim] ILs with anions such as SCN⁻, HSO₄⁻, CH₃COO⁻ and I⁻ were destabilizers for the native form of insulin. Moreover, imidazolium-based ILs were also found to enhance the aggregated structure in insulin [115]. In support, Bae [101] and Hwang et al. [103] investigated the effect of imidazolium-based ILs on the aggregation properties of α -synuclein. Their results indicated the increase in the aggregated structure of the protein due to the ILs [101, 103].

6. Influence of mixture of ILs on the structure and stability of proteins

It is now obvious after examining the effect of various ILs (from different families of ILs) that some of the industrially important ILs acted as destabilizers for the proteins. Therefore, the search to offset the negative effects of ILs on proteins came into limelight. Therefore, the maintenance of ILs as the “green solvent medium” is a great challenge for a chemist or biochemist [116]. There are reports available in the literature that projects the negative effects of the ILs on the proteins. Klähn et al. [117, 118] reported the destabilization of *Candida antarctica* lipase B (CALB) in imidazolium- or guanidinium-based ILs through MD simulations. Further, very recently our research group has shown the destabilization of *heme* proteins in the presence of ammonium-based ILs [119]. We stress that all these results can be considered as an alarm for a chemist and biochemist to search for the novel method of counteraction for the denaturation action of ILs on the biomolecules.

In this context, the mixtures of ILs have been of continuing interest, of great fundamental practical importance and increasingly received a lot of attention from both academia and industry [120–123]. Recently, mixtures of ILs exhibit interesting and increased scope to the access of the properties, which are not readily apparent from those of the individual IL. Keeping this in mind, Lozano and coworkers [124] showed that [Bmim][Cl] behaved as a powerful enzyme-deactivating agent for cellulase. On the other hand, hydrophobic IL butyltrimethylammonium bis(trifluoromethylsulfonyl)imide ([N₁₁₁₄][NTf₂]) clearly enhanced the enzyme thermal stability. Apparently, the mixture of [N₁₁₁₄][NTf₂] and [Bmim][Cl] greatly improved the thermal stability of cellulase with respect to [Bmim][Cl] alone. By increasing the hydrophobic IL concentration, the deactivation effect of [Bmim][Cl] was reduced, which could be attributed to the preservation of the essential water molecules around the protein [124].

Similarly, the highest hydrolytic activity of immobilized lipase was obtained when the hydrophilic IL, 1-ethyl-3-methylimidazolium tetrafluoroborate ([Emim][BF₄]), was used as an additive, while the highest stability of immobilized lipase was obtained by using hydrophobic IL,

[C₁₆mim][Tf₂N] [125]. When Lee et al. [125] used the binary mixtures of these two ILs as additives, the optimal immobilized lipase showed both high activity and stability. The hydrolysis and esterification activities of lipase co-immobilized with the mixture of 1:1 at molar ratio of [Emim][BF₄] and [C₁₆mim][Tf₂N] were 10-fold and 14-fold greater than in silica gel without ILs, respectively. Therefore, the binary mixtures of these ILs as additives were used to obtain the optimal immobilized lipase which shows both high activity and stability [125].

Very recently, our group also showed the influence of mixture of two ILs on the structure and the stability of CT [126]. Evidently, the fluorescence and CD spectral results demonstrated that [Bmim][Br] alone acts as a stabilizer at low concentrations, while it acts as a destabilizer at high concentrations for the native structure of CT. On the other hand, [Bmim][I] is a destabilizer at all the concentrations. Nevertheless, the denaturing ability of [Bmim][I] was compensated by the [Bmim][Br]. Further, to offset the action of [Bmim][Br] on deleterious action of [Bmim][I] is more pronounced at lower concentration (0.025 M) than at higher concentrations. As shown in **Figure 1**, the fluorescence intensity maximum (I_{max}) for CT in buffer was 73.6 a.u., in 0.025 M [Bmim][Br] was 71.5 a.u. and in 0.2 M [Bmim][I] was 39.7 a.u. [126].

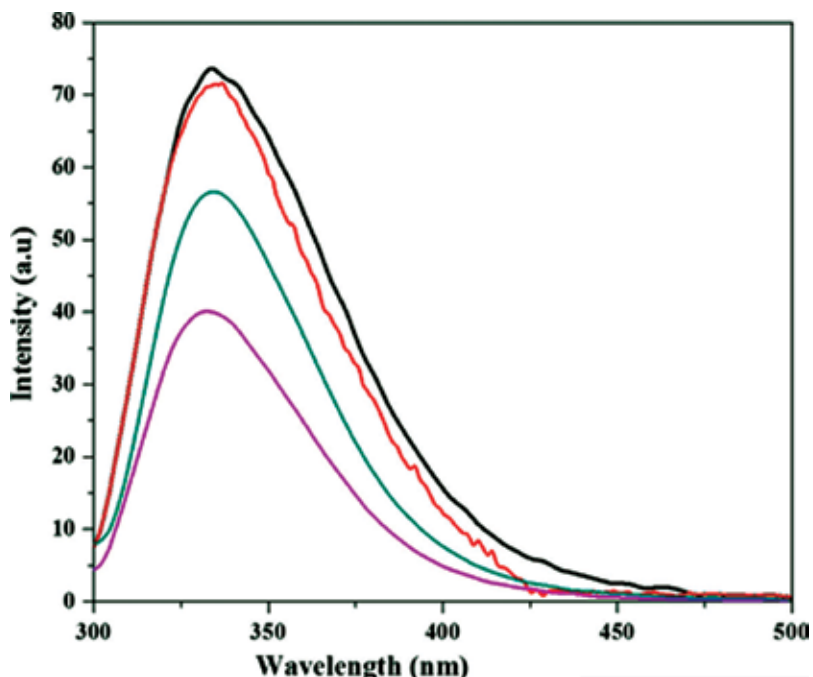
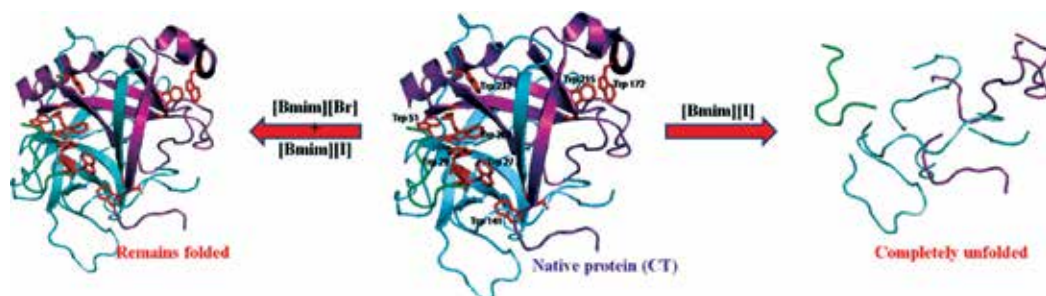


Figure 1. Fluorescence intensity changes for α -chymotrypsin (CT) in Tris-HCl buffer (black color line), 0.025 M [Bmim][Br] (red color line), 0.2 M [Bmim][I] (magenta color line) and 0.025 M [Bmim][Br] + 0.2 M [Bmim][I] mixture (dark cyan color) (Ref. [126]).

Interestingly, after addition of 0.025 M [Bmim][Br] to 0.2 M [Bmim][I], it is noticeable how the fluorescence spectra of the CT were clearly modified compared with the I_{max} for the CT in [Bmim][I], although the intensity was lower in the presence of [Bmim][Br] + [Bmim][I] than that of the native protein, which is, however, certainly larger than that of [Bmim][I].

The main reason behind the enhancement of intensity with the addition of [Bmim][Br] into the protein solution having [Bmim][I] is the movement of Trp toward a more hydrophobic environment and therefore high fluorescence intensity is observed due to higher quantum yield. Obviously, the mixture of the ILs may improve the stability of CT structure [126]. This phenomenon is schematically shown in **Scheme 1**.



Scheme 1. The presence of [Bmim][Br] counteracts the strong denaturation action of [Bmim][I] (Ref. [126]).

In 2006, the Lee group published a pioneering work [127] that showed that the effect of chloride impurity on the activity and stability of lipase in 1-octyl-3-methylimidazolium bis(trifluoromethylsulfonyl)imide ([Omim][Tf₂N]) and [Omim][Cl] ILs. In result, the activity of enzyme exponentially decreased with increasing Cl⁻ content in [Omim][Tf₂N] and the activity of lipase in [Omim][Tf₂N] mixture containing 2% [Omim][Cl] was only about 2% of the activity in pure [Omim][Tf₂N]. The reason provided by the authors for the decrease in the activity of the enzyme in Cl⁻ ILs is due to the denaturation of the enzyme in these ILs. As mentioned before, the activity of the enzyme linearly decreased at about 5% for every 1% increase in [Omim][Cl] with there being no activity in [Omim][Tf₂N] containing about 20% [Omim][Cl] [127]. In another work of the Lee group [128], they systematically showed that the highest lipase activity was obtained in water-miscible [Bmim][TfO] which can dissolve a high concentration of glucose, while the highest stability of lipase was shown in hydrophobic [Bmim][Tf₂N]. The optimal activity and stability of lipase could be obtained in the mixture of [Bmim][TfO] and [Bmim][Tf₂N]. Therefore, the productivity obtained by using IL mixtures was higher than those in pure ILs [128]. A later study by this same research group reported that higher enzyme activity was achieved under ultrasound irradiation on lipase-catalyzed esterification of fructose in the mixture of [Bmim][TfO] and [Omim][Tf₂N] [129]. These results show that enzymatic reaction in ILs mixture under ultrasound irradiation is an effective method for enzyme activity and stability resulting in economic competitiveness of green process [129]. It is well documented that 100% conversion of cellulose to useful biochemical process in the presence of the mixture of ILs at low temperature, which overcomes the long intrinsic phase problem in the conversion of biomass to chemicals [130, 131]. Yao et al. [132] reported the activity and stability of *Candida rugosa* lipase in binary ILs.

Mixing of two different ILs, which show different physicochemical properties, can easily make new ILs because hydrophobic ILs and hydrophilic ILs are generally miscible. The mixing of

different ILs may be a very useful method to make new IL solvent media for the structure and stability of biomolecules. These results improve knowledge of the excellent properties of IL mixtures as stabilizers for the native conformation of protein, since IL mixtures are able to stabilize enzymes and are suitable as reaction media for enzymatic biotransformations of industrial interest. Currently, these discoveries have opened new opportunities for obtaining better activity and improvement of stability of proteins in the mixtures of ILs.

7. The significant and specific contribution of ILs on protein stability

Practically, the native conformations of the globular proteins have adapted to environmental stresses that normally denature the proteins and the nature has provided a mechanism of adaptation that some of the cosolvents protect against denatured proteins [133, 134]. In fact, the protecting cosolvents stabilize the proteins against denaturing stresses and their presence in the cell does not alter protein functional activity [135]. The protein aggregation and its cold and thermal denaturation have been recognized as a major manifestation of instability that can severely affect a protein's functionality. As a group of novel green solvents, ILs have attracted extensive attention and gained popularity to overcome these physiological stresses. As discussed in earlier sections, ILs are potential cosolvent media for preservation of biomolecules because of their high stability and unusual solvent properties. We saw some of the ILs acted as efficient additives for the suppression of protein aggregation. Also, in the previous sections, we observed that the ILs behaved differently with various proteins. From the obtained results, we concluded that the stability of the proteins in ILs is completely dependent on the interactions of the ions of ILs with AA residues at the surface of the proteins.

In this section, we support the concept of novel behavior of ILs and explain the prevention of the self-aggregation of proteins, refolding of thermally and chemically perturbed proteins and also counteracting effects of ILs against the thermally and cold denaturation of proteins. Therefore, mechanistic insight into the effects of ILs on preventing all the deleterious effects on the proteins is desired for the understanding and designing of protein processes in biophysical chemistry and biotechnology.

As mention before, in 2000, Summers and Flowers [64] have observed that EAN has the ability to prevent lysozyme aggregation and is an efficient refolding additive for a completely denatured protein. Further, EAN has been utilized as a precipitating agent for the crystallization of lysozyme, providing crystals with good diffraction [135]. In another study, ammonium-based ILs such as EAF, PAF, 2-methoxyethylammonium formate (MOEAF) and Ethanolammonium formate (EtAF) not only acted as good stabilizers for the lysozyme native structure but also they protected the protein against thermal unfolding [67]. Subsequently, EAN IL not only stabilized the lysozyme native structure for long term rather it acted as a refolding agent preventing the lysozyme from aggregation. Bisht et al. [136] noticed that the presence of 1% v/v ammonium-based ILs can increase the activity of lysozyme up to 13% also refolded the urea-induced unfolded lysozyme structure. Interestingly, EAN has been observed to be possessing multicharacter in protein stability [64, 66, 67, 70]. We believe that information will surely help in understanding the microscopic mechanism existing between protein and ILs, particularly EAN.

Apparently, Lange et al. [73] explicitly elucidated that the set of imidazolium-based ILs such as [Emim]⁺, [Bmim]⁺ and [Hexmim]⁺ cations with a fixed anion Cl⁻ can also be considered as refolding agents. The stability of lysozyme in these ILs was observed to decrease significantly as the alkyl chain of the ILs increased from ethyl, butyl to hexyl. Nonetheless, all ILs acted as refolding enhancers for the completely denatured lysozyme structure. A later study found that a series of the ILs such as [Mmim][Cl], [Emim][Cl], [Pmim][Cl], [Bmim][Cl], [Penmim][Cl], [Hexmim][Cl], [Hepmim][Cl], [Omim][Cl], [Ddmim][Cl], [i-Bmim][Cl] and [Bemim][Cl] were applied to the denatured lysozyme structure and a significant refolding of the protein was observed. Among the ILs, in the presence of [Bmim][Cl], the refolding yield reached up to maximum of 84% [137]. The less hydrophobic ILs such as N-alkylpyridinium chlorides [EtPy][Cl], [BPy][Cl] and [HexPy][Cl] were effective in enhancing the refolding agents for the lysozyme structure and yielded up to 46–69% refolding [76]. As a consequence, the results conclude that more hydrophobic ILs behaved as a denaturants for lysozyme while the same ILs acted as refolding agents for the denatured lysozyme structure. In support to the above-mentioned facts, Takekiyo et al. [72] observed that the secondary structure of lysozyme was refolded in the 6–10 M concentration range of imidazolium-based IL, whereas the tertiary structure breaks down. Upon increase in the concentration more than 10 M of [Bmim][NO₃], the secondary structure of the protein was still observed to be in a partially refolded state, while the tertiary structure was completely disrupted.

Very recently, at low concentration of [Bmim][Cl], the cyt c starts to unfold and again starts refolding with increasing concentration of the IL [138]. These results suggest a partial refolding of the secondary structure of cyt c in [Bmim][Cl]. The [Emim][Cl] was a very efficient in promoting refolding of the recombinant plasminogen activator (rPA) [139]. The delicate balance of favorable interactions with side chains and unfavorable interactions with the peptide backbone provides a molecular explanation of how this IL suppresses protein aggregation and simultaneously promotes refolding. Nonetheless, the protein denatured at high concentrations of [Emim][Cl] which indicates strong favorable interactions between AA side chains and ions of the IL [139].

The effect of EAN on renaturation of cyt c has been shown by Jaganathan et al. [140] and the results show that EAN in the range of 10⁻⁴ M helps in refolding of the protein from urea (8 M)-induced denaturation of cyt c. On the other hand, it was observed that at moderate concentrations (50–150 mM) [Emim][CH₃COO] did not induce any significant effect over Mb structure, however, [Bmim][BF₄], at the same concentrations significantly destabilized the Mb [141]. Further, there was minimal variation in the structure of Mb, when the mixture of 1.4 M GdnHCl and 150 mM of [Emim][CH₃COO] IL was used as a cosolvent. That is, the protein is not completely unfolded. While in the presence of 150 mM [Bmim][BF₄]⁺ 1 M of GdnHCl, the Mb completely unfolds. Thus, if compared, a combination of imidazolium cation with [CH₃COO] anion in an IL is more biocompatible and giving protection against GdnHCl denaturation action on Mb native structure than those in ILs containing [BF₄] anion. Moreover, it is interesting to note that some of the imidazolium-based ILs could be used as anticancer solvents [142].

IL such as triethylammonium acetate (TEAA) was found to be an efficient refolding additive for a thermally unfolded CT structure [143]. The refolding ability of TEAA against thermally denatured CT structure was monitored using ¹H NMR. In addition, the fluorescence, CD and

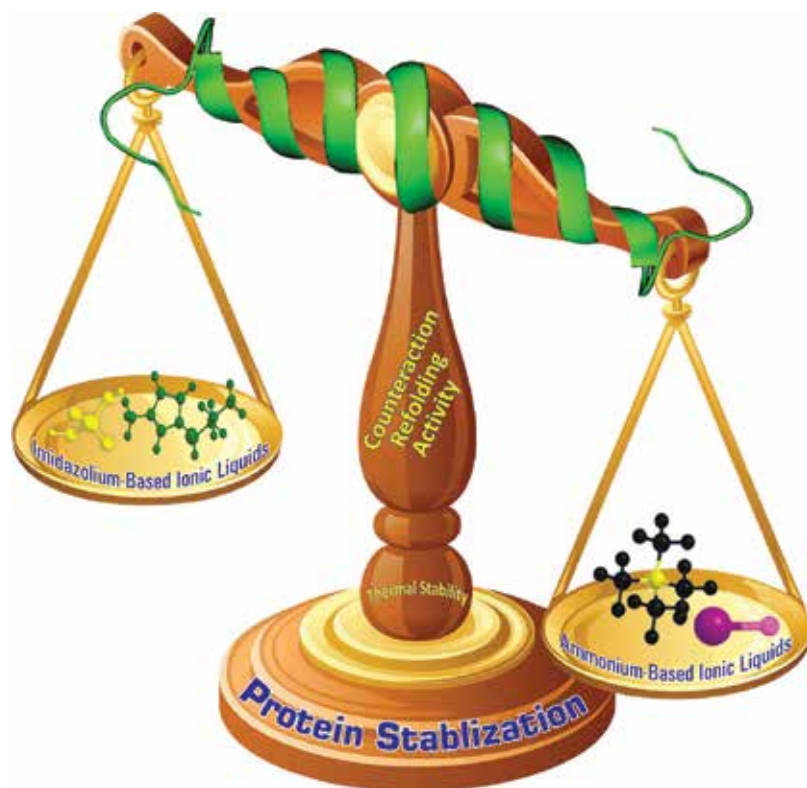
NMR results confirmed that TEAA strongly counteracted the deleterious actions of well-known denaturant, urea, on the CT structure [144]. It was demonstrated that TEAA and urea mixture substantially increased the T_m values which showed the counterbalance of the urea-induced denaturation of CT. Most importantly, deleterious action 5 M urea on CT was counteracted by only 1 M TEAA.

It has been already noted that a protic IL triethylammonium phosphate (TEAP) acted as a refolding additive for the urea-induced chemical denatured state of the two enzymes, CT and succinylated Concanavalin A (S Con A) [22]. In one of the studies by Attri and Venkatesu, TEAP was shown to be acting as an efficient refolding agent for thermally denatured S Con A [145]. In 2013, Attri and Choi [146] showed that TEAP strongly attenuated the detrimental action of atmospheric pressure plasma jet (APPJ) on CT. This ammonium-based IL TEAP is able to maintain the structural integrity as well as activity of CT even after the exposure of APPJ [147]. The results show that one can use both enzyme and plasma simultaneously without affecting the enzyme structure and activity on the material surface, which can prove to be applicable in various fields.

Recent studies on ammonium-based ILs offer some valuable information to prevent the self-aggregation of the proteins. In this regard, Awanish and Venkatesu [148] for the first time showed ammonium-based ILs as a novel solvent for offsetting self-aggregation of insulin in the presence of TMA, TEAS, TMAP, TEAP and TMAA. Therefore, the native structure of insulin was found to be stabilized in the presence of ammonium-ILs by unfavorable interactions with the surface of protein. The stability studies of insulin in ILs have opened a new way that can lead us to overcome the aggregation properties of insulin. This will not only increase the shelf life of insulin, whereas suitable formulations of insulin in biocompatible ILs can lead to safe and durable insulin formulations in pharmaceutical products. The ammonium-based ILs such as ethylammonium mesylate (EaM), diethylammonium mesylate (DeaM)-stabilized *tobacco mosaic virus*, whereas triethylammonium mesylate (TeaM) caused a change in the secondary structure of the virus [149].

From the literature and from our own experience, it can be suggested that ammonium-based ILs are more biocompatible as compared to the imidazolium-based ILs [44, 140–155]. Yu et al. [150] explored the stability of laccase in the presence of both ammonium- and imidazolium-based ILs such as [TMA][TfO], [Bmim][TfO] and [Bmpyr][TfO]. They found that only ammonium-based ILs [TMA][TfO] stabilized laccase, while [Bmim][TfO] and [Bmpyr][TfO] destabilized it. The contrasting nature of ammonium family ILs is also consistent with Rodrigues et al. [151], where among different families of ILs only ammonium-containing IL shows higher activity as compared to imidazolium-based ILs for *Thermomyces lanuginosus* lipase (TLL). **Scheme 2** shows the difference between the biocompatibility behaviors of ammonium- and imidazolium-based ILs.

On the other hand, Jha et al. [152] have explored the influence of a of imidazolium-based IL, 1-allyl-3-methylimidazolium chloride ([Amim][Cl]), on the stability of Hb. Unprecedented improvement in the stability of Hb in the presence of [Amim][Cl] at the lower concentration of [Amim][Cl] was observed by the authors [153]. Furthermore, the effect of [Amim][Cl] on bromelain stability and activity was investigated in another work. They observed that at low concentrations (0.01–0.10 M) of [Amim][Cl], there is ostensible only change in the stability and activity of BM.

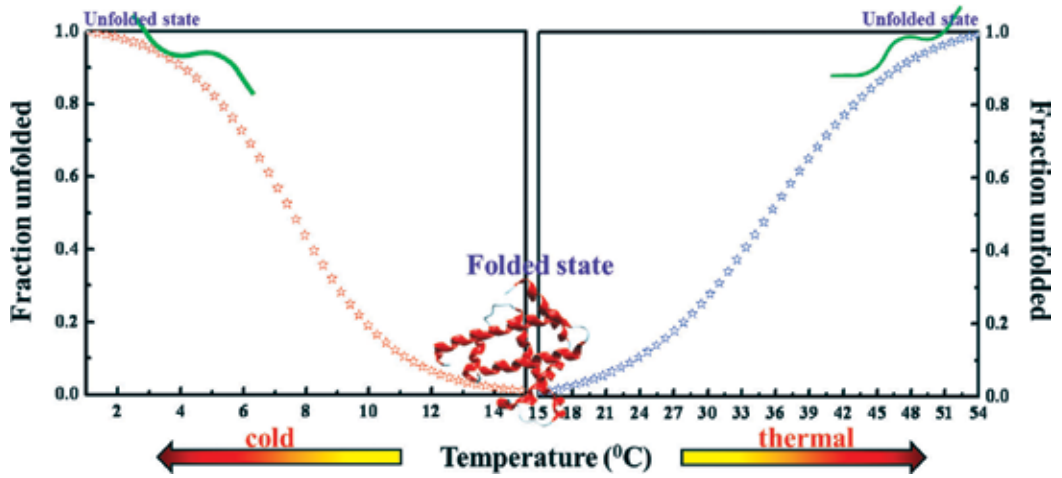


Scheme 2. The biocompatible behavior of ammonium-based ILs as compared to imidazolium-based ILs for proteins (Ref. [44]).

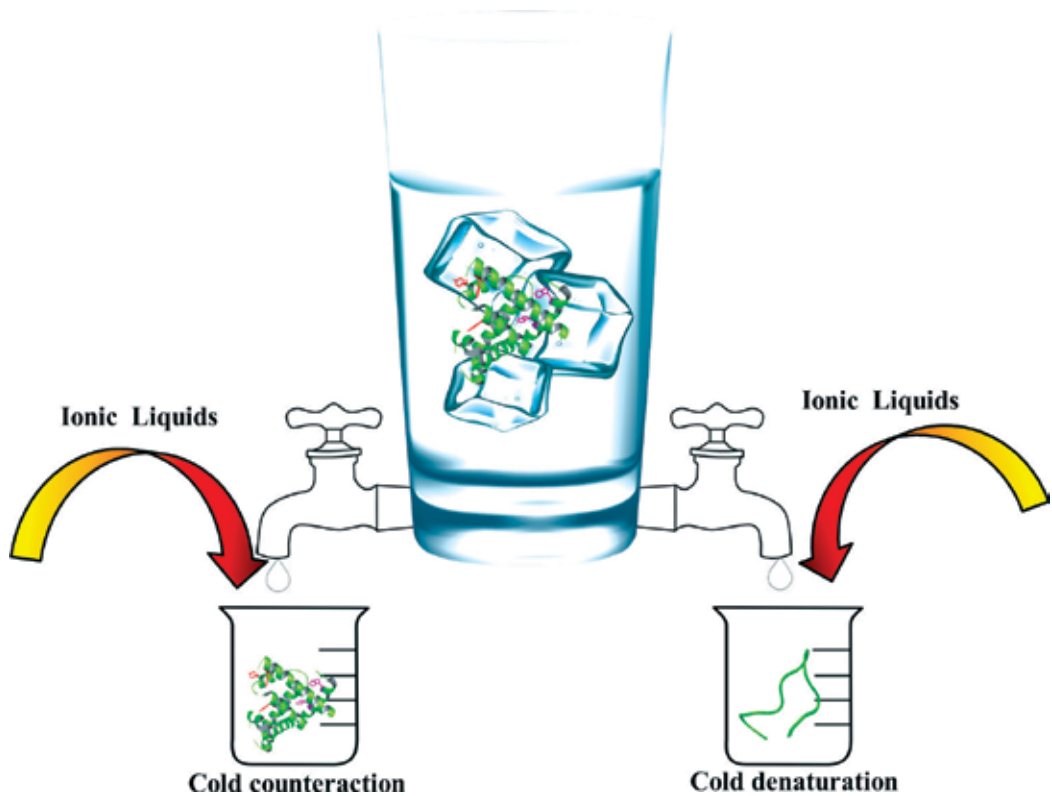
However, we cannot overlook the wide applications and uses of imidazolium-based ILs in various fields. Therefore, it is very important to emphasize the role of these ILs in biomedical applications, for example, counteraction of cold-induced unfolding of Mb and CT structures.

Cold denaturation is a fundamental fact in aqueous solutions where the native structure of globular protein disorders on extreme cooling [156]. Unlike thermal denaturation, whereby a native protein is disrupted at high temperature, cold denaturation is accompanied by decreases in both the system entropy and enthalpy [150]. As shown in **Scheme 3**, very recently we experimentally observed in one of our recent studies that the cold-induced unfolding of Mb and CT approaches closely a two-state folding mechanism similar to that experienced in the thermal denaturation of proteins [157].

Interestingly, for the first time, ILs having CH_3COO^- or Br^- with $[\text{Bmim}]^+$ proved to counteract the cold-induced unfolding of Mb and CT structures. Nevertheless, ILs containing Cl^- , HSO_4^- and SCN^- with $[\text{Bmim}]^+$ failed to prevent the Mb and CT structures against cold denaturation. These findings are concluded through **Scheme 4**.



Scheme 3. Schematic representation of two-state unfolding transitions in a protein with temperature (Ref. [157]).



Scheme 4. The ability of the ILs to offset the cold-induced unfolding of proteins.

An advantage of studying cold denaturation of globular proteins in ILs will certainly help us to encounter the reversible unfolding of proteins. Apparently, both cold and heat effects can lead to the unfolding of the proteins, which causes several human diseases. Evidently, the novel character of ILs offsets both the deleterious actions on protein keeping it in a proper folded conformation. It is hoped that the results obtained from these studies will be useful in recommending tailor-made ILs for various applications in biological systems as well as novel pharmaceutical applications.

Obviously, full access to the cold- and thermal-induced unfolding of proteins in ILs is still lacking. The interaction of the ions with protein surface is a complex result of the ability of the ions to enhance and disrupt water structure and internal protein residue interactions that contribute to the overall protein stability. Therefore, it is not necessary that only the IL is responsible for stabilization or destabilization of a protein under varying conditions, rather the solvent environment is equally responsible which creates variations in the interactions of the ILs with the protein surface. Apparently, ILs may stabilize or destabilize the proteins which are solely dependent on the molecular environment in the protein's surroundings. However, based on the literature survey and our experience, these studies might be inapplicable to all proteins in general (other than investigated proteins). Therefore, a lot of studies in this regard are essentially required to build a universal conclusion on ILs to protect the protein against various external stresses.

8. Conclusions

The extents of stabilization ability of ILs on the proteins vary and usually depend upon the combination of ions (both cation and anion). The activity and stability of protein in ILs that depend not only on the nature of the ions of IL but also on the functional groups of AAs sequences arrangement of the protein. Therefore, interactions of ions of ILs with proteins are important for understanding the effects shown by them on proteins whether in stabilization or destabilization. The results based on experiments revealed that the concentration of the ILs can play a major role in stabilizing/destabilizing a particular protein and also the alkyl chain length of the cation. Some of the novel characters in protein stability by ILs have been highlighted in this chapter. Prevention of self-aggregation and counteraction against extreme heat, cold and chemicals by ILs have been systematically presented. Cold counteraction is a new approach to stabilize proteins in ILs. This will help in increasing the stability of protein-based pharmaceutical products, which sometimes become inactive due to cold-induced denaturation of the proteins when stored at low temperature. Similarly, self-aggregation in proteins is also an issue which we believe can be controlled using biocompatible ILs. However, a very little amount of literature is available in this field of research.

Acknowledgments

We gratefully acknowledge Physical Chemistry Chemical Physics and Royal Society of Chemistry for reusing our figures such as **Figure 1** and **Schemes 1–3**.

Author details

Awanish Kumar¹, Meena Bisht², Indrani Jha² and Pannuru Venkatesu^{2*}

*Address all correspondence to: venkatesup@hotmail.com

1 Department of Chemistry, Massachusetts Institute of Technology, Cambridge, MA, USA

2 Department of Chemistry, University of Delhi, Delhi, India

References

- [1] Freemantle M, An Introduction to Ionic Liquids, The Royal Society of Chemistry, Cambridge, UK; 2010.
- [2] Kavitha T, Attri P, Venkatesu P, Ramadevi R S, *J. Phys. Chem. B*, 2012; **116**: 4561–4574.
- [3] Rogers R D, Seddon K R, *Science*, 2003; **302**: 792–793.
- [4] Seddon K R, *J. Chem. Tech. Biotechnol.*, 1997; **68**: 351–356.
- [5] Koel, M. (2009). Ionic liquids in chemical analysis, In: *Analytical Chemistry Series*, first edition, CRC Press Taylor & Francis Group, ISBN-13: 978-1-4200-4646-5, USA.
- [6] Reddy P M, Venkatesu P, *J. Phys. Chem. B*, 2011; **115**: 4752–4757.
- [7] Zhao D, Wu M, Kou Y, Min E, *Catal. Today*, 2002; **74**: 157–189.
- [8] Walden P, *Bull. Acad. Imper. Sci. (St. Petersburg)*, 1914; **8**: 405–422
- [9] Hurley F H, Wier T P, *J. Electrochem. Soc.*, 1951; **98**: 207–212.
- [10] Wilkes J S, Levisky J A, Wilson R A, Hussey C L, *Inorg. Chem.*, 1982; **21**: 1263–1264.
- [11] Wilkes J S, *Green Chem.*, 2002; **4**: 73–80.
- [12] Welton T, *Chem. Rev.*, 1999; **99**: 2071–2084.
- [13] Hallett J P, Welton T, *Chem. Rev.*, 2011; **111**: 3508–3576.
- [14] Freire M G, Claudio A F M, Araujo J M M, Coutinho J A P, Marrucho I M, Lopes J N C, Rebelo L P N, *Chem. Soc. Rev.*, 2012; **41**: 4966–4995.
- [15] Zhang S, Sun N, He X, Lu X, Zhang X, *J. Phys. Chem. Ref. Data*, 2006; **35**: 1475–1517.
- [16] Kumar A, Reddy P M, Venkatesu P, *RSC Adv.*, 2012; **2**: 6939–6947.
- [17] Attri P, Venkatesu P, Hofman T, *J. Phys. Chem. B*, 2011; **115**: 10086–10097.
- [18] Wang Z, Wu P, *RSC Adv.*, 2012; **2**: 7099–7108.
- [19] Khara D C, Kumar J P, Mandal N, Samanta A, *J. Phys. Chem. B*, 2013; **117**: 5156–5164.
- [20] Gordon C M, *Appl. Catal. A*, 2001; **222**: 101–117.

- [21] Parvulescu V I, Hardacre C, *Chem. Rev.*, 2007; **107**: 2615–2665.
- [22] Crowhurst L, Lancaster N L, Arlandis J M P, Welton T, *J. Am. Chem. Soc.*, 2004; **126**: 11549–11555.
- [23] Armand M, Endres F, MacFarlane D R, Ohno H, Scrosati B, *Nat. Mater.*, 2009; **8**: 621–629.
- [24] Chen X, Liu J, Wang J, *Anal. Methods*, 2010; **2**: 1222–1226.
- [25] Lin Y, Zhao A, Tao Y, Ren J, Qu X, *J. Am. Chem. Soc.*, 2013; **135**: 4207–4210.
- [26] Yang Z, *J. Biotechnol.*, 2009; **144**: 12–22.
- [27] Zhao H, *J. Chem. Technol. Biotechnol.*, 2010; **85**: 891–907.
- [28] Zhao H, *J. Chem. Technol. Biotechnol.*, 2006; **81**: 877–891.
- [29] Zhao H, *J. Mol. Catal. B Enzym.*, 2005; **37**: 16–25.
- [30] Kumar A, Venkatesu P, *Int. J. Biol. Macromol.*, 2014; **63**: 244–253.
- [31] Egorova K S, Ananikov V P, *ChemSusChem.*, 2014; **7**: 336–360.
- [32] Martins M A P, Frizzo C P, Moreira D N, Zanatta N, Bonacorso H G, *Chem. Rev.*, 2008; **108**: 2015–2050.
- [33] Fedorov M V, Kornyshev A A, *Chem. Rev.*, 2014; **114**: 2978–3036.
- [34] Sun X, Luo H, Dai S, *Chem. Rev.*, 2012; **112**: 2100–2128.
- [35] van Rantwijk F, Sheldon R A, *Chem. Rev.*, 2007; **107**: 2757–2785.
- [36] Greaves T L, Drummond C J, *Chem. Rev.*, 2008; **108**: 206–237.
- [37] Plechkova N V, Seddon K R, *Chem. Soc. Rev.*, 2008; **37**: 123–150.
- [38] Petkovic M, Seddon K R, Rebelo L P N, Pereira C S, *Chem. Soc. Rev.*, 2011; **40**: 1383–1403.
- [39] Kumar A, Venkatesu P, Taha M, Lee M J, *Curr. Biochem. Eng.*, 2014; **1**: 125–140.
- [40] Moniruzzaman M, Kamiya N, Goto M, *Org. Biomol. Chem.*, 2010; **8**: 2887–2899.
- [41] Weingärtner H, Cabrele C, Herrmann C, *Phys. Chem. Chem. Phys.*, 2012; **14**: 415–426.
- [42] Plaquevent J C, Levillain J, Guillen F, Malhiac C, Gaumont A C, *Chem. Rev.*, 2008; **108**: 5035–5060.
- [43] Constantinescu D, Weingärtner H, Herrmann C, *Angew. Chem. Int. Ed.*, 2007; **46**: 8887–8889.
- [44] Jha I, Venkatesu P, *Phys. Chem. Chem. Phys.*, 2015; **17**: 20466–20484.
- [45] Greaves T L, Drummond C J, *Chem. Rev.*, 2015; **115**: 11379–11448.
- [46] Dong K, Zhang S, *Chem. Eur. J.*, 2012; **18**: 2748–2761.

- [47] Nuthakki B, Greaves T L, Krodkiewska I, Weerawardena A, Burgar M I, Mulder R J, Drummond C J, *Aust. J. Chem.*, 2007; **60**: 21–28.
- [48] Angell C A, Byrne N, Belieres J P, *Acc. Chem. Res.*, 2007; **40**: 1228–1236.
- [49] Esperanc J M S S, Lopes J N C, Tariq M, Santos L M N B F, Magee J W, Rebelo L P N, *J. Chem. Eng. Data*, 2010; **55**: 3–12.
- [50] Markusson H, Belieres J P, Johansson P, Angell C A, Jacobsson P, *J. Phys. Chem. A*, 2007; **111**: 8717–8723.
- [51] Fumino K, Wulfa A, Ludwig R, *Phys. Chem. Chem. Phys.*, 2009; **11**: 8790–8794.
- [52] Yoshizawa M, Xu W, Angell C A, *J. Am. Chem. Soc.*, 2003; **125**: 15411–15419.
- [53] Welton T, *Green Chem.*, 2011; **13**: 225–225.
- [54] Peplow M, Warning Shot for Green Chemistry, *news@nature.com*, 2005, DOI: 10.1038/news051031-8, Online: <http://www.nature.com/news/2005/051031/full/news051031-8.html>.
- [55] Pham T P T, Cho C W, Yun Y S, *Water Res.*, 2010; **44**: 352–372.
- [56] Docherty K M, Kulpa C F, *Green Chem.*, 2005; **7**: 185–189.
- [57] Stepnowski P, Stładanowski A C, Ludwiczak A, Laczynska E, *Hum. Exp. Toxicol.*, 2004; **23**: 513–517.
- [58] Cull S G, Holbrey J D, Vargas-Mora V, Seddon K R, Lye G J, *Biotechnol. Bioeng.*, 2000; **69**: 227–233.
- [59] Erbedinger M, Mesiano A J, Russell A J, *Biotechnol. Prog.*, 2000; **16**: 1129–1131.
- [60] Lau R M, van Rantwijk F, Seddon K R, Sheldon R A, *Org. Lett.*, 2000; **2**: 4189–4191.
- [61] Tavares, A.P.M.; Rodríguez, O.; Macedo, E.A. New Generations of Ionic Liquids Applied to Enzymatic Biocatalysis. In *Ionic Liquids-New Aspects for the Future*; Kadokawa, J., Ed.; InTech: Rijeka, Croatia, 2013; pp. 537–556. Available online: <http://www.intechopen.com/books/ionicliquids-new-aspects-for-the-future/new-generations-of-ionic-liquids-applied-to-enzymatic-biocatalysis>.
- [62] Moniruzzaman M, Kamiya N, Nakashima K, Goto M, *Green Chem.*, 2008; **10**: 497–500.
- [63] Park S, Kazlauskas R J, *Curr. Opin. Biotechnol.*, 2003; **14**: 432–437.
- [64] Summers C A, Flowers II R A, *Protein Sci.*, 2000; **9**: 2001–2008.
- [65] de Diego T, Lozano P, Gmouh S, Vaultier M, Iborra J. L, *Biotechnol. Bioeng.*, 2004; **88**: 916–924.
- [66] Byrne N, Wang L, Belieres J, Angell C A, *Chem. Commun.*, 2007: 2714–2716.
- [67] Mann J P, Cluskey A M, Atkin R, *Green Chem.*, 2009; **11**: 785–792.

- [68] Byrne N, Angell C A, *Chem. Commun.*, 2009; **7**: 1046–1048.
- [69] Bisht M, Jha I, Venkatesu P, *ChemistrySelect*, 2016; **1**: 3510–3519.
- [70] Mangialardo S, Gontrani L, Leonelli F, Caminiti R, Postorino P, *RSC Adv.*, 2012; **2**: 12329–12336.
- [71] Wang Z, Dang L, Han Y, Jiang P, Wei H, *J. Agric. Food Chem.*, 2010; **58**: 5444–5448.
- [72] Takekiyo T, Yamazaki K, Yamaguchi E, Abe H, Yoshimura Y, *J. Phys. Chem. B*, 2012; **116**: 11092–11097.
- [73] Lange C, Patil G, Rudolph R, *Protein Sci.*, 2005; **14**: 2693–2701.
- [74] Mester P, Wagner M, Rossmanith P, *Anal. Bioanal. Chem.*, 2010; **397**: 1763–1766.
- [75] Pei Y, Li L, Li Z, Wang J, *Sep. Sci. Technol.*, 2012; **47**: 277–283.
- [76] Yamamoto E, Yamaguchi S, Nagamune T, *Appl. Biochem. Biotechnol.*, 2011; **164**: 957–967.
- [77] Rawat K, Bohidar H, *J. Phys. Chem. B*, 2012; **116**: 11065–11074.
- [78] Rawat K, Bohidar H, *Int. J. Biol. Macromol.*, 2015; **73**: 23–30.
- [79] Zhou L, Danielson N D, *J. Chromatogr. B*, 2013; **940**: 112–120.
- [80] Kohlmann C, Robertz N, Leuchs S, Dogan Z, Lütz S, Bitzer K, Na’amnieh S, Greiner L, *J. Mol. Catal. B Enzym.*, 2011; **68**: 147–153.
- [81] Ferdjani S, Ionita M, Roy B, Dion M, Djeghaba Z, Rabiller C, Tellier C, *Biotechnol. Letts.*, 2011; **33**: 1215–1219.
- [82] Baker S N, McCleskey T M, Pandey S, Baker G A, *Chem. Commun.*, 2004: 940–941.
- [83] Kaftzik N, Wasserscheid P, Kragl U, *Org. Proc. Res. Dev.*, 2002; **6**: 553–557.
- [84] Zhao H, Campbell S M, Jackson L, Song Z, Olubajo O, *Tetrahedron Asymmetry*, 2006; **17**: 377–383.
- [85] Zhao H, Olubajo O, Song Z, Sims A L, Person T E, Lawal R A, Holley L A, *Bioorg. Chem.*, 2006; **34**: 15–25.
- [86] Fan Y, Zhang S, Wang Q, Li J, Fan H, Shan D, *Spectrochim. Acta Part A Mol. Biomol. Spectrosc.*, 2013; **105**: 297–303.
- [87] Persson M, Bornscheuer U T, *J. Mol. Catal. B Enzym.*, 2003; **22**: 21–27.
- [88] Lai J Q, Li Z, Lü Y H, Yang Z, *Green Chem.*, 2011; **13**: 1860–1868.
- [89] Chiappe C, Neri L, Pieraccini D, *Tetrahedron Lett.*, 2006; **47**: 5089–5093.
- [90] Otrelo-Cardoso A R, Schwuchow V, Rodrigues D, Cabrita E J, Leimkühler S, Romão M J, Santos-Silva T, *Plos One*, 2014; **9**: e87295.
- [91] Jia R, Hu Y, Liu L, Jiang L, Zou B, Huang H, *ACS Catal.*, 2013; **3**: 1976–1983.

- [92] Figueiredo A M, Sardinha J, Moore G R, Cabrita E J, *Phys. Chem. Chem. Phys.*, 2013; **15**: 19632–19643.
- [93] Fan Y, Zhang S, Wang Q, Li J, Fan H, Shan D, *Appl. Spectrosc.*, 2013; **67**: 648–655.
- [94] Bekhouche M, Blum L J, Doumèche B, *J. Phys. Chem. B*, 2012; **116**: 413–423.
- [95] Ajloo D, Sangian M, Ghadamgahia M, Evini M, Saboury A A, *Int. J. Biol. Macromol.*, 2013; **55**: 47–61.
- [96] Dabirmanesh B, Daneshjou S, Sepahi A A, Ranjbard B, Khavari-Nejad R A, Gill P, Heydari A, Khajeh K, *Int. J. Biol. Macromol.*, 2011; **48**: 93–97.
- [97] Jaeger V W, Pfaendtner J, *ACS Chem. Biol.*, 2013; **8**: 1179–1186.
- [98] Shigemi M, Takekiyo T, Yoshimura Y, *High Press. Res.*, 2013; **33**: 265–270.
- [99] Alvarez-Guerra E, Irabien A, *J. Chem. Technol. Biotechnol.*, 2015; **90**: 939–946.
- [100] Bai Z, Chao Y, Zhang M, Han C, Zhu W, Chang Y, Li H, Sun Y, *J. Chem.*, 2013; Article ID 938154, <http://dx.doi.org/10.1155/2013/938154>
- [101] Bae S Y, Kim S, Hwang H, Kim H K, Yoon H C, Kim J H, Lee S Y, Kim T D, *Biochem. Biophys. Res. Commun.*, 2010; **400**: 531–536.
- [102] Byrne N, Angell C A, *J. Mol. Biol.*, 2008; **378**: 707–714.
- [103] Hwang H, Choi H, Kim H K, Jo D H, Kim T D, *Anal. Biochem.*, 2009; **386**: 293–295.
- [104] Mester P, Wagner M, Rossmann P, *Separ. Purific. Technol.*, 2012; **97**: 211–215.
- [105] Monogioudi E, Permi P, Filpponen I, Lienemann M, Li B, Argyropoulos D, Buchert J, Mattinen M L, *J. Agric. Food Chem.*, 2011; **59**: 1352–1362.
- [106] Takács B, Nagy L, Kollár L, Nagy G, *Anal. Lett.*, 2010; **43**: 1734–1745.
- [107] Pinto P C A G, Saraiva M L M F S, Lima J L F C, *Anal. Sci.*, 2008; **24**: 1231–1238.
- [108] Paljevac M, Habulin M, Knez Z, *CI & CEQ*, 2006; **12**: 181–186.
- [109] Curto V F, Scheuermann S, Owens R M, Ranganathan V, MacFarlane D R, Benito-Lopez F, Diamond D, *Phys. Chem. Chem. Phys.*, 2014; **16**: 1841–1849.
- [110] Chiappe C, Leandri E, Lucchesi S, Pieraccini D, Hammock B D, Morisseau C, *J. Mol. Catal. B Enzym.*, 2004; **27**: 243–248.
- [111] Li T, Li B, Dong S, Wang E, *Chem. Eur. J.*, 2007; **13**: 8516–8521.
- [112] Debeljuh N, Barrow C J, Henderson L, Byrne N, *Chem. Commun.*, 2011; **47**: 6371–6373.
- [113] Tomlinson S R, Kehr C W, Lopez M S, Schlup J R, Anthony J L, *Ind. Eng. Chem. Res.*, 2014; **53**: 2293–2298.
- [114] Ebrahimi M, Hosseinkhani S, Heydari A, Khavari-Nejad R A, Akbar J, *Photochem. Photobiol. Sci.*, 2012; **11**: 828–834.

- [115] Kumar A, Venkatesu P, RSC Adv., 2014; **4**: 4487–4499.
- [116] Reddy P M, Umapathi R, Venkatesu P, Phys. Chem. Chem. Phys., 2014; **16**: 10708–10718.
- [117] Klähn M, Lim G S, Seduraman A, Wu P, Phys. Chem. Chem. Phys., 2011; **13**: 1649–1662.
- [118] Klähn M, Lim G S, Wu P, Phys. Chem. Chem. Phys., 2011; **13**: 18647–18660.
- [119] Jha I, Attri P, Venkatesu P, Phys. Chem. Chem. Phys., 2014; **16**: 5514–5526.
- [120] Castiglione F, Raos G, Appetecchi G B, Montanino M, Passerini S, Moreno M, Famulari A, Mele A, Phys. Chem. Chem. Phys., 2010; **12**: 1784–1792.
- [121] Niedermeyer H, Hallett J P, Villar-Garcia I J, Hunt P A, Welton T, Chem. Soc. Rev., 2012; **41**: 7780–7802.
- [122] Chatel G, Pereira J F B, Debbeti V, Wang H, Rogers R D, Green Chem., 2014; **16**: 2051–2083.
- [123] Ruana C, Li T, Niu Q, Lu M, Lou J, Gao W, Sun W, Electrochim. Acta, 2012; **64**: 183–189.
- [124] Lozano P, Bernal B, Bernal J M, Pucheault M, Vaultier M, Green Chem., 2011; **13**: 1406–1410.
- [125] Lee S H, Doan T T N, Ha S H, Chang W J, Koo Y M, J. Mol. Catal. B Enzym., 2007; **47**: 129–134.
- [126] Reddy P M, Umapathi R, Venkatesu P, Phys. Chem. Chem. Phys., 2015; **17**: 184–190.
- [127] Lee S H, Ha S H, Lee S B, Koo Y M, Biotechnol. Letts., 2006; **28**: 1335–1339.
- [128] Lee S H, Ha S H, Hiep N M, Chang W J, Koo Y M, J. Biotechnol., 2008; **133**: 486–489.
- [129] Ha S H, Hiep N M, Koo Y M, Biotechnol. Bioprocess Eng., 2010; **15**: 126–130.
- [130] Long J, Guo B, Li X, Jiang Y, Wang F, Tsang S C, Wang L, Yu K M K, Green Chem., 2011; **13**: 2334–2338.
- [131] Gurau G, Wang H, Qiao Y, Lu X, Zhang S, Rogers R D, Pure Appl. Chem., 2012; **84**: 745–754.
- [132] Yao P, Pu X, Huang X, Int. J. Biol. Macromol., 2015; **77**: 243–249.
- [133] Ortiz-Costa S, Sorenson M M, Sola-Penna M, Arch. Biochem. Biophys., 2002; **408**: 272–278.
- [134] Yancey P H, Clark M E, Hand S C, Bowlus R D, Somero G N, Science, 1982; **217**: 1214–1222.
- [135] Garlitz J A, Summers C A, Flowers R A, Borgstahl G E, Acta Crystallogr. D, 1999; **55**: 2037–2038.
- [136] Bisht M, Kumar A, Venkatesu P, RSC Adv., 2016; **6**: 18763–18777
- [137] Yamaguchi S, Yamamoto E, Tsukiji S, Nagamune T, Biotechnol. Prog., 2008; **24**: 402–408.

- [138] Takekiyo T, Nihei A, Yamazaki K, Aono M, Abe H, Yoshimura Y, *J. Solution Chem.*, 2014; **43**: 1701–1709.
- [139] Tischer A, Pultke H, Topf A, Auton M, Lange C, Lilie H, *FEBS J.*, 2014; **281**: 1738–1749.
- [140] Jaganathan M, Ramakrishnan C, Velmurugan D, Dhathathreyan A, *J. Mol. Struct.*, 2015; **1081**: 334–341.
- [141] Fiebig O C, Mancini E, Caputo G, Vaden T D, *J. Phys. Chem. B*, 2014; **118**: 406–412.
- [142] Malhotra S V, Kumar V, *Bioorg. Med. Chem. Letts.*, 2010; **20**: 581–585.
- [143] Attri P, Venkatesu P, Kumar A, *Phys. Chem. Chem. Phys.*, 2011; **13**: 2788–2796.
- [144] Attri P, Venkatesu P, Kumar A, Byrne N, *Phys. Chem. Chem. Phys.*, 2011; **13**: 17023–17026.
- [145] Attri P, Venkatesu P, *Int. J. Biol. Macromol.*, 2012; **51**: 119–128.
- [146] Attri P, Jha I, Choi E H, Venkatesu P, *Int. J. Biol. Macromol.*, 2014; **69**: 114–123.
- [147] Attri P, Choi E H, *Plos One*, 2013; **8**: 1–11.
- [148] Kumar A, Venkatesu P, *RSC Adv.*, 2013; **3**: 362–367.
- [149] Byrne N, Rodoni B, Constable F, Varghese S, Davis J H, Jr., *Phys. Chem. Chem. Phys.*, 2012; **14**: 10119–10121.
- [150] Yu X, Zou F, Li Y, Lu L, Huang X, Qu Y, *Int. J. Biol. Macromol.*, 2013; **56**: 62–68.
- [151] Rodrigues V, Ruivo D, Rodríguez A, Deive F J, Esperança J M S S, Marrucho I M, Gome C M, Rebelo L P N, *Green Chem.*, 2014; **16**: 4520–4523.
- [152] Jha I, Venkatesu P, *ACS Sustain. Chem. Eng.*, 2016; **4**: 413–421.
- [153] Jha I, Bisht M, Venkatesu P, *J. Phys. Chem. B*, 2016; **120**: 5625–5633.
- [154] Jha I, Kumar A, Venkatesu P, *J. Phys. Chem. B*, 2015; **119**: 8357–8368
- [155] Bisht M, Kumar M, Venkatesu P, *Int. J. Biol. Macromol.*, 2015; **81**: 1074–1081
- [156] Yang C, Jang S, Pak Y, *Nat. Commun.*, 2014; **5**: 1–8.
- [157] Kumar A, Rani A, Venkatesu P, Kumar A, *Phys. Chem. Chem. Phys.*, 2014; **16**: 15806–15810.

Ionic Liquid-Induced Unique Structural Transitions of Proteins

Takahiro Takekiyo and Yukihiro Yoshimura

Additional information is available at the end of the chapter

<http://dx.doi.org/10.5772/65886>

Abstract

The structural transitions of proteins in aqueous solutions of various ionic liquids (ILs) over a wide concentration range (x (mol% IL) = 0–30) were investigated using Fourier-transform infrared and near-UV circular dichroism spectroscopy combined with small-angle X-ray scattering. The proteins in the aqueous IL solutions showed two structural transition patterns: (i) the folded state \rightarrow unfolded state \rightarrow partial globular state (α -helical formation disrupted tertiary structure) and (ii) the folded state \rightarrow unfolded state \rightarrow aggregation (amyloid-like aggregation or disordered aggregation). We found that the helical formation of proteins in the condensed IL solutions was strongly related to the competition between the low polarity and denaturation effect of ions. Moreover, the amyloid-like aggregate formation correlated with the competition between the size of the confined water assemblies in the IL layer and the IL-amino acid residue interactions. On the basis of these results, we discussed the future applications of ILs, including their use as cryoprotectants for proteins and as agents for the suppression of amyloid formation.

Keywords: protein, aqueous ionic liquid solution, aggregation, helix formation, optical spectroscopy

1. Introduction

Aqueous mixtures of proteins and ionic liquids (ILs), which comprise organic cations and anions and remain in the liquid state below 373 K, are employed in protein engineering applications, such as protein storage media, biocatalysts, and buffers [1–3]. Although these applications are based on the unique solvent properties of these mixtures, such as their solubility in water and solution structure [2, 4], the detailed relationship between the proteins and aqueous IL solutions at the molecular level is unclear. Thus, to realize the protein engineering

applications of ILs, numerous studies have been conducted on the structural stability and activity of proteins in aqueous IL solutions [2–8].

For instance, Lange et al. [6] demonstrated that the addition of imidazolium-based ILs (up to 4 M) to renaturation buffers caused high protein renaturation without protein aggregation, whereas addition to the folded protein induced a decrease in the structural stability. Many aqueous IL solutions are found to degrade the structural stability and activity of proteins at x (mol% IL) < 6 [2, 3, 7, 8]. This decrease in protein stability in dilute aqueous IL solutions can be explained by the Hofmeister series [7, 8]. This series ranks the relative influence of ions on the physical behavior of a wide variety of aqueous processes ranging from colloidal assembly to protein folding. Originally, it was assumed that the influence of ions on protein folding was caused at least in part by “making” and “breaking” bulk water structures [9]. However, these investigations of protein stability in dilute aqueous IL solutions have not sufficiently considered essential properties of ILs. Thus, it is necessary to obtain basic information on protein stability over a wide IL concentration range to realize protein engineering using ILs.

Recently, intriguing phenomena such as protein refolding and aggregate formation have been observed in condensed IL solutions ($x > 10$) or pure IL. Imidazolium-based or alkylammonium-based ILs at a concentration of $x > 10$ induce the formation of α -helical structures of protein, such as human interleukin-2 [10] and succinylated concanavalin A [11]. Moreover, Hwang et al. [12] showed that imidazolium- and pyridinium-based ILs promoted amyloid formation in α -synuclein and α -lactalbumin. Similarly, Debeljuh et al. [13] demonstrated that addition of protic ILs, such as triethylammonium-based ILs, to A β 1–40 peptide promotes amyloid aggregation. These intriguing protein-refolding/amyloid-formation phenomena in condensed ILs or pure ILs may be related to the essential properties of ILs and cannot be explained by Hofmeister series, as in the case of protein unfolding in dilute aqueous IL solutions.

Related to these phenomena, the solvent properties of ILs, such as viscosity and dielectric constant, drastically change at a certain IL concentration [2]. These changes depend on the amount of water in the mixture. In addition, it is known that IL solutions adopt a nanoheterogeneous structure with a polar domain, i.e., the ionic parts of the cations and anions, and a nonpolar domain, i.e., the alkyl chain of the cations [14–16]. In binary solutions under water-rich conditions [17], IL-water mixtures adopt IL-aggregated structures that are surrounded by bulk water molecules; therefore, the nanoheterogeneity of these systems is relatively low. However, under IL-rich conditions wherein the mixtures exhibit molten-salt-like behavior, the water molecules are scattered in the polar domain and self-assemble in the ILs. The water molecules in this state are termed “confined water” [18, 19] and the nanoheterogeneity of these systems is higher. As mentioned earlier, these solvent properties may contribute to unique structural transitions of the proteins. Thus, detailed information on protein stability over a wide range of IL concentrations is valuable, and this information would facilitate the use of ILs in protein engineering applications.

This manuscript aims to determine the structural stabilities of various model proteins over a wide concentration range of ILs using optical spectroscopy combined with small-angle X-ray scattering (SAXS). The origin of the structural transitions of proteins in condensed aqueous IL solutions has been discussed.

2. Experimental methodology

2.1. Materials

Chicken lysozyme, bovine ribonuclease A (RNase A) and bovine β -lactoglobulin (β -LG), horse cytochrome *c*, bovine myoglobin, bovine rhodanese, and bovine insulin were purchased from Sigma and were used without further purification. The ILs 1-butyl-3-methylimidazolium chloride ([bmim][Cl]) (Kanto Chemical Co.), [bmim][NO₃] (Sigma), [bmim][SCN] (Sigma), 1-ethyl-3-methylimidazolium nitrate ([emim][NO₃]) (Iolitec), methylammonium nitrate (MAN) (Iolitec), ethylammonium nitrate (EAN) (Iolitec), and propylammonium nitrate (PAN) (Iolitec) were used in this study. All aqueous mixtures with concentrations of x (mol% IL) were prepared by mixing the required amount of the IL and D₂O (Kanto Chemical Co.) at room temperature. The prepared concentrations of the aqueous IL solutions were $x = 0$ –30 because of the overlap of the cations with proteins in the Fourier-transform infrared (FTIR) spectra. The concentrations of the proteins were adjusted to 20 mg mL⁻¹, which does not result in protein aggregation in water ($x = 0$). Samples were loaded into a transmission cell with CaF₂ windows and a Teflon spacer (50 μ m) for FTIR and near-UV circular dichroism (CD) spectral measurement under the same protein conditions as used in the condensed ILs. These spectral analyses were performed using the GRAMS software (Galactic Software).

2.2. FTIR spectroscopy

The amide I' vibrational mode (deuterated peptide groups) in FTIR spectra is highly sensitive to the secondary structure of proteins, and thus it serves as an indicator of α -helix and β -sheet formation [20]. FTIR spectra were recorded using a Nicolet 6700 FTIR spectrometer equipped with a mercury-cadmium-telluride liquid-nitrogen detector. Typically, 512 interferograms were collected to obtain spectra with a resolution of 4 cm⁻¹. Solvent spectra were also measured under the same conditions as those used for the protein solution measurements and were subtracted from the protein solution spectra.

2.3. CD spectroscopy

Near-UV CD spectra in the range of 250–300 nm are sensitive to the presence of specific rigid packing interactions between aromatic side chains, indicating changes in the tertiary structure [21]. CD spectra were measured over a wavelength range of 250–300 nm on a JASCO J-820 spectropolarimeter. Typically, spectra were accumulated at a scan rate of 20 nm min⁻¹ in 0.1 nm steps. Five scans were averaged for each spectrum. The obtained spectra were converted into mean residue ellipticity units using $[\theta] = \theta_{\text{obs}} / (10ncl)$, where θ_{obs} is the observed ellipticity, l is the path length, c is the protein concentration, and n is the number of residues.

2.4. SAXS

SAXS is a powerful technique for investigating protein size and the presence of protein aggregation [22]. SAXS experiments were conducted using a Kratky camera system (BioSAXS-1000, Rigaku Co.) at a brilliance of 56.0 kW mm⁻². CuK α radiation ($\lambda = 0.1542$ nm) was selected and

collimated using a parabolic multilayer mirror. The beam was focused by a converting optical tool (CBO-*f*, Rigaku Co.). The beam size was 0.5 mm (V) \times 0.1 mm (H) at the sample position, and the camera distance was 500 mm. The combination of the 2D Kratky block and focusing optics can achieve a wide q range. Here the scattering vector q is defined as $4\pi\sin\theta/\lambda$ (nm^{-1}). A 2D detector (PILATUS 100 K/R) was used. Samples were put into quartz capillaries with a diameter of 1.0 mm and a thickness of 0.1 mm. The scattering of the aqueous IL solutions was subtracted, and the final scattering curve was obtained using the program *PRIMUS*.

3. Results and discussion

3.1. Structural transition of proteins in aqueous solutions with [bmim]-based ILs

As representative results, **Figure 1a** and **b** shows the FTIR amide I' spectra of myoglobin and cytochrome *c* in aqueous solutions under concentrations of [bmim][NO₃] up to $x = 30$. The amide I' spectra of both proteins change significantly as a function of [bmim][NO₃] concentration. The peaks at ca. 1615 and ca. 1690 cm^{-1} , which are due to the intermolecular β -sheet structure and indicate myoglobin aggregation [23], are observed above $x = 5$. However, no such peaks appear for cytochrome *c* over the studied [bmim][NO₃] concentrations.

To further investigate the changes in the secondary structure of both proteins, we plotted the changes in the maximum absorbance (Abs) values of these two proteins against the [bmim][NO₃] concentrations, as shown in **Figure 1c** and **d**. For myoglobin, the first decrease in the Abs value, indicating myoglobin unfolding, is observed in the region $x = 1$ –5. The second decrease in the Abs value, indicating the formation of an intermolecular β -sheet structure, is observed at $x > 7$. Thus, the addition of [bmim][NO₃] to myoglobin causes the fold \rightarrow unfold \rightarrow intermolecular β -sheet transition.

Conversely, a drastic decrease in Abs for cytochrome *c* is observed up to $x = 7$, and it is noteworthy that the Abs value increases at $x > 7$. From the second-derivative analysis of the FTIR spectra, the peak at ca. 1645 cm^{-1} indicates an increase in the disordered structure up to $x = 7$, and further addition causes the increase in the peak at ca. 1655 cm^{-1} , which indicates an α -helical structure (inset in **Figure 1d**). Based on these FTIR spectra, the increase in Abs at $x > 7$ is due to the partial refolding of the secondary structure of cytochrome *c*. However, the partial refolding at $x > 7$ is not sufficiently confirmed by only the FTIR result. If the partial refolding of cytochrome *c* occurs at $x > 7$, the whole cytochrome *c* size would be smaller than in the unfolded state and larger than in the folded state. Therefore, to further investigate the state of cytochrome *c* in aqueous [bmim][NO₃] solutions, we performed SAXS measurements.

Figure 2a shows a Guinier plot of cytochrome *c* in aqueous [bmim][NO₃] solutions where the radius of gyration (R_g) was estimated. The Guinier equation is defined as follows:

$$I(q) = I(0)\exp(-R_g^2 q^2) \quad (1)$$

where $I(0)$ is the intensity at $q = 0$. The Guinier equation is valid in the range of $R_g q < 1$. In this study, despite the fact that the range $0 < R_g q < 2$ was employed, a linear relationship in the

Guinier plots is observed. In aqueous [bmim][NO₃] solutions, the R_g values of cytochrome *c* were obtained in the same manner. The R_g values of cytochrome *c* are 13.4 Å for $x = 0$, 25.0 Å for $x = 5$, and 15.0 Å for $x = 20$. The R_g values at $x = 0$ and 5 are in good agreement with those of the folded state ($R_g = 13.8$ Å) and unfolded state ($R_g = 24.0$ Å) reported by Cinelli et al. [24]. As speculated above, the R_g value of cytochrome *c* at $x = 20$ is larger than that at $x = 0$ and smaller than that at $x = 5$. Thus, cytochrome *c* at $x = 20$ takes a more compact structure than at $x = 5$ and does not completely unfold without aggregation.

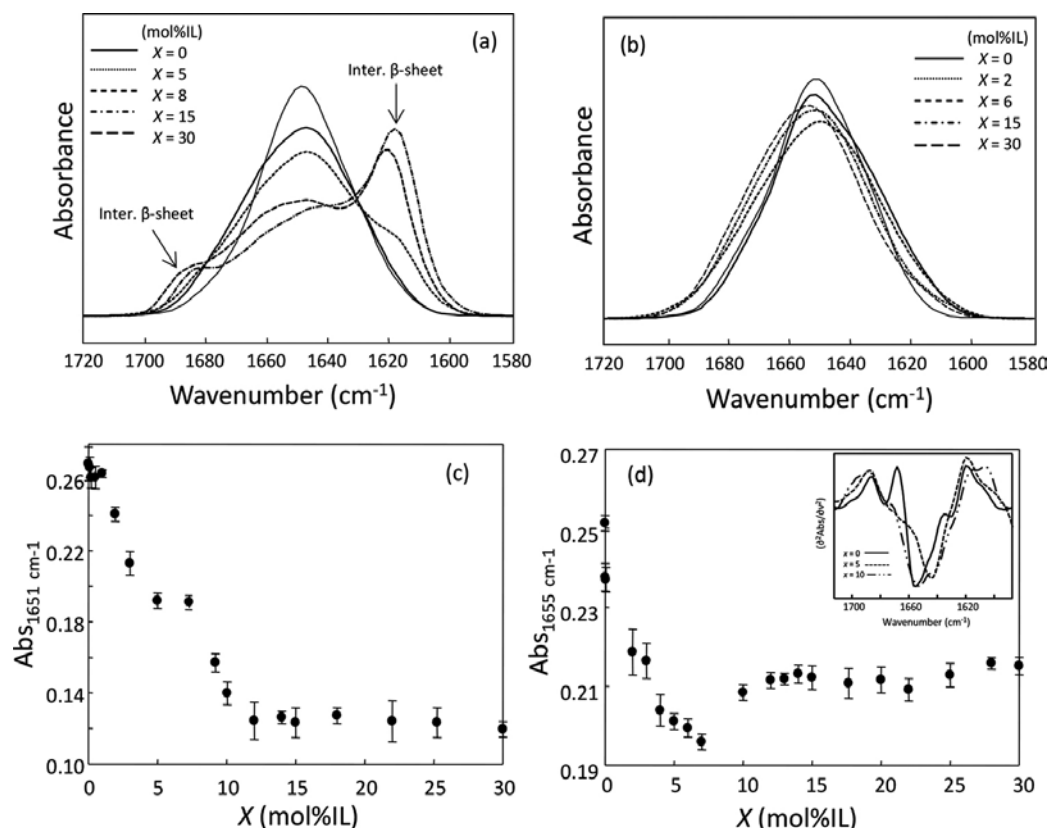


Figure 1. FTIR spectra in the amide I' region of (a) myoglobin and (b) cytochrome *c* in aqueous [bmim][NO₃] solutions at several [bmim][NO₃] concentrations. Changes in absorbance of (c) myoglobin ($Abs_{1651\text{cm}^{-1}}$) and (d) cytochrome *c* ($Abs_{1655\text{cm}^{-1}}$) as a function of [bmim][NO₃] concentration. Inset figure shows the second derivative spectra of cytochrome *c* in aqueous [bmim][NO₃] solutions at $x = 0, 5$, and 10 , respectively.

A similar result is also obtained using Kratky plots (Figure 2b). Kratky plots provide insight into the compactness of a protein, i.e., a bell shape in the plot indicates a globular protein, whereas a plateau, seen in the high q region, suggests that the protein is unfolded. The addition of [bmim][NO₃] shifts the peak of the bell shape to a smaller q region, indicating that the size of cytochrome *c* increases with increasing [bmim][NO₃] concentration. This implies that cytochrome *c* in aqueous [bmim][NO₃] solutions, even at high [bmim][NO₃] concentrations, is not completely unfolded. Combination with FTIR and SAXS

results indicate that the aqueous [bmim][NO₃] solution at $x = 20$ causes cytochrome *c* to partially refold without aggregation.

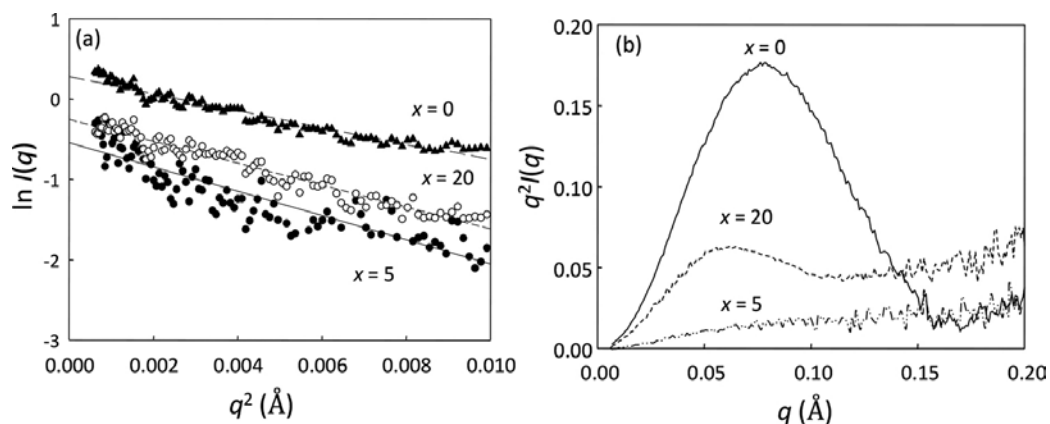


Figure 2. (a) Guinier plots and (b) Kratky plots of cytochrome *c* in aqueous [bmim][NO₃] solutions at $x = 0, 5,$ and 20 .

Next, we measured the changes in the tertiary structure of both proteins induced by [bmim][NO₃] using near-UV CD spectroscopy (**Figure 3a** and **b**). Although the negative CD intensity at 290 nm for myoglobin and 288 nm for cytochrome *c* due to the aromatic residues drastically decreases at [bmim][NO₃] concentrations of up to $x = 7$, no increase in the negative CD intensity occurs above $x = 7$ (**Figure 3c** and **d**). This indicates that an increase in the [bmim][NO₃] concentration completely disrupts the tertiary structure of both proteins.

The results from the FTIR, SAXS, and near-UV CD analyses show that aqueous [bmim][NO₃] solutions of up to $x = 5$ – 7 cause myoglobin and cytochrome *c* to unfold. Further addition of [bmim][NO₃] induces formation of the intermolecular β -sheet for myoglobin and the partially globular (PG) state, which is the α -helical formation disrupted tertiary structure, for cytochrome *c*. Consequently, changes in the concentration of [bmim][NO₃] induce structural transitions of the folded state \rightarrow unfolded state \rightarrow intermolecular β -sheet aggregation for myoglobin, and the folded state \rightarrow unfolded state \rightarrow PG state for cytochrome *c*. Similar structural transitions are observed in other proteins (β -LG, lysozyme, and RNase A) in aqueous solutions with other [bmim]-based ILs ([bmim][Cl] and [bmim][SCN]), except for cytochrome *c* in condensed [bmim][SCN] solutions (cytochrome *c* in this media takes the disordered-rich aggregate) [24–28]. **Figure 4** summarizes the structural transitions of proteins in aqueous solutions over a wide IL concentration range.

The most remarkable result is that condensed solutions with [bmim]-based ILs cause the formation of an α -helical structure, and intermolecular β -sheets or disordered-rich aggregation. From the previous results, the former state is similar to the intermediate in the on- or off-pathway for the protein folding process [29], and the latter state is similar to the amyloid structure associated with neurodegenerative conditions such as Parkinson's disease [30, 31] and the structure of the inclusion body in expression proteins [30, 32]. Thus, it is important to reveal the origin of the structural formation of proteins in condensed aqueous IL solutions in

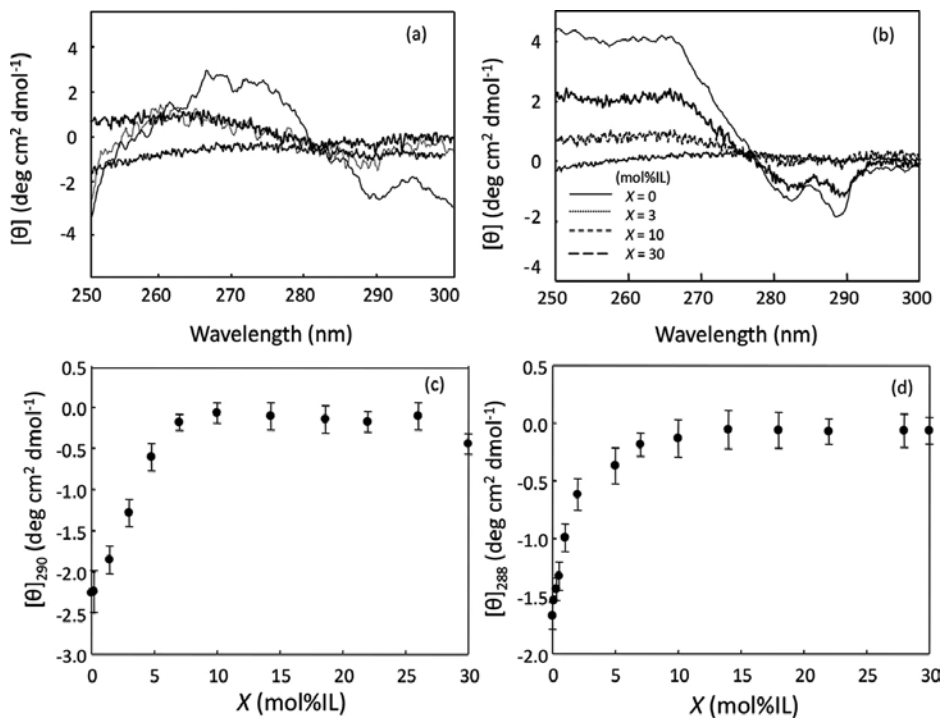


Figure 3. Near-UV CD spectra in the amide I' region of (a) myoglobin and (b) cytochrome *c* in aqueous [bmim][NO₃] solutions at several [bmim][NO₃] concentrations. Changes in ellipticity of (c) myoglobin ([θ]₂₉₀) and (d) cytochrome *c* ([θ]₂₈₈) as a function of [bmim][NO₃] concentration.

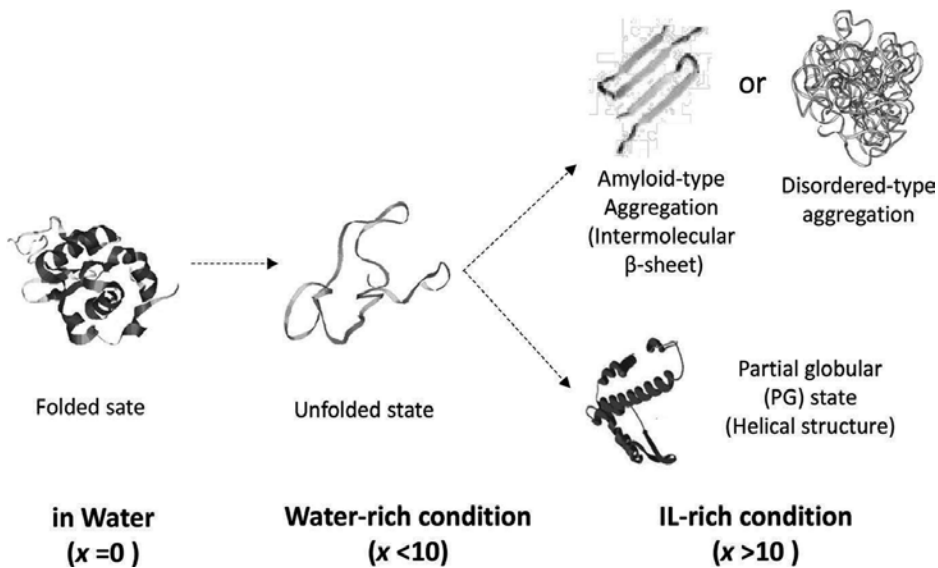


Figure 4. Summary of structural transition of proteins in aqueous ILs solutions.

view of protein engineering application using ILs. In the following sections, we discuss the preferential formation of the α -helical structure (PG state) in Section 3.2, and intermolecular β -sheet aggregation in Section 3.3.

3.2. Helix formation ability of ILs for proteins

We found that condensed aqueous solutions with [bmim]-based ILs induce the helical formation disrupted tertiary structure (PG state) for some proteins. Generally, it is well known that β -LG and RNase A, having substantial β -sheet contents, take non-native helical formations in aqueous alcohol solutions, such as 2,2,2-trifluoroethanol [33–35]. This is termed alcohol denaturation. The PG state in condensed IL solutions structurally resembles that from alcohol denaturation. Here, we focused on the details of helical formation ability of ILs for β -LG and RNase A.

Figure 5a and **b** shows the FTIR spectra of β -LG and RNase A in aqueous [bmim][NO₃] solutions of several concentrations. On the whole, the absorbance of both proteins at ca. 1635 cm⁻¹, indicating intramolecular β -sheet structure, decreases, and that at ca. 1656 cm⁻¹, indicating the α -helix structure, increases with [bmim][NO₃] concentration (**Figure 5a** and **c**). Both proteins undergo helix formation at high [bmim][NO₃] concentrations, though β -LG forms an intermolecular β -sheet structure in addition to an α -helical structure. Characterization of the helix formation in condensed aqueous [bmim][NO₃] solutions reveals that it is similar to that seen for alcohol denaturation, which results in a direct β - α transition. However, it is intriguing whether the condensed [bmim][NO₃] solutions induce direct β - α transition, as in the case of alcohol denaturation.

We assessed the second-derivative FTIR spectra of β -LG and RNase A in aqueous [bmim][NO₃] solutions at different concentrations of [bmim][NO₃] (**Figure 5c** and **d**). Increasing the [bmim][NO₃] concentration up to $x = 1$ – 5 causes a decrease in the intramolecular β -sheet structure and an increase in the disordered structure of both proteins. With further addition of [bmim][NO₃] (up to $x = 30$), the disordered structure decreases and the α -helical content increases. Conversely, our previous FTIR spectra showed that the intramolecular β -sheet structure of β -LG in the aqueous TFE solution drastically decreases with increasing TFE concentration, and the α -helical content increases without the appearance of the disordered structure [26]. Importantly, the metastable intermediate, i.e., native β -sheet \rightarrow disordered structure \rightarrow non-native α -helix, in the β - α transition process, can be observed in aqueous [bmim][NO₃] solutions. Unlike alcohol denaturation (direct β - α transition), the aqueous [bmim][NO₃] solutions cause helix formation in β -LG and RNase A through an intermediate disordered structure. Although similar helix formation ability is observed in [bmim][Cl], its ability is weaker than [bmim][NO₃]. Besides, [bmim][SCN], representing a strong denaturant, does not show helix formation ability.

Here we discuss the origin of helix-forming ability of [bmim]-based ILs for β -LG and RNase A. Generally, alcohol denaturation is thought to arise from solvent properties such as low polarity. Low solvent polarity weakens the hydrophobic interactions that stabilize the compact native structure of proteins while simultaneously strengthening the intramolecular electrostatic interactions, such as hydrogen bonds, and stabilizing secondary structures, particularly the α -helix. The dielectric constant (ϵ) of the [bmim]-based ILs is low ($\epsilon = 10$ – 20) [36], similar

to that seen in alcohols (32.6 for methanol [37] and 27 for TFE [38]). The results suggest that [bmim]-based ILs cause an enhancement of the intramolecular hydrogen bonding in proteins by removing water molecules from their proximity. Accordingly, the similar solvent polarity of aqueous [bmim]-based ILs and aqueous alcohol solutions likely causes the structural changes observed for both proteins and stabilizes their α -helix structure. While the condensed [bmim][SCN] solutions, which is a strong denaturant, did not show the helix formation for β -LG and RNase A. Thus, the helix-forming ability of [bmim]-based ILs depended on the anionic species, and is related to the competition between the low polarity of condensed IL and denaturant effect of anions showing the anion-protein interaction.

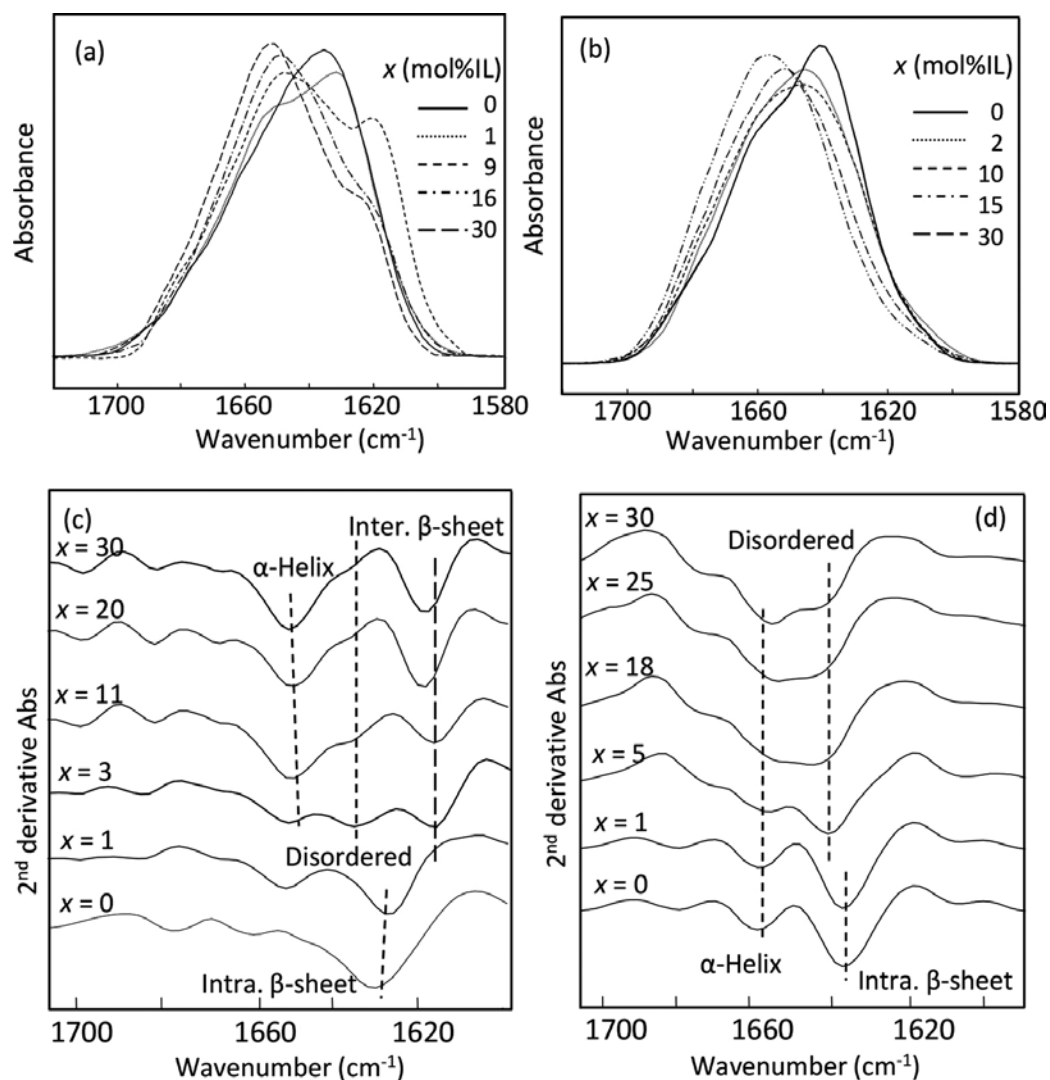


Figure 5. FTIR (a and b) and second derivative (c and d) spectra of β -LG and RNase A in aqueous [bmim][NO₃] solutions at several [bmim][NO₃] concentrations.

Next we discuss the generality of helix formation of ILs with NO_3^- . The helix-forming ability of $[\text{bmim}][\text{NO}_3]$ for proteins has been connected to its low polarity; however, similar solution properties are also observed in other ILs with NO_3^- anion. To elucidate the generality of helix formation of β -sheet-rich proteins in ILs with NO_3^- , we compared two imidazolium-based ILs ($[\text{bmim}][\text{NO}_3]$ and 1-ethyl-3-methylimidazolium nitrate ($[\text{emim}][\text{NO}_3]$)) and the three alkylammonium nitrates (RAN-ILs): MAN, EAN, and PAN.

As a representative result, the FTIR spectra of RNase A in condensed aqueous solutions with various ILs at $x = 30$ are shown in **Figure 6a**. Although the FTIR spectral shape of RNase A in MAN shows slight RNase A unfolding, those with other ILs show a decrease in the native sheet structure and an increase in the helix structure. The amounts of α -helix structures in RNase A and β -LG were determined using a curve-fitting method (**Figure 6b**). Notably, the amounts of α -helix structures in RNase A (\circ) and β -LG (\bullet) with the ILs (except for MAN) are essentially the same (within estimated experimental errors). This indicates that the effect of IL cations on the secondary structure of both proteins is negligible. The orders of solvent-induced helix formation of RNase A and β -LG are $\text{D}_2\text{O} \ll \text{MAN} \ll [\text{emim}][\text{NO}_3] < \text{EAN} \sim \text{PAN} \sim [\text{bmim}][\text{NO}_3]$ (the value of α -helical content of β -LG in $[\text{bmim}][\text{NO}_3]$ is slightly lower than those in EAN, PAN, and $[\text{bmim}][\text{NO}_3]$ by the formation of intermolecular β -sheets). The present results indicate that condensed aqueous ILs with NO_3^- solutions show a high helix-forming ability for β -sheet-rich proteins, such as RNase A and β -LG.

On the basis of these results, we can conclude that the helix-forming ability of IL depended on the anionic species rather than the cationic species. Besides, this ability is strongly related to the competition between the low polarity and denaturation effect of anions.

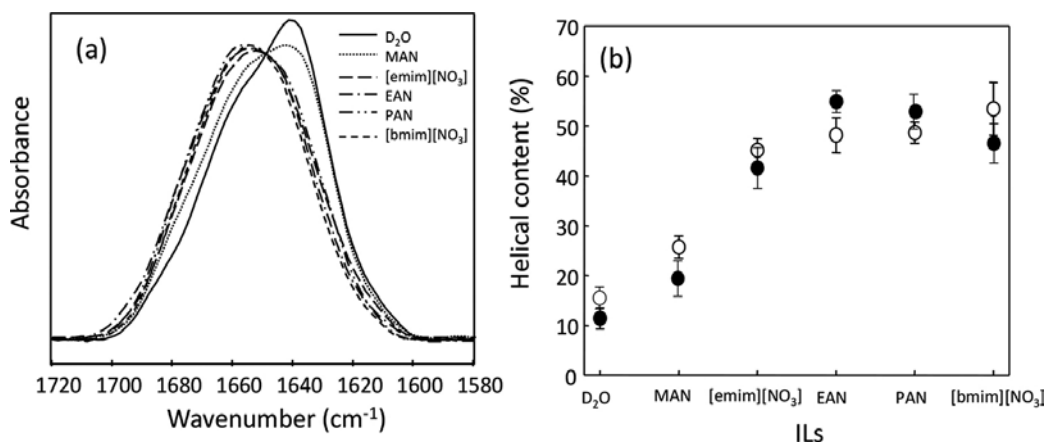


Figure 6. (a) FTIR spectra in the amide I region of RNase A at various ILs with NO_3^- ($x = 30$). (b) Contents of the α -helical structures of RNase A and β -LG at various ILs with NO_3^- ($x = 30$).

3.3. Ionic liquid-induced amyloid-like aggregation

Another intriguing phenomena associated with condensed IL solutions are the formation of intermolecular β -sheet structures (i.e., amyloid-like aggregation). As mentioned in Section 3.1,

amyloid-like aggregation is related to neurodegenerative diseases such as Parkinson's disease and the structure of the inclusion body [30–32]. The origin of amyloid-like aggregate formation in ILs is related to the suppression of protein aggregation. Consequently, we focused on amyloid-like aggregate formation in condensed aqueous solutions of [bmim][NO₃] and [bmim][SCN].

First, we address the case of [bmim][NO₃]. **Figure 7a** shows the FTIR spectra of the eight model proteins, which have different secondary structures and sizes in condensed aqueous [bmim][NO₃] solutions ($x = 20$). The FTIR spectra of rhodanese, α -chymotrypsin, β -LG, myoglobin, and clearly present peaks at ca. 1615 and ca. 1690 cm⁻¹, are indicating amyloid-like aggregation. In contrast, the four remaining proteins (lysozyme, RNase A, cytochrome *c*, and insulin) do not present these two peaks. Similar FTIR spectra are also obtained from an aqueous [bmim][Cl] solution at $x = 20$. To investigate whether the four proteins aggregate, their SAXS profiles were recorded [39]. The SAXS curves show a drastic increase in $I(q)$ below $q = 0.03$ nm⁻¹ for rhodanese, α -chymotrypsin, β -LG, myoglobin, indicating protein aggregation. However, the other four proteins do not aggregate, as indicated by their SAXS

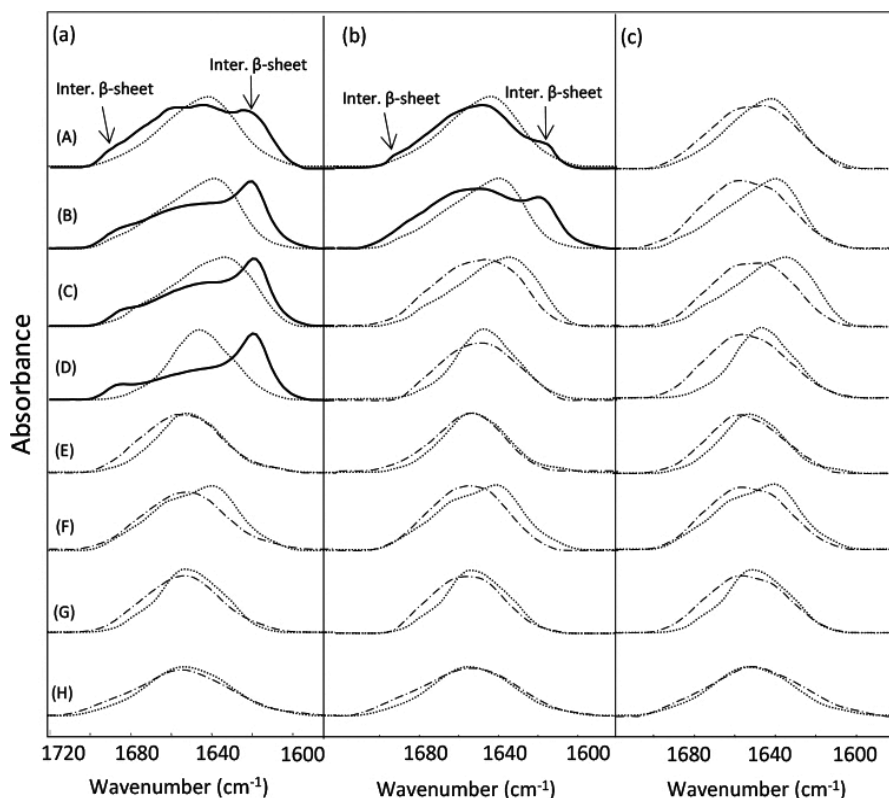


Figure 7. FTIR spectra of various proteins ((A) rhodanese, (B) α -chymotrypsin, (C) β -LG, (D) myoglobin, (E) lysozyme, (F) RNase A, (G) cytochrome *c*, and (H) insulin) in water (dotted line) and in ILs ((a) [bmim][NO₃], (b) [emim][NO₃], and (c) EAN) solutions ($x = 20$). The solid and dashed-dotted lines represent aggregated and nonaggregated proteins, respectively.

curves, which do not show a significant increase in $I(q)$ below $q = 0.03 \text{ nm}^{-1}$. These results are consistent with those from the FTIR experiments. The FTIR and SAXS results indicate that aqueous [bmim][NO₃] solutions at $x = 20$ promote the formation of amyloid-like aggregates in rhodanese, α -chymotrypsin, β -LG, and myoglobin, whereas the same solutions inhibit aggregation for lysozyme, RNase A, cytochrome *c*, and insulin.

Here, to investigate the influence of the imidazolium cation alkyl chain length on the decrease in amyloid-like aggregation, FTIR spectra were recorded for proteins in aqueous solutions ($x = 20$) of [emim][NO₃], which has a shorter alkyl chain length (**Figure 7b**). Intriguingly, the two peaks indicating an intermolecular β -sheet structure are observed for rhodanese and α -chymotrypsin. Conversely, the spectra of the other proteins do not contain these peaks, and the six remaining proteins form an α -helical structure, as in the case of [bmim][NO₃]. The protein size at which aggregation occurs in aqueous [emim][NO₃] solutions is larger than that in aqueous [bmim][NO₃] solutions. Thus, the formation of amyloid-like aggregates depends on the alkyl chain length of the cation.

In order to gain insight into the amyloid-like aggregate formation, we have focused on the solution structure and protein size. As discussed in Section 1, it has been suggested that the structural changes of proteins in aqueous IL solutions are strongly related to the solution structures of these media. 1-Alkyl-3-methylimidazolium-based ILs form nanoheterogeneous structures containing polar and nonpolar domains. The solutions exhibit molten-salt-like behavior, and the water molecules are scattered in the polar domain and self-assemble into confined-water-type domains under IL-rich conditions. The SAXS and small-angle neutron scattering (SANS) results imply that confined water exists in aqueous [bmim][NO₃] solutions at $x = 20$ [18, 19]. Moreover, an increase in alkyl chain length results in an enhancement of nanoheterogeneity [40]. Thus, in the condensed aqueous IL solutions, a decrease in the alkyl chain length of the cation may induce an increase in the size of the confined water domains. In terms of the relationship between the protein structure and the solution structure of the aqueous IL solutions, it has been suggested that proteins in condensed IL solutions are hydrated with water molecules in IL layers [3, 41, 42]. Jaganathan et al. [41] demonstrated the organization of ILs around hydrated cytochrome *c* in high-concentration ILs using molecular dynamics simulations. Similarly, according to the analysis of transfer free energy (ΔG_t) in cyclic dipeptides from water to aqueous IL solutions conducted by Attri and Venkatesu [42], ILs interact unfavorably with protein surfaces, thus promoting the formation of hydration layers around the proteins.

On the basis of these results, we propose that aggregated proteins in aqueous [bmim][NO₃] or [emim][NO₃] solutions at $x = 20$ are even less sufficiently hydrated than the small-sized proteins; therefore, protein-protein interactions are enhanced. However, the nonaggregated proteins selectively interact with water molecules at aggregated water sites in the polar domains. Consequently, the formation of amyloid-like aggregates is strongly related to the size of the confined water domains in the IL layer. Unfortunately, further elucidation of the direct correlation between the protein size and confined water in aqueous IL solutions is difficult. Further experimental studies, such as investigations into the influence of aggregated water in aqueous IL solutions with/without proteins using SAXS and SANS methods, are required.

Next, we discuss amyloid-like aggregation in aqueous [bmim][SCN] solutions showing the strong denaturant. **Figure 8** shows the FTIR spectra of five of the investigated proteins (cytochrome *c*, myoglobin, lysozyme, RNase A, and β -LG) at $x = 30$. Remarkably, the spectra of four of the proteins (with the spectrum of cytochrome *c* being the exception) clearly present peaks attributable to intermolecular β -sheet structures.

To further investigate the changes in the secondary structures of the proteins, we determined their intermolecular- β -sheet contents ($\beta\%$) using curve-fitting analysis. The $\beta\%$ values at $x = 30$ are 0% for cytochrome *c*, $11 \pm 1.6\%$ for myoglobin, $34 \pm 3.5\%$ for lysozyme, $21 \pm 4.0\%$ for RNase A, and $17 \pm 3.2\%$ for β -LG. Compared with the case of [bmim][NO₃], the amyloid-like aggregation patterns do not correlate with the protein size or with their secondary structures. Thus, the origin of the amyloid-like aggregation in aqueous [bmim][SCN] solutions is an interesting topic. When structural transitions of proteins occur in aqueous solutions with salts and ILs, the cations and anions interact directly with specific amino acid residues on the proteins [43, 44], and this interaction is enhanced in condensed IL solutions. Consequently, we focused on the relationship between the secondary-structure content of the proteins in the condensed ILs and their amino acid residue contents.

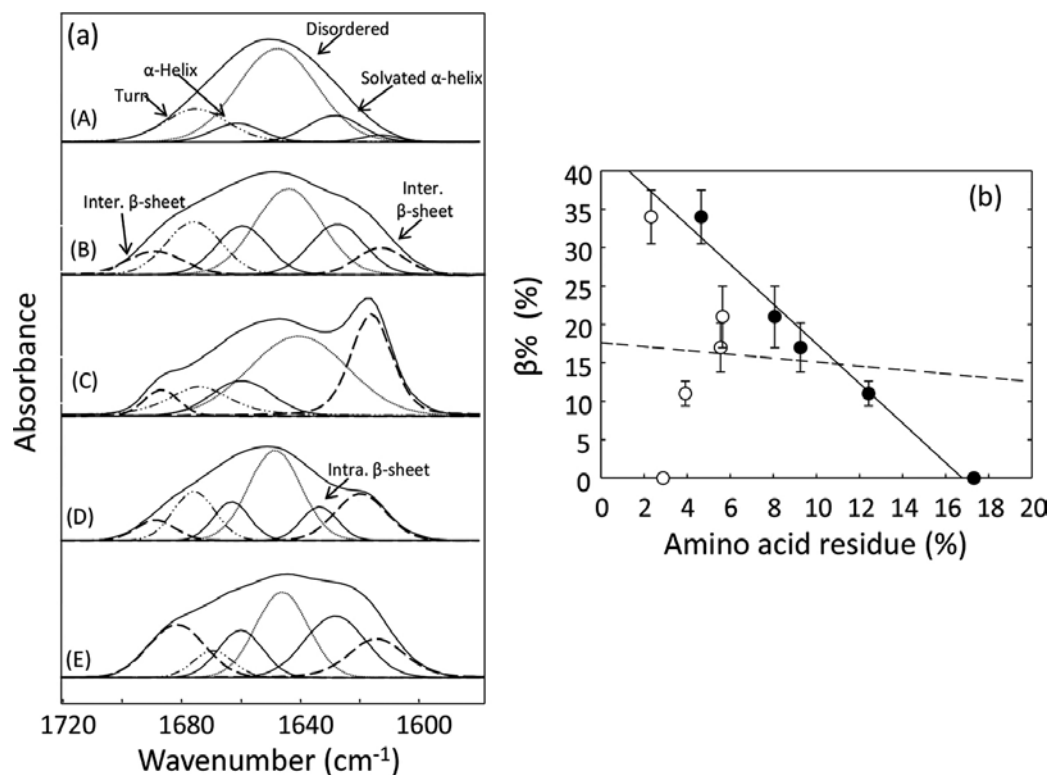


Figure 8. (a) Curve-fitted FTIR spectra in the amide I' region of (A) cytochrome *c*, (B) myoglobin, (C) lysozyme, (D) RNase A, and (E) β -LG in aqueous [bmim][SCN] solutions at $x = 30$. (b) Relationship between the $\beta\%$ and amino acid residues. Closed and open circles represent Lys and Gln residues, respectively.

To investigate the correlation between the $\beta\%$ values and the occurrence of 20 amino acid residues in the five investigated proteins, we determined the correlation coefficient (R^2) of the relationship between $\beta\%$ and the 20 amino acid residues of the proteins using the slope of **Figure 8b**. **Figure 9a** shows R^2 value between amino acid residues of protein and $\beta\%$. The value of $\beta\%$ appears to be dependent on the presence of hydrophilic amino acid residues, such as those on Lys, Arg, and Glu residues, rather than on the presence of hydrophobic or aromatic amino acid residues, such as those on Ile, Tyr, and Phe residues. The amino acid residues with $R^2 > 0.7$ are those on Lys, Arg, and Glu residues. Because Lys and Arg residues contain an amino group and Asn and Glu residues contain a carboxyl group, the former tend to interact with SCN^- ions while the latter tend to interact with $[\text{bmim}]^+$ ions. An important result is that the Lys residues exhibit the highest R^2 value. A straightforward interpretation of this result is that SCN^- ions bind mainly to the Lys residues of proteins in aqueous solutions. The present result is consistent with the previous X-ray diffraction studies that the SCN^- ions weakly bind to the Lys and Arg residues of proteins in the crystalline state [45, 46].

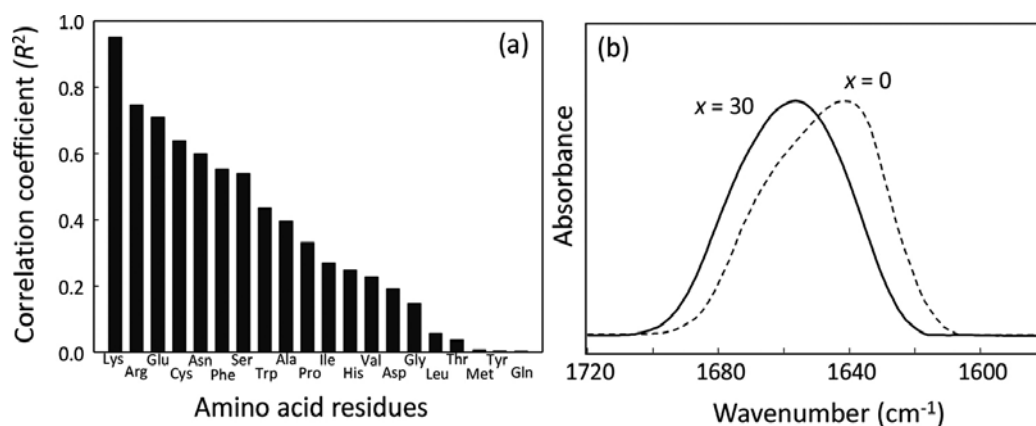


Figure 9. (a) Correlation coefficients (R^2) between amino acid residues of proteins and the content of intermolecular β -sheet structure ($\beta\%$). (b) FTIR spectra of PLL in aqueous $[\text{bmim}][\text{SCN}]$ solutions at $x = 0$ and 30.

Here, we can speculate that a Lys-rich polypeptide does not form an intermolecular β -sheet structure in aqueous $[\text{bmim}][\text{SCN}]$ solutions if Lys residues are directly related to the formation of intermolecular β -sheet structures. To confirm this speculation, we measured the FTIR spectra of poly-L-lysine (PLL) (Lys = 100%) in aqueous $[\text{bmim}][\text{SCN}]$ solutions at $x = 0$ and 30. They are significantly different from the spectra of the model proteins, in which PLL does not present the two peaks associated with intermolecular β -sheet formation. Accordingly, we propose that the SCN^- ions bind primarily to Lys residues in the proteins, and that Lys-rich proteins do not undergo intermolecular β -sheet formation in the presence of $[\text{bmim}][\text{SCN}]$. Thus, the formation of amyloid-like aggregates by the addition of $[\text{bmim}][\text{SCN}]$ is related to IL-amino acid residue interactions.

These results indicate that the origin of amyloid-like aggregate formation in $[\text{bmim}][\text{NO}_3]$ is different from that in $[\text{bmim}][\text{SCN}]$. The former is due to the relationship between the protein size and the confined water size in the IL layer, while the latter is due to IL-amino acid

residue interactions. The SCN^- anion is a stronger denaturant than the NO_3^- anion. As the denaturation effect of the anions becomes stronger, the origin of amyloid-like aggregation in condensed IL solutions changes from solution structural properties to the IL-amino acid residue interactions.

3.4. Future application of protein engineering

We have discussed the unique structural transitions of proteins in aqueous solutions with [bmim]-based ILs. Aqueous [bmim]-based IL solutions induce two structural transition patterns: the folded state \rightarrow unfolded state \rightarrow intermolecular β -sheet aggregation for myoglobin, and the folded state \rightarrow unfolded state \rightarrow partial globular state. These transitions are strongly related to solution properties, such as the presence of confined water around the IL layers (i.e., the nanoheterogeneity), a low polarity, and IL-amino acid residue interaction. On the basis of these results, we propose that future applications of ILs in protein engineering may be as cryoprotectants for proteins and as agents for the suppression of amyloid formation.

The inhibition of ice-nucleation and a high structural reversibility of proteins without protein aggregation are important criteria for a protein cryoprotectant. Recently, Yoshimura et al. reported that the aqueous IL solutions in the wide IL concentration range exhibit glassy formation at 77 K [47]. In addition, the present study shows that condensed IL solutions cause the helical formation for some proteins without protein aggregation. Related to these results, we found that low temperatures (77 K) induce structural reversibility for lysozyme in aqueous [bmim][NO_3] solutions [48]. After cooling, the lysozyme structure shows reversible transition without aggregation. Similar results were obtained in the case of RNase A in aqueous solutions of choline dihydrogen phosphate [49]. Thus, condensed IL solutions forming the glassy state at 77 K that induce helical formation without protein aggregation may be applicable as cryoprotectants for proteins, specifically as cryopreservation agents for recombinant proteins. However, in order to use ILs as cryoprotectants, it is necessary to investigate the enzyme activity in condensed IL solutions after cooling and removal of the IL from aqueous protein solutions.

As mentioned in Section 3.3, we have demonstrated that specific IL-amino acid residue interactions in condensed IL solutions cause inhibition of amyloid-like aggregation (i.e., intermolecular β -sheet structures). Related to this, we found that [bmim][SCN], EAN, and PAN ILs suppress thermally induced insulin amyloid formation [50]. Furthermore, condensed solutions of EAN or PAN demonstrate a high protectant ability for the structure of monomeric insulin. The affinity between ILs and specific amino acid residues in insulin is the main cause of the suppression of insulin amyloid formation. Thus, ILs can potentially be used as agents for the suppression of amyloid aggregation.

We proposed the applications of ILs in protein engineering as cryoprotectants for proteins and as agents for the suppression of amyloid formation using properties of the condensed IL solutions. In addition to these, the solution properties of condensed IL solution (the presence of confined water around the IL layers, a low polarity, and IL-amino acid residue interaction) will have a wide potential for applications of ILs in protein engineering in the future.

4. Conclusion

We have investigated the structural transition of proteins in aqueous solutions of ILs over a wide concentration range using FTIR and near-UV CD spectroscopy combined with SAXS. Aqueous IL solutions induced two structural transition patterns; (i) the folded state → unfolded state → partial globular state (α -helical formation disrupted tertiary structure), and (ii) the folded state → unfolded state → aggregation (amyloid-like aggregation or disordered aggregation). These transition patterns are strongly related to the condensed IL solution properties, such as the presence of confined water in the IL layers, low polarity, denaturant effect of anions, and IL-amino acid residue interactions. On the basis of these results, we proposed the new application of ILs as novel cryoprotectants and amyloid suppression agents. The present results will be basic information for the design of ILs for protein engineering applications. Although we have fully investigated the structural properties of proteins in aqueous IL solutions, detailed information on enzyme activity and methods for the removal of ILs from these media is still required to use the protein engineering applications.

Author details

Takahiro Takekiyo* and Yukihiro Yoshimura

*Address all correspondence to: take214@nda.ac.jp

Department of Applied Chemistry, National Defense Academy, Hashirimizu, Yokosuka, Japan

References

- [1] van Rantwijk F, Sheldon R A. Biocatalysis in ionic liquids. *Chem. Rev.* 2007; 107: 2757–2785.
- [2] Weingärtner H, Cabrele C, Herrman C. How ionic liquids can help to stabilize native proteins. *Phys. Chem. Chem. Phys.* 2012; 14: 415–426.
- [3] Tietze A A, Bordusa F, Giernoth R, Imhof D, Lenzer T, Mrestani-Klaus C, Neudorf I, Oum K, Reith D, Stark A. On the nature of interactions between ionic liquids and small amino-acid-based biomolecules. *ChemPhysChem.* 2013; 14: 4044–4064.
- [4] Greaves T L, Drummond C J. Protic ionic liquids: evolving structure-property relationship and expanding application. *Chem. Rev.* 2015; 115: 11379–11448.
- [5] Summers C A, Flowers R A. Protein renaturation by the liquid organic salt ethylammonium nitrate. *Protein Sci.* 2000; 9: 2001–2008.

- [6] Lange C, Patil G, Rudolph R. Ionic liquids as refolding additives: *N'*-alkyl and *N'*-(ω -hydroxyalkyl) *N*-methylimidazolium chlorides. *Protein Sci.* 2005; 14: 2693–2701.
- [7] Constantinescu D, Herrman C, Weingärtner H. Pattern of protein unfolding and protein aggregation in ionic liquids. *Phys. Chem. Chem. Phys.* 2010; 12: 1756–1763.
- [8] Constantinescu D, Weingärtner H, Herrman C. Protein denaturation by ionic liquids and the Hofmeister series: a case study of aqueous solutions of ribonuclease A. *Angew. Chem. Int. Ed.* 2007; 46: 8887–8889.
- [9] Zhang Y, Cremer P S. Interaction between macromolecules and ions: the Hofmeister series. *Curr. Opin. Chem. Biol.* 2006; 10: 658–663.
- [10] Weaver K D, Vrikkis R M, Van Vorst M P, Trullinger J, Vijayaraghavan R, Foureau D M, McKillop I H, MacFarlane D R, Kruger J K, Elliott G D. Structure and function of proteins in hydrated choline dihydrogen phosphate ionic liquid. *Phys. Chem. Chem. Phys.* 2012; 14: 790–801.
- [11] Attei P, Venkatesu P. Ammonium ionic liquids as convenient co-solvents for the structure and stability of succinylated con A. *J. Chem. Thermodyn.* 2012; 52: 78–88.
- [12] Hwang H, Choi H, Kim H–K, Jo D H, Kim T D. Ionic liquids promote amyloid formation from α -synuclein. *Anal. Biochem.* 2009; 386: 293–295.
- [13] Debeljuh N, Barrow C J, Byrne N. The impact of ionic liquids on amyloid fibrilization of A β 16–22: tuning the rate of fibrilization using a reverse Hofmeister strategy. *Phys. Chem. Chem. Phys.* 2011; 13: 16534–16536.
- [14] Triolo A, Russina O, Bleif H–J, DiCola E. Nanoscale segregation in room temperature ionic liquids. *J. Phys. Chem. B.* 2006; 111: 4641–4644.
- [15] Lopes J N A C, Pádua A A H. Nanostructural organization in ionic liquids. *J. Phys. Chem. B.* 2006; 110: 3330–3335.
- [16] Wang Y, Voth G A. Tail aggregation and domain diffusion in ionic liquids. *J. Phys. Chem. B.* 2006; 110: 18601–18608.
- [17] Jiang W, Wang Y, Voth G A. Molecular dynamics simulation of nanostructural organization in ionic liquid/water mixtures. *J. Phys. Chem. B.* 2007; 111: 4812–4818.
- [18] Abe H, Takekiyo T, Shigemi M, Yoshimura Y, Tsuge S, Hanasaki T, Onishi K, Takata S, Suzuki J. Direct evidence of confined water in room-temperature ionic liquids by complementary use of small-angle X-ray and neutron scattering. *J. Phys. Chem. Lett.* 2014; 5: 1175–1180.
- [19] Abe H, Takekiyo T, Yoshimura Y, Saihara K, Shimizu A. Anomalous freezing of nanoconfined water in room temperature ionic liquid, 1-butyl-3-methylimidazolium nitrate. *ChemPhysChem.* 2016; 17: 1136–1142.

- [20] Smeller L, Meersman F, Heremans K. Refolding studies under pressure: the folding landscape of lysozyme in pressure-temperature plane. *Biochim. Biophys. Acta.* 2006; 1764: 497–505.
- [21] Kelly S M, Jess T J, Price N C. How to study proteins by circular dichroism. *Biochim. Biophys. Acta.* 2005; 1751: 119–139.
- [22] Kozak M. Glucose isomerase from streptomyces rubiginosus—potential molecular weight standard for small-angle x-ray scattering. *J. Appl. Cryst.* 2005; 38: 555–558.
- [23] Hiramatsu H, Kitagawa T. FT-IR approaches on amyloid fibril structure. *Biochim. Biophys. Acta.* 2006; 1764: 100–107.
- [24] Cinelli S, Spinozzi F, Itri R, Finet S, Carsughi F, Onori G, Mariani P. Structural characterization of the pH-denatured states of ferricytochrome-c by synchrotron small angle X-ray scattering. *Biophys. J.* 2001; 81: 3522–3533.
- [25] Takekiyo T, Yamazaki K, Yamaguchi E, Abe H, Yoshimura Y. High ionic liquid concentration-induced structural change of protein in aqueous solution: a case study of lysozyme. *J. Phys. Chem. B.* 2012; 116: 11092–11097.
- [26] Takekiyo T, Koyama Y, Yamazaki K, Abe H, Yoshimura Y. Ionic liquid-induced formation of α -helical structure of β -lactoglobulin. *J. Phys. Chem. B.* 2013; 117: 10142–10148.
- [27] Takekiyo T, Nihei A, Aono M, Abe H, Yoshimura Y. Optical spectroscopic studies on structural changes of helical-rich proteins in aqueous solutions of ionic liquids. *J. Sol. Chem.* 2014; 43: 1707–1709.
- [28] Takekiyo T, Yamaguchi E, Yoshida K, Kato M, Yamaguchi T, Yoshimura Y. Intercation site between the protein aggregates and thiocyanate ion in aqueous solution: a case study of 1-butyl-3-methylimidazolium thiocyanate. *J. Phys. Chem. B.* 2015; 119: 6536–6544.
- [29] Englasnder S W, Mayne L. The nature of protein folding pathways. *Proc. Natl. Acad. Sci. USA.* 2014; 111: 15873–15880.
- [30] Chiti F, Dobson C M. Protein misfolding, functional amyloids, and human diseases. *Annu. Rev. Biochem.* 2006; 75: 333–336.
- [31] Fink A L. Protein aggregation: folding aggregates, inclusion bodies and amyloid. *Fold. Des.* 1998; 3: R9–R23.
- [32] De Groot N S, Sabate R, Ventura S. Amyloids in bacterial inclusion bodies. *Trend. Biochem. Sci.* 2009; 34: 408–416.
- [33] Shiraki K, Nishikawa K, Goto Y. Trifluoroethanol-induced stabilization of the α -helical structure of β -lactoglobulin: implication for non-hierarchical protein folding. *J. Mol. Biol.* 1995; 245: 180–194.
- [34] Uversky V N, Narizhneva N V, Kirschstein S O, Winter S, Löber G. Conformational transitions provoked by organic solvents in β -lactoglobulin: can a molten globule

- like intermediate be induced by the decrease in dielectric constant? *Fold. Des.* 1997; 2: 163–172.
- [35] Hirota N, Mizuno K, Goto Y. Group additive contributions to the alcohol-induced α -helix formation of melittin: implication for the mechanism of the alcohol effects on proteins. *J. Mol. Biol.* 1998; 275: 365–378.
- [36] Wakai C, Oleinikova A, Ott M, Weingärtner H. How polar are ionic liquids? Determination of the static dielectric constant of an imidazolium-based ionic liquid by microwave dielectric spectroscopy. *J. Phys. Chem. B.* 2005; 109: 17028–17030.
- [37] Kindt J T, Schmuttenmaer C A. Far-infrared dielectric properties of polar liquids by femtosecond terahertz pulse spectroscopy. *J. Phys. Chem.* 1996; 100: 10373–10379.
- [38] Chitra R, Smith P E. Properties of 2,2,2-trifluoroethanol and water mixtures. *J. Chem. Phys.* 2001; 114: 426–435.
- [39] Takekiyo T, Fukudome K, Yamazaki K, Abe H, Yoshimura Y. Protein aggregation and partial globular state in aqueous 1-alkyl-3-methylimidazolium nitrate solutions. *Chem. Phys. Lett.* 2014; 602: 22–27.
- [40] Hayes R, Warr G G, Atkin R. Structure and nanostructure in ionic liquids. *Chem. Rev.* 2015; 115: 6357–6426.
- [41] Jaganathan M, Ramakrishnan C, Velmurugan D, Dhathathereyan A. Understanding ethylammonium nitrate stabilized cytochrome c-molecular dynamics and experimental approach. *J. Mol. Struct.* 2015; 1081:334–341.
- [42] Attri P, Venkatesu P. Thermodynamic characterization of the biocompatible ionic liquid effects on protein model compounds and their functional groups. *Phys. Chem. Chem. Phys.* 2011; 13: 6566–6575.
- [43] Shammans S L, Knowles T P J, MacPhee C E, Welland M E, Dobson C M, Devlin G L. Perturbation of the stability of amyloid fibrils through alteration of electrostatic interaction. *Biophys. J.* 2011; 100: 2783–2791.
- [44] Shu Y, Liu M, Chen S, Chen X, Wang J. New insight into molecular interactions of imidazolium ionic liquids with bovine serum albumin. *J. Phys. Chem. B.* 2011; 115: 12306–12314.
- [45] Hamiaux C, Prangé T, Riès-Kautt M, Ducruix A, Lafont S, Astier J P, Veesler S. The dodecameric structure of bovine pancreatic trypsin inhibitor (BPTI) crystallized from thiocyanate at 2.7 Å resolution. *Acta Crystallogr. D.* 1999; 55: 103–113.
- [46] Vaney M C, Broutin I, Retailleau P, Douangamath A, Lafont S, Hamiaux C, Prangé T, Ducruix A, Riès-Kautt M. Structural effects on monovalent anions on polymorphic lysozyme crystals. *Acta Crystallogr. D.* 2001; 57: 929–940.
- [47] Yoshimura Y, Kimura H, Okamoto C, Miyashita T, Imai Y, Abe, Y. Glass transition behavior of ionic liquid, 1-butyl-3-methylimidazolium tetrafluoroborate- H_2O mixed solutions. *J. Chem. Thermodyn.* 2011; 43: 410–412.

- [48] Shigemi M, Mori T, Yamazaki K, Takekiyo T, Abe H, Yoshimura Y. Structural changes of lysozyme in aqueous ionic liquid solution upon heating. *Cryobiol. Cryotech.* (in Japanese) 2013; 59: 145–148.
- [49] Takekiyo T, Yamazaki K, Yoshimura Y. Structural reversibility of protein by the use of a hydrophilic ionic liquid: choline dihydrogen phosphate. *Cryobiol. Cryotech.* (in Japanese) 2012; 58: 147–151.
- [50] Takekiyo T, Yamaguchi E, Abe H, Yoshimura Y. Suppression effect on the formation of insulin amyloid by the use of ionic liquids. *ACS Sustain. Chem. Eng.* 2016; 4: 422–428.

Green Composites from Ionic Liquid-Assisted Processing of Sustainable Resources: A Brief Overview

Hamayoun Mahmood, Muhammad Moniruzzaman,
Suzana Yusup and Hazizan Md. Akil

Additional information is available at the end of the chapter

<http://dx.doi.org/10.5772/65796>

Abstract

The massive use of synthetic, petroleum-based polymeric composites has disturbed the fragile environmental equilibrium of our planet. Composites made solely from polysaccharides can offer unique intrinsic properties such as renewability, biodegradability, easy availability, eco-friendliness, facile processing, flexibility, and exciting physico-mechanical characteristics. The development of green processing of lignocellulosic materials and bio-based polymers such as cellulose, starch, chitin, and chitosan, the most abundant biorenewable materials on earth, is urgent from the perspectives of both environmental protection and sustainability in materials industries. Recently, the enormous potential of ionic liquids (ILs) as an alternative to ecologically harmful conventional organic solvents has been well recognized. Presently, a wide range of pronounced approaches have been explored to further improve the performance of ionic liquid-based processing of polysaccharides for green composite manufacturing. This review presents recent technological developments in which the advantages of ionic liquids as a dissolution medium for polysaccharides for production of plethora of green composites have been gradually realized.

Keywords: ionic liquids, polysaccharides, biocomposites, biofilms, biofiber, plasticization, biopolymer, lignocellulose

1. Introduction

Ionic liquids (ILs) are termed as “liquid salts” and entirely composed of ions. Most of these materials are liquids at ambient or far below ambient temperature and have been widely used as a potential alternative to toxic, hazardous, volatile, and highly flammable organic solvents

[1–3]. Various unique and attractive physicochemical properties of ILs, such as remarkable thermal and chemical stability [4, 5], extremely low vapor pressure [6], high solvation interactions with inorganic and organic compounds [7], broad electrochemical window, and sharp ionic conductivity, make ILs promising candidates for the replacement of volatile organic compounds (VOCs) for polysaccharide dissolution and modification [8]. ILs have been accredited as “designer solvents” as their properties can be tailored by appropriate combinations of anions and cations [9]. The combination of all these unique properties has triggered the use of ILs as environmentally benign dissolution media for lignocellulose and various biopolymers for the manufacturing of different composite products [10].

The extensive use of petroleum-based polymers and composites and their existing anti-natural processing methods has disturbed the fragile environmental equilibrium and exhausting limited petroleum reserves [11]. A fierce public debate regarding the future of the earth and the need for transition toward a CO₂ neutral bio-based economy was emphasized in the UN conference on climate change [12]. To this end, polymeric carbohydrates, e.g., starch, cellulose, chitin, inulin, chitosan, lignin, etc., are natural polymers found abundantly in nature as structural building elements and could be potential alternatives for petroleum-based nonbiodegradable polymers [13].

Manufacturing of sustainable composites demands not only the assortment of renewable or biodegradable resources for their manufacturing but also the utilization of mild pretreatment methods that avoid the use and production of hazardous by products [14, 15]. The strong inter- and intramolecular hydrogen bonding and the highly recalcitrant nature of the biopolymers and lignocellulose offer a critical challenge to extend the novel applications of these materials in composite industries [16, 17]. In this regard, various pretreatment technologies were developed to reduce the recalcitrance of lignocellulosic polymers, which apply chemical or hydrothermal treatments after mechanical comminution. However, most of the current pretreatment methods exhibit several drawbacks. Some pretreatments have to be tailored to the specific biopolymer material and or may cause decomposition of biopolymer constituents to side products, which can severely hinder downstream processing of these materials [18]. Further, some pretreatment technologies require strong acids or bases and extreme conditions of temperatures and pressures for which special equipment are necessary. Therefore, the development of alternative processing techniques for widespread potential applications of bio-based polymeric carbohydrates and lignocellulosic agricultural waste for fabrication of biocomposite material still remains challenging [19, 20].

Ionic liquids have attracted numerous interest as a new and highly effective solvent for a plethora of biodegradable polymers and lignocellulosic materials. Thus, the technological utilization of such materials for biocomposite manufacturing could be enhanced remarkably by their dissolution in ILs rather than the use of conventional organic solvents [5, 21]. Various reports on dissolution of a wide variety of polysaccharides in ILs over the past 10–15 years suggested that by using ILs, efficient selective extraction of the components is also feasible [22]. The main purpose of the present work is to depict a short overview of the state of the art on the current role of ILs as dissolution medium to explore polysaccharide-based sustainable raw materials for engineered green materials applications.

2. Ionic liquids and their properties

Typical ionic liquids consist of an organic cation with an inorganic anion with melting point usually below 100°C, and they persist in liquid state for a wide temperature range (typically <400 °C). ILs could be capable of having a broad range of intermolecular interactions with biopolymers including hydrogen bonding, dispersive, ionic, and dipolar [23]. Some ILs are considered as highly polar solvents due to their excellent solvation properties. A number of techniques could be used to predict the polarity of ILs, such as solvatochromic dyes [24], partition [25], and fluorescence probe methods [26]. Generally, ILs are immiscible with most of the organic solvents like hexane and ether but miscible with most of the polar solvents, such as ketones, lower alcohols, and dichloromethane [27]. Furthermore, ILs can also be classified into two categories: hydrophilic and hydrophobic based on their solubility in water. Usually, ILs exhibit higher viscosities in comparison with ordinary molecular solvents which significantly impede the dissolution of polysaccharide materials in ILs. Different organic cosolvents such as dimethylformamide, dimethylsulfoxide, and 1, 3-dimethyl-2-imidazolidinone have been successfully applied to cope with higher viscosities [28].

3. A comparison of ILs with conventional organic solvents for polysaccharide dissolution and modification

In addition to the greener aspects and the excellent physicochemical properties, some important merits of the ILs over conventional organic solvents for bio-based polymers could be summarized as follows:

- Ionic liquids are tunable solvents, and hence they can be designed by appropriate selection of cations and anions for particular application which is generally not possible using conventional organic solvents [29].
- ILs can dissolve biopolymers under relatively mild conditions of temperature and time and at normal atmospheric pressure which offer remarkable benefit to ILs in comparison with other molecular solvents. The dissolution of cellulose at the temperature of 45 °C for 30 min in the alkyl-substituted imidazolium-based ILs was reported [30, 31].
- ILs have also been proved to be highly effective solvents for lignocellulosic materials under solid biomass loadings of as high as 50 % in a continuous pretreatment reactor [32]. Thus, the feasibility of high-throughput continuous pretreatment could enhance the potential for use of IL-based pretreatment as a cost-effective and highly invaluable technology for fabrication of sustainable composite materials from polysaccharide raw materials.

4. Ionic liquid-assisted processing of polysaccharides for biocomposites

Composites are engineered materials fabricated from two or more components usually referred as reinforcement and matrix. However, for the composites fabricated from polysac-

charide materials, the end-product properties could be fitted without strict distinction for reinforcement and matrix. The present section briefly describes the IL-based preparation of different composite products from polysaccharides or their sources. Keeping in view the ethical standards, the sources may include plant cell walls or some sort of living species.

4.1. Biofilms and biofibers

Although petroleum-based synthetic polymer products have offered excellent services to modern society, their extensive use has become a serious threat to the environment. Therefore, interest has been focused for the exploitation of natural biopolymers. Cellulose is a linear polysaccharide, which exhibited outstanding characteristics and broad range of applications as engineering material. Generally, it does not melt or dissolve in ordinary solvents, which makes its processing extremely difficult. Recently, the capabilities of ILs to dissolve cellulose have significantly impacted its processing for fabrication of biodegradable plastic films [9, 22].

Dissolution and regeneration of cellulosic biofilms from IL [bmim][Cl] by using cotton pulp as raw cellulose source was reported by Liu et al. [33]. It was observed that solubility of cellulose could reach up to 13 wt% at 90°C in 7 h. Takegawa et al. [34] fabricated the bicomponent biopolymer film with cellulose and chitin each dissolved separately in the ILs [amim][Br] and [bmim][Cl], respectively, at 100 °C. The biofilms became more elastic by decreasing the relative ratio of chitin to cellulose in the final product. Further, **Figure 1** depicts the scheme of successful dissolution and regeneration of the native skin collagen in IL [bmim][Cl] [35]. The possible mechanism of dissolution of collagen in IL was also suggested which was based mainly on the hydrogen bond breaking.

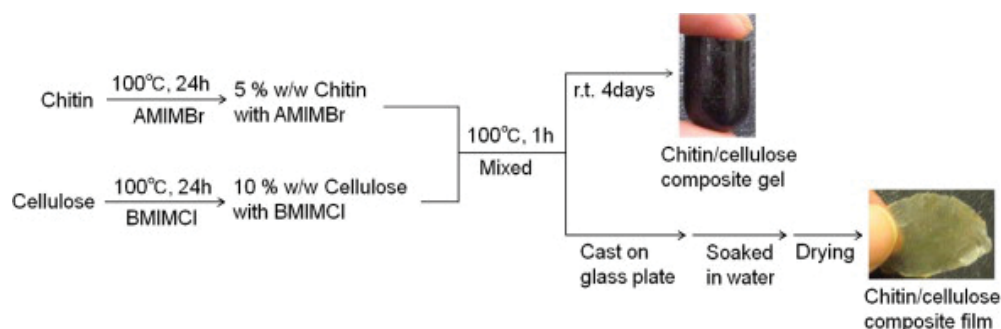


Figure 1. Schematic representation for preparation of collagen/cellulose composite materials using IL [bmim][Cl].

Electrospinning of polymer solution has turned up as a dominant technology for the preparation of fibrous materials with high specific surface area, controllable compositions, and high porosities for various applications. Particularly, the electrospinning of biopolymers for fabrication of biofiber has attracted numerous interests not only because of the renewable resources but also due to the advantageous characteristics of these biomacromolecules such

as biocompatibility, biodegradability, and significant specificity [5]. With the aim to replace commonly used noxious solvents, ILs have been investigated as new, nonvolatile, and nonflammable media for the electrospinning of biopolymers. A typical electrospinning apparatus based on IL-assisted dissolution and regeneration of cellulose is shown in **Figure 2**.

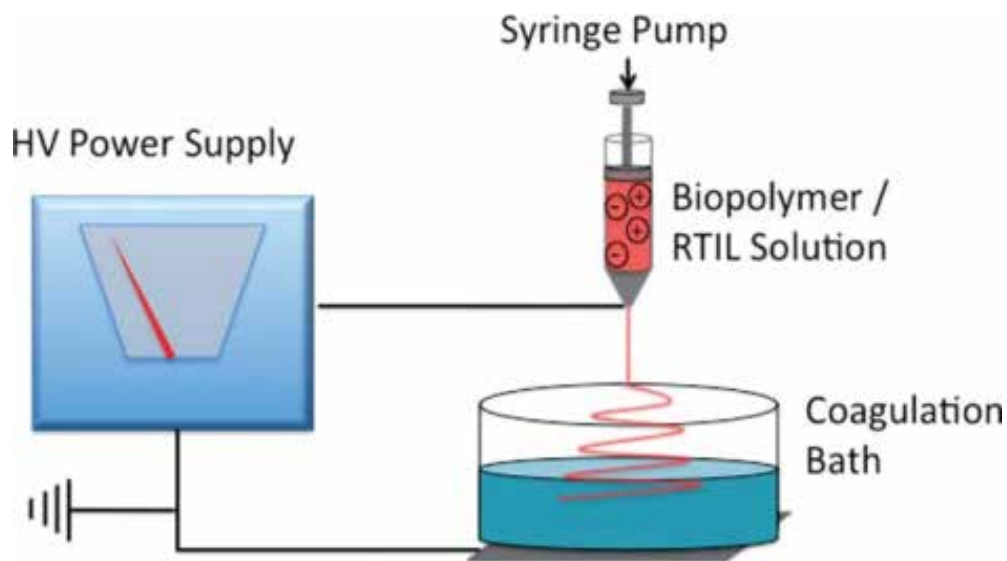


Figure 2. A typical electrospinning apparatus for IL-based processing of biofibers.

Polaskova et al. [36] dissolved raw pine wood in IL [emim][OAc] and utilized wet electrospinning technique to transform it into microfibers (1–4 μm). It was noted that 5% wood loading in IL was the most appropriate concentration for electrospinning, and further increase in the biomass loading up to 10% could complicate the process due to significant increase in the viscosity of solution. Similarly, electrospinning technology was utilized to obtain nonwoven nanoscale fibers from regenerated cellulose in the IL [bmim][Cl] [37]. The influence of the viscosity of biopolymer solution IL on the structure and size of the resulting biofiber was explored. Besides, Qin et al. [38] noted that high-molecular-weight and high purity chitin powder could be recovered after complete dissolution of raw crustacean shells in IL [emim][OAc] (**Figure 3**). The direct fabrication of chitin fibers and films from the extract solution was also reported. The conversion of cellulose and starch into fibrous material by making their homogeneous solution in IL [bmim][Cl] was described [39]. As explained in **Figure 4**, the fine linear material was obtained by raising the viscous biopolymer mixture with the help of a spatula and subsequently soaked into acetone to remove IL and then vacuum dried. The fabricated fiber showed the compatibilized fibrous structure of ca. 100–200 μm with higher thermal stability than that of gel made from the same biopolymers in [bmim][Cl]. Branched fibers with the size range of micro- to nanometer were extruded from 10% (w/w) of cellulose-heparin solution in the IL by using electrospinning technique [40].

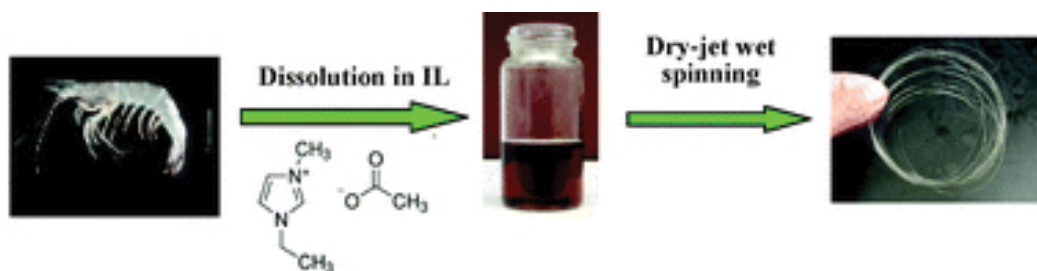


Figure 3. Preparation of chitin fiber from IL solution of crustacean shells.

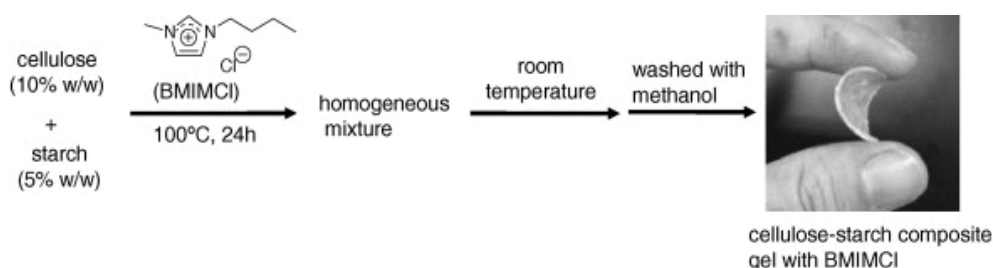


Figure 4. Cellulose-starch composite gel (a) and fiber (b).

4.2. Role of ionic liquids to provide alternative raw materials for wood composite industry

Although woody biomass has been the most promising raw material for production of composite panels, the excessive deforestation and at the same time increasing demand for wood composite panels has evoked a critical raw material issue in the wood composite industry [41]. Therefore, extensive research has been focused for the possibilities of using lignocellulosic residues of agro-industries as a direct substitute for wood fiber for the manufacturing of products such as fiberboard, particleboard, plywood, and so on [42]. Every year, about 184.6 million tons of lignocellulosic solid waste is being generated worldwide only from the oil palm industry [43]. The effective utilization of these lignocellulosic materials for manufacturing of industrial products would be highly helpful for development of agricultural-based economy in the rural areas.

Recently, we have reported the pretreatment of oil palm biomass with imidazolium-based ILs to produce cellulose-rich fiber (CRF) which was subsequently compounded with thermoplastic starch biopolymer binder to fabricate thermo-molded “green” composite board [44, 45]. Oil palm frond (OPF) samples were ground into particle size below 250 μm and pretreated with IL 1-butyl-3-methylimidazolium ([bmim][Cl]) or 1-ethyl-3-methylimidazolium diethyl phosphate ([emim][dep]) prior to mix with thermoplastic starch biopolymer. Finally, the compounded mixture was hot-pressed at 170°C and 25 MPa in a 30 ton Carver Laboratory Machine (CARVER, Inc., USA) [44].

During dissolution of lignocellulose particle in IL, some bonds between major biopolymer components are broken down leading to the swelling of plant cell wall. Separation of hydrogen and oxygen atoms occurs as a result of interaction of IL with lignocellulose which causes it to dissolve due to the disruption in the intermolecular and intramolecular hydrogen bonds. A fraction of hemicellulose and lignin is decreased in the pretreated material due to partial removal of these components. The results of lignocellulosic characterization of OPF samples before and after pretreatment showed that untreated OPF contained 26.4 %, 47.6 %, and 26 % of cellulose, hemicellulose, and lignin, respectively. This composition was changed to, respectively, 48%, 38%, 14% for pretreatment with IL [bmim][Cl], and 41% cellulose, 49% hemicellulose, and 10% lignin were achieved for IL [emim][dep]-treated fiber [44, 45].

Investigation of the thermal properties of lignocellulosic materials is important to explore their suitability for thermo-mechanical processing of biocomposite where the glass transition temperature of certain thermoplastic polymers is above 200°C. The thermal decomposition profiles obtained by TGA for untreated IL-treated OPF fibers are sketched in **Figure 5a**. These measurements clearly indicated that the thermal stability of the fiber was increased after pretreatment with IL. Indeed, treatment with both ILs [bmim][Cl] and [emim][dep] had a significant impact on the thermal decomposition profiles of the OPF fibers, raising the temperature at which the thermal degradation was initiated. This increase in the thermal stability of lignocellulosic fiber could be due to the removal of some constituents with lower thermal stability than cellulose. Besides, the thermal decomposition profiles of the composites fabricated from both treated and untreated fibers are provided in **Figure 5b**. It could be noted that the modifications occurred in the thermal properties of the fibers as a result of ILs pretreatment embarked a positive influence on the thermal properties of the fabricated composite as implied by their relatively higher thermal stability. It was observed that IL pretreatment increased the 10 % loss temperature (T_{10}) from 206°C to 225°C and 223°C for biocomposites manufactured from ILs [bmim][Cl] and [emim][dep] treated fibers, respectively. In fact, the improved thermal properties of the IL-treated biocomposites indicated that IL pretreatment was capable to increase the interfacial adhesion of the OPF fiber with polymer binder so that a higher amount of thermal energy was essential to break these fiber-binder linkages [44].

Furthermore, mechanical testing of the fabricated biocomposite panels before and after IL pretreatment in the flexural mode was also conducted to find the properties such as bending strength and bending modulus. **Figure 6** schematically depicts the details of the bending test. The obtained results plainly indicated that pretreatment of OPF fiber with both ILs [bmim][Cl] and [emim][dep] had a noteworthy impact on the bending strength and bending modulus. The bending strength of the untreated composite was found to be 4.9 MPa, which was increased to 8.3 and 8.9 MPa after the pretreatment with ILs [emim][dep] and [bmim][Cl], respectively. It could be possible that IL pretreatment reconstituted the lignocellulose structure by providing a more accessible interfacial area for thermoplastic binder flow during the thermo-molding step. This could lead to the improved fiber-matrix interfacial adhesion which consequently increased the bending properties [44].

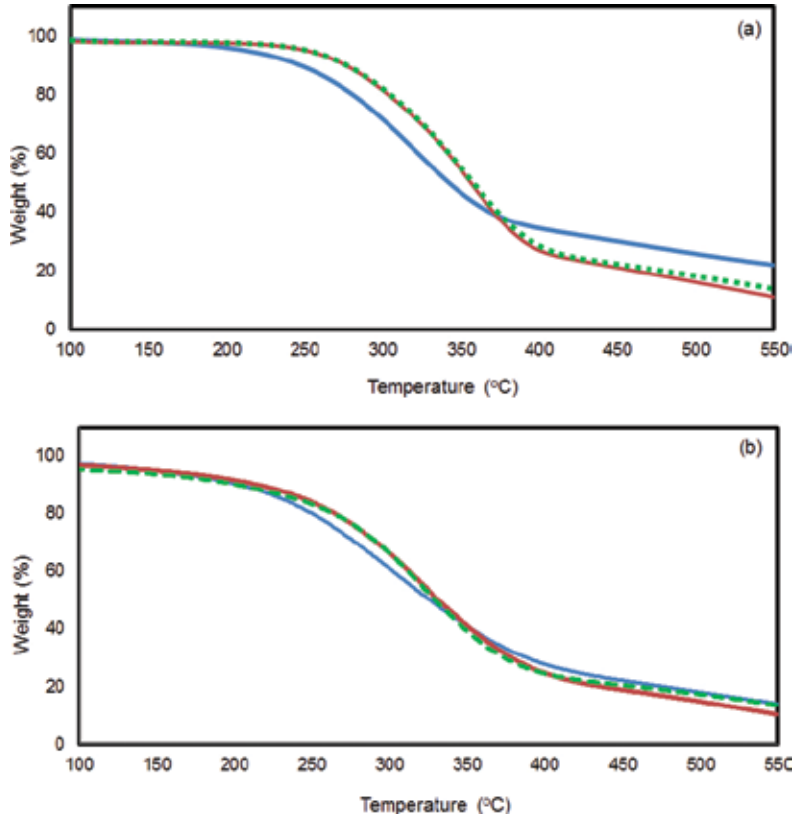


Figure 5. TGA profiles for untreated and IL-treated OPF fibers (a) and the fabricated composites (b).

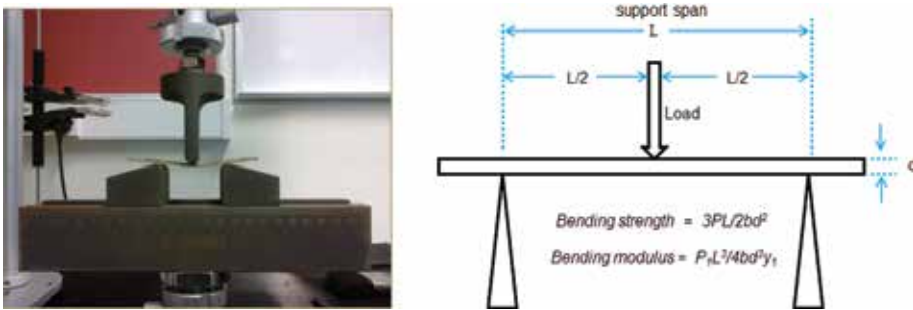


Figure 6. Schematics of the flexural test of composite board. P = peak load, P_1 = load at proportional limit, y_1 = deflection at proportional limit, and L , b , and d = length, width, and depth of specimen.

Thus, ionic liquid-treated composite panels exhibited superior mechanical and thermal properties because of partial removal of noncellulosic impurities from the lignocellulosic fiber after IL pretreatment. These studies demonstrated that IL-facilitated pretreatment technology

could be highly promising and green alternative route for efficient utilization of lignocellulosic biomass in the wood composite industries.

5. Future prospects

Processing of natural fiber reinforcements and a wide variety of biopolymer materials with IL for manufacturing of various biocomposite products would achieve commercial success only if the advantages of ILs outweigh its limitations, the most important of which is prices of ILs as compared to the value of the material processed [46]. In general, the design of a certain pretreatment process and selection of appropriate conditions for efficient and economical processing of biocomposite materials would need an adjustment between conflicting objectives which could be restrained by the use multi-objective optimization tool in design and selection of particular pretreatment process [47].

Process modeling for the pretreatment operation could be highly beneficial to estimate thermal energy consumption for dissolution step and the associated cost so that the comparison with other conventional pretreatment technologies would be made. Additionally, molecular-level simulation could be helpful to better understand the interaction mechanism of ILs with biological molecules [48, 49]. Furthermore, the physicochemical characteristics of IL may also be tuned by optimized selection of both cation and anion, and the careful selection of processing conditions may allow the more efficient utilization of ILs in the production of green composite materials from lignocellulosic and biopolymer-based sustainable raw materials [50].

Table 1 provides a cost comparison for ILs with conventional organic solvents. Although the cost of ILs has always been one of the major issues, all ILs are not expensive, particularly, when considered at large scale [51]. Recently, the ILs derived from “low-cost” feedstock or from renewable raw materials may open new pathways for synthesis of cost-effective and competitive ILs for pretreatment of natural fibers and polymers for biocomposite manufacturing [52, 53].

	Pretreatment solvent	Price (\$/g)
Ionic liquid	[bmim]Cl	0.262
	[emim]Cl	0.325
	[bmim][OAc]	0.696
	[amim]Cl	6.250
Solvent	MeOH	0.041
	DMSO	0.453
	NMMO	2.010
	DMF	0.094
	H ₂ SO ₄	0.574

Table 1. Price comparison of some ILs used for lignocellulose dissolution with ordinary biomass pretreatment solvents.

The major aspects that should be focused for the future research work in IL-based processing of various biofibers and biopolymers could be summarized as:

- “Dry” pretreatment under high biomass loading
- Development of low-cost ILs
- Applicability to a wide range of raw materials
- Minimum dissolution time
- Optimization of IL recycling to reduce losses
- “Greenness” of ILs (environmental and health impact)

Acknowledgements

The authors would like to acknowledge Universiti Teknologi PETRONAS for University Research Internal Fund (URIF) under grant 0153AA-B80 and Universiti Sains Malaysia for research grant 203.PBAHAN.6071337 for this research work.

Author details

Hamayoun Mahmood¹, Muhammad Moniruzzaman^{1*}, Suzana Yusup¹ and Hazizan Md. Akil²

*Address all correspondence to: m.moniruzzaman@petronas.com.my

1 Department of Chemical Engineering, Universiti Teknologi Petronas, Perak Darul Ridzuan, Malaysia

2 School of Materials and Minerals Resources Engineering, Universiti Sains Malaysia, Penang, Malaysia

References

- [1] M. Moniruzzaman, H. Mahmood, M. F. Ibrahim, S. Yusup, and Y. Uemura, "Effects of pressure and temperature on the dissolution of cellulose in ionic liquids," *Advanced Materials Research*, vol. 1133, pp. 588-592, 2016.
- [2] N. M. Konda, J. Shi, S. Singh, H. W. Blanch, B. A. Simmons, and D. Klein-Marcuschamer, "Understanding cost drivers and economic potential of two variants of ionic liquid

- pretreatment for cellulosic biofuel production," *Biotechnology for Biofuels*, vol. 7, p. 1, 2014.
- [3] H. Mahmood, M. H. A. bin Ahmad Sayukhi, M. Moniruzzaman, and S. Yusup, "Synthesis of ionic liquid polymer incorporating activated carbon for carbon dioxide capture and separation," *Advanced Materials Research*, vol. 1133, pp. 566-570, 2016.
- [4] M. Moniruzzaman and T. Ono, "Separation and characterization of cellulose fibers from cypress wood treated with ionic liquid prior to laccase treatment," *Bioresource Technology*, vol. 127, pp. 132-137, 2013.
- [5] P. Mäki-Arvela, I. Anugwom, P. Virtanen, R. Sjöholm, and J.-P. Mikkola, "Dissolution of lignocellulosic materials and its constituents using ionic liquids—a review," *Industrial Crops and Products*, vol. 32, pp. 175-201, 2010.
- [6] M. Moniruzzaman and T. Ono, "Ionic liquid assisted enzymatic delignification of wood biomass: a new 'green' and efficient approach for isolating of cellulose fibers," *Biochemical Engineering Journal*, vol. 60, pp. 156-160, 2012.
- [7] F. Ibrahim, M. Moniruzzaman, S. Yusup, and Y. Uemura, "Dissolution of cellulose with ionic liquid in pressurized cell," *Journal of Molecular Liquids*, vol. 211, pp. 370-372, 2015.
- [8] M. Moniruzzaman, K. Ino, N. Kamiya, and M. Goto, "Lipase incorporated ionic liquid polymers as active, stable and reusable biocatalysts," *Organic & Biomolecular Chemistry*, vol. 10, pp. 7707-7713, 2012.
- [9] A. Brandt, J. Gräsvik, J. P. Hallett, and T. Welton, "Deconstruction of lignocellulosic biomass with ionic liquids," *Green Chemistry*, vol. 15, pp. 550-583, 2013.
- [10] R. Financie, M. Moniruzzaman, and Y. Uemura, "Enhanced enzymatic delignification of oil palm biomass with ionic liquid pretreatment," *Biochemical Engineering Journal*, vol. 110, pp. 1-7, 2016.
- [11] A. N. Netravali and S. Chabba, "Composites get greener," *Materials Today*, vol. 6, pp. 22-29, 2003.
- [12] K. Protocol, "United Nations framework convention on climate change," *Kyoto Protocol, Kyoto*, vol. 19, 1997.
- [13] I. Šimkovic, "What could be greener than composites made from polysaccharides?," *Carbohydrate Polymers*, vol. 74, pp. 759-762, 2008.
- [14] C. Vila, A. Campos, C. Cristovao, A. Cunha, V. Santos, and J. Parajó, "Sustainable biocomposites based on autohydrolysis of lignocellulosic substrates," *Composites Science and Technology*, vol. 68, pp. 944-952, 2008.
- [15] M. Moniruzzaman, T. Ono, M. A. Bustam, S. Yusup, and Y. Uemura, "Pretreatment of wood biomass with ionic liquids: a "Green" approach to separate cellulose for use in oilfield application," *Journal of Applied Sciences*, vol. 15, p. 531, 2015.

- [16] M. Abe, Y. Fukaya, and H. Ohno, "Extraction of polysaccharides from bran with phosphonate or phosphinate-derived ionic liquids under short mixing time and low temperature," *Green Chemistry*, vol. 12, pp. 1274-1280, 2010.
- [17] M. Sivapragasam, M. Moniruzzaman, and M. Goto, "Recent advances in exploiting ionic liquids for biomolecules: solubility, stability and applications," *Biotechnology Journal*, vol. 11, pp. 1000-1013, 2016.
- [18] R. Financie, M. Moniruzzaman, Y. Uemura, and N. Osman, "Recent advances of using ionic liquid in lignocellulosic biomass degradation," in *Applied Mechanics and Materials*, vol. 625, pp. 834-837, 2014.
- [19] S. Kalia, B. Kaith, and I. Kaur, "Pretreatments of natural fibers and their application as reinforcing material in polymer composites—a review," *Polymer Engineering & Science*, vol. 49, pp. 1253-1272, 2009.
- [20] M. Moniruzzaman, K. Nakashima, N. Kamiya, and M. Goto, "Recent advances of enzymatic reactions in ionic liquids," *Biochemical Engineering Journal*, vol. 48, pp. 295-314, 2010.
- [21] M. Moniruzzaman, Y. Hayashi, M. M. R. Talukder, E. Saito, and T. Kawanishi, "Effect of aprotic solvents on the enzymatic activity of lipase in AOT reverse micelles," *Biochemical Engineering Journal*, vol. 30, pp. 237-244, 2006.
- [22] M. Zavrel, D. Bross, M. Funke, J. Büchs, and A. C. Spiess, "High-throughput screening for ionic liquids dissolving (ligno-) cellulose," *Bioresource Technology*, vol. 100, pp. 2580-2587, 2009.
- [23] S. Bahrani, S. Raeissi, and M. Sarshar, "Experimental investigation of ionic liquid pretreatment of sugarcane bagasse with 1,3-dimethylimidazolium dimethyl phosphate," *Bioresource Technology*, vol. 185, pp. 411-415, 2015.
- [24] C. Reichardt, "Polarity of ionic liquids determined empirically by means of solvatochromic pyridinium N-phenolate betaine dyes," *Green Chemistry*, vol. 7, pp. 339-351, 2005.
- [25] M. H. Abraham, A. M. Zissimos, J. G. Huddleston, H. D. Willauer, R. D. Rogers, and W. E. Acree, "Some novel liquid partitioning systems: water-ionic liquids and aqueous biphasic systems," *Industrial & Engineering Chemistry Research*, vol. 42, pp. 413-418, 2003.
- [26] A. Chapeaux, L. D. Simoni, M. A. Stadtherr, and J. F. Brennecke, "Liquid phase behavior of ionic liquids with water and 1-octanol and modeling of 1-octanol/water partition coefficients," *Journal of Chemical & Engineering Data*, vol. 52, pp. 2462-2467, 2007.
- [27] M. Moniruzzaman, N. Kamiya, and M. Goto, "Activation and stabilization of enzymes in ionic liquids," *Organic & Biomolecular Chemistry*, vol. 8, pp. 2887-2899, 2010.

- [28] L. Wu, S.-H. Lee, and T. Endo, "Effect of dimethyl sulfoxide on ionic liquid 1-ethyl-3-methylimidazolium acetate pretreatment of eucalyptus wood for enzymatic hydrolysis," *Bioresource Technology*, vol. 140, pp. 90-96, 2013.
- [29] S. H. Lee, T. V. Doherty, R. J. Linhardt, and J. S. Dordick, "Ionic liquid-mediated selective extraction of lignin from wood leading to enhanced enzymatic cellulose hydrolysis," *Biotechnology and Bioengineering*, vol. 102, pp. 1368-1376, 2009.
- [30] Y. Fukaya, K. Hayashi, M. Wada, and H. Ohno, "Cellulose dissolution with polar ionic liquids under mild conditions: required factors for anions," *Green Chemistry*, vol. 10, pp. 44-46, 2008.
- [31] M. Moniruzzaman, N. Kamiya, K. Nakashima, and M. Goto, "Water-in-ionic liquid microemulsions as a new medium for enzymatic reactions," *Green Chemistry*, vol. 10, pp. 497-500, 2008.
- [32] A. S. A. da Silva, R. S. S. Teixeira, T. Endo, E. P. Bon, and S.-H. Lee, "Continuous pretreatment of sugarcane bagasse at high loading in an ionic liquid using a twin-screw extruder," *Green Chemistry*, vol. 15, pp. 1991-2001, 2013.
- [33] Z. Liu, H. Wang, Z. Li, X. Lu, X. Zhang, S. Zhang, *et al.*, "Characterization of the regenerated cellulose films in ionic liquids and rheological properties of the solutions," *Materials Chemistry and Physics*, vol. 128, pp. 220-227, 2011.
- [34] A. Takegawa, M.-a. Murakami, Y. Kaneko, and J.-i. Kadokawa, "Preparation of chitin/cellulose composite gels and films with ionic liquids," *Carbohydrate Polymers*, vol. 79, pp. 85-90, 2010.
- [35] Z. Meng, X. Zheng, K. Tang, J. Liu, Z. Ma, and Q. Zhao, "Dissolution and regeneration of collagen fibers using ionic liquid," *International Journal of Biological Macromolecules*, vol. 51, pp. 440-448, 2012.
- [36] M. Polaskova, R. Cermak, V. Verney, P. Ponizil, S. Commereuc, M. F. C. Gomes, *et al.*, "Preparation of microfibrils from wood/ionic liquid solutions," *Carbohydrate Polymers*, vol. 92, pp. 214-217, 2013.
- [37] S.-L. Quan, S.-G. Kang, and I.-J. Chin, "Characterization of cellulose fibers electrospun using ionic liquid," *Cellulose*, vol. 17, pp. 223-230, 2010.
- [38] Y. Qin, X. Lu, N. Sun, and R. D. Rogers, "Dissolution or extraction of crustacean shells using ionic liquids to obtain high molecular weight purified chitin and direct production of chitin films and fibers," *Green Chemistry*, vol. 12, pp. 968-971, 2010.
- [39] J.-i. Kadokawa, M.-a. Murakami, A. Takegawa, and Y. Kaneko, "Preparation of cellulose-starch composite gel and fibrous material from a mixture of the polysaccharides in ionic liquid," *Carbohydrate Polymers*, vol. 75, pp. 180-183, 2009.

- [40] G. Viswanathan, S. Murugesan, V. Pushparaj, O. Nalamasu, P. M. Ajayan, and R. J. Linhardt, "Preparation of biopolymer fibers by electrospinning from room temperature ionic liquids," *Biomacromolecules*, vol. 7, pp. 415-418, 2006.
- [41] M. Abdel-Aal, R. Nasser, P. Khan, and H. Al-Mefarrej, "Anatomical and physical characterisations of some lignocellulosic residues and their suitability for fibre production," *Journal of Environmental Biology*, vol. 36, p. 543, 2015.
- [42] M. V. Madurwar, R. V. Ralegaonkar, and S. A. Mandavgane, "Application of agro-waste for sustainable construction materials: a review," *Construction and Building Materials*, vol. 38, pp. 872-878, 2013.
- [43] S. E. Hosseini, M. Abdul Wahid, M. Jamil, A. A. Azli, and M. F. Misbah, "A review on biomass-based hydrogen production for renewable energy supply," *International Journal of Energy Research*, vol. 39, pp. 1597-1615, 2015.
- [44] H. Mahmood, M. Moniruzzaman, S. Yusup, and H. M. Akil, "Pretreatment of oil palm biomass with ionic liquids: a new approach for fabrication of green composite board," *Journal of Cleaner Production*, vol. 126, pp. 677-685, 2016.
- [45] H. Mahmood, M. Moniruzzaman, S. Yusup, and H. M. Akil, "Particulate composites based on ionic liquid-treated oil palm fiber and thermoplastic starch adhesive," *Clean Technologies and Environmental Policy*, vol. 18, pp. 2217-2226, 2016.
- [46] D. Klein-Marcuschamer, B. A. Simmons, and H. W. Blanch, "Techno-economic analysis of a lignocellulosic ethanol biorefinery with ionic liquid pre-treatment," *Biofuels, Bioproducts and Biorefining*, vol. 5, pp. 562-569, 2011.
- [47] K. G. Satyanarayana, G. G. Arizaga, and F. Wypych, "Biodegradable composites based on lignocellulosic fibers—an overview," *Progress in Polymer Science*, vol. 34, pp. 982-1021, 2009.
- [48] H. Wu, M. Mora-Pale, J. Miao, T. V. Doherty, R. J. Linhardt, and J. S. Dordick, "Facile pretreatment of lignocellulosic biomass at high loadings in room temperature ionic liquids," *Biotechnology and Bioengineering*, vol. 108, pp. 2865-2875, 2011.
- [49] A. George, K. Tran, T. J. Morgan, P. I. Benke, C. Berrueco, E. Lorente, *et al.*, "The effect of ionic liquid cation and anion combinations on the macromolecular structure of lignins," *Green Chemistry*, vol. 13, pp. 3375-3385, 2011.
- [50] P. Jessop, F. Ahmadpour, M. Buczynski, T. Burns, N. Green Ii, R. Korwin, *et al.*, "Opportunities for greener alternatives in chemical formulations," *Green Chemistry*, vol. 17, pp. 2664-2678, 2015.
- [51] N. V. Plechkova and K. R. Seddon, "Applications of ionic liquids in the chemical industry," *Chemical Society Reviews*, vol. 37, pp. 123-150, 2008.

- [52] H. Zhao, G. A. Baker, Z. Song, O. Olubajo, T. Crittle, and D. Peters, "Designing enzyme-compatible ionic liquids that can dissolve carbohydrates," *Green Chemistry*, vol. 10, pp. 696-705, 2008.
- [53] M. Stasiewicz, E. Mulkiwicz, R. Tomczak-Wandzel, J. Kumirska, E. Siedlecka, M. Gołbiowski, *et al.*, "Assessing toxicity and biodegradation of novel, environmentally benign ionic liquids (1-alkoxymethyl-3-hydroxypyridinium chloride, saccharinate and acesulfamates) on cellular and molecular level," *Ecotoxicology and Environmental Safety*, vol. 71, pp. 157-165, 2008.

Electrochemistry

Ionic Liquids as Electrodeposition Additives and Corrosion Inhibitors

Zhang Qibo and Hua Yixin

Additional information is available at the end of the chapter

<http://dx.doi.org/10.5772/65807>

Abstract

Ionic liquids (ILs) are molten salts with a melting point of 100°C or below and solely consist of cations and anions. As a kind of novel green solvent, ILs have been obtained broad and deep investigations, and enormous progresses in various fields have been made during the recent 20 years. Despite the fact that the application studies of ILs have been proposed in various fields, no processes have yet been developed to an industrial scale. However, the main interests are still focused on their industrial applications. In this chapter, two perspective applications of ILs in electrochemical fields including additives for metal electrodeposition and inhibitors for metal anti-corrosion were introduced.

Keywords: ionic liquids, additives, metal electrodeposition, corrosion inhibitors, adsorption

1. Introduction

Additives are widely used in electrodeposition of metals and alloys due to their special functions in the deposition process. These additives are found to affect both the deposition and crystal-building processes through their adsorbates at the electrode surface [1]. Traditional colloidal and some organic additives have gained wide industrial use and achieved good additive effect, even though they can be decomposed easily and are not environmentally friendly due to their disadvantages, such as thermal stability, bad chemical and high toxicity. Consequently, there is a continuing search for better additives that combine good stability, high efficiency and environmentally friendliness. The effect of corrosion inhibitors is similar to that of electrodeposition additives to some extent, as their excellent corrosion resistance performance on metals is attributed to their adsorption on the metal surface, which protects the metal from attack by the acidic solutions [2]. However, most commercially available

picking inhibitors are toxic compounds that should be replaced by new environmentally-friendly ones. Research studies in the field of 'green' corrosion inhibitors have been aimed at using cheap, effective molecules with low or 'zero' environmental impact [3].

Ionic liquids (ILs) are organic salts that are liquids at ambient temperature and comprised entirely of organic cations and organic/inorganic anions. Due to the unique structure characteristics, ILs have many attractive properties and attract a great deal of interest in various fields [4–17]. Some of the most important prosperities of ILs are their thermal stability and avirulence, which make them potential additives for metal electrodeposition and green inhibitors for metal anti-corrosion. In our previous studies, alkylimidazolium, alkylpyridinium and quaternary ammonium-based ionic liquids were observed to be an excellent levelling agent in zinc [18–22] and copper [23–25] electrodeposition and showed favourable corrosion resistant on metals such as aluminium [26], copper [27] and mild steel [2].

2. Why use ILs as electrodeposition additives and corrosion inhibitors?

As mentioned above, the effect mechanism of electrodeposition additives and corrosion inhibitors is quite similar. Both are dependent on their surface adsorbability to achieve the expected additive effect. The main difference from each other could be the use of additives is under electric field and their electrode surface adsorption behaviour will be influenced by the electric field distribution, while the corrosion inhibitors are used without galvanization and their adsorption mainly depends on certain physico-chemical properties of the inhibitor group, such as electron density at the donor atom, π -orbital character and the electronic structure of the molecule [28].

ILs are composed entirely of organic cations and organic/inorganic anions that are liquid at low temperature. Their relatively high cationic configuration makes them readily adsorb on the cathode surface under the electric field. In addition, some functional groups such as $-C=N-$ group and electronegative nitrogen in the molecule of imidazolium ILs enables them spontaneous adsorption on the metal surface due to the specific interaction between these functional groups and the metal surface [2]. Furthermore, the high thermal stability, negligible vapour pressure and environmentally benign characteristics of ILs allow them to be considered as very promising replacements for the traditional volatile organic solvents. Therefore, it is hopeful to overcome these defects of traditional additives and toxic organic corrosion inhibitors, and help to realize additives with good stability and inhibitors with avirulence by using ILs as metal electrodeposition additives and corrosion inhibitors, respectively.

The application studies of ILs have been proposed varying from precious metal processing [29–40] to mineral leaching [41–44]; however, very few have come to practical fruition although several are at a pilot scale [45–47]. Except some technical difficulties that are hard to solve at our present state of knowledge [48], the relatively prohibitive high cost of ILs is also a main reason for delaying their industrial application [44]. In comparing to the use ILs as electrolytes for metal electrodeposition and rechargeable batteries, where the

reproducible operation in these ILs requires either a strictly controlled inert gas atmosphere with extremely low water concentration or at least closed vessel conditions with limited contamination [49], the applications of ILs in electrodeposition additives and corrosion inhibitors are not only cost accepted with the trace amount of consumption, but also have more practical operability.

On the basis of these discussions, it is accepted that the applications of ILs as additives for metal electrodeposition and corrosion inhibitors are with favourable industrial application prospect, as in our opinion they are very likely to initiatively realize the zero breakthrough of industrial applications of ILs.

3. Additives for metal electrodeposition

In modern electrodeposition and electrowinning practice, it is well known that the introduction of one or more inorganic or organic additives in the electrolyte leads to produce smooth, free of voids and compacted metallic deposits at the cathode. The quantity of additives required is always considerably small, but their action is often specific [50]. Although the number of these additives studied in electrodeposition is very high, their action mechanism can be divided into two main categories, which are levelling additive and brightening additive. Levelling additive [51] has been defined as the additive with the ability to produce deposit relatively thinner on small protrusions and then decrease in depth on height of the small surface irregularities. While brightening additive [52] can be defined as the ability to obtain fine deposits with the crystallites smaller than the wavelengths of visible light. In this section, we reported the use of a series of novel 1-alkyl-3-methylimidazolium hydrosulphate ILs, namely, [BMIM]HSO₄, [HMIM]HSO₄ and [OMIM]HSO₄ as additives in zinc electrodeposition from the acidic sulphate electrolyte. Furthermore, effects of ILs on copper electrodeposition from acidic sulphate electrolyte were also introduced.

3.1. Additives for zinc electrodeposition

Zinc electrodeposition is very sensitive when it comes into contact with some types of impurities in augmenting simultaneous evolution of hydrogen during zinc ion electroreduction from aqueous solutions. Apart from occluding hydrogen into the zinc deposit, hydrogen evolution will increase specific electric energy consumption and decrease current efficiency (CE), bringing about an increment in the level of internal stress to produce pitted deposits [19]. To counteract the harmful effect of metallic impurities, achieve high CE and produce a smooth, levelled and dense cathodic deposit, additives such as glue and gum arabic are most often used. In addition, enormous organic additives [53–62] have been proposed for use as additives and some authorities have reported them to work better than glue or gum arabic. We have reported that 1-alkyl-3-methylimidazolium hydrosulphate ILs ([BMIM]HSO₄ [18], [HMIM]HSO₄ and [OMIM] HSO₄ [19]) had a pronounced inhibiting effect on Zn²⁺ electroreduction and all were efficient as levelling agents for zinc electrodeposition.

Figure 1(a) shows the effect of [BMIM]HSO₄ on the CE during zinc electrodeposition. The CE increases with the initial addition of [BMIM]HSO₄ and steadily decreases at higher concentrations. Without additives, the CE is ~89%, whereas at 5 mg dm⁻³ [BMIM]HSO₄ the CE was ~92.7% and then fell to 87.8% at 50 mg dm⁻³. The trend observed in CE with increasing [HMIM]HSO₄ and [OMIM]HSO₄ concentration is similar to that for [BMIM]HSO₄, where we obtained a CE of 92.9–92.2% with the addition of 2 mg·dm⁻³ [HMIM]HSO₄ and 1 mg dm⁻³ [OMIM]HSO₄, respectively, but at higher concentrations there is a reduction. The CE decreases with increasing additive concentrations in the order [OMIM]HSO₄ > [HMIM]HSO₄ > [BMIM]HSO₄, which reflects increasing adsorbability at the electrode surface with increasing molecular size and hence molecular mass [62, 63].

The cyclic voltammograms recorded for zinc electrodeposition from acidic sulphate solution in the absence and presence of ILs additive [BMIM]HSO₄ are presented in **Figure 1(b)**. The voltammograms were initiated at point 'A' (-0.70 V versus SCE), scanned in the negative direction and reversed at -1.30 V in the positive direction. The nucleation overpotential (NOP) for zinc deposition on an aluminium substrate is defined as the potential difference between the electroreduction potential of zinc ions at 'B' and the crossover potential at 'D', which is regarded as an indicator of the extent of polarization of a cathode [64]. It is clear that the addition of additives has a significant effect on the zinc electrocrystallization process as shown in **Figures 1(b)** and 2–4, where the NOP values increase substantially, along with the reduction of the cathodic process area. The strong adsorption of the additives on the electrode surface is usually held to be responsible for this. The extent of absorption appears to be in the order [OMIM]HSO₄ > [HMIM]HSO₄ > [BMIM]HSO₄, which shows the adsorbability of the studied additives and reflects their effect on the process of deposition. The analysis of the kinetic parameters [18, 19] indicates that the presence of ILs does not have any significant effect on the Tafel slopes and transfer coefficients, suggesting that they do not change the zinc electrodeposition mechanism in the absence of additives.

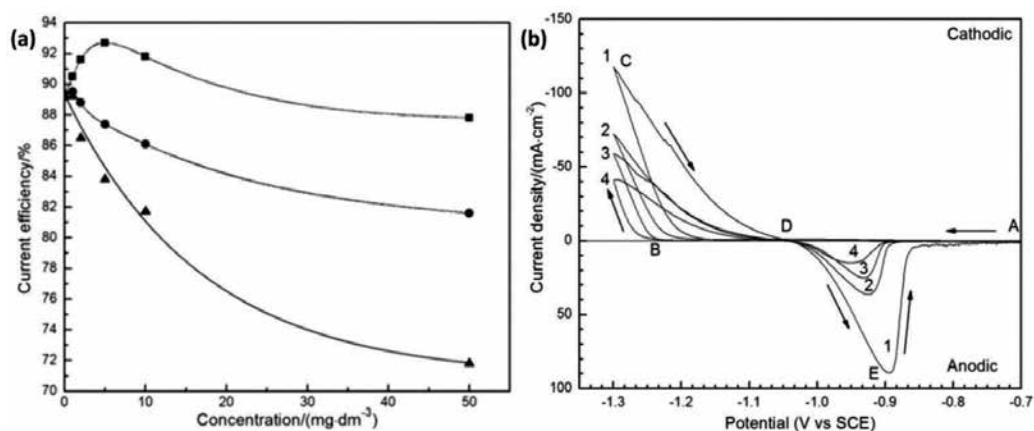


Figure 1. (a) Effect of additives on current efficiency during zinc electrodeposition. (■) [BMIM]HSO₄, (●) [HMIM]HSO₄ and (▲) [OMIM]HSO₄. (b) Cyclic voltammograms of acidic zinc sulphate solutions in the absence and presence of 5 mg dm⁻³ different additives. (1) Blank, (2) [BMIM]HSO₄, (3) [HMIM]HSO₄ and (4) [OMIM]HSO₄ [18, 19].

The investigated additives significantly changed the morphology of the zinc deposits as compared with those obtained from solutions without additives, as shown in **Figure 2**. The zinc deposit obtained from addition-free electrolyte is bright but not smooth and consists of hexagonal platelets of moderate size (**Figure 2a**). Introducing the additives into the solution did not affect the shape of the crystals but improved the quality of deposits by reducing the platelet sizes and giving smooth and compact deposits (**Figure 2b** and **d**) with changing the preferred crystal orientations [18, 19].

Moreover, the addition of [BMIM]HSO₄ was observed to relieve the harmful effect of impurities, such as copper, iron, cobalt, nickel and lead, to some extent and led to a reduction of the impurity content in the zinc deposits and improved the CE and the quality of the cathodic deposits [65]. Considering the anodic reaction, [BMIM]HSO₄ was also found to have a catalytic effect on oxygen evolution by stimulating the reaction rate constant. Introduction of 5 mg dm⁻³ [BMIM]HSO₄ can markedly reduce the oxygen evolution charge transfer resistance by at least 50% [66]. [BMIM]HSO₄ manifested superior chemical and thermal stabilities compared with traditional industrial additives, gelatine and gum arabic. The inhibition effects of gelatine and gum arabic on the zinc electrocrystallization weakened significantly under observation because of their partial degradation after 12-h long-time successive electrolysis and high temperature (90°C) treatments. In contrast, 24-h long-term successive electrolysis and high-temperature treatments have no effect on the activity of [BMIM]HSO₄ [67].

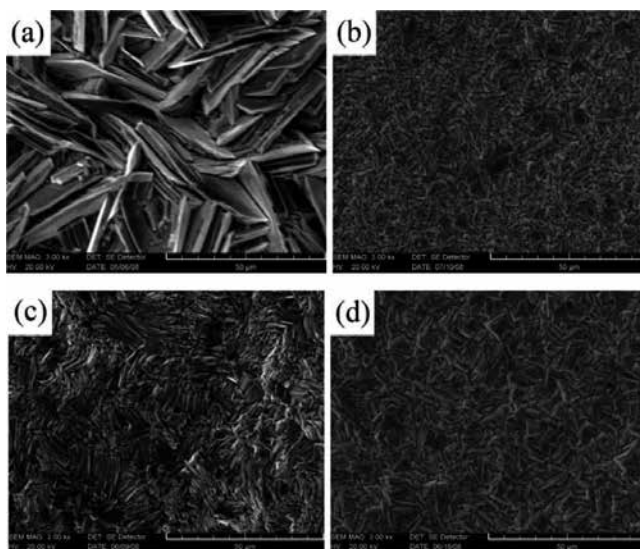


Figure 2. Scanning electron micrographs of zinc deposits in the presence of different additives. (a) Blank, (b) [BMIM]HSO₄-5 mg·dm⁻³, (c) [HMIM]HSO₄-10 mg·dm⁻³ and (d) [OMIM]HSO₄-10 mg·dm⁻³ [18, 19].

The inhibition effect of [BMIM]HSO₄ for zinc electrodeposition was also found in a typical plating solution (0.1 M ZnSO₄ + 0.5 M Na₂SO₄) [22], in which [BMIM]HSO₄ can induce the formation of finer-grained deposits by the adsorption of additive in the first stages of deposition

(Figure 3a and d). The corrosion behaviour of Q235 steel with coating by a thin layer of zinc in the presence of [BMIM]HSO₄ exhibited more excellent protection of the base metal in comparison to the additive-free one in 3.5% NaCl solution (Figure 3e).

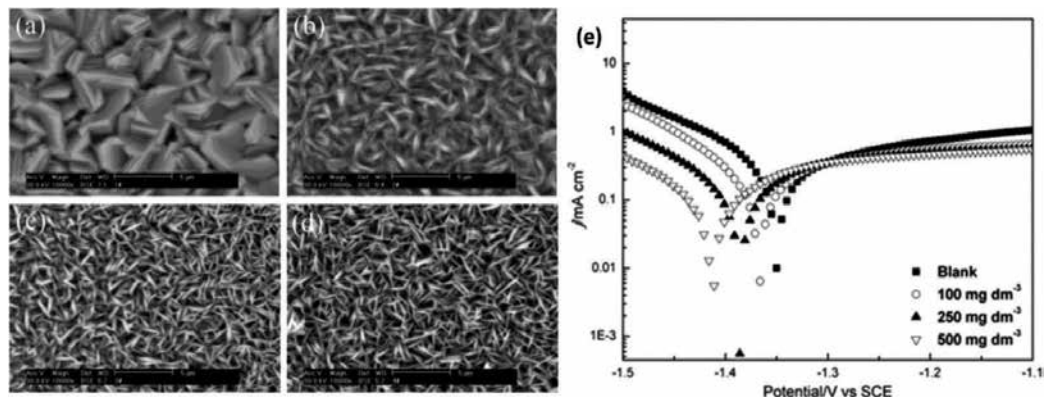


Figure 3. SEM micrographs of zinc electrodeposits produced on GC electrode from solution 0.1 M ZnSO₄ + 0.5 M NaSO₄, pH 2.6 in the absence and presence of [BMIM]HSO₄. (a) Blank, (b) 100 mg dm⁻³, (c) 250 mg dm⁻³ and (d) 500 mg dm⁻³. The deposition potential was -1.30 V and $Q = 1.00 \pm 0.01$ C (e). Potentiodynamic polarization curves of Q235 steel substrate free and coated by a thin layer of zinc from the baths in the presence of different concentrations of [BMIM]HSO₄ in 3.5% NaCl solutions. The deposition charges, Q_d , were approximately 1.00 ± 0.01 C [22].

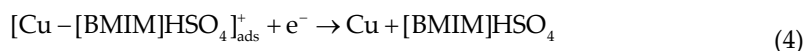
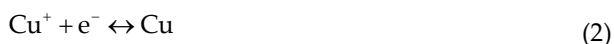
3.2. Additives for copper electrodeposition

Copper electrodeposition from acidic sulphate electrolyte with different small amounts of certain additives has been investigated extensively and it is well known that they lead to significant changes in the properties and orientation of the deposit [68]. Appropriate amounts of additives are necessary for the formation of fine-grained, smooth and compact deposits. Additives, such as thiourea [69–71], gelatine [72, 73] and animal glue [74], are commonly used as levelling and brightening agents in copper electrodeposition and electrowinning in order to produce smooth, free of voids and porosity copper deposits. Although advances have been made, in many cases the use of these additives is still carried out in an empirical way, and there are still many unknown aspects concerning the mechanism of action of additives.

Recently, we have investigated the effect of [BMIM]HSO₄ on copper electrodeposition [21]. Its effects on the morphology of cathodic deposits and the kinetic parameters of the cathodic process were deeply studied. Similar to the case for zinc electrodeposition, the addition of [BMIM]HSO₄ was found to have a strong inhibiting effect on the electroreduction process, and the effect is more pronounced at higher additive concentrations.

The kinetic parameters obtained show that the presence of [BMIM]HSO₄ has an inhibiting effect on the kinetics of the copper discharge process with slight changes in the copper electrodeposition reaction pathway, indicated by the changes in Tafel slopes and the corresponding charge transfer coefficient [21]. A possible mechanism of the action of this additive may

be explained as follows: cathodic surface can effectively adsorb [BMIM]HSO₄. When we add [BMIM]HSO₄ in the electrolyte, the additive molecules adsorb at the cathodic surface and interact with the Cu⁺ ions produced from Eq. (1) to form a copper-[BMIM]HSO₄ complex Eq. (3) by these equations:



We attribute the inhibition effect of [BMIM]HSO₄ on the process of copper electroreduction to the adsorption of the complex at active sites, where it may receive an electron from the cathode and discharge copper atoms which are embedded at the active sites (Eq. (4)). The [BMIM]HSO₄ will be released and can then become a complex.

The effect of [BMIM]HSO₄ on the complex-plane impedance diagrams is illustrated in **Figure 4**. The complex-plane impedance spectra obtained from the additive-free solution exhibit two capacitive features at high frequencies followed by an inductive loop at low-frequency values (**Figure 4a**). On the other hand, two intermediate-frequency capacitive features, far more separated at high concentration of additive (**Figure 4b and c**) in the presence of [BMIM]HSO₄, are obtained; that implies that two adsorbed species play a role in the process of copper electroreduction and the addition of [BMIM]HSO₄ brought about a change in the copper electroreduction mechanism.

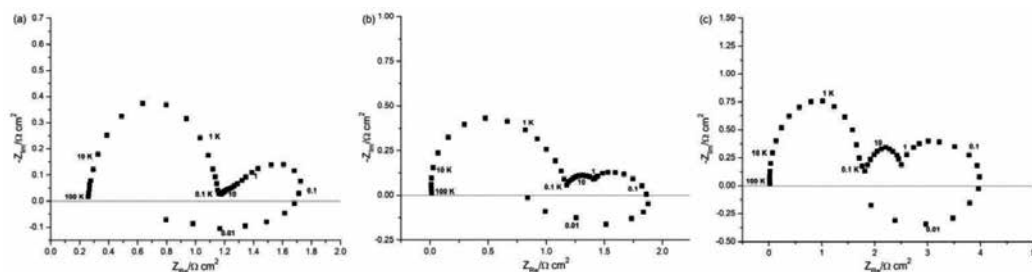


Figure 4. Impedance plots for copper electrodeposition at $E = -0.15$ V in the absence (a) and presence of [BMIM]HSO₄ (b) 10 mg·dm⁻³, (c) 50 mg·dm⁻³ [21].

Figure 5 shows the SEM images of copper deposits obtained by small-scale electrolysis from the sulphate electrolyte in the absence and presence of [BMIM]HSO₄. As it can be seen from **Figure 5(b and c)**, introducing [BMIM]HSO₄ has brought a notable effect on the surface quality of the copper deposits as compared with those gained from the additive-free bath

(Figure 5a) consisting of comparatively large, coarse grains. The size of the copper grain is smaller and continuously decreases with increasing additive concentrations in the presence of [BMIM]HSO₄ (Figure 5b and c). The fact that there was a blockage of the electrocrystallization process is indicated by the results. Blockage of the crystal growth process is the action of [BMIM]HSO₄, which induces a relative improvement in the process of nucleation. This results in a finer grained deposit. It is also noteworthy that the copper deposits' morphology remains essentially unchanged, irrespective of the additive concentration. The influence of [BMIM]HSO₄ on the crystallographic structure of the deposits is presented in Figure 5(d). The copper deposit consists of (111), (200), (220), (311) and (222) crystal orientations without additives. The addition of 10 mg·dm⁻³ [BMIM]HSO₄ inhibited the growth in the direction of the (111), (311), (222) planes and promoted the growth of the (220) plane.

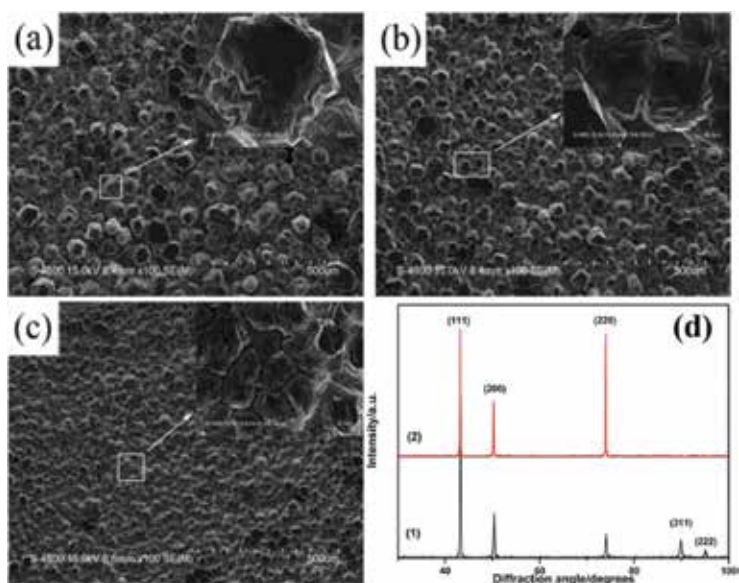


Figure 5. Scanning electron micrographs of copper deposits in the absence and presence of [BMIM]HSO₄: (a) Blank, (b) 10 mg·dm⁻³ and (c) 50 mg·dm⁻³. (Insets: local magnified graphs). (d) XRD patterns for the copper deposits in the absence and presence of [BMIM]HSO₄ (1) Blank, (2) 10 mg·dm⁻³ [21].

Pyridinium-based ionic liquids were also found to be readily adsorbed on the metallic surface similar to that of imidazolium-based ILs [21], which provide a larger potential group to be researched as novel metal electrodeposition additives. We have previously studied the effects of two alkylpyridinium ILs (py-iLs), including N-butylpyridinium hydrogen sulphate (BpyHSO₄) and N-hexylpyridinium hydrogen sulphate (HpyHSO₄), on copper electrodeposition from acidic sulphate electrolyte [22]. BpyHSO₄ and HpyHSO₄ both turn out to be efficient levelling additives in copper electrodeposition, which leads to more levelled and fine-grained cathodic deposits. Copper electrodeposition is associated with the growth process and a nucleation. The addition of py-iLs has a blocking effect on copper electrodeposition, which causes a blockage of the nuclei growth process and some improvement in the process of nucleation. Both additives increase the cathodic polarization of copper through their adsorption on the

cathodic surface and block the kinetics of the Cu^{2+} reduction process. A higher inhibition effect is offered by HpyHSO_4 than by BpyHSO_4 , which may be due to HpyHSO_4 's stronger adsorbability and complexation in comparison with BpyHSO_4 .

For further nucleation investigation [23], the initial stages of the process of copper electrodeposition take place through a three-dimensional instantaneous nucleation with diffusion-controlled growth of the nuclei. We changed the practically instantaneous nucleation mechanism observed in the additive-free solution to become more progressive for the additives in the solution. The blocking effect of alkyipyridinium hydrosulphate-based ILs on the copper electrocrystallization process through its cathodic adsorption on the active sites of the electrode surface brought about this change in the nucleation mechanism and, as a consequence, caused a decrease in the nucleation and growth rate of these nuclei and induced the formation of levelled and finer grained copper electrodeposits.

To be distinguished from alkyimidazolium and alkyipyridinium-based ILs, for which their additive effects were found to come from surface adsorption together with complexing action, quaternary ammonium-based ILs feature their action simply through specific adsorption [25]. The typically feasible cathodic adsorption of quaternary ammonium-based ILs, including tetraethylammonium hydrogen sulphate (NEt_4HSO_4 , **Figure 6a**) and tetrabutyl-ammonium hydrogen sulphate (NBu_4HSO_4 , **Figure 6b**), may have been caused by electrostatic attractive forces between dissolved quaternary ammonium cations and the electrically charged surface of the cathode, which can be schematically described in **Figure 6(c)**. Furthermore, the possible difference applied during the process of electrodeposition makes the charge on the cathode surface more negative and enhances the adsorption of positively charged quaternary ammonium ions. At a lower additive concentration, the alkyl chain of these quaternary ammonium cations may be oriented in the direction of the electrolyte. Nevertheless, a horizontal arrangement to the cathode can also be made of them. As there is an increment in the concentration of added ILs, the alkyl chain may trend for a vertical arrangement to improve absorption [75].

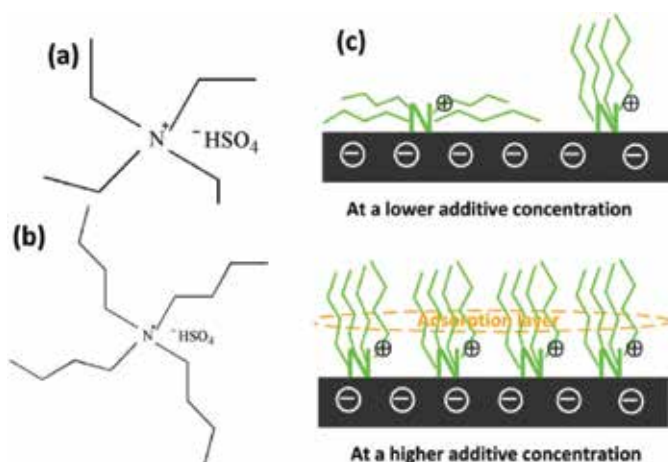


Figure 6. Structures of quaternary ammonium-based ILs used. (a) NEt_4HSO_4 , (b) NBu_4HSO_4 and (c) the proposed surface adsorption of NBu_4^+ at different additive concentrations on the cathode [25].

In this manner, more quaternary ammonium cations can adsorb at the cathode surface and act together to form a layer above the head group; this will block the cathode surface and bring about an increment in the inhibition effect on the approach of the Cu^{2+} species and the resulting electroreduction reaction. Longer alkyl chain will result in greater surface adsorbability of the ILs cations because of the alkyl group's electron releasing ability [76], which is found to improve with any increment in the alkyl chain. Therefore, NBu_4HSO_4 provides a higher inhibition effect than NEt_4HSO_4 .

4. Corrosion inhibitors

Because of the general aggressiveness of acid solutions, inhibitors are commonly used to reduce the corrosive attack on metallic materials. Numerous possible inhibitors have been investigated. Amongst them there are inorganic inhibitors [77], but in much greater numbers there are organic compounds. Most of the effective organic inhibitors used contain heteroatoms such as oxygen, nitrogen, sulphur, phosphorous and multiple bonds in the organic compound molecules through which they can adsorb on the metals surface [78–83]. The adsorption behaviour could include two main modes [1]. They are chemisorption (involving chemical combination between the metal and the adsorbate where electrons are shared and/or transferred, usually leading to the formation of covalent bonds) and physisorption (involving physical force such as van der Waals and pure electrostatic attraction between the charged metal and the charged inhibitor molecules). The former may occur if the inhibitor contains lone pairs of electrons, multiple bonds or conjugated p-type bond system. And there is no electron transfer and no electron sharing in the later adsorption mode. In this section, we reported the effect of some alkylimidazolium ILs on the corrosion inhibition of metals such as mild steel, aluminium and copper in acid solution.

4.1. Mild steel

Acid solutions are widely used in industry, such as acid pickling, industrial acid cleaning, acid descaling and oil well acidizing. However, due to their general aggressiveness, inhibitors are generally used in these processes to control metal dissolution. There are various organic inhibitors that tend to decrease the corrosion rate of steel and iron in acidic solutions [28, 83–86]. ILs with imidazolium [87–92] and pyridinium cations [93, 94] have showed excellent corrosion inhibition performance on mild steel in an acidic environment. We have first investigated the acid corrosion inhibition process of mild steel [2] in 1 M HCl by 1-butyl-3-methyl-imidazolium chlorides (BMIC) and 1-butyl-3-methyl-imidazolium hydrogen sulphate ($[\text{BMIM}]\text{HSO}_4$) and found that the studied inhibitors are mixed type inhibitors. For both inhibitors, the inhibition efficiency increased with an increase in the concentration of the inhibitor and the effectiveness of the two inhibitors are in the order $[\text{BMIM}]\text{HSO}_4 > \text{BMIC}$.

Figure 7 shows the Nyquist plot diagram for mild steel in 1 M HCl solution in the absence and presence of BMIC and $[\text{BMIM}]\text{HSO}_4$. It is clear from these figures that the impedance spectra obtained yield a semi-circular shape, suggesting that the corrosion of the mild steel in 1 M HCl solution is mainly controlled by a charge transfer process [95, 96]. A similar profile

of the Nyquist plots observed in the absence and presence of the inhibitors indicates that the addition of inhibitors does not change the mechanism for the dissolution of mild steel in HCl.

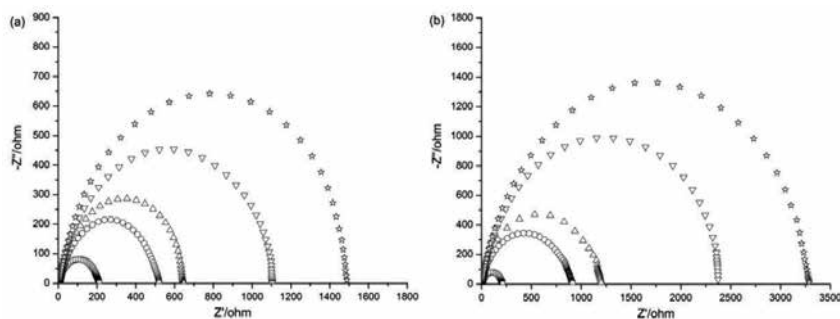


Figure 7. Nyquist plots for mild steel in 1 M HCl solution in the absence (\square) and presence of 5×10^{-4} (\circ), 1×10^{-3} (\triangle), 5×10^{-3} (∇) and 1×10^{-2} M (\diamond) inhibitor at 303 K: (a) BMIC, (b) [BMIM]HSO₄ [2].

The corrosion mechanism of iron in hydrochloric acid was proposed [97, 98] as follows. We assume that coulombic attraction first adsorbed Cl⁻ anion is onto the positively charged metal surface. Then the inhibitor molecules can be adsorbed via electrostatic interactions between the negatively charged metal surface and the positively charged molecules. These adsorbed inhibitor molecules come together with (FeCl⁻)_{ads} species to form monomolecular layers (by forming a complex) on the surface of the steel; it protects the surface of the steel from attack by chloride ions and prevents the oxidation reaction of (FeCl⁻)_{ads} as seen in steps (b→d). In contrast, in competition with hydrogen ions reducing hydrogen evolution (e→g), the protonated imidazolium molecules are also adsorbed at cathodic sites.

These are the steps followed by the anodic dissolution of iron:

- a. $\text{Fe} + \text{Cl}^- \leftrightarrow (\text{FeCl}^-)_{\text{ads}}$
- b. $(\text{FeCl}^-)_{\text{ads}} \leftrightarrow (\text{FeCl})_{\text{ads}} + \text{e}^-$
- c. $(\text{FeCl})_{\text{ads}} \rightarrow (\text{FeCl}^+) + \text{e}^-$
- d. $(\text{FeCl}^+) \leftrightarrow \text{Fe}^{2+} + \text{Cl}^-$

The cathodic hydrogen evolution follows the steps:

- e. $\text{Fe} + \text{H}^+ \leftrightarrow (\text{FeH}^+)_{\text{ads}}$
- f. $(\text{FeH}^+)_{\text{ads}} + \text{e}^- \rightarrow (\text{FeH})_{\text{ads}}$
- g. $(\text{FeH})_{\text{ads}} + \text{H}^+ + \text{e}^- \rightarrow \text{Fe} + \text{H}_2$

Meanwhile, the presence of the electron-donating groups on the imidazolium base structure, such as Cl and S, increases the electron density on the nitrogen of the -C=N- group due to their ability of offer free electrons. In particular, the ability of S atom is more excellent than that of Cl [99]. Therefore, [BMIM]HSO₄ is more effective than BMIC in inhibiting the corrosion of mild steel in HCl.

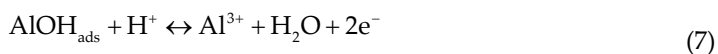
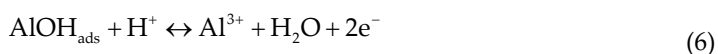
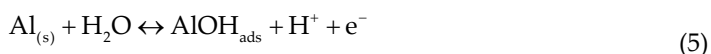
The characteristics of adsorption of the imidazolium base inhibitors on the mild steel in 1.0 M HCl solution follow Langmuir's adsorption isotherm. The analysis of thermodynamic parameters [2] such as equilibrium constant and standard free energy indicate that the inhibitors are physically adsorbed on the metal surface and the adsorption of inhibitor molecule with the corroding mild steel surface is a spontaneous and exothermic process [100].

4.2. Aluminium

A rapidly formed compact, strongly adherent and continuous oxide film may be responsible for the resistance of aluminium against corrosion in aqueous media [101, 102]. Consequently, many industries, such as reaction vessels, pipes, machinery and chemical batteries, have come to rely heavily on aluminium and its alloys. Hydrochloric acid solutions are employed for pickling, chemical and electrochemical etching of aluminium [103]. Having aggressive ions such as chloride, however, creates a huge localized attack [104]. The corrosion inhibition of aluminium in an acid medium has been reported while using hydrazone [105], anionic surfactants [106] and amino acid [107] as inhibitors. We have studied the corrosion inhibition performance of three alkylimidazolium ILs namely 1-butyl-3-methylimidazolium chlorides, 1-hexyl-3-methylimidazolium chlorides (HMIC) and 1-octyl-3-methyl-imidazolium chlorides (OMIC) on the corrosion of aluminium in 1.0 M HCl [22]. All the inhibitors studied could be classified as mixed type inhibitors with the obvious inhibition effect on both cathodic and anodic reactions of the corrosion process. The inhibition efficiency increased with an increase in the concentration of inhibitor and the effectiveness of these inhibitors was in the order of OMIC > HMIC > BMIC. Similar to the adsorption behaviour of imidazolium base inhibitors on the mild steel, the adsorption of these inhibitors on the aluminium surface also obeyed Langmuir adsorption isotherm and had a physical mechanism involving a spontaneous and exothermic process.

The Nyquist plots (**Figure 8**) for aluminium in 1.0 M HCl solution showed that the impedance spectra are made up of a large capacitive loop at high frequencies, which is followed by a small inductive one at low-frequency values. There is a relationship between the high-frequency capacitive loop and the charge transfer of the corrosion process and the double layer behaviour, and the inductive loop could be interpreted in terms of the relaxation processes in the oxide film covering the electrode surface [108] or attributed to the stabilization of the layer by the adsorbed intermediate products of the corrosion reaction on the electrode surface involving inhibitor molecules as well as reactive products [109].

A general mechanism for the dissolution of aluminium in the presence of chloride ions would be similar to that reported in the literature [110, 111].





The water molecules originally adsorbed on the surface are partly displaced by the adsorption of imidazolium compounds on the aluminium surface; this blocks the formation of AlOH_{ads} (Eq. (5)). Thus, we can prevent both the oxidation reaction of AlOH_{ads} to Al^{3+} as shown by step (Eq. (6)) and the complexation reaction between the hydrated cation $[\text{AlOH}]^{2+}$ species that are formed in step (Eq. (7)) and chloride ions (Eq. (8)). Moreover, these protonated molecules also compete with the hydrogen ions, which will curtail the evolution of hydrogen. The presence of the electron-donating group (Cl) on the imidazolium base structure is observed to increase the electron density on the nitrogen of the $-\text{C}=\text{N}-$ group and to result in high inhibition efficiency. In particular, this effect appears more pronounced with the increase in the chain length of the alkyl connecting with $\text{N}_{(3)}$ of the imidazolium ring. Therefore, the effectiveness of these inhibitors with the sequence of $\text{OMIC} > \text{HMIC} > \text{BMIC}$ is obtained.

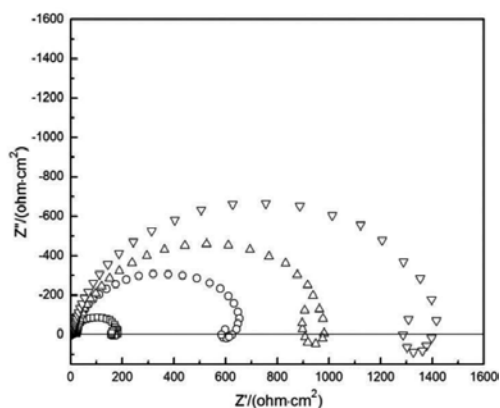


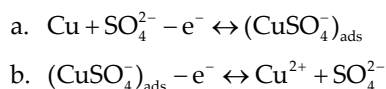
Figure 8. Effect of inhibitors on the impedance response of aluminum in 1.0 M HCl solution in the absence (\square) and presence of 5×10^{-4} M (\circ) BMIC, (\triangle) HMIC, (∇) OMIC at 303 K [26].

4.3. Copper

Copper and its alloys have been found widespread applications in many industrial processes such as industrial equipment, building construction, electricity, electronics, coinages and ornamental parts due to their electrical, thermal, mechanical and corrosion resistance properties [112]. However, the presence of aggressive ions such as chlorides, sulphates or nitrates creates extensive localized attack [113]. One effective approach to protect metals against the general aggression of acid solutions is the use of organic inhibitors, which can effectively control the metal dissolution and eliminate the undesirable acid consumption. Many organic compounds including triazole, imidazole, thiazole, tetrazole, indole and its derivatives [114, 115] have been developed as corrosion inhibitors to inhibit copper corrosion in aggressive environments. As an example of ILs, alkylimidazolium-based ILs ($[\text{BMIM}]\text{HSO}_4$, $[\text{HMIM}]\text{HSO}_4$ and $[\text{OMIM}]\text{HSO}_4$) have proved to be excellent inhibitors for the corrosion inhibition of copper

in 0.5 mol·L⁻¹ H₂SO₄ solution [27], which behave as mixed type inhibitors with a pre-dominantly cathodic action. The corresponding electrochemical impedance results suggested that these imidazolium-based molecules act by adsorbing at the copper/solution interface. The adsorption of these imidazolium-based compounds on the copper surface in an acidic solution is found to fit the Langmuir adsorption isotherm and occurs by a physisorption-based mechanism involving a spontaneous process.

The anodic dissolution of copper proceeds via a two-step reaction mechanism and can be described as follows: [116]



where $(\text{CuSO}_4^-)_{\text{ads}}$ is an adsorbed species at the copper surface and does not diffuse into the bulk solution [52]. Consequently, the mass transport has little influence on dissolution of copper.

It is assumed that the negative sulphated ions are first adsorbed onto the positively charged metal surface by columbic attraction. Since the imidazolium group as well as nitrogen atom in the heteroaromatic ring of imidazolium compounds can be protonated in acidic solutions [117]. The protonated inhibitor molecules can be adsorbed through electrostatic interactions between the positively charged molecules and the negatively charged metal surface [2]. These adsorbed imidazolium compound molecules will interact with $(\text{CuSO}_4^-)_{\text{ads}}$ ions generated from (a) to form a protective layer (by forming a complex) at active sites, which hides both mass and charge transfers and blocks the further oxidation reaction of $(\text{CuSO}_4^-)_{\text{ads}}$ to Cu^{2+} as shown in step (b).

5. Conclusions

In this chapter, two perspective application studies of ILs in using as additives for metal electrodeposition and inhibitors for metal anti-corrosion were summarized. It was shown that ILs had some intrinsic advantages over traditional organic agents. Due to their stability, high conductivity, low vapour pressure and environmental friendly nature, ILs were excellent levelling agents for both zinc and copper electrodeposition, which were superior to traditional additives, and showed favourable corrosion resistant performance on mild steel, aluminium and copper in acidic solutions.

It is apparent that the future for ILs-based technology in these two aspects is extremely bright; however, more fundamental aspects issues have to be solved so that their applications will become a practical reality instead of laboratorial studies. What is the adsorption mechanism of ILs on the metal surface? What is the effect of ILs on the nucleation and growth of metal? And how is the influence of ILs on the structures of electric double layer, etc.? All these issues are the critical problems for further study.

Author details

Zhang Qibo* and Hua Yixin

*Address all correspondence to: qibozhang@kmust.edu.cn

Key Lab of Ionic Liquids Metallurgy, Faculty of Metallurgical and Energy Engineering, Kunming University of Science and Technology, Kunming, Yunnan, China

References

- [1] Paunovic M, Schlesinger M. *Fundamental of Electrochemical Deposition*. A John Wiley & Sons, Inc., Publication. Hoboken, New Jersey, 2006, 168.
- [2] Zhang Q B, Hua Y X. Corrosion inhibition of mild steel by alkyylimidazolium ionic liquids in hydrochloric acid. *Electrochim. Acta*, 2009, 54(6): 1881.
- [3] Scendo M. The effect of purine on the corrosion of copper in chloride solutions. *Corros. Sci.*, 2007, 49(2): 373.
- [4] Sheldon R. Catalytic reactions in ionic liquids. *Chem. Commun*, 2001, 7(23): 2399.
- [5] Zhao D, Wu M, Kou Y, Min E. Ionic liquids: Applications in catalysis. *Catal. Today*, 2002, 74(1–2): 157.
- [6] Wasserscheid P, Welton T. *Ionic Liquids in Synthesis*. Wiley-VCH, Weinheim, 2003, 48.
- [7] Moens L, Blake D M, Rudnicki D L, Hale M J. Advanced thermal storage fluids for solar parabolic trough systems. *J. Solar Energy Eng.*, 2003, 125(1): 112.
- [8] Makoto U, Takeda M, Toriumi A, Kominato A, Hagiwara R, Yasuhiko I. Application of low-viscosity ionic liquid to the electrolyte of double-layer capacitors. *J. Electrochem. Soc.*, 2003, 150(4): A499.
- [9] Antonietti M, Kuang D, Smarsly B, Zhou Y. Ionic liquids for the convenient synthesis of functional nanoparticles and other inorganic nanostructures. *Angew. Chem. Int. Ed.*, 2004, 43(38): 4988.
- [10] Balducci A, Bardi U, Caporali S, Mastragostino M, Soavi F. Ionic liquids for hybrid super capacitors. *Electrochem. Commun.*, 2004, 6(6): 566.
- [11] Sato T, Maruo T, Marukane S, Takagi K. Ionic liquids containing carbonate solvent as electrolytes for lithium ion cells. *J. Power Sources*, 2004, 138(1–2): 253.
- [12] Kubisa P. Application of ionic liquids as solvents for polymerization processes. *Prog. Polym. Sci.*, 2004, 29(1): 3.
- [13] Anderson J L, Armstrong D W, Wei G T. Ionic liquids in analytical chemistry. *Anal. Chem.*, 2006, 78(9): 2892.

- [14] Pandey S. Analytical applications of room-temperature ionic liquids: A review of recent efforts. *Anal. Chim. Acta*, 2006, 556(1): 38.
- [15] Winterton N. Solubilization of polymers by ionic liquids. *J. Mater. Chem.*, 2006, 16(44): 4281.
- [16] Izgorodina E I, Forsyth M, MacFarlane D R. On the components of the dielectric constants of ionic liquids: Ionic polarization? *Phys. Chem. Chem. Phys.*, 2009, 11(14): 2452
- [17] Imanishi A, Tamura M, Kuwabata S. Formation of Au nanoparticles in an ionic liquid by electron beam irradiation. *Chem. Commun.*, 2009(13): 1775
- [18] Zhang Q B, Hua Y X. Effects of 1-butyl-3-methylimidazolium hydrogen sulfate-[BMIM]HSO₄ on zinc electrodeposition from acidic sulfate electrolyte. *J. Appl. Electrochem.*, 2009, 39(2): 261.
- [19] Zhang Q B, Hua Y X. Effects of [HMIM]HSO₄ and [OMIM]HSO₄ on the electrodeposition of zinc from sulfate electrolytes. *J. Appl. Electrochem.*, 2009, 39(8): 1185.
- [20] Zhang Q B, Hua Y X, Dong T G, Zhou D G. Effects of temperature and current density on zinc electrodeposition from acidic sulfate electrolyte with [BMIM]HSO₄ as additive. *J. Appl. Electrochem.*, 2009, 39(8): 1207.
- [21] Zhang Q B, Hua Y X, Wang Y T, Lu H J, Zhang X Y. Effects of ionic liquid additive [BMIM]HSO₄ on copper electrodeposition from acidic sulfate electrolyte. *Hydrometallurgy*, 2009, 98(3–4): 291.
- [22] Zhang Q B, Hua Y X. Influence of [BMIM]HSO₄ on electrodeposition and corrosion behavior of Zn coatings from acidic sulfate bath. *Surf. Interface Anal.*, 2012, 44(9): 1254.
- [23] Zhang Q B, Hua Y X, Ren Y X, Chen L Y. Influence of alkylpyridinium ionic liquids on copper electrodeposition from acidic sulfate electrolyte. *J. Cent. South Univ.*, 2013, 20: 2096.
- [24] Zhang Q B, Hua Y X, Wang R. Initial stages of copper electrodeposition from acidic sulfate solution in the presence of alkylpyridinium hydrosulfate ionic liquids. *Sci. China Chem.*, 2013, 56(11): 1586.
- [25] Zhang Q B, Yu X L, Hua Y X, Xue W. The effect of quaternary ammonium-based ionic liquids on copper electrodeposition from acidic sulfate electrolyte. *J. Appl. Electrochem.*, 2015, 45(1): 79.
- [26] Zhang Q B, Hua Y X. Corrosion inhibition of aluminium in hydrochloric acid solution by alkylimidazolium ionic liquids. *Mater. Chem. Phys.*, 2010, 119(1–2): 57.
- [27] Zhang Q B, Hua Y X. Effect of alkylimidazolium ionic liquids on the corrosion inhibition of copper in sulfuric acid solution. *Acta Phys. Chim. Sin.*, 2011, 27(3), 655–663.
- [28] Emregül K C, Hayvali M. Studies on the effect of vanillin and protocatechualdehyde on the corrosion of steel in hydrochloric acid. *Mater. Chem. Phys.*, 2004(2–3), 83: 209.
- [29] Piersma B J, Ryan D M, Schumacher E R, Reichel T L. Electrodeposition and stripping of lithium and sodium on inert electrodes in room temperature chloroaluminate molten salts. *J Electrochem. Soc*, 1996, 143(3): 908.

- [30] Katayama Y, Morita T, Yamagata M, Miura T. Electrodeposition of metallic lithium on a tungsten electrode in 1-butyl-1-methylpyrrolidinium bis (trifluoromethanesulfone) imide room-temperature molten salt. *Electrochemistry*, 2003, 71(12): 1033.
- [31] Howlett P C, MacFarlane D R, Hollenkamp A F. High lithium metal cycling efficiency in a room-temperature ionic liquid. *Electrochem. Solid-State Lett.*, 2004, 7(5): A97.
- [32] Gray G E, Kohl P A, Winnick J. Stability of sodium electrodeposited from a room temperature chloroaluminate molten salt. *J. Electrochem. Soc.*, 1995, 142(11): 3636.
- [33] Zhang M, Kamavaram V, Reddy R G. Aluminum electrowinning in ionic liquids at room temperature. *J. Manag.*, 2004, 56(11): 334.
- [34] Zhang M, Kamavaram V, Reddy R G. Aluminum electrowinning in ionic liquids at low temperature. *Light Metals*, 2005, (1): 583.
- [35] Wu B, Reddy R G, Rogers R D. Aluminum reduction via near room temperature electrolysis in ionic liquids. *Light Metals*, 2001, (1): 237.
- [36] Mukhopadhyay I, Aravinda C L, Borissov D, Freyland W. Electrodeposition of Ti from $TiCl_4$ in the ionic liquid 1-methyl-3-butyl-imidazolium bis (trifluoro methyl sulfone) imide at room temperature: Study on phase formation by in situ electrochemical scanning tunneling microscopy. *Electrochim. Acta*, 2005, 50(6): 1275.
- [37] Endres F, Abedin S Z E, Saad A Y, Moustafa E M, Borissenko N, Price W E, Wallace G G, MacFarlane D R, Newman P J, Bund A. On the electrodeposition of titanium in ionic liquids. *Phys. Chem. Chem. Phys.*, 2008, 10(16): 2189.
- [38] NuLi Y, Yang J, Wang P. Electrodeposition of magnesium film from BMIMBF₄ ionic liquid. *Appl. Surf. Sci.*, 2006, 252(23): 8086.
- [39] NuLi Y, Yang J, Wu R. Reversible deposition and dissolution of magnesium from BMIMBF₄ ionic liquid. *Electrochem. Commun.*, 2005, 7(11): 1105.
- [40] Cheek G T, O'Grady W E, Abedin S Z E, Moustafa E M, Endres F. Studies on the electrodeposition of magnesium in ionic liquids. *J. Electrochem. Soc.*, 2008, 155(1): D91.
- [41] Whitehead J A, Lawrence G A, McCluskey A. Green leaching: Recyclable and selective leaching of gold-bearing ore in an ionic liquid. *Green Chem.*, 2004, 6(7): 313.
- [42] Whitehead J A, Zhang J, Pereira N, McCluskey, Lawrence G A. Application of 1-alkyl-3-methyl-imidazolium ionic liquids in the oxidative leaching of sulphidic copper, gold and silver ores. *Hydrometallurgy*, 2007, 88(1–4): 109.
- [43] Luczak J, Joskowska M, Hupka J. Imidazolium ionic liquids in mineral processing. *Physicochem. Prob. Miner. Proc*, 2008, 42(3): 223.
- [44] Dong T G, Hua Y X, Zhang Q B, Zhou D G. Leaching of chalcopyrite with Brønsted acidic ionic liquid at ambient pressure and low temperature. *Hydrometallurgy*, 2009, 99(1–2): 33.
- [45] Maase M, Cornils B, Herrmann W A, Horvath I T, Leitner W, Mecking S, Olivier-Bourbigou H, Vogt D. *Multiphase Homogeneous Catalysis*. Wiley-VCH Verlag GmbH & Co. KGaA, Weinheim, Germany, 2005, 560.

- [46] Chauvin Y, Olivier H, Wyrvalski C N, Simon L C, Souza R, Dupont J. Oligomerization of n-butenes catalyzed by nickel complexes dissolved in organochloroaluminate ionic liquids. *J. Catal.*, 1997, 165(2): 275.
- [47] Transforming Metal Finishing Processes, 2009. http://www.ionmet.eu/fileadmin/ionmet/Dissemination/eStrategies_IONMET.pdf.
- [48] Tian G C, Li J, Hua Y X. Application of ionic liquids in hydrometallurgy of nonferrous metals. *Trans. Nonferrous Met. Soc. China*, 2010, 20(3): 513.
- [49] Zhang M, Kamavaram V, Reddy R G. Ionic liquids metallurgy: Novel electrolytes for metals extraction and refining technology. *Miner. Metall. Proc.*, 2006, 23(3): 177.
- [50] Oniciu L, Muresan. Some fundamental aspects of levelling and brightening in metal electrodeposition. *J. Appl. Electrochem.*, 1991, 21(7): 565.
- [51] Thomas J D. Leveling, definition, measurement, and understanding. *Proc. Am. Electroplat. Soc.*, 1956, 43(1): 60.
- [52] Kardos O, Foulke D G. *Advances in Electrochemistry and Electrochemical Engineering*. Vol. 2 (edited by Ch. W. Tobias), Interscience Publishers, New York, 1966, 145.
- [53] Piron D L, Mathieu D, Amboise M D. Zinc electrowinning with 2-butyne-1,4-diol. *Can. J. Chem. Eng.*, 1987, 65(4): 685.
- [54] Hosny A Y. Electrowinning of zinc from electrolytes containing anti-acid mist surfactant. *Hydrometallurgy*, 1993, 32(2): 261.
- [55] Karavasteva M, Karaivanov SA. Electrowinning of zinc at high current density in the presence of some surfactants. *J. Appl. Electrochem.*, 1993, 23(7): 763.
- [56] Karavasteva M. The electrodeposition of metal impurities during the zinc electrowinning at high current density in the presence of some surfactants. *Hydrometallurgy*, 1994, 35(3): 391.
- [57] Das S C, Singh P, Hefter G T. Effects of 2-picoline on zinc electrowinning from acidic sulfate electrolyte. *J. Appl. Electrochem.*, 1996, 26(12): 1245.
- [58] Das S C, Singh P, Hefter G T. The effects of 4-ethylpyridine and 2-cyanopyridine on zinc electrowinning from acidic sulfate solutions. *J. Appl. Electrochem.*, 1997, 27(6): 738.
- [59] Tripathy B C, Das S C, Singh P, Hefter G T. Zinc electrowinning from acidic sulfate solutions: Part I: Effects of sodium lauryl sulfate. *J. Appl. Electrochem.*, 1997, 27(6): 673.
- [60] Tripathy B C, Das S C, Singh P, Hefter G T. Zinc electrowinning from acidic sulphate solutions. Part III: Effects of quaternary ammonium bromides. *J. Appl. Electrochem.*, 1999, 29(10): 1229.
- [61] Tripathy B C, Das S C, Hefter G T, Singh P. Zinc electrowinning from acidic sulphate solutions Part II: Effects of triethylbenzylammonium chloride. *J. Appl. Electrochem.*, 1998, 28(9): 915.

- [62] Tripathy B C, Das S C, Singh P, Heffer G T, Misra V N. Zinc electrowinning from acidic sulphate solutions Part IV: Effects of perfluorocarboxylic acids. *J. Electroanal. Chem.*, 2004, 565(1): 49.
- [63] Stupnisek-Lisac E, Podbrscek S, Soric T. Non-toxic organic zinc corrosion inhibitors in hydrochloric acid. *J. Appl. Electrochem.*, 1994, 24(8): 779
- [64] Mohanty U S, Tripathy B C, Singh P, Das S C. Effect of pyridine and its derivatives on the electrodeposition of nickel from aqueous sulfate solutions. Part II: Polarization behaviour. *J. Appl. Electrochem.*, 2001, 31(9): 969.
- [65] Zhang Q B, Hua Y X. Effect of ionic liquid additive [BMIM]HSO₄ on zinc electrodeposition from impurity-containing sulfate electrolyte. Part I: Current efficiency, surface morphology and crystal orientations. *J. Appl. Electrochem.*, 2011, 41(4): 481.
- [66] Zhang Q B, Hua Y X. Effect of the ionic liquid additive-[BMIM]HSO₄ on the kinetics of oxygen evolution during zinc electrowinning. *Acta Phys. Chim. Sin.*, 2011, 27(1): 149.
- [67] Zhang Q B, Hua Y X. Stability of [BMIM]HSO₄ for using as additive during zinc electrowinning from acidic sulfate solution. *J. Cent. South Univ.*, 2012, 19: 2451.
- [68] Bonou L, Eyraud M, Denoyl R, Massiani Y. Influence of additives on Cu electrodeposition mechanisms in acid solution: Direct current study supported by non-electrochemical measurements. *Electrochim. Acta*, 2002, 47(26): 4139.
- [69] Varvara S, Muresan L, Nicoara A, Maurin G, Popescu I C. Kinetic and morphological investigation of copper electro-deposition from sulfate electrolytes in the presence of an additive based on ethoxyacetic alcohol and triethyl-benzylammonium chloride. *Mater. Chem. Phys.*, 2001, 72(3): 332.
- [70] Suarez D F, Olson F A. Nodulation of electro-deposited copper in the presence of thiourea. *J. Appl. Electrochem.*, 1992, 22(4): 1002.
- [71] Cofré P, Bustos A. Voltammetric behaviour of the copper (II)-thiourea system in sulphuric acid medium at platinum and glassy carbon electrodes. *J. Appl. Electrochem.*, 1994, 24(6): 564.
- [72] Turner D R, Johnson G R. The effect of some addition agents on the kinetics of copper electro-deposition from a sulfate solution. I. Cathode potential-current density relation. *J. Electrochem. Soc.*, 1962, 109 (9): 798.
- [73] Johnson G R, Turner D R. The effect of some addition agents on the kinetics of copper electrodeposition from a sulfate solution. II. Rotating disk electrode experiments. *J. Electrochem. Soc.*, 1962, 109(9): 918.
- [74] Muresan L, Varvara S, Maurin G, Dorneanu S. The effect of some organic additives upon copper electrowinning from sulphate electrolytes. *Hydrometallurgy*, 2000, 54(2-3): 161.
- [75] Fuchs-Godec R. The adsorption, CMC determination and corrosion inhibition of some N-alkyl quaternary ammonium salts on carbon steel surface in 2 M H₂SO₄. *Colloid Surf. A Physicochem. Eng. Asp.*, 2006, 280: 130-139.

- [76] Egashira M, Nakagawa M, Watanabe I, Okada S, Yamaki J. Cyano-containing quaternary ammonium-based ionic liquid as a 'co-solvent' for lithium battery electrolyte. *J. Power Sources*, 2005, 146: 685.
- [77] Igual M A, García A J, Guiñón J L, Pérez H V. Comparison of inorganic inhibitors of copper, nickel and copper-nickels in aqueous lithium bromide solution. *Electrochim. Acta*, 2004, 50(4): 957.
- [78] Quraishi M A, Ansari F A. Fatty acid oxadiazoles as corrosion inhibitors for mild steel in formic acid. *J. Appl. Electrochem.*, 2006, 36(3): 309.
- [79] Quraishi M A, Rafiquee M Z A, Saxena N, Khan S. Fatty acid thiosemicarbazides as corrosion inhibitors for mild steel in hydrochloric acid solution. *J. Corros. Sci. Eng.*, 2006, 10(1): 3.
- [80] Rehim S S Abd El, Hassan H H, Amin M A. The corrosion inhibition study of sodium dodecyl benzene sulphonate to aluminum and its alloys in 1.0 M HCl solution. *Mater. Chem. Phys.*, 2003, 78(2): 337.
- [81] Bentiss F, Traisnel M, Chaibi N, Mernari B, Vezin H, Lagrenee M. 2, 5-Bis (n-methoxyphenyl)-1,3,4-oxadiazoles used as corrosion inhibitors in acidic media: Correlation between inhibition efficiency and chemical structure. *Corros. Sci.*, 2002, 44(10): 2271.
- [82] Lebrini M, Lagrenee M, Vezin H, Gengembre L, Bentiss F. Electrochemical and quantum chemical studies of new thiadiazole derivatives adsorption on mild steel in normal hydrochloric acid medium. *Corros. Sci.*, 2005, 47(2): 485.
- [83] Wahdan M H, Hermas A A, Morad M S. Corrosion inhibition of carbon-steels by propargyltriphenylphosphonium bromide in H_2SO_4 solution. *Mater. Chem. Phys.*, 2002, 76(2): 111.
- [84] Bentiss F, Traisnel M, Lagrenee M. The substituted 1,3,4-oxadiazoles: A new class of corrosion inhibitors of mild steel in acidic media. *Corros. Sci.*, 2000, 42(1): 127.
- [85] Li X, Tang L, Li L, Mu G, Liu G. Synergistic inhibition between o-phenanthroline and chloride ion for steel corrosion in sulphuric acid. *Corros. Sci.*, 2006, 48(2): 308.
- [86] Benabdellah M, Aouniti A, Dafali A, Hammouti B, Benkaddour M, Yahyi A, Ettouhami A. Investigation of the inhibitive effect of triphenyltin 2-thiophene carboxylate on corrosion of steel in 2 M H_3PO_4 solutions. *Appl. Surf. Sci.*, 2006, 252(23): 8341.
- [87] Ashassi-Sorkhabi H, Eshaghi M. Corrosion inhibition of mild steel in acidic media by [BMIm]Br ionic liquid. *Mater. Chem. Phys.*, 2009, 114(1): 267
- [88] Murulana L C, Singh A K, Shukla S K, Kabanda M M, Ebenso E E. Experimental and quantum chemical studies of some bis (trifluoromethyl-sulfonyl) imide imidazolium-based ionic liquids as corrosion inhibitors for mild steel in hydrochloric acid solution. *Ind. Eng. Chem. Res.*, 2012, 51(40): 13282.
- [89] Guzmán-Lucero D, Olivares-Xometl O, Martínez-Palou R, Likhanova N V, Domínguez-Aguilar M A, Garibay-Febles V. Synthesis of selected vinylimidazolium ionic liquids

and their effectiveness as corrosion inhibitors for carbon steel in aqueous sulfuric acid. *Ind. Eng. Chem. Res.*, 2011, 50(12): 7129.

- [90] Zhou X, Yang H, Wang F. [BMIM] BF₄ ionic liquids as effective inhibitor for carbon steel in alkaline chloride solution. *Electrochim. Acta*, 2011, 56(11): 4268.
- [91] Kowsari E, Payami M, Amini R, Ramezanzadeh B, Javanbakht M. Task-specific ionic liquid as a new green inhibitor of mild steel corrosion. *Appl. Surf. Sci.*, 2014, 289: 478.
- [92] Yousefi A, Javadian S, Dalir N, Kakemam J, Akbari J. Imidazolium-based ionic liquids as modulators of corrosion inhibition of SDS on mild steel in hydrochloric acid solutions: Experimental and theoretical studies. *RSC Adv.*, 2015, 5(16): 11697.
- [93] Likhanova N V, Dominguez-Aguilar M A, Olivares-Xometl O, Nava-Entzana N, Arce E, Dorantes H. The effect of ionic liquids with imidazolium and pyridinium cations on the corrosion inhibition of mild steel in acidic environment. *Corros. Sci.*, 2010, 52(6): 2088.
- [94] Messali M. A green microwave-assisted synthesis, characterization and comparative study of new pyridinium-based ionic liquids derivatives towards corrosion of mild steel in acidic environment. *J. Mater. Environ. Sci.*, 2011, 2(2): 174–185.
- [95] Achouri M E, Kertit S, Goultaya H M, Nciri B, Bensouda Y, Perez L, Infante M R, Elkacemi K. Corrosion inhibition of iron in 1 M HCl by some gemini surfactants in the series of alkanediyl- α,ω -bis-(dimethyl tetradecyl ammonium bromide). *Prog. Org. Coat.*, 2001, 43(4): 267.
- [96] Chetouani A, Aouniti A, Hammouti B, Benchat N, Benhadda T, Kertit S. Corrosion inhibitors for iron in hydrochloric acid solution by newly synthesised pyridazine derivatives. *Corros. Sci.*, 2003, 45(8): 1675.
- [97] Li W, He Q, Pei C, Hou B. Experimental and theoretical investigation of the adsorption behaviour of new triazole derivatives as inhibitors for mild steel corrosion in acid media. *Electrochim. Acta*, 2007, 52(22): 6386.
- [98] Yurta A, Balaban A, Kandemir S U, Bereket G, Erk B. Investigation on some Schiff bases as HCl corrosion inhibitors for carbon steel. *Mater. Chem. Phys.*, 2004, 85(2–3): 420.
- [99] Fang J, Li J. Quantum chemistry study on the relationship between molecular structure and corrosion inhibition efficiency of amides. *J. Mol. Struct. (Theochem.)*, 2002, 593(1–3): 179.
- [100] Gomma G K, Wahdan M H. Schiff bases as corrosion inhibitors for aluminum in hydrochloric acid solution. *Mater. Chem. Phys.*, 1995, 39(3): 209.
- [101] Gayle R T, Schueller S, Taylor R, Hajcsar E E. Evaluation of natural oxides on aluminum in neutral borate electrolyte. *J. Electrochem. Soc.*, 1992, 139(10): 2799.
- [102] Lee E J, Pyun S J. The effect of oxide chemistry on the passivity of aluminium surfaces. *Corros. Sci.*, 1995, 37(1): 157.
- [103] Metikos-Hukovic M, Babic R, Grubac Z. The study of aluminum corrosion in acidic solution with nontoxic inhibitors. *J. Appl. Electrochem.*, 2002, 32(1): 35.

- [104] El-Etre A Y. Inhibition of aluminum corrosion using *Opuntia* extract. *Corros. Sci.*, 2003, 45(11): 2485.
- [105] Ahmed A I, El-Asklany A H, Fouda A S. Effect of some hydrazone compounds on the corrosion behavior of aluminum in HCl and NaOH solutions. *J. Ind. Chem. Soc.*, 1985, 62(7): 367.
- [106] Zhao T P, Mu G N. The adsorption and corrosion inhibition of anion surfactants on aluminium surface in hydrochloric acid. *Corros. Sci.*, 1999, 41(10): 1937.
- [107] Fouda A S, El-Semongy M M. The Effect of some amino acids on the corrosion of aluminium in hydrochloric acid solution. *J. Ind. Chem. Soc.*, 1982, 59(1): 89.
- [108] Al-Kharafi F M, Badawy W A. Phosphoric acid passivated niobium and tantalum EIS-comparative study. *Electrochim. Acta*, 1995, 40(16): 1811.
- [109] Yurt A, Ulutas S, Dal H. Electrochemical and theoretical investigation on the corrosion of aluminium in acidic solution containing some Schiff bases. *Appl. Surf. Sci.*, 2006, 253(2): 919.
- [110] Ford F P, Burstein G T, Hoar T P. Bare surface reaction rates and their relation to environment controlled cracking of aluminum alloys. *J. Electrochem. Soc.*, 1980, 127(6): 1325.
- [111] Nguyen T H, Foley R T. The chemical nature of aluminum corrosion. *J. Electrochem. Soc.*, 1982, 129(3): 464.
- [112] Tavakoli H, Shahrabi T, Hosseini M G. Synergistic effect on corrosion inhibition of copper by sodium dodecylbenzenesulphonate (SDBS) and 2-mercaptobenzoxazole. *Mater. Chem. Phys.*, 2008, 109(2): 281.
- [113] Zucchi F, Grassi V, Frignani A, Trabanelli G. Inhibition of copper corrosion by silane coatings. *Corros. Sci.*, 2004, 46(11): 2853.
- [114] Zhao Y S, Pang Z Z. The action mechanism of MMI as corrosion inhibitor of copper for hydrochloric acid pickling. *Acta Phys. Chim. Sin.*, 2003, 19(5): 419–422.
- [115] Scendo M, Poddebniak D, Malyszko J. Indole and 5-chloroindole as inhibitors of anodic dissolution and cathodic deposition of copper in acidic chloride solutions. *J. Appl. Electrochem.*, 2003, 33(3–4): 287–293.
- [116] Smyrl W H, Bockris J O M, Conway B E, Yeager E, White R E. *Comprehensive Treatise of Electrochemistry*. Plenum Press, New York, 1981, Vol. 4.
- [117] Quraishi M A, Rafiquee M Z A, Khan S, Saxena N. Corrosion inhibition of aluminium in acid solutions by some imidazoline derivatives. *J. Appl. Electrochem.*, 2007, 37(10): 1153–1162.

Ionic Liquid Enhancement of Polymer Electrolyte Conductivity and their Effects on the Performance of Electrochemical Devices

Siti Nor Farhana Yusuf, Rosiyah Yahya and
Abdul Kariem Arof

Additional information is available at the end of the chapter

<http://dx.doi.org/10.5772/65752>

Abstract

Ionic liquids (ILs) are molten salts at ambient temperature and consist of poorly coordinating cations and anions. They have good electrical conductivity with a wide voltage window and high thermal stability, but negligible vapor pressure. ILs can enhance ionic conductivity when added to polymer electrolytes. Conductivity enhancement is due to the additional ions supplied by the IL, the plasticizing nature of the IL and the low viscosity that facilitates ion mobility. The plasticizing nature of ILs softens the polymer chain giving rise to easier polymer segmental motion. Increase in polymer segmental motion implies that IL can increase amorphousness of a polymer electrolyte (PE). This article discusses the involvement of ionic liquid as electrolytes in selected devices, namely dye sensitized photovoltaics, batteries, fuel cells and supercapacitors.

Keywords: polymer electrolyte, ionic liquid, dye-sensitized photovoltaic, supercapacitors, fuel cells

1. Introduction

An ionic liquid (IL) is a molten salt at room temperature (RT). They consist of cations and anions that are weakly coordinating [1]. Ionic liquids (ILs) have thermal stability as high as 473–573 K, wide potential windows and high electrical conductivity [2].

ILs have low melting temperature and negligible vapor pressure. They are therefore green solvents making them suitable for applications in industries [3]. The negligible vapor pressure prevents loss of solvent to the environment. To economize space, abbreviations are used in this article. These are listed at the end of the article.

2. ILs in polymer electrolytes (PEs)

ILs have been introduced in PEs for conductivity enhancement. Kumar and Hashmi [4] have introduced EMImTf, in PVdF-HFP- NaCF_3SO_3 PE system. EMImTf is a room temperature ionic liquid (RTIL). The PVdF-HFP with EMImTf PE system gave an electrical conductivity of the order 10^{-1} S m^{-1} at room temperature (RT), good thermal stability and wide potential window.

EMImBF₄ [5] has also been shown to increase ionic conductivity of PVdF-HFP-LiBF₄ PE system from 4.4×10^{-5} to $2.0 \times 10^{-3} \text{ S m}^{-1}$. The incorporation of EMImBF₄ introduced additional mobile ions namely EMIm⁺ and BF₄⁻. This increased the concentration of mobile ions that is one of the parameters that govern ionic conductivity. The additional charge carriers also interacted with the electron donors of the polymer, which reduced the polymer-polymer intermolecular interaction. This will soften the polymer chains resulting in increased polymer segmental motion. Increased polymer segmental motion implied increased structural disorder or amorphousness of the PE system. Ion conduction only takes place in the amorphous region of the PE, hence with increased amorphousness, conductivity of the PE also increased.

The PP₂₄TFSI ionic liquid has been added with LiTFSI to impart Li⁺ ion transport [6]. The electrolyte displayed ionic conductivity of the order 10^{-2} S m^{-1} and potential stability window is 2.7 V versus Li⁺/Li. GPEs have also been successfully prepared by incorporating the Li⁺-IL mixture into PVdF-HFP. The GPE containing 80 wt. % IL solution attained an ionic conductivity of the order 1 S m^{-1} at 383 K.

The BMImBF₄ ionic liquid [7] conductivity was expected to decrease on addition of PVdF-HFP to the IL. This is because, on adding polymer to the IL will increase the IL viscosity. This should decrease the ionic mobility, and hence conductivity. However, the sample with 10 wt. % polymer and 90 wt. % IL exhibited RT conductivity which is higher than the pristine BMImBF₄. This observation can be clarified successfully using the polymer breathing model. The model assumes that the polymer chains can open and fold. Chain opening is analogous to “inhaling” and chain folding to “exhaling”. This inhaling-exhaling process of the polymeric chain led to volume and local pressure changes that either dissociate ion pairs and increased number density of mobile ions or reduce viscosity and increased ionic mobility, both of which, will result in conductivity enhancement [8]. However, at high polymer content, viscosity effect would dominate.

One of the possible ways to determine the choice of an IL is by considering the type of alkyl chain. Different alkyl chains have different chain lengths. As an example, consider the three SPE samples chitosan/[C₂mim][C_nSO₃], chitosan/[C₂mim][C_nSO₄] and chitosan/[C₂mim][diC_nPO₄]). [C₂mim]⁺ is the 1-ethyl-3-methylimidazolium cation [9] with sulfonate, sulfate and dialkylphosphate anions. The alkyl chains are determined by n. For the sulfonate anion, the subscript n values were 1, 2 and 4; for the sulfate anion, n values were 1 and 2 and n also had values of 1 and 2 for the dialkylphosphate anions. The highest conducting chitosan/[C₂mim][C₁SO₃] sample exhibited a conductivity of 7.78 S m^{-1} at 298 K and 0.75 S m^{-1} at 373 K. Shorter alkyl chain length ILs exhibited higher conductivity due to their lower viscosity that facilitates ion mobility, hence higher conductivity. This can therefore be a method of choosing the appropriate IL for conductivity enhancement.

Another example of an IL-PE system consisted of PVA, $\text{CH}_3\text{COONH}_4$ and BmImBr ionic liquid [10]. The IL increased the amorphousness of the polymer electrolyte and this enhanced ionic mobility. The plasticizing nature of the IL contributed to the softening of the polymer backbone that increased segmental motion. The segmental motion will bring a cation coordinated to the electron donor atom of the PVA near to another possible site and on compression of the chain, the cation can jump to the vacant site with low, but sufficient activation energy and will then be transported away from its former site as the segmental motion moves forward.

BMImTf was incorporated into a PEMA/PVdF-HFP blend with LiTf being the Li^+ source [1]. The 49 wt. % PEMA-21 wt. % (PVdF-HFP)-30 wt. % LiTf exhibited an increase in RT maximum conductivity on addition of 60 wt. % BMImTf from 2.9×10^{-5} to $8.59 \times 10^{-3} \text{ S m}^{-1}$. At low BMImTf content, the number density of mobile ions was observed to influence the ionic conductivity, but the mobility and diffusion coefficient were more dominant at higher BMImTf contents. Incorporation of BMImTf also increased thermal stability. This is advantageous as the high decomposition temperature enables the polymer electrolyte to be used at elevated temperatures. The addition of BMImPF₆ into corn starch-based electrolyte with LiPF₆ salt also increased ionic conductivity [11]. This was attributed to the amorphousness of the sample.

We have shown that IL can enhance ion transport in an electrolyte. IL acts as a plasticizer, increased the amorphousness of a PE and the segmental motion of the polymeric chain. IL can also improve thermal stability.

3. ILs in dye-sensitized photovoltaic systems

Dye-sensitized solar cell (DSSC) is one of the third generation photovoltaic technologies that have been developed. It uses cheap materials that do not require tedious purifications, easy to fabricate and has high efficiency [12]. A DSSC consists of three main parts, namely (i) photoactive electrode or photoanode, (ii) Pt counter electrode and (iii) electrolyte with a redox mediator, for example, I^-/I_3^- as shown in **Figure 1**.

The DSSC mimics the process of photosynthesis. The sensitizer absorbs solar energy that excites the dye molecules and oxidizes them. The electrons released are injected into the mesoporous nano-TiO₂ conduction band (TiO₂ is normally used as part of the photoanode). After leaving the photoanode, the electrons move to the cathode where they reduce the I_3^- ions of the redox couple into I^- ions. The I^- ions then return the electrons to the oxidized dye molecules. The dye molecules are regenerated, the circuit is completed and current flows. The electrolyte is a key DSSC component. The high device photon to current efficiency is also associated with electrolyte conductivity. For a DSSC with I^-/I_3^- redox couple, the contribution to conductivity by the I^- ions is important. IL can be used to increase the iodide mobility, which may result in high DSSC efficiency.

An EMImI ionic liquid has been employed in a DSSC. However, EMImI can easily crystallize and this will prevent them from entering the pores of the nanocrystalline semiconducting TiO₂ films. In order to inhibit EMImI from crystallizing, another type of IL, TIPIL can be added to EMImI electrolyte [13]. Hence, without TIPIL and if EMImI crystallizes, the photon to electricity conversion efficiency will be low [14]. The electrolyte containing TIPIL had

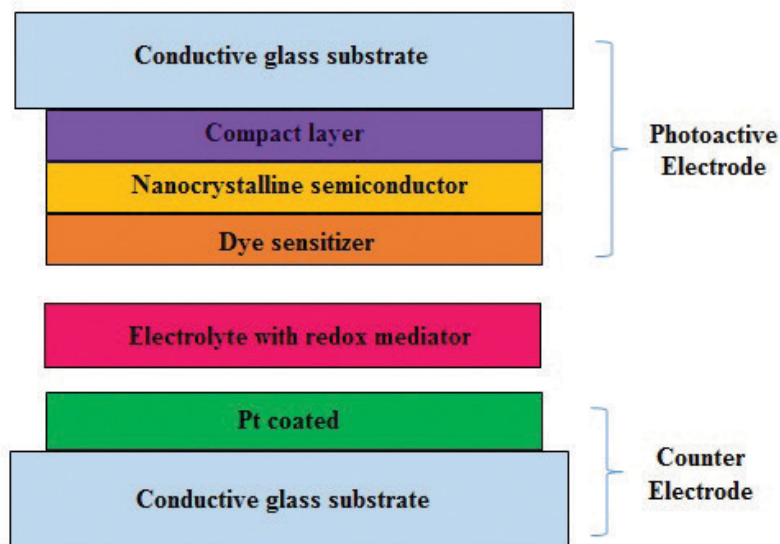


Figure 1. Configuration of DSSC.

improved the photovoltaic efficiency of the DSSC to 5.37%, which was about an 18% increase in efficiency compared to the DSSC without TIPIL. The inhibiting effect toward EMImI crystal growth decreased surface tension between EMImI and the dyed-TiO₂ films and improved interfacial wetting. The stability of the cell was also improved and thus able to maintain more than 90% of the initial efficiency after the aging test. The device using EMImI with I⁻/I₃⁻ redox mediator electrolyte without TIPIL exhibited a decrease of durability in less than 10 days. Hence the use of a crystallizing inhibiting IL can help to maintain stability of the DSSC.

Imidazolium iodide ILs have been used widely as a solvent in electrolytes containing I⁻/I₃⁻ redox mediator for the fabrication of DSSCs [11–15]. However, the high viscosity of pure imidazolium iodide IL can obstruct diffusion of the I⁻ and I₃⁻ ions of the mediator, thus limiting solar cell performance [15]. Also, if the I⁻ concentration is large, the dye molecules that have been excited (D*) can be reduced by the iodide ions, forming reduced dye molecules (D⁻) and iodine radicals I* following the reaction [16]



The reduced dye molecules can either inject the electrons into the TiO₂ following the equation



and this leads to photocurrent which will be benefit the device performance. The reduced dye can also react with an I₃⁻ ion according to the equation below.



This is a recombination reaction that will result in electron loss and is “parasitic” to the DSSC performance because it can result in a decrease in photocurrent. If this happens, it implies that recombination reaction is dominant over electron injection and cell efficiency will be reduced. Hence, to reduce I-ion concentration and viscosity of the electrolyte, binary or double ILs were used in electrolyte preparation [17–20] and this can avoid efficiency loss.

Since iodine has a negative effect on the efficiency when used in large concentrations, liquid electrolytes free from iodine had to be prepared [17]. Iodine in the electrolyte gives rise to polyiodides such as I_3^- or I_5^- according to the equation:



At high iodine content, polyiodide concentration in the mesoporous dyed-TiO₂ matrix will also increase. Polyiodides can assist electron recombination and also aid in solar cell increasing dark current. A high I₂ content can also result in enhanced light absorption by the carrier mediator. This will make the dye molecules harvest less light and led to the decrease in V_{OC} and J_{SC} .

DSSCs with configuration FTO (fluorine tin oxide)/photoanode/IL-CB/Pt/FTO and FTO/photoanode/IL-PACB/Pt/FTO have been fabricated [21]. The electrolytes were I₂-free. Here CB stands for carbon black and PACB for polyaniline-loaded carbon black. FTO or fluoride tin oxide was the current collector. The IL was either BMImI or MPImI. With CB, the efficiencies exhibited were 4.38% (MPImI/CB) and 3.68% (BMImI/CB). The MPImI/PACB containing cell exhibited an efficiency of 5.81% under 1 Sun illumination. The working of the I₂-free DSSC is similar to the I₂ containing DSSC, but the I₃⁻ ion was formed by iodide oxidation. The IL in the electrolyte can provide sufficient I⁻ anion that under illumination



Hence, I⁻ anion can be oxidized to I₃⁻ anion and the redox couple is generated.

DSSC using PACB has been investigated at RT and at 343 K. Its performance was superior to a DSSC using organic solvent electrolyte.

Another type of gel electrolyte that is I₂-free has been prepared using a mixture of KI and DMPImI that has been gelled [22]. The DSSC employing the GPE achieved a photon conversion efficiency of 6.44%. The I₂-free gel electrolyte was able to reduce electron recombination and solar cell dark current. The I₂-free electrolyte system demonstrated a method to be used in the fabrication of DSSCs for performance improvement.

As IL is considered a “green” solvent, it has also been applied in the DSSCs with natural dyes as sensitizer [23]. The electrolyte was 2.33 wt. % functionalized alkoxide precursor + 47.24 wt. % sulfolane + 23.62 wt. % 3-methoxypropionitrile + 10.87 wt. % AcOH + 3.54 wt. % LiI + 3.54 wt. % MPImI + 1.77 wt. % I₂ + 6.02 wt. % TBP + 1.06 wt. % GuSCN. TBP and GuSCN were introduced to help increase J_{SC} as well as V_{OC} .

IL is often used in devices as electrolyte, but fabrication of devices using liquid electrolytes (LEs) is difficult. LEs are volatile and may leak [24, 25]. This will cause the electrode to corrode

and the dye to decompose in the medium [26, 27]. On top of these, sealing and stability problems are also associated with LEs [28, 29]. The use of IL, though beneficial is not leakage-proof due to its liquid state. To overcome this, IL can be added into polymers [30–35], gelators [24, 36] and nanoparticles [37] to form gel or quasi-solid-state electrolytes. The use of gel electrolytes solves electrolyte leakage problem, enhances robustness and increases stability [38]. According to Ref. [39], a gel-type membrane is obtained when an IL solution is immobilized in a polymer matrix. The solvents trapped in the host polymer exhibit good electrolyte conductivity. Electrolyte-photoanode and electrolyte-cathode contacts were also improved. This will also contribute to improve efficiency of the DSSCs [25, 40]. Gel electrolyte is also an alternative to replace solid electrolytes in DSSC. This is because solid electrolyte cannot fill the pores of the nanosemiconducting mesoporous TiO_2 . This causes dye regeneration problems, recombination enhancement and efficiency lowering [2].

The PEO:KI:I₂ membrane has been added with EMImTFSI. The IL has low viscosity of 0.034 Pa S at 298 K. The IL increased ionic conductivity of the membrane and improved efficiency of DSSC [41]. The conductivity increase can be accredited to the charge carriers supplied by the IL. The IL also increased amorphousness of the electrolyte. Adding another IL of low viscosity, namely, (EMImTf) into a PEO:NaI:I₂ system [42] reduced crystallinity and enhanced the ionic conductivity. As for the DSSC performance, the addition of EMImTf enhanced J_{sc} by about four times and the solar cell efficiency by more than three times. This work seems to show that mobility of the iodide ions and efficiency are related. By adding EMImDCN into a PEG plasticized PEO:NaI:I₂ system, the performance of DSSC improved from 0.74% with no IL to 3.02% at 1 Sun illumination. This again showed conductivity-efficiency relationship and the role of IL as plasticizer [43].

PAN-based GPEs have been prepared using three salts, namely, LiI, Pr₄NI and BMImI IL. The highest RT conductivity was 0.393 S m⁻¹ [28]. When used in DSSC with mesoporous TiO_2 , the cell exhibited J_{sc} of 206 A m⁻² and efficiency 5.41%. The efficiency, V_{oc} and J_{sc} varied with electrolyte composition. These can be explained based on Li⁺ and Pr₄N⁺ adsorption on the mesoporous TiO_2 surface that shifted the Fermi level of the semiconductor to a more positive or negative energy level that would certainly affect electron injection into the TiO_2 conduction band and J_{sc} and the V_{oc} , since the distance between the Fermi and the redox mediator levels can be shortened or lengthened. The ternary iodide electrolyte that includes LiI, Pr₄NI and BMImI ionic liquid uncovers the advantage of a ternary system that has been shown to increase the DSSC efficiency by 30%.

The DSSC [44] with GPE composed of P(VP-co-VAc), ethylene and propylene carbonates, KI and I₂ also showed efficiency enhancement when MPImI ionic liquid was added. Again IL played the role as a plasticizing agent that increased the amorphousness of the electrolyte and eventuated in conductivity enhancement. The IL softened the polymer backbone, increased segmental mobility and provided new pathways for ionic motion. The large MPIm⁺ cation enabled easier I⁻ anion dissociation that helped to increase J_{sc} as the MPImI concentration increased. The smaller K⁺ cation used in the same electrolyte reduced electron movement through the mesoporous nano- TiO_2 layer in the photoanode causing a shift in the TiO_2 conduction band toward the redox potential. This led to increased J_{sc} and efficiency of the DSSCs.

Huo et. al [36] investigated quasi-solid-state DSSC (QS-DSSCs) prepared using the low molecular mass $C_{18}H_{36}O_3$. $C_{18}H_{36}O_3$ is commonly used as gelling agent for organic solvents. The ILs studied were MPImI, MBImI and MHImI and were gelled with $C_{18}H_{36}O_3$. The electrolytes contained I_2 , LiI and N-MBI in MPImI, MBImI and MHImI ionic liquids, respectively, to form ILGEs. The ILGEs with different Im^+ cation alkyl chain lengths influenced adsorption competition between Im^+ and Li^+ , electron recombination or transport, charge diffusion, TiO_2 conduction band shift and distribution of surface states. The ILGE containing Im^+ cation with extended alkyl chain length can delay electron recombination, enhanced J_{sc} and improves IPCE. The DSSC with MHImI exhibited the highest efficiency of 3.25%. All DSSCs based on ILGEs exhibited stable photovoltaic performance.

Electrolyte solidification may solve problems associated with leakage of organic solvents. However, issues associated with evaporation and toxicity still limit the DSSCs long-term operation. To overcome problems due to toxicity and evaporation, the use of low viscosity ILs were suggested. ILs can also dissolve polysaccharides and biomacromolecules. It has been shown [38] that a DSSC using a solvent free $LiI + I_2 + BMImI + EMiDCA + TBP$ -based solidified electrolyte exhibited efficiency of ~4%. Electrolyte solidification can also be done using synthetic polymers.

GPEs are electrolytes that contain mobile cations and anions. Thus the electrolyte can be polarized. For example, since in DSSCs with iodide/triiodide redox mediators require iodide ion conductivity, it would be useful to "immobilize" the cations and increase the anion transport or transference number [35]. This has led to the synthesis of an electrolyte in which, the cation is constrained to the polymer backbone. This is known as a PIL. A PIL with the cation constrained to the polymer backbone is therefore a single ion conductor. A DSSC using PMAPII as the PIL-based GPE and PEDOT-NF as the counter electrode has been reported in Ref. [45]. The transference number of the imidazolium cations is reduced due to their being immobilized, but the iodide anions can easily migrate. The PIL formed a stable GPE with increased I^- transference number. The most conducting electrolyte ($0.49 S m^{-1}$) contained 16 wt. % PMAPII. The DSSC with the PIL GPE and PEDOT-NF electrode showed 8.12% efficiency. The performance was better than the liquid electrolyte DSSC and Pt counter electrode that exhibited an efficiency of 7.20%.

An IL-imbibed polymer gel electrolyte has been designed [46] using an IL solvent, an IL iodide source and a polymer. The solvent was BMImCl. The iodide source was MPImI ionic liquid and poly(HEMA/GR), a hydrophilic and lipophilic host matrix. The host matrix possesses unique microporosity, extraordinary absorption and good electrolyte loading and retention to form a stable gel. The interconnected poly(HEMA/GR) framework stores the IL electrolyte. The GPE had high room temperature conductivity and good stability. The DSSC exhibited 7.15% efficiency. This was higher than the 6% efficiency exhibited by DSSC employing acetonitrile-based electrolyte-imbibed in the same polymer host. The V_{oc} of the DSSC with the IL-imbibed GPE was 0.76 V and J_{sc} was 0.014 A. The product of V_{oc} and J_{sc} is $106.2 W m^{-2}$. The MPD was $71.1 W m^{-2}$. The electrolyte concept of imbibing IL into a polymer host indicates the potential application in DSSCs.

As another example, the solvent BMImNO₃ and the iodide ion supplier, MPImI, have been imbibed into poly(AA/GR) and poly(AA/CTAB) to form stable ion conducting medium in gel

form [47]. These polymer are also “hydrophilic and lipophilic” or amphiphilic. The imbibed poly(AA/GR) GPE exhibited RT electrical conductivity of 1.78 S m^{-1} and that of IL imbibed poly(AA/CTAB) GPE was 1.84 S m^{-1} . The efficiencies were 7.19% and 7.15%, respectively. The DSSCs employing acetonitrile-based GPEs with the same matrices exhibited lower efficiencies of less than 7%.

Besides imidazolium, other ILs based on sulfonium and ammonium have also been used in DSSCs. Sulfonium ion-based ILs mostly had higher conductivity than ammonium ion-based ILs due to their lower viscosity. DSSCs employing IL with asymmetric diethylalkylsulfonium cation, $[\text{Et}_2(\text{n-C}_4\text{H}_9)\text{S}]^+$, showed efficiency of 4.61% while DSSC using IL based on quaternary ammonium-based cations, $[\text{Et}_3(\text{n-C}_8\text{H}_{17})\text{N}]^+$, showed 3.95% efficiency [15]. This is due to the high charge-transfer conductivity.

The above examples illustrate how ILs have been used to improve conductivity and enhance DSSC performance.

4. ILs in fuel cells

Fossil fuels cannot be renewed, pollute the environment and are the primary cause of global warming. To minimize some of these problems, it is necessary to produce energy using approaches that do not “destroy” the environment. One approach is to use hydrogen fuel cells in which water is a product besides electricity. Fuel cells are chemical to electrical energy converters. They are classed according to their operating temperature and electrolyte.

PEMFCs use hydrogen or methanol as the fuels. PEMFCs are used in transportation and also portable applications. PEMFCs have shown high electrical efficiency. They do not produce pollutant and they are easy to install. For application in PEMFC, the membranes should have high proton conductivity, good mechanical strength, dimensionally stable and good chemical, electrochemical and thermal stabilities [48].

Polymer electrolytes with addition of IL have been employed in fuel cells. Imidazolium type aprotic IL has been introduced into sulfonated poly (ether ketone) or SPEK for short. The electrolyte was prepared by solution casting [49]. The electrical conductivity was two orders of magnitude higher than the IL-free SPEK membrane even under anhydrous condition. The membrane was able to operate successfully under anhydrous condition between 313 and 413 K. The plasticizing effect of the ILs has made the electrolyte membrane flexible. The ability of the membrane to operate at 413 K shows its potential as a candidate for PEMFC. The same group has also prepared anhydrous H^+ conducting composite membranes with BMImTf ionic liquid [50]. Under anhydrous condition, the H^+ conductivity of the membranes was of the order 10^{-1} S m^{-1} between 303 and 413 K. The H^+ conductivity increased with temperature and IL content. The T_g was observed to decrease implying that the IL has penetrated the polymer chains and enhanced segmental motion of the SPEK/ethylene glycol polymer.

The effects of IL cation on the PEMFC performance have been investigated by Gao et. al [51] using $[\text{N1114}]^+$, $[\text{Epdy}]^+$ and $[\text{EMIm}]^+$ cations. The fuel cell worked poorly when the

imidazolium IL of [EmIm]HSO₄ was used as an electrolyte. The maximum current density was only 100 A m⁻². The MPD was 16 W m⁻². When the IL was replaced with non-imidazolium IL, [Epdy]HSO₄, the current density increased to 700 A m⁻². When [N1114]HSO₄ IL was employed, the current density drastically increased to around 1750 A m⁻² and the MPD increased to 650 W m⁻². Fuel cell with [N1114]HSO₄ can work at 400 A m⁻² with voltage higher than 0.65 V for nearly 1 h without significant decrease in performance. To verify the better performance of [N1114]⁺ and [Epdy]⁺ ILs over [EMIm]⁺, calculations using Gaussian 03 was carried out to determine the adsorption energy of these cations on protonated platinum cluster surface. Higher adsorption energy reflects more cation adsorption on the Pt surface. The higher adsorption energy also implies that many of a particular cation species are occupying the surface of the Pt catalyst. The calculations showed that [EMIm]⁺ exhibited the highest adsorption energy of 249 kJ mol⁻¹ followed by [Epdy]⁺ (200 kJ mol⁻¹) and [N1114]⁺ that exhibited only 7.5 kJ mol⁻¹. Hence the electrochemical active surface area was reduced by the [EMIm]⁺ IL molecules compared to [N1114]⁺ and [Epdy]⁺ ILs. These results explain why fuel cell performance with [N1114]⁺ was higher than that with [Epdy]⁺ and [EMIm]⁺ ILs.

Graphite oxide (GO) has been successfully functionalized using 3-aminopropyltriethoxysilane IL [52]. The functionalized GO was used in high temperature PEMFCs as an additive in a polybenzimidazole (PBI) anion exchange membrane (AEM). The composite membrane had H⁺ conductivity of 3.5 and 2.5 S m⁻¹ at 418 K for 3.5 and 2.0 per repeat units of PBI when imbibed with low concentrations of phosphoric acid (PA). The acidic groups in the 3-aminopropyltriethoxysilane IL functionalized GO such as carboxyl and epoxy oxygen groups, could facilitate proton hopping. This enables the membrane to be used in PEMFC. The functionalized ILGO has enhanced the H⁺ conduction even with low PA loading. The ILGO performance in enhancing the PA imbibed PBI conductivity signaled its suitability for use in PEMFC. The ILGO bonds with H₃PO₄ and provides pathways for fast H⁺ transport. Hence, the ILGO is able to enhance conductivity without requiring high PA loading. This indicates that the ILGO-PBI film has potential for application in fuel cells. When tested in PEMFC, the ILGO-PBI-PA membranes showed overwhelming performance over a PBI-PA membrane. The MPDs of the fuel cells employing PBI and ILGO-PBI with the oxygen group located in GO were 2.6 W m⁻² and 3.2 W m⁻² with the higher MPD for 3.5 per repeat unit. The enhanced performance has been attributed to the higher H⁺ conductivity.

Fang et al. [53] have copolymerized [VMI]I and [VBI]Br with styrene for alkaline fuel cell (AFC) application. The ionic conductivity of these [VBI]Br:styrene and [VMI]I:styrene AEM was 2.26 S m⁻¹ and 1.32 S m⁻¹ at 303 K, respectively. The water uptake and ion exchange capacity are 56.8% and 1.26 mmol g⁻¹, respectively. The membrane was chemically stable even after treatment in high NaOH concentrations at 333 K for 120 h. The H₂/O₂ fuel cell with [VBI]Br:styrene of molar ratio 10:18 exhibited V_{OC} of 1.07 V. The MPD of the H₂/O₂ fuel cell was 1160 W m⁻² at J_{sc} of 2300 A m⁻² at 333 K. These results demonstrate bright prospect of AEMs for AFC.

Novel OH⁻ AEMs with IL consisting of butanediyl-1,4-bis(N-dodecylimidazole bromide) cation has been synthesized for AFC [54]. The anionic conductivity of the electrolyte film reached 4.19 S m⁻¹ at 353 K. This work showed that AEMs based on imidazolium cations have potential for application in AFCs.

Ortiz-Martínez et al. [55] have embedded a polymer-IL membrane into a carbon cathode for application in microbial fuel cells (MFCs). The IL was methyltrioctylammonium chloride. The MFC works when organic matter is oxidized by microbes and the electrons produced are transferred to the carbon cathode. The cell achieved a volumetric MPD of 0.613 W m^{-3} , which is about 10 times higher than the output of typical membranes. Coulombic efficiency also increased from 19.18 to 64.96%. The results obtained by these researchers indicate the potential application of embedded polymer IL membrane-cathode assembly in MFCs. This approach also improved contact between the separator and cathode.

SILMs also have potential for use in MFCs as proton exchange membranes. SILMs have been evaluated by Hernández-Fernández et al. [56]. The ILs used were [BMIm⁺] and [OMIM⁺] and [MTOA⁺] cation combined with Cl⁻, BF₄⁻, PF₆⁻ and TFSI⁻ anions. The voltage of the MFC with different SILMs was monitored continuously for more than 160 h. The fuel cell using the supported [OMIM⁺][PF₆⁻] film attained the highest voltage of $\sim 0.14 \text{ V}$. It is unfortunate that the IL in the film has the highest toxicity. The highest chemical oxygen demand (COD) removal for the MFCs has been achieved using [MTOA⁺][Cl⁻]. Its value was 89.1%. Its noncotoxicity is comparable to the commercial membranes such as Ultrex[®] and Nafion[®] with 88.3% and 90.7%, respectively.

In another study Ref. [57] [MTOA⁺][Cl⁻], [OMIM⁺][PF₆⁻], [P4,4,4,1⁺][MeSO₄⁻] and [P4,4,4,1⁺][TOS⁻] IL-based membranes were evaluated. The highest COD removal value was still achieved by the [MTOA⁺][Cl⁻]-based membrane while the [P4,4,4,1⁺][TOS⁻] and Nafion[®]117 membranes exhibited slightly lower CODs. In terms of volumetric power density (VPD), [P4,4,4,1⁺][TOS⁻] membrane offered higher VPD (0.795 W m^{-3}) compared to Nafion[®]117 (0.756 W m^{-3}). The fuel cell based on [MTOA⁺][Cl⁻] membrane exhibited 0.237 W m^{-3} . Overall performance among the ILs applied, [P4,4,4,1⁺][TOS⁻] showed better performance than Nafion[®]117 in terms of VPD and COD removal.

5. IL in lithium batteries

Due to their high energy density, lithium ion batteries (LIBs) have become attractive power sources for many applications such as mobiles, cameras and laptops. The specific energy in Wh kg^{-1} that can be delivered by LIBs, Ni-MH, Ni-Cd and lead acid batteries is 160, 90, 45 and 40, respectively. Hence lead acid batteries can only deliver 25% of the energy that can be supplied by LIBs.

Li et al. [58] have prepared a novel CPE with a PIL, namely, poly((4-vinylbenzyl) trimethylammonium bis(trifluoromethanesulfonyl)imide) as the host, DEME-TFSI ionic liquid, LiTFSI salt and nanosilica filler. PIL-based electrolytes with IL could effectively improve the electrode/electrolyte interface, which signaled a direction for the application of PIL electrolytes in LIBs. The compatible PIL-IL combination provides stable PEs with minimized phase separation and leakage. The electrical conductivity increased with IL content attributed to the increased amorphousness brought about by the plasticizing effect of DEME-TFSI. At 60% IL content, the electrolyte conductivity was $7.58 \times 10^{-2} \text{ S m}^{-1}$ at 333 K. The

assembled Li/PIL-IL-LiTFSI-SiO₂/LiFePO₄ cell showed that the IL was able to penetrate into the electrode and exhibited discharge capacity of ~136 Ah kg⁻¹ at 0.1 C. The cell recorded capacity fading of 0.075 Ah kg⁻¹ per cycle for 40 cycles. The specific discharge capacity of the cell was still 134 Ah kg⁻¹ even after 50 cycles.

ILGPE has been prepared by photocuring a mixture containing MPPIpTFSI ionic liquid, LiTFSI and ethoxylated bisphenol A diacrylate, a long chain monomer [59]. MPPIpTFSI had a sufficiently high conductivity to be applied in electrochemical devices and its wide voltage stability (5.8 V versus Fc/Fc⁺) provided good compatibility with the LiFePO₄ cathode. The IL-GPE conductivity was $6.4 \times 10^{-3} \text{ S m}^{-1}$ at 298 K and increased with temperature to 0.48 S m^{-1} at 368 K. The IL-GPE electrochemical stability was ~4.8 V versus Li/Li⁺. The cell Li/IL-GPE/LiFePO₄ displayed stable cyclability with capacity that is 4% less than the LiFePO₄ theoretical capacity at C/20 rate and 298 K. This showed that the IL-GPE provides good electrode/electrolyte interfacial contact and is a promising electrolyte for flexible LIBs.

A SPE system comprising PVdF host, an ionic liquid MePrPipNTf₂, LiTFSI salt and VC have been prepared by Swiderska-Mocek [60]. VC is an additive to help form the solid electrolyte interphase (SEI) layer. The conductivity of the elastic membrane was 0.44 S m^{-1} at 298 K. The activation energy was 12.4 kJ mol^{-1} . The IL-incorporated membrane decomposed at 583 K. The high decomposition temperature signaled the safe use of the membrane in lithium polymer batteries at elevated temperatures. The Li⁺ cell with the quaternary electrolyte PVdF + LiTFSI + MePrPipNTf₂ + VC can display good cyclability and safely deliver high specific capacities with LiFePO₄ cathode. The researchers also used LiMn₂O₄ in place of LiFePO₄ [61]. The LiMn₂O₄ cathode also exhibited good specific capacity. The full LiMn₂O₄/quaternary PE/Li₄Ti₅O₁₂ cell displayed good cycling performance indicating that the PE can also be safely used with LiMn₂O₄ as cathode in LIBs.

Yang et al. [62] have used poly(VdF-co-HFP)-based GPEs with LiTFSI salt and B₄MePyTFSI for application in LIB. The ILGPE 66.7 wt. % (PVdF-HFP/LiTFSI)-33.3 wt. % B₄MePyTFSI exhibited a maximum Li⁺ ionic conductivity of 0.20 S m^{-1} . The Li/ILGPE/LiFePO₄ cell showed high capacity and good cyclability.

The ionic liquid BMImBF₄ was introduced into PVDF-HFP/PMMA-LiClO₄ blend membrane [63]. The GPE was microporous. After addition of IL into the microporous GPE, T_g was observed to decrease. However the IL uptake into the membrane increased. The reason was that the IL that interacted with the polymer disrupted some of the PVDF-HFP crystalline phases and increased amorphousness that decreased T_g of the GPE. The addition of LiClO₄ also helped to expand the amorphous zone. The LiFePO₄/GPE/Li coin-type cell exhibited good cyclability.

PIL-plastic crystal CPE consisting of P(DADMA)TFSI PIL, succinonitrile (SN) and LiTFSI as the Li⁺ ion source [64]. The 40%PIL-40%SN-20%LiTFSI (designated as 50% SN) electrolyte exhibited a high ambient conductivity, a wide potential window and good mechanical strength. The Li/50% SN/LiFePO₄ cell discharged at C/10 rate delivered a capacity of ~150 Ah kg⁻¹ at 298 K and has good capacity retention. The findings illustrated the fact that the electrolyte has great potential in LIBs.

6. IL in supercapacitors

The application of supercapacitors for energy storage can help to minimize dependence on fossil fuels. According to Mysyk et al. [65], supercapacitors have energy density higher than electrolytic capacitors. They also have power density higher than rechargeable batteries. Supercapacitors bridge the gap between electrolytic capacitors and rechargeable batteries. Supercapacitors can be divided into three general classes. There are electrical double layer capacitors (EDLCs), pseudocapacitors and hybrid capacitors. Each class is characterized by its charge storage mechanism. These mechanisms are non-Faradaic, Faradaic and a combination of both. Non-Faradaic mechanism can be likened to electrostatic charge storage. Faradaic reaction is a heterogeneous charge transfer reaction that occurs on the surface of an electrode.

Supercapacitors comprise an anode, electrolyte and a cathode [66]. The potential stability window of the electrolyte determines the supercapacitor voltage. The electrode and electrolyte also determine the power density and cyclability of the supercapacitor. Hence, it is important to choose the proper electrolyte [67].

A lot of attention has been given to carbon-based capacitors. This is because these carbonaceous materials possess diversified morphologies, excellent cycling stability, high power capability and conductivity [68, 69]. EMImBF₄ was introduced as an ion conducting medium in an EDLC of AC nanofibers. Propylene carbonate (PC) that can dissolve EMImBF₄ was also added into the electrolyte. Without PC, the EDLC delivered a decreasing capacitance from ~78 to ~60 F g⁻¹. On addition of PC, the capacitance delivered maintained at ~80 F g⁻¹. This showed that PC helped to recover the lost capacitance by breaking the interaction between the carbon micropore wall and EMIm⁺ cation and also releasing the immobile ions in the micropores during the cycling. By incorporating Cu(II) into EMImBF₄ [70], the electrochemical capacitors exhibited good stability with only ~9% capacitance loss after 500 cycles. The capacitance is higher than that obtained from an EDLC using pure EMImBF₄ as electrolyte. The average specific capacitance is 108 F g⁻¹ for EMImBF₄ and 225 F g⁻¹ for EMImBF₄ with Cu(II). The increase indicated that the Faradaic pseudocapacitance associated with the Cu species has contributed considerably to the total capacitance of the EDLC.

The ionic liquid DEME-BF₄, with wide potential window of 6 V also showed high potential for electrochemical capacitors. Its conductivity at 25°C is considerably high, 4.8 mS cm⁻¹ [71]. Aliphatic quaternary ammonium-based ILs are expected to show higher cathodic stability since its melting point is higher compared to aromatic ILs. EDLC with showed little gas release and smaller capacity fade at 373 K. This implies that AC electrodes and DEME-BF₄ electrolyte combination contributed to cell stability compared to the EDLC using TEA-BF₄/PC, which exhibited a large capacity fade at 373 K. The DEME-BF₄ EDLC retained 85% of its initial capacity even after 500 cycles.

According to Yuyama et al. [72], ILs with BF₄⁻ anion exhibited better stability and performance compared to PF₆⁻ and TFSI⁻ anions when used in EDLCs. The equivalent series resistance (ESR) and direct current (dc) resistance at 298 K and 243 K decreased accordingly as TFSI⁻ > PF₆⁻ > BF₄⁻. According to Fletcher et al. [69], dc resistance and ESR decreased with increasing temperature and this can be accredited to the decreasing IL electrolyte viscosity.

Decrease in viscosity led to the increase in anion and cation self-diffusion. This implied that ion dissociation and ionic mobility have increased at elevated temperatures.

A carbon-based supercapacitor has been fabricated using protic ionic liquid (PrIL) as novel electrolyte [65]. PrILs are created when one proton is transferred between a Brønsted acid and base. When compared to aprotic ILs, PrILs are cheaper and easier to synthesize [73]. Cyclic voltammograms of PrILs exhibit reversible redox peaks. This indicated pseudo-Faradaic charge transfer. Oxidative HNO_3 treatment of AC augmented surface performance and resulted in enhanced capacitance that is attributed to pseudo-Faradaic contribution. PrIL-based capacitors show a wider potential window than capacitors using aqueous H_2SO_4 . AC-PrIL combination shows promise for supercapacitors with good energy characteristics. Et_3HTFSI PrIL has been used as an ion conducting medium in supercapacitors with AC electrodes [74]. Supercapacitors with less than 200 ppm of H_2O in $\text{NEt}_3\text{H TFSI}$ electrolyte are able to operate at 2.5 V. At water concentration of 200 ppm the electrolyte was considered dry. The voltage of AC-PrIL-based supercapacitors will be affected if the electrolyte contains a significant amount of water. The cell voltage will then not be able to exceed 1.2 V, that is, the potential window of water. Brandt et. al [75] have studied various carbon-based supercapacitors using various PrILs such as Et_3NHTFSI , Me_3NHTFSI and PYRNO_3 as electrolytes for long-term cycling stability. They reported that the supercapacitor employing PrIL-based supercapacitors exhibited stability even after 30,000 cycles. The supercapacitors can also perform over wide temperature range. The PC- Me_3NHTFSI mixed electrolyte can be used even at temperatures down to 250 K. The supercapacitor containing the protic IL Et_3NHTFSI showed stable performance from 283 to 333 K.

Timperman et al. [67] have described the use of eutectic PrIL mixtures of PYRNO_3 and PYRTFSI as ion conducting medium for application in AC-based supercapacitors. The capacitors showed good capacity retention. Using electrolyte with $[\text{PYR}]/[\text{NO}_3]$ ratio of 0.72 at 298 K, the capacitor showed more than 95% efficiency at 1.5 V for at least 80 h and at 2.0 V for 110 h.

The performance of IL electrolytes consisting of various cations such as EMIm^+ and BMP^+ and TFSI^- , BF_4^- and DCA^- anions have been investigated [76]. BMP-DCA ionic liquid showed excellent electrolyte behavior for supercapacitor with graphene nanosheet (GNS) electrodes. The supercapacitor delivered 235 F g^{-1} specific capacitance, energy density of 88 Wh kg^{-1} and specific power 17.5 kW kg^{-1} at 298 K. IL electrolytes perform better at high temperatures. This is because their conductivity increased with temperature and their viscosity decreased. The decrease in viscosity led to enhancement in ionic mobility. This led to increased conductivity. Stability was also maintained at elevated temperatures.

One of the challenges facing IL supercapacitors is to improve electrolyte accessibility to the nanocarbon surface. According to Trigueiro et al. [77], the wettability of the electrodes with an IL electrolyte can be facilitated by the poly(IL) molecules electrostatically linked to reduced graphene oxide (RGO) surface electrode, producing high specific capacitance. As an example, a $[\text{MPPy}][\text{TFSI}]$ -modified RGO electrode (PIL:RGO) exhibited a drop in specific capacitance of only 20% as scan rate increased from 10 to 30 mV s^{-1} at 298 K, while an RGO capacitor lost 42% of its specific capacitance under similar conditions. The effective intercalation and distribution of the poly(IL) molecules in the RGO nanosheets contributed to the improved

wettability as well as interaction with the IL. These results implied that 80% capacity is retained for PIL:RGO and 58% RGO capacitors. At 333 K, 70% of the capacity was retained for PIL:RGO and 61% capacity retention for RGO-based supercapacitors.

Another approach to obtain stable polymer electrolytes thermally and electrochemically is by incorporating RTIL into polymer electrolytes [78]. Pandey et. al [79] has compared the EDLC performance using electrolyte in the solid-state and ionic liquid incorporated polymer electrolytes. The electrodes of EDLCs comprised multiwalled carbon nanotube (MWCNT). The polymer electrolytes consisted of PEO, triflate salts of magnesium and lithium and EMImTf ionic liquid. The ambient conductivity was $\sim 10^{-2} \text{ S m}^{-1}$. The addition of IL increased the polymer backbone flexibility and enhanced segmental motion. The use of the triflate salts and IL introduced $\text{Li}^+/\text{Mg}^{2+}$, EMIm^+ and CF_3SO_3^- free ions. The presence of many types of mobile ionic species increased the possibility of formation of more double layers where energy was stored. The enhanced flexibility is also useful for proper electrode-electrolyte contact. Incorporating EMImTf resulted in a substantial increment of PEO-Mg(Tf)₂ electrolyte conductivity. MWCNT with Li-based and Mg-based electrolyte could deliver between 1.7 and 2.1 F g^{-1} and between 2.6 and 3.0 F g^{-1} , specific capacitance, respectively. Without IL incorporation the capacitance per unit mass were $\sim 0.03 \text{ F g}^{-1}$ and $\sim 0.01 \text{ F g}^{-1}$ for the Mg- and Li-system, respectively. This showed IL contribution on EDLC capacitance.

Ayalneh Tiruye et al. [78] have assembled supercapacitors containing two parts of a pyrrolidinium-based PIL, that is, pDADM TFSI and three parts $\text{PYR}_{14}\text{TFSI}$ ionic liquid. A supercapacitor with PIL-based PE delivered specific capacitance and specific energy of 100 F g^{-1} and 32 Wh kg^{-1} , respectively. At 333 K, specific energy increased to 42 Wh kg^{-1} at discharge current density 1 mA cm^{-2} . These values are a little less than that using pristine $\text{PYR}_{14}\text{TFSI}$, but are higher than that of supercapacitors using conventional polymer electrolytes. The IL-based polymer electrolytes have a wide potential window that allowed operation of the all solid-state supercapacitors at voltages of 3.5 V.

The addition of BmImCl into the $\text{PVA}/\text{CH}_3\text{COONH}_4$ electrolyte enhanced the ionic conductivity due to its strong plasticizing effect, environmental friendly nature and high ion content [80]. In the presence of IL, the polymer chains become more flexible, thus the polymer segmental motion increased. This assisted ionic transport that conferred the high ionic conductivity. This result agreed with the differential scanning calorimetric (DSC) analysis as subambient T_g was observed on addition of IL. At these sub-ambient temperatures, the polymer electrolyte is in the rubbery state as the surrounding temperature is much higher than T_g . The molecules in the polymer matrix are allowed to undergo orientation and conformational changes in the rubbery phase. Moreover, the physicochemistry of IL such as viscosity and dielectric constant also contribute to ionic conductivity enhancement. EDLC fabricated with the most conducting ion conducting polymer can be charged up to 4.8 V. By doping IL into the polymer electrolyte also increased the capacitive nature of EDLC as the specific capacitance of 28.36 F g^{-1} was achieved. The inclusion of IL not only improved the electrode-electrolyte interfacial contact, but also improved the electrolyte and EDLC properties. Therefore, this is also a good prospect for improving the electrochemical performance of an EDLC.

The ionic liquid, BmImBr has been introduced into a PVA/CH₃COONH₄ PE system for application in EDLC [81]. The EDLC delivered a capacitance of 21.89 F g⁻¹ and continued to do so for 250 cycles.

An electrical conductivity of 0.73 S m⁻¹ was achieved at 393 K upon adulteration of 50 wt. % BmImCl to the PVA/CH₃COONH₄ PE system [80]. This is accompanied with the lowering of T_g. The primary cause of reduction in T_g was the ability of the IL to plasticize. Plasticization softened the polymer backbone, increased segmental motion thus helped in facilitating ionic transport. On addition of the IL containing ion conducting medium, the amorphousness of the membrane was observed to increase. It was also observed that the polymer electrolyte exhibited a wider potential stability range. The presence of IL has also improved the electrochemical behavior of the EDLC delivering 2.39 Wh kg⁻¹ of specific energy and 19.79 W kg⁻¹ of specific power with Coulombic efficiency above 90%. The specific capacitance of 28.36 F g⁻¹ was obtained with better electrochemical characteristics.

Addition of BMImTf ionic liquid in PVA/CH₃COONH₄ PE system [82] resulted in the polymer electrolyte exhibiting strong adhesive properties. Thus, better electrode-electrolyte interfacial contact can be provided. The specific capacitance of the EDLC obtained was 2.02 from 0.14 F g⁻¹ without IL. This implied that the IL-based polymer electrolytes possessed higher dielectric constant compared to the IL-free polymer electrolyte. The addition of IL has also extended the electrolyte voltage window and improved thermal stability.

The BdMImBF₄ ionic liquid was added into a gel matrix that comprised a blended host of PVP/PVdF-HFP and magnesium triflate salt. The gel was used in an EDLC [83]. The interaction between the IL and the polar groups of the polymer chain increased amorphousness of the GPE. The ionic conductivity achieved a maximum value of 0.29 S m⁻¹ after 7.5 wt. % of BdMImBF₄ was added. The calculated specific energy and power were 14 Wh kg⁻¹ and 21 W kg⁻¹, respectively.

7. Summary

ILs consist of poorly coordinating cations and anions and are molten salts at room temperature. They have high thermal stability, wide potential window and high electrical conductivity. ILs are green solvents with negligible vapor pressure. IL such as EMImTf, EMImBF₄ and PP₂₄TFSI, to name a few can enhance ionic conductivity when added to PEs. Conductivity enhancement is attributed to the additional ions supplied by the IL, the plasticizing nature of the IL and its low viscosity that facilitates ion mobility. The plasticizing nature of ILs softens the polymer backbone resulting in the increase in polymer segmental motion. This implies that IL can increase amorphousness of a PE. ILs with short alkyl chains are less viscous and hence suitable for facilitating ion mobility. However, IL containing Im⁺ cation with long alkyl chain length can delay electron recombination, enhance J_{sc} and improves IPCE in DSSCs. EMImTFSI, EMImTf and EMImDCN are low viscosity ILs that are able to increase ionic conductivity of and PEO:NaI:I₂ systems. It is also to be noted that most sulfonium ion-based ILs have higher conductivity than ammonium ion-based ILs due to the lower viscosity of the

former. Incorporation of ILs, for example, BMImTf can increase thermal stability of a PE such as in 49 wt. % PEMA-21 wt. % (PVdF-HFP)-30 wt. % LiTf sample. DMPImI is an ionic liquid that has been added to a PEO-PEG-KI system to produce an I₂-free GPE that was able to reduce electron recombination and dark current in a DSSC. Imidazolium type aprotic IL when added into sulfonated poly (ether ketone) or SPEK not only increased ionic conductivity, but also enabled the membrane to operate under anhydrous condition between at elevated temperatures. The ability of the membrane to operate at 413 K shows its potential as a candidate for PEMFC. The MePrPipNTf₂ incorporated into a PVdF + LiTFSI + VC electrolyte system decomposed at a high temperature of ~583K. This signaled the safe use of the membrane in lithium polymer batteries at elevated temperatures. The ILGPE 66.7 wt. % (PVdF-HFP/LiTFSI)-33.3 wt. % B₄MePyTFSI exhibited a maximum Li⁺ ionic conductivity of 0.20 S m⁻¹. The Li/ILGPE/LiFePO₄ cell showed high capacity and good cyclability. The addition of BmImCl to the PVA/CH₃COONH₄ PE system is accompanied with the lowering of T_g, wider potential stability range and improved EDLC electrochemical behavior.

Abbreviations

[C ₂ mim][C _n SO ₃]	1-Ethyl-3-methylimidazolium sulfonate; (subscript n had values n = 1, 2, 4 as methanesulfonate, ethanesulfonate and butanesulfonate, respectively)
[C ₂ mim][C _n SO ₄]	1-Ethyl-3-methylimidazolium sulfate (subscript n had values n = 1, 2 as methanesulfonate and ethanesulfonate, respectively)
[C ₂ mim][diC _n PO ₄]	1-Ethyl-3-methylimidazolium phosphate (subscript n had values n = 1, 2 as dimethanephosphate and diethanephosphate, respectively)
[EmIm]HSO ₄	Ethylmethyl imidazolium hydrosulfate
[Epyd]HSO ₄	Ethyl pyridinium hydrosulphate
[MPPy][TFSI]	Poly(1-methyl-1-propylpyrrolidinium bis(trifluoromethylsulfonyl)imide)
[MTOA ⁺]	Methyl trioctyl ammonium cation
[MTOA ⁺][Cl ⁻]	Methyl trioctyl ammonium chloride
[N1114] ⁺	Trimethylethyl amide cation
[N1114]HSO ₄	Trimethylethyl amide hydrosulphate
[OMIM ⁺][PF ₆ ⁻]	1-Octyl-3-methylimidazolium hexafluorophosphate
[P4,4,4,1 ⁺][TOS ⁻]	Triisobutyl(methyl)phosphonium tosylate,
[P4,4,4,1 ⁺][MeSO ₄ ⁻]	Tributylmethyl phosphonium methylsulfate
[VBI]Br	1-Vinyl-3-butylimidazolium bromide
[VMI]I	1-Vinyl-3-methylimidazolium iodide
AC	Activated carbon
AFC	Alkaline fuel cell
B ₄ MePyTFSI	1-Butyl-4-methylpyridinium bis(trifluoromethanesulfonyl)imide
BdMImBF ₄	1-Butyl-2,3-dimethylimidazolium tetrafluoroborate

BF_4^-	Tetrafluoroborate anion
BMI mBF_4	1-Butyl-3-methylimidazolium tetrafluoroborate
BmImBr	1-Butyl-3-methylimidazolium bromide
BMI mCl	1-Butyl-3-methylimidazolium chloride
BMI mI	1-Butyl-3-methylimidazolium iodide
BMI mNO_3	1-Butyl-3-methylimidazolium nitrate
BMI mPF_6	1-Butyl-3-methylimidazolium hexafluorophosphate
BMI mTf	1-Butyl-3-methylimidazolium trifluoromethanesulfonate
BMP $^+$	N-Butyl-N-methylpyrrolidinium cation
$\text{C}_{18}\text{H}_{36}\text{O}_3$	12-Hydroxystearic acid
CPE	Composite polymer electrolyte
DCA $^-$	Dicyanamide anion
DEME- BF_4	N,N-diethyl-N-methyl-N-(2-methoxyethyl)ammonium tetrafluoroborate
DEME-TFSI	N,N-diethyl-N-methyl-N-(2-methoxyethyl) ammonium bis (trifluoromethanesulfonyl) imide
DMPImI	1,2-Dimethyl-3-propylimidazolium iodide
DSSC	Dye-sensitized solar cell
EMiDCA	1-Ethyl-3-methyl dicyanamide
EMIm $^+$	1-Ethyl-3-methylimidazolium cation
EMIm BF_4	1-Ethyl-3-methylimidazolium tetrafluoroborate
EMImDCN	1-Ethyl-3-methylimidazolium dicyanamide
EMImI	1-Ethyl-3-methylimidazolium iodide
EMImTf	1-Ethyl-3-methylimidazolium trifluoromethanesulfonate
EMImTFSI	1-Ethyl-3-methylimidazolium bis(trifluoromethylsulfonyl)imide
Epd y^+	Ethyl pyridinium cation
Et_3NHTFSI	Triethylammonium bis(tetrafluoromethylsulfonyl)imide
FF	Fill factor
GPE	Gel polymer electrolyte
GuSCN	Guanidine thiocyanate
IL	Ionic liquid
ILGE	Ionic liquid gel electrolyte
ILGO	Ionic liquid graphite oxide
IPCE	Incident photon-to-electron conversion efficiency
J_{sc}	Short-circuit current density
LGPE	Ionic liquid gel polymer electrolyte
Li PF_6	Lithium hexafluorophosphate
LiTf	Lithium trifluoromethanesulfonate

LiTFSI	Lithium bis(tetrafluoromethylsulfonyl)imide
$\text{Li}_4\text{Ti}_5\text{O}_{12}$	Spinel lithium titanate
MBImI	1-Methyl-3-butylimidazolium iodide
Me_3NHTFSI	Trimethylammonium bis(tetrafluoromethylsulfonyl)imide
MEMP-BF ₄	N-(2-methoxyethyl)-N-methylpyrrolidinium
MePrPip ⁺	N-methyl-N-propylpiperidinium cation
MePrPipNTf ₂	N-methyl-N-propylpiperidinium bis(trifluoromethanesulfonyl)imide
MHImI	1-Methyl-3-hexylimidazolium iodide
MPD	Maximum power density
MPIImI	1-Methyl-3-propylimidazolium iodide
MPPipTFSI	N-methyl-N-propylpiperidinium bis(trifluoromethanesulfonyl)imide
N-MBI	N-methylbenzimidazole
NTf ₂ ⁻	Bis(trifluoromethanesulfonyl)imide anion
P[VP-co-VAc]	Poly[1-vinylpyrrolidone-co-vinyl acetate]
PAN	Polyacrylonitrile
PBI	Polybenzimidazole
pDADMTFSI	Poly(diallyldimethylammonium) bis(trifluoromethanesulfonyl)imide
PE	Polymer electrolyte
PEDOT-NF	Poly(3,4-ethylenedioxythiophene) nanofibers
PEG	Polyethylene glycol
PEMA	Poly(ethyl methacrylate)
PEMFC	Proton exchange membrane fuel cells
PEO	Poly(ethylene oxide)
PIL	Polymeric ionic liquid
PMAPII	Poly(1-methyl 3-(2-acryloyloxypropyl) imidazolium iodide)
Poly(AA/CTAB)	Poly(acrylic acid/cetyltrimethylammonium bromide)
Poly(AA/GR)	Poly(acrylic acid/gelatin)
Poly(HEMA/GR)	Poly(hydroxyethyl methacrylate/glycerol)
PP ₂₄ TFSI	N-butyl-N-ethylpiperidinium N,N-bis(trifluoromethane)sulfonimide
Pr ₄ NI	Tetrapropyl ammonium iodide
PrIL	Protic ionic liquid
PVA	Polyvinyl alcohol
PVdF-HFP	Poly(vinylidene fluoride-co-hexafluoropropylene)
PVP/PVdF-HFP	Poly(vinyl pyrrolidone)/poly(vinylidene fluoride-co-hexafluoropropylene)

PMMA	Poly(methyl methacrylate)
PYR ₁₄ TFSI	(N-butyl-N-methylpyrrolidinium bis(trifluoromethylsulfonyl)imide)
PYRNO ₃	Pyrrolidinium nitrate
PYRTFSI	Pyrrolidinium bis(trifluoromethanesulfonyl)imide
RT	Room temperature
RTIL	Room temperature ionic liquid
SILM	Supported IL membrane
SPE	Solid polymer electrolyte
SPEK	Sulfonated poly (ether ketone)
TBP	Tert-butylpyridine
TEA-BF ₄ /PC	Tetraethylammonium tetrafluoroborate/propylene carbonate
TFSI ⁻	Bis(trifluoromethylsulfonyl)imide anion
T _g	Glass transition temperature
TIPIL	Three-armed imidazolium phenoxy ionic liquid
VC	Vinylene carbonate
V _{oc}	Open circuit voltage

Acknowledgements

Authors would like to thank University of Malaya for the UMRG Grant no. RP003-13AFR.

Author details

Siti Nor Farhana Yusuf, Rosiyah Yahya and Abdul Kariem Arof*

*Address all correspondence to: akarof@um.edu.my

Department of Physics, Centre for Ionics University Malaya, University of Malaya, Kuala Lumpur, Malaysia

References

- [1] Sim LN, Majid SR, and Arof AK. Effects of 1-butyl-3-methyl imidazolium trifluoromethanesulfonate ionic liquid in poly(ethyl methacrylate)/poly(vinylidene fluoride-co-hexafluoropropylene) blend based polymer electrolyte system. *Electrochimica Acta*. 2014;123:190–197. <http://dx.doi.org/10.1016/j.electacta.2014.01.017>

- [2] Jayaweera EN, Ranasinghe CSK, Kumara GRA, Wanninayake WMNMB, Senarathne KGC, Tennakone K, Rajapakse RMG, and Ileperuma OA. Novel method to improve performance of dye-sensitized solar cells based on quasi-solid gel-polymer electrolytes. *Electrochimica Acta*. 2015;152:360–367. <http://dx.doi.org/10.1016/j.electacta.2014.11.156>
- [3] Romero A, Santos A, Tojo J, and Rodríguez A. Toxicity and biodegradability of imidazolium ionic liquids. *Journal of Hazardous Materials*. 2008;151:268–273.
- [4] Kumar D and Hashmi SA. Ionic liquid based sodium ion conducting gel polymer electrolytes. *Solid State Ionics*. 2010;181:(8–10):416–423. <http://dx.doi.org/10.1016/j.ssi.2010.01.025>
- [5] Tang J, Muchakayala R, Song S, Wang M, and Kumar KN. Effect of EMIMBF₄ ionic liquid addition on the structure and ionic conductivity of LiBF₄-complexed PVdF-HFP polymer electrolyte films. *Polymer Testing*. 2016;50:247–254. <http://dx.doi.org/10.1016/j.polymertesting.2016.01.023>
- [6] Fericola A, Weise FC, Greenbaum SG, Kagimoto J, Scrosati B, and Soletto A. Lithium-ion-conducting electrolytes: From an ionic liquid to the polymer membrane. *Journal of the Electrochemical Society*. 2009;156:(7):A514–A520. <http://dx.doi.org/10.1149/1.3122885>
- [7] Shalu, Chaurasia SK, Singh RK, and Chandra S. Thermal stability, complexing behavior, and ionic transport of polymeric gel membranes based on polymer PVdF-HFP and ionic liquid, [BMIM][BF₄]. *The Journal of Physical Chemistry B*. 2013;117:(3):897–906. <http://dx.doi.org/10.1021/jp307694q>
- [8] Chandra S, Sekhon SS, Srivastava R, and Arora N. Proton-conducting gel electrolyte. *Solid State Ionics*. 2002;154–155:609–619. [http://dx.doi.org/10.1016/S0167-2738\(02\)00505-2](http://dx.doi.org/10.1016/S0167-2738(02)00505-2)
- [9] Leones R, Sentanin F, Nunes SC, Esperança JMSS, Gonçalves MC, Pawlicka A, Bermudez VdZ, and Silva MM. Effect of the alkyl chain length of the ionic liquid anion on polymer electrolytes properties. *Electrochimica Acta*. 2015;184:171–178. <http://dx.doi.org/10.1016/j.electacta.2015.09.163>
- [10] Liew C-W, Arifin KH, Kawamura J, Iwai Y, Ramesh S, and Arof AK. Electrical and structural studies of ionic liquid-based poly(vinyl alcohol) proton conductors. *Journal of Non-Crystalline Solids*. 2015;425:163–172. <http://dx.doi.org/10.1016/j.jnoncrysol.2015.06.008>
- [11] Ramesh S, Liew C-W, and Arof AK. Ion conducting corn starch biopolymer electrolytes doped with ionic liquid 1-butyl-3-methylimidazolium hexafluorophosphate. *Journal of Non-Crystalline Solids*. 2011;357:(21):3654–3660. <http://dx.doi.org/10.1016/j.jnoncrysol.2011.06.030>
- [12] O'Regan B and Grätzel M. A low-cost, high-efficiency solar cell based on dye-sensitized colloidal TiO₂ films. *Nature*. 1991;353:4.
- [13] Cong S, Yi Q, Gao M, Wang H, Su Y, Zhao J, Sun Y, Lou Y, and Zou G. Three-armed imidazolium phenoxy ionic liquid as a novel crystal growth inhibitor for solid-state dye-sensitized solar cells. *Materials Letters*. 2015;160:135–138. <http://dx.doi.org/10.1016/j.matlet.2015.07.113>

- [14] Cong S, Yi Q, Wang Y, Zhao J, Sun Y, and Zou G. High viscous light-scattering crystal growth inhibitors for solid-state dye-sensitized solar cells. *Journal of Power Sources*. 2015;280:7.
- [15] Lee C-P, Peng J-D, Velayutham D, Chang J, Chen P-W, Suryanarayanan V, and Ho K-C. Trialkylsulfonium and tetraalkylammonium cations-based ionic liquid electrolytes for quasi-solid-state dye-sensitized solar cells. *Electrochimica Acta*. 2013;114:303–308. <http://dx.doi.org/10.1016/j.electacta.2013.09.087>
- [16] Nishida S, Harima Y, and Yamashita K. Kinetic studies of the reductive quenching of photoexcited tris(2,2'-bipyrazine) ruthenium (II) by an oxalate ion in the photoelectrochemical system. *Inorganic Chemistry*. 1989;28:5.
- [17] Chen J, Peng T, Shi W, Li R, and Xia J. An efficient binary ionic liquid based quasi solid-state electrolyte for dye-sensitized solar cells. *Electrochimica Acta*. 2013;107:231–237. <http://dx.doi.org/10.1016/j.electacta.2013.06.014>
- [18] Cosar B, Icli KC, Yavuz HI, and Ozenbas M. Photovoltaic performance of bifacial dye sensitized solar cell using chemically healed binary ionic liquid electrolyte solidified with SiO₂ nanoparticles. *Electrochimica Acta*. 2013;87:425–431. <http://dx.doi.org/10.1016/j.electacta.2012.09.117>
- [19] Lin HH, Peng JD, Suryanarayanan V, Velayutham D, and Ho KC. Perfluoro anion based binary and ternary ionic liquids as electrolytes for dye-sensitized solar cells. *Journal of Power Sources*. 2016;311:167–174. <http://dx.doi.org/10.1016/j.jpowsour.2016.02.029>
- [20] Lee H-F, Wu J-L, Hsu P-Y, Tung Y-L, Ouyang F-Y, and Kai J-J. Enhanced photovoltaic performance and long-term stability of dye-sensitized solar cells by incorporating SiO₂ nanoparticles in binary ionic liquid electrolytes. *Thin Solid Films*. 2013;529:2–6. <http://dx.doi.org/10.1016/j.tsf.2012.06.025>
- [21] Lee C-P, Chen P-Y, Vittal R, and Ho K-C. Iodine-free high efficient quasi solid-state dye-sensitized solar cell containing ionic liquid and polyaniline-loaded carbon black. *Journal of Materials Chemistry*. 2010;20:(12):2356–2361. <http://dx.doi.org/10.1039/B922350A>
- [22] Ri JH, Jin J, Xu J, Peng T, and Ryu KI. Preparation of iodine-free ionic liquid gel electrolyte using polyethylene oxide (PEO)-polyethylene glycol (PEG) and its application in Ti-foil-based dye-sensitized solar cells. *Electrochimica Acta*. 2016;201:251–259. <http://dx.doi.org/10.1016/j.electacta.2016.03.197>
- [23] Rapsomanikis A, Sygkridou D, Voutsinas E, and Stathatos E. Transparent quasi-solid state dye-sensitized solar cells sensitized with naturally derived pigment extracted from red seaweed. *Current Applied Physics*. 2016;16:(6):651–657. <http://dx.doi.org/10.1016/j.cap.2016.03.018>
- [24] Huo Z, Dai S, Zhang C, Kong F, Fang X, Guo L, Liu W, Hu L, Pan X, and Wang K. Low molecular mass organogelator based gel electrolyte with effective charge transport property for long-term stable quasi-solid-state dye-sensitized solar cells. *The Journal of Physical Chemistry B*. 2008;112:(41):12927–12933. <http://dx.doi.org/10.1021/jp8052168>

- [25] Shi J, Peng S, Pei J, Liang Y, Cheng F, and Chen J. Quasi-solid-state dye-sensitized solar cells with polymer gel electrolyte and triphenylamine-based organic dyes. *ACS Applied Materials & Interfaces*. 2009;1(4):944–950. <http://dx.doi.org/10.1021/am9000375>
- [26] Dissanayake MAKL, Jayathissa R, Seneviratne VA, Thotawatthage CA, Senadeera GKR, and Mellander BE. Polymethylmethacrylate (PMMA) based quasi-solid electrolyte with binary iodide salt for efficiency enhancement in TiO₂ based dye sensitized solar cells. *Solid State Ionics*. 2014;265:85–91. <http://dx.doi.org/10.1016/j.ssi.2014.07.019>
- [27] Bandara TMWJ, Jayasundara WJMJSR, Dissanayake MAKL, Furlani M, Albinsson I, and Mellander BE. Effect of cation size on the performance of dye sensitized nanocrystalline TiO₂ solar cells based on quasi-solid state PAN electrolytes containing quaternary ammonium iodides. *Electrochimica Acta*. 2013;109:609–616. <http://dx.doi.org/10.1016/j.electacta.2013.07.089>
- [28] Bandara TMWJ, Jayasundara WJMJSR, Dissanayake MAKL, Fernando HDNS, Furlani M, Albinsson I, and Mellander BE. Quasi solid state polymer electrolyte with binary iodide salts for photo-electrochemical solar cells. *International Journal of Hydrogen Energy*. 2013. <http://dx.doi.org/10.1016/j.ijhydene.2013.05.163>
- [29] Li W, Kang J, Li X, Fang S, Lin Y, Wang G, and Xiao X. A novel polymer quaternary ammonium iodide and application in quasi-solid-state dye-sensitized solar cells. *Journal of Photochemistry and Photobiology A: Chemistry*. 2005;170:1-6. <http://dx.doi.org/10.1016/j.jphotochem.2004.07.016>.
- [30] Bandara TMWJ, Aziz MF, Fernando HDNS, Careem MA, Arof AK, and Mellander B-E. Efficiency enhancement in dye-sensitized solar cells with a novel PAN-based gel polymer electrolyte with ternary iodides. *Journal of Solid State Electrochemistry*. 2015;19:7.
- [31] Aziz MF, Buraidah MH, Careem MA, and Arof AK. PVA based gel polymer electrolytes with mixed iodide salts (K⁺ and Bu₄N⁺) for dye-sensitized solar cell application. *Electrochimica Acta*. 2015;182:217–223.
- [32] Noor MM, Buraidah MH, Careem MA, Majid SR, and Arof AK. An optimized poly(vinylidene fluoride-hexafluoropropylene)–NaI gel polymer electrolyte and its application in natural dye sensitized solar cells. *Electrochimica Acta*. 2014;121:159–167. <http://dx.doi.org/10.1016/j.electacta.2013.12.136>
- [33] Arof AK, Aziz MF, Noor MM, Careem MA, Bandara LRAK, Thotawatthage CA, Rupasinghe WNS, and Dissanayake MAKL. Efficiency enhancement by mixed cation effect in dye-sensitized solar cells with a PVdF based gel polymer electrolyte. *International Journal of Hydrogen Energy*. 2014;39(6):2929–2935. <http://dx.doi.org/10.1016/j.ijhydene.2013.07.028>
- [34] Aziz MF, Noor IM, Sahraoui B, and Arof AK. Dye-sensitized solar cells with PVA–KI–EC–PC gel electrolytes. *Optical and Quantum Electronics*. 2014;46(1):133–141. <http://dx.doi.org/10.1007/s11082-013-9722-0>

- [35] Hassan HC, Abidin ZHZ, Careem MA, and Arof AK. Chlorophyll as sensitizer in I^-/I_3^- -based solar cells with quasi-solid-state electrolytes. *High Performance Polymers*. 2014;26:(6):647–652. <http://dx.doi.org/10.1177/0954008314540310>
- [36] Huo Z, Tao L, Wang L, Zhu J, Chen S, Zhang C, Dai S, and Zhang B. Effect of alkyl chain length of imidazolium cations on the electron transport and recombination kinetics in ionic gel electrolytes based quasi-solid-state dye-sensitized solar cells. *Electrochimica Acta*. 2015;168:313–319. <http://dx.doi.org/10.1016/j.electacta.2015.04.007>
- [37] Yupapin PP, Pivsa-Art S, Ohgaki H, Tiautit N, Puratane C, Panpinit S, and Saengsuwan S. 11th Eco-energy and materials science and engineering (11th EMSES) effect of SiO_2 and TiO_2 nanoparticles on the performance of dye-sensitized solar cells using PVDF-HFP/PVA gel electrolytes. *Energy Procedia*. 2014;56:378–385. <http://dx.doi.org/10.1016/j.egypro.2014.07.170>
- [38] Bidikoudi M, Perganti D, Karagianni C-S, and Falaras P. Solidification of ionic liquid redox electrolytes using agarose biopolymer for highly performing dye-sensitized solar cells. *Electrochimica Acta*. 2015;179:228–236. <http://dx.doi.org/10.1016/j.electacta.2015.02.122>
- [39] Nicotera I, Coppola L, Oliviero C, Castriota M, and Cazzanelli E. Investigation of ionic conduction and mechanical properties of PMMA–PVdF blend-based polymer electrolytes. *Solid State Ionics*. 2006;177:(5–6):581–588. <http://dx.doi.org/10.1016/j.ssi.2005.12.028>
- [40] Saito Y, Kataoka H, Capiglia C, and Yamamoto H. Ionic conduction properties of PVDF–HFP type gel polymer electrolytes with lithium imide salts. *The Journal of Physical Chemistry B*. 2000;104:(9):2189–2192. <http://dx.doi.org/10.1021/jp993723h>
- [41] Singh PK, Kim K-W, and Rhee H-W. Electrical, optical and photoelectrochemical studies on a solid PEO-polymer electrolyte doped with low viscosity ionic liquid. *Electrochemistry Communications*. 2008;10:4.
- [42] Singh PK, Kim K-W, and Rhee H-W. Development and characterization of ionic liquid doped solid polymer electrolyte membranes for better efficiency. *Synthetic Metals*. 2009;159:4.
- [43] Singh PK, Bhattacharya B, Mehra MR, and Rhee H-W. Plasticizer doped ionic liquid incorporated solid polymer electrolytes for photovoltaic application. *Current Applied Physics*. 2011;11:616–619 <http://dx.doi.org/10.1016/j.cap.2010.10.012>.
- [44] Ng HM, Ramesh S, and Ramesh K. Efficiency improvement by incorporating 1-methyl-3-propylimidazolium iodide ionic liquid in gel polymer electrolytes for dye-sensitized solar cells. *Electrochimica Acta*. 2015;175:169–175. <http://dx.doi.org/10.1016/j.electacta.2015.01.076>
- [45] Jeon N, Hwang DK, Kang YS, Im SS, and Kim D-W. Quasi-solid-state dye-sensitized solar cells assembled with polymeric ionic liquid and poly(3,4-ethylenedioxythiophene) counter electrode. *Electrochemistry Communications*. 2013;34:1–4. <http://dx.doi.org/10.1016/j.elecom.2013.05.009>

- [46] Li Q, Tang Q, Du N, Qin Y, Xiao J, He B, Chen H, and Chu L. Employment of ionic liquid-imbibed polymer gel electrolyte for efficient quasi-solid-state dye-sensitized solar cells. *Journal of Power Sources*. 2014;248:816–821. <http://dx.doi.org/10.1016/j.jpowsour.2013.10.027>
- [47] Li Q, Tang Q, He B, and Yang P. Full-ionic liquid gel electrolytes: Enhanced photovoltaic performances in dye-sensitized solar cells. *Journal of Power Sources*. 2014;264:83–91. <http://dx.doi.org/10.1016/j.jpowsour.2014.04.095>
- [48] Smitha B, Sridhar S, and Khan AA. Solid polymer electrolyte membranes for fuel cell applications – a review. *Journal of Membrane Sciences*. 2005;259.
- [49] Malik RS, Tripathi SN, Gupta D, and Choudhary V. Novel anhydrous composite membranes based on sulfonated poly (ether ketone) and aprotic ionic liquids for high temperature polymer electrolyte membranes for fuel cell applications. *International Journal of Hydrogen Energy*. 2014;39:(24):12826–12834. <http://dx.doi.org/10.1016/j.ijhydene.2014.06.060>
- [50] Malik RS, Verma P, and Choudhary V. A study of new anhydrous, conducting membranes based on composites of aprotic ionic liquid and cross-linked SPEEK for fuel cell application. *Electrochimica Acta*. 2015;152:352–359. <http://dx.doi.org/10.1016/j.electacta.2014.11.167>
- [51] Gao J, Guo Y, Wu B, Qi L, Li B, Liu J, Wang Z, Liu W, Gu J, and Zou Z. Impact of cation selection on proton exchange membrane fuel cell performance with trimethylethyl amide, ethylpyridinium and ethylmethyl imidazolium ionic liquid carried by poly(vinylidene fluoride) membrane as electrolyte. *Journal of Power Sources*. 2014;251:432–438. <http://dx.doi.org/10.1016/j.jpowsour.2013.11.038>
- [52] Wang C, Lin B, Qiao G, Wang L, Zhu L, Chu F, Feng T, Yuan N, and Ding J. Polybenzimidazole/ionic liquid functionalized graphene oxide nanocomposite membrane for alkaline anion exchange membrane fuel cells. *Materials Letters*. 2016;173:219–222. <http://dx.doi.org/10.1016/j.matlet.2016.03.057>
- [53] Fang J, Lyu M, Wang X, Wu Y, and Zhao J. Synthesis and performance of novel anion exchange membranes based on imidazolium ionic liquids for alkaline fuel cell applications. *Journal of Power Sources*. 2015;284:517–523. <http://dx.doi.org/10.1016/j.jpowsour.2015.03.065>
- [54] Wang J-L, Wang L-L, Feng R-J, and Zhang Y. Synthesis and characterization of novel anion exchange membranes containing bi-imidazolium-based ionic liquid for alkaline fuel cells. *Solid State Ionics*. 2015;278:144–151. <http://dx.doi.org/10.1016/j.ssi.2015.06.010>
- [55] Ortiz-Martínez VM, Salar-García MJ, Hernández-Fernández FJ, and de los Ríos AP. Development and characterization of a new embedded ionic liquid based membrane-cathode assembly for its application in single chamber microbial fuel cells. *Energy*. 2015;93, Part 2:1748–1757. <http://dx.doi.org/10.1016/j.energy.2015.10.027>
- [56] Hernández-Fernández FJ, de los Ríos AP, Mateo-Ramírez F, Juárez MD, Lozano-Blanco LJ, and Godínez C. New application of polymer inclusion membrane based on ionic liquids as proton exchange membrane in microbial fuel cell. *Separation and Purification Technology*. 2016;160:51–58. <http://dx.doi.org/10.1016/j.seppur.2015.12.047>

- [57] Salar-García MJ, Ortiz-Martínez VM, de los Ríos AP, and Hernández-Fernández FJ. A method based on impedance spectroscopy for predicting the behavior of novel ionic liquid-polymer inclusion membranes in microbial fuel cells. *Energy*. 2015;89:648–654. <http://dx.doi.org/10.1016/j.energy.2015.05.149>
- [58] Li M, Wang L, Yang B, Du T, and Zhang Y. Facile preparation of polymer electrolytes based on the polymerized ionic liquid poly((4-vinylbenzyl)trimethylammonium bis(trifluoromethanesulfonylimide)) for lithium secondary batteries. *Electrochimica Acta*. 2014;123:296–302. <http://dx.doi.org/10.1016/j.electacta.2013.12.179>
- [59] Stepniak I, Andrzejewska E, Dembna A, and Galinski M. Characterization and application of N-methyl-N-propylpiperidinium bis(trifluoromethanesulfonyl)imide ionic liquid-based gel polymer electrolyte prepared in situ by photopolymerization method in lithium ion batteries. *Electrochimica Acta*. 2014;121:27–33. <http://dx.doi.org/10.1016/j.electacta.2013.12.121>
- [60] Swiderska-Mocek A. Application of quaternary polymer electrolyte based on ionic liquid in $\text{LiFePO}_4/\text{Li}$, $\text{Li}_4\text{Ti}_5\text{O}_{12}/\text{Li}$ and $\text{LiFePO}_4/\text{Li}_4\text{Ti}_5\text{O}_{12}$ batteries. *Electrochimica Acta*. 2014;139:337–344. <http://dx.doi.org/10.1016/j.electacta.2014.07.042>
- [61] Swiderska-Mocek A and Naparstek D. Compatibility of polymer electrolyte based on N-methyl-N-propylpiperidinium bis(trifluoromethanesulphonyl)imide ionic liquid with LiMn_2O_4 cathode in Li-ion batteries. *Solid State Ionics*. 2014;267:32–37. <http://dx.doi.org/10.1016/j.ssi.2014.09.007>
- [62] Yang P, Liu L, Li L, Hou J, Xu Y, Ren X, An M, and Li N. Gel polymer electrolyte based on polyvinylidene fluoride-co-hexafluoropropylene and ionic liquid for lithium ion battery. *Electrochimica Acta*. 2014;115:454–460. <http://dx.doi.org/10.1016/j.electacta.2013.10.202>
- [63] Zhai W, Zhu H-J, Wang L, Liu X-M, and Yang H. Study of PVDF-HFP/PMMA blended micro-porous gel polymer electrolyte incorporating ionic liquid [BMIM]BF₄ for Lithium ion batteries. *Electrochimica Acta*. 2014;133:623–630. <http://dx.doi.org/10.1016/j.electacta.2014.04.076>
- [64] Li X, Zhang Z, Li S, Yang L, and Hirano S-I. Polymeric ionic liquid-plastic crystal composite electrolytes for lithium ion batteries. *Journal of Power Sources*. 2016;307:678–683. <http://dx.doi.org/10.1016/j.jpowsour.2016.01.032>
- [65] Mysyk R, Raymundo-Piñero E, Anouti M, Lemordant D, and Béguin F. Pseudocapacitance of nanoporous carbons in pyrrolidinium-based protic ionic liquids. *Electrochemistry Communications*. 2010;12(3):414–417. <http://dx.doi.org/10.1016/j.elecom.2010.01.007>
- [66] Xiong P, Zhu J, and Wang X. Recent advances on multi-component hybrid nanostructures for electrochemical capacitors. *Journal of Power Sources*. 2015;294:31–50. <http://dx.doi.org/10.1016/j.jpowsour.2015.06.062>
- [67] Timperman L, Vigeant A, and Anouti M. Eutectic mixture of protic ionic liquids as an electrolyte for activated carbon-based supercapacitors. *Electrochimica Acta*. 2015;155:164–173. <http://dx.doi.org/10.1016/j.electacta.2014.12.130>

- [68] Shiraishi S, Miyauchi T, Sasaki R, Nishina N, Oya A, and Hagiwara R. Electric double layer capacitance of activated carbon nanofibers in ionic liquid: EMImBF₄. *Electrochemistry*. 2007;8:619–621.
- [69] Fletcher SI, Sillars FB, Carter RC, Cruden AJ, Mirzaeian M, Hudson NE, Parkinson JA, and Hall PJ. The effects of temperature on the performance of electrochemical double layer capacitors. *Journal of Power Sources*. 2010;195:(21):7484–7488. <http://dx.doi.org/10.1016/j.jpowsour.2010.05.043>
- [70] Sun G, Li K, and Sun C. Electrochemical performance of electrochemical capacitors using Cu(II)-containing ionic liquid as the electrolyte. *Microporous and Mesoporous Materials*. 2010;128:(1–3):56–61. <http://dx.doi.org/10.1016/j.micromeso.2009.07.027>
- [71] Sato T, Masuda G, and Takagi K. Electrochemical properties of novel ionic liquids for electric double layer capacitor applications. *Electrochimica Acta*. 2004;49:(21):3603–3611. <http://dx.doi.org/10.1016/j.electacta.2004.03.030>
- [72] Yuyama K, Masuda G, Yoshida H, and Sato T. Ionic liquids containing the tetrafluoroborate anion have the best performance and stability for electric double layer capacitor applications. *Journal of Power Sources*. 2006;162:(2):1401–1408. <http://dx.doi.org/10.1016/j.jpowsour.2006.09.002>
- [73] Yoshizawa M, Xu W, and Angell CA. Ionic liquids by proton transfer: vapor pressure, conductivity, and the relevance of ΔpK_a from aqueous solutions. *Journal of the American Chemical Society*. 2003;125:(50):15411–15419. <http://dx.doi.org/10.1021/ja035783d>
- [74] Demarconnay L, Calvo EG, Timperman L, Anouti M, Lemordant D, Raymundo-Piñero E, Arenillas A, Menéndez JA, and Béguin F. Optimizing the performance of supercapacitors based on carbon electrodes and protic ionic liquids as electrolytes. *Electrochimica Acta*. 2013;108:361–368. <http://dx.doi.org/10.1016/j.electacta.2013.07.001>
- [75] Brandt A, Pires J, Anouti M, and Balducci A. An investigation about the cycling stability of supercapacitors containing protic ionic liquids as electrolyte components. *Electrochimica Acta*. 2013;108:226–231. <http://dx.doi.org/10.1016/j.electacta.2013.06.118>
- [76] Huang P-L, Luo X-F, Peng Y-Y, Pu N-W, Ger M-D, Yang C-H, Wu T-Y, and Chang J-K. Ionic liquid electrolytes with various constituent ions for graphene-based supercapacitors. *Electrochimica Acta*. 2015;161:371–377. <http://dx.doi.org/10.1016/j.electacta.2015.02.115>
- [77] Trigueiro JPC, Lavall RL, and Silva GG. Supercapacitors based on modified graphene electrodes with poly(ionic liquid). *Journal of Power Sources*. 2014;256:264–273. <http://dx.doi.org/10.1016/j.jpowsour.2014.01.083>
- [78] Ayalneh Tiruye G, Muñoz-Torrero D, Palma J, Anderson M, and Marcilla R. All-solid state supercapacitors operating at 3.5 V by using ionic liquid based polymer electrolytes. *Journal of Power Sources*. 2015;279:472–480. <http://dx.doi.org/10.1016/j.jpowsour.2015.01.039>

- [79] Pandey GP, Kumar Y, and Hashmi SA. Ionic liquid incorporated PEO based polymer electrolyte for electrical double layer capacitors: A comparative study with lithium and magnesium systems. *Solid State Ionics*. 2011;190:(1):93–98. <http://dx.doi.org/10.1016/j.ssi.2011.03.018>
- [80] Liew C-W, Ramesh S, and Arof AK. Good prospect of ionic liquid based-poly(vinyl alcohol) polymer electrolytes for supercapacitors with excellent electrical, electrochemical and thermal properties. *International Journal of Hydrogen Energy*. 2014;39:(6):2953–2963. <http://dx.doi.org/10.1016/j.ijhydene.2013.06.061>
- [81] Liew C-W, Ramesh S, and Arof AK. Characterization of ionic liquid added poly(vinyl alcohol)-based proton conducting polymer electrolytes and electrochemical studies on the supercapacitors. *International Journal of Hydrogen Energy*. 2015;40:(1):852–862. <http://dx.doi.org/10.1016/j.ijhydene.2014.09.160>
- [82] Liew C-W, Ramesh S, and Arof AK. Investigation of ionic liquid-doped ion conducting polymer electrolytes for carbon-based electric double layer capacitors (EDLCs). *Materials & Design* 2016;92:829–835. <http://dx.doi.org/10.1016/j.matdes.2015.12.115>
- [83] Syahidah SN and Majid SR. Ionic liquid-based polymer gel electrolytes for symmetrical solid-state electrical double layer capacitor operated at different operating voltages. *Electrochimica Acta* 2015;175:184–192. <http://dx.doi.org/10.1016/j.electacta.2015.02.215>

Recent Advances in Electrocatalytic Applications of Ionic Liquids

Yu Lin Hu

Additional information is available at the end of the chapter

<http://dx.doi.org/10.5772/65808>

Abstract

Ionic liquids have emerged as an environmentally friendly alternative to the volatile organic solvents. Being designer solvents, they can be modulated to suit the reaction conditions, therefore earning the name “task-specific ionic liquids.” Though primarily used as solvents, they are now finding applications in various fields such as catalysis, electrochemistry, spectroscopy, and material science to mention a few. The goal of this chapter is focused on the electrocatalytic applications of ionic liquids, which can be used as catalysts and catalytic supports in electrochemistry. Their scope has marched beyond academic research laboratories to industries where their practical applications have been leading to various sustainable technologies. Flexibility to modulate properties by changing design endows freedom to a chemist to design an ionic liquid according to one’s own requirement. To conclude, it can be said that the field of ionic liquid electrocatalysis holds enormous possibilities to be explored.

Keywords: ionic liquid, electrochemistry, electrocatalysis, sensors, electrodeposition, electroredox, application

1. Introduction

Ionic liquids (ILs) are organic salts remaining liquid even under ambient temperatures [1]. They consist of organic cations (e.g., imidazolium, pyridinium, pyrrolidinium, phosphonium, ammonium) and organic/inorganic anions with side chains of alkyl or different functional groups and aromatic moieties (e.g., trifluoromethanesulfonate, bis(trifluoromethyl)sulfonyl imide) [2, 3]. Characteristic interesting properties of these liquid salts include good thermal stability, wide liquid temperature range, considerable ionic conductivity, a broad electrochem-

ical window, and a wide solubility and miscibility range [4, 5]. Due to these advantages, they have been considered as environmental benign solvents compared to volatile organic solvents and “green designer solvents.” As a result, ILs are widely used in various chemical transformations such as electrocatalysis, electrosynthesis, electrodeposition, electrochemical capacitor, and lithium batteries (**Figure 1**) [6]. Nowadays, ionic liquids are of immensely growing importance for the electrochemical technology [7–9]. The applications of ILs reveal new perspectives in electrocatalysis and other branches of applied electrochemistry [10–12].

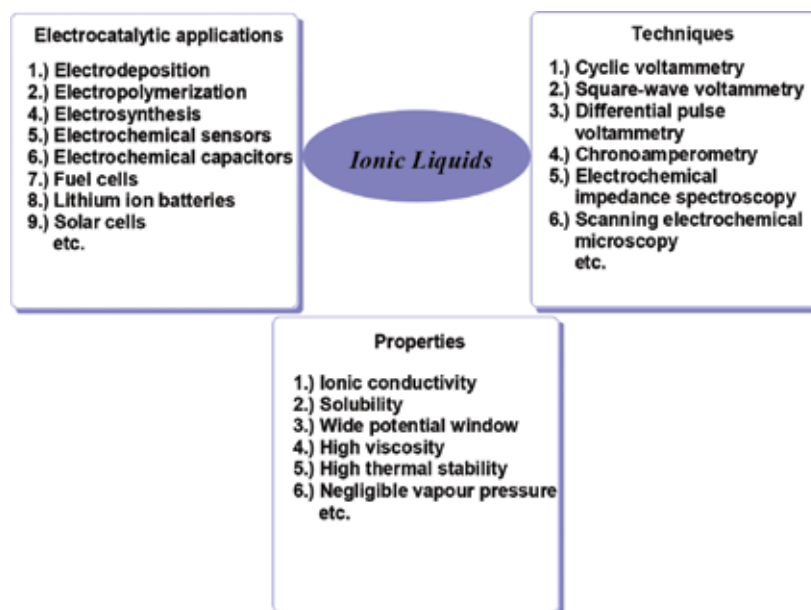


Figure 1. Schematic representation of the general properties of ILs, electrochemical techniques, and electrochemical applications of ILs.

Electrocatalysis is a special type of catalysis that speeds up the rate of an electrochemical reaction occurring on electrode surfaces or at liquid/solid interfaces [13]. In this chapter, we mainly overviewed recent advances in electrocatalytic applications of ionic liquids such as electrosensing, electrodeposition, electroredox, and electropolymerization.

2. Electrochemical applications of ionic liquids

2.1. Electrochemical sensors

Nonenzymatic amperometric sensor for direct determination of some electroactive molecules is an attractive alternative technique to solve the disadvantages of enzymatic biosensors [14]. They have received continuously increasing interest in the recent years [15, 16]. ILs are used primarily as modifying materials of electrodes (IL can interact with other materials to get

composites which exhibit the synergistic effects [17]) for the fabrication of sensors due to their performance of achieving electron transfer (DET) directly. The modified electrodes in electroanalysis offer several advantages. They can not only lower the overpotential but also increase the reaction rate and sensitivity and improve selectivity. These advantages have been evidenced by numerous experiments.

Rahman et al. [18] reported the synthesis of ionic liquid [CIPr]NTf₂ by simple metathesis reaction at room temperature (**Figure 2**). The [CIPr]NTf₂ can fabricate the chemical sensor with conducting coating binders onto glassy carbon electrodes, which showed high selective and sensitivity on sensing applications. The performances of the fabricated sensors are excellent in terms of selectivity, sensitivity, detection limit, etc. This novel approach was introduced a well-organized route of efficient chemical sensor development for environmental pollutants and health-care fields in broad scales.

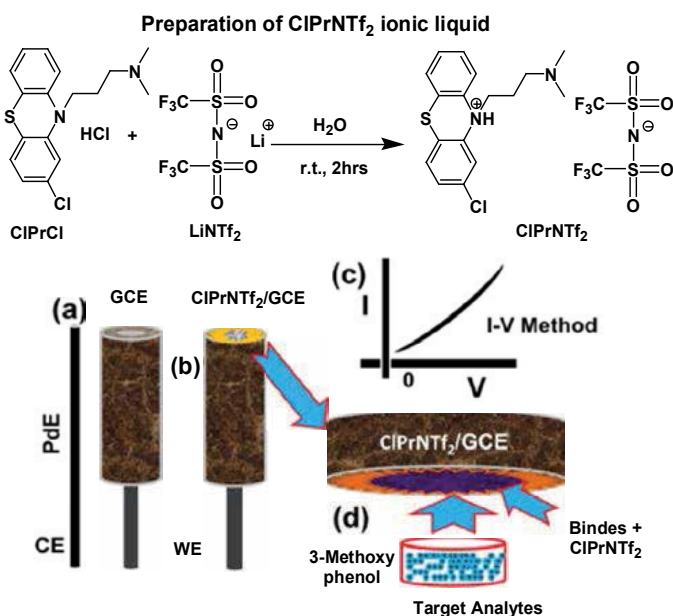


Figure 2. Preparation of CIPrNTf₂ and the mechanism of sensor development. (a) CIPrNTf₂ coated GCE with conducting coating binders, (b) detection I-V method (theo-retical), (c) observed I-V responses by CIPrNTf₂/GCE, and (d) proposed adsorption mechanisms of 3-methoxy phenol detection in presence of CIPrNTf₂ onto GCE.

Atta et al. [19] fabricated reduced cyclodextrin/ionic liquid crystal/graphene composite electrode for the determination of some neurotransmitters such as dopamine (DA), epinephrine (EP), and norepinephrine (NEP) (**Figure 3**). Besides the pre-concentrating effect of CD, this electrode expected large graphene surface area, good electron mobility, and high ionic stability and conductivity of ionic liquid. Optimization of the sensor performance was presented and resulted in a better current signal. The sensor was sensitive and successfully applied for direct determination of EP in human urine samples with good recovery results.

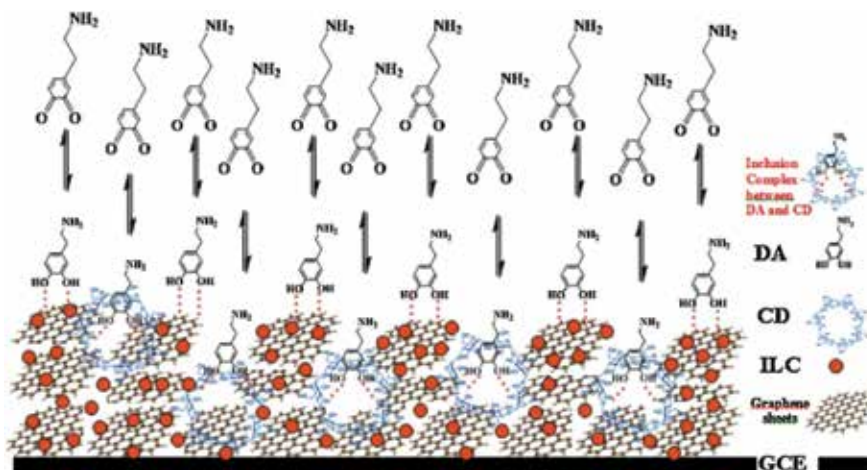


Figure 3. Schematic representation of the proposed sensor with the inclusion complex between the studied compounds and CD.

Yu et al. [20] fabricated an ionic liquid- Fe_3O_4 nanoparticle-graphite composite electrode (IL- Fe_3O_4 NPs-GP) (**Figure 4**). A hydrophobic ionic liquid BMP-TFSA was used to combine Fe_3O_4 NPs and graphene paper (GP) and to substitute paraffin oil that is conventionally used as the organic binder for preparing carbon-paste electrodes. The electrode showed good stability and the synergistic effect from the combination of IL and Fe_3O_4 NPs, exhibiting a high sensitivity but a narrower dynamic range with a detection limit of 0.5 IM.

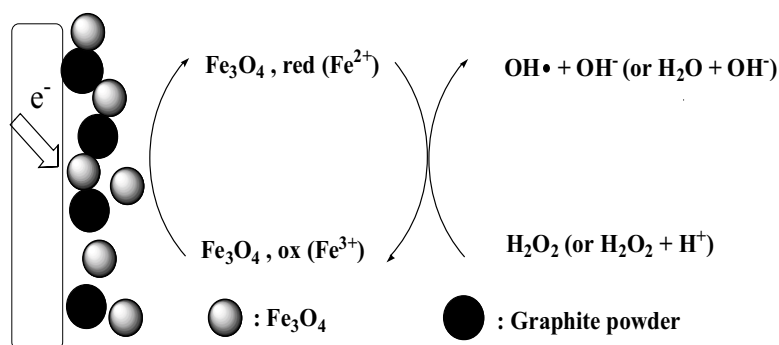


Figure 4. IL- Fe_3O_4 NPs-GP electrode for detection of H_2O_2 .

He et al. [21] reported the synthetic method for the free-standing GP-supported graphene-CNT-IL nanocomposite graphene-CNT-IL/GP (**Figure 5**), which was formulated by blending three-dimensional porous graphene-carbon nanotube (CNT) assembly with ionic liquid on two-dimensional graphene paper (GP). The results showed that the graphene-CNT-IL/GP exhibited excellent sensing characteristics in terms of selectivity, reproducibility, and sensitivity in electrochemical detection of glucose.

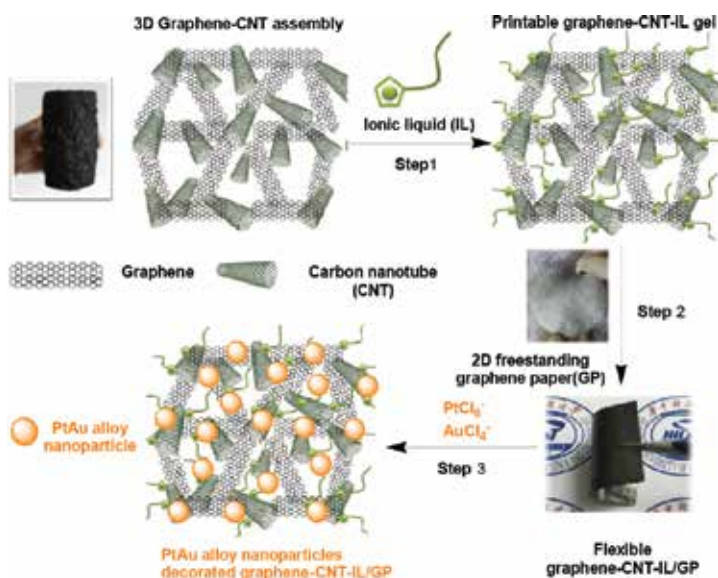


Figure 5. Preparation process of PtAu alloy nanoparticle decorated graphene-CNT-IL/GP.

Okuzaki et al. [22] synthesized the transparent ionic liquid/polyurethane (IL/PU) gels firstly (**Figure 6**). They observed that with increasing the IL content from 0 wt% to 40 wt%, both ionic conductivity and electric-double-layer capacitance increased, respectively, while the compression modulus slightly decreased. After that, the workers fabricated the IL/PU/PEDOT:PSS composites by sandwiching the IL/PU gel between two conductive polymer films (PEDOT:PSS) as flexible and soft electrodes, which showed excellent bending toward anode.

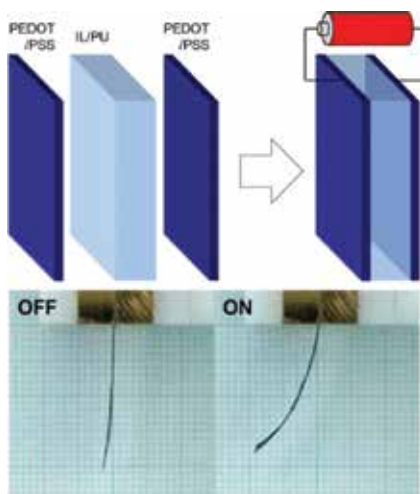


Figure 6. Illustration of IL/PU/PEDOT:PSS composite actuator.

Xia et al. [23] fabricated the molecularly imprinted electrochemical biosensor based on chitosan/ionic liquid-graphene composites modified electrode (CS/IL-GR/GCE) for determination of bovine serum albumin (BSA) (**Figure 7**). The synergistic effects of chitosan, ionic liquid, and graphene nanocomposites improved the electrochemical response and the sensitivity of the sensor. The fabricated sensor possessed a high selectivity, good reproducibility, excellent stability, and acceptable recovery, which indicated the potential application in clinical field.

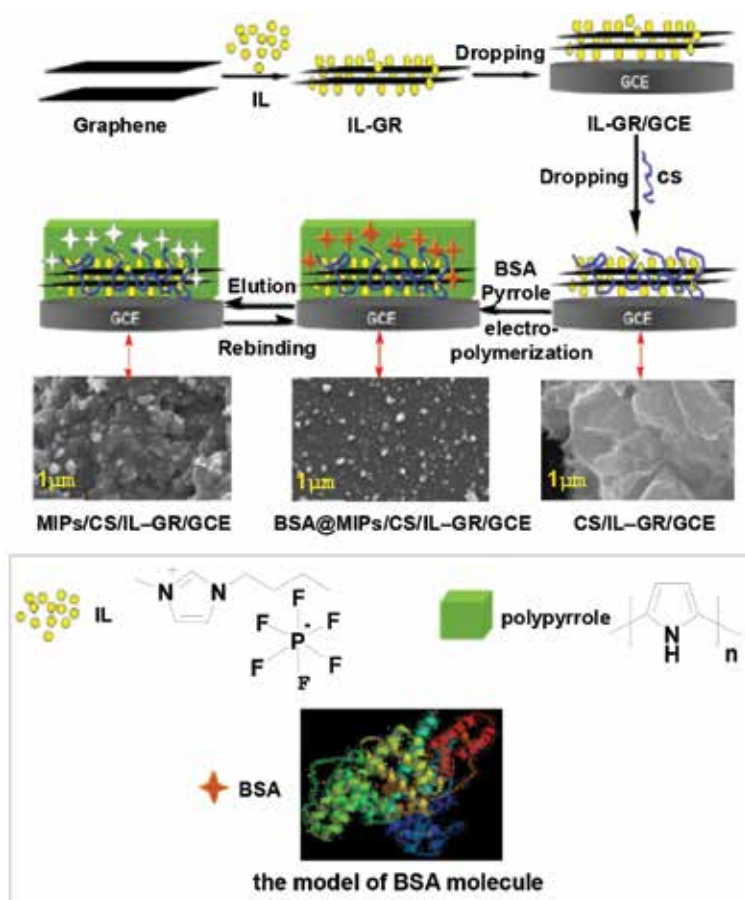


Figure 7. Schematic diagram of the preparation procedure of the molecularly imprinted electrochemical sensor.

Zhao and Hao [24] constructed an analytical approach for detecting diaminopyridine derivatives using a molecular imprinting-electrochemical sensor synthesized with 6-aminouracil and 2,6-diaminopyridine (**Figure 8**). Ionic liquid and graphene can assist 2,6-diaminopyridine-imprinted core-shell nanoparticles in electrochemical reaction by increasing conductivity. This proposed method has been demonstrated appropriate sensitivity and selectivity, with a linear range of 0.0500–35.0 mg kg⁻¹ and a detection limit as low as 0.0275 mg kg⁻¹.

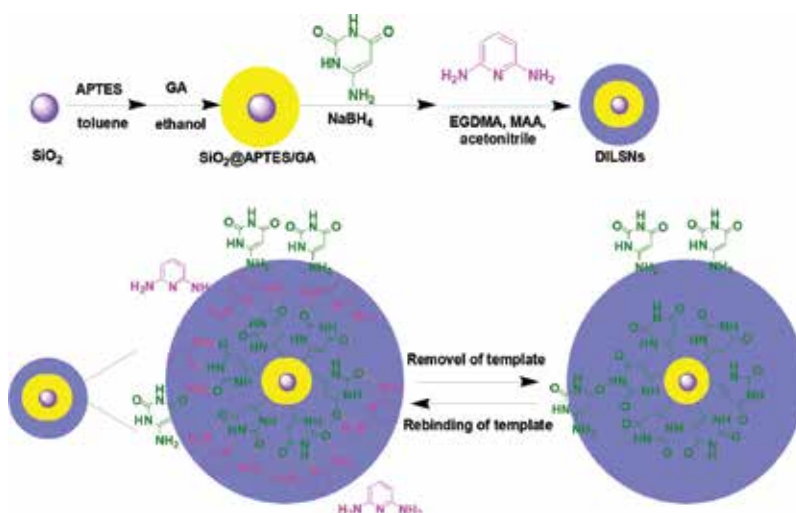


Figure 8. Illustration of the construction of the 2,6-DAP-imprinted core-shell nanoparticles (DICSNs).

Wang et al. [25] synthesized the GNS/Pd nanocomposites by the incorporation of different kinds of ionic liquid (IL) to increase the electrode sensing current toward different analytes (**Figure 9**). They found that BMP-TFSI IL is beneficial for glucose detection, whereas the electrode with BMP-DCA IL shows high sensitivity toward ascorbic acid (AA). Angle-resolved X-ray photoelectron spectroscopy analyses indicate that GNSs can create an aligned cation/anion orientation in the adsorbed IL film, with the anions preferentially occupying the topmost surface. As a result, the electrode sensitivity and selectivity are mainly determined by the IL constituent anions. Chen et al. [26] reported the ultra-sensitive gaseous NH₃ sensor (ECL sensor) based on ionic liquid mediated for directly detecting gaseous NH₃ (**Figure 10**). The NH₃ECL sensor has a very high sensitivity and an excellent selectivity against common interfering gases.

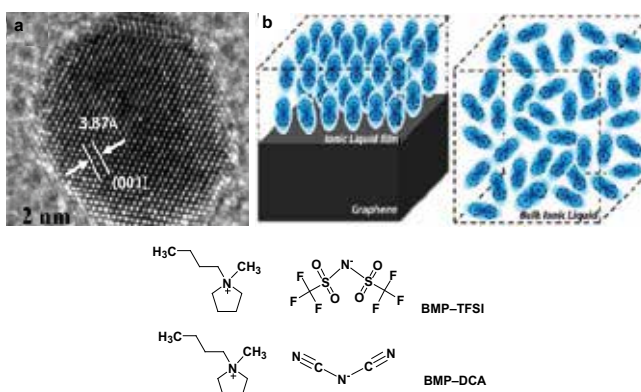


Figure 9. (a) High-resolution TEM micrograph of synthesized Pd nanoparticle means sampling depth is low and (b) schematic of constituent ion orientation in ILs based on different underlying supports.

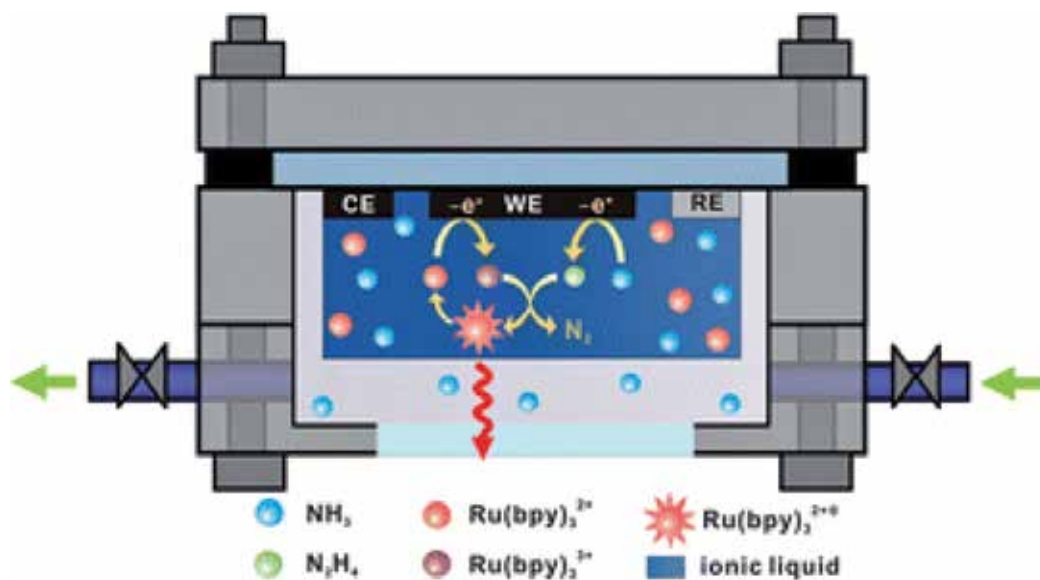


Figure 10. Illustrative ECL sensor for directly detecting gaseous NH_3 .

2.2. Electrodeposition

Electrodeposition is an important process, which has been widely applied in industry from functional and decorative anticorrosion to wear-resistant coatings [27]. Aqueous electrolytes are traditionally used in the electrodeposition, and they suffer from limitations such as gas evolution, narrow potential windows, environmental hazards, and necessity for complexing agents [28–30]. Consequently, to overcome these shortcomings, several alternative electrolytes have been developed to substitute for aqueous solvent, although organic solvents have a wider electrochemical potential window; however, their toxicity, volatility, and handling are the major problems for their industrial applications [30]. Ionic liquids (ILs) are green and important electrolytes in electrode position of metals and can circumvent these limitations. Many studies have demonstrated IL electrolytes are favorable for electrode position of nanocrystalline metals, while in aqueous media, pulsed electrode position and addition of additives are required, which often complicates the reaction mechanisms significantly [31].

Suryanto et al. [27] achieved the electrode position of silver onto glassy carbon, gold, and indium tin oxide-coated glass substrates from three room-temperature protic ionic liquids (PILs) (Figure 11). The results showed that the electrode position took place through a progressive nucleation and diffusion controlled 3D growth reaction mechanism. The silver micro-/nanoparticles were then employed as electrocatalysts in oxygen reduction reaction and had excellent catalytic activity. This research provided promise for using protic ionic liquids as alternative electrolytes for the electrode position of metals and nanostructured electrocatalysts.

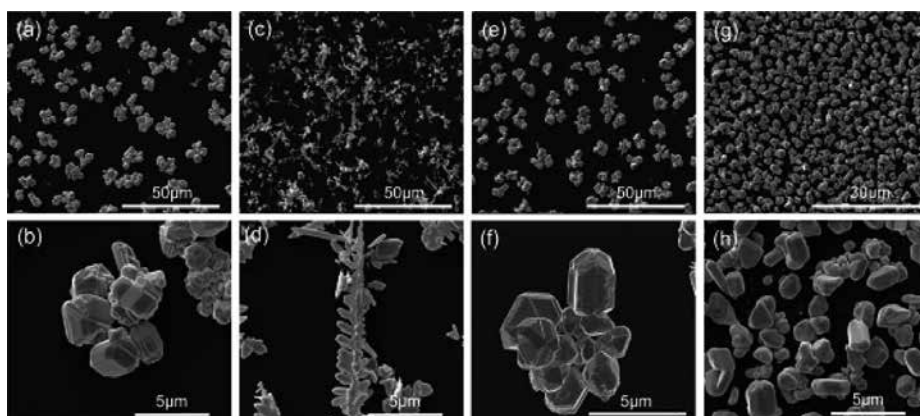


Figure 11. SEM images of silver electrodeposited onto a GC electrode from EAN containing 0.1 M Ag^+ with different deposition parameters. (a and b) $E_{\text{dep}} = -0.2 \text{ V}$, $t = 30 \text{ s}$; (c and d) $E_{\text{dep}} = -0.6 \text{ V}$, $t = 30 \text{ s}$; (e and f) $E_{\text{dep}} = -0.2 \text{ V}$, $t = 60 \text{ s}$; and (g and h) $E_{\text{dep}} = -0.2 \text{ V}$, $t = 300 \text{ s}$.

Martis and coworkers [32] investigated the nickel-multiwalled carbon nanotube (Ni/MWCNT) composites electrodeposited in choline chloride/urea-based deep eutectic solvent on a copper substrate (**Figure 12**). Electrodeposition of Ni/MWCNT composites could be easily achieved due to the excellent dispersion stability of MWCNTs in DES nickel chloride solution. Different morphologies and high surface roughness of MWCNTs to the coating were observed through the uniform distribution in the nickel matrix. The results showed that coating with oxygen-functionalized MWCNTs exhibited better corrosion resistance and higher stability than that with pristine MWCNTs.

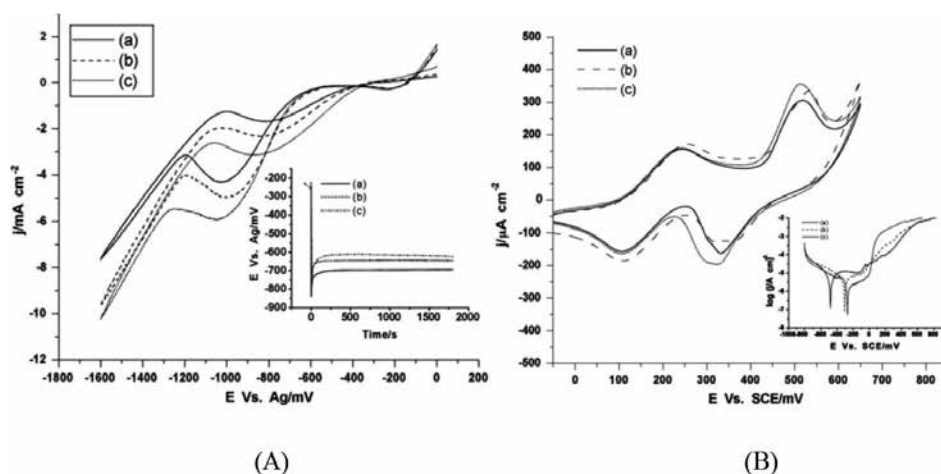


Figure 12. A: Cyclic voltammograms for a copper electrode (a) DES + 0.3 M NiCl_2 , (b) O-MWCNT + 0.3 M NiCl_2 , and (c) P-MWCNT in DES + 0.3 M NiCl_2 , SR = 0.02V/s. B: Cyclic voltammograms for (a) bare nickel, (b) Ni/O-MWCNTs, and (c) Ni/P-MWCNTs.

Mascia et al. [33] studied the electrochemical deposition of Cu/Nb composites by using 1-butyl-1-methylpyrrolidinium bis(trifluoromethylsulfonyl)imide as solvent (**Figure 13**). Structural and chemical analyses indicated that the obtained deposits cover uniformly the electrode surface and exhibit individual layers with a characteristic size ranging between 50 and 100 nm.

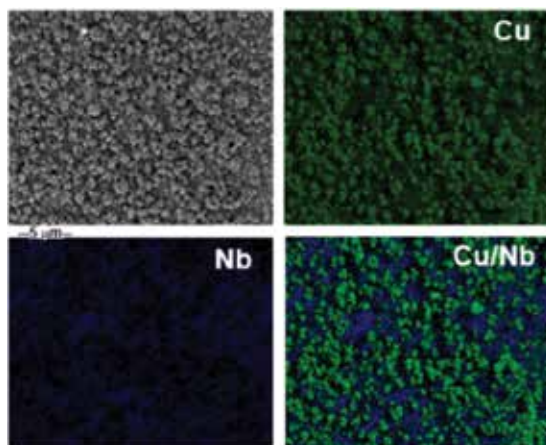


Figure 13. SEM micrograph and elemental maps of the Cu/Nb electrodeposit obtained in dual bathmode: first deposit of copper prepared at -0.75 V for 1800 s, followed by niobium deposit obtained at -1.5 V for 3600 s. The procedure was repeated twice.

Izgorodin et al. [34] synthesized a novel material based on manganese oxide catalyst, which is sensitized and stabilized through a surface phosphorylation reaction in the ionic liquid electrode position reaction (**Figure 14**). The results showed that the surface of the MnOx contained phosphorous at a P/Mn ratio of 1/2, indicating that the surface layer contained phosphate and oxide characteristics. The stability of the catalyst was enhanced and more than 25 h of continuous water oxidation is demonstrated.

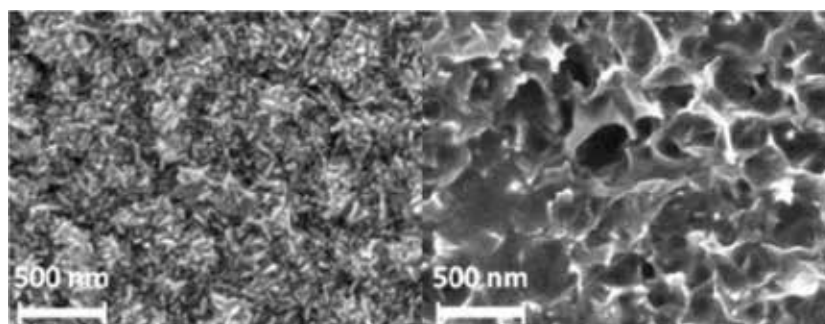


Figure 14. SEM images of the manganese dioxide substrate before (left) and after (right) surface phosphorylation treatment.

Serrà et al. [35] demonstrated a method for grow mesoporous films of Pt-poor alloys (Co_3Pt and CoPt_3) through electrode position in ionic liquid-water microemulsions (**Figure 15**). The electrolytic aqueous solution in the IL/W system favors a significant deposition rate. The mesoporous alloys exhibit excellent durability in acidic and alkaline media, maintaining their peculiar morphology, and this prepared catalysts efficient for the methanol electrooxidation in alkaline media.

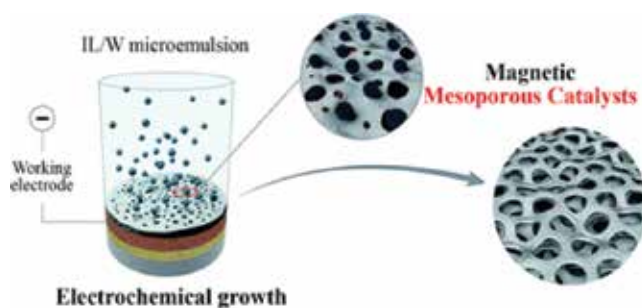


Figure 15. Illustrative approach to grow mesoporous films of Pt-poor alloys (Co_3Pt and CoPt_3), based on electrodeposition in ionic liquid-in-water (IL/W) microemulsions.

Bakkar and Neubert [36] conducted the electrode position of aluminum in air, after preparation of ionic liquids in a glove box and covering them by a nonwater-absorbable layer of particular organic compound (**Figure 16**). The functional aluminum layers were successfully deposited from a first-generation ionic liquid $\text{AlCl}_3/[\text{EMIm}]\text{Cl}$ (60/40 mol%) on low-carbon steel. SEM/EDX assessments showed that uniform, dense, and adherent Al layers were obtained. Furthermore, adherence of Al to the steel substrate was improved via in situ electrochemical etching.

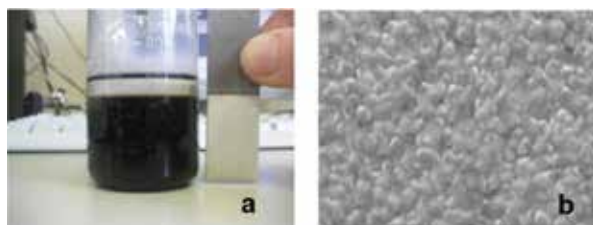


Figure 16. (a) Photograph of a beaker containing $\text{AlCl}_3/[\text{EMIm}]\text{Cl}$ ionic liquid insulated from air by a floating layer of decane, in addition to Al electroplated steel strip. (b) SEM micrograph of electrodeposited Al onto low-carbon steel substrate from $\text{AlCl}_3/[\text{EMIm}]\text{Cl}$ (60/40 mol%) ionic liquid protected from air by a layer of decane at a potential of -500 mV at ambient atmosphere.

Hekmata et al. [37] arranged the multiwall carbon nanotubes (MWCNTs) in nanochannels of anodic aluminum oxide template (AAO) by electrophoretic deposition (EPD) to make a vertically aligned carbon nanotube (VA-CNT)-based electrode (**Figure 17**). The stabilized CNTs in a water-soluble room-temperature ionic liquid (1-methyl-3-octadecylimidazolium bromide)

were deposited in the pores of AAO templates which were conductive by deposition of Ni nanoparticles in the bottom of pores. The capacitive performance of prepared electrodes was analyzed with a maximum value of 50 Fg^{-1} at the scan rate of 20 mV s^{-1} that was achieved for the specific capacitance.

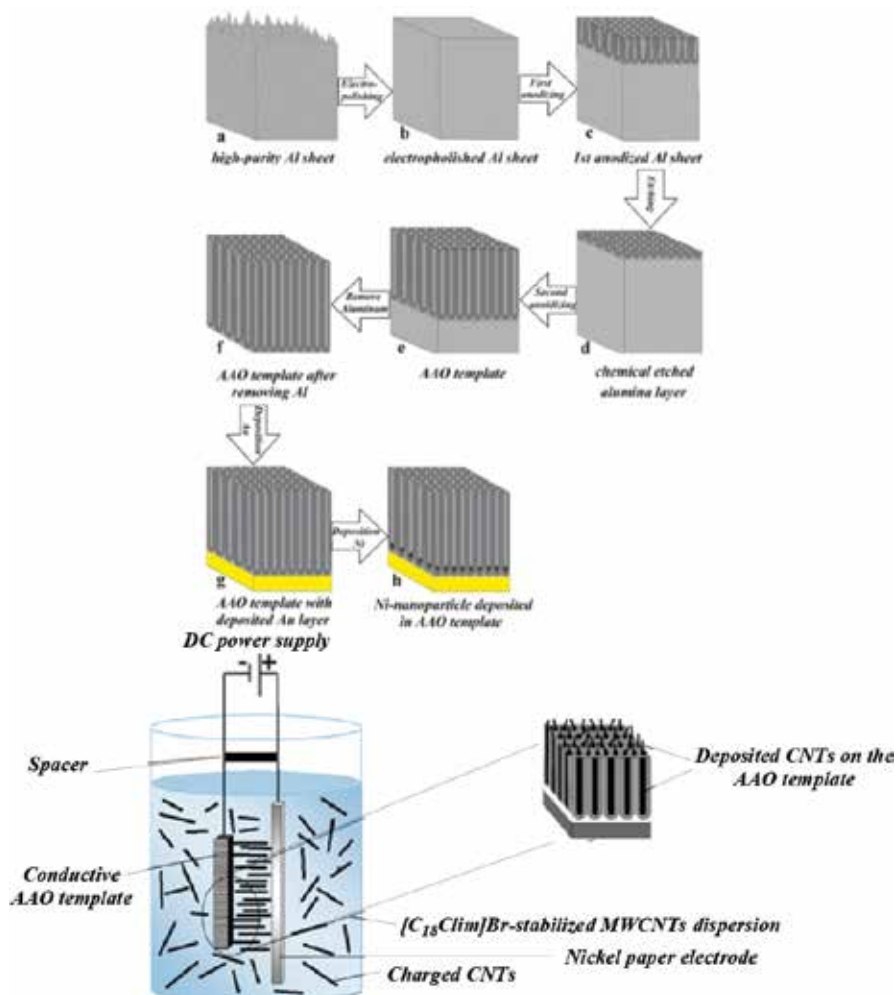


Figure 17. Schematic diagram of an EPD cell for electrophoretic deposition of well-dispersed CNTs on the cathode (as prepared AAO template).

Caporali et al. [38] assessed the feasibility of the use of highly concentrated solutions of ionic liquids to achieve high rates of metal electrodeposition (**Figure 18**). Different ionic liquids containing five transition metals were obtained by dissolving Tf_2N salts of the metals (Ag, Cu, Co, Ni, and zinc) in $[\text{bmim}][\text{Tf}_2\text{N}]$ in a 1:2 molar ratio. The experimental results showed that with the exception of the Ni system, for all the ILs, it was possible to achieve the electroreduction of the metal operating in a normal air atmosphere.

Abebe et al. [39] prepared 4,4-bipyridinium-based ionic liquids which exhibited good metal coordinating abilities and were able to dissolve metal salts at high concentrations (**Figure 19**). The ionic liquid ($[C_4\text{Bipyr}][\text{Tf}_2\text{N}]$) exhibited a large liquidus range and a wide electrochemical window. Moreover, the successful electrodeposition of Cu (II) to Cu (0) from a solution of $\text{Cu}(\text{NO}_3)_2$ in $[C_4\text{Bipyr}][\text{Tf}_2\text{N}]$ showed the potential of this new type of ionic liquids for electro-deposition.

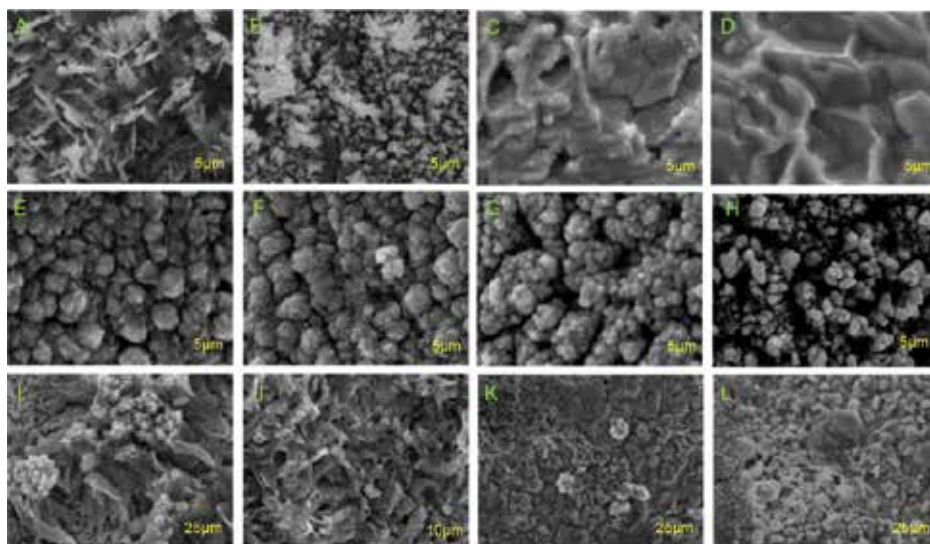


Figure 18. (a) SEM of silver coatings deposited from “wet” (A and B) and “dry” (C and D) $\text{AgTf}_2\text{N}:[\text{bmim}][\text{Tf}_2\text{N}]$ 1:2 molar ratio solution. (b) SEM of copper layers deposited from “wet” $\text{Cu}(\text{Tf}_2\text{N})_2: [\text{bmim}][\text{Tf}_2\text{N}]$ 1:2 molar ratio solution as a function of the applied potential. (E) -0.55 V, (F) -0.70 V, (G) -0.85 V, and (H) -0.90 V. (c) SEM of copper layers deposited from “wet” $\text{Co}(\text{Tf}_2\text{N})_2: [\text{bmim}][\text{Tf}_2\text{N}]$ 1:2 molar ratio solution. (I) -1.30 V “dry” solution and (J) -1.30 V “wet” solution. (d) SEM of zinc layers deposited from “wet” $\text{Zn}(\text{Tf}_2\text{N})_2: [\text{bmim}][\text{Tf}_2\text{N}]$ 1:2 molar ratio solution. (K) -1.30 V “dry” solution and (L) -1.30 V “wet” solution.

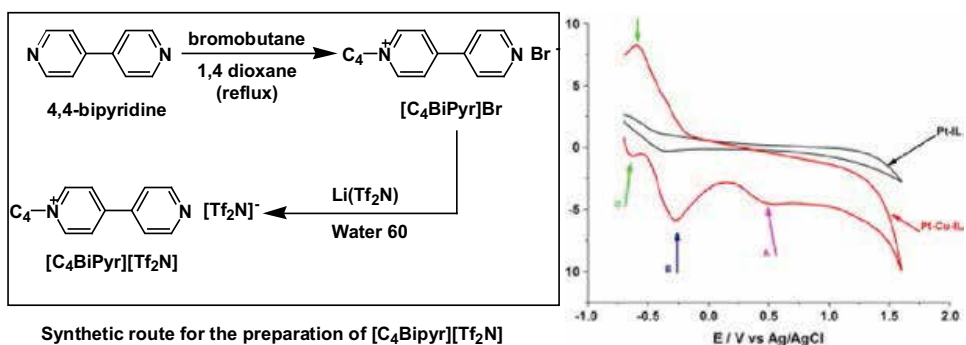


Figure 19. Cyclic voltammogram for the neat $[C_4\text{Bipyr}][\text{Tf}_2\text{N}]$ (black trace) and the solution of $\text{Cu}(\text{NO}_3)_2$ in $[C_4\text{Bipyr}][\text{Tf}_2\text{N}]$ (red trace).

Kosta et al. [40] proposed an electrochemical route to obtain CuI films (**Figure 20**). The approach was based on the electrochemical reduction of I_2 in a solution of copper bis(trifluoromethanesulfonyl)imide salt in 1-butyl-1-methylpyrrolidinium bis(trifluoromethanesulfonyl)imide room-temperature ionic liquid. The mechanisms pointed out that the CuI formation occurred from the chemical reaction between the Cu^{2+} and I^- generated from the I_2 reduction. The researchers also investigated the electrodeposition from organic solvent-based media and found that the solvent nature affected strongly to the nanocrystal packing density. The electrodeposition of ZnO/CuI heterostructures, with high transmittance in the visible range (i.e., >75%), was also reported. The current density-voltage characteristic of the resulting device exhibited clear rectifying behavior with a rectification of $\sim 2 \times 10^3$ at $V = \pm 1.5$ V.

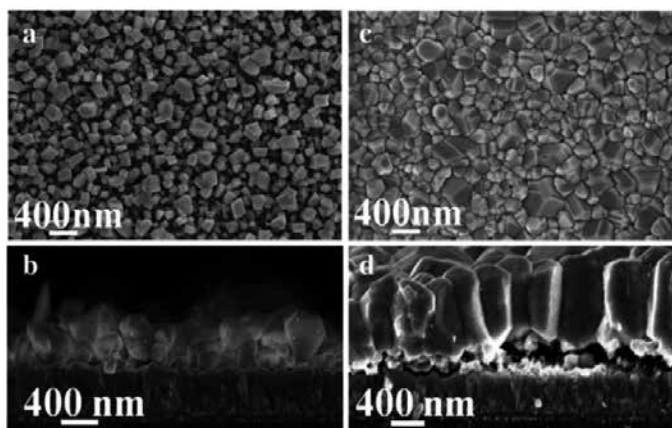


Figure 20. FESEM micrographs of the top view and cross section of films obtained from PYR14TFSI (a and b) and isopropanol (c and d)-based media.

2.3. Electroredox

Mourada et al. [41] described the biredox ionic liquid electrolytes in which both anion and cation are functionalized with anthraquinone and 2,2,6,6-tetramethylpiperidiny-1-oxyl (TEMPO) groups, respectively (**Figure 21**). At the same time, they carried out the in-depth investigations based on crossed experimental and theoretical studies to elucidate how the bulkiness of ions bearing a redox moiety impacted electron and mass transfers and accordingly the efficiency of electrochemical devices. In such redox species, the electron transfer was not governed by the overall size of the solvated redox species, which took preferential orientation toward the surface.

Yoo et al. [42] investigated the electrical performance of a Li-air cell with ionic liquid electrolytes operating at high temperature. A continuum-based model was used to quantify the performance of the Li-air cell, with an ionic liquid (MPPY-TFSI) electrolyte as a function of operating temperature (**Figure 22**). The molecular dynamics (MD) simulations indicated that oxygen solubility in ionic liquid increases with temperature, which is very favorable for high-

temperature operation. The continuum-based cell level simulation results showed that the battery performance can be improved significantly by increasing operating temperature. Simulation results also revealed that by increasing the operating temperature, the specific capacity can be improved significantly for high load current density. They also investigated the effect of different temperatures on the performance of Li-air battery, and the results showed that the transport limitation of oxygen and lithium ions could be alleviated at higher temperatures.

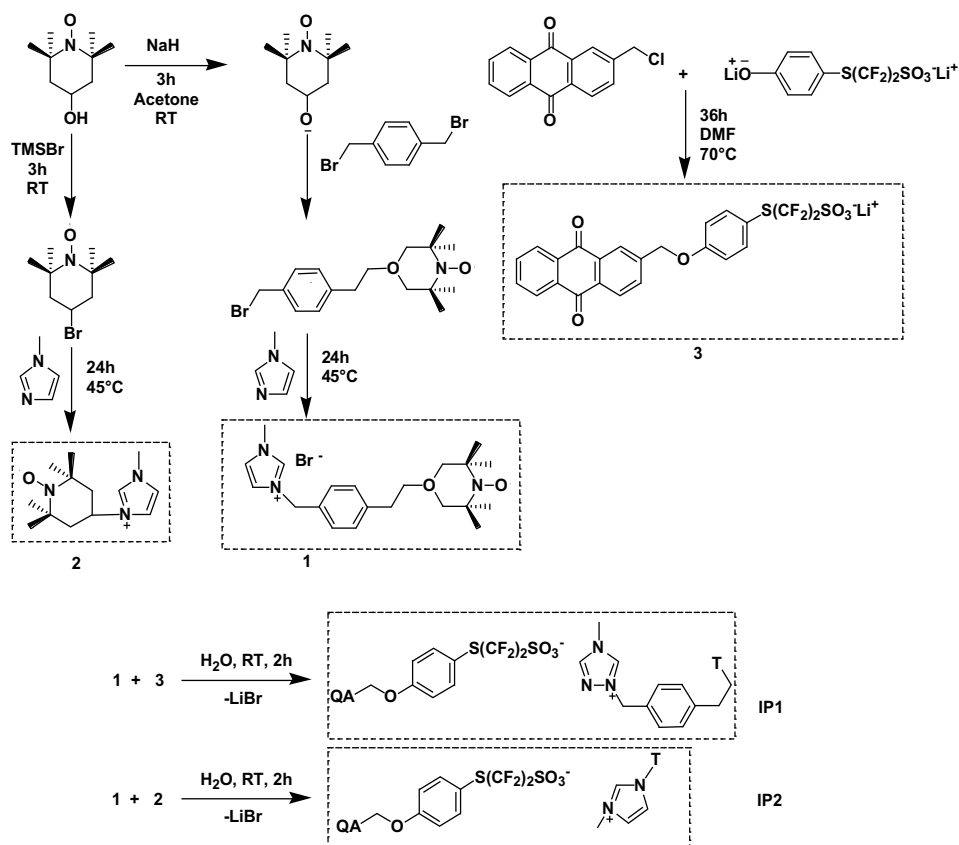


Figure 21. Synthesis route to obtain redox cationic and anionic species for the biredox ILs named IP1 and IP2. QA and T denote the anthraquinone and TEMPO moiety, respectively.

Ueda et al. [43] investigated the electrochemical stability of a fullerene (C_{60}) thin film supported on Au(1 1 1) in an ionic liquid electrolyte $[C_4mpyrr][Tf_2N]$ (**Figure 23**). The obtained result indicated that the dissolution of the C_{60} film was caused by cation insertion and accelerated by the generation of multiple redox states of C_{60}^{n-} ($n = 1 - 6$) during the continuous scans. The redox states of C_{60} in $[C_4mpyrr][Tf_2N]$ could be clearly controlled by the scan rate and temperature.

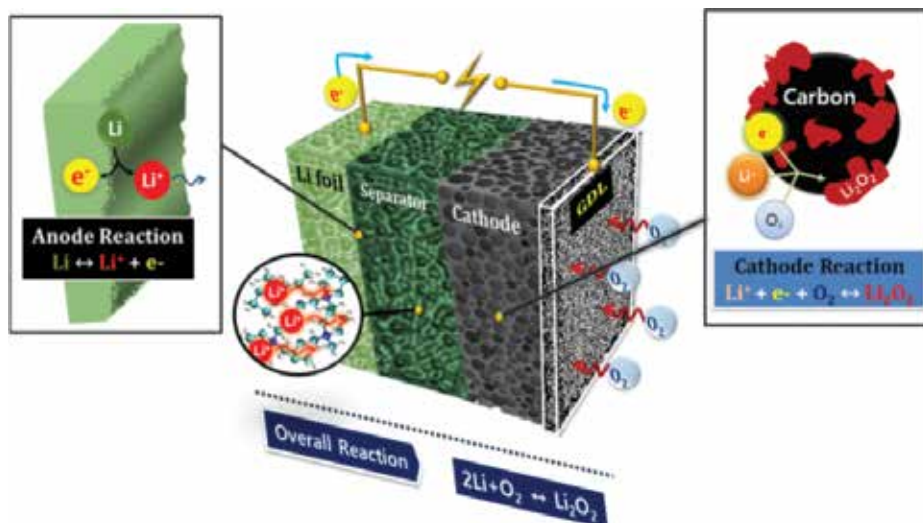


Figure 22. Illustration of Li-air battery with corresponding electrochemical reactions at anode and cathode side.

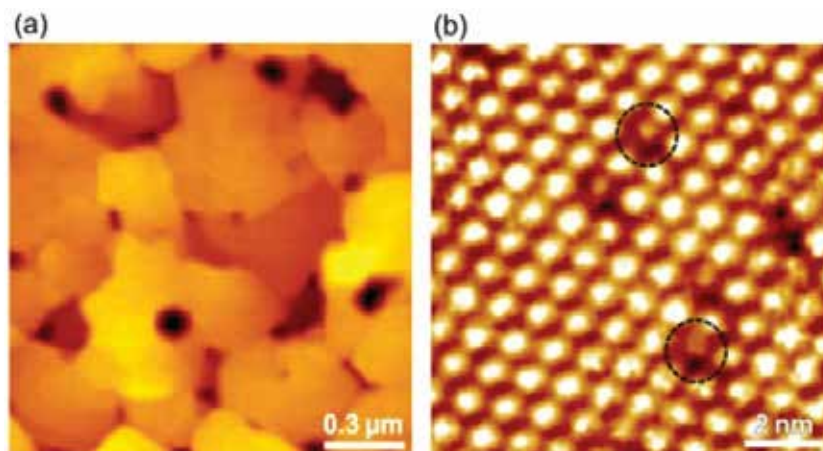


Figure 23. (a) AFM image ($1.5 \times 1.5 \mu\text{m}^2$) and (b) high-resolution STM image ($10 \times 10 \text{nm}^2$) of C_{60} -deposited Au/mica surface. Note that STM image was obtained under electrochemical condition in 0.1 M HClO_4 .

Sonkaria et al. [44] carried out the ionic liquid-induced synthesis of a graphene intercalated ferrocene nanocatalyst (**Figure 24**), which was the first demonstration approach for the assembly of ferrocene in ionic liquids. Hooshyari et al. [45] prepared two types of innovative composite membranes based on polybenzimidazole (PBI) containing dicationic ionic liquid PDC_3 and monocationic ionic liquid PMC_6 as electrolyte for high-temperature fuel cell applications under anhydrous conditions (**Figure 25**). The analyses of results displayed high proton conductivity and thermal stability. Moreover, the fuel cell performance of PA doped PDC_3 composite membranes was enhanced at high temperatures.

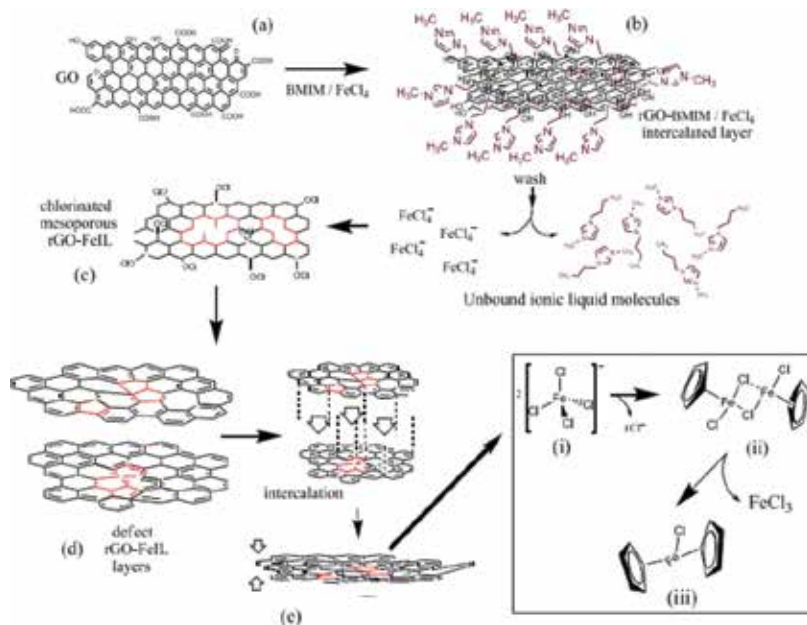


Figure 24. Chemical events between rGO and FeII leading to the intercalation of Fe at defect positions (shown in red) stabilized by a ferrocene/ferrocenyl configuration.

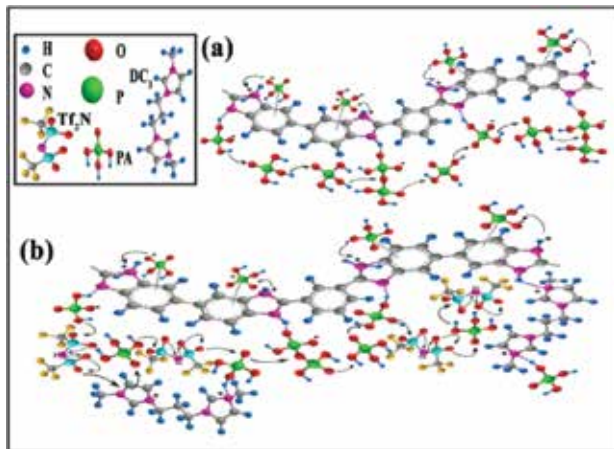


Figure 25. Schemes of the proton transport mechanism for (a) PA-PBI and (b) PPDC_{3x} membranes.

Ueda et al. [46] investigated the control of the redox states of highly charged C₆₀ anions in two ionic liquids (ILs) (**Figure 26**). The results showed that highly charged reduced states of C₆₀⁵⁻ and C₆₀⁶⁻ could be produced and detected at room temperature by using an electrochemical interface between a multilayered C₆₀ adlayer on a Au(1 1 1) electrode and N-butyl-N-methyl-

pyrrolidinium-based IL, whereas a tributylmethylammonium-based IL provided less than four redox waves of C_{60} . The results of the present study suggested that both a wide potential window and the interaction between C_{60} anions and IL cations are important for controlling the multiple redox states of C_{60} at room temperature.

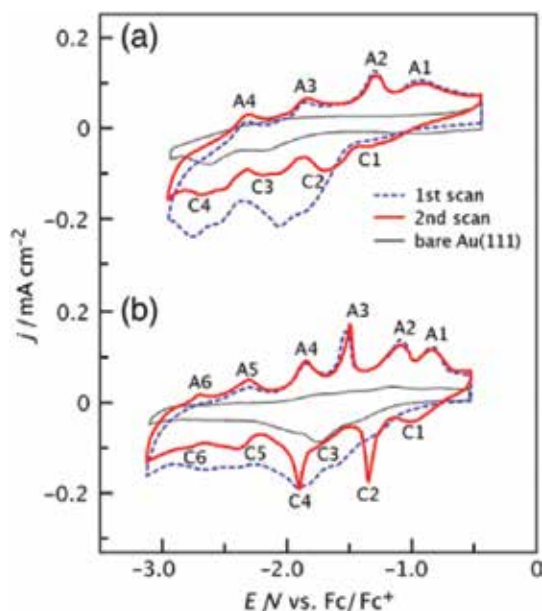


Figure 26. Typical cyclic voltammograms of a clean Au(1 1 1) electrode (gray line) and a C_{60} -modified Au(1 1 1) electrode obtained in [TFSI]⁻-based ILs with (a) $[N_{1,4,4,4}]^+$ and (b) $[C_4\text{mpyr}]^+$, respectively, at 25 °C. The blue dotted and red solid lines indicate the first and second scans, respectively, of the C_{60} -modified Au(1 1 1) single-crystal electrode. The scan rate was 0.5 V s⁻¹.

Fu et al. [47] presented a spontaneous vertical phase separation (SVPS) self-assembled bilayers structure with BenMeIm-Cl ionic liquid (IL) interfacial bottom layer and a photoactive top layer via a single spin-coated step of BenMeIm-Cl IL and organic donor-acceptor composite and achieved a PCE as high as 8% based on IPSCs with PTB7 as the donor (**Figure 27**). The presence of BenMeIm-Cl IL reduced the work function of ITO and led to a better energy-level matching for efficient charge transfer. The driving force of SVPS self-assembled structure was from the relative surface energy difference between organic materials and BenMeIm-Cl ILs, together with their interactions with the substrates. This self-assembled process procedure paved the way to simplify the manufacturing of low-cost and large-area organic electronic devices. Chen et al. [48] studied the metal binary sulfides (TiS_2 , FeS_2), in either powder or thin film forms, Li insertion electrodes for rechargeable lithium batteries. They exploited the equilibrium solubility of molecular sulfur into ionic liquids at its melting point (120°C), to prepare thin films of both Co_9S_8 and FeS_x (**Figure 28**). The researchers demonstrated that the growth of Co_9S_8 films involved the reaction of soluble sulfur with the electrodeposited Co metallic layer.

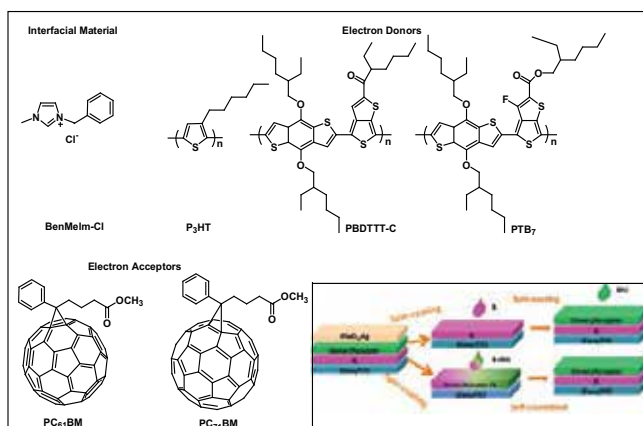


Figure 27. Chemical structures of BenMeIm-Cl IL and BHJ materials.

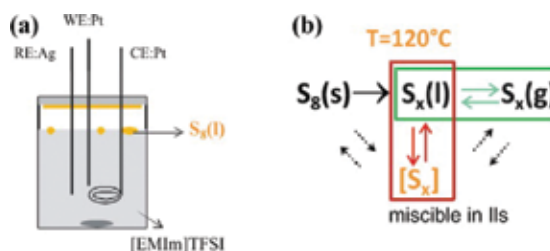


Figure 28. (a) Schematic setup of sulfur in the electrochemical cell and (b) possible equilibria of different phases of sulfur in [EMIm]TFSI.

2.4. Other applications

Viaua et al. [49] studied the electropolymerization of pyrrole films in three room-temperature ionic liquids: bmim-PF₆, emim-TFSA, and bmp-TFSA (**Figure 29**). The experimental results showed that the difference of activity from one polymer film to the other was mainly attributed to the difference of viscosity between the solvents used. Li et al. [50] prepared the composite films of poly(3,4-ethylenedioxythiophene) (PEDOT) doped with various functional ionic liquids by electropolymerization process on indium-doped tin oxide (ITO) conducting glasses (**Figure 30**). The ITO glasses coated with the composite films were used as the counter electrodes in dye-sensitized solar cells, and various imidazolium cations with different alkyl chains and anions were used as the ionic liquids. Palombi et al. [51] investigated the double electrosynthesis of 3-((4S)-benzyl-2-oxo-oxazolidin-3-carbonyl)-heptane-2,6-dione (2a) at the cathodic and anodic compartments of a divided glass cell in ionic liquid [Emim]BF₄ (**Figure 31**). In this electrolysis, ionic liquid played the role of solvent/electrolyte system for the cathodically initiated reaction and electrolyte/pre-catalyst for the anodic one. Dong et al. [52] synthesized the monodisperse poly(ionic liquid) particles for use as high-performance

anhydrous polyelectrolyte-based smart electrorheological materials (**Figure 32**). The results showed that the ionic liquid particles possessed strong electrorheological effect in dry state and the electrorheological effect depended on the size of cation/anion parts.

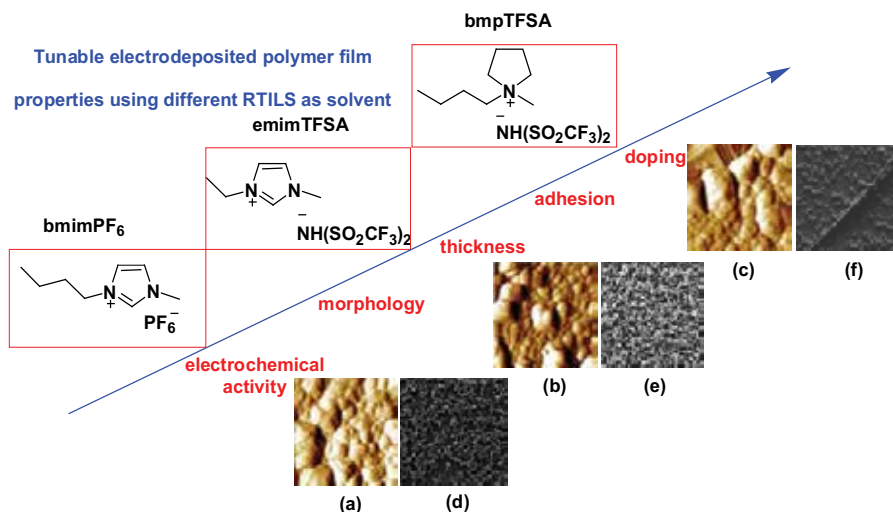


Figure 29. AFM images of PPy-bmim-PF₆ (a), PPy-emim-TfSA (b), and PPy-bmp-TfSA (c). SEM images of PPy-bmim-PF₆ (d), PPy-emim-TfSA (e), and PPy-bmp-TfSA (f).

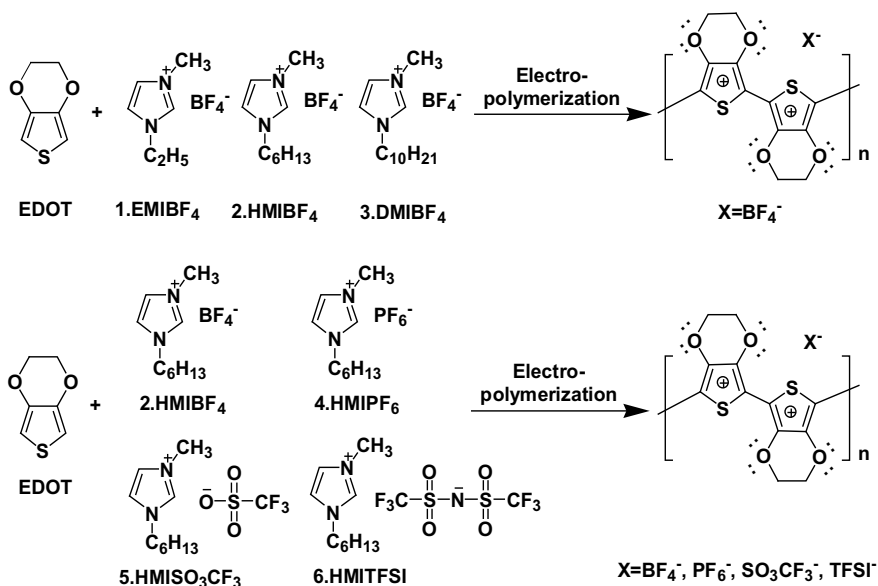


Figure 30. Illustrative electropolymerization process for the PEDOT counter electrodes (a) doped with various alkyl chains in imidazolium cations and (b) doped with different anions.

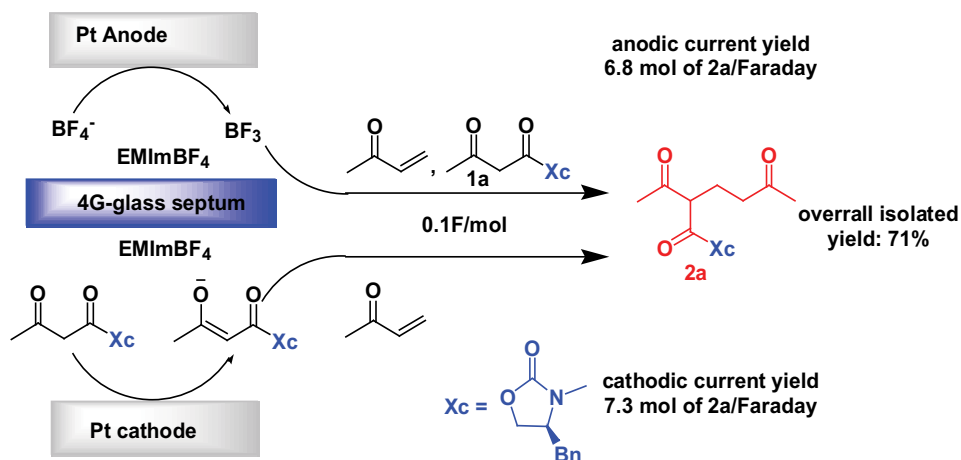


Figure 31. Synthesis of Michael adduct 2a by paired electrolysis in BF_4 -based ionic liquid.

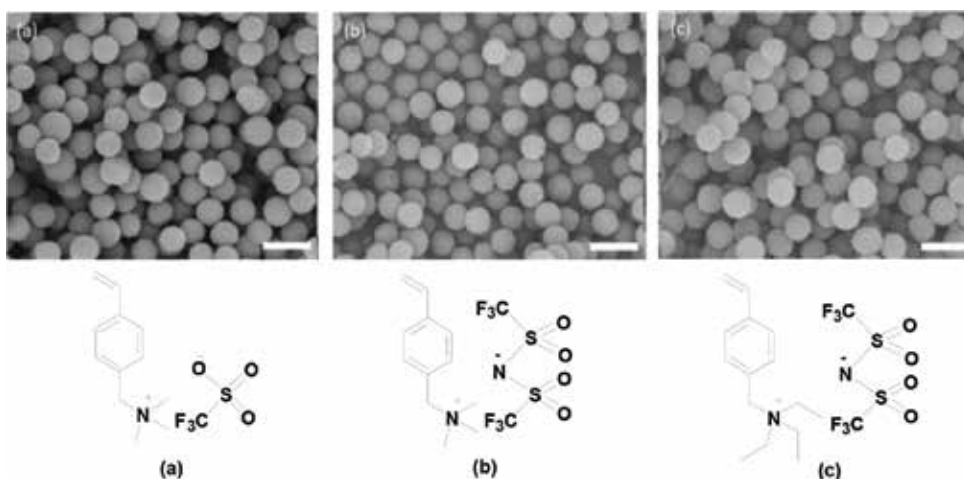


Figure 32. The SEM images of PIL particles: (a) poly(VBTMA $^+$ CF $_3$ SO $_3^-$), (b) poly(VBTMA $^+$ (CF $_3$ SO $_2$) $_2$ N $^-$), and (c) poly(VBTEA $^+$ (CF $_3$ SO $_2$) $_2$ N $^-$).

Kaminski et al. [53] presented an innovative methodology for a liquid-liquid extraction process based on an electrically induced emulsion of ionic liquid 1-[bmim][MeSO $_4$] as the extracting solvent dispersed in an organic mixture (Figure 33), and this liquid-liquid extraction provided an environmentally friendly process as an alternative to azeotropic distillation. Martínez et al. [54] studied the performance of terracotta separators modified with the same ionic liquid [Emim][NTf $_2$], neat, and also mixed with PTFE binder (Figure 34). They found the operational limitations when the IL was integrated in the ceramic separator, there was a significant enhancement of the MFC performance when added as part of the activated layer mixture of the cathode. Najafabadi and Gyenge [55] reported the simultaneous anodic and cathodic GN

production in two types of electrochemical cells in aprotic ionic liquid electrolytes (Figure 35). They demonstrated a synergistic exfoliation effect when the iso-molded graphite anode and cathode were subjected to a constant cell potential, generating up to three times higher exfoliation yields than single electrode studied on each side.

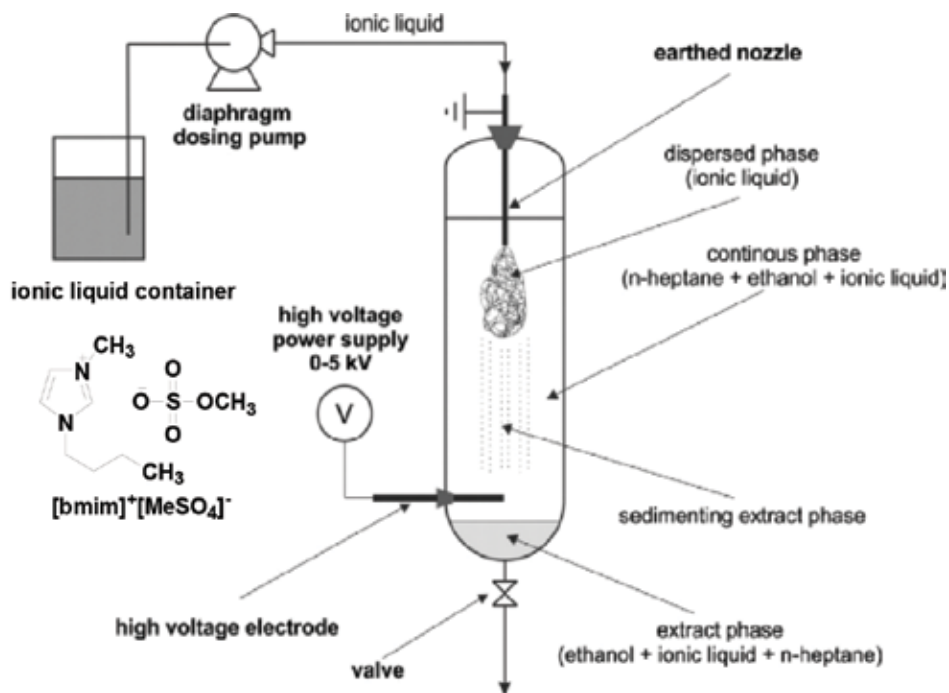


Figure 33. Scheme of the general experimental arrangement.

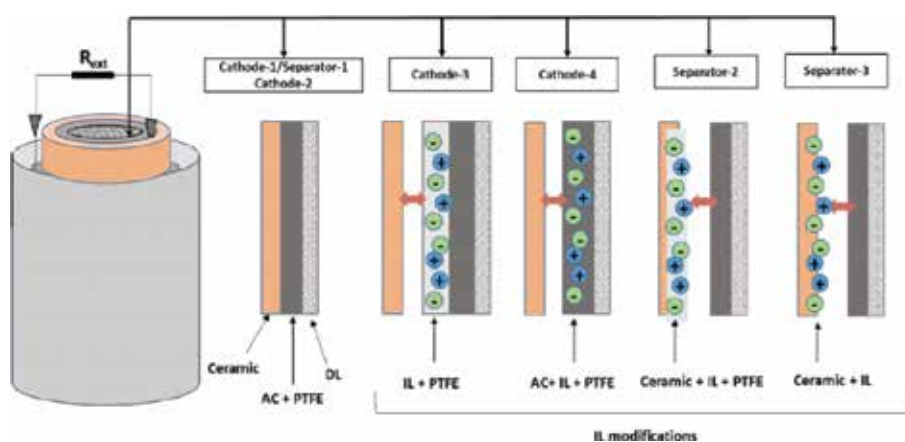


Figure 34. Configuration of the cathodes and the separators.

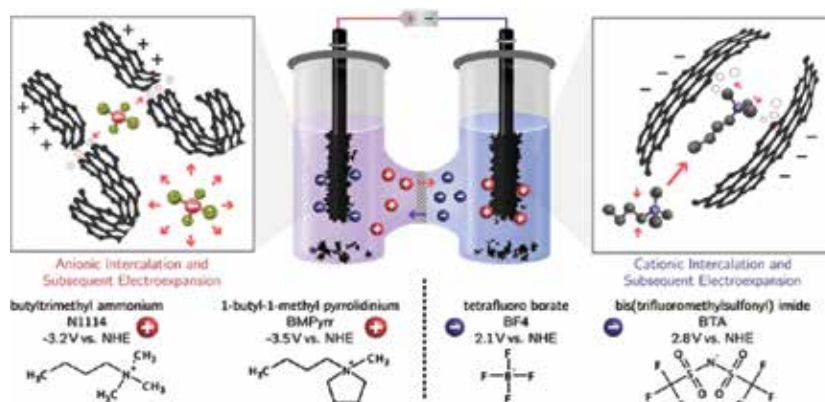


Figure 35. Electro-exfoliation of graphitic anodes and cathodes in ionic liquids.

3. Conclusions

In summary, a remarkable amount of progress has been made in recent years in the field of electrocatalysis in the presence of ionic liquids. Despite the impressive progress, a number of challenges still remain: the current studies mainly focus on the applications of ILs while lacking of systematicness in its theoretical research. There is absolutely a need for the search of inherent structures, purity, distribution, and orientation of ILs at electrode interface. We do believe that ionic liquids as a green solvent, which is expected to replace the water, organic solvents, and molten salt, will play a greater role in electrocatalytic system.

Author details

Yu Lin Hu

Address all correspondence to: huyulin1982@163.com

College of Materials and Chemical Engineering, China Three Gorges University, Yichang, PR China

References

- [1] H. Karkhanechi, S. Salmani, and M. Asghari, "A Review on Gas Separation Applications of Supported Ionic Liquid Membranes," *ChemBioEng Reviews*, vol. 2, pp. 290–302, 2015.

- [2] S. Zahn, G. Bruns, J. Thar, and B. Kirchner, "What Keeps Ionic Liquids in Flow?" *Physical Chemistry Chemical Physics*, vol. 10, pp. 6921–6924, 2008.
- [3] Z. Lei, C. Dai, and Bi. Chen, "Gas Solubility in Ionic Liquids," *Chemical Reviews*, vol. 114, pp. 1289–1326, 2014.
- [4] H.W. Gao, M.Y. Xi, L. Xu, and W. Sun, "Sensitive Determination of ATP using a Carbon Paste Electrode Modified with a Carboxyl Functionalized Ionic Liquid," *Microchimica Acta*, vol. 174, pp. 115–122, 2011.
- [5] H.W. Gao, M.Y. Xi, X.W. Qi, M. Lu, T.R. Zhan, and W. Sun, "Application of a Hydroxyl Functionalized Ionic Liquid Modified Electrode for the Sensitive Detection of Adenosine-5'-Monophosphate," *Journal of Electroanalytical Chemistry*, vol. 664, pp. 88–93, 2012.
- [6] M.J.A. Shiddiky, and A.A.J. Torriero, "Application of Ionic Liquids in Electrochemical Sensing Systems," *Biosensors and Bioelectronics*, vol. 26, pp. 1775–1787, 2011.
- [7] A. Bard, and L.R. Faulkner, "Electrochemical Methods. Fundamentals and Applications," John Wiley & Sons, New York, 2001.
- [8] F. Endres, "Ionic Liquids: Solvents for the Electrodeposition of Metals and Semiconductors," *ChemPhysChem*, vol. 3, pp. 144–154, 2012.
- [9] M. Armand, F. Endres, D.R. MacFarlane, H. Ohno, and B. Scrosati, "Ionic-Liquid Materials for the Electrochemical Challenges of the Future," *Nature Materials*, vol. 8, pp. 621–629, 2009.
- [10] P. Simon, and Y. Gogotsi, "Materials for Electrochemical Capacitors," *Nature Materials*, vol. 7, pp. 845–854, 2008.
- [11] D.R. MacFarlane, J.M. Pringle, P.C. Howlett, and M. Forsyth, "Ionic Liquids and Reactions at the Electrochemical Interface," *Physical Chemistry Chemical Physics*, vol. 12, pp. 1659–1669, 2010.
- [12] H. Liu, Y. Liu, and J. Li, "Ionic Liquids in Surface Electrochemistry," *Physical Chemistry Chemical Physics*, vol. 12, pp. 1685–1697, 2010.
- [13] A. Halder, M.W. Zhang, and Q.J. Chi, "Electrocatalytic Applications of Graphene–Metal Oxide Nanohybrid Materials," *In Advanced Catalytic Materials: Photocatalysis and Other Current Trends*, Chapter 14, InTech Open Access Publishers, 2016, pp. 379–413.
- [14] J.Y. Wu, Y.Q. Miao, X.C. Liang, Z.Y. Yang, Y. Yang, and R.Z. Ouyang "Promotion Effect of Bismuth on Nickel Electrodeposition and Its Electrocatalysis to Glucose Oxidation," *Electroanalysis*, vol. 26, pp. 856–863, 2014.
- [15] F. Sun, L. Li, P. Liu, and Y.F. Lian, "Nonenzymatic Electrochemical Glucose Sensor Based on Novel Copper Film," *Electroanalysis*, vol. 23, pp. 395–401, 2011.

- [16] H. Yu, J. Jin, X. Jian, Y. Wang, and G.C. Qi, "Preparation of Cobalt Oxide Nanoclusters/Overoxidized Polypyrrole Composite Film Modified Electrode and Its Application in Nonenzymatic Glucose Sensing," *Electroanalysis*, vol. 25, pp. 1665–1674, 2013.
- [17] B.Z. Liu, B. Xiao, and L.Q. Cui, "Electrochemical Analysis of Carbaryl in Fruit Samples on Graphene Oxide-Ionic Liquid Composite Modified Electrode," *Journal of Food Composition and Analysis*, vol. 40, pp. 14–18, 2015.
- [18] M.M. Rahman, H.M. Marwania, A.A. Alshehrib, H.A. Albar, J. Bisquertc, and A.M. Asiria, "Room Temperature Stable ClPrNTf₂ Ionic Liquid Utilizing for Chemical Sensor Development," *Journal of Organometallic Chemistry*, vol. 811, pp. 74–80, 2016.
- [19] N.F. Atta, E.H. El-Ads, Y.M. Ahmed, and A. Galal, "Determination of Some Neurotransmitters at Cyclodextrin/Ionic Liquid Crystal/Graphene Composite Electrode," *Electrochimica Acta*, vol. 199, pp. 319–331, 2016.
- [20] C.L. Yu, N.C. Lo, H. Cheng, T. Tsuda, T. Sakamoto, Y.H. Chen, S. Kuwabata, and P.Y. Chen, "An Ionic Liquid-Fe₃O₄ Nanoparticles-Graphitecomposite Electrode Used for Nonenzymatic Electrochemical Determination of Hydrogen Peroxide," *Journal of Electroanalytical Chemistry*, vol. 729, pp. 109–115, 2014.
- [21] W.S. He, Y.M. Sun, J.B. Xi, A.A.M. Abdurhman, J.H. Ren, H.W. Duan, "Printing Graphene-Carbon Nanotube-Ionic Liquid Gel on Graphene Paper: Towards Flexible Electrodes with Efficient Loading of PtAu Alloy Nanoparticles for Electrochemical Sensing of Blood Glucose," *Analytica Chimica Acta*, vol. 903, pp. 61–68, 2011.
- [22] H. Okuzaki, S. Takagi, F. Hishiki, and R. Tanigawa, "Ionic Liquid/Polyurethane/PEDOT: PSS Composites for Electro-Active Polymer Actuators," *Sensors and Actuators B*, vol. 194, pp. 59–63, 2014.
- [23] J.F. Xia, X.Y. Cao, Z.H. Wang, M. Yang, F.F. Zhang, B. Lu, F. Li, L. Xia, Y.H. Li, and Y.Z. Xia, "Molecularly Imprinted Electrochemical Biosensor Based on Chitosan/Ionic Liquid-graphene Composites Modified Electrode for Determination of Bovine Serum Albumin," *Sensors and Actuators B*, vol. 225, pp. 305–311, 2016.
- [24] P.N. Zhao, and J.C. Hao, "2,6-Diaminopyridine-Imprinted Polymer and Its Potency to Hair-Dye Assay Using Graphene/Ionic Liquid Electrochemical Sensor," *Biosensors and Bioelectronics*, vol. 64, pp. 277–284, 2015.
- [25] C.H. Wang, C.H. Yang, and J.K. Chang, "High-Selectivity Electrochemical Non-Enzymatic Sensors Based on Graphene/Pd Nanocomposites Functionalized with Designated Ionic Liquids," *Biosensors and Bioelectronics*, in press, doi:10.1016/j.bios.2016.03.071.
- [26] L.C. Chen, D.J. Huang, Y.J. Zhang, T.Q. Dong, C. Zhou, S.Y. Ren, Y.W. Chi, and G.N. Chen, "Ultrasensitive GaseousNH₃Sensor Based onIonic Liquid- mediated Signal-on Electrochemiluminescence," *Analyst*, vol. 137, pp. 3514–3519, 2012.

- [27] B.H.R. Suryanto, C.A. Gunawan, X.Y. Lu, and C. Zhao, "Tuning the Electrodeposition Parameters of Silver to Yield Micro/Nano Structures from Room Temperature Protic Ionic Liquids," *Electrochimica Acta*, vol. 81, pp. 98–105, 2012.
- [28] Rudolf, "Holze Electrodeposition from Ionic Liquids". F. Endres, A.P. Abbott, and D.R. MacFarlane (Eds). Wiley-VCH, Weinheim, 2008, vol. 13, pp. 1633–1634, 2009.
- [29] D. Grujicic, B. Pesic, "Electrodeposition of Copper: The Nucleation Mechanisms," *Electrochimica Acta*, vol. 47, pp. 2901–2912, 2002.
- [30] M. Galova, "M. Schlesinger, M. Paunovic (Eds). Modern Electroplating, 4th ed. Wiley, New York, pp. 848, 2000.
- [31] A.P. Abbott, and K.J. McKenzie, "Application of Ionic Liquids to the Electrodeposition of Metals," *Physical Chemistry Chemical Physics*, vol. 8, pp. 4265, 2006.
- [32] P. Martis, V.S. Dilimon, J. Delhalle, and Z. Mekhalif, "Electro-generated Nickel/Carbon Nanotube Composites in Ionic Liquid," *Electrochimica Acta*, vol. 55, pp. 5407–5410, 2010.
- [33] M. Mascia, A. Vacca, L. Mais, S. Palmas, E. Musu, and F. Delogu, "Electrochemical Deposition of Cu and Nb from Pyrrolidinium Based Ionic Liquid," *Thin Solid Films*, vol. 571, pp. 325–331, 2014.
- [34] A. Izgorodin, R. Hocking, O. Winther-Jensen, M. Hilder, B. Winther-Jensen, "Phosphorylated Manganese Oxide Electrodeposited from Ionic Liquid as a Stable, High Efficiency Water Oxidation Catalyst," *Catalysis Today*, vol. 200, pp. 36–40, 2013.
- [35] A. Serrà, E. Gómez, I.V. Golosovsky, J. Nogués, and E. Vallés, "Effective Ionic-liquid Microemulsion Based Electrodeposition of Mesoporous Co-Pt Films for Methanol Oxidation Catalysis in Alkaline Media," *Journal of Materials Chemistry A*, vol. 4, pp. 7805–7814, 2016.
- [36] A. Bakkar, and V. Neubert, "A New Method for Practical Electrodeposition of Aluminium from Ionic Liquids," *Electrochemistry Communications*, vol. 51, pp. 113–116, 2015.
- [37] F. Hekmata, B. Sohrabi, M.S. Rahmanifar, and A. Jalali, "Electrophoretic Deposition of Multi-walled Carbon Nanotubes on Porous Anodic Aluminum Oxide Using Ionic Liquid as a Dispersing Agent," *Applied Surface Science*, vol. 341, pp. 109–119, 2015.
- [38] S. Caporali, P. Marcantelli, C. Chiappe, and C.S. Pomelli, "Electrodeposition of Transition Metals from Highly Concentrated Solutions of Ionic Liquids," *Surface & Coatings Technology*, vol. 264, pp. 23–31, 2015.
- [39] A. Abebe, S. Admassie, I.J. Villar-Garcia, and Y. Chebude, "4,4-Bipyridinium Ionic Liquids Exhibiting Excellent Solubility for Metal Salts: Potential Solvents for Electrodeposition," *Inorganic Chemistry Communications*, vol. 29, pp. 210–212, 2013.
- [40] I. Kosta, E. Azaceta, L. Yate, G. Cabañero, H. Grande, and R. Tena- Zaera, "Cathodic Electrochemical Deposition of CuI from Room Temperature Ionic Liquid-based Electrolytes," *Electrochemistry Communications*, vol. 59, pp. 20–23, 2015.

- [41] E. Mourada, L. Coustana, S.A. Freunberger, A. Mehd, A. Viouxa, F. Favier, and O. Fontainea, "Biredox Ionic Liquids: Electrochemical Investigation and Impact of Ion Size on Electron Transfer," *Electrochimica Acta*, vol. 206, pp. 513–523, 2016.
- [42] K. Yoo, A.M. Dive, S. Kazemiabnavi, S. Banerjee, and P. Dutta, "Effects of Operating Temperature on the Electrical Performance of a Li-air Battery Operated with Ionic Liquid Electrolyte," *Electrochimica Acta*, vol. 194, pp. 317–329, 2016.
- [43] H. Ueda, K. Nishiyama, and S. Yoshimoto, "Electrochemical Stability of C₆₀ Thin Film Supported on a Au(111) Electrode at a Pyrrolidinium-based Ionic Liquid Interface," *Electrochimica Acta*, vol. 210, pp. 155–162, 2016.
- [44] S. Sonkaria, H.-T. Kim, S.Y. Kim, N. Kumari, Y.G. Kim, V. Khare, and S.H. Ahn, "Ionic Liquid-Induced Synthesis of a Graphene Intercalated Ferrocene Nanocatalyst and its Environmental Application," *Applied Catalysis B: Environmental*, vol. 182, pp. 326–335, 2016.
- [45] K. Hooshyari, M. Javanbakht, and M. Adibi, "Novel Composite Membranes Based on PBI and Dicationic Ionic Liquids for High Temperature Polymer Electrolyte Membrane Fuel Cells," *Electrochimica Acta*, vol. 205, pp. 142–152, 2016.
- [46] H. Ueda, K. Nishiyama, and S. Yoshimoto, "Multiple Redox State Control of Fullerene at Room Temperature Through Interfacial Electrochemistry of Ionic Liquids," *Electrochemistry Communications*, vol. 43, pp. 102–104, 2014.
- [47] P. Fu, L.Q. Huang, W. Yua, D. Yang, G.J. Li, L.Y. Zhou, J. Zhang, and C. Li, "Efficiency Improved for Inverted Polymer Solar Cells with Electrostatically self-assembled BenMeIm -Cl Ionic Liquid Layer as Cathode Interface Layer," *Nano Energy*, vol. 13, pp. 275–282, 2015.
- [48] Y.H. Chen, J.M. Tarascon, and C. Guéry, "Exploring Sulfur Solubility in Ionic Liquids for the Electrodeposition of Sulfide Films with Their Electrochemical Reactivity Toward Lithium." *Electrochimica Acta*, vol. 99, pp. 46–53, 2013.
- [49] L. Viaua, J.Y. Hihna, S. Lakarda, V. Moutarlier, V. Flaudb, and B. Lakarda, " Full Characterization of Polypyrrole Thin Films Electrosynthesized in Room Temperature Ionic Liquids, Water or Acetonitrile," *Electrochimica Acta*, vol. 137, pp. 298–310, 2014.
- [50] C.T. Li, C.P. Leea, M.S. Fana, P.Y. Chen, R. Vittal, K.C. Ho, "Ionic Liquid-Doped Poly(3,4-ethylenedioxythiophene) Counter Electrodes for Dye- Sensitized Solar Cells: Cationic and Anionic Effects on the Photovoltaic Performance," *Nano Energy*, vol. 9, pp. 1–14, 2014.
- [51] L. Palombi, "A Study on Designing a Paired Electrolysis for Electro-induced Michael Addition Using Tetrafluoroborate-Based Ionic Liquid as Electrolysis Medium and Pre-Catalyst in a Divided Cell," *Electrochimica Acta*, vol. 56, pp. 7442–7445, 2011.
- [52] Y.Z. Dong, J.B. Yin, J.H. Yuan, and X.P. Zhao "Microwave-Assisted Synthesis and High-performance Anhydrous Electrorheological Characteristic of Monodisperse Poly(Ionic

- Liquid) Particles with Different Size of Cation/Anion Parts," *Polymer*, vol. 97, pp. 408–417, 2016.
- [53] K. Kaminski, M. Krawczyk, J. Augustyniak, L.R. Weatherley, J. Petera, Electrically Induced Liquid-Liquid Extraction from Organic Mixtures with the Use of Ionic Liquids. *Chemical Engineering Journal*, vol. 235, pp. 109–123, 2014.
- [54] V.M. Ortiz-Martínez, I. Gajda, M.J. Salar-García, J. Greenman, F.J. Hernández- Fernández, and I. Ieropoulos, "Study of the Effects of Ionic Liquid-Modified Cathodes and Ceramic Separators on MFC Performance," *Chemical Engineering Journal*, vol. 291, pp. 317–324, 2016.
- [55] A.T. Najafabadi, and E. Gyenge, "Synergistic Production of Graphene Microsheets by Simultaneous Anodic and Cathodic Electro-exfoliation of Graphitic Electrodes in Aprotic Ionic Liquids," *Carbon*, vol. 84, pp. 449–459, 2015.

Purification of Rare Earth Amide Salts by Hydrometallurgy and Electrodeposition of Rare Earth Metals Using Ionic Liquids

Masahiko Matsumiya

Additional information is available at the end of the chapter

<http://dx.doi.org/10.5772/66300>

Abstract

This paper reports a novel bench-scale hydrometallurgical procedure and electrodeposition using triethyl-pentyl-phosphonium bis(trifluoromethyl-sulfonyl)amide ([P₂₂₂₅][TFSA]) ionic liquids (ILs) for the recovery of rare earth (RE) metals from spent Nd-Fe-B magnets. The hydrometallurgical treatments were carried out at bench scale to produce RE amide salts of high purity. In the leaching process employing 1.7 kg of oxidized Nd-Fe-B fine powder and 14.2 L of an acid medium of 1,1,1-trifluoro-*N*-[(trifluoromethyl)sulfonyl]methanesulfonamide (H[TFSA]), selective leaching of RE ions (85.7±5.8% Nd) was performed at bench scale. Then, Fe (<99.9%) was successfully separated from RE ions in the deionization process. The total amount of the recovered amide salts through the evaporation treatment using a spray dryer was 3.57 kg. From the CV/EQCM measurements for Nd(III) at 373 K, a clear cathodic peak with the mass increased, and the $\eta\rho$ decreased was observed at -2.79 V. Considering our previous investigations, the reduction of Nd(III)/Nd(0) was indicated as $[\text{Nd}^{\text{III}}(\text{TFSA})_5]^{2-} + 3e^- \rightarrow \text{Nd}(0) + 5[\text{TFSA}]^-$. In addition, the M_{app} value in the range of -2.49 V ~ -2.94 V was 46.8 g mol⁻¹, which was close to the theoretical value for the electrodeposition reaction of Nd(III)/Nd(0), 48.1 g mol⁻¹. Moreover, the electrodeposition of Nd(0) was carried out under the condition of -3.20 V versus Fc/Fc⁺ at 373 K. The electrodeposits were identified with the metallic Nd in the middle layer investigated by X-ray diffraction and X-ray photoelectron spectroscopy. Finally, we demonstrated that the novel recovery process consisted of hydrometallurgy and electrodeposition using ILs was effective by calculating material flow.

Keywords: electrodeposition, hydrometallurgy, ionic liquids, neodymium metal

1. Introduction

Rare earth (RE) elements are currently regarded to be the most critical elements necessary for sustainable applications, and their RE groups play an important role in the development of future high-tech industries. Significant price fluctuations and high demand have raised their potential recovery from end-of-life products [1]. It is important to recover them from urban mining and secondary products containing permanent magnets.

Hydrometallurgical treatment is widely applied as an effective method for extracting RE components from primary sources and is potential in reclaiming these elements [2]. As listed in **Table 1**, the various techniques effective for the recovery of RE elements, such as chemical vapor transport [3], solvent extraction [4], electrolytic method [5], and hydrometallurgical processes [6, 7], have been listed, although a number of recovery methods for RE elements on the laboratory scale have not been so widespread. There was almost no information about the plants and processing paths. From the above situation, this study focused on a bench-scale hydrometallurgy to separate and recover RE components from spent Nd-Fe-B magnet. The preliminary research in our procedure is reported in the previous publications [8, 9].

Methods	Remarks	Reference
Chemical vapor transport	59% Nd and 68% Dy were recovered from scrap of RE intermetallic materials.	[3]
Solvent extraction and liquid-membrane transport	The selective permeation of Nd and Dy by IL based supported liquid-membrane using <i>N,N</i> -dioctyldiglycolamic acid.	[4]
Electrolysis	Polarization on Pt electrode led to recover Nd and Dy metals in fused Na ₂ SO ₄ from Nd and Dy oxides	[5]
Electrochemical process	Mass ratio between Nd and Dy was indicated as 121 from RE-Ni alloys	[6]
Hydrometallurgical process	The recovery efficiencies were indicated as 69.7% Nd and 51% Dy from magnetic waste sludge	[7]

Table 1. Various recovery techniques for rare earths.

Pyrometallurgical treatment using high-temperature molten salts (HTMSs) is generally known as a conventional method for the recovery of RE metals. However, the HTMSs such as fluorides [10, 11] consumes a large amount of thermal energy owing to the high melting points of molten salts; thus, the recovery method of RE metals from HTMS baths is inappropriate as a next-generation technique. From the standpoint of saving energy, the development of a recovery process for RE metals with reduced energy consumption is hopeful in the near future. For this purpose, we have proposed an electrowinning-recovery method of the REs using ILs, which have unique physicochemical properties, such as high ionic conductivity, a wide electrochem-

ical window, low vapor pressure, and incombustibility [12]. The electrochemical behaviors and the electrodepositions of RE metals such as La, Sm, Eu, and Yb in ILs are reported [13, 14]. We have already demonstrated the electrochemical behaviors and the electrodepositions of Nd [15–18] and Dy metals [19, 20] using hydrophobic ILs, such as triethyl-pentyl-phosphonium bis(trifluoromethyl-sulfonyl) amide [P_{2225}][TFSA] and 2-hydroxyethyl-trimethyl-ammonium bis(trifluoromethyl-sulfonyl) amide [$N_{1112}OH$][TFSA]. In addition, we have developed the wet separation processes such as the solvent extraction using the hydrophobic ILs [21–23] and the precipitation separation [8, 9]. The wet separation process was combined with the electrodeposition for the recovery of the Nd and Dy metals from the practical wastes of Nd-Fe-B magnets.

For the purpose of the analysis of reduction behavior of Nd(III) in ILs, in situ investigation using an electrochemical quartz crystal microbalance (EQCM) was conducted in this study. The EQCM technique is based on the piezoelectric properties of a quartz crystal and can detect a nano-level mass change in a quartz crystal electrode during electrochemical experiments from the resonance frequency of the quartz [24]. Although a conventional oscillator technique, namely self-excited or active technique EQCM, was inoperative in some ILs due to their high viscosity, the possibility of applying EQCM measurements with the use of separately excited or passive technique in highly viscous fluids including ILs was recently demonstrated and the cases of successful application have been reported [25–30]. On the EQCM measurement, the resonance resistance can also be measured and reflects a product of the viscosity and the density of the media near the quartz crystal electrode [28] and the viscoelasticity of the electrodeposits [26, 27, 31, 32]. Thus, the change in the mass and the viscoelasticity of the electrodeposits on the electrode and the product of the viscosity and the density of the electrolyte near the electrode, relating to the concentration of a soluble species particularly in the case of ILs [25, 26] and corresponding to the electrochemical behavior, can simultaneously be observed by using the EQCM measurements, and very useful information for the specific examination of the electrode reaction can be acquired.

In this study as a new attempt, the electrochemical behavior of Nd(III) in ILs was analyzed by EQCM measurement at elevated temperatures because it is desirable to decrease the overpotential of the electrodeposition and to increase the diffusion rate of the metallic species by lowering the viscosity by means of elevating the temperature. There were a few reports about the theoretical equations: the Sauerbrey equation [24] and Kanazawa-Gordon [33]. However, these equations were not applied at elevated temperatures [25, 34]; therefore, we have demonstrated that the applicability of EQCM method in a medium temperature range around 373 K was revealed in the previous study [35]. In addition, we discuss the electroreduction behavior of Nd(III) in ILs on the potentiostatic condition in this study.

Considering the fundamental electrochemical investigations, the electrodeposition on the condition of constant potential was carried out on a relatively large scale. The Nd metal recovered by electrodeposition is applicable in the production of new Nd-Fe-B magnets because Nd metal of high purity is obtained by polishing the oxide layer after electrodeposition using ILs. Finally, we demonstrated the effectiveness of hydrometallurgy and electrodeposition process through the material flow.

2. Experimental

2.1. Pretreatment process

The spent Nd-Fe-B magnets were recovered from voice coil motors (VCMs) that were heated in an electric furnace at 623 K for 3 h for the demagnetization treatment. After demagnetization, the magnetic flux density was measured using a digital TESLA meter. The residual magnetic force field of this sample was almost zero, and the percentage of demagnetization was >99.9%. Then, the Ni-Cu-Ni triple layer on the Nd-Fe-B sample was removed by a grinding machine. After the stripping of the layer, fragments of Nd-Fe-B sample were pulverized using a stamp mill. The fine powders obtained were sieved to less than 150 μm and heated at 90 K h^{-1} to 1133 K, which was kept for 3 h in an electric furnace in order to oxidize the Nd-Fe-B components. After the roasting process, these fine powders were reground again by the automatic grinder. The surface area and the particle size (D_{50}) of oxidized Nd-Fe-B sample measured by the Brunauer-Emmett-Teller (BET) method were 0.630 $\text{m}^2 \text{g}^{-1}$ and 59.43 μm , respectively.

2.2. Bench-scale leaching

The fine powders of oxidized Nd-Fe-B sample (1.7 kg) were leached in 14.2 L of a 1.0 M aqueous solution of 1,1,1-trifluoro-*N*-[(trifluoromethyl)sulfonyl]methanesulfonamide ($\text{HN}(\text{SO}_2\text{CF}_3)_2$, H[TFSA]). The leaching solution was heated at 323 K, stirring at 500 rpm. The leaching behavior was researched from the potential (E)-pH diagram for Fe- H_2O and Nd- H_2O systems. Therefore, the oxidation-reduction potential (ORP) and pH in the leaching solution were measured by a high-precision digital meter (MM-60R, DKK-TOA Corp.). The quantification of Fe^{2+} was available for the complexation of $[\text{Fe}(\text{phen})_3]^{2+}$ using 1,10-phenanthroline. The concentration of Fe^{2+} was measured by an ultraviolet-visible-near-infrared (UV-Vis-NIR) spectrometer (Perkin Elmer, Lambda750) at 508 nm [36, 37]. The concentration of Fe^{3+} was calculated from the total amount of Fe^{2+} and Fe^{3+} ions obtained from inductively coupled plasma atomic emission spectroscopy (ICP-AES) analysis (ICPE-9000, Shimadzu Co.). All of the precise concentrations for metallic species were quantitatively determined from ICP-AES analysis.

2.3. Bench-scale deironization and preparation of RE salts

Dried oxygen gas was introduced into the leaching solution with a flow rate of 5.0 L min^{-1} after the leaching process. The oxidizing agent for Fe^{2+} was effective in the leaching solution at $\text{pH} > 3.2$. Some kinds of alkali metal hydroxides [8, 9] were acted as precipitation agents in the previous study, and the perfect removal of the iron components was successfully carried out at laboratory scale. The deironization treatment without precipitation agents is important as a further development, because the additive materials contaminated the final RE salts. Considering the leaching process, reuse of the oxidized Nd-Fe-B powder as a precipitation agent is desirable, because RE_2O_3 in the oxidized Nd-Fe-B sample was selectively leached in the H[TFSA] solution. The oxidized Nd-Fe-B fine powder was also available for sediment formation of $[\text{Fe}(\text{OH})_x]^{3-x}$ precipitates in this study. A small amount of the oxide Nd-Fe-B powder was introduced carefully into leaching solution while the alternation in pH was

measured. The best terminal point of the precipitation reaction for $[\text{Fe}(\text{OH})_x]^{3-x}$ was found to be $\text{pH} = 4.92\text{--}4.93$ because no iron component was detected in the leaching solution. It was important to develop a rapid solid-liquid separation technique because $[\text{Fe}(\text{OH})_x]^{3-x}$ precipitates are colloidal and the separation from colloidal precipitates is very difficult. Therefore, hematite ($\alpha\text{-Fe}_2\text{O}_3$) containing oxidized Nd-Fe-B sample was applied as a seed crystal in the formation of $[\text{Fe}(\text{OH})_x]^{3-x}$ precipitates. The formation of $[\text{Fe}(\text{OH})_x]^{3-x}$ precipitates with a large particle size greatly contributed to the filtration in solid-liquid separation. Finally, the $[\text{Fe}(\text{OH})_x]^{3-x}$ precipitates were completely removed from the leaching solution.

After the deironization treatment, a turquoise filtrate was obtained; the color of the solution was based on the RE components. The evaporation treatment of the filtrate was carried out by a spray dryer (SD-1000, EYELA Co., Ltd.). In the operation of the spray dryer, the inlet temperature was maintained at 473 ± 1.6 K and dried nitrogen gas was introduced through the evaporation part at 105 ± 5.0 kPa. Then, the $\text{H}[\text{TFSA}]$ filtrate was introduced using a roller pump at 150 mL h^{-1} . In order to recover the dried $\text{M}(\text{TFSA})_n$ salts, the recovery part was heated at 413 ± 1.5 K with a heating mantle. The amount of $\text{M}(\text{TFSA})_n$ salts for one batch and the total amount of $\text{M}(\text{TFSA})_n$ salts were >300 g and 3.57 kg, respectively. The amount of metallic components in the $\text{M}(\text{TFSA})_n$ salts was measured by ICP-AES analysis.

2.4. Electrochemical analysis

The resistance of a quartz oscillator and resonance frequency were observed using an EQCM system, (Seiko EG&G, QCA922) applying AT-cut platinum-coated [9 MHz, $\varphi = 5.0$ mm, Seiko EG&G, QA-A9M-PT(P)] with a well-type cell (Seiko EG&G, QA-CL4PK) as shown in **Figure 1**. The employed O-rings (Seiko EG&G, P-S75B) had a high resistance for heat and low expansibility. The temperature of the EQCM system was elevated using a heating mantle controlled by a thermostat with a proportional-integral-derivative (PID) controller. The temperature was slowly increased at a rate of $1.0\text{--}1.5 \text{ K min}^{-1}$ to prevent the strain occurring in the crystal structure of the quartz. The bath temperature was measured using a K-type thermocouple ($\varphi = 1.6$ mm). The cell covered with the heating mantle was connected to the EQCM system with an extension cord (Seiko EG&G, QCA922-10-EX10). In terms of the functionality of EQCM technique at elevated temperatures, the relationship between the viscosity and the density of Nd(III) samples, $\eta\rho$ values, the shifts of the resonance frequency, and the resistance before and after contacting the samples with the quartz have been already revealed in the previous study [35].

The voltammetric measurements were carried out using an electrochemical analyzer (ALS-440A, BAS Inc.,) with the EQCM system employing the Pt-coated quartz oscillator as a working electrode. Two Pt wires with 0.5 mm inside diameter were used as a counter and a quasi-reference electrode (QRE). The counter electrode was surrounded by a Vycor glass filter at the bottom in order to prevent the diffusion of decomposition components from the anode into the electrolyte. The Pt QRE showed a high stability and a good reproducibility of the potential at elevated temperatures. The potential was compensated for the IL standard using a ferrocene (Fc)/ferrocenium (Fc⁺) redox couple. Before all the electrochemical measurements, the dissolved oxygen was removed from the electrolytes by bubbling Ar gas for 30 min, and

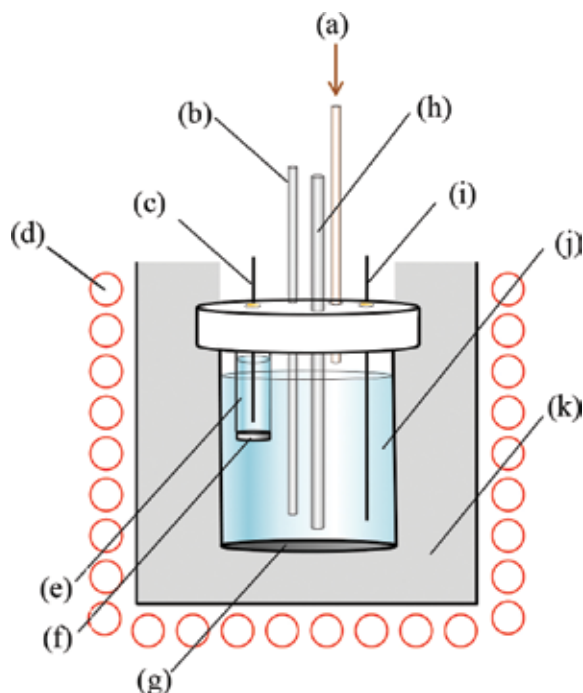


Figure 1. The schematic illustration of EQCM cell with separate system: (a) Ar flow, (b) K-type thermocouple-1 (for recording by a data logger), (c) Pt wire (counter electrode), (d) heating mantle, (e) separated electrolyte, (f) Vycor glass, (g) quartz oscillator coated with Pt (working electrode), (h) K-type thermocouple-2 (for controlling temperature by PID), (i) Pt wire (quasi-reference electrode), (j) main electrolyte, (k) heat insulator.

the measurements were conducted under flowing Ar gas in the cell with a rate of 20 ml min^{-1} . Cyclic voltammetry (CV) of 0.01 M Fc in $[\text{P}_{2225}][\text{TFSA}]$ was carried out at 298 K with a sweep rate of 1.0 mV s^{-1} after iR compensation (RC constant: 977.3) in order to confirm EQCM behavior while there was an outer-sphere electron-transfer reaction of Fc/Fc^+ . The electrochemical behavior of Nd(III) in $[\text{P}_{2225}][\text{TFSA}]$ was investigated by CV measurements of 0.05 M Nd(III) in $[\text{P}_{2225}][\text{TFSA}]$ at 373 K with a sweep rate of 2.0 mV s^{-1} . For the analysis of the electrodeposition behavior of Nd(0) from Nd(III) in $[\text{P}_{2225}][\text{TFSA}]$, the controlled potential electrolysis (CPE) under $-3.20 \text{ V vs. Fc}/\text{Fc}^+$ was performed at 373 K using 0.05 and 0.10 M Nd(III) in $[\text{P}_{2225}][\text{TFSA}]$ as electrolytes.

2.5. Electrodeposition

A schematic illustration of the electrodeposition cell is shown in **Figure 2**. In the electrodeposition with the three-electrode system, a copper substrate with a surface area of $2.0 \times 10^{-2} \text{ m}^2$ and a platinum were employed as the working electrode and quasi-reference electrode, respectively. Fe rod was employed as a counter electrode and was surrounded with a glass tube via a Vycor glass filter at the bottom to prevent the diffusion of dissolved $[\text{Fe}(\text{TFSA})_3]^-$ complexes from the anode into the electrolyte. The electrolytic bath was stirred at 500 rpm , because the current during electrodeposition decreased immediately to the limiting current

when the bath was not stirred. The overpotential was constant at -3.20 V versus Fc/Fc^+ at 373 K during potentiostatic electrodeposition in a glovebox. After electrodeposition, the electrodeposits were leached into a super-dehydrated acetone ($>99.5\%$, Wako Pure Chemical Industries, Ltd., water content <10 ppm) in a glovebox to remove the electrolyte thoroughly. The surface morphology of the electrodeposits was observed by scanning electron microscopy (SEM) and the composition of the electrodeposits was analyzed by energy dispersive X-ray analysis (EDX) (JSM-6510LA, JED-2300, JEOL, Ltd.). The metallic state and the crystallinity of the electrodeposits were evaluated by X-ray photoelectron spectroscopy (XPS) (Quantera SXM, ULVAC-PHI, Inc) and X-ray diffraction (XRD) (RINT-2500, Rigaku Co.), respectively.

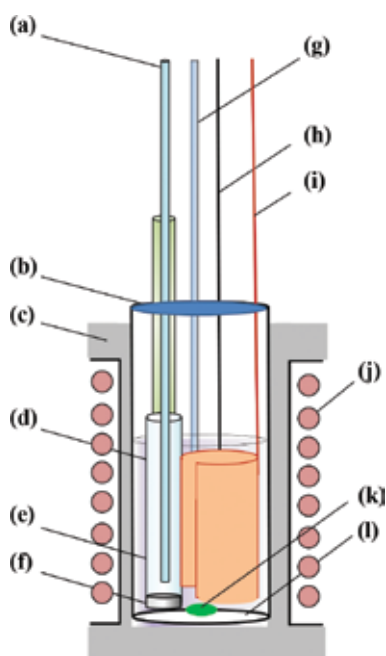
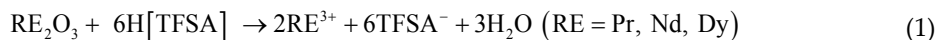


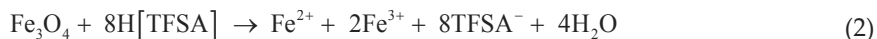
Figure 2. The schematic illustration of the electrodeposition cell with three-electrode system, (a) Fe rod (anode), (b) Teflon cap, (c) heat insulator, (d) soda-lime glass tube, (e) $[\text{P}_{2225}][\text{TFSA}]$, (f) Vycor glass filter, (g) K-type thermocouple, (h) Pt wire (Q.R.E.), (i) Cu substrate (cathode), (j) heating mantle, (k) stirrer, and (l) $[\text{P}_{2225}][\text{TFSA}]$ including $\text{M}(\text{TFSA})_n$ or $\text{Nd}(\text{TFSA})_3$.

3. Results and discussion

3.1. Leaching behavior at bench scale

The leaching reactions of the oxidized Nd-Fe-B sample were represented as follows:





The leaching behavior in H[TFSA] solution using the oxidized Nd-Fe-B fine powder as a precipitation agent is shown in **Figure 3**. The leaching percentage of Nd and Fe for 66h in the H[TFSA] solution were $85.7 \pm 5.8\%$ and $5.8 \pm 0.1\%$, respectively. A drastic increase in the pH value was observed at the initial stage of the leaching process, which indicates that leaching reaction Eq. (1) mainly occurred in this system. The leaching behavior accounted for the potential (E)-pH diagrams of Fe-H₂O and Nd-H₂O systems as shown in **Figure 4**. The actual measurement data in the bench scale is also plotted in the potential (E)-pH diagram. From the E -pH diagram, at $E = -0.75$ and $\text{pH} < 1.0$, the most stable states of Fe and Nd components were found to be solid Fe₂O₃ and Nd³⁺ ion, respectively. This result indicated that the selective leaching of Nd³⁺ (leaching percentage > 90%) was carried out at bench scale.

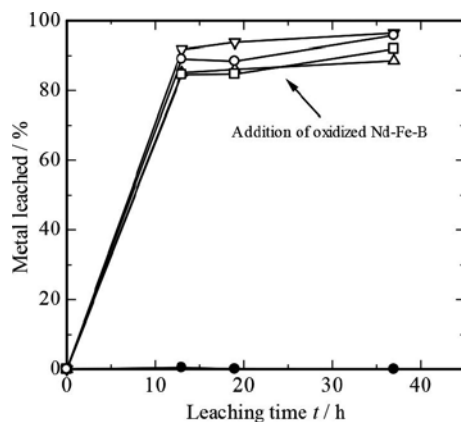


Figure 3. The leaching behavior of each metallic component in H[TFSA] solution at bench scale.

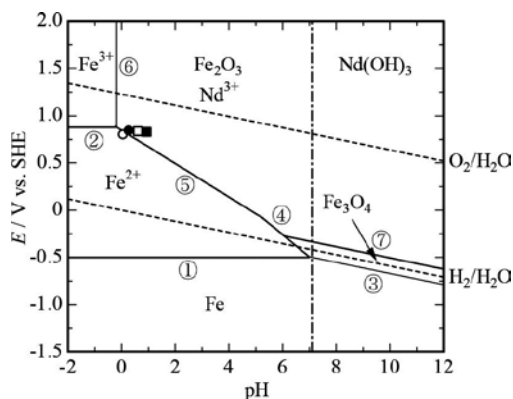
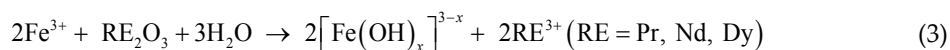


Figure 4. Potential(E)-pH diagram of Fe-H₂O and Nd-H₂O systems. Leaching time ○:3 h, ●:15 h, □:18 h, ■:21 h.

3.2. Deironization and purification of RE amide salts at bench scale

The effective treatment for deironization is precipitation separation through the oxidation from Fe²⁺ to Fe³⁺ by oxygen bubbling, because [Fe(OH)_x]^{3-x} precipitates are formed under acidic pH conditions [8, 9]. The precipitation reaction using the oxidized Nd-Fe-B sample was expressed as follows:



[Fe(OH)_x]^{3-x} is generally a colloidal precipitate, and it is very difficult to separate from the H[TFSA]_n solution. Therefore, we applied a seed crystal method, and hematite (α-Fe₂O₃) in oxidized Nd-Fe-B sample was employed as a seed crystal for the formation of [Fe(OH)_x]^{3-x} precipitates. The precipitate with a large particle size greatly facilitated the filtration in the solid-liquid separation treatment. From the ICP-AES analysis, the separation percentage of Fe component was confirmed to be >99.9%. This result allowed us to conclude that the oxidized Nd-Fe-B sample was applicable for perfect removal of iron component as a seed crystal.

After the solid-liquid separation, the evaporation treatment of filtrate was performed using an improved spray dryer to effectively recover dried M(TFSA)_n (M = Pr, Nd, Dy, B, Al, K, and trace elements) salts. The refining conditions of the H[TFSA]_n solution for the oxidized Nd-Fe-B sample are listed in **Table 2**. The total amount of recovered M(TFSA)_n and the average

Run no.	Flow rate /mL min ⁻¹	Blower flow rate/m ³ min ⁻¹	Volume of H[TFSA] aq./mL	Amount of M(TFSA) _n /g	Recovery Yield/%
1	2.5	0.35-0.50	150	35.10	82.4
2	2.5	0.35-0.50	300	73.25	84.7
3	2.5	0.35-0.50	450	110.81	88.1
4	2.7	0.35-0.50	600	154.13	89.8
5	2.7	0.15-0.35	750	201.97	91.8
6	2.7	0.15-0.35	1050	273.85	91.2
7	2.9	0.15-0.35	1200	314.59	91.6
8	2.9	0.15-0.35	1200	320.62	93.7
9	2.9	0.15-0.35	1200	321.73	93.5
10	2.9	0.15-0.35	1200	325.64	94.4
11	2.9	0.15-0.35	1200	329.89	95.3
12	2.9	0.15-0.35	1200	328.74	94.6
13	2.9	0.15-0.35	1200	387.83	95.8
14	2.9	0.15-0.35	1200	393.32	96.8
				Total: 3571.5 g	Ave.: 91.7%

Table 2. The refining condition of leaching solution by spray dryer.

recovery yield were 3571.5 g and 91.7%, respectively. The obtained $M(\text{TFSA})_n$ salt was a fine pale purple powder, and the water content in the $M(\text{TFSA})_n$ salt was less than 10 ppm. The composition of the recovered $M(\text{TFSA})_n$ salts is tabulated in **Table 3**. The stoichiometric number of $M(\text{TFSA})_n$ and average molecular weight were 3.00 and 943.68, respectively. In addition, the average RE component in $M(\text{TFSA})_n$ was 96.81%. This series of results allowed us to conclude that the separation factor of Fe in the deironization treatment was >99.9% and the recovery yield of $M(\text{TFSA})_n$ salts was 82.4–96.8% using a spray dryer at bench scale.

Run no.	Pr	Nd	Dy	RE [*]	Fe	B	Molecular weight of $M(\text{TFSA})_n$	n ^{**}
1	20.81	72.87	2.48	96.16	0.00	3.84	938.15	3.00
2	20.76	73.55	2.47	96.78	0.00	3.22	943.46	3.00
3	19.80	74.96	2.06	96.82	0.00	3.18	943.77	3.00
4	19.39	74.78	2.46	96.63	0.00	3.37	942.11	3.00
5	19.83	74.58	2.46	96.87	0.00	3.13	944.26	3.00
6	19.80	74.77	2.40	96.96	0.00	3.04	944.26	3.00
7	19.53	74.85	2.53	96.91	0.00	3.09	944.71	3.00
8	19.86	74.87	2.05	96.78	0.00	3.22	943.42	3.00
9	20.01	74.80	2.00	96.82	0.00	3.18	943.78	3.00
10	20.07	74.84	1.99	96.90	0.00	3.10	944.52	3.00
11	21.05	73.93	1.97	96.95	0.00	3.05	944.98	3.00
12	20.10	74.77	2.13	96.99	0.00	3.01	945.40	3.00
13	19.75	74.99	2.16	96.89	0.00	3.11	944.45	3.00
14	20.01	74.73	2.12	96.87	0.00	3.13	944.23	3.00
Ave.	20.06	74.52	2.23	96.81	0.00	3.19	943.68	3.00

^{*}RE indicates the summation of the composition for Pr, Nd, and Dy.

^{**} n indicates the stoichiometric number of $M(\text{TFSA})_n$ salts.

Table 3. The composition (wt.%) of recovered $M(\text{TFSA})_n$ salts on the condition of **Table 1**.

3.3. Theory

A frequency shift (Δf) observed on the EQCM analyzer includes effects relating to the mass change (Δm) in the quartz crystal electrode (Δf_m) and the viscosity (η) and the density (ρ) of the liquid adjacent to the quartz ($\Delta f_{\eta\rho}$).

$$\Delta f = \Delta f_m + \Delta f_{\eta\rho} \quad (4)$$

The relationship between Δf_m and Δm is expressed by the Sauerbrey equation [24].

$$\Delta f_m = \frac{2f_0^2 \Delta m}{A(\mu_q \rho_q)^{1/2}} \quad (5)$$

where f_0 is the fundamental resonance frequency, A is the surface area of the electrode (0.196 cm²), μ_q is the shear modulus of quartz (2.95×10^{10} kg m⁻¹ s⁻² at 298 K), and ρ_q is the density of quartz (2.65×10^3 kg m⁻³ at 298 K). On the other hand, $\Delta f_{\eta\rho}$ is proportional to the square root of the product of the liquid viscosity and density, $(\eta\rho)^{1/2}$ demonstrated by Kanazawa-Gordon [33].

$$\Delta f_{\eta\rho} = -f_0^2 \left(\frac{\eta\rho}{\pi\mu_q\rho_q} \right) \quad (6)$$

Although a frequency shift by the aqueous solution contacting the quartz is small, in the case of employing ILs as the electrolyte, it is necessary to consider the influence of $\Delta f_{\eta\rho}$ due to the exceedingly high viscosity of ILs. In the EQCM measurements, the resonance resistance (R) can simultaneously be measured, and $(\eta\rho)^{1/2}$ is also estimated from R value [38].

$$R = \frac{A(2\pi f_0 \eta\rho)^{1/2}}{k^2} \quad (7)$$

where k is an electromechanical coupling factor and often used when the electrical model of the quartz crystal oscillator is converted to a mechanical model. The k value was estimated from the shifts in the resonance frequency and the resistances before and after the liquid sample came into contact with the quartz according to Eqs. (6) and (7), respectively, for each measurement in this study. Δf_m is isolated from the total shift of frequency (Δf) by using Eqs. (4), (6), and (7). In addition, the apparent molar mass, M_{app} , of the electrodeposited species can be calculated by using Δm estimated from Δf_m , the electrical charge Q passed during electrodeposition, and the Faraday constant F .

$$M_{app} = \frac{F\Delta m}{\Delta Q} \quad (8)$$

The theoretical value of M_{app} based on the reduction reaction of Nd(III) + 3e⁻ → Nd(0) was 48.1 g mol⁻¹. The theoretical equations of the EQCM measurements related to the frequency response are based on the analysis of an admittance spectrum of the quartz crystal near its resonance frequency [39]. The responses of the resonance frequency and the resistance to $(\eta\rho)^{1/2}$ of the adjacent liquid to the quartz crystal are derived from the solutions of the equation, describing the steady-state shear waves in the AT-cut quartz oscillator under the condition that the transverse velocity of the surface of the quartz oscillator is identical with that of the adjacent liquid and that the force exerted by the liquid on the quartz is equal and opposite to the force

exerted by the quartz on the liquid [33, 38]. Strictly speaking, the estimation of Δm from Δf_m by Eq. (4) is valid for thin and rigid films coated on the quartz. Moreover, $\Delta f_{\eta\rho}$ and R reflect not only the viscosity and the density of contacting liquid with the quartz but also the roughness, the viscoelastic properties, and the films [31, 32]. By considering these parameters in combination, it is possible to discuss detailed states on the surface of the quartz electrode accompanied by the electrochemical behaviors.

3.4. Electrochemical analysis

For the investigation of the reduction behavior for Nd(III) in $[P_{2225}][TFSA]$, cyclic voltammetry with EQCM measurements (CV/EQCM) were carried out at elevated temperatures. The EQCM behavior was confirmed in advance by CV/EQCM at 298 K measuring Fc/Fc⁺ redox couple in $[P_{2225}][TFSA]$. The potential difference, ΔE_p , between the anode and cathode peak was 67 mV after iR compensation. The ΔE_p value was close to the theoretical value; 59 mV in a reversible and one-electron reaction at 298 K and thus the observation of the electrochemical behavior was confirmed with high precision. Moreover, there were no significant alternations for the mass and $\eta\rho$ values in this reversible reaction. The results indicated that no changes of Δm and $\Delta\eta\rho$ were detected during the outer-sphere electron-transfer reaction and consistent with the Ref. [26].

The CV/EQCM results for Nd(III) in $[P_{2225}][TFSA]$ at 373 K were shown in **Figure 5**. A clear cathodic peak with the mass increased and the $\eta\rho$ decreased was observed at -2.79 V. Considering our previous investigations [15–18], the reduction of Nd(III)/Nd(0) was indicated as follows:



The M_{app} value in the range of -2.49 V \sim -2.94 V calculated from the mass change was 46.8 g mol⁻¹, which was close to the theoretical value for the electrodeposition reaction of Nd(III)/Nd(0), 48.1 g mol⁻¹. Moreover, the observed decrease of the $\eta\rho$ value indicated that the concentration of Nd(III) near the electrode was locally decreased by consuming Nd(III) in the electrodeposition reduction of Nd(III)/Nd(0). This is based on the $\eta\rho$ change in the IL system that largely depends on the concentration of the metal ion. Therefore, these results are an evidence for the electrodeposition reaction of Nd(III)/Nd(0). At a more negative potential than -2.79 V, the mass and $\eta\rho$ increased with the comparatively low values of M_{app} for 0.05 M Nd(III) in $[P_{2225}][TFSA]$. This behavior indicated that the cathodic decomposition products from IL were generated on the electrode surface. A part of side chain of $[P_{2225}]^+$ would be decomposed on the cathode considering the M_{app} value estimated in this potential range (-2.96 V \sim -3.30 V). In addition, in the range of $0 \sim -2.0$ V the mass unexpectedly increased during slight current and no change in the $\eta\rho$ value for 0.05 M Nd(III) in $[P_{2225}][TFSA]$. There was no observation of mass increase in the EQCM analysis for neat $[P_{2225}][TFSA]$ in this potential. Therefore, it was deduced that the reaction would be the formation of divalent species; Nd(II) $[Nd(III) + e^- \rightarrow Nd(II)]$. The related disproportionation reaction $[2Nd(III) + Nd(0) \rightarrow 3Nd(II)]$ would occur in the IL system.

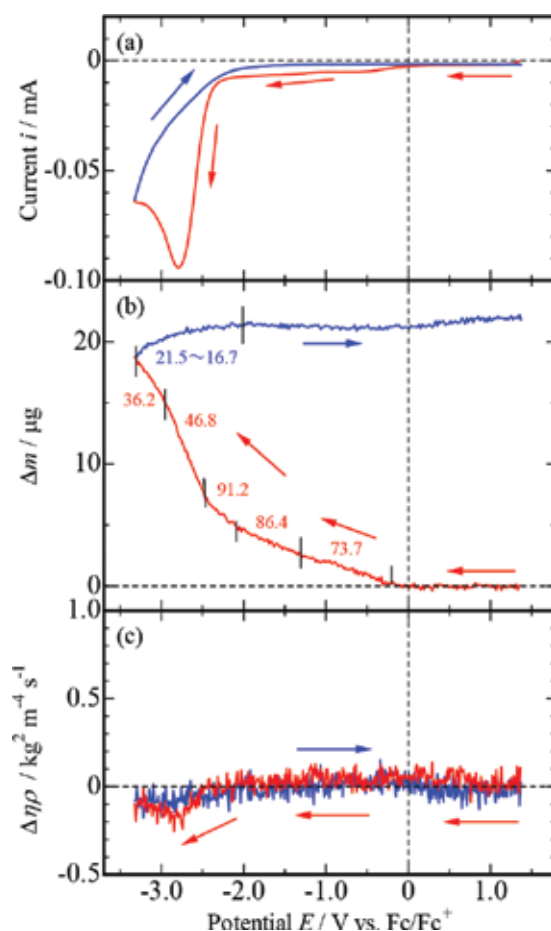


Figure 5. CV/EQCM analysis for 0.05 M Nd(III) in $[\text{P}_{2225}][\text{TFSA}]$ at 373 K with 2.0 mV s^{-1} ; (a) voltammogram, (b) the mass change, and (c) the change in $\eta\rho$ values.

The controlled potential electrolysis with EQCM measurements (CPE/EQCM) at -3.20 V was conducted with 0.05 and 0.10 M Nd(III) in $[\text{P}_{2225}][\text{TFSA}]$ at 373 K. The parameters of Δm and $\Delta\eta\rho$ were plotted as a function of the charge density Q_d passed during CPE as shown in **Figure 6**. The calculated values of M_{app} in 0.05 and 0.10 M Nd(III) at the initial stage of CPE/EQCM analysis were 49.1 and 49.6 g mol^{-1} , respectively, which were close to the theoretical value when the reduction of Nd(III)/Nd(0) occurred, 48.1 g mol^{-1} , so that the electrodeposition of Nd(0) metal was also proved from the CPE/EQCM analysis. The total values of M_{app} in 0.10 M solution, 18.4 ~ 29.8 g mol^{-1} , were larger than those in 0.05 M solution, 7.7 ~ 18.6 g mol^{-1} . These results indicated that the competition reaction for Nd(III)/Nd(0) reduction and IL decomposition would occur and depend on the Nd(III) concentration. The value of $\eta\rho$ after 0.45 C cm^{-2} increased and the IL decomposition was also deduced from this result because the $\eta\rho$ change implied that the quantity of the soluble species increase near the electrode and/or the viscoelastic film might be formed on the electrode surface [27, 31, 32, 40] by the IL decomposition.

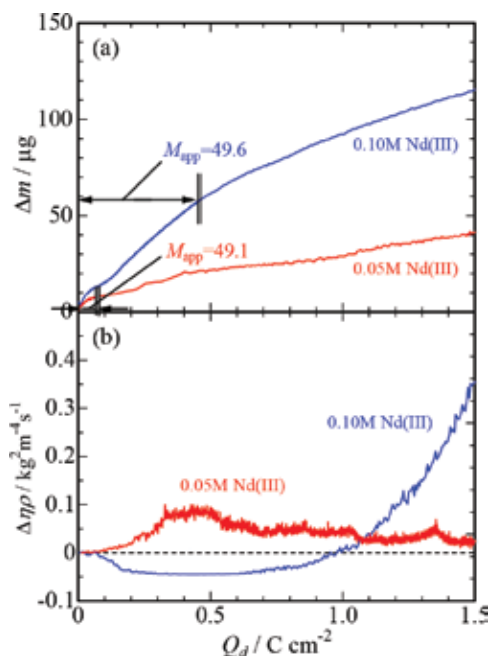


Figure 6. CPE/EQCM analysis for 0.05 and 0.10 M Nd(III) in $[\text{P}_{2225}][\text{TFSA}]$ induced on -3.20 V at 373 K; (a) the mass change and (b) the change in $\eta\rho$ values.

Run no.	Overpotential, η/V vs. Fc/Fc^+	Transported charge, Q/C	Weight change, $\Delta w/\text{g}$	Current efficiency, $\epsilon/\%$
1	-3.20	6054.6	Anode:-1.694	Anode:96.7
			Cathode:+2.184	Cathode:72.4
2	-3.20	6634.8	Anode:-1.794	Anode:93.4
			Cathode:+2.541	Cathode:76.9
3	-3.20	7618.2	Anode:-2.094	Anode:95.0
			Cathode:+2.832	Cathode:74.6

Table 4. The potentiostatic electrodeposition condition using $[\text{P}_{2225}][\text{TFSA}]$ including $\text{M}(\text{TFSA})_3$ at 373 K.

Run no.	Composition/wt.%								
	C	N	O	F	P	S	Fe	Cu	Nd
1	5.52	0.84	12.38	0.46	0.31	0.96	0.02	15.82	63.69
2	3.62	0.43	9.62	0.32	0.18	0.68	0.00	13.64	71.51
3	4.82	0.68	10.23	0.36	0.23	0.82	0.00	12.46	70.40

Table 5. The composition of Nd electrodeposits analyzed by EDX.

3.5. Electrodeposition

Considering the above fundamental electrochemical behavior of Nd(III), the electrodeposition of Nd(0) was carried out, and the condition was listed in **Table 4**. The electrodeposition was smoothly performed on the high anodic current efficiency. The current slowly decreased to the limiting current during electrodeposition. After the electrodeposition, the blackish electrodeposits were obtained on the Cu substrate. The electrodeposits observed by SEM had a granular morphology with a nonuniform size distribution. This morphology is considered to be explained from the fact that the initial stage of nucleation and growth occurred according to the progressive nucleation model [15]. The quantitative analysis using EDX for the electrodeposits obtained from the electrodeposition at -3.20 V versus Fc/Fc⁺ is summarized in **Table 5**. The results indicated that the electrodeposits on Cu substrate comprised mainly Nd component. However, a small amount of O component was also included in the electrodeposits, suggesting that the oxidizing Nd metal with O atoms would occur. In order to investigate the chemical bond state of Nd, XPS analysis with Al-K α was carried out on the electrodeposits. The metallic and oxide components for Nd correspond to the binding energies of Nd3d_{5/2} at 980.5–981.0 eV and 981.7–982.3 eV, respectively, in the case of monochromated Al-K α line [41]. The Nd3d_{5/2} spectra for the middle layer and top surface of electrodeposits are shown in **Figure 7**. For an in-depth analysis of the middle layer, the oxide layer of the electrodeposits was perfectly removed with an Ar ion beam, that is, (a) 0.42 μ m under the electrodeposits. The peak maximum in the Nd3d_{5/2} spectrum acquired for the layers below 0.42 μ m was at 980.77 eV. Hence, the electrodeposits obtained through electrodeposition using [P₂₂₂₅][TFSA] with M(TFSA)₃ were identified as Nd metal and partial oxide mixtures. This result indicated that metallic Nd would have been electrodeposited on the Cu substrate and subsequently oxidized by O in the electrolyte, that is, residual water or dissolved oxygen. The XRD profile of the electrodeposits is shown in **Figure 8** with the profile from Ref. [42] for Nd metal. The position of 2θ of the electrodeposits was nearly identical to that of Nd metal. Therefore, the electrodeposits were identified to be crystalline Nd metal.

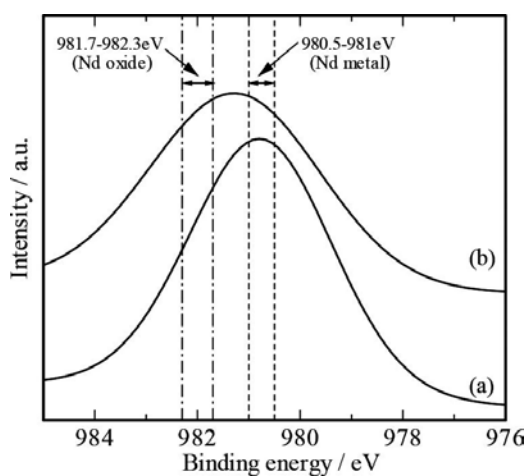


Figure 7. XPS spectra for Nd3d_{5/2} region of electrodeposits (a) middle layer at 0.42 μ m, (b) top surface.

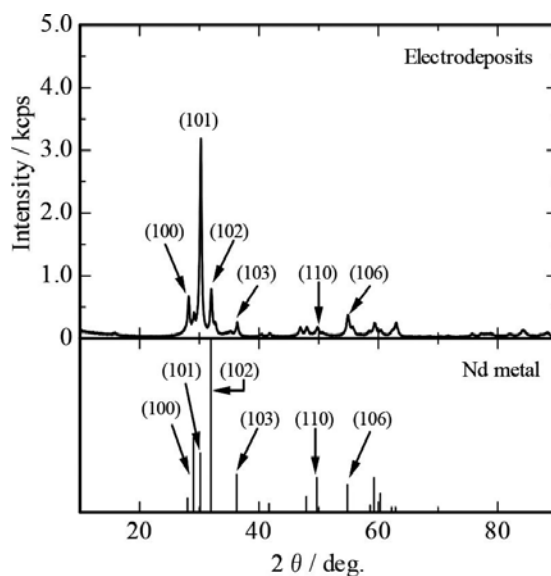


Figure 8. XRD profile of the Nd electrodeposits obtained from $[P_{2225}][TFSA]$.

3.6. Material flow of VCM recycling

As described earlier, it is worthwhile to evaluate the material flow from a series of processes such as pretreatment, hydrometallurgy, and electrodeposition using $[P_{2225}][TFSA]$ melts. The whole material flow is shown in **Figure 9**, and the recovery target in this material flow was based on the oxidized Nd-Fe-B wastes after the roasting process. As the first step of hydrometallurgy, the selective leaching of RE components ($85.7 \pm 5.8\%$ Nd and $5.8 \pm 0.1\%$ Fe in 66 h) was performed in the leaching process. Then, the deironization treatment was carried out using precipitation formation of $[Fe(OH)_x]^{3-x}$, and the residual Fe component was perfectly removed in this process. After the deironization process, the $M(TFSA)_n$ salts with high purity were obtained from the evaporation by a spray dryer, and the yield of $M(TFSA)_n$ salts was as high as 91.7%. Scaling up for the vaporization treatment is relatively simple because a large-scale spray dryer can be available through cooperation with an associated company. A series of hydrometallurgy indicates that 78.6% ($356.0 \text{ g}/453.0 \text{ g} \times 100$) Nd and 77.9% ($10.9 \text{ g}/14.0 \text{ g}$) Dy can be recovered as purified $M(TFSA)_n$ salts from the initial oxidized Nd-Fe-B powder. After the hydrometallurgical process, $M(TFSA)_n$ salts were available as an electrolytic bath in the electrodeposition process. In terms of material flow, the induced overpotential ($E = -3.20 \text{ V vs. } Fc/Fc^+$) and the cathodic current efficiency ($\epsilon = 74.6\%$) were determined from the actual electrodeposition results described above. Assuming that the total transported charge is $Q = 7618.2 \times 10^2 \text{ C}$ (100 times at laboratory scale) under proper conditions based on the scaling-up electrolytic bath, 283.2 g of Nd metal can be recovered during the electrodeposition process, and the recovery yield calculated from the starting material (453.0 g Nd) was estimated to be 62.5%. Therefore, the recovery process based on hydrometallurgy and electrodeposition using $[P_{2225}][TFSA]$ was applicable for practical Nd-Fe-B wastes. From the economic point of view,

H[TFSA] is currently slightly expensive compared with mineral acids. However, H[TFSA] can be prepared through an ion-exchange reaction of residual components. Studies to further improve the recovery process are now in progress.

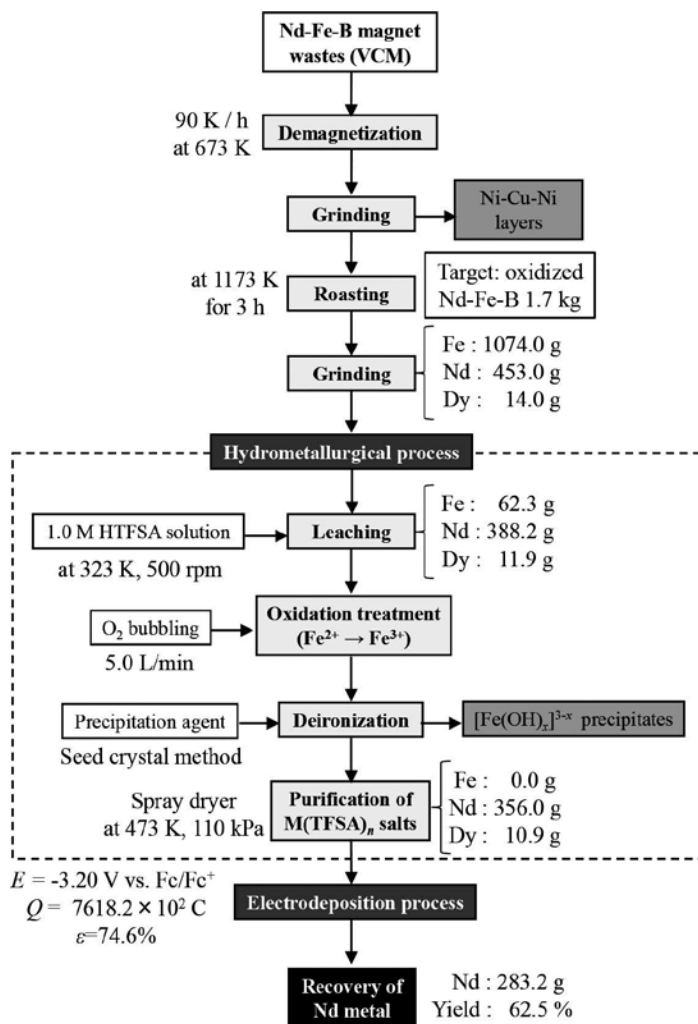


Figure 9. Material flow of hydrometallurgy and electrodeposition using [P₂₂₂₅][TFSA].

4. Conclusion

Hydrometallurgical process based on leaching, deironization, and purification of rare earth (RE) amide salts were carried out at bench scale. In the leaching process using 1.7 kg of oxidized Nd-Fe-B sample and 14.2 L of an aqueous solution of 1,1,1-trifluoro-N-[(trifluoromethyl)

sulfonyl]methanesulfonamide ($\text{HN}(\text{SO}_2\text{CF}_3)_2$, $\text{H}[\text{TFSA}]$), The leaching percentage of Nd and Fe for 66h in the $\text{H}[\text{TFSA}]$ solution were $85.7 \pm 5.8\%$ and $5.8 \pm 0.1\%$, respectively. Moreover, the oxidized Nd-Fe-B sample applied as a precipitation agent in the deionization process, and $>99.9\%$ Fe component was successfully separated from RE components. Finally, 3.57 kg of purified amide salts ($\text{M}(\text{TFSA})_3$, $\text{M} = \text{Pr, Nd, Dy, B, Al}$, and trace elements) were recovered through the evaporation process using an improved spray dryer and the percentage of RE components for amide salts was 96.81%.

The cyclic voltammetry (CV) with electrochemical quartz crystal microbalance (EQCM) was applied at elevated temperatures in this study. CV/EQCM measurements for the investigation of the reduction behavior related to Nd(III) in triethyl-pentyl-phosphonium bis(trifluoromethyl-sulfonyl)amide ($[\text{P}_{2225}][\text{TFSA}]$) were conducted at 373 K. At the potential of -2.79 V, the objective electrodeposition, Nd(III)/Nd(0) was confirmed because a clear cathodic peak was observed and the apparent molar mass, M_{app} was calculated to be 46.8 g mol^{-1} , and this value was consistent with the theoretical value for Nd(III)/Nd(0), 48.1 g mol^{-1} . At more negative potential than -2.79 V, the mass and $\eta\rho$ increased with the comparatively low values of M_{app} for 0.05 M Nd(III) in $[\text{P}_{2225}][\text{TFSA}]$. This behavior indicated that the cathodic decomposition reaction of IL occurred on the electrode surface. Moreover, from the controlled potential electrolysis with EQCM (CPE/EQCM) measurements at -3.20 V versus Fc/Fc^+ in the solutions of 0.05 and 0.10 M Nd(III) in $[\text{P}_{2225}][\text{TFSA}]$ at 373 K, the electrodeposits of Nd(0) metal were confirmed at the initial stage considering the M_{app} values (49.1 and 49.6 g mol^{-1}). The electrodeposition of Nd was carried out under potentiostatic conditions of -3.20 V versus Fc/Fc^+ at 373 K. The electrodeposits in the middle layer $0.15 \mu\text{m}$ below the surface were identified to be Nd metal from the analysis of SEM/EDX, XPS, and XRD. Finally, the material flow of whole process allowed us to conclude that the novel recovery process was effective for practical use.

Acknowledgements

This study was partly supported by the Grant-in-Aid for Scientific Research (No. 15H02848) from the Ministry of Education, Culture, Sports, Science, and Technology, Japan.

Author details

Masahiko Matsumiya

Address all correspondence to: mmatsumi@ynu.ac.jp

Graduate School of Environment and Information Sciences, Yokohama National University, Hodogaya-ku, Yokohama, Japan

References

- [1] K. Binnemans, P. T. Jones, B. Blanpain, T. Van Gerven, Y. X. Yang, A. Walton, M. Buchert, Recycling of rare earths: a critical review, *J. Clean. Prod.* 51 (2013) 1-22.
- [2] C. Tunsu, M. Petranikova, M. Gergoric, C. Ekberg, T. Retegan, Reclaiming rare earth elements from end-of-life products: a review of the perspectives for urban mining using hydrometallurgical unit operations, *Hydrometallurgy* 156 (2015) 239-258.
- [3] K. Murase, K. Machida, G. Adachi, Recovery of rare metals from scrap of rare earth intermetallic material by chemical vapor transport, *J. Alloys Compd.* 217 (1995) 218-225.
- [4] Y. Baba, F. Kubota, N. Kamiya, M. Goto, Selective recovery of dysprosium and neodymium ions by a supported liquid membrane based on ionic liquids, *Solvent Extr. Res. Dev., Jpn.* 18 (2011) 193-198.
- [5] M. Fukumoto, M. Odera, K. Yokoyama, M. Hara, Dissolution of Dy_2O_3 and Nd_2O_3 by electrolysis of fused Na_2SO_4 and the recovery of Dy and Nd, *Corros. Eng.* 61 (2012) 278-282.
- [6] T. Nohira, S. Kobayashi, K. Kondo, K. Yasuda, R. Hagiwara, T. Oishi, H. Konishi, Electrochemical formation of RE-Ni (RE = Pr, Nd, Dy) alloys in molten halides, *ECS Trans.* 50(11) (2013) 473-482.
- [7] J. P. Rabatho, W. Tongamp, Y. Takasaki, K. Haga, A. Shibayama, Recovery of Nd and Dy from rare earth magnetic waste sludge by hydrometallurgy, *J. Mater. Cycles Waste Manag.* 15 (2013) 171-178.
- [8] M. Matsumiya, K. Ishioka, T. Yamada, M. Ishii, S. Kawakami, Recovery of rare earth metals from voice coil motors using bis(trifluoromethylsulfonyl)amide melts by wet separation and electrodeposition, *Int. J. Miner. Process.* 126 (2014) 62-69.
- [9] K. Ishioka, M. Matsumiya, M. Ishii, S. Kawakami, Development of energy-saving recycling process for rare earth metals from voice coil motor by wet separation and electrodeposition using metallic-TFSA melts, *Hydrometallurgy* 144-145 (2014) 186-194.
- [10] C. Hamela, P. Chamelot, P. Taxil, Neodymium(III) cathodic processes in molten fluorides, *Electrochim. Acta* 49 (2004) 4467-4476.
- [11] E. Stefanidaki, C. Hasiotis, C. Kontoyannis, Electrodeposition of neodymium from $LiF-NdF_3-Nd_2O_3$ melts, *Electrochim. Acta* 46 (2001) 2665-2670.
- [12] H. Matsumoto, H. Sakaebe, K. Tatsumi, Preparation of room temperature ionic liquids based on aliphatic onium cations and asymmetric amide anions and their electrochemical properties as a lithium battery electrolyte, *J. Power Sources* 146 (2005) 45-50.
- [13] S. Legeai, S. Diliberto, N. Stein, C. Boulanger, J. Estager, N. Papaiconomou, M. Draye, Room-temperature ionic liquid for lanthanum electrodeposition, *Electrochem. Commun.* 10 (2008) 1661-1664.

- [14] M. Yamagata, Y. Katayama, Y. Miura, Electrochemical behavior of samarium, europium, and ytterbium in hydrophobic room-temperature molten salt systems, *J. Electrochem. Soc.* 153 (2006) E5-E9.
- [15] M. Matsumiya, *Application of Ionic Liquids on Rare Earth Green Separation and Utilization*, Springer (2016) 117-153.
- [16] H. Kondo, M. Matsumiya, K. Tsunashima, S. Kodama, Attempts to the electrodeposition of Nd from ionic liquids at elevated temperatures, *Electrochim. Acta*, 66 (2012) 313-319.
- [17] M. Ishii, M. Matsumiya, S. Kawakami, *ECS Trans.* 50(11) (2012) 549-560.
- [18] M. Matsumiya, M. Ishii, K. Kazama, S. Kawakami, Electrochemical analyses of diffusion behaviors and nucleation mechanisms for neodymium complexes in [DEME][TFSA] ionic liquid, *Electrochim. Acta* 146 (2014) 371-377.
- [19] R. Kazama, M. Matsumiya, N. Tsuda, K. Tsunashima, *Electrochim. Acta* 113 (2013) 269-279.
- [20] A. Kurachi, M. Matsumiya, K. Tsunashima, S. Kodama, Electrochemical behavior and electrodeposition of dysprosium in ionic liquids based on phosphonium cations, *J. Appl. Electrochem.* 42 (2012) 961-968.
- [21] M. Matsumiya, Y. Kikuchi, T. Yamada, S. Kawakami, Extraction of rare earth ions by tri-*n*-butylphosphate/phosphonium ionic liquids and the feasibility of recovery by direct electrodeposition, *Sep. Purif. Technol.* 130 (2014) 91-101.
- [22] Y. Kikuchi, M. Matsumiya, S. Kawakami, Extraction of rare earth ions from Nd-Fe-B magnet wastes with TBP in tricaprylmethylammonium nitrate, *Solvent Extr. Res. Dev., Jpn.* 21(2) (2014) 137-145.
- [23] S. Murakami, M. Matsumiya, T. Yamada, K. Tsunashima, *Solvent Extr. Ion Exch.* 34(2) (2016) 172-187.
- [24] G. Z. Sauerbrey, Verwendung von schwingquarzen zur wägung dünner schichten und zur mikrowägung, *Z. Phys.* 155 (1959) 206-222.
- [25] A. Ispas, B. Adolphi, A. Bund, F. Endres, On the electrodeposition of tantalum from three different ionic liquids with the bis(trifluoromethyl sulfonyl) amide anion, *Phys. Chem. Chem. Phys.* 12 (2010) 1793-1803.
- [26] N. Serizawa, Y. Katayama, T. Miura, EQCM measurement of Ag(I)/Ag reaction in an amide-type room-temperature ionic liquid, *J. Electrochem. Soc.* 156(11) (2009) D503-D507.
- [27] N. Serizawa, S. Seki, K. Takei, H. Miyashiro, K. Yoshida, K. Ueno, N. Tachikawa, K. Dokko, Y. Katayama, M. Watanabe, T. Miura, EQCM measurement of deposition and dissolution of lithium in Glyme-Li salt molten complex, *J. Electrochem. Soc.* 160(9) (2013) A1529-A1533.

- [28] F. Endres, S. Z. E. Abedin, A. Y. Saad, E. M. Moustafa, N. Borissenko, W. E. Price, G. G. Wallace, D. R. MacFarlane, P. J. Newman, A. Bund, On the electrodeposition of titanium in ionic liquids, *Phys. Chem. Chem. Phys.* 10 (2008) 2189-2199.
- [29] E. M. Moustafa, S. Z. E. Abedin, A. Shkurankov, E. Zschippang, A. Y. Saad, A. Bund, F. Endres, Electrodeposition of Al in 1-butyl-1-methylpyrrolidinium bis(trifluoromethylsulfonyl)amide and 1-ethyl-3-methylimidazolium bis(trifluoromethylsulfonyl)amide ionic liquids: in situ STM and EQCM studies, *J. Phys. Chem. B* 111 (2007) 4693-4704.
- [30] A. P. Abbott, A. Nandhra, S. Postlethwaite, E. L. Smith, and K. S. Ryder, Electroless deposition of metallic silver from a choline chloride-based ionic liquid: a study using acoustic impedance spectroscopy, SEM and atomic force microscopy, *Phys. Chem. Chem. Phys.* 9 (2007) 3735-3743.
- [31] H. Muramatsu, A. Egawa, T. Ataka, Reliability of correlation between mass change and resonant frequency change for a viscoelastic-film-coated quartz crystal, *J. Electroanal. Chem.* 388 (1995) 89-92.
- [32] K. Naoi, Y. Oura, M. Maeda, S. Nakamura, Electrochemistry of surfactant-doped polypyrrole film(I): formation of columnar structure by electropolymerization, *J. Electrochem. Soc.* 142(2) (1995) 417-422.
- [33] K. K. Kanazawa, J. G. Gordon II, Frequency of a quartz microbalance in contact with liquid, *Anal. Chem.* 57 (1985) 1770-1771.
- [34] A. Ispas, M. Pölleth, H. T. B. Khanh, A. Bund, J. Janek, Electrochemical deposition of silver from 1-ethyl-3-methylimidazolium trifluoromethanesulfonate, *Electrochim. Acta* 56 (2011) 10332-10339.
- [35] N. Sasaya, M. Matsumiya, S. Murakami, K. Nishihata, K. Tsunashima, Investigation into applicability of EQCM methods at elevated temperature for ionic liquids, *Electrochim. Acta* 194 (2016) 304-309.
- [36] J. Xu, P. Che, Y. Ma, More sensitive way to determine iron using an iron(II)-1,10-phenanthroline complex and capillary electrophoresis, *J. Chromatogr. A* 749 (1996) 287-294.
- [37] T. Hirokawa, K. Nishimoto, F. Nishiyama, Isotachophoretic separation of Fe(II) and Fe(III) by using 1,10-phenanthroline as a complex-forming agent, *J. Chromatogr. A* 723 (1996) 389-394.
- [38] H. Muramatsu, E. Tamiya, I. Karube, Computation of equivalent circuit parameters of quartz crystals in contact with liquids and study of liquid properties, *Anal. Chem.* 60 (1988) 2142-2146.
- [39] A. Bund, G. Schwitzgebel, Investigations on metal depositions and dissolutions with an improved EQCMB based on quartz crystal impedance, *Electrochim. Acta* 45 (2000) 3703-3710.

- [40] K. Naoi, M. Mori, Y. Shinagawa, Study of deposition and dissolution processes of lithium in carbonate based solutions by means of the quartz crystal microbalance, *J. Electrochem. Soc.* 143(8) (1996) 2517-2522.
- [41] J. F. Moulder, W. F. Stickle, P. E. Sobol, K. D. Bomben, *Handbook of X-ray Photoelectron Spectroscopy*, Perkin-Elmer Corp., Eden Prairie, MN (1992).
- [42] G. C. Che, J. Liang, Y. Yi, Crystal structure of X-ray diffraction properties, *J. Metall.* 22 (1986) B206-B211.

Electrodeposition from Deep Eutectic Solvents

R. Bernasconi, G. Panzeri, A. Accogli, F. Liberale,
L. Nobili and L. Magagnin

Additional information is available at the end of the chapter

<http://dx.doi.org/10.5772/64935>

Abstract

Deep eutectic solvents constitute a class of compounds sharing many similarities with properly named ionic liquids. The accepted definition of ionic liquid is a fluid (liquid for $T < 100\text{ }^{\circ}\text{C}$) consisting of ions, while DES are eutectic mixtures of Lewis or Brønsted acids and bases. Their most attractive properties are the wide potential windows and the chemical properties largely different from aqueous solutions. In the last few decades, the possibility to electrodeposit decorative and functional coatings employing deep eutectic solvents as electrolytes has been widely investigated. A large number of the deposition procedures described in literature, however, cannot find application in the industrial practice due to competition with existing processes, cost or difficult scalability. From one side, there is the real potential to replace existing plating protocols and to find niche applications for high added-value productions; to the other one, this paves the path towards the electrodeposition of metals and alloys thermodynamically impossible to be obtained via usual aqueous solution processes. The main aim of this chapter is therefore the critical discussion of the applicability of deep eutectic solvents to the electrodeposition of metals and alloys, with a particular attention to the industrial and applicative point of view.

Keywords: electrodeposition, deep eutectic solvents, metals, alloys

1. Introduction

The electrodeposition of metals for industrial surface finishing is nowadays a well-established industrial practice. Many processes are available to obtain a wide variety of coatings on most of

the substrates used in manufacturing. There are however some important limitations, as not all the metal/substrate combinations are possible in the current state of the art. This is connected to the nature of the electrolytes used for the vast majority of the plating processes, which are water based. Water is the most obvious choice to formulate a plating electrolyte, and in the majority of the cases, it is also the most convenient from the point of view of the results obtained. This solvent however presents some limitations: narrow potential window, reactivity towards specific metals, high hydrogen evolution in specific conditions, etc. If metal plating is limited to aqueous solutions, many possibilities are therefore precluded.

A possible way to extend the range of coating/substrate combinations is the use of non-aqueous solvents, characterized by extended potential windows and improved chemical inertness. A notable amount of scientific literature is available on a high number of non-aqueous systems. Deep eutectic solvents (DESs) are a particular class of such systems, and in the last few decades, they are finding application in the electrodeposition of many metals and alloys. This chapter is intended to be a review of the current state of art for electrodeposition from DESs and a critical discussion of the realistic applicability of DESs with particular attention to the industrial point of view.

2. Chemistry of DESs

Despite the fact that the physical properties of DESs are similar to those of other ionic liquids (ILs), their chemical properties exhibit peculiarities, which make them suitable for specific and different applications [1]. Melting point of two components strongly depends upon their reciprocal interaction: when considering a binary mixture of A+B, the difference in the freezing point at the eutectic composition compared to that of a theoretical ideal mixture is directly proportional to the interaction between the two single components A and B. The stronger the interaction, the larger will be the depression of the mixture melting point [1, 2]. This effect is schematically shown in the phase diagram presented in **Figure 1**.

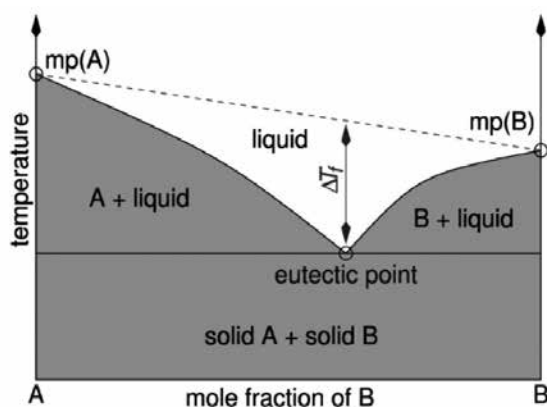


Figure 1. Eutectic formation in a two components phase diagram [1].

The word eutectic comes from a Greek word that means “easily melted” and indicates the temperature where the phases simultaneously crystallize from molten solution [2]. DESs includes a wide range of liquids close to the eutectic composition of the mixtures; differently from ionic liquids, which are formed primarily of one type of discrete anion and cation, they can contain a variety of anionic and cationic species [1]. They are mainly obtained by the complexation of a quaternary ammonium salt with a metal salt or an hydrogen bond donor (HBD) and can be schematically expressed by the general formula $\text{Cat}^+\text{X}^-\text{zY}$, where Cat^+ is in principle any ammonium, phosphonium or sulfonium cation and X^- is a Lewis base, generally a halide anion [1]. The interaction occurs between X^- and z molecules of Y , either a Lewis or Brönsted acid. Depending on the nature of the complexing agent used, four types of DESs can be categorized [1]. Such classification is presented in **Table 1**.

Type	General formula	Examples of terms
Type I	$\text{Cat}^+\text{X}^-\text{zMCl}_x$	$\text{M} = \text{Zn, Sn, Fe, Al, Ga, In}$
Type II	$\text{Cat}^+\text{X}^-\text{zMCl}_{x,y}\text{H}_2\text{O}$	$\text{M} = \text{Cr, Co, Cu, Ni, Fe}$
Type III	$\text{Cat}^+\text{X}^-\text{zRZ}$	$\text{Z} = \text{CONH}_2, \text{COOH, OH}$
Type IV	$\text{MCl}_x + \text{RZ} = \text{MCl}_{x-1}^+ \cdot \text{RZ} + \text{MCl}_x + 1^-$	$\text{M} = \text{Al, Zn}$ and $\text{Z} = \text{CONH}_2, \text{OH}$

Table 1. Classification of DESs and examples [1].

Up to now, the most widely Cat^+ species studied have been based on pyridinium, imidazolium and quaternary ammonium species [2]. As in traditional ionic liquid systems, the strongest depression of the freezing point is encountered when imidazolium-based DESs are used, due the intense interaction between the anion and the complexing agent. The simple handling and manufacture of DESs is one reason for their success. Mixing the two components, a mild endothermic reaction occurs, requiring only a gentle heating and stirring [2]. Moreover, they are water insensitive, which make it unnecessary to work in a glovebox with a controlled atmosphere.

2.1. Type I eutectics

Type I DESs formed from MCl_x and quaternary ammonium salt are the analogues of the well-studied metal halide/imidazolium salt systems [1]. Despite the fact they include a wide range of eutectic mixtures, from famous chloroaluminate/imidazolium to less common EMIC with different metal halides (FeCl_2 , AgCl , CuCl , LiCl , CdCl_2 , CuCl_2 , SnCl_2 , ZnCl_2 , LaCl_3 , YCl_3 , SnCl_4 , etc. [3]), the number of non-hydrated metal halides with a suitable low melting point is limited. Among them, the only ones which form ionic liquids with pyridinium, imidazolium and quaternary ammonium halides are FeCl_3 , ZnCl_2 , SnCl_2 , CuCl , InCl_3 , CdCl_2 , AuCl_3 [2]. ZnCl_2 -based DESs have been studied deeper in detail with respect to other systems: it was found that ZnCl_3^- , Zn_2Cl_5^- and Zn_3Cl_7^- species are present in the liquid, with proportions depending on the ionic liquid composition [2, 5]. They differ in dimensions and charge density one from the other and thus have peculiar electrostatic interactions with the cation. For

example, since ZnCl_3 ions are smaller and have stronger electrostatic interactions, the freezing point increases [2]. It is difficult to model the potential energy between the ions due to the complex nature of the anion and the non-centrosymmetric charge distribution on the cation. However, considering simultaneously the freezing point difference between the quaternary ammonium salts and the complexed metal salt and the potential energy, a correlation can be found: the variation of interionic potential energy and of the freezing temperature are indeed strictly related [2]. It was found that is possible to extrapolate the phase behaviour from simple ionic size considerations and that the symmetry has a minimum effect on the depression of the freezing point. Endres et al. show that the cation has a little effect on the freezing point of the eutectic-based ionic liquids: smaller cations depress the freezing point more because the correspondent halide salts have a higher freezing point [2]. Considering different cation dimensions, the two effects are to some extent compensated and the freezing point does not almost change. The ions size strictly influences both the conductivity and the viscosity of the type I eutectics: anhydrous zinc and iron salts based on DESs show lower conductivity and higher viscosity with respect to corresponding aluminium ionic liquids because of the larger ion size. In general, imidazolium-based liquids have lower viscosity and higher conductivity than the pyridinium or quaternary ammonium eutectics formed under the analogous conditions.

2.2. Type II eutectics

The number of metals that can be incorporated into an ionic liquid can be increased by using hydrated metal halides and choline chloride (ChCl) [1]. The presence of water decreases the melting point since the lattice energy is decreased too. Therefore, hydrated salts are more prone to form mixtures with quaternary ammonium salts that are liquid at ambient temperature with respect to anhydrous salts [2]. Examples of metal salts mixed with ChCl are $\text{CrCl}_3 \cdot 6\text{H}_2\text{O}$, $\text{MgCl}_2 \cdot 6\text{H}_2\text{O}$, $\text{CoCl}_2 \cdot 6\text{H}_2\text{O}$, $\text{LaCl}_3 \cdot 6\text{H}_2\text{O}$, $\text{CuCl}_2 \cdot 2\text{H}_2\text{O}$ [1]. Studies on the first mixture showed how the main charge carrying species are $[\text{Choline}]^+$ and $[\text{Cl}_3\text{H}_2\text{O}]^-$: this is consistent with the highest conductivity of these liquid compared to anhydrous salt mixtures [1]. The addition of Li^+ ions from LiCl does not cause the expected increase of the conductivity, probably due to the high ion solvation or to its high association with the anion. These systems are more temperature sensitive with respect to anhydrous metal salts. Although different metal salts can be theoretically deposited from these type of eutectic mixtures, up to now only Cr and Co have been deposited. Since hydrated systems are being considered, the deposition of Al and other low reduction potential metals is not possible due to the limited potential window [2].

2.3. Type III eutectics

These eutectics are formed from choline chloride and hydrogen bond donors [1]. They are able to solvate different metal species, including chlorides and oxides. Since the number of hydrogen bond donors is high, they constitute a group of easily tuneable liquids, adjustable for specific peculiar applications. Hydrogen bond donors (HBDs) include amides, carboxylic acids and alcohols [1]. These eutectic mixtures are easy to prepare and handle, as they are almost unreactive with water and biodegradable. For some of these eutectics, depression of

the freezing point is extremely high, even higher than 200°C for the oxalic acid-zinc chloride system [6].

2.4. Type IV eutectics

A metal chloride hydrate and a hydrogen bond donor mainly form these eutectic mixtures. Type IV eutectics are very interesting due to the production of cationic metal complexes, guaranteeing a high metal ion concentration close to the electrode surface [7]. A noteworthy example is ZnCl_2 , which forms eutectic compounds with different substances such as urea, acetamide, ethylene glycol and 1,6-hexanediol [1].

3. Physical properties of DESs

3.1. Viscosity

Viscosity is one of the most important properties of DESs due to its practical and industrial relevance. Although numerous works are present in scientific literature, there is a lack of information on DESs' behaviour at pressures different from ambient one and for related applications [8]. Typical DESs viscosity ranges from tens to hundreds of mPa s at temperatures around ambient one or slightly higher [1, 2, 8]. Some exceptions occur, for example, in the case of compounds containing $\text{ChCl} + \text{ZnCl}_2$ in a 1:2 molar ratio, which can give rise to viscosity of 85,000 mPa s at room temperature [9]. The most remarkable DESs for practical purposes are in general those with low viscosities, close to the widely used organic solvents or water-based solutions. It is important to note that differences in experimental methods, sample preparation and impurities can affect significantly the measure obtained [8].

The presence of impurities is the variable that more deeply affects the rheological behaviour of these systems. Moreover, some of DESs are non-Newtonian fluids: this feature can influence the viscosity analysis methods for this kind of system. The hygroscopic nature of many DESs strongly influences their viscosity, which can change of even two orders of magnitude from dehydrated to hydrated eutectics [8]. An example is that of ChCl and oxalic acid equimolar mixtures, whose viscosity passes from 5363 to 44.49 mPa s when water is absorbed [9]: water addition could be an easy method for tuning the viscosity and it is indeed applied in different cases. However, because water may compete with CO_2 in absorption sites occupation in systems tailored for CO_2 absorption, the efficiency could be depressed affecting the obtained result [10, 11]. Moreover, the presence of water could be detrimental for some electrodeposition procedures [1, 2, 8].

The temperature-viscosity dependence has been deeply investigated in literature following Arrhenius equation or Vogel-Fulcher-Tammann one [7]. As intuitively predictable, viscosity decreases with increasing temperature. In particular, using an approach based on a temperature-viscosity fitting through an Arrhenius model, it is possible to calculate the activation energy E_a and therefore the strength of intermolecular forces in DESs [2, 12, 13]. Low-viscosity DESs have low E_a values, whereas more viscous systems show higher activation energies.

Abbot and co-workers [8], following the same approach used to relate melting temperature and activation energy of molten salts, found out an almost linear relationship also for DESs: larger melting points are indeed associated with larger E_a (and subsequently larger viscosity) (Figure 2).

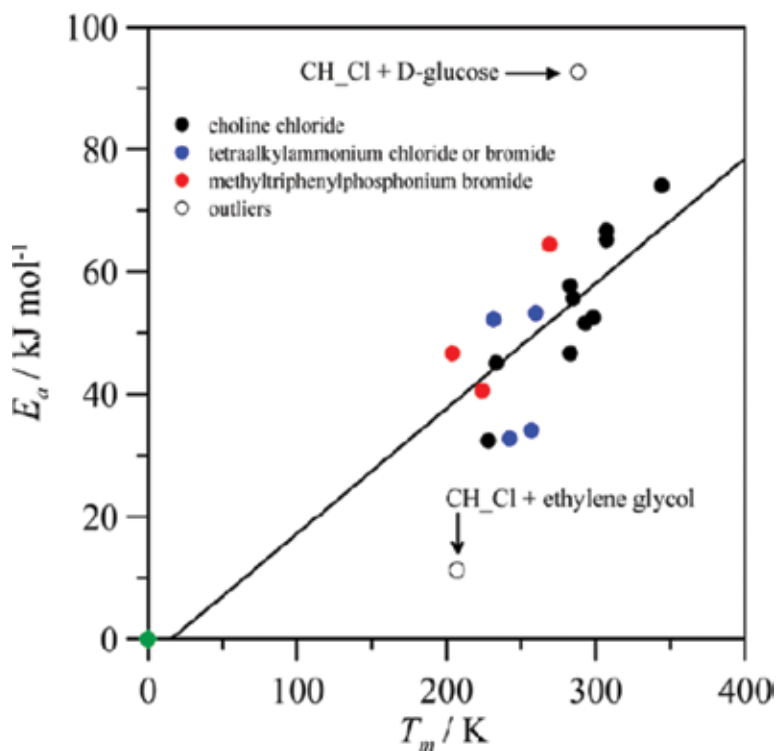


Figure 2. The almost linear relationship between activation energy and temperature [13].

In the case of DESs, ions have a relatively large size if compared with the voids between the ions themselves. Such voids represent the free space between the different moieties that constitute the DES and are generally called holes. Relating viscosity data in the light of hole-theory approach [14–16], for which viscosity and electrical conductivity are correlated with availability of holes in the fluid, it is possible to evince that DESs with larger holes lead to less viscous fluids. Deviation from this general trend is shown when very viscous systems are taken into account.

3.2. Conductivity

Conductivity cannot be considered separately from viscosity, since the two are strictly related. Generally, a low viscosity is usually associated with a high conductivity and vice versa [8]. Low viscosity DESs have conductivity in the order of even tens of mS cm^{-1} [16], while for most common high density DESs an order of magnitude lower is usually observed. A theoretical

approach for determining conductivity can be followed using the hole-theory approach [15, 16]. Because of both holes availability and kind of bonds between ions and HBDs have to be taken into account, achievement of a univocal trend in all the analysed systems is difficult to obtain. During conductivity modelling, many aspects from chemical to hydrodynamic ones have to be taken into account. The typical trend implies an increase in conductivity when higher quantities of salts are used [16], but this is not always true, since both the type of salt and HBD and their interaction have to be considered. Some DESs indeed manifest deviation from the general trend: for example, ChCl:ethylene glycol-based DESs show a maximum in conductivity, which then decreases after a certain salt concentration [8]. The conductivity dependence on temperature is well described by an Arrhenius model, through which analogous computation to those used for viscosity can lead to activation energy evaluation [8].

Viscosity and conductivity are usually plotted together in the so-called Walden plot, where molar conductivity and the inverse of viscosity, that is fluidity, are represented in a logarithmic scale [8]. The obtained data are compared with an ideal line passing through the origin for a potassium chloride solution. The deviation from ideality is higher in the case of DESs with respect to common ILs, since in the first case ions and HBDs complexes have to be considered [16]. An example of Walden plot is reported in **Figure 3** [8].

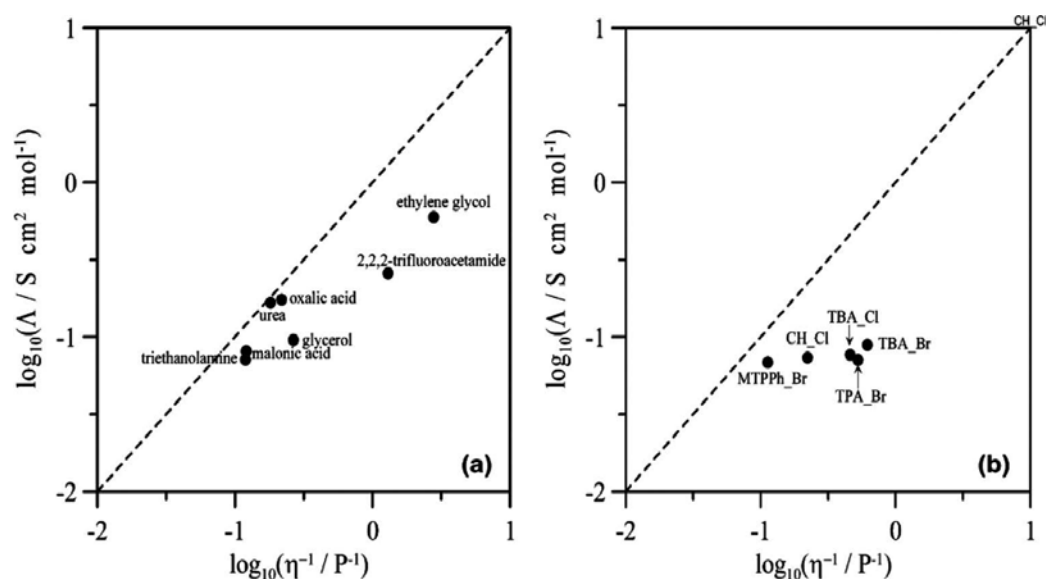


Figure 3. Walden plots for a series of DESs [13].

The deviation from the ideal line is associated with the systems ionicity: low viscous liquids have lower ionicity i.e. high deviation, whereas high DESs show the opposite behavior [15]. Ionicity is influenced by both salt nature and interaction between ions and different HBDs [8, 15]. Nowadays, although good correlation between effective experimentally measured conductivity and theoretically predicted one has been proved with some models for a set of

DESs, a unique broadly applicable method for conductivity is still not available or, at least, not reliable [8]. An important factor which governs both viscosity and conductivity is the diffusion coefficient of molecules present in ILs [17, 18] influenced by both hole size distribution and intermolecular forces [8].

3.3. Electrochemical reactions

Due to their practical application, DESs electrochemical properties are very important: they are evaluated by means of cyclic voltammetries and electrochemical impedance spectroscopy [19]. The material used as working electrode has obviously a relevant influence, and peculiarities are revealed for each material selected. Many studies have been performed on mixtures, revealing some differences with respect to high-temperature molten salts [4]: the differential capacitance indeed increases with temperature for all the electrodes studied with the exception of Au [1]. For example, when different HBDs are used for the same ChCl system, specificities are encountered related to the HBD type: it has indeed an influence on the negative limit of polarization [1]. Moreover, an increase in temperature of DESs results in narrower electrochemical windows and in larger capacitance currents [1]. Although the electrochemical window is generally smaller than pure ILs one, it is suitable for a wide range of electrochemical purposes [1, 8]. In the cathodic part of CV curves, again for ChCl-based DESs, a layer of HBDs molecules adheres to the electrode surface, while choline cations are in contact with the electrolyte [1]. When passing to less negative potentials, the absorption of anions occurs replacing partially positive choline ions [1]. The Helmholtz type layer model of the double layer at large negative potential is validated from very similar results obtained by replacing choline with other cations, such as acetylcholine [1]. Because of DESs ionic character is dependent on their chemical-physical properties, the comprehension of metal ions behaviour in the liquid is really important. Many efforts have been made by Abbott's group to determine, through equilibrium electrochemical measurements, the activity coefficients for metal salts in DESs and how they vary with concentration [16]. Understanding the activity of a solute in solution is indeed fundamental for using the full potential of a reactive species. Comparing the redox potentials of metal couples in an established DES mixture with those in an aqueous medium allows understanding the potentialities of a system for electrodeposition purposes and other applications. However, since there is plenty of factors influencing them, a univocally valid model cannot be found.

4. Electrodeposition of metals from DESs

Due to their good properties as electrolytes, electrodeposition is an obvious possible application for DESs. Nowadays, this technique is one of the most used surface finishing methods in industrial applications. It consists mainly in the formation of a solid metal coating on the electrode surface starting from metal cations dispersed in the electrolyte, reduced on the cathode under an electrical potential. This electrochemical process is used to functionalize surface to obtain required properties, for example hardness, corrosion and wear resistances, abrasion, brightness, magnetism, electrocatalysis [20]. Although electrodeposition can be

carried out using several solvents, due to the well-known baths chemistry and handling, electrodeposition of metals and alloys is performed usually from aqueous solutions. The number of metallic coatings obtaining from aqueous baths is strictly related to those having redox potential higher than the water one: this narrow potential window entails gas evolution with subsequent hydrogen embrittlement phenomena and the formation of insoluble oxides and/or hydroxides on the electrode surface (passivation) which hinder the deposition of thick metallic coatings. Moreover, many of the traditional aqueous solutions are based on toxic components and show low current efficiency [e.g. Cr(VI) plating]. For these reasons and especially for the possibility to electrodeposit metals having Nernst potential well below water decomposition one, for example titanium, aluminium, tungsten suitable for many industrial applications (e.g. anti-corrosion, batteries) that cannot be plated starting from aqueous solutions, electrodeposition based on deep eutectic solvents (DESs) could be the alternative [21]. DESs show high solubility for metal and metal oxides and hydroxides allowing the possibility to avoid passivation phenomena during electrodeposition or electropolishing, to plate thicker metal layers and to use them in electrochemical processes such as metal recovery and metal separation. Furthermore, the wider potential window, the absence of water (no embrittlement phenomena), the relatively high conductivity compared to other non-aqueous solvents, the relatively low cost, simply preparation and biodegradability make them suitable for industrial electrodeposition processes, although these are not economically competitive with respect to the existing ones. However, the instability of DES baths, while the electrodeposition proceeds, has to be solved prior to a possible industrial transfer [2]. Electrodeposition from DESs could be the way to easily circumvent legislative restriction related to aqueous precursor toxicity used in current technological electroplating systems (Ni, Cr, Co) known to be carcinogenic and the related high disposal costs [1, 21]. In case of DESs deposition, morphology and adhesion of the growing metal coatings are dependent on applied current density, DES composition and presence of additive. As in case of aqueous-based baths, the plating process can be carried out under constant current or constant voltage regimes [2]. In this dissertation, electrodeposition of the most popular metallic coatings starting from DESs made of ChCl and either ethylene glycol or glycerol or urea are shown.

4.1. Nickel

Nickel metal coatings can be successfully obtained by dissolving nickel chloride dehydrate salts both in ChCl:urea and ChCl:ethylene glycol [16, 22]: coatings morphology obtained from DESs baths is completely different compared to the aqueous plated Ni, due to the different thermodynamics and kinetics of the two processes [23]. Recent works demonstrate that the addition of different components into DESs-based electrolyte can induce changes in terms of microstructure, morphology and redox behavior of the Ni(II) ion. Let us consider the case of nicotinic acid [23] and ethylenediamine [24], whose addition in a ChCl: urea bath affects the morphology and the microstructure of the metal coatings and allows obtaining high uniform and shiny deposits. The effect of these species on the electrodeposition process can be ascribed to the formation of Ni(II) complexes and their subsequent absorption on the electrode surface. These phenomena decrease the nickel deposition current and its nucleation lowering the particles size. The effect of process temperature on the coating quality was investigated by Gu

et al. [25] performing electrodeposition at ambient temperature and at 90°C using a ChCl:ethylene glycol bath on a brass foil. This work demonstrates that the surface roughness increases with temperature due to the formation of nanosheets with a thickness of 10–20 nm and grains size of about 10–50 nm. This phenomenon is related to a decrease of DES viscosity causing an increase of ion species mobility, enhancing in this way the deposition process and the nucleation of Ni. The obtained coating shows also low corrosion potential. Abbott et al. [22] have also studied the Ni electrodeposition starting from the ChCl:ethylene glycol DES bath, obtaining a dark grey deposit: the addition of ethylenediamine and acetylacetamide in this kind of electrolyte induces the suppression of the Ni underpotential deposition. Due to the growing industrial interest on composite materials, several studies have been done in order to develop electrodeposition process starting from DESs. Using Ni as matrix, compact Ni-multiwalled carbon nanotubes (MWCNTs) were deposited on copper substrate. In order to have a high efficient deposition process, a homogeneous dispersion of MWCNTs into the electrolyte has to be guaranteed. This has been obtained dispersing MWCNTs into ChCl:urea DES before the addition of soluble Ni chloride salt. Morphology, crystallinity and roughness of Ni coating were affected by the presence of MWCNTs [26].

4.2. Chromium

For several decades, hard chromium plating has been the most used metallic coating employed for several applications, especially to protect components operating in high wear and corrosion environment. This was due to its high hardness and its natural ability to inhibit corrosion. Due to its significant use in the industry, chromium electroplating based on Cr(VI) aqueous electrolyte is the highest optimized process. However, a series of issues, with most important the extremely negative environmental impact of the hard chromium plating process, due to the use of the carcinogenic hexavalent chromium, has led to a number of directives and legislation related to the restriction of this method [27]. This favours the necessity of finding less hazardous method replacing the present one. Up to now, some Cr(III) processes are on the market, but the obtained results are not repeatable. As demonstrated by recent scientific studies, the Cr electrodeposition from DESs could be the way to achieve metallic coatings having same properties of Cr(VI) ones. In particular, Abbott et al. have reported DESs obtained mixing ChCl with trivalent chromium chloride salts [28, 29]: in this electrolyte, electrodeposition process with a very high current efficiency (>90%) leads to a formation of a very thick and adherent chromium layer. Modifying the Cr(III)-based electrolyte is possible to plate coatings with different morphologies: soft but not microcracked (dull black), hard chromium (hardness > 700 HV, increased up to 1500 HV after thermal treatment) and very thin layer with a mirror appearance. The same research group demonstrated that the addition of LiCl into the bath promotes the formation of nanocrystalline crack-free black chromium deposit, suitable for decorative applications, with good corrosion resistance [30].

4.3. Zinc

Due to its peculiar features such as low cost and protection against corrosion, zinc has a paramount importance into the metal finishing industry. Because of Zn electrodeposition from

aqueous solution is inexpensive and produces very good coatings, the study of electroplating from DESs is mostly used for Zn alloys production [1]. However, several studies have been done in order to understand the Zn deposition process using different DESs, in particular ChCl:urea [31] and ChCl:ethylene glycol [32]. Compared to aqueous electrodeposited Zn having a dendritic structure, those ones plated with DES shows very different morphologies. Using ChCl:ethylene glycol bath, deposited Zn shows very thin platelets with the planar face perpendicular to the electrode surface, according to progressive nucleation mechanism. In case of ChCl:urea, zinc coating has a rice-grain morphology, consistent with a rapid nucleation mechanism. The effects induced by the addition of some chelating agents such as acetonitrile, ammonia and ethylenediamine on the electrochemical process were studied [31]: these additives act as brightener but at the same time affect the electrodeposition process and lead to the formation of macro-crystalline deposit like in water. This phenomenon can be ascribed to the adsorption inhibition of chloride on the electrode surface induced by the presence of ammonia and ethylenediamine. Because of the addition of complexing agent to ChCl:urea and ChCl:ethyleneglycole baths does not change the metal species present in the baths ($[ZnCl_4]^{2-}$), it is possible to deduce that the morphology variation after their addition is caused by the chemical processes taking place in the diffusion layer or on the cathodic surface rather than in the bulk [16, 33]. Another important study was performed by Bakkar et al., in which the electrodeposition of Zn using ChCl based electrolytes on magnesium substrates [34]. Mg and its alloys are difficult to be electroplated and so cannot be used as substrate in aqueous solution due to their water-sensitiveness, their tendency to form MgO and/or Mg(OH)₂ film inhibiting adhesion of the electrodeposited coating and their high reactivity inducing formation of loose immersion layers on the surface by replacement that stops the following electrodeposition. Furthermore, magnesium suffers of microgalvanic deterioration if it is in contact with cathodic metals in a wet environment: this means that Mg is subjected to strong corrosion attack by aqueous electrolytes. Developing an electrodeposition process based on DESs could be an important turning point for a successful application of protective coatings on magnesium largely used in automobiles, aerospace and electronics industries. The authors have compared the efficiency of several ChCl-based DESs, in particular 1 ChCl:2 urea, 1 ChCl:2 ethylene glycol, 1 ChCl:1 malonic acid, 1 ChCl:2 glycerol and 1 ChCl:2 ZnCl₂. From this study, it is possible to evince that Mg has the lowest corrosion rate in 1 ChCl:2 urea, the most feasible mixture for successful Zn electrodeposition, whereas the other mixtures produce powdery deposits or Mg corrosion. In particular, in case of 1 ChCl:2 glycerol pitting phenomena on Mg surface occur. The application of pulsed cathodic current during the electroplating process helps for the production of smooth, uniform and corrosion-resistant Zn coating, similar to that of pure zinc [34].

4.4. Aluminium

Aluminium is one of the metals that cannot be plated in aqueous media because of its Nernst potential, well below the water decomposition one. Moreover, the high stability of aluminium oxide makes it high resistant to corrosion, but unfortunately this means that it cannot be electroplated from aqueous electrolytes [21]. In any case, aluminium electrodeposition is an important technological target due to its application in electronic, energy storage and anti-

corrosion fields. During the last years, many efforts have been put on aluminium electrodeposition from pure ionic liquids (ILs). However, the high hygroscopic nature of AlCl_3 -based ILs obligates to prepare and handle them under inert gas atmosphere, delaying progresses in this kind of process [35]. Several kinds of electroplating processes for Al deposition have been developed starting from DESs, both I type and IV type. Although the anodic reaction of this process is still low and the deposition rate has to be increased, the simple addition of acetamide to AlCl_3 allows obtaining an electrolyte suitable for Al electrodeposition, relatively insensitive to water. Electrolytes characterization has shown that both cationic and anionic aluminium species, namely $[\text{AlCl}_2]^+$ and $[\text{AlCl}_4]^-$, are present [1].

4.5. Copper

Since Cu electrodeposition is very common in surface finishing industry, many studies involving DESs copper plating have been done. In particular, Popescu et al. have studied Cu electrodeposition from ChCl combined with urea, malonic acid, oxalic acid and ethylene glycol, using as CuCl as copper source [36]. From those studies, it is possible to evince that the better deposit can be obtained from ChCl :oxalic acid and ChCl :ethylene glycol: the coating was fine, homogeneous and adherent. Furthermore, Abbott et al. have produced different kind of Cu deposits depending on Cu concentration into ChCl :ethylene glycol DES: bright nanostructured deposit corresponding to progressive nucleation of Cu was obtained for concentrations 0.01–0.1 M; for concentration lower than 0.01 M, black deposit was formed corresponding to a spontaneous nucleation of Cu [37]. Using chronoamperometry, impedance spectroscopy and cyclic voltammetry (CV) analyses into ChCl :ethylene glycol DES, Murtomaki et al. have studied the electron transfer kinetics of $\text{Cu}^+/\text{Cu}^{2+}$: the reaction was found to be quasi reversible and the [38]. In some cases electrodeposition from DESs not containing chloride ions can be advantageous. This is valid in general when a metallic layer is deposited on thin layers of metals sensitive to chloride corrosion, like nickel or iron. In the case of copper, deposition from a chloride free DES was studied for instance by Bernasconi et al [39] using a choline chloride dihydrogen citrate:ethylene glycol mixture with anhydrous copper sulfate as metal source. Abbott et al. have studied the electrodeposition of composite Cu coating with SiC and Al_2O_3 . The addition of these particles does not affect the morphology and the size of Cu particles. The amount of particles dispersed into the DESs is directly related to the composition of the composite materials [37].

4.6. Silver and other metals

Silver electrodeposition from ChCl :ethylene glycol DES was performed using Cu as substrate: Ag not only oxidizes the copper substrate, but it is deposited on the electrode surface on the same time, forming a very shiny nanocrystalline coating. Gomez et al. have evaluated the chloride anion function during the electrodeposition process in 2 urea: choline chloride DES by means of voltammetric and chronoamperometric analyses [40]. The work reveals that Ag deposition takes place as 3D nucleation and growth process under diffusion control. The best hypothesis is that chloride induces the formation of rounded grains at short deposition times hindering uncontrolled directional growth. Adding SiC and Al_2O_3 particles to ChCl :ethylene

glycol DES, the Ag coating morphology is not affected by the particles presence. The most important point is that the hardness of the Ag coating from DESs after the incorporation of the particles is higher with respect to the same deposit obtained from aqueous electrolytes. Moreover, this value is not dependent on the reinforcing particles size. Al_2O_3 reinforced coatings show a low friction coefficient. Because of the lithium salts modify the mechanism of metal nucleation, LiF was added during the Ag deposition, inducing higher hardness leaving the structure unchanged [41, 42]. Magnesium metal can be plated using dimethylformamide and magnesium chloride hexahydrate-based DES. Cyclic voltammetry analyses indicate that the deposition of this metal is irreversible whereas from X-ray diffraction analyses, it is possible to evince that the plated coatings are Mg_2Cu and MgO , revealing that an alloy with Cu substrate is formed [43]. Rahman et al. have studied indium electrodeposition starting from 1ChCl: 2urea DES at which indium sulphate is added [44]. The electrodeposition was performed on Au and Mo. To determine the type of nucleation, the current-time transients were normalized and compared to the theoretical dimensionless current-time transients obtained from Scharifker-Hills model. The work reveals that indium electrodeposition on molybdenum electrode proceeds via instantaneous nucleation with diffusion-controlled growth, whereas on the Au electrode, the deposition proceeds via progressive nucleation. The surface roughness decreases at higher current density [44].

5. Electrodeposition of alloys from DESs

A significant amount of scientific work is present on the electrodeposition of pure metals from DESs. The interest in such systems is even greater considering the electrodeposition of alloys; the use of aprotic liquids (e.g. DES) avoids the limited potential window and hydrogen evolution issues of aqueous solutions [1, 45]. Thus, the number of possible metallic elements combination is largely increased. The study on systems already affirmed in the galvanic industry increases the amount of useful information on DES without claiming new possible industrial solution. On the contrary, for example, the possibility to deposit alloys containing rare earth elements with relatively ease may represent a unique and valid solution also outside academics [1, 45].

5.1. Corrosion resistant alloys

The demand of corrosion resistant coating is one of the highest in the surface finishing market, consequently great efforts are put in finding new solutions to improve nowadays processes. DES may avoid problems related to bath toxicity of existing process or for improving process efficiency [1, 43]. One example is the electrodeposition of Zn alloy, largely employed in the galvanic industry, for example ZnNi, ZnFe, ZnMn. The main advantage over the aqueous solutions is related to the reduction of hydrogen evolution, causing substrate embrittlement and poor deposit quality [45]. In addition, the relatively high redox potential difference between Zn and the correspondent alloying element complicates the deposition process, and anomalous deposition is observed. Employing DES system, chlorometallate ions are formed in the solution shifting the redox potential; higher compositional control of the deposits is

obtained. Fashu et al. show a significant dependence of composition and surface morphology of ZnNi deposits, obtained from choline chloride-urea solution, on electrolyte concentration, temperature and voltage applied; alloy composition can thus be tuned significantly with different process parameters [46]. Abbot et al. reported the electrodeposition of ZnSn alloys, candidates for replacing Cd, from ethylene glycol-based solution; ChCl:urea and ChCl:ethylene glycol DESs containing 0.5 M ZnCl₂:0.05 M SnCl₂ are studied in terms of deposit composition and morphology [47]. In view of corrosion resistance coatings, different alloys have been reported in literature.

You et al. carried out a study on NiCo alloys from ChCl:ethylene glycol; Ni-rich alloys with 4–40 wt.% Co showed an important improvement with respect to pure Ni deposit in the corrosion potential [48]. In a similar DES system, Saravanan et al. replace Ni with Cr evaluating both microstructure and potentiodynamic polarization behaviour in the composition interval 65–81 wt.% Co of CoCr deposits [49]. The same research group obtained NiFeCr deposits containing approximately 53–61% Fe, 34–41% Ni and 4–15% Cr from ChCl:ethylene glycol [50]. Zhang et al. successfully deposited CrP coating from a Cr(III) solution by adding ammonium hypophosphite (NH₄H₂PO₂) to a ChCl:ethylene glycol deep eutectic solvent containing CoCl₂ salts [51]. Employing the same system, You et al. firstly deposited NiP alloy coatings at room temperature; deposits with 8 wt.% P have been evaluated from the corrosion point of view [48].

5.2. Magnetic alloys

With progressive improvements and miniaturization in the microelectronic industries, the ability to obtain functional thin films is fundamental. Magnetic alloys have assumed a crucial role in a huge number of microelectromechanical system (MEMS), for example actuators, sensors [52]. In addition, the huge potential in biomedical applications of wirelessly controlled microrobots has attracted the attention of many researchers [53]. Nowadays, electrodeposition from aqueous solution is largely employed for the fabrication of magnetic films, for example FeCo, FeCoNi and CoPt, while few studies are present employing DES solvent. In the field of MEMS application, Guillamat et al. successfully obtain hard-magnetic CoPt without the need of subsequent heat treatments [54], avoiding a critical fabrication step for microelectromechanical system with layered and complex architecture. Yanai et al. showed the suitability of ChCl:ethylene glycol-based DES for FeNi alloys where deposits composition has shown to be easily controlled varying the reagent in the bath [55].

On the other hand, complex systems are commercially available for high performances magnets: SmCo, AlNiCo and NeFeB alloys. The correspondent metallic products are mainly fabricated through sintering or casting; the presence of rare earth metals or elements having high negative reduction potential limits the suitability of electrodeposition processes. Gomez, Cojocar and co-workers firstly succeeded in the electrodeposition of SmCo alloys employing a choline chloride–urea solution [40, 56]; the relative ease, low cost and precision of this process may represent an alternative to the metallurgical ones.

5.3. Semiconductors and photovoltaic alloys

With the emerging field of thin films solar cells, electrodeposition process started to gain importance also in the photovoltaic field. Unlike common vacuum techniques employed in the semiconductors industries, electrodeposition is a low-temperature atmospheric process allowing the fabrication of small features with high precision and control [57]. Among the active materials, CdTe is the most extensively studied chalcogenide material in the field of electrodeposition; the process is affirmed, and efforts are paid to bring the process to high volume production. On the other hand, Cu(In,Ga)Se₂ (CIGS) is the material having the best absorbing properties [56]. Studies on aqueous solution show the difficulties in controlling the composition, for example non-linearity between the metal concentration in solution and in the deposit; moreover, the process is characterized by very low faradaic efficiency (5%) due to Ga low reduction potential [58]. Malaquias et al. proposed a Mo/Cu/InGa metal stack subsequently selenized to obtain CIGS [58]; InGa deposition has been successfully carried out from 1ChCl:1Urea system [59]. Steichen et al. proposed a similar route for the fabrication of CuGaSe₂(CGS) active material; controlled electrodeposition of CuGa alloy is proposed using the same DES solution [60].

5.4. Alloys for electrocatalysis

Electrocatalytic processes are largely employed in the industry in different area of interest such as hydrogen production, energy conversion/production, electroplating. The employment of a catalyst is in fact a fundamental pillar of all the electrochemical processes. For example, nickel alloys have assumed an important role in water electrolysis process, both for the hydrogen and oxygen evolution reaction [61]. Vijayakumar et al. successfully deposited NiCoSn alloy from 1ChCl:2EG system and evaluated the improvement with respect to NiSn and CoSn alloys, obtained from the same solution, in terms of catalytic activity in 1 M KOH alkaline solution [59]. PtCo alloys are characterized by high electrocatalytic activities as well, and Guillamat et al. successfully electrodeposited alloys with different composition between 54 and 90% wt. Pt [54].

6. Industrial applicability and implemented processes

A series of concerns must be considered when evaluating the realistic applicability of DESs electrodeposition in the industry. The main driving force for the development of new surface finishing processes is of course the need to improve existing industrial processes or to introduce brand new ones. For this reason, also electrodeposition from deep eutectic solvents must open new possibilities with respect to the current state of the art in order to be implemented as an industrial finishing process. Almost all the plating technologies used nowadays in the galvanic field use aqueous-based solutions. Each new DES-based process is therefore in competition with its homologous water-based counterpart, and possible advantages and disadvantages of its substitution must be carefully weighted. Aqueous solutions are widely used, the know-how for their employment is well established and in most cases their cost is

highly competitive. For this reason, in order to be accepted as realistic alternatives for water-based treatments, DESs must present significant advantages. This part of the chapter is intended to be an analysis of the realistic possibility to see large-scale applications for DES-based electroplating in the next few decades, as anticipated by some existing reviews [35]. Some pilot projects, already used on smaller scales, are presented as well to give a perspective and to demonstrate that, if the application is well calibrated, DESs can find application in industry.

6.1. Industrial applicability of metal deposition from DESs

As reported previously in this chapter, in principle DESs can be used to electrodeposit the main commodities metals: copper, nickel and zinc. From the practical point of view, however, their application to the deposition of coatings on most of the metals used in the industry (iron, copper, brass, nickel and their alloys) to produce functional parts is not realistic. These substrates are in general easy to plate after suitable pretreatments, and a wide variety of aqueous-based solutions is available for the most common metals [20]. A good example is copper, which can be deposited from alkaline, nearly neutral or acidic solutions reaching high thicknesses, excellent surface finishing and cathodic efficiencies [62]. The same is true also for nickel or zinc [62]. Moreover, deposits from DES-based solutions present in general a lower quality with respect to the ones from aqueous solutions. This is not always true, as Abbott et al. demonstrated in the case of nickel [63]. In this case, however the comparison is done between non-additive aqueous nickel baths and a choline chloride-based DES, while in industrial practice, solutions are most of the times modified with suitable additives to improve properties of the deposit (hardness, ...) or surface finishing.

There are however some applications where plating commodities metals from a non-aqueous solution are preferable, like in the case of substrates that are not easy to metalize (e.g. aluminium and magnesium). These metals are widely used, in general as alloys, for their low weight and good mechanical properties. The application of metallic layers on their surface is not trivial, since they tend to quickly passivate (or corrode, according to the pH of the electrolyte) upon exposure to the plating solution [64–66]. As already previously exposed, Mg alloys are in particular the most difficult due to their tendency to form MgO and/or Mg(OH)₂ film inhibiting adhesion of the electrodeposited coating and their high reactivity inducing formation of loose immersion layers on the surface by replacement that stop the successive electro-deposition. Furthermore, Mg is subjected to strong corrosion attack by aqueous electrolytes. The use of DES-based electrolytes can allow the deposition on aluminium or magnesium without specific pretreatments. This was demonstrated by Abbott et al. [22], Florea et al. [67] and Bernasconi et al. [68] in the case of nickel on aluminum and by Bakkar et al. [34] in the case of zinc on magnesium. Compact metallic layers can be applied on Al 1100 alloys and Mg-RE alloys by using a 1:2 mixture of choline chloride and urea additivated with metal ions and, in the case of nickel, a suitable complexing agent (ethylenediamine). The resulting coatings present good adhesion and corrosion behaviour. Other metals, such as chromium, can be plated on the resulting nickel if it is used as adhesion layer, producing thus multilayers [68].

A notable case in which it may be preferable to use DESs on an easy to plate substrate like steel is zinc deposition. Zinc is efficiently deposited from aqueous solutions, but, in this case, a considerable amount of the current supplied is lost for hydrogen evolution. Besides the low cathodic efficiency, the hydrogen produced can cause many problems to high-strength steels, inducing an embrittlement of the material [45, 69]. It can be thus beneficial to use DES-based electrolytes to plate zinc due to their low hydrogen evolution.



Figure 4. A chrome plating pilot plant part of the IONMET consortium activities [80].

Another possible application is the electrodeposition of some metals that are difficult or costly to electrodeposit from aqueous solutions. These may include highly reactive metals like samarium [40, 56] or inert metals such as indium [44]. In addition, the electrodeposition of metals which reduction potential falls outside the electrochemical window of water, like Al [70], can be in principle achieved. Their plating however must be performed in inert atmosphere with anhydrous solutions and a coating quality lower than imidazolium-based ionic liquids is in general achieved [71, 72]. For this reason, DESs do not offer real advantages with respect to other ionic liquids. Silver and other precious metals, characterized by high reduction potentials, can present some advantages when electrodeposited from DESs. Typically, these metals require strongly complexed electrolytes or the presence of intermediate plating steps to avoid undesired displacement deposition (resulting in poor adhesion) [62]. DESs strongly complex metallic ions, and for this reason, their use can result in good quality layers. Examples may include Ag [73] and Pd [74].

A particular case is represented by chromium plating. Functional chromium coatings are usually obtained from Cr(VI) containing solutions, but Cr(VI) is a recognized carcinogenic and environmentally hazardous chemical [75]. For this reason, it will be progressively banned from the industrial practice. EU is currently eliminating Cr(VI) as a chromium source in the case of decorative coatings, since Cr(III)-based aqueous solutions constitute a good alternative [76].

This is unfortunately not true in the case of functional hard chromium and aqueous solutions are not able nowadays to provide properties comparable to those coming from Cr(VI)-based electrolytes. DES-based Cr(III) solutions on the contrary showed promising results. In particular, cracked and crack-free thick coatings have been obtained from CrCl₃/choline chloride mixtures with cathodic current efficiencies higher than Cr(VI)-based electrolytes [29, 30, 45].

Not many examples of plants using DES-based electrodeposition processes are available nowadays, and all of them are pilot or semi-industrial projects. The Abbott group [77] at the University of Leicester is the most active in the industrialization of DES-based processes with its collaboration in the IONMET consortium [78], created under the 6th EU Framework Programme of Research. IONMET, in collaboration with Scionix [79], realized the ionic liquid demonstrator (ILD), which is a multi-application pilot plant facility to showcase the application of ionic liquids. Industrial electroplating of chromium and nickel was demonstrated at ILD. The IONMET consortium itself is scaling up many laboratory processes [78, 80], the most interesting one being hard chromium plating from DESs. Scionix is the largest world manufacturer of ionic liquids for industrial applications and of DESs in particular (**Figure 4**) [79]. Some patents are available as well for general metal deposition [81] or for specific applications: Ag [82], Au [83], superhydrophobic Ni layers [84], Fe [85], Zn and Ni [86] and Ga [87].

Some patents are available as well for general metal deposition [78] or for specific applications: Ag [79], Au [80], superhydrophobic Ni layers [81], Fe [82], Zn and Ni [83] and Ga [84].

6.2. Industrial applicability of alloys deposition from DESs

The considerations exposed in the case of metals deposition can be adapted to the plating of alloys. In particular, many different alloys are difficult to electrodeposit from aqueous solutions. The reasons are mainly correlated to the properties of some metals, which present high reactivity or refractoriness in water.

ZnMn alloys are difficult to plate in aqueous mediums due to the low reduction potential of manganese and to its reactivity [88]. These alloys, useful for corrosion protection, can be however obtained from choline chloride/urea mixtures [89] with good coating properties. On the contrary, Mo-based alloys are difficult to obtain in a wide composition range due to the inertness of molybdenum. The use of DES to obtain these alloys, also in this case promising for corrosion protection, can extend the compositional range with respect to water solutions (like in the case of NiMo and CoMo [90]). Always in the field of Zn-based materials, ZnSn is a particular case of alloy that can be deposited in water but present some advantages when plated in DESs. This material, a good option to replace cadmium in anticorrosion coatings, is plated from aqueous solutions [47], but composition control is easier when the deposition is performed in strongly complexing electrolytes like DESs [47]. Plating with DESs also avoids excessive hydrogen evolution, which may result in embrittlement of the coating. Similar considerations can be done for ZnNi and ZnFe.

Due to their negative standard reduction potential and high reactivity, almost all the rare earth-based alloys are not easy to plate in water-based solutions. Many of these alloys, like SmCo,

present however interesting properties, suitable for magnetic recording devices. The use of DESs for their electrochemical deposition can remove many obstacles with respect to aqueous plating. This was demonstrated by Gomez et al. [40, 56], which obtained high coercivity layers from a choline chloride/urea DES.

From the applicative point of view, for alloys the IONMET consortium is currently scaling up laboratory scale ZnSn deposition to perform barrel plate on industrial scale [78]. This is so far the only notable example of industrial application for alloys plating from DESs. Also in the case of alloys deposition, like in the case of pure metals, some patents for industrial processes are available: CrNi [91], CIGS [92] and AuSn [93].

6.3. Industrial applicability of electroless and displacement deposition from DESs

In this part are treated some processes not strictly related to electrodeposition but of some industrial interest. In the case of electroless and displacement deposition, few processes are available and almost none of them can be applied in current industrial practice. Some notable exceptions are the displacement deposition of some noble metals for PCB technology.

Water-based solutions for immersion plating of PCB contacts are currently used for corrosion protection of electrical contact, but some critical issues have been reported from their use [35]. Novel DES-based processes have been developed in the case of silver application on copper [45, 94] or copper application on aluminium [78]. **Figure 5** represents a PCB treated with immersion silver deposition.

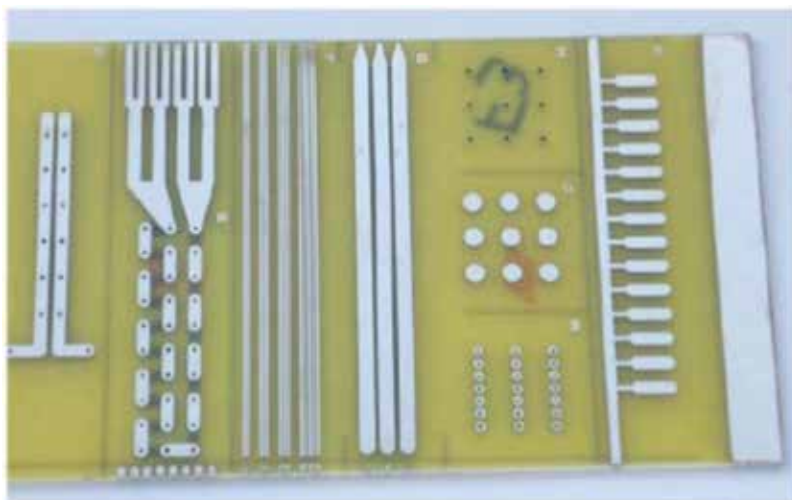


Figure 5. A PCB presenting copper tracks immersion plated with Ag from DESs [79].

ENIG-like processes have been developed as well, with gold deposited on nickel-plated contacts [94, 95]. The neutral nature of the DES can help avoiding the “black pads” effect,

induced by an excessive corrosion of Ni in the Au electrolyte. This advantage can increase the industrial attractiveness of such processes.

7. Conclusions

Deep eutectic solvents have the real potential to widen the panorama of modern galvanic techniques. Their application on large-scale production is however subordinated to the challenge of competing with well-established technologies and industrial systems not always easy to adapt to new techniques. As demonstrated by the examples presented, deep eutectic solvents are slowly leaving the laboratories to approach a real usage in plating plants. The next few decades will be the reference timeframe to understand whether these electrolytes have the possibility to be accepted as complements to existing water-based processes.

Author details

R. Bernasconi, G. Panzeri, A. Accogli, F. Liberale, L. Nobili and L. Magagnin*

*Address all correspondence to: luca.magagnin@polimi.it

Department of Chemistry, Materials and Chemical Engineering "Giulio Natta", Politecnico di Milano, Milano, Italy

References

- [1] Smith EL, Abbott AP, Ryder KS. Deep eutectic solvents (DESs) and their applications. *Chem Rev* 2014;114(21):11060–11082.
- [2] Endres F, MacFarlane D, Abbott A. *Electrodeposition from ionic liquids*. : John Wiley & Sons; 2008.
- [3] Sitze MS, Schreiter ER, Patterson EV, Freeman RG. Ionic liquids based on FeCl₃ and FeCl₂. Raman scattering and ab initio calculations. *Inorg Chem* 2001;40(10):2298–2304.
- [4] Seventh International Conference on Molten Salts. : The Electrochemical Society Montreal, Quebec, Canada; 1990.
- [5] Lecocq V, Graille A, Santini CC, Baudouin A, Chauvin Y, Basset JM, et al. Synthesis and characterization of ionic liquids based upon 1-butyl-2, 3-dimethylimidazolium chloride/ZnCl₂. *New journal of chemistry* 2005;29(5):700–706.

- [6] Abbott AP, Boothby D, Capper G, Davies DL, Rasheed RK. Deep eutectic solvents formed between choline chloride and carboxylic acids: versatile alternatives to ionic liquids. *J Am Chem Soc* 2004;126(29):9142–9147.
- [7] Abbott AP, Al-Barzinjy AA, Abbott PD, Frisch G, Harris RC, Hartley J, et al. Speciation, physical and electrolytic properties of eutectic mixtures based on CrCl₃·6H₂O and urea. *Physical Chemistry Chemical Physics* 2014;16(19):9047–9055.
- [8] Abbott AP, Capper G, Davies DL, Rasheed R. Ionic liquids based upon metal halide/substituted quaternary ammonium salt mixtures. *Inorg Chem* 2004;43(11):3447–3452.
- [9] Florindo C, Oliveira F, Rebelo L, Fernandes AM, Marrucho I. Insights into the synthesis and properties of deep eutectic solvents based on cholinium chloride and carboxylic acids. *ACS Sustainable Chemistry & Engineering* 2014;2(10):2416–2425.
- [10] Su WC, Wong DSH, Li MH. Effect of water on solubility of carbon dioxide in (amino-methanamide 2-hydroxy-N, N, N-trimethylethanaminium chloride). *Journal of Chemical & Engineering Data* 2009;54(6):1951–1955.
- [11] Aparicio S, Atilhan M. Water effect on CO₂ absorption for hydroxylammonium based ionic liquids: A molecular dynamics study. *Chem Phys* 2012;400:118–125.
- [12] Emi T, Bockris JO. Semiempirical calculation of 3.7 RTm term in the heat of activation for viscous flow of ionic liquid. *J Phys Chem* 1970;74(1):159–163.
- [13] García G, Aparicio S, Ullah R, Atilhan M. Deep eutectic solvents: Physicochemical properties and gas separation applications. *Energy Fuels* 2015;29(4):2616–2644.
- [14] Abbott AP, Capper G, Gray S. Design of improved deep eutectic solvents using hole theory. *ChemPhysChem* 2006;7(4):803–806.
- [15] Abbott AP, Harris RC, Ryder KS. Application of hole theory to define ionic liquids by their transport properties. *The Journal of Physical Chemistry B* 2007;111(18):4910–4913.
- [16] Zhang Q, Vigier KDO, Royer S, Jérôme F. Deep eutectic solvents: syntheses, properties and applications. *Chem Soc Rev* 2012;41(21):7108–7146.
- [17] Abbott AP, Harris RC, Ryder KS, D'Agostino C, Gladden LF, Mantle MD. Glycerol eutectics as sustainable solvent systems. *Green Chem* 2011;13(1):82–90.
- [18] D'Agostino C, Harris RC, Abbott AP, Gladden LF, Mantle MD. Molecular motion and ion diffusion in choline chloride based deep eutectic solvents studied by ¹H pulsed field gradient NMR spectroscopy. *Physical Chemistry Chemical Physics* 2011;13(48):21383–21391.
- [19] Figueiredo M, Gomes C, Costa R, Martins A, Pereira CM, Silva F. Differential capacity of a deep eutectic solvent based on choline chloride and glycerol on solid electrodes. *Electrochim Acta* 2009;54(9):2630–2634.
- [20] Gamburg YD, Zangari G. *Theory and practice of metal electrodeposition*. : Springer Science & Business Media; 2011.

- [21] Abbott AP, McKenzie KJ. Application of ionic liquids to the electrodeposition of metals. *Physical Chemistry Chemical Physics* 2006;8(37):4265–4279.
- [22] Abbott A, El Ttaib K, Ryder K, Smith E. Electrodeposition of nickel using eutectic based ionic liquids. *Transactions of the IMF* 2008;86(4):234–240.
- [23] Yang H, Guo X, Birbilis N, Wu G, Ding W. Tailoring nickel coatings via electrodeposition from a eutectic-based ionic liquid doped with nicotinic acid. *Appl Surf Sci* 2011;257(21):9094–9102.
- [24] Abbott AP, Capper G, Davies DL, McKenzie KJ, Obi SU. Solubility of metal oxides in deep eutectic solvents based on choline chloride. *Journal of Chemical & Engineering Data* 2006;51(4):1280–1282.
- [25] Gu C, Tu J. One-step fabrication of nanostructured Ni film with lotus effect from deep eutectic solvent. *Langmuir* 2011;27(16):10132–10140.
- [26] Martis P, Dilimon V, Delhalle J, Mekhalif Z. Electro-generated nickel/carbon nanotube composites in ionic liquid. *Electrochim Acta* 2010;55(19):5407–5410.
- [27] Saha R, Nandi R, Saha B. Sources and toxicity of hexavalent chromium. *Journal of Coordination Chemistry* 2011;64(10):1782–1806.
- [28] Ferreira ES, Pereira C, Silva A. Electrochemical studies of metallic chromium electrodeposition from a Cr (III) bath. *J Electroanal Chem* 2013;707:52–58.
- [29] Abbott AP, Capper G, Davies DL, Rasheed RK. Ionic liquid analogues formed from hydrated metal salts. *Chemistry—A European Journal* 2004;10(15):3769–3774.
- [30] Abbott AP, Capper G, Davies DL, Rasheed RK, Archer J, John C. Electrodeposition of chromium black from ionic liquids. *Trans Inst Met Finish* 2004;82:14–17.
- [31] Abbott AP, Barron JC, Frisch G, Gurman S, Ryder KS, Silva AF. Double layer effects on metal nucleation in deep eutectic solvents. *Physical Chemistry Chemical Physics* 2011;13(21):10224–10231.
- [32] Smith EL, Barron JC, Abbott AP, Ryder KS. Time resolved in situ liquid atomic force microscopy and simultaneous acoustic impedance electrochemical quartz crystal microbalance measurements: a study of Zn deposition. *Anal Chem* 2009;81(20):8466–8471.
- [33] Abbott AP, Barron JC, Frisch G, Ryder KS, Silva AF. The effect of additives on zinc electrodeposition from deep eutectic solvents. *Electrochim Acta* 2011;56(14):5272–5279.
- [34] Bakkar A, Neubert V. Electrodeposition onto magnesium in air and water stable ionic liquids: from corrosion to successful plating. *Electrochemistry Communications* 2007;9(9):2428–2435.
- [35] Smith E. Deep eutectic solvents (DESs) and the metal finishing industry: where are they now? *Transactions of the IMF* 2013;91(5):241–248.

- [36] Popescu AJ, Constantin V, Olteanu M, Demidenko O, Yanushkevich K. Obtaining and structural characterization of the electrodeposited metallic copper from ionic liquids. *Rev Chim* 2011;62(6):626–632.
- [37] Abbott AP, El Ttaib K, Frisch G, McKenzie KJ, Ryder KS. Electrodeposition of copper composites from deep eutectic solvents based on choline chloride. *Physical Chemistry Chemical Physics* 2009;11(21):4269–4277.
- [38] Lloyd D, Vainikka T, Murtomäki L, Kontturi K, Ahlberg E. The kinetics of the Cu²⁺/Cu redox couple in deep eutectic solvents. *Electrochim Acta* 2011;56(14):4942–4948.
- [39] Bernasconi R, Zebajradi M, Magagnin L. Copper electrodeposition from a chloride free deep eutectic solvent. *J Electroanal Chem* 2015;758:163–169.
- [40] Gómez E, Cojocar P, Magagnin L, Valles E. Electrodeposition of Co, Sm and SmCo from a deep eutectic solvent. *J Electroanal Chem* 2011;658(1):18–24.
- [41] Abbott AP, El Ttaib K, Frisch G, Ryder KS, Weston D. The electrodeposition of silver composites using deep eutectic solvents. *Physical Chemistry Chemical Physics* 2012;14(7):2443–2449.
- [42] Abbott AP, Nandhra S, Postlethwaite S, Smith EL, Ryder KS. Electroless deposition of metallic silver from a choline chloride-based ionic liquid: a study using acoustic impedance spectroscopy, SEM and atomic force microscopy. *Physical Chemistry Chemical Physics* 2007;9(28):3735–3743.
- [43] Wang H, Jia Y, Wang X, Yao Y, Yue D, Jing Y. Electrochemical deposition of magnesium from analogous ionic liquid based on dimethylformamide. *Electrochim Acta* 2013;108:384–389.
- [44] Rahman M, Bernasconi R, Magagnin L. Electrodeposition of indium from a deep eutectic solvent. *Journal Of Optoelectronics And Advanced Materials* 2015;17(1–2):122–126.
- [45] Abbott AP, Ryder K, König U. Electrofinishing of metals using eutectic based ionic liquids. *Transactions of the IMF* 2013.
- [46] Fashu S, Gu C, Zhang J, Bai W, Wang X, Tu J. Electrodeposition and characterization of Zn–Sn alloy coatings from a deep eutectic solvent based on choline chloride for corrosion protection. *Surf Interface Anal* 2015;47(3):403–412.
- [47] Abbott AP, Capper G, McKenzie KJ, Ryder KS. Electrodeposition of zinc–tin alloys from deep eutectic solvents based on choline chloride. *J Electroanal Chem* 2007;599(2):288–294.
- [48] You Y, Gu C, Wang X, Tu J. Electrochemical Synthesis and Characterization of Ni–P Alloy Coatings from Eutectic–Based Ionic Liquid. *J Electrochem Soc* 2012;159(11):D642–D648.

- [49] Saravanan G, Mohan S. Structure, composition and corrosion resistance studies of Co–Cr alloy electrodeposited from deep eutectic solvent (DES). *J Alloys Compounds* 2012;522:162–166.
- [50] Gengan Saravanan SM. Electrodeposition of Fe–Ni–Cr alloy from Deep Eutectic System containing Choline chloride and Ethylene Glycol. *Int. J. Electrochem. Sci* 2011;6:1468–1478.
- [51] Zhang J, Gu C, Tong Y, Gou J, Wang X, Tu J. Microstructure and corrosion behavior of Cr and Cr–P alloy coatings electrodeposited from a Cr (iii) deep eutectic solvent. *RSC Advances* 2015;5(87):71268–71277.
- [52] Chin T. Permanent magnet films for applications in microelectromechanical systems. *J Magn Magn Mater* 2000;209(1):75–79.
- [53] Zheng L, Chen L, Huang H, Li X, Zhang L. An overview of magnetic micro-robot systems for biomedical applications. *Microsystem Technologies*, published online on May 2016:1–17.
- [54] Guillamat P, Cortés M, Vallés E, Gómez E. Electrodeposited CoPt films from a deep eutectic solvent. *Surface and Coatings Technology* 2012;206(21):4439–4448.
- [55] Yanai T, Shiraishi K, Watanabe Y, Nakano M, Ohgai T, Suzuki K, et al. Electroplated Fe–Ni Films Prepared From Deep Eutectic Solvents. *IEEE Trans Magn* 2014;50(11):1–4.
- [56] Cojocar P, Magagnin L, Gomez E, Valles E. Using deep eutectic solvents to electrodeposit CoSm films and nanowires. *Mater Lett* 2011;65(23):3597–3600.
- [57] Deligianni H, Ahmed S, Romankiw LT. The next frontier: electrodeposition for solar cell fabrication. *Interface-Electrochemical Society* 2011;20(2):47.
- [58] Malaquias JC, Regesch D, Dale PJ, Steichen M. Tuning the gallium content of metal precursors for Cu (In, Ga) Se 2 thin film solar cells by electrodeposition from a deep eutectic solvent. *Physical Chemistry Chemical Physics* 2014;16(6):2561–2567.
- [59] Malaquias JC, Steichen M, Thomassey M, Dale PJ. Electrodeposition of Cu–In alloys from a choline chloride based deep eutectic solvent for photovoltaic applications. *Electrochim Acta* 2013;103:15–22.
- [60] Steichen M, Thomassey M, Siebentritt S, Dale PJ. Controlled electrodeposition of Cu–Ga from a deep eutectic solvent for low cost fabrication of CuGaSe 2 thin film solar cells. *Physical Chemistry Chemical Physics* 2011;13(10):4292–4302.
- [61] Vijayakumar J, Mohan S, Kumar SA, Suseendiran S, Pavithra S. Electrodeposition of Ni–Co–Sn alloy from choline chloride-based deep eutectic solvent and characterization as cathode for hydrogen evolution in alkaline solution. *Int J Hydrogen Energy* 2013;38(25):10208–10214.
- [62] Schlesinger M, Paunovic M. *Modern electroplating*. : John Wiley & Sons; 2011.

- [63] Abbott AP, Ballantyne A, Harris RC, Juma JA, Ryder KS. A comparative study of nickel electrodeposition using deep eutectic solvents and aqueous solutions. *Electrochim Acta* 2015;176:718–726.
- [64] Gray J, Luan B. Protective coatings on magnesium and its alloys—a critical review. *J Alloys Compounds* 2002;336(1):88–113.
- [65] Song G. Recent progress in corrosion and protection of magnesium alloys. *Advanced Engineering Materials* 2005;7(7):563–586.
- [66] Travers WJ. Plating on Aluminum. *Transactions of The Electrochemical Society* 1939;75(1):201–208.
- [67] Florea A, Anicai L, Costovici S, Golgovici F, Visan T. Ni and Ni alloy coatings electrodeposited from choline chloride-based ionic liquids—electrochemical synthesis and characterization. *Surf Interface Anal* 2010;42(6-7):1271–1275.
- [68] Bernasconi R, Magagnin L. Electrodeposition of nickel from DES on aluminium for corrosion protection. *Surface Engineering*, published online on May 2016:1–5.
- [69] Casanova T, Soto F, Eyraud M, Crousier J. Hydrogen absorption during zinc plating on steel. *Corros Sci* 1997;39(3):529–537.
- [70] Huynh T, Dao QP, Truong T, Doan N, Ho S. Electrodeposition of Aluminum on Cathodes in Ionic Liquid Based Choline Chloride/Urea/ALCL⁺ sub 3⁺. *Environment and Pollution* 2014;3(4):59.
- [71] El Abedin SZ, Moustafa E, Hempelmann R, Natter H, Endres F. Additive free electrodeposition of nanocrystalline aluminium in a water and air stable ionic liquid. *Electrochemistry Communications* 2005;7(11):1111–1116.
- [72] Zein El Abedin S, Moustafa E, Hempelmann R, Natter H, Endres F. Electrodeposition of Nano-and Microcrystalline Aluminium in Three Different Air and Water Stable Ionic Liquids. *ChemPhysChem* 2006;7(7):1535–1543.
- [73] Florea A, Petica A, Anicai L, Visan T. Preliminary studies of silver coatings formation from choline chloride based ionic liquids. *UPB Buletin Stiintific, Series B: Chemistry and Materials Science* 2010;72(2):115–126.
- [74] Lanzinger G, Böck R, Freudenberger R, Mehner T, Scharf I, Lampke T. Electrodeposition of palladium films from ionic liquid (IL) and deep eutectic solutions (DES): physical-chemical characterisation of non-aqueous electrolytes and surface morphology of palladium deposits. *Transactions of the IMF* 2013;91(3):133–140.
- [75] Baruthio F. Toxic effects of chromium and its compounds. *Biol Trace Elem Res* 1992;32(1–3):145–153.
- [76] nomorehex.org. Available at: nomorehex.org/LEGISLATION/EU-MANDATE. Accessed 07/10, 2016.

- [77] Leicester Ionic Liquids G. University of Leicester. Available at: www.leicester-ils.co.uk. Accessed 07/10, 2016.
- [78] Ionmet, New Ionic Liquid Solvent Technology to Transform Metal Finishing. Available at: www.ionmet.eu. Accessed 07/10, 2016.
- [79] Scionix. Available at: www.scionix.co.uk. Accessed 07/10, 2016.
- [80] Smith E, Fullarton C, Harris R, Saleem S, Abbott A, Ryder K. Metal finishing with ionic liquids: scale-up and pilot plants from IONMET consortium. *Transactions of the IMF* 2013;88(6):285–293.
- [81] Kuzmanovic B, Van Strien CJG, Bartel CE, Zeitler M, Speelman JC, inventors. AnonymousMethod to electrodeposit metals using ionic liquids. US20090236227A1. 2009 09/24.
- [82] Method for preparing silver by utilizing ionic liquid through electrodeposition at low temperature. Anonymous CN103046081A. 2013 04/17.
- [83] Gold plating liquid and gold plating method. Anonymous CN101319339A. 2008 12/10.
- [84] Nickel electroplating liquid, and preparation method for super-hydrophobic nickel plating layer using same. Anonymous CN102199783A. 2011 09/28.
- [85] Deep eutectic solution iron electroplating solution. Anonymous CN104099645A. 2014 10/15.
- [86] Method of electroplating zinc, nickel, molybdenum and their alloys by using ionic liquid. Anonymous CN102191517A. 2014 04/30.
- [87] Bhattacharya RN, inventor. AnonymousElectrodeposition of gallium for photovoltaics. US20140202870A1. 2014 07/24.
- [88] John S, Silaimani S, Anand V, Vasudevan T. Zinc-Manganese alloy plating-A critical review. *Bull Electrochem* 2002;18(9):407–412.
- [89] Chung P, Cantwell P, Wilcox G, Critchlow GW. Electrodeposition of zinc–manganese alloy coatings from ionic liquid electrolytes. *Transactions of the IMF* 2008;86(4):211–219.
- [90] Costovici S, Manea A, Visan T, Anicai L. Investigation of Ni-Mo and Co-Mo alloys electrodeposition involving choline chloride based ionic liquids. *Electrochim Acta* 2016;207:97–111.
- [91] Chen L, Yang Z, Brindley WJ, Kinstler MD, SAXTON BR, inventors. Electrodeposited nickel-chromium alloy. WO2015088859A2. 2015 06/18.
- [92] Method for coplating copper indium gallium selenium prefabricated layer by using ionic liquid through complex waveform pulse. Anonymous CN103866360A. 2014 06/18.

- [93] The method of electroless deposition of nanocrystalline structure gold-tin alloy plating. Anonymous CN103469264A. 2015 10/21.
- [94] Wang Y, Cao X, Wang W, Mitsuzak N, Chen Z. Immersion gold deposition from a chloroauric acid–choline chloride solution: Deposition kinetics and coating performances. *Surface and Coatings Technology* 2015;265:62–67.
- [95] Ballantyne A, Forrest G, Goosey M, Griguceviciene A, Juodkazyte J, Kellner R, et al. Advanced surface protection for improved reliability PCB systems (ASPIS). *Circuit World* 2012;38(1):21–29.

Electrodeposition of Zn, Cu, and Zn-Cu Alloys from Deep Eutectic Solvents

Xingli Zou, Xionggang Lu and Xueliang Xie

Additional information is available at the end of the chapter

<http://dx.doi.org/10.5772/65883>

Abstract

Deep eutectic solvents (DESs) comprising choline chloride (ChCl) with either urea or ethylene glycol (EG) have been successfully used as powerful and potential electrolytes for extracting metals from their corresponding metal oxide precursors. In this work, for electrodeposition of Zn and Zn-Cu alloys, ChCl/urea-based DES was employed. Cyclic voltammetry study demonstrates that the reduction of Zn(II) to Zn is a diffusion-controlled quasi-reversible, one-step, two electrons transfer process. Micro-/nanostructured Zn and Zn-Cu alloys films have been electrodeposited directly from their metal oxide precursors in DES, and the Zn and Zn-Cu alloy films exhibit homogeneous morphologies with controlled particle sizes. Besides, the electrodeposition of Cu from CuO in the eutectics based on ChCl with urea and EG has been investigated, respectively. The higher coordinated Cu species in the ChCl/urea-based DES are obviously more difficult to reduce, and higher overpotential is needed to drive the nucleation process compared with the lower coordinated Cu species in the ChCl/EG-based DES. The surface morphology of the Cu electrodeposits is significantly affected by the type of DES and the electrodeposition potentials. Furthermore, the Cu electrodeposits obtained in the ChCl/urea-based DES possess more dense microstructures than those produced in the ChCl/EG-based DES.

Keywords: electrodeposition, deep eutectic solvents, metal oxides, cyclic voltammetry, morphology

1. Introduction

The electrodeposition of Zn, Cu, and Zn-Cu alloys for corrosion-resistant coatings and electrochemical applications such as electrocatalysis and electronic devices has received considerable attention in recent years [1–7]. The electrodeposition of Zn, Cu, and Zn-Cu alloys

is commonly performed in aqueous electrolyte solutions. Traditional Zn plating is mainly carried out in sulfuric acidic aqueous baths [8, 9]. Generally, Zn is extracted from zinc sulfide ore. The ore is mined from the earth's crust and beneficiated by flotation methods that produce zinc sulfide concentrates. The mineral concentrates are oxidized to metal oxides during high temperature roasting and then the metal oxides are leached with sulfuric acid to produce zinc sulfate solution. Finally, the Zn electrodeposits are obtained from the zinc sulfate electrolyte under constant current electrolysis [10, 11]. However, the traditional Zn electrodeposition process is very sensitive to impurities and requires effective purification methods to produce pure Zn [12]. Copper electrodeposition is mostly performed in aqueous solutions, which possess high solubility of copper salts (e.g., CuCl_2 and CuSO_4) and high electrolyte conductivity. However, the acid- and cyanide-based aqueous electrolytes are corrosive and the inevitable hydrogen evolution reaction commonly occurs during the electrolysis process [13]. Consequently, finding new alternative electrolytes for the electrodeposition of Zn, Cu, and Zn-Cu alloy films at low temperature has become the focus in recent years.

More recently, the direct electrochemical reduction of metal oxides/compounds to metals/alloys in molten salts has been extensively studied because of its low energy consumption and environmental compatibility [14, 15]. This previous innovative work shows that the production of metallic/coating materials directly from their metal oxide precursors in liquid salt is a promising route. Low-temperature electrolytic production of iron film from iron oxide in alkaline solution has been studied in our previous work [16], which showed that metal oxide has the potential to be used as a precursor for the electrodeposition at low temperature; the electrochemical process can be controlled effectively and the electrodeposition process generally exhibits acceptable current efficiency. However, in comparison with aqueous solutions, room temperature ionic liquids (RTILs) have attracted much interest as promising electrolyte candidates for metal electrodeposition due to their remarkable characteristics, such as high thermal and chemical stability, negligible vapor pressure, wide electrochemical windows, high ionic conductivity, simplicity of handling, and good solubility for quite a lot of metal salts [17–19]. The hydrogen embrittlement and hydrogen evolution reactions occurring in aqueous solutions can be avoided by using ionic liquids as electrolytes. The electrodeposition of Zn has been investigated in many ionic liquids, particularly in AlCl_3 -based ionic liquids [20] and chlorozincate ionic liquids [21]. In addition, the electrodeposition of Zn from ZnCl_2 precursor has also been studied in choline chloride (ChCl)-based deep eutectic solvents (DESs) [22–26]. Liu et al. [27] illustrated the electrodeposition of Zn films from zinc triflate ($\text{Zn}(\text{TfO})_2$) in 1-butyl-1-methylpyrrolidinium trifluoromethylsulfonate ($[\text{Py}_{1,4}]\text{TfO}$) and 1-ethyl-3-methylimidazolium trifluoromethylsulfonate ($[\text{EMIm}]\text{TfO}$) ionic liquids. Zheng et al. [28] investigated the electrodeposition of Zn films from ZnO in imidazolium chloride/urea ionic liquid, which suggested that ZnO has appreciable solubility in the electrolyte. Besides, the electrochemical behavior of copper species (e.g., CuCl and CuCl_2) has been investigated in a range of ionic liquids such as Lewis acidic, basic chloroaluminate ionic liquids, and air-/water-stable ionic liquids based on $[\text{BF}_4]^-$, $[\text{N}(\text{CN})_2]^-$, and $[\text{Tf}_2\text{N}]^-$ [29–34]. Although these ionic liquids show many advantages in electrodeposition of Cu, issues such as toxicity, cost, and tedious synthesis procedures may limit their realistic applications [35]. Furthermore, many air-/water-stable ionic liquids are not

ideal electrolyte for copper salts such as nitrates, halides, and sulfates because of their poor solubilities [36]. Chen et al. [37] attempted to introduce the cuprous ions into the ionic liquid by the anodic dissolution of a Cu electrode, however, it is a time-consuming process. Therefore, searching for suitable ionic liquid-metal precursors systems for the electrodeposition of Zn, Cu, and Zn-Cu alloys is extremely needed.

DESs, which are made from quaternary ammonium salts mixed with hydrogen bond donors, such as carboxylic acids, alcohols, and amides, are promising electrolytes for electrodeposition application [38, 39]. The DESs are simple to prepare, relatively stable in air and moisture, many are biodegradable, and are relatively low cost [40–47]. Moreover, the DESs show considerable selective solubilities for many metal oxides, which may provide a new route for preparation of metals from metal oxide precursors in the DESs [48, 49]. In comparison with ZnCl_2 , CuCl , and CuCl_2 precursors [22–26], ZnO , Cu_2O , and CuO have potential to be used directly as new promising precursors for the electrodeposition of Zn, Cu, and Zn-Cu alloys films in DESs without chloridization pretreatment. ChCl /urea-based DES has been used as a potential solvent for Zn recovery from waste oxide residues [50]. Yang and Reddy [41, 42] studied the electrodeposition of Zn and Pb films from their oxide precursors in the ChCl /urea-based DES due to their relatively high solubilities in the DES. Tsuda et al. [43] investigated the electrochemical behavior of Cu_2O in the same DES, and they found that Cu can be directly electrodeposited from Cu_2O precursor. More recently, we have also found that micro-/nanostructured Zn and Cu films can be electrodeposited from ZnO and CuO precursors in DESs, respectively [44, 45]. Zhang et al. [46] also demonstrated that the electrochemical synthesis of uniform Cu nanoparticles from Cu_2O can be achieved in ChCl /urea-based DES. This previous work generally showed that zinc and copper oxides have the potential to be used as the precursors for the direct electrodeposition of Zn, Cu, and Zn-Cu alloys films in DESs.

2. Electrodeposition of Zn from ZnO in ChCl /urea-based DES

2.1. Cyclic voltammetry (CV) analysis

The blank CV curve obtained from a platinum working electrode in ChCl /urea-based DES at 333 K is illustrated in **Figure 1(a)**. The cathodic limit is approximately -1.2 V and the anodic limit is about 1.2 V. It can be seen from the blank CV that the electrochemical window of the ChCl /urea-based DES is approximately 2.4 V. **Figure 1(b)** shows the CV curve obtained from a platinum working electrode in the ChCl /urea-based DES dissolved with 0.1 M ZnO at 333 K and potential range of -1.3 to -0.1 V. As evidenced from this figure, the single cathodic current peak observed at about -1.1 V is attributed to the reduction of Zn^{2+} to the metal Zn, the anodic current peak occurred at approximately -0.95 V and is due to the stripping of the electrodeposited Zn.

In order to further investigate the electrochemical behavior of Zn, CV experiments using a platinum electrode as working electrode at different scan rates in ChCl /urea-ZnO (0.1 M) were also performed systematically, and the CV curves are shown in **Figure 2(a)**.

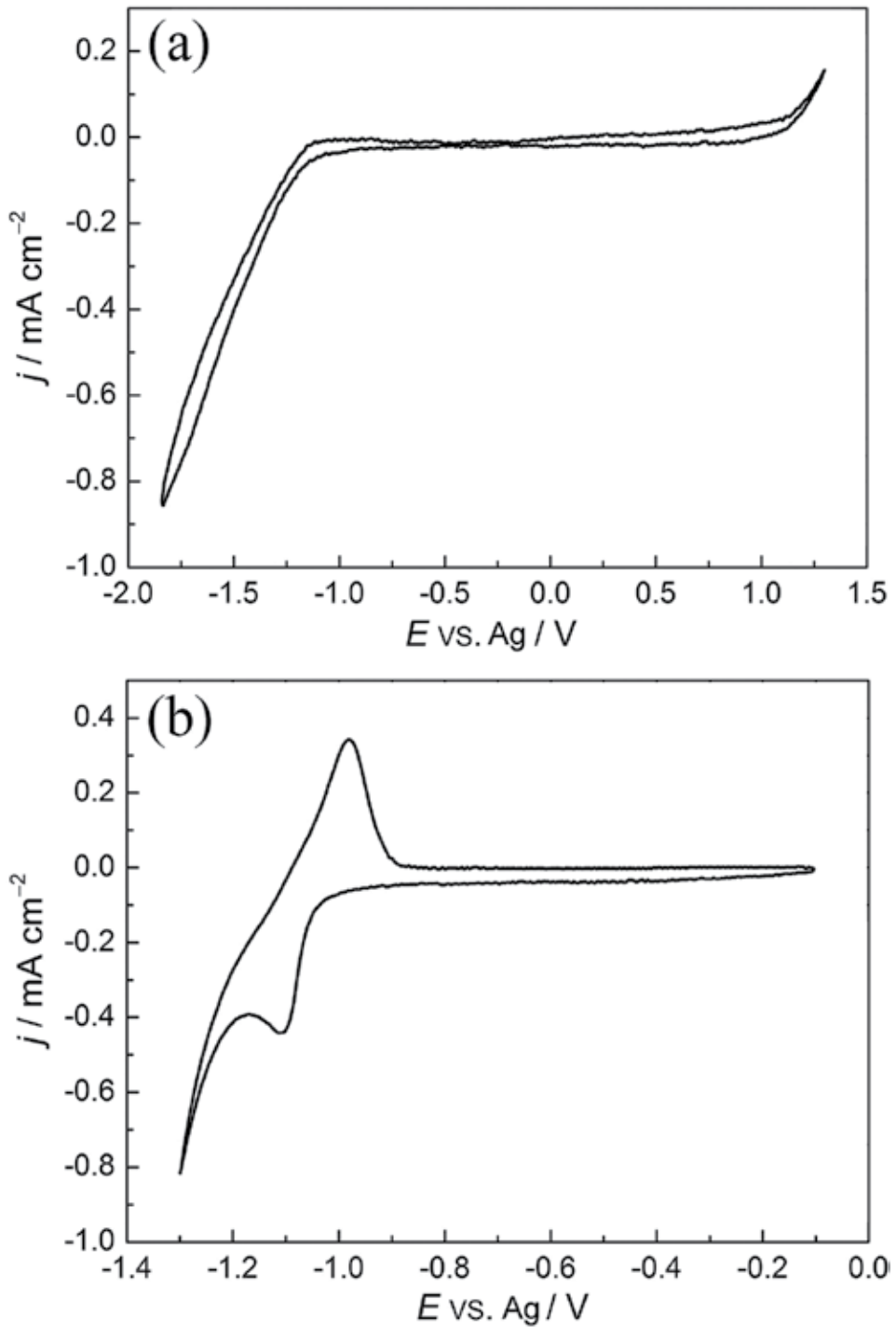


Figure 1. (a) CV curve of a Pt electrode in pure ChCl/urea at 333 K with a scan rate of 10 mV s⁻¹. (b) CV curve of a Pt electrode in ChCl/urea-ZnO (0.1 M) at 333 K with a scan rate of 10 mV s⁻¹.

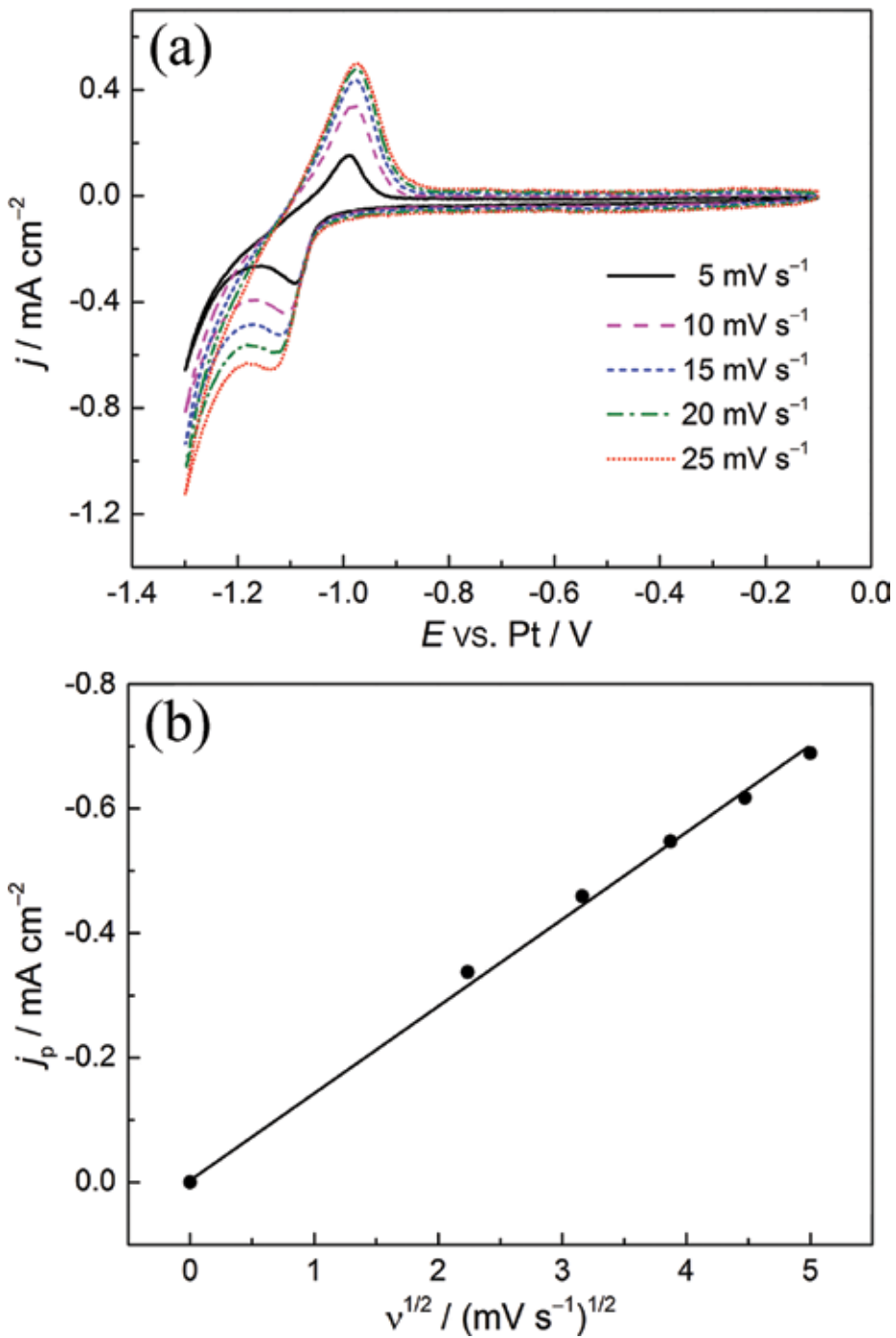


Figure 2. (a) CV curve of a Pt electrode in ChCl/urea-ZnO (0.1 M) at 333 K with different scan rates. The scan rates were 5, 10, 15, 20, and 25 mV s⁻¹, respectively. (b) Relationship between cathodic peak current density (j_{pc}) and square root of scan rate ($v^{1/2}$) calculated from (a).

The cathodic and anodic peak's current densities increase with the increase of scan rate, and the cathodic and anodic peak potentials shift to more negative and positive sides, respectively. In **Figure 2(b)**, the cathodic peak current density (j_{pc}) vary linearly as a function of the square root of scan rate ($v^{1/2}$), implying the reduction process of Zn(II) is mainly diffusion-controlled. Besides, the cathodic peak and half-peak potentials $|E_{pc} - E_{pc/2}|$ increase with the increase of scan rate. At the lowest scan rate, the difference in the value of 42 mV is larger than the value for the reversible process (31 mV at 333 K). All of these results suggest that the reduction of Zn(II) to Zn in ChCl/urea-based DES is a diffusion-controlled quasi-reversible process [51].

For a quasi-reversible charge transfer process, the diffusion coefficient of Zn(II) can be determined by the irreversible Randles-Sevick equation (1) [51], which is applicable to the quasi-reversible systems as well [52, 53],

$$j_{pc} = 0.4958nFAC_{Zn(II)}D_{Zn(II)}^{1/2} \left(\frac{\alpha n_a Fv}{RT} \right)^{1/2} \quad (1)$$

where j_{pc} is the cathodic peak current density, F is the Faraday constant, n is the number of exchanged electrons, $C_{Zn(II)}$ is the Zn(II) species concentration, A is the electrode area, $D_{Zn(II)}$ is the diffusion coefficient of Zn(II) species, v is the scan rate, α is the transfer coefficient, n_a is the electron transfer number in the rate determining step, R is the gas constant, and T is the absolute temperature. The value α can be obtained from Eq. (2) [51]:

$$\left| E_{pc} - E_{pc/2} \right| = 1.857RT/\alpha n_a F \quad (2)$$

where E_{pc} and $E_{pc/2}$ are the cathodic peak potential and half-peak potential, respectively. According to Eq. (2) and the data obtained from **Figure 2(a)**, the average transfer coefficient can be calculated as 0.53. Substituting this and other parameters in Eq. (1), the diffusion coefficient of Zn(II) in ChCl/urea-based DES is determined to be $6.21 \times 10^{-9} \text{ cm}^2 \text{ s}^{-1}$ at 333 K, which is smaller than that of Zn(II) in $\text{Bu}_3\text{MeN-TFSI}$ ($1.6 \times 10^{-7} \text{ cm}^2 \text{ s}^{-1}$ [54]) and $\text{AlCl}_3\text{-EMIC}$ ($2.6 \times 10^{-6} \text{ cm}^2 \text{ s}^{-1}$ [55]) ionic liquids. The relatively low mobility of Zn(II) species may be ascribed to the formation of large, sterically hindered Zn-complex anions when ZnO is dissolved in the DES [44] and high viscosity of the ChCl/urea-based DES [56].

2.2. Morphology and phase composition analyses of the electrodeposited Zn films

The SEM images of the Zn films electrodeposited at different electrodeposition temperatures are shown in **Figure 3**. It is obvious that the microstructure of the Zn films changes gradually with increasing the electrodeposition temperature. As illustrated in **Figure 3(a)**, compact Zn films with particle size approximately 400 nm can be obtained at 333 K. The particle size of the Zn electrodeposits apparently increases with increasing electrodeposition temperature (**Figure 3b-d**). In addition, the interspaces between the Zn particles

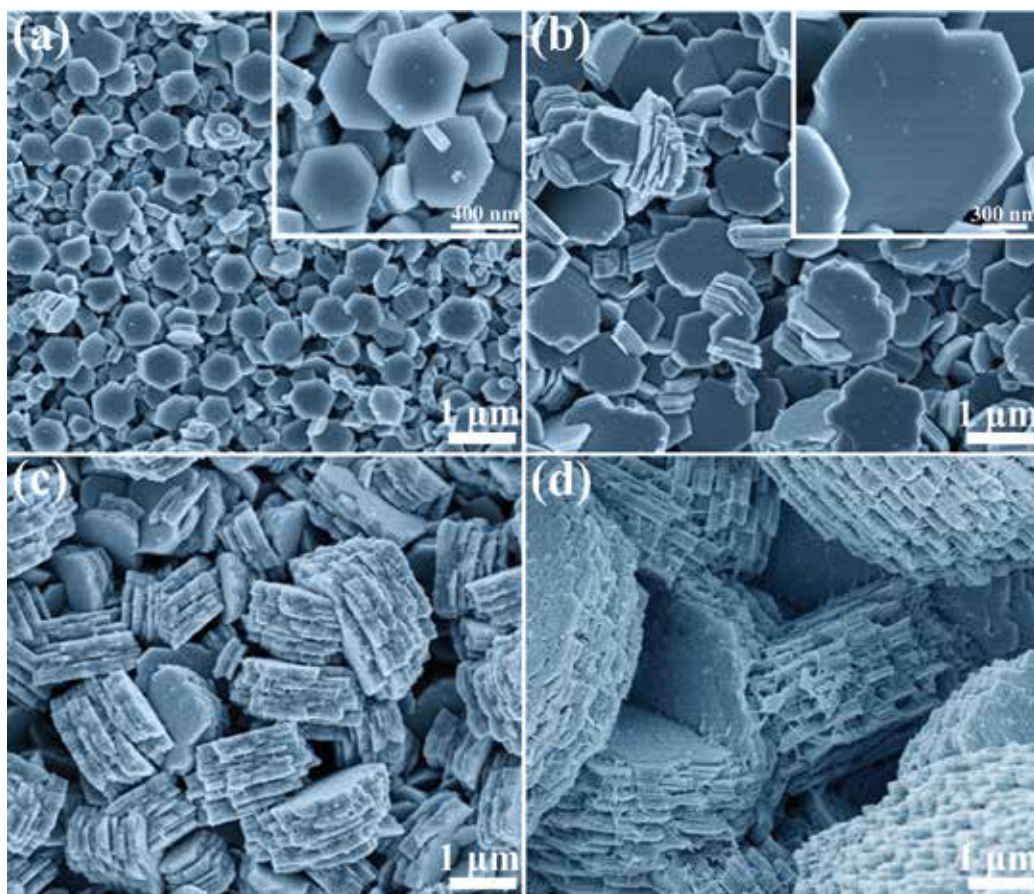


Figure 3. SEM images of the Zn electrodeposits obtained from ChCl/urea–ZnO (0.1 M) at -1.15 V on a Cu substrate at different temperatures: (a) 333 K, (b) 343 K, (c) 353 K, and (d) 363 K for 2 h.

also increase gradually with the growth of the particles, which result in the Zn films become porous. The Zn electrodeposits with hexagonal structure (**Figure 3a**) continue to further nucleate and grow to form polygonal Zn plates (**Figure 3b**) and then transform to multilayer structure (**Figure 3c–d**). The Zn particles gradually change from dispersive nanoparticle to multilayer microparticle with irregular shapes. It should be noted that the morphology change during the electrodeposition process is mainly attributed to the increased electrodeposition rate and the electrodeposition temperature. It is worth noting that the morphology of the electrodeposited Zn can be influenced by the electrodeposition temperature.

X-ray diffraction (XRD) pattern of the Zn electrodeposits on a Cu substrate obtained from 0.1 M ZnO in ChCl/urea-based DES is shown in **Figure 4**. It can be seen that only two metallic phases, Zn and Cu (substrate), are identified. It is obvious that the electrodeposit is composed of high purity Zn.

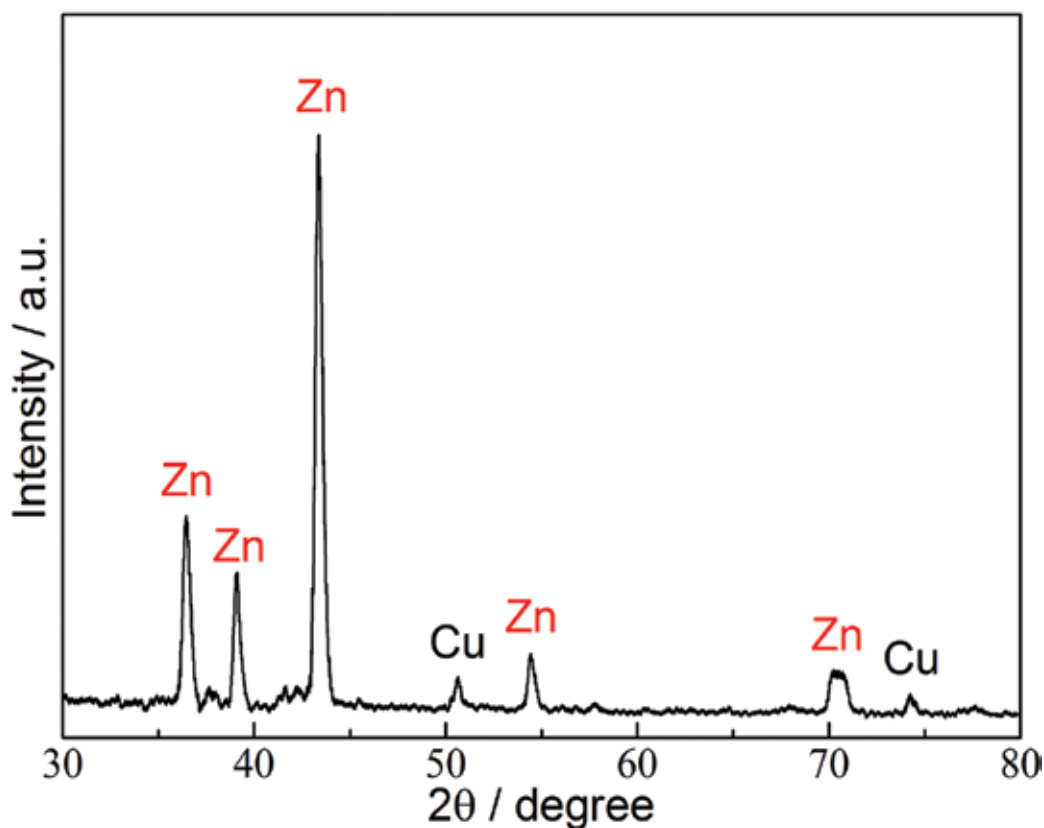


Figure 4. XRD pattern of the Zn electrodeposits obtained from ChCl/urea–ZnO (0.01 M) on a Cu substrate at -1.15 V and 333 K.

3. Electrodeposition of Cu from CuO in ChCl/EG and ChCl/urea-based DESs

3.1. CV study

In order to investigate the electrochemical behavior of Cu, CV analysis was carried out in ChCl/EG–CuO (0.01 M)- and ChCl/urea–CuO (0.01 M)-based DESs, and the CV curves are shown in **Figure 5**. For comparison, **Figure 5(a)** and **(b)** illustrates the voltammetric behavior of Cu(II) in the ChCl/EG–CuO (0.01 M) and ChCl/urea–CuO (0.01 M) electrolytes, respectively, and the CVs were recorded at 353 K with a scan rate of 10 mV s^{-1} . Two redox couples (c_1/a_1 and c_2/a_2) are occurred in each CV curve. The redox couple (c_1/a_1) is assigned to the reaction of $\text{Cu(II)} + e^- \leftrightarrow \text{Cu(I)}$, and the redox couple (c_2/a_2) is attributed to the reaction of $\text{Cu(I)} + e^- \leftrightarrow \text{Cu}$. As shown in **Figure 5(a)** and **(b)**, the peak current density for the reduction of Cu(I)/Cu(0) in the ChCl/EG system is higher than that in the ChCl/urea system. Moreover, the redox potentials of the Cu(II)/Cu(I) and Cu(I)/Cu(0) couples in the ChCl/urea system occur at potentials more negative than those observed in the ChCl/EG system. The different redox potentials

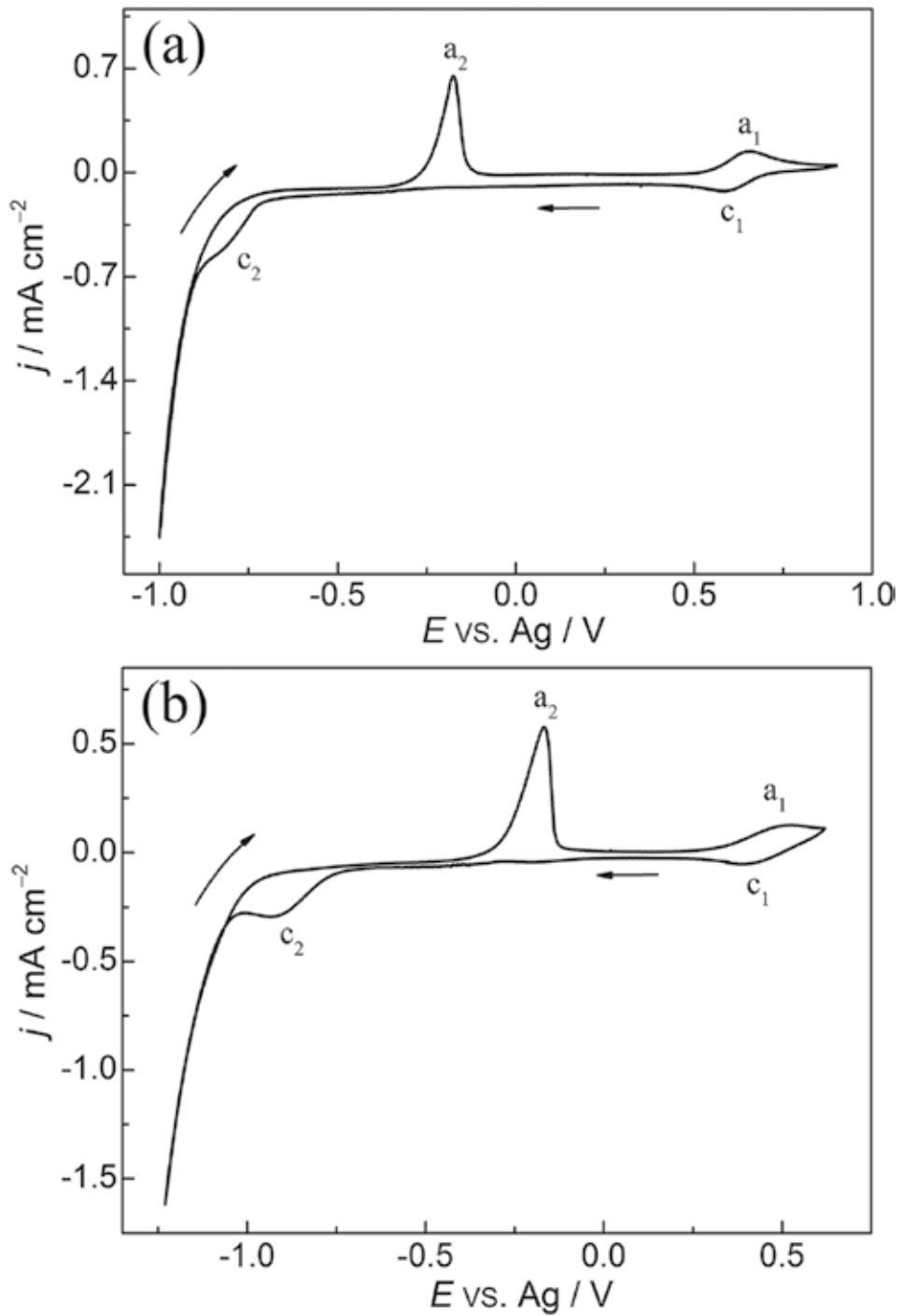


Figure 5. CV curves of a Fe electrode in (a) $\text{ChCl/EG-CuO (0.01 M)}$ and (b) $\text{ChCl/urea-CuO (0.01 M)}$ at 353 K with a scan rate of 10 mV s^{-1} .

may be attributed to the differences in ligand activity between the two DESs. There is a strong coordination between the chloride ions and urea, which can effectively decrease the activity of chloride compared with EG [25]. These results can be ascribed to the lower viscosity of the ChCl/EG system and the facile charge-transfer kinetics in the ChCl/EG system compared to that of the ChCl/urea system [41]. Therefore, the lower coordinated Cu species in the ChCl/EG ionic liquid are obviously more easier to be reduced, whereas the higher coordinated Cu species in the ChCl/urea ionic liquid are more difficult to be reduced.

3.2. Characterization of the Cu electrodeposits

The SEM images of the Cu films electrodeposited in ChCl/EG ionic liquid at different electrodeposition potentials are shown in **Figure 6**. In **Figure 6(a)**, a porous and nonuniform electrodeposit is formed. As the electrodeposition potential was made progressively negative to -0.80 V, the agglomeration of Cu particles occurred. The Cu particles generated at high cathodic potential are composed of some larger agglomerates with fine nanoscale particles (**Figure 6c**). **Figure 6(d)** shows the EDS spectra of the Cu film corresponding to **Figure 6(b)**. Only two elements Cu and Fe (substrate) are determined from the EDS spectra.

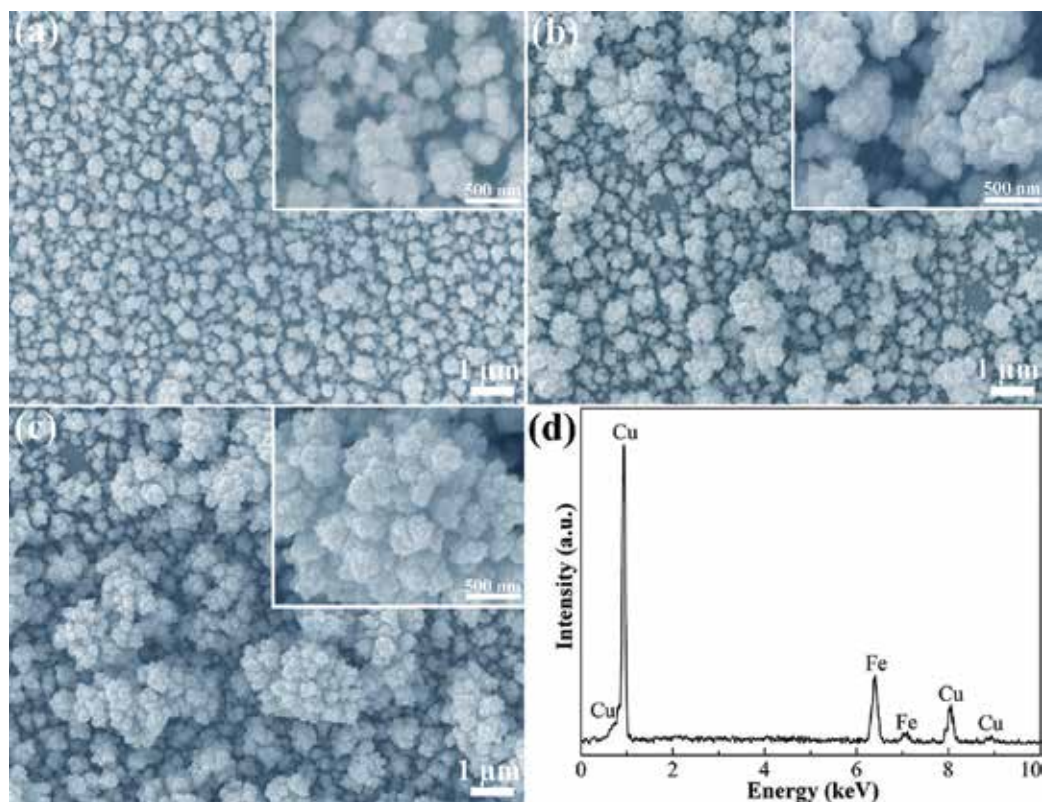


Figure 6. SEM images of the Cu electrodeposits obtained on a Fe substrate in ChCl/EG–CuO (0.01 M) at (a) -0.75 V, (b) -0.80 V, and (c) -0.85 V and 353 K for 3 h, and (d) EDS spectra of the electrodeposited Cu film corresponding to (b).

It is indicated that the electrodeposition potential has significant influences on the morphology of Cu electrodeposits.

The SEM images of the Cu films electrodeposited in ChCl/urea ionic liquid at different electrodeposition potentials are shown in **Figure 7**. As evidenced in **Figure 7(a)**, the uniform, dense, and compact electrodeposits are formed at -0.90 V. As the electrodeposition potential increases to -0.95 and -1.00 V, some spherical nodular electrodeposits are formed and become more porous (**Figure 7b** and **c**). **Figure 7(d)** shows the EDS spectra of the Cu film corresponding to **Figure 7(b)**. Only two elements Cu and Fe (substrate) are determined from the EDS spectra. The differences in morphology are probably due to the different Cu species formed in the electrolyte, the higher coordinated and lower superficial diffusion of Cu species in ChCl/urea ionic liquid results in a homogenous distribution of particles with particle size smaller than those observed in ChCl/EG ionic liquid.

XRD patterns of the Cu electrodeposits on a Fe substrate obtained from 0.01 M CuO in ChCl/EG and ChCl/urea ionic liquids are shown in **Figure 8(a)** and **(b)**. It can be seen that only two metallic phases Cu and Fe (substrate) are identified in both media. It is evidenced that the electrodeposit is composed of high purity Cu.

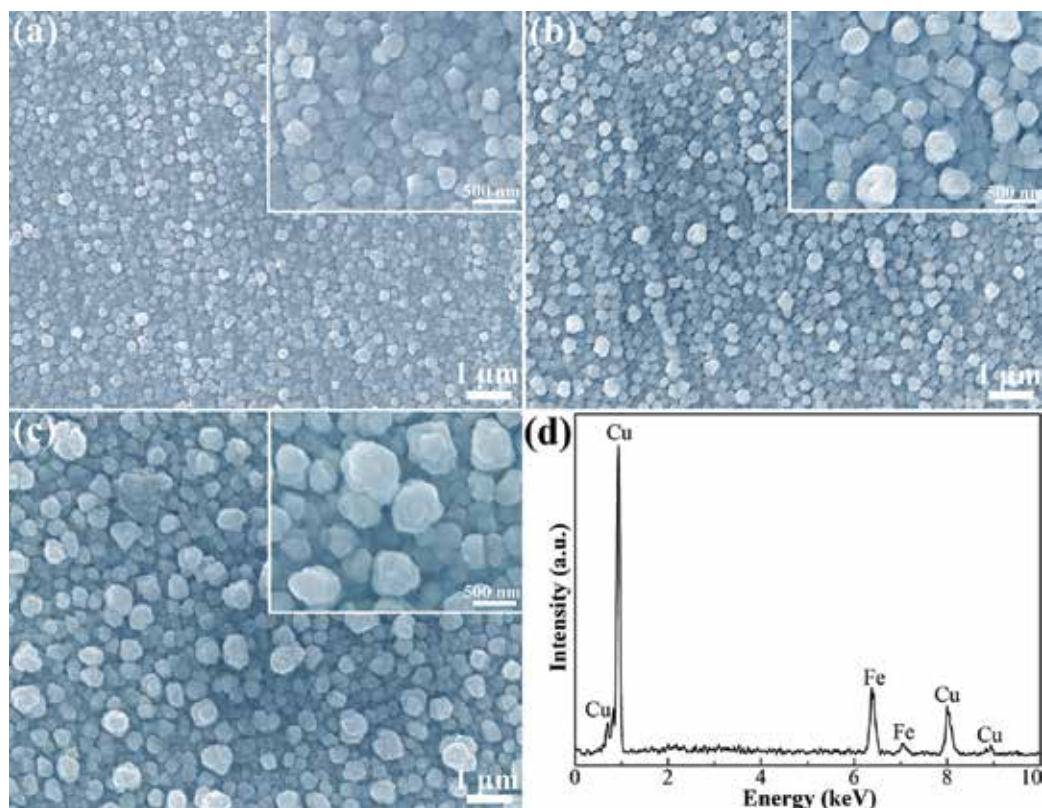


Figure 7. SEM images of the Cu electrodeposits obtained on a Fe substrate in ChCl/urea–CuO (0.01 M) at (a) -0.90 V, (b) -0.95 V, (c) -1.00 V and 353 K for 3 h, and (d) EDS spectra of the electrodeposited Cu film corresponding to (b).

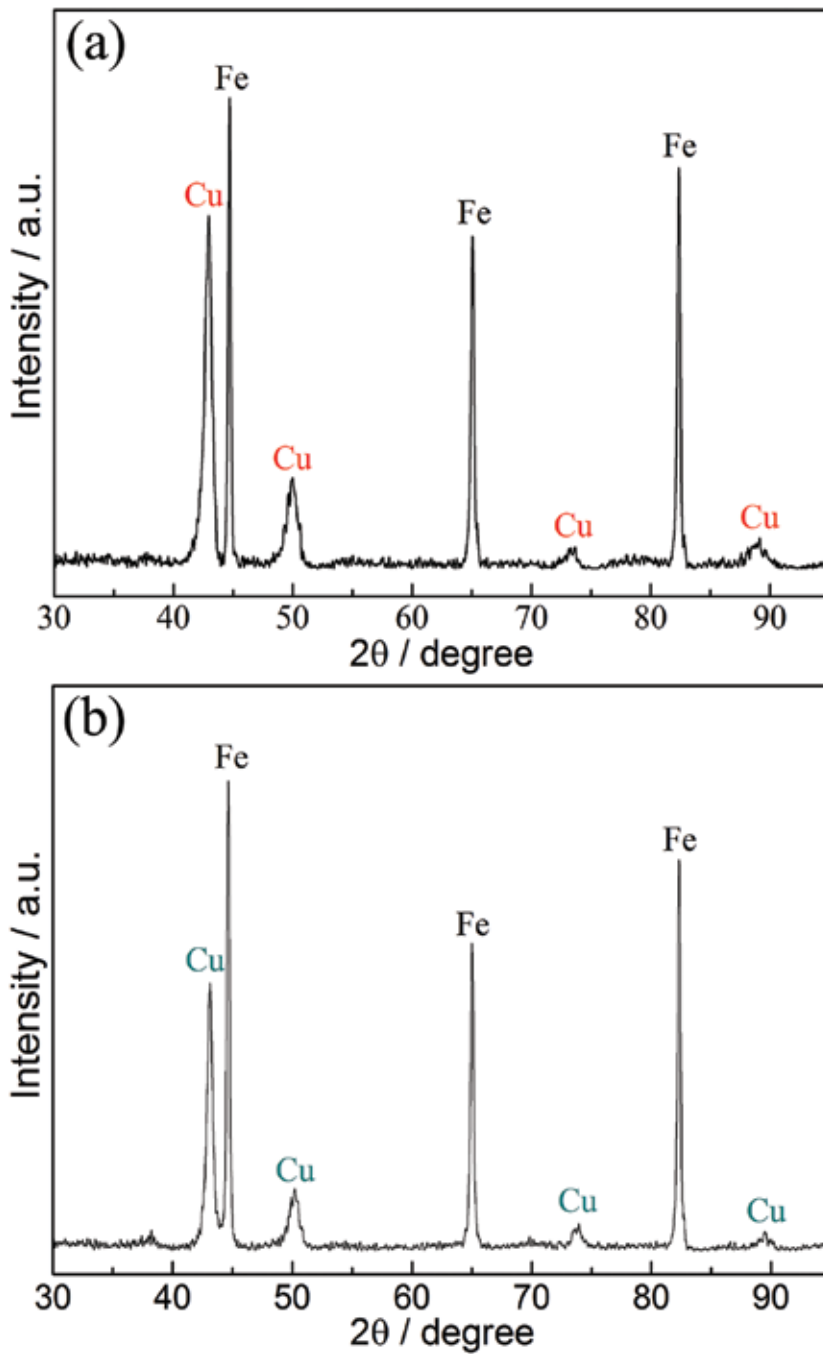


Figure 8. XRD patterns of the Cu electrodeposits obtained on a Fe substrate in (a) ChCl/EG-CuO (0.01 M) at -0.80 V and 353 K for 3 h and (b) ChCl/urea-CuO (0.01 M) at -0.95 V and 353 K for 3 h.

4. Electrodeposition of Zn-Cu alloys in ChCl/urea-based DES

4.1. CV analysis

Figure 9 shows the CV curve of the ChCl/urea ionic liquid dissolved with 0.01 M CuO and 0.1 M ZnO on a Fe electrode at 343 K with a scan rate of 10 mV s⁻¹. There are three reduction peaks on the cathodic branch of the voltammogram. The two cathodic reduction peaks observed at approximately 0.25 V (labeled as c₁) and -0.85 V (c₂) are attributed to the Cu(II) to Cu(I) reduction process and the Cu(I) to Cu reduction process, respectively. The reduction peak at about -1.15 V (c₃) can be ascribed to the Zn(II) to Zn reduction process. When the scan is reversed, four oxidation peaks (a₁, a₂, a₃, and a₄), as shown in **Figure 9**, are observed in the potential range of -1.10 to 0.50 V. The oxidation peaks for pure Cu (a₁ and a₂) and pure Zn (a₄) are at about 0.32, -0.30, and -1.05 V, respectively, and the oxidation peak (a₃) is for the Zn-Cu electrodeposits between the two potentials (a₂ and a₄).

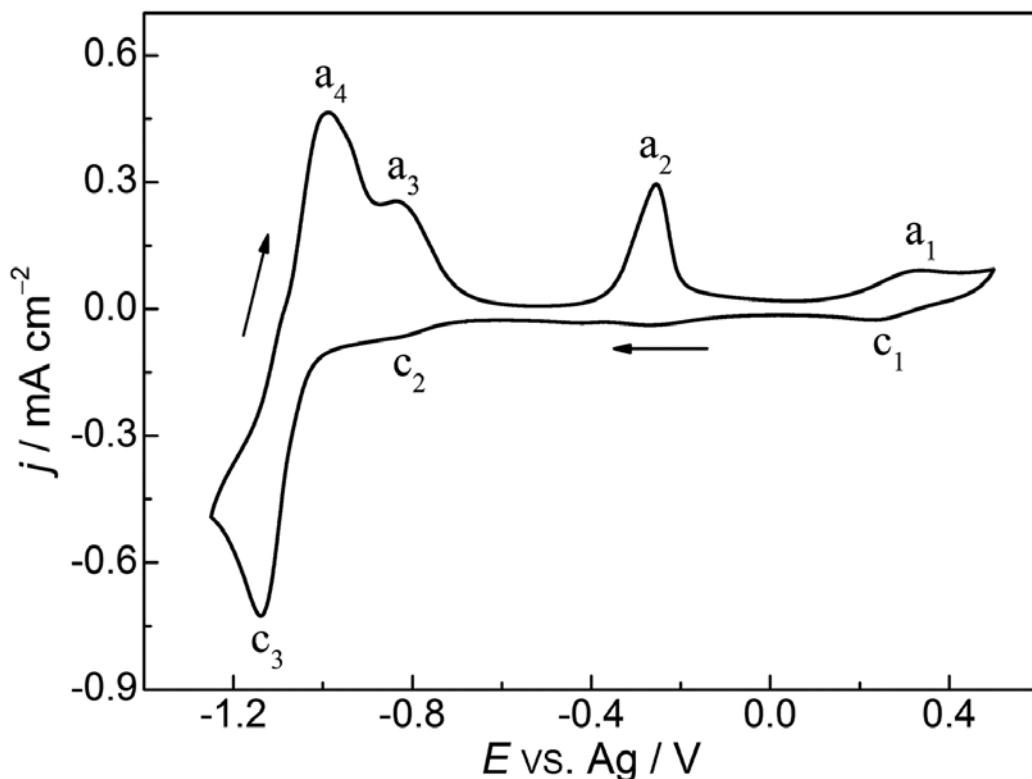


Figure 9. CV curve of a Fe electrode in ChCl/urea ionic liquid containing 0.1 M ZnO and 0.01 M CuO at 343 K with a scan rate of 10 mV s⁻¹.

4.2. Morphology and phase composition analyses of the electrodeposited Zn-Cu films

The XRD patterns of the Zn-Cu alloys electrodeposited on a Fe substrate in the ChCl/urea ionic liquid containing 0.1 M ZnO and 0.01 M CuO at different potentials and 343 K for 3 h are shown in **Figure 10(a)**. It can be seen that the dominate phases of the Zn-Cu films electrodeposited at -1.05 V are Cu_5Zn_8 and Cu (substrate). As the electrodeposition potential increases to -1.10 V, two new phases (CuZn_5 , Zn) are observed and the Cu_5Zn_8 phase is disappeared. It is mainly the result of increasing the Zn electrodeposition rate under more negative potential. **Figure 10(b)** and **(c)** shows the SEM images of the Zn-Cu alloys electrodeposited in the ChCl/urea ionic liquid containing 0.1 M ZnO and 0.01 M CuO at different cathodic potentials and 343 K for 3 h. The Zn-Cu electrodeposit obtained at -1.05 V is composed of spherical clusters with some void space between the particles (**Figure 10b**). When the potential changes from -1.05 to -1.10 V, the agglomeration of Zn-Cu particles is observed and the electrodeposits are porous and nonuniform (**Figure 10c**).

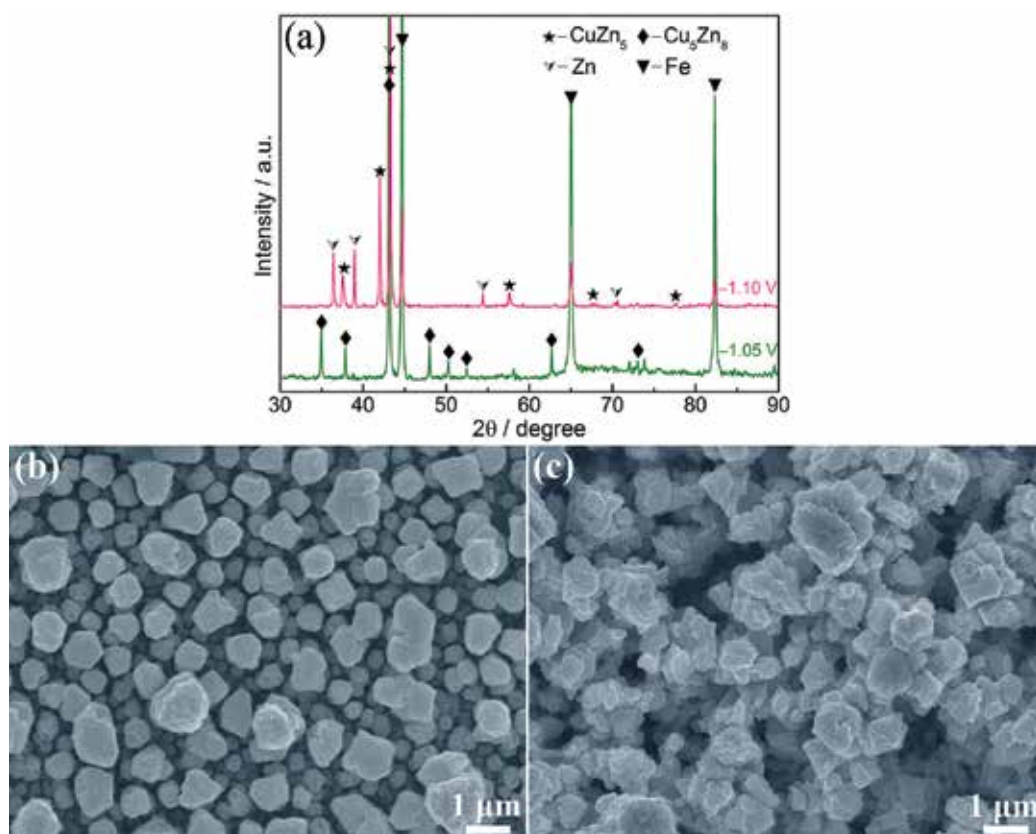


Figure 10. (a) XRD patterns of the Cu-Zn alloys electrodeposited on a Fe substrate in the ChCl/urea ionic liquid containing 0.1 M ZnO and 0.01 M CuO at different cathodic potentials and 343 K for 3 h. (b) and (c) SEM images of the Cu-Zn electrodeposits obtained on a Fe substrate in the 12CU ionic liquid containing 0.1 M ZnO and 0.01 M CuO at 343 K for 3 h, (b) -1.05 V and (c) -1.10 V.

5. Conclusions

The electrodeposition of Zn, Cu, and Zn-Cu alloys from ZnO/CuO precursors has been investigated in DESs. Electrochemical measurements showed that the Zn electrodeposition is a diffusion-controlled quasi-reversible, one-step, two electrons transfer process. The diffusion coefficient of Zn(II) was estimated to be $6.21 \times 10^{-9} \text{ cm}^2 \text{ s}^{-1}$ at 333 K. Uniform, dense, and compact Zn electrodeposits can form under suitable electrodeposition potentials and lower temperatures. Besides, the electrodeposition of Cu from CuO in the eutectics based on ChCl with urea and EG has been respectively investigated and compared. The voltammetric measurements show the electrodeposition of Cu in ChCl/EG and ChCl/urea systems through a two-step process. The higher coordinated Cu species in the ChCl/urea ionic liquid are more difficult to be reduced. The surface morphology of the Cu electrodeposits can be significantly affected by the ionic liquids and the electrodeposition potential. Furthermore, the Cu electrodeposits obtained in the ChCl/urea ionic liquid possess more homogenous microstructures than those produced in the ChCl/EG ionic liquid. In addition, the Zn-Cu alloy films have also been electrodeposited directly from their metal oxide precursors in ChCl/urea-based DES, the phase composition of the Zn-Cu alloys depends on the electrodeposition potential. These results may have implications on the electrodeposition of other alloy films from oxide precursors in DESs system.

Acknowledgements

The authors thank China National Funds for Distinguished Young Scientists (No. 51225401), the National Natural Science Foundation of China (Nos. 51304132 and 51574164), the National Basic Research Program of China (No. 2014CB643403), the Science and Technology Commissions of Shanghai Municipality (No. 14JC1491400), and the Young Teacher Training Program of Shanghai Municipal Education Commission for financial support. The authors also thank the Instrumental Analysis and Research Center of Shanghai University for materials characterization.

Author details

Xingli Zou*, Xionggang Lu* and Xueliang Xie

*Address all correspondence to: xlzou@shu.edu.cn and luxg@shu.edu.cn

State Key Laboratory of Advanced Special Steel & Shanghai Key Laboratory of Advanced Ferrometallurgy & School of Materials Science and Engineering, Shanghai University, Shanghai, China

References

- [1] Liu H, Szunerits S, Xu WX. Preparation of superhydrophobic coatings on zinc as effective corrosion barriers. *ACS Appl. Mat. Interfaces*. 2009;1:1150–1153. DOI: 10.1021/am900100q

- [2] Liu Z, Zein El Abedin S, Endres F. Electrodeposition and stripping of zinc from an ionic liquid polymer gel electrolyte for rechargeable zinc-based batteries. *J. Solid State Electrochem.* 2014;**18**:2683–2691. DOI: 10.1007/s10008-014-2526-8
- [3] Fashu S, Gu C, Wang XX. Influence of electrodeposition conditions on the microstructure and corrosion resistance of Zn-Ni alloy coatings from a deep eutectic solvent. *Surf. Coat. Technol.* 2014;**242**:34–41. DOI: 10.1016/j.surfcoat.2014.01.014
- [4] Abbott A, Frisch G, Ryder K. Electroplating using ionic liquids. *Annu. Rev. Mater. Res.* 2013;**43**:335–358. DOI: 10.1146/annurev-matsci-071312-121640
- [5] Peterson A, Abild-Pedersen F, Studt FX. How copper catalyzes the electroreduction of carbon dioxide into hydrocarbon fuels. *Energy Environ. Sci.* 2010;**3**:1311–1315. DOI: 10.1039/c0ee00071j
- [6] Ding Y, Chen M, Erlebacher J. Metallic mesoporous nanocomposites for electrocatalysis. *J. Am. Chem. Soc.* 2004;**126**:6876–6877. DOI: 10.1021/ja0320119
- [7] Miura S, Honma H. Advanced copper electroplating for application of electronics. *Surf. Coat. Technol.* 2003;**169-170**:91–95. DOI: 10.1016/S0257-8972(03)00165-8
- [8] Brown A, Melsenhelder J, Yao N. The alkaline electrolytic process for zinc production: a critical evaluation. *Ind. Eng. Chem. Prod. Res. Dev.* 1983;**22**:263–272. DOI: 10.1021/i300010a020
- [9] Guillaume P, Leclerc N, Boulanger CX. Investigation of optimal conditions for zinc electrowinning from aqueous sulfuric acid electrolytes. *J. Appl. Electrochem.* 2007;**37**:1237–1243. DOI: 10.1007/s10800-007-9377-2
- [10] Yan H, Downes J, Boden PX. A model for nanolaminated growth patterns in Zn and Zn-Co electrodeposits. *J. Electrochem. Soc.* 1996;**143**:1577–1583. DOI: 10.1149/1.1836682
- [11] Gomes A, da Silva Pereira M. Pulsed electrodeposition of Zn in the presence of surfactants. *Electrochim. Acta* 2006;**51**:1342–1350. DOI: 10.1016/j.electacta.2005.06.023
- [12] Mackinnon D, Brannen J, Kerby R. The effect of lead on zinc deposit structures obtained from high purity synthetic and industrial acid sulphate electrolytes. *J. Appl. Electrochem.* 1979;**9**:55–70. DOI: 10.1007/BF00620587
- [13] Nikolić N, Popov K, Pavlović LjX. The effect of hydrogen codeposition on the morphology of copper electrodeposits. I. The concept of effective overpotential. *J. Electroanal. Chem.* 2006;**588**:88–98. DOI: 10.1016/j.jelechem.2005.12.006
- [14] Abdelkader A, Kilby K, Cox AX. DC voltammetry of electro-deoxidation of solid oxides. *Chem. Rev.* 2013;**113**:2863–2886. DOI: 10.1021/cr200305x
- [15] Zou X, Lu X, Zhou ZX. Electrochemical extraction of Ti_5Si_3 silicide from multicomponent Ti/Si-containing metal oxide compounds in molten salt. *J. Mater. Chem. A* 2014;**2**:7421–7430. DOI: 10.1039/c3ta15039a
- [16] Zou X, Gu S, Cheng HX. Facile electrodeposition of iron films from $NaFeO_2$ and Fe_2O_3 in alkaline solutions. *J. Electrochem. Soc.* 2015;**162**:D49–D55. DOI: 10.1149/2.0751501jes

- [17] Endres F, Abbott A, MacFarlane D (Eds.). *Electrodeposition from Ionic Liquids*. Wiley-VCH, Weinheim, 2008.
- [18] Castner Jr E, Wishart J. Spotlight on ionic liquids. *J. Chem. Phys.* 2010;**132**:120901–120909. DOI: 10.1063/1.3373178
- [19] Hartley J, Ip C, Forrest GX. EXAFS Study into the speciation of metal salts dissolved in ionic liquids and deep eutectic solvents. *Inorg. Chem.* 2014;**53**:6280–6288. DOI: 10.1021/ic500824r
- [20] Dogel J, Freyland W. Layer-by-layer growth of zinc during electrodeposition on Au(111) from a room temperature molten salt. *Phys. Chem. Chem. Phys.* 2003;**5**:2484–2487. DOI: 10.1039/b303388k
- [21] Hsiu S, Huang J, Sun IX. Lewis acidity dependency of the electrochemical window of zinc chloride–1-ethyl-3-methylimidazolium chloride ionic liquids. *Electrochim. Acta* 2002;**47**:4367–4372. DOI: 10.1016/S0013-4686(02)00509-1
- [22] Abbott A, Barron J, Ryder K. Electrolytic deposition of Zn coatings from ionic liquids based on choline chloride. *Trans. Inst. Met. Finish.* 2009;**87**:201–207. DOI: 10.1179/174591909X438857
- [23] Whitehead A, Pözl M, Gollas B. Zinc electrodeposition from a deep eutectic system containing choline chloride and ethylene glycol. *J. Electrochem. Soc.* 2010;**157**:D328–D334. DOI: 10.1149/1.3364930
- [24] Abbott A, Barron J, Frisch GX. Double layer effects on metal nucleation in deep eutectic solvents. *Phys. Chem. Chem. Phys.* 2011;**13**:10224–10231. DOI: 10.1039/C0CP02244F
- [25] Abbott A, Barron J, Frisch GX. The effect of additives on zinc electrodeposition from deep eutectic solvents. *Electrochim. Acta* 2011;**56**:5272–5279. DOI: 10.1016/j.electacta.2011.02.095
- [26] Pereira N, Fernandes P, Pereira CX. Electrodeposition of zinc from choline chloride-ethylene glycol deep eutectic solvent: effect of the tartrate ion. *J. Electrochem. Soc.* 2012;**159**:D501–D506. DOI: 10.1149/2.004209jes
- [27] Liu Z, Abedin S, Endres F. Electrodeposition of zinc films from ionic liquids and ionic liquid/water mixtures. *Electrochim. Acta* 2013;**89**:635–643. DOI: 10.1016/j.electacta.2012.11.077
- [28] Zheng Y, Dong K, Wang QX. Electrodeposition of zinc coatings from the solutions of zinc oxide in imidazolium chloride/urea mixtures. *Sci. China: Chem.* 2012;**55**:1587–1597. DOI: 10.1007/s11426-012-4682-y
- [29] Endres F. Ionic liquids: Solvents for the electrodeposition of metals and semiconductors. *Chemphyschem.* 2002;**3**:144–154. DOI: 10.1002/1439-7641
- [30] Endres F, Schweizer A. The electrodeposition of copper on Au(111) and on HOPG from the 66/34 mol% aluminium chloride/1-butyl-3-methylimidazolium chloride room temperature molten salt: an EC-STM study. *Phys. Chem. Chem. Phys.* 2000;**2**:5455–5462. DOI: 10.1039/B006040M

- [31] Chen P, Sun I. Electrochemical study of copper in a basic 1-ethyl-3-methylimidazolium tetrafluoroborate room temperature molten salt. *Electrochim. Acta* 1999;**45**:441–450. DOI: 10.1016/S0013-4686(99)00275-3
- [32] Murase K, Nitta K, Hirato TX. Electrochemical behaviour of copper in trimethyl-n-hexylammonium bis((trifluoromethyl)sulfonyl)amide, an ammonium imide-type room temperature molten salt. *J. Appl. Electrochem.* 2001;**31**:089–1094. DOI: 10.1023/A:1012255601793
- [33] Zein El Abedin S, Saad A, Farag HX. Electrodeposition of selenium, indium and copper in an air- and water-stable ionic liquid at variable temperatures. *Electrochim. Acta* 2007;**52**:2746–2754. DOI: 10.1016/j.electacta.2006.08.064
- [34] Chen P, Deng M, Zhuang D. Electrochemical codeposition of copper and manganese from room-temperature N-butyl-N-methylpyrrolidinium bis(trifluoromethylsulfonyl)imide ionic liquid. *Electrochim. Acta* 2009;**54**:6935–6940. DOI: 10.1016/j.electacta.2009.07.016
- [35] Endres F, Zein El Abedin S. Air and water stable ionic liquids in physical chemistry. *Phys. Chem. Chem. Phys.* 2006;**8**:2101–2116. DOI: 10.1039/B600519P
- [36] Haerens K, Matthijs E, Binnemans KX. Electrochemical decomposition of choline chloride based ionic liquid analogues. *Green Chem.* 2009;**11**:1357–1365. DOI: 10.1039/B906318H
- [37] Chen P, Chang Y. Voltammetric study and electrodeposition of copper in 1-butyl-3-methylimidazolium salicylate ionic liquid. *Electrochim. Acta* 2012;**75**:339–346. DOI: 10.1016/j.electacta.2012.05.024
- [38] Abbott A, Capper G, Davies DX. Novel solvent properties of choline chloride/urea mixtures. *Chem. Commun.* 2003:70–71. DOI: 10.1039/B210714G
- [39] Abbott A, Boothby D, Capper GX. Deep eutectic solvents formed between choline chloride and carboxylic acids: versatile alternatives to ionic liquids. *J. Am. Chem. Soc.* 2004;**126**:9142–9147. DOI: 10.1021/ja048266j
- [40] Abbott A, Ttaib K, Frisch GX. Electrodeposition of copper composites from deep eutectic solvents based on choline chloride. *Phys. Chem. Chem. Phys.* 2009;**11**:4269–4277. DOI: 10.1039/B817881J
- [41] Yang H, Reddy R. Electrochemical deposition of zinc from zinc oxide in 2:1 urea/choline chloride ionic liquid. *Electrochim. Acta* 2014;**147**:513–519. DOI: 10.1016/j.electacta.2014.09.137
- [42] Yang H, Reddy R. Fundamental studies on electrochemical deposition of lead from lead oxide in 2:1 urea/choline chloride ionic liquids. *J. Electrochem. Soc.* 2014;**161**:D586–D592. DOI: 10.1149/2.1161410jes
- [43] Tsuda T, Boyd L, Kuwabata SX. Electrochemistry of copper(I) oxide in the 66.7–33.3 mol % urea–choline chloride room-temperature eutectic melt. *J. Electrochem. Soc.* 2010;**157**:F96–F103. DOI: 10.1149/1.3377117

- [44] Xie X, Zou X, Lu XX. Electrodeposition of Zn and Cu-Zn alloy from ZnO/CuO precursors in deep eutectic solvent. *Appl. Surf. Sci.* 2016;**385**:481–489. DOI: 10.1016/j.apsusc.2016.05.138.
- [45] Xie X, Zou X, Lu XX. Voltammetric study and electrodeposition of Cu from CuO in deep eutectic solvents. *J. Electrochem. Soc.* 2016; **163**:D537–D543. DOI:10.1149/2.1241609jes.
- [46] Zhang Q, Abbott A, Yang C. Electrochemical fabrication of nanoporous copper films in choline chloride-urea deep eutectic solvent. *Phys. Chem. Chem. Phys.* 2015;**17**:14702–14709. DOI: 10.1039/c5cp01276g
- [47] Ru J, Hua Y, Wang DX. Mechanistic insight of in situ electrochemical reduction of solid PbO to lead in ChCl-EG deep eutectic solvent. *Electrochim. Acta* 2015;**186**:455–464. DOI: 0.1016/j.electacta.2015.11.013
- [48] Abbott A, Capper G, Davies DX. Selective extraction of metals from mixed oxide matrixes using choline-based ionic liquids. *Inorg. Chem.* 2005;**44**:6497–6499. DOI: 10.1021/ic0505450
- [49] Abbott A, Capper G, Davies DX. Solubility of metal oxides in deep eutectic solvents based on choline chloride. *J. Chem. Eng. Data* 2006;**51**:1280–1282. DOI: 10.1021/je060038c
- [50] Abbott A, Collins J, Dalrymple IX. Processing of electric arc furnace dust using deep eutectic solvents. *Aust. J. Chem.* 2009;**62**:341–347. DOI: 10.1071/CH08476
- [51] Bard A, Faulkner L. *Electrochemical methods: Fundamentals and Applications*. John Wiley & Sons, New York, 2000.
- [52] Nagaishi R, Arisaka M, Kimura TX. Spectroscopic and electrochemical properties of europium (III) ion in hydrophobic ionic liquids under controlled condition of water content. *J. Alloys Compd.* 2007;**431**:221–225. DOI: 10.1016/j.jallcom.2006.05.048
- [53] Kuznetsov S, Gaune-Escard M. Kinetics of electrode processes and thermodynamic properties of europium chlorides dissolved in alkali chloride melts. *J. Electroanal. Chem.* 2006;**595**:11–22. DOI: 10.1016/j.jelechem.2006.02.036
- [54] Chen P, Hussey C. The electrodeposition of Mn and Zn-Mn alloys from the room-temperature tri-1-butylmethylammonium bis((trifluoromethane)sulfonyl)imide ionic liquid. *Electrochim. Acta* 2007;**52**:1857–1864. DOI: 10.1016/j.electacta.2006.07.049
- [55] Pitner W, Hussey C. Electrodeposition of zinc from the Lewis acidic aluminum chloride-1-methyl-3-ethylimidazolium chloride room temperature molten salt. *J. Electrochem. Soc.* 1997;**144**:3095–3103. DOI: 10.1149/1.1837965
- [56] Abbott A, Azam M, Frisch GX. Ligand exchange in ionic systems and its effect on silver nucleation and growth. *Physical Chemistry Chemical Physics*. 2013;**15**:17314–17323. DOI: 10.1039/c3cp52674g

Liquid Crystals

Ionic Liquid Crystals Based on Pyridinium Salts

Viorel Cîrcu

Additional information is available at the end of the chapter

<http://dx.doi.org/10.5772/65757>

Abstract

This chapter describes the liquid crystalline properties of the ionic liquid crystals (ILC) based on pyridinium salts as well as their metal-containing compounds with an emphasis on the recent systems described in literature. The main factors that influence the liquid crystalline properties of pyridinium ILC are discussed. Selected thermal data are given according to mesogenic group employed and its position (either N-substitution or pyridinium ring substitution) and the number of structural cationic units (mono-, di-, or polycationic pyridinium ILC).

Keywords: ionic liquids, liquid crystals, pyridinium salts

1. Introduction

Ionic liquid crystals (ILCs) are extensively studied nowadays due to their unique properties resulting from the combination of liquid crystal (LC) and ionic liquid (IL) properties. Several reviews covering this topic were published in the recent years [1–3]. The field of ILCs is continuously growing as many recent applications were found: solar cells, membranes, battery materials, electrochemical sensors, or electroluminescent switches. Different factors are responsible for governing the nature of ILC phases, such as the molecular shape, location, and size of ionic groups, intermolecular interactions, and microphase segregation. Thus, the hydrophobic interactions between the long alkyl chain groups, ionic, dipole-dipole, anion-cation hydrogen bonding, and cation- π interactions together with the π - π stacking of the aromatic rings, all have a contribution to the stabilization of the liquid crystalline phase. For instance, there is a strong tendency to stabilize lamellar (smectic) phases, with SmA the most common phase for ILC, due to electrostatic interactions and ion-ion stacking in ILC. The combination of all these factors leads to LC behavior ranges from typical calamitic materials to discotic. The imidazolium or pyridinium derivatives, one of the most studied classes of ILC, with weakly coordinating anions, such as tetrafluoroborate (BF_4^-) and hexafluorophosphate (PF_6^-), are well known for their high thermal and electrochemical stabilities. It is worth to

mention here that the pyridinium-based ILC has been known for a long time, displaying very similar properties with the related imidazolium-based ILC.

The most common types of LC phases displayed by ILCs are represented in **Figure 1**. Their identification relies upon three characterization techniques: polarizing optical microscopy (POM), differential scanning calorimetry (DSC), and powder X-ray diffraction (XRD). The usual textures seen by POM for different mesophases are presented in **Figure 2**. It is very common to see the SmA phase of ionic mesogens as a so-called oily streak texture by POM, in particular during heating runs (**Figure 2**). When cooling from the isotropic state, very often the SmA phase can develop spontaneous homeotropic alignment due to interactions developed between the cationic groups and the glass substrate surface (the samples are sandwiched between two microscope slides), and further orientation of the mesogenic groups. As a result, the microscopy image contains large dark regions corresponding to these homeotropic alignments.

The POM technique is an important tool for mesophase identification, but an ultimate technique that confirms unequivocally the phase type is the XRD method. The later one can give also important information regarding the internal organization within the mesophase resulting from the different molecular packing related to the chemical structure of the ionic mesogens and the nature of interactions between them.

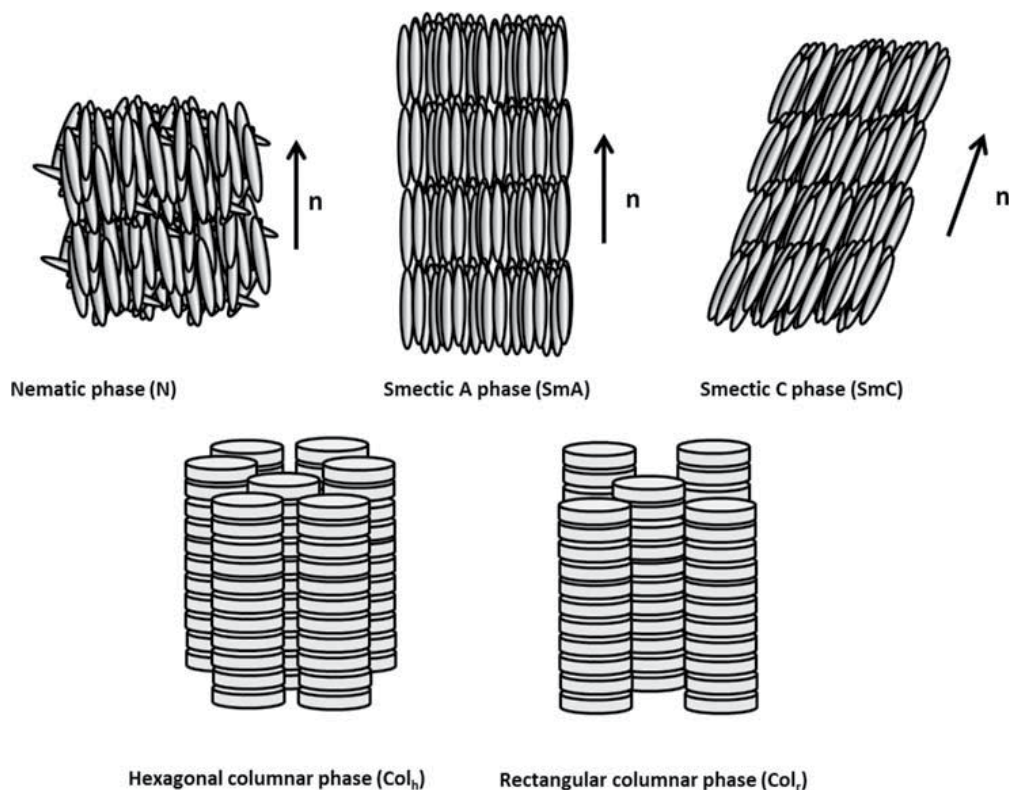


Figure 1. Schematic representation of the most common liquid crystalline phases encountered for ionic liquid crystals.

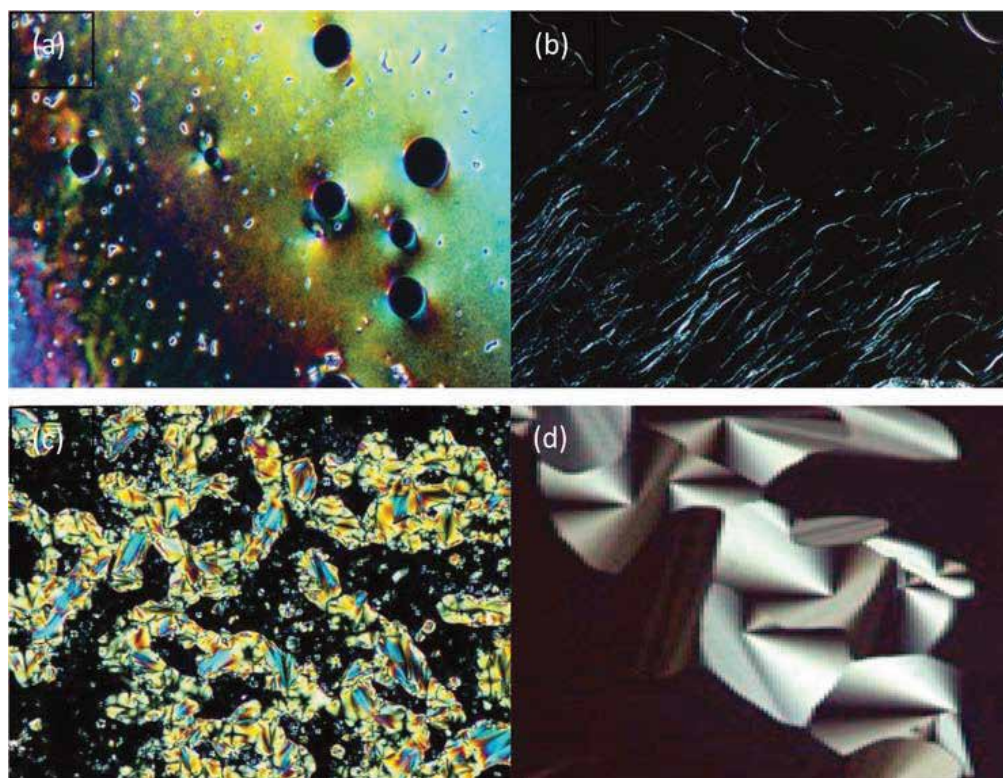


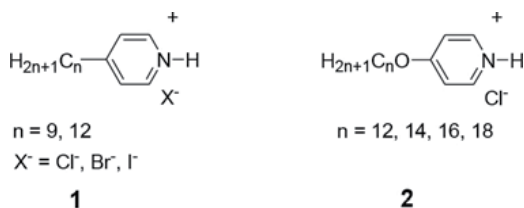
Figure 2. Typical textures for LC phases: marbled texture of a nematic phase (a), oily-streaks texture for a SmA phase on heating run (b), focal conical fan-shaped texture for SmA phase (c), and fan-shaped texture of a hexagonal columnar phase Col_h (d).

The thermal behavior as well as the mesophase type of pyridinium-based ILCs depends on several factors: the position and the nature of the mesogenic group attached to the pyridinium ring and the counterion employed. These structural factors will be discussed further and selected examples will be presented to illustrate their influence on the mesomorphic behavior. The pyridinium-based ILC classification was made according to mesogenic group used and its position (either N-substitution or pyridinium ring substitution) and the number of cationic units contained in their structure (mono-, di-, or polycationic pyridinium ILC).

2. Monocationic pyridinium ionic liquid crystals

2.1. Simple protonated pyridinium salts

The simplest 4-alkyl substitution protonated pyridinium salts with halide as counterions (1) show no liquid crystalline properties as they melt straight to the isotropic phase. Such products have been synthesized by reaction between the corresponding hydrogen halide with their corresponding 4-alkyl pyridine compounds [4].



2a, $n = 12$ Cr 92 Cr' 122 SmA 133 dec

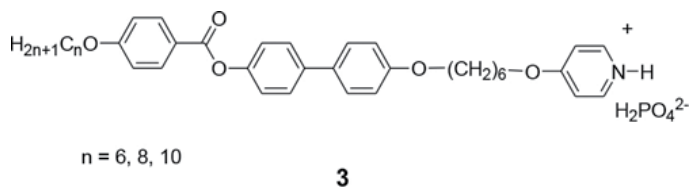
2b, $n = 14$ Cr 95 Cr' 122 SmA 139 dec

2c, $n = 16$ Cr 95 Cr' 124 SmA 142 dec

2d, $n = 18$ Cr 93 Cr' 124 SmA 145 dec

By changing the alkyl group with an alkoxy group, the resulting protonated chloride pyridinium salts show a SmA phase, with decomposition near the isotropization process. The melting and isotropization temperatures of these products were very insensitive to the chain lengths, suggesting that the hydrophobic interactions are the least significant factor in the thermal behavior of such protonated pyridinium salts [5].

A series of more elaborated protonated pyridinium salts have been prepared by the reaction between pyridine derivatives and phosphoric acid with the aim of studying their anhydrous proton conduction. X-ray diffraction measurements suggested that the pyridinium salts formed a bilayer structure with head-to-head configuration in the SmA phase [6].

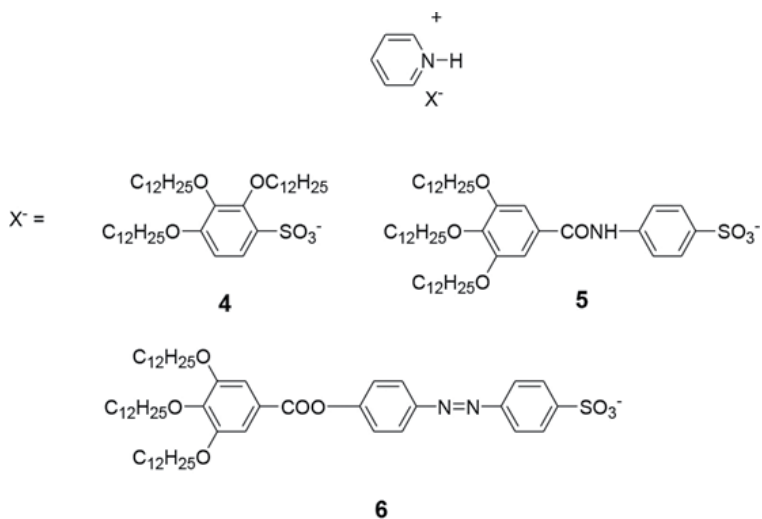


3a, $n = 6$; Cr 170 SmA 235 dec

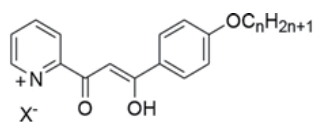
3b, $n = 8$; Cr 169 SmA 232 dec

3c, $n = 10$; Cr 159 SmA 213 dec

The protonated pyridinium cation was employed to generate liquid crystalline materials having as counterions a series of wedge-shaped benzenesulfonate mesogens **4–6** [7, 8]. Compound **4**, having a rather unusual substitution pattern, 2,3,4-tris(dodecyloxy)benzenesulfonate, exhibits a reversible transition from a columnar disordered phase into an ordered columnar during the slow heating and cooling cycles. The thermal behavior of pyridinium salts **5** and **6** was compared to thermal properties of their corresponding benzenesulfonic acid and its sodium salts. It was found that **5** and **6** exhibit much lower transition temperatures than the sulfonic acids (the corresponding sulfonic acid of **6** was not stable upon drying) and sodium salts, respectively.

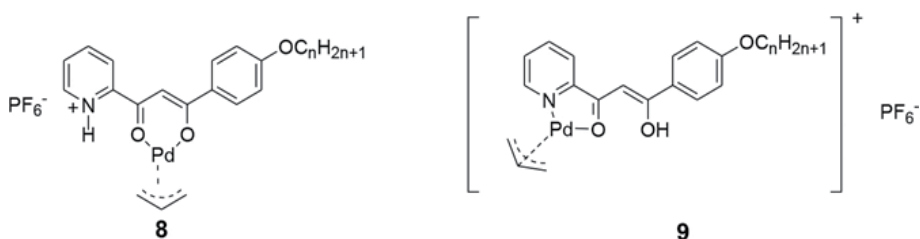


4, Cr 30 Cr' 53 Cr" 80 Col_{hd} 122 Iso
5, Cr 39 M 65 Iso
6, Cr 94 Col 200 Iso (dec)



n = 10, 12, 14, 16, 18
 X⁻ = Cl⁻, [ZnCl₄]²⁻

7



n = 12, 14, 16, 18

8, n = 14, Cr 84 Cr' 158 SmC 170 Iso **9**, n = 14, Cr 76 SmC 173 Iso

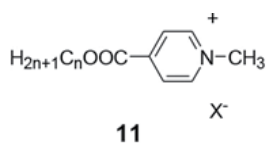
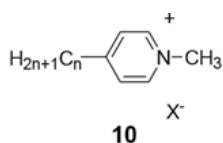
When the protonated pyridinium moiety is part of a α -diketone compound, the resulting β -diketone pyridinium chloride salts are not mesomorphic. Replacement of chloride anion with the tetrachlorozincate ion produced mesomorphic ionic salts displaying a SmA phases over a

broad temperature range [9]. The same authors reported the thermal behavior and photophysical properties of the metal-free β -diketone pyridinium ligands, and their allyl-palladium(II) complexes (**8**, **9**) [10, 11]. Interestingly, an equilibrium between **8** and **9** exists in solution. Another peculiar aspect about these complexes is that normally, the β -diketone ligands are first deprotonated before coordination to the metal center. Pd(II) metallomesogens with tetradecyloxy groups display a SmC phase, with reduced mesomorphic range for the protonated compound. The emission properties of Pd(II) complexes were preserved in the LC state.

2.2. N-alkylated pyridinium salts

2.2.1. N-methyl pyridinium salts

A clear trend for isotropization temperatures was seen for N-methyl pyridinium salts, meaning that, based on strong dependence of these temperatures on the alkyl chain length, longer alkyl chain length in position 4 of the pyridinium ring lead to higher transition temperatures. Moreover, it was observed that the 1-methyl-4-alkoxycarbonylpyridinium iodides salts have thermochromic properties. Color changes were observed on heating at both crystal to crystal and crystal to mesophase transitions, while such an observation could not be made for the 1-methyl-4-alkylpyridinium iodides salts [4, 12, 13].



10a, $n = 8$, $X^- = I^-$: Cr 103 Iso

10b, $n = 10$, $X^- = I^-$: Cr 113 Iso

10c, $n = 11$, $X^- = I^-$: Cr 116 SmA Iso

10d, $n = 12$, $X^- = I^-$: Cr 113 SmA 153 Iso

10e, $n = 12$, $X^- = ClO_4^-$: Cr 93 SmA 95 Iso

10f, $n = 13$, $X^- = I^-$: Cr 112 SmA 188 Iso

10g, $n = 14$, $X^- = I^-$: Cr 116 SmA 209 Iso

11a, $n = 10$, $X^- = I^-$: Cr 86 SmA154 Iso

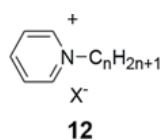
11b, $n = 12$, $X^- = I^-$: Cr 94 SmA 178 Iso

11c, $n = 14$, $X^- = I^-$: Cr 99 SmA 182 Iso

11d, $n = 16$, $X^- = I^-$: Cr 103 SmA 182 Iso

2.2.2. Other N-alkylated pyridinium salts

The simple N-alkylated chloride pyridinium salts **12** were obtained by reacting the corresponding alkyl chloride and pyridine, while the tetrachlorometalates, where $M = Co(II)$ or $Ni(II)$, were prepared by the reaction between these chloride pyridinium salts and anhydrous metallic chlorides [14]. The N-alkylated pyridinium chloride salts with a chain length below 12 units do not display liquid-crystal behavior.

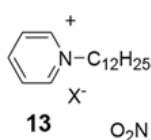


$X^- = \text{Cl}^-, [\text{MCl}_4]^{2-}$ (where M = Co, Ni)
 $n = 12, 14, 16, 18$

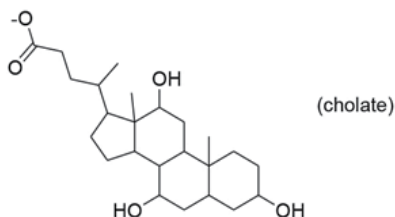
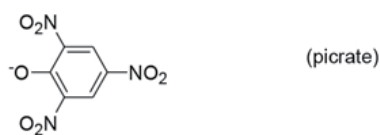
$X^- = \text{PF}_6^-$
 $n = 12, 14, 16, 18$

$X^- = \text{C}_m\text{H}_{2m+1}\text{OSO}_3^-$
 $m = 10, 12, 14, 16, 18, 20$
 $n = 6, 8, 10, 12, 14, 16, 18, 20$

$X^- = [\text{CuCl}_4]^{2-}$
 $n = 6, 9-18$



$X^- =$



12a, $n = 16$, $X^- = \text{PF}_6^-$: Cr 104 Cr' 126 SmA 138 Iso

12b, $n = 18$, $X^- = \text{PF}_6^-$: Cr 107 Cr' 126 SmA 176 Iso

12c, $n = 12$, $X^- = [\text{CuCl}_4]^{2-}$: Cr 54 Col_h 76 Iso

Importantly, these salts (**12**) exhibit a SmA phase with relatively large mesophase ranges that become relatively independent of the chain length for alkyl chain length greater than 14 carbon atoms. On the contrary, for the tetrachlorometalate(II) salts, the mesophase stability increases monotonically with an increase in chain length. While initially, the n-dodecyl derivative has been found to show only a SmA phase, later it was reported that this compound showed cubic and smectic A phases on the heating run, and columnar (16–46°C), cubic (46–66°C), and smectic A (46–143°C) phases on the cooling run. The authors found that the phase transition temperatures were strongly influenced by a glass surface and on the thermal history [15].

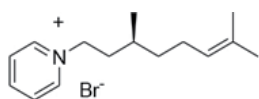
Replacement of chloride anion with bulkier hexafluorophosphate anion led to mesophase destabilization for pyridinium salts with alkyl chain shorter than 16 carbon atoms. Extensive studies were performed for N-alkyl pyridinium salts with alkylsulfates as counterion, all of them displaying a typical SmA phase, the mesophase temperature range depending on the combination of chain lengths of both N-alkyl and the aliphatic chain connected to the sulfate group [16, 17].

The tetrachlorocuprate pyridinium salts show a very interesting and rich polymorphism for alkyl chain longer than or equal to 12 carbon atoms, with hexagonal columnar, cubic, and SmA phases appearing in the order of increasing the chain length and/or temperature [18].

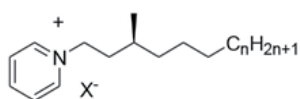
By exchanging the chloride anion with biologically active picrate, dodecylbenzenesulfonate, or cholate anions, different thermal behavior was found [19]. Thus, only the compound with dodecylbenzenesulfonate anion displayed a SmA phase stable up to 152°C, while the other two showed no liquid crystalline properties. The absence of mesomorphic properties in the case of picrate anion was attributed to the formation of interlayer 3-D hydrogen bond network between pyridinium and picrate ions.

2.2.3. Chiral *N*-alkylated pyridinium salts

Recently, a series of *N*-alkylated pyridinium salts containing a chiral center in the four positions with respect to nitrogen atoms have been prepared and investigated by Laschat et al. [20, 21]. Their thermal properties were compared to their imidazolium counterparts. Generally, these salts show a SmA phase, with melting and isotropization temperatures lower than the temperatures of their corresponding imidazolium counterparts. The mesophase stability range depends on the alkyl group length as well as on the counterion and it was found to decrease in the following order: $\text{Br}^- > \text{OAc}^- > \text{BF}_4^- > \text{I}^- > \text{SCN}^-$. The pyridinium salts with hexafluorophosphate anion show no liquid crystalline properties.



14



$\text{X}^- = \text{Br}^-, \text{I}^-, \text{SCN}^-, \text{BF}_4^-, \text{PF}_6^-, \text{OAc}^-$
 $n = 6-9$

15

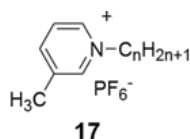
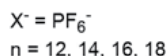
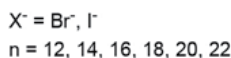
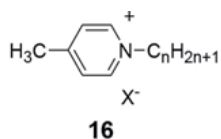
15a , $n = 9$, $\text{X}^- = \text{Br}^-$: Cr -8 Cr' -1 SmA 173 Iso	15d , $n = 9$, $\text{X}^- = \text{BF}_4^-$: Cr -19 Cr' 1 SmA 140 Iso
15b , $n = 9$, $\text{X}^- = \text{I}^-$: Cr -6 Cr' 41 SmA 171 Iso	15e , $n = 9$, $\text{X}^- = \text{PF}_6^-$: Cr 63 Cr' 80 Cr'' 126 Iso
15c , $n = 9$, $\text{X}^- = \text{SCN}^-$: Cr 2 Cr' 21 SmA 135 Iso	15f , $n = 9$, $\text{X}^- = \text{OAc}^-$: Cr 0 SmA 162 Iso

For chiral 1-citronellylpyridinium bromide salt **14**, only a glass transition was detected and no mesomorphism was evidenced.

2.2.4. *N*-alkylated pyridinium salts derived from picoline

The pyridinium salts derived from either 4- or 3-picoline, **16** and **17**, have been extensively studied [12, 22–24]. Their mesophase stability (SmA phase) depends strongly on the alkyl chain length as well as on the position of methyl group on the pyridinium ring. The mesophase temperature range increases significantly with increasing the alkyl chain length, while the alkyl substitution at the 3- and 4-positions on the pyridinium ring leads to a decrease in the melting point compared with the corresponding unsubstituted pyridinium salts. The effect of pyridinium ring substitution was also seen on the mesophase broadness, the pyridinium salts derived from 4-picoline having a much broader mesomorphic range compared to those derived from 3-picoline. Regarding the internal mesophase structure, the molecules are

considered to pack in an interdigitated fashion, with the anions sandwiched between the pyridinium rings.



16a, $n = 18$, $X^- = Br^-$: Cr 92 SmA 158 Iso

16b, $n = 20$, $X^- = Br^-$, Cr 84 SmA 197 Iso

16c, $n = 22$, $X^- = Br^-$, Cr 91 SmA 207 Iso

16d, $n = 22$, $X^- = I^-$: Cr 99 SmA 198 Iso

17a, $n = 12$, $X^- = PF_6^-$: Cr 56 Iso

17b, $n = 14$, $X^- = PF_6^-$: Cr 71 Iso

17c, $n = 16$, $X^- = PF_6^-$: Cr 75 Iso 60 SmA 55 Cr

17d, $n = 18$, $X^- = PF_6^-$: Cr 88 Iso 84 SmA 77 Cr

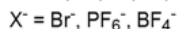
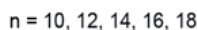
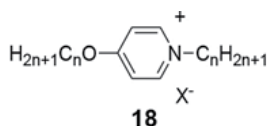
16e, $n = 12$, $X^- = PF_6^-$: Cr 55 Iso

16f, $n = 14$, $X^- = PF_6^-$: Cr 68 Iso

16g, $n = 16$, $X^- = PF_6^-$: Cr 74 Iso 61 SmA 58 Cr

16h, $n = 18$, $X^- = PF_6^-$: Cr 87 SmA 94 Iso

A series of N-alkylated pyridinium salts, having an alkoxy group in 4-position of pyridinium ring, were synthesized by the reaction of either N-alkyl-4-pyridones or 4-alkoxypyridines with corresponding alkyl bromides. Further, hexafluorophosphate and tetrafluoroborate pyridinium salts could be prepared by a metathesis reaction with the ammonium salts.



18a, $n = 12$, $X^- = Br^-$: Cr 70 SmA 120 Iso

18b, $n = 12$, $X^- = PF_6^-$: Cr 72 Iso 53 SmA 17 Cr

18c, $n = 12$, $X^- = BF_4^-$: Cr 39 SmA 77 Iso

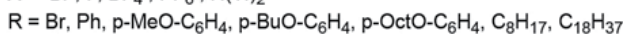
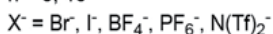
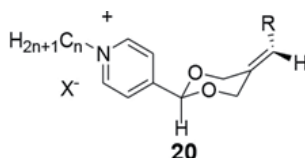
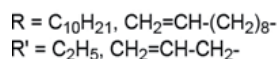
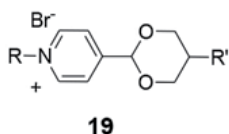
18d, $n = 14$, $X^- = Br^-$: Cr 77 SmA 140 Iso

18e, $n = 14$, $X^- = PF_6^-$: Cr 67 SmA 94 Iso

18f, $n = 14$, $X^- = BF_4^-$: Cr 51 SmA 98 Iso

These salts exhibit smectic A phase. The transition temperatures, both melting and clearing, as well as the mesophase stability were influenced by the alkyl chain length and the counterion type. The hexafluorophosphate anion, PF_6^- , produced smaller mesophase ranges, followed by tetrafluoroborate anion, BF_4^- , when compared to bromide pyridinium salts as a consequence of a weaker cation-anion interaction for the BF_4^- or PF_6^- than for the Br^- [5].

Pyridinium salts with a 1,3-dioxane ring attached in 4-position were prepared and their liquid crystalline properties were investigated [25, 26]. A very wide range for the SmA mesophase (between -24 and 150°C) was found for ionic thermotropic liquid crystal system having two rings in its central core (**19**) reported by Haramoto et al. [25]. Based on the same design, chiral pyridinium liquid crystals **20** show an interesting thermal behavior [26].



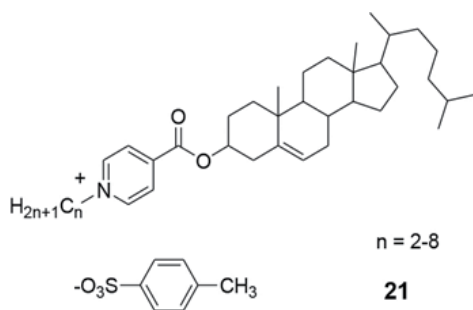
19a, Cr -24 SmA 150 Iso (R = $\text{C}_{10}\text{H}_{21}$, R' = C_2H_5)

20a, n = 10, R = $\text{C}_{18}\text{H}_{37}$, X⁻ = I⁻: SmX 41 N 90 Iso (dec.)

20b, n = 10, R = p-BuO-C₆H₄, X⁻ = I⁻: N 47 Iso

20c, n = 10, R = C_8H_{17} , X⁻ = Br⁻: SmC 53 Iso

First, LC phases were observed only for long alkyl chains on both sides of the molecule. Furthermore, the authors found that the enantiomeric purity influences significantly the nature of the mesophase (chiral nematic phase N* for pure single enantiomeric compounds and nematic and smectic phases for racemic mixture) and only slightly the transition temperatures between solid state and LC phase and LC phase and isotropic state. Moreover, the LC phase stability depends on the counterion size (higher stability for halide and tetrafluoroborate anions) due to the contribution of bigger anions to decreasing the packing of the mesomorphic cationic units. Yousif et al. found an enantiotropic cholesteric phase (N*) for a series of quaternized cholesteryl isonicotinates with tosylate counterions [27]. The assignment of such



21a, n = 2, Cr 225 N* 241 Iso

21b, n = 3, Cr 176 N* 228 Iso

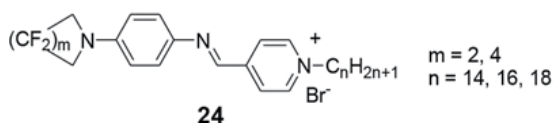
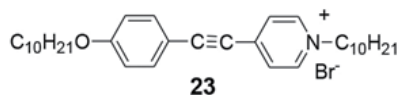
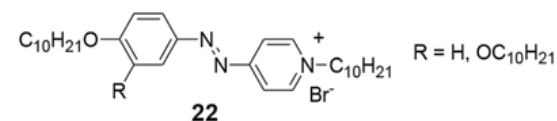
21c, n = 4, Cr 194 N* 225 Iso

21d, n = 5, Cr 181 N* 219 Iso

21e, n = 6, Cr 183 N* 236 Iso

21f, n = 7, Cr 177 N* 237 Iso

21g, n = 8, Cr 149 N* 218 Iso



22a, R = H, Cr 119 SmA 138 Iso

22b, R = C₁₀H₂₁, Cr 86 SmA 119 Iso

23, Cr 174 SmA 183 dec

24a, m = 2, n = 14, Cr 87 M 156 Iso (dec.)

24b, m = 2, n = 16, Cr 90 M 159 SmA 175 Iso (dec)

24c, m = 4, n = 14, Cr 80 Iso

24d, m = 4, n = 16, Cr 80 Iso

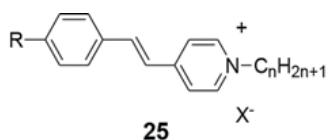
a mesophase was made based on polarizing optical microscopy when a planar texture with bright oily streaks was identified for such compounds. No additional XRD studies were undertaken to characterize this phase.

Several other pyridinium ILCs having a second aromatic ring connected to the 4-position of the pyridinium ring via a linking group (azo, **22**, acetylene, **23**, or imine, **24**) were designed and investigated [28, 29]. Their thermal properties are influenced by the alkyl chain length, the nature of linking groups, while the dominant factor for **24** was the size of perfluorinated ring [29].

2.2.5. *N*-Alkyl-4'-substitution-stilbazolium halides

N-alkyl-stilbazolium ILC, having different groups at the 4'-position of the stilbazolium head unit, were investigated by several authors [23, 30, 31]. The 4'-substitution at the stilbazolium unit has a great influence on the LC properties. For instance, the compounds with NO₂ or CN groups and bromide as counterion show a relatively narrow temperature range of the LC phase [30]. By introduction of chloride anions, the LC phase stability increases and the compounds decompose before reaching the isotropic phase. The use of dialkylamino group at the 4'-position in the stilbazolium core led to a significant decrease of the temperature range of the mesophase. For compounds **25a-f**, the substituents at the 4'-position of stilbazolium core increase the stability of the SmA phase in the following order: OCH₃ > OH > H, meaning that the mesomorphic behavior is also influenced by dipolar interactions resulting from OH and OCH₃ groups [23]. All these salts show an increase of the SmA phase range with increasing the alkyl chain length. On the other hand, the stability of the SmA phase is influenced by the size

of the counterion; lower melting and clearing temperatures were seen for iodide compared to bromide stilbazolium salts.



$n = 5 - 10$	$n = 14, 16, 18$	$n = 14, 16, 18, 20, 22$
$R = \text{NO}_2, \text{CN}$	$R = \text{N}(\text{CH}_3)_2$	$R = \text{OH}, \text{OCH}_3, \text{H}$
$X^- = \text{Cl}^-, \text{Br}^-, \text{I}^-$	$X^- = \text{Br}^-$	$X^- = \text{Br}^-, \text{I}^-$

25a, $R = \text{H}$, $n = 18$, $X^- = \text{Br}^-$: Cr 153 SmA 217 Iso (dec)

25b, $R = \text{H}$, $n = 18$, $X^- = \text{I}^-$: Cr 189 Iso

25c, $R = \text{OH}$, $n = 18$, $X^- = \text{Br}^-$: Cr 172 SmA 230 Iso (dec)

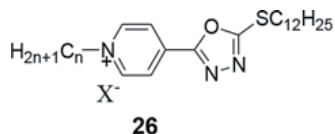
25d, $R = \text{OH}$, $n = 18$, $X^- = \text{I}^-$: Cr 130 SmA 184 Iso

25e, $R = \text{OCH}_3$, $n = 18$, $X^- = \text{Br}^-$: Cr 63 SmA 255 Iso (dec)

25f, $R = \text{OCH}_3$, $n = 18$, $X^- = \text{I}^-$: Cr 62 Cr' 245 Iso (dec)

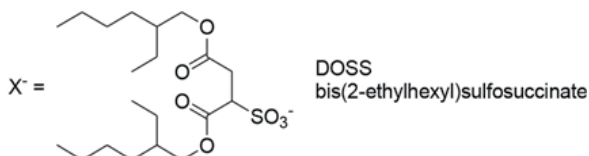
2.2.6. Monocationic oxadiazole pyridinium salts

The pyridinium bromide salts **26a-d**, all of them show a SmA phase with a slight increase of clearing temperatures on increasing the alkyl chain length. By replacing the bromide ion with



$n=10,12,14,16$; $X^-=\text{Br}^-$

$n=12$ $X^- = \text{C}_m\text{H}_{2m+1}\text{-SO}_3^-$
 $m=10, 14$



26a, $n = 10$, $X^- = \text{Br}^-$: Cr 64 Cr' 117 SmA 172 Iso

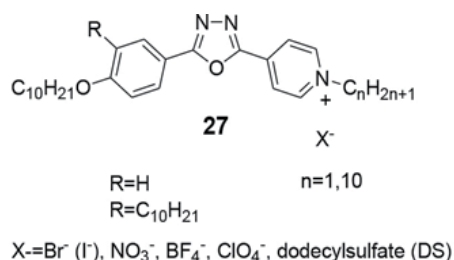
26b, $n = 12$, $X^- = \text{Br}^-$: Cr 74 Cr' 119 SmA 185 Iso

26c, $n = 14$, $X^- = \text{Br}^-$: Cr 70 Cr' 118 SmA 186 Iso

26d, $n = 16$, $X^- = \text{Br}^-$: Cr 85 Cr' 115 SmA 189 Iso

alkyl sulfate ions, a significant depression of clearing temperature was achieved (about 40°C) [32]. On the other hand, a total suppression of liquid crystalline phase was observed when the bis(2-ethylhexyl)-sulfosuccinate ion (DOSS) was employed. Interestingly, the pyridinium bromide salts display thermochromic properties [33]. Thus, the crystal to SmA transition of such compounds was accompanied with a color change from pale yellow to bright red that is almost fully reversible upon cooling. Such thermochromic effect was not observed on changing the bromide anion for alkylsulfate or DOSS ions. The origin of the thermochromic properties was attributed by authors to a charge-transfer couple formation between the bromide and the pyridinium ring.

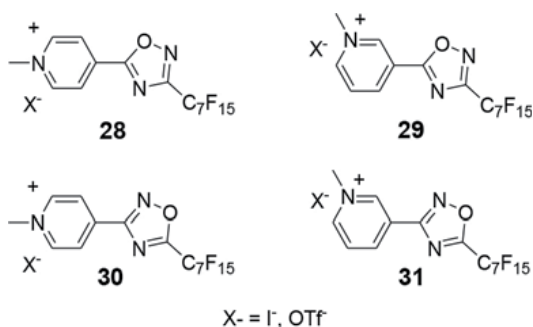
More recently, a systematic study of liquid crystalline and photophysical properties of a series of pyridinium salts was reported [34, 35], where the 1,3,4-oxadiazole unit connects one pyridinium ring and one mono- or di-substitution phenyl ring with alkoxy groups.



- 27a**, n = 1, R = H, X⁻ = BF₄⁻: Cr 193 SmA 256 dec
27b, n = 1, R = H, X⁻ = ClO₄⁻: Cr 202 SmA 257 dec
27c, n = 1, R = H, X⁻ = DS: Cr 122 SmA 208 dec
27d, n = 10, R = H, X⁻ = Br⁻: Cr 182 SmA 193 dec
27e, n = 10, R = H, X⁻ = NO₃⁻: Cr 126 SmA 171 dec
27f, n = 10, R = H, X⁻ = BF₄⁻: Cr 153 SmA 213 Iso
27g, n = 10, R = H, X⁻ = ClO₄⁻: Cr 167 SmA 217 Iso
27h, n = 10, R = H, X⁻ = DS: Cr 135 SmA 172 Iso
27i, n = 10, R = C₁₀H₂₁, X⁻ = Br⁻: Cr 148 SmA 194 dec

The N-decyl pyridinium salts exhibit SmA mesomorphism, regardless of the counterion, while their N-methyl counterparts show decomposition and no liquid crystalline properties for iodine and nitrate anions, and, for the remaining anions (BF₄⁻, ClO₄⁻, and DS), the salts decompose before reaching the isotropic phase from the previous SmA phase, suggesting that the thermal properties (melting point, mesophase range, and clearing or decomposition temperature) are sensitive to counterion exchange. Moreover, the two pyridinium salts with DS as counterion are similar in terms of thermal behavior, and this was explained by XRD studies. These compounds have a monolayered SmA phase, instead of a bilayered SmA phase found for the others compounds of the series, and the same molecular lengths (due to the presence of the same counterion), and such a different mesophase structure could account for their similar behavior.

An interesting example showing how the 3'- or 4'-substitution pattern of the pyridinium ring affects the thermal behavior is represented by the iodides and trifluoromethanesulfonates salts derived from perfluoroalkylated 1,2,4-oxadiazolylpyridines 28–31 [36]. Thus, the 3'-substitution derivatives exhibited liquid crystalline properties (SmX phase) on a narrow temperature range, while the corresponding 4'-substitution derivatives were found to pass from the crystalline state straight to the isotropic phase. Such a behavior was attributed to a charge delocalization over the entire structure, including the oxadiazole ring, which makes the cation/anion electrostatic interactions weaker and, thus, leading to the mesophase detabilization for 4'-substitution compounds.



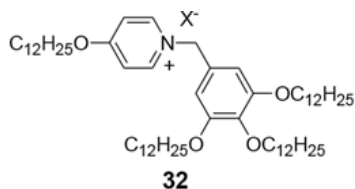
29a, X⁻ = I⁻: Cr 97 SmX 150 Iso

31a, X⁻ = I⁻: Cr 113 SmX 135 Iso

The fact that only the iodide salts showed liquid crystalline properties was explained by the greater coordinating ability of the iodide anions with respect to the trifluoromethanesulfonates anions. Moreover, all iodide salts showed thermochromism phenomena suggesting prospective applications in optoelectronics.

2.3. Monocationic pyridinium salts with mesogenic groups attached to nitrogen atom

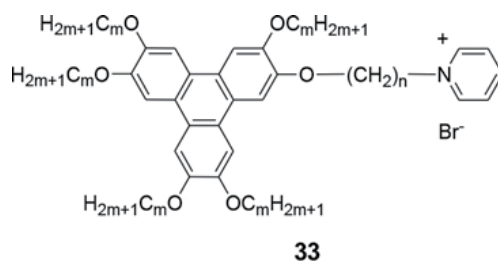
A series of pyridinium salts with the 3,4,5-tridodecyloxybenzyl moiety attached to nitrogen atom and different counterions (bromide, nitrate, tetrafluoroborate, and hexafluorophosphate) **32** were prepared starting from 4-hydroxypyridine [37].



X⁻ = Br⁻, NO₃⁻, BF₄⁻, PF₆⁻

32a, X⁻ = Br⁻: Cr 63 Col₁ 108 Iso 105 Col₁ 74 Col₂

The pyridinium bromide salt shows one enantiotropic columnar mesophase and one additional monotropic columnar phase at lower temperatures. The size of counterion has a significant contribution to the LC phase stability. Surprisingly, when the bromide ion (Br^-) was replaced with bulkier counterions (NO_3^- , BF_4^- , and PF_6^-), the resulting products showed no liquid crystalline behavior. The photoluminescent properties of these pyridinium salts were investigated both in solution and solid state and it has been shown that their emission is only slightly influenced by the nature of counterion employed.

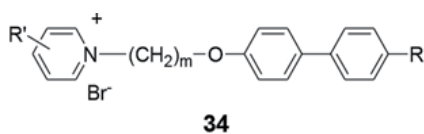


$$m = 4, n = 5, 6, 7$$

$$m = 5, 6, n = 5$$

33a, $m = 4$, $n = 6$, Cr 84 Col 95 Iso

The classical triphenylene unit was connected to pyridinium ring via a flexible methylene flexible chain to give discotic liquid crystals [38]. The mesophase was identified to be a columnar phase based on microscopy observations of optical textures. The stability of this columnar phase was found to depend both on the peripheral alkyl chain length as well as the methylene spacer length. Thus, the stability of columnar phase increases by increasing the number of carbon atoms on the peripheral chains of the triphenylene core, while longer spacer connecting the triphenylene unit with the pyridine ring destabilized the mesophase.



$$m = 6, 10$$

$$R = \text{CN}, -\text{OC}_n\text{H}_{2n+1}, n = 3, 10$$

$$R' = \text{H}, 4\text{-ethyl}, 2\text{-ethyl}, 3,5\text{-dimethyl}$$

34a, $m = 6$, $n = 3$, $R' = \text{H}$, Cr 151 SmA 159 Iso

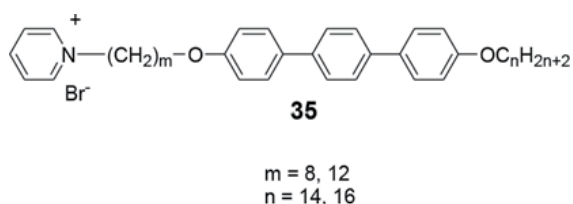
34b, $m = 10$, $n = 10$, $R' = \text{H}$, Cr 136 SmC 165 Iso

34c, $m = 10$, $n = 10$, $R' = 2\text{-ethyl}$, Cr 75 SmC 116 SmA 180 Iso

Interesting results were obtained for pyridinium bromides salts containing a biphenyl core and alkyl chains of different lengths **34** [39]. The substitution of the pyridine ring greatly influences the thermal behavior of these salts. While the unsubstituted pyridinium groups promote

mesomorphism (SmA and SmC phases), the 2- and 4-ethyl-substitution pyridinium groups give rise to liquid crystalline phases only with sufficiently long alkyl chains (decyl chains on both sides of the biphenyl core). The salts having a 3,5-dimethyl substitution pyridine ring do not show any liquid crystalline properties. Moreover, the substitution pattern at the pyridinium groups resulted in different types of smectic phases (SmA, SmC, and SmE).

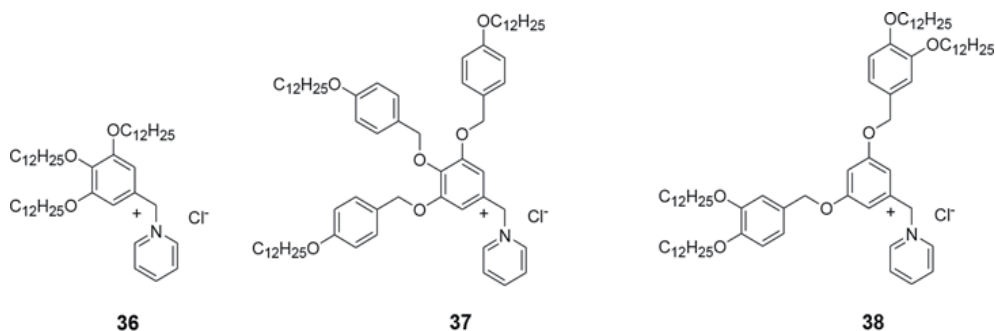
When an additional ring was added, the new pyridinium bromide salts **35** with a triphenylene moiety displayed tilted smectic mesophases (SmC) with molecules stacked in a double layer morphology, as indicated by XRD studies [40]. The tilt angle of these compounds shows a great temperature dependence, and, in fact, at lower temperature being closed to 0°.



The XRD studies together with molecular modeling indicated that π - π interactions counterbalance the strong ionic forces leading to a full segregation of molecular parts in the smectic structures.

2.3.1. Dendritic pyridinium ionic liquid crystals

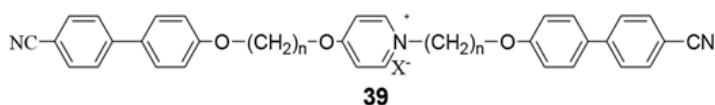
Pyridinium chloride salts having dendritic building blocks connected to the nitrogen atom have been investigated by Percec et al. [41]. Depending on the number of peripheral alkoxy groups, these molecules were found to form columns or spheres, leading to 2D hexagonal columnar phases or a 3D cubic phase, respectively.



36, Cr 65 Col_h 166 Iso
37, Cr 15 Cr' 35 Cr'' 57 Col_h 159 Iso
38, Cr 17 Cr' 92 Col_h 129 Cub 164 Iso

2.3.2. Nematic pyridinium ionic liquid crystals

Starting from 4-hydroxypyridine, it is possible to attach two cyanobiphenyl mesogenic units, via flexible alkyl spacer, on both sides of the pyridinium ring giving rise to a series of nematic pyridinium liquid crystals [42]. The nematic phase has numerous technological applications due to its highest fluidity of all LC phases and hence the possibility to align it by applying an external electric/magnetic field. Moreover, the nematic phase is commonly used in electro-optical devices. The nematic phase is quite rare in the case of ILCs, several examples have been reported so far for ammonium [43, 44], imidazolium [45–48], pyridinium-based ILC [49], or miscellaneous type of ILC [50–54]. Generally, as the smectic phases are the most common phases for ILCs, especially due to electrostatic interactions, the nematic phase can be seen rather as an exception. It has to be reminded here the cholesteryl-containing compounds 21a-g that display a cholesteric phase (chiral nematic phase N*) at relatively high temperatures and on a narrow temperature range. Compounds **39**, all of them with the exception of **39d** and **39e**, displayed a monotropic nematic phase on cooling from the isotropic state. This is the first example of a series of ILC that exhibit a long range nematic phase, no matter the counterion or spacer length between the ionic core and the mesogenic group.



$n = 6, 9, 10$

$X^- = \text{Br}^-, \text{NO}_3^-, \text{BF}_4^-, \text{PF}_6^-, \text{OTf}^-, \text{SCN}^-$

39a, $n = 6$, $X^- = \text{Br}^-$: Cr 120 Cr'144 Iso 70 N 23 g

39b, $n = 6$, $X^- = \text{NO}_3^-$: Cr 81 Iso 65 N 22 g

39c, $n = 6$, $X^- = \text{BF}_4^-$: Cr 57 Cr'85 Cr''102 Iso 60b N 24 g

39d, $n = 6$, $X^- = \text{PF}_6^-$: Cr 119 Iso 21 g

39e, $n = 6$, $X^- = \text{OTf}^-$: Cr 62 Cr'89 Iso 23 g

39f, $n = 6$, $X^- = \text{SCN}^-$: Cr 121 Iso 70 N 24 g

39g, $n = 9$, $X^- = \text{Br}^-$: Cr 128 Iso 89 N 28 g

39h, $n = 9$, $X^- = \text{NO}_3^-$: Cr 92 Cr' 103 Iso 92 N 26 g

39i, $n = 9$, $X^- = \text{BF}_4^-$: Cr 84 Cr'97 Iso 76 N 22 g

39j, $n = 9$, $X^- = \text{PF}_6^-$: Cr 114 Iso 41 N 21 g

39k, $n = 9$, $X^- = \text{OTf}^-$: Cr 104 Iso 45 N 20 g

39l, $n = 9$, $X^- = \text{SCN}^-$: Cr 92 Cr'110 Iso 89 N 21 g

39m, $n = 10$, $X^- = \text{Br}^-$: Cr 114 Iso 83 N 47 Cr

39n, $n = 10$, $X^- = \text{NO}_3^-$: Cr 99 Iso 86 N 25 g

39o, $n = 10$, $X^- = \text{BF}_4^-$: Cr 91 Iso 68 N 20 g

39p, $n = 10$, $X^- = \text{PF}_6^-$: Cr 120 Iso 40 N 21 g

39r, $n = 10$, $X^- = \text{OTf}^-$: Cr 72 Iso 44 N 10 g

39s, $n = 10$, $X^- = \text{SCN}^-$: Cr 95 Iso 82 N 40 Cr

The nematic phase was identified by using the combination of the three techniques: POM, DSC, and XRD, as well as, miscibility studies with 5 CB and doping with a chiral compound. A

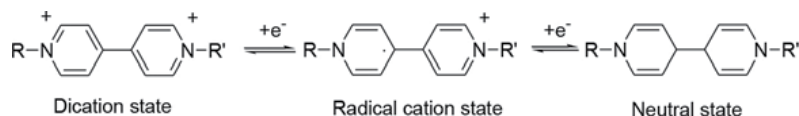
marbled texture or thread-like texture could be seen by POM, which flashed brightly under pressure, while several samples also exhibited regions with not well developed Schlieren texture. Previous examples of pyridinium ILC showing a Schlieren texture were assigned to a SmC phase [39]. For this reason, additional XRD studies were undertaken to rule out the possibility of misinterpretation of experimental data. Indeed, the diffractograms showed no sharp peaks in the low-angle region, but just a broad signal centered at 4.5 Å assigned to the average intermolecular separation, close to the typical value for liquid crystalline phases, confirming the nematic phase nature. Additional confirmation came from miscibility studies with common nematic LC, a mixture of **39i** 40% wt. and 5 CB displayed the N-Iso transition at 54°C. Furthermore, doping **39i** with a chiral dopant, a typical fingerprint texture could be seen by POM, a good indication of nematic phase. It has been shown that the temperature range of the liquid crystalline phase is greatly influenced by the spacer length and the nature of counterion employed. In fact, the very bulky PF₆⁻ and OTf⁻ anions have a great contribution to the destabilization of nematic phase.

The NMR data are strongly dependent on the anion-cation interaction specific to ILC, and they can be related to the presence of hydrogen-bonding interactions that cause downfield chemical shift of the related H atoms for imidazolium- and pyridinium-based ILC. Stronger interactions with anions lead to further downfield chemical shifts, in particular for C-H adjacent to nitrogen atom. The chemical shifts of these protons, from the ¹H NMR spectra of pyridinium salts **39a-s**, were found to follow the order: Br⁻ > SCN⁻ ~ NO₃⁻ > OTf⁻ > BF₄⁻ > PF₆⁻.

3. Dicationic bis(pyridinium) and polycationic pyridinium salts

3.1. 4,4'-Bipyridinium-based ionic liquid crystals

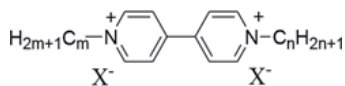
The 4,4'-bipyridinium salts or viologens are a special class of materials that show interesting properties, such as electrochromism and electrical conductivity, which were successfully employed in producing liquid crystalline materials. The reports dealing with liquid crystals based on 4,4'-bipyridinium salts significantly grew after 2000. It is important to mention that such materials can be part of a two steps reduction process, and this process is reversible, as depicted below.



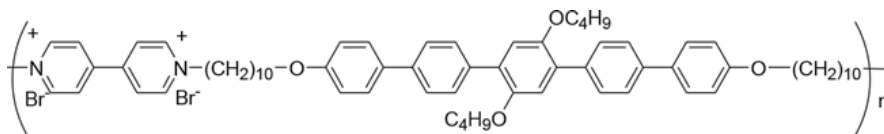
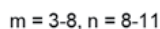
Additionally, it is of interest to note here that many dicationic and tetracationic ILC based on the 4,4'-bipyridinium rigid core (viologen-based ILC) have been investigated so far, displaying mesomorphic properties typically of calamitic and discotic materials [55–59].

The mesogenic properties of compounds based on asymmetric viologen salts of bis(trifluoromethanesulfonyl)amide ([NTf₂]⁻) **40** were influenced by their symmetry. It was found that the strongly asymmetric system does not display mesomorphic behavior, having low melting points (below 40°C). The less asymmetric products exhibit a smectic phase (SmB) with a wide

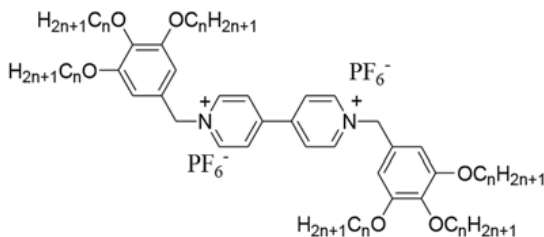
range of stability, from about 0°C up to above 140°C. More structural changes on these 4,4'-bipyridinium systems, in general, give rise to more ordered smectic phases. 4,4'-bipyridine group can also be employed to prepare polymeric liquid crystals **41**, and one example bearing a pentaphenylene connecting group via flexible chain length is presented below [60]. This polymeric ionic liquid crystal shows single layer smectic-type mesophases, both tilted (SmC) and orthogonal (SmA) phases.



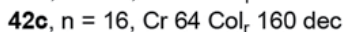
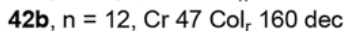
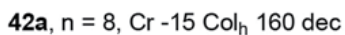
40



41



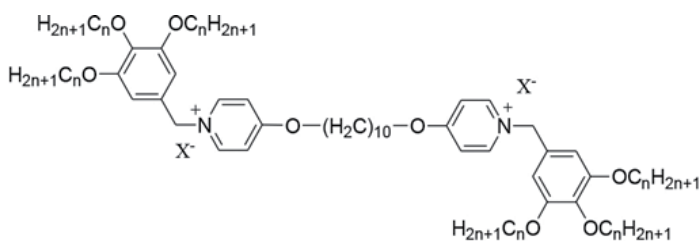
42



Columnar phases could be obtained for liquid crystals bearing two 3,4,5-tris(alkoxy) benzyl units attached to the 4,4'-bipyridinium moiety [61]. The viologen product bearing six octyloxy chains shows a hexagonal columnar (Col_h) phase, while the analogues with longer alkoxy chains (12 or 16) show rectangular columnar (Col_r) phases. For these products, the clearing temperatures could not be measured due to thermal degradation before reaching the isotropic state. Different molecular packing (Col_h or Col_r) was explained by formation of more elliptical molecular structures for compounds with elongated terminal alkoxy chains that may prefer to form the Col_r phases.

3.2. Dicationic bis(pyridinium) salts with flexible linker

Bis(pyridinium) salts with flexible spacers **43** derived from 4-hydroxypyridine containing mesogenic 3,4,5-tris(alkoxy)benzyl moieties (alkyl = dodecyl or tetradecyl) on each side and various counterions, such as bromide (Br^-), hexafluorophosphate (PF_6^-), tetrafluoroborate (BF_4^-), and triflate (OTf^-), were reported recently [62]. While there are numerous examples of dicationic pyridinium ILC, this one represents the first example of this type. These dicationic pyridinium salts display an enantiotropic liquid crystalline behavior with a hexagonal columnar (Col_h) phase assigned on the basis of their characteristic texture, pseudo-focal conic and spherulitic textures, when observed by POM and XRD studies. The temperature range of the hexagonal columnar phase is greatly influenced by the terminal chain length (12 or 14) and the nature of counterion employed. For example, the triflate salt with 12 carbon atoms in the terminal chains, **43d**, has the lowest melting point, 15°C , below ambient temperature and does not show any mesogenic behavior. It was found that the thermal behavior resembles the general trend found for pyridinium ILC, where transition temperatures show a decreasing tendency with an increase in the size of anions. Furthermore, the compounds with higher number of carbon atoms have higher melting points and isotropization temperatures with broader mesophase ranges (31°C for **43a** and 40°C for **43e**).



43

$n = 12, 14$

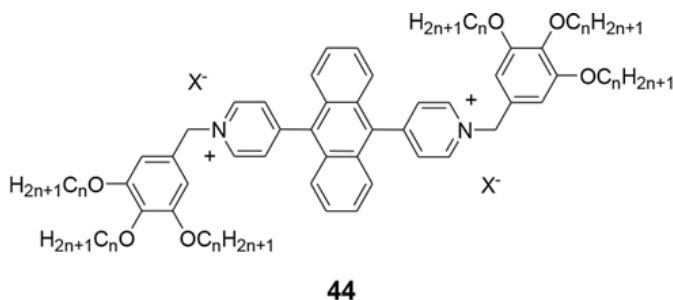
$X^- = \text{Br}^-, \text{PF}_6^-, \text{BF}_4^-, \text{OTf}^-$

- | | |
|--|--|
| 43a , $n = 12$, $X^- = \text{Br}^-$: Cr 21 Cr' 39 Col_h 70 Iso | 43e , $n = 14$, $X^- = \text{Br}^-$: Cr 39 Col_h 79 Iso |
| 43b , $n = 12$, $X^- = \text{PF}_6^-$: g 8 Col_h 87 Iso | 43f , $n = 14$, $X^- = \text{PF}_6^-$: Cr 34 Col_h 100 Iso |
| 43c , $n = 12$, $X^- = \text{BF}_4^-$: Cr 14 Col_h 84 Iso | 43g , $n = 14$, $X^- = \text{BF}_4^-$: Cr 37 Col_h 77 Iso |
| 43d , $n = 12$, $X^- = \text{OTf}^-$: Cr 15 Iso | 43h , $n = 14$, $X^- = \text{OTf}^-$: Cr 36 Col_h 47 Iso |

The study of emission properties of these luminescent bis(pyridinium) salts revealed a weak emission in dichloromethane solutions at room temperature, with quantum yields up to 4.4%. Their solid-state emission is significantly red shifted by comparison to solution emission spectra recorded in dichloromethane, suggesting a more complex emission mechanism, probably an aggregate-type emission in solid state [62].

3.3. Dicationic bis(pyridinium) salts with a rigid core

Dicationic pyridinium salts with an anthracene moiety connecting two pyridine rings substitution with tris(alkoxy)benzyl groups **44** were designed and investigated for their liquid crystalline properties and stimulus responsive luminescence [63].



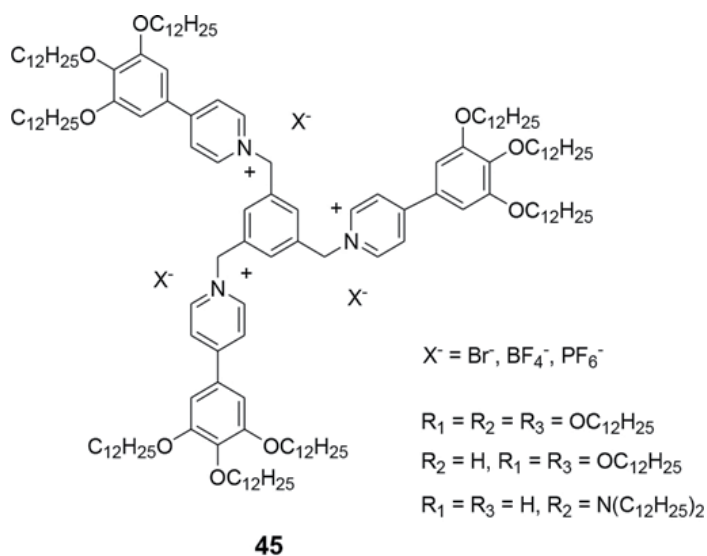
$n = 8, 12$
 $X^- = Br^-, BF_4^-, PF_6^-$

44a, $n = 8$, $X^- = Br^-$: Cr 197 Col_r 228 dec **44d**, $n = 12$, $X^- = Br^-$: Cr 203 Col_r 235 dec
44b, $n = 8$, $X^- = PF_6^-$: Cr 216 Iso 151 Col_r **44e**, $n = 12$, $X^- = PF_6^-$: Cr 220 Iso 148 Col_r
44c, $n = 8$, $X^- = BF_4^-$: Cr 181 Col_r 218 dec **44f**, $n = 12$, $X^- = BF_4^-$: Cr 185 Col_r 205 dec

The anthracene moiety act as a fluorophore in the center of molecules, and the solvate of pyridinium salts **44**, $n = 1$, show piezoluminescence by grinding. The anion has an influence on the LC phase stability and thus, the long alkyl chain derivatives **44a-f** show either enantiotropic (for bromide and tetrafluoroborate salts) or monotropic (in the case of hexafluorophosphate salts) rectangular columnar phases.

3.4. Tripodal pyridinium ILC

Photoluminescent tripodal pyridinium-based ionic liquid crystals were reported by Kato et al. [64, 65]. These tricationic pyridinium salts show thermotropic hexagonal or rectangular columnar phases or cubic phases with a large temperature ranges. The columnar or cubic phase stability is given by the difference in the anion size. For small-size anions (bromide), the cationic pyridinium cores should be packed more closely through electrostatic interactions and hence, the molecules prefer to self-assemble in cubic structures at higher temperatures (**45a**). Upon photoirradiation with UV light, these pyridinium salts emit blue-green or green light with photoluminescence quantum yields rather low, 3–6% in solution [65].



45a, $X^- = \text{Br}^-$: Cr 77 Col_h 179 Cub 245 Iso

45b, $X^- = \text{BF}_4^-$: Cr -3 Col_h 160 Iso

45c, $X^- = \text{PF}_6^-$: Cr 13 Cr' 24 Col_r 245 Iso

Acknowledgements

This work was supported by a grant of the Romanian Authority for Scientific Research, CNCS-UEFISCDI, and project number PN-II-ID-PCE-2011-3-0384.

Author details

Viorel Cîrcu

Address all correspondence to: viorel.circu@chimie.unibuc.ro

Inorganic Chemistry Department, University of Bucharest, Bucharest, Romania

References

- [1] K. V. Axenov, S. Laschat, Thermotropic ionic liquid crystals, *Materials*, 2011, 4, 206–259. DOI: 10.3390/ma4010206
- [2] K. Binnemans, Ionic liquid crystals, *Chem. Rev.*, 2005, 105, 4148–4204. DOI: 10.1021/cr0400919

- [3] K. Goossens, K. Lava, C. W. Bielawski, K. Binnemans, *Chem. Rev.*, 2016, 116, 4643–4807. DOI: 10.1021/cr400334b
- [4] E. J. R. Sudholter, J. B. F. N. Engberts, W. H. de Jeu, Thermotropic liquid-crystalline behavior of some single- and double-chained pyridinium amphiphiles, *J. Phys. Chem.*, 1982, 86, 1908–1913. DOI: 10.1021/j100207a035
- [5] J.-T. Lu, C.-K. Lee, I. J. B. Lin, Ionic liquid crystals derived from 4-hydroxypyridine, *Soft Matter*, 2011, 7, 3491–3501. DOI: 10.1039/c0sm01376e
- [6] X. Yang, S. Tan, T. Liang, B. Wei, Y. Wu, Synthesis, characterization, and electrochemical properties of smectic pyridinium salts with inorganic dihydrogen phosphate ions, *Ionics*, 2016, 22, 85–92. DOI: 10.1007/s11581-015-1524-x
- [7] X. Zhu, B. Tartsch, U. Beginn, M. Müller, Wedge-shaped molecules with a sulfonate group at the tip—a new class of self-assembling amphiphiles, *Chem. Eur. J.*, 2004, 10, 3871–3878. DOI: 10.1002/chem.200400050
- [8] U. Beginn, L. Yan, S. N. Chvalun, M. A. Shcherbina, A. Bakirov, M. Möller, Thermotropic columnar mesophases of wedge-shaped benzenesulfonic acid mesogens, *Liq. Cryst.*, 2008, 35, 1073–1093. DOI: 10.1080/02678290802376107
- [9] M. J. Mayoral, P. Ovejero, J. A. Campo, J. V. Heras, E. Pinilla, M. R. Torres, M. Cano, Ionic liquid crystals from β -diketonyl containing pyridinium cations and tetrachlorozincate anions, *Inorg. Chem. Commun.*, 2009, 12, 214–218. DOI: 10.1016/j.inoche.2008.12.016
- [10] M. J. Mayoral, P. Ovejero, J. A. Campo, J. V. Heras, E. Oliveira, B. Pedras, C. Lodeiro, M. Cano, Exploring photophysical properties of new boron and palladium(II) complexes with β -diketone pyridine type ligands: from liquid crystals to metal fluorescence probes, *J. Mater. Chem.*, 2011, 21, 1255–1263. DOI: 10.1039/c0jm02698k
- [11] M. J. Mayoral, P. Cornago, R. M. Claramunt, M. Cano, Pyridyl and pyridiniumyl β -diketones as building blocks for palladium(II) and allyl-palladium(II) isomers. Multinuclear NMR structural elucidation and liquid crystal behaviour, *New J. Chem.*, 2011, 35, 1020–1030. DOI: 10.1039/c0nj00938e
- [12] C. G. Bazuin, D. Guillon, A. Skoulios, J.-F. Nicoud, The thermotropic mesophase structure of two long-chain alkyl pyridinium halides, *Liq. Cryst.*, 1986, 1, 181–188. DOI: 10.1080/02678298608086504
- [13] J. J. H. Nusselder, J. B. F. N. Engberts, H. A. Van Doren, Liquid crystalline and thermochromic behaviour of 4-substituted 1-methylpyridinium iodide surfactants, *Liq. Cryst.*, 1993, 13, 213–225. DOI: 10.1080/02678299308026295
- [14] C. J. Bowlas, D. W. Bruce, K. R. Seddon, Liquid-crystalline ionic liquids, *Chem. Commun.*, 1996, 1625–1626. DOI: 10.1039/CC9960001625
- [15] S. Ujiie, A. Mori, Cubic mesophase formed by thermotropic liquid crystalline ionic systems-effects of polymeric counter ion, *Mol. Cryst. Liq. Cryst.*, 2005, 437, 1269–1275.

- [16] C. Cruz, B. Heinrich, A. C. Ribeiro, D. W. Bruce, D. Guillon, Structural study of smectic A phases in homologous series of N-alkylpyridinium alkylsulphates, *Liq. Cryst.*, 2000, 27, 1625–1631. DOI: 10.1080/026782900750037185
- [17] D. W. Bruce, S. Estdale, D. Guillon, B. Heinrich, Mesomorphic N-alkylpyridinium dodecylsulphates, *Liq. Cryst.*, 1995, 19, 301–305. DOI: 10.1080/02678299508031983
- [18] F. Neve, O. Francescangeli, A. Crispini, J. Charmant, $A_2[MX_4]$ Copper(II) pyridinium salts. From ionic liquids to layered solids to liquid crystals, *Chem. Mater.*, 2001, 13, 2032–2041. DOI: 10.1021/cm000804d
- [19] T. Mihelj, V. Tomašić, Thermal behavior of dodecylpyridinium-based surfactant salts with varied anionic constituent, *J. Dispers. Sci. Technol.*, 2014, 35(4), 581–592. DOI: 10.1080/01932691.2013.811683
- [20] G. Kohnen, M. Tosoni, S. Tussetschläger, A. Baro, S. Laschat, Counterion Effects on the mesomorphic properties of chiral imidazolium and pyridinium ionic liquid, *Eur. J. Org. Chem.*, 2009, 5601–5609. DOI: 10.1002/ejoc.200900730
- [21] M. Tosoni, S. Laschat, A. Baro synthesis of novel chiral ionic liquids and their phase behavior in mixtures with smectic and nematic liquid crystals, *Helv. Chim. Acta*, 2004, 87, 2742–2749. DOI: 10.1002/hlca.200490247
- [22] M. Tabrizian, A. Soldera, M. Couturier, C. G. Bazuin, Pyridinium salt liquid crystals effect of mesogen extension and alkyl chain length, *Liq. Cryst.*, 1995, 18, 475–482. DOI: 10.1080/02678299508036647
- [23] D. Ster, U. Baumeister, J. Chao, C. Tschierske, G. Israel, Synthesis and mesophase behaviour of ionic liquid crystals. *J. Mater. Chem.*, 2007, 17, 3393–3400. DOI: 10.1039/b705519f
- [24] C. M. Gordon, J. D. Holbrey, A. R. Kennedy, K. R. Seddon, Ionic liquid crystals: hexafluorophosphate salts, *J. Mater. Chem.*, 1998, 8, 2627–2636. DOI: 10.1039/A806169F
- [25] Y. Haramoto, S. Ujiie, M. Nanasawa, New pyridinium type ionic liquid crystal compounds with a 1,3-dioxane ring in the principal structure, *Liq. Cryst.*, 1996, 21, 923–925. DOI: 10.1080/02678299608032911
- [26] J. Baudoux, P. Judeinstein, D. Caharda, J.-C. Plaquevent, Design and synthesis of novel ionic liquid/liquid crystals (IL2Cs) with axial chirality, *Tetrahedron Lett.*, 2005, 46, 1137–1140. DOI: 10.1016/j.tetlet.2004.12.097
- [27] Y. Z. Yousif, A. A. Othman, W. A. Al-masoudi, P. R. Alapati, Some novel cholesteric liquid crystals, *Liq. Cryst.*, 1992, 12, 363–368. DOI: 10.1080/02678299208031053
- [28] J. Tao, J. Zhong, P. Liu, S. Daniels, Z. Zeng, Pyridinium-based ionic liquid crystals with terminal fluorinated pyrrolidine, *J. Fluor. Chem.*, 2012, 144, 73–78. DOI: 10.1016/j.jfluchem.2012.07.009
- [29] N. G. Filippi, D. Zambelli Mezalira, S. Ovalle, E. Westphal, Study of the mesomorphic behaviour through the structure modification of azo and acetylene pyridinium and imidazolium-based ionic liquid crystals, *Liq. Cryst.*, 2016. DOI: 10.1080/02678292.2016.1199817

- [30] Y. Kosaka, T. Kato, T. Uryu, Thermotropic liquid crystalline ionic stilbazoles and their miscible mixtures with non-ionic carbazoyl compounds, *Liq. Cryst.*, 1995, 18, 693–698. DOI: 10.1080/02678299508036678
- [31] K. Binnemans, C. Bex, R. Van Deun, Ionic liquid crystals with hemicyanine chromophores, *J. Incl. Phenom. Macrocycl. Chem.*, 1999, 35, 63. DOI: 10.1023/A:1008146431142
- [32] D. Haristoy, D. Tsiourvas, Novel ionic liquid-crystalline compounds bearing oxadiazole and pyridinium moieties as prospective materials for optoelectronic applications, *Chem. Mater.*, 2003, 15, 2079–2083. DOI: 10.1021/cm021365g
- [33] D. Haristoy, D. Tsiourvas, Effect of counterions on the thermotropic and thermochromic properties of ionic liquid crystals, *Liq. Cryst.*, 2004, 31, 697–703. DOI: 10.1080/02678290410001675110
- [34] E. Westphal, D. Henrique da Silva, F. Molin, H. Gallardo, Pyridinium and imidazolium 1,3,4-oxadiazole ionic liquid crystals: a thermal and photophysical systematic investigation, *RSC Adv.*, 2013, 3, 6442–6454. DOI: 10.1039/C3RA23456H
- [35] J. A. Pedro, J. R. Mora, E. Westphal, H. Gallardo, H. D. Fiedler, F. Nome, Photophysical study and theoretical calculations of an ionic liquid crystal bearing oxadiazole, *J. Mol. Struct.*, 2012, 1016, 76–81. DOI: 10.1016/j.molstruc.2012.02.046
- [36] F. Lo Celso, I. Pibiri, A. Triolo, R. Triolo, A. Pace, S. Buscemib, N. Vivona, Study on the thermotropic properties of highly fluorinated 1,2,4-oxadiazolylpyridinium salts and their perspective applications as ionic liquid crystals, *J. Mater. Chem.*, 2007, 17, 1201–1208. DOI: 10.1039/b615190f
- [37] A. Pana, F. L. Badea, M. Ilis, T. Staicu, M. Micutz, I. Pasuk, V. Cîrcu, Effect of counterion on the mesomorphic behavior and optical properties of columnar pyridinium ionic liquid crystals derived from 4-hydroxypyridine, *J. Mol. Struct.*, 2015, 1083, 245–251. DOI: 10.1016/j.molstruc.2014.11.059
- [38] S. Kumar, S. K. Pal, Ionic discotic liquid crystals: synthesis and characterization of pyridinium bromides containing a triphenylene core, *Tetrahedron Lett.*, 2005, 46, 4127–4130. DOI: 10.1016/j.tetlet.2005.03.201
- [39] L. Cui, V. Sapagovas, G. Lattermann, Synthesis and thermal behaviour of liquid crystalline pyridinium bromides containing a biphenyl core, *Liq. Cryst.*, 2002, 29, 1121–1132. DOI: 10.1080/02678290210155589
- [40] R. G. Santos-Martell, A. Cenicerros-Olguín, L. Larios-López, R. J. Rodríguez-González, D. Navarro-Rodríguez, B. Donnio, D. Guillon, Synthesis and thermotropic liquid-crystalline properties of N-alkylpyridinium bromides substituted with a terphenylene moiety, *Liq. Cryst.*, 2009, 36, 787–797. DOI: 10.1080/02678290903060618
- [41] M. R. Imam, M. Peterca, U. Edlund, V. S. K. Balagurusamy, V. Percec, Dendronized supramolecular polymers self-assembled from dendritic ionic liquids, *J. Polym. Sci.: Part A: Polym. Chem.*, 2009, 47, 4165–4193. DOI: 10.1002/pola.23523

- [42] A. Pană, I. Pasuk, M. Micutz, V. Cîrcu, Nematic ionic liquid crystals based on pyridinium salts derived from 4-hydroxypyridine, *CrystEngComm.*, 2016, 18, 5066–5069. DOI: 10.1039/C6CE00618C
- [43] W. Li, J. Zhang, B. Li, M. Zhang, L. Wu, Branched quaternary ammonium amphiphiles: nematic ionic liquid crystals near room temperature, *Chem. Commun.*, 2009, 5269–5271. DOI: 10.1039/B909605A
- [44] L. Lu, N. Sharma, G.A.N. Gowda, C.L. Khetrapal, R.G. Weiss, Enantiotropic nematic phases of quaternary ammonium halide salts based on trioctadecylamine, *Liq. Cryst.*, 1997, 22, 23–28. DOI: 10.1080/026782997209630
- [45] K. Goossens, P. Nockemann, K. Driesen, B. Goderis, C. Görller-Walrand, K. Van Hecke, L. Van Meervelt, E. Pouzet, K. Binnemans, T. Cardinaels, Imidazolium ionic liquid crystals with pendant mesogenic groups, *Chem. Mater.*, 2008, 20, 157–168. DOI: 10.1021/cm702321c
- [46] A. Pană, M. Ilis, M. Micutz, F. Dumitrascu, I. Pasuk, V. Cîrcu, Liquid crystals based on silver carbene complexes derived from dimeric bis(imidazolium) bromide salts, *RSC Adv.*, 2014, 4, 59491–59497. DOI: 10.1039/C4RA11023D
- [47] S. Ahn, S. Yamakawa, K. Akagi, Liquid crystallinity-embodied imidazolium-based ionic liquids and their chiral mesophases induced by axially chiral tetra-substituted binaphthyl derivatives, *J. Mater. Chem. C*, 2015, 3, 3960–3970. DOI: 10.1039/C4TC02968B
- [48] X. H. Cheng, X. Q. Bai, S. Jing, H. Ebert, M. Prehm, Self-assembly of imidazolium-based rodlike ionic liquid crystals: transition from lamellar to micellar organization, *Chem. Eur. J.*, 2010, 16, 4588–4601. DOI: 10.1002/chem.200903210
- [49] X. Liu, J. L. Liu, B. Cai, X. M. Ren, A charge transfer salt consisted of bis(maleonitriledithiolato)zincate dianion and 1,1'-didecyl-4,4'-bipyridinium exhibiting uncommon nematic mesophase behavior, *Inorg. Chem. Commun.*, 2011, 14, 1428–1431. DOI: 10.1016/j.inoche.2011.05.038
- [50] M. Ghedini, D. Pucci, Cyclopalladation of 5-(1-hexyl)-2[[4'-(1-undecyloxy)phenyl]]-pyrimidine. Synthesis and characterization of mononuclear complexes, *J. Organomet. Chem.*, 1990, 395, 105–112. DOI: 10.1016/0022-328X(90)85265-Z
- [51] A. Liebmann, C. Mertesdorf, T. Plesnivý, H. Ringsdorf, J. H. Wendorff, Complexation of transition metal ions with substituted aza macrocycles: induction of columnar mesophases by molecular recognition, *Angew. Chem. Int. Ed. Engl.*, 1991, 30, 1375–1377. DOI: 10.1002/anie.199113751
- [52] J. W. Goodby, G. H. Mehl, I. M. Saez, R. P. Tuffin, G. Mackenzie, R. Auzely-Velty, T. Benvegnu, D. Plusquellec, Liquid crystals with restricted molecular topologies: supermolecules and supramolecular assemblies, *Chem. Commun.*, 1998, 2057–2070. DOI: 10.1039/A802762E
- [53] B. Ringstrand, A. Jankowiak, L. E. Johnson, P. Kaszynski, D. Pocięcha, E. Gorecka, Anion-driven mesogenicity: a comparative study of ionic liquid crystals based on the [closo-1-

- CB₉H₁₀]⁻ and [closo-1-CB₁₁H₁₂]⁻ clusters, *J. Mater. Chem.*, 2012, 22, 4874–4880. DOI: 10.1039/C2JM15448J
- [54] A. Jankowiak, J. Kanazawa, P. Kaszynski, R. Takita, M. Uchiyama, [closo-1-CB₁₁H₁₁-1-Ph]⁻ as a structural element for ionic liquid crystals, *J. Organomet. Chem.*, 2013, 747, 195–200. DOI: 10.1016/j.jorganchem.2013.05.034
- [55] V. Causin, G. Saielli, Effect of asymmetric substitution on the mesomorphic behaviour of low-melting viologen salts of bis(trifluoromethanesulfonyl)amide. *J. Mater. Chem.* 2009, 19, 9153–9162. DOI: 10.1039/b915559g
- [56] V. Causin, G. Saielli, Effect of a structural modification of the bipyridinium core on the phase behaviour of viologen-based bistriflimide salts. *J. Mol. Liq.* 2009, 145, 41–47. DOI: 10.1016/j.molliq.2008.11.013
- [57] G. Casella, V. Causin, F. Rastrelli, G. Saielli, Viologen-based ionic liquid crystals: induction of a smectic A phase by dimerisation, *Phys. Chem. Chem. Phys.*, 2014, 16, 5048–5051. DOI: 10.1039/C3CP54628D
- [58] M. Bonchio, M. Carraro, G. Casella, V. Causin, F. Rastrelli, G. Saielli, Thermal behaviour and electrochemical properties of bis(trifluoromethanesulfonyl)amide and dodecatungstosilicate viologen dimers, *Phys. Chem. Chem. Phys.*, 2012, 14, 2710–2717. DOI: 10.1039/C2CP23580C
- [59] G. Casella, V. Causin, F. Rastrelli, G. Saielli, Ionic liquid crystals based on viologen dimers: tuning the mesomorphism by varying the conformational freedom of the ionic layer, *Liq. Cryst.*, 2016, 43, 1161–1173. DOI: 10.1080/02678292.2016.1161852
- [60] J. C. Díaz-Cuadros, L. Larios-López, R. J. Rodríguez-González, B. Donnio, D. Guillon, D. Navarro-Rodríguez, Ionic liquid crystals bearing bipyridinium and pentaphenylene groups, *J. Mol. Liq.*, 2010, 157, 133–141. DOI: 10.1016/j.molliq.2010.09.002
- [61] K. Tanabe, T. Yasuda, M. Yoshio, T. Kato, Viologen-based redox-active ionic liquid crystals forming columnar phases, *Org. Lett.*, 2007, 9(21), 4271–4274. DOI: 10.1021/ol701741e.
- [62] A. Pană, M. Iliş, T. Staicu, I. Pasuk, V. Cîrcu, Columnar bis(pyridinium) ionic liquid crystals derived from 4-hydroxypyridine: synthesis, mesomorphism and emission properties. *Liq. Cryst.*, 2016, 43, 381–392. DOI: 10.1080/02678292.2015.1116630
- [63] S. Kohmoto, T. Chuko, S. Hisamatsu, Y. Okuda, H. Masu, M. Takahashi, K. Kishikawa, Piezoluminescence and liquid crystallinity of 4,4'-(9,10-anthracenediyl)bipyridinium salts crystal. *Growth Des.*, 2015, 15 (6), 2723–2731. DOI: 10.1021/acs.cgd.5b00028
- [64] K. Tanabe, Y. Suzui, M. Hasegawa, T. Kato, Full-color tunable photoluminescent ionic liquid crystals based on tripodal pyridinium, pyrimidinium, and quinolinium salts, *J. Am. Chem. Soc.* 2012, 134, 5652–5661. DOI: 10.1021/ja3001979
- [65] K. Tanabe, T. Yasuda, T. Kato, Luminescent ionic liquid crystals based on tripodal pyridinium salts, *Chem. Lett.*, 2008, 37, 1208–1209. DOI: 10.1246/cl.2008.1208

Ionic Liquids/Ionic Liquid Crystals for Safe and Sustainable Energy Storage Systems

Sudha J. Devaki and Renjith Sasi

Additional information is available at the end of the chapter

<http://dx.doi.org/10.5772/65888>

Abstract

Ionic liquid crystals are organic salts having synergistic properties of ionic liquids and liquid crystalline materials endowed with non-covalently bound delocalised ion pairs of large organic cations and anions. They can undergo stimulus-responsive anisotropic phase change, followed by enhancement in ionic diffusion and conductivity, which makes them ideal candidates as electrolyte in energy storage systems. Our goal in this chapter is to survey the key developments in the field of ionic liquid crystalline electrolytes and to generate curiosity in the wider research community in tackling challenges in the electrolyte materials for sustainable energy related devices, such as supercapacitors, Li batteries, fuel cells and dye-sensitized solar cells (DSSCs).

Keywords: ionic liquids, ionic liquid crystals, energy storage, supercapacitors, batteries

1. Introduction

Research and development, in the arena of sustainable energy, is receiving overwhelming interest due to the rapid proliferation of portable nano-electronic devices and also evolution in lifestyle. Due to the depletion of petroleum-based energy resources, researchers are turning towards the energy production from wind, solar, tidal, hydro and geothermal energy sources. But these resources are intermittent with time and season. Safe, sustainable and clean strategies for energy storage, such as supercapacitors, batteries, fuel cells, etc. have been explored tremendously in recent years to store energy in a sustainable way. Electrodes and electrolytes are the main components present in the energy storage devices. Electrolytes are the materials through which the transport of ions takes place from anode to cathode and vice versa, during charge-discharge processes. Transport and diffusion of ions through the electrolyte are largely influenced by various material parameters, such as viscosity, porosity and ionic conductivity

of the electrolytes. Among the presently used liquid electrolytes, ionic liquids (ILs) are delivering excellent performance due to their high ionic conductivity, wide electrochemical stability window, good thermal stability, wide liquidity range, non-volatility and non-toxicity. Being composed of ion pairs bound by non-covalent interactions, they are bestowed with innumerable fascinating properties suitable for various applications [1, 2]. Generally, ionic liquids contain the cationic centres, such as nitrogen, oxygen, sulphur, phosphorous atoms and counter anions, such as halides, hexafluorophosphate (PF_6^-), tetrafluoroborate (BF_4^-), bis-triflimide [$(\text{CF}_3\text{SO}_2)_2\text{N}^-$], etc. as shown in **Figure 1** [3–10].

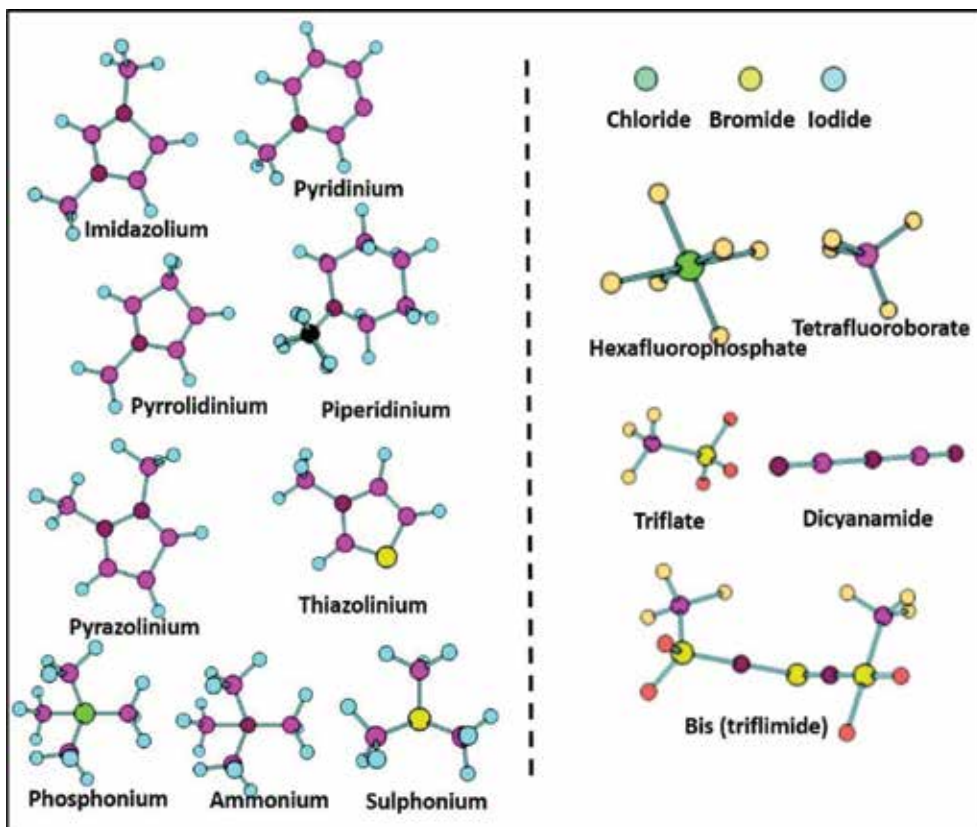


Figure 1. Common cations and anions of ionic liquids.

The structural design of ionic liquids is playing a very important role as it is decisive for controlling the temperature limits, self-assembly and associate functional properties. Self-assembly processes are mainly controlled by the type of cations, anions and side-chains. In ILs, only delocalised charge centres are present which makes the intra-molecular interactions less intense to gift them their exquisite properties. The organic cations and anions of ILs are often stabilised by resonance with highly delocalised charges. Ions with lower symmetry or without symmetry are another major feature of ILs, which restricts the molecular packing into a low-energy crystal structure, ultimately lowering the melting point [11, 12]. Their physical and functional properties could be well tuned, since they are capable for infinite number of

structural variation by changing cations, anions and the substituents [13–17]. They exhibit high degree of miscibility with a wide array of organic and inorganic materials, since they contain both organic cations and inorganic anions or vice versa. ILs is found to have higher affinity towards CO₂ and water vapour. This could be explored in devising gas separators for removing moisture or poisonous gases from the mixtures and also helping in CO₂ sequestration and reducing the greenhouse effect [18–22]. The main criteria for exploiting a compound as an electrolyte for electrochemical energy storage systems are high ionic conductivity, non-volatility, non-flammability, high thermal stability and good electrochemical window. Electrochemical window can be defined as the limiting potential range, in which, the electrolyte is electrochemically stable and is free from any unwanted redox reactions. As the electrochemical window of electrolyte is directly related to the energy density, high EC window is necessary for electrolytes for energy storage systems. In comparison with the commercially used electrolytes, ILs has greater ionic conductivities and better potential windows to draw superior energy storage performances. Unlike aqueous electrolytes with limited potential window less than 1 V, IL-based electrolytes have very high window of 3–4 V, very high ionic conductivity, very good liquidity range and thermal stability for efficient energy storage applications, such as electrochemical supercapacitors, Li-ion batteries, Na- or Mg-batteries, Fuel cells, etc. [23].

Compared to ILs, ionic liquid crystals (ILCs) are receiving importance in flexible electronics as safe and efficient electrolytes. They exhibit synergistic properties of both ionic liquids and liquid crystals. Just like ILs, ILCs are also solely composed of ions bound with ionic interactions in different extents. Liquid crystals are often regarded as the fourth state of matter, with ordering in-between highly rigid crystalline lattices and disordered liquid state. Mesophase formed between solid and liquid phases exhibit impressive properties due to positional order and flow properties. Rotating isotropic spherical molecules are responsible for the plastic crystal formation, whereas, the non-covalent interactions are behind the anisotropic behaviour of liquid crystals. Ionic interactions are often responsible for strong crystalline ordering, whereas, other non-covalent interactions like hydrogen bonding, van der Waals forces and layer-by-layer self-assembly are responsible for liquid crystalline mesophase formation. In addition to the cationic and anionic centres, long alkyl side-chains and functional groups are present in ILCs for modulating the mesophase self-assembly. They are the real smart materials for realising multi-functional applications, such as stimuli-responsive conductors for energy storage devices, electrochromic supercapacitors, flexible batteries, etc. Stimuli-responsive phase transition of ILCs enables to modulate the direction of ionic conduction in them as shown in **Figure 2**. Based on the order and texture of mesogens, mesophases exhibited by ILCs are mainly of two types: nematic phase and smectic phase [24]. Mesogenic molecules tend to align along the molecular axis in the nematic phase (1D ordered). Smectic phase is more ordered where the molecules are arranged in layers (2-dimensionally ordered). Based on the extent of ordering of mesogens within the layers, smectic phase is subdivided into Sm A, Sm B, Sm C, Sm D, Sm F, Sm G, etc. Sm A is the least ordered one, among all the smectic mesophases [25–28]. Tschierske defined the LC state as a condensed matter state, in which, there is orientational and/or positional long-range order in at least one direction and no fixed position for individual molecules [25]. Columnar and cubic phases are other major mesophases observed in ionic liquid crystals. Based on the lattice in which columns are arranged, columnar phase is divided into hexagonal columnar (Col_h), rectangular (Col_r) and oblique

columnar (Col_h) phases [29, 30]. Molecules with bent-core or banana shape displayed unique mesophases different from the normal mesophases [30–34].

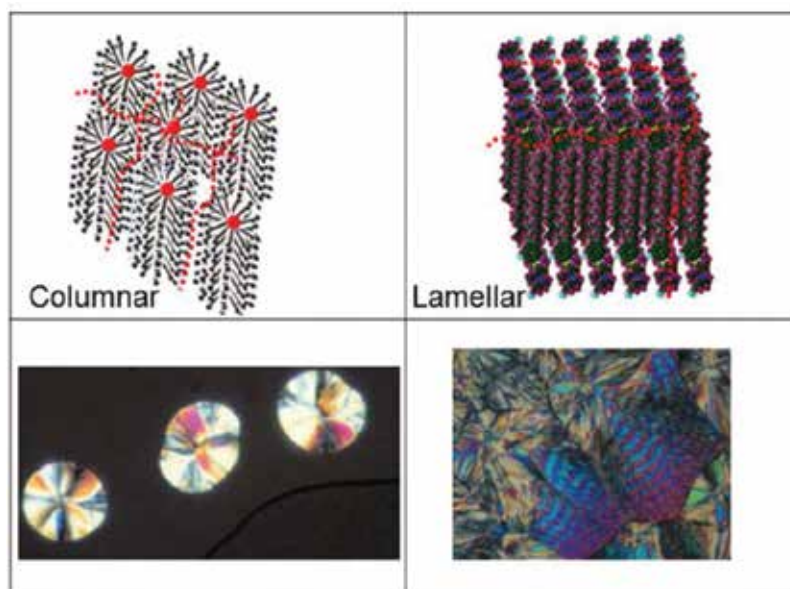


Figure 2. Conducting channels generated by the controlled self-assembly of ILCs. Columnar and lamellar phases with their polarised light microscopic (PLM) images.

Generally, for such mesophases, functional properties like refractive index, dielectric permittivity, magnetic susceptibility, conductivity, elasticity, etc. are measured to have different values in different directions (anisotropy). Since the molecular kinetic energy is high for the LC phase, it is capable to undergo self-adjustments in response to the external stimuli. For thermotropic ILCs, crystalline phase changes to mesophase on heating and then to isotropic phase on further heating. On cooling from isotropic melt, mesophase is revisited and finally crystalline phase on further cooling. If the mesophase is observed both in the heating as well as cooling ramp, such ILCs are known as enantiotropic ILCs. In some occasions, the mesophase is observed only during cooling from the isotropic phase. This type of ILCs belongs to the category of monotropic ILCs. Liquid-crystalline phase arises, due to the introduction of solvent or by varying concentration, which is regarded as lyotropic ILCs. On cooling the ionic liquid crystalline molecule from isotropic phase, the relative variation of intermolecular interactions and molecular kinetic energy leads to the formation of liquid crystalline mesophases. The alignment of charge carriers along the mesophase boundaries will produce conducting nano-channels for improving the ionic conduction [27, 28]. Mesophases exhibit characteristic birefringent textures, when examined under PLM.

LC phase in ILCs can be induced in response to thermal, concentration, potential, magnetic, light as well as mechanic stimuli. Unlike other stimuli, light could make the shift in conduction direction without making any physical contact with the mesophase, avoiding mechanical disintegration to the phase. Soberats et al. reported light-induced re-orientation of an imidazolium ionic liquid crystal effecting variation in the ionic conduction directions, transverse and longitudinal [35]. Mesophase formation of ILCs is accompanied with the formation of

nano-sized ionic channels in 1-, 2-, or 3-dimensions, due to the controlled self-assembly. These ionic channels are able to conduct charge carriers across the mesophase. The dimensions and directions of the nano-channels are controlled by the extent of self-assembly, and hence, the stimuli responsive mesophase formation can indirectly affect ionic conduction too [36, 37]. This photo-responsive ILC contains an azobenzene-core, which undergoes Cis-trans isomerisation when subjected to UV irradiation. Cis-trans isomerisation will shift the orientation of charge carriers, which are aligned in perpendicular direction to the molecular axis with concomitant mesophase transition from homogeneous to homeotropic smectic phases. Ordered charge carriers can be tuned and oriented with respect to external stimuli, which can be used as the electrolyte for various applications.

Liquid-crystalline phase formation of a quaternary ammonium ionic liquid crystal (Qs) in response to temperature or concentration by the controlled self-assembly of mesogens was studied from Sasi et al., recently [37]. Studies showed that the nature of the mesophase formed relies on the surface alignment of self-assemblies, topographical defects and molecular ordering, which are governed by various non-covalent interactions among the molecules, temperature and polarity of the solvent. Investigation of the LC phase formation, under PLM, reveals polymorphic textures including crystalline, plastic crystalline, nematic, hexagonal columnar phases, randomly oriented molecular layers as shown in **Figure 3**. In the nematic phase, molecular layers are uniaxially oriented and the plane of molecular layers may be perpendicular to the director. However, columnar layers are biaxially oriented and the molecular layers in this phase are perpendicular to the layer planes. A slight tilt in the director angle is responsible for the observation of various textures arising from the difference in the nature of defects.

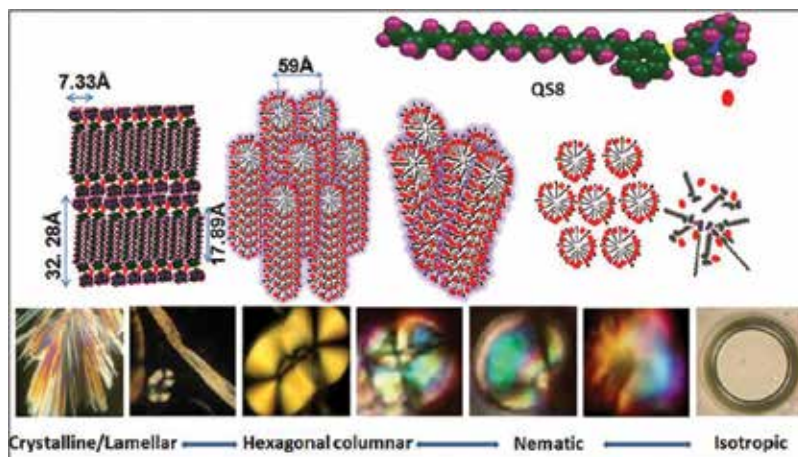


Figure 3. Mesophase formation by the self-assembly of mesogens and corresponding textural variation. Reproduced with permission from [37].

Generally, at room temperature, Qs are three -dimensionally ordered crystalline solids with highly birefringent spherulitic textures. During cooling from melt, they undergo transition to the gyroid-type of 1-dimensionally ordered nematic phase, further to hexagonal columnar phase by gaining the positional order. Further cooling may lead to the formation of lamellar and crystalline phases. Formations of conducting mesophase, in response to external stimuli, are mainly

attributed to the variation of molecular kinetic energy and the extent of intermolecular interactions. In the crystalline phase, molecules are tightly-packed together by means of very strong intermolecular interactions and consequently, they will exhibit the least amount of molecular kinetic energy. On the contrary, isotropic liquid is characterised by lower intermolecular interactions and very high molecular kinetic energy. Crystalline state has 3-dimensional orientational, positional and translational orders. But in the mesophase, the crystalline order is reduced and the degree of freedom of molecules gets enhanced so that a fluidic phase is resulted.

Ionic conductivity exhibited by ILCs is receiving significant importance and finding applications in electronic devices and drug delivery systems [38–46]. As the temperature increases, the 3-dimensionally ordered crystalline phase decreases and transforms into 2- or 1-dimensionally ordered LC phases, where there is more freedom for the transport of charge carriers, leading to higher conductivity. This conductivity enhancement with temperature is attributed to the thermotropic phase transitions that can be further envisaged from the temperature-dependent variation of charge diffusion coefficient (D) values. Similarly, lyotropic liquid-crystalline phase formation of the Qs is studied by means of conductivity and rheological analysis. Storage modulus increases with self-assembly and finally transformed into highly organized gel phase.

2. As electrolytes for energy storage systems

For any electrochemical energy storage systems (EESs), electrodes, electrolytes and separators are the main components [47, 48]. Electrolytes are considered as the heart of an EES, being the charge transport medium, which facilitates the ionic charge carriers for maintaining the device reactions alive. Electrolyte with good ionic conductivity and electrochemical window is necessary for exploiting maximum device performance [49]. Electrolyte plays an important role in controlling the cycle stability, rate capability, specific capacity and safety of the EESs. Choice of electrolyte is crucial in deriving the maximum output, since it could eliminate the possible parasitic side reactions effectively. Non-aqueous electrolytes have extended electrochemical windows to extract high energy and power densities. Conventional non-aqueous electrolytes used for energy systems are composed of ionic salts dissolved in volatile organic solvents. This is not at all safe, since there is a possibility of generating electric sparks when the system is charged at high rates, which can lead to the explosion of the device by burning easy flammable electrolytes. Also, the leakage of poisonous electrolytes while crimping the cell or on standing for long will also create serious environmental problems. ILs and ILCs with high ionic conductivity, high EC window and environmentally benign nature prove to be better alternates for conventional electrolytes in realising high performing energy storage devices [50]. Solid electrolytes like gel-polymer electrolytes and ionogels electrolytes, which are derived from ILs, are also found to be suitable for powering energy storage systems. Ion-conducting polymeric films can also be prepared by cross-linking the polymerizable side-chains in the self-assembled systems including liquid electrolytes, plasticisers and polymerizable mesogens. Also, ILCs with ordered ion channels were found to be extremely advantageous over conventional I/I_3^- couple, which shuttles the energy transport in dye-sensitized solar cells (DSSCs). This book chapter reviews various ILs, ILCs and their derived electrolyte systems employed for various energy storage systems and their advantages over conventional electrolytes.

2.1. Supercapacitors

Supercapacitors are widely employed as electrochemical energy storage devices as a replacement or complementary to batteries. High power density, faster charge-discharge rates, better cycle stability and service life of supercapacitors make them far superior to other energy storage systems [51]. They found to be more common in industrial and automobile applications rather than consumer electronics. Unlike batteries, which need considerable time for initial recharge, supercapacitors possess faster charge and discharge to facilitate regenerative pulse and peak assists necessary for starting the engine. Their capacity to generate intense high power discharge in short periods could be suitable to produce flash lamps for aerospace applications. Faster responses of supercapacitors are attributed to fast surface processes like adsorption or desorption of charge carriers at the electrode-electrolyte interface.

Based on the charging mechanism, supercapacitors are divided into two categories, such as electrical double-layer capacitors (EDLC) and pseudo-capacitors. In EDLC, the electrical energy is stored by the formation of Helmholtz double layers at the electrode-electrolyte interface. The width of the charge separation influenced the capacitance of the device to a great extent. In EDLC, the storage mechanism mainly involves the adsorption and desorption of charge carriers on the porous organic electrodes. Various porous carbon derivatives, such as graphite, mesoporous activated carbon, CNTs and conducting polymers were frequently employed for performing the function of porous electrodes. Capacitive action of pseudo-capacitors involves the charge transfer in-between the electrodes by means of faradaic reactions. Normally transition metal oxide derived electrodes which can provide smooth electron transfer were deployed for generating high-performing pseudo-capacitors. Symmetric and asymmetric supercapacitors are differed by the nature of electrodes used for fabricating them. Two electrodes with identical capacitances are used for fabricating symmetric supercapacitors, but two distinctly different electrodes are used for asymmetric supercapacitors [52].

Device structure of supercapacitors constituted by two same or different electrodes, are separated by an ion-transparent dielectric membrane wetted with ionic electrolytes. On charging, the electrodes get polarised, so that, the ions from the electrolyte will migrate towards oppositely charged electrodes and gets adsorbed over the electrode surface resulting in the formation of double layers. Each electrode will associate with a layer of diffused charges from the electrolyte, and hence, the whole device will function as two capacitors separated by a resistor. Double-layer capacitance (C) is directly related to the specific surface area (S) of the electrodes and inversely related to the distance (d) between ions and electrodes.

$$C = \frac{\epsilon_0 \epsilon_r S}{d} \quad (1)$$

So, activated carbon electrodes with very high surface area are tenable to deliver extremely high capacitive behaviour. If C1 and C2 are the individual capacitances, then the total capacitance of the entire device can be given as,

$$\frac{1}{C} = \frac{1}{C_1} + \frac{1}{C_2} \quad (2)$$

The storable energy of a capacitor quadratically related to the potential window of the electrolyte is ,

$$E = \frac{1}{2} C V^2 = \frac{1}{2} QV \quad (3)$$

where, V is the potential window and Q is the charge stored in the capacitor. The potential window is limited by the decomposition potential of the electrolyte used. In the case of aqueous electrolytes, it is not possible to go beyond 1 V, whereas for non-aqueous electrolytes, the decomposition potential is quite high to deliver very good energy density. Acetonitrile-based systems could be used up to 2.8 V and propylene carbonate-based systems can go around 3 V. Potential-driven break down of dielectric material will also affect device performance, which will limit application of very high potentials also. As pointed out earlier, de-merits of conventional electrolytes pave the way for new non-conventional safety electrolytes for powering supercapacitors [53]. Initially, ILs was used as high-conducting electrolytes for supercapacitors by dissolving in suitable solvents. Even though they have extra-high conductivity and performed exceedingly well with porous carbon electrodes, the energy density is limited by the decomposition potential of the solvent used. ILs with excellent electrochemical window, generally greater than 3 V, could be used alone as high-conducting electrolytes. Anions of ILs are oxidised only at high potentials and the reduction of cations also require very low potentials, giving them very high electrochemical windows and rendering very high energy densities. In comparison with ILs with halide anions, the ones with fluorine containing coordinate anions displayed higher EC windows. Apart from the EC window, ion size, ion type, interaction of ions with solvent and electrodes will also influence the overall performance of the devices [54]. Equivalent series resistance (ESR), an important quality parameter of supercapacitors, is strongly influenced by the ion type, conductivity as well as the viscosity of the electrolyte. If the ions are too heavy, less diffusible or too viscous, it will considerably drag down the electrolyte conductivity and increase the ESR. This will affect the storage efficiency, as the ESR is inversely related to the power density of the device as,

$$P = \frac{V^2}{4 \cdot ESR \cdot m} \quad (4)$$

where V represents the potential window and m is the active mass of the electrodes. Also, the interaction of the electrolytes with solvents or electrodes also has a strong role to play in deciphering the cycle stability of the system. High temperature stability of ILs was found to be promising in exploiting them as electrolytes for powering supercapacitors for a wide range of temperatures. Delivering power at extreme condition seems to be difficult with conventional electrolytes, as they may be either in frozen or gaseous state in which the charge conduction is impossible. Inception of ILs with wide liquid range helped to solve this difficulty to a greater extent. This will be suitable in producing high-power short-pulse arc lamps for polar regions, space stations and in mines. It was found that the viscosity of ILs could be reduced by suitable formulation of eutectic mixture of two or more ILs with identical anions, which can also be applied to a wide range of temperatures due to the depression in freezing points of ILs.

Lin et al. reported the use of a mixture of piperidinium and pyrrolinium ILs for preparing the electrolyte for supercapacitors for temperatures ranging from -50 to 100°C [55]. It delivered an outstanding capacitance of 180 F/g , which was attributed to a wide EC window of 3.5 V . Similarly, Ruiz et al. demonstrated a mixture of pyrrolidinium IL in butyronitrile as power electrolyte for supercapacitors for temperatures ranging from -20 to 80°C [56]. Low-viscous ILs has higher conductivity and capacitive performance than high-viscous ILs, due to better ionic mobility. Likewise, variation of anionic or cationic sizes also has a prominent effect on the performance. ILs with PF_6^- or BF_4^- anions have better capacitive performance over other anions, because their ionic size is complementary to the pores of the mesoporous carbon electrodes, which is widely employed in supercapacitors. Clever structural design of ILs could also improve the device performance. Rennie et al. extensively studied on this aspect and found that the ILs with ether-bonded alkyl side-chains possesses higher capacitance in comparison with others. They found that the presence of ether bond could induce significant flexibility to the structural design. It could lower the viscosity and further enhance the conductivity, which in turn improves the capacitive performance [57]. Xu et al. explored a new kind of ILs with fluorohydrogenate anions with comparatively lower viscosity and better ionic conductivities to be used as conducting medium in a wide range of applications, mainly supercapacitors and other energy storage systems [58].

Like ILs, their solid analogues and secondary derivatives, such as ILCs, ionogels, etc. are also receiving technological importance in energy storage systems [59]. Presence of well-ordered conducting channels provide them strong propensity to transport and store charges. ILCs could be explored as electrolytes either in the solution state in suitable solvents or in their conducting liquid crystalline mesophase. Thermotropic mesophase formation improves the molecular conductivity to extract better capacitance at high temperatures. We have exploited the lyotropic mesophase formation of an imidazolium ionic liquid crystal in acetonitrile to derive a high-conducting electrolyte for supercapacitors. Unlike pure solution, where the ion density is very low, liquid-crystalline phase have high ionic density and weight-specific performance to yield superior performance. Not only the ionic concentration, but also the ionic mobility is important in governing the storage performance. Lyotropic columnar phase of ILC found to be adequate with conductivity and lower viscosity to be employed in supercapacitors as electrolytes. In mesophase, self-assembly of mesogens provide adequate nano-oriented pathways to effect charge diffusion with ease for developing double layers in response to the subjected potential. Lyotropic columnar mesophase yielded a specific capacitance of 134 F/g with 80% capacitance retention, after 2000 cycles [60]. Schematic diagram showing the capacitive behaviour of ionic liquid crystalline electrolyte in powering high-performance supercapacitors and corresponding liquid crystalline phases are given in **Figure 4**.

In the LC phase, the charge carriers are aligned by the molecular self-assembly and have considerable degree of freedom to migrate to corresponding electrodes on charging, forming electrical double layers. While on discharge, when the electrodes are depolarised, ions move away from the electrodes to the centre depleting the double layers. These processes are highly reversible to achieve better cycle stability. Solid ionic electrolytes have also been obtained by mixing ionic liquids with polymer binders or carbon materials to generate safe energy storage systems. Zhang et al. prepared a flexible gel-polymer electrolyte containing

1-butyl-3-methylimidazolium chloride and Li_2SO_4 in a matrix of poly(vinyl alcohol) to be used as flexible safe electrolyte for supercapacitors [61]. The high ionic conductivity and a high fracture strain of the electrolyte is benefited by delivering a specific capacitance of 136 F/g, with a maximum energy density of 10.6 Wh/kg and a power density of 3400 W/kg. The conductivity and capacitive behaviour of supercapacitors remains with negligible fade, even after the repeated bending cycles illustrated the flexibility of electrolyte and its application in future plastic electronics. Similarly, many reports are there in utilising ILs or ILCs in combinations with PEO, PVDF, PHEMA, etc. to materialise highly conducting and flexible ionogels for powering supercapacitors.

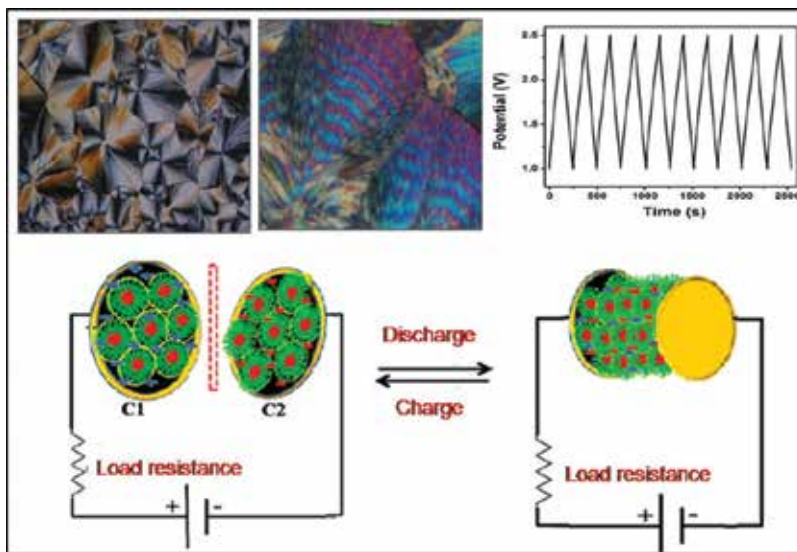


Figure 4. Bio-based ionic liquid crystal as electrolyte for supercapacitors. Reproduced with permission from [60].

2.2. Lithium-ion batteries

Like supercapacitors, or comparatively to a higher extent, Li-ion batteries attracted the scientific interest particularly because of its higher energy density and superior performance [62, 63]. In Li-ion batteries, device structure is more or less similar to that of supercapacitors with a separator soaked with electrolyte, sandwiched in-between a pair of electrodes (cathode and anode). A typical device structure of the Li-ion battery is depicted in **Figure 5**. Similar to pseudo-capacitors, the energy storage is realised by the Li-ion transport across the permeable separator. Leakage and flammability issues associated with conventional volatile organic electrolytes lead to the inception of safe, cost-effective and eco-friendly electrolytes, mainly ILs [64]. Low evaporation power and less flammable nature make them more safe and convenient. Initially, quaternary ammonium or phosphonium salts with triflate anions were explored for electrolyte applications. Less viscous and cathodically stable ILs are necessary for effective lithium cycling. Fluorinated anions, such as BF_4^- , PF_6^- , TFSI^- , etc. were found to be more efficient in realising better Li intercalation reactions. As the size of anion significantly affects the ionic transport, Matsumoto et al showed high-rate cycling of Li/LiCoO₂ cell with smaller sulphonamide anions [65].

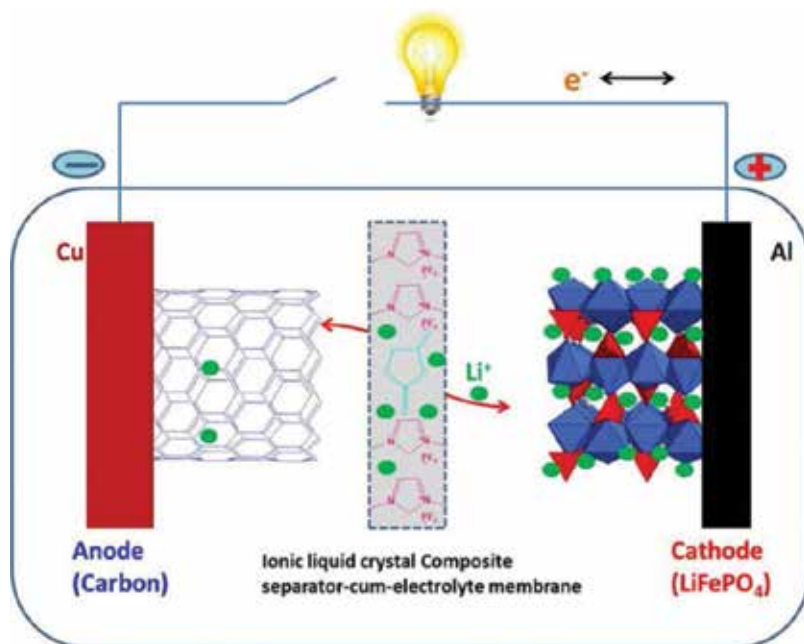


Figure 5. Design of Li-ion battery incorporating ionic liquid crystal membrane separator.

It was observed that bulkier cations of ILs, sometimes, form inhibiting layers on the surface of carbonaceous anodes hindering cell reactions. Fluorinated anions are able to remove such unwanted layer formation and rule out the need for secondary additives for this purpose. IL-based electrolytes demonstrated their excellent performance with variety of electrode materials. High redox stability of ILs will help to explore new horizon of electrodes with high-voltage stabilities, so that the energy and power densities could be improved [66]. The main factor, which needs to be addressed while choosing a solvent for Li batteries, is the handling of dissolved Li-ions and its influence on charge transport, while cell reactions are on. Structural design of ILs by incorporating anionic or cationic functionality to interact with dissolved ions or the usage of external additives or diluents were also tried to eliminate filament formation and other undesirable reactions by the dissolved Li-ions. IL structural design has a special role to play on the formation of protective film (solid electrolyte interface, SEI) and also to modulate ion transport, charge transfer and electrolyte stability [67]. Each ILs has definite reaction pathways for modulating the Li-ion transfer, depending on the association or other interaction of the constituting ions. Considering the needs, such as safety, sustainability, strength, cycle stability and high temperature operability, new designs and methodologies were introduced. Inception of thin and flexible batteries further added much interest towards IL-based electrolytes. Even though many studies have invested to analyse the energy storage performance of IL-based electrolyte in combination with a large array of electrode materials, the commercialisation of them is still uncertain. High-cost of ILs, in comparison with conventional carbonate solvents, may be one of the major hindering factors. In order to solve the situation, efforts were taken to reduce the cost of ILs by introducing new low-cost cations or anions with simple

strategies. Bio-based ILs/ILCs with negligible production cost and comparable performance could be prepared by suitable modification of industrial waste by-products like cashew nut shell liquid (CNSL). They can be used for powering energy storage systems either as such or in combination with solvents or as solid films or gels with suitable polymeric binder. Since the conversion of waste to value-added electrolytes seems to be a double benefit to the society, it can be a remedy for pollution as well as a sustainable energy storage pathway. Similarly, dicyanamide $[\text{N}(\text{CN})_2]^-$ with highly delocalised negative charge proves to be a better alternate for fluorinated anions to produce low-cost ionic liquids. Their highly delocalised ionic charge is responsible for the extremely low freezing points, which they have [68].

Thermo-mechanical stability of ILs/ILCs is utilised for generating stable batteries with different categories of electrodes and with good cycling stability. Rate performance of the cells also found to be improved, due to the better conductivity, tuneable viscosity and reversibility of IL-based electrolytes. But, in some cases, rate capability is significantly affected by the ion-association with ILs during cell cycling, which enhances the viscosity and thereby hinders cycling efficiency. In contrary to this, fluorosulfonamide anion containing ILs displayed high-rate performance with higher Li-ion concentrations, but lacked the device stability. Mixture electrolytes containing ILs and conventional solvents, found a better strategy to cope up with the desired conductivity and device stability. Recently, newer electrode combinations such as Li-air, Li-S, Na, Mg and Al batteries have formulated to overcome the shortcomings of Li-ion batteries [69]. In all these new-generation batteries also, ILs seems to be a better alternate for ionic shuttling. Their wide operation window and liquid range will be applicable in many more upcoming storage systems.

Solid-state electrolytes, which could function as both electrolyte and separator, could be generated by integrating ILs/ILCs with polymeric binders [69]. Schematic diagram showing the separator composed of ILC-based hybrid membrane that functions as both separator and electrolyte is given in **Figure 5**. High conductivity, porosity, better Li-ion transport, high electrolyte affinity and uptake, mechanical stability and thermal stability are the main requisites for solid electrolytes [70]. Kato et al. developed thermotropic liquid crystalline (LC) electrolytes for lithium-ion batteries for the first time by the self-assembly of rod-like LC molecule having a cyclic carbonate moiety with lithium salts and is used to form self-assembled two-dimensional ion-conductive pathways. Electrochemical and thermal stability and efficient ionic conduction is observed for the liquid crystal and is employed as an electrolyte in lithium-ion batteries with highly reversible charge–discharge for both positive and negative electrodes [71]. Presence of ambiphilic ILs/ILCs will definitely improve the electrolyte affinity and further ionic transport upheld the reaction kinetics and improves efficiency. Flexible, wearable storage batteries are the future directives of new age storage systems.

2.3. Fuel cells

Fuel cells are unanimously agreed to be one of the green technologies for sustainable energy, due to their high energetic efficiency and low environmental impact. These devices directly convert chemical energy to electrical energy with water as by-product, thereby omitting toxic emissions prevalent with fossil fuels [72]. They have been explored in space crafts and subma-

rines to power the arc lamps and to make use of by-product water for drinking purpose. The major working elements of fuel cells are bipolar plates, diffusion layers, electrodes (anodes and cathodes) and the electrolytes. Mainly, aqueous solutions with acidic or basic nature have been used as the electrolyte for conventional fuel cells. Even though fuel cell technology possesses an eventful 150-year-old history, no one had succeeded in using proton carriers other than hydronium ions or hydroxide ions in a fuel cell, until last few decades. Obviously, it confined the fuel cell science within the aqueous electrolytes of acid or basic character. The effective potential range also limited below 1 V, due to the use of aqueous electrolyte alone. In addition, the operating temperature range also limited to below 100°C, when aqueous electrolytes are employed. In proton exchange membrane (PEM) fuel cell, the core is called the membrane electrode assembly (MEA), which comprises the PEM placed between two electrodes. Different functions of PEMs are separating the gaseous reactants, conducting protons from the anode to the cathode, electrically insulating the electrons and supporting the catalyst. The necessary requirements an exchange membrane should have to function exquisitely are excellent proton conductivity in dry and wet states, unflinching mechanical strength and dimensional stability, chemical, electrochemical and thermal stability under the working conditions, low fuel and oxygen crossover, easy conformation to form a membrane electrode assembly and low-cost **Figure 6** [74, 75].

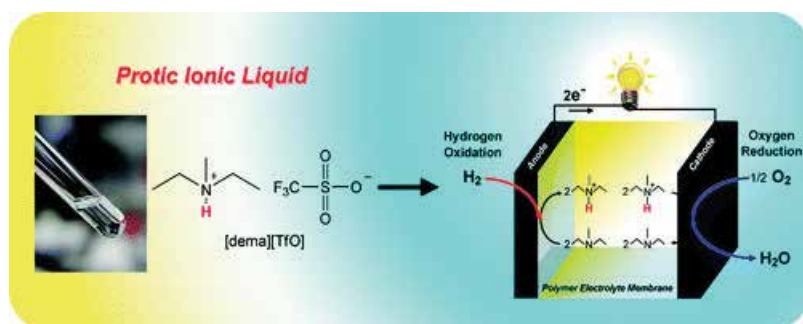


Figure 6. Application of protic ILs in fuel cells as electrolytes. Reproduced with permission from [73].

Nafion (perfluorosulfonic acid) ionomer is one of the most widely used membranes in PEMFC devices because of its chemical inertness, high ionic conductivity and better mechanical strength. But, the conductivity of the Nafion usually reduces when the temperature goes beyond 100°C, as the evaporation of water will hinder the ionic mobility considerably. Even then, elevated temperatures are advantageous because the contamination tolerance of the catalyst is improved and even low purity hydrogen could be benefited at higher temperatures. It would also eradicate both carbon monoxide poisoning and noble metal catalyst corrosion frequently associated with aqueous electrolytes. In addition, electrode reaction kinetics also improved at elevated temperatures. All these issues could be solved by introducing room temperature ionic liquids as the electrolytes either by gelling ILs with polymers or polymerizing polymerizable ionic liquids. Protic ionic liquids could be generally considered as a salt of a Bronsted acid and a Bronsted base. The transfer of a proton from an acid to a base

leads to the formation of hydrogen-bonded networks between proton donor and acceptors. Protic ILs with more fluidity found to have more conductivity also underlines that the conduction follows vehicular mechanism. IL-based solid electrolyte membranes have exquisite conductivity and thermo-mechanical stability and are also free from water. Mainly, azoles like imidazole, pyrazole, triazole, benzimidazole, etc. or amines are the proton relay molecules in IL-based electrolytes with a wide pH range, which opens a new horizon to design alternate low-cost electrode materials, with an aim to replace expensive and scarce platinum electrodes. Protonated imidazole derivatives are found to have an excellent conductivity and it conducts like water through Grotthuss conduction mechanism [76–78].

The main challenge in employing ILs in PEMs is choosing the suitable molecular design of the ion pair, so that the whole requirements for the membrane electrolyte in a fuel cell including mechanical stability without compromising the proton transport activity are attained. Lee et al. fabricated a SPI/[dema][TfO] membrane for PEMFCs under non-humidified conditions, which fetch a peak power density of 100 mW cm^{-2} and maximum current density of 400 mA cm^{-2} at 120°C [73]. However, this membrane has an unstable three-phase boundary in the catalyst layer formed by leaked [dema][TfO]. Lee et al. reported many fuel cell varieties with the ILs provided by Ohno et al. [79]. But, the mechanical integrity of the solid electrolytes needs to be improved. Relatively, a new approach for fabricating mechanically stable and high-conducting solid electrolytes is the polymerization of ionic liquid monomers. Ionic liquid monomer $[\text{HSO}_3\text{-BVIm}][\text{TfO}]$ was polymerized by Díaz et al. and employed in a PEMFC at 25°C under anhydrous conditions, measuring a maximum current density of 154 mA cm^{-2} and a peak power density of 33.1 mW cm^{-2} [80]. These membranes were thermally stable up to 300°C . Utilisation of organic plastic crystals or ionic liquid crystals as high-conducting solid safety electrolytes is another intriguing strategy. Membranes based on the cellulose acetate supported with [choline][DHP] doped with various acids were studied by Rana et al. [81]. Belieres et al. recently identified that the small cation NH_4^+ could be useful in replacement of H_3O^+ [82]. Also, IL-based electrolytes with nitrate anion prove to have narrow ranges of current density, in which, there appears to be almost no energy barrier to oxygen reduction. The reasons for this are still not clarified, though they are presumably related to some instability of the nitrate anion. Hagiwara et al. proposed the application of fluorohydrogenate ionic liquid in fuel cells [83, 84]. In principle, the FHFC needs no humidification, since the fluorohydrogenate ion conduction does not require the presence of water. They have also demonstrated composite membranes consisting of 2-hydroxyethyl methacrylate (HEMA) and EMPyr(FH)1.7F and achieved a maximum power density of 200 mW cm^{-2} .

2.4. Dye-sensitized solar cells (DSSCs)

DSSC is a third-generation photovoltaic device, which can convert solar energy into electrical energy in a more convenient and cost-effective way than the conventional semi-conducting photovoltaics [85]. They can be also designed as flexible and multi-coloured forms. The device structure of DSSCs include a photosensitizer (often organic dyes that is why the name dye-sensitized), a photo anode comprised of semiconducting nano-particles with well-adjusted conduction band to accept electrons, a counter electrode (mainly Pt based) and electrolyte. The theoretical maximum efficiency that could be extracted from a DSSC is around 20% only,

but simple and convenient device structure, easy fabrication and comparatively low cost active materials made DSSC so popular. As we pointed out electrolyte is one of the major components of DSSC, the main function of which is to facilitate a conducting pathway to keep the electron transfer mechanism alive by regenerating the oxidised dye by providing electrons.

Normally I^-/I_3^- couple in acetonitrile is used as electrolyte in DSSCs to regenerate the dyes. Volatile solvent and toxic additives make the use of this electrolyte undesirable even if they gave very good efficiency. Repeated exposure to the solar heating may evaporate the solvents so that the device efficiency lowered due to poor charge transport. Quest for alternate electrolytes found ILs/ILCs as one among possible candidates. Combination of redox active salts with ILs is often employed for generating the ionic couple which can produce faster charge transport. Viscosity and conductivity of ILs are the determining factors for improving charge transport. High-viscous ILs often fails to harvest good efficiencies owing to poor ionic diffusion and transport. Eutectic mixtures of ILs were employed by many groups as a low-viscous high-conducting electrolyte system with good efficiencies. It was also found that addition of Lithium salt with IL in combination with TiO_2 based photoanode could lower the conduction band of TiO_2 to improve the electron injection between dye and TiO_2 [86]. Similarly more basic anions like dicyanamide will also influence the conduction levels to modify the V_{oc} of DSSC and thereby efficiency. Better redox couple diffusion, fast electron transfer, slow recombination due to high electron diffusion lengths, excellent electrochemical reversibility are the main advantages of using IL based electrolytes over conventional ones. Even then, the paradigm remains in finding appropriate ILs with energy levels closer to the dye for its fast regeneration, but at the same time it should be in a level so that V_{oc} remain unaltered. Cobalt based redox couples have used very recently in harnessing very high efficiencies; a positive sign. Cobalt based systems in conjugation with ILs may lead to much better performances. Since the efficiency of DSSC is influenced by a large number of factors optimisation of each one with IL electrolytes is essential. Different photosensitizers like porphyrins, Ru-based inorganic dyes, organic molecules, etc. have been studied for solar energy conversion in combination with IL electrolytes. A porphyrin based dye recorded a 4.9% efficiency with $[C_2mim][B(CN)_4]$ -based IL electrolytes [87–90].

ILs and ILCs are more suitable for flexible DSSCs since they could be easily formed in the form of thin films with the combination of some polymeric binders. Large scale batch to batch production of thin film electrolytes will definitely revise the face of modern solar technology. Easy miscibility of ILs with conventional polymers and non-volatility made them highly desirable for safe, flexible and durable energy conversions. Moisture sensitivity and atmospheric stability of the electrolyte membranes should also be optimum. Instead of easy corrodible ITO/FTO electrodes new stable substrates have to be designed and developed for working with IL based electrolytes. Semiconducting metal nano-particles, carbon derivatives and polymers can also function as electrode materials.

Quasi-solidified electrolytes obtained by gelling ILs with polymers or ionogels can also utilised for DSSCs. It will reduce leakage problems, improve connectivity, flexibility, etc. Use of ILCs as electrolytes is another possible option. Being solid-state analogues of ILs,

ILCs have ions with a definite structural order to impart excellent solid-state conductivities. They could be further exploited for stimuli responsive conduction or temperature dependent storage, etc. Modern device structures for performing under dim light or extreme conditions will be in reality when combined IL/ILC electrolytes. It will also be suitable for wearable or stretchable device architectures to harness energy in a more sustainable manner.

Quasi-solid electrolytes were also developed by dissolving poly (ionic liquid) in room temperature IL harvested a good PCE of 5.92% with excellent long-term stability. The superior performance is attributed to the improved conductivity owing to the extended charge transport networks via the π - π stacking of imidazolium rings [91]. Gunko et.al prepared new electrolytes by suspending smaller amounts of graphene flakes in RTILs to extract more than 25 times improved photovoltaic performance [92]. Kuang et al. used carbon black- IL mixture as better performing electrolyte without adding iodine to yield 6.37% [93]. Jang et al. used an efficient ionic plastic crystal derived from imidazolium iodide salt as an excellent electrolyte for solid-state DSSCs with high PCE of 7.8% [94].

The plastic crystal electrolyte membrane was fabricated over the dye-adsorbed TiO_2 by melt processing. Wang et al. developed ionogels with silica nano-particles and ILs is to used as high-performing solid DSSC electrolytes [95]. Schematic diagram showing the electronic transfer between silica-ionic liquid quasi-solid electrolytes to the dye to re-generate it on photo-oxidation in solid-state DSSC is given in **Figure 7**. Polymer electrolytes composed of conventional polymer binders and ionic liquids could also employed for solid-state DSSC applications. Recently, Kato and co-workers developed high-temperature stable liquid crystalline electrolytes for DSSCs. The self-assembly of a carbonate mesogen and an IL forms 2D ion channels for the smooth passage of I^-/I_3^- couple, harvesting till date better performance up to 120°C . Utilisation of ionic liquid crystalline electrolytes helps in fabricating quasi-solid-state DSSCs with excellent power conversion efficiencies over a wide temperature range.

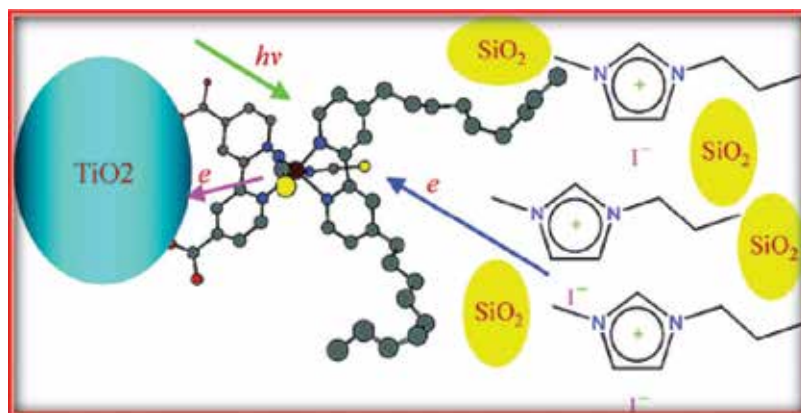


Figure 7. Quasi-solid-state electrolytes based on ionic liquids for DSSCs. Reproduced with permission from [95].

2.5. Other applications

Apart from the above discussed energy applications, ionic liquids and ionic liquid crystals were also exploited in systems like thin film transistors, thermo-electrochemical cells, hydrogen storage applications, etc. Application of ILs/ILCs with more eco-friendly nature will generate safe and sustainable energy storage for the future. Application of ILs as gate electrolytes in thin film transistors has paved way to the modern flexible electronics [96–99].

3. Conclusions

The present survey on the electrolyte systems used in various energy devices suggests that ionic liquid crystals are demonstrated as efficient electrolyte systems because of their anisotropic phase induced exciting channels, such as high ionic conductivity and diffusion along with excellent thermal stability, low dimensionally ordered phase, low vapour pressure and non-toxicity. They can be considered as prospectable and sustainable materials for bringing safe and affordable electronic devices. Their ability to formulate solid electrolyte films, in combination with polymers, can make revolution in the field of flexible, wearable, bendable supercapacitors, fuel cells and batteries.

Author details

Sudha J. Devaki* and Renjith Sasi

*Address all correspondence to: sudhajd2001@yahoo.co.in

Chemical Science and Technology Division, CSIR-NIIST, Trivandrum, Kerala, India

References

- [1] S. Zhang, J. Sun, X. Zhang, J. Xin, Q. Miao and J. Wang. Ionic liquid-based green processes for energy production. *Chem. Soc. Rev.* 2014; 43 :7838–7869.
- [2] M. Smiglak, J. M. Pringle, X. Lu, L. Han, S. Zhang, H. Gao, D. R. MacFarlane and R. D. Rogers. Ionic liquids for energy, materials, and medicine. *Chem. Commun.* 2014; 50: 9228–9250.
- [3] N. D. Khupse and A. Kumar. Ionic liquids: New materials with wide applications. *Indian J. Chem.* 2010; 49A: 635–648.
- [4] R. Hayes, G. G. Warr and R. Atkin. Structure and nanostructure in ionic liquids. *Chem. Rev.* 2015; 115: 6357–6426.
- [5] G.-H. Min, T. Yim, H. Y. Lee, D. H. Huh, E. Lee, J. Mun, S. M. Oh and Y. G. Kim. Synthesis and properties of ionic liquids: Imidazolium tetrafluoroborates with unsaturated side chains. *Bull. Korean Chem. Soc.* 2006; 27:847–852.

- [6] A. Aupoix, B. Pegot and G. Vo-Thanh. Synthesis of imidazolium and pyridinium-based ionic liquids and application of 1-alkyl-3-methylimidazolium salts as pre-catalysts for the benzoin condensation using solvent-free and microwave activation. *Tetrahedron*. 2010; 66:1352–1356.
- [7] H. Tokuda, K. Hayamizu, K. Ishii, Md. A. B. H. Susan and M. Watanabe, Physicochemical properties and structures of room temperature ionic liquids. 2. Variation of alkyl chain length in imidazolium cation. *J. Phys. Chem. B*. 2005; 109: 6103–6110.
- [8] N. Kumar, S. Goindi, S. Kumar and A. K. Jana. The effect of N-alkyl substituents on the usability of imidazolium cation-based ionic liquids in microemulsion systems: A technical note. *American Assoc. Pharm. Sci.* 2013; 14:551–557. DOI: 10.1208/s12249-013-9939-z.
- [9] Y. Bi, L. Zhao, Q. Hu, Y. Gao and L. Yua. Aggregation behavior of imidazolium-based surface-active ionic liquids with photoresponsive cinnamate counter ions in the aqueous solution. *Langmuir*. 2015; 31 (46):12597–12608.
- [10] M. T. Garcia, I. Ribosa, L. Perez, A. Manresa and F. Comelles. Aggregation behavior and antimicrobial activity of ester-functionalized imidazolium- and pyridinium-based ionic liquids in aqueous solution. *Langmuir*. 2013; 29: 2536–2545.
- [11] W. Xu, T. Wang, N. Cheng, Q. Hu, Y. Bi, Y. Gong and L. Yu. Experimental and DFT studies on the aggregation behavior of imidazolium-based surface-active ionic liquids with aromatic counter ions in aqueous solution. *Langmuir*. 2015; 31: 1272–1282.
- [12] D. Kobayashi, K. Fujita, N. Nakamura and H. Ohno. A simple recovery process for biodegradable plastics accumulated in cyanobacteria treated with ionic liquids. *Appl. Microbiol. Biotechnol.* 2015; 99: 1647–1653.
- [13] A. S. M. C. Rodrigues, M. A. A. Rocha, H. F. D. Almeida, C. M. S. S. Neves, J. A. Lopes-da-Silva, M. G. Freire, J. A. P. Coutinho and L. M. N. B. F. Santos. Effect of the methylation and N–H acidic group on the physicochemical properties of imidazolium-based ionic liquids. *J. Phys. Chem. B*. 2015; 119: 8781–8792.
- [14] M. Wang, X. Pan, J. Chen and S. Dai. Regulating the mesogenic properties of imidazolium salts by modifying N3-substituents. *Sci. China Chem.* 2015; 1–7. DOI: 10.1007/s11426-015-5390-1.
- [15] R. Tao and S. L. Simon. Rheology of imidazolium-based ionic liquids with aromatic functionality. *J. Phys. Chem. B*. 2015; 119: 11953–11959.
- [16] J. F. Wishart and E. W. Castner, Jr. The physical chemistry of ionic liquids. *J. Phys. Chem. B*. 2007; 111: 1–2. DOI: 10.1021/jp072262u
- [17] T. L. Greaves and C. J. Drummond. Protic ionic liquids: Properties and applications. *Chem. Rev.* 2008; 108: 206–237.
- [18] K. Ghandi. A review of ionic liquids, their limits and applications. *Green Sustain. Chem.* 2014; 4: 44–53.

- [19] D. Han and K. H. Row. Recent applications of ionic liquids in separation technology. *Molecules*. 2010; 15: 2405–2426. DOI: 10.3390/molecules15042405
- [20] G. Laus, G. Bentivoglio, H. Schottenberger, V. Kahlenberg, H. Kopacka, T. Röder and H. Sixta. Ionic liquids: Current developments, potential and drawbacks for industrial applications. *Lenzinger Ber.* 2005; 84: 71–85.
- [21] G. Singh and A. Kumar. Ionic liquids: Physico-chemical, solvent properties and their applications in chemical processes. *Indian J. Chem.* 2008; 47A: 495–503.
- [22] X. Zhang, X. Zhang, H. Dong, Z. Zhao, S. Zhang and Y. Huang. Carbon capture with ionic liquids: Overview and progress. *Energy Environ. Sci.* 2012; 5: 6668–6681.
- [23] A. Noda, Md. A. B. H. Susan, K. Kudo, S. Mitsushima, K. Hayamizu and M. Watanabe. Brønsted acid–base ionic liquids as proton-conducting nonaqueous electrolytes. *J. Phys. Chem. B*. 2003; 107: 4024–4033.
- [24] T. Kato. From nanostructured liquid crystals to polymer-based electrolytes. *Angew. Chem. Int. Ed.* 2010; 49: 7847–7848.
- [25] J. W. Goodby, P. J. Collings, T. Kato, C. Tschierske, H. Gleeson and P. Raynes, editors. *Handbook of Liquid Crystals. Vol. 3: Nematic and Chiral Nematic Liquid Crystals*. 2nd ed. Wiley-VCH: Weinheim; 2014.
- [26] G. W. Gray and J. W. Goodby, editors. *Smectic Liquid Crystals: Textures and Structures*. Leonard Hill: Glasgow, London; 1984.
- [27] C. Tschierske. Development of structural complexity by liquid-crystal self-assembly. *Angew. Chem. Int. Ed.* 2013; 52: 8828–8878.
- [28] T. Ichikawa, M. Yoshio, A. Hamasaki, T. Mukai, H. Ohno and T. Kato. Self-organization of room-temperature ionic liquids exhibiting liquid-crystalline bicontinuous cubic phases: Formation of nano-ion channel networks. *J. Am. Chem. Soc.* 2007; 129: 10662–10663.
- [29] J. P. F. Lagerwall and F. Giesselmann. Current topics in smectic liquid crystal research. *Chem. Phys. Chem.* 2006; 7: 20–45.
- [30] J. W. Goodby, P. J. Collings, T. Kato, C. Tschierske, H. Gleeson and P. Raynes, *Handbook of Liquid Crystals. Vol. 4: Smectic and Columnar Liquid Crystals*. 2nd ed. Wiley-VCH: Weinheim; 2014.
- [31] C. Tschierske. 6 Non-conventional soft matter. *Annu. Rep. Sect. C (Phys. Chem)*. 2001; 97: 191–267.
- [32] M. Lehmann, C. Kohn, H. Meier, S. Renkerb and A. Oehlhof. Supramolecular order of stilbenoid dendrons: Importance of weak interactions. *J. Mater. Chem.* 2006; 16: 441–451.
- [33] R. A. Reddy and C. Tschierske. Bent-core liquid crystals: Polar order, superstructural chirality and spontaneous desymmetrisation in soft matter systems. *J. Mater. Chem.* 2006; 16: 907–961.

- [34] K. Binnemans. Ionic liquid crystals. *Chem. Rev.* 2005; 105: 4148–4204.
- [35] B. Soberats, E. Uchida, M. Yoshio, J. Kagimoto, H. Ohno and T. Kato. Macroscopic photo-control of ion-transporting pathways of a nanostructured imidazolium-based photoresponsive liquid crystal. *J. Am. Chem. Soc.* 2014; 136: 9552–9555.
- [36] K. Goossens, K. Lava, C. W. Bielawski and K. Binnemans. Ionic liquid crystals: Versatile materials. *Chem. Rev.* 2016; 116: 4643–4807.
- [37] R. Sasi, T. P. Rao and S. J. Devaki. Bio-based ionic liquid crystalline quaternary ammonium salts: Properties and applications. *ACS Appl. Mater. Interfaces.* 2014; 6: 4126–4133.
- [38] G. Pelzl, I. Wirth and W. Weissflog. The first 'banana phase' found in an original Vorländer substance. *Liq. Cryst.* 2001; 28: 969–972.
- [39] K. Goossens, P. Nockemann, K. Driesen, B. Goderis, C. Görller-Walrand, K. Van Hecke, L. Van Meervelt, E. Pouzet, K. Binnemans and T. Cardinaels. Imidazolium ionic liquid crystals with pendant mesogenic groups. *Chem. Mater.* 2008; 20: 157–168.
- [40] J. Pernak, M. Smiglak, S. T. Griffin, W. L. Hough, T. B. Wilson, A. Pernak, J. Zabielska-Matejuk, A. Fojutowski, K. Kita and R. D. Rogers. Long alkyl chain quaternary ammonium-based ionic liquids and potential applications. *Green Chem.* 2006; 8: 798–806.
- [41] A. Abate, A. Petrozza, G. Cavallo, G. Lanzani, F. Matteucci, D. W. Bruce, N. Houbenov, P. Metrangolo and G. Resnati. Anisotropic ionic conductivity in fluorinated ionic liquid crystals suitable for optoelectronic applications. *J. Mater. Chem. A.* 2013; 1: 6572–6578.
- [42] H. Shimura, M. Yoshio, A. Hamasaki, T. Mukai, H. Ohno and T. Kato. Electric-field-responsive lithium-ion conductors of propylene carbonate-based columnar liquid crystals. *Adv. Mater.* 2009; 21: 1591–1594.
- [43] A. Kotlewski, B. Norder, W. F. Jager, S. J. Picken and E. Mendes. Can morphological transitions in fibrils drive stiffness of gels formed by discotic liquid crystal organogelators?. *Soft Matter.* 2009; 5: 4905–4913.
- [44] T. Kato. Self-assembly of phase-segregated liquid crystal structures. *Science.* 2002; 295: 2414–2418.
- [45] Y. Iinuma, K. Kishimoto, Y. Sagara, M. Yoshio, T. Mukai, I. Kobayashi, H. Ohno and T. Kato. Uniaxially parallel alignment of a smectic A liquid-crystalline rod-coil molecule and its lithium salt complexes using rubbed polyimides. *Macromolecules.* 2007; 40: 4874–4878.
- [46] D. Tanaka, H. Ishiguro, Y. Shimizu and K. Uchida. Thermal and photoinduced liquid crystalline phase transitions with a rod–disc alternative change in the molecular shape. *J. Mater. Chem.* 2012; 22: 25065–25071.
- [47] F. Béguin, V. Presser, A. Balducci and E. Frackowiak. Carbons and electrolytes for advanced supercapacitors. *Adv. Mater.* 2014; 26: 2219–2251.
- [48] J. Wang, H. L. Xin and D. Wang. Recent progress on mesoporous carbon materials for advanced energy conversion and storage. *Part. Part. Syst. Charact.* 2014; 31: 515–539.

- [49] C. Zhong, Y. Deng, W. Hu, J. Qiao, L. Zhangd and J. Zhang. A review of electrolyte materials and compositions for electrochemical supercapacitors. *Chem. Soc. Rev.* 2015; 44: 7484–7539.
- [50] Y.-S. Ye, J. Rick and B.-J. Hwang. Ionic liquid polymer electrolytes. *J. Mater. Chem. A.* 2013; 1: 2719–2743.
- [51] A. González, E. Goikolea, J. A. Barrena and R. Mysyk. Review on supercapacitors: Technologies and materials. *Renew. Sustain. Energy Rev.* 2016; 58: 1189–1206.
- [52] F. Beguin and E. Frackowiak, editors. *Supercapacitors Materials, Systems, and Applications*. Wiley-VCH Verlag GmbH & Co. KGaA, Boschstr. 12, 69469 Weinheim, Germany; 2013.
- [53] L. Demarconnay, E. G. Calvo, L. Timperman, M. Anouti, D. Lemordant, E. Raymundo-Pin˜ero, A. Arenillas, J. A. Menéndez and F. Béguin. Optimizing the performance of supercapacitors based on carbon electrodes and protic ionic liquids as electrolytes. *Electrochim. Acta.* 2013; 108: 361–368.
- [54] G. Feng, R. Qiao, J. Huang, S. Dai, B. G. Sumpter and V. Meunier. The importance of ion size and electrode curvature on electrical double layers in ionic liquids. *Phys. Chem. Chem. Phys.* 2011; 13: 1152–1161.
- [55] R. Lin, P.-L. Taberna, S. Fantini, V. Presser, C. R. Pérez, F. Malbosc, N. L. Rupesinghe, K. B. K. Teo, Y. Gogotsi and P. Simon. Capacitive nergy storage from –50 to 100°C using an ionic liquid electrolyte. *J. Phys. Chem. Lett.* 2011; 2(19): 2396–2401.
- [56] V. Ruiz, T. Huynh, S. R. Sivakkumar and A. G. Pandolfo. Ionic liquid–solvent mixtures as supercapacitor electrolytes for extreme temperature operation. *RSC Adv.* 2012; 2: 5591–5598.
- [57] A. J. Rennie, N. Sanchez-Ramirez, R. M. Torresi and P. J. Hall. Ether-bond-containing ionic liquids as supercapacitor electrolytes. *J. Phys. Chem. Lett.* 2013; 4: 2970–2974.
- [58] F. Xu, K. Matsumoto and R. Hagiwara. Phase behavior of 1-dodecyl-3-methylimidazolium fluorohydrogenate salts (C₁₂MIm(FH)(n)F, n = 1.0-2.3) and their anisotropic ionic conductivity as ionic liquid crystal electrolytes. *J. Phys. Chem. B.* 2012; 116(33): 10106–10112.
- [59] H. Gao and K. Lian. Proton-conducting polymer electrolytes and their applications in solid supercapacitors: A review. *RSC Adv.* 2014; 4: 33091–33113.
- [60] R. Sasi, S. Sarojam and S. J. Devaki. High performing biobased ionic liquid crystal electrolytes for supercapacitors. *ACS Sustainable Chem. Eng.* 2016; 4: 3535–3543.
- [61] X. Zhang, L. Wang, J. Peng, P. Cao, X. Cai, J. Li and M. Zhai. A flexible ionic liquid gelled PVA-Li₂SO₄ polymer electrolyte for semi-solid-state supercapacitors. *Adv. Mater. Interfaces.* 2015; 2: DOI: 10.1002/admi.201500267.
- [62] N.-S. Choi, J.-G. Han, S.-Y. Ha, I. Park and C.-K. Back. Recent advances in the electrolytes for interfacial stability of high-voltage cathodes in lithium-ion batteries. *RSC Adv.* 2015; 5: 2732–2748.

- [63] J. B. Goodenough and K.-S. Park. The li-ion rechargeable battery: A perspective. *J. Am. Chem. Soc.* 2013; 135: 1167–1176.
- [64] D. Larcher and J.-M. Tarascon. Towards greener and more sustainable batteries for electrical energy storage. *Nat. Chem.* 2015; 7: 19–29.
- [65] H. Matsumoto, H. Sakaebe, K. Tatsumi, M. Kikuta, E. Ishiko and M. Kono. Fast cycling of Li/LiCoO₂ cell with low-viscosity ionic liquids based on bis(fluorosulfonyl)imide [FSI]. *J. Power Sources.* 2006; 160(2): 1308–1313.
- [66] Y. Shao, F. Ding, J. Xiao, J. Zhang, W. Xu, S. Park, J.-G. Zhang, Y. Wang and J. Liu. Making li-air batteries rechargeable: Material challenges. *Adv. Funct. Mater.* 2013; 23: 987–1004.
- [67] S. Fang, L. Qu, D. Luo, S. Shen, L. Yang and S. Hirano. Novel mixtures of ether-functionalized ionic liquids and non-flammable methylperfluorobutylether as safe electrolytes for lithium metal batteries. *RSC Adv.* 2015; 5: 33897–33904.
- [68] D. R. MacFarlane, M. Forsyth, P. C. Howlett, M. Kar, S. Passerini, J. M. Pringle, H. Ohno, M. Watanabe, F. Yan, W. Zheng, S. Zhang and J. Zhang. Ionic liquids and their solid-state analogues as materials for energy generation and storage. *Nat. Rev. Mater.* 2016. DOI: 10.1038/natrevmats.2015.5.
- [69] A. Luntz. Beyond lithium ion batteries. *J. Phys. Chem. Lett.* 2015; 6(2): 300–301.
- [70] Shalu, V. K. Singh and R. K. Singh. Development of ion conducting polymer gel electrolyte membranes based on polymer PVdF-HFP, BMIMTFSI ionic liquid and the Li-salt with improved electrical, thermal and structural properties. *J. Mater. Chem. C.* 2015; 3: 7305–7318.
- [71] J. Sakuda, E. Hosono, M. Yoshio, T. Ichikawa, T. Matsumoto, H. Ohno, H. Zhou and T. Kato. Liquid-crystalline electrolytes for lithium-ion batteries: Ordered assemblies of a mesogen-containing carbonate and a lithium salt. *Adv. Funct. Mater.* 2015; 25: 1206–1212.
- [72] M. Diaz, A. Ortiz, I. Ortiz. Progress in the use of ionic liquids as electrolyte membranes in fuel cells. *J. Membr. Sci.* 2014; 469: 379–396 .
- [73] S.-Y. Lee, A. Ogawa, M. Kanno, H. Nakamoto, T. Yasuda, M. Watanabe. Nonhumidified intermediate temperature fuel cells using protic ionic liquids. *J. Am. Chem. Soc. USA,* 2010; 132(28): 9764–9773.
- [74] K. Kordeesch, G. Simader, editors. *Fuel Cells and Their Applications.* VCH; 1996.
- [75] K. D. Kreur, editor. *Handbook of Fuel Cells: Fundamental, Technology & Applications.* Vol. 3 (eds Vielstich, W., Lamm, A. & Gasteiger, H. A.) ed. Wiley; 2003.
- [76] S. Yu, B. C. Benicewicz. Synthesis and properties of functionalized polybenzimidazoles for high-temperature PEMFCs. *Macromolecules.* 2009; 42 (22): 8640–8648.
- [77] C. Yang, P. Costamagn, S. Srinivasan, J. Benziger, A. B. Bocarsly. Approaches and technical challenges to high temperature operation of proton exchange membrane fuel cells. *J. Power Sources.* 2001; 103(1): 1–9.

- [78] M. Yamada and I. Honma. Anhydrous protonic conductivity of a self-assembled acid–base composite material. *J. Phys. Chem. B.* 2004; 108(18): 5522–5526.
- [79] H. Ohno, editor. *Electrochemical Aspects of Ionic Liquids.* John Wiley & Sons, USA. 2011; DOI: 10.1002/0471762512
- [80] M. Díaz, A. Ortiz, M. Vilas, E. Tojo, I. Ortiz. Performance of PEMFC with new polyvinyl-ionic liquids based membranes as electrolytes. *Int. J. Hydrogen Energy.* 2014; 39(8): 3970–3977.
- [81] U. A. Rana, I. Shakir, R. Vijayraghavan, D. R. MacFarlane, M. Watanabe, M. Forsyth. Proton transport in acid containing choline dihydrogen phosphate membranes for fuel cell. *Electrochim. Acta.* 2013; 111: 41–48.
- [82] J.-P. Belieres, D. Gervasio, C. A. Angell. Binary inorganic salt mixtures as high conductivity liquid electrolytes for >100°C fuel cells. *Chem. Commun.* 2006; 4799–4801.
- [83] R. Hagiwara, T. Nohira, K. Matsumoto, Y. Tamba. A fluorohydrogenate ionic liquid fuel cell operating without humidification. *Electrochem. Solid-State Lett.* 2005; 8: A231–A233.
- [84] P. Kiatkittikul, T. Nohira, R. Hagiwara. Nonhumidified fuel cells using N-ethyl-N-methylpyrrolidinium fluorohydrogenate ionic liquid-poly(vinylidene fluoride-hexafluoropropylene) composite membranes. *Energies.* 2015; 8: 6202–6214. DOI: 10.3390/en8066202.
- [85] B. O'Regan and M. Gratzel. A low-cost, high-efficiency solar cell based on dye-sensitized colloidal TiO₂ films. *Nature.* 1991; 353: 737–740.
- [86] Y. Bai, J. Zhang, Y. Wang, M. Zhang and P. Wang. Lithium-modulated conduction band edge shifts and charge-transfer dynamics in dye-sensitized solar cells based on a dicyanamide ionic liquid. *Langmuir.* 2011; 27: 4749–4755.
- [87] M. Gorlov and L. Kloo. Ionic liquid electrolytes for dye-sensitized solar cells. *Dalton Trans.* 2008; 2655–2666.
- [88] R. Kawano, H. Matsui, C. Matsuyama, A. Sato, Md. A. B. H. Susan, N. Tanabe, M. Watanabe. High performance dye-sensitized solar cells using ionic liquids as their electrolytes. *J. Photochem. Photobiol., A: Chem.* 2004; 164: 87–92.
- [89] S. M. Zakeeruddin and M. Gratzel. Solvent-free ionic liquid electrolytes for mesoscopic dye-sensitized solar cells. *Adv. Funct. Mater.* 2009; 19: 2187–2202.
- [90] V. Armel, J. M. Pringle, M. Forsyth, D. R. MacFarlane, D. L. Officer and P. Wagner. Ionic liquid electrolyte porphyrin dye sensitised solar cells. *Chem. Commun.* 2010; 46: 3146–3148.
- [91] X. Chen, J. Zhao, J. Zhang, L. Qiu, D. Xu, H. Zhang, X. Han, B. Sun, G. Fu, Y. Zhang and F. Yan. Bis-imidazolium based poly(ionic liquid) electrolytes for quasi-solid-state dye-sensitized solar cells. *J. Mater. Chem.* 2012; 22: 18018–18024.
- [92] L. J. Brennan, S. T. Barwich, A. Satti, A. Faure and Y. K. Gunko. Graphene–ionic liquid electrolytes for dye sensitised solar cells. *J. Mater. Chem. A.* 2013; 1: 8379–8384.

- [93] B.-X. Lei, W.-J. Fang, Y.-F. Hou, J.-Y. Liao, D.-B. Kuang, C.-Y. Su. All-solid-state electrolytes consisting of ionic liquid and carbon black for efficient dye-sensitized solar cells. *J. Photochem. Photobiol., A: Chem.* 2010; 216: 8–14.
- [94] D. Hwang, D. Y. Kim, S. M. Jo, V. Armel, D. R. MacFarlane, D. Kim and S.-Y. Jang. Highly efficient plastic crystal ionic conductors for solid-state dye-sensitized solar cells. *Sci. Rep.* 2013; 3. DOI: 10.1038/srep03520.
- [95] P. Wang, S. M. Zakeeruddin, P. Comte, I. Exnar and M. Grätzel. Gelation of ionic liquid-based electrolytes with silica nanoparticles for quasi-solid-state dye-sensitized solar cells. *J. Am. Chem. Soc.* 2003; 125(5): 1166–1167.
- [96] D. Högberg, B. Soberats, S. Uchida, M. Yoshio, L. Kloo, H. Segawa and T. Kato. Nanostructured two-component liquid-crystalline electrolytes for high-temperature dye-sensitized solar cells. *Chem. Mater.* 2014; 26: 6496–6502.
- [97] D. R. MacFarlane, N. Tachikawa, M. Forsyth, J. M. Pringle, P. C. Howlett, G. D. Elliott, J. H. Davis, Jr., M. Watanabe, P. Simon and C. A. Angell. Energy applications of ionic liquids. *Energy Environ. Sci.* 2014; 7: 232–250.
- [98] S. Thiemann, S. J. Sachnov, F. Pettersson, R. Bollström, R. Österbacka, P. Wasserscheid and J. Zaumseil. Cellulose-based ionogels for paper electronics. *Adv. Funct. Mater.* 2014; 24: 625–634.
- [99] S. H. Kim, K. Hong, W. Xie, K. H. Lee, S. Zhang, T. P. Lodge and C. D. Frisbie. Electrolyte-gated transistors for organic and printed electronics. *Adv. Mater.* 2013; 25: 1822–1846.

Physical Properties

Predicting Density and Refractive Index of Ionic Liquids

Mercedes G. Montalbán, Mar Collado-González,
F. Guillermo Díaz-Baños and Gloria Víllora

Additional information is available at the end of the chapter

<http://dx.doi.org/10.5772/65790>

Abstract

The determination of the physicochemical properties of ionic liquids (ILs), such as density and refractive index, is essential for the design of processes that involve ILs. Density has been widely studied in ILs because of its importance whereas refractive index has received less attention even though its determination is rapid, highly accurate and needs a small amount of sample in most techniques. Due to the large number of possible cation and anion combinations, it is not practical to use trial and error methods to find a suitable ionic liquid for a given function. It would be preferable to predict physical properties of ILs from their structure. We compile in this work different methods to predict density and refractive index of ILs from literature. Especially, we describe the method developed by the authors in a previous work for predicting density of ILs through their molecular volume. We also correlate our experimental measurements of density and refractive index of ILs in order to predict one of the parameters knowing the other one as a function of temperature. As the measurement of refractive index is very fast and needs only a drop of the ionic liquid, this is also a very useful approach.

Keywords: ionic liquids, density, refractive index, ionic volume, molecular volume, prediction, correlation

1. Introduction

Ionic liquids (ILs) are organic salts with low melting point so most of them are liquid at room temperature. During the last years, scientists and engineers have shown a huge interest for ILs in research and industrial fields because of their capacity for being chemical and biochemical reaction media. ILs are also of interest because they can be considered a new group of

polar and nonaqueous solvents. Their most important advantage as solvents is that they possess negligible vapor pressure [1]. For that, they are well known as “green solvents” compared to conventional volatile organic compounds (VOCs). Other relevant properties of the ILs are that they are highly stable from the chemical and thermal points of view. However, ILs are mainly valued because of the possibility of modulating their physical and chemical properties, such as melting point, viscosity, density, hydrophobicity and polarity by selecting the appropriate anion and cation and, in this way, they can be used for a specific application. For this reason, some authors have called them “designer solvents.” Hence the number of different combinations of anions and cations that can be chosen to form potential ILs is enormous [2]. Some years ago, Álvarez-Guerra and Irabien [3] claimed that “more than 10^6 different ILs may be synthesized, with 10^{12} binary combinations and 10^{18} ternary systems possible,” while the number of traditional solvents widely used in industry is around a few hundred. The excellent properties of the ILs permit their application in many different fields such as synthesis, catalysis, electrochemistry, separation technology, analytical chemistry and nanotechnology [4].

In order to design processes involving ILs, it is essential to determine and understand some of their physicochemical properties, such as density and refractive index [5]. On the one hand, density of ILs is related to the mechanics and engineering components of a process and is usually used to determine parameters like rates of liquid-liquid phase separation, mass transfer, power requirements of mixing and pumping and equipment sizing [6]. In fact, density of ILs is necessary to solve material or energy balance equations of chemical processes in industry [7]. On the other hand, refractive index of ILs is more linked to specific chemical properties like the structuredness, polarity and relative hydrogen bonding donating and accepting ability which help to determine solubilities, partition constants and reaction rates [8]. In general, refractive index of a compound is especially used to verify a material and check its purity, or to determine the concentration of a mixture. It is also related to the forces between molecules or their behavior in solution [9] and can be easily correlated with certain properties of the material such as the dielectric constant, density and surface tension by means of thermodynamic equations [10].

We compile in this chapter different methods to predict density and refractive index of ILs from the literature. Especially, we describe the method developed by the authors in a previous work for predicting density of ionic liquids through their molecular volume. We also correlate our experimental measurements of density and refractive index for a set of ionic liquids in order to predict one of the parameters knowing the other one as a function of temperature [6].

2. Prediction methods of density of ionic liquids

Density (ρ) is defined as the mass (m) per volume unit (V), $\rho = m/V$, and is one of the most relevant physical properties of a chemical compound.

As it has been mentioned before, nowadays the possible number of combinations of cation/anion to form ILs is huge. For this reason, it is almost impossible to measure experimentally

the density of all the feasible ILs. In addition, it is not worthwhile to use trial and error methods to find the suitable IL for a specific application. Therefore, developing reliable predictive methods and correlations to estimate the density of ILs in a wide range of temperature is essential. Furthermore, this kind of method allows a better understanding of the influence of the structure of the ILs on the density and on other physicochemical properties [7].

During the last years, authors have developed different methods to estimate density of ILs. We have compiled in this chapter published studies concerning methods to predict or estimate density of ILs according to the classification established by Padászyński and Domańska [7]. Briefly, some authors have used methods based on quantitative structure-property relationships (QSPRs) [11–15] and on artificial neural networks (ANNs) [16–18]. Other authors have developed estimation methods for density of ILs by adopting equation of state (EoS) [19–29]. There are also some studies in which the estimation of density of ILs is carried out by group contribution methods (GCMs) [6, 7, 10, 30–37] and correlations between density and other properties such as refractive index, molar refraction or surface tension [6, 38–42]. In order to improve the predicting capabilities, it is usual to find in the literature a combination of methods included in different categories of this classification.

2.1. Estimation by quantitative structure-property relationships (QSPRs)

A QSPR model is a mathematical model that links the structure-derived features of a chemical compound to a physicochemical property. They are based on quantum chemistry calculations. This is their great advantage and, at the same time, their main drawback. While virtually any imagined compound can be studied with no previous experimental knowledge, usually the calculations are not easy and only can be developed by very specialized research groups.

In the literature, we can find several QSPR models to predict density of ILs. Trohalaki et al. [13] developed a QSPR model by the use of CODESSA software. They use three types of descriptors (electrostatic, quantum mechanical and thermodynamic) in order to predict the density of triazolium-based ILs. Palomar et al. [15] determined the density of 40 imidazolium-based ILs using COSMO-RS. In this model, thermodynamic data are obtained from the molecular surface polarity of the individual compounds of the mixture. A year later, they combined COSMO-RS with ANN to get a computational approach with a new descriptor which was useful to simulate the density of 45 imidazolium-based ILs [14]. Interestingly, this approach allows them to propose a design strategy which introduces the desired IL properties as input into inverse neural networks to obtain a selection of counterions. Lazzús [18] used a QSPR model with 11 descriptors based on semiempirical calculations to estimate the density of ILs as a function of temperature and pressure. Specifically, the range of temperature and pressure was 258–393 K and 0.09–207 MPa, respectively. Finally, El-Harbawi et al. [11] proposed a new QSPR model using MATLAB™ software for the development of the algorithm and the same molecular descriptors used by Shen et al. [24]. The code was written based on a combination of multiple linear regression and polynomial equation.

2.2. Estimation by artificial neural networks (ANNs)

ANN is an especially efficient computer algorithm to approximate any function with a finite number of discontinuities by learning the relationships between input and output vectors [43]. ANNs are usually suitable to model chemical properties whose behavior is highly nonlinear because nonlinear relationships are well described with ANN. The predicting capabilities of this method depend on the quality of the algorithm for learning and very importantly on the quality, quantity and nature of experimental (or calculated) data used for the learning process. Some authors have developed approaches to estimate density of ILs based on ANN combined with a GCM.

Properties of chemical compounds like boiling point, critical temperature, critical pressure, vapor pressure, heat capacity, enthalpy of sublimation, heat of vaporization, density, refractive index, surface tension, viscosity, thermal conductivity, and acentric factor have been analyzed by ANN in the literature [44]. For instance, Valderrama et al. [17] proposed a combined GCM + ANN method which divides the molecule in defined groups but instead of determining the value of the group contributions, an ANN is used to get the relationship between the dependent and independent variables. In this way, the relationship between density and molecular structure was determined. Lazzús [16] also proposed in a first paper another combined (GCM + ANN) method, which uses a feedforward backpropagation neural network. It is shown that this network is very efficient in representing nonlinear relationships among properties. Specifically, the network, which was programmed with the software MATLAB, consists of a multilayer network, in which the flow of information spreads forward through the layers while the propagation of the error is back. In this way, he predicted the density of 72 ILs as a function of temperature and pressure. Later, Lazzús [18] published the estimation results obtained with another similar model replacing standard backpropagation with particle swarm optimization (PSO) because some authors had shown that PSO-based ANN led to a better training performance and predicting capacity and a faster convergence rate than the standard backpropagation algorithm. Briefly, PSO is a population-based optimization tool, where the system is initialized with a population of random particles and the algorithm searches for optima by updating generations [45]. In a PSO system, each particle is “flown” through the multidimensional search space, adjusting its position in search space according to its own experience and that of neighboring particles. The particle therefore makes use of the best position encountered by itself and that of its neighbors to position itself toward an optimal solution. The performance of each particle is evaluated using a predefined fitness function, which encapsulates the characteristics of the optimization problem [46].

2.3. Estimation by equation of state (EoS)

Equations of state are well known for determining the relationship between pressure, temperature, volume and composition of components providing a theoretical way to calculate some physical properties such as density. Therefore, some equations of state have been used to estimate density of ILs in the literature. Usually the proposed EoS contains some constants whose values have been obtained by previous fitting of the available experimental results. The main advantage is the simplicity in the use of these methods but a possible drawback is that

to obtain the density of the desired compound usually some previous experimental (or calculated) data of certain critical properties (temperature, pressure, volume, ...) are needed.

Goharshadi and Moosavi [19] proposed a simple EoS (called GMA EoS) to predict the density of phosphonium and imidazolium-based ILs at different temperatures and pressures. Valderrama and Zarricueta [21] used ten expressions based on the corresponding state principle to estimate the density of ILs and analyzed one of them in depth to obtain a new generalized, accurate and simple model using only the critical properties and the molecular weight of the ionic liquid. As several authors have claimed that the dependence between density and temperature is linear, the proposal of Valderrama and Zarricueta was to linearize the Valderrama and Abu-Sharkh model [47] to end up with a simple and totally predictive model, the linear generalized model, to estimate the density of ILs with acceptable accuracy.

Ji and Adidharma [26] modeled the density of three families of ILs ($[C_n\text{mim}][\text{Tf}_2\text{N}]$, $[C_n\text{mim}][\text{BF}_4]$ and $[C_n\text{mim}][\text{PF}_6]$) in a wide temperature and pressure range by the usage of a model published in previous works [48–50]. Specifically, this model uses a heterosegmented statistical associating fluid (hetero-SAFT) equation of state which can predict the properties of an ionic liquid based on the information of its alkyl substituent, cation head and anion. However, this model does not taken into account the electrostatic interactions. On the contrary, Wang et al. [23, 27] included an electrostatic term to residual Helmholtz energy expressed by mean spherical approximation (MSA) and they improved the results.

Abildskow et al. [22] used the statistical mechanical fluctuation solution theory to develop two models which provide a direct connection between integrals of the molecular direct correlation function and isothermal derivatives of pressure and density. In this way, they can predict densities of ILs at elevated pressures.

Shen et al. [24] extended the Valderrama and Robles [51] group contribution model for the critical properties to the estimation of densities of ILs at different temperatures and pressures representing the critical properties by the modified the Lydersen-Joback-Reid group contribution method and predicting the density by the Patel-Teja (PT) equation of state.

Patel and Joshipura [25] used a simple correlation presented by Nasrifar and Moshfeghian [52] in conjunction with the predictive-Soave-Redlich-Kwong (PSRK) equation of state to estimate density of ILs.

More recently, Mahboub and Farrokhpour [28] developed a molecular modeling of ILs incorporating the perturbed thermodynamic linear Yukawa isotherm regularity (LYIR) equation of state, which is derived based on an effective nearest neighboring pair attractive interaction of the Yukawa potential. They used this model to predict the densities of ILs up to high pressures (35 MPa) and in the temperature range 293.15–393.15 K. To use the LYIR for ILs, a simple molecular model was proposed to describe their molecular structure, in which they were considered as a liquid consisting of the ion pairs moving together in the fluid, and each ion pair was assumed to be a one-center spherical united atom. Farzi and Esmaeilzadeh [29] used the Esmaeilzadeh-Roshanfekar EoS obtained in a previous paper [53] to predict density of ILs. This EoS is based on the Patel-Teja EoS and Peng-Robinson EoS and offer better results than these two equations especially near the critical areas.

2.4. Estimation by group contribution methods (GCMs)

Other authors have preferred to develop GCMs to estimate the density of ILs. First of all, we will revise briefly the published studies in the literature and after that we will detail our own predictive method based on a GCM. In these methods, the desired property is obtained as individual contribution of each of the components of the final compound. Then, predictions are obtained using available simple equations. The main drawback of these methods is that their predictive capability depends on previous experimental (or calculated) data. With some exceptions, it is impossible to predict density if no data are available for both of the components of an ionic liquid. On the other hand, usually good predictions can be obtained very easily for any combination of known counterions in a few minutes.

Slattery et al. [32] supported that a strong relationship exists between molecular volumes and density. Thus they described this relationship and predict the density of ILs only from their molecular volumes and an anion-dependent correlation. They considered the molecular volume as the sum of the individual contributions of the anion and the cation. Ye and Shreeve [36] widened a predictive method proposed by Jenkins et al. [54] for estimation of thermochemical radius and closed packed volume of single ions and used it as GCM for ILs. The method provided good density prediction results but, unfortunately, is limited to room temperature and ambient pressure. To solve this disadvantage, Gardas and Coutinho [31] extended this method estimating three coefficients independent of the ionic liquid which take into account the influence of temperature and pressure on the molecular volume. In this way, they can predict the density of ILs in a wide range of temperature (273.15–393.15 K) and pressure (0.10–100 MPa). Jacquemin et al. [34, 35] studied the suitability of GCMs to predict density of ILs. The study was based on an assumption proposed by Rebelo et al. [55, 56] that the molar volume of the ILs can be obtained from the effective molar volumes of the ions considering the ionic liquid as an “ideal” mixture. Qiao et al. [30] introduced the interaction between several substitutes on the same center in the partition of groups. For that, the same group structure attached to different substitutes may have different group values. Padiuszyński and Domańska [7] proposed a simple and generalized correlation to estimate the density of ILs as a function of temperature and pressure. They divided the ILs in 177 functional groups which are classified in three subgroups: cation cores, anion cores and substituents. In this way, they obtained the group contributions to molar volume for each of the functional groups and the universal coefficients describing the relationship pressure-density-temperature. Lately, Keshavarz et al. [37] provided a simple correlation to predict density of ILs based on their size, structure and types of cations and anions. They introduced two correcting terms which take into account the effect that some specific cations and anion may have in the ionic packing leading to its increase or decrease and hence affect to the density values. Finally, Kermanioryani et al. [33] found new group contribution parameters using the Gardas and Coutinho model [31] to predict the density of ILs more accurately.

Recently, we have proposed our own method to predict density of ILs [6]. It can be considered as a GCM and it is based on the prediction of the molecular volume of ILs from the ionic volume. It will be described in detail in the following paragraphs.

<i>T</i> /K	V_m/nm^3	$\alpha_p \times 10^{-4}/\text{K}^{-1}$	V_m/nm^3	$\alpha_p \times 10^{-4}/\text{K}^{-1}$	V_m/nm^3	$\alpha_p \times 10^{-4}/\text{K}^{-1}$
	[emim⁺][BF₄⁻]		[bmim⁺][BF₄⁻]		[hmim⁺][BF₄⁻]	
293.15	0.2561	5.93	0.3119	5.96	0.3676	6.06
303.15	0.2577		0.3134		0.3698	
313.15	0.2592		0.3152		0.3721	
323.15	0.2607		0.3171		0.3744	
333.15	0.2623		0.3190		0.3766	
343.15	0.2638		0.3209		0.3789	
	[omim⁺][BF₄⁻]		[emim⁺][TfO⁻]		[bmim⁺][TfO⁻]	
293.15	0.4234	6.14	0.3112	6.08	0.3691	6.19
303.15	0.4260		0.3131		0.3714	
313.15	0.4286		0.3150		0.3737	
323.15	0.4313		0.3169		0.3760	
333.15	0.4339		0.3189		0.3784	
343.15	0.4366		0.3208		0.3808	
	[bmim⁺][OCSO₄⁻]		[bmim⁺][PF₆⁻]		[hmim⁺][PF₆⁻]	
293.15	0.5401	6.09	0.3442	6.13	0.3996	6.14
303.15	0.5434		0.3463		0.4021	
313.15	0.5467		0.3485		0.4045	
323.15	0.5500		0.3506		0.4070	
333.15	0.5534		0.3528		0.4096	
343.15	0.5568		0.3549		0.4121	
	[omim⁺][PF₆⁻]		[emim⁺][NTf₂⁻]		[bmim⁺][NTf₂⁻]	
293.15	0.4556	6.18	0.4264	6.65	0.4834	6.72
303.15	0.4584		0.4292		0.4866	
313.15	0.4612		0.4321		0.4903	
323.15	0.4641		0.4349		0.4933	
333.15	0.4670		0.4378		0.4966	
343.15	0.4699		0.4408		0.5003	
	[hmim⁺][NTf₂⁻]		[omim⁺][NTf₂⁻]		[emim⁺][EtSO₄⁻]	
293.15	0.5397	6.71	0.5959	6.78	0.3160	5.47
303.15	0.5434		0.5999		0.3177	
313.15	0.5470		0.6040		0.3195	
323.15	0.5507		0.6081		0.3212	
333.15	0.5544		0.6122		0.3230	
343.15	0.5581		0.6164		0.3248	

Table 1. Experimental values of molecular volume, V_m , and thermal expansion coefficient, α_p , of the studied ILs at temperatures T ranging from 293.15 to 343.15 K at pressure $p = 0.1$ MPa.

It is known that volume is more informative about structure and packing efficiency than density, and the conclusions and predictions obtained for volume can be immediately translated to density values. The molecular volume V_m (or formula-unit volume) of a salt is a physical observable and is defined as the sum of the ionic volumes, V_{ion} , of the constituent ions [32]. For a binary ionic liquid, V_m is given by:

$$V_m = V_{cat} + V_{an} \quad (1)$$

If we define the molecular volume (V_m) as

$$V_m = (M_w / \rho) / N_A \quad (2)$$

In Eq. (2), where M_w is the molecular weight and N_A is Avogadro's constant, we can study the influence in V_m (see **Table 1** for numerical values) of the characteristics of the ions.

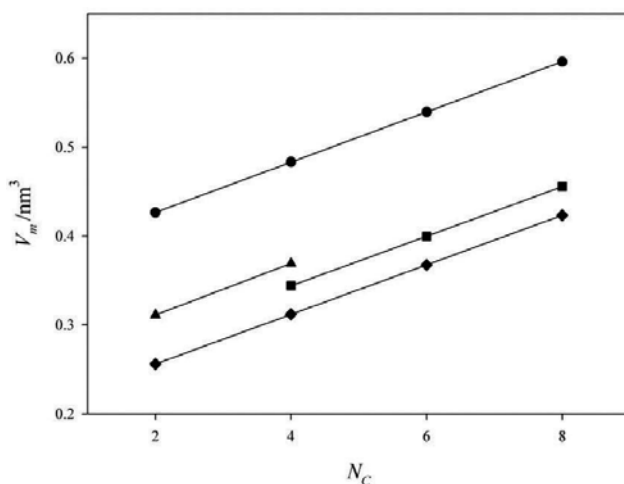


Figure 1. Dependence of the ILs' molecular volume V_m at 293.15 K on the alkyl chain length of the cation. ● [NTf₂⁻], linear fitting: $V_m = 0.3702 + 0.02823 N_C$, $r^2 = 0.99998$; ▲ [TfO⁻], linear fitting: $V_m = 0.2533 + 0.02895 N_C$, $r^2 = 1$; ■ [PF₆⁻], linear fitting: $V_m = 0.2327 + 0.02785 N_C$, $r^2 = 0.99999$; ◆ [BF₄⁻], linear fitting: $V_m = 0.20035 + 0.02788 N_C$, $r^2 = 0.99999$.

Regarding the cations, our data (see **Figure 1** and **Table 1**) reveal a linear increase of V_m with increasing alkyl chain length, and so, with the volume of the cation. From the slope of the linear fit to dV_m/dN_C , with N_C being the number of carbons of the imidazolium alkyl chain, the volume of one methylene group ($-\text{CH}_2-$) is calculated to be $0.0281 \pm 0.0004 \text{ nm}^3$ (between 0.0279 and 0.0289 nm^3) at 293.15 K, corresponding to a molar volume of $17 \text{ cm}^3 \text{ mol}^{-1}$. These values agree well with the calculations of Kolbeck et al. [57] (0.0283 nm^3), Glasser [58] (0.0272 – 0.0282 nm^3) and Tariq et al. [39] ($17 \text{ cm}^3 \text{ mol}^{-1}$) at 298.15 K. Therefore, according to our results the increase in V_m per added methylene group is always the same, irrespective of the nature of the anion

of the ionic liquid, and, as a consequence, the volume that the cation occupies varies linearly with the number of carbons. Then, we can conclude that the length of the chain does not change significantly the interaction between ions or the packing efficiency of cations.

IL	$M_w/\text{g}\cdot\text{mol}^{-1}$	$M_{Wanion}/\text{g}\cdot\text{mol}^{-1}$	V_{an}/nm^3	$\rho_{an}/\text{g}\cdot\text{mol}^{-1}\cdot\text{nm}^{-3}$
[emim ⁺][NTf ₂ ⁻]	391.31	280.133	0.270	1035.995
[bmim ⁺][NTf ₂ ⁻]	419.37		0.287	976.073
[hmim ⁺][NTf ₂ ⁻]	447.43		0.298	940.991
[omim ⁺][NTf ₂ ⁻]	475.47		0.308	909.818
[bmim ⁺][PF ₆ ⁻]	284.18	144.961	0.148	978.144
[hmim ⁺][PF ₆ ⁻]	312.24		0.158	919.803
[omim ⁺][PF ₆ ⁻]	340.29		0.168	864.922
[emim ⁺][TfO ⁻]	260.23	149.062	0.155	960.451
[bmim ⁺][TfO ⁻]	288.29		0.173	861.132
[emim ⁺][BF ₄ ⁻]	197.97	86.802	0.100	867.153
[bmim ⁺][BF ₄ ⁻]	226.02		0.116	748.939
[hmim ⁺][BF ₄ ⁻]	254.08		0.126	691.099
[omim ⁺][BF ₄ ⁻]	282.13		0.135	641.078
[emim ⁺][EtSO ₄ ⁻]	236.29	125.126	0.160	782.037
[bmim ⁺][OCSO ₄ ⁻]	348.50	209.280	0.344	608.372

Table 2. The molecular weight of the ionic liquid (M_w), molecular weight of the anion (M_{Wanion}), volume (V_{an}), and density of the molecular volume not occupied by the cation (ρ_{an}) for all investigated ILs obtained from the method proposed by Slattery et al. [32] for a temperature (T) of 293.15 K at pressure $p = 0.1$ MPa.

We can study the effect of the volume of the ion in the global V_m . The ionic volume is a measure of the size of an ion, equally valid for symmetrical and nonsymmetrical ions. But, to obtain quantitatively the volume of the constituents in an ionic liquid is not a trivial task. One way is to define the contribution of one of the ions to the molecular volume and, from Eq. (1), to obtain the other ionic volume. To do so, Slattery et al. [32] have proposed to derive the volume of the cation from crystal structures (e.g., the CCDC Database) [59] containing the ion of interest in combination with a reference ion of known volume or predicted by the contribution methods proposed by Rebelo et al. [55] and Jacquemin et al. [34, 35]. From the cationic volumes obtained by Slattery et al. [32] and our experimental molecular volume for each temperature, it is possible to assess the fraction of the molecular volume not occupied by the cation, V_{an} , and the density of it, ρ_{an} ($\rho_{an} = M_{Wanion}/V_{an}$). The values of V_m , M_w , M_{Wanion} , V_{an} and ρ_{an} are reported in **Table 2**. We think that this is not a good approximation. Ionic volume assigns a certain fraction of the total molecular volume to one of the ions. When doing so, the ionic volume is a measure not only of the volume of the actual molecular structure of the ion, but also of the interionic separation. This interionic separation must be the consequence of the interactions between

ions, mainly due to electrostatic attraction, but also of geometry of their molecular structures, their polarizability, their ability to establish some other type of interactions (i.e., hydrogen bond) and other factors. Then, it is not plausible to assume that the volume of the cation is not affected by the anion in front (like it is proposed in this method), and, at the same time, to assume that the volume of the anion changes with the cation in a very significant amount (i.e., from **Table 2**, for $[\text{BF}_4^-]$ we find a 35% increase from $[\text{emim}^+]$ to $[\text{omim}^+]$). Another question is that in this treatment the effect of temperature on the ionic volumes is not clear. Clearly, if we assume that molecular structure (i.e., covalent bonds) are temperature-independent in a certain temperature range, but an increment in T decreases density (and increases V_m), then the increment in ionic volumes should mean that the interionic distances increase. Following our argument, if there is no change in molecular structure that justifies a significant change in the geometry of packing, the main reason for the increase in the interionic distance should be a decrease in the strength of interaction, what should have other known consequences as the decrease in viscosity.

We now propose an alternative way to assign the ionic volume, and so to explain the experimental results of density. Volume of a given chemical structure can be theoretically calculated. We used the web page chemicalize.org [60] to obtain the van der Waals volume of the ions studied. This volume is not comparable with the ionic volume, because it only takes into account the isolated molecular structure and it is independent of the temperature. We propose below a way to assign the ionic volumes from the theoretically calculated volumes of the components and the experimental measurements of density, which takes into account the effect of temperature.

Cation	Structural volume/nm ³ (theoretical)	Ionic volume/nm ³ (this work)	Ionic volume/nm ³ (Slattery et al. [32])
$[\text{emim}^+]$	0.11553	0.19142	0.156
$[\text{bmim}^+]$	0.14945	0.24762	0.196
$[\text{hmim}^+]$	0.18341	0.30388	0.242
$[\text{omim}^+]$	0.21735	0.36012	0.288

Table 3. Volume of molecular structure from theoretical calculation (structure volume), ionic volume proposed in this work and ionic volume proposed by Slattery et al. [32] for the alkyl methylimidazolium cations present in the ILs studied in this work at 293.15 K at pressure $p = 0.1$ MPa.

From the values of the theoretical van der Waals volume obtained for the set of alkyl methylimidazolium cations used in this work (see **Table 3**), it is straightforward to assign a molecular volume to one methylene group ($-\text{CH}_2-$), $V_{(\text{CH}_2)\text{Theo}} = 0.01697 \pm 0.00001$ nm³. If we compare with the value obtained from experimental values of density at 293.15 K, $V_{(\text{CH}_2)\text{Density}} = 0.0281 \pm 0.0004$ nm³, the increment is 65.7%. In our hypothesis, this increment includes the fraction corresponding to the cation of interionic distance. Given that this increment is the same regardless of the length of the alkyl chain of the cation or the anion in front, it is reasonable to assume that this increment is approximately the same for the theoretically calculated volume of the whole molecule, which allows us to assign a ionic volume of the cation.

For comparison purposes, **Table 3** includes ionic volume for the cations used in this work proposed by Slattery et al. [32]. Their values are systematically lower than ours. In addition they propose a $V_{-CH_2-} = 0.023 \text{ nm}^3$, lower than ours and others found in the literature (see above). While Slattery et al. [32] proposed a constant absolute increment of ionic volume, we propose a constant percentual increment of ionic volume with alkyl chain length.

Using Eq. (1), we can obtain the ionic volume occupied by the anions at 293.15 K (see **Table 4**).

Anion	Structural volume/nm ³ (theoretical)	Ionic volume/nm ³ (this work)	% increment
[BF ₄ ⁻]	0.05420	0.0634 ± 0.0008	17
[PF ₆ ⁻]	0.07135	0.0952 ± 0.0007	33
[TfO ⁻]	0.08520	0.1201 ± 0.0010	41
[EtSO ₄ ⁻]	0.09639	0.1242	29
[NTf ₂ ⁻]	0.15671	0.2349 ± 0.0002	50
[OcSO ₄ ⁻]	0.19820	0.2919	47

Table 4. van der Waals volume of molecular structure from theoretical calculation (structural volume) and ionic volume proposed in this work for anions present in the ILs studied at 293.15 K at pressure $p = 0.1 \text{ MPa}$.

We find various advantages in this procedure. First, we are able to obtain a plausible ionic volume for the anions participating in the ionic liquid studied. Our results show that the ionic volume of the anion is not affected significantly by the length of the alkyl chain of the cation.

The second consequence of our approximation is that there is a very good correlation between the molecular volume with both, volume of the cation and also with the volume of the anion.

Indeed, in **Figure 2**, we observe that volume of the anion is the fundamental factor to determine the molecular volume (the higher the volume of the anion, the higher V_m). According to theoretical calculations (**Table 4**), the order of volumes is: [OcSO₄⁻] > [NTf₂⁻] > [EtSO₄⁻] > [TfO⁻] > [PF₆⁻] > [BF₄⁻]. As we mentioned before, it is very likely that some other factors (geometry of the anion, distribution of charge,...) have some influence in the global volume, but according to our results their importance is smaller than the volume of the anion. These data explain the trend observed in the experimental values of the density.

Using our treatment, we can obtain the increment of anionic volume with respect to the theoretical volume of the molecular structure (**Table 4**). This increment takes into account interionic distances and effect of temperature and could be taken as a measure of the packing quality. If we assume this idea, we conclude that packing quality is higher for small molecules, but when the size of the anion becomes similar to the cation, the packing quality decreases, reaches a certain level and probably other factors than volume become significant.

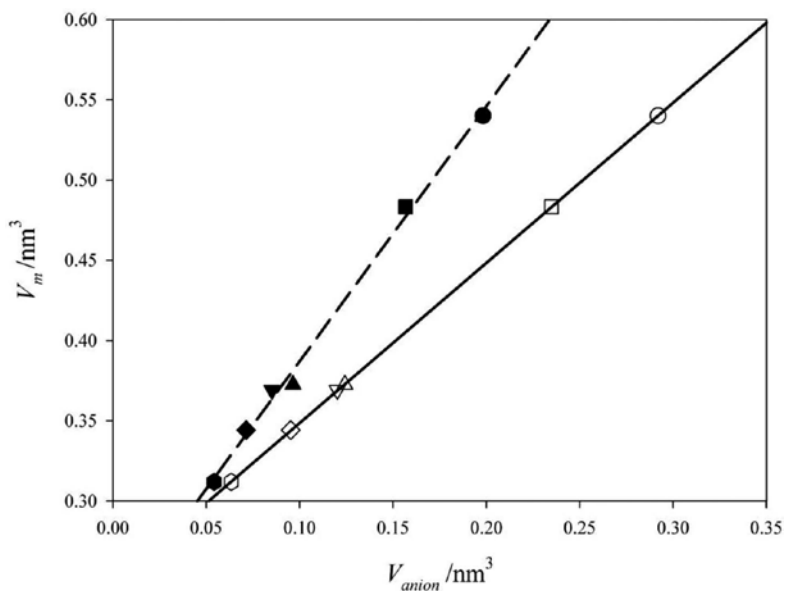


Figure 2. Molecular volume at 293.15 K of ILs based on [bmim⁺] versus volume of anion. ● [OCSO₄⁻]; ■ [NTf₂⁻]; ▲ [EtSO₄⁻]; ▼ [TfO⁻]; ◆ [PF₆⁻]; ● [BF₄⁻]. V_m for [bmim⁺][EtSO₄⁻] is not measured but predicted. Full symbols are for van der Waals theoretically calculated anionic volume. Empty symbols are for our proposed ionic volume obtained from averages over experimental measurements of density (Table 4). In this plot, standard deviations are smaller than symbols. Fitting results: - - - theoretical volume $V_m = 1.592 V_{an} + 0.2279 \text{ nm}^3$, $r^2 = 0.9956$. — — — ionic volumes $V_m = 0.9980 V_{an} + 0.2489 \text{ nm}^3$, $r^2 = 0.99999$.

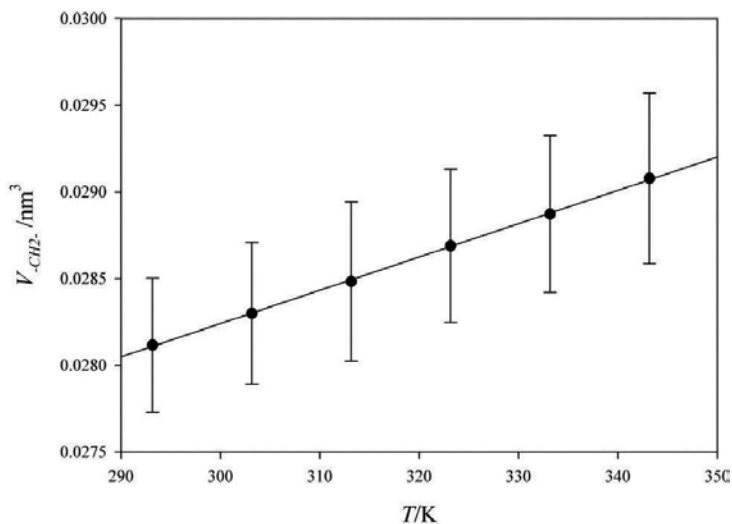


Figure 3. Dependence of the ionic volume of $-\text{CH}_2-$ ionic (obtained from density experimental values) on temperature. All numerical data can be found in Table 6. Linear fit: $V_{-\text{CH}_2-} = 0.02247 + 1.922 \times 10^{-5} T$; $r^2 = 0.9996$.

Finally, this treatment allows us to predict with high accuracy the densities of all the combinations at all temperatures of these anions and cations by obtaining molecular volumes of ILs after assigning proper ionic volumes to its constituents. Indeed, following the method we have used for $T = 293.15$ K for the rest of temperatures studied, we obtain (see **Figure 3**) a linear dependence $V_{CH_2} = 1.922 \times 10^{-5} T + 0.02247 \text{ nm}^3$ ($r^2 = 0.9996$) of the ionic volume of CH_2 with temperature (numerical values in **Table 5**).

<i>T</i> /K	Ionic volume/nm ³	S.D.	% increase
293.15	0.0281	0.0004	65.7
303.15	0.0283	0.0004	66.8
313.15	0.0285	0.0005	67.8
323.15	0.0287	0.0004	69.1
333.15	0.0289	0.0005	70.1
343.15	0.0291	0.0005	71.3

% increase = $32.83 + 0.112 T$; $r^2 = 0.9990$.

Table 5. Effect of temperature (T) on ionic volume of $-CH_2-$ and % of increase over theoretically calculated van der Waals volume.

Knowing this quantitative dependence the ionic volume of alkyl imidazolium cations with different alkyl chain lengths can be properly assigned for any temperature. We propose the following equation:

$$V_{al-imid} = V_{al-imid-theo} (1.328 + 1.120 \times 10^{-3} T) \quad (3)$$

Or in terms of number of carbons

$$V_{al-imid} = (0.08159 + 0.01697 N_C) (1.328 + 1.120 \times 10^{-3} T) \quad (4)$$

In Eq. (3), $V_{al-imid}$ is the ionic volume of any alkyl imidazolium cation and $V_{al-imid-theo}$ is the calculated theoretical van der Waals volume, both in nm³. In Eq. (4), N_C is the number of carbons and T is the temperature in Kelvin. Although the limits of validity should be established it is likely that the range of application of these equations is rather broad.

Regarding the dependence of the ionic volumes of the anions studied in this work on temperature, in all cases we find a very good linear dependence, with a tendency to higher slopes for higher ionic volumes (see **Figure 4** and **Table 6** for numerical values). From our results, the ionic volume of these ions can be predicted for any temperature:

$$V_{BF_4} = V_{BF_4theo} (1.083 + 0.365 \times 10^{-3} T) = 0.0587 + 1.98 \times 10^{-5} T \quad (5)$$

$$V_{PF_6} = V_{PF_6theo} (1.171 + 0.596 \times 10^{-3} T) = 0.0835 + 4.25 \times 10^{-5} T \quad (6)$$

$$V_{NTf_2} = V_{NTf_2theo} (1.201 + 1.032 \times 10^{-3} T) = 0.1882 + 16.17 \times 10^{-5} T \quad (7)$$

$$V_{TfO} = V_{TfOtheo} (1.200 + 0.738 \times 10^{-3} T) = 0.1022 + 6.29 \times 10^{-5} T \quad (8)$$

$$V_{EtSO_4} = V_{EtSO_4theo} (1.156 + 0.468 \times 10^{-3} T) = 0.1114 + 4.51 \times 10^{-5} T \quad (9)$$

$$V_{OctSO_4} = V_{OctSO_4theo} (1.233 + 0.829 \times 10^{-3} T) = 0.0835 + 16.44 \times 10^{-5} T \quad (10)$$

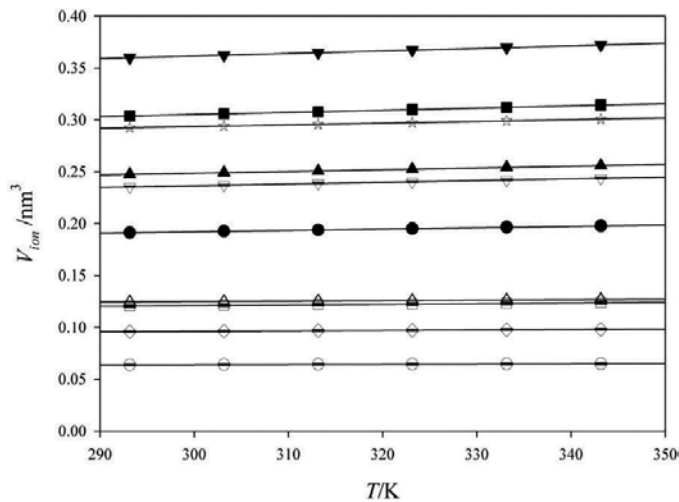


Figure 4. Ionic volume (V_{ion}) versus temperature (T). This figure shows the linear dependence of ionic volume on temperature, which is higher for bigger structures. All numerical data (including fitting parameters) can be found in **Table 6**. ● [emim⁺]; ▲ [bmim⁺]; ■ [hmim⁺]; ▼ [omim⁺]; ○ [BF₄⁻]; ▽ [NTf₂⁻]; □ [TfO⁻]; ▲ [EtSO₄⁻]; ◇ [PF₆⁻]; ★ [OcSO₄⁻].

In Eqs. (5–10), V_{anion} is the ionic volume of each anion and $V_{anion-theo}$ is the calculated theoretical van der Waals volume, both in nm³. T is the temperature in Kelvin.

To check our procedure we have compared the calculated densities from Eqs. (1–10) with our experimental values and some others found in the literature [34, 39, 40, 61–68]. As an illustration, some results are plotted in **Figure 5** (see also **Tables 7** and **8** for numerical values).

T/K	[emim ⁺]	[bmim ⁺]	[hmim ⁺]	[omim ⁺]	[BF ₄ ⁻]	[NTf ₂ ⁻]	[TfO ⁻]	[EtSO ₄ ⁻]	[PF ₆ ⁻]	[OctSO ₄ ⁻]
293.15	0.1914	0.2476	0.3039	0.3601	0.0640	0.2356	0.1206	0.1246	0.0959	0.2925
303.15	0.1927	0.2492	0.3059	0.3625	0.0642	0.2372	0.1213	0.1250	0.0964	0.2942
313.15	0.1939	0.2508	0.3078	0.3648	0.0644	0.2390	0.1220	0.1256	0.0969	0.2959
323.15	0.1953	0.2527	0.3101	0.3674	0.0645	0.2404	0.1225	0.1259	0.0972	0.2973
333.15	0.1966	0.2543	0.3121	0.3698	0.0648	0.2421	0.1232	0.1264	0.0978	0.2991
343.15	0.1980	0.2506	0.3143	0.3724	0.0649	0.2437	0.1238	0.1268	0.0980	0.3007
$a \times 10^3 / \text{nm}^3 \cdot \text{K}^{-1}$	0.1309	0.1693	0.2078	0.2462	0.0198	0.1617	0.0629	0.0451	0.0425	0.1644
b/nm^3	0.1530	0.1979	0.2829	0.2878	0.0587	0.1882	0.1022	0.1114	0.0835	0.2443
r^2	0.9996	0.9996	0.9996	0.9996	0.9828	0.9994	0.9979	0.9962	0.9924	0.9997

Table 6. Dependence of the ionic volumes (in nm³) of all the ions studied in this work on the temperature (T). Fitting parameters to equation $V_{ion} = aT + b$ are also included.

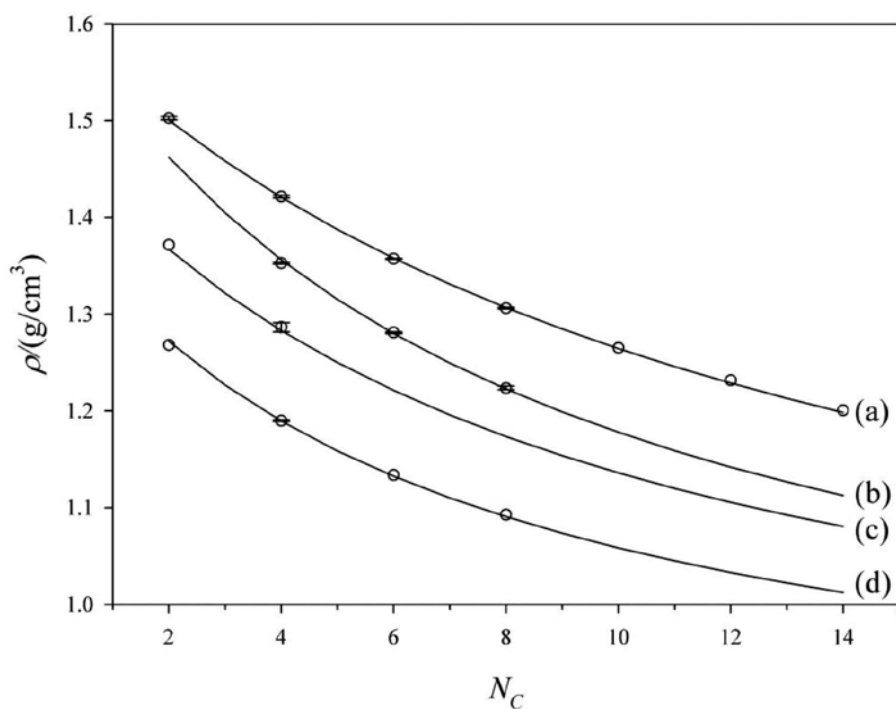


Figure 5. Density at 313.15 K of different ILs versus number of carbons of the alkyl chain of the cation. The anions are: (a) [NTf₂⁻]; (b) [PF₆⁻]; (c) [TfO⁻]; (d) [BF₄⁻]. ○ Experimental (averaged from different sources, see **Table 8** for numerical values); (— — —) predicted from Eqs. (5–10). For experimental values, the error bars are smaller than the size of the symbol.

		$\rho/(g/cm^3)$									
Experimental (different sources)		Exp. Average $\pm \sigma$		Predicted	Error [*]	Error [*]					
[NTf ₂ ⁻]											
[emim ⁺]	1.5238 ¹	1.5197 ²	1.5229 ³	1.5234 ³	1.5260 ⁴	1.5232	0.0023	1.5215	-0.0016	-0.11	
[bmim ⁺]	1.4403 ¹	1.4408 ²	1.4427 ³	1.4402 ³	1.4389 ⁵	1.4405 ⁵	1.4406	0.0012	1.4408	0.0003	0.02
[hmim ⁺]	1.3763 ¹	1.3755 ²	1.3751 ³	1.3754 ⁶	1.3750 ⁶		1.3755	0.0005	1.3770	0.0015	0.11
[omim ⁺]	1.3248 ¹	1.3234 ²	1.3245 ³	1.3281 ⁴			1.3252	0.0020	1.3251	-0.0001	-0.01
[c ₁₀ mim ⁺]		1.2828 ²	1.2824 ³				1.2826	0.0003	1.2821	-0.0005	-0.04
[c ₁₂ mim ⁺]		1.2490 ²					1.2490		1.2459	-0.0031	-0.25
[PF ₆ ⁻]											
[bmim ⁺]	1.3707 ¹	1.3679 ²	1.3698 ³	1.3681 ³	1.3704 ⁵	1.3716 ^{7,8}	1.3698	0.0015	1.3734	0.0036	0.26
[hmim ⁺]	1.2973 ¹	1.2964 ²	1.2979 ^{7,8}				1.2972	0.0008	1.2964	-0.0008	-0.06
[omim ⁺]	1.2402 ¹	1.2378 ²	1.2396 ^{7,8}				1.2392	0.0012	1.2385	-0.0007	-0.06
[BF ₄ ⁻]											
[emim ⁺]	1.2833 ¹						1.2833		1.2869	0.0036	0.28
[bmim ⁺]	1.2031 ¹	1.2029 ²	1.2049 ^{3,9}	1.2038 ³			1.2037	0.0009	1.2041	0.0004	0.04
[hmim ⁺]	1.1475 ¹						1.1475		1.1467	-0.0008	-0.07
[omim ⁺]	1.1064 ¹						1.1064		1.1044	-0.0020	-0.18
[TfO ⁻]											
[emim ⁺]	1.3884 ¹						1.3884		1.3848	-0.0036	-0.26
[bmim ⁺]	1.2966 ^x	1.3035 ²	1.3013 ³	1.2900 ¹⁰			1.2979	0.0060	1.2998	0.0019	0.15

¹This work.
²Tariq et al. [39].
³Jacquemin et al. [34].
⁴Gardas et al. [63].
⁵Troncoso et al. [64].
⁶Łachwa et al. [65].
⁷Pereiro and Rodríguez [66].
⁸Pereiro and Rodríguez [67].
⁹Iglesias-Otero et al. [62].
¹⁰Bonhôte et al. [68].
^x Error, in g/cm³.
^{*} Error, in %.

Table 7. Comparison of predicted (this work) and experimental (different sources) densities (ρ) for different ILs at temperature $T = 293.15$ K at pressure $p = 0.1$ MPa.

$\rho/(\text{g}/\text{cm}^3)$												
Experimental (different sources)					Exp. Average $\pm \sigma$		Predicted	Error*	Error*			
[NTf ₂ ⁻]												
[emim ⁺]	1.5037 ¹	1.4996 ²	1.5029 ³	1.5034 ³	1.5038 ⁴	1.5027	0.0018	1.5005	-0.0022	-0.15		
[bmim ⁺]	1.4202 ¹	1.4216 ²	1.4230 ⁶	1.4198 ⁵	1.4214 ⁵	1.4235 ³	1.4212 ³	1.4215	0.0015	1.4210	-0.0005	-0.04
[hmim ⁺]	1.3580 ¹	1.3572 ²	1.3569 ³	1.3570 ⁶		1.3573	0.0005	1.3581	0.0008	0.06		
[omim ⁺]	1.3070 ¹	1.3055 ²	1.3070 ³	1.3056 ⁴		1.3063	0.0008	1.3070	0.0007	0.05		
[c ₁₀ mim ⁺]		1.2653 ²	1.2653 ³			1.2653	0.0000	1.2646	-0.0007	-0.06		
[c ₁₂ mim ⁺]		1.2318 ²				1.2318		1.2289	-0.0029	-0.23		
[c ₁₄ mim ⁺]		1.2006 ²				1.2006		1.1985	-0.0021	-0.17		
[PF ₆ ⁻]												
[bmim ⁺]	1.3540 ¹	1.3513 ²	1.3533 ³	1.3518 ³	1.3534 ⁵	1.3528 ⁷		1.3528	0.0010	1.3562	0.0034	0.25
[hmim ⁺]	1.2815 ¹	1.2804 ²				1.2810	0.0008	1.2801	-0.0009	-0.07		
[omim ⁺]	1.2250 ¹	1.2224 ²				1.2237	0.0018	1.2227	-0.0010	-0.08		
[BF ₄ ⁻]												
[emim ⁺]	1.2681 ¹					1.2681		1.2721	0.0040	0.31		
[bmim ⁺]	1.1905 ¹	1.1887 ²	1.1901 ³	1.1889 ³	1.1908 ⁶	1.1907 ⁸		1.1900	0.0009	1.1898	-0.0002	-0.01
[hmim ⁺]	1.1337 ¹					1.1337		1.1328	-0.0009	-0.08		
[omim ⁺]	1.0929 ¹					1.0929		1.0908	-0.0021	-0.19		
[TfO ⁻]												
[emim ⁺]	1.3716 ¹					1.3716		1.3673	-0.0043	-0.31		
[bmim ⁺]	1.2808 ¹	1.2877 ²	1.2856 ³	1.2924 ⁷		1.2866	0.0048	1.2832	-0.0034	-0.26		

¹This work.
²Tariq et al. [39].
³Jacquemin et al. [34].
⁴Gardas et al. [63].
⁵Troncoso et al. [64].
⁶Gomes de Azevedo et al. [61].
⁷Soriano et al. [40].
⁸Iglesias-Otero et al. [62].
^{*}Error, in g/cm³.
^{*}Error, in %.

Table 8. Comparison of predicted (this work) and experimental (different sources) densities (ρ) for different ILs at temperature $T = 313.15$ K at pressure $p = 0.1$ MPa.

Tariq et al. [39] showed the experimental density of some ILs composed with combinations of cations and anions not used for our research group. A further test for our method is to predict volumes of these ions. For $T = 293.15$ K, we obtain the volume of methylsulfate ([MeSO₄⁻]) and acetate ([OAc⁻]): $V_{\text{MeSO}_4} = 0.0956 \text{ nm}^3$; $V_{\text{OAc}} = 0.0640 \text{ nm}^3$. The volume of the trihexyl(tetradecyl)phosphonium cation ([P_{6,6,6,14}⁺]) can be obtained from data of three different ILs: [P_{6,6,6,14}⁺][NTf₂⁻]; [P_{6,6,6,14}⁺][TfO⁻]; [P_{6,6,6,14}⁺][OAc⁻]. We obtain $V_{[\text{P}_{6,6,6,14}^+] } = 0.945 \pm 0.002 \text{ nm}^3$. We can see that

although $[P_{6,6,14}^+][OAc^-]$ is formed by two anions not used to obtain the equations proposed in this work, the result obtained is very close to the ones obtained from the other ILs.

To have an idea of the quality of the predictions we can use the average deviation from experimental values. Then, we can compare our values (see **Tables 7** and **8**) with those obtained by Tariq et al. [39]. Those average deviations are between $\sigma_{ave} = 0.21$ and $\sigma_{ave} = 1.29$. Our method gives $\sigma_{ave} = 0.13$.

As a summary, with our results we should be able to predict, prior to synthesis, the density and molecular volumes for IL with alkyl imidazolium cations and with different anions (and very likely combinations of ions of similar chemical structure) in a wide range of temperatures from easily accessible theoretical calculations of the structure of the proposed ions.

2.5. Estimation by correlations between density and other properties

The last approach to estimate density is through correlations between density and other properties. Obviously, no prediction can be obtained if these correlations have not been previously established. But these methods can be especially interesting if the measurement of the property used is easier or cheaper than the measurement of the density. A good example is the refractive index.

There are some authors who have studied the relationship between density and refractive index in order to predict one of the properties from the other one due to the experimental measurement of refractive index only needs a drop of the ionic liquid and it is very fast. However, in the case of density the determination requires higher volumes of ionic liquid and it takes more time. Tariq et al. [39] and Soriano et al. [38, 40] used different empirical models (Lorentz-Lorenz, Dale-Gladstone, Eykman, Oster, Arago-Biot and Newton equations) to predict density of ILs from their refractive index. Other authors such as Deetlefs et al. [41] and Gardas et al. [42] used the parachor to estimate density. Parachor is a surface-tension-weighted molar volume, which constitutes a link between the structure, density and surface tension of the ILs. Deetlefs et al. [41] also used the refraction molar to estimate density.

We detail in the following paragraphs our prediction of the density from the refractive index.

It is known that the density and refractive index (n) were correlated using several empirical equations of the form:

$$f(n) = k\rho \quad (11)$$

where $f(n)$ is a function of the refractive index, k is an empirical constant that depends on the liquid and the wavelength at which the refractive index is measured and ρ is the density of the liquid. The $f(n)$ function is associated with several empirical equations. In this work, we have used the most common equations, those of Lorentz-Lorenz (Eq. (12)), Dale-Gladstone (Eq. (13)), Eykman (Eq. (14)), Oster (Eq. (15)), Arago-Biot (Eq. (16)) and Newton (Eq. (17)), which have also been used by different authors to correlate the density with the refractive index.

$$f(n) = (n^2 - 1) / (n^2 + 2) \tag{12}$$

$$f(n) = (n - 1) \tag{13}$$

$$f(n) = (n^2 - 1) / (n + 0.4) \tag{14}$$

$$f(n) = (n^2 - 1)(2n^2 + 1) / n^2 \tag{15}$$

$$f(n) = n \tag{16}$$

$$f(n) = n^2 - 1 \tag{17}$$

System	L-L	D-G	Eykman	Oster	A-B	Newton
[emim ⁺][BF ₄ ⁻]	0.1948	0.3220	0.4289	1.9418	1.1130	0.7752
[bmim ⁺][BF ₄ ⁻]	0.2125	0.3524	0.4687	2.1276	1.1966	0.8518
[hmim ⁺][BF ₄ ⁻]	0.2251	0.3738	0.4969	2.2585	1.2586	0.9055
[omim ⁺][BF ₄ ⁻]	0.2359	0.3923	0.5212	2.3719	1.3102	0.9523
[emim ⁺][TfO ⁻]	0.1881	0.3128	0.4155	1.8914	1.0442	0.7594
[bmim ⁺][TfO ⁻]	0.2027	0.3375	0.4481	2.0415	1.1208	0.8204
[bmim ⁺][OcSO ₄ ⁻]	0.2620	0.4407	0.5825	2.6791	1.3885	1.0865
[bmim ⁺][PF ₆ ⁻]	0.1813	0.2996	0.3992	1.8059	1.0404	0.7203
[hmim ⁺][PF ₆ ⁻]	0.1947	0.3224	0.4291	1.9450	1.1052	0.7775
[omim ⁺][PF ₆ ⁻]	0.2061	0.3418	0.4546	2.0638	1.1607	0.8263
[emim ⁺][NTf ₂ ⁻]	0.1679	0.2784	0.3703	1.6809	0.9457	0.6729
[bmim ⁺][NTf ₂ ⁻]	0.1789	0.2969	0.3947	1.7933	1.0031	0.7186
[hmim ⁺][NTf ₂ ⁻]	0.1888	0.3137	0.4168	1.8959	1.0526	0.7605
[omim ⁺][NTf ₂ ⁻]	0.1969	0.3275	0.4350	1.9797	1.0952	0.7946
[emim ⁺][EtSO ₄ ⁻]	0.2286	0.3853	0.5088	2.3446	1.2020	0.9525
S.D.	0.0032	0.0020	0.0025	0.0016	0.0099	0.0018

Table 9. Parameters $k/\text{cm}^3\cdot\text{g}^{-1}$ for the different empirical equations from Eq. (6) for the equations proposed by Lorentz-Lorenz (L-L), Dale-Gladstone (D-G), Eykman, Oster, Arago-Biot (A-B) and Newton.

All these equations assume that the relation between density and refractive index is temperature-independent. But, from our results (see **Tables 1** and **9**) it can be deduced that k in Eq. (11) has a certain dependence on T (as it is illustrated below in **Figure 5** in the case of Eq. (16)).

Nevertheless, as a first approximation, and assuming that the dependence is small, it is worth finding the equation that best fits our experimental results. In this approximation we shall assume that $k = f(n)\rho$ only depends on the nature of ionic liquid. The value for each ionic liquid is obtained as the average for all the temperatures. The standard deviation is obtained as described in Eq. (18). From these calculations (**Table 9**), we conclude that the Oster equation is the one that best fitted our experimental results.

$$S.D = \left[\frac{\sum (z_{\text{exp}} - z_{\text{calc}})^2}{n} \right]^{\frac{1}{2}} \quad (18)$$

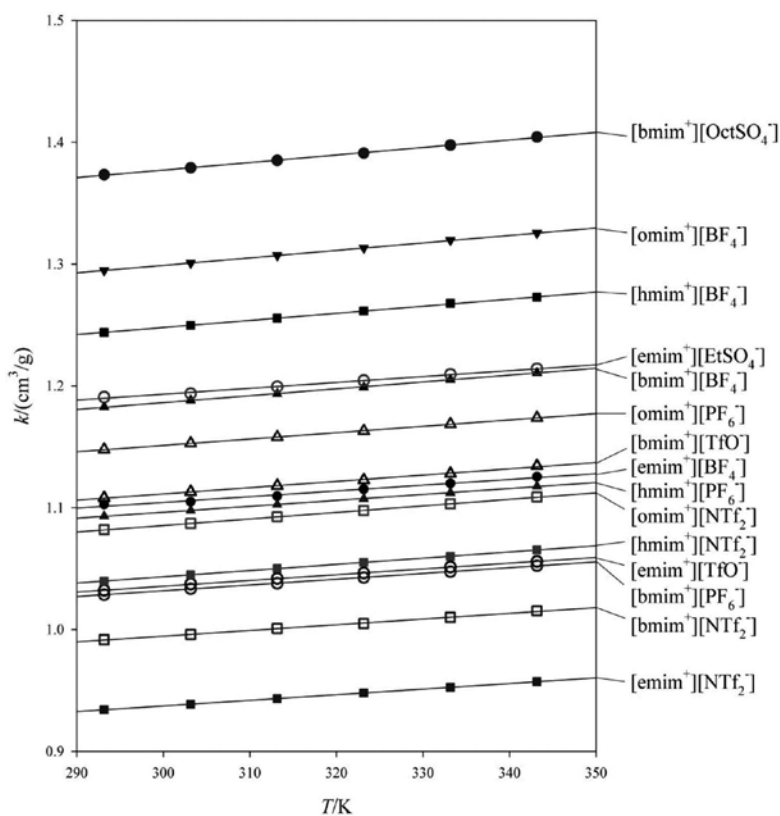


Figure 6. Values of $k = n/\rho$ of different ILs for different temperatures. Parameters for linear fitting can be found in **Table 10**.

As mentioned above, a small dependence of k on T can be observed from our experimental results, and, as a consequence, we used another approach, defining $k = n/\rho$ and fitting the results to a linear equation in the form $k = k_0T + k_1$. **Figure 6** (numerical values can be found in **Table 10**) shows the good quality of the fittings.

ILs	$k_0 \times 10^4/\text{cm}^3 \cdot \text{g}^{-1} \cdot \text{K}^{-1}$	$k_1/\text{cm}^3 \cdot \text{g}^{-1}$	r^2	S.D.
[emim ⁺][BF ₄ ⁻]	4.709	0.9632	0.9882	0.0009
[bmim ⁺][BF ₄ ⁻]	5.632	1.0174	0.9992	0.0003
[hmim ⁺][BF ₄ ⁻]	5.829	1.0731	0.9994	0.0002
[omim ⁺][BF ₄ ⁻]	6.139	1.1149	0.9999	0.0001
[emim ⁺][TfO ⁻]	4.712	0.8942	0.9996	0.0002
[bmim ⁺][TfO ⁻]	5.140	0.9572	0.9971	0.0005
[bmim ⁺][O ₂ CSO ₄ ⁻]	6.189	1.1916	0.9991	0.0003
[bmim ⁺][PF ₆ ⁻]	4.717	0.8904	0.9998	0.0001
[hmim ⁺][PF ₆ ⁻]	4.888	0.9496	0.9997	0.0001
[omim ⁺][PF ₆ ⁻]	5.221	0.9946	0.9997	0.0001
[emim ⁺][NTf ₂ ⁻]	4.622	0.7986	1.0000	0.00003
[bmim ⁺][NTf ₂ ⁻]	4.695	0.8538	0.9981	0.0003
[hmim ⁺][NTf ₂ ⁻]	5.123	0.8896	0.9999	0.0001
[omim ⁺][NTf ₂ ⁻]	5.351	0.9250	0.9997	0.0002
[emim ⁺][EtSO ₄ ⁻]	4.831	1.0482	0.9952	0.0006
			Average	0.0003

Table 10. Fitting parameters for $k = n/\rho$ (n , refractive index, ρ density) of ILs studied to a linear equation ($k = k_0T + k_1$).

As a consequence, we think that a very good and simple description of the correlation between density and the refraction index can be obtained by including the dependence on T . If we compare the S.D. results with those in **Table 9** for any of the equations proposed, a substantial improvement in the quality of the fitting can be observed. Given the quality of the data, once the quantitative relation between density and refractive index is known in a range of temperatures, it is possible just to measure one of these properties at any temperature (probably even outside the range) to know the value of the other with a high degree of precision.

3. Prediction methods of refractive index of ionic liquids

The refractive index (n) can be defined as the ratio of the speed of light in vacuum to that in a given medium [69]. Research studies focused on the modeling and even on the measurement of the refractive index of ILs are scarce in the literature even though its measurement is very simple and fast [9]. However, due to the high number of potential ILs we think it is substantially relevant to develop methods to estimate the refractive index of ILs prior to synthesis.

Some of the studies related to the estimation of refractive index are listed here. The first prediction model in the literature was developed by Deetlefs et al. [41]. They calculated the mo-

lar refraction to predict the refraction indices of ILs from their surface tension. However, all the parameters involved in this model should be experimentally measured or correlated with other experimental properties; thus, it is not suitable to predict refractive indices of new ILs. In addition, it was developed only from 9 ILs so it is far away of being a universal method. The next model was published by Gardas and Coutinho [10] who developed a GCM to predict refractive index of ILs from 245 experimental values of refractive index of ILs in the temperature range from 283.15 to 363.15 K. All the ILs used to model the refractive index were based on imidazolium salts (with different anions) thus this model is not appropriate to estimate the refractive index of ILs with another cation. The same method was used by Freire et al. [70] and Soriano et al. [38] who broadened the method by incorporating some new ILs. Xu et al. [71] synthesized a new ionic liquid ($[C_3\text{mim}][\text{Val}]$) and measured its refractive index in the temperature range of 298.15–333.15 K. After that, they estimated the refractive index for the homologue ILs ($[C_n\text{mim}][\text{Val}]$; $n = 2, 4, 5, 6$) following the same procedure than Deetlefs et al. [41]. This model is also very limited because it was developed only for a specific family of ILs. Finally, Sattari et al. [9] tried to solve the limitations of the rest of the predictive models of refractive index of ILs developing a widely applicable model based on a QSPR method using genetic function approximation (GFA). They used experimental data of 82 ILs with a great variety of structures and developed a 9-parameter model with very good prediction results.

4. Conclusions

Many efforts have been done during the last years to develop a great variety of prediction methods of density of ILs. Thus they have reached a high degree of perfection. Prediction methods of density of ILs can be classified in five categories although the methods are sometimes a combination of more than one category: i) QSPR, ii) ANN, iii) EoS, iv) GCM, and v) correlations between density and other properties.

QSPR models are based on quantum chemistry calculations and this is their great advantage and, at the same time, their main drawback. While virtually any imagined compound can be studied with no previous experimental knowledge, usually the calculations are not easy and only can be developed by very specialized research groups.

ANN is an especially efficient computer algorithm whose main advantage is that it is usually suitable to model chemical properties whose behavior is highly nonlinear because nonlinear relationships are well described with ANN. However, the predicting capabilities of this method depend on the quality of the algorithm for learning and very importantly on the quality, quantity and nature of experimental (or calculated) data used for the learning process.

Equations of state are well known for determining the relationship between pressure, temperature, volume and composition of components providing a theoretical way to calculate some physical properties such as density. The main advantage of this method is the simplicity in their use but a possible drawback is that to obtain the density of the desired compound

usually some previous experimental (or calculated) data of certain critical properties (temperature, pressure, volume,...) are needed.

In the GCM methods, the desired property is obtained as individual contribution of each of the components of the final compound. Then, predictions are obtained using available simple equations. The main drawback of these methods is that their predictive capability depends on previous experimental (or calculated) data. With some exceptions, it is impossible to predict density if no data are available for both of the components of an ionic liquid. On the other hand, usually good predictions can be obtained very easily for any combination of known counterions in a few minutes.

Estimating the density of ILs by correlations between this property and other physical properties is especially interesting if the measurement of the property used is easier or cheaper than the measurement of the density like in the case of refractive index. Nevertheless, the main drawback is that no prediction can be obtained if previous correlations have not been properly established.

Our method provides a fast and simple way to predict the density of ILs with alkyl imidazolium cations and with different anions (and very likely combinations of ions of similar chemical structure) based on the molecular volume in a wide range of temperatures from simple theoretical calculations of the structure of the proposed ions.

The correlation between density and the refraction index is usually described in the literature by equations which are assumed to be temperature-independent; we have shown that a substantial improvement can be obtained if the dependence on temperature is included.

Prediction of refractive index of ILs has not been so widely studied in the literature like in the case of density because the relationships between this property and the ion constituents of the ILs are not so direct and accessible. For this reason, more studies in this field are required.

We support the idea that ILs can be designed with adjustable properties (at least density and refractive index, but very probably some others) based on the structure of the cation and anion chosen. Our method may provide valuable contributions for the design and study of present and future ILs.

Acknowledgements

This work was partially supported by FEDER/ERDF funds from the European Commission, the Spanish Ministry of Economy and Competitiveness (MINECO) (Ref. CTQ2014-57467-R) and the research support programme of the Seneca Foundation of Science and Technology of Murcia, Spain (Ref. 19499/PI/14). Mercedes G. Montalbán acknowledges support from MINECO (FPI grant, BES-2012-053267).

Author details

Mercedes G. Montalbán¹, Mar Collado-González², F. Guillermo Díaz-Baños² and Gloria Villora^{1*}

*Address all correspondence to: gvillora@um.es

¹ Department of Chemical Engineering, Faculty of Chemistry, Regional Campus of International Excellence "Campus Mare Nostrum," University of Murcia, Murcia, Spain

² Department of Physical Chemistry, Faculty of Chemistry, Regional Campus of International Excellence "Campus Mare Nostrum," University of Murcia, Murcia, Spain

References

- [1] Keskin S, Kayrak-Talay D, Akman U, Hortaçsu Ö. A review of ionic liquids towards supercritical fluid applications. *J Supercrit Fluids* 2007;43:150–180. DOI: 10.1016/j.supflu.2007.05.013
- [2] Montalbán MG, Collado-González M, Trigo R, Díaz Baños FG, Villora G. Experimental measurements of octanol-water partition coefficients of ionic liquids. *J Adv Chem Eng* 2015;5:133. DOI: 10.4172/2090-4568.1000133
- [3] Álvarez-Guerra M, Irabien A. Design of ionic liquids: an ecotoxicity (*Vibrio fischeri*) discrimination approach. *Green Chem* 2011;13:1507–1516. DOI: 10.1039/c0gc00921k
- [4] Bogdanov MG, Kantlehner W. Simple prediction of some physical properties of ionic liquids: the residual volume approach. *Z Naturforsch B* 2009;64:215–222. DOI: 10.1515/znb-2009-0212
- [5] Heintz A. Recent developments in thermodynamics and thermophysics of non-aqueous mixtures containing ionic liquids. A review. *J Chem Thermodyn* 2005;37:525–535. DOI: 10.1016/j.jct.2005.04.003
- [6] Montalbán MG, Bolívar CL, Díaz Baños FG, Villora G. Effect of temperature, anion, and alkyl chain length on the density and refractive index of 1-alkyl-3-methylimidazolium-based ionic liquids. *J Chem Eng Data* 2015;60:1986–1996. DOI: 10.1021/je501091q
- [7] Paduszyński K, Domańska U. A new group contribution method for prediction of density of pure ionic liquids over a wide range of temperature and pressure. *Ind Eng Chem Res* 2012;51:591–604. DOI: 10.1021/ie202134z
- [8] Huddleston JG, Visser AE, Reichert WM, Willauer HD, Broker GA, Rogers RD. Characterization and comparison of hydrophilic and hydrophobic room temperature

- ionic liquids incorporating the imidazolium cation. *Green Chem* 2001;3:156–164. DOI: 10.1039/b103275p
- [9] Sattari M, Kamari A, Mohammadi AH, Ramjugernath D. Prediction of refractive indices of ionic liquids – a quantitative structure-property relationship based model. *J Taiwan Inst Chem Eng* 2015;52:165–180. DOI: 10.1016/j.jtice.2015.02.003
- [10] Gardas RL, Coutinho JAP. Group contribution methods for the prediction of thermo-physical and transport properties of ionic liquids. *AIChE J* 2009;55:1274–1290. DOI: 10.1002/aic.11737
- [11] El-Harbawi M, Samir BB, Babaa MR, Mutalib MIA. A new QSPR model for predicting the densities of ionic liquids. *Arab J Sci Eng* 2014;39:6767–6775. DOI: 10.1007/s13369-014-1223-3
- [12] Lazzús JA. $\rho(T, p)$ model for ionic liquids based on quantitative structure-property relationship calculations. *J Phys Org Chem* 2009;22:1193–1197. DOI: 10.1002/poc.1576
- [13] Trohalaki S, Pachter R, Drake GW, Hawkins T. Quantitative structure – property relationships for melting points and densities of ionic liquids. *Energ Fuels* 2005;19:279–284. DOI: 10.1021/ef049858q
- [14] Palomar J, Torrecilla JS, Ferro VR, Rodríguez F. Development of an a priori ionic liquid design tool. 1. integration of a novel COSMO-RS molecular descriptor on neural networks. *Ind Eng Chem Res* 2008;47:4523–4532. DOI: 10.1021/ie800056q
- [15] Palomar J, Ferro VR, Torrecilla JS, Rodríguez F. Density and molar volume predictions using COSMO-RS for ionic liquids. An approach to solvent design. *Ind Eng Chem Res* 2007;46:6041–6048. DOI: 10.1021/ie070445x
- [16] Lazzús JA. ρ -T-P prediction for ionic liquids using neural networks. *J Taiwan Inst Chem Eng* 2009;40:213–232. DOI: 10.1016/j.jtice.2008.08.001
- [17] Valderrama JO, Reátegui A, Rojas RE. Density of ionic liquids using group contribution and artificial neural networks. *Ind Eng Chem Res* 2009;48:3254–3259. DOI: 10.1021/ie801113x
- [18] Lazzús JA. Estimation of density as a function of temperature and pressure for imidazolium-based ionic liquids using a multilayer net with particle swarm optimization. *Int J Thermophys* 2009;30:883–909. DOI: 10.1007/s10765-009-0591-5
- [19] Goharshadi EK, Zebarjad SM. Thermodynamic properties of the mixtures of some ionic liquids with alcohols using a simple equation of state. *J Mol Liq* 2009;149:66–73. DOI: 10.1016/j.molliq.2009.08.004
- [20] Gadamsetty S V, Joshipura MH, Saxena P. A review on property prediction of ionic liquids using cubic equation of state. Institute of Technology, Nirma University, Ahmedabad. 8–10th December 2011;1:1–5.

- [21] Valderrama JO, Zarricueta K. A simple and generalized model for predicting the density of ionic liquids. *Fluid Phase Equilib* 2009;275:145–151. DOI: 10.1016/j.fluid.2008.10.002
- [22] Abildskov J, Ellegaard MD, O'Connell JP. Densities and isothermal compressibilities of ionic liquids—modeling and application. *Fluid Phase Equilib* 2010;295:215–229. DOI: 10.1016/j.fluid.2010.04.019
- [23] Wang J, Li Z, Li C, Wang Z. Density prediction of ionic liquids at different temperatures and pressures using a group contribution equation of state based on electrolyte perturbation theory. *Ind Eng Chem Res* 2010;49:4420–4425. DOI: 10.1021/ie901590h
- [24] Shen C, Li C, Li X, Lu Y, Muhammad Y. Estimation of densities of ionic liquids using Patel–Teja equation of state and critical properties determined from group contribution method. *Chem Eng Sci* 2011;66:2690–2698. DOI: 10.1016/j.ces.2011.03.027
- [25] Patel NK, Joshipura MH. Generalized PSRK model for prediction of liquid density of ionic liquids. *Procedia Eng* 2013;51:386–394. DOI: 10.1016/j.proeng.2013.01.054
- [26] Ji X, Adidharma H. Thermodynamic modeling of ionic liquid density with heterosegmented statistical associating fluid theory. *Chem Eng Sci* 2009;64:1985–1992. DOI: 10.1016/j.ces.2009.01.018
- [27] Wang J, Li C, Shen C, Wang Z. Towards understanding the effect of electrostatic interactions on the density of ionic liquids. *Fluid Phase Equilib* 2009;279:87–91. DOI: 10.1016/j.fluid.2009.02.011
- [28] Sohrabi Mahboub M, Farrokhpour H. Molecular thermodynamic modeling of ionic liquids using the perturbation-based linear Yukawa isotherm regularity. *J Phys Condens Matter* 2016;28:235101. DOI: 10.1088/0953-8984/28/23/235101
- [29] Farzi R, Esmaeilzadeh F. Prediction of densities of pure ionic liquids using Esmaeilzadeh-Roshanfekar equation of state and critical properties from group contribution method. *Fluid Phase Equilib* 2016;423:101–108. DOI: 10.1016/j.fluid.2016.04.020
- [30] Qiao Y, Ma Y, Huo Y, Ma P, Xia S. A group contribution method to estimate the densities of ionic liquids. *J Chem Thermodyn* 2010;42:852–855. DOI: 10.1016/j.jct.2010.02.007
- [31] Gardas RL, Coutinho JAP. Extension of the Ye and Shreeve group contribution method for density estimation of ionic liquids in a wide range of temperatures and pressures. *Fluid Phase Equilib* 2008;263:26–32. DOI: 10.1016/j.fluid.2007.09.016
- [32] Slattery JM, Daguene C, Dyson PJ, Schubert TJS, Krossing I. How to predict the physical properties of ionic liquids: a volume-based approach. *Angew Chemie* 2007;119:5480–5484. DOI: 10.1002/anie.200700941
- [33] Kermanioryani M, Mutalib MIA, Dong Y, Lethesh KC, Ben Ghanem OBO, Kurnia KA, Aminuddin NF, Leveque J-M. Physicochemical properties of new imidazolium-based

- ionic liquids containing aromatic group. *J Chem Eng Data* 2016;61:2020–2026. DOI: 10.1021/acs.jced.5b00983
- [34] Jacquemin J, Ge R, Nancarrow P, Rooney DW, Costa Gomes MF, Padua AAH, Hardacre C. Prediction of ionic liquid properties. I. Volumetric properties as a function of temperature and pressure. *J Chem Eng Data* 2008;53:716–726. DOI: 10.1021/je8002817
- [35] Jacquemin J, Nancarrow P, Rooney DW, Gomes MFC, Husson P, Majer V, Padua AAH, Hardacre C. Prediction of ionic liquid properties. II. Volumetric properties as a function of temperature and pressure. *J Chem Eng Data* 2008;53:2133–2143. DOI: 10.1021/je8002817
- [36] Ye C, Shreeve JM. Rapid and accurate estimation of densities of room temperature ionic liquids and salts. *J Phys Chem A* 2007;3:5–10. DOI: 10.1021/je200883w
- [37] Keshavarz MH, Pouretedal HR, Saberi E. A simple method for prediction of density of ionic liquids through their molecular structure. *J Mol Liq* 2016;216:732–737. DOI: 10.1016/j.molliq.2016.01.095
- [38] Soriano AN, Doma BT, Li M-H. Density and refractive index measurements of 1-ethyl-3-methylimidazolium-based ionic liquids. *J Taiwan Inst Chem Eng* 2010;41:115–121. DOI: 10.1016/j.jtice.2009.07.002
- [39] Tariq M, Forte PAS, Gomes MFC, Lopes JNC, Rebelo LPN. Densities and refractive indices of imidazolium- and phosphonium-based ionic liquids: effect of temperature, alkyl chain length, and anion. *J Chem Thermodyn* 2009;41:790–798. DOI: 10.1016/j.jct.2009.01.012
- [40] Soriano AN, Doma BT, Li MH. Measurements of the density and refractive index for 1-n-butyl-3-methylimidazolium-based ionic liquids. *J Chem Thermodyn* 2009;41:301–307. DOI: 10.1016/j.jct.2008.08.010
- [41] Deetlefs M, Seddon KR, Shara M. Predicting physical properties of ionic liquids. *Phys Chem Chem Phys* 2005;8:642–649. DOI: 10.1039/b513453f
- [42] Gardas RL, Rooney DW, Hardacre C. Development of a QSPR correlation for the parachor of 1,3-dialkyl imidazolium based ionic liquids. *Fluid Phase Equilib* 2009;283:31–37. DOI: 10.1016/j.fluid.2009.05.008
- [43] Hagan MT, Demuth HB, Beale M, De Jesús O. *Neural Network Design*. 2nd Ed. Oklahoma State University, Stillwater, Oklahoma, USA. 2014.
- [44] Taskinen J, Yliruusi J. Prediction of physicochemical properties based on neural network modelling. *Adv Drug Deliv Rev* 2003;55:1163–1183. DOI: 10.1016/S0169-409X(03)00117-0
- [45] Jiang Y, Hu T, Huang C, Wu X. An improved particle swarm optimization algorithm. *Appl Math Comput* 2007;193:231–239. DOI: 10.1016/j.amc.2007.03.047

- [46] Da Y, Xiurun G. An improved PSO-based ANN with simulated annealing technique. *Neurocomputing* 2005;63:527–533. DOI: 10.1016/j.neucom.2004.07.002
- [47] Valderrama JO, Abu-Sharkh BF. Generalized rackett-type correlations to predict the density of saturated liquids and petroleum fractions. *Fluid Phase Equilib* 1989;51:87–100. DOI: 10.1016/0378-3812(89)80356-5
- [48] Tan SP, Ji X, Adidharma H, Radosz M. Statistical associating fluid theory coupled with restrictive primitive model extended to bivalent ions. SAFT2: 1. Single Salt + Water Solutions. *J Phys Chem B* 2006;110:16694–16699. DOI: 10.1021/jp0625107
- [49] Ji X, Tan SP, Adidharma H, Radosz M. Statistical associating fluid theory coupled with restrictive primitive model extended to bivalent ions. SAFT2: 2. Brine/Seawater properties predicted. *J Phys Chem B* 2006;110:16700–16706. DOI: 10.1021/jp062511z
- [50] Ji X, Adidharma H. Ion-based SAFT2 to represent aqueous single- and multiple-salt solutions at 298.15 K. *Ind Eng Chem Res* 2006;45:7719–7728. DOI: 10.1021/ie060649y
- [51] Valderrama JO, Robles PA. Critical properties, normal boiling temperatures, and acentric factors of fifty ionic liquids. *Ind Eng Chem Res* 2007;46:1338–1344. DOI: 10.1021/ie0603058
- [52] Nasrifar K, Moshfeghian M. A saturated liquid density equation in conjunction with the predictive-Soave-Redlich-Kwong equation of state for pure refrigerants and LNG multicomponent systems. *Fluid Phase Equilib* 1998;153:231–242. DOI: 10.1016/S0378-3812(98)00422-1
- [53] Esmaeilzadeh F, Roshanfekr M. A new cubic equation of state for reservoir fluids. *Fluid Phase Equilib* 2006;239:83–90. DOI: 10.1016/j.fluid.2005.10.013
- [54] Jenkins HDB, Roobottom HK, Passmore J, Glasser L. Relationships among ionic lattice energies, molecular (formula unit) volumes, and thermochemical radii. *Inorg Chem* 1999;38:3609–3620. DOI: 10.1021/ic9812961
- [55] Rebelo LPN, Najdanovic-Visak V, Gomes de Azevedo R, Esperança JMSS, Nunes da Ponte M, Guedes HJR, Visak ZP, de Sousa HC, Szydłowski J, Canongia Lopes JN, Cordeiro TC. Phase behavior and thermodynamic properties of ionic liquids, ionic liquid mixtures, and ionic liquid solutions. In: Rogers RD, Seddon KR, editors. *Ionic Liquids IIIA: Fundamentals, Progress, Challenges, and Opportunities*, pp. 270–291. DOI: 10.1021/bk-2005-0901.ch021
- [56] Esperança JMSS, Guedes HJR, Blesic M, Rebelo LPN. Densities and derived thermodynamic properties of ionic liquids. 3. Phosphonium-based ionic liquids over an extended pressure range. *J Chem Eng Data* 2006;51:237–242. DOI: 10.1021/je050358g

- [57] Kolbeck C, Lehmann J, Lovelock KRJ, Cremer T, Paape N, Wasserscheid P, Fröba AP, Maier F, Steinrück H-P. Density and surface tension of ionic liquids. *J Phys Chem B* 2010;114:17025–17036. DOI: 10.1021/jp1068413
- [58] Glasser L. Lattice and phase transition thermodynamics of ionic liquids. *Thermochim Acta* 2004;421:87–93. DOI: 10.1016/j.tca.2004.03.015
- [59] Allen FH. The Cambridge Structural Database: a quarter of a million crystal structures and rising. *Acta Crystallogr B* 2002;58:380–388. DOI: 10.1107/S0108768102003890
- [60] [Internet]. Available from: <http://www.chemicalize.org/> (accessed 2016-07-15).
- [61] Gomes de Azevedo R, Esperança JMSS, Szydłowski J, Visak ZP, Pires PF, Guedes HJR, Rebelo LPN. Thermophysical and thermodynamic properties of ionic liquids over an extended pressure range: [bmim][NTf₂] and [hmim][NTf₂]. *J Chem Thermodyn* 2005;37:888–899. DOI: 10.1016/j.jct.2005.04.018
- [62] Iglesias-Otero MA, Troncoso J, Carballo E, Romaní L. Density and refractive index in mixtures of ionic liquids and organic solvents: correlations and predictions. *J Chem Thermodyn* 2008;40:949–956. DOI: 10.1016/j.jct.2008.01.023
- [63] Gardas RL, Freire MG, Carvalho PJ, Marrucho IM, Fonseca IMA, Ferreira AGM, Coutinho JAP. High-pressure densities and derived thermodynamic properties of imidazolium-based ionic liquids. *J Chem Eng Data* 2007;52:80–88. DOI: 10.1021/je060247x
- [64] Troncoso J, Cerdeiriña CA, Sanmamed YA, Romaní L, Rebelo LPN. Thermodynamic properties of imidazolium-based ionic liquids: densities, heat capacities, and enthalpies of fusion of [bmim][PF₆] and [bmim][NTf₂]. *J Chem Eng Data*. 2006;51:1856–1859.
- [65] Łachwa J, Morgado P, Esperança JMSS, Guedes HJR, Canongia Lopes JN, Rebelo LPN. Fluid-phase behavior of {1-hexyl-3-methylimidazolium bis(trifluoromethylsulfonyl) imide, [C₆mim][NTf₂], + C₂–C₈ n -alcohol} mixtures: liquid–liquid Equilibrium and excess volumes. *J Chem Eng Data* 2006;51:2215–2221. DOI: 10.1021/je060307z
- [66] Pereiro AB, Rodríguez A. Thermodynamic properties of ionic liquids in organic solvents from (293.15 to 303.15) K. *J Chem Eng Data* 2007;52:600–608. DOI: 10.1021/je060497d
- [67] Pereiro AB, Rodríguez A. Study on the phase behaviour and thermodynamic properties of ionic liquids containing imidazolium cation with ethanol at several temperatures. *J Chem Thermodyn* 2007;39:978–989. DOI: 10.1016/j.jct.2006.10.017
- [68] Bonhôte P, Dias A-P, Papageorgiou N, Kalyanasundaram K, Grätzel M. Hydrophobic, highly conductive ambient-temperature molten salts. *Inorg Chem* 1996;35:1168–1178. DOI: 10.1021/ic951325x

- [69] Deetlefs M, Seddon KR, Shara M. Neoteric optical media for refractive index determination of gems and minerals. *New J Chem* 2006;30:317–326. DOI: 10.1039/b513451j
- [70] Freire MG, Teles ARR, Rocha MAA, Schröder B, Neves CMSS, Carvalho PJ, Evtuguin DV, Santos LMNBF, Coutinho JAP. Thermophysical characterization of ionic liquids able to dissolve biomass. *J Chem Eng Data* 2011;56:4813–4822. DOI: 10.1021/je200790q
- [71] Xu W-G, Ma X-X, Li L, Tong J, Guan W. Prediction of physicochemical properties of valine ionic liquids [Cnmim][Val] (n = 2, 3, 4, 5, 6) by empirical methods: 2. *Ind Eng Chem Res* 2012;51:4105–4111. DOI: 10.1021/ie201530b

Thermodynamic Properties of Ionic Liquids

Liu Qingshan, Mou Lin, Zheng Qige and Xia Quan

Additional information is available at the end of the chapter

<http://dx.doi.org/10.5772/65792>

Abstract

Basic physicochemical properties were discussed at different temperatures for 18 hydrophobic ionic liquids (ILs) which containing imidazolium and pyridinium as cations, separately. The ILs include 1-ethyl-3-methylimidazolium tris(pentafluoroethyl)trifluorophosphate ($[C_2mim][PF_3(CF_2CF_3)_3]$), 1-acetonitrile-3-ethylimidazolium bis(trifluoromethylsulfonyl)imide ($[MCNMIM][NTf_2]$), 1-(cyanopropyl)-3-methylimidazolium bis(trifluoromethylsulfonyl)imide ($[PCNMIM][NTf_2]$), 1-ethanol-3-ethylimidazolium bis(trifluoromethylsulfonyl)imide ($[EOHMIM][NTf_2]$), 1-butylamide-3-ethylimidazolium bis(trifluoromethylsulfonyl)-imide ($[CH_2CONHBuEIM][NTf_2]$), N-alkylpyridinium bis(trifluoromethylsulfonyl)imide $\{[C_npy][NTf_2] (n = 2, 3, 4, 5, 6)\}$, N-alkyl-3-methylpyridinium bis(trifluoromethylsulfonyl)imide $\{[C_n3Mpy][NTf_2] (n = 3, 4, 6)\}$, and N-alkyl-4-methylpyridinium bis(trifluoromethylsulfonyl)imide $\{[C_n4Mpy][NTf_2] (n = 2, 4, 6)\}$. The molar volume, standard molar entropy, and lattice energy were estimated by the empirical and semiempirical equations. The dependences of density, dynamic viscosity, and electrical conductivity on temperature are discussed in the measured temperature range. It is found that with the increasing temperature, the density and dynamic viscosity decreased, while the electrical conductivity increases. The influences of microstructures of ILs, such as the introduction of the methylene, methyl, and functional groups on cations, on their basic physicochemical properties are discussed.

Keywords: ionic liquid, density, surface tension, dynamic viscosity, electrical conductivity

1. Introduction

Ionic liquids (ILs) are salts while can exist as liquid at room temperature or near room temperature, which are completely composed of ions [1–3]. Compared with traditional organic solvents, ILs have exhibited outstanding properties, such as negligible vapor pressures, nonflammable, wide electrochemical window, high electrical conductivity, adjustable acidity, high dissolving

capacity for inorganic and organic compounds or polymers and can be recycled, etc. Moreover, ILs can be designed through the introduction of functional groups on anion or cation to modify their physicochemical properties. As the new designed and functional solvents, ILs have been used in fields of synthesis, extraction, catalysis, electrochemistry, etc. The basic physicochemical properties of ILs are of great importance for their design and applications; however, related data are very deficient. Therefore, IL's properties and related theoretical studies have received increasing attention.

2. Preparation of ionic liquids

All ionic liquids (ILs) were synthesized according to the reported method [4] except $[\text{CH}_2\text{CONHBuEIM}][\text{NTf}_2]$ and $[\text{C}_2\text{mim}][\text{PF}_3(\text{CF}_2\text{CF}_3)_3]$.

The chloride (or bromide) type compounds were synthesized by the N-alkylation reaction. A slight excess of halide was added dropwise into N-alkyl compounds by stirring at 353 K for 24 h. The products were recrystallized from acetonitrile/ethyl acetate solution several times. The products were dried under high vacuum for 48 h at 353 K before the synthesis of the target products. The $[\text{C}_2\text{mim}][\text{PF}_3(\text{CF}_2\text{CF}_3)_3]$ was supplied by Merck Co. (batch: S9588301). The compound $[\text{CH}_2\text{CONHBuEIM}][\text{NTf}_2]$ was synthesized according to the reported method [5]. Chloroacetyl chloride was added to n-butylamine drop by drop in the same molar ratio in an ice bath. After completion of the reaction, the organic layer was separated then washed with $\omega(\text{HCl}) = 5\%$ or $\omega(\text{NaHCO}_3) = 5\%$ until the water layer became neutral. The product (chloroacetyl-n-butylamine) was dried under vacuum conditions. Acetonitrile was chosen as a solvent, ethylimidazole was added to chloroacetyl-n-butylamine in a small excess molar ratio to allow the complete reaction of chloroacetyl-n-butylamine at 85°C for 18 h. The product was recrystallized twice with acetonitrile and ethyl acetate ester. The resulting product was vacuum dried to obtain pure $[\text{EimCH}_2\text{CONHBu}]\text{Cl}$.

The hydrophobic ILs were synthesized in the distilled water by the traditional ion exchange reaction. The chloride (or bromide) type compounds were placed in a flask and dissolved with distilled water, an equivalent amount of lithium bis[(trifluoromethyl)sulfonyl]imide (LiNTf_2) salt was also dissolved in distilled water and added to the flask. The solution was stirred vigorously for 3 h. The bottom liquid was washed with distilled water until no halogen as detected by $\text{AgNO}_3/\text{HNO}_3$ solution (the mass fraction of halogen was reckoned to be less than 50 ppm). The products were finally dried on vacuum drying line at 353 K before the determination of the thermodynamic properties. The final products were characterized by ^1H NMR spectra.

3. Water content

The impurity of the water is the most serious influence factor to the properties of ILs. Since the residual water cannot be removed by conventional methods in the ILs. The mass fraction of the residual water was determined by a Cou-Lo Aquamax Karl Fischer moisture meter (v.10.06)

before and after the measurement of properties. The water mass fractions of the ILs are lower than 300×10^{-6} and 500×10^{-6} for before and after the property determination, respectively.

4. Property measurement

4.1. Density

The densities of ILs were measured by a Westphal balance (or an automated SVM3000 Anton Paar rotational Stabinger viscometer-densimeter with a cylinder geometry) in the temperature range of $T = (283.15 \text{ to } 338.15) \pm 0.05$ K. The density values were recorded at every 5 K. For the Westphal balance method, the sample was placed in a cell with a jacket.

4.2. Surface tension

Using the tensiometer (DP-AW type produced by Sang Li Electronic Co.) of the forced bubble method, the surface tension of the ILs was measured with the experimental error that is $\pm 0.1 \text{ mJ}\cdot\text{m}^{-2}$. The temperature was controlled by a thermostat. The uncertainties of the measurement are in the range of $\pm 0.2 \text{ mJ}\cdot\text{m}^{-2}$.

4.3. Dynamic viscosity

The dynamic viscosity of the ILs was measured using an Ostwald viscometer (or an automated SVM3000 Anton Paar rotational Stabinger viscometer-densimeter with a cylinder geometry, the principle is based on a modified Couette according to a rapidly rotating outer tube and a relatively slow rotating inner measuring bob). The values were recorded at every 5 K. The uncertainties were estimated to be $\pm 1\%$.

4.4. Electrical conductivity

The electrical conductivity of the ILs was carried out using a MP522 conductivity instrument with the cell constants of 1 cm^{-1} (the cell was calibrated with the aqueous KCl solution). The uncertainty was reckoned to less than $\pm 1\%$. The temperature was regulated by a thermostat with a precision of ± 0.05 K. The experimental data were reported per 5 K after 30 min thermal equilibrium time.

5. Formulas

5.1. Density

A straight line can be obtained according to plot $\ln\rho$ against T/K . And the $\ln\rho$ against T/K can be fitted by the following empirical equation:

$$\ln\rho/\text{g}\cdot\text{cm}^{-3} = b - \alpha T/K \quad (1)$$

where b is an empirical constant and α is the thermal expansion coefficient.

At 298.15 K, the molecular volume, V , standard molar entropy, S^0 , and lattice energy, U_{POT} of the ILs can be obtained from the experimental density by the following equations:

$$V = M/(N \cdot \rho) \quad (2)$$

$$S^0 = 1246.5 \cdot (V) + 29.5 \quad (3)$$

$$U_{\text{POT}} = 1981.2 \cdot (\rho/M)^{1/3} + 103.8 \quad (4)$$

where M is molar mass, ρ is the density, and N is the Avogadro's constant.

5.2. Surface tension

The surface tension, γ , has the relationship with the temperature in terms of the Eötvös equation:

$$\gamma V^{2/3} = k(T_c - T) \quad (5)$$

where V is the molar volume of the liquid, T_c is the critical temperature, and k , is an empirical constant.

The parachor, P , was estimated by the following equation:

$$P(298.15 \text{ K}) = (M \gamma^{1/4})/\rho \quad (6)$$

where M is molar mass, ρ is the density, and γ is surface tension.

The molar enthalpy of vaporization, $\Delta_1^g H_m^0$, was estimated by the following equation:

$$\Delta_1^g H_m^0(298.15\text{K})/\text{kJ} \cdot \text{mol}^{-1} = 0.01121(\gamma V^{2/3} N^{1/3}) + 2.4 \quad (7)$$

where V is molar volume, γ is surface tension, and N is Avogadro's constant.

At 298.15 K, according to the literature studies [6, 7], the interstice volume, v , can be estimated by interstice model theory:

$$v = 0.6791 (k_b T/\gamma)^{3/2} \quad (8)$$

herein, k_b is the Boltzmann constant, T is thermodynamic temperature, and γ is the surface tension of ILs.

According to Yang et al., the molar volume of ILs is composed of the volume of inherent and interstices; herein, the molar volume of the interstice is, $\sum v = 2Nv$, the molar volume of the ILs can be calculated by the following equation:

$$V = V_i + 2Nv \quad (9)$$

herein, V is the molar volume, V_i is the inherent volume, and $2Nv$ is the interstice volume.

At 298.15 K, Yang et al. pointed out that the expansion volume of ILs only results from the interstices expansion following the temperature increase. Then, the thermal expansion coefficient, α , can be estimated by the interstice model theory by the following equation:

$$\alpha = (1/V)(\partial V/\partial T)_p = 3Nv/VT \quad (10)$$

5.3. Dynamic viscosity

The temperature dependence of the dynamic viscosity for ILs can be fitted using the Vogel-Fulcher-Tammann (VFT) equation:

$$\eta = \eta_0 \cdot \exp(B/(T - T_0)) \quad (11)$$

where η is the dynamic viscosity; η_0 , B , and T_0 are the fitting parameters.

Usually, the Arrhenius equation was used to fit the dynamic viscosity and the equation is:

$$\eta = \eta_\infty \cdot \exp(E_\eta/(k_B T)) \quad (12)$$

where E_a is the activation energy for dynamic viscosity, η_∞ is the maximum dynamic viscosity, and k_B is the Boltzmann constant.

According to Vila et al. [12], the VFT equation for dynamic viscosity was related to the Arrhenius equation, $\eta_0 = \eta_\infty$ and $B = E_\eta/k_B$. The activation energy of dynamic viscosity was introduced in the final version VFT equation. The final version of the VFT equation can be expressed as follows:

$$\eta = \eta_\infty \cdot \exp(E_\eta/(k_B(T - T_0))) \quad (13)$$

5.4. Electrical conductivity

Usually, the VFT is also used for the fitting of temperature dependence on electrical conductivity. Herein, the temperature dependence of electrical conductivity of the ILs was also fitted according to the following VFT equation:

$$\sigma = \sigma_0 \cdot \exp(-B/(T - T_0)) \quad (14)$$

here σ is the electrical conductivity; σ_0 , B , and T_0 are fitting parameters.

Sometimes, the Arrhenius equation is also used to fit the electrical conductivity:

$$\sigma = \sigma_{\infty} \cdot \exp(-E_{\sigma}/(k_B T)) \quad (15)$$

where E_{σ} is the activation energy, which indicates the energy needed for the ion to hop into a free hole, σ_{∞} is the maximum electrical conductivity, and k_B is the Boltzmann constant.

According to the discussion, Vila et al. [8] have introduced the activation energy of electrical conductivity in the VFT equation by establishing the fitting parameters of the VFT equation with the Arrhenius equation: $\sigma_0 = \sigma_{\infty}$ and $B = E_{\sigma}/k_B$. The final version of the VFT equation can be expressed as follows:

$$\sigma = \sigma_{\infty} \cdot \exp(-E_{\sigma}/(k_B(T - T_0))) \quad (16)$$

5.5. Walden rule

The classical Walden rule was usually used for the assessing of the ionicity of ILs [9, 10]. The ionic mobilities (represented by the equivalent conductivity $\Lambda = F \sum \mu_i Z_i$) and the fluidity ϕ ($\phi = \eta^{-1}$) of the medium can be related to the Walden rule through the ions move. On the basis of this fact, the relationship of the molar electrical conductivity and dynamic viscosity for ILs can be described by the following equation:

$$\Lambda \eta = k \quad (17)$$

where Λ is the molar electrical conductivity, η is the dynamic viscosity, and k is a temperature dependent constant. The Walden's product (in [S·cm²·mol⁻¹][mP·s]) can be calculated at 298.15 K.

6. Density and surface tension of ionic liquid [C₂mim][PF₃(CF₂CF₃)₃] and prediction of properties [C_nmim][PF₃(CF₂CF₃)₃] ($n = 1, 3, 4, 5, 6$)

As organic salts, the ionic liquids (ILs) have shown many excellent properties, such as the low melting temperature, good solvation, and nonvolatility. So, the industrial and scientific communities have applied ILs in a broad range as the green organic solvents. In particular, the air- and water-stable hydrophobic ILs have been used in some special fields as the stable ILs. Actually, the most ILs are hydrophilic, so, 1-alkyl-3-methylimidazolium bis(trifluoromethylsulfonyl)imide (C_nmimNTf₂) has attracted serious concern as an air- and water-stable hydrophobic compound. And the properties were reporting in succession when the air- and water-stable hydrophobic compounds were synthesized. As another air- and water-stable hydrophobic type IL 1-ethyl-3-methylimidazolium tris(pentafluoroethyl)trifluorophosphate [C₂mim][PF₃(CF₂CF₃)₃] was provided by Merck Co. This is also the air- and water-stable hydrophobic IL. So, the study on the properties of this type ILs is significant in many concerned fields.

The structure of [C₂mim][PF₃(CF₂CF₃)₃] is shown in **Figure 1**.

The experimental measured values of density and surface tension of IL [C₂mim][PF₃(CF₂CF₃)₃] are listed in **Table 1** [11].

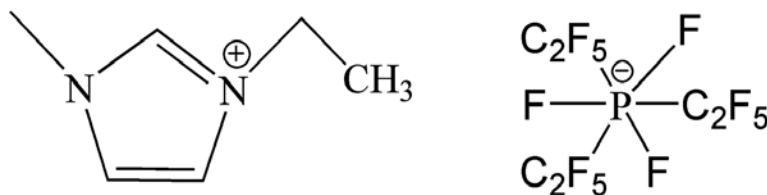


Figure 1. The structure of IL ([C₂mim][PF₃(CF₂CF₃)₃]).

<i>T</i> /K	283.15	288.15	293.15	298.15	303.15	308.15
ρ /g cm ⁻³	1.72705	1.72113	1.71517	1.70926	1.70332	1.69740
γ /mJ m ⁻²	35.3	35.1	34.9	34.8	34.6	34.4
<i>T</i> /K	313.15	318.15	323.15	328.15	333.15	338.15
ρ /g cm ⁻³	1.69150	1.68562	1.67975	1.67388	1.66804	1.66221
γ /mJ m ⁻²	34.2	34.1	34.0	33.8	33.6	33.4

Table 1. Experimental values of density, ρ , and surface tension, γ , of IL [C₂mim][PF₃(CF₂CF₃)₃] from 283.15 to 338.15 K.

By plotting $\ln \rho$ against $(T - 298.15)$ K, a straight line can be obtained (see **Figure 2**) according to Eq. (1). According to Eq. (1), the correlation coefficient is $R = 0.9999$, the standard deviation $s = 3.0 \times 10^{-5}$ g cm⁻³, $b = 0.53603$, the thermal expansion coefficient of the IL is $\alpha = 6.96 \times 10^{-4}$ K⁻¹ at 298.15 K, respectively.

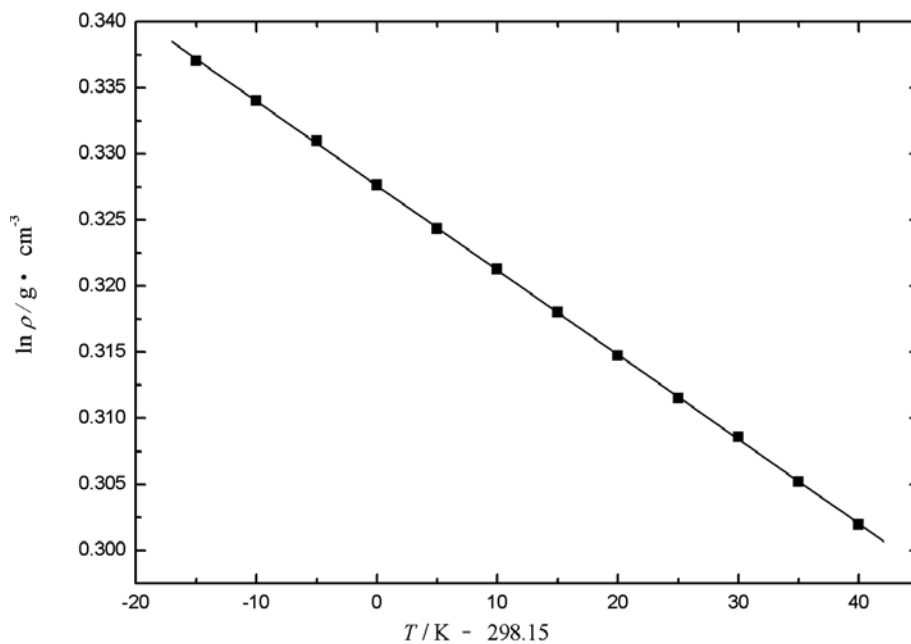


Figure 2. Plot of $\ln \rho$ vs. $T/K - 298.15$ of IL [C₂mim][PF₃(CF₂CF₃)₃].

The experiment values of γ against $(T - 298.15)$ K can be fitted according to the linear equation (see **Figure 3**). According to the linear equation, the correlation coefficient and standard deviation can be obtained and the values are 0.998 and $0.04 \text{ mJ}\cdot\text{m}^{-2}$, respectively. In **Figure 3**, the surface entropy, $S_a = -(\partial\gamma/\partial(T - 298.15))_p$, can also be obtained and the value is $33.4 \times 10^{-3} \text{ mJ}\cdot\text{K}^{-1}\cdot\text{m}^{-2}$ at 298.15 K. At 298.15 K, the surface energy can be calculated from the surface tension value by the imperial equation, $E_a = \gamma - T(\partial\gamma/\partial(T - 298.15))_p$, and the value is $44.8 \text{ mJ}\cdot\text{m}^{-2}$. Compared with surface energies of the fused salts and organic liquids, the value of the IL $[\text{C}_2\text{mim}][\text{PF}_3(\text{CF}_2\text{CF}_3)_3]$ is close to the organic liquids, even less than some organic liquids, for example, $146 \text{ mJ}\cdot\text{m}^{-2}$ for NaNO_3 , $67 \text{ mJ}\cdot\text{m}^{-2}$ for benzene, and $51.1 \text{ mJ}\cdot\text{m}^{-2}$ for octane. This fact shows that the interaction energy between ions in $[\text{C}_2\text{mim}][\text{PF}_3(\text{CF}_2\text{CF}_3)_3]$ is less than that in fused salts. The physicochemical properties (molecular volume, V_m , parachor, P , thermal expansion coefficient, α , standard entropy, S^0 , lattice energy, U_{pot} , and molar enthalpy of vaporization, $\Delta_1^s H_m^0$) were estimated by using the experimental data of density and surface tension according to Eqs. (1)–(7).

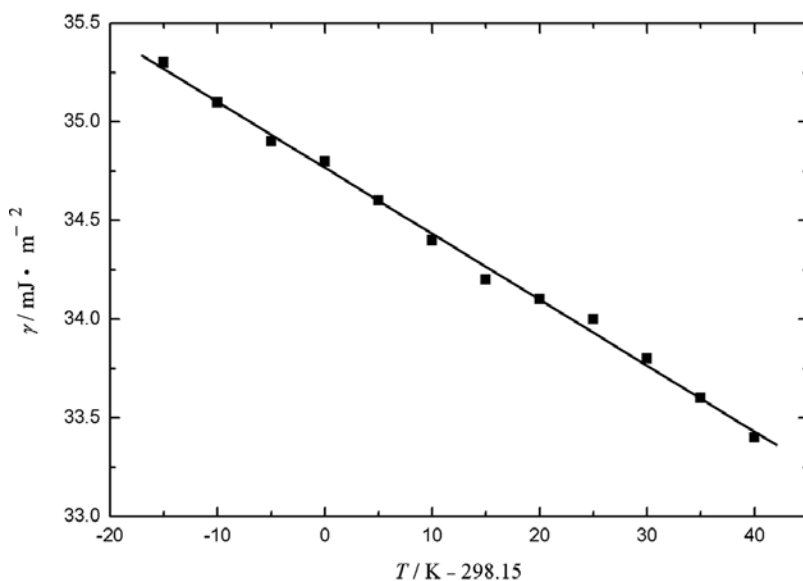


Figure 3. Plot of γ vs. $T/\text{K} - 298.15$ of IL $[\text{C}_2\text{mim}][\text{PF}_3(\text{CF}_2\text{CF}_3)_3]$.

The contribution of the methylene ($-\text{CH}_2-$) group to the molecular volumes can be obtained according to the literature studies [12, 13]. The values of the ILs $[\text{C}_n\text{mim}][\text{BF}_4]$, $[\text{C}_n\text{mim}][\text{NTf}_2]$, $[\text{C}_n\text{mim}][\text{AlCl}_4]$, and $[\text{C}_n\text{mim}][\text{Ala}]$ are 0.0272, 0.0282, 0.0270 and 0.0278 nm^3 , respectively. From the above values, the contribution of the methylene to the molecular volume can be considered to be similar. So, the mean value of the contribution can be calculated to be 0.0275 nm^3 , the physicochemical properties (density, standard entropy, lattice energy) of the homologues of $[\text{C}_n\text{mim}][\text{PF}_3(\text{CF}_2\text{CF}_3)_3]$ ($n = 1, 3, 4, 5, 6$) can be predicted. All of the predicted data are listed in **Table 2**.

Properties	[C ₁ mim] [PF ₃ (CF ₂ CF ₃) ₃] ^p	[C ₂ mim] [PF ₃ (CF ₂ CF ₃) ₃] ^e	[C ₃ mim] [PF ₃ (CF ₂ CF ₃) ₃] ^p	[C ₄ mim] [PF ₃ (CF ₂ CF ₃) ₃] ^p	[C ₅ mim] [PF ₃ (CF ₂ CF ₃) ₃] ^p	[C ₆ mim] [PF ₃ (CF ₂ CF ₃) ₃] ^p
<i>M</i> /g·mol ⁻¹	542.15	556.18	570.20	584.23	598.26	612.29
<i>V_m</i> /nm ³	0.5130	0.5405	0.5680	0.5955	0.6230	0.6505
<i>ρ</i> /g·cm ⁻³	1.75552	1.70926 ^m	1.66756	1.62962	1.59516	1.56356
<i>S</i> ⁰ /J·K ⁻¹ ·mol ⁻¹	669.0	703.3	737.5	771.8	806.1	840.3
<i>U_{pot}</i> /kJ·mol ⁻¹	397	392	387	383	379	375
<i>V</i> /cm ⁻³ ·mol ⁻¹	308.8	325.4	341.9	358.5	375.0	391.6
<i>p</i>	757.8	792.1	826.4	860.7	895.0	929.3
$\Delta_1^{\text{g}}H_m^0$ / kJ·mol ⁻¹	161.9	157.8	160.3	161.1	162.0	163.1
10 ²⁴ <i>v</i> /cm ³	25.93	27.63	28.48	29.65	30.75	31.78
Σv /cm ³	31.22	33.33	34.29	35.70	37.03	38.26
10 ² Σv / <i>V</i>	10.11	10.22	10.29	9.96	9.87	9.77
10 ⁴ α /K ⁻¹		6.96 ^m				
10 ⁴ α /K ⁻¹	5.10	5.14	5.04	5.00	4.96	4.91
γ 10 ³ /N·m ⁻¹	36.3	34.8 ^m	34.1	33.2	32.4	31.7

Notes: ^m measurement value; ^p data in the column were predicted values; ^e data in the column were estimated values.

Table 2. Estimated and predicted values of physicochemical properties of IL [C_{*n*}mim][PF₃(CF₂CF₃)₃] (*n* = 1, 2, 3, 4, 5, 6) at 298.15 K.

According to the literature [12, 13], the contribution per methylene (–CH₂–) to parachor is 31.1 for [C_{*n*}mim][AlCl₄] and 37.5 for [C_{*n*}mim][Ala]. An average value of the contribution can be calculated to be 34.3. So, the average value can be used to predict the parachor of the ILs [C_{*n*}mim][PF₃(CF₂CF₃)₃] (*n* = 1, 3, 4, 5, 6). According to Eq. (6), the surface tension can be calculated from the predicted density and parachor. The molar enthalpy of vaporization, $\Delta_1^{\text{g}}H_m^0$, can be obtained from the predicted density and surface tension. The data are listed in **Table 2**.

According to the predicted values of density and surface tension, the other properties can be predicted and the values are also listed in **Table 2**.

According to the interstice model and Eqs. (8)–(10) [6, 7], the interstice volume, *v*, the molar volume of ionic liquids, *V*, consists of the inherent volume, *V_i* and the volume of the interstices; the molar volume of the interstice, $\Sigma v = 2Nv$, the thermal expansion coefficient, α , can be predicted from the interstice model at 298.15 K. All of the data obtained from estimation and prediction are listed in **Table 2**.

Table 2 shows the comparison of the predicted and experimental thermal expansion coefficients of [C₂mim][PF₃(CF₂CF₃)₃] at 298.15 K. The difference of the two values is about 26%. So, the predicted values of the expansion coefficient can be as the reference data when lack of reliable experimental values.

For the majority materials, the volume expansions are in the range of 10–15% from the solid state to the liquid state. From **Table 2**, the estimated and predicted interstice fractions are in the range of 9–11% for the serious ILs $[C_n\text{mim}][PF_3(CF_2CF_3)_3]$ ($n = 1, 2, 3, 4, 5, 6$) at 298.15 K. The values are in good agreement with the reported values. Therefore, the interstice model theory can be used for calculation of the thermal expansion coefficient.

Conclusion

In this section, the density and surface tension of the imidazolium-type hydrophobic IL $[C_2\text{mim}][PF_3(CF_2CF_3)_3]$ ($n = 1, 2, 3, 4, 5, 6$) were determined and predicted in the temperature range of 283.15–338.15 K. According to the estimated equations and interstice model theory, the thermodynamic properties of the serious ILs were calculated by the empirical and semiempirical equations at 298.15 K. The effect of the methylene on molecular volume and parachor was discussed and used for the prediction of the thermodynamic properties of ILs. From the predicted values of thermal expansion coefficient, the other predicted values can be used as the reference data when lack the reliable experimental values.

7. Density, dynamic viscosity, and electrical conductivity of imidazolium-type hydrophobic functional ionic liquids

Ionic liquids (ILs) have exhibited outstanding physicochemical properties, such as good solvation, negligible vapor pressure, good thermal stability, and designability. ILs have been used as the green solvents in industrial and scientific areas. The functional ionic liquids (FILs) have been paid much more attention because of the designability [14–24]. The physicochemical properties can be designed according to the introduction of the functional groups, such as $-\text{CN}$, $-\text{OH}$, and $-\text{CH}_2-\text{O}-\text{CH}_3$.

Egashira et al. [14–16] have introduced the cyano group on the imidazolium FILs and quaternary ammonium FILs, respectively. The FILs have been applied in the lithium batteries as electrolyte components. The FILs have showed an improved cycle behavior compared with the electrolyte based on a tetraalkylammonium ionic liquid without a cyano group. The quaternary ammonium-based FILs containing a cyano group showed the better stability of the cathodic than the imidazolium-based FILs. Hardacre et al. [17, 18] have also synthesized two series pyridinium type FILs. The effect of electron-withdrawing groups on the properties was discussed according to the presence of the nitrile or trifluoromethyl in this type FILs. The introduction of the two functional groups leads to the increasing of the melting temperature compared the traditional ILs. On the basis of this fact, the authors have observed the liquid charge-transfer complexes form upon contacting electron-rich aromatics with an electron withdrawing group appended 1-alkyl-4-cyanopyridinium ionic liquids. Zhang et al. [19] have studied the solubilities of C_2H_4 and CO_2 in the cyano-type imidazolium FILs using the gas chromatography. Compared with the 1,3-dialkylimidazolium-type ILs, the cyano-type FILs result in a remarkable decrease of the interactions of hydrocarbons. The cyano-type ILs have exhibited the advanta-

geous properties. As the solvent, it can be applied as a suitable reaction media and ligands in catalytic reactions, as an electrolyte in lithium batteries, as a solvent for extraction of metals and dissolution of cellulose.

Although the FILs have been applied in some areas, the physicochemical properties are not enough for the application [20–22]. In this chapter, the properties of 1-acetonitrile-3-ethylimidazolium bis(trifluoromethylsulfonyl)imide [MCNMIM][NTf₂], 1-(cyanopropyl)-3-methylimidazolium bis[(trifluoromethyl) sulfonyl]imide [PCNMIM][NTf₂], 1-ethanol-3-ethylimidazolium bis(trifluoromethylsulfonyl)imide [EOHMIM][NTf₂], 1-butylamide-3-ethylimidazolium bis(trifluoromethylsulfonyl)-imide [CH₂CONHBuEIM][NTf₂] were compared with the traditional ILs 1-alkyl-3-methylimidazolium bis(trifluoromethylsulfonyl)imide [C_nMIM][NTf₂], (*n* = 2, 4) and 1-alkyl-2,3-dimethylimidazolium bis(trifluoromethylsulfonyl)imide [C_nMMIM][NTf₂], (*n* = 2, 4).

The structure of [EMIM][NTf₂], [BMIM][NTf₂], [EMMIM][NTf₂], [BMMIM][NTf₂], [MCNMIM][NTf₂], [PCNMIM][NTf₂], [EOHMIM][NTf₂], and [CH₂CONHBuEIM][NTf₂] is shown in **Figure 4**.

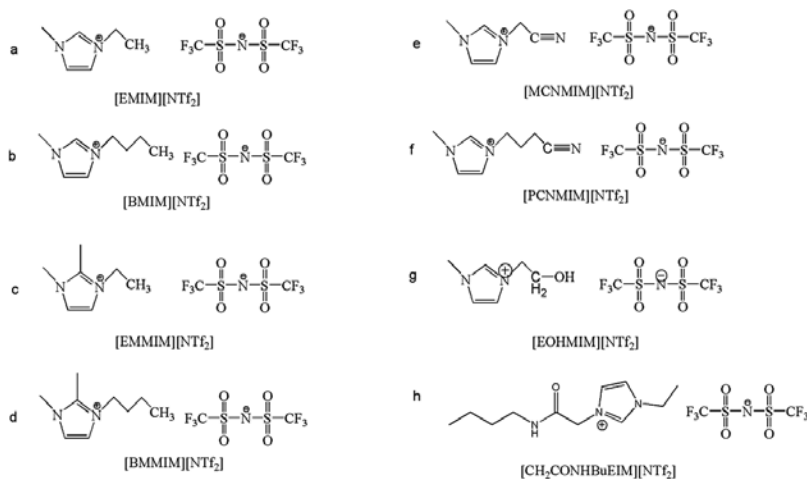


Figure 4. The structures of the (a) [EMIM][NTf₂], (b) [BMIM][NTf₂], (c) [EMMIM][NTf₂], (d) [BMMIM][NTf₂], (e) [MCNMIM][NTf₂], (f) [PCNMIM][NTf₂], (g) [EOHMIM][NTf₂], and (h) [CH₂CONHBuEIM][NTf₂].

The density, dynamic viscosity, and electrical conductivity of the four FILs are listed in **Tables 3–5** [23–25].

The temperature dependences on the density of the FILs [MCNMIM][NTf₂], [PCNMIM][NTf₂], [EOHMIM][NTf₂], and [CH₂CONHBuEIM][NTf₂] are plotted in **Figure 5**.

In order to compare the influences of methylene and functional group on the properties of ILs, the values of density, dynamic viscosity, and electrical conductivity for ILs are listed in **Table 6** at 298.15 K. The ILs are [EMIM][NTf₂], [BMIM][NTf₂], [EMMIM][NTf₂], [BMMIM][NTf₂], [MCNMIM][NTf₂], [PCNMIM][NTf₂], [EOHMIM][NTf₂], and [CH₂CONHBuEIM][NTf₂], respectively.

	[MCNMIM] [NTf ₂]	[PCNMIM] [NTf ₂]	[EOHMIM] [NTf ₂]	[CH ₂ CONHBuEIM] [NTf ₂]
283.15	1.6259	1.5290	1.5886	1.4310
288.15	1.6205	1.5239	1.5836	1.4270
293.15	1.6150	1.5191	1.5786	1.4227
298.15	1.6097	1.5143	1.5737	1.4180
303.15	1.6046	1.5097	1.5688	1.4135
308.15	1.5996	1.5051	1.5639	1.4090
313.15	1.5946	1.5006	1.5591	1.4044
318.15	1.5898	1.4961	1.5542	1.3997
323.15	1.5848	1.4916	1.5494	1.3954
328.15	1.5799	1.4870	1.5446	1.3910
333.15	1.5751	1.4826	1.5398	1.3867
338.15	1.5702	1.4781	1.5350	1.3823
343.15	1.5654	1.4737	1.5302	
348.15	1.5606	1.4692	1.5255	
353.15	1.5558	1.4648	1.5207	

Table 3. Experimental values of density, $\rho/\text{kg}\cdot\text{m}^{-3}$, of [MCNMIM][NTf₂], [PCNMIM][NTf₂], [EOHMIM][NTf₂], and [CH₂CONHBuEIM][NTf₂] from 283.15 to 353.15 K at atmosphere pressure.

	[MCNMIM] [NTf ₂]	[PCNMIM] [NTf ₂]	[EOHMIM] [NTf ₂]	[CH ₂ CONHBuEIM] [NTf ₂]
283.15	1140	612.68	213.4	
288.15	708.6	419.66	153.7	
293.15	463.4	303.31	114.1	
298.15	315.5	222.35	86.89	777.5
303.15	222.8	166.86	67.66	517.3
308.15	162.4	131.14	53.88	359.0
313.15	121.7	99.090	43.52	255.2
318.15	93.56	78.438	35.85	187.9
323.15	73.61	63.791	29.83	138.9
328.15	58.99	55.023	25.20	106.0
333.15	47.93	44.728	21.52	82.1
338.15	39.70	37.515	18.46	64.4
343.15	33.27	29.223	16.08	53.3
348.15	28.11	26.418	14.06	43.5
353.15	24.06	23.573	12.44	35.8

Table 4. Experimental values of dynamic viscosity, $\eta/\text{mPa}\cdot\text{s}$, of [MCNMIM][NTf₂], [PCNMIM][NTf₂], [EOHMIM][NTf₂], and [CH₂CONHBuEIM][NTf₂] from 283.15 to 353.15 K at atmosphere pressure.

	[MCNMIM] [NTf ₂]	[PCNMIM] [NTf ₂]	[EOHMIM] [NTf ₂]	[CH ₂ CONHBuEIM] [NTf ₂]
283.15	0.283		1.319	0.0606
288.15	0.439	0.612	1.794	0.0985
293.15	0.648	0.841	2.37	0.1527
298.15	0.919	1.125	3.05	0.233
303.15	1.294	1.473	3.87	0.332
308.15	1.727	1.874	4.81	0.467
313.15	2.25	2.33	5.89	0.639
318.15	2.85	2.88	7.04	0.854
323.15	3.60	3.49	8.30	1.106
328.15	4.41	4.17	9.67	1.414
333.15	5.36	4.94	11.12	1.774
338.15	6.44	5.78	12.77	2.19
343.15	7.56	6.66	14.47	
348.15	8.78	7.60	16.26	
353.15	10.12		18.15	

Table 5. Experimental values of electrical conductivity, $\sigma/\text{mS}\cdot\text{cm}^{-1}$, of [MCNMIM][NTf₂], [PCNMIM][NTf₂], [EOHMIM][NTf₂], and [CH₂CONHBuEIM][NTf₂] from 283.15 to 353.15 K at atmosphere pressure.

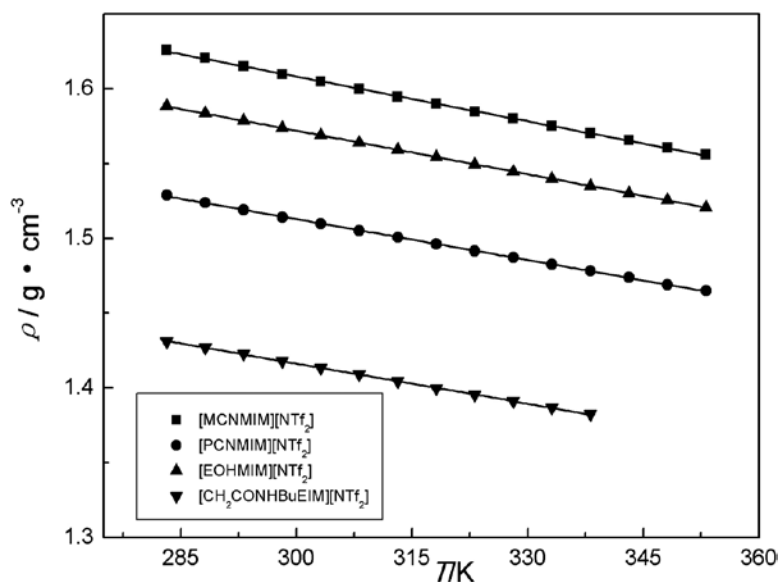


Figure 5. Density vs. temperature plots for FILs [MCNMIM][NTf₂], [PCNMIM][NTf₂], [EOHMIM][NTf₂], and [CH₂CONHBuEIM][NTf₂].

	MW g mol ⁻¹	V cm ³ mol ⁻¹	ρ kg m ⁻³	η mPa s	σ mS cm ⁻¹
[EMIM][NTf ₂]	391.31	257.75	1.5182 ^a	32.0 ^a	8.96 ^a
[BMIM][NTf ₂]	419.36	291.91	1.4366 ^a	51.7 ^a	3.98 ^a
[EMMIM][NTf ₂]	405.33	271.48	1.4931 ^a	72.2 ^a	3.89 ^a
[BMMIM][NTf ₂]	433.38	304.70	1.4224 ^a	101.6 ^a	2.12 ^a
[MCNMIM][NTf ₂]	402.29	249.92	1.6097 ^b	315.5 ^b	0.919 ^b
[PCNMIM][NTf ₂]	430.34	284.18	1.5143 ^c	222.35 ^c	1.125 ^c
[EOHMIM][NTf ₂]	407.30	258.8	1.5737	86.89	3.05
[CH ₂ CONHBuEIM][NTf ₂]	490.47	345.89	1.4180	777.5	0.233

Table 6. Comparison of density, ρ , dynamic viscosity, η , and electrical conductivity, σ , of [EMIM][NTf₂], [BMIM][NTf₂], [EMMIM][NTf₂], [BMMIM][NTf₂], [MCNMIM][NTf₂], [PCNMIM][NTf₂], [EOHMIM][NTf₂], and [CH₂CONHBuEIM][NTf₂] at 298.15 K at atmosphere pressure.

From **Table 6**, based on the same anion, at 298.15 K, the density follows the order of ILs [CH₂CONHBuEIM][NTf₂] < [BMMIM][NTf₂] < [BMIM][NTf₂] < [EMMIM][NTf₂] < [PCNMIM][NTf₂] < [EMIM][NTf₂] < [EOHMIM][NTf₂] < [MCNMIM][NTf₂].

The dynamic viscosity follows the order of ILs [EMIM][NTf₂] < [BMIM][NTf₂] < [EMMIM][NTf₂] < [EOHMIM][NTf₂] < [BMMIM][NTf₂] < [PCNMIM][NTf₂] < [MCNMIM][NTf₂] < [CH₂CONHBuEIM][NTf₂].

The electrical conductivity follows the order of ILs [CH₂CONHBuEIM][NTf₂] < [MCNMIM][NTf₂] < [PCNMIM][NTf₂] < [BMMIM][NTf₂] < [EOHMIM][NTf₂] < [EMMIM][NTf₂] < [BMIM][NTf₂] < [EMIM][NTf₂].

As shown in **Table 6**, the three series ILs have exhibited the same tendency for density after the introduction of methylene on the alkyl side chain. Usually, for dynamic viscosity and electrical conductivity, the introduction of methylene leads to the dynamic viscosity increase and electrical conductivity decrease, such as [EMIM][NTf₂] and [BMIM][NTf₂]; [EMMIM][NTf₂] and [BMMIM][NTf₂]. However, for the FILs, the values exhibited the contrary tendency with the traditional ILs. The dynamic viscosity values of FIL [PCNMIM][NTf₂] are lower than FIL [MCNMIM][NTf₂] and the electrical conductivity values of FIL [PCNMIM][NTf₂] are higher than FIL [MCNMIM][NTf₂] in the temperature range. The abnormal results have been also discovered for traditional pyridinium-type ILs from our group (see here). For the pyridinium-type ILs, the electrical conductivity values increase when the methyl group is introduced on position 4. The dynamic viscosity values decrease when the methyl group is introduced on position 4. We believed that the electron-withdrawing and electron-donating groups play the important role to the effect of the properties. -CN is the electron-withdrawing group, -CH₂- and -CH₃ are the electron-donating group. For the two series ILs, the presence of the -CN and -CH₃ leads to the cations that have the relatively symmetry structure after the introduction of -CH₂-. Then, the cation and anion have the relatively far away and the force of them becomes weak. So, these two types of ILs exhibited the high fluidity after the introduction of -CH₂-.

As indicated in **Table 6**, the density and dynamic viscosity of the FILs are higher than the nonfunctional ILs, and the electrical conductivity is lower than the nonfunctional ILs after the introduction of the $-\text{CN}$ or $-\text{CH}_2\text{OH}$ functional group on the imidazolium ring, this result leads to the increasing of Van der Waals force between the cation and the anion relative to the nonfunctional ILs. The order of the effect of the group to the thermodynamic properties is: $-\text{CN} > -\text{CH}_2\text{OH} > -\text{CH}_3$.

According to Eqs. (1)–(4), the calculated values of the thermal expansion coefficient molecular volume, standard molar entropy, and lattice energy are calculated and listed in **Table 7**, respectively.

Property	[MCNMIM] [NTf ₂]	[PCNMIM] [NTf ₂]	[EOHMIM] [NTf ₂]	[CH ₂ CONHBuEIM] [NTf ₂]
MW/(g mol ⁻¹)	402.29	430.34	407.30	490.47
V/(nm ³)	0.4151	0.4721	0.4299	0.5746
10 ⁴ α/(K ⁻¹)	6.26	6.09	6.23	6.36
V _m /(cm ⁻³ mol ⁻¹)	249.9	284.18	258.8	345.89
S ⁰ /(J K ⁻¹ mol ⁻¹)	547.0	617.9	565.4	745.7
U _{pot} /(kJ mol ⁻¹)	418	405	414	613

Table 7. Calculated values of thermodynamic properties of FILs [MCNMIM][NTf₂], [PCNMIM][NTf₂], [EOHMIM][NTf₂], and [CH₂CONHBuEIM][NTf₂] at 288.15–338.15 K under atmospheric pressure.

From **Table 7**, the contribution of the methylene to the molecular volume is 0.0285 nm³ for the cyano-type FILs [MCNMIM][NTf₂] and [PCNMIM][NTf₂]. The value is in good agreement with the reported values of 0.0280 nm³ for ILs [C_npy][NTf₂] [4, 26], 0.0282 nm³ for [C_nmim][NTf₂], 0.0277 nm³ for [C_n3mpy][NTf₂] (*n* = 3, 4, 6) [27], and 0.0289 nm³ for [C_n4mpy][NTf₂] (*n* = 2, 4, 6) [27] at 298.15 K. The lattice energies of the FILs are much lower than traditional salts, such as U_{POT, CsI} = 613 kJ mol⁻¹ [28]. Usually, the ILs exhibit the low lattice energy [4, 23–27]. And it is the reason that the ILs having the relatively low melting temperature can exist in the liquid state at room temperature.

Usually, the Vogel-Fulcher-Tammann (VFT) is used for the fitting of temperature dependence on dynamic viscosity. The temperature dependences on dynamic viscosity of the FILs [MCNMIM][NTf₂], [PCNMIM][NTf₂], [EOHMIM][NTf₂], and [CH₂CONHBuEIM][NTf₂] are plotted in **Figure 6**.

The best fitted values of η₀, B, T₀, and the correlation coefficient, R, are listed in **Table 8** from the empirical Eq. (11). From **Table 8**, the obtained correlation coefficient values, R, are better than 0.9999. The results indicate that the experimental dynamic viscosity of the FILs [MCNMIM][NTf₂], [PCNMIM][NTf₂], [EOHMIM][NTf₂], and [CH₂CONHBuEIM][NTf₂] can be fitted by the VFT equation.

According to Eq. (12), the 1000/T dependence of ln η was plotted for four FILs [MCNMIM][NTf₂], [PCNMIM][NTf₂], [EOHMIM][NTf₂], and [CH₂CONHBuEIM][NTf₂] (see **Figure 7**).

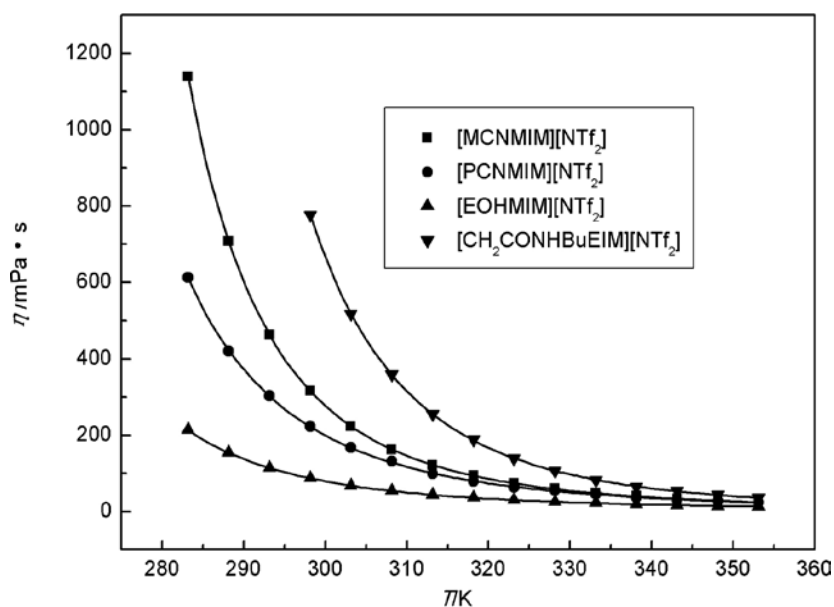


Figure 6. Dynamic viscosity vs. temperature plots for FILs [MCNMIM][NTf₂], [PCNMIM][NTf₂], [EOHMIM][NTf₂], and [CH₂CONHBuEIM][NTf₂].

Property	[MCNMIM][NTf ₂]	[PCNMIM][NTf ₂]	[EOHMIM][NTf ₂]	[CH ₂ CONHBuEIM][NTf ₂]
η_0 /(mPa s)	0.2166	0.1600	0.2144	0.0820
B /K	728.8	882.1	692.3	990.9
$10^5 E_\eta$ /eV	62.9	76.1	59.7	85.5
T_σ /K	198.1	176.2	182.9	189.9
R	0.99999	0.99989	0.99999	0.99998

Table 8. Fitted parameter values of η_0 , B , T_σ and correlation coefficient, R , and E_η .

The $1000/T$ dependences on $\ln \eta$ of the four FILs [MCNMIM][NTf₂], [PCNMIM][NTf₂], [EOHMIM][NTf₂], and [CH₂CONHBuEIM][NTf₂] are also fitted in the temperature range (**Figure 7**). The values of the correlation coefficient, R , are 0.9878, 0.9937, 0.9926, and 0.9943, respectively. The values are obvious lower than the correlation coefficient values, $R = 0.99999$, 0.99989, 0.99999, and 0.99998, which obtained according to the VFT equation. So, the same result indicated that the dynamic viscosity values of [MCNMIM][NTf₂], [PCNMIM][NTf₂], [EOHMIM][NTf₂], and [CH₂CONHBuEIM][NTf₂] cannot be fitted according to the Arrhenius Eq. (12). From **Figure 7**, it can be obviously observed that the measurement points lie far away from the fitted straight lines.

According to Eq. (13), the activation energies of dynamic viscosity for the FILs [MCNMIM][NTf₂], [PCNMIM][NTf₂], [EOHMIM][NTf₂], and [CH₂CONHBuEIM][NTf₂] were calculated and are listed in **Table 8**.

From **Table 5**, the temperature dependences on electrical conductivity of the FILs [MCNMIM][NTf₂], [PCNMIM][NTf₂], [EOHMIM][NTf₂], and [CH₂CONHBuEIM][NTf₂] are plotted in **Figure 8**.

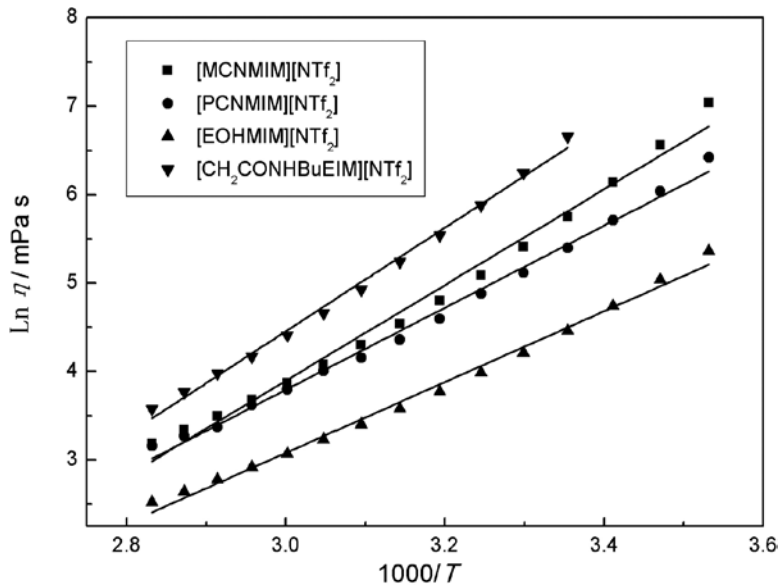


Figure 7. Plot of $\ln \eta$ vs. $1000/T$ for FILs [MCNMIM][NTf₂], [PCNMIM][NTf₂], [EOHMIM][NTf₂], and [CH₂CONHBuEIM][NTf₂].

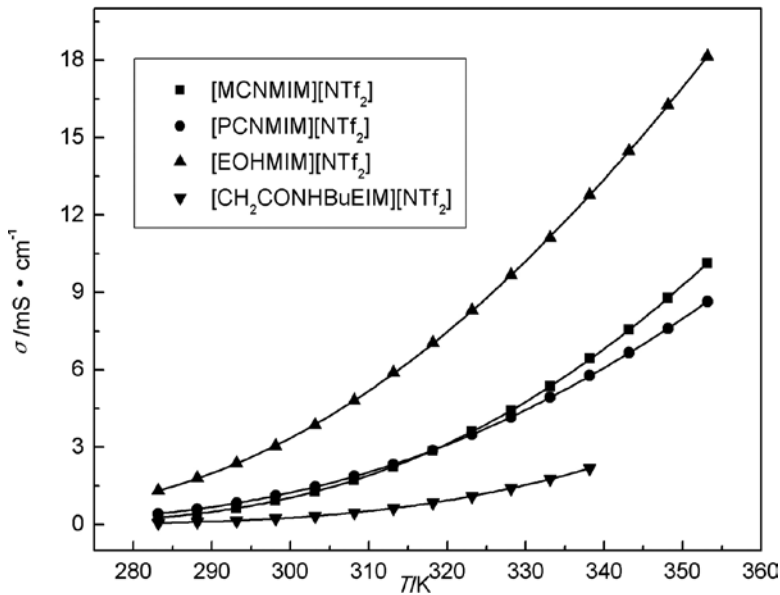


Figure 8. Electrical conductivity vs. temperature plots for FILs [MCNMIM][NTf₂], [PCNMIM][NTf₂], [EOHMIM][NTf₂], and [CH₂CONHBuEIM][NTf₂].

The best fitted values of σ_0 , B , T_0 , and the correlation coefficient, R , are listed in **Table 9** from the empirical Eq. (14). From **Table 9**, the obtained correlation coefficient, R , is better than 0.9999. The results indicate that the measurement electrical conductivity of the FILs [MCNMIM][NTf₂], [PCNMIM][NTf₂], [EOHMIM][NTf₂], and [CH₂CONHBuEIM][NTf₂] can be fitted by the VFT equation.

According to Eq. (15), the $1000/T$ dependence on $\ln \sigma$ was plotted of four FILs [MCNMIM][NTf₂], [PCNMIM][NTf₂], [EOHMIM][NTf₂], and [CH₂CONHBuEIM][NTf₂] (see **Figure 9**).

Property	[MCNMIM][NTf ₂]	[PCNMIM][NTf ₂]	[EOHMIM][NTf ₂]	[CH ₂ CONHBuEIM][NTf ₂]
$\sigma_0/(\text{S}\cdot\text{cm}^{-1})$	0.64	0.49	0.56	0.82
B/K	621.3	661.8	551.9	860.5
$10^3 E_0/\text{eV}$	53.6	57.1	47.6	74.3
T_0/K	203.0	189.3	192.0	192.9
R	0.99997	0.99997	0.99998	0.99999

Table 9. Fitted parameter values of σ_0 , B , T_0 , correlation coefficient, R and E_0 .

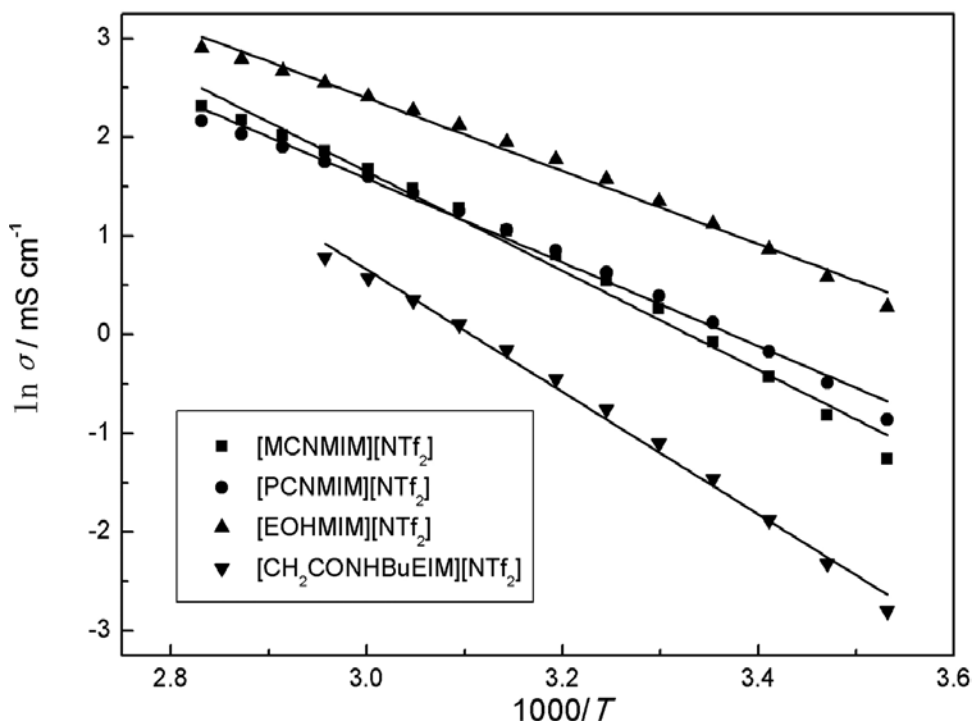


Figure 9. Plot of $\ln \sigma$ and $\ln \sigma_0$ vs. $1000/T$ for FILs [MCNMIM][NTf₂], [PCNMIM][NTf₂], [EOHMIM][NTf₂], and [CH₂CONHBuEIM][NTf₂].

In **Figure 9**, the $1000/T$ dependences on $\ln \sigma$ of the four FILs [MCNMIM][NTf₂], [PCNMIM][NTf₂], [EOHMIM][NTf₂], and [CH₂CONHBuEIM][NTf₂] are fitted in the temperature range. The values of the correlation coefficient, R , are 0.9878, 0.9908, 0.9905, and, 0.9930, respectively. The same results can be obtained that the values are much lower than the correlation coefficient values, $R = 0.99997, 0.99998, 0.99998, \text{ and } 0.99999$, which obtained by the VFT equation (see **Table 9**). So, the measurement electrical conductivity of [MCNMIM][NTf₂], [PCNMIM][NTf₂], [EOHMIM][NTf₂], and [CH₂CONHBuEIM][NTf₂] does not well follow the Arrhenius Eq. (15). From **Figure 9**, it can be obviously seen that the measurement points lie far away from the fitted straight lines.

The activation energies of electrical conductivity for four FILs [MCNMIM][NTf₂], [PCNMIM][NTf₂], [EOHMIM][NTf₂], and [CH₂CONHBuEIM][NTf₂] were also calculated by Eq. (16) and are listed in **Table 9**.

At 298.15 K, the Walden's product (in [S·cm²·mol⁻¹][mP·s]) for the four FILs [MCNMIM][NTf₂], [PCNMIM][NTf₂], [EOHMIM][NTf₂], and [CH₂CONHBuEIM][NTf₂] can be determined according to Eq. (17), and the values are 73, 71, 69, and 63, respectively.

According to Eq. (17), the $\log \Lambda$ dependences on $\log \eta^{-1}$ are illustrated in **Figure 10** for the four FILs [MCNMIM][NTf₂], [PCNMIM][NTf₂], [EOHMIM][NTf₂], and [CH₂CONHBuEIM][NTf₂] from 283.15 to 353.15 K.

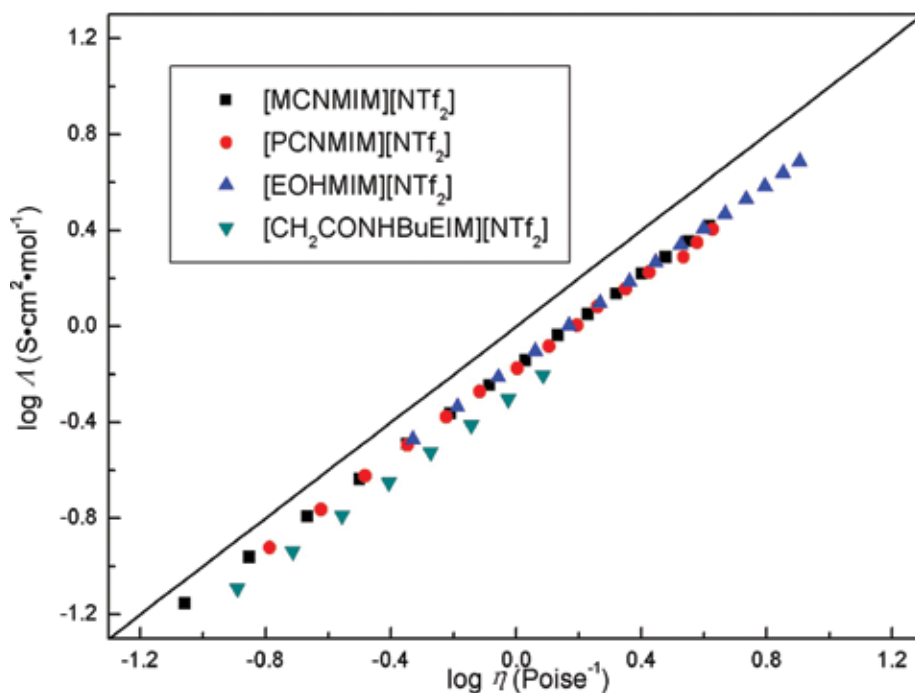


Figure 10. Plot of $\lg \Lambda$ vs. $\lg \eta^{-1}$ for the four FILs [MCNMIM][NTf₂], [PCNMIM][NTf₂], [EOHMIM][NTf₂], and [CH₂CONHBuEIM][NTf₂] from 283.15 to 353.15 K. The solid straight line is the ideal line for aqueous KCl solutions.

Usually, the Walden rule can be used for the presentation of the independent ions of the liquid. If the Walden points close to the ideal line, the liquid can be considered as a relative ideal liquid. The ideal line position was determined according to the aqueous KCl solution at high dilution. As an ideal line, the slope of the ideal line should be unity and not have any interaction of the ions [10, 29, 30]. In **Figure 10**, it can be seen that the approximately straight lines can be obtained according to the experimental points. The results indicate that the FILs [MCNMIM][NTf₂], [PCNMIM][NTf₂], [EOHMIM][NTf₂], and [CH₂CONHBuEIM][NTf₂] follow the Walden rule to some extent. The slopes of the lines for the four FILs [MCNMIM][NTf₂], [PCNMIM][NTf₂], [EOHMIM][NTf₂], and [CH₂CONHBuEIM][NTf₂] are 0.941, 0.927, 0.939, and 0.913, respectively. The lines for the two FILs below are close to the ideal KCl line, as shown in **Figure 10**. Most of the reported traditional ILs [9, 10, 29, 31] and our previous studied ILs [24–27, 32, 33] have the same trend. From the result, the FILs [MCNMIM][NTf₂], [PCNMIM][NTf₂], [EOHMIM][NTf₂], and [CH₂CONHBuEIM][NTf₂] can be named “sub-ionic” [34].

Conclusion

The density, dynamic viscosity, and electrical conductivity of the FILs [MCNMIM][NTf₂], [PCNMIM][NTf₂], [EOHMIM][NTf₂], and [CH₂CONHBuEIM][NTf₂] were measured at the temperature from 283 to 353 K. The others thermodynamic properties of the FILs, like thermal expansion coefficient, molecular volume, standard molar entropy, and lattice energy, were estimated according to the classical empirical equations. The introduction of the methylene group on the –CN (electron-withdrawing group) type series FILs leads to a different change in the dynamic viscosity, and electrical conductivity with the traditional ILs. The dynamic viscosity values of FIL [PCNMIM][NTf₂] are lower than FIL [MCNMIM][NTf₂] and the electrical conductivity values of FIL [PCNMIM][NTf₂] are higher than FIL [MCNMIM][NTf₂] in the temperature range. The temperature dependences on the dynamic viscosity and electrical conductivity values of the ILs can be satisfactorily fitted by the VFT equation. However, the experimental values do not follow the Arrhenius behavior described by the Arrhenius equation.

8. Density, dynamic viscosity, and electrical conductivity of pyridinium-based hydrophobic ionic liquids

Actually, most of the studied ILs are hydrophilic-type ILs. The hydrophobic ILs have been paid much more attention in many fields as a special functional ILs. The bis(trifluoromethylsulfonyl)imide [NTf₂][−] as an air- and water-stable anion has been applied in many fields [35–37]. These types of anion ILs have exhibited a relatively wide liquid range, higher electrical conductivity, and thermal stability than the hydrophilic-type ILs. However, the study of thermodynamic properties of the [NTf₂]-type ILs mainly focuses on the imidazolium-type cation ILs [38–40]. The study of the pyridinium type cation-based ILs is still not

enough [41]. The systematical research on the properties including density, dynamic viscosity, and electrical conductivity is still scarce which can provide the well information of the suitable IL for a specific purpose.

In this section, the basic physicochemical properties of three series of N-alkylpyridinium bis(trifluoromethylsulfonyl)imide {[C_npy][NTf₂] (n = 2, 3, 4, 5, 6)}, N-alkyl-3-methylpyridinium bis(trifluoromethylsulfonyl)imide {[C_n3Mpy][NTf₂] (n = 3, 4, 6)}, and N-alkyl-4-methylpyridinium bis(trifluoromethylsulfonyl)imide {[C_n4Mpy][NTf₂] (n = 2, 4, 6)} were discussed. The methyl group was introduced on positions 3 and 4 of the pyridinium ring, respectively. The basic physicochemical properties, including density, dynamic viscosity, and electrical conductivity, were measured by the traditional methods. The other physicochemical properties, including molecular volume, standard molar entropy, lattice energy, were estimated in terms of empirical and semiempirical equations on the basis of the experimental value. The effect of the methylene and methyl groups on the properties is discussed at 298.15 K.

The structures of ILs [C_npy][NTf₂] (n = 2, 3, 4, 5, 6), [C_n3Mpy][NTf₂] (n = 3, 4, 6), and [C_n4Mpy][NTf₂] (n = 2, 4, 6) are shown in **Figure 11**.

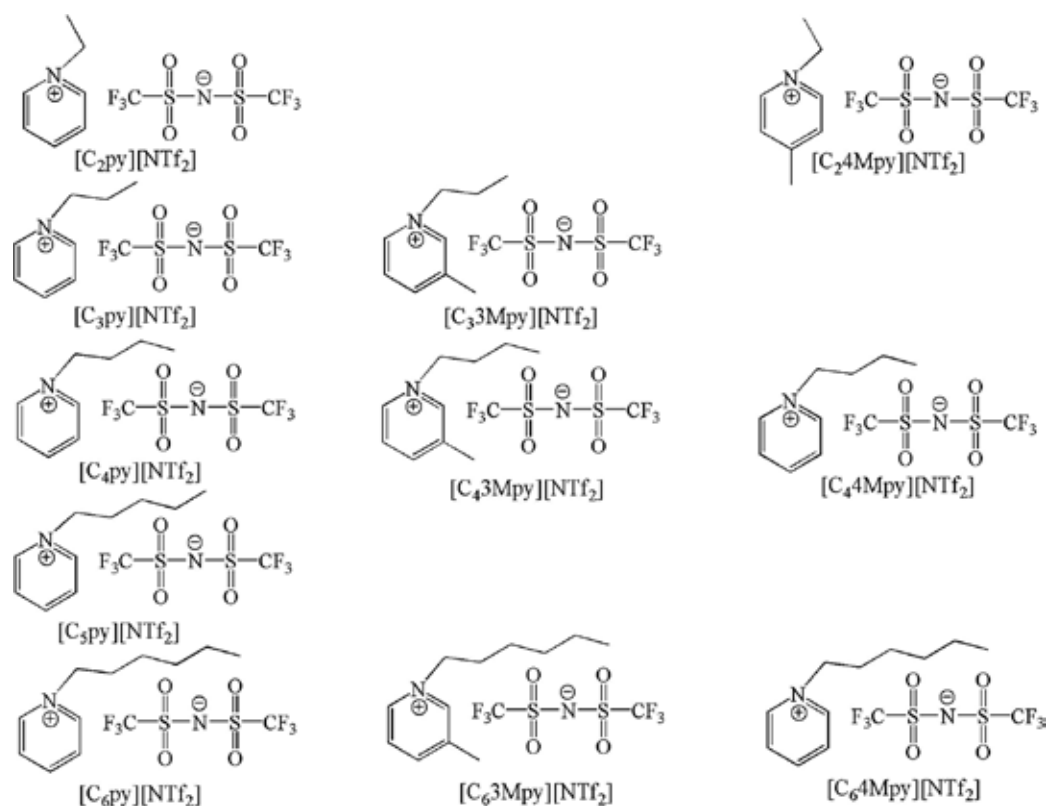


Figure 11. The structure of ILs [C_npy][NTf₂] (n = 2, 3, 4, 5, 6), [C_n3Mpy][NTf₂] (n = 3, 4, 6), and [C_n4Mpy][NTf₂] (n = 2, 4, 6).

8.1. N-Alkyl type pyridinium type ionic liquids

The results of the density, surface tension, dynamic viscosity, and electrical conductivity of the ILs $[C_n\text{py}][\text{NTf}_2]$ ($n = 2, 3, 4, 5, 6$) are listed in Tables 10–13 [4, 31, 33].

	$[C_2\text{py}][\text{NTf}_2]$	$[C_3\text{py}][\text{NTf}_2]$	$[C_4\text{py}][\text{NTf}_2]$	$[C_5\text{py}][\text{NTf}_2]$	$[C_6\text{py}][\text{NTf}_2]$
283.15				1.4331	1.4008
288.15	1.5457			1.4296	1.3966
293.15	1.5414			1.4259	1.3923
298.15	1.5375		1.4547	1.4214	1.3877
303.15	1.5332		1.4506	1.4169	1.3831
308.15	1.5291	1.4845	1.4462	1.4128	1.3789
313.15	1.5249	1.4800	1.4417	1.4083	1.3744
318.15	1.5205	1.4757	1.4372	1.4038	1.3699
323.15	1.5164	1.4710	1.4332	1.3989	1.3655
328.15	1.5122	1.4667	1.4291	1.3942	1.3615
333.15	1.5078	1.4623	1.4245	1.3893	1.3569
338.15	1.5037	1.4574	1.4205	1.3851	1.3525

Table 10. Experimental values of density of ILs $[C_n\text{py}][\text{NTf}_2]$ ($n = 2, 3, 4, 5, 6$).

	$[C_2\text{py}][\text{NTf}_2]$	$[C_3\text{py}][\text{NTf}_2]$	$[C_4\text{py}][\text{NTf}_2]$	$[C_5\text{py}][\text{NTf}_2]$	$[C_6\text{py}][\text{NTf}_2]$
283.15				33.1	32.5
288.15	37.7			32.8	32.2
293.15	37.6			32.7	32.0
298.15	37.4		33.4	32.5	31.7
303.15	37.1		33.2	32.2	31.6
308.15	36.9		32.9	32.0	31.4
313.15	36.7		32.8	31.8	31.2
318.15	36.6		32.4	31.5	31.0
323.15	36.4		32.1	31.3	30.8
328.15	36.1		32.0	31.1	30.6
333.15	35.9		31.8	30.8	30.3
338.15	35.6		31.5	30.5	30.1

Table 11. Experimental values of surface tension of ILs $[C_n\text{py}][\text{NTf}_2]$ ($n = 2, 3, 4, 5, 6$).

	[C ₂ py][NTf ₂]	[C ₃ py][NTf ₂]	[C ₄ py][NTf ₂]	[C ₅ py][NTf ₂]	[C ₆ py][NTf ₂]
298.15	39.4		58.3	71.9	84.5
303.15	32.5		46.7	57.1	66.4
308.15	27.1	33.0	38.0	45.6	53.2
313.15	23.2	27.6	31.4	37.2	43.1
318.15	20.0	23.3	26.4	30.6	35.2
323.15	17.3	19.8	22.4	25.6	29.1
328.15	15.2	17.1	19.2	21.7	24.5
333.15	13.5	14.9	16.6	18.4	20.9
338.15	11.9	13.5	14.4	15.8	17.9

Table 12. Experimental values of dynamic viscosity of ILs [C_{*n*}py][NTf₂] (*n* = 2, 3, 4, 5, 6).

	[C ₂ py][NTf ₂]	[C ₃ py][NTf ₂]	[C ₄ py][NTf ₂]	[C ₅ py][NTf ₂]	[C ₆ py][NTf ₂]
283.15			1.67	1.04	0.76
288.15			1.91	1.37	1.00
293.15	5.01		2.50	1.77	1.30
298.15	5.99		3.21	2.22	1.66
303.15	7.06		3.95	2.75	2.08
308.15	8.24		4.73	3.36	2.57
313.15	9.53	7.19	5.63	4.03	3.11
318.15	10.90	8.30	6.70	4.81	3.87
323.15	12.33	9.55	7.79	5.63	4.46
328.15	14.28	10.83	8.96	6.53	5.38
333.15	16.09	12.23	10.19	7.42	6.21
338.15	17.84	13.65	11.47	8.24	7.12

Table 13. Experimental values of electrical conductivity of ILs [C_{*n*}py][NTf₂] (*n* = 2, 3, 4, 5, 6).

From **Tables 10–13**, it can be concluded that the density and electrical conductivity decrease as the alkyl side chain length of the cation increases for the N-alkyl type pyridinium ILs. The dynamic viscosity increases with the extension of the alkyl side chain of the cation for the three series of N-alkyl type pyridinium ILs.

According to Eqs. (1)–(10), the thermodynamic properties are calculated and listed in **Table 14**, respectively.

Property	[C ₂ py][NTf ₂]	[C ₄ py][NTf ₂]	[C ₅ py][NTf ₂]	[C ₆ py][NTf ₂]
10 ³ S _a /mJ·K ⁻¹ ·m ⁻²	41.6	47.9	46.2	41.8
E _a /mJ·m ⁻²	49.8	47.7	46.3	44.1
V _m /nm ³	0.4196	0.4754	0.5030	0.5320
S ⁰ /J·K ⁻¹ ·mol ⁻¹	552.5	622.1	656.4	692.6
10 ⁷ k/J·K ⁻¹	1.131	1.590	1.503	1.316
T _c /K	1618	1212	1271	1429
T _v /K	970	727	763	857
U _{pot} /kJ·mol ⁻¹	417	404	399	393
V/cm ³ ·mol ⁻¹	252.6	286.2	302.8	320.2
p	625.0	688.9	723.5	759.9
Δ [‡] H _m ⁰ /kJ·mol ⁻¹	143.8	139.1	140.9	142.9
10 ²⁴ v/cm ³	24.80	29.38	30.67	31.77
Σv/cm ³	29.86	35.38	36.92	38.25
10 ² Σv/V	11.82	12.36	12.19	11.95
10 ⁴ α/K ⁻¹ (exp.)	5.63	5.99	6.30	6.40
10 ⁴ α/K ⁻¹ (cal.)	5.95	6.22	6.13	6.01

Table 14. Estimated values of physicochemical properties of [C_npy][NTf₂] at 298.15 K.

From **Table 14**, the thermal expansion coefficients are 5.63×10^{-4} , 5.99×10^{-4} , 6.30×10^{-4} , and $6.40 \times 10^{-4} \text{ K}^{-1}$ for [C₂py][NTf₂], [C₄py][NTf₂], [C₅py][NTf₂], and [C₆py][NTf₂], respectively. The values are in good agreement in the range of 5×10^{-4} to $7 \times 10^{-4} \text{ K}^{-1}$ obtained by Jacquemin et al. [40]. From **Table 14**, compared with the fused salts and organic liquids, for example, $E_a = 146 \text{ mJ}\cdot\text{m}^{-2}$ for NaNO₃, $E_a = 67 \text{ mJ}\cdot\text{m}^{-2}$ for benzene and $E_a = 51.1 \text{ mJ}\cdot\text{m}^{-2}$ for octane. The values of surface energy of the samples are close to the organic liquids. This fact shows that the interaction energy between ions in the samples is less than fused salts. The values of the molecular volume are 0.4196 nm³ for [C₂py][NTf₂], 0.4754 nm³ for [C₄py][NTf₂], 0.5030 nm³ for [C₅py][NTf₂], and 0.5320 nm³ for [C₆py][NTf₂] at 298.15 K. The plotting V_m against the number of the carbons, n , in the alkyl chain of the samples ([C_npy][NTf₂]) can be described (see **Figure 4**). The average contribution of the methylene to the molecular volume can be obtained by the slop of the fitting equation. The value is 0.0280 nm³ at 298.15 K. The value is close to the values of 0.0272 nm³ for imidazolium-type ILs [C_nmim][BF₄] and 0.0282 nm³ for imidazolium-type [C_nmim][NTf₂].

The molar masses of cations of the ILs [C_npy][NTf₂] ($n = 2, 4, 5, 6$) are listed in **Table 15**. The plotting V_m against the molar mass of cations of the samples ([C_npy][NTf₂]) can be obtained (see **Figure 12**). The intercept of the linear regression can be approximately regarded the volume of the anion, NTf₂⁻, the value is 0.2032 nm³. The volume value of NTf₂⁻ is much higher than 0.1390 nm³ for AlCl₄⁻ [42] and 0.1548 nm³ GaCl₄⁻ [43]. The volume values of the cations and the radii are listed in **Table 15**.

	$\rho/\text{g}\cdot\text{cm}^{-3}$	V_m/nm^3	M_+	V_f/nm^3	r_s/nm
$[\text{C}_2\text{py}][\text{NTf}_2]$	1.5375	0.4196	108.16	0.2164	0.372
$[\text{C}_4\text{py}][\text{NTf}_2]$	1.4547	0.4754	136.22	0.2722	0.402
$[\text{C}_5\text{py}][\text{NTf}_2]$	1.4214	0.5030	150.24	0.2998	0.415
$[\text{C}_6\text{py}][\text{NTf}_2]$	1.3877	0.5320	164.27	0.3288	0.428

Table 15. Estimated volumetric properties of the ILs $[\text{C}_n\text{py}][\text{NTf}_2]$ $n = 2, 4, 5, 6$ at 298.15 K.

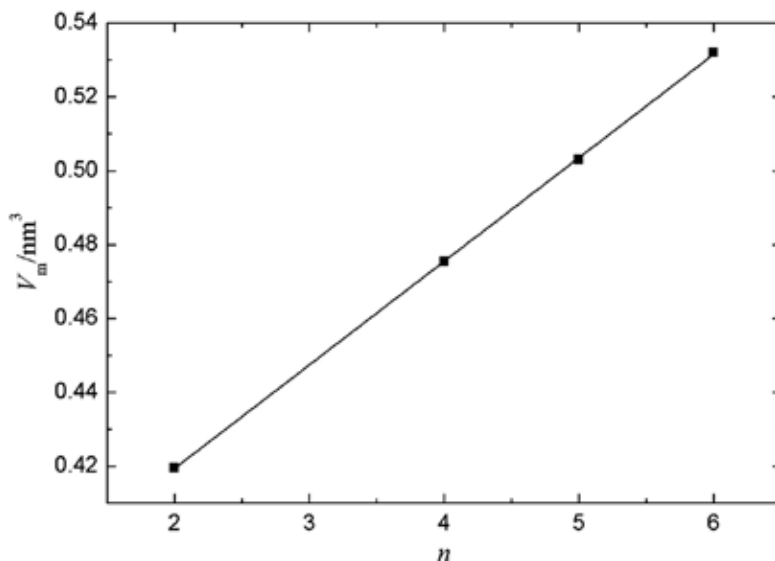


Figure 12. Plot of V_m vs. n at 298.15 K, the correlation coefficient is $R = 0.9999$ for ILs $[\text{C}_n\text{py}][\text{NTf}_2]$ ($n = 2, 4, 5, 6$).

According to Eq. (5), by plotting the $\gamma V_m^{2/3}$ against T , straight lines were obtained (see **Figure 13**). From the plot, the value of empirical constant (k) and critical temperature (T_c) can be obtained according to the fitting equation and the values are listed in **Table 16**. Rebelo et al. [44] have reported that the normal boiling point, T_b , is approximately $0.6T_c$ for ILs. Herein, the normal boiling point, T_b , can be calculated and the values are also listed in **Table 16**. For the majority of organic liquids, $k \approx 2.1 \times 10^{-7} \text{ J}\cdot\text{K}^{-1}$, but for fused salts, $k = 0.4 \times 10^{-7} \text{ J}\cdot\text{K}^{-1}$ for fused NaCl [7]. It indicated that ILs $[\text{C}_n\text{py}][\text{NTf}_2]$ ($n = 2, 4, 5, 6$) have the medium polarity between organic liquids and fused salts in terms of the value of the k .

From **Table 14**, the values of estimation of the thermal expansion coefficient are in good agreement with experimental values. It also can be seen that the estimation values of interstice fractions, $\sum v/V$, are in the range of 11–13% for the ILs $[\text{C}_n\text{py}][\text{NTf}_2]$ ($n = 2, 4, 5, 6$). For the majority materials, the volume expansions are in the range of 10–15% from the solid state to liquid state. For the ILs $[\text{C}_n\text{py}][\text{NTf}_2]$ ($n = 2, 4, 5, 6$), the values are in good agreement with the reported values. Therefore, the interstice model theory can be used for calculation of the thermal expansion coefficient of pyridinium-based ILs.

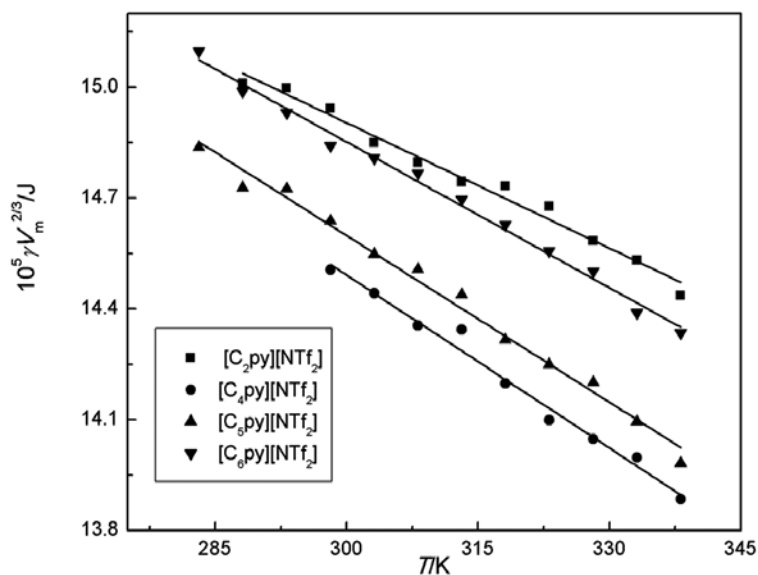


Figure 13. Plot of $\gamma V_m^{2/3}$ vs. T (K) for ILs $[C_n\text{py}][\text{NTf}_2]$ ($n = 2, 4, 5, 6$).

	$[C_2\text{py}][\text{NTf}_2]$	$[C_4\text{py}][\text{NTf}_2]$	$[C_5\text{py}][\text{NTf}_2]$	$[C_6\text{py}][\text{NTf}_2]$
$10^7 k/\text{J}\cdot\text{K}^{-1}$	1.131	1.559	1.503	1.316
T_v/K	1618	1230	1815	1429
T_c/K	971	738	1089	857

Table 16. The estimated values of k , T_v , and T_c for ILs $[C_n\text{py}][\text{NTf}_2]$ $n = 2, 4, 5, 6$.

According to **Table 12** and Eq. (11), the temperature dependence on dynamic viscosity values of the ILs can also be fitted using the VFT Eq. (11), see **Figure 14**.

The best fitting parameters of η_0 , B , T_0 , and the corresponding correlation coefficient, R , are listed in **Table 17**. From **Table 17**, the obtained values of the correlation coefficient, R , are 0.9999, which indicates that the VFT equation can be used for fitting the experimental dynamic viscosity.

According to Eq. (13), the activation energies of dynamic viscosity for $[C_n\text{py}][\text{NTf}_2]$ ($n = 2, 4, 5, 6$) were calculated by Eq. (13) and are listed in **Table 17**.

According to Eq. (12), the $1000/T$ dependence of $\ln \eta$ was plotted for $[C_n\text{py}][\text{NTf}_2]$ ($n = 2, 3, 4, 5, 6$) (see **Figure 15**).

The $1000/T$ dependences on $\ln \eta$ of the for $[C_n\text{py}][\text{NTf}_2]$ ($n = 2, 3, 4, 5, 6$) were fitted in the temperature range (see **Figure 15**). The values of the correlation coefficient, R , are 0.9976, 0.9965,

0.9977, 0.9984, and 0.9983, respectively. The values are obviously lower than the values (all of the values are 0.9999) which obtained by the empirical VFT equation. So, the measurement dynamic viscosity of $[C_n\text{py}][\text{NTf}_2]$ ($n = 2, 3, 4, 5, 6$) does not follow the Arrhenius Eq. (12). From **Figure 15**, it can also be obviously seen that the measurement points lie far away from the fitted straight lines. The FILs $[\text{MCNMIM}][\text{NTf}_2]$, $[\text{PCNMIM}][\text{NTf}_2]$, $[\text{EOHMIM}][\text{NTf}_2]$, and $[\text{CH}_2\text{CONHBuEIM}][\text{NTf}_2]$ have also exhibited the same result.

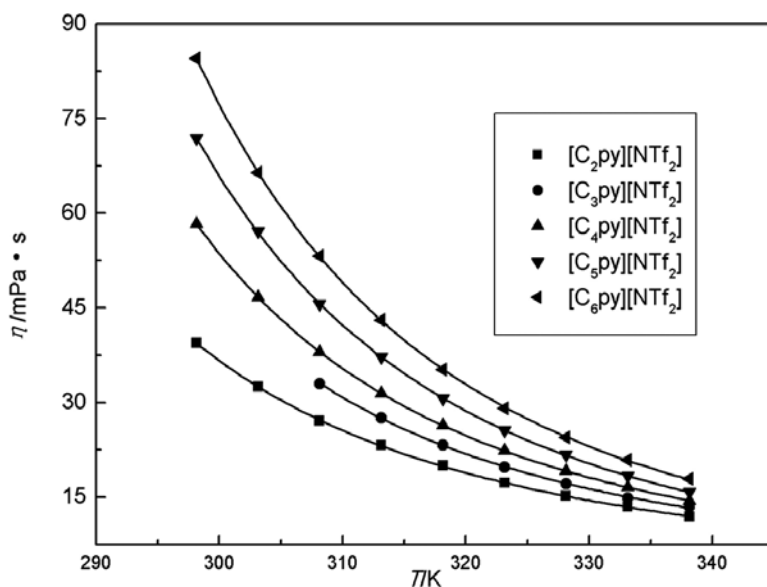


Figure 14. Plot of dynamic viscosity, η , vs. temperature, T , of ILs $[C_n\text{py}][\text{NTf}_2]$ ($n = 2, 3, 4, 5, 6$).

Property	$[C_2\text{py}][\text{NTf}_2]$	$[C_4\text{py}][\text{NTf}_2]$	$[C_5\text{py}][\text{NTf}_2]$	$[C_6\text{py}][\text{NTf}_2]$
$\eta_0/(\text{mPa}\cdot\text{s})$	0.3907	0.2021	0.0758	0.0645
B/K	531.7	695.1	966.2	1036.0
$10^3 E_a/\text{eV}$	45.9	60.0	83.4	89.4
T_0/K	182.9	175.4	157.2	153.8
R	0.9999	0.9999	0.9999	0.9999

Table 17. Fitted values of dynamic viscosity of η_0 , B , E_a , T_0 and R according to Eqs. (11) and (13).

According to **Table 13** and Eq. (14), the temperature dependences of electrical conductivity values of the ILs can also be fitted using the VFT Eq. (14), see **Figure 16**.

The best-fitting parameters of σ_0 , B , T_0 and the corresponding correlation coefficient, R , are listed in **Table 18**. From **Table 18**, the obtained values of the correlation coefficient, R , are 0.9996, which indicates that the VFT equation can be used for fitting the experimental electrical conductivity.

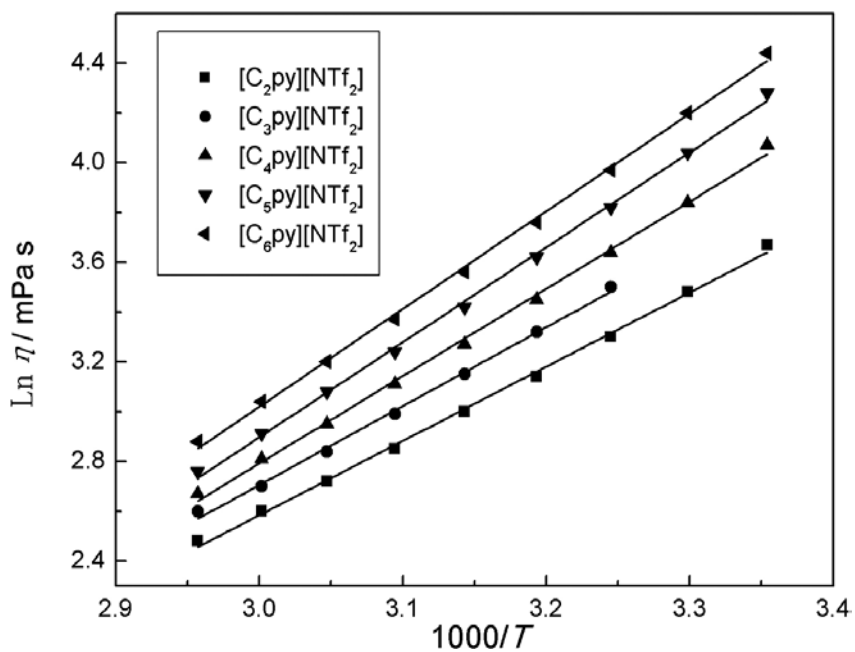


Figure 15. Plot of dynamic viscosity, η , vs. temperature, T , of $[\text{C}_n\text{py}][\text{NTf}_2]$ ($n = 2, 3, 4, 5, 6$).

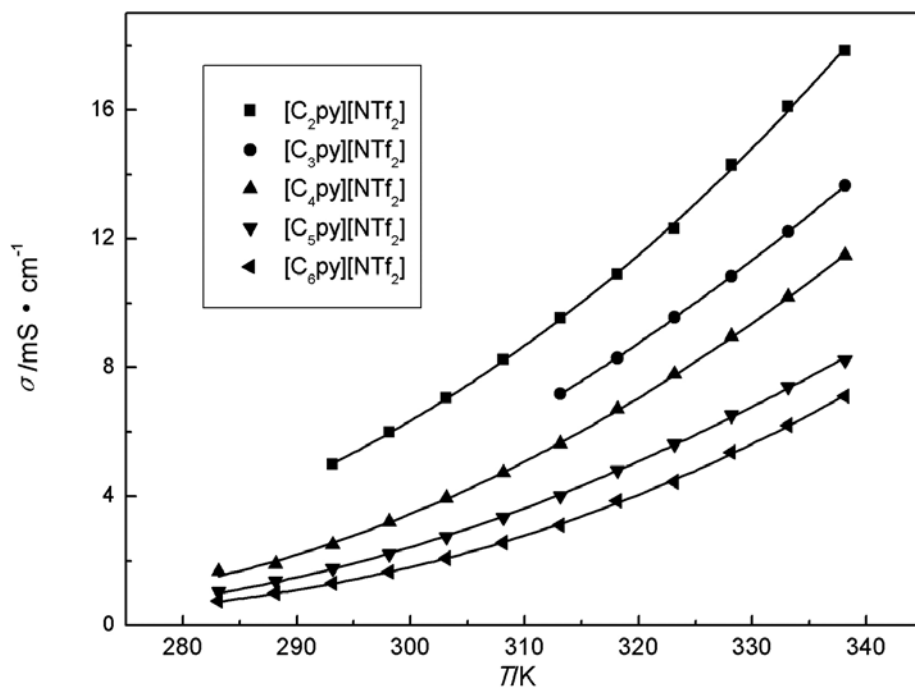


Figure 16. Plot of electrical conductivity, σ , vs. temperature, T , of $[\text{C}_n\text{py}][\text{NTf}_2]$ ($n = 2, 3, 4, 5, 6$).

Property	[C ₂ py][NTf ₂]	[C ₄ py][NTf ₂]	[C ₅ py][NTf ₂]	[C ₆ py][NTf ₂]
σ_0 /(S·cm ⁻¹)	2.39	0.47	0.23	0.81
B/K	1067.5	577.7	472.9	803.1
10 ⁵ E _σ /eV	92.1	49.9	40.8	69.3
T ₀ /K	119.9	182.3	196.5	168.4
R	0.9996	0.9996	0.9996	0.9996

Table 18. Fitted values of electrical conductivity of σ_0 , B, E_σ, T₀ and R according to Eqs. (15) and (17).

According to Eq. (16), the activation energies of dynamic viscosity for [C_npy][NTf₂] (n = 2, 4, 5, 6) were calculated by Eq. (16) and are listed in **Table 18**.

According to Eq. (15), the 1000/T dependence on ln σ was also plotted for the [C_npy][NTf₂] (n = 2, 4, 5, 6) (see **Figure 17**).

In **Figure 17**, the 1000/T dependence on ln σ of the [C_npy][NTf₂] (n = 2, 3, 4, 5, 6) was fitted in the temperature range. The values of the correlation coefficient, R, are 0.9990, 0.9990, 0.9939, and 0.9970, respectively. The values are also lower than the values (all of the values of R = 0.9996) which obtained by the empirical VFT equation (see **Table 18**). So, the measurement electrical conductivity does not follow the Arrhenius Eq. (15). In **Figure 17**, it can also be seen that the measurement points lie far away from the fitted straight lines. The FILs [MCNMIM][NTf₂], [PCNMIM][NTf₂], [EOHMIM][NTf₂], and [CH₂CONHBuEIM][NTf₂] have also exhibited the same result.

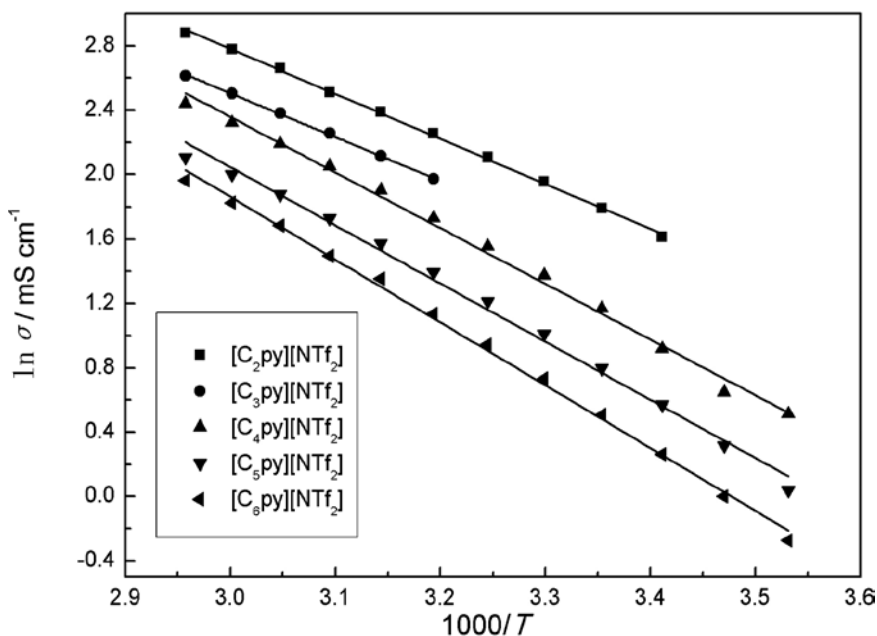


Figure 17. Plot of Ln σ vs. 1000/T of ILs [C_npy][NTf₂] (n = 2, 3, 4, 5, 6).

The Walden's product (in $[S \cdot \text{cm}^2 \cdot \text{mol}^{-1}][\text{mP} \cdot \text{s}]$) can be calculated according to Eq. (17). The values are 60, 54, 48, 45 for $[\text{C}_2\text{py}][\text{NTf}_2]$, $[\text{C}_4\text{py}][\text{NTf}_2]$, $[\text{C}_3\text{py}][\text{NTf}_2]$, and $[\text{C}_6\text{py}][\text{NTf}_2]$ at 298.15 K, respectively. From the results, the values are decrease with the methylene introduced.

According to Eq. (17), the $\log \Lambda$ dependence on $\log \eta^{-1}$ is illustrated in **Figure 18** for the $[\text{C}_n\text{py}][\text{NTf}_2]$ ($n = 2, 3, 4, 5, 6$) from 283.15 to 338.15 K.

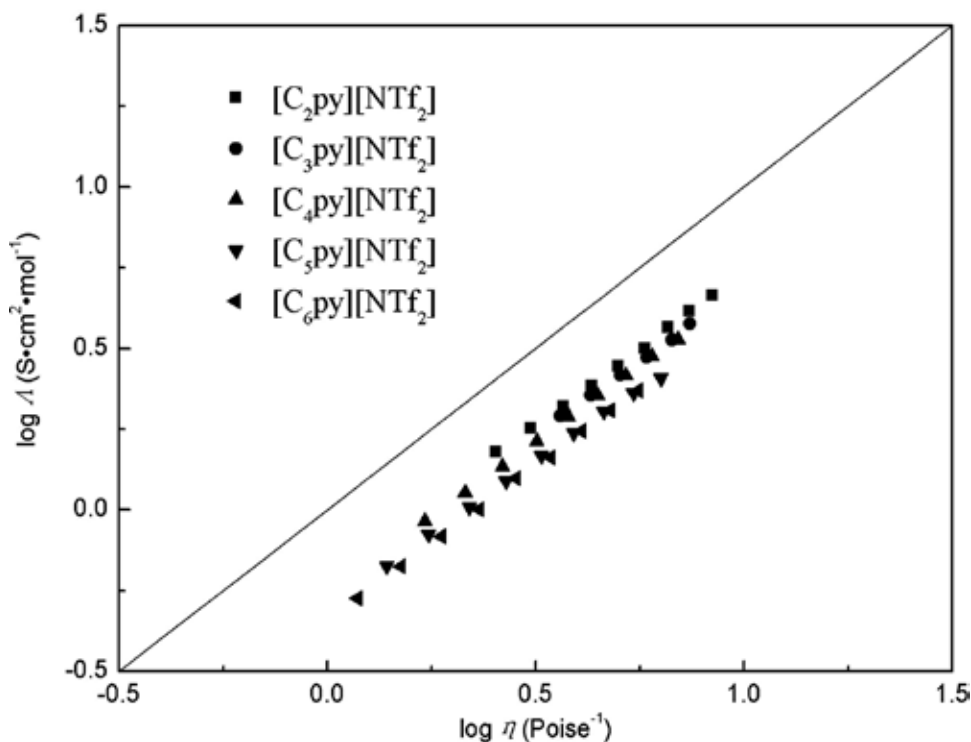


Figure 18. Walden plots for samples at temperature from 283.15 to 338.15 K for $[\text{C}_n\text{py}][\text{NTf}_2]$ ($n = 2, 3, 4, 5, 6$).

Usually, the Walden rule can be used for the presentation of the independent ions of the liquid. If the Walden points close to the ideal line, the liquid can be considered as a relative ideal liquid. The ideal line position was determined according to the aqueous KCl solution at high dilution. As an ideal line, the slope of the ideal line should be unity and not have any interaction of the ions [10, 29, 30]. In **Figure 10**, it can be seen that the approximately straight lines can be obtained according to the experimental points.

Like the FILs, the Walden rule can also be used for the presentation of the independent ions of the ILs $[\text{C}_n\text{py}][\text{NTf}_2]$ ($n = 2, 3, 4, 5, 6$). From **Figure 18**, it can be seen that the approximately straight lines can be obtained according to the experimental values. The fitted slopes of the lines for the ILs $[\text{C}_n\text{py}][\text{NTf}_2]$ ($n = 2, 3, 4, 5, 6$) are 0.941, 0.906, 0.935, 0.893, and 0.959, respectively. The lines for the ILs below are close to the ideal KCl line from **Figure 18**. Most of the reported traditional ILs [9, 10, 29–31] have the same tendency. Herein, the ILs $[\text{C}_n\text{py}]$

[NTf₂] (*n* = 2, 3, 4, 5, 6) can be called “subionic.” It means that the ILs [C_{*n*}py][NTf₂] (*n* = 2, 3, 4, 5, 6) did not yield the expected conductivity from the high fluidities because on average the proton transfer is incomplete. The behavior of the ILs [C_{*n*}py][NTf₂] (*n* = 2, 3, 4, 5, 6) as if there is only a small population of ions and the “ionicity” of the ILs is therefore reduced [34].

8.2. N-Alkyl-3-methyl or N-alkyl-4-methyl type pyridinium-type ionic liquids

Two series ILs [C_{*n*}3Mpy][NTf₂] (*n* = 3, 4, 6) and [C_{*n*}4Mpy][NTf₂] (*n* = 2, 4, 6) were synthesized in this section. From **Figure 11**, the two series ILs introduced the methyl group on the pyridinium ring and the positions are position 3 and 4, respectively.

The values of the density, dynamic viscosity, and electrical conductivity are listed in **Tables 19–21** [27, 33, 45].

In order to compare the density, dynamic viscosity, and electrical conductivity with the N-alkyl type pyridinium-type ILs at 298.15 K, the values of the three series pyridinium-based ILs are listed in **Table 22**.

<i>T</i> /K	[C ₃ 3Mpy][NTf ₂]	[C ₄ 3Mpy][NTf ₂]	[C ₆ 3Mpy][NTf ₂]	[C ₂ 4Mpy][NTf ₂]	[C ₄ 4Mpy][NTf ₂]	[C ₆ 4Mpy][NTf ₂]
278.15	1.4685 ^c	1.4399	1.3781 ^c	1.5100 ^c	1.4373 ^c	1.3695 ^c
283.15	1.4640 ^c	1.4357	1.3736	1.5052	1.4328	1.3653
288.15	1.4596	1.4315	1.3697	1.5010	1.4284	1.3608
293.15	1.4556	1.4271	1.3653	1.4961	1.4234	1.3563
298.15	1.4514	1.4226	1.3615	1.4920	1.4187	1.3518
303.15	1.4471	1.4183	1.3570	1.4877	1.4140	1.3474
308.15	1.4426	1.4142	1.3529	1.4830	1.4093	1.3429
313.15	1.4380	1.4098	1.3487	1.4783	1.4047	1.3385
318.15	1.4332	1.4051	1.3447	1.4734	1.4002	1.3341
323.15	1.4287	1.4007	1.3403	1.4688	1.3958	1.3296
328.15	1.4245	1.3964	1.3360	1.4644	1.3913	1.3252
333.15	1.4203	1.3921	1.3317	1.4599	1.3869	1.3208
338.15	1.4160	1.3876	1.3280	1.4551	1.3825	1.3165
343.15	1.4113 ^c	1.3832 ^c	1.3237 ^c	1.4506 ^c	1.3777 ^c	1.3121
348.15	1.4069 ^c	1.3787 ^c	1.3195 ^c	1.4460 ^c	1.3731 ^c	1.3078
353.15	1.4025 ^c	1.3742 ^c	1.3154 ^c	1.4414 ^c	1.3686 ^c	1.3034

Note: ^c calculated values.

Table 19. Experimental values of density, ρ , of two series ILs [C_{*n*}3Mpy][NTf₂] (*n* = 3, 4, 6) and [C_{*n*}4Mpy][NTf₂] (*n* = 2, 4, 6) at pressure $p = 0.1$ MPa.

T/K	[C ₃ mpy][NTf ₂]	[C ₄ mpy][NTf ₂]	[C ₆ mpy][NTf ₂]	[C ₂ 4mpy][NTf ₂]	[C ₄ 4mpy][NTf ₂]	[C ₆ 4mpy][NTf ₂]
278.15	160.80 ^c	177.0 ^c	276.16 ^c	79.45 ^c	159.65 ^c	253.47 ^c
283.15	118.12 ^c	133.3 ^c	199.61 ^c	61.98 ^c	118.57 ^c	181.62
288.15	89.08 ^c	102.3 ^c	147.89 ^c	49.30 ^c	90.07 ^c	133.92
293.15	68.73 ^c	79.9 ^c	112.00 ^c	39.89 ^c	69.82 ^c	101.07
298.15	54.12	63.2	86.59	32.75	55.14	77.989
303.15	43.46	51.1	67.83	27.31	44.20	61.301
308.15	35.27	41.4	54.23	23.10	35.85	49.031
313.15	29.18	34.0	44.24	19.69	29.61	39.755
318.15	24.32	28.4	36.21	16.95	24.77	32.729
323.15	20.87	23.9	29.97	14.66	20.85	27.381
328.15	17.94	20.3	25.08	12.85	17.86	23.111
333.15	15.15	17.5	21.31	11.34	15.37	19.709
338.15	13.40	15.2	18.28	10.10	13.42	16.968
343.15	11.74	13.0	15.88	9.07	11.65	14.729
348.15	10.37	11.3	13.71	8.19	10.15	12.866
353.15	9.19	10.0	11.99	7.43	8.89	11.324
358.15				6.76	7.94	
363.15				6.19	7.20 ^c	

Note: ^c calculated values.

Table 20. Experimental values of dynamic viscosity, η , of two series ILs [C_{*n*}3Mpy][NTf₂] (*n* = 3, 4, 6) and [C_{*n*}4Mpy][NTf₂] (*n* = 2, 4, 6) at pressure *p* = 0.1 MPa.

From **Table 22**, the density of the three series of pyridinium-type ILs decreases with the introduction of the methylene group on the alkyl side chain of the pyridinium-type ILs. The result is the same with the imidazolium-type ILs [12, 13]. The introduction of the methyl group on the pyridinium-type ILs leads the apparent decrease of the density. However, the degree of decreasing is different on the position 3 and 4 of the pyridinium ring. The introduction of the methyl group on position 4 leads the more decrease than position 3 on the pyridinium ring. The order is as follows: [C₂py][NTf₂] > [C₂4mpy][NTf₂]; [C₄py][NTf₂] > [C₄3mpy][NTf₂] > [C₄4mpy][NTf₂]; [C₆py][NTf₂] > [C₆3mpy][NTf₂] > [C₆4mpy][NTf₂].

As shown in **Table 22**, the electrical conductivity of the three series pyridinium-type ILs decreases with the introduction of the methylene group on the alkyl side chain of the pyridinium-type ILs. But, the introduction of the methyl group on the ring leads to the different change tendency for electrical conductivity. For density, the values are decrease with the introduction of the methyl group on positions 3 and 4 of the pyridinium ring. However, the electrical conductivity decreases after the introduction of methyl group on position 3 and increases after the introduction of the methyl group on position 4 of the pyridinium ring. The tendency is just the reverse and the order is as follow: [C₂py][NTf₂] < [C₂4mpy][NTf₂]; [C₄3mpy][NTf₂] < [C₄py][NTf₂] < [C₄4mpy][NTf₂]; [C₆3mpy][NTf₂] < [C₆py][NTf₂] < [C₆4mpy][NTf₂].

T/K	[C ₃ 3mpy][NTf ₂]	[C ₄ 3mpy][NTf ₂]	[C ₆ 3mpy][NTf ₂]	[C ₂ 4mpy][NTf ₂]	[C ₄ 4mpy][NTf ₂]	[C ₆ 4mpy][NTf ₂]
278.15	1.524	1.00	0.495	3.39 ^c	1.24	0.592 ^c
283.15	1.990	1.32	0.670	4.24	1.66	0.839
288.15	2.53	1.72	0.885	5.25	2.15	1.101
293.15	3.18	2.17	1.157	6.38	2.73	1.447
298.15	3.93	2.72	1.480	7.63	3.41	1.852
303.15	4.76	3.35	1.869	9.01	4.19	2.31
308.15	5.71	4.09	2.31	10.50	5.09	2.83
313.15	6.71	4.90	2.83	12.08	6.00	3.46
318.15	7.86	5.76	3.42	13.78	7.02	4.15
323.15	9.04	6.90	4.06	15.54	8.17	4.87
328.15	10.36	7.96	4.77	17.50	9.41	5.71
333.15	11.79	9.10	5.53	19.55	10.75	6.52
338.15	13.29	10.31	6.38	21.7	12.07	7.56
343.15	14.85	11.60	7.28	23.9 ^c	13.56 ^c	8.61
348.15	16.50	12.96	8.22	26.2 ^c	15.10 ^c	9.68
353.15	18.28	14.37	9.20	28.5 ^c	16.70 ^c	10.75

Note: ^c calculated values.

Table 21. Experimental values of electrical conductivity, σ , of two series ILs [C_{*n*}3Mpy][NTf₂] (*n* = 3, 4, 6) and [C_{*n*}4Mpy][NTf₂] (*n* = 2, 4, 6) at pressure *p* = 0.1 MPa.

	$\rho/(\text{g}\cdot\text{cm}^{-3})$	$\eta/(\text{mPa}\cdot\text{s})$	$\sigma/(\text{mS}\cdot\text{cm}^{-1})$
[C ₂ py][NTf ₂]	1.5375	39.4	5.99
[C ₄ py][NTf ₂]	1.4547	58.3	3.21
[C ₅ py][NTf ₂]	1.4214	71.9	2.22
[C ₆ py][NTf ₂]	1.3877	84.5	1.66
[C ₃ 3mpy][NTf ₂]	1.4514	54.12	3.93
[C ₄ 3mpy][NTf ₂]	1.4226	63.2	2.72
[C ₆ 3mpy][NTf ₂]	1.3615	86.59	1.480
[C ₂ 4mpy][NTf ₂]	1.4920	32.75	7.63
[C ₄ 4mpy][NTf ₂]	1.4187	55.14	3.41
[C ₆ 4mpy][NTf ₂]	1.3518	77.989	1.852

Table 22. The comparison of density, ρ , dynamic viscosity, η , and electrical conductivity, σ , of three series pyridinium-based ILs at 298.15 K and pressure *p* = 0.1 MPa.

For the dynamic viscosity, the values of the three series pyridinium-type ILs increase with the introduction of the methylene group on the alkyl side chain of pyridinium-type cation ILs. Like the electrical conductivity, the dynamic viscosity also exhibited the difference tendency with the density after the introduction of the methyl group on the pyridinium ring. However, the tendency is in contrast to the electrical conductivity. For dynamic viscosity, the values increase with the introduction of the methyl group on position 3 of the pyridinium ring and decrease with the introduction of the methyl group on position 4 of the pyridinium ring with the non-substituting pyridinium ring. The order is as follows: $[C_2py][NTf_2] > [C_24mpy][NTf_2]; [C_43mpy][NTf_2] > [C_4py][NTf_2] > [C_44mpy][NTf_2]; [C_63mpy][NTf_2] > [C_6py][NTf_2] > [C_64mpy][NTf_2]$.

According to **Table 19**, the temperature dependence of the density values can be plotted and fitted according to the linear equation (**Figure 19**).

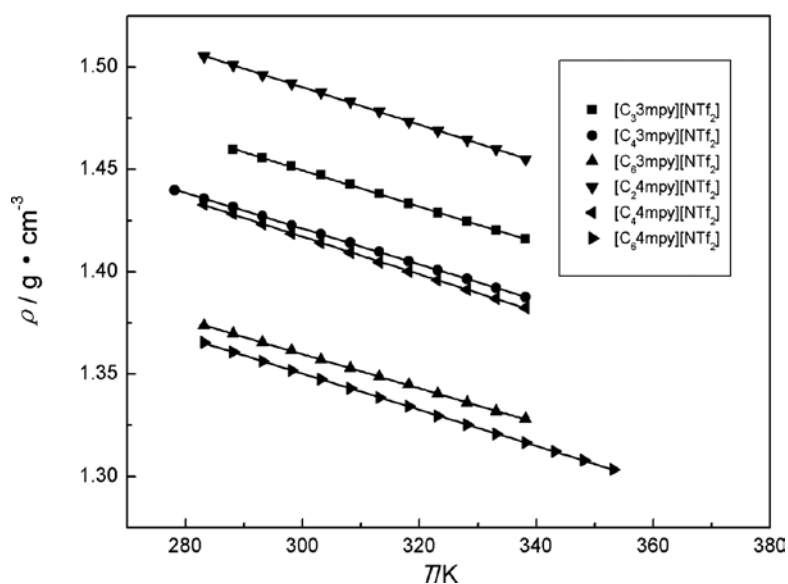


Figure 19. Plot of density, ρ , vs. temperature, T , for two series ILs $[C_n3Mpy][NTf_2]$ ($n=3, 4, 6$) and $[C_n4Mpy][NTf_2]$ ($n=2, 4, 6$).

The thermal expansion coefficient, α , molecular volume, V_m , standard molar entropy, S^0 , and lattice energy, U_{pot} were calculated from experimental density using the empirical Eqs. (1)–(4). The obtained data from the empirical equations are listed in **Table 23**.

From **Table 23**, the thermal expansion coefficients are $6.12 \times 10^{-4} K^{-1}$ for $[C_33mpy][NTf_2]$, $6.20 \times 10^{-4} K^{-1}$ for $[C_43mpy][NTf_2]$, $6.19 \times 10^{-4} K^{-1}$ for $[C_63mpy][NTf_2]$, $6.17 \times 10^{-4} K^{-1}$ for $[C_24mpy][NTf_2]$, $6.52 \times 10^{-4} K^{-1}$ for $[C_44mpy][NTf_2]$, and $6.62 \times 10^{-4} K^{-1}$ for $[C_64mpy][NTf_2]$, respectively. The values are in good agreement with the range of 5×10^{-4} to $7 \times 10^{-4} K^{-1}$ obtained by Jacquemin et al. [44]. According to **Table 23**, the mean contributions of the methylene to the molecular volume are 0.0277 nm^3 for $[C_n3mpy][NTf_2]$ ($n=3, 4, 6$) and 0.0289 nm^3 for $[C_n4mpy][NTf_2]$ ($n=2, 4, 6$) at 298.15 K. The values are in good agreement with the values of 0.0280 nm^3 for ILs $[C_npy][NTf_2]$ [4, 26].

From **Table 20**, the temperature dependence on dynamic viscosity can be fitted according to VFT Eq. (11), see **Figure 20**.

Property	[C ₃ 3mpy][NTf ₂]	[C ₄ 3mpy][NTf ₂]	[C ₆ 3mpy][NTf ₂]	[C ₂ 4mpy][NTf ₂]	[C ₄ 4mpy][NTf ₂]	[C ₆ 4mpy][NTf ₂]
MW/(g·mol ⁻¹)	416.35	430.38	458.43	402.33	430.38	458.43
V _m /(nm ³)	0.4765	0.5025	0.5593	0.4479	0.5039	0.5633
10 ⁴ α/(K ⁻¹)	6.12	6.20	6.19	6.17	6.52	6.62
V/(cm ⁻³ ·mol ⁻¹)	286.9	302.5	336.7	269.7	303.4	339.1
S ⁰ /(J·K ⁻¹ ·mol ⁻¹)	623.5	655.9	726.7	587.8	657.6	731.7
U _{pol} /(kJ·mol ⁻¹)	404	399	389	410	399	388

Table 23. Estimated values of physicochemical properties of two series pyridinium-based ILs at 298.15 K.

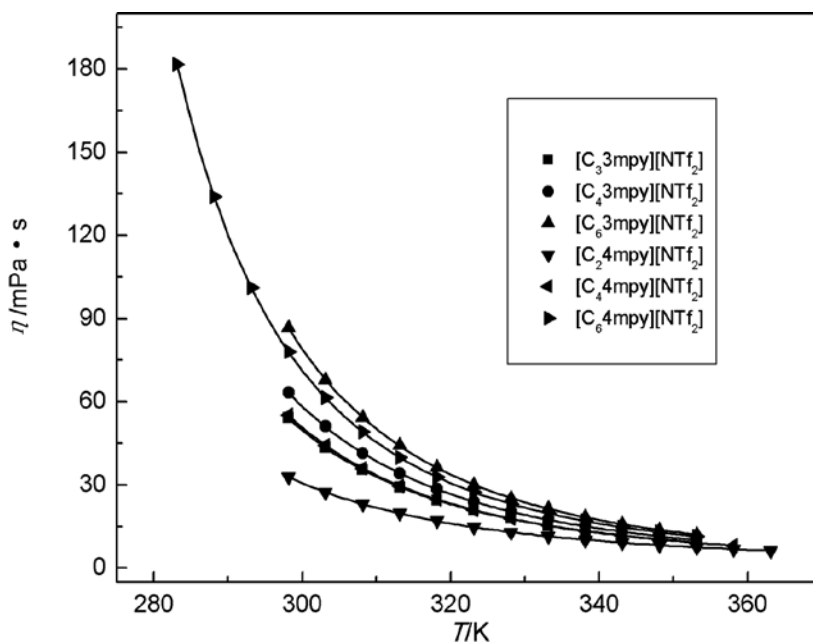


Figure 20. Plot of dynamic viscosity, η , vs. temperature, T , for two series ILs [C_n3Mpy][NTf₂] ($n = 3, 4, 6$) and [C_n4Mpy][NTf₂] ($n = 2, 4, 6$).

The best-fitting parameters of η_0 , B , T_0 and the corresponding correlation coefficient, R , are listed in **Table 24**. From **Table 24**, the obtained values of the correlation coefficient, R , are higher than 0.9999, which indicates that the VFT equation can be used for fitting the experimental dynamic viscosity.

According to Eq. (13), the activation energies of dynamic viscosity for the two series ILs $[C_n 3Mpy][NTf_2]$ ($n = 3, 4, 6$) and $[C_n 4Mpy][NTf_2]$ ($n = 2, 4, 6$) were calculated and are listed in **Table 24**.

The $1000 T^{-1}$ dependence on $\ln \eta$ was plotted for the ILs $[C_n 3Mpy][NTf_2]$ ($n = 3, 4, 6$) and $[C_n 4Mpy][NTf_2]$ ($n = 2, 4, 6$) (see **Figure 21**) according to Eq. (12).

Property	$[C_3 3mPy][NTf_2]$	$[C_4 3mPy][NTf_2]$	$[C_6 3mPy][NTf_2]$	$[C_2 4mPy][NTf_2]$	$[C_4 4mPy][NTf_2]$	$[C_6 4mPy][NTf_2]$
η_0 /(mPa·s)	0.1523	0.0474	0.0749	0.1768	0.0859	0.1170
B /K	751.0	1151.7	997.9	720.6	914.6	847.2
$10^3 E_a$ /eV	64.8	99.4	86.1	62.2	79.9	73.1
T_0 /K	170.3	138.1	156.6	160.2	156.6	167.9
R^2	0.99999	0.9999	0.99999	0.99997	0.99996	0.99999

Table 24. Fitted parameter values of η_0 , B , T_0 and correlation coefficient, R^2 , by Eq. (11) and E_a by Eq. (13).

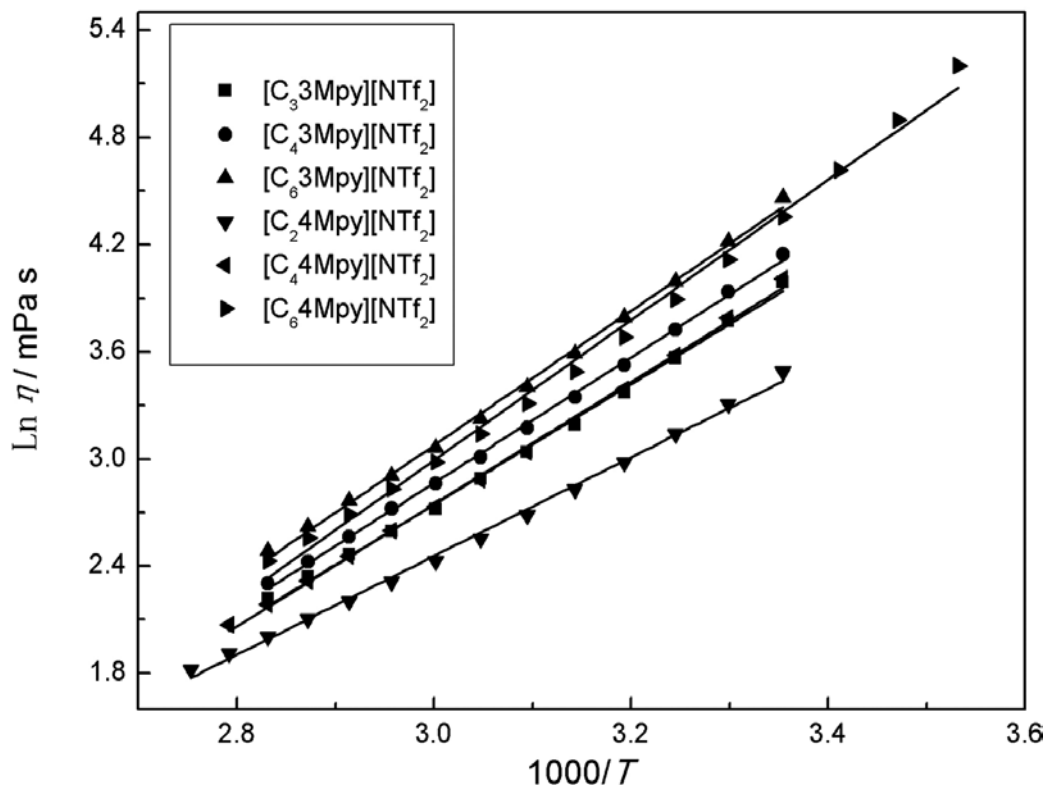


Figure 21. Plot of $\ln \eta$ vs. $1000/T$ of ILs $[C_n 3Mpy][NTf_2]$ ($n = 3, 4, 6$) and $[C_n 4Mpy][NTf_2]$ ($n = 2, 4, 6$).

In **Figure 21**, the $1000/T$ dependences on $\ln \eta$ of the two ILs $[C_n\text{3Mpy}][\text{NTf}_2]$ ($n = 3, 4, 6$) and $[C_n\text{4Mpy}][\text{NTf}_2]$ ($n = 2, 4, 6$) were fitted in the temperature range. The values of the correlation coefficient, R , are 0.9972, 0.9987, 0.9978, 0.9966, 0.9981, and 0.9947, respectively. The values are much lower than the values (all of the values are higher than $R = 0.9999$) which fitted according to the empirical VFT equation (see **Table 24**). So, the measurement dynamic viscosity cannot be well fitted with the Arrhenius Eq. (12). From **Figure 21**, it can also be obviously obtained that the measurement points lie far away from the straight fitting lines. The FILs $[\text{MCNMIM}][\text{NTf}_2]$, $[\text{PCNMIM}][\text{NTf}_2]$, $[\text{EOHMIM}][\text{NTf}_2]$, and $[\text{CH}_2\text{CONHBuEIM}][\text{NTf}_2]$ have also exhibited the same result.

From **Table 21**, the temperature dependence on electrical conductivity can be fitted according to VFT Eq. (14), see **Figure 22**.

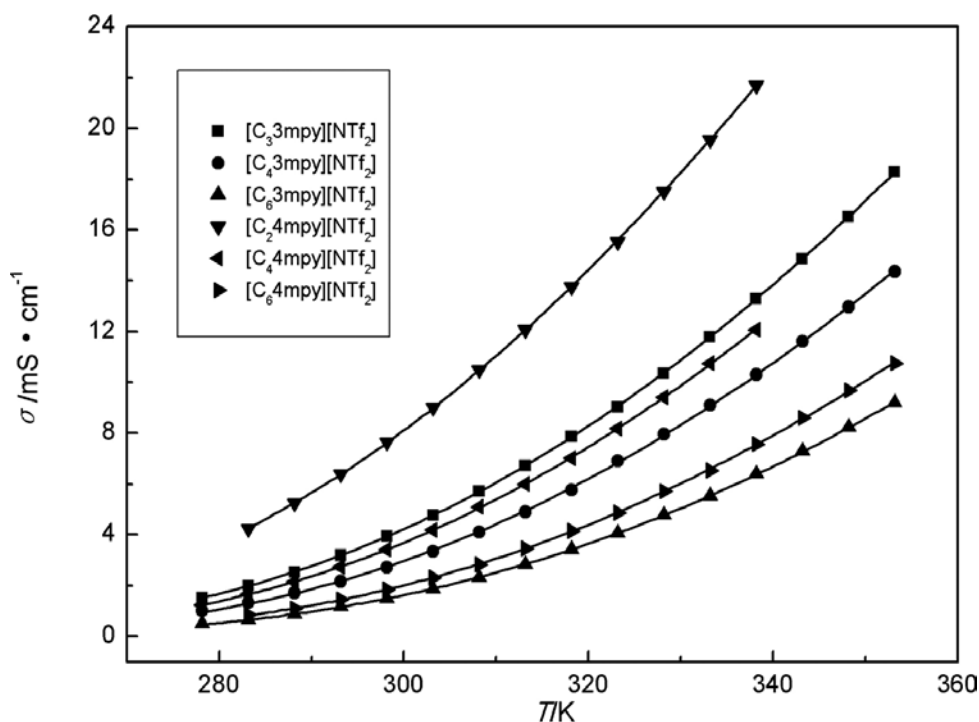


Figure 22. Plot of electrical conductivity, σ , vs. temperature, T , of two ILs $[C_n\text{3Mpy}][\text{NTf}_2]$ ($n = 3, 4, 6$) and $[C_n\text{4Mpy}][\text{NTf}_2]$ ($n = 2, 4, 6$).

The best-fitting parameters of σ_∞ , B , T_∞ and the corresponding correlation coefficient, R , are listed in **Table 25**. From **Table 25**, the obtained values of the correlation coefficient, R , are higher than 0.9999, which indicates that the VFT equation can be used for fitting the experimental electrical conductivity.

The activation energies of electrical conductivity for the two series ILs $[C_n3Mpy][NTf_2]$ ($n=3, 4, 6$) and $[C_n4Mpy][NTf_2]$ ($n=2, 4, 6$) were calculated by Eq. (16) and are listed in **Table 25**.

The $1000/T$ dependence on $\ln \sigma$ was plotted for the two series ILs $[C_n3Mpy][NTf_2]$ ($n=3, 4, 6$) and $[C_n4Mpy][NTf_2]$ ($n=2, 4, 6$) (see **Figure 23**) by Eq. (15).

Property	$[C_33Mpy][NTf_2]$	$[C_43Mpy][NTf_2]$	$[C_63Mpy][NTf_2]$	$[C_24Mpy][NTf_2]$	$[C_44Mpy][NTf_2]$	$[C_64Mpy][NTf_2]$
$\sigma_0/(S \cdot cm^{-1})$	0.64	0.49	0.47	0.64	0.50	0.46
B/K	650.2	608.4	684.6	574.6	586.5	647.3
$10^5 E_a/eV$	56.1	52.4	59.0	49.5	50.6	55.9
T_0/K	170.7	181.0	179.3	168.5	180.4	181.0
R^2	0.99996	0.9999	0.99992	0.99997	0.99996	0.99999

Table 25. Fitted parameter values of σ_0 , B , T_0 and correlation coefficient, R^2 , by Eq. (15) and E_a by Eq. (17).

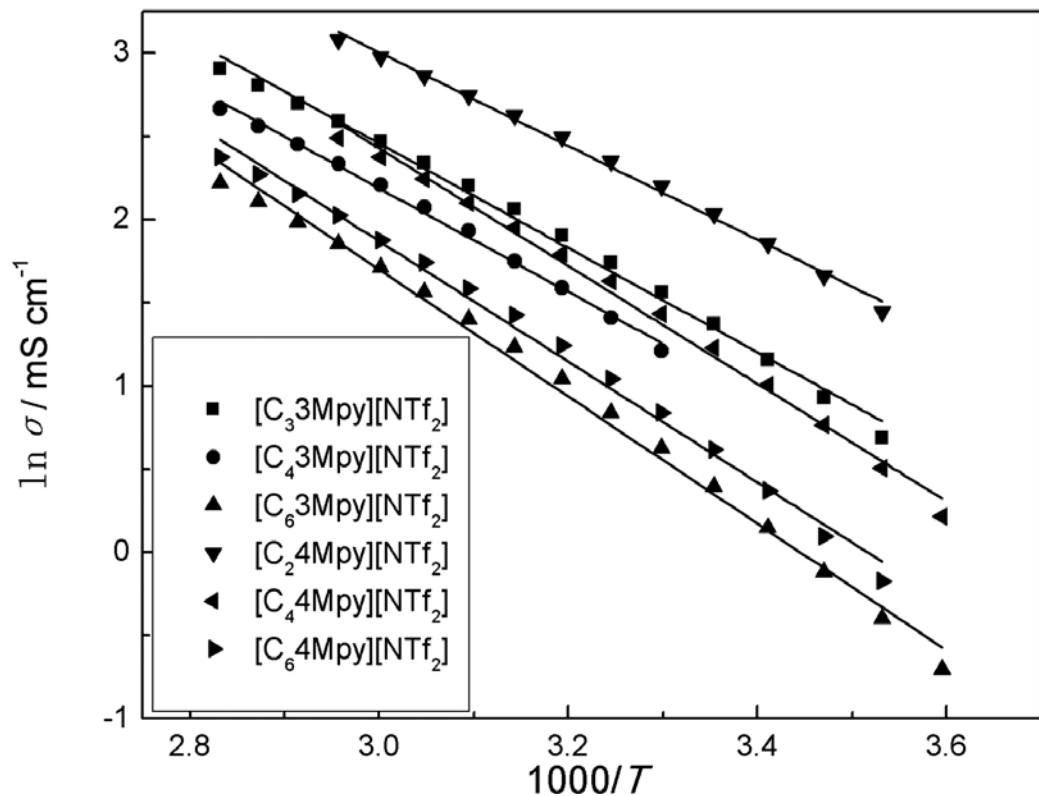


Figure 23. Plot of $\ln \sigma$ vs. $1000/T$ of ILs for the two series ILs $[C_n3Mpy][NTf_2]$ ($n=3, 4, 6$) and $[C_n4Mpy][NTf_2]$ ($n=2, 4, 6$).

In **Figure 23**, the $1000/T$ dependence on $\ln \sigma$ of the two ILs $[C_n\text{Mpy}][\text{NTf}_2]$ ($n = 3, 4, 6$) and $[C_n\text{Mpy}][\text{NTf}_2]$ ($n = 2, 4, 6$) was fitted in the temperature range. The values of the correlation coefficient, R , are 0.9957, 0.9935, 0.9933, 0.9943, 0.9958, and 0.9936, respectively. The values are much lower than the values (all of the values are higher than $R = 0.9999$) which fitted by the empirical VFT equation (see **Table 25**). So, the measurement values cannot be well fitted with the Arrhenius Eq. (15). From **Figure 23**, the measurement points can also be obviously shown far away from the straight fitting lines. The FILs $[\text{MCNMIM}][\text{NTf}_2]$, $[\text{PCNMIM}][\text{NTf}_2]$, $[\text{EOHMIM}][\text{NTf}_2]$, and $[\text{CH}_2\text{CONHBuEIM}][\text{NTf}_2]$ have also exhibited the same result.

According to Eq. (17), the Walden products (in $[\text{S}\cdot\text{cm}^2\cdot\text{mol}^{-1}][\text{cP}]$) are calculated and the values are 61 for $[C_3\text{Mpy}][\text{NTf}_2]$, 52 for $[C_4\text{Mpy}][\text{NTf}_2]$, 43 for $[C_6\text{Mpy}][\text{NTf}_2]$, 67 for $[C_2\text{Mpy}][\text{NTf}_2]$, 53 for $[C_4\text{Mpy}][\text{NTf}_2]$, and 49 for $[C_6\text{Mpy}][\text{NTf}_2]$ at 298.15 K. From the results we found that the values are also decrease with the introduction of the methylene group such as the N-alkyl pyridinium-type ILs.

$\log \Lambda$ dependence on $\log \eta^{-1}$ was plotted for the ILs $[C_n\text{Mpy}][\text{NTf}_2]$ ($n = 3, 4, 6$) and $[C_n\text{Mpy}][\text{NTf}_2]$ ($n = 2, 4, 6$) from 273.15 to 353.15 K according to Eq. (17) (see **Figure 24**).

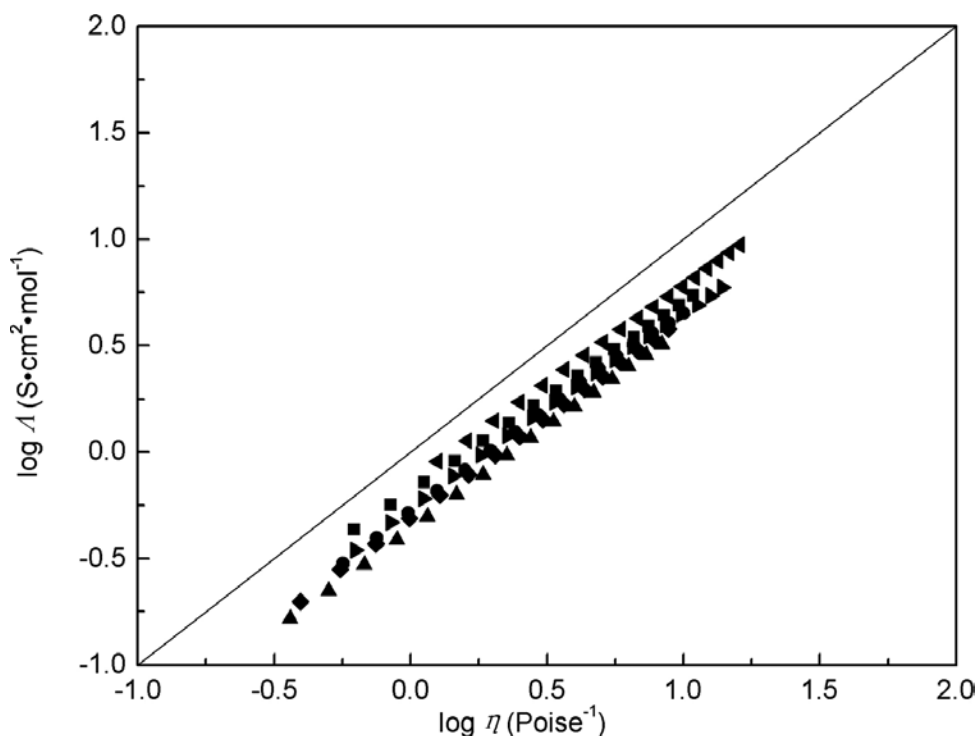


Figure 24. Walden plots for samples at temperature from 273.15 to 353.15 K.

From **Figure 24**, it can be observed that the curves are approximately straight lines. The slopes of the lines for the ILs $[C_n\text{3mpy}][\text{NTf}_2]$ ($n = 3, 4, 6$) and $[C_n\text{4mpy}][\text{NTf}_2]$ ($n = 2, 4, 6$) are 0.887, 0.949, 0.954, 0.915, 0.912, and 0.946, respectively. The position of the ideal line was established using aqueous KCl solutions at high dilution. The lines of the ILs $[C_n\text{3mpy}][\text{NTf}_2]$ ($n = 3, 4, 6$) and $[C_n\text{4mpy}][\text{NTf}_2]$ ($n = 2, 4, 6$) lie below and closely to the ideal KCl line. The ILs $[C_n\text{3mpy}][\text{NTf}_2]$ ($n = 3, 4, 6$) and $[C_n\text{4mpy}][\text{NTf}_2]$ ($n = 2, 4, 6$) are “subionic” [38].

Conclusion

The density, surface tension, dynamic viscosity, and electrical conductivity of the three series hydrophobic pyridinium-type ILs $[C_n\text{py}][\text{NTf}_2]$ ($n = 2, 3, 4, 5, 6$), $[C_n\text{3Mpy}][\text{NTf}_2]$ ($n = 3, 4, 6$), and $[C_n\text{4Mpy}][\text{NTf}_2]$ ($n = 2, 4, 6$) were determined at atmospheric pressure in the temperature range of 278–363 K. The thermal expansion coefficient, molecular volume, standard molar entropy, and lattice energy of the samples were estimated in terms of empirical and semiempirical equations. The density and electrical conductivity decrease with the introduction of the methylene group on the alkyl side chain of the pyridinium type. However, the dynamic viscosity exhibited the inverse tendency. Compared with the methylene group, the introduction of the methyl group on the pyridinium ring exhibited the irregular tendency to the density, dynamic viscosity and electrical conductivity. The order is as follows: $[C_2\text{4mpy}][\text{NTf}_2] < [C_2\text{py}][\text{NTf}_2]$, $[C_4\text{4mpy}][\text{NTf}_2] < [C_4\text{3mpy}][\text{NTf}_2] < [C_4\text{py}][\text{NTf}_2]$, and $[C_6\text{4mpy}][\text{NTf}_2] < [C_6\text{3mpy}][\text{NTf}_2] < [C_6\text{py}][\text{NTf}_2]$ for density; $[C_2\text{4mpy}][\text{NTf}_2] < [C_2\text{py}][\text{NTf}_2]$, $[C_4\text{4mpy}][\text{NTf}_2] < [C_4\text{py}][\text{NTf}_2] < [C_4\text{3mpy}][\text{NTf}_2]$, and $[C_6\text{4mpy}][\text{NTf}_2] < [C_6\text{py}][\text{NTf}_2] < [C_6\text{3mpy}][\text{NTf}_2]$ for dynamic viscosity; $[C_2\text{4mpy}][\text{NTf}_2] > [C_2\text{py}][\text{NTf}_2]$, $[C_4\text{4mpy}][\text{NTf}_2] > [C_4\text{py}][\text{NTf}_2] > [C_4\text{3mpy}][\text{NTf}_2]$, and $[C_6\text{4mpy}][\text{NTf}_2] > [C_6\text{py}][\text{NTf}_2] > [C_6\text{3mpy}][\text{NTf}_2]$ for electrical conductivity. According to the correlation coefficients, the empirical equation can be satisfactorily used for the fitting of the dynamic viscosity and electrical conductivity of the pyridinium-type ILs. However, the Arrhenius equation cannot be used for the fitting of the measurement values.

Author details

Liu Qingshan*, Mou Lin, Zheng Qige and Xia Quan

*Address all correspondence to: 13478787524@163.com

Shenyang Agriculture University, College of Science, Shenyang, Liaoning, P. R. China

References

- [1] J. Fuller, R. T. Carlin. Structural and Electrochemical Characterization of 1,3-bis-(4-methylphenyl)imidazolium Chloride. *J. Chem. Crystallogr.* 1994;24(8):489–493. DOI: 10.1007/BF01666725

- [2] C. M. Gordon, J. D. Holbrey, A. R. Kennedy, K. R. Seddon. Ionic Liquid Crystals: Hexafluorophosphate Salts. *J. Mater. Chem.* 1998;8(12):2627–2636. DOI: 10.1039/A806169F
- [3] P. Bonhôte, A. P. Dias, N. Papageorgiou, K. Kalyanasundaram, M. Grätzel. Hydrophobic, Highly Conductive Ambient-Temperature Molten Salts. *Inorg. Chem.* 1996;35(5):1168–1178. DOI: 10.1021/ic951325x
- [4] Q. S. Liu, M. Yang, P. F. Yan, X. M. Liu, Z. C. Tan, U. W. Biermann. Density and Surface Tension of Ionic Liquids $[C_n\text{py}][\text{NTf}_2]$ ($n = 2, 4, 5$). *J. Chem. Eng. Data.* 2010;55(11):4928–4930. DOI: 10.1021/jc100507n
- [5] H. Li, Z. Li, J. Yin, C. Li, Y. Chi, Q. Liu, X. Zhang, U. W. Biermann. Liquid-Liquid Extraction Process of Amino Acids by a New Amide-Based Functionalized Ionic Liquid. *Green Chem.* 2012;14(6):1721–1727. DOI: 10.1039/C2GC16560K
- [6] J. Z. Yang, X. M. Lu, J. S. Gui, W. G. Xu. A New Theory for Ionic Liquids—The Interstice Model Part 1. The Density and Surface Tension of Ionic Liquid EMISE. *Green Chem.* 2004;6(11):541–543. DOI: 10.1039/B412286K
- [7] Q. G. Zhang, J. Z. Yang, X. M. Lu, J. S. Gui, M. Huang. Studies on an Ionic Liquid Based on FeCl_3 and its Properties. *Fluid Phase Equilib.* 2004;226(1):207–211. DOI: 10.1016/j.fluid.2004.09.020
- [8] J. Vila, P. Ginés, J. M. Pico, C. Franjo, E. Jiménez, L. M. Varela, O. Cabeza. Temperature Dependence of the Electrical Conductivity in EMIM-Based Ionic Liquids: Evidence of Vogel-Tamman-Fulcher Behavior. *Fluid Phase Equilib.* 2006;242(2):141–146. DOI: 10.1016/j.fluid.2006.01.022
- [9] M. Yoshizawa, W. Xu, C. A. Angell. Ionic Liquids by Proton Transfer: Vapor Pressure, Conductivity, and the Relevance of $\Delta_p K_a$ from Aqueous Solutions. *J. Am. Chem. Soc.* 2003;125(50):15411–15419. DOI: 10.1021/ja035783d
- [10] W. Xu, E. I. Cooper, C. A. Angell. Ionic Liquids: Ion Mobilities, Glass Temperatures, and Fragilities. *J. Phys. Chem. B.* 2003;107(25):6170–6178. DOI: 10.1021/jp0275894
- [11] Q. S. Liu, J. Tong, Z. C. Tan, U. W. Biermann, J. Z. Yang. Density and Surface Tension of Ionic Liquid $[C_2\text{mim}][\text{PF}_3(\text{CF}_2\text{CF}_3)_3]$ and Prediction of Properties $[C_n\text{mim}][\text{PF}_3(\text{CF}_2\text{CF}_3)_3]$ ($n = 1, 3, 4, 5, 6$). *J. Chem. Eng. Data.* 2010;55(7):2586–2589. DOI: 10.1021/jc901035d
- [12] J. Tong, Q. S. Liu, W. G. Xu, D. W. Fang, J. Z. Yang. Estimation of Physicochemical Properties of Ionic Liquids 1-Alkyl-3-Methylimidazolium Chloroaluminate. *J. Phys. Chem. B.* 2008;112(14):4381–4386. DOI: 10.1021/jp711767z
- [13] D. W. Fang, W. Guan, J. Tong, Z. W. Wang, J. Z. Yang. Study on Physicochemical Properties of Ionic Liquids Based on Alanine $[C_n\text{mim}][\text{Ala}]$ ($n = 2, 3, 4, 5, 6$). *J. Phys. Chem. B.* 2008;112(25):7499–7505. DOI: 10.1021/jp801269u
- [14] M. Egashira, S. Okada, J. I. Yamaki, D. A. Dri, F. Bonadies, B. Scrosati. The Preparation of Quaternary Ammonium-Based Ionic Liquid Containing a Cyano Group and its Properties in a Lithium Battery Electrolyte. *J. Power Sources.* 2004;138(1–2):240–244. DOI: 10.1016/j.jpowsour.2004.06.022

- [15] M. Egashira, H. Todo, N. Yoshimoto, M. Morita, J. I. Yamaki. Functionalized Imidazolium Ionic Liquids as Electrolyte Components of Lithium Batteries. *J. Power Sources*. 2007;174(2):560–564. DOI: 10.1016/j.jpowsour.2007.06.123
- [16] M. Egashira, M. Nakagawa, I. Watanabe, S. Okada, J. I. Yamaki. Cyano-Containing Quaternary Ammonium-Based Ionic Liquid as a ‘Co-Solvent’ for Lithium Battery Electrolyte. *J. Power Sources*. 2005;146(1–2):685–688. DOI: 10.1016/j.jpowsour.2005.03.069
- [17] C. Hardacre, J. D. Holbrey, C. L. Mullan, M. Nieuwenhuyzen, W. M. Reichert, K. R. Seddon, S. J. Teat. Ionic Liquid Characteristics of 1-Alkyl-N-Cyanopyridinium and 1-Alkyl-N-(Trifluoromethyl)pyridinium Salts. *New J. Chem.* 2008;32(11):1953–1967. DOI: 10.1039/B805063E
- [18] C. Hardacre, J. D. Holbrey, C. L. Mullan, M. Nieuwenhuyzen, T. G. A. Youngs, D. T. Bowronb, S. J. Teat. Solid and Liquid Charge-Transfer Complex Formation Between 1-Methylnaphthalene and 1-Alkyl-Cyanopyridinium Bis{(trifluoromethyl)sulfonyl} imide Ionic Liquids. *Phys. Chem. Chem. Phys.* 2010;12(8):1842–1853. DOI: 10.1039/B921160H
- [19] J. Zhang, Q. Zhang, B. Qiao, Y. Deng. Solubilities of the Gaseous and Liquid Solutes and Their Thermodynamics of Solubilization in the Novel Room-Temperature Ionic Liquids at Infinite Dilution by Gas Chromatography. *J. Chem. Eng. Data*. 2007;52(6):2277–2283. DOI: 10.1021/je700297c
- [20] E. D. Bates, R. D. Mayton, I. Ntai, J. H. Davis, Jr. CO₂ Capture by a Task-Specific Ionic Liquid. *J. Am. Chem. Soc.* 2002;124(6):926–927. DOI: 10.1021/ja017593d
- [21] Y. Cai, Y. Peng. Amino-Functionalized Ionic Liquid as an Efficient and Recyclable Catalyst for Knoevenagel Reactions in Water. *Catal. Lett.* 2006;109(1):61–64. DOI: 10.1007/s10562-006-0057-3
- [22] S. Hu, T. Jiang, Z. Zhang, A. Zhu, B. Han, J. Song, Y. Xie, W. Li. Functional Ionic Liquid from Biorenewable Materials: Synthesis and Application as a Catalyst in Direct Aldol Reactions. *Tetrahedron Lett.* 2007;48(32):5613–5617. DOI: 10.1016/j.tetlet.2007.06.051
- [23] Q-S. Liu, J. Liu, X-X. Liu, S-T. Zhang. Density, Dynamic Viscosity, and Electrical Conductivity of Two Hydrophobic Functionalized Ionic Liquids. *J. Chem. Thermodyn.* 2015;90:39–45. DOI: 10.1016/j.jct.2015.06.010
- [24] Q. S. Liu, Z. Li, U. W. Biermann, C. P. Li, X. Liu. Thermodynamic Properties of a New Hydrophobic Amide-Based Task-Specific Ionic Liquid [EimCH₂CONHBu][NTf₂]. *J. Chem. Eng. Data*. 2013;58(1):93–98. DOI: 10.1021/je301001g
- [25] Q. S. Liu, H. Liu, L. Mou. Properties of 1-(Cyanopropyl)-3-Methylimidazolium Bis[(trifluoromethyl)sulfonyl]imide. *Acta. Phys. Chim. Sin.* 2016;32(3):617–623. DOI: 10.3866/PKU.WHXB201512171
- [26] Q. S. Liu, M. Yang, P. P. Li, S-S. Sun, U. W. Biermann, Z-C. Tan, Q-G. Zhang. Physicochemical Properties of Ionic Liquids [C₃py][NTf₂] and [C₆py][NTf₂]. *J. Chem. Eng. Data*. 2011;56(11):4094–4101. DOI: 10.1021/je200534b

- [27] Q. S. Liu, P. P. Li, U. W. Biermann, J. Chen, X. Liu. Density, Dynamic Viscosity, and Electrical Conductivity of Pyridinium-based Hydrophobic Ionic Liquids. *J. Chem. Thermodyn.* 2013;66:88–94. DOI: 10.1016/j.jct.2013.06.008
- [28] D. R. Lide. *Handbook of Chemistry and Physics*. 84th ed. U.S.A: LLC; 2003–2004. 2616 p. ISBN: 0–8493–0484–9
- [29] C. A. Angell, N. Byrne, J. P. Belieres. Parallel Developments in Aprotic and Protic Ionic Liquids: Physical Chemistry and Applications. *Acc. Chem. Res.* 2007;40(11):1228–1236. DOI: 10.1021/ar7001842
- [30] D. R. MacFarlane, M. Forsyth, E. I. Izgorodina, A. P. Abbott, G. Annat, K. Fraser. On the Concept of Ionicity in Ionic Liquids. *Phys. Chem. Chem. Phys.* 2009;11(25):4962–4967. DOI: 10.1039/B900201D
- [31] K. Matsumoto, R. Hagiwara. A New Series of Ionic Liquids Based on the Difluorophosphate Anion. *Inorg. Chem.* 2009;48(15):7350–7358. DOI: 10.1021/ic9008009
- [32] Q. S. Liu, P. F. Yan, M. Yang, Z. C. Tan, C. P. Li, U. W. Biermann. Dynamic Viscosity and Conductivity of Ionic Liquids [C_npy][NTf₂] (*n* = 2, 4, 5). *Acta. Phys. Chim. Sin.* 2011;27(12):2762–2766. DOI: 10.3866/PKU.WHXB20112762
- [33] Q. S. Liu, P. P. Li, U. W. Biermann, X. X. Liu, J. Chen. Density, Electrical Conductivity, and Dynamic Viscosity of N-Alkyl-4-Methylpyridinium Bis(trifluoromethylsulfonyl)imide. *J. Chem. Eng. Data* 2012;57(11):2999–3004. DOI: 10.1021/je3004645
- [34] J. P. Belieres, C. A. Angell. Protic Ionic Liquids: Preparation, Characterization, and Proton Free Energy Level Representation. *J. Phys. Chem. B.* 2007;111(18):4926–4937. DOI: 10.1021/jp067589u
- [35] G. T. Kim, G. B. Appetecchi, F. Alessandrini, S. Passerini. Solvent-Free, PYR1ATFSI Ionic Liquid-Based Ternary Polymer Electrolyte Systems: I. Electrochemical Characterization. *J. Power Sources.* 2007;171(2):861–869. DOI: 10.1016/j.jpowsour.2007.07.020
- [36] O. K. Kamijima, M. Yoshida, L. Yang. Application of Sulfonium-, Thiophenium-, and Thioxonium-Based Salts as Electric Double-layer Capacitor Electrolytes. *J. Power Sources.* 2010;195(19):6970–6976. DOI: 10.1016/j.jpowsour.2010.04.028
- [37] M. Lazzari, M. Mastragostino, A. G. Pandolfo, V. Ruiz, F. Soavi. Role of Carbon Porosity and Ion Size in the Development of Ionic Liquid Based Supercapacitors. *J. Electrochem. Soc.* 2011;158(1):A22–A25. DOI: 10.1149/1.3514694
- [38] H. Tokuda, S. Tsuzuki, M. A. B. H. Susan, K. Hayamizu, M. Watanabe. How Ionic Are Room-Temperature Ionic Liquids? An Indicator of the Physicochemical Properties. *J. Phys. Chem. B.* 2006;110(39):19593–19600. DOI: 10.1021/jp064159v
- [39] F. S. Oliveira, M. G. Freire, P. J. Carvalho, J. A. P. Coutinho, J. N. Canongia Lopes, L. P. N. Rebelo, I. M. Marrucho. Structural and Positional Isomerism Influence in the Physical Properties of Pyridinium NTf₂-Based Ionic Liquids: Pure and Water-Saturated Mixtures. *J. Chem. Eng. Data.* 2010;55(10):4514–4520. DOI: 10.1021/je100377k

- [40] J. Jacquemin, P. Husson, A. A. H. Padua, V. Majer. Density and Viscosity of Several Pure and Water-Saturated Ionic Liquids. *Green Chem.* 2006;8(2):172–180. DOI: 10.1039/B513231B
- [41] A. Seduraman, P. Wu, M. Klähn. Extraction of Tryptophan with Ionic Liquids Studied with Molecular Dynamics Simulations. *J. Phys. Chem. B.* 2012;116(1):296–304. DOI: 10.1021/jp206748z
- [42] J. Tong, M. Hong, W. Guan, J. B. Li, J. Z. Yang. Studies on the Thermodynamic Properties of New Ionic Liquids: 1-Methyl-3-Pentylimidazolium Salts Containing Metal of Group III. *J. Chem. Thermodyn.* 2006;38(11):1416–1421. DOI: 10.1016/j.jct.2006.01.017
- [43] J. Tong, Q. Liu, W. Guan, J. Yang. Estimation of Physicochemical Properties of Ionic Liquid $C_6MIGaCl_4$ Using Surface Tension and Density. *J. Phys. Chem. B.* 2007;111(12):3197–200. DOI: 10.1021/jp068793k
- [44] L. P. N. Rebelo, J. N. C. Lopes, J. M. S. S. Esperança, E. Filipe. On the Critical Temperature, Normal Boiling Point, and Vapor Pressure of Ionic Liquids. *J. Phys. Chem. B.* 2005;109(13):6040–6043. DOI: 10.1021/jp050430h
- [45] Q. G. Zhang, Y. Wei, S. S. Sun, C. Wang, M. Yang, Q. S. Liu, Y. A. Gao. Study on Thermodynamic Properties of Ionic Liquid N-Butyl-3-Methylpyridinium Bis(trifluoromethylsulfonyl)imide. *J. Chem. Eng. Data.* 2012;57(8):2185–2190. DOI: 10.1021/je300153f

Behavior of Ionic Liquids Under Nanoconfinement Greatly Affects Actual Friction

Toshio Kamijo, Hiroyuki Arafune, Takashi Morinaga,
Takaya Sato and Kazue Kurihara

Additional information is available at the end of the chapter

<http://dx.doi.org/10.5772/65758>

Abstract

Ionic liquids (ILs) are organic salts consisting of anions and cations that exist as liquids at room temperature. ILs exhibit many attractive properties such as negligible volatility, low flammability, and relatively high thermal stability. These properties can be varied in a controlled fashion through systematic changes in the molecular structure of their constituent ions. Some recent studies have aimed to use ILs as new lubricant materials. However, the behavior of ILs as lubricants on the sliding interfaces has not been elucidated. In this chapter, we describe the nano- and macrolubrication properties of some ILs with different types of anions using resonance shear measurement (RSM) and conventional ball-on-plate-type tribotests, respectively. This study reveals that the properties observed by RSM for nanoscale systems can provide important insights for the study of the friction coefficients (macrolubrication properties) obtained by tribotests.

Keywords: tribology, lubricant, nanolubrication, confinement, friction coefficient

1. Introduction

Ionic liquids (ILs) are expected to be promising candidate materials for new lubricants [1–5]. In particular, their stability under severe conditions, such as ultrahigh vacuum [6, 7] and high temperatures [8], has attracted increasing interest. To choose ILs suitable for use as lubricants, it is important to understand the characteristics of the target materials. However, currently, the details of the lubrication mechanism of ILs are not clearly understood.

The tribological properties of ILs have been studied using a macroscopic tribotester. Most previous research has focused on the lubricating behavior of ILs in the boundary lubrication

regime at high loads of several GPa and on their tribochemical reactions with solid surfaces [9–13]. The formation of tribochemical layers on metal surfaces from ILs containing a halogen such as fluorine under sliding conditions has been studied by X-ray photoelectron spectroscopy (XPS) [9–12], scanning electron microscope with energy dispersive X-ray spectroscopy (SEM-EDS) [9–11], and time-of-flight secondary ion mass spectrometry (TOF-SIMS) [12]. Therefore, ILs have also been used as additives for the formation of a tribochemical layer under high loads of several GPa [14–16]. When used, these layers have been considered to contribute to the reduction of friction in the system.

On the other hand, due to the interest in applying ILs as lubricants, the properties of ILs confined in a nanoscale space have also been studied by atomic force microscopy (AFM) [17–19] and the surface force apparatus (SFA) [20, 21]. The oscillating forces observed by both AFM and SFA demonstrated the layered structure of ILs in narrow gaps. However, the relationship between these nanoscale properties and the macrolubrication properties is still not fully understood even for the same surface and ILs. Motivated by this problem, we have recently used resonance shear measurement (RSM) to show that some ILs form a layered structure in the nanoscale space created by the sliding surface [21, 22]. We also revealed that a nanostructure consisting of only several IL layers had a large influence on macroscale friction.

In this chapter, we describe the nano- and macrolubrication properties of some ILs (**Table 1**) with different anions by using RSM and a conventional ball-on-plate-type tribotester, respectively. This study reveals that ILs with different structures form different nanolayered structures and that their nanoscale behaviors are correlated with their macroscale tribology. In addition to providing information related to the lubrication mechanism of ILs, we also describe the principles for choosing an IL as a lubricant.

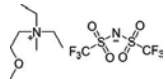
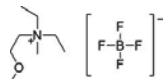
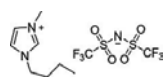
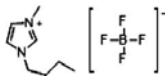
Ionic liquid	Abbreviation	Structure	MW/g	$\rho/\text{g cm}^{-3}$	MV/nm ³	D_m/nm	Viscosity/ mPa s
<i>N,N</i> -diethyl- <i>N</i> -methyl- <i>N</i> -(2-methoxyethyl) ammonium bis (trifluoromethane sulfonyl) imide	[DEME][TFSI]		426.40	1.42	0.49	0.79	77 [22]
<i>N,N</i> -diethyl- <i>N</i> -methyl- <i>N</i> -(2-methoxyethyl) ammonium tetrafluoroborate	[DEME][BF ₄]		233.06	1.17	0.33	0.69	400 [22]
1-Butyl-3-methylimidazolium bis(trifluoromethyl sulfonyl) imide	[BMIM][TFSI]		419.36	1.44	0.48	0.78	58.4 [21]
1-Butyl-3-methylimidazolium tetrafluoroborate	[BMIM][BF ₄]		226.02	1.20	0.31	0.68	124.6 [21]

Table 1. Name, abbreviation, structure, molecular weight (MW), density (ρ), molecular volume (MV), ion pair diameter (D_m), and viscosity (η) of ILs. D_m is determined from (ρ) assuming a cubic packing geometry according to the method described by Horn et al. [23].

2. Nanolubrication properties

2.1. RSM for nanoscale properties of ILs

RSM was performed using an in-house resonance shear system based on an SFA [22], as shown schematically in **Figure 1**. The experimental setup and procedures for RSM are described in detail in a previous publication [21]. Silica sheets used as samples were prepared following the procedure reported by Horn et al. [24]. The root mean square (RMS) roughness value measured by AFM (Toyo Corporation, Agilent 5100 AFM/SPM Microscope) over an area of $5 \times 5 \mu\text{m}^2$ for the silica sheets was 0.31 nm. Using RSM, the resonance curve between the molecularly smooth silica sheets was measured across IL films at a surface separation D with a resolution of 0.1 nm. The value of D was determined from the fringes of equal chromatic order (FECO) analysis. In brief, two back-silvered silica sheets (thickness of ca. 2–4 μm) were glued onto cylindrical quartz lenses (with a radius of curvature (R) of ca. 20 mm) and mounted onto the RSM system. The RSM system was composed of the upper surface unit suspended by a pair of vertical leaf springs and the lower surface unit mounted on a horizontal leaf spring. The upper surface unit was connected to a four-section piezo tube. In this case, it can be laterally oscillated at various frequencies (ω) by an application of a sinusoidal input voltage (U_{in}). The deflection (Δx) of the leaf spring was detected as an output voltage (U_{out}) by a capacitance probe (Microsense 4830, Japan ADE Ltd.). Then, resonance curves were recorded at various D values as the normalized amplitude ($U_{\text{out}}/U_{\text{in}}$) as a function of the frequency ω . RSM was conducted at room temperature (295 ± 0.5 K) and at a humidity of less than 25% maintained by placing silica gel in the sample chamber.

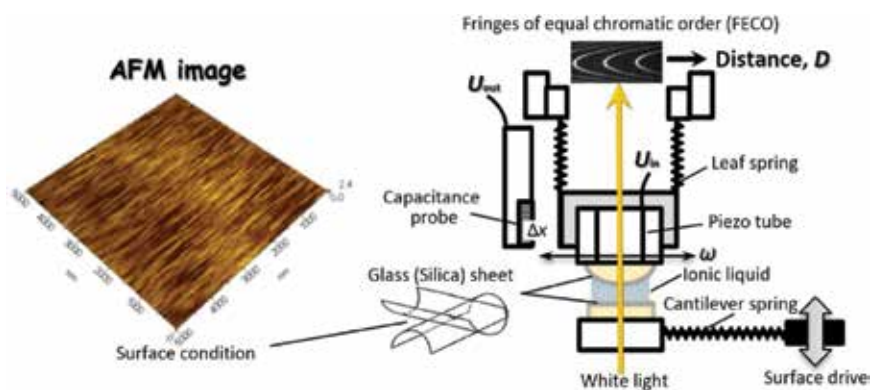


Figure 1. Schematic of the RSM system. The surfaces are in the crossed-cylinder geometry.

The RSM system measured the surface force and resonance shear response by continuously changing the thickness of the liquid film confined between two solid surfaces with a nanometer resolution. The liquid thickness was controlled and determined using interferometric methods in the surface force apparatus. The shear response via resonance method provided a sensitive method for detecting the tiny changes in the liquid properties between the substrates, allowing

us to evaluate the viscosity change associated with liquid structuring, frictional/lubricational property, as well as other properties, by simply changing the liquid film thickness.

Figure 2 shows the typical resonance shear curves for different surface separations. The resonance curves for the two reference states of separation in air (AS) and for silica-silica contact (SC) were measured prior to the RSM of a liquid (**Figure 2**). In the absence of a liquid, the system parameters (mass, damping parameter, and spring constant for the apparatus) determined the AS and SC resonance curves. In the presence of a liquid, the resonance curve at long distances showed a peak at a low frequency that was almost the same as the AS peak. The peak intensity U_{out}/U_{in} was lower than the AS peak intensity, corresponding to the energy dissipation due to the bulk viscosity of the liquid. With decreasing D value, the amplitude of the resonance peaks first decreased, and then, the peak disappeared with a further decrease in the distance. For a further decrease in the surface separation, broad resonance curves were observed at intermediate frequencies between the AS and SC frequencies, and the peak frequencies started to shift toward the SC peak because of the weak coupling of the upper and lower surfaces mediated by the confined liquid [25]. When the applied load (N) was further increased by decreasing the surface separation, the peak frequency shifted further toward the SC peak and the amplitude increased, until finally, for a surface separation of 0 nm, the amplitude was almost identical to that of the SC peak. This means that the liquid was completely removed from the gap between the silica surfaces [26]. Similarly, when the applied load (N) was further increased while the surface separation was fixed at a certain distance, the peak frequency also shifted further toward the SC peak frequency, while the amplitude increased. This means that the liquid remained between the silica surfaces at a certain surface separation due to the stronger coupling of the upper and lower surfaces with the increasing applied load.

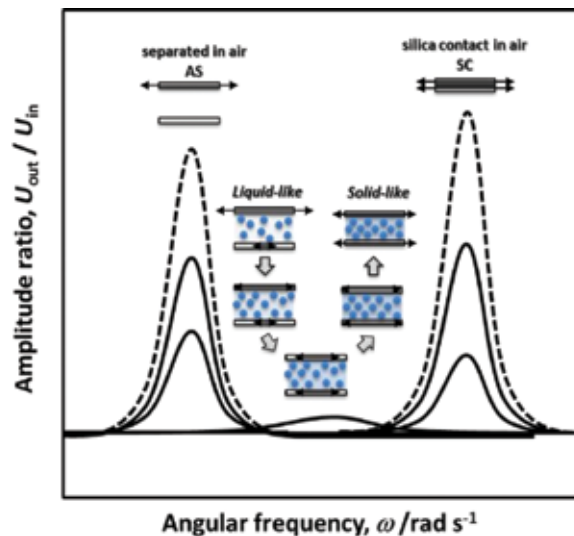


Figure 2. Typical resonance shear curves with different surface separations.

The RSM system described above was used to study the nanolubrication properties of ILs between smooth silica surfaces. **Figure 3(a)** and **(b)** shows the resonance curves for [DEME][TFSI] and [DEME][BF₄] ILs confined between silica surfaces at various separation distances. For reference, the resonance curves for AS and SC were measured prior to the resonance shear measurement of the ILs (**Figure 3**). In the absence of the ILs, the system parameters (mass, damping parameter, and spring constant for the apparatus) determined the AS and SC resonance curves. In the presence of [DEME][TFSI], the resonance curve at $D = 228.1$ nm showed a peak at a frequency of 185 rad s^{-1} that was almost the same as the AS peak. The peak intensity $U_{\text{out}}/U_{\text{in}}$ was lower than the AS peak intensity, corresponding to the energy dissipation due to the bulk viscosity of the IL. With decreasing D value, the amplitude of the resonance peaks started to decrease at 10.2 nm and disappeared at $D = 4.9$ nm. In the range from $D = 4.9$ to 2.5 nm, broad resonance curves were observed at intermediate frequencies between the AS and SC frequencies, and the peak frequency started to shift toward the SC peak because of the weak coupling of the upper and lower surfaces mediated by the confined [DEME][TFSI] [21]. When the applied load (N) was increased further, the surface separation did not change and remained at 2.5 nm (**Figure 4**); however, the peak frequency shifted further toward that of the SC peak and the amplitude increased. This means that [DEME][TFSI] remained between the silica surfaces at the separation of 2.5 nm, and the coupling of the upper and lower surfaces became stronger with the increased applied load.

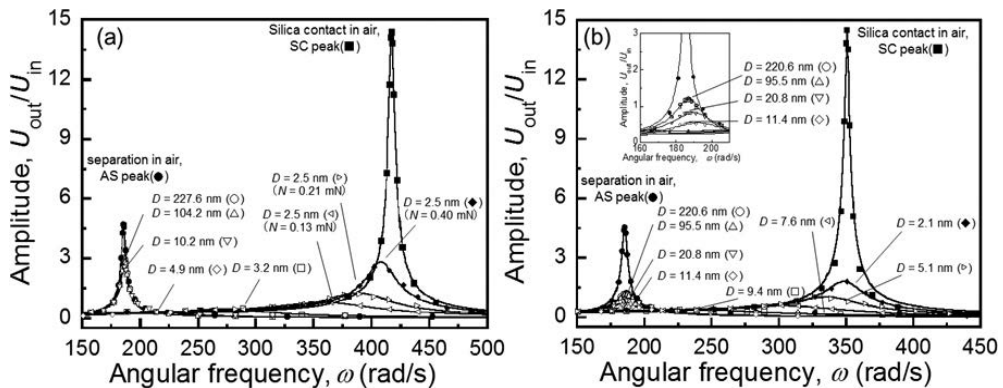


Figure 3. Resonance curves for (a) [DEME][TFSI] and (b) [DEME][BF₄] confined between the silica surfaces at various separation distances under an applied load N . Resonance curves for AS and SC are also shown [22]. Solid lines denote the best fit curves to a physical model [27].

The resonance shear behavior of [DEME][BF₄] (**Figure 3(a)**) was similar to that of [DEME][TFSI], except in the small D region below 2.5 nm (**Figure 3(b)**). The resonance curves at 186 rad s^{-1} did not change in the D range from 220.6 to 95.5 nm, and their amplitudes started to decrease at $D = 20.8$ nm. The resonance frequencies of these curves were almost the same as the frequency of the AS peak. The amplitude of the resonance peaks gradually decreased with decreasing D from 20.8 to 11.4 nm and disappeared at $D = 9.4$ nm. This distance is higher than the disappearance distance ($D = 4.9$ nm) for [DEME][TFSI]. In the range from $D = 9.4$ to 2.1 nm, broad resonance curves were observed at intermediate frequencies, and the peak

frequencies started to shift toward the frequency of the SC peak because of the weak coupling of the upper and lower surfaces mediated by the confined [DEME][BF₄]. When the applied load (N) was further increased, the surface separation remained at 2.1 nm (**Figure 4**), indicating that [DEME][BF₄] remained trapped between the silica surfaces.

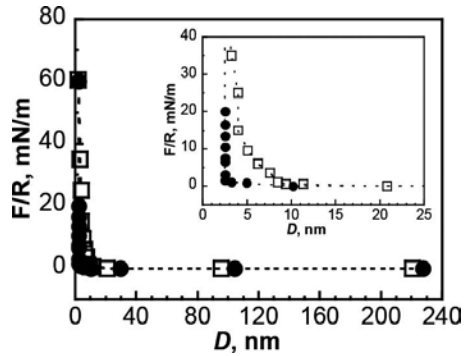


Figure 4. Profiles of normal force normalized by surface curvature radius (F/R) as a function of surface separation D between silica surfaces in [DEME][TFSI] (●) and [DEME][BF₄] (□) [22].

2.2. Dynamics of ILs by changing the load applied to the two friction surfaces

Figure 5 plots the relative intensity (I_r) of the resonance peak, that is, the ratio of the peak intensity for confined ILs is divided by the SC peak intensity as a function of applied load. This intensity ratio is a measure of the lubrication behavior of the confined ILs, with smaller values indicating better lubrication behavior. With an increase in the applied load from 0.21 to 0.33 mN, the I_r values of [DEME][TFSI] clearly increased from ca. 0.09 to 0.16 and then plateaued when the load was increased to 0.40 mN. The I_r of [DEME][BF₄] showed a behavior similar to that of [DEME][TFSI], gradually increasing from ca. 0.07 to 0.12 as the applied load increased from 0.19 to 0.50 mN, and reaching a plateau when the load was increased to 0.70 mN. The noteworthy difference between the two ILs was observed at higher loads (>0.4 mN), with the 0.18 I_r value obtained for [DEME][TFSI] being significantly larger than the 0.12 value obtained for [DEME][BF₄]. These results indicate that, under higher loads (>0.4 mN), [DEME][BF₄] is a better lubricant than [DEME][TFSI]. Additionally, RSM revealed that an IL layer with ca. 2 nm thickness was maintained between the silica surfaces even under high applied loads (>0.4 mN). The plateau of the relative intensity under applied loads (>0.4 mN) indicated that the IL layer confined between the silica surfaces maintained its lubricating properties.

2.3. Effective viscosity (η_{eff}) of the confined ILs measured to quantitatively measure lubrication performance

We analyzed the resonance curves using a previously developed physical model [27] to obtain a quantitative understanding of the properties of the confined ILs. The details of the analytical procedure are described in the literature [21, 27]. **Figure 6** plots the effective viscosity (η_{eff}) obtained for the ILs using the model versus the separation distance between the silica surfa-

ces. The η_{eff} values at larger separations were constant and essentially identical to the bulk IL viscosity of 400 for [DEME][BF₄] and 77 mPa s for [DEME][TFSI]. However, the η_{eff} value increased sharply with decreasing D below 11.4 nm for [DEME][TFSI] and below 10.4 nm for [DEME][BF₄]. The η_{eff} value for [DEME][TFSI] confined in the nanospace ($D \leq 4.9$ nm) was one to two orders of magnitude higher than that at larger separations ($D \geq 10.2$), and the η_{eff} value for [DEME][BF₄] confined in the nanospace ($D \leq 9.4$ nm) was about one order of magnitude higher than that at larger separations ($D \geq 11.4$). Note that in the nanospace, the η_{eff} value of [DEME][TFSI] was higher than that of [DEME][BF₄], whereas in the bulk, the opposite was the case and the viscosity of [DEME][BF₄] was higher than that of [DEME][TFSI]. This behavior is similar to the trend shown by the ILs [BMIM][TFSI] and [BMIM][BF₄] confined between the silica surfaces [21], even though the cations used in this study are different from those used in Ref. [21].

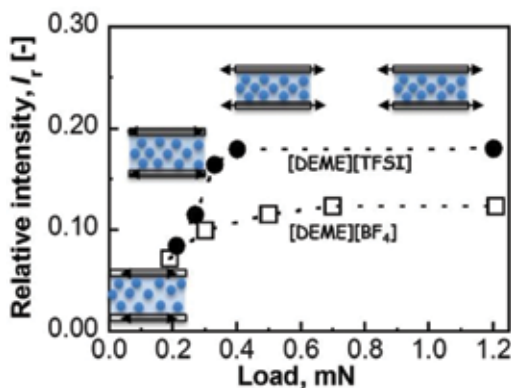


Figure 5. Relative intensity (peak intensity confined ILs/SC peak intensity) versus the applied load for [DEME][TFSI] (●) and [DEME][BF₄] (□) [22].

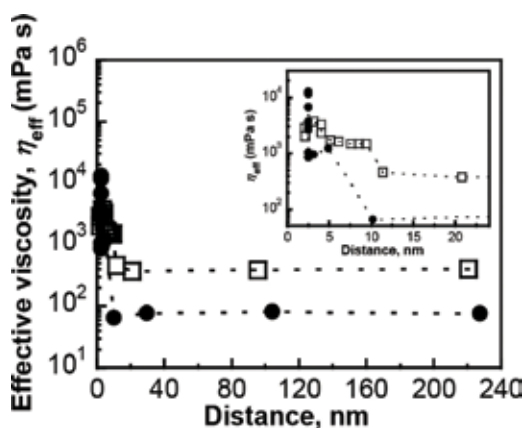


Figure 6. Effective viscosity η_{eff} versus the separation distance for [DEME][TFSI] (●) and [DEME][BF₄] (□) [22].

We suppose that the rapid increase in the effective viscosity with decreasing distance observed in **Figure 6** corresponds to the distance at which the formation of a solid-like structure due to the confinement is initiated. For [DEME][BF₄], the sharp viscosity increase began at a clearly shorter distance than that for [DEME][TFSI], indicating that this ammonium salt restructures more readily than the TFSI salt, or in other words, that the BF₄ salt is more easily crystallized. This consideration is also supported by the results of the crystallization temperature measurement using differential thermal calorimetry (DSC) [28]. As indicated by the DSC measurements, [DEME][BF₄], for which the viscosity increases at a relatively long distance, shows a distinct crystallization temperature, whereas the TFSI salt only shows a glass transition temperature but not a crystallization temperature. The same trend is found for aromatic ILs. The viscosity of [BMIM][TFSI], which has a specific crystallization temperature, rises rapidly at a large distance, whereas the viscosity of [BMIM][BF₄], which does not show a crystallization temperature, rises rapidly only at a short distance [29].

Figure 7 plots η_{eff} versus the applied load. The η_{eff} values for [DEME][TFSI] and [DEME][BF₄] increased with the applied load and plateaued when the load was increased to 0.4 mN. At higher loads (>0.4 mN), η_{eff} of ca. 13,000 for [DEME][TFSI] was larger than the ca. 3000 value obtained for [DEME][BF₄].

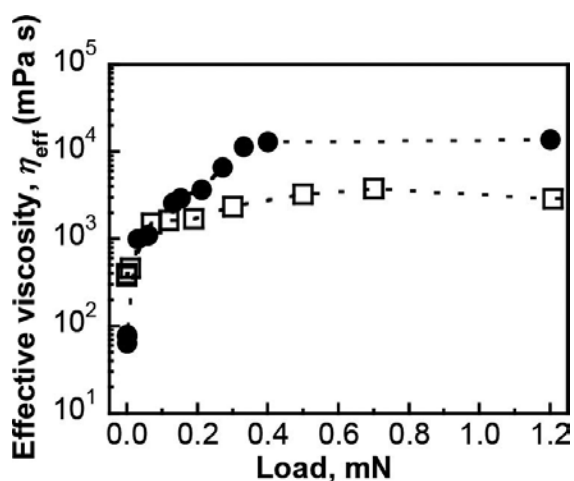


Figure 7. Plots of the effective viscosity η_{eff} versus the applied load for [DEME][TFSI] (●) and [DEME][BF₄] (□) [22].

In the RSM, the facing silica surfaces were completely separated to avoid partial contact and to allow the analysis of the boundary lubrication property of the confined liquid at a certain separation distance. In this configuration, an increase in the viscosity of the lubricant layer under confinement directly leads to increased friction at the sliding interface. The results obtained from RSM showed that the η_{eff} of [DEME][BF₄] is lower than that of [DEME][TFSI] at a similar separation distance (ca. 2 nm), meaning that under such confinement, the lubrication performance of [DEME][BF₄] is better than that of [DEME][TFSI]. We thus concluded that, for higher loads (>0.4 mN), [DEME][BF₄] is a better lubricant than [DEME][TFSI].

3. Macroscopic tribological properties

3.1. Reciprocating-type tribotests for evaluation of macroscopic properties

Friction measurements were carried out using a conventional reciprocating tribotester, TRIBOGEAR TYPE 38 (Shinto Scientific Co. Ltd., Tokyo), using a glass ball of 10 mm ϕ and a glass plate. To obtain a clean surface, the glass ball and glass plate were treated in fresh nitric acid at 373 K for 75 min. The RMS roughness values measured by AFM for the glass ball and plate were 9.9 and 1.2 nm over an area of 5 \times 5 μ m², respectively. A schematic of the tribotester is shown in **Figure 8**. The measurements were performed at a movement distance of 10 mm, with a sliding velocity ranging from 5.0 \times 10⁻⁴ to 3.0 \times 10⁻² m s⁻¹ under an applied load of 196–980 mN at room temperature (295 \pm 0.5 K). The friction force was measured by an all-in-one load converter from a gauge attached to the sample holder and was recorded as a function of time. The friction coefficient (μ) was calculated as the friction force divided by the normal load. Friction coefficients obtained for at least five trials were recorded and averaged.

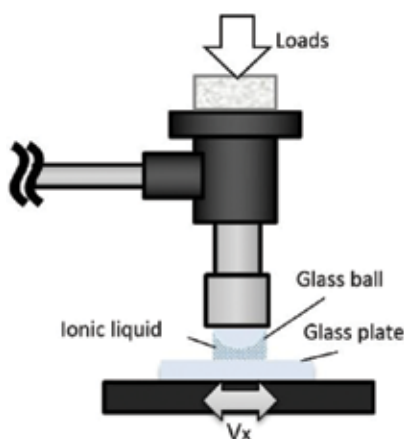


Figure 8. Schematic of reciprocating-type tribotester.

The Stribeck diagram of the friction behavior is used to explain the rubbing phenomena occurring in lubricated contacts [30]. A schematic representation of the Stribeck diagram is shown in **Figure 9**. For high values of $\eta V/N$, the friction coefficient is linearly ascending due to fluid film lubrication, and the friction is related to the viscous dragging forces in the fluid film. When the load increases or fluid viscosity and/or velocity decreases, the $\eta V/N$ factor falls. Then, the fluid film becomes thinner, and consequently, the friction coefficient decreases down to the minimum value. For even smaller $\eta V/N$ values, the fluid film thickness is further reduced and solid-to-solid contact starts to occur, leading to an increase in the friction coefficient as the $\eta V/N$ factor decreases. Such a rise in the friction coefficient is also related to the fluid viscosity increase in some regions of the contact area under high contact pressure. These phenomena characterize the mixed lubrication regime. Further reduction in the $\eta V/N$ factor strengthens

the solid-to-solid contact, and the film thickness becomes smaller than the height of the surface asperities, leading to the transition of the boundary lubrication regime.

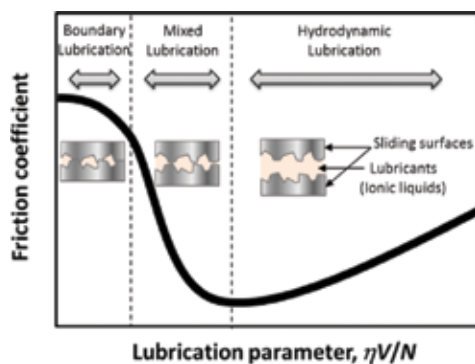


Figure 9. Schematic of Stribeck diagram; friction coefficient as a function of the lubrication parameter: $\eta V/N$. η : fluid viscosity, V : sliding velocity, N : normal load.

We studied the boundary lubrication properties of ILs between a glass ball and a glass plate by using a macroscopic tribotester. **Figure 10** plots the friction coefficients between a glass ball and a glass plate in [DEME][TFSI] or [DEME][BF₄] versus the sliding velocity (V) divided by the load (L) ($\text{m s}^{-1} \text{N}^{-1}$). The measurements were conducted by sliding a glass plate over a distance of 10 mm at various sliding velocities from 5.0×10^{-4} to $3.0 \times 10^{-2} \text{ m s}^{-1}$ and under various applied loads from 196 to 980 mN at 298 K. The friction coefficient for [DEME][BF₄] increased from 0.05 to 0.08 as the V/L parameter decreased from 1.5×10^{-1} to 5.1×10^{-3} and was nearly constant at $\mu \approx 0.08$ over the V/L range of 5.1×10^{-3} to 1.0×10^{-3} . The friction coefficient results for [DEME][TFSI] were similar to those for [DEME][BF₄]; however, the friction coefficient observed in the region of V/L ranging from 1.5×10^{-1} to 1.0×10^{-4} was significantly higher than that of [DEME][BF₄]. Such dependence of the friction coefficient on V/L corresponds to the shift in the lubrication regime of [DEME][TFSI] and [DEME][BF₄] from mixed lubrication to boundary lubrication. As a control, the friction coefficient was measured between the glass ball and glass plate without an IL and was found to be ≈ 0.7 at the sliding velocity of $1.0 \times 10^{-3} \text{ m s}^{-1}$ and under a normal load of 196 mN. Thus, the presence of ILs at the glass-glass interface dramatically reduced the friction coefficient to less than 20% of the value obtained without ILs.

3.2. Comparison of measurement results revealing a correlation between the macroscale friction phenomena and the physicochemical properties of ILs in nanospace

For a confined IL, boundary lubrication is dominant, and the contribution of hydrodynamic lubrication due to the change in lubricant thickness is not effective. Therefore, the difference in boundary lubrication under the measurement conditions between [DEME][BF₄] and [DEME][TFSI] can be explained based on the effective viscosity obtained from RSM. The obtained RSM results showed that the η_{eff} of [DEME][BF₄] was lower than that of [DEME][TFSI] when these ILs were maintained at a similar separation distance (ca. 2 nm), indicating that the

lubrication performance of [DEME][BF₄] is better than that of [DEME][TFSI] under such confined conditions. The inversion of the order of IL viscosities under confinement from the order of bulk viscosity values appears to be due to the differences in the layering structure of the ILs due to the differences in their anion structure.

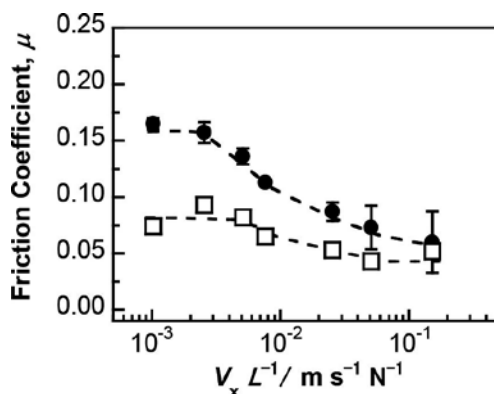


Figure 10. Friction coefficient between a glass ball and a glass plate in [DEME][TFSI] (●), in [DEME][BF₄] (□), by sliding the glass plate over a distance range of 10 mm at sliding velocity of $5.0 \times 10^{-4} \text{ m s}^{-1}$ – $3.0 \times 10^{-2} \text{ m s}^{-1}$ and under an applied load of 196–980 mN at 298 K. Dashed lines are guides to the eyes [22].

We now discuss the possible structural origin for the observed viscosity effects. Canova et al. studied the layering structure of ILs ([BMIM][TFSI] and [BMIM][BF₄]) confined to a silica contact plane using molecular dynamics simulations. For [BMIM][TFSI], it was found that ion pairs orient alternately to form a checker-board structure. This means that each ion is forced to contact ions with the same charge during shearing [31]. The repulsive force between the ions with the same sign of the charge destabilizes the crystal structure of the IL and triggers an overall restructuring of inner molecular layers to form a more stable configuration, resulting in high friction. In contrast, [BMIM][BF₄] formed a layer-by-layer structure where cations and anions did not suffer from such repulsions because each ion layer is sandwiched between the oppositely charged layers, leading to smooth shearing and low friction. Even though the cations used in our study are different from those studied by Canova et al., based on this insight, we ascribe the better boundary lubrication performance of [DEME][BF₄] relative to that of [DEME][TFSI] to the differences in the layered structures of these ILs under confinement.

The RSM showed that ILs were maintained between the silica surfaces at a surface separation of 2.5 nm for [DEME][TFSI] and 2.1 nm for [DEME][BF₄], which are usually referred to as hard-wall thicknesses. Assuming a cubic packing geometry and following Horn et al.'s [23] method, the diameters of the ion pairs determined from the density were 0.79 nm for [DEME][TFSI] and 0.69 nm for [DEME][BF₄]. Based on these values, we determined that in both systems, three layers of ILs were trapped between the silica surfaces. The dramatic reduction in the friction coefficient in “the boundary lubrication region” with ILs was presumably due to the presence of the three layers of ILs between the silica surfaces under an applied load of 196 mN.

These results indicated that the tribotester macroscopic tribological properties correspond to the nanoscale lubrication properties obtained from nanoscopic RSM.

4. Conclusion

We performed RSM and reciprocating-type tribotests to evaluate the friction properties of lubrication systems consisting of some types of ILs between the silica surfaces. In the case of [DEME][BF₄] and [DEME][TFSI], the RSM results revealed that IL layers with a thickness of ca. 2 nm remained between the silica surfaces under applied loads. For these conditions, the effective viscosity of the IL including BF₄ anion was smaller than that of the IL including the TFSI anion. Similarly, in the boundary lubrication regime, the friction coefficient μ of [DEME][BF₄] obtained by the tribotests was lower than that of [DEME][TFSI]. Even though the RSM and tribotest measurement were performed under different applied loads, the difference in the friction coefficient between [DEME][TFSI] and [DEME][BF₄] in the boundary lubrication regime observed by the tribotest corresponded to their behavior under confinement between the silica surfaces, as observed by RSM. These results indicate that the nanoscale properties observed by RSM can provide important insights for the study of the friction coefficients (macrolubrication properties) obtained by the tribotests.

Acknowledgements

This work was supported in part by the “Green Tribology Innovation Network” Advanced Environmental Materials Area, Green Networks of Excellence (GRENE) program and Grants-in-Aid for Scientific Research (nos. 25810091, 26820034, and 30399258) sponsored by the Ministry of Education, Culture, Sports, Science and Technology (MEXT) in Japan.

Author details

Toshio Kamijo¹, Hiroyuki Arafune¹, Takashi Morinaga¹, Takaya Sato^{1*} and Kazue Kurihara^{2,3}

*Address all correspondence to: takayasa@tsuruoka-nct.ac.jp

1 Department of Creative Engineering, National Institute of Technology, Tsuruoka College, Tsuruoka, Japan

2 Institute of Multidisciplinary Research for Advanced Materials (IMRAM), Tohoku University, Aoba-ku, Sendai, Japan

3 WPI-Advanced Institute of Materials Research (WPI-AIMR), Tohoku University, Aoba-ku, Sendai, Japan

References

- [1] Ye C, Liu W, Chen Y, Yu L. Room-temperature ionic liquids: a novel versatile lubricant. *Chem. Commun.* 2001;21:2244–2245. DOI: 10.1039/b106935g
- [2] Minami I. Ionic liquids in tribology. *Molecules* 2009;14:2286–2305. DOI: 10.3390/molecules14062286
- [3] Zhou F, Liang Y, Liu W. Ionic liquid lubricants: designed chemistry for engineering applications. *Chem. Soc. Rev.* 2009;38:2590–2599. DOI: 10.1039/b817899m
- [4] Kondo H. Tribochemistry of ionic liquid lubricant on magnetic media. *Adv. Tribol.* 2012;2012:1–20. DOI: 10.1155/2012/526726
- [5] Somers A, Howlett P, MacFarlane D, Forsyth M. A review of ionic liquid lubricants. *Lubricants* 2013;1:3–21. DOI: 10.3390/lubricants1010003
- [6] Suzuki A, Shinka Y, Masuko M. Tribological characteristics of imidazolium-based room temperature ionic liquids under high vacuum. *Tribol. Lett.* 2007;27:307–313. DOI: 10.1007/s11249-007-9235-8
- [7] Street KW, Morales W, Koch VR, Valco DJ, Richard RM, Hanks N. Evaluation of vapor pressure and ultra-high vacuum tribological properties of ionic liquids. *Tribol. Trans.* 2011;54:911–919. DOI: 10.1080/10402004.2011.606963
- [8] Phillips BS, John G, Zabinski JS. Surface chemistry of fluorine containing ionic liquids on steel substrates at elevated temperature using mössbauer spectroscopy. *Tribol. Lett.* 2007;26:85–91. DOI: 10.1007/s11249-006-9020-0
- [9] Lu Q, Wang H, Ye C, Liu W, Xue Q. Room temperature ionic liquid 1-ethyl-3-hexylimidazolium-bis(trifluoromethylsulfonyl)-imide as lubricant for steel–steel contact. *Tribol. Int.* 2004;37:547–552. DOI: 10.1016/j.triboint.2003.12.003
- [10] Jiménez AE, Bermúdez MD, Iglesias P, Carrión FJ, Martínez-Nicolás G. 1-N-alkyl-3-methylimidazolium ionic liquids as neat lubricants and lubricant additives in steel–aluminium contacts. *Wear* 2006;260:766–782. DOI: 10.1016/j.wear.2005.04.016
- [11] Liu X, Zhou F, Liang Y, Liu W. Tribological performance of phosphonium based ionic liquids for an aluminum-on-steel system and opinions on lubrication mechanism. *Wear* 2006;261:1174–1179. DOI: 10.1016/j.wear.2006.03.018
- [12] Kamimura H, Kubo T, Minami I, Mori S. Effect and mechanism of additives for ionic liquids as new lubricants. *Tribol. Int.* 2007;40:620–625. DOI: 10.1016/j.triboint.2005.11.009
- [13] Qu J, Chi M, Meyer HM, Blau PJ, Dai S, Luo H. Nanostructure and composition of tribo-boundary films formed in ionic liquid lubrication. *Tribol. Lett.* 2011;43:205–211. DOI: 10.1007/s11249-011-9800-z

- [14] Qu J, Bansal DG, Yu B, Howe JY, Luo H, Dai S, Li H, Blau PJ, Bunting BG, Mordukhovich G, Smolenski DJ. Antiwear performance and mechanism of an oil-miscible ionic liquid as a lubricant additive. *ACS Appl. Mater. Interfaces* 2012;4:997–1002. DOI: 10.1021/am201646k
- [15] Zhou Y, Dyck J, Graham TW, Luo H, Leonard DN, Qu J. Ionic liquids composed of phosphonium cations and organophosphate, carboxylate, and sulfonate anions as lubricant antiwear additives. *Langmuir* 2014;30:13301–13311. DOI: 10.1039/b817899m
- [16] Lo ER, Reichelt M, Salgado J. Ionic liquids based on phosphonium cations as neat lubricants or lubricant additives for a steel/steel contact. *ACS Appl. Mater. Interfaces* 2014;6:13115–13128. DOI: 10.1021/am502980m
- [17] Hayes R, El Abedin SZ, Atkin R. Structure in confined room-temperature ionic liquids. *J. Phys. Chem. B* 2009;113:7049–7052. DOI: 10.1021/jp902837s
- [18] Atkin R, Warr GG. Pronounced structure in confined aprotic room-temperature ionic liquids. *J. Phys. Chem. C* 2007;111:5162–5168. DOI: 10.1021/jp902837s
- [19] Werzer O, Cranston ED, Warr GG, Atkin R, Rutland MW. Ionic liquid nanotribology: mica–silica interactions in ethylammonium nitrate. *Phys. Chem. Chem. Phys.* 2012;14:5147–5152. DOI: 10.1039/c1cp23134k
- [20] Perkin S, Albrecht T, Klein J. Layering and shear properties of an ionic liquid, 1-ethyl-3-methylimidazolium ethylsulfate, confined to nano-films between mica surfaces. *Phys. Chem. Chem. Phys.* 2010;12:1243–1247. DOI: 10.1039/b920571c
- [21] Ueno K, Kasuya M, Watanabe M, Mizukami M, Kurihara K. Resonance shear measurement of nanoconfined ionic liquids. *Phys. Chem. Chem. Phys.* 2010;12:4066–4071. DOI: 10.1039/b923571j
- [22] Kamijo T, Arafune H, Morinaga T, Honma S, Sato T, Hino M, Mizukami M, Kurihara K. Lubrication properties of ammonium-based ionic liquids confined between silica surfaces using resonance shear measurements. *Langmuir* 2015;31:13265–13270. DOI: 10.1021/acs.langmuir.5b03354
- [23] Horn RG, Evans DF, Ninham BD. Double-layer and solvation forces measured in a molten salt and its mixtures with water. *J. Phys. Chem.* 1988;92:3531–3537. DOI: 10.1021/J100323a042
- [24] Horn RG, Smith DT, Haller W. Surface forces and viscosity of water measured between silica sheets. *Chem. Phys. Lett.* 1989;162:404–408. DOI: 10.1016/0009-2614(89)87066-6
- [25] Dushkin CD, Kurihara K. Nanotribology of thin liquid-crystal films studied by the shear force resonance method. *Colloids Surf. A Physicochem. Eng. Asp.* 1997;129–130:131–139. DOI: 10.1016/S0927-7757(97)00031-9

- [26] Mizukami M, Kusakabe K, Kurihara K. Shear resonance measurement on structuring of liquids confined between mica surfaces. *Prog. Colloid Polym. Sci.* 2004;128:105–108. DOI: 10.1007/b97098
- [27] Mizukami M, Kurihara K. A new physical model for resonance shear measurement of confined liquids between solid surfaces. *Rev. Sci. Instrum.* 2008;79:113705. DOI: 10.1063/1.3012811
- [28] Maru MM, Tanaka DK. Consideration of Stribeck diagram parameters in the investigation on wear and friction behavior in lubricated sliding. *J. Braz. Soc. Mech. Sci. Eng.* 2007;29:55–62. DOI: 10.1590/S1678-58782007000100009
- [29] Sato T, Masuda G, Takagi K. Electrochemical properties of novel ionic liquids for electric double layer capacitor applications. *Electrochim. Acta* 2004;49:3603–3611. DOI: 10.1016/j.electacta.2004.03.030
- [30] Tokuda H, Tsuzuki S, Susan M.A.B.H., Hayamizu K, Watanabe, M. How ionic are room-temperature ionic liquids? An indicator of the physicochemical properties. *J. Phys. Chem. B* 2006;110:19593–19600. DOI: 10.1021/jp064159v
- [31] Canova F. F., Matsubara H., Mizukami M., Kurihara K., Shluger A.L. Shear dynamics of nanoconfined ionic liquids. *Phys. Chem. Chem. Phys.* 2014;16:8247–8256. DOI: 10.1039/c4cp00005f

Ecotoxicity of Ionic Liquids Towards *Vibrio fischeri*: Experimental and QSAR Studies

Mohamed Ibrahim Abdul Mutalib and
Ouahid Ben Ghanem

Additional information is available at the end of the chapter

<http://dx.doi.org/10.5772/65795>

Abstract

Ionic liquids (ILs) have gained significant attention within the academic and industrial circle owing to their attractive and unique characters. However, the usual green image of the ionic liquids mainly associated with their low vapour pressure has become increasingly doubtful. Several recent studies have highlighted the underestimated ILs toxicity which has not been adequately addressed. Therefore, improving the understanding of the ionic liquids toxicity towards aquatic organisms will undoubtedly lead to formulation of right solutions to address the toxicity problem hence contributing towards the development of green and sustainable ILs-based technology. The chapter provides a collective review of studies conducted on the effect of ILs structure on toxicity, specifically focussing on the various types of cations and anions, and the length of the alkyl chain attached. Based on the qualitative outcome from the review, a discussion on the development of statistical modelling on the impact of ILs structural features towards the overall toxicity is presented. The application of quantitative structure activity relationship (QSAR) for developing the predictive model for toxicity is highlighted.

Keywords: ionic liquids, ecotoxicity, *Vibrio fischeri*, structural features, QSAR

1. Introduction

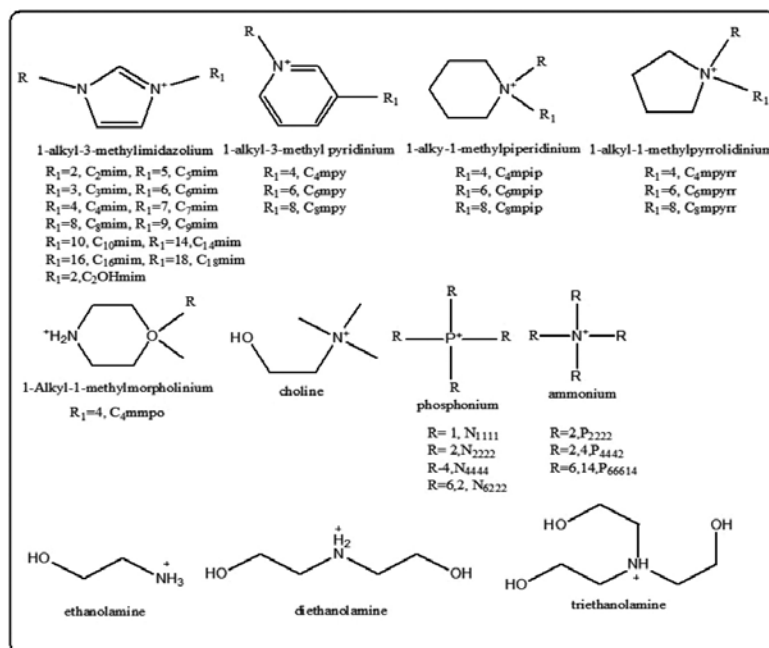
One of the major developments made on green solvents focuses on the design of new and more environmental friendly solvents. From the green chemistry perspective, green solvent should be non-toxic, readily biodegradable and is synthesized using the environmental friendly synthesis procedure, whilst at the same time able to meet the application target technologically and economically [1, 2]. For several years, ionic liquids (ILs) have been gaining significant attention as the candidate for future 'green solvents' from the scientific and indus-

trial community. It has shown several advantages over the volatile organic solvents (VOCs), among others, covering three major aspects namely:

1. Extremely low vapour pressure in comparison to the VOCs resulting in insignificant vaporization losses to the atmosphere.
2. Inflammable as opposed to the flammable VOCs hence easier to handle and store.
3. Non-toxic perception due to minute losses through vaporization into the atmosphere compared to the VOCs.

Whilst most studies have converged opinion on the first two aspects, the third has been increasingly contested. The work presented focuses on addressing the latter in order to provide further clarity pertaining to the issue of ILs toxicity. It has been generally agreed that the unique feature which enables ILs to capture significant interest is the ability to design them for specific application by changing the cation and anion coupling to meet specified physical, chemical and biological properties. To date, significant number of ILs has been developed and most of them are now commercially available. In addition, there are few more millions of possible ILs that could be theoretically synthesized [3].

ILs are mainly designed to be inflammable, non-volatile, and non-explosive media with a high thermal stability [4]. Due to their hardly measurable vapour pressure, they are not expected to contribute towards atmospheric pollution. On the contrary, most of them display high aqueous solubility. Even the supposedly most hydrophobic IL was found to exert some degree of solubility hence allowing their possible dispersion into aquatic systems, raising concerns on their subsequent environmental impact [5, 6]. Given the almost



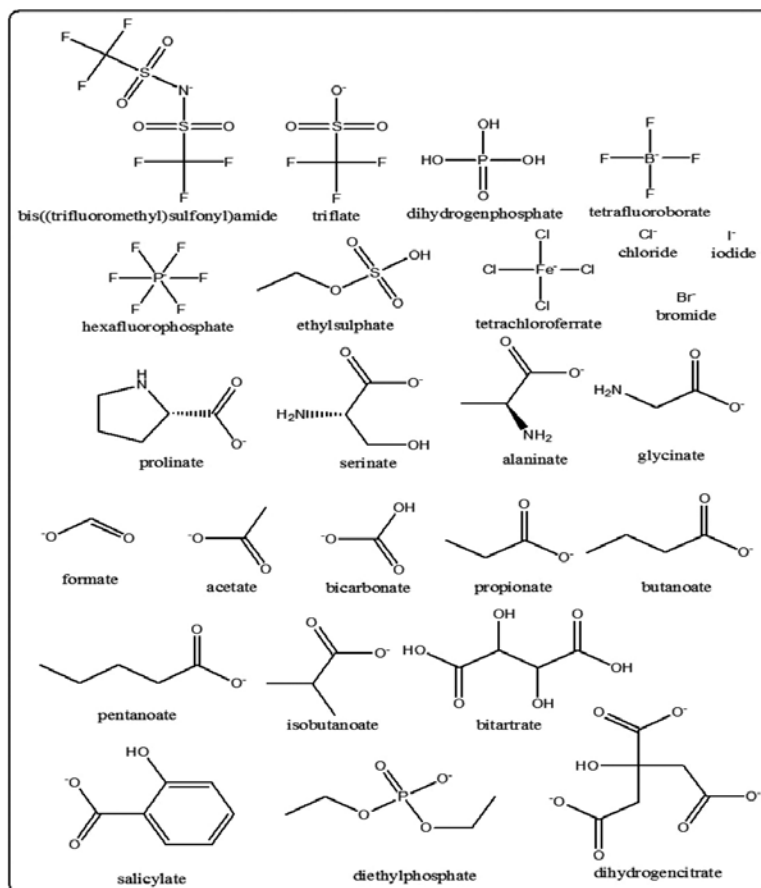


Figure 1. Structures of cations and anions discussed in the study.

unlimited combinations of possible ILs that could be developed, the toxicity determination could become highly laborious and extremely costly as well as time consuming. Developing predictive methods would require systematic understanding of the complex interactions between the cation and anion pairings leading to the toxicity properties, which are not easily done.

On another note, recent studies have pointed towards some possible draw backs on the use of ILs on an industrial scale. One of the major concerns highlighted was from aquatic toxicity studies showing potential drastic impact of some ILs which was considered as being green, on various aquatic organisms. A number of these ILs were found to possess higher toxicity than some of the acute organic solvents. Therefore, evaluating their overall toxicity has become of primary interest to the industries and public at large prior to their bulk application. This necessitates the development of a predictive method to substitute the laborious manual toxicity measurement in light of the increasing interest on ILs applications.

It has been known for some time that the structural feature of ILs may have different contributions on the ILs overall toxicity. Hence, a systematic study to assess the variation of the ILs structure on its overall toxicity has to be commissioned separately. The review attempted at investigating the influence of the changes in ILs structural features involves: (i) the cation core and the functional group substituent, (ii) the length of the alkyl chain substituent, and (iii) anion nature, on the ILs toxicity using bioluminescent *Vibrio fischeri*. The effective concentration at 50% i.e. EC_{50} values for 83 ILs were collected from different literature reports in order to configure the effect of changing the functional group and the structure of the ILs on its toxicity. All the various functional group substituents together with their different structures reflected on the cation and anion are shown in **Figure 1**. The study also introduces some further insight into the recent development pertaining to the quantitative structure activity relationship models (QSAR) which are proposed as the approach for developing models for predicting ILs toxicity based on the *V. fischeri*.

2. Ecotoxicity measurement using *V. fischeri*

The bioluminescent *V. fischeri* is a Gram-negative, rod-shaped bacterium that bioluminesces through a population-dependent mechanism called quorum sensing [7, 8]. The Microtox assay system (MAS) against bioluminescent *V. fischeri* was often chosen as the first sequence in a test battery to evaluate the toxicity of chemicals due to their simple, quick, good sensitivity and cost-effectiveness as well as a widely acceptable method for ecotoxicity assessments [9, 10]. In addition, *V. fischeri* is also sensitive to a wide variety of toxic substances hence making it a popular proxy method for detecting environmental pollutants for ecotoxicity studies. Furthermore, *V. fischeri* is also considered as a common test organism, well published in the Aquatic Toxicity Information Retrieval database (AQUIRE) produced by the US Environmental Protection Agency (EPA). Several other large environmental-based organizations have also recommended these species for aquatic toxicity assessment [11, 12]. It was earlier reported that *V. fischeri* assay yielded fairly replicable results which were comparable to those obtained using the standard tests, with an advantage of only requiring about 5% of the actual work involved in the standard procedures. Therefore, it was suggested that the MAS be used as a pre-screening tool in the hazard assessment of chemicals [13].

In the reported study, the ILs are classified based on their EC_{50} values according to the hazard ranking as described by Passino and Smith [14], shown in **Table 1**.

Hazard ranking	Concentration of ILs in $mg L^{-1}$
Practically harmless	100–1000
Moderately toxic	10–100
Slightly toxic	1–10
Highly toxic	0.1–1

Table 1. Hazard ranking classification for aquatic organisms.

2.1. Effect of the cation core

Numerous cations have been used to create ILs such as imidazolium and pyridinium, which have been appearing mostly in past ILs studies particularly for the room temperature ionic liquids (RTILs). In the study, the influences of the cation core on the ILs toxicity were investigated using imidazolium-, pyridinium-, pyrrolidinium-, piperidinium- and morpholinium-based cations. The structure with regards to the chain length variation on the cation core was kept within 1-butyl-(1 or 3)-methyl (cation) bromide ILs [15], as shown in **Table 2**, group A.

Ionic liquid names	Abbreviation	EC ₅₀ in mg L ⁻¹
Group A		
1-Butyl-1-methylimidazolium bromide	[C ₄ mim][Br]	1002
1-Hexyl-1-methylimidazolium bromide	[C ₆ mim][Br]	334
1-Octyl-1-methylimidazolium bromide	[C ₈ mim][Br]	50.9
1-Butyl-1-methylpiperidinium bromide	[C ₄ mpip][Br]	3958
1-Hexyl-1-methylpiperidinium bromide	[C ₆ mpip][Br]	230
1-Octyl-1-methylpiperidinium bromide	[C ₈ mpip][Br]	29.3
1-Butyl-1-methylpyrrolidinium bromide	[C ₄ mpyrr][Br]	5525
1-Hexyl-1-methylpyrrolidinium bromide	[C ₆ mpyrr][Br]	387
1-Octyl-1-methylpyrrolidinium bromide	[C ₈ mpyrr][Br]	50.8
1-Butyl-3-methylpyridinium bromide	[C ₄ mpy][Br]	130.48
1-Hexyl-3-methylpyridinium bromide	[C ₆ mpy][Br]	29.99
1-Octyl-3-methylpyridinium bromide	[C ₈ mpy][Br]	1.77
1-Butyl-1-methylmorpholinium bromide	[C ₄ mmor][Br]	66,729
1-Methylimidazole	[mim]	2864
1-Methylmorpholine	[mmor]	2328
Pyridine	[py]	867
1-Methylpiperidine	[mpip]	700
1-Methylpyrrolidine	[mpyrr]	493
2,3-Dimethylpyridine	[2,3mpy]	238
3,5-Dimethylpyridine	[3,5mpy]	65.9
2,3,5-Trimethylpyridine	[2,3,5mpy]	43
Group B		
1-Propyl-3-methylimidazolium tetrafluoroborate	[C ₃ mim][BF ₄]	1846.44
1-Butyl-3-methylimidazolium tetrafluoroborate	[C ₄ mim][BF ₄]	801.88
1-Pentyl-3-methylimidazolium tetrafluoroborate	[C ₅ mim][BF ₄]	331.29

Ionic liquid names	Abbreviation	EC ₅₀ in mg L ⁻¹
1-Hexyl-3-methylimidazolium tetrafluoroborate	[C ₆ mim][BF ₄]	384.44
1-Heptyl-3-methylimidazolium tetrafluoroborate	[C ₇ mim][BF ₄]	73.81
1-Octyl-3-methylimidazolium tetrafluoroborate	[C ₈ mim][BF ₄]	7.25
1-Nonyl-3-methylimidazolium tetrafluoroborate	[C ₉ mim][BF ₄]	1.55
1-Decyl-3-methylimidazolium tetrafluoroborate	[C ₁₀ mim][BF ₄]	0.20
1-Ethyl-3-methylimidazolium chloride	[C ₂ mim][Cl]	3134.68
1-Butyl-3-methylimidazolium chloride	[C ₄ mim][Cl]	515.49
1-Hexyl-3-methylimidazolium chloride	[C ₆ mim][Cl]	164.78
1-Octyl-3-methylimidazolium chloride	[C ₈ mim][Cl]	2.36
1-Decyl-3-methylimidazolium chloride	[C ₁₀ mim][Cl]	0.15
1-Tetradecyl-3-methylimidazolium chloride	[C ₁₄ mim][Cl]	0.22
1-Hexadecyl-3-methylimidazolium chloride	[C ₁₆ mim][Cl]	0.58
1-Octadecyl-3-methylimidazolium chloride	[C ₁₈ mim][Cl]	10.46
1-Ethyl-3-methylimidazolium bis((trifluoromethyl) sulfonyl)amide	[C ₂ mim][NTf ₂]	330.23
1-Propyl-3-methylimidazolium bis((trifluoromethyl) sulfonyl)amide	[C ₃ mim][NTf ₂]	240.18
1-Butyl-3-methylimidazolium bis((trifluoromethyl) sulfonyl)amide	[C ₄ mim][NTf ₂]	141.99
1-Pentyl-3-methylimidazolium bis((trifluoromethyl) sulfonyl)amide	[C ₅ mim][NTf ₂]	46.87
1-Hexyl-3-methylimidazolium bis((trifluoromethyl) sulfonyl)amide	[C ₆ mim][NTf ₂]	22.8
1-Heptyl-3-methylimidazolium bis((trifluoromethyl) sulfonyl)amide	[C ₇ mim][NTf ₂]	19.25
1-Octyl-3-methylimidazolium bis((trifluoromethyl) sulfonyl)amide	[C ₈ mim][NTf ₂]	6.44
Tetramethylammonium bromide	[N ₁₁₁₁][Br]	>15405.0
Tetraethylammonium bromide	[N ₂₂₂₂][Br]	21016.00
Tetrabutylammonium bromide	[N ₄₄₄₄][Br]	600.28
Hexyltriethylammonium bromide	[N ₆₂₂₂][Br]	64.65
Tetrabutylphosphonium bromide	[P ₂₂₂₂][Br]	174.03
Tributylethylphosphonium diethylphosphate	[P ₄₄₄₂][Br]	451.71
Trihexyl(tetradecyl)phosphonium bromide	[N ₆₆₆₁₄][Br]	1449.09
Group C		
Cholinium bicarbonate	[Chol][Bic]	>20000
Cholinium butanoate	[Chol][But]	884.1

Ionic liquid names	Abbreviation	EC ₅₀ in mg L ⁻¹
Cholinium acetate	[Chol][Ac]	673.21
Cholinium dihydrogenphosphate	[Chol][DHPhosp]	572.72
Cholinium propanoate	[Chol][Prop]	487.9
Cholinium chloride	[Chol]Cl	469.34
Cholinium salicylate	[Chol][Sal]	236.11
Cholinium bitartrate	[Chol][Bit]	37.9
Cholinium dihydrogencitrate	[Chol][DHCit]	37.23
2-Hydroxyethanolamine formate	[2-HEA][F]	700
2-Hydroxyethanolamine butanoate	[2-HEA][B]	2239
2-Hydroxydiethanolamine formate	[2-HDEA][F]	800
2-Hydroxydiethanolamine acetate	[2-HDEA][ace]	1750
2-Hydroxydiethanolamine propionate	[2-HDEA][Pr]	650
2-Hydroxydiethanolamine butanoate	[2-HDEA][B]	800
2-Hydroxydiethanolamine isobutanoate	[2-HDEA][iB]	850
2-Hydroxydiethanolamine pentanoate	[2-HDEA][Pe]	350
2-Hydroxytriethanolamine butanoate	[2-HTEA][B]	501
2-Hydroxytriethanolamine pentanoate	[2-HTEA][Pe]	461
1-Ethyl-3-methylimidazolium chloride	[C ₂ mim][Cl]	9213.24
1-Ethyl-3-methylimidazolium hexafluorophosphate	[C ₂ mim][PF ₆]	4250.70
1-Ethyl-3-methylimidazolium ethylsulphate	[C ₂ mim][EtSO ₄]	2974.71
1-Ethyl-3-methylimidazolium bis((trifluoromethyl) sulfonyl)amide	[C ₂ mim][NTf ₂]	1631.25
1-Ethyl-3-methylimidazolium triflate	[C ₂ mim][TfO]	1430.13
1-Ethyl-3-methylimidazolium acetate	[C ₂ mim][Ace]	1321.25
1-Ethyl-3-methylimidazolium tetrachloroferrate	[C ₂ mim][FeCl ₄]	9.99
1-(2-Hydroxyethyl)-3-methylimidazolium glycinate	[C ₂ OHmim][Gly]	11649.23
1-(2-Hydroxyethyl)-3-methylimidazolium alaninate	[C ₂ OHmim][Ala]	8123.27
1-(2-Hydroxyethyl)-3-methylimidazolium serinate	[C ₂ OHmim][Ser]	10526
1-(2-Hydroxyethyl)-3-methylimidazolium prolinat	[C ₂ OHmim][Pro]	14509
1-(2-Hydroxyethyl)-3-methylimidazolium bis((trifluoromethyl)sulfonyl)amide	[C ₂ OHmim][NTf ₂]	4896.94
1-(2-Hydroxyethyl)-3-methylimidazolium iodide	[C ₂ OHmim][I]	1972.20
Group D		
Methanol	MeOH	320400
Dimethyl sulfoxide	DMSO	98359.84

Ionic liquid names	Abbreviation	EC ₅₀ in mg L ⁻¹
Ethanol	EtOH	34947.67
2-Propanol	IPA	35389.50
Acetonitrile	Acn	24172.03
Acetone	Ace	17140.62
N,N-Dimethylformamide	DMAc	20130.66
Dichloromethane	DCM	2877.80
Chloroform	CHCl ₃	671.32
Cyclohexane	CYHEX	226.52
Pyridine	py	212.90
Benzene	bz	102.97
Toluene	TOL	19.70

Table 2. Ionic liquids ecotoxicity against *Vibrio fischeri* expressed in mg. L⁻¹.

Although the EC₅₀ values for the five ILs fall under the same category i.e. practically harmless, the impact of the cation variations on the overall toxicity are found to be obvious. The result on EC₅₀ values highlighted that the imidazolium-based ILs exhibited about 4–5 magnitude higher toxicity measurement compared to piperidinium- and pyrrolidinium-based ILs respectively. The most toxic IL is the one based on pyridinium cation where a slightly higher toxicity values were observed compared to the imidazolium analogue. Meanwhile the morpholinium cation demonstrates far less toxicity behaviour than the other counterparts with EC₅₀ value reaching as high as 66,729 mg L⁻¹. The piperidinium and morpholinium exhibited almost similar cationic core structure where the latter can simply be established by replacing the carbon atom located opposite to the amine group in the piperidinium structure, with an oxygen atom. Despite the slight structural differences, the presence of the oxygenated atom in the morpholinium cation led to its significant toxicity reduction in the order of 17 times, compared to the piperidinium-based IL. This finding augurs well with the earlier work reported by Samori et al. [16, 17].

The toxicity of some starting reactant for the cation used in the ILs synthesized in the study were tested against *V. fischeri*, with results shown in **Table 2**, group A. The EC₅₀ values for 1-methylimidazolium, 1-methylpyrrolidinium, 1-methylpiperidinium, 1-methylmorpholinium, pyridinium, 2,3-dimethylpyridine, 3,5-dimethylpyridine and 2,3,5-dimethylpyridine are found to be 2864 mg L⁻¹, 493 mg L⁻¹, 700 mg L⁻¹, 2328 mg L⁻¹, 867 mg L⁻¹, 238 mg L⁻¹, 65.9 mg L⁻¹ and 43 mg L⁻¹, respectively. The reported toxicity of these compounds did not show any clear and logical pattern linking the toxicity to the ILs structure. Hence, there were not any structure-toxicity relationships that could be established. As an example, the results show that 1-methylpyrrolidinium and 1-methylpiperidinium cation-based ILs displayed 5.8 and 4 times higher toxicity respectively, when compared to 1-methylimidazolium, which is contrary to the anticipated trend which predicts imidazolium-based to have higher toxicity than the earlier two ILs.

Generally, it was extremely difficult to establish sensible and systematic structure-toxicity relationship with exception to the observation involving relationship between the position and the number of methyl groups attached to the pyridine cation and the effect on toxicity of the ILs as a whole. Also, the result indicates an important general trend which shows that the ILs with the cation structure containing aromatic, are always more toxic than the non-aromatic ones. According to Ventura et al. [6] and Kurnia et al. [18], the aromatic cation are more soluble in water and therefore capable of directly exhibiting its high toxicity effect on the aqua environment compared to the non-aromatic-based ILs which are much less soluble. However, it is worth to note that the toxicity of the non-cyclic cations such as sulphonium, ammonium and phosphonium has not been rigorously studied. Nevertheless, the present study still takes into account of the toxicity involving few ammonium and phosphonium ILs reported earlier and the results are included.

2.2. Effect of alkyl chain length

It is known that the alkyl chain length of the cation has a strong effect on the physical and chemical properties of the ILs. For example, the extension of the cation side resulting from a longer alkyl chain commonly results in lower density and solubility, slower diffusion rate and increases viscosity [19, 20]. In addition, it was also observed that the cation alkyl chain length has a pronounced effect on the ecotoxicity towards microorganisms. Most of the established ecotoxicity data covering not only *V. fischeri* but also other organisms such as cell, green algae, fish, and bacteria employed for investigating the influence of the alkyl chain length on the ionic liquid toxicity. **Table 2** group B provides the EC_{50} values for different counters to represent the impact of the alkyl chain length associated with different cation type on the ILs toxicity. Viboud et al. [15] have reported the effect of butyl, hexyl and octyl on the toxicity for 1-alkyl-1-methylimidazolium [C_n mim][Br], 1-alkyl-1-methylpyrrolidinium bromide [C_n mpyr][Br] and 1-alkyl-1-methyl piperidinium bromide [C_n mpip][Br]. It was noticeable that the EC_{50} values sharply decreases with the reduction in the alkyl chain length of the cation, indicating clear toxicity relationship.

The type of cation also seems to have an important role in changing the toxicity effect of the ILs when its' substituent chain length are further extended. For the shorter alkyl chain (butyl), the pyrrolidinium cation demonstrated lower toxicity compared to piperidinium and imidazolium, respectively. The recorded EC_{50} value of [C_4 mpyr][Br] is 5525 mg L⁻¹ and this marked a reduction of 109-fold in the EC_{50} value, signifying a tremendous increase in toxicity when the side alkyl chain was extended from four to eight carbon atoms. For the piperidinium type, the recorded effect was even more drastic with the toxicity increased by 135-fold from 3958 mg L⁻¹ for [C_4 mpip][Br] to 29.3 mg L⁻¹ for [C_8 mpip][Br]. Between the three cations, imidazolium recorded the lowest rate of increase in toxicity with the increase in the alkyl chain length, where the increment was only by 20-fold from 1002 mg L⁻¹ for [C_4 mim][Br] to 50.9 mg L⁻¹ for [C_8 mim][Br]. The lowest rate of increase in toxicity could be explained by the fact that imidazolium is already possessing highest toxicity even with shorter alkyl chain length compared to the others.

A similar study has been conducted for pyridinium-based ILs by Docherty and Kulpa [21] who studied the effect of butyl, hexyl and octyl substituents on the toxicity of 1-alkyl-3-meth-

lpyridinium bromide-based ILs. A similar increasing trend in the toxicity associated with increasing alkyl chain length was observed. As expected, the least toxic compound of this cation type is the butyl-based ILs with EC_{50} value of 130.48 mg L^{-1} . The EC_{50} value reduces to 29.99 mg L^{-1} through the addition of two carbon atoms to the alkyl chain (hexyl) resulting in a fourfold increase in toxicity. Switching the hexyl substituent to an octyl causes an increase in toxicity i.e. by 17-fold compared to the hexyl-based IL and up to 73-fold compared to the butyl-based IL.

Generally, it can be stated that increase in the side chain for the pyrrolidinium- and piperidinium-based ILs produces more pronounced effect than those of the aromatic-based cation such as imidazolium- and pyridinium-based ILs. Although there were almost zero data reported for much longer alkyl chain except for imidazolium-type ILs which will be further discussed below, the increasing trend of the toxicity with respect to the increase in the side alkyl chain reveals that longer extension on the alkyl chain beyond C_9 and above, will produce highly toxic ILs and therefore should be avoided.

For the longer alkyl chain, Ranke et al. [22] studied the toxicities for 1-alkyl-3-methylimidazolium tetrafluoroborate with alkyl chain varied from C_3 to C_{10} . Based on their EC_{50} values, as can be seen from **Table 2** group B, the tetrafluoroborate-based ILs having alkyl chain length up to heptyl, can still be classified as practically harmless. Further extension of the alkyl chain will lead to more toxic effect on the *V. fischeri*, with the C_8 - and C_9 -based ILs classified as slightly toxic ILs. A more drastic increase in toxicity was observed when the alkyl chain length reaches decyl with the resultant IL producing a highly toxic one. A similar study has been done by Stolte et al. [23] where they investigated the toxicities for 1-alkyl-3-methylimidazolium chloride with alkyl chain varied from C_2 to C_{10} with an increment rate of two carbon atoms at a time, and for C_{14} , C_{16} and C_{18} . It is clear that chloride-based ILs showed a slightly more toxic character than their tetrafluoroborate counter parts which is a result of the contribution from the halide anion. In agreement with what have been discussed above, the toxicity of the chloride-based ILs was found to follow the same trend observed for tetrafluoroborate-based ILs. The alkyl chain length extension of ethyl, butyl and hexyl are categorized as practically harmless, whereas the octyl is found to be slightly toxic. Increasing the alkyl chain from 8 to 10 carbon atoms causes a reduction of 15-fold on the EC_{50} values. The EC_{50} value reduces from 2.36 mg L^{-1} for $[C_8\text{mim}][\text{Cl}]$ to 0.15 mg L^{-1} for $[C_{10}\text{mim}][\text{Cl}]$, producing the most toxic IL for $[C_n\text{mim}][\text{Cl}]$ ILs. Also for the latter, the toxicity hazard impact increases to highly toxic when compared to the slightly toxic octyl. The reported EC_{50} values of $[C_{14}\text{mim}][\text{Cl}]$ and $[C_{16}\text{mim}][\text{Cl}]$ were 0.22 mg L^{-1} and 0.58 mg L^{-1} , respectively.

Despite the above highlighted findings, a temporary reverse effect was observed for the ILs when the alkyl chain reaches decyl, where a noticeable increase in the EC_{50} value indicating reduction in the toxicity of the ILs. The observed effect continues until the chain length reaches C_{17} before reversing back to the earlier trend. As a result, the hazard ranking of $[C_{18}\text{mim}][\text{Cl}]$ changes back to a slightly toxic effect, similar to the earlier hazard ranking for the ILs when the alkyl chain was at C_8 . Hence it can still be concluded that for long alkyl side chains beyond C_8 , the dependence between the chain length and toxicity is still valid.

The toxicity of hydrophobic $[C_n\text{mim}][\text{NTf}_2]$ -based ILs was also discussed by Ventura et al. [6]. For these ILs, the alkyl chain is varied from C_2 to C_8 (see **Table 2** group B). The reported EC_{50} values are found to be comparable and it follows a similar trend observed for the chloride and tetrafluoroborate-based ILs. The exception was only observed for the short alkyl chain, where $[\text{NTf}_2]$ -based ILs exhibited higher toxicity than their corresponding $[\text{BF}_4]$ and $[\text{Cl}]$ anions. For instance, the EC_{50} value for $[\text{C}_2\text{mim}][\text{NTf}_2]$ is 330.23 mg L^{-1} which is 5.6-fold more toxic than $[\text{C}_3\text{mim}][\text{BF}_4]$ despite having shorter alkyl chain attached to the cation, and 9.5-fold more toxic than $[\text{C}_2\text{mim}][\text{Cl}]$. On the contrary, for the $[\text{C}_8\text{mim}]$ -based ILs, much smaller differences in EC_{50} values were reported for the three different anions, where the values for $[\text{C}_8\text{mim}][\text{Cl}]$, $[\text{C}_8\text{mim}][\text{NTf}_2]$ and $[\text{C}_8\text{mim}][\text{BF}_4]$ were 2.36 mg L^{-1} , 6.44 mg L^{-1} and 7.25 mg L^{-1} , respectively. This could be explained based on earlier reported work that the *V. fischeri* organism was less sensitive to the hydrophobic ILs than other organisms such as *Folsomia candida* [24].

Phosphonium-based ILs also showed a similar behaviour as discussed earlier where its toxicity reduces as the alkyl chain length grew longer than decyl. For instance, the reported EC_{50} value for trihexyl(tetradecyl)phosphonium bromide is $1449.09 \text{ mg L}^{-1}$, eightfold greater than the EC_{50} value of tetrabutylphosphonium bromide i.e. 174.09 mg L^{-1} [25], as presented in **Table 2** group B. The phenomenon is well reported in the literature for highly lipophilic substances ($\log K_{ow} > 5$) known as the cut-off effect. For this phenomenon, different explanations were presented based either on insufficient solubility i.e. nominal concentration deviating from real test concentration, or on kinetic aspects i.e. slower uptake due to steric effects for compounds with a large molecular size [2, 26].

The increasing trend in toxicity with alkyl chain length was also confirmed for quaternary ammonium-based ILs [25]. As can be seen from the tabulated data shown in **Table 2** group B, tetramethylammonium bromide and tetraethylammonium bromide show non-toxic behaviour with EC_{50} values greater than 5000 mg L^{-1} . The toxicity of these ILs increases i.e. EC_{50} value reduces to 600.28 mg L^{-1} , for tetrabutylammonium bromide. Further noticeable increase in toxicity was observed for hexyltriethylammonium bromide with EC_{50} value reduces to 64.65 mg L^{-1} .

Generally it can also be seen that the quaternary ammonium-based ILs exhibits lower toxicity against *V. fischeri* than the ILs with cyclic cations (aromatic and non-aromatic).

2.3. Effect of the anions

The anion chemistry has a great impact on the alteration of the ILs properties. Most of ILs properties such as melting point, hydrophobicity, chemical and thermal stabilities, ability to dissolve organic and inorganic solutes and miscibility with organic solvent rely mainly on the type of the anion [27–29]. Although there is no clear pattern that could be drawn for the anion influence on the ILs toxicity, recent studies have given more attention towards the impact of anions type on ILs toxicity. The data reported for the anion effect are tabulated in **Table 2** group C. Ventura et al. [30] investigated the toxicity of 10 ILs with 9 of them comprising the cholinium cation with different anions. Cholinium-based ILs has received significant attention due to its non-toxic and biocompatible nature [31–33]. Using cholinium as the cation, the study on the impact of various anions on toxicity of the ILs was conducted. The bicarbonate

anion was found to be the least toxic whilst the dihydrogen citrate being the most toxic. In fact, there was no EC_{50} value reported for cholinium bicarbonate due to its unnaturally high value. The maximum luminescence inhibition caused by this IL was as low as 35% at a very high concentration of 20,000 mg L⁻¹.

Judging on the anion structure, the butanoate anion which corresponds to the addition of propanoate and acetate anions with one and two methyl group, respectively is expected to possess higher toxicity due to longer alkyl chain on its structure. However, the toxicity reported for the cholinium cation did not show any consequence leading to noticeable toxicity increase with increase in the alkyl chain on the anion side. Except for cholinium bitartrate and cholinium dihydrogencitrate which are classified as moderately toxic with EC_{50} values lower than 100 mg L⁻¹, the other seven compounds reported fell under practically harmless class. The reported ecotoxicity data also demonstrated that some classic ILs, pairing the imidazolium or pyridinium cation with alkyl chain varied from C₁ to C₆ with similar anions, may possess lower toxicity than the one exerted by the cholinium cation. Hence, contrary to the effect of alkyl chain length on the IL cation towards ILs toxicity, the same effect is proven to be inconclusive for the anion.

Overall, the order of toxicity sequence reported in increasing order is bicarbonate < butanoate < acetate < dihydrogenphosphate < propanoate < chloride < salicylate < bitartrate < dihydrogencitrate.

Another recent work concerning the anion impact on IL toxicity is the study conducted by Peric et al. [34] where they investigated the ecotoxicity of compounds based on substituted amines as the cations including monoethanolamine, [2-HEA], diethanolamine [2-HDEA] and triethanolamine [2-HTEA], paired with organic acids with different numbers of carbon atoms (formic, propionic, butanoic, isobutanoic and pentanoic acid) as the anions. From the reported data, it is apparent that the alkyl chain length did show some influence on the ILs toxicity. The 2-hydroxydiethanolamine pentanoate [2-HDEA][Pe] was found to be the most toxic with EC_{50} values of 350 mg L⁻¹, followed by 2-hydroxytriethanolamine pentanoate [2-HTEA][Pe] with EC_{50} of 461 mg L⁻¹. The two ILs have pentanoic as its anion, indicating the presence of five carbon atoms in the anion side chain. The toxicity exerted by the two ILs demonstrated stronger influence by the cation structure although [2-HDEA][Pe] displayed a 1.3-fold higher toxicity than the [2-HTEA][Pe] despite the latter having a larger cation size. The lower toxicity of [2-HTEA] is attributed mainly to the presence of three hydroxyl groups (-OH) in the cation structure as opposed to only two in [2-HDEA]. As a matter of fact, the observation agrees well with the conclusion stated earlier on the influence of the oxygenated atom within the cation structure which tends to lower the ILs toxicity. Interestingly, this is not always true for the butanoate anion as the toxicity trend displayed different results. The 2-hydroxydiethanolamine butanoate [2-HDEA][B] was reported to be 1.6-fold less toxic than the 2-hydroxytriethanolamine butanoate (2-HTEAB) despite having more hydroxyl (-OH) group attached to it. In this respect, the authors argued that the noticeable increase in the toxicity is due to the more dominant effect contributed from the longer alkyl chain length of the anion. The argument is rather controversial as it was earlier explained that the trend on the effect of the alkyl chain length of the anion on toxicity is inconclusive and lesser compared to the cation. Nevertheless, all the studied ILs were non-toxic and fell under the class of practically harmless.

It is worthy to highlight that it may be worthwhile to use some of the carboxylic acid anions such as decanoic and undecanoic acid which have longer alkyl chains, to synthesize novel ILs for undertaking the study to confirm the effect of the alkyl chain of the anion to the ILs toxicity.

More recently, Montalbán et al. [35] studied the toxicity of 1-ethyl-3-methylimidazolium-based ILs using six different anions including PF_6^- , TfO⁻, NTf_2^- , Cl⁻, Ace and EtSO_4^- . Due to the short alkyl chain used, the six ILs possess very low toxicity and hence all of them were classified as practically harmless. The reduction in toxicity of these ILs follow the trend of $\text{Ace} > \text{TfO} > \text{NTf}_2 > \text{EtSO}_4 > \text{PF}_6 > \text{Cl}$. Contrary to the above finding, Alvarez-Guerra and Irabien [36] studied the toxicity of tetrachloroferrate(III) anion with the same cation and found a very low EC_{50} value i.e. 9.99 mg L^{-1} indicating highly toxic behaviour. Clearly, the $[\text{FeCl}_4]^-$ anion contributes to the extreme toxicity effect when compared to the earlier six anions and the alkyl chain length used. The $[\text{FeCl}_4]^-$ found to possess toxicity of 132-fold higher compared to [Ace] which was the most toxic among the former anions. According to the QSAR model developed by Alvarez-Guerra and Irabien [36], it was similarly suggested that the highly toxic behaviour exerted by the anion was due to the presence of Fe in its structure, exerting a significant influence on the toxicity.

Based on past reported work, introducing amino acid anion to the structure of the ILs can be considered as a convenient approach to reduce its toxicity. Interestingly, the claim has yet to be experimentally proven. In our recent work [37], the variation of the toxicity of 1-(2-hydroxyethyl)-3-methylimidazolium, $[\text{C}_2\text{OHmim}]^+$ by pairing it with four different types of amino acid anions namely glycinate, alaninate, serinate and prolinatate was studied towards the *V. fischeri*. The reported EC_{50} for the amino acid-based ILs was found to be greater than 5000 mg L^{-1} , which highlighted their non-toxic behaviour. The toxicity of the same cation when paired with $[\text{NTf}_2]^-$ and [I] anions as reported earlier by Alvarez-Guerra and Irabien [36] in EC_{50} values was $4896.94 \text{ mg L}^{-1}$ and $1972.20 \text{ mg L}^{-1}$, respectively as shown in **Table 2** group C. This indicates a marked change in toxicity when changing the anion from amino acid type. Nevertheless, there was a recent report by Egorova et al. [38] contravening the role of the amino acid anion in ILs in lowering the ILs toxicity and the fact that they should not be seen as entirely green compounds for initial design. Nonetheless, the comparison between the EC_{50} values of 1-(2-hydroxyethyl)-3-methylimidazolium-based ILs has sufficiently indicated a clear impact of the amino acid anions on lowering the toxicity of the ILs compared to the [I] and $[\text{NTf}_2]^-$ -based ILs. Furthermore, the toxicity of $[\text{C}_2\text{OHmim}][\text{Ala}]$ which is the most toxic among the amino acid-based ILs, displayed even lower toxicity than $[\text{C}_2\text{OHmim}][\text{NTf}_2]^-$ and $[\text{C}_2\text{OHmim}][\text{I}]$ by 1.6 and 4-fold, respectively.

Generally, it can be argued that the impact contributed by the anion on the toxicity did not show any strong systematic relationship involving its structure i.e. alkyl chain length as demonstrated in the case of the cation. However, changing the type of the anion would be crucial as it can change the ILs' toxicity significantly.

2.4. Toxicity of starting material and organic solvent

Volatile organic solvents (VOCs) are considered as a major source of atmospheric pollution. They exert high vapour pressure hence have high volatility leading to their significant losses to the atmosphere. Their vapour can be highly toxic depending on the type of component

and its respective concentration thus posing toxic exposure to process operators and the surrounding community. This is where ILs, having significantly low volatility, was promoted by many researchers as the ideal replacement to VOCs for many of the industrial application. However, several studies have reported comparable EC_{50} values towards *V. fischeri* for some of the common VOCs (Table 2 group D) compared to several common ILs. Hence, the idea of ILs being a greener alternative to the VOCs has to be carefully evaluated. In fact, most of VOCs displayed lower toxicity to the *V. fischeri* than some of the least toxic ILs discussed earlier.

3. Quantitative structure activity/property relationship (QSAR/QSPR)

Quantitative structure activity/property relationships (QSAR/QSPR) are models which can be used to predict the relationship between the chemical compound structure and a desired end measure which could refer to any type of physical, chemical or biological activities/properties [39]. Reliable experimental data is crucial at the model development stage in order to produce good prediction model. However, the more extensive the experimental data used, the more time and resources required causing higher cost.

The main aim of the QSAR development is to develop reliable predictive models with minimum possible experimental data thus reducing the time and resources required. The basic principles of the development of the QSAR/QSPR as outlined by Todeschini and Consonni [40] are;

1. The property of interest of the studied compound must have some strong form of relationship with their molecular structure.
2. Similar compounds judging from the orientation of the molecular structure, must behave in a similar fashion.

As the QSAR/QSPR modelling involves computational work, it reflects the benefits as below;

- low costs and high productivity levels especially dealing with data from large chemical libraries,
- more environmental friendly approach leading to reduction in necessary chemical experiments and/or animal testing, which could be further reduced with selection of good descriptor linking the molecular structure to the property of interest,
- possibility to predict properties of newly synthesized compounds based on its chemical structure without the need to conduct any experimental or test procedure.

In this study, ILs toxicity is the property of interest and an attempt was made to develop efficient relationship with the ILs molecular structure. There have been several QSAR models reported for predicting ILs ecotoxicity against *V. fischeri*. Nevertheless, all the QSAR/QSPR models developed suffer from limitation due to the lack of experimental data involving some specific family of ILs. The main differences between the various QSAR/QSPR models were mainly on the selection of the descriptors used in developing the predictive model, and the algorithm learning methods used to establish the relationships between input descriptor and the identified property of interest.

The evaluation of the model accuracy and stability are highly important. The correlation coefficient (R^2) was used mostly as the statistical parameter to evaluate the model accuracy. However, the high R^2 value (close to 1) does not necessarily mean that the model is reliable and stable. Therefore, model validation is another important step to ascertain the model stability which signifies the ability to display consistently good prediction for ILs especially for data outside the experimental range used during model development stage. In other words, validation of the QSAR models is a crucial issue for judging its ability in predicting similar properties of new ILs set not included during model development [41].

Different methods were adopted to validate the QSAR/QSPR models such as internal, external and cross-validation [42]. Most of the developed models used the multiple linear regression technique (MLR) which was widely employed due to its simplicity, transparency and reproducibility as well as easy interpretability [43]. It also provides useful statistical parameter for evaluating the significance of the selected descriptors (i.e. P -value and t -statistic), thus guiding the elimination of insignificant descriptors that have none or insignificant impact on the model performance.

In most cases reported, the end measure for ecotoxicity of ILs towards *V. fischeri* was expressed as $\log EC_{50}$ in $\mu\text{mol L}^{-1}$. In the extensive literature study conducted, the pioneering work found on QSAR/QSPR model dealing with the toxicity of ILs towards *V. fischeri* was developed by Couling et al. [25]. The model was developed using four descriptors namely E-state indices, surface area, surface charge density and shadow parameter. This model was able to predict the toxicity with accuracy producing R^2 value of 0.78. Luis et al. [44] and [45] later developed novel QSAR models based on multiple linear regression method to predict the ecotoxicity. In their two studies, they proposed the used of group contribution approach i.e. the functional group, as molecular descriptors, in order to assess the contribution of different structural elements on the overall toxicity of ILs. Supposedly, an ionic liquids structure could be divided into three main components namely the cation, the anion and the substitution group, and each group could further be divided into subgroups based on their toxicity effect. In their earlier model, nine descriptors were used to represent a medium dataset obtained for 43 ILs. In their later model, the number of descriptors was increased to 15 as the dataset was expanded to 96 ILs. Despite the effort of increasing the number of descriptors with a larger pool of ILs, the later multiple linear regression models hardly produced improvement compared to the earlier, both displaying only acceptable regression statistics with $R^2 = 0.925$ and 0.924, respectively. This was due to the fact that the group contribution descriptors were used as independent variables for the prediction of a dimensionless toxicity value. Alvarez-Guerra and Irabien [36] proposed a new approach for estimating the ecotoxicity of ILs by means of partial least square-discriminant analysis (PLS-DA) to classify the ecotoxicity for relatively large dataset comprising of 148 ILs. The developed model was able to achieve a high correlation coefficient value of 0.929. The same dataset was used later by Das and Roy [46] to develop their ecotoxicity predictive model. Various two-dimensional chemical descriptors were used to build the input dataset code including constitutional, topological, connectivity, information indices, extended topo-chemical atom (ETA) indices, atom-type E-state indices and molecular properties, using the DragonTM software. The regression model produced an R^2 value of 0.739 when tested using external validation i.e. using data set outside the data range used during

the model development stage. The achievement has led to more QSAR models developed to predict ILs toxicity against *V. fischeri*, which are summarized in **Table 3**.

No of IL	Method	Molecular descriptor	Descriptor type	R ²	Ref
25	GFA ^a	4	Electronic, spatial, structural, thermodynamic, and topological descriptors	0.78	[25]
43	MLR	9	Group contribution	0.925	[44]
96	MLR	15	Group contribution	0.924	[45]
148	PLS-DA ^b	94	Negative or positive effect	Tr = 0.963 Te = 0.929	[36]
157	MLR	28	Topological index	0.908	[47]
10 & 19	MCA ^c	1	Number of aliphatic carbons & number of carbons in the cation	0.934 & 0.861	[15]
147	MLR	12	DRAGON	Tr = 0.936 Te = 0.757	[46]

^a Genetic function approximation.
^b Partial least squares-discriminant analysis.
^c Multifactorial analysis.

Table 3. Summary of published QSAR models for predicting the ecotoxicity for *V. fischeri*.

There were two aspects clearly noticeable from the comparison made across all the published models. These are the variation in the dataset size and the number and type of molecular descriptors used. It is worth highlighting that adding new ILs which pair different elements in their structure, not considered in the earlier models, would require new set of descriptors for better molecular representation and good applicability of the QSAR model. For instance, Viboud et al. [15] developed two linear QSAR models for relatively small datasets containing 10 and 19 ILs. The first dataset which comprised pyridinium bromide-based ILs was expanded by the addition of 9 ILs pairing different cations (imidazolium, pyrrolidinium and piperidinium). Although a single descriptor was used in the model construction, good correlation coefficients was achieved i.e. 0.934 and 0.861, respectively. However, it is clear that expanding dataset size would affect the model accuracy resulting in the accuracy drop. Therefore, many QSAR models developed to cover relatively huge dataset were constructed using higher number of molecular descriptors to cover the significant variation in all the molecular structure. So far, the largest dataset used comprised 157 ILs covering 74 cations and 22 anions, studied by Yan et al. [47]. They used linear regression to propose a predictive model with good correlation coefficient i.e. $R^2 = 0.908$, using large number of topological descriptors i.e. 28.

Overall, it can be concluded that the application of proper method for the selection of molecular descriptor, and the model validation method used, become the key factors in influencing the outcome of the QSAR/QSPR model developed. With the right selection of the molecular descriptors, the accuracy and reliability of the predictive models developed could be enhanced significantly.

With such capability, the design of ILs for any application could be made to consider its toxicity thus enabling greener ILs developed for industrial application right from the design stage.

4. Conclusion

The collective study on the relationship between ILs ecotoxicity towards luminescent marine bacterium *V. fischeri* has demonstrated the impact of the ILs structure on the overall toxicity. Although, most of ILs highlighted in the works discussed were practically rated between harmless to moderately toxic towards luminescent marine bacterium *V. fischeri*, few of them were found to be highly toxic with an EC_{50} values lower than 1 mg L^{-1} . These ILs are mainly characterized by the presence of a cyclic cation having long alkyl chain attachment. The extension of the alkyl side chain leads to increase in the ILs hydrophobicity, and hence increasing the toxicity drastically.

There seems to be consensus from the past literature that the alkyl chain length appeared to be the dominant parameter controlling the ILs toxicity towards different aquatic organisms including *V. fischeri* and other trophic organisms such as cress (*Lepidium sativum*), mammalian cells (IPC-81), limnic unicellular green algae (*Scenedesmus vacuolatus*), enzymes (acetylcholinesterase), wheat (*Triticum aestivum*) and duckweed (*Lemna minor*). Therefore, the focus on the ILs design for low toxicity should be focussed on the ILs structure including the type of chemical elements attached to it. Two useful guidelines that could be applied to consistently design low toxicity ILs are the utilisation of shorter alkyl chain varied from (C_1 to C_4) attached to the ILs cation, and functional group containing oxygen paired to its atom on the ILs cation side. Any alkyl chain used as extension on the ILs cation should be kept at less than C_4 since the toxicity increases significantly beyond the limit. Past toxicity studies have also displayed that the non-aromatic cation such as piperizinium, pyrrolidinium and morpholinium, shows lower toxicity compared to the imidazolium and pyridinium cations which contained an aromatic structure.

Besides the above factors highlighted on ILs cation affecting its toxicity, the proper selection of the anion moiety could also have impact on controlling its toxicity. With the exception of the $FeCl_4$ anion which showed very high toxicity behaviour towards *V. fischeri*, the other anion types demonstrated heterogeneous and diverse effect on the ILs toxicity. It was difficult to ascertain an identifiable pattern that could explain the toxicity variation. Even the effect of the side alkyl chain length for the carboxylic acids-based anions does not show any clear trend relating to the changes in the corresponding ILs toxicity. Also, for some of the anions possessing more than one oxygenated atom in their structure, the expected reduction in toxicity as seen in the cations' effect, was not evidenced. Hence, it can be concluded that although changing the anions' structure and content can alter the chemical and physical properties of the ionic liquids but the effect on ILs toxicity remained uncertain.

Overall, from the aquatic toxicity point of view, ILs may not seem to necessarily perform better when compared to the organic solvent, which it supposed to replace for many industrial applications. However, considering their negligible impact on the atmosphere as a result of extremely low vapour pressure as well as being non-flammable, and coupled with the unique

tuning ability to meet specific industrial requirements, ILs can still be largely considered as promising class of greener material. In view of the need to perform the toxicity assessment to confirm fully green behaviour, the QSAR/QSPR method can be the key towards providing the predictive ability which could guide the design of novel greener ILs for industrial application.

Author details

Mohamed Ibrahim Abdul Mutalib* and Ouahid Ben Ghanem

*Address all correspondence to: ibrahmat@petronas.com.my

Department of Chemical Engineering, Universiti Teknologi PETRONAS, Bandar Seri Iskandar, Perak, Malaysia

References

- [1] M. C. Bubalo, K. Radošević, I. R. Redovniković, J. Halambek, and V. G. Srček, "A brief overview of the potential environmental hazards of ionic liquids," *Ecotoxicology and Environmental Safety*, vol. 99, pp. 1–12, 2014.
- [2] M. Matzke, J. Arning, J. Ranke, B. Jastorff, and S. Stolte, "Design of Inherently Safer Ionic Liquids: Toxicology and Biodegradation," in *Handbook of Green Chemistry*, ed: Wiley-VCH Verlag GmbH & Co. KGaA, 2010.
- [3] J. S. Torrecilla, J. García, E. Rojo, and F. Rodríguez, "Estimation of toxicity of ionic liquids in leukemia rat cell line and acetylcholinesterase enzyme by principal component analysis, neural networks and multiple linear regressions," *Journal of Hazardous Materials*, vol. 164, pp. 182–194, 2009.
- [4] M. Armand, F. Endres, D. R. MacFarlane, H. Ohno, and B. Scrosati, "Ionic-liquid materials for the electrochemical challenges of the future," *Nature Materials*, vol. 8, pp. 621–629, 2009.
- [5] T. Zhou, L. Chen, Y. Ye, L. Chen, Z. Qi, H. Freund, *et al.*, "An overview of mutual solubility of ionic liquids and water predicted by COSMO-RS," *Industrial and Engineering Chemistry Research*, vol. 51, pp. 6256–6264, 2012.
- [6] S. P. Ventura, A. M. Gonçalves, T. Sintra, J. L. Pereira, F. Gonçalves, and J. A. Coutinho, "Designing ionic liquids: the chemical structure role in the toxicity," *Ecotoxicology*, vol. 22, pp. 1–12, 2013.
- [7] A. M. Stevens and E. Greenberg, "Quorum sensing in *Vibrio fischeri*: essential elements for activation of the luminescence genes," *Journal of Bacteriology*, vol. 179, pp. 557–562, 1997.
- [8] L. Boynton, "Using bioluminescent bacteria to detect water contaminants," *JUS SJWP*, vol. 4, pp. 29–41, 2009.
- [9] S. Girotti, E. N. Ferri, M. G. Fumo, and E. Maiolini, "Monitoring of environmental pollutants by bioluminescent bacteria," *Analytica Chimica Acta*, vol. 608, pp. 2–29, 2008.

- [10] B. T. Johnson, "Microtox[®] acute toxicity test," in *Small-scale freshwater toxicity investigations*, ed: Springer Netherlands, 2005, pp. 69–105.
- [11] P. C. Mishra and N. Behera, *Advances in Ecology and Environmental Sciences*: APH Publishing, 1995.
- [12] W.-c. Wang, J. W. Gorsuch, and W. R. Lower, *Plants for toxicity assessment* vol. 2: ASTM International, Philadelphia, 1990.
- [13] D. De Zwart and W. Slooff, "The Microtox as an alternative assay in the acute toxicity assessment of water pollutants," *Aquatic Toxicology*, vol. 4, pp. 129–138, 1983.
- [14] D. R. Passino and S. B. Smith, "Acute bioassays and hazard evaluation of representative contaminants detected in Great Lakes fish," *Environmental Toxicology and Chemistry*, vol. 6, pp. 901–907, 1987.
- [15] S. Viboud, N. Papaiconomou, A. Cortesi, G. Chatel, M. Draye, and D. Fontvieille, "Correlating the structure and composition of ionic liquids with their toxicity on *Vibrio fischeri*: a systematic study," *Journal of Hazardous Materials*, vol. 215, pp. 40–48, 2012.
- [16] C. Samorì, A. Pasteris, P. Galletti, and E. Tagliavini, "Acute toxicity of oxygenated and nonoxygenated imidazolium-based ionic liquids to *Daphnia magna* and *Vibrio fischeri*," *Environmental Toxicology and Chemistry*, vol. 26, pp. 2379–2382, 2007.
- [17] C. Samorì, D. Malferrari, P. Valbonesi, A. Montecavalli, F. Moretti, P. Galletti, et al., "Introduction of oxygenated side chain into imidazolium ionic liquids: evaluation of the effects at different biological organization levels," *Ecotoxicology and Environmental Safety*, vol. 73, pp. 1456–1464, 2010.
- [18] K. A. Kurnia, T. E. Sintra, C. M. Neves, K. Shimizu, J. N. C. Lopes, F. Gonçalves, et al., "The effect of the cation alkyl chain branching on mutual solubilities with water and toxicities," *Physical Chemistry Chemical Physics*, vol. 16, pp. 19952–19963, 2014.
- [19] S. Li, J. L. Ban~uelos, J. Guo, L. Anovitz, G. Rother, R. W. Shaw, et al., "Alkyl chain length and temperature effects on structural properties of pyrrolidinium-based ionic liquids: a combined atomistic simulation and small-angle X-ray scattering study," *The Journal of Physical Chemistry Letters*, vol. 3, pp. 125–130, 2011.
- [20] H. Tokuda, K. Hayamizu, K. Ishii, M. A. B. H. Susan, and M. Watanabe, "Physicochemical properties and structures of room temperature ionic liquids. 2. Variation of alkyl chain length in imidazolium cation," *The Journal of Physical Chemistry B*, vol. 109, pp. 6103–6110, 2005.
- [21] K. M. Docherty and J. C. F. Kulpa, "Toxicity and antimicrobial activity of imidazolium and pyridinium ionic liquids," *Green Chemistry*, vol. 7, p. 185, 2005.
- [22] J. Ranke, K. Mölter, F. Stock, U. Bottin-Weber, J. Poczobutt, J. Hoffmann, et al., "Biological effects of imidazolium ionic liquids with varying chain lengths in acute *Vibrio fischeri* and WST-1 cell viability assays," *Ecotoxicology and Environmental Safety*, vol. 58, pp. 396–404, 2004.

- [23] S. Stolte, M. Matzke, J. Arning, A. Bösch, W.-R. Pitner, U. Welz-Biermann, et al., "Effects of different head groups and functionalised side chains on the aquatic toxicity of ionic liquids," *Green Chemistry*, vol. 9, pp. 1170–1179, 2007.
- [24] M. Matzke, S. Stolte, K. Thiele, T. Juffernholz, J. Arning, J. Ranke, et al., "The influence of anion species on the toxicity of 1-alkyl-3-methylimidazolium ionic liquids observed in an (eco) toxicological test battery," *Green Chemistry*, vol. 9, pp. 1198–1207, 2007.
- [25] D. J. Couling, R. J. Bernot, K. M. Docherty, J. K. Dixon, and E. J. Maginn, "Assessing the factors responsible for ionic liquid toxicity to aquatic organisms via quantitative structure–property relationship modeling," *Green Chemistry*, vol. 8, pp. 82–90, 2006.
- [26] P. T. Anastas, P. Wasserscheid, and A. Stark, *Handbook of green chemistry, green solvents, ionic liquids* vol. 6: John Wiley & Sons, 2014.
- [27] Z. Yang and W. Pan, "Ionic liquids: Green solvents for nonaqueous biocatalysis," *Enzyme and Microbial Technology*, vol. 37, pp. 19–28, 2005.
- [28] F. van Rantwijk, F. Secundo, and R. A. Sheldon, "Structure and activity of *Candida antarctica* lipase B in ionic liquids," *Green Chemistry*, vol. 8, pp. 282–286, 2006.
- [29] P. Vidya and A. Chadha, "The role of different anions in ionic liquids on *Pseudomonas cepacia* lipase catalyzed transesterification and hydrolysis," *Journal of Molecular Catalysis B: Enzymatic*, vol. 57, pp. 145–148, 2009.
- [30] S. P. Ventura, F. A. e Silva, A. M. Goncalves, J. L. Pereira, F. Goncalves, and J. A. Coutinho, "Ecotoxicity analysis of cholinium-based ionic liquids to *Vibrio fischeri* marine bacteria," *Ecotoxicology and Environmental Safety*, vol. 102, pp. 48–54, 2014.
- [31] Z. Li, X. Liu, Y. Pei, J. Wang, and M. He, "Design of environmentally friendly ionic liquid aqueous two-phase systems for the efficient and high activity extraction of proteins," *Green Chemistry*, vol. 14, pp. 2941–2950, 2012.
- [32] S. Sekar, M. Surianarayanan, V. Ranganathan, D. R. MacFarlane, and A. B. Mandal, "Choline-based ionic liquids-enhanced biodegradation of azo dyes," *Environmental Science and Technology*, vol. 46, pp. 4902–4908, 2012.
- [33] M. Petkovic, K. R. Seddon, L. P. Rebelo, and C. Silva Pereira, "Ionic liquids: a pathway to environmental acceptability," *Chemical Society Reviews*, vol. 40, pp. 1383–1403, 2011.
- [34] B. Peric, J. Sierra, E. Marti, R. Cruanas, M. A. Garau, J. Arning, et al., "(Eco)toxicity and biodegradability of selected protic and aprotic ionic liquids," *Journal of Hazardous Materials*, vol. 261, pp. 99–105, 2013.
- [35] M. G. Montalbán, J. M. Hidalgo, M. Collado-González, F. G. D. Baños, and G. Villora, "Assessing chemical toxicity of ionic liquids on *Vibrio fischeri*: Correlation with structure and composition," *Chemosphere*, vol. 155, pp. 405–414, 2016.
- [36] M. Alvarez-Guerra and A. Irabien, "Design of ionic liquids: an ecotoxicity (*Vibrio fischeri*) discrimination approach," *Green Chemistry*, vol. 13, p. 1507, 2011.

- [37] O. B. Ghanem, N. Papaiconomou, M. A. Mutalib, S. Viboud, M. El-Harbawi, Y. Uemura, *et al.*, "Thermophysical properties and acute toxicity towards green algae and *Vibrio fischeri* of amino acid-based ionic liquids," *Journal of Molecular Liquids*, vol. 212, pp. 352–359, 2015.
- [38] K. S. Egorova, M. M. Seitkalieva, A. V. Posvyatenko, and V. Ananikov, "Unexpected increase of toxicity of amino acid-containing ionic liquids," *Toxicology Research*, vol. 4, pp. 152–159, 2015.
- [39] R. N. Das and K. Roy, "Advances in QSPR/QSTR models of ionic liquids for the design of greener solvents of the future," *Molecular Diversity*, vol. 17, pp. 151–196, 2013.
- [40] R. Todeschini and V. Consonni, *Handbook of molecular descriptors* vol. 11: John Wiley & Sons, 2008.
- [41] K. Roy, R. N. Das, P. Ambure, and R. B. Aher, "Be aware of error measures. Further studies on validation of predictive QSAR models," *Chemometrics and Intelligent Laboratory Systems*, vol. 152, pp. 18–33, 2016.
- [42] R. Veerasamy, H. Rajak, A. Jain, S. Sivadasan, C. P. Varghese, and R. K. Agrawal, "Validation of QSAR models-strategies and importance," *International Journal of Drug Design and Discovery*, vol. 3, pp. 511–519, 2011.
- [43] Roy, Kunal, Supratik Kar, and Rudra Narayan Das. "Statistical Methods in QSAR/QSPR," in *A Primer on QSAR/QSPR Modeling: Fundamental Concepts*. Springer, pp. 37–59, 2015.
- [44] P. Luis, I. Ortiz, R. Aldaco, and A. Irabien, "A novel group contribution method in the development of a QSAR for predicting the toxicity (*Vibrio fischeri* EC 50) of ionic liquids," *Ecotoxicology and Environmental Safety*, vol. 67, pp. 423–429, 2007.
- [45] P. Luis, A. Garea, and A. Irabien, "Quantitative structure–activity relationships (QSARs) to estimate ionic liquids ecotoxicity EC 50 (*Vibrio fischeri*)," *Journal of Molecular Liquids*, vol. 152, pp. 28–33, 2010.
- [46] R. N. Das and K. Roy, "Development of classification and regression models for *Vibrio fischeri* toxicity of ionic liquids: green solvents for the future," *Toxicology Research*, vol. 1, pp. 186–195, 2012.
- [47] F. Yan, Q. Shang, S. Xia, Q. Wang, and P. Ma, "Topological study on the toxicity of ionic liquids on *Vibrio fischeri* by the quantitative structure-activity relationship method," *Journal of Hazardous Materials*, vol. 286C, pp. 410–415, 2015.

Dielectric Characteristics of Ionic Liquids and Usage in Advanced Energy Storage Cells

Attila Gölle

Additional information is available at the end of the chapter

<http://dx.doi.org/10.5772/66948>

Abstract

Before the application of ionic liquids, it is important to know their fundamental physical and chemical properties. Practical experience has shown that it is important to look at these materials in the behaviour of the function frequency and temperature. To understand obtained information understanding the molecular-physic bases is needed. Research and application of ionic liquids have attracted an increasing attention in the areas of nuclear industry, oil and gas industry, petrochemical industry, chemical and electrochemical industry. The number of studies dealing with the question is proliferating which opens up new horizons in the field of chemical operations in microwave field with ionic liquids (organic chemical synthesis, catalytic operations, etc.). As a result of the relatively high destroying temperature of ionic liquids, a wider temperature range of operations can be done and it offers environmental friendly solution in the replacement of the toxic solvents with generally low evaporating temperatures. The area of application is becoming more widespread as electrolyte of novel battery cells. Being aware of the physical and chemical properties of ionic liquids is necessary in order to apply them. The main goal of this research was to test the dielectric properties, viscosity and temperature dependence of the electrical conductivity. Based on our results, we can claim that significant temperature dependence of the three properties can be shown in the case of ionic liquids. These findings are crucial for the usability of applications, planning and preparing of production and optimization processes. The significance and importance of these results become even more obvious if we consider the fact that these energy storage cells are exposed to large temperature differences. The present study discusses the

sample materials, their usage possibilities and the results of the research from the previous work of the author. In the case of ionic liquids, it is important to know their behaviour in electric field. In lot of cases, there is no fundamental difference between the static and dynamic behaviours. Static state (like in accumulators) is similar to the dynamic. Ionic liquids are well characterized and grouped with their dielectric behaviour. First of all a short summarizing of basics of the electrical permittivity and then a modelling procedure will be shown modelling lots of parameters using dielectric characteristic of material. At the end the practical usage and application will be shown by using ionic liquids as the electrolyte of batteries.

Keywords: ionic liquids, energy storage cells, conductivity, temperature dependence, viscosity

1. The electrical permittivity of ionic liquids: the concept of dielectric constant

1.1. The introduction of the concept of the dielectric constant

Charge carriers in ideally sealants are not able to move. Perfect vacuum is considered to be an ideal insulation for the fluid. In reality, in the practical devices containing the vacuum (such as vacuum switches), the vacuum is always bounded with material that allocates charge carriers in the vacuum; therefore, they cannot be considered as perfect insulators in practice [2].

Dielectric is a solid, liquid or gaseous substance, which acts as an electrically insulating material. Resistivity is greater than $10^8 \Omega m$. In dielectric there are practically no free charge carriers. Polarization occurs in the dielectric materials as a result of electric field. It is the permittivity characteristics of the substances that affect the amount of electric field. The dielectric constant is a scalar value.

Electric field strength from the charge by r distance created by a point charge Q from the context of

$$E = \frac{Q}{4\pi \cdot \varepsilon \cdot r^2} \rightarrow \varepsilon = \frac{Q}{4\pi \cdot E \cdot r^2} \quad (1)$$

so:

$$[\varepsilon] = \frac{[Q]}{[E] \cdot [r^2]} = \frac{1As}{1\frac{V}{m} \cdot 1m^2} = 1\frac{As}{Vm} \quad (2)$$

The proportionality factor is between the electrical permittivity of the prevailing electric field of a given electrical offset (D) and electric field (E), which is characterized by filling the space at the point of medium volume and independent of the electric field in the material:

$$\varepsilon = \frac{D}{E} \quad (3)$$

The electrical permittivity of a point in space is a multiplication of the relative constant of the vacuum permittivity and the permittivity of room-filling material at the point:

$$\varepsilon = \varepsilon_0 \cdot \varepsilon_r \quad (4)$$

where $\varepsilon_0 \approx 8,852 \cdot 10^{-12} \frac{As}{Vm}$, the permittivity of the vacuum, the so-called dielectric field constant and ε_r is a value without dimension, the permittivity of the material, the so-called dielectric value of the material.

Most of the insulation applied in practice have the relative permittivity of insulation value of a digit. Water has particularly high value, due to the highly polar water molecules and high dipole moments.

In most computing procedures, the relative dielectric constant of air can be considered with the value of 1 because of its difference from one is in the order of 10^{-4} .

1.2. Electric field in the insulating material

The value of the field of the electric charge can be obtained from the very simple relationship:

$$D = \varepsilon_0 E \quad (5)$$

The introduction of the displacement vector, which is formally a simple relationship between the dielectric constant and the electric field strength [3]. The situation is complicated when the insulation material is placed in the chamber. This is a natural thing since the smallest building blocks of matter are charged particles, although they usually seem to be neutral in the outgoing direction. In a small part of the chamber, the same amount of positive and negative charges can be found, but we know that these charges are influenced by the electric field force and the consequence of the previously neutral dielectric material that creates a force field as well. This effect of the external space will change the field of force.

1.3. Electrophysiological approach

The value of a capacitor can be calculated by the following equation:

$$C_0 = \frac{\varepsilon_0 \cdot A}{4\pi \cdot d} \quad (6)$$

where C is the capacitance, A is the surface area of opposing arms, d is the distance of armaments and ε is the dielectric constant of material positioned between the plates. If there

is a vacuum between the condenser armatures, the measured capacity of the condenser is marked C_0 . If there is electrically insulating material between the armaments, the capacitance increases:

$$C = \varepsilon_r \cdot C_0 \quad (7)$$

The relationship shows that the value of the dielectric constant is at least one or greater than one value.

Then $\varepsilon_r = \frac{C}{C_0}$ or in relative units, $\varepsilon_r = \frac{C+C_0}{C_0}$

If the capacitance change is large ($C \gg C_0$), the values of the two previous relationships do not differ significantly. The obtained dielectric constant value is marked ε' and this metric number characterizes the interaction between the material and the electromagnetic field. The dielectric constant is a number that shows how many times greater the capacity of a given capacitor filled with dielectric material is than in the vacuum.

1.4. Interpretation of the dissipation factor

If an ideal lossless capacitor is coupled in AC circuit, $\varphi = 90^\circ$ phase shift is generated between the voltage and the current of the capacitor (**Figure 1**).

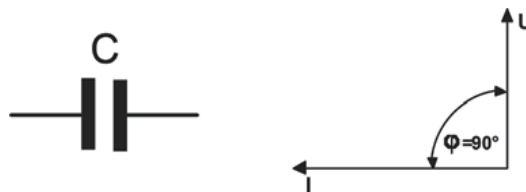


Figure 1. Phase between current and volt of capacitor.

In this case the capacitor behaves like a lossless impedance (reactive resistance). Accordingly, the capacitor does not absorb energy from the circuit. The context of the AC power load can be seen

$W = U I \cos\varphi$ where $\varphi = 90^\circ$ $\cos\varphi = 0$ and so $W = 0$.

If there is a dielectric material between the capacitor armatures, the dielectric loss is created. This can be modelled with an ideal capacitor and a resistor coupled in parallel.

The value of the reciprocal of the resistance is often presented as electrical conductivity. In this case, the phase difference between voltage and current will be less than 90° (**Figure 2**).

The dielectric material absorbs electromagnetic energy from the space (directly from the circuit) and consequently the movement of the dielectric molecules increases. Part of the electrical energy is converted into heat, so dielectric loss occurs. The magnitude of the losses is called phase angle supplementary angle and it equals to the tangent of the loss angle:

$$\delta = 90^\circ - \phi \tag{8}$$

The $\tan \delta$ is an analytically similar electro-physical constant to ϵ . From the magnitude of $\tan \delta$, even more reliable conclusions can be obtained about the purity of a substance than some cases from the dielectric constants. The $\tan \delta$ of a capacitor comprising a parallel loss resistance is calculated as follows:

$$\tan \delta = \frac{1}{\omega \cdot C \cdot R} = \frac{G_a}{\omega_0 \cdot C_a} \tag{9}$$

where G_a is the electrical conductivity of the dielectric, measured together with the dielectric capacitance of C_a .

So $\tan \delta = \frac{\epsilon''}{\epsilon'}$ than $\epsilon'' = \epsilon' \cdot \tan \delta$.

Therefore ϵ'' is a value without dimension that characterizes the amount of absorbed energy by the material from the electromagnetic space.

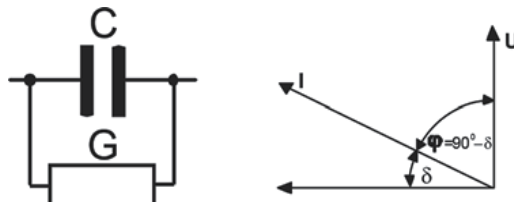


Figure 2. Lossless capacitor.

1.5. Molecular physics approach

Two groups of the dielectric structure are distinguished regarding the structure of materials.

a. Non-polar molecules

In the case of non-polar molecules, the molecules of the insulating material are neutral if there is no outward electric field. The positive and negative electric charge centres of gravity are in the same point and they only constitute small dipoles, depending on the outer space's field strength. This group includes, for example, a symmetrical hydrocarbons without permanent dipole moment molecules (methane, acetylene, benzene, naphthalene) and molecules consist of two identical atoms (F₂, Cl₂) and the noble gases.

b. Polar molecules

In the case of polar molecules, the molecules of the dielectric are situated in an unsettled manner without an electric field. The positive and negative potentials of the centre of gravity in these materials do not coincide and they have dipole moment without an electric field (permanent dipole moment). The electric field handles and deforms these

dipoles of the molecule and the electric field is trying to turn to the direction of the field despite of the heat movement. This group contains molecules that are related together with electrovalent or ion binding (e.g. water, alcohols, compounds containing a carboxyl group, an amino group). So polar molecules and materials can be polarized by the deformation and orientation effects of the outdoor electric space (Figure 3).

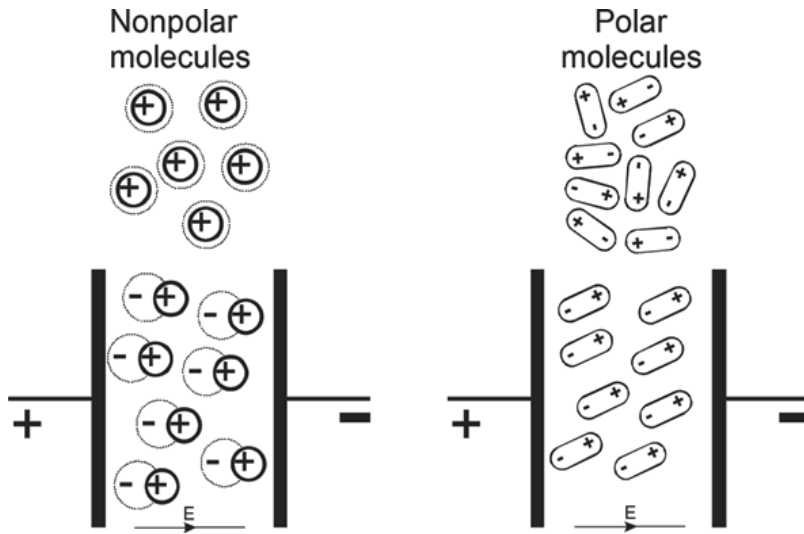


Figure 3. Arrangement of non-polar and polar molecules.

The dielectric polarization is composed of several parts:

Polarization shift

1. The electron cloud shifts from relative to the nucleus without having to change relative positions of the nuclei inside the molecule.
(elektron polarization, P_e)
2. Atoms or ions are shifted relative to each other.
(atomic or ion polarization, P_a).

Orientation polarization.

The dipoles are arranged in the effect of the outing field

($-P_o$).

1.6. The effect of temperature on the dielectric constant (temperature dependence)

In non-polar solvents, the resulting dipole molecules are always arranged in the direction of the field and this state is not formed by the heat movement significantly; therefore, the dielectric constant of the non-polar material does not depend on temperature. In the case of

polar materials, the temperature increase causes dielectric constant decreasing (incoordination is increasing).

The polarization of polar materials, as has been previously mentioned, is made up of displacement and polarization orientation. In the case of polarization orientation, the thermal motion of molecules prevents the orientation effect of the field and prevents molecules from turning into the direction of the field.

This effect is greater when the temperature and the heat movement are higher.

The polarization level depends on the number and strength of the dipole and the intensity of the thermal motion. There are some liquid compound temperature coefficients in **Table 1**. As shown, the temperature coefficient increases with the increase of the value of polarity.

Material	Temperature coefficient
Benzene	0.00160
Chlorine-benzene	0.00174
Ethylene chloride	0.0553
Nitro-benzene	0.185
Pure water	0.366

Table 1. Temperature coefficient of the dielectric constant in case of liquid compounds.

1.7. The effect of frequency changing to the dielectric constant (frequency dependence)

The dielectric constant depends on many other things, mostly the frequency at measurement. This can easily be seen if we introduce the concept of the complex dielectric constant:

$$\varepsilon^* = \varepsilon' - j\varepsilon'' \tag{10}$$

The ε'' is the dielectric power consumption from the electric field, thus referred to as the absorption coefficient or loss numbers sometimes. There is the following relation between ε' , ε'' and $\text{tg}\delta$:

$$\text{tg}\delta = \frac{\varepsilon''}{\varepsilon'} \tag{11}$$

The following figure shows the frequency dependence of ε'' and ε' . ε' retains its value by a certain frequency (approximately 10^8 Hz). Here the electric field and the polarization are in phase and the dielectric constant is maximum (**Figure 4**). This is called the quasi-static dielectric constant values [4].

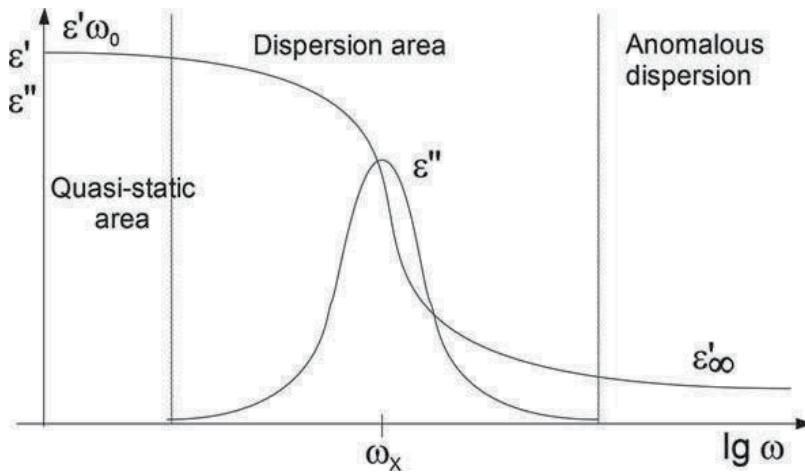


Figure 4. Frequency dependency of ϵ'' és ϵ' .

With increasing the frequency, the dielectric constant (ϵ'_{ω_0}) is retained until you reach certain frequency areas, areas of anomalous dispersion, where the dielectric constant is reduced to a constant value (ϵ'_{∞}). This value of n is called the refractive index in the next context on the basis of Maxwell's equation:

$$\epsilon'_{\infty} = n^2 \tag{12}$$

Theoretically, this can be explained by the electrons, atoms and atomic groups and the permanent dipoles can track slow changes of the field in the quasi-static area. Significant change occurs when the frequency of the alternating space is increased to a greater extent. Above a certain frequency, the permanent dipoles cannot follow the changes of space rapidly, so the orientation polarization no longer contributes to the total polarization. The dipole orientation cannot keep up with the force field and suffers delayed phase shift. Then we can talk about the anomalous dispersion of the dielectric constant. According to the Debye's theory of dispersion, this situation depends on the viscosity (η), the molecular radius (r):

$$\tau = \frac{4\pi \cdot \eta \cdot r^3}{k \cdot T} \tag{13}$$

τ is the so-called relaxation time τ ($\tau = 1/\omega_x$), the measured value of the relaxation rate. This is the time period, while the orientation polarization reduces e -fold by switching off the static field afterwards [5].

The absorption coefficient ϵ'' behaves differently depending on the frequency. The quasi-static and high-frequency field ϵ'' are almost immeasurably small. Only the dispersion area can be measured and reaches its maximum at a frequency ω_x . The theoretical analysis of the frequency dependence of the dielectric constant begins to form detailed in Debye equations:

$$\epsilon^* = \epsilon'_{\infty} + \frac{\epsilon'_{\omega_0} - \epsilon'_{\infty}}{1 + j\omega\tau} \tag{14}$$

1.8. The Cole-Cole diagram

The real and the imaginary part is obtained by applying the following relationships:

$$\epsilon' = \epsilon'_{\infty} + \frac{\epsilon'_{\omega_0} - \epsilon'_{\infty}}{1 + \omega^2 \tau^2} \quad \epsilon'' = \left(\epsilon'_{\omega_0} - \epsilon'_{\infty} \right) \frac{\omega \tau}{1 + \omega^2 \tau^2} \quad (15)$$

Where ϵ'_{∞} and ϵ'_{ω_0} are the high frequency and static dielectric constant and τ and ω are the frequency and relaxation time, which is characterized by the formation and cessation of the polarization ratio. These relationships are derived both from liquids and solids and can also be used, although they are from different models.

From the combination of relationships above, we can obtain the following relationships:

$$\left(\epsilon' - \frac{\epsilon'_{\omega_0} + \epsilon'_{\infty}}{2} \right)^2 + (\epsilon'')^2 = \left(\frac{\epsilon'_{\omega_0} - \epsilon'_{\infty}}{2} \right)^2 \quad (16)$$

The formula above gives the equation of the circle. Accordingly, in the diagram ϵ'' with as ordinate and ϵ' with as abscissa, a semicircle is obtained.

Figure 5 shows an ideal Cole-Cole diagram, when the behaviour of that material fits the above equations. In this case, the centre of the circle is at the abscissa and a different behaviour lies when the centre of semicircle lies below the abscissa. From the ideal Debye behaviour analysis of the differential structure, this is a useful research method.

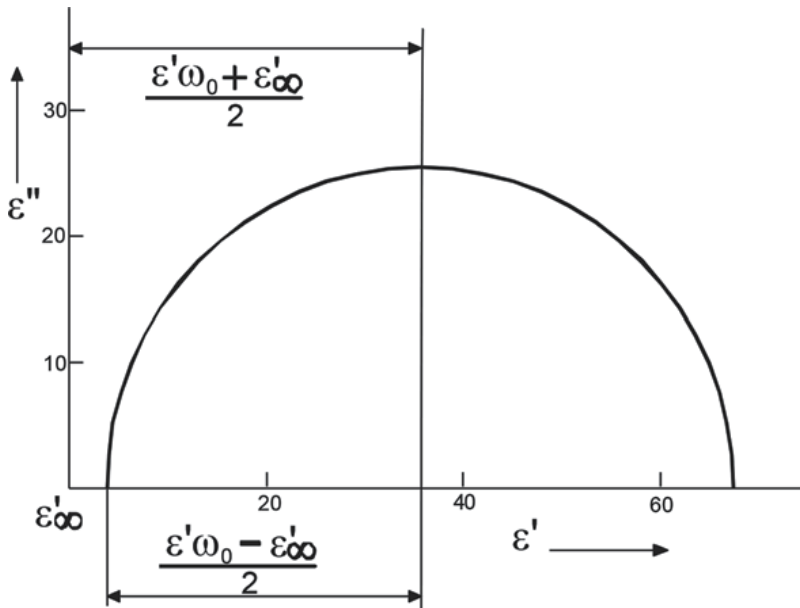


Figure 5. Cole-Cole diagram, ideal Debye behaviour.

2. Materials in electromagnetic field

During the microwave treatment, temperature of the sample continuously rises and its dielectric properties also change [6]. From the generator's viewpoint, the value of terminating impedance represented by the transmission line changes accordingly. For the microwave generator, the transmission line acts as an impedance terminator whose value depends on the wavelength and on the geometric properties of the transmission line [7]. The impedance of transmission line also depends on the dielectric properties of the material which are either partially or fully filling the transmission line. Since the temperature of the sample changes due to the energy impact, the value of the impedance terminator represented by parameters the transmission line also changes together with the sample properties. During the energy impact, the varying dielectric properties of the sample change the axial distribution of the microwave energy in the transmission line; therefore, the amount of energy absorbed in the sample also changes.

Because of the constant microwave energy input, temperature-dependent energy-, impedance- and dielectric conditions are developed. Some of them (e.g. temperature, dielectric property) are measurable; others can only be determined by computation [8]. By constructing a model containing the parameters of the transmission line and the sample placed in the transmission line, it is possible to determine the continuously varying parameters during the heating.

3. Modelling of power and temperature dependence of ionic liquids

During treatment and usage, outgoing energy is transferred to a material sample placed in an applicator of given geometric parameters. As a result of the energy transfer, the sample absorbs energy from the microwave field depending on its dielectric properties. The degree of energy absorption is directly proportional to the dielectric loss and proportional to the square root of the dielectric constant. The temperature of the sample continuously increases due to the energy transfer and the dielectric properties of the sample also change with the rising temperature. Although the microwave energy supply is constant, time- and temperature-dependent energy impedance and dielectric relations are developed. A part of them is measurable, but the other part of them cannot be directly measured; they can only be computed from the previously measured ones. In a closed model which contains the parameters of the sample and the waveguide, the continuously changing parameters can be determined in relation of the temperature. These parameters are as follows: attenuation of the transmission line, temporal change of the sample temperature, dielectric properties of the sample, loss factor of the sample, penetration depth, impedance of the transmission line and standing wave ratio reflection factor. The modelling procedure was invented on the University of Pannonia by the research group. The above parameters can be modelled as a function of the sample's temperature or as a function of time [9].

The power leaving the generator enters and propagates in the transmission line as a wave. The medium in the transmission line—according to its dielectric properties—modifies the portrait of lines of force and takes energy from the electromagnetic field. The electromagnetic wave

reflected from the shortcut at the end of the transmission line leaves the line towards the generator. The ratio of forwarding and reflected waves is the standing wave ratio and it depends first of all on the dielectric loss of the medium filling the transmission line. The standing wave ratio is infinity in the ideal case (there is no sample, i.e. loss in the transmission line) if the transmission line is closed with the wave impedance of the line. Since the standing wave ratio is given as the ratio of forwarding and reflected waves, it is greater than one if the transmission line has loss and it equals to the ratio of powers entering and leaving the transmission line.

That is, knowing the standing wave ratio r and the generator power P_M , it is possible to determine the power entering the transmission line. Since the medium's (sample's) dielectric parameters are functions of the temperature, it is necessary to appear the temperature dependence in the formulae explicitly. Denoting the microwave power entering the transmission line by P_A and the generator's power by P_M , the following formula holds:

$$P_A(T) = \frac{1}{r(T)} P_M \quad (17)$$

A part of this, power will dissipate and heat up the sample placed inside the transmission line. The amount of power absorbed in the sample depends on the sample's dielectric properties: it is directly proportional to the dielectric loss and inversely proportional to the square root of the dielectric constant. The coefficient 0.5126 is an experimental value [10]:

$$P_D(T) = 0.5126 \frac{\varepsilon''(T)}{\sqrt{\varepsilon'(T)}} P_A(T) \quad (18)$$

The temperature dependence of the dielectric parameters is respected in the above formula. The power absorbed in the sample increases its temperature; the degree of warming depends on the specific heat (C_p) and the density (ρ) of the sample. A sample having greater specific heat or density warms slower. The change of temperature is given as follows:

$$\frac{dT}{dt} = K \frac{1}{C_p \rho} P_D(T) \quad (19)$$

where K is a coefficient regarding the volume of the sample and its unit is $1/\text{cm}^3$. The formula gives the speed of temperature change; on the other hand, the integral of the formula with respect to time gives the value of the temperature in the sample as a function of time. The temperature dependence of the dielectric parameters (ε' , ε'') of the sample can be measured with a microwave dielectrometer designed by the author of this paper [11]; thus, it is possible to define the relationships $\varepsilon'(T)$ and $\varepsilon''(T)$ regarding the specific sample material by fitting polynomials on the resulted data.

The impedance of the transmission line is a function of its geometric parameters and the dielectric properties of the sample. The characteristic wave impedance Z_{0t} of the transmission line depends on the size of the transmission line sizes (in two dimensions) and the wavelength (λ_g) of the electromagnetic wave propagates inside according to the following formula:

$$Z_{0t} = \frac{2Z_{0l}b}{a\sqrt{1-\left(\frac{\lambda_g}{2a}\right)^2}} = 754 \frac{4,4}{9,4\sqrt{1-\left(\frac{12,24}{18,8}\right)^2}} = 465\Omega \quad (20)$$

where Z_{0l} is the open air wave impedance of the air (377 Ω), is the electromagnetic wavelength a and b are the dimensions of the transmission line (9.4 cm, 4.4 cm), respectively. Note that Z_{0t} is independent of the sample properties and depends only on the transmission line geometry and wavelength. From Z_{0t} and the dielectric loss, it is possible to calculate the overall impedance (of the transmission line and the sample) as a function of temperature [12]:

$$Z_T(T) = \frac{Z_{0t}}{\sqrt{\epsilon'(T)}} \left(1 - \frac{3}{8} (\text{tg}\delta(T))^2 + j\frac{1}{2} \text{tg}\delta(T) \right) \quad (21)$$

From the overall impedance and the wave impedance, one can determine the reflection coefficient of the transmission line:

$$|\Gamma(T)| = \frac{Z_T(T) - Z_{0t}}{Z_T(T) + Z_{0t}} \quad (22)$$

Afterwards, it is possible to express the standing wave ratio:

$$r(T) = \frac{1 + |\Gamma(T)|}{1 - |\Gamma(T)|} \quad (23)$$

From the standing wave ratio, it is possible to give the power entering the transmission line knowing the generator power, as it was mentioned before. Now, it is possible to build a model from the above equations, which has the following input parameters: microwave generator power, density of the sample, specific heat of the sample, sample specific dielectric characteristics as a function of temperature, transmission line and wavelength parameters.

3.1. Modelling set-up in filled cavity

Overall we can obtain an overall figure about modelling of microwave cavity filled with ionic liquid or other material (Figure 6).

The model structure has been implemented in MatLab® environment (Figure 7). First the pure water has been investigated. The temperature dependence of dielectric values of water is described by Eq. (24) This equation is from the literature [13] and showed in (Figure 8):

$$\epsilon'(T) = 87 - 0.36T \quad \epsilon''(T) = 283/T - 1.17 \quad (24)$$

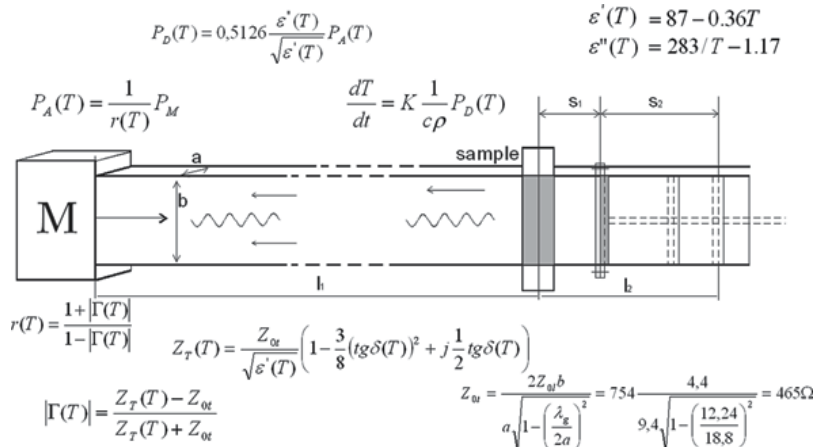


Figure 6. Overall modelling of the filled cavity.

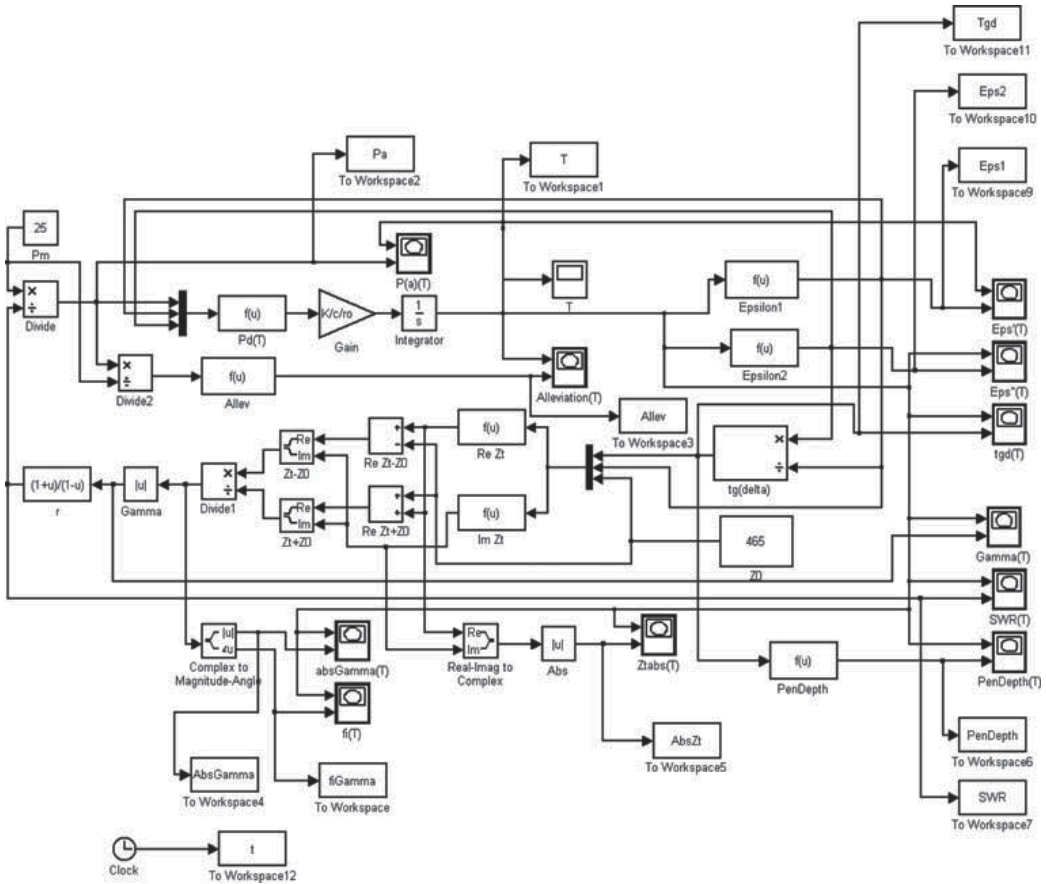


Figure 7. The MatLab model for simulation.

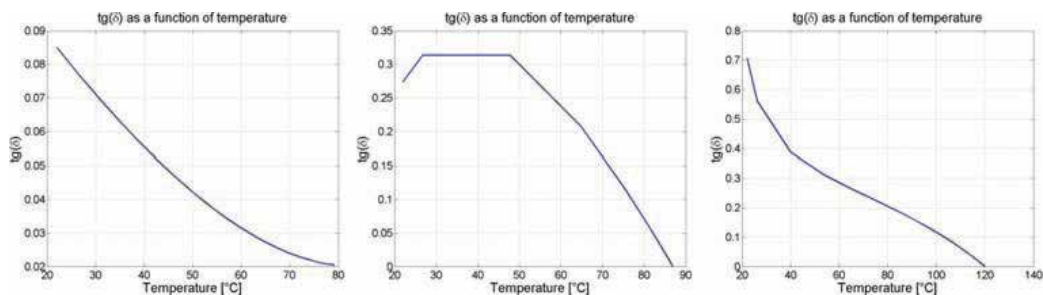


Figure 8. Results from the model. $\text{tg}(\delta)(T)$ values of different materials.

4. Introduction of battery cell

Dielectric constant and dielectric dissipation factors are the main parameters in the modelling of microwave behaviour of ionic liquids, in addition the parameters characterizing the polarizability and the microwave energy absorption. The static dielectric constant of ionic liquids cannot be approached with traditional measurement methods because they are characterized by high electrical conductivity which results in intense shortcut. Systematic study of these contexts has not been conducted so far because the subject is relatively new; however, the results are very important in the planning and controlling of chemical reactions.

At the end of the 1990s, the discovery of ionic liquids opened new ways of technological applications especially in the area of chemistry and in particular green chemistry. Their special chemical and physical properties make it very beneficial and important since the use of energy storage units, particularly mobile phones, electric vehicles and uninterruptible power supply systems, is widely used [1]. Recently, room temperature ionic liquids (RTILs) have been extensively studied as electrolytes of lithium ion batteries from cellular phones to electric vehicles. RTILs are good options for the electrolyte bases of a safe lithium battery due to their unique properties [14, 15].

RTILs are known for being thermally stable and non-flammable and they might have the capacity to improve the safety of electrochemical devices with aprotic solvents, such as Li batteries and supercapacitors in abuse.

The high ionic conductivity of 1-Ethyl-3-methylimidazolium tetrafluoroborate (EMIM-BF_4) is comparable to those of organic solvent electrolytes and its viscosity is low which makes it a good electrolyte for Li batteries. Li battery applications can benefit from these and we also found that a Li/LiCoO_2 cell with RTILs as an electrolyte base works reversibly, indicating that QAimide RTILs are quite stable even at the Li reduction potential. We can claim that RTILs improve the safety of Li-ion batteries with carbon-negative electrodes. For improving the safety of Li-metal batteries, RTILs seem to be the most promising and applicable electrolytes, which could also be important for higher energy densities [16].

A set of four imidazolium ionic liquids (solid at room temperature) and one imidazolium ionic solid were screened for their potentials as electrolytes in manganese dioxide-free Leclanché batteries, equipped with a zinc anode and graphite cathode [17].

It is important to note that the ionic liquid 1-ethyl-3-methylimidazolium hydrogen sulphate (EMIM-HSO₄) similar to many other ionic liquids, such as those based on nitrate and dihydrogenphosphate anions, has also been found to work well in this battery design. Novel batteries are designed using standard cathode materials such as MnO₂, PbO₂, NiO and AgO and anode materials such as Zn, Sn and Pb. Additionally, by using a solid polymer electrolyte composed of polyvinyl alcohol and anionic liquid, new types of solid-state batteries are demonstrated with discharge voltages ranging up to 1.8 V, depending upon the type of cathode and anode used [18].

Ionic liquids like 1-butyl-3-methylimidazolium tetrafluoroborate (IMIM-BF₄) or hexafluorophosphate (IMIM-PF₆) and 1-butyl-4-methylpyridinium tetrafluoroborate (PyBF₄) were mixed with organic solvents such as butyrolactone (BL) and acetonitrile (ACN). A lithium salt (LiBF₄ or LiPF₆) was added to these mixtures for possible application in the field of energy storage (batteries or supercapacitors). Viscosities, conductivities and electrochemical windows at a Pt electrode of these electrolytes were investigated. All the studied electrolytes are stable towards oxidation and exhibit a vitreous phase transition, which has been determined by application of the conductivity measurements. Mixtures containing the BF₄⁻ anion exhibit the lowest viscosity and the highest conductivity [19].

Aromatic cations, such as 1-ethyl-3-methylimidazolium (EMI), have been used for as the cationic component of the RTILs. The EMI cation is the best cation to form the RTIL, which has a low viscosity and low melting point, with various anions. However, the electrochemical stability as a lithium battery electrolyte was not satisfactory since the cathodic limiting potential is ca. +1.0 V versus Li/Li⁺ and additives, such as thionyl chloride, were essential for improving the coulombic efficiency for lithium deposition in an RTIL based on EMI [20].

There are several combinations of alkylimidazolium cations and inorganic and organic anions have been investigated to date. A survey of these salts including fluoroanions will be given in [21].

4.1. Methods

Several properties of ionic liquids should be examined before its application in batteries; therefore, we used different measurement methods at our disposal on a number of ionic liquids. The different microwave measurements included processes such as checking the temperature rise in microwave field and measuring microwave dielectric properties at 2.45 GHz frequency, electrical conductivity according to temperature and viscosity changes depending on the temperature.

We used CEM Discover unit to measure the velocity of temperature rise of ionic liquids. The CEM Discover unit is a widely used and available apparatus in microwave chemistry. The device has a cylindrical operating space and on the cylindrical peripheral surface, there are many slots where microwave energy can enter; this way the high homogeneity of the microwave field is ensured. We measured the temperature at the bottom of the compartment with an infrared thermometer. The amount of the tested samples was 0.5 g, which were placed in an inner diameter of 12.5 mm of borosilicate cylindrical glass flask.

It is important to note that during microwave treatment, a conversion process takes place in which the microwave energy interacts with the treated material and the material converts the electric energy into thermal energy according to its characteristic dielectric properties. During this process, the measurable increase of the temperature in the treated material is the macroscopically observable result. The rate of the temperature increase depends on the microwave field and the treated material properties, which is described in the following equation:

$$\Delta T/\Delta t = P_v/\rho C_p = jE^2 f \epsilon''/\rho C_p \quad (25)$$

where the $\Delta T/\Delta t$ is the velocity of temperature rising in Kelvin per second, P_v is the absorbed power in the sample, ρ is the density of the sample, C_p is the specific heat of the sample, E^2 is the strength of the electromagnetic field in the sample, f is the frequency of the field and ϵ'' is the dielectric loss; j means this is a complex value [15]. This formula shows that the temperature of the treated material is influenced by a number of factors. Testing their effects separately is not simple, because ρ , ϵ , C_p features themselves are temperature dependent and it is difficult to measure this value accurately inside the material. In the case of strictly homogeneous series of examined compounds, the situation is more simplified, because some simplifications are permissible.

Assuming ρ and C_p do not change significantly in the function of temperature, the multiplication ρC_p was almost considered to be constant, so that the rate of temperature rise is determined by E and ϵ'' only. Further simplifications can be made if the device is single mode with the same volume and shape and the microwave energy is constant during the investigation. The value of E is determined by ϵ' and ϵ'' and the rate of temperature rise is essentially determined by ϵ'' value.

4.2. Measurement set-up of ionic liquids

Figure 9 depicts the schematic representation of the self-designed experimental set-up applied for automatic and online measurement of dielectric properties of ionic liquids in a definite temperature range. It is composed of the following devices and instruments: cylindrical sample holder unit, thermostat, peristaltic pump, waveguide, temperature sensor, displaceable piston, stepper motor, magnetron, detectors, control unit and a PC.

The IL sample, which is placed in the thermostat to keep it at the desired constant temperature, is flown across the waveguide having a length of about 3λ through the sample holder tube with the help of a peristaltic pump. The electric energy is transformed into microwave energy by the magnetron. The stepper motor is controlled by a microprocessor control unit, which contains an Intel 8-bit microcontroller, 12-bit A/D converters for receiving the four diode-detector signals, a stepper motor driver and a RS-232 serial interface to connect it to the PC. The control unit collects the detector signals and the temperature data determined by the temperature sensor and sends them to the PC. Furthermore it controls the position of the short circuit displaceable piston on the basis of algorithm software elaborated for this purpose.

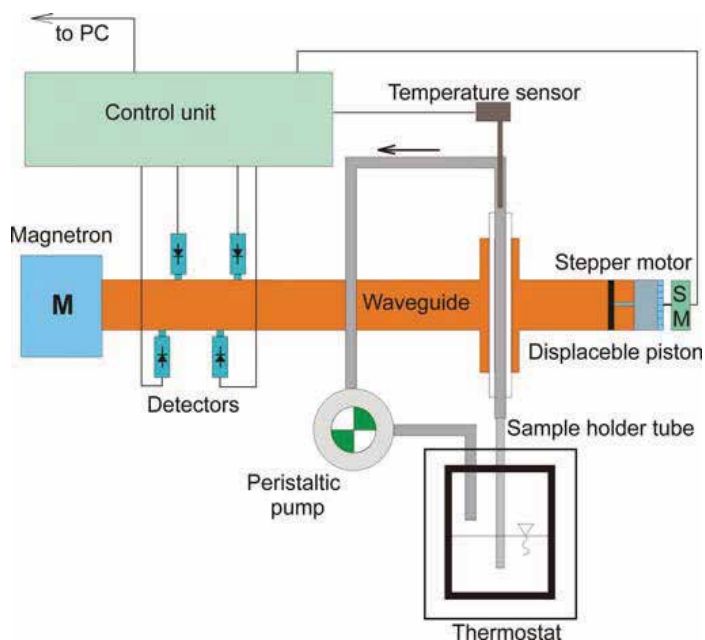


Figure 9. Scheme of the experimental set-up.

The method is based on the compensation of phase change due to the microwave energy absorption of the liquid sample. The short circuit piston situated behind the sample must be actuated for compensation. The energy conditions created by the wave front in the waveguide are measured by four diode detectors.

Dielectric constants, dielectric loss factors and the temperature dependence of the dielectric properties of ionic liquids intended to be used in batteries were determined by the above-described self-designed microwave dielectrometric apparatus (Figure 3) at the frequency of 2.45 GHz and at different temperatures (30°C, 40°C, 50°C, 60°C, 70°C, 80°C, 90°C, 100°C, 110°C and 120°C). The speed of the change in temperature depends on the electrical field strength in the material (E), the absorbed microwave power, (P_v) density (ρ), the specific heat capacity (C_p) and the dielectric loss factor ϵ'' and can be given by Eq. (1) [11].

4.3. Results and obtained characteristics

The temperature increase of the new type of ionic liquids was examined, as it is shown in Figure 10 and in Table 2.

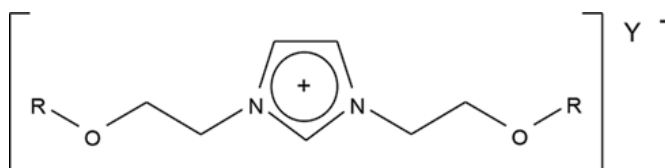


Figure 10. The structure of investigated ionic liquids.

Compound	R	Y	Compound	R	Y
1	CH ₃	BF ₄	8	C ₄ H ₉	PF ₆
2	C ₂ H ₅	BF ₄	9	C ₂ H ₅	Cl
3	C ₃ H ₇	BF ₄	10	C ₂ H ₅	Br
4	C ₄ H ₉	BF ₄	11	C ₂ H ₅	SCN
5	CH ₃	PF ₆	12	C ₂ H ₅	N(CN) ₂
6	C ₂ H ₅	PF ₆	13	C ₂ H ₅	N(SO ₂ CF ₃) ₂
7	C ₃ H ₇	PF ₆			

Table 2. The formulas of investigated ionic liquids.

The effect of R groups was examined in the case of two anions—BF₄ (compounds 1–4) and PF₆ (compounds 5–8) at 3–5 watts of microwave energy.

Our results show that there is a negative correlation between the R group carbon number and the temperature elevation rate: a decrease in the previous increases the latter. By increasing the microwave power significantly, the temperature speeds converge to each other and sometimes change this order, but this is not typical in **Figure 11**. Overall, the rate of temperature rising follows the order of ϵ' and ϵ'' suggesting that in a strictly homologous series, the temperature rise of ionic liquids is determined by ϵ'' [18].

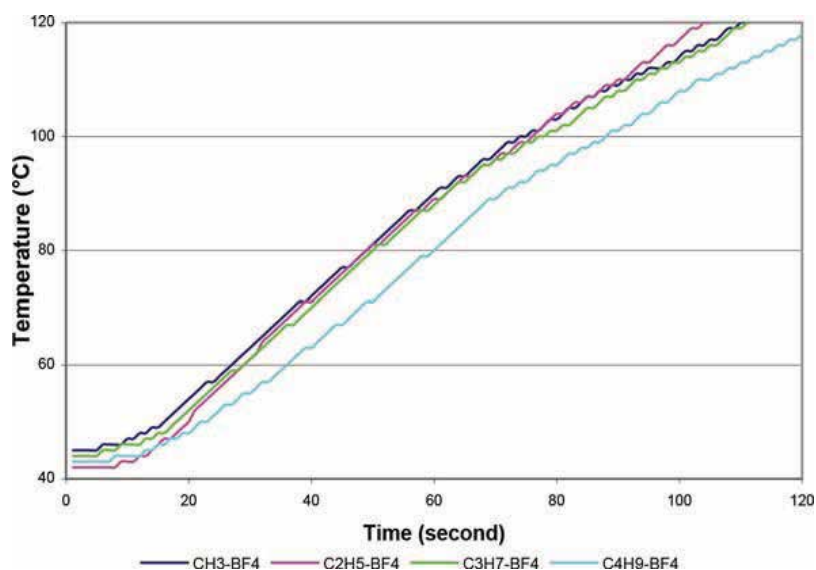


Figure 11. Temperature rising of 1-butyl-3-methylimidazolium tetrafluoroborates at 3 W.

After the temperature rising data rate, we investigated two additional parameters of the ionic liquids used in the advanced batteries, i.e. viscosity and electrical conductivity. Both properties are the functions of temperature and they were examined between 20°C and 100–120°C temperature range. The sample material was heated through a heat exchanger, so the viscosity

was measured up to 95°C. Water was used as a heat transfer material and it was not possible to achieve 100°C. The measurements were performed in a SV-10 type of vibration viscometer (A&D Ltd. Japan). The following figures show that the viscosity in room temperature is high, typically several hundred Pa*s and it decreases rapidly with the temperature rising similar to a $y=1/x$ curve. Reaching the 100°C temperature, the value of viscosity can be ten times lower than at the initial value as we can see in **Figure 12**.

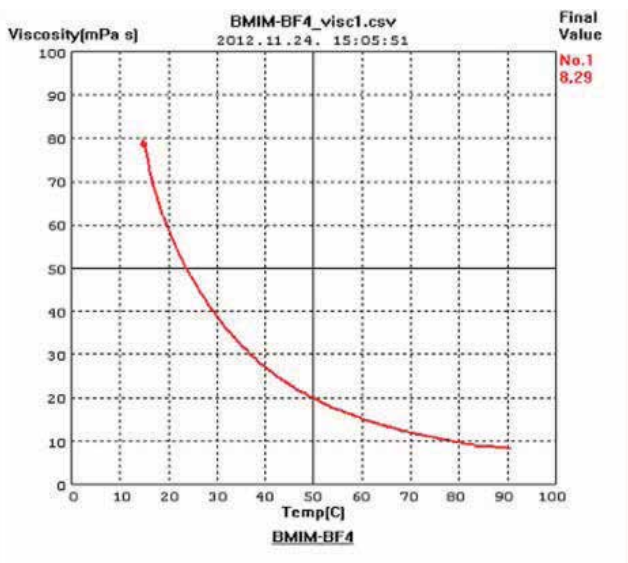


Figure 12. Viscosity of BMIM-BF₄ in the function of the temperature.

The investigation of the viscosity may be important; therefore, it basically influences the mobility of ions in the electrolyte, which can affect the conductivity and thus the internal resistance of the battery cell. By cooling ionic liquids, the viscosity is increasing rapidly. Around freezing temperature the ionic liquids were already similar to a “honey density” mass.

Since the energy storage cells are used in a wide temperature range, it is important to know that the electrical conductivity of the electrolytes is a function of temperature.

In **Figure 13** five different electrical conductivity plots of ionic liquids in the function of temperature can be seen. It clearly shows that it is not BMIM-BF₄ which has the highest conductivity value, but the conductivity value, depending on the temperature of this material, increases with the greatest intensity [7].

Results in **Figure 14** are both new and impressive. The dielectric constant value of BMIM-BF₄ reaches a value of 1 at close to 100°C, similarly to the value of the vacuum and if the temperature is raised further, the value will decrease to the negative range. This outcome suggests that the electrical conductivity is rising greatly with an increase in temperature and this compound is no longer an insulating material but a conductor. Therefore it is important to keep the temperature in an adequate range when batteries are used and especially in the charging period.

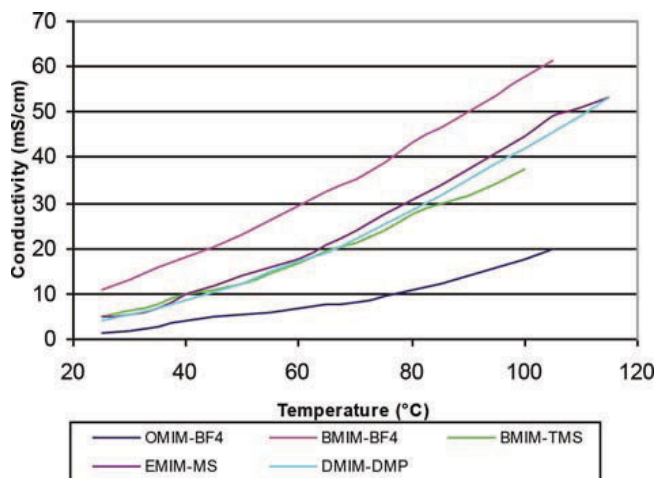


Figure 13. Conductivity of five compounds in a function of temperature.

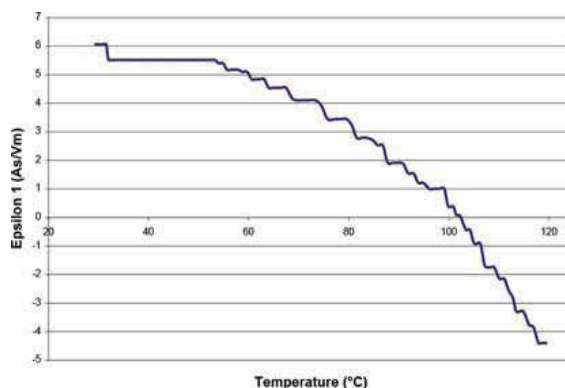


Figure 14. Dielectric constant of BMIM-BF4 in a function of the temperature.

The dielectric constant (E_1) and dielectric loss factor values of ILs built up of the same $[\text{BF}_4]$ anion and six previously described cations containing alkyl chains with different lengths ($[\text{DiEtMeIm}]$, $[\text{DiEtEtIm}]$, $[\text{DiEtPrIm}]$ and $[\text{DiEtBuIm}]$) at different temperatures between 30°C and 120°C are shown in **Figure 15**, respectively.

At the initial measuring temperature of 30°C, all four of the studied ILs have similar dielectric constants around 7. With the increase in temperature, the E_1 values for $[\text{DiEtMeIm}][\text{BF}_4]$, $[\text{DiEtEtIm}][\text{BF}_4]$ and $[\text{DiEtPrIm}][\text{BF}_4]$ slightly increase up to 13, while the dielectric constant for $[\text{DiEtBuIm}][\text{BF}_4]$ shows a sudden break at 90°C and at 120°C it reaches the value as high as 27. This could be explained with some sudden changes in the structure of the ILs or in the physicochemical interactions between the anion and the cation. Excluding the results for $[\text{DiEtBuIm}][\text{BF}_4]$, the values at elevated temperature show that the highest E_1 value belongs to $[\text{DiEtMeIm}][\text{BF}_4]$, followed by $[\text{DiEtEtIm}][\text{BF}_4]$ and then by the $[\text{DiEtPrIm}][\text{BF}_4]$; hence, the dielectric constant increases with the decrease in the alkyl chain length of the cation.

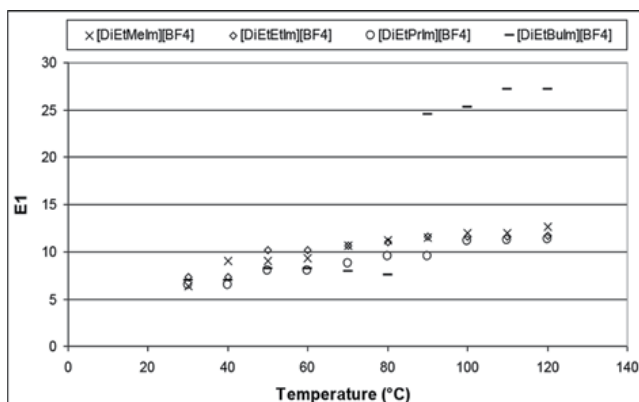


Figure 15. Dielectric constant of ILs containing common $[BF_4]$ anion and different cations.

Taking into account the dielectric constant, dielectric loss and electrical conductivity results of all the investigated ILs, it can be concluded that the alkyl chain length of the cation and the structure of the anion strongly influence the dielectric properties of the ILs and that the highest G value is exhibited by the $[DiEtMeIm][BF_4]$ IL at $30^\circ C$ temperature; hence, it is the most suitable candidate for battery applications. Furthermore, it can be stated that implementing the knowledge about the connection between the IL structure and the dielectric properties another ILs should be studied in order to select the ones most adequate for electrolyte application.

5. Conclusion

Based on our study, ionic liquids turned out to be excellent candidates for environmentally sound, green electrolytes in batteries due to their useful features, such as wide electrochemical windows, high inherent conductivities, high thermal and electrochemical stability, tuneable physicochemical properties, etc. Before making decisions about their applicability, careful measurements on their dielectric properties should be done.

Although techniques aiming at the determination of the dielectric properties of ILs have been the main focus of several studies, so far no convincing findings can be found in the literature due to the fact that most measurements are based on classical methods. As it was detailed in this study, these methods are doomed to failure because of the high conductivity of ILs.

Based on the analyses of previous results, it can be concluded that the physical, chemical and electrical parameters of ionic liquids are greatly temperature dependent when used in energy storage cells. In any case, when they are applied, we should specify the range of application temperature. Stepping out of this range of the energy storage cell may not meet the expected specification values, or in the worst case, it may be permanently damaged.

Acknowledgements

The present study discusses the sample materials, their usage possibilities and the results of the research from the previous work of the author.

Author details

Attila Göllei

Address all correspondence to: gollei.attila@virt.uni-pannon.hu

Department of Electrical Engineering and Information Technology, University of Pannonia, Veszprém, Hungary

References

- [1] Göllei A., Magyar A.: Ionic liquids in advanced energy storage cells. *Hungarian Journal of Industry & Chemistry* 41(1) (2013): 11–15.
- [2] Edvin I.: *Microwaves technics and radar locators*, Textbook Publishing, Budapest (1958). [Edvin I.: *Mikrohullámok technikája és rádiólokátorok*, Tankönyvkiadó, Budapest (1958).]
- [3] Károly S.: *Electromagnetic Theory*, Academic Press, Budapest (1973) ISBN 963 05 3413 4. [Károly S.: *Villamosságtan*, Akadémiai Kiadó, Budapest (1973) ISBN 963 05 3413 4.]
- [4] Nagy Sándor B.: *Dielectrometry*, Technical Publishing House, Budapest (1970) [Nagy Sándor B.: *Dielektrometria*, Műszaki Könyvkiadó Budapest (1970).
- [5] Kingston H.M., Haswell S.J.: *Microwave-Enhanced Chemistry*, American Chemical Society, Washington, DC (1997).
- [6] Knoerzer K., Regier M., Schubert H.: Computational model for calculating temperature distributions in microwave food applications. *Innovative Food Science and Emerging Technologies* 9 (2008): 374–384.
- [7] Zhu J., Kuznetsov A.V., Sandeep K.P.: Mathematical modeling of continuous flow microwave heating of liquids. *International Journal of Thermal Sciences* 46 (2007): 328–341.
- [8] Johns P.B.: Simulation of electromagnetic wave interactions by transmission-line modeling (TLM). *Wave Motion* 10(6) (1998): 597–610.
- [9] Göllei A., Magyar A. and Gerzson M.: Investigating energetic and impedance relations of microwave transmission line filled with dielectric material. *Progress in Electromagnetics*

Research Symposium Proceedings, Cambridge, USA, July 5–8, 2010. pp 23–27.
DOI:10.2529/PIERS091216050152.

- [10] MacDowell J.F.: Microwave heating of nepheline glass-ceramics, *American Ceramic Society Bulletin* 63 (1984): 282–286.
- [11] Göllei A. et al.: Apparatus and method to measure dielectric properties (ϵ' and ϵ'') of ionic liquids, *Review of Scientific Instruments* 80 (2009): 044703; doi:10.1063/1.3117352.
- [12] Almássy Gy.: *Microwave handbook*, XII-3, Technical Publishing House, Budapest, 1973. [Almássy, Gy: *Mikrohullámú kézikönyv*; XII-3. Műszaki Könyvkiadó, Bp, 1973.]
- [13] Kegel, K.: *Electric Thermal Engineering Technical Manual*, Technical Publishing House, Budapest, 1978. [Kegel, K.: *Villamos Hőtechnikai Kézikönyv*, Műszaki Könyvkiadó, Budapest, 1978.]
- [14] Alarco, P.J., Yaser, A.L., Ravet, N., Armand, M.: Lithium conducting pyrazoliumimides plastic crystals: a new solid state electrolyte matrix. *Solid State Ionics*, 172 (2004): 1–4, 53–56, 0167-2738.
- [15] Schiffmann R.F.: Microwave and dielectric drying, in: Mujamder A.S.(Ed), 2nd., *Handbook of Industrial Drying*, vol 1, Marcel Dekker, New York, 1995, pp. 345–372.
- [16] Hikari S., Hajime M., Kuniaki T.: Application of room temperature ionic liquids to Li batteries. *Electrochimica Acta* 53 (2007): 1048–1054.
- [17] Zhang Z., Gao X., Yang L.: Electrochemical properties of room temperature ionic liquids incorporating BF₄ and TFSI anions as green electrolytes. *Chinese Science Bulletin* 50(18) (2005): 2005–2009.
- [18] Gao, X.H., Zhu, M.J., Zhang, Z.X. et al., Research on room temperature molten salts with alkylated imidazolium salt as electrolytes. *ChemicalWorld* 45(Supplement I) (2004): 156–157 (in Chinese).
- [19] Nishida, T., Tashiro, Y., Yamamoto, M.: Physical and electrochemical properties of 1-alkyl-3-methylimidazolium tetrafluoroborate for electrolyte. *Journal of Fluorine Chemistry* 120 (2003): 135–141.
- [20] Matsumoto H., Sakaebe H., Tatsumi K.: Preparation of room temperature ionic liquids based on aliphatic onium cations and asymmetric amide anions and their electrochemical properties as a lithium battery electrolyte. *Journal of Power Sources* 146 (2005): 45–50.
- [21] Hagiwara R., Ito Y.: Room temperature ionic liquids of alkylimidazolium cations and fluoroanions. *Journal of Fluorine Chemistry* 105 (2000):221–227.

Separations

Ionic Liquids in Multiphase Systems

Stella Nickerson, Elizabeth Nofen, Denzil Frost and
Lenore L. Dai

Additional information is available at the end of the chapter

<http://dx.doi.org/10.5772/65281>

Abstract

Ionic liquids (ILs) can be used to replace one or more phases in conventional oil/water emulsions including Pickering emulsions—surfactant-free emulsions which utilize nano- or micron-sized particles to stabilize the immiscible liquid-liquid interface. Due to the extreme tunability of both the ILs and particles used, the study of IL-based Pickering emulsions yields novel emulsion morphologies and insights into the ionic liquid-liquid-particle interactions present. This work discusses extensive experimental work on IL-based Pickering emulsions and IL/liquid interfaces, emphasizing unique phenomena—such as “bridging” between emulsion droplets and spontaneous particle transport across the interface—never observed in more conventional Pickering emulsions. Molecular dynamics (MD) simulations of particles at the IL/liquid interface are also discussed, and fundamental insights from these simulations are used to enhance understanding of the unique interface behavior revealed by experiment.

Keywords: ionic liquids, emulsions, Pickering emulsions, particles, colloids, interfaces

1. Introduction

The unique properties and rich variety of ionic liquids (ILs) make them promising for a wide range of applications and the potential of pure ILs is multiplied by introducing them to multicomponent systems. Ionic liquids’ complex interactions with other materials enable multiphase systems that are both theoretically fascinating and potentially useful. This work focuses in particular on systems involving solid particles and immiscible liquid phases. It explores ionic liquid-liquid interfaces and their role in ionic liquid Pickering emulsions through both experimental and simulation approaches, including several unique and fascinating interface phenomena. **Figure 1** illustrates some of these phenomena—particle self-assembly on an emulsion surface, particle “bridging” between emulsion droplets, and spontaneous transport

across the liquid-liquid interface—as well as an example of the molecular dynamics (MD) simulations used to further explore the fundamentals of IL interactions with other phases. There continues to be active research in Pickering emulsions [1, 2], immiscible phases [3, 4], and ILs [5–9], and one particularly relevant application is employing ionic liquid-in-water emulsions as “a new class of fluorescent sensors for metal ions” [9].

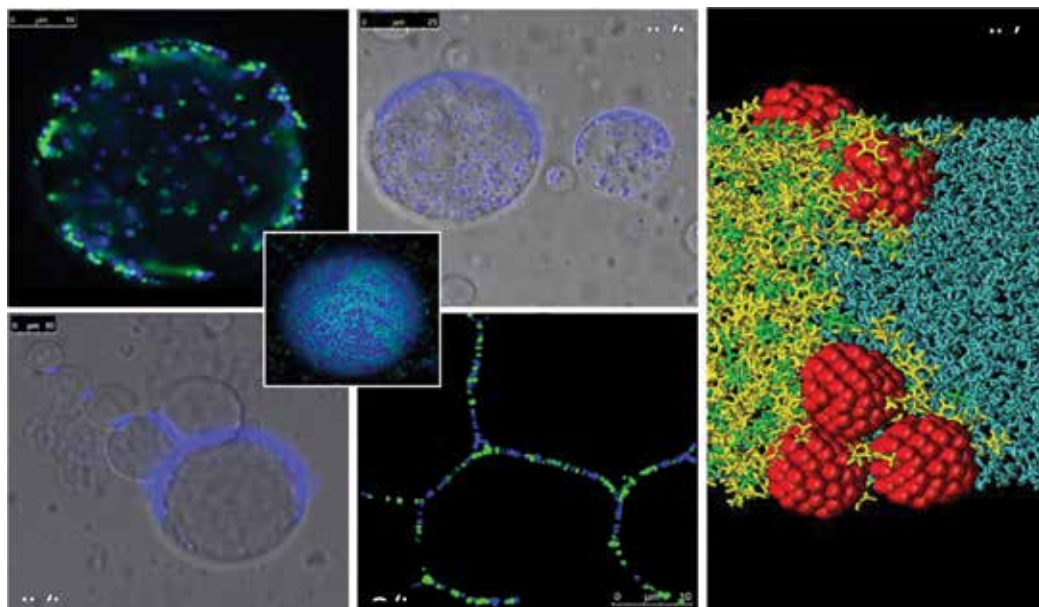


Figure 1. Upper left: confocal microscopy image of an IL-in-water emulsion droplet. Upper-middle: confocal microscopy image of IL-in-IL emulsion droplets. Lower left and lower-middle: particle bridging between emulsion droplets. Right: MD simulation of nanoparticles at IL/water interface.

Given the complex and unusual molecular-scale interactions at ionic liquid/liquid interfaces, it is reasonable to suspect that they might behave differently than conventional aqueous/organic interfaces. Accepting this, the challenge becomes identifying those unique behaviors and developing applications based on them. It is equally important to develop fundamental theories of these interfaces and their interactions with, for example, solid particles. This work outlines the progress made toward these goals.

2. Ionic liquid-liquid interfaces and particle interactions

2.1. Unique morphologies of aqueous and nonaqueous ionic liquid Pickering emulsions

The extremely high tunability of the material properties of ionic liquids (ILs), caused by the virtually endless combinations of anions and cations, allows ILs to be unique candidates for the study of liquid-liquid interfaces. Additionally, by incorporating particles into these IL-liquid systems, novel and varied behaviors can be achieved. These suggest unique

applications in extraction, catalysis, reaction schemes, etc., and provide even more extensive tunability through the complex interactions of differing choices of particles and ionic liquids. Surfactant-free, solid-stabilized Pickering emulsions can act as templates for these studies in which the ionic liquid subsists as the droplet phase, continuous phase, or both phases in the emulsion. Deviating from the conventional oil-in-water emulsion systems, employing ILs allows for interesting interfacial phenomena due to the charged nature of the IL and other factors intrinsic to the liquid including ion ordering, interfacial tension, etc.

Our first foray into ionic liquid-based Pickering emulsions was to simply replace the droplet phase in a conventional oil-in-water emulsion with an IL to create an IL-in-water Pickering emulsion [10]. While IL-in-water Pickering emulsions had been created previously, their use of silica nanoparticles prevented easy observation of the resulting particle morphology [11, 12], and thus, fluorescent micron-sized particles were used in this work. The hydrophobic IL 1-butyl-3-methylimidazolium hexafluorophosphate ([BMIM][PF₆]), which is immiscible with water, was chosen for the droplet phase. In order to observe the effect of particle hydrophobicity and surface charge and learn the resultant particle morphology on the droplets and the partition preference of the particles, 1 μm fluorescent surface-treated polystyrene (PS) particles were employed in conjunction with a confocal laser-scanning microscope. For this work, the various surface chemistries of the PS were sulfate ($-\text{SO}_3\text{H}$, S-PS, blue color), aldehyde sulfate ($-\text{CHO}$ and $-\text{SO}_3\text{H}$, AS-PS, green color), or amine ($-\text{NH}_2$, A-PS, green color). The S-PS and AS-PS particles were relatively hydrophobic and negatively charged, while the A-PS particles were relatively hydrophilic and positively charged.

Figure 2 shows the resulting droplet morphologies and partition preferences of the particles, each image showing a [BMIM][PF₆] IL emulsion droplet suspended in water. The three images on the left of the figure show the resulting surface coverage of the droplet when a single particle type is used, while the two large images on the right, with additional smaller representative images of selected systems in the middle, show the morphology when two differing particle types are mixed in the emulsion at equal concentrations. All of the larger images, whether a single or binary particle type was used, show the aggregated domain morphology in which the IL droplet is nearly fully covered by the particles. In the binary systems, there is no significant partitioning of the particles on the droplet interface, that is to say, the particles are well mixed. For the A-PS and S-PS/A-PS particle systems, some fully covered droplets were observed in addition to the aggregated domain morphology. Full covered droplets were never seen in the S-PS, AS-PS, or S-PS/AS-PS systems, likely suggesting that the hydrophobicity or contact angle plays a role, as the A-PS particles were the only hydrophilic particles used. This contact angle difference could thus allow for closer packing on the IL droplet. This hypothesis is further confirmed by the partition preference of the particles for either the water phase or the ionic liquid phase. For the S-PS, A-PS, and S-PS/A-PS systems, many A-PS particles remain in the water phase, while the S-PS particles prefer the IL phase, even being extracted into the IL droplets (as seen for the cross section of the S-PS/A-PS droplet in the middle of **Figure 2**). The AS-PS particles also show a higher affinity for the IL-water interface, and the S-PS/AS-PS system further shows this behavior with a large amount of both S-PS and AS-PS particles being extracted into the IL phase, as seen in the cross section droplet

for the S-PS/AS-PS system. As the Gibbs free energy of adhesion to the interface is very high for microparticles, and the particles were originally dispersed in the water phase, this extraction phenomenon is quite interesting as it defies the general thermodynamic thinking. This is likely due to the fact that the S-PS and AS-PS particles are hydrophobic, and thus prefer the hydrophobic IL phase, rather than the aqueous. Thus the surface chemistry of the particles was found to have a significant effect on the resultant droplet morphologies and extraction characteristic of the IL, with the resultant emulsion scheme being tuned by the hydrophobicity of the particle type or types chosen. However, it is important to that such extraction has never been reported in systems involving oil-water interfaces thus the uniqueness of ILs plays a critical role.

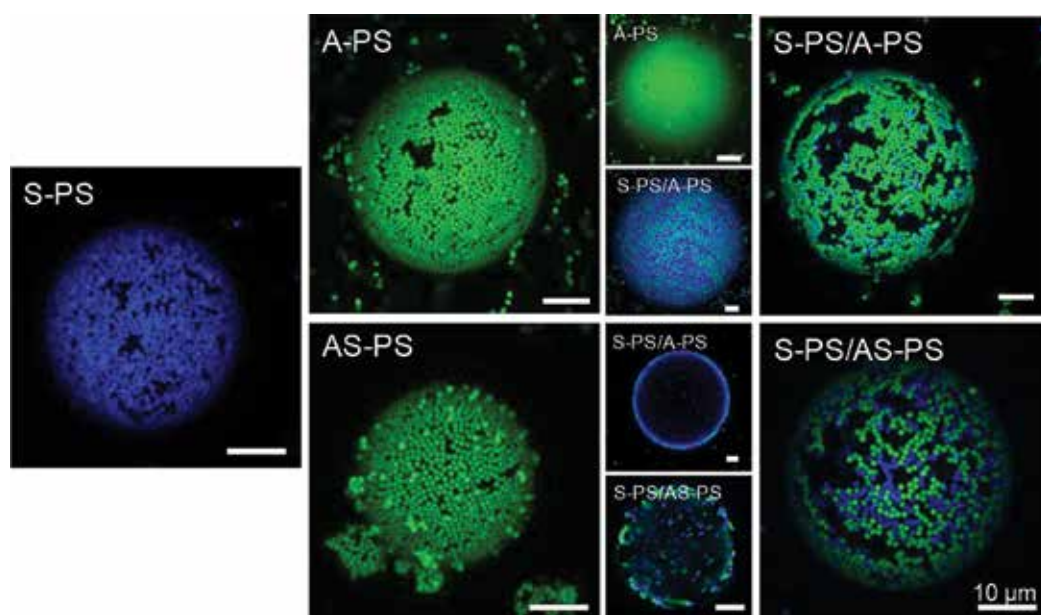


Figure 2. Various observed particle morphologies on [BMIM][PF₆] IL droplets in water for a variety of PS particle surface chemistries with 1 μm particle diameters in all images. All scale bars are 10 μm.

After studying the effect of having an ionic liquid as the droplet phase of a Pickering emulsion, we then turned to using the IL as the continuous phase, to form oil-in- or water-in-ionic liquid Pickering emulsions [13, 14]. Polydimethylsiloxane (PDMS) oil was used, and the same [BMIM][PF₆] IL was used for either oil-in- or water-in-IL emulsions, as this IL is immiscible with both water and the PDMS oil used. For the particle types, 1 μm fluorescent surface-treated polystyrene particles were again employed with the same surface chemistries as the IL-in-water Pickering emulsion work, including sulfate (–SO₃H, S-PS, blue color), aldehyde sulfate (–CHO and –SO₃H, AS-PS, green color), and amine (–NH₂, A-PS, green color), adding the carboxylate (–COOH, C-PS, red color) for this work. It is worthwhile to note that the S-PS and AS-PS are relatively hydrophobic while the C-PS and A-PS are relatively hydrophilic, with all particles exhibiting a negative surface charge in water, except for A-PS, which is positively charged.

The simple inversion of the droplet phase/continuous phase identities in these IL-based Pickering emulsions lead to a very interesting and novel particle morphology not seen in the conventional oil-in-water or IL-in-water emulsions, that of particle bridging. **Figure 3** outlines this phenomenon for both the oil-in-IL and water-in-IL Pickering emulsions studied, focusing on emulsions of S-PS, AS-PS, C-PS, and A-PS particles. In the oil-in-IL emulsions, for the negatively charged particles used (S-PS, AS-PS, and C-PS), a clear bridged morphology was observed in which the particles preferred inter-oil droplet bridges rather than the oil-IL interface, with this liquid-liquid interface being nearly completely devoid of particles. For the A-PS (positively charged) system, some bridges were observed, but the main morphology consisted of the particles sparsely covering the visible oil droplets, with more particles simply dispersed in the continuous IL phase. As both C-PS and A-PS are hydrophilic, this shows that for these systems, particle surface charge rather than hydrophobicity plays a more important role in terms of the bridge formation. Additionally, the bridges formed were monolayers between connected droplets, and the bridges prevented droplet coalescence by hindering drainage of the inter-droplet film. Also, there was no particle transport into the oil droplet phase, which was expected, as there is no particle extraction with conventional oil-in-water Pickering emulsions [15, 16].

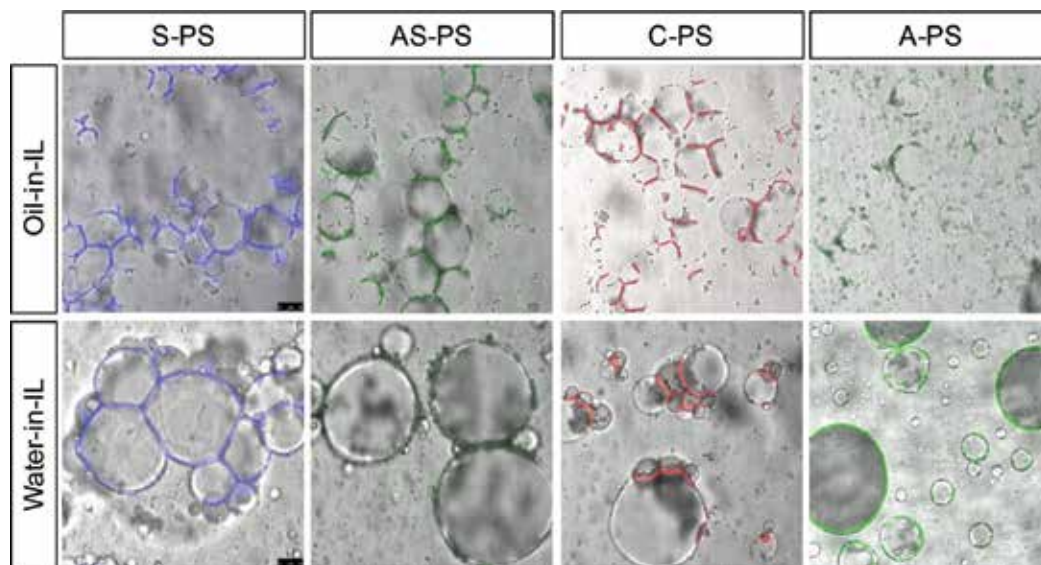


Figure 3. Various observed particle morphologies on (upper row) PDMS droplets and (bottom row) water droplets in a [BMIM][PF₆] IL continuous phase for a variety of PS particle surface chemistries with 1 μm particle diameters in all images. The 25 μm scale bar is valid for all images.

For the water-in-IL Pickering emulsions, a similar trend was observed in which the negatively charged S-PS, AS-PS, and C-PS showed bridging, while the positively charged A-PS did not, with no particle extraction seen in any of the cases. It is interesting that the bridging phenomenon occurs in these systems, as the particles were originally dispersed in water, thus it was first hypothesized that the water droplets would reabsorb the particles, making bridge

formation impossible. However, the bridging did similarly occur, with more compact structures seen rather than the long chains of droplets observed in the oil-in-IL systems. This occurrence provides an interesting look at the importance of contact angle, as the same particles stabilize the aqueous/nonaqueous emulsions to yield similar bridged morphologies. We may want to add the practical significance—instead of particle stabilization, the bridging caused a creamy layer and made the emulsions less stable.

2.2. Ionic liquid-in-ionic liquid Pickering emulsions

Prior to our work on the subject, ionic liquid-in-ionic liquid Pickering emulsions had not been studied [17]. While many IL systems are miscible due to ion exchange, immiscible ionic liquid pairs do exist, and we chose two systems to study: (1) trihexyltetradecylphosphonium *bis*-(2,2,4-trimethylphenyl)-phosphinate ($[P_{66614}][Phos]$) and ethylammonium nitrate (EAN) and (2) $[P_{66614}][Phos]$ and $[BMIM][PF_6]$. Imidazolium- and phosphonium-based ILs are known to form an immiscible pair, which is thought to be caused by strong hydrogen bonds formed when the imidazolium ions diffuse into the phosphonium IL, increasing the degree of order within the phosphonium IL, resulting in a negative entropy of mixing. However, while it was observed that the $[BMIM][PF_6]$ IL slowly gelled the $[P_{66614}][Phos]$ IL over time, the diffusion between the two ILs was slow enough to allow for droplets to remain stable for hours, and thus their subsequent droplet morphology study. For the $[P_{66614}][Phos]/EAN$ system, it was quite stable against mixing as long as EAN was the continuous phase of the emulsion.

The chemical structures of the ILs used can be seen in the right schematic of **Figure 4**. As far as droplet morphologies are concerned, the $[P_{66614}][Phos]/EAN$ system showed very similar results as the $[BMIM][PF_6]$ -in-water Pickering emulsions we studied previously, as seen in the leftmost column of images in **Figure 4**. The S-PS and C-PS systems showed aggregated domains of particles at the interface with particle absorption into the droplet. The A-PS system interestingly showed a different morphology, that of droplet bridging, as seen in the oil/water-in-IL emulsions, with no particle absorption, as typical of the bridged systems. Previously, A-PS particles were the only particles that did not form bridges in either water/IL or oil/IL systems, so the presence of bridging in the IL-in-IL system was unexpected. This allows for the overarching hypothesis describing the modulation of particle morphology in these IL-based Pickering emulsion systems that an active surface chemistry is required in order for particles to exclusively form bridges. For a further explanation, the major difference between this system and the bridging systems reported previously is that the continuous phase here is protic. This is significant as in order for A-PS particles to assume a surface charge, the amine groups needed to accept a proton and can do so from the protic EAN. This is further illuminated by observing the $[P_{66614}][Phos]$ -in- $[BMIM][PF_6]$ system in which the S-PS and C-PS particle types form bridges, while the A-PS does not. It is hypothesized that the anion $[BMIM][PF_6]$ can remove the acidic hydrogens of the sulfate and carboxylate surface chemistries, activating them, and thus allowing for bridging to occur. This driving force does not exist in the $[P_{66614}][Phos]/EAN$ system, and thus bridging does not occur there for S-PS and C-PS. For the A-PS in $[P_{66614}][Phos]/[BMIM][PF_6]$, again there are no protons to activate the surface chemistry, and thus bridging does not occur. Overall, it is clear that the particle self-assembly phenomena is a strong function of the continuous phase/IL type and that phenomena generally unique to IL-based Pickering emulsions, including exclusive bridging and particle absorption, can also

occur when both phases are ILs. These results additionally show that these morphologies can be tuned by the constituent ILs, not only the particles, and can have important implications for various IL-based applications.

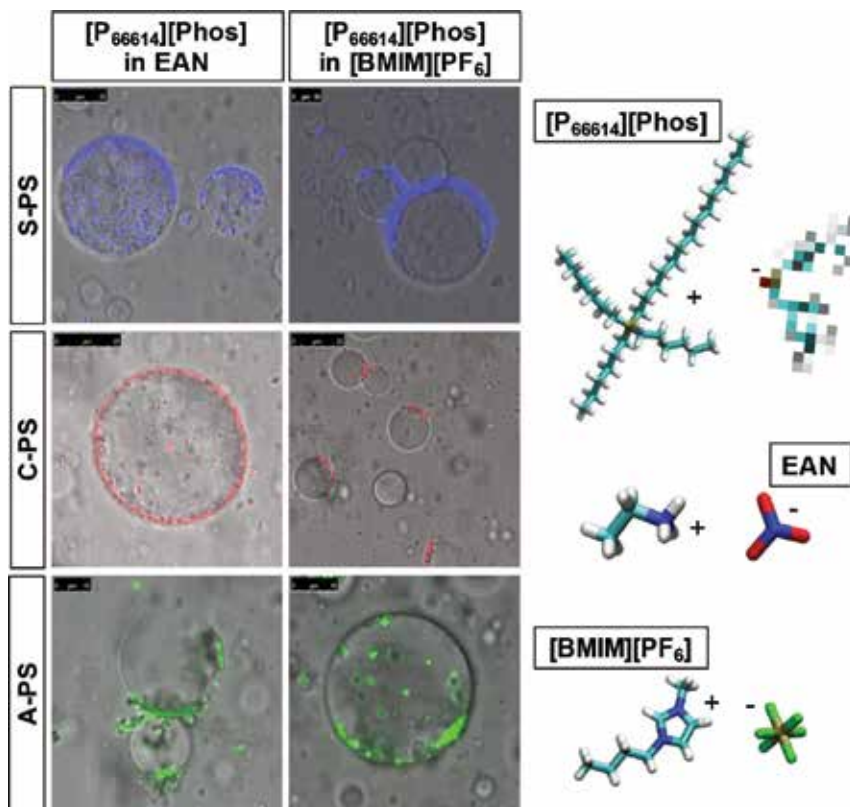


Figure 4. Confocal laser-scanning fluorescent images of IL-in-IL Pickering emulsions, including [P₆₆₆₁₄][Phos]-in-EAN and [P₆₆₆₁₄][Phos]-in-[BMIM][PF₆], stabilized by 1 μm particle diameter PS particles. The right schematic shows generated chemical structures of the IL molecules for visualization purposes.

Further research in this area includes ionic liquid emulsions stabilized by more exotic particles—microgel particles, for example. Work by Monteillet et al., for example, finds that microgels self-assemble on the surface of IL emulsion droplets in a similar manner to the solid particles discussed above. These microgel particles, however, are responsive to various stimuli such as pH and temperature, making the emulsion system itself responsive and opening up still further potential applications [5].

2.3. Spontaneous particle transport across the ionic liquid interface

During our extensive study of ionic liquid-based Pickering emulsions, we noticed the separate and unique phenomenon of microparticle extraction across the liquid-liquid interface [18]. Spontaneous particle transport defies traditional understanding of the thermodynamics of particle-interface interactions and suggests intriguing and novel physics taking place at the

molecular scale. For this work, 1 μm fluorescent sulfate-treated polystyrene particles were again employed ($-\text{SO}_3\text{H}$, S-PS, blue color) and dispersed in the water phase. The water phase was then carefully brought into contact with the particle free IL [P_{66614}][Phos], by placing droplets in contact with one another on a glass slide. The interface was then observed over time with a confocal laser-scanning microscope to observe the resulting particle motion.

Figure 5 shows the spontaneous microparticle transport for both (a) a single particle and (b) a cluster of particles from the water phase to the IL phase. The adhesive Gibbs energy for a microparticle at the liquid-liquid interface is in the order of 10^7 kT, thus prior to this work, spontaneous particle transport was not observed, instead propelling the particles by shear forces or functionalizing them with surfactants was required to see this phenomenon. The single particle moved through the interface onto the IL side at $t = 0.8$ s, and moving past the interface and into the IL, the particle remained attached to the IL/water interface for a time before finally detaching. For the particle cluster, it moved through the interface at $t = 0.4$ s, followed by two more particles at $t = 4.3$ s. The latter event forced the first cluster to detach from the interface, with only one particle of the cluster remaining attached until complete absorption at $t = 15.6$ s.

Figure 5(c) shows the proposed mechanism for the microparticle transport across the liquid-liquid interface, from the water phase to the IL phase, showing spontaneous particle extraction by the IL. This is due to the association of the ions with the particle surfaces that can be thought of as multiple equilibrium constants driving this association and the subsequent particle motion. Because the ILs removed particles from the continuous phase, we hypothesized that the dissolved IL ions in this phase played a role in the absorption process, as it is known that IL solubility in water depends on both the hydrophobicities of the cation and anion. A series of equilibrium relationships were used to describe the mechanism, as seen in **Figure 5(c)**. K_1 represents the equilibrium between IL ions in the IL phase and those IL ions dissolved in the aqueous or solvent phase. The dissolved ions can then interact with and cover the particles dispersed in the aqueous phase. This is likely given the previous observations of the particle extraction for S-PS particles in the studied IL-based Pickering emulsions. Similarly, K_2 represents the equilibrium between ion-covered particles dispersed in the aqueous phase and the particles extracted into the IL phase. This explanation allows for identification of IL-particle-solvent systems that may be adequate to experience particle absorption. For example, [P_{66614}][Phos] is minimally soluble in water, thus exhibiting a low K_1 , but the constituent ions would exhibit strong binding to the particles, exhibiting a high K_2 . This supports the fact that [P_{66614}][Phos] was one of the most efficient ILs for particle absorption and fits with the results seen for extraction with a myriad of other ILs in our work on the subject [18].

Thus, the study of ionic liquids and their interfaces with other liquids and solid particles reveal many interesting phenomena, including fully covered emulsion droplets, droplet/particle bridging, particle transport into the IL during emulsification and spontaneously, and a combination of these phenomena for the same emulsion system depending on the particle type. These phenomena are unique to IL-based emulsions, not seen in their traditional oil/water emulsion counterparts, and were likely due to the charged nature of the ionic liquid and additionally due to the behavior of their substituent cations and anions at the particle-IL

and liquid-IL interfaces. Additionally, the discovery of spontaneous transport of microparticles through a liquid-liquid interface was highlighted to show the intrinsic, powerful particle extraction capability of ionic liquids.

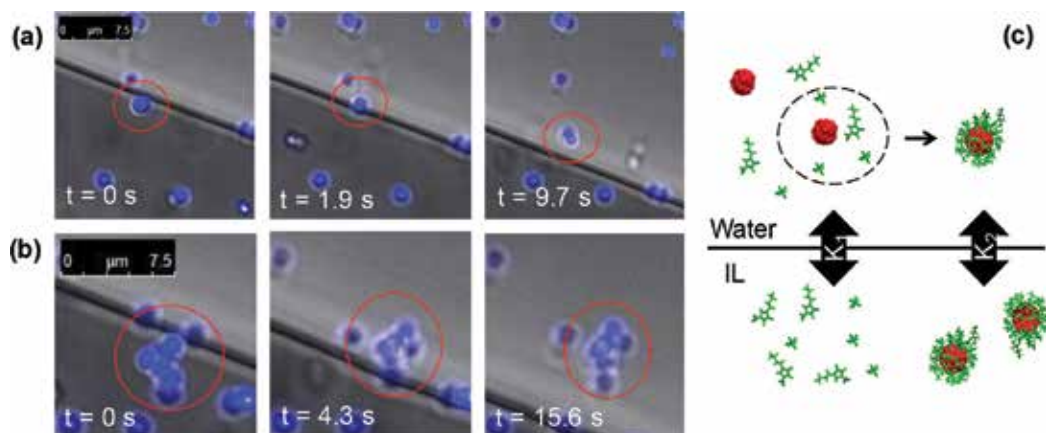


Figure 5. Images showing the microparticle transport phenomenon across the IL-water interface for (a) a single 1 μm S-PS particle and (b) a cluster of S-PS particles over time. (c) Schematic of the proposed mechanism for the observed spontaneous particle transport. Adapted from Ref. [18].

3. Insights from molecular dynamic simulations

The unique nature of ionic liquids is largely due to molecular-scale effects—bulky, asymmetric organic molecules that resist steric packing, ionic charges distributed across each IL molecule, and the endless tunability provided by the ability to mix and match cation/anion pairs. Given the importance of the molecular scale to ILs and their behaviors, it is vital to study IL systems at the level of individual molecules and atoms. Molecular dynamics (MD) simulations provide a valuable tool in this effort. By modeling the forces between atoms and predicting the behavior of molecules, we can gain insight into the fundamental physics of ILs in multiphase systems and are able to form solid theories on the phenomena explored in our experimental work.

3.1. Particle self-assembly at ionic liquid interfaces at the molecular-scale

Our first molecular dynamics study of ionic liquids in multiphase systems used a model IL and a model nanoparticle to examine the behavior of particles at IL/water and IL/oil interfaces [19]. The IL was chosen as 1-butyl-3-methylimidazolium hexafluorophosphate ([BMIM][PF₆]), perhaps the most commonly studied IL, and because it is immiscible with both water and hexane (our model oil). Furthermore, a force field model had been developed for it specifically tuned to surface properties [20]. For the nanoparticle, we took a diamond lattice, cut it off in a roughly spherical shape, and saturated the surface with hydrogen. This model was taken to represent hydrophobic nanoparticles as a class. Two interfaces were simulated—IL/water and

IL/hexane—both with and without nanoparticles. The systems simulated with nanoparticles are shown in **Figure 6**.

As shown in that figure, the second immiscible liquid phase makes a dramatic difference to the self-assembly of nanoparticles at the liquid-liquid interface. When the second phase is water, the hydrophobic nanoparticles are partially absorbed into the IL phase. However, when the second phase is hydrophobic oil, the particles prefer to remain on the hexane-side of the interface. This has obvious implications for several potential applications of these systems, including particle extraction from an oil or water phase or the formation of microscale structure from particles adhered to emulsion droplets.

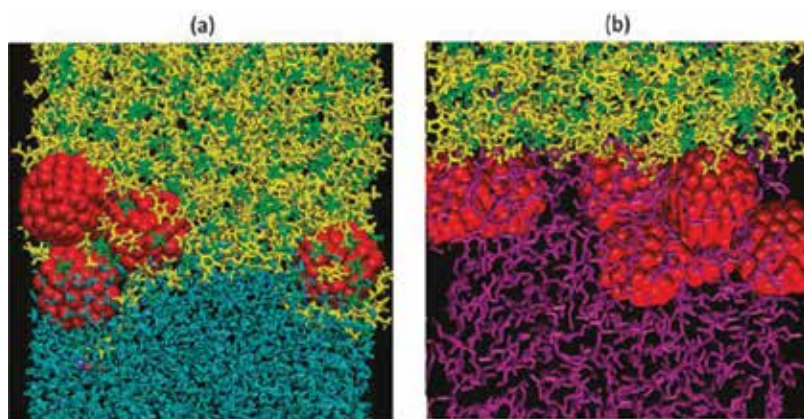


Figure 6. Snapshots from MD simulations of particles at the (a) IL/water and (b) IL/hexane interface. [BMIM] is yellow, [PF₆]⁻ is green, particles are red, water is blue, and hexane is purple. Adapted from Ref. [19].

While the molecules of the liquid phases influence particle behavior, the opposite is equally true. By comparing the simulations of the systems with nanoparticles to those without, we were able to examine the effect of nanoparticles on the interface through various analytical techniques. **Figure 7** illustrates two of those techniques—calculating density profiles and ordering parameters. Mass density profiles are a simple way to illustrate the physical distribution of molecules across the system. The ordering parameter S_z is a measure of how flat the carbon chain on the IL cation (the butyl in 1-butyl-3-methylimidazolium) lies against the plane of the interface. When S_z is zero, there is no particular ordering of ionic liquid atoms—they are oriented in all directions. S_z rising indicates that the IL cation is orienting itself flat against the plane of the interface, creating an ordered pattern of molecules. This ordering is similar to that widely observed in molecular dynamics studies of other ionic liquid interfaces including the IL/oil [21], IL/graphite [22], IL/gold [23], and IL/vapor interfaces [24, 25]. Drawing from this wide range of studies, it can confidently be said that ordering of ionic liquid molecules is a fundamental trait of IL interfaces, and it is no surprise that it affects and is affected by particles at the interface. Such ordering has also been confirmed experimentally through spectroscopy [26].

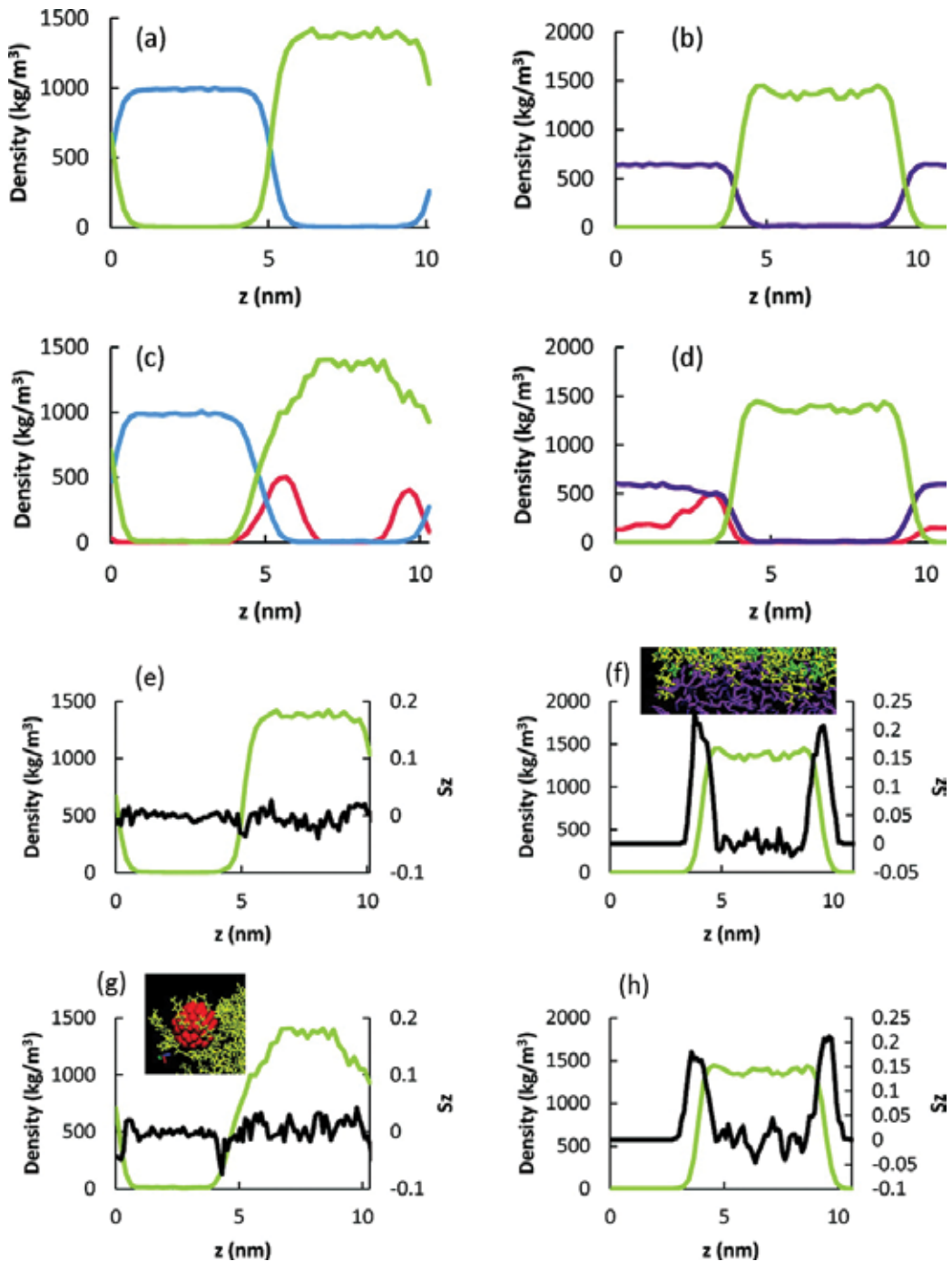


Figure 7. Density profiles and ordering parameters for IL/water (a, c, e, g) and IL hexane (b,d,f,h) systems without (a, b, e, f) and with (c, d, g, h) particles. The four figures above (a, b, c, d) show density profiles for water (blue), IL (green), and particles (red). The four figures below (e, f, g, h) compare the IL density profile to the ordering parameter S_z , a measure of how flat the IL cation molecules lay against the interface. Adapted from Ref. [19].

Figure 7 illustrates the impact of the particles on the IL/water interface. In the case of the IL/water system, the addition of particles broadens the interface, with potential relevance to interface properties such as surface tension. However, this does not occur in the IL/hexane system, likely because the hydrophobic oil is especially repulsive to [BMIM][PF₆] molecules. Instead, the density of the IL features a slight bump at the IL/hexane interface. Examining the ordering parameter S_z explains this oddity— S_z spikes up at the interface as [BMIM] molecules lie laterally against the surface. This ordering likely explains, in part, why particles equilibrate on the hexane side of the interface—absorption into the IL would disrupt this ordering.

This study gave an important insight into the effect of the second, non-IL, liquid phase on the self-assembly of particles at the interface. It also demonstrated that the particles influence the interface as well. These effects occur at the molecular scale because of the interactions between atoms in the IL and other phases, and are vital to fully understanding corresponding behavior at the macroscale.

3.2. Particle effects: particle hydrophobicity and charge

The initial MD study described in Section 3.1 was inherently limited. It only examined one type of ionic liquid and one type of particle. Two further studies allowed us to examine the effect of changing particle properties on self-assembly. This is an extremely important variable to study if we are to derive conclusions about real-world phenomena. In particular, one of the most promising applications for ILs in multiphase systems is the extraction of sand particles from water or oil, and sand is made up of hydrophilic silica that cannot be expected to behave like our model hydrophobic carbon particle. Another important factor is particle charge. Many particles of interest have some charge, which would obviously have an effect on the ions making up ionic liquids. Therefore, we completed two studies. Both simulated the same [BMIM][PF₆]/water and [BMIM][PF₆]/hexane interfaces as the original study. The first compared two types of particles—the same hydrophobic carbon particle as before, and a new, hydrophilic silica particle meant to behave similarly to, for example, a grain of sand [26]. The second utilized the carbon particle but arbitrarily varied the charge [27].

These systems were analyzed using the same techniques utilized in the first study. Some results were as expected. For example, the hydrophilic silica particle equilibrated on the opposite side of the interface from the hydrophobic carbon particle—on the water side in the IL/water system, and on the IL side in the IL/hexane system. Though this result was predictable, it is highly encouraging to one of the most exciting potential applications of these systems—oil spill clean-up. If silica particles are naturally absorbed into the ionic liquid phase when it is placed alongside oil, ionic liquids may be able to passively clean oil by absorbing grains of sand.

Somewhat more interestingly, the silica particle did not adhere as strongly to the IL/water interface as the carbon particle did to the IL/hexane interface. In fact, many of the silica particles remained in the water phase throughout the simulation. This indicates that a silica particle, or particles with similar properties, would be less effective at stabilizing Pickering emulsions than more hydrophobic particles. The silica particles also had the fascinating effect of eliminating the “ordering” of cation molecules at the IL/hexane interface. This suggests that the particle intermediates the repulsive forces between the two liquid phases. (This observation in part inspired aspects of another study described in Section 3.3 below.)

In Section 3.1, it was concluded that the presence of the particle at the interface affected properties of that interface. In particle, a hydrophobic particle broadened and softened the IL/water interface, leading to a region of relatively intermingled water and IL molecules. Particle charge was found to have a significant influence on this effect. In the IL/water system, a neutral particle widened the interface significantly more than either negatively or positively charged particles, and the interface tended to narrow as the charge grew strongly positive. The effect on the IL/hexane system showed the opposite trend, with a neutral particle resulting in a narrower interface than either a negative or positive charge. This indicates that particle charge contributes to a complex system of balanced coulombic forces affecting the interactions of all elements within the interfaces.

Another technique that was utilized in the first study (though that data was not described in this work) was the potential of mean force (PMF). A PMF diagram allows researchers to compare the energy effects of physical configurations with a simulation system. In the case of these particle/interface studies, a particle was forcibly dragged from midway in the water or hexane phase to midway within the IL phase. Snapshots were saved of the system with the particles at intervals of 0.2 nm. Then, each of these snapshots were taken as the starting point of a new simulation. This time, however, the particle was frozen in place. The system energies were then recorded as the system moved around the frozen particle and plotted against the distance of the particle from the interface. The result is shown in **Figure 7**.

Graphs (a) and (b) in **Figure 8** compare carbon and silica particles. Graphs (c) and (d) compare carbon particles with -4 , neutral, and $+4$ charges. The equilibrium state of each system is at the lowest point of the energy. This allows us to confirm some things that we already know—that carbon particles equilibrate just inside the IL phase in the IL/water system and just inside the hexane phase in the IL/hexane system, that the hydrophilic and hydrophobic particles exhibit roughly opposing trends. From (c) we determine that [BMIM][PF₆] has stronger, more attractive interactions with a neutral particle than either a negative or positively charged one. We also see that in the hexane system, the particle tends to equilibrate at the interface regardless of charge. This again shows the powerful influence of the second liquid phase. In a multiphase system, all elements affect all others in profound ways. When one of those phases is an ionic liquid with its complex constituent ions, the interactions become even more elaborate, allowing for the unusual behavior and intriguing phenomena revealed by experiment.

3.3. Ionic liquid effects: IL cation and anion influence on interface/particle interactions

The previous studies all utilized the ionic liquid [BMIM][PF₆]. This is a solid choice for a model IL since it is widely studied, and a well-tested model is available. However, one of the greatest assets of ionic liquids is their near endless variety, tunability, and adaptability. Different ionic liquids differ from each other in profound ways, and we are inherently unable to make definitive statements on the nature of IL interfaces after only studying one IL. The final study described here aims to address that issue. It compares four ionic liquids: 1-ethyl-3-methylimidazolium hexafluorophosphate ([EMIM][PF₆]), 1-butyl-3-methylimidazolium hexafluorophosphate ([BMIM][PF₆]), 1-hexyl-3-methylimidazolium hexafluorophosphate ([HMIM][PF₆]), and 1-butyl-3-methyl bis(trifluoromethylsulfonyl)imide ([BMIM][Tf₂N]). The length of the carbon chain on the cation is directly correlated to the hydrophobicity

of the IL, so adjusting the length makes for a convenient comparison. Tf_2N is both more hydrophobic than PF_6 and allows us to study an IL with an anion of a different shape. We are particularly interested in any insight this might give to the phenomenon of spontaneous particle transport across the interface as described in Section 2.3, which varies widely with different ILs. This study also varied the number of particles, simulating systems of zero, eight, and thirty-two particles. This was done to allow a further study of particle effects on the rest of the system.

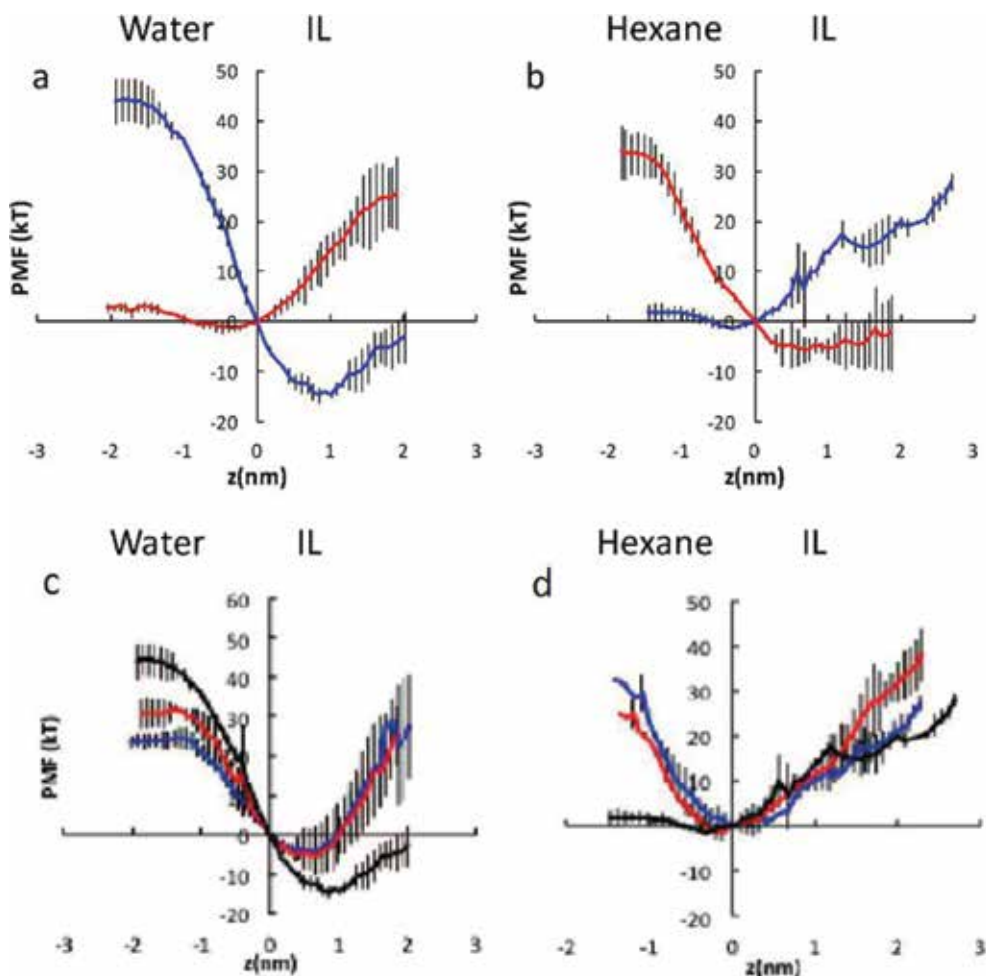


Figure 8. Potential of mean force (PMF) diagrams. (a) and (b) compare carbon (blue) and silica (red) particles. (c) and (d) compare carbon particles with -4 (red), neutral (black), and $+4$ (blue) charges. Adapted from Refs. [26, 27].

Adding particles to these systems reveals how these interface properties affect particle/interface interactions. **Figure 9** shows snapshots from the 32-particle simulations of each interface system. To some extent all four interfaces behave similarly, equilibrating with the particles aggregated at the surface and a thin layer of IL molecules wrapping around, insulating the

hydrophobic nanoparticles from the water phase. However, the [EMIM][PF₆] also seems to have drawn water molecules into the ionic liquid phase with them. [BMIM][PF₆] and [HMIM][PF₆] also seem to be doing this to different extents. The [BMIM][Tf₂N] system, however, shows a sharp interface with very little uptake into the IL. Density profiles confirm these suspicions.

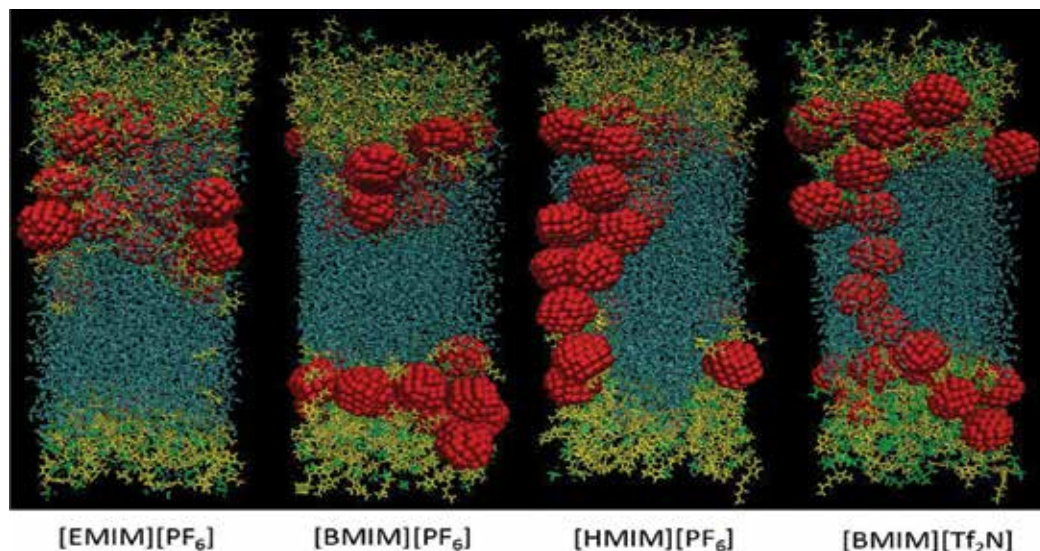


Figure 9. Snapshots from simulations of four IL interfaces with 32 particles.

Given these observations, it would seem that differences in hydrophobicity do not entirely explain the differing behavior of the IL interfaces. Hydrophobicity is certainly a factor—after all, relatively hydrophilic EMIM experiences more interface-broadening than hydrophobic HMIM. However, HMIM does not experience the same IL-crowding at the interface. The difference is not hydrophobicity but the shape of the anion, with Tf₂N being linear and capable of lying flat on the interface, while PF₆ is round. Applying these observations to the particle transport exhibited in **Figure 5**, it becomes clear that a major relevant difference between [BMIM][Tf₂N] (no transport) and [P₆₆₆₁₄][Phos] (strong transport), both highly hydrophobic ILs, may be the shape of the anion, with Tf₂N much more linear and much more rigid than phosphinate with its branching chains.

The results of the thirty-two particle simulations are intriguing for another reason. [EMIM][PF₆], water, and particles form a broad, intermingled interface, with the particles quickly aggregating into a single cluster (this behavior was also observed in the parallel simulation runs). Hydrophobic [HMIM][PF₆] and [BMIM][Tf₂N], on the other hand, maintain relatively distinct interfaces, and the nanoparticles are not quickly drawn into a large cluster. In the [HMIM][PF₆] snapshot, the particles can be seen drawing ions out into the water phase. This confirms prior suspicions that nanoparticles intermedicate the repulsive interactions between water and the ionic liquid molecules. This creates a unique energy-favorable region with

water, ionic liquid, and particles commingling. This observation was further confirmed by calculating interaction energies between the ILs and water for system with varying numbers of particles. It was found that changing the number of particles had a profound effect on the repulsive and attractive forces between ionic liquids and water. This may explain phenomena such as spontaneous transport of particles across the IL-water interface—the particles themselves distort and broaden the interface, changing their fundamental nature and the energetic physics which typically cause particles to adhere strongly to the interface.

4. Summary and discussion

The unique properties of ionic liquids lend themselves to a multitude of applications relying on various diverse and intriguing systems. This work has focused on multiphase systems where IL undergo complex interactions with other materials. In particular, this work explored ionic-liquid-based Pickering emulsions (stabilized by solid particles) and the behavior of particles at ionic liquid/liquid interfaces. These systems exhibit several remarkable phenomena including “bridging” of particles in between emulsion droplets and, perhaps most intriguingly, spontaneous transport of particles across the liquid/liquid interface. The unique behavior and properties of ionic liquids in these systems make them potentially relevant to a variety of applications including oil spill cleanup, drug delivery, and the creation of novel materials. What is more, the unusual nature of ionic liquids makes their study a vital tool in fully understanding the fundamental nature of physical systems such as liquid/liquid interfaces and Pickering emulsions. Molecular dynamics simulations, in particular, reveal how the properties of ionic liquids at the molecular level influence the behaviors of the systems. Further work in this field may take a variety of directions including developing practical extraction techniques based on ionic liquids, developing novel materials utilizing or based on ionic liquid Pickering emulsions, or environmentally responsive emulsions. Regardless, ionic liquids in multiphase systems promise continued relevance to both scientific advancement and practical application in the years to come.

Author details

Stella Nickerson, Elizabeth Nofen, Denzil Frost and Lenore L. Dai*

*Address all correspondence to: lenore.dai@asu.edu

School for Engineering of Matter, Transport Energy, Arizona State University, Tempe, Arizona, United States of America

References

- [1] Destribats, M.; Rouvet, M.; Gehin-Delval, C.; Schmitt, C.; Binks, B.P. Emulsions stabilized by whey protein microgel particles: towards food-grade Pickering emulsions. *Soft Matter* **2014**, *10*, 6941–6954.

- [2] Tikekar, R.V. Fate of curcumin encapsulated in silica nanoparticle stabilized Pickering emulsion during storage and simulated digestion. *Food Res. Int.* **2013**, *51*, 370–377.
- [3] Zhu, Z.; Chen, D.; Wu, G. Molecular dynamic simulation of asphaltene co-aggregation with humic acid during oil spill. *Chemosphere* **2015**, *138*, 412–421.
- [4] Nagarkar, S.; Velankar, S.S. Rheology and morphology of model immiscible polymer blends with monodisperse spherical particles at the interface. *J. Rheol.* **2013**, *57*, 901–926.
- [5] Monteillet, H.J.M.; Workamp, M.J.; Li, X.; Schuur, B. Multi-responsive ionic liquid emulsions stabilized by microgels. *Chem. Commun.* **2014**, *50*, 12197–12200.
- [6] Luczak, J.; Paszkiewicz, M.; Krukowska, A.; Malankowska, A. Ionic liquids for nano- and microstructures preparation. Part 1: properties and multifunctional role. *Adv. Colloid Interface Sci.* **2016**, *230*, 13–28.
- [7] Federicia Canova, F.; Mizukami, M.; Imamura, T.; Kurihara, K.; Shluger, A.L. Structural stability and polarization of ionic liquid films on silica surfaces. *Phys. Chem. Chem. Phys.* **2015**, *17*, 17661–17669.
- [8] Anouti, M. Room-temperature molten salts: protic ionic liquids and deep eutectic solvents as media for electrochemical application. Chapter in *Electrochemistry in Ionic Liquids: Volume 1: Fundamentals*, **2015**.
- [9] Bettoschi, A. Highly stable ionic liquid-in-water emulsions as a new class of fluorescent sensors for metal ions: the case study of Fe³⁺ sensing. *RSC Adv.* **2015**, *5*, 37385–37391.
- [10] Ma, H.; Dai, L. Particle self-assembly in ionic liquid-in-water Pickering emulsions. *Langmuir* **2011**, *27*, 508–512.
- [11] Binks, B.P.; Fletcher, P.D.I.; Dyab, A.K.F. Novel emulsions of ionic liquids stabilised solely by silica nanoparticles. *Chem. Commun.* **2003**, *20*, 2540–2541.
- [12] Binks, B.P.; Dyab, A.K.F.; Fletcher, P.D.I. Contact angles in relation to emulsions stabilised solely by silica nanoparticles including systems containing room temperature ionic liquids. *Phys. Chem. Chem. Phys.* **2007**, *9*, 6391–6397.
- [13] Walker, E.M.; Frost, D.S.; Dai, L.L. Particle self-assembly in oil-in-ionic liquid Pickering emulsions. *J. Colloid Interface Sci.* **2011**, *363*, 307–313.
- [14] Frost, D.S.; Schoepf, J.J.; Nofen, E.M.; Dai, L.L. Understanding droplet bridging in ionic liquid-based Pickering emulsions. *J. Colloid Interface Sci.* **2012**, *383*, 103–109.
- [15] Tarimala, S.; Dai, L.L. Structure of microparticles in solid-stabilized emulsions. *Langmuir* **2004**, *20*, 3492–3494.
- [16] Dai, L.L.; Tarimala, S.; Wu, C.; Guttula, S.; Wu, J. The structure and dynamics of microparticles at Pickering emulsion interfaces. *Scanning* **2008**, *30*, 87.
- [17] Frost, D.S.; Nofen, E.M.; Dai, L.L. Particle self-assembly at ionic liquid-based interfaces. *Adv. Colloid Interface Sci.* **2014**, *206*, 92–105.

- [18] Frost, D.S.; Ngan, M.; Dai, L.L. Spontaneous transport of microparticles across liquid-liquid interfaces. *Langmuir* **2013**, *29*, 9310–9315.
- [19] Frost, D.S.; Dai, L.L. Molecular dynamics simulations of nanoparticle self-assembly at ionic liquid-water and ionic liquid-oil interfaces. *Langmuir* **2011**, *27*, 11339–11346.
- [20] Bhargava, B.L.; Balasubramanian, S. Refined potential model for atomistic simulations of ionic liquid [bmim][PF₆]. *J. Chem. Phys.* **2007**, *127*, 114510.
- [21] Iwahashi, T.; Ishiyama, T.; Sakai, Y.; Ouchi, Y. Liquid/liquid interface layering of 1-butanol and [bmim]PF₆ ionic liquid: a nonlinear vibrational spectroscopy and molecular dynamics simulation study. *Phys. Chem. Chem. Phys.* **2015**, *17*, 24587–24597.
- [22] Maolin, S.; Fuchun, Z.; Guozhong, W.; Haiping, F.; Chunlei, W.; Shimou, C. Yi, Z.; Jun, H. Ordering layers of [bmim][PF₆] ionic liquid on graphite surfaces: molecular dynamics simulation. *J. Chem. Phys.* **2008**, *128*, 134504.
- [23] Ferreira, E.S.C.; Pereira, C.M.; Cordeiro, M.N.D.S.; dos Santos, D.J.V.A. Molecular dynamics study of the gold/ionic liquids interface. *J. Phys. Chem. B* **2015**, *119*, 9883–9892.
- [24] Heggen, B.; Zhao, W.; Leory, F.; Dammers, A.J.; Muller-Plathe, F. Interfacial properties of an ionic liquid by molecular dynamics. *J. Phys. Chem. B* **2010**, *114*, 6954–6961.
- [25] Bhargava, B.L.; Balasubramanian, S. Layering at an ionic liquid-vapor interface: a molecular dynamics simulation study of [bmim][PF₆]. *J. Am. Chem. Soc.* **2006**, *128*, 10073–10078.
- [26] Frost, D.S.; Machas, M.; Dai, L.L. Molecular dynamics studies on the adaptability of an ionic liquid in the extraction of solid nanoparticles. *Langmuir* **2012**, *28*, 13924–13932.
- [27] Frost, D.S.; Dai, L.L. Molecular dynamics simulations of charged nanoparticle self-assembly at ionic liquid-water and ionic liquid-oil interfaces. *J. Chem. Phys.* **2012**, *136*, 084706.

Imidazolium-Based Ionic Liquid Binary Solvent System as an Extraction Medium in Enhancing the Rotenone Yield Extracted from *Derris elliptica* Roots

Zetty Shafiqah Othman, Nur Hasyareeda Hassan and Saiful Irwan Zubairi

Additional information is available at the end of the chapter

<http://dx.doi.org/10.5772/66777>

Abstract

Rotenone, is a biopesticide which can be isolated from *Derris* species roots. However, procuring significant amount of rotenone using green alternative solvent rather than harmful organic solvents for commercialization is a challenge to be faced. Therefore, an approach using imidazolium-based ionic liquids (ILs) as an extraction medium was employed in this study. Five different types of binary solvent systems comprising a combination of acetone and five respective ionic liquids (ILs) of (1) [BMIM] Cl; (2) [BMIM] OAc; (3) [BMIM] NTf₂; (4) [BMIM] OTf; and (5) [BMPy] Cl were used in the normal soaking extraction (NSE) of rotenone for a 24-hour extraction. The yield of the rotenone, % (w/w), and its concentration (mg/mL) in the dried roots was quantitatively determined by means of the reversed-phase high-performance liquid chromatography (RP-HPLC) and thin-layer chromatography (TLC). The results showed that a binary solvent system of [BMIM] OTf:acetone was the best solvent system combination compared to other solvent systems ($p < 0.05$). It contributed to the highest rotenone content of $2.69 \pm 0.21\%$ (w/w) (4.04 ± 0.34 mg/ml) at the 14th hour of the exhaustive extraction time. In conclusion, a combination of certain ILs with a selective organic solvent has been proven to be able to increase a significant amount of bioactive constituents in the phytochemical extraction process.

Keywords: rotenone, *Derris* sp., binary solvent system, imidazolium-based, ionic liquids

1. Introduction

The destructive effects of numerous pests from the time immemorial led to a large decline in crop yield. Through the advent of chemical pesticides, this crisis was resolved to a great extent.

However, an overdose, overdependence on and uncontrolled usage of synthetic pesticides eventually created pest resistance which simultaneously led to frequent applications, application of bulk quantity of pesticide and a high cost [1]. In addition, the violative pesticides' residues had contributed to food safety concern among consumers. Therefore, an eco-friendly alternative is needed to overcome the drawbacks of synthetic pesticides. As agricultural-industrial tools, biopesticides demonstrate exemplary benefits over chemically synthesized pesticides through harnessing the natural capabilities of organisms and their molecular constituents in minimizing the crop and plant damages from pests, affording the opportunity for protection, maintenance of biodiversity, and commerce-strengthening alternatives for organic farming and safe guarding of human health. Rotenone is one of the biopesticides that can be extracted from *Derris* and *Lonchocarpus* plants' roots [2]. It exhibits a strong pesticidal activity due to its strong paralysis action (knock-down effect) on cold-blooded animals. Besides, its high degradability, exceptionally selective and poor absorption across the gut and skin of humans enhances its eco-friendly usage [3–7]. In accordance with that, the extraction process plays a major role in optimizing the extraction of the yield of rotenone compound. Conventionally, organic solvents were used as an extraction medium and the selection of solvent systems largely depended on the specific nature of the bioactive compound from natural products. Rotenone is an isoflavonoid and it does not dissolve in water but it dissolves in organic solvents. According to John and Ron [4], the solubility of pure rotenone in acetone is 0.066 g/ml, ethanol, 0.002 g/ml and chloroform, 0.47 g/ml. However, a research completed by Zubairi [8] showed that acetone extracted more rotenone and other bioactive constituents compared to a high-polarity solvent as it could extract rotenone from from 39.5% up to 72.8% compared to chloroform and ethanol.

Although conventional organic solvents have been used for so long as the extraction medium, their drawbacks such as volatility, toxicity, and flammability that lead to several human risks and environmental problems, limit its usage as an extractant. Taking all these into account, there have been several studies conducted on the exploration of ionic liquids (ILs) compatibility as green solvents for plant extraction. According to Fu et al. [9], ILs can be used as an alternative green solvent to replace volatile organic solvents. ILs are organic salts in the liquid state under ambient temperature that comprise a normally charge-stabilized organic cation paired with an organic or inorganic anion. They display a wide range of unique properties such as high thermal stability, nonflammability, insignificant vapor pressure, and low chemical reactivity. In addition to that, they also have fine tunable density, viscosity, polarity, and miscibility with other common solvents through the change of the cation and anion [10]. Some of ILs are also immiscible with organic solvents which define their polar alternative with nonaqueous nature for two-phase systems and ILs can be recycled that this enhances their green properties. The viscosity of ILs also plays a crucial role in the extraction and separation of bioactive compounds from plants. Their viscosity is affected by a range of intermolecular interactions such as electrostatic, van der Waals forces, and hydrogen bonding interaction [11]. The increase in temperature and asymmetry of ILs' anions lead to the decrease in their viscosity. For instance, using the imidazolium cationic species, the viscosity can be intensified by increasing the substituted alkyl chain length or branching due to more van der Waals interactions between the ions themselves [11–14]. Some ILs also are immiscible in water (formation of

biphasic systems) and the organic species have a high solubility in these ILs, making them ideal solvents for bioactive compound extraction from plants and as mobile phase modifiers to improve liquid chromatography separation of bioactive targets. The usage of ILs as plant bioactive constituent extractants has a great impact and potential as they alleviate the environmental pollution and improve the selectivity and extraction yields of interesting compounds in sample pretreatment process compared to conventional organic solvents.

However, due to their charged and asymmetric structures, ILs have a relatively high polarity [15], as they do not have a good affinity with weak-polar compounds, thus causing a reduction in the distribution of weak-polar compounds in the IL phase. The viscosity of ILs increases with longer alkyl chain of ILs in accordance with the strong electrostatic and hydrogen bonding interaction between ions [16, 17]. The high viscosity of ILs will hinder the mixing and transferring of properties in the extraction process by influencing the dissolution of the compounds in ILs. In exchange, the mixture of ILs and polar molecular solvents as an extraction medium could be an effective approach to solve their flaws. Besides creating a wide-adjusted range of solvent polarity, hydrophobicity, hydrogen-bond acidity, and basicity [18, 19], the addition of miscible molecular solvents as co-solvents helps to break the microscopic hydrogen-bond network and the aggregation of ILs, which significantly reduces the viscosity and improves the mixing and transferring process in their mediated extraction [20, 21]. The rotenone compound is an acidic isoflavonoid compound that consists of ketonic chemical groups (R-C(=O)-R) [22] which has the potential of interacting with intermediate-polar solvents. It can be easily dissolved in moderate-polar organic solvents (e.g., methanol, chloroform, and acetone) [23] and is sparingly soluble in water [24]. For that reason, a combination of any ILs with a moderate polarity of organic solvents would perhaps increase the chances of extracting a high rotenone content due to its low viscosity and mediate polarity property and the high tendency of interaction between rotenone compound with the anion and cation of ILs. The previous study indicated that solubility of flavonoids and their derivatives can be increased by using ILs as the of flavonoids are greatly anion-dependent [25]. The anionic potency of both organic solvents and ILs in extracting a large amount of bioactive compounds (e.g., rotenone) and moving into solvent systems is significantly undeniable as both chemicals facilitate the extraction process via salvation power and multiple interactions (e.g., hydrogen bonding, polarity, ionic/charge-to-charge, and π - π , π - n) with the analytes [26, 27].

2. Imidazolium-based ionic liquids as a green extraction medium

2.1. Structural features of ionic liquids

Ionic liquids (ILs) are organic salts in the liquid state under ambient temperature that comprise a normally charged stabilized organic cation paired with an organic or inorganic anion. The widely used cations (**Figure 1**) are ammonium, sulfonium, imidazolium, pyridinium, pyrrolidinium, tetraalkylammonium, phosphonium, picolinium, and the functionalized cations with different substitutions [28, 29]. On the other hand, anions are weakly basic inorganic or organic compounds that have a diffuse or protected negative charge [28]. ILs based on halides such as $[\text{BF}_4]^-$, or $[\text{PF}_6]^-$ ions are not preferred due to their

unfavorable properties and they are also strongly hygroscopic [26]. The most preferred anions are the ones which are more complex, perfluorated anions such as bis(trifluoromethane sulfonyl) amide or trifluoromethanesulfonate or halogen-free ions such as dicyandiamide, tosylate, or n-alkyl sulfates (**Figure 1**) [30]. The environment constituted by ionic liquids is completely different from that of polar and nonpolar molecular solvents. In addition to the existing interactions in conventional organic solvents such as hydrogen bonding, dipole-dipole, and van der Waals interactions, ionic liquids have strong electrostatic interactions.

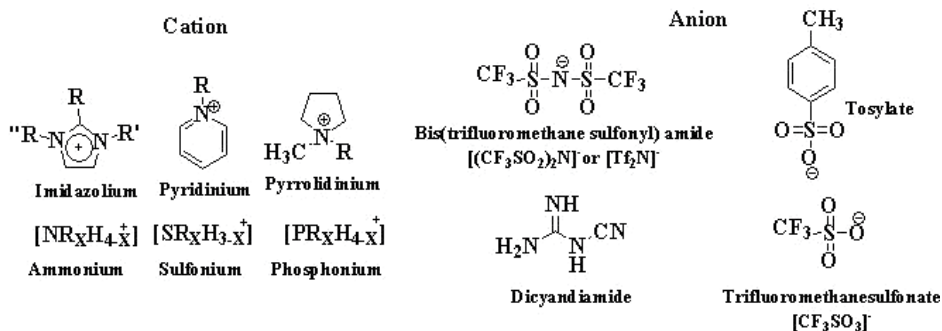


Figure 1. Some typical cations and anions.

2.2. Imidazolium-based ionic liquid characterization

Among all ionic liquids, the ionic liquid based on imidazolium cation is widely used and studied due to the stability of the imidazolium ring and its excellent liquescency [31] which is resulted from its electronic structure of the aromatic cation. With delocalized 3-centre-4-electron configuration across the N₁-C₂-N₃ moiety, a double bond between C₄ and C₅ at the opposite side of the ring, and a weak delocalization in the central region (**Figure 2**) [32], the hydrogen atoms C₂-H, C₄-H and C₅-H carry almost the same charge but carbon C₂ is positively charged owing to the electron deficit in the C=N bond, whereas C₄ and C₅ are practically neutral. The resulting acidic proton or hydrogen on the C₂ carbon is the key for understanding the properties of the ionic liquids (ILs) and it is presented that the hydrogen on the C₂ carbon (C₂-H) binds specifically with solute molecules [33, 34] or its counter ion [35] as a good hydrogen bond donor.



Figure 2. Electronic structure of 1,3-dialkylimidazolium cation.

2.3. Structural organization of imidazolium-based ionic liquids

Long-range coulomb interaction may play a major role in ionic liquids which are composed solely of ions by creating the structure and dynamics that are unique to ionic liquids without being associated with molecular liquids [36]. From macroscopic point of view, ionic liquids can be considered as a continuum system characterized by their macroscopic constants such as boiling point, vapor pressure, density, and surface tension. However, from microscopic point of view, they are a discontinuum system consisting of individual, mutually interacting molecules characterized by molecular properties such as dipole moment, electronic polarizability, hydrogen-bond donor (HBD), and hydrogen bond acceptor (HBA) capability, electron pair donor (EPD) and electron pair acceptor (EPA). The types and degrees of these interactions control and determine the macroscopic properties of ionic liquids and their possibilities for various applications. Specifically, the ionic liquids' structure exhibits a unique spatial heterogeneity due to their inherent polar/nonpolar phase separation. The underlying reason for the microphase segregation resulted from the interplay between electrostatic interaction (between polar imidazolium ring and anion) and van der Waals interaction with the nonpolar alkyl tails of the cation [37]. In fact, charge-charge distribution and anion size affect the nanostructural segregation of ionic liquids. As the ions' size increases, the charge becomes more delocalized and the cation-anion interaction is reduced resulting in less charge ordering and nanostructural segregation [38]. On the other hand, divalent anions such as sulfate (SO_4^{2-}), thiosulfate ($\text{S}_2\text{O}_3^{2-}$), chromate (CrO_4^{2-}), dichromate ($\text{Cr}_2\text{O}_7^{2-}$), carbonate (CO_3^{2-}), and oxalate ($\text{C}_2\text{O}_4^{2-}$) increase the electrostatic interaction between cation and anion and enhance intermolecular structuring. Besides, it was observed that the size of structural heterogeneities depended on alkyl chain length [37, 39].

2.4. Physicochemical properties of imidazolium-based ionic liquids

Ionic liquids are constituted exclusively by ions and hence they experience a strong interionic interaction that yield a long-lived association of ions [40]. The nature and types of cation-anion interactions and intermolecular forces in bulk ionic liquids affect their physical and chemical properties and how they interact with other solutes [41]. The examples of conformational heterogeneity of cations and anions are the coexisting *trans-trans* and *trans-gauche* conformations of n-butyl chain in 1-butyl-3-methylimidazolium cation and bisimide [Tf_2N] anion conformational which forms *trans-* and *cis* conformers and this seems to be crucial in lowering their ionic liquid melting point [42]. Ionic liquids which comprise a low symmetry cation possess a low melting point than the one with a higher symmetry due to weak intermolecular interactions and good distribution of charge in the cation.

Generally, ionic liquids (ILs) are denser than water. The density (ρ) of ionic liquids (ILs) decreases with the increase in organic cation bulkiness and anion selection affects ILs' density. Normally, the density of ILs varies in the range of 1.05–1.36 g/cm³ at ambient temperature [43, 44]. In terms of ILs' thermal stability, a research conducted had observed that thermal stability was dependent on both the cation and the anion of ILs. Ngo et al. [45] reported that imidazolium-based cations exhibited a higher thermal stability than tetraalkylammonium cations based on thermal gravimetric analysis (TGA) and differential scanning calorimetry

(DSC). In addition, imidazolium-based ILs have a thermal stability that increases in the following order: $[\text{Cl}]^-$, $[\text{Br}]^-$, $[\text{I}]^- < [\text{BF}_4]^- < [\text{CF}_3\text{SO}_3]^- < [\text{NTf}_2]^- < [\text{PF}_6]^-$ and Ngo et al. [45] also reported that IL-based organic anions have a higher thermal stability than that of those based on inorganic anions.

The viscosity of ILs also plays a crucial role in the extraction and separation of bioactive compounds from plants. Their viscosity is affected by a range of intermolecular interactions such as electrostatic, van der Waals forces, and hydrogen bonding interaction [11]. The increase in temperature and asymmetry of IL anions leads to the decrease in their viscosity. For instance, using imidazolium cationic species, the viscosity can be increased by increasing the substituted alkyl chain length or branching due to higher van der Waals interactions between the ions themselves [12–14]. Ionic liquids also have their own polarity values according to Kamlet-Taft parameters such as dipolarity or polarizability (π^*), hydrogen bond basicity (β), and hydrogen bond acidity (α) [46]. Although measurement has not been made for a large number of ionic liquids, the general trend suggests that the π^* values for ionic liquids are higher than that of alkyl chain alcohol, while the α values are less than those of water and alkyl chain alcohols and also the magnitude of β is determined by the anion of ionic liquids. **Tables 1** and **2** display the summary of some physicochemical properties of ILs and Kamlet-Taft parameters for some ionic liquids.

ILs			
Cation	Anion	Density (g/ml)	Viscosity (cP)
[EMIM] ⁺	[BF ₄] ⁻	1.248	66
	[PF ₆] ⁻	1.373	450
[BMIM] ⁺	[BF ₄] ⁻	1.208	233
	[PF ₆] ⁻	1.373	400
	[Br] ⁻	1.134	Solid
	[Cl] ⁻	1.12	Solid
	[CF ₃ SO ₃] ⁻	1.29	90
	[(CF ₃ SO ₃) ₂ N] ⁻	1.42	52
[AMIM] ⁺	[NTf ₂] ⁻	1.404	48
	[BF ₄] ⁻	1.213	321
[HMIM] ⁺	[BF ₄] ⁻	1.075	211
	[PF ₆] ⁻	1.304	800
[OMIM] ⁺	[BF ₄] ⁻	1.11	440
	[Cl] ⁻	1	16,000
[MPPyr] ⁺	[NTf ₂] ⁻	1.44	39
[C ₂ H ₅ NH ₃] ⁺	[HCOO] ⁻	0.99	11.5
[BMPyrrol] ⁺	[NTf ₂] ⁻	1.4	71

Table 1. Summary of some physicochemical properties of ILs at 25°C.

ILs	α	β	π^*
[OMIM][BF ₄] [49]	0.62	0.41	0.98
[OMIM][NTf ₂]	0.60	0.29	0.96
[HMIM][NTf ₂] [48]	0.65	0.26	0.97
[HMIM][Cl] [49]	0.48	0.94	1.02
[HMIM][Br][49]	0.45	0.74	1.09
[BMIM][BF ₄] [49]	0.77	0.39	1.04
	0.63	0.37	1.05
[BMIM][NTf ₂]	0.72	0.24	0.90 [47]
	0.64	0.25	0.97 [48]
	0.61	0.23	0.99
[BMIM][(C ₈)OSO ₃] [49]	0.69	0.79	0.89
[BMIM][PF ₆]	0.68	0.21	1.02 [49]
	0.65	0.25	1.02
	0.63	0.24	1.02 [49]
	0.63	0.19	1.04
[BMIM][SBF ₆]	0.62	0.15	1.04
[BMIM][OTf]	0.62	0.49	1.00
[BMIM][MeCO ₂]	0.57	1.18	0.89 [50]
	0.43	1.05	1.04 [51]
	0.48	1.20	0.96
[BMIM][N(CN) ₂]	0.54	0.60	1.05
[BMIM][MeSO ₄]	0.53	0.66	1.06
[BMIM][PrCO ₂] [51]	0.51	1.23	0.92
[BMIM][(HO)C ₁ CO ₂] [51]	0.44	0.87	1.12
[BMIM][EtCO ₂] [51]	0.48	1.16	0.94
[BMIM][Me ₂ PO ₄]	0.45	1.13	0.98
[BMIM][MeSO ₃]	0.44	0.77	1.02
[BMIM]O ₂ CCH ₂ CH(OH)CO ₂] [51]	0.41	1.00	1.10
[BMIM][O ₂ CCH ₂ CH ₂ CO ₂] [51]	0.39	1.08	1.09
[BMIM][O ₂ CCHCHCO ₂] [51]	0.34	1.02	1.11
[BM ₂ IM][BF ₄]	0.39	0.36	1.08
[BM ₂ IM][NTf ₂]	0.38	0.26	1.02
[EMIM][NTf ₂]	0.71	0.23	0.98 [48]
	0.42	0.10	1.02 [47]
	0.63	0.23	1.00
[EMIM][(C ₆)SO ₄]	0.65	0.71	0.98

ILs	α	β	π^*
[EMIM][[(C ₈)SO ₄]	0.65	0.77	0.93
[EMIM][MeCO ₂]	0.57	1.06	0.97
[(HO) ³ (HO) ² C ₃ C ₁ IM][Cl]	1.12	0.99	0.82
[(HO) ³ (HO) ² C ₃ C ₁ IM][N(CN) ₂]	0.87	0.47	1.17
[(HO) ³ (HO) ² C ₃ C ₁ IM][NTf ₂]	1.20	0.13	1.15
[(HO) ³ (HO) ² C ₃ C ₁ C ₁ IM][N(CN) ₂]	0.87	0.47	1.17
[(HO) ³ (HO) ² C ₃ C ₁ C ₁ IM][NTf ₂]	0.93	0.11	1.14
[(HO) ³ C ₃ C ₁ IM][MeCO ₂]	0.51	0.99	1.08
[(HO) ³ C ₂ C ₁ IM][NTf ₂]	1.14	0.28	1.08
[(HO) ³ C ₂ C ₁ IM][MeCO ₂]	0.53	0.90	1.04

Table 2. Kamlet-Taft parameters for some imidazolium-based ionic liquids.

2.5. Ionic liquid binary solvent system as phytochemical extractant

The usage of ILs as plant bioactive constituents' extractants has a great impact and potential as they alleviate the environmental pollution and improve the selectivity and extraction yields of interesting compounds in the sample pre-treatment process compared to conventional organic solvents. However, ILs have a relatively high polarity due to their charged and asymmetric structures [15], which cause them not to have a good affinity with weak-polar compounds and thus this gives rise to a reduction in the distribution of weak-polar compounds in the IL phase. Although a longer alkyl chain of ILs has a lower polarity, their viscosity is large in accordance with the strong electrostatic and hydrogen bonding interaction between the ions [16, 17]. This drawback impairs the mixing and transferring properties in the extraction process by influencing the dissolution of the compounds in ILs. In exchange, the mixture of ILs and organic molecular solvents as an extraction medium could be an effective approach to solve their flaws. Besides creating a wide-adjusted range of solvent polarity, hydrophobicity, hydrogen-bond acidity, and basicity [18, 19], the addition of miscible molecular solvents as cosolvents helps to break the microscopic hydrogen-bond network and the aggregation of ILs, which significantly reduces the viscosity of ILs and improves the mixing and transferring process in their mediated extraction [20, 21].

3. Materials and methods

3.1. Sample collection and preparation

Derris elliptica roots were first collected from Ladang 2, Faculty of Agriculture, Universiti Putra Malaysia, UPM, Malaysia. The collected roots (**Figure 3a**) were cleaned and cut into smaller parts prior to rapid drying. The cleaned parts of the roots were placed in the freezer to maintain their freshness and dried using a vacuum oven at the temperature of $28 \pm 2^\circ\text{C}$ for 24

hours. Once dried, the roots were ground into smaller particles of the size of approximately 0.86 ± 0.20 mm (**Figure 3b**). The selected sieved, ground samples were weighed prior to the normal soaking extraction process (NSE).

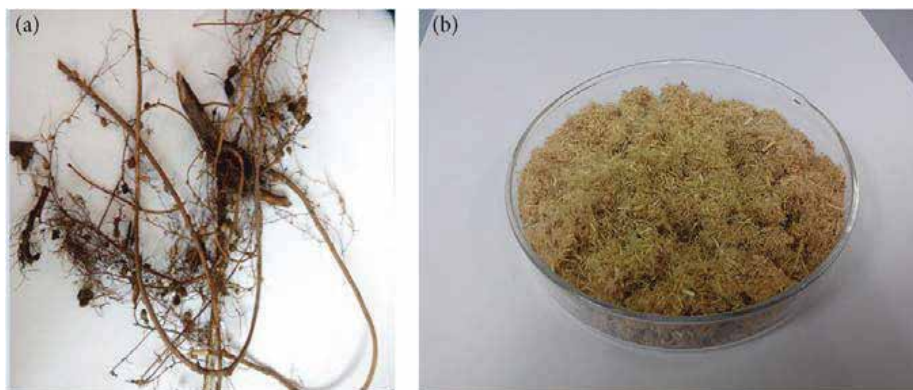


Figure 3. (a) *Derris elliptica* roots and (b) ground fine roots.

3.2. Preparation of binary solvent system

The binary solvent system comprises five selected ILs which are listed as follows: (1) 1-butyl-3-methylimidazolium chloride, [BMIM] Cl; (2) 1-butyl-3-methylimidazolium acetate, [BMIM] OAc; (3) 1-butyl-3-methylimidazolium bis(trifluorosulfonyl)imide, [BMIM] NTf₂; (4) 1-butyl-3-methylimidazolium trifluoromethanesulfonate, [BMIM] OTf; and (5) 1-butyl-1-methylpyrrolidinium chloride, [BMPy] Cl. The binary solvent systems were prepared by adding 2 ml of respective ILs into a round bottom flask (with stopper) containing 18 ml of organic solvent (acetone) with the ratio of 1: 9. To avoid any moisture absorption due to the hygroscopic properties of some ILs, the ILs' collection was carried out in the glove box. The mixtures were stirred by using a magnetic stirrer for 5–6 hours to homogenize the combined solvents. The ratio of 1:9 was based on the exploratory experiment results (data not shown). The mixing of the ILs in acetone was considered homogeneous if no apparent residue appeared in the flask.

3.3. Normal soaking extraction (NSE)

The extraction process was conducted at room temperature ($28 \pm 2^\circ\text{C}$) by using a combination of five different types of ILs and acetone with a mixing ratio of 1:9. The optimized parameters were utilized in accordance to protocols of Zubairi et al. [52, 53] as presented in **Table 3**. The extraction process was carried out by soaking 0.50 g of dried roots in 10 ml of the solvent systems for 24 hours with the solvent-to-solid ratio of 10 ml/g ($n = 3$). The liquid crude extract was collected twice at the 14th hour and 24th hour prior to the reversed-phase high-performance liquid chromatography (RP-HPLC) and thin-layer chromatography (TLC) analysis.

Solvent-to-solid ratio (mg/ml)	10
Weight of raw material (g)	0.50
Raw material particle size (mm)	0.86 ± 0.20
Temperature (°C)	28 ± 2
ILs-to-acetone ratio	1:9
Extraction time (hour)	14

Table 3. Processing parameters used in the rotenone extraction process.

3.4. Liquid crude extract collection

The liquid crude extracts were collected at the 14th hour and 24th hour and placed in the labeled vials. There were 18 samples in total of five different types of solvent system used in three replicates ($n = 3$). Acetone was used as a control solvent. Later, the collected samples were placed in a freezer (-18°C) to prevent any thermal degradation.

3.5. Preparation of fine debris-free liquid crude extract

The collected liquid crude extracts were diluted using analytical grade acetonitrile, Sigma-Aldrich, 95% (v/v) with the dilution factor (DF) of 20. Then, the extracts were filtered by using polytetrafluoroethylene (PTFE—0.45 μm pore size) vacuum filtration to remove any fine debris. A 2-ml vial was used to store the extracts prior to the qualitative and quantitative analyses.

3.6. Qualitative analysis using thin-layer chromatography

MERCK Silica gel 60 F₂₅₄ TLC aluminum sheet was used as a stationary phase to observe the presence of rotenone in the liquid crude extracts ($n = 3$). The migrations of rotenone markers were compared with rotenone standard. The markers and their migrated distance were visualized and determined under UV light of 254 and 365 nm wavelengths, respectively. In the development chamber, chloroform and n-hexane were combined and utilized as a mobile phase system with the ratio of 70:30. The retardation factors (R_f) of each extract were calculated by using Eq. (1).

$$\text{Retardation factor } (R_f) = \frac{\text{Migration distance of substance}}{\text{Migration distance of solvent front}} \quad (1)$$

3.7. Quantitative analysis using reversed-phase high-performance liquid chromatography

Approximately 21.80 mg of rotenone standard Dr. Ehrenstorfer GmbH, 93.80% (w/w) was diluted with 50 ml of acetonitrile in a volumetric flask. The stock solution was filtered using Whatman™ filter paper no. 2 with 8 μm pore size. The quantitative analysis was completed by using Symmetry® C18 5 μl column, Waters with the internal diameter of 4.6

and 150 mm in length. The physical parameters involved in the RP-HPLC are as follows: (1) 0.7 ml/min flow rate; (2) injection volume of 20 μ l; (3) mobile phase of acetonitrile and deionized water with the ratio of 60:40 and (4) photodiode array detector (PDA) wavelength of 294 nm.

4. Results and discussion

4.1. Solubility of ionic liquids (ILs) in acetone

To enhance the rotenone extraction capacity, several ionic liquids were selected preliminarily. However, there was a drawback with regard to their solubility in organic solvents. The solubility of the selected ILs in acetone was observed by conducting a normal mixing with the ratio of 1:9. An exploratory experiment implemented revealed that the higher the amount of ILs used in the mixture, the higher the tendency of the ILs to produce undissolved solid residue (data not shown). Of the five selected ILs, only 1-butyl-3-methylimidazolium acetate, [BMIM] OAc, 1-butyl-3-methylimidazolium bis(trifluorosulfonyl)imide, [BMIM] NTf₂, and 1-butyl-3-methylimidazolium trifluoromethanesulfonate, [BMIM] OTf could be easily homogenized. In contrast, 1-butyl-3-methylimidazolium chloride, [BMIM] Cl and 1-butyl-1-pyrrolidinium chloride, [BMPy] Cl required a longer time to be homogenized (with the aid of heating at 80°C prior to mixing with acetone) which this could be possibly due to their physical properties (solid form at ambient temperature) and a specific range of organic solvent polarity, so that the solubility of the ILs in the organic solvent could be achieved. Theoretically, ionic liquids are miscible with an organic solvent of a medium to a high dielectric constant (ϵ) and they become immiscible with a low dielectric constant (ϵ) [54, 55]. Thus, the solubility of all of the selected ILs was considered satisfactory as there was no apparent residue appeared in the flask due to the high dielectric constant of acetone that aided the solubility of both chemicals.

4.2. Qualitative analysis of rotenone

The qualitative analysis of thin-layer chromatography (TLC) was performed to identify the existence of rotenone in the extracts of all of the binary solvent systems used. **Figure 4** displays the images of rotenone markers visualized under the UV light of 254 nm. All samples exhibited the presence of rotenone markers in the extracts. On the other hand, **Table 4** shows the migration distance (cm) and retardation factor (R_f) of rotenone in a standard solution and liquid crude extracts. The results indicated that the rotenone's R_f value in a standard solution and all extracts (including control) were determined to be insignificantly different when compared to each other ($p > 0.05$). However, there were still a lot of impurities (unknown markers left behind rotenone) as presented in **Figure 4**. For that reason, a purification process of the liquid crude extracts via high-vacuum pressure liquid chromatography (VLC) is highly recommended as to increase the accuracy of rotenone and its derivative compounds' identification [54, 56].

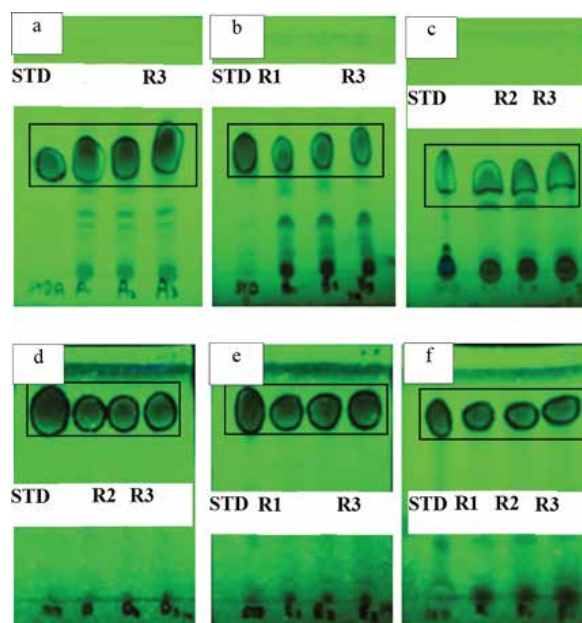


Figure 4. Visualization of rotenone migration markers of five different types of binary solvent systems used at the 14th hour of extraction. The markers were visualized on the alumina-based TLC plate under the UV light of 254 nm. (a) Acetone; (b) [BMIM] Cl; (c) [BMIM] Oac; (d) [BMIM] NTF₂; (e) [BMIM] OTF and (f) [BMP] Cl. The dark circled markers of STD and R (R1, R2, and R3) represent the rotenone standard and replication of each of the binary solvent systems used.

Binary solvent system	Rotenone migration distance, D_s (cm)		Retardation factor (R_f)	
	14 hour	24 hour	14 hour	24 hour
Rotenone standard ^a	1.80 ± 0.05	2.60 ± 0.03	0.45 ± 0.04	0.65 ± 0.03
Control (acetone)	2.03 ± 0.06	2.60 ± 0.01	0.51 ± 0.02	0.65 ± 0.04
[BMIM] Cl + acetone	1.93 ± 0.06	2.20 ± 0.02	0.49 ± 0.01	0.55 ± 0.01
[BMIM] Oac + acetone	1.53 ± 0.06	1.40 ± 0.04	0.39 ± 0.01	0.35 ± 0.01
[BMIM] NTF ₂ + acetone	3.20 ± 0.01	2.17 ± 0.06	0.80 ± 0.01	0.54 ± 0.01
[BMIM] OTF + acetone	3.20 ± 0.08	1.70 ± 0.07	0.80 ± 0.08	0.43 ± 0.06
[BMP] Cl + acetone	3.10 ± 0.00	2.93 ± 0.06	0.78 ± 0.00	0.74 ± 0.01

^a Rotenone standard was prepared in acetone + ILs.

Table 4. Qualitative analysis of rotenone via TLC on varied binary solvent systems.

4.3. Quantitative analysis of rotenone content

Table 5, Figures 5 and 6 show the concentration (mg/ml) and yield of rotenone, % (w/w), respectively, from five different types of binary solvent systems extracted at the 14th hour

and 24th hour. The dependent variables were calculated based on the external standard method of RP-HPLC. The retention times of the rotenone in the standard solution (8.83 mins) and liquid crude extract (8.82 mins) are shown in **Figures 7 and 8**, respectively. Overall, it was observed that the binary solvent system of 1-butyl-3-methylimidazolium trifluoromethanesulfonate, [BMIM] OTf produced the highest rotenone concentration of 4.04 ± 0.34 and 4.19 ± 0.48 mg/ml as compared to the others ionic liquids and control solvent (acetone) ($p < 0.05$) at the 14th hour and 24th hour, respectively. The highest yield of rotenone ($2.69 \pm 0.21\%$ (w/w) and $2.03 \pm 0.11\%$ (w/w) in dried roots) was also determined in the 1-butyl-3-methylimidazolium trifluoromethanesulfonate, [BMIM] OTf solvent system at the 14th hour and 24th hour, respectively. However, both of the optimized processing parameters and the control extract (acetone) reported in the previous study resulted in only $2.44 \pm 0.02\%$ (w/w) [8] and $2.44 \pm 0.09\%$ (w/w) with the concentration of 3.65 ± 0.13 mg/ml respectively. The results were approximately 10.25% lower than that of the yield of rotenone extracted using a combination of [BMIM] OTf: acetone ($p < 0.05$).

This phenomenon can be explained from the perspective of the types of ILs. Of the five different ILs, four of them have the same cation but different anions ([BMIM] OTf, [BMIM] OAc, [BMIM] NTf₂, [BMIM] Cl), and one with the same anion but a different cation ([BMPy] Cl). The increase of the rotenone yield is related to the anion and cation of ILs as ILs have different polarities depending on the anion and cation presence. ILs' polarity is referred to Kamlet-Taft parameters such as polarity (π^*), hydrogen bond basicity (β) and hydrogen bond acidity (α) [46]. ILs' hydrogen bond basicity (β) depends on anion, while hydrogen bond acidity (α) depends on the cation. [BMIM] OTf has lower hydrogen bond basicity compared to [BMIM] OAc and [BMIM] Cl, but higher than that of [BMIM] NTf₂ ($[\text{OAc}]^- > [\text{Cl}]^- > [\text{OTf}]^- > [\text{NTf}_2]^-$) and has hydrogen bond acidity higher than that of [BMPy] Cl.

The rotenone compound is an acidic isoflavonoid compound that consists of ketonic chemical groups (R-C(=O)-R) [22] which has the potential of interacting with intermediate-polar solvents. It can be easily dissolved in moderate-polar organic solvents (e.g., methanol, chloroform, and acetone) [23] and sparingly soluble in water [24]. These are the factors that lead to the increase in the rotenone yield extracted when [BMIM] OTf with mid polarities is used as the extraction medium. The abundant presence of anion [OTf]⁻ helped to attract more hydroxyl groups of rotenone to form more hydrogen bonds [25, 26]. With respect to the impact of the ILs' cation, [BMIM] Cl and [BMPy] Cl on rotenone extraction, it was discovered that the rotenone yield extracted was high when the cation [BMIM]⁺ was used. This was due to the presence of an acid proton in the imidazole ring [32], which had the potential to form the hydrogen bond with oxygen of the rotenone compounds. The significant increase in the rotenone content can be explained in relation to several aspects as follows: (1) the trend of functional groups of rotenone toward foreign charge and (2) the capacity of the IL in the vicinity of various charges. For that reason, any combination of ionic liquids and middle-polar organic solvents does not only optimize the absorption of solute into the solvent due to the low viscosity but is also even able to increase the opportunities for extracting higher rotenone compounds.

The previous study also revealed that the solubility of flavonoids and their derivatives could be increased by using ILs, as the components were greatly an anion-dependent [25]. The anionic potency of both organic solvent and ILs in extracting a large amount of bioactive compounds (e.g., rotenone) and moving into the solvent systems was significantly undeniable as both chemicals facilitated the extraction process via solvation power and multiple interactions (e.g., hydrogen bonding, polarity, ionic charge-to-charge, and π - π , π -n) with the analysis [26, 27].

Solvent system type	Concentration (mg/ml) (\pm SD)		Yield (% w/w) (\pm SD)	
	14 hour	24 hour	14 hour	24 hour
Acetone (control)	3.65 \pm 0.13	3.50 \pm 0.02	2.44 \pm 0.09	1.73 \pm 0.09
[BMIM] Cl:Acetone	2.73 \pm 0.00	2.57 \pm 0.02	2.00 \pm 0.06	1.55 \pm 0.01
[BMIM] OAc:Acetone	2.51 \pm 0.02	2.69 \pm 0.14	1.60 \pm 0.01	1.18 \pm 0.06
[BMIM] NTf ₂ :Acetone	3.70 \pm 0.11	3.80 \pm 0.03	2.42 \pm 0.14	2.07 \pm 0.07
[BMIM] OTf:Acetone	4.04 \pm 0.34	4.19 \pm 0.48	2.69 \pm 0.21	2.03 \pm 0.11
[BMPy] Cl:Acetone	2.66 \pm 0.20	2.37 \pm 0.26	1.78 \pm 0.08	1.27 \pm 0.16

Table 5. Rotenone quantitative analysis using RP-HPLC using different binary solvent systems at the 14th hour and 24th hour of extraction time.

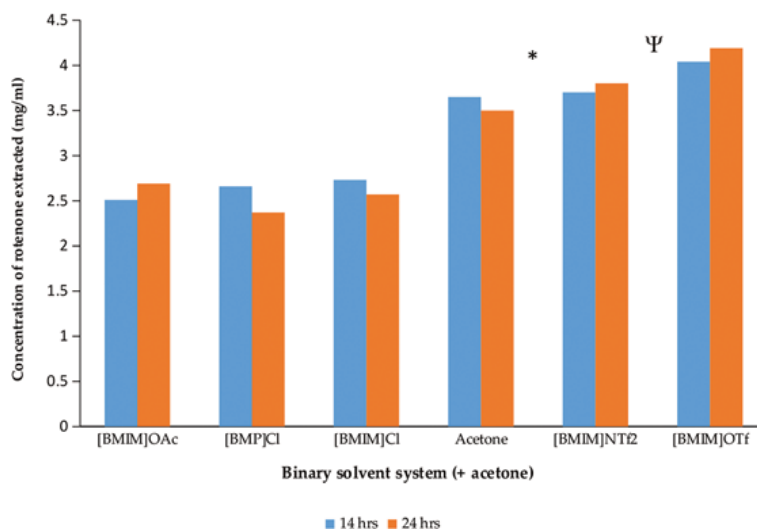


Figure 5. Concentration of rotenone (mg/ml) with respect to five different types of binary solvent systems. $^{\Psi}p < 0.05$ —[BMIM] OTf: acetone was the best binary solvent system to procure the highest rotenone concentration (mg/ml) ($n = 3$). $^*p < 0.05$ —[BMIM] NTf₂: acetone and acetone extract produced a high concentration as compared to the [BMIM] OAc, [BMPy] Cl and [BMIM] Cl.

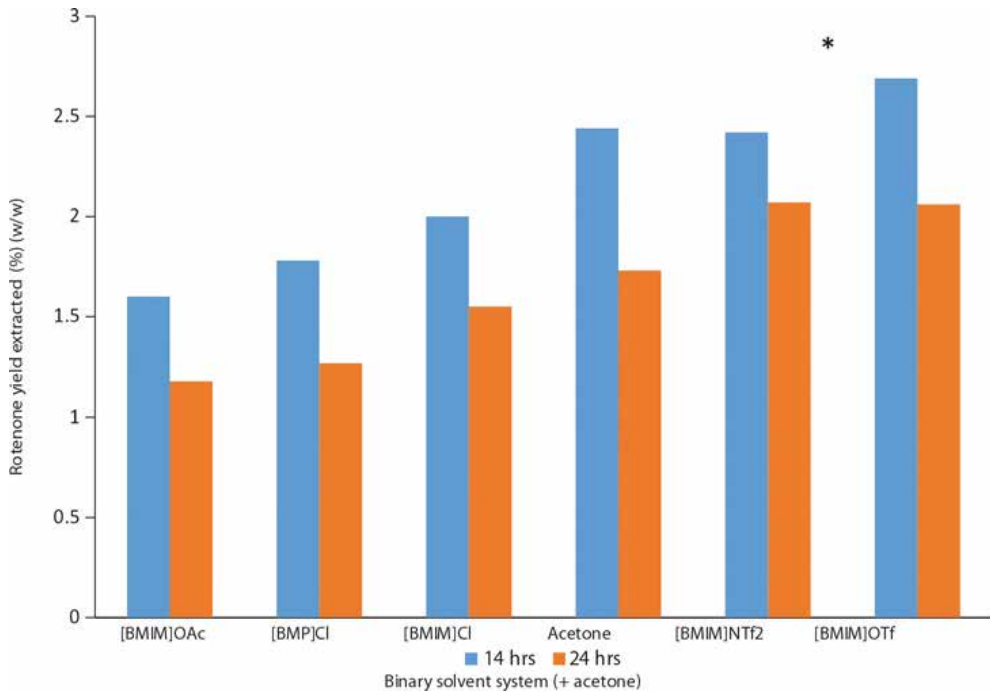


Figure 6. Yield of rotenone, % (w/w) in dried roots with respect to five different types of binary solvent systems. * $p < 0.05$ – [BMIMI] OTf : acetone was the best binary solvent system to procure the highest rotenone content in dried roots ($n = 3$).

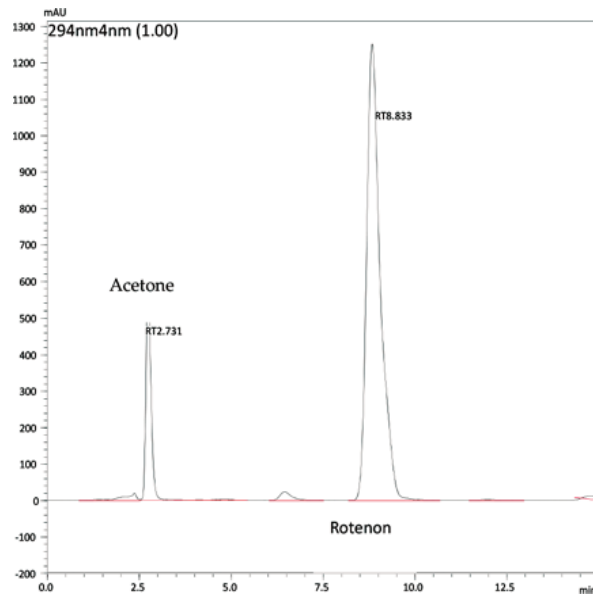


Figure 7. Chromatogram of rotenone standard.

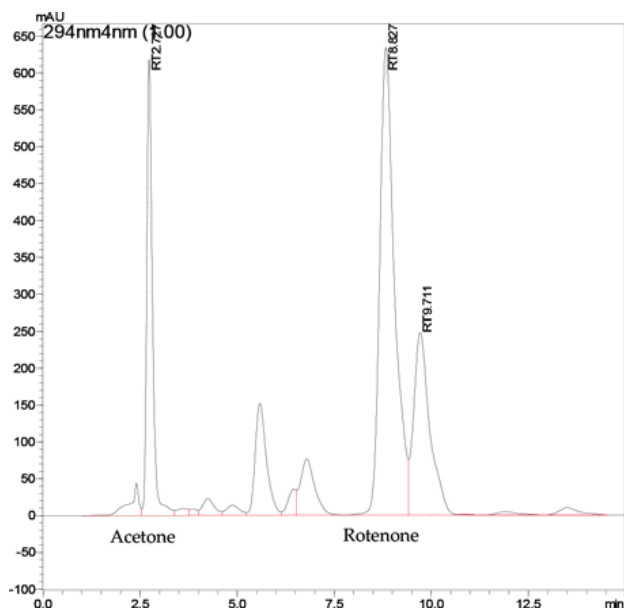


Figure 8. Chromatogram of [BMIM] OTf: acetone binary solvent system at the 14th hour.

5. Conclusion

In conclusion, the best ionic liquid to assist the organic solvent (acetone) extraction system was 1-butyl-3-methylimidazolium trifluoromethanesulfonate, [BMIM] OTf. The selected binary solvent system had contributed to the highest rotenone content of $2.69 \pm 0.21\%$ (w/w) with a concentration of 4.04 ± 0.34 mg/ml at the 14th hour (the time of the exhaustive extraction as reported in the previous study). The rotenone content was 10.25% higher than the optimized parameter of the acetone extract (control) ($p < 0.05$). Therefore, the addition of certain ionic liquids to the organic solvent will potentially give rise to a significant increase in the amount of bioactive constituent in the phytochemical extraction process. Further study is required to optimize several processing parameters especially on the mixing ratio between the ILs and organic solvent in order to verify the increase in the rotenone content as the solubility problem between both chemicals, is relatively prominent.

Acknowledgements

We would like to thank the Ministry of Higher Education (MOHE), Malaysia for providing financial support to this project (FRGS/2/2013/TK04/UKM/03/1 and GGPM-2013-078).

Author details

Zetty Shafiqah Othman, Nur Hasyareeda Hassan and Saiful Irwan Zubairi*

*Address all correspondence to: saiful-z@ukm.edu.my

Faculty of Science and Technology, School of Chemical Sciences and Food Technology,
Universiti Kebangsaan Malaysia (UKM), Bangi, Selangor, Malaysia

References

- [1] Stoll, G. Natural Crop Protection Based on Local Farm Resources in the Tropics and Subtropics, Weikersheim, Margraf Publishers Scientific Books, Germany. 1988.
- [2] Gingerich, W. H. Tissue distribution and elimination of rotenone in rainbow trout. *Aquatic Toxicology*. 1986; **8**(1):27–40.
- [3] Ray David, E. Pesticides derived from plants and other organism. In *Handbook of Pesticide Toxicology*, volume 2, Classes of Pesticides. Wayland J. Hayes & Edward R. Laws (eds.) Academic Press, NY. 1991.
- [4] John, R. A. and Ron, R. K. Insect control. *Journal of Economic Entomology*. 1944; **37**: 400–408.
- [5] Andel, T. V. The diverse uses of fish-poison plants in Northwest Guyana. *Economic Botany*. 2000; **54**(4): 500–512.
- [6] Schnick, R. A. A review of literature on the use of rotenone in fisheries. United States Department of the Interior, Fish and Wildlife Service, Wisconsin. 1974.
- [7] Bradbury, A. Rotenone and Trout Stocking n.p. Washington Department of Game Fisheries Management Division. 1986.
- [8] Zubairi, S. I. The yield and biological activity (LC50) of rotenone extracted from *Derris elliptica*, Universiti Teknologi Malaysia, Faculty of Chemical and Natural Resources Engineering. 2006.
- [9] Fu, X., Shugui, D. and Yu, Z. Comparison of extraction abilities between ionic liquids and dichloromethane. *Chinese Journal of Analytical Chemistry*. 2006; **34**(5): 598–602.
- [10] Bogdanov, M. G., Petkova, D., Hristeva, S., Svinyarov, I. and Kantlehner, W. New guanidinium-based room-temperature ionic liquids. Substituent and anion effect on density and solubility in water. *Zeitschrift für Naturforschung. B, A Journal of Chemical Sciences*. 2010; **65**(1): 37.

- [11] Endres, F. and El Abedin, S. Z. Air and water stable ionic liquids in physical chemistry. *Physical Chemistry*. 2006; **8**(18): 2101–2116.
- [12] Bonhote, P., Dias, A. -P., Papageorgiou, N., Kalyanasundaram, K. and Grätzel, M. Hydrophobic, highly conductive ambient-temperature molten salts. *Inorganic Chemistry*. 1996; **35**(5): 1168–1178.
- [13] Handy, S. T. Room temperature ionic liquids: different classes and physical properties. *Current Organic Chemistry*. 2005; **9**(10): 959–988.
- [14] Rooney, D., Jacquemin, J. and Gardas, R. Thermophysical properties of ionic liquids. *Topics in Current Chemistry* 2009; **290**: 185–212.
- [15] Reichardt, C. Polarity of ionic liquids determined empirically by means of solvatochromic pyridinium N-phenolate betaine dyes. *Green Chemistry*. 2005; **7**(5): 339–351.
- [16] Huddleston, J. G., Visser, A. E., Reichert, W. M., Willauer, H. D., Broker, G. A. and Rogers, R. D. Characterization and comparison of hydrophilic and hydrophobic room temperature ionic liquids incorporating the imidazolium cation. *Green Chemistry*. 2001; **3**(4): 156–164.
- [17] Xie, L.-L., Favre-Reguillon, A., Wang, X.-X., Fu, X., Pellet-Rostaing, S., Toussaint, G., Geantet, C., Vrinat, M. and Lemaire, M. Selective extraction of neutral nitrogen compounds found in diesel feed by 1-butyl-3-methyl-imidazolium chloride. *Green Chemistry*. 2008; **10**(5): 524–531.
- [18] Mancini, P. M., Fortunato, G. G. and Vottero, L. R. Molecular solvent/ionic liquid binary mixtures: designing solvents based on the determination of their microscopic properties. *Physics and Chemistry of Liquids*. 2004; **42**(6): 625–632.
- [19] Mellein, B. R., Aki, S. N., Ladewski, R. L. and Brennecke, J. F. Solvatochromic studies of ionic liquid/organic mixtures. *The Journal of Physical Chemistry B*. 2007; **111**(1): 131–138.
- [20] Heintz, A. Recent developments in thermodynamics and thermophysics of non-aqueous mixtures containing ionic liquids. A review. *The Journal of Chemical Thermodynamics*. 2005. **37**(6): 525–535.
- [21] Gómez, E., González, B., Domínguez, Á., Tojo, E. and Tojo, J. Dynamic viscosities of a series of 1-alkyl-3-methylimidazolium chloride ionic liquids and their binary mixtures with water at several temperatures. *Journal of Chemical and Engineering Data*. 2006; **51**(2): 696–701.
- [22] Ahmad, F. and Raji, H. Kimia hasilan semula jadi dan tumbuhan ubatan. *Dewan Bahasa dan Pustaka*. 1993.
- [23] Cabizza, M., Angioni, A., Melis, M., Cabras, M., Tuberoso, C. V. and Cabras, P. Rotenone and rotenoids in cube resins, formulations, and residues on olives. *Journal of Agricultural and Food Chemistry*. 2004; **52**(2): 288–293.
- [24] Dhaouadi, A., Monser, L. and Adhoum, N. Removal of rotenone insecticide by adsorption onto chemically modified activated carbons. *Journal of Hazardous Materials*. 2010; **181**(1): 692–699.

- [25] Guo, Z., Lue, B.-M., Thomasen, K., Meyer, A. S. and Xu, X. Predictions of flavonoid solubility in ionic liquids by COSMO-RS: experimental verification, structural elucidation, and solvation characterization. *Green Chemistry*. 2007; 9(12): 1362–1373.
- [26] Anderson, J. L., Ding, J., Welton, T. and Armstrong, D. W. Characterizing ionic liquids on the basis of multiple solvation interactions. *Journal of the American Chemical Society*. 2002; 124(47): 14247–14254.
- [27] Du, F.-Y., Xiao, X.-H. and Li, G.-K. Application of ionic liquids in the microwave-assisted extraction of trans-resveratrol from *Rhizma Polygoni Cuspidati*. *Journal of Chromatography A*. 2007; 1140(1): 56–62.
- [28] Gonfa, G., Bustam, M., Man, Z. and Mutalib, M. A. Unique structure and solute–solvent interaction in imidazolium based ionic liquids: A review. *Asian Transactions on Engineering*. 2011; 1: 24–34.
- [29] Geetanjali S. and Anil K. Ionic liquids: Physico-chemicals, solvent properties and their applications in chemical processes. *Indian Journal of Chemistry*. 2008; 47A: 495–503.
- [30] Weingärtner, H. Understanding ionic liquids at the molecular level: facts, problems, and controversies. *Angewandte Chemie International Edition*. 2008; 47(4): 654–670.
- [31] Nobuoka, K., Kitaoka, S., Iio, M., Harran, T. and Ishikawa, Y. Solute–solvent interactions in imidazolium camphorsulfonate ionic liquids. *Physical Chemistry Chemical Physics*. 2007; 9(44): 5891–5896.
- [32] Hunt, P. A., Kirchner, B. and Welton, T. Characterising the electronic structure of ionic liquids: An examination of the 1-butyl-3-methylimidazolium chloride ion pair. *Chemistry: A European Journal*. 2006; 12(26): 6762–6775.
- [33] Aggarwal, A., Lancaster, N. L., Sethi, A. R. and Welton, T. The role of hydrogen bonding in controlling the selectivity of Diels–Alder reactions in room-temperature ionic liquids. *Green Chemistry*. 2002; 4(5): 517–520.
- [34] Znamenskiy, V. and Kobrak, M. N. Molecular dynamics study of polarity in room-temperature ionic liquids. *The Journal of Physical Chemistry B*. 2004; 108(3): 1072–1079.
- [35] Dieter, K. M., Dymek, C. J., Heimer, N. E., Rovang, J. W. and Wilkes, J. S. Ionic structure and interactions in 1-methyl-3-ethylimidazolium chloride-aluminium chloride molten salts. *Journal of the American Chemical Society*. 1988; 110(9): 2722–2726.
- [36] Iwata, K., Okajima, H., Saha, S. and Hamaguchi, H.O. Local structure formation in alkyl-imidazolium-based ionic liquids as revealed by linear and nonlinear Raman spectroscopy. *Accounts of Chemical Research*. 2007; 40(11): 1174–1181.
- [37] Raju, S. and Balasubramanian, S. Molecular dynamics simulation of model room temperature ionic liquids with divalent anions. *Indian Journal of Chemistry-Section A: Inorganic, Physical, Theoretical and Analytical Chemistry*. 2010; 49(5-6): 721–726.

- [38] Deetlefs, M., Hardacre, C., Nieuwenhuyzen, M., Padua, A. A., Sheppard, O. and Soper, A. K. Liquid structure of the ionic liquid 1,3-dimethylimidazolium bis ((trifluoromethyl) sulfonyl) amide. *The Journal of Physical Chemistry B*. 2006; **110**(24): 12055–12061.
- [39] Triolo, A., Russina, O., Bleif, H.-J. and Di, C. E. Nanoscale segregation in room temperature ionic liquids. *The Journal of Physical Chemistry B*. 2007; **111**(18): 4641–4644.
- [40] Zhao, W., Leroy, F., Heggen, B., Zahn, S., Kirchner, B., Balasubramanian, S. and Müller-Plathe, F. Are there stable ion-pairs in room-temperature ionic liquids? Molecular dynamics simulations of 1-n-butyl-3-methylimidazolium hexafluorophosphate. *Journal of the American Chemical Society*. 2009; **131**(43): 15825–15833.
- [41] Fernandes, A. M., Rocha, M. A., Freire, M. G., Marrucho, I. M., Coutinho, J. A. and Santos, L. M. Evaluation of cation–anion interaction strength in ionic liquids. *The Journal of Physical Chemistry B*. 2011; **115**(14): 4033–4041.
- [42] Hamaguchi, H. O., Saha, S., Ozawa, R. and Hayashi, S. Raman and X-ray Studies on the Structure of [bmim] X. In *ACS Symposium Series Oxford University Press*. 2005; **901**: 68–78.
- [43] Pringle, J. M., Golding, J., Baranyai, K., Forsyth, C. M., Deacon, G. B., Scott, J. L. and MacFarlane, D. R. The effect of anion fluorination in ionic liquids—physical properties of a range of bis (methanesulfonyl) amide salts. *New Journal of Chemistry*. 2003; **27**(10): 1504–1510.
- [44] Xu, W., Wang, L.-M., Nieman, R. A. and Angell, C. A. Ionic liquids of chelated orthoborates as model ionic glassformers. *The Journal of Physical Chemistry B*. 2003; **107**(42): 11749–11756.
- [45] Ngo, H. L., LeCompte, K., Hargens, L. and McEwen, A. B. Thermal properties of imidazolium ionic liquids. *Thermochimica Acta*. 2000; **357**: 97–102.
- [46] Kamlet, M.J., Abboud, J. L. M., Taft, R. W. *Progress in Physical Organic Chemistry*. 1981; **13**: 485.
- [47] Coleman, S., Byrne, R., Minkovska, S. and Diamond, D. Thermal reversion of spirooxazine in ionic liquids containing the [NTf₂][−] anion. *Physical Chemistry*. 2009; **11** (27): 5608–5614.
- [48] Chiappe, C. and Pieraccini, D. Determination of ionic liquids solvent properties using an unusual probe: The electron donor-acceptor complex between 4,4'-bis (dimethylamino)-benzophenone and tetracyanoethene. *The Journal of Physical Chemistry A*. 2006; **110**(14): 4937–4941.
- [49] Jeličić, A., García, N., Löhmannsröben, H.-G. and Beuermann, S. Prediction of the ionic liquid influence on propagation rate coefficients in methyl methacrylate radical polymerizations based on Kamlet-Taft solvatochromic parameters. *Macromolecules*. 2009; **42**(22): 8801–8808.

- [50] Doherty, T. V., Mora-Pale, M., Foley, S. E., Linhardt, R. J. and Dordick, J. S. Ionic liquid solvent properties as predictors of lignocellulose pretreatment efficacy. *Green Chemistry*. 2010; **12**(11): 1967–1975.
- [51] Wu, Y., Sasaki, T., Kazushi, K., Seo, T. and Sakurai, K. Interactions between spiropyrans and room-temperature ionic liquids: photochromism and solvatochromism. *The Journal of Physical Chemistry B*. 2008. **112**(25): 7530–7536.
- [52] Zubairi, S. I., Sarmidi, M. R. and Aziz, R. A. The effects of raw material particles size, types of solvents and solvent-to-solid ratio on the yield of rotenone extracted from *Derris elliptica* roots. *Sains Malaysiana*. 2014; **43**(5): 707–713.
- [53] Zubairi, S. I., Sarmidi, M. R. and Aziz, R. A. A preliminary study of rotenone exhaustive extraction kinetic from *Derris elliptica* dried roots using normal soaking extraction (NSE) method. *Advances in Environmental Biology*. 2014; **8**(4): 910–915.
- [54] Touchstone, J. C. *Practice of Thin Layer Chromatography*. John Wiley & Sons. 1992.
- [55] Poole, C. F. and Poole, S. K. Extraction of organic compounds with room temperature ionic liquids. *Journal of Chromatography A*. 2010; **1217**(16): 2268–2286.
- [56] Zubairi, S. I., Sarmidi, M. R. and Aziz, R. A. Identification of bio-active constituents from *Derris elliptica* liquid crude extract using liquid chromatographic method coupled with high vacuum pressure. *Advances in Environmental Biology*. 2014; **8**(2): 437–440.

Use of Ionic Liquids in Solid-Liquid Separation Processes

Lavinia Lupa , Petru Negrea and Adriana Popa

Additional information is available at the end of the chapter

<http://dx.doi.org/10.5772/65890>

Abstract

This chapter reports the possible use of ionic liquids (ILs) in solid-liquid separation processes by their immobilization in suitable solid supports. This method presents some benefits such as economical one—due to the fact that a smaller quantity of ILs is used and the loss of ILs in the aqueous phase is avoided; and second the efficiency benefit—because the advantages of the ILs are combined with the properties of the solid support, and this enhances the removal process of metal ions from aqueous solutions and could be successfully used in the removal processes of metal ions from aqueous solutions containing trace amounts. The type of solid supports used for the immobilization of different ILs, and the methods used for the immobilization were discussed. Also the adsorption efficiency of these ionic liquid immobilized solid supports in the removal process of different metal ions (Cr, Hg, Pt, Au, Pd, Cs, Sr, Tl, etc.) from aqueous solutions were presented. The inorganic materials present a higher efficiency to be used as solid supports for the immobilization of the ILs. It was observed that the physical method of impregnation, especially ultrasonication, has a positive effect on the adsorption capacities of the materials obtained.

Keywords: ionic liquids, heavy metals, impregnation, encapsulation, adsorption

1. Introduction

The huge quantities of waste, discharged from various industries and from human activities, and their negative effect on human health and the environment, have led to some stringent regulations. These have driven researchers to find and develop some new efficient methods for the removal and recovery of organic and mineral contaminants from discharged wastes.

Many separation techniques have been proposed especially for the treatment of wastewaters containing heavy metals, such as precipitation [1, 2] ion-exchange [3, 4] liquid-liquid

extraction [5, 6] and membrane processes [7]. These processes may encounter some technical, economical and environmental problems, which limit their application [8]. Even if the precipitation processes results in an efficiency of 90%, the disadvantage remains that precipitation agents are needed to reach the maximum admitted value for discharge. Thus, after treatment, huge amounts of highly contaminated sludge and filter backwash liquid remain [8–10]. Ion exchange, the most extensively used method is expensive for large-scale applications [9]. Membrane processes, especially reverse osmosis, also present economic disadvantages [8, 10].

A widely applied method for the separation of metal ions from an aqueous solution is solvent extraction. Recently, this method has become more attractive because instead of using volatile organic compounds (VOCs) ionic liquids (ILs) or so-called “green extractants” were used, due to their well-known properties [11–13]. Even so, the liquid-liquid extraction method has some drawbacks such as: use of large quantities of ILs [10, 14], the possible loss of IL in the aqueous phase due to incomplete phase separations [15–19], it can only be considered efficient for the treatment of aqueous solutions with high metal concentrations [9, 18–21]. Therefore, there is an increased demand to find alternative technologies to overcome the drawbacks of the liquid-liquid extractions, which should be competitive, efficient and environmentally friendly to achieve targets for sustainable growth. An answer to this problem is the use of ionic liquid in solid-liquid separation processes. This can happen if the ILs are immobilized in a suitable solid support. In this way (i) the minimum amount of ILs is consumed, (ii) the extraction and stripping step is combined into a single step, (iii) the immobilization reduces the loss of ILs in the aqueous phase, (iv) the advantages of the ILs are combined with the properties of the solid support, and this enhances the removal process of metal ions from aqueous solutions, (v) the ILs immobilized solid support obtained can be used for the removal of metal ions from dilute and complex solutions with possible use in simple fixed bed columns for commercial applications [14, 22–25].

This chapter reports various aspects of the use of ILs in solid-liquid separation processes by their immobilization in suitable solid support such as:

1. The type of materials used as solid supports for the immobilization of various ILs.
2. The kind of methods used for the immobilization of various ILs onto suitable solid supports.
3. The use of solid support immobilized with ILs in the process of removing various metal ions from aqueous solutions using solid-liquid separation processes.

2. Materials used as solid support for ILs immobilization

The use of ILs immobilized on a suitable solid support represents a link between the solvent extraction and adsorption processes, for the separation of various pollutants from aqueous solutions. The product obtained should develop an increased selectivity, a higher degree of adsorbent-adsorbate interactions, and should have mechanical stability [26]. All these prop-

erties are influenced by the used solid support, by the type of the immobilized ILs and by the method used for the immobilization of the ILs onto the solid support.

A number of different inorganic and organic solid supports have been tested for the immobilization of ILs during the last decade. The surface properties and the specific surface area are the two most relevant criteria used for the selection of a suitable solid support [25, 26]. Some researchers consider that the macroporous organic polymers are suitable to be used as solid supports due to their high surface area and good mechanical stability, faster kinetics for the removal of contaminant even from dilute solutions, ease of regeneration and high adsorption capacity. On the other hand, other researchers consider that inorganic types of solid support present some advantages over organic supports such as higher thermal and chemical stability, well-ordered periodic pore structure and controllable pore diameter [26]. Therefore, in this section, the discussion is about the most frequently used solid supports, the ones used for immobilization of ILs, which are reported in literature, and also the considerations that have led to the researches focus on them.

Polymer-supported reagents are widely employed in the separation of metal ions. Amberlite XAD resins were a kind of commercial resin frequently used as a solid support for the immobilization of various ILs [18, 20, 24, 25] with uniform pore size distribution, high surface area and good mechanical and chemical stability. Their surface properties differ in function depending on their structure [27, 28]: XAD-2, XAD-4 are hydrophobic, XAD-7 and XAD-8 are moderate hydrophilic and have a higher polarity compared with the other two. For these reasons, the group of Guibal, Gallardo and Navarro used XAD-7 resin as a solid support for the impregnation of tetraalkyl phosphonium ionic liquid—tetradecyl (trihexyl) phosphonium chloride—Cyphos IL-101 and used the obtained materials in the removal of cadmium, zinc and bismuth, respectively [24, 27, 28]. Yang et al. impregnated the Amberlite XAD-7 resin with Cyphos IL-104 in order for it to be used for Cr(VI) removal from aqueous solutions [20]. Cr(VI) removal was also studied by Saha et al. [29] through adsorption onto Amberlite XAD-7 impregnated with Aliquat 336. Kalidhasan et al. used an ion exchange resin as a solid support because this type of resin has a high degree of metal recovery and selectivity. Their study was made with Dowex 1 x 8, a styrene-divinylbenzene polymeric resin containing quaternary ammonium functional groups with chloride (Cl^-) and a total exchange capacity of 1.2 mequiv/mL. They impregnated Aliquat 336 ionic liquid onto Dowex [30]. Popa and co-workers used styrene-divinylbenzene as a solid support grafted with different pendant groups (triphenylphosphonium, *iso*-propylphosphonate and aminoethylaminomethyl) [31]. Styrene-divinylbenzene grafted with aminoethylaminomethyl groups was impregnated with three different ionic liquids: (trihexyl) tetradecyl phosphonium—Cyphos IL-101, 1-octyl-3-methyl imidazolium tetrafluoroborate—OmimBF₄; and 1-butyl-3-methyl imidazolium hexafluorophosphate—(BmimPF₆). This was done in order to determine the synergistic effect of the functional groups grafted on the polymer and the functional groups from the impregnated ionic liquid in the removal process of Tl⁺ and Sr²⁺ ions from aqueous solutions [32].

The disadvantage of synthetic resins is the fact that at the end of their life cycle they must be degraded and their thermal degradation produces toxic gaseous compounds. For this reason, an appropriate elimination procedure should be developed. This disadvantage could be

eliminated by using some biopolymers (such as alginate, cellulose and chitosan) as a solid support as they have a thermal degradation which is much more environmentally friendly than that of synthetic resins [9, 21]. Using the biopolymers or renewable resources as a solid support for the immobilization of ILs, the process will conform with the principle of sustainable development [10]. The research group of Guibal, Vincent, Campos and other co-workers reported that the Cyphos IL-101 immobilized in biopolymer capsules of alginate and gelatin leads to the obtaining of an efficient sorbent material which was used with success in the processes of recovering of Hg, Pd, Bi, Au and Pt from acidic solutions [9, 10, 21, 33–35].

Zhang et al. [36] proposed the use of poly(vinyl alcohol) (PVA)-alginate matrix gel as a solid support for the immobilization of [A336][MTBA] IL as a new kind of solid-phase extractant for an efficient recovery of Hg(II) from aqueous solutions. PVA is a water-soluble material containing large amounts of hydroxide groups, but it cannot be degraded by microorganism, has a higher mechanical strength and larger durability in high acidic solutions than alginate gel. For this reason, they wanted to design a novel, simple, competitive and environmentally friendly solid-phase sorbent for treatment of wastewaters [36].

Kalidhasan et al. [37] studied the possible adsorption enhancement of cellulose, a natural biodegradable polysaccharide, by its impregnation with methyl trioctyl ammonium chloride. Through appropriate modification of the cellulose by immobilization with an IL, an adsorbent with good mechanical properties is obtained.

Li et al. [38, 39] reported the adsorption performance of an ionic liquid/chitosan/graphene composite. Both materials chitosan and graphene are recognized as excellent adsorbents due to their high surface area and their active sites: amino and hydroxyl groups for chitosan and carbonyl, carboxylic and alcoholic functional groups for graphene. However, their individual use presents some drawbacks such as possible oxidation in acidic solutions, and they are difficult to recycle due to their small size. These individual problems were eliminated by Li and co-workers through the synthesis of a chitosan-graphene oxide composite (MCGO). The MCGO obtained was used as a platform for the impregnation of IL [38–40].

Other researchers focussed on the use of Fe_3O_4 magnetic nanoparticles (MNPs) as a solid support for IL immobilization because of their properties such as unique size and magnetic properties. These were also chosen due to other advantages: ease of preparation and surface modification, high adsorption capacity due to their high surface area, and their simple and convenient separation from solution using a magnetic field [41–44]. The immobilization of IL on MNPs is advantageous because it prevents the aggregation and oxidation of the nanoparticles during the solid-liquid separation processes. Mehdinia et al. [41] used the individual MNPs for the immobilization of Aliquat 336 IL; Chen et al. [42] immobilized 1-alkyl-3 vinyl imidazolium chloride onto MNPs coated with SiO_2 and Zheng et al. [43] studied the immobilization of 1-vinyl-3-hexyl imidazolium bromide on Fe_3O_4 co-precipitated with SiO_2 . Cheng et al. also used a superparamagnetic mesoporous core/shell nanocomposite ($\text{Fe}_3\text{O}_4@n\text{SiO}_2@m\text{SiO}_2$) as a solid support for amino ionic liquids (Si-DHIM- NH_2). The adsorbent obtained was used for removing dye from aqueous solutions [45].

Carbon-based materials are the most widely used adsorbent materials, due to their attractive properties (large surface area, favourable chemical and thermal stability, ease of surface functionalization and modification). Thus, other researchers used these kinds of materials as solid supports for the immobilization of ionic liquids. Activated carbon obtained from palm shell was impregnated with task-specific ionic liquids (trioctyl methyl ammonium thiosalicylate (TOMATS)) by Ismaiel and his collaborators in order to remove mercury from contaminated water. The modification of palm shell-activated carbon by immobilization of the IL led to an increased efficiency in the removal of Hg(II) in comparison with the efficiency of virgin-activated carbon. This is due to the increased number of functional groups (thio groups) present on the surface of the activated carbon [46]. Tokalioglu et al. [47] reported the use of carbon nanospheres as a solid support for IL immobilization.

Nanosized metal oxides, such as Al₂O₃, SiO₂ and TiO₂, have attracted a lot of interest as adsorbents in the solid-liquid separation processes due to their high surface area; crystalline and well-ordered periodic pore structure and chemical, thermal and radiation stability. The main disadvantage of these solids is their lack of selectivity, which can lead to a decrease in adsorption capacity when, in some matrixes there are various interfering ions present with the target metal. This problem can be overcome by chemical or physical modification of the sorbent surface. Therefore, a lot of researchers studied the possible use of these metal oxides as solid supports for the immobilization of ILs [48–58]. Amjadi and Samadi [48] modified the surface of TiO₂ by coating it with 1-hexadecyl-3-methyl imidazolium bromide. Sprynskyy et al. [49] reported the adsorption performance of diatomite modified by chemical treatment with 1-ethyl-3-methyl imidazolium chloride solution in the removal of uranium ions from aqueous solutions. The metal oxide most extensively used as a solid support for IL immobilization is SiO₂. **Table 1** summarizes literature reports on the types of ILs, which have been immobilized onto silica and their applications in solid-liquid separation processes.

In addition to studying silica as a possible solid support for the immobilization of ILs, the research group of Lupa, Negrea and co-workers, tested Florisil, which is a magnesium silicate [58–60]. They impregnated onto Florisil trihexyl (tetradecyl) phosphonium chloride—Cyphos IL-101 ionic liquid and used the adsorbent obtained in the removal of Sr²⁺ [58] and Cs⁺ [59] from aqueous solutions. Also they determined the adsorption performance of Florisil impregnated with various ILs: Cyphos IL-101, OmimBF₄ and BmimPF₆ in the removal process of Tl⁺ ions from aqueous solutions [60]. Another study was carried out by the same group of researchers on the impregnation of Cyphos IL-101 on various organic solid supports (Dowex resin, Amberlite XAD7 and dibenzo-18-Crown-6-crown ether) and inorganic solid supports (Florisil and silica) and their use in the removal of Cd, Pb, Co, Ni, Cr, Cs, Sr, Tl and La. It was demonstrated that the type of solid support used for the immobilization of the ILs affected the adsorption properties of the resulting material [26]. In this study, the highest adsorption capacities were achieved by the inorganic solid supports. This can be explained by the fact that after the impregnation process the particles of the ILs studied were more homogeneously distributed and bonded onto the surface of the inorganic solid supports compared to the organic solid supports, as can be seen from the SEM images presented [26].

No.	Type of ILs immobilized	Method of ILs immobilization	Application of the obtained ILs immobilized silica	References
1.	1-butyl-3-methyl imidazolium hexafluorophosphate [C ₄ MIM][PF ₆]	Stirring method	Cadmium pre-concentration	[50]
2.	N-methyl imidazole	Stirring in the presence of acetonitrile and 3-chloropropyltriethoxysilane	Removal of 12 sulfonylurea herbicides	[51]
3.	Tropine-type chiral ionic liquid with proline anion	Chemical bonding method	Separation of Cu ²⁺ , Fe ³⁺ , Mn ²⁺ and Ni ²⁺ Separation of racemic amino acids	[52]
4.	Trihexyl (tetradecyl) phosphonium bis 2,4,4-trimethyl pentyl phosphonate—Cyphos IL-104	Sol-gel method	Removal of Cr(III,VI)	[53]
5.	Trialkyl methyl ammonium bis 2,4,4-trimethyl pentyl phosphonate—[A336][C272]	Sol-gel method	Removal of Cr(III,VI)	[53]
6.	Trihexyl (tetradecyl) phosphonium bis 2,4,4-trimethyl pentyl phosphonate—Cyphos IL-104 mixed with imidazolium ionic liquid C _n mim ⁺ PF ₆ ⁻	Sol-gel method	Extraction of Yttrium	[54]
7.	1-octyl-3-methyl imidazolium hexafluorophosphate (C ₈ mim ⁺ PF ₆ ⁻) and trialkyl phosphine oxides (Cyanex 923)	Sol-gel method	Extraction of Yttrium	[55]
8.	N,N-EPANTf ₂ which was impregnated onto silica gel activated through chemically bound method with 3-aminopropyltrimethoxysilane (APTMS)	Stirring method	Separation of Zr(IV)	[56]
9.	Trihexyl (tetradecyl) phosphonium chloride—Cyphos IL-101	Dry method of impregnation	Adsorption of Cs ⁺ from aqueous solutions	[57]
10.	Trihexyl (tetradecyl) phosphonium chloride—Cyphos IL-101	Dry method of impregnation	Adsorption of Sr ²⁺ from aqueous solutions	[58]

Table 1. Type of ILs immobilized onto silica.

3. Methods used for the immobilization of ILs on solid supports

There are both chemical and physical methods used for the immobilization of ILs onto suitable solid supports. The chemical methods of immobilization include: the encapsulation of the IL into microcapsules, the chemical bonding method and the sol-gel method. The immobilization of the ILs using a physical technique may be achieved through different processes such as: wet method, dry method, impregnation in the presence of a modifying agent, the dynamic method or ultrasonication method [14, 19, 28].

The immobilization of ILs through encapsulation is, in most cases, carried out in biopolymers, this technique being intensively studied by the research group of Guibal [10, 21, 33–35]. The schematic flow process for obtaining ILs immobilized in biopolymer capsules through encapsulation is presented in **Figure 1**. In the first step, the IL is mixed with a NaOH solution,

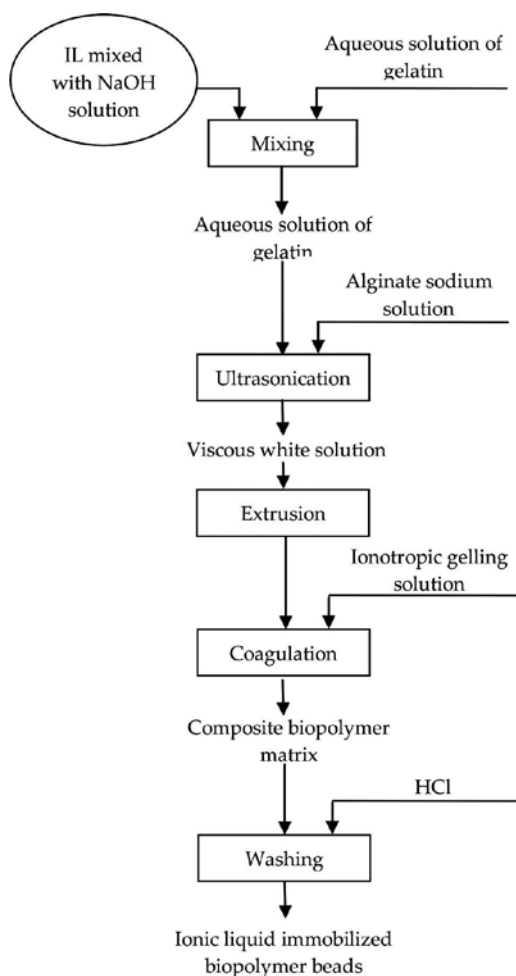


Figure 1. The process of IL immobilization in biopolymer capsules through encapsulation.

then it is mixed with an aqueous solution of gelatin. To the gelatin-ionic liquid solution is added alginate sodium solution and the suspension is ultrasonicated thus obtaining a slightly viscous white solution. This is extruded through a nozzle into an ionotropic gelling solution of CaCl_2 . The beads obtained are kept in the coagulation bath overnight before being rinsed with HCl solution. In order to avoid the degradation of the composite biopolymer matrix, the obtained capsules are stored in 0.1 M HCl solution [10, 21, 33–35]. Zhang et al. also used the encapsulation method for the immobilization of ILs. They introduced PVA into the alginate solid support to enhance the strength and durability of the beads. Before the extrusion step, they blended the PVA alginate solution with the IL ([A336][MTBA]) for 6 h at 500 rpm and 30°C [36].

Shanthana Lakshmi et al. [61] immobilized Cyphos IL-101 in polymer microspheres using the phase-inversion technique. In the first step a Phase I is obtained, a casting solution to form the microspheres, which contain the polymer and the IL dissolved in *N,N*-dimethylformamide. The microspheres pass through a second oil phase (dodecane) and then into a coagulation bath (Phase III—a mixture of ethanol and double-distilled water). In the coagulation bath, the phase inversion is induced by exchange across the interface of the solvent from the polymer solution with a non-solvent [61].

Qian et al. immobilized a tropine-type chiral ionic liquid with proline anion on silica gel by a chemical bonding method. In the first step, they activated the surface of the silica gel, mixed the tropine 3-iodopropyl trimethoxysilane and potassium iodide in ethanol, and then mixed all the reagents and left the reaction to perform at 110°C . The compound which resulted was added to a mixture of L-proline and sodium hydroxide solution and stirred continuously for 48 h [52].

Other researchers immobilized ILs onto magnetic nanoparticle surfaces by free radical copolymerization [42, 43]. The reaction is performed under a nitrogen atmosphere and each of the papers mentions different times taken for the reaction (6–24 h) and different temperatures (70 – 110°C). Liu and co-workers used the sol-gel method for the immobilization of the IL onto silica-based materials [53, 54].

The use of chemical processes to immobilize the IL onto a suitable solid support involves the use of a lot of reagents which limit their application from the economical point of view. Therefore, physical processes are most widely used. The physical method which has been tested most is the dry method of impregnation because researchers consider that through this process the stability of the extractant on the solid support is increased [24, 25, 27, 28, 57–59]. The schematic process of ILs immobilization onto a solid support, using the dry method of impregnation, is presented in **Figure 2**.

Some researchers activate the surface of the solid supports before impregnation [27, 28]. Also the ionic liquid is dissolved in a volatile diluent (ketone, methanol and ethanol). The two components are kept in contact for at least 24 h. Subsequently, the diluent is evaporated and pure ionic liquid remains inside the pores of the support. The evaporation of the diluent is achieved through drying in an oven at 50°C for 24 h or by using roto-vapour.

Because the immobilization of the IL by the dry method of impregnation involves a lot of time for contact between the IL and the solid support, some researchers used the stirring method [20, 29, 41, 46–50]. They stirred these two phases (the IL dissolved in a diluent and the solid support), different stirring times are reported, and then filtered, washed and dried the solid support immobilized with the IL in order to evaporate the diluent. The total time taken for the immobilization of the IL on a solid support using the stirring method depends on how much treatment is carried out on the solid support before impregnation, and how many steps of the washing there are before the final product is obtained.

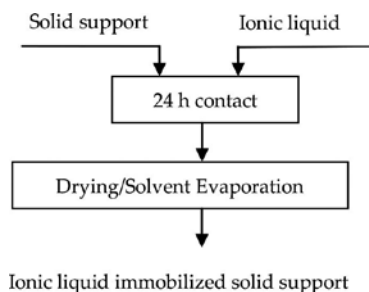


Figure 2. The obtaining of ionic liquid immobilized on a solid support using the dry method of impregnation.

Negrea et al. studied the influence of the impregnation method on the adsorption capacity of the resulting materials. For the immobilization of Cyphos IL-101 on Florisil and Silica solid supports, the methods they used for impregnation were: the dry method, the stirring method, the dynamic column method and the ultrasound method. The materials obtained were used in the removal of Cs^+ ions from aqueous solutions [62]. The materials obtained through the various methods they studied were characterized using FTIR, BET, SEM and EDX analysis. It was observed that the method used for the impregnation of the IL onto the solid support influences the surface morphology of the product obtained. This led to the materials having different adsorption capacities in the removal of Cs^+ ions from aqueous solutions. The most efficient method of impregnation proved to be the ultrasound method with which the distribution of the ILs particles onto the surface of the studied solid supports was uniform. This method also resulted in the highest adsorption capacity of Cs^+ [62].

Other researchers used the ultrasonication method for the immobilization of the ionic liquid onto a solid support because it is an economic alternative process, which is not so time-consuming [30, 37–40, 45, 60].

The research group of Lupa, Negrea and co-workers studied the influence of the ultrasonication conditions (amplitude and time of ultrasonication) upon the immobilization of Cyphos IL-101, OmimBF₄ and BmimPF₆ onto Florisil. It was observed that in order to obtain a stable and homogenous impregnation of the solid support with the studied IL, it is not necessary to increase the ultrasonication time, but a higher amplitude should be used. Increasing the ultrasonication time leads to the conglomeration of the IL particles on the solid support affecting in this way the reproducibility of the adsorption experiments [63]. Increasing the amplitude of sonication assures an easier transmission of the IL particles through the liquid

media until it reaches the cavities of the solid support. Through this process, instead of the 24 h of impregnation needed in case of the dry method, the immobilization is achieved in 10 min. After the immobilization of the IL onto the solid support through ultrasonication, the suspension is dried for 24 h at 50°C for solvent evaporation. This time could be minimized if the evaporation of the solvent is carried out using a roto-vapour. The same group of researchers studied the possibility of IL immobilization using the process of pellicular vacuum solvent vaporization using a roto-vapour. They studied the influence of the impregnation conditions: stirring time and temperature in the case of the immobilization of the 1-n-hexyl-3-methyl imidazolium chloride on Florisil. The material obtained was used in the removal of Tl ions from aqueous solutions [66]. It was observed that to improve the adsorption capacity of the obtained ionic-liquid impregnated material, it is not necessary to increase the stirring time during the impregnation process, but it is necessary to increase the temperature. The temperature increase led to a large quantity of ionic liquid being impregnated onto the solid support and to a shorter time for solvent evaporation [66].

4. Use of ionic liquid immobilized solid supports for the removal of metal ions from aqueous solutions

Ionic liquid immobilized solid supports were used for the removal of different metal ions from various samples such as: wastewater, sea water and hydrochloric acid solution. The adsorption efficiency of the studied materials was determined using the mass balance equation:

$$q = \frac{(C_0 - C_e) \cdot V}{m} \quad (1)$$

where C_0 and C_e represent the initial and equilibrium concentration of the studied metal ion [mg/L]; V is the volume of the aqueous solution sample containing the metal ion [L] and m represents the mass of the used ionic liquid immobilized solid support [g].

This section presents the results of studies on the adsorption efficiency obtained by various ionic liquid immobilized solid supports used in the removal of metal ions from different samples. Identifying the adsorbent with the greatest capacity of adsorption is difficult as the experimental conditions vary from one study to another. However, in most of the adsorption studies, the following were analyzed to find their influence on adsorption capacity: pH, contact time between the adsorbent and adsorbate, and initial concentration of the metal ions. With some exceptions, when more models are tested, the equilibrium data were fitted with Langmuir and Freundlich isotherms and the kinetic data were discussed using the pseudo-first order and pseudo-second order kinetic models.

Gallardo et al. studied zinc (II) extraction from HCl acid solutions using Amberlite XAD7 impregnated with Cyphos IL-101 through the dry method. They studied the influence of the HCl concentration, the content of the Cyphos IL-101 upon the uptake efficiency and sorption isotherms [27]. Compared to the raw Amberlite XAD7, the adsorption capacity was 10 times

higher when resin impregnated with Cyphos IL-101 was used in the removal of Zn(II) from acidic solutions. They reported that the impregnated materials could be regenerated after adsorption using Na₂SO₄, H₂SO₄ or HNO₃. Also sorption and desorption efficiencies were maintained almost constantly over five sorption/desorption cycles [27]. The removal of lead ions was studied by Sun et al. [40] through adsorption onto graphene oxide and magnetic chitosan ionic-liquid and by Tokalioglu et al. [47] using carbon nanospheres coated with an ionic liquid. In the first case, an adsorption capacity of 85 mg/g was obtained, while the carbon nanospheres coated with ionic liquid gave an adsorption capacity of 50.3 mg/g.

A lot of studies were made on the removal of Cr ions from aqueous solutions. Chromium compounds are widely applied in many industries (pigments, metallurgy, electroplating, leather tanning, stainless steel production, steel, photography) giving rise to huge quantities of wastewater containing chromium [20, 53]. The discharged chromium exists in two important states of oxidation, Cr(III) and Cr(VI). Cr(VI) is more toxic than Cr(III) because of its ability to oxidize other substances. In **Table 2**, there is a summary of the adsorption capacities of different ionic liquid immobilized solid supports in the removal of Cr(VI) from aqueous solutions. It can be observed from the data presented in **Table 2** that the highest adsorption capacity was given by the Dowex 1 x 8 in the removal process of Cr(VI) from aqueous solutions. This could be explained by the fact that Dowex is known to be a good ion exchanger and so it may be that the success in this removal process results from a combination between adsorption and ion

Solid support	Ionic liquid	Immobilization method	q _m , mg/g	Work conditions	References
Amberlite XAD-7	Cyphos IL-104	Stirring method 0.25 g of IL/1 g of SS	44.85	S:L = 4 g/L; t = 60 min; T = 298 K; pH = not mentioned (n.m.)	[19]
Amberlite XAD-7	Aliquat 336	Stirring method 2 g of IL/1 g of SS	50.44	S:L = 1.6 g/L; t = 24 h; T = 298 K; pH = 6	[29]
Dowex 1 x 8	Aliquat 336	Ultrasonication 6 mL of IL/1 g of SS	230.9	S:L = 10 g/L; t = 30 min, T = 300 K; pH = 3.5-4	[30]
Cellulose	MeTOACl	Ultrasonication	38.94	S:L = 10 g/L; t = n.m., T = room temp.; pH = 2	[37]
Magnetic chitosan/graphene oxide	N-(3-Aminopropyl)-imidazole	Ultrasonication 1 g IL/1 g SS	107.99	S:L = 1g/L; t = 60 min, T = 303 K; pH = 2	[38]
Magnetic chitosan/graphene oxide	Tetraoctylammonium bromide	Ultrasonication 1 g IL/1 g SS	145.35	S:L = 1g/L; t = 40 min, T = 303 K; pH = 3	[39]
Silica	Cyphos IL-104	Sol-gel method	19.31	S:L = 4 g/L; t = 4 h; T = 298 K; pH = 6	[53]
Silica	[A336][C272]	Sol-gel method	15.29	S:L = 4 g/L; t = 4 h; T = 298 K; pH = 6	[53]

Table 2. The adsorption capacities developed by ionic liquid immobilized solid support in the removal process of Cr(VI) from aqueous solutions.

exchange. Also high adsorption capacities were obtained by magnetic chitosan/graphene oxide immobilized with different ionic liquids. The mixture between an organic solid support (chitosan) and an inorganic one (Fe_3O_4) leads to the enhancement of the adsorption capacity of the obtained product. The lowest adsorption capacity was obtained by the silica impregnated with the studied ILs using the sol-gel method of impregnation. The materials obtained through the impregnation of the IL onto the solid supports by ultrasonication presented the highest efficiency in the removal process of Cr(VI) from aqueous solutions.

Ionic liquids immobilized through encapsulation in biopolymer capsules were used in the removal of some precious metals such as: Au, Pd, Hg, Pt. The work conditions and the obtained adsorption capacities of the ionic liquid immobilized biopolymers are presented in **Table 3**. It can be observed that the Cyphos IL-101 immobilized in microcapsules of gelatin and alginate composite were efficient in removing Hg, Pd, Bi, Au, Pt ions from acid solutions. Adsorption capacities of over 100 mg/g were obtained. [A336][MTBA] immobilized through encapsulation in alginate beads functionalized with PVA developed a smaller adsorption capacity for the removal of Hg(II) ions from aqueous solutions. A higher adsorption capacity for the removal of Hg(II) from aqueous solutions resulted from using TOMATS impregnated onto palm shell activated carbon. In this case, equilibrium is achieved after 3 h of shaking.

Solid support	Ionic liquid	Immobilization method	Removed metal	q_m , mg/g	Work conditions	References
Composite polymer (gelatin and alginate)	Cyphos IL-101	Encapsulation	Hg	150	S:L = 0.2 g/L; t = 96 h; T = 298 K; In the presence of HCl solution	[10]
			Pd	130-145	S:L = 0.6 g/L; t = 72 h; T = 298 K; In the presence of HCl solution	[21]
			Bi	110-130	S:L = 0.25 g/L; t = 96 h; T = 298 K; In the presence of HCl solution	[33]
			Au	140	S:L = 0.6 g/L; t = 96h; T = 298 K; In the presence of HCl solution	[34]
			Pt	177	S:L = 0.6 g/L; t = 48-72 h; T = 298 K; In the presence of HCl solution	[35]
PVA alginate gel beads	[A336][MTBA]	Encapsulation	Hg	49.89	S:L = 1 g/L; t = 24 h; T = 298 K; pH = 6	[36]
Palm shell activated carbon	TOMATS	Orbital shacking	Hg	83.33	S:L = 20 g/L; t = 3 h; T = 308 K; pH = 8	[46]

Table 3. The efficiency of the IL immobilized in biopolymer capsules in the removal process of metal ions from aqueous solutions.

Ionic liquid impregnated solid supports were also used as adsorbent materials in the removal of some radionuclides from aqueous solutions. It can be observed from **Table 4** that ionic liquid impregnated solid support can be used for the removal of radionuclides from aqueous solutions containing trace amounts. The materials impregnated with the studied ionic liquid developed a higher efficiency when the ultrasonication is used for the impregnation of the IL onto the solid support. The inorganic materials presented a higher efficiency than the organic materials as solid support for the impregnation of the IL.

Solid support	Ionic liquid	Immobilization method	Removed metal	$q_{m,r}$ mg/g	Work conditions	References
Diatomite	1-ethyl-3-methylimidazolium chloride	Stirring method	U(VI)	88	S:L = 1 g/L; t = n.m.; T = 298 K; pH = 4.2	[49]
Florisil	Cyphos IL-101	Dry method	Cs(I)	3.086	S:L = 4 g/L; t = 2 h; T = 298 K; pH = 8	[59]
Silica	Cyphos IL-101	Dry method	Cs(I)	1.48	S:L = 4 g/L; t = 2 h T = 298 K; pH = 8	[57]
Florisil	Cyphos IL-101	Ultrasound	Cs(I)	2.95	S:L = 4 g/L; t = 1 h, T = 298 K; pH = 3.5	[63]
Florisil	OmimBF ₄	Ultrasound	Cs(I)	2.27	S:L = 4 g/L; t = 1 h, T = 298 K; pH = 3.5	[64]
Florisil	BmimPF ₆	Ultrasound	Cs(I)	1.6	S:L = 4 g/L; t = 1 h, T = 298 K; pH = 3.5	[65]
Florisil	Cyphos IL-101	Dry method	Sr(II)	2.94	S:L = 4 g/L; t = 2 h; T = 298 K; pH = 6	[58]
Silica	Cyphos IL-101	Dry method	Sr(II)	3.97	S:L = 4 g/L; t = 2 h; T = 298 K; pH = 6	[58]
Functionalized styrene divinylbenzene	OmimBF ₄	Ultrasonication	Sr(II)	15.6	S:L = 4 g/L; t = 2 h; T = 298 K; pH = 3.5	[32]
Functionalized styrene divinylbenzene	BmimPF ₆	Ultrasonication	Sr(II)	13.7	S:L = 4 g/L; t = 2 h; T = 298 K; pH = 3.5	[32]
Functionalized styrene	Cyphos IL-101	Ultrasonication	Sr(II)	8.13	S:L = 4 g/L; t = 2 h; T = 298	[32]

Solid support	Ionic liquid	Immobilization method	Removed metal	q_m , mg/g	Work conditions	References
divinylbenzene					K; pH = 3.5	
Functionalized styrene divinylbenzene	OmimBF ₄	Ultrasonication	Tl(I)	4.83	S:L = 4 g/L; t = 2 h; T = 298 K; pH = 3.5	[32]
Functionalized styrene divinylbenzene	BmimPF ₆	Ultrasonication	Tl(I)	3.92	S:L = 4 g/L; t = 2 h; T = 298 K; pH = 3.5	[32]
Functionalized styrene divinylbenzene	Cyphos IL-101	Ultrasonication	Tl(I)	2.94	S:L = 4 g/L; t = 2 h; T = 298 K; pH = 3.5	[32]
Florisil	OmimBF ₄	Ultrasonication	Tl(I)	8.48	S:L = 2 g/L; t = 2 h; T = 298 K; pH = 3.5	[60]
Florisil	BmimPF ₆	Ultrasonication	Tl(I)	7.97	S:L = 2 g/L; t = 2 h; T = 298 K; pH = 3.5	[60]
Florisil	Cyphos IL-101	Ultrasonication	Tl(I)	11.1	S:L = 2 g/L; t = 2 h; T = 298 K; pH = 3.5	[60]
Florisil	1-hexyl-3-methylimidazolium chloride	Pellicular vacuum solvent vaporization	Tl(I)	2.95	S:L = 40 g/L; t = 2 h; T = 298 K; pH = 3.5	[66]

Table 4. The adsorption capacities developed by ionic liquid immobilized solid support in the removal process of different radionuclides from aqueous solutions.

5. Conclusion

Ionic liquids could be used in the solid-liquid separation processes by their immobilization in suitable solid supports. In this way, the loss of ILs into the aqueous phase is avoided, and a smaller amount of IL is used. The ionic liquid immobilized solid supports could be efficiently used for metal ions removal from aqueous solutions even from dilute samples. Through the immobilization of IL onto different solid supports, the adsorption performance of the materials is enhanced because of the combination of the advantages of the IL and the properties of the solid support. The type of materials used as solid support for ILs immobilization, and the method used for the immobilization process influences the adsorption efficiency of the product obtained. Regarding to the materials, silica and Amberlite XAD-7 have been the most tested as solid supports. The most immobilized ionic liquids were quaternary phosphonium ionic liquid and imidazolium type. The immobilization of the ILs in biopolymers was performed through encapsulation. Between the chemical and physical methods used for the immobiliza-

tion of ILs, the second one proved to be more advantageous. The materials obtained through the impregnation of the IL onto the solid supports by ultrasonication presented the highest efficiency in the removal process of metal ions from aqueous solutions. Even if the results are very promising, a wider combination of solid supports and ILs can be tested, opening the door to explore new challenges.

Acknowledgements

This work was supported by a grant of the Romanian National Authority for Scientific Research, CNCS – UEFISCDI, project number PN-II-RU-TE-2012-3-0198”.

Author details

Lavinia Lupa^{1*}, Petru Negrea¹ and Adriana Popa²

*Address all correspondence to: lavinia.lupa@upt.ro

1 Faculty of Industrial Chemistry and Environmental Engineering, Politehnica University of Timisoara, Timisoara, Romania

2 Institute of Chemistry Timisoara of Romanian Academy, Romanian Academy, Timisoara, Romania

References

- [1] Soylak M, Saracoglu S, Divrikli U, Elci L: Coprecipitation of heavy metals with erbium hydroxide for their flame atomic absorption spectrometric determinations in environmental samples. *Talanta*. 2005;66:1098–1102, DOI:10.1016/j.talanta.2005.01.030.
- [2] Munter R: Technology for the removal of radionuclides from natural water and waste management: state of the art. *Proceedings of the Estonia Academy of Science*. 2013; 62:122–132, DOI: 10.3176/proc.2013.2.06.
- [3] Lehto J, Brodtkin L, Harjula R: SrTreat: A highly effective ion exchanger for the removal of radioactive strontium from nuclear waste solutions. *Radioactive Waste Management and Environmental Remediation*. ASME. 1997;245–248.
- [4] Hamed MM, Attallah MF, Shehata FA: Synthesis, characterization and sorption behaviour of some radionuclides on zirconium tungstate ion-exchanger. *Arab Journal of Nuclear Science and Applications*. 2012;45:37–50.

- [5] Zhang X, Yin G, Hu Z: Extraction and separation of gallium, indium and thallium with several carboxylic acids from chloride media. *Talanta*. 2003;59(5):905–912. DOI:10.1016/S0039-9140(02)00646-X.
- [6] Wei GT, Yang Z, Chen CJ: Room temperature ionic liquid as a novel medium for liquid/liquid extraction of metal ions. *Analytica Chimica Acta*. 2003;488:183–192. DOI:10.1016/S0003-2670(03)00660-3.
- [7] Esmeray E, Aydin ME: Comparison of natural radioactivity removal methods for drinking water supplies: A review, *Journal of International Environmental Applications & Science*. 2008;3:142–146.
- [8] Ciopec M, Popa A, Negrea A, Lupa L, Negrea P, Voda R, Davidescu CM, Ilia G: Comparative characteristics of some material polymers impregnated with ionic liquid for removal of radionuclides. *Environmental Engineering and Management Journal*. 2015;14(6):1287–1294.
- [9] Guibal E, Vincent T, Jouannin C: Immobilization of extractants in biopolymer capsules for the synthesis of new resins: a focus on the encapsulation of tetraalkyl phosphonium ionic liquids. *Journal of Materials Chemistry*. 2009;19:8515–8527. DOI: 10.1039/b911318e.
- [10] Guibal E, Campos Gavilan K, Bunio P, Vincent T, Trochimczuk A: Cyphos IL 101 (tetradecyl(trihexyl)phosphonium chloride) immobilized in biopolymer capsules for Hg(II) recovery from HCl solutions. *Separation Science and Technology*. 2008;43(9–10):2406–2433. DOI: 10.1080/01496390802118970.
- [11] Mahamuni SV, Wadgaonkar PP, Anuse MA: Rapid liquid–liquid extraction of thallium(III) from succinate media with 2-octylaminopyridine in chloroform as the extractant. *Journal of the Serbian Chemical Society*. 2008;73(4):435–451.
- [12] Anderson L, Armstrong DW, Wei GT: Ionic liquids in analytical chemistry. *Analytical Chemistry*. 2006;78(9):2892–2902. DOI: 10.1021/ac069394o.
- [13] Nakashima K, Kubota F, Maruyama T, Goto M: Ionic liquids as a novel solvent for lanthanide extraction. *Analytical Sciences*. 2003;19:1097–1098.
- [14] Chen J, editor. *Application of Ionic Liquids on Rare Earth Green Separation and Utilization*: Springer-Verlag Berlin Heidelberg; 2016. 14p. DOI: 10.1007/978-3-662-47510-2.
- [15] Heitzman H, Young BA, Rausch DJ, Rickert P, Stepinski DC, Doetz ML: Fluorous ionic liquids as solvents for the liquid-liquid extraction of metal ions by macrocyclic polyethers. *Talanta*. 2006;69(2):527–531. DOI: 10.1016/j.talanta.2005.09.046.
- [16] Visser AE, Rogers RD: Room temperatures ionic liquids: new solvents for f- element separations and associated solution chemistry. *Journal of Solid State Chemistry*. 2003;171(1–2):109–113. DOI: 10.1016/S0022-4596(02)00193-7.

- [17] Ajioka T, Oshima S, Hirayama N: Use of 8-sulfonamidoquinoline derivatives as chelate extraction reagents in ionic liquid extraction system. *Talanta*. 2008;74(4):903–908. DOI: 10.1016/j.talanta.2007.07.020.
- [18] Sun X, Peng B, Ji Y, Chen J, Li D: The solid-liquid extraction of yttrium from rare earth by solvent (ionic liquid) impregnated resin coupled with complexing method. *Separation and Purification Technology*. 2008;63:61–68. DOI: 10.1016/j.seppur.2008.03.038.
- [19] Vidal L, Riekkola ML, Canals A: Ionic liquid-modified materials for solid-phase extraction and separation. *Analytica Chimica Acta*. 2012;715:19–41. DOI: 10.1016/j.aca.2011.11.050.
- [20] Yang XY, Zhang JP, Guo L, Zhao H, Zhang Y, Chen J: Solvent impregnated resin prepared using ionic liquid Cyphos IL 104 for Cr(VI) removal. *Transactions of Nonferrous Metals Society of China*. 2012;12:3126–3130. DOI: 10.1016/S1003-6326(12)61764-6.
- [21] Vincent T, Parodi A, Guibal E: Immobilization of Cyphos IL-101 in biopolymer capsules for the synthesis of Pd sorbents. *Reactive & Functional Polymers*. 2008;68:1159–1169. DOI: 10.1016/j.reactfunctpolym.2008.04.001.
- [22] Sun X, Li Y, Chen J, Ma J: Solvent impregnated resin prepared using task-specific ionic liquids for rare earth separation. *Journal of Rare Earths*. 2009;27:932–936. DOI: 10.1016/S1002-0721(08)60365-8.
- [23] Fontanals N, Borrull F, Marce RM: Ionic liquids in solid-phase extraction. *Trac-Trends in Analytical Chemistry*. 2012;41:15–26. DOI: 10.1016/j.trac.2012.08.010.
- [24] Arias A, Saucedo I, Navarro R, Gallardo V, Martinez M, Guibal E: Cadmium(II) recovery from hydrochloric acid solutions using Amberlite XAD-7 impregnated with tetraalkyl phosphonium ionic liquid. *Reactive & Functional Polymers*. 2011;71:1059–1070. DOI: 10.1016/j.reactfunctpolym.2011.07.008.
- [25] Blahusiak M, Schlosser S, Martak J: Extraction of butyric acid by a solvent impregnated resin containing ionic liquid. *Reactive & Functional Polymers*. 2011;7:736–744. DOI: 10.1016/j.reactfunctpolym.2011.04.002.
- [26] Negrea A, Ciopec M, Lupa L, Gabor A: Influence of the solid support base impregnated with IL on the sorption of various radionuclides from aqueous solutions. *AWERProcedia Advances in Applied Science*. 2013;1:241–250.
- [27] Gallardo V, Navarro R, Saucedo I, Avila M, Guibal E: Zinc(II) extraction from hydrochloric acid solutions using Amberlite XAD-7 impregnated with Cyphos IL 101 (tetradecyl(trihexyl)phosphonium chloride). *Separation Science and Technology*. 2008;43(9–10):2434–2459. DOI: 10.1080/01496390802119002.
- [28] Navarro R, Ruiz P, Saucedo I, Guibal E: Bismuth(II) recovery from hydrochloric acid solutions using Amberlite XAD-7 impregnated with a tetraalkyl phosphonium ionic

- liquid. *Separation and Purification Technology*. 2014;135:268–277. DOI: 10.1016/j.seppur.2014.02.023.
- [29] Saha B, Gill RJ, Bailey DG, Kabay N, Arda M: Sorption of Cr(VI) from aqueous solution by Amberlite XAD-7 resin impregnated with Aliquat 336. *Reactive & Functional Polymers*. 2004;60:223–244. DOI: 10.1016/j.reactfunctpolym.2004.03.003.
- [30] Kalidhasan S, Santhana Krishna Kumar A, Rajesh V, Rajesh N: An efficient ultrasound assisted approach for the impregnation of room temperature ionic liquid onto Dowex 1 x 8 resin matrix and its application toward the enhanced adsorption of chromium (VI). *Journal of Hazardous Materials*. 2012;213–214:249–257. DOI: 10.1016/j.hazmat.2012.01.093.
- [31] M. Ciopec, A. Popa, A. Negrea, L. Lupa, P. Negrea, R. Voda, C.M. Davidescu, G. Ilia: Comparative characteristics of some material polymers impregnated with ionic liquid for removal of radionuclides. *Environmental Engineering and Management Journal*. 2015;14(6):1287–1294.
- [32] A. Popa, M. Ciopec, A. Negrea, L. Lupa, P. Negrea, C.M. Davidescu, G. Ilia, N. Duteanu: Use of styrene-divinylbenzene grafted with aminoethylaminomethyl groups and various ionic liquids in the removal process of thallium and strontium. *Pure and Applied Chemistry*. 2014;86(11):1741–1753. DOI 10.1515/pac-2014-0702.
- [33] Campo K, Domingo R, Vincent T, Ruiz M, Sastre AM, Guibal E: Bismuth recovery from acidic solutions using Cyphos IL-101 immobilized in a composite biopolymer matrix. *Water Research*. 2008;42:4019–4031. DOI: 10.1016/j.watres.2008.07.024.
- [34] Campos K, Vincent T, Bunio P, Trochimczuk A, Guibal E: Gold recovery from HCl solutions using Cyphos IL-101 (a quaternary phosphonium ionic liquid) immobilized in biopolymer capsules. *Solvent Extraction and Ion Exchange*. 2008;26:570–601. DOI: 10.1080/07366290802301572.
- [35] Vincent T, Parodi A, Guibal E: Pt recovery using Cyphos IL-101 immobilized in biopolymer capsules. *Separation and Purification Technology*. 2008;62:470–479. DOI: 10.1016/j.seppur.2008.02.025.
- [36] Zhang Y, Kogelnig D, Morgenbesser C, Stojanovic A, Jirsa F, Lichtscheidl-Schultz I, Krachler R, Li Y, Keppler BK: Preparation and characterization of immobilized [A336] [MTBA] in PVA-alginate gel beads as novel solid-phase extractants for an efficient recovery of Hg(II) from aqueous solutions. *Journal of Hazardous Materials*. 2011;196:201–209. DOI: 10.1016/j.jhazmat.2011.09.018.
- [37] Kalidhasan S, Santhana KrishnaKumar A, Rajesh V, Rajesh N: Ultrasound-assisted preparation and characterization of crystalline cellulose-ionic liquid blend polymeric materials: A prelude to the study of its application toward the effective adsorption of chromium. *Journal of Colloid and Interface Science*. 2012;367:398–408. DOI: 10.1016/j.jcis.2011.09.062.

- [38] Li L, Liu F, Duan H, Wang X, Li J, Wang Y, Luo C: The preparation of novel adsorbent materials with efficient adsorption performance for both chromium and methylene blue. *Colloids and Surface B: Biointerfaces*. 2016;141:253–259. DOI: 10.1016/j.colsurfb.2015.06.023.
- [39] Li L, Luo C, Li X, Duan H, Wang X, Preparation of magnetic ionic liquid/chitosan/graphene oxide composite and application for water treatment. *International Journal of Biological Macromolecules*. 2014;66:172–178. DOI: 10.1016/j.ijbiomac.2014.02.031.
- [40] Sun W, Li, L, Luo C, Fan L, Synthesis of magnetic graphene nanocomposites decorated with ionic liquids for fast lead ion removal. *International Journal of Biological Macromolecules*. 2016;85:246–251. DOI: 10.1016/j.ijbiomac.2015.09.061.
- [41] Mehdinia A, Shegefti S, Shemirani F. A novel nanomagnetic task specific ionic liquid as a selective sorbent for trace determination of cadmium in water and fruit samples. *Talanta*. 2015;144:1266–1272. DOI: 10.1016/j.talanta.2015.08.012.
- [42] Chen L, Huang X, Zhang Y, Yuan D: A new polymeric ionic liquid-based magnetic adsorbent for the extraction of inorganic anions in water samples. *Journal of Chromatography A*. 2015;1403:37–44. DOI: 10.1016/j.chroma.2015.05.021.
- [43] Zheng X, He L, Duan Y, Jiang X, Xiang G, Zhao W, Zhang S: Poly(ionic liquid) immobilized magnetic nanoparticles as new adsorbent for extraction and enrichment of organophosphorous pesticides from tea drinks. *Journal of Chromatography A*. 2014;1358:39–45. DOI: 10.1016/j.chroma.2014.06.078.
- [44] Karimi M, Shabani AMH, Dadfarnia S: Magnetic nanoparticles coated with ionic liquid as a sorbent for solid phase extraction of chromium (VI) prior to its determination by electrothermal atomic absorption spectrometry. *Journal of Brazilian Chemical Society*. 2016;27:144–152. DOI: 10.5935/0103-5053.20150263.
- [45] Cheng J, Shi L, Lu J: Amino ionic liquids-modified magnetic core/shell nanocomposite as an efficient adsorbent for dye removal. *Journal of Industrial and Engineering Chemistry*. 2016;36:206–214. DOI:10.1016/j.jiec.2016.02.2014.
- [46] Ismaiel AA, Aroua MK, Yusoff R: Pallm shell activated carbon impregnated with task-specific ionic-liquids as a novel adsorbent for the removal of mercury from contaminated water. *Chemical Engineering Journal*. 2013;225:306–314. DOI: 10.1016/j.cej.2013.03.082.
- [47] Tokalioglu S, Yavuz E, Sahan H, Colak SG, Ocakoglu K, Kacer M, Patat S: Ionic liquid coated carbon nanospheres as a new adsorbent for fast solid phase extraction of trace copper and lead from sea water, wastewater, street dust and spice samples. *Talanta*. 2016;159:222–230. DOI: 10.1016/j.talanta.2016.06.022.
- [48] Amjadi M, Samadi A: Modified ionic liquid-coated nanometer TiO₂ as a new solid phase extraction sorbent for preconcentration of trace nickel. *Colloids and Surface A*:

- Physicochemical and Engineering Aspects. 2013;434:171–177. DOI: 10.1016/j.colsurfa.2013.04.059.
- [49] Sprynskyy M, Kowalkowski T, Tutu H, Cukrowska EM, Buszewski B: Ionic liquid modified diatomite as a new effective adsorbent for uranium ions removal from aqueous solution. *Colloids and Surface A: Physicochemical and Engineering Aspects*. 2015;465:159–167. DOI: 10.1016/j.colsurfa.2014.10.042.
- [50] Liang P, Peng L: Ionic liquid-modified silica as sorbent for preconcentration of cadmium prior to its determination by flame atomic absorption spectrometry in water samples. *Talanta*. 2010;81:673–677. DOI: 10.1016/j.talanta.2009.12.056.
- [51] Fang G, Chen J, Wang J, He J, Wang S: N-methylimidazolium ionic liquid-functionalized silica as a sorbent for selective solid-phase extraction of 12 sulfonylurea herbicides in environmental water and soil samples. *Journal of Chromatography A*. 2010;1217:1567–1574. DOI: 10.1016/j.chroma.2010.01.010.
- [52] Qian G, Song H, Yao S: Immobilized chiral tropine ionic liquid on silica gel as adsorbent for separation of metal ions and racemic amino acids. *Journal of Chromatography A*. 2016;1429:127–133. DOI: 10.1016/j.chroma.2015.11.083.
- [53] Liu Y, Guo L, Zhu L, Sun X, Chen J, Removal of Cr(III, VI) by quaternary ammonium and quaternary phosphonium ionic liquids functionalized silica materials. *Chemical Engineering Journal*. 2010;158:108–114. DOI: 10.1016/j.cej.2009.12.012.
- [54] Liu Y, Zhu L, Sun X, Chen J, Luo F: Silica materials doped with bifunctional ionic liquid extractant for Yttrium extraction. *Industrial Engineering and Chemical Research*. 2009;48:7308–7313. DOI: 10.1021/ie900468c.
- [55] Liu Y, Sun X, Luo F, Chen J: The preparation of sol-gel materials doped with ionic liquids and trialkyl phosphine oxides for Yttrium(III) uptake. *Analytica Chimica Acta*. 2007;604(2):107–113. DOI: 10.1016/j.aca.2007.10.005.
- [56] Marwani HM, Alsafrani AE, Asiri AM, Rahman MM: Silica-gel particles loaded with an ionic liquid for separation of Zr(IV) prior to its determination by ICP-OES. *Sensors*. 2016;16(7):1001–10015. DOI: 10.3390/s16071001.
- [57] Negrea A, Lupa L, Ciopec M, Negrea P: Silica impregnated with Cyphos IL-101 for Cs⁺ adsorption. *Environmental Engineering and Management Journal*. 2014;13(8): 2005–2013.
- [58] Negrea A, Lupa L, Ciopec M, Negrea P: Characterization of strontium adsorption from aqueous solutions using inorganic materials impregnated with ionic liquid. *International Journal of Chemical Engineering and Applications*. 2013;4(5): 326–330. DOI: 10.7763/IJCEA.2013.V4.319.
- [59] Lupa L, Negrea A, Ciopec M, Negrea P: Cs⁺ removal from aqueous solutions through adsorption onto Florisil impregnated with trihexyl(tetradecyl)phosphonium chloride. *Molecules*. 2013;18:12845–12856. DOI: 10.3390/molecules181012845.

- [60] Lupa L, Negrea A, Ciopec M, Negrea P, Voda R: Ionic liquids impregnated onto inorganic support used for thallium adsorption from aqueous solutions. *Separation and Purification Technology*. 2015;155:75–82. DOI: 10.1016/j.seppur.2015.06.043.
- [61] Shanthana Lakshmi D, Figoli A, Fiorani G, Carraro M, Giorno L, Drioli E: Preparation and characterization of ionic liquid polymer microspheres [PEEKWC/DMF/CYPHOS IL 101] using the phase-inversion technique. *Separation and Purification Technology*. 2012;97:179–185. DOI:10.1016/j.seppur.2012.01.045.
- [62] Negrea A, Lupa L, Ciopec M, Negrea P, Voda R, Ianasi C: Study of different impregnation methods of inorganic supports with ionic liquid. *Journal of Environmental Protection and Ecology*. 2013;14:1785–1793.
- [63] Negrea A, Lupa L, Ciopec M, Negrea P, Hulka I: Studies regarding the Florisil impregnation with ionic liquid through ultrasonication. *International Journal of Chemical Engineering and Applications*. 2014;5(5):424–428. DOI: 10.7763/IJCEA.2014.V5.422.
- [64] Negrea A, Lupa L, Ciopec M, Voda R, Negrea P, Hulka I: Ultrasonication impregnation of Florisil with 1-octyl-3-methylimidazolium tetrafluoroborate used as adsorbent in the removal process of Cs⁺ from aqueous solutions. *WIT Transactions on Ecology and the Environment*. 2014;182:223–232. DOI: 10.2495/WPI40201.
- [65] Lupa L, Negrea A, Ciopec M, Voda R, Negrea P: Studies regarding the influence of the ultrasonication conditions on the adsorption performance of obtained ionic liquid impregnated materials. *International Journal of Chemical Engineering and Applications*. 2015;6(6):410–416. DOI: 10.7763/IJCEA.2015.V.520.
- [66] Negrea P, Popa A, Lupa L, Voda R: Thallium removal through adsorption onto ionic liquid-impregnated solid support: influence of the impregnation conditions. *International Journal of Environmental Science and Technology*. DOI: 10.1007/s13762-016-1017-0.

Supported Ionic Liquid Membranes for Metal Separation

Pius Dore Ola and Michiaki Matsumoto

Additional information is available at the end of the chapter

<http://dx.doi.org/10.5772/65754>

Abstract

Metals are widely used in various areas of human life, and their existence in the environment at high concentrations has become a cause for concern. Metals can enter the human body and disturb the human metabolic system. Therefore, research to recover metals from their matrix both from industrial wastewater and from ores or scraps containing metals is of great importance. One of the separation techniques proposed to overcome those issues involves using supported ionic liquid membranes (SILMs). This chapter summarizes the recovery of metals using SILM. In SILM, an ionic liquid that acts as an extractant is embedded in small pores of a polymer support. The latest type of physical impregnation of ionic liquid, which is the type most commonly used in metal separation, is called polymer inclusion membrane (PIM). PIMs were prepared by casting a solution containing an ionic liquid, a plasticizer and a base polymer to form a thin, flexible and stable film. A PIM including ionic liquids has a similar configuration to SILM, and it is considered to be a kind of SILM. In this chapter, effects on the stability and selectivity in SILM and PIM for metal separation are reviewed.

Keywords: liquid membrane, ionic liquid, metal, separation, supported membrane

1. Introduction

The separation of metals has become a hot topic of research in recent years. This is because metals are widely used in many aspects of human life, and their existence in the environment at high concentrations is a cause for concern. Although some metals are essential for the human body, their presence in high concentrations will disturb the human metabolic system. Therefore, research on recovering metals from their matrix both from industrial wastewater and from ores and ore scrap is of great importance. In hydrometallurgy, several conventional methods are being used to remove and recover heavy metals from aqueous solutions.

These methods include chemical precipitation [1], reverse osmosis [2], adsorption [3], ion exchange [4] and solvent extraction processes [5]. Those techniques have their own inherent limitations such as low efficiency, sensitive operation conditions, production of secondary sludge, high capital and operating costs, and expensive disposal [6]. Hence, more efficient and cost-effective removal and recovery methods are sought to overcome these problems.

One technique proposed to overcome those issues involves using supported ionic liquid membranes (SILMs). This technique is superior to the above techniques because the advantages of the liquid membrane and ionic liquid are included in the technique of SILM. The advantages of liquid membranes such as combining the extraction and stripping into a single step and using a very small amount of solvent give SILM very low capital and operating costs and make it easy to scale up. Using ionic liquid as an extractant in this technique increases the efficiency and selectivity of SILM. In addition, the very low vapour pressure and very high viscosity of ionic liquid give the best stability of the liquid membrane, which also absolutely affects the flux and selectivity and is environmentally friendlier.

The properties and applications of SILMs are greatly affected by support types, supporting methods and kind of ionic liquid used. The supporting method could be chemical or physical. The physical immobilization of an ionic liquid can be conducted through simple impregnation [7], sol-gel method [8], encapsulation [9], and so on. In chemical immobilization, the ionic liquid is bound to solid support via covalent bonding [10, 11]. The kind of ionic liquids determines the efficiency and selectivity of separation.

This chapter reviews use of supported ionic liquid membranes for separation of metals. At the beginning, it is important to briefly present a summary of supported liquid membrane using ionic liquid and metal separation using this method to ensure the better understanding regarding this topic. Then, we review several articles discussing the effect of related parameters such as type of solid support and supporting method as well as kind of ionic liquids on the stability of the membrane, efficiency and selectivity of metal separation.

2. Supported liquid membrane and ionic liquid

A membrane is a semipermeable barrier between two phases. If membranes are viewed as semipermeable phase separator, then the concept of membranes including solids as polymer or ceramic films can be extended to include liquids, and these are defined as liquid membranes (LMs). A liquid membrane system involves a liquid that is immiscible with the source (feed) and receiving (product) solutions and serves as a semipermeable and barrier between two liquid and gas phases [12]. Liquid membrane separation combines the solvent extraction and stripping (back-extraction) in a single step [13]. The great potential for energy saving, low capital and operating costs, and the possibility to use expensive extractants due to the small amount of the membrane phase make SLMs an area attracting the special attention of both researchers and practitioners.

The transport in a membrane is a dynamic and non-equilibrium process. The transporting compound dissolved in the feed aqueous solution has to dissolve in the organic, hydrophobic

membrane phase and diffuse through it to enter the aqueous stripping phase. Although it is possible to transport the hydrophobic compound through the hydrophilic membrane, this review concerns the transport of water-soluble compounds such as metal ions. The mass transfer in this system takes place due to the difference in the chemical potential across the membrane as a driving force.

According to the configuration definition, three groups of liquid membranes are usually considered as illustrated in **Figure 1**: bulk (BLM), supported or immobilized (SLM or ILM) and emulsion (ELM) liquid membrane transport [12]. A supported liquid membrane (SLM) is one of the three-phase liquid membrane systems in which the membrane phase (liquid) is held by capillary force in the pores of microporous polymeric and inorganic film. The immobilized liquid is a membrane phase, and a microporous film serves as a support for the membrane [13]. SLM was reported for the first time by Scholander [14], who used thin cellulose acetate filters impregnated with an aqueous haemoglobin for oxygen transport.

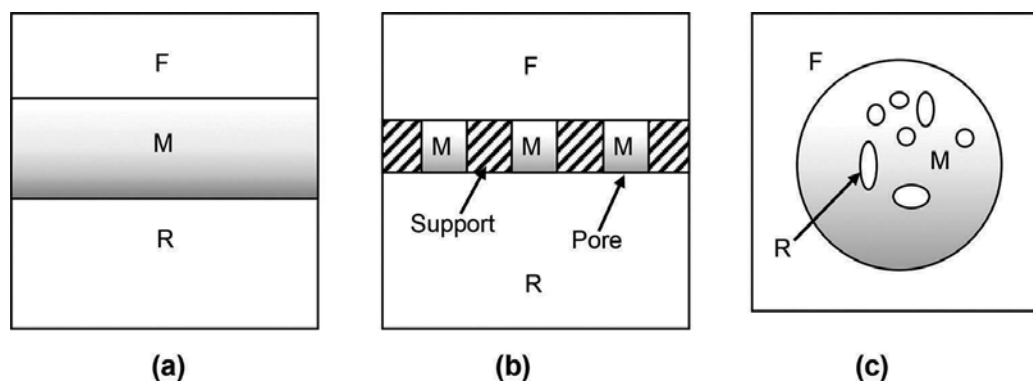
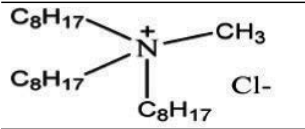
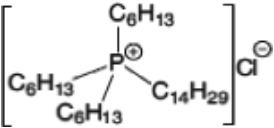
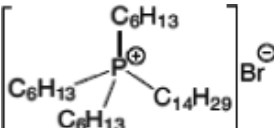
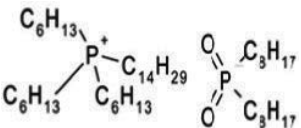


Figure 1. Liquid membranes: (a) bulk, (b) supported and (c) emulsion. (F: feed, M: membrane, R: receiving).

Successful applications of SLMs are possible due to their advantages compared to other separation methods. The main advantages of SLMs are the small amounts of organic phase and extractant (carrier) used, which allows for use of expensive extractants, one-step mass transfer, the possibility of achieving high separation factors, enrichment of extracted compound(s) during separation and low separation costs. Nevertheless, there are some problems limiting the practical application of SLMs. The main problem is the stability of the liquid membrane, caused by leakage and/or losses of membrane phase components during the transport process. Ionic liquids (ILs) come to solve the problem of membrane instability.

ILs are organic salts remaining as liquids under ambient temperatures. They normally consist of an organic cation (e.g. imidazolium, pyridinium, pyrrolidinium, phosphonium, ammonium) and inorganic anion (e.g. tetrafluoroborate, hexafluorophosphate, chloride) or, increasingly, an organic anion (e.g. trifluoromethylsulphonate, bis[(trifluoromethyl) sulphonyl] imide) [15]. The main advantages of these media are their near-zero vapour pressure, which means that they will not evaporate easily from the pores of membranes, have good chemical and thermal stability, and have a large temperature range where they are stable. They also

will not be replaced easily from the pores of the membrane due to their very high viscosity. The properties of ILs (hydrophobicity, viscosity, solubility, etc.), which can be varied by altering the substitutive group on the cation or the combined anion [16], make them more widely applicable in many physical and chemical fields. Therefore, they have been considered environmentally benign solvents as compared to volatile organic solvents. The structures of common ILs used in metal separation are shown in **Table 1**. Most ILs show the pronounced miscibility in the aqueous phases due to their polar nature. ILs have to be hydrophobic as shown in **Table 1** to extract the metal ions from the aqueous phases. For this reason, the ILs used in the metal separation were limited to those listed in **Table 1**.

Molecular structure	Product name Chemical name	Viscosity ^a cP	Water content ^a , wt %
	Aliquat-336 <i>N</i> -Methyl- <i>N,N</i> - <i>N</i> - <i>tri</i> octylammonium chloride	1450 (79.05) ^b	4.3 (20.3) ^b
	Cyphos IL-101 Trihexyl(tetradecyl) phosphonium chloride	1824 (95.8) ^b	0.67 (12.8) ^b
	Cyphos IL-102 Trihexyl(tetradecyl) phosphonium bromide	2094 (190.4) ^b	0.002 (6.1) ^b
	Cyphos IL-104 Trihexyltetradecylphosphonium bis-2,4,4-trimethylpentyl phosphinate	805.8	Not measured

^a25°C.

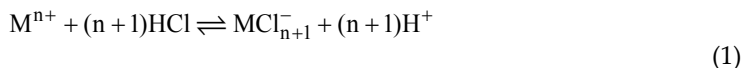
^bThese values were determined using water-saturated ionic liquid.

Table 1. Structures of common ILs used in metals separation.

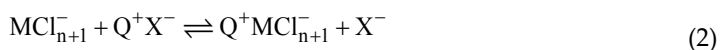
3. Metal separation using supported ionic liquid membrane (SILM)

An interesting field of application of supported ionic liquid membranes is the removal of metal ions from aqueous solutions. In this review, SLMs with IL as a metal carrier dissolved in the conventional organic solvent were excluded, and SLMs impregnated with IL or the mixture of IL and metal extractant in the absence of conventional solvents were discussed as SILM. In the SILMs impregnated with IL only, metals are slowed to be separated from their matrix if the metal ions are in the form of an anionic complex that reacts with the cation of

ionic liquid in the membrane. Aqueous solution of metal ions in hydrogen chloride was used as the feed phase in order to form the anionic metal complex, although other forms such as nitrate and sulphate were also used in several investigations. The reactions of metal ions (M^{n+}) and HCl to form the complex are as follows:



Furthermore, at the feed solution-membrane interface, the complex of MCl_{n+1}^{-} enters into the membrane because of the anion-exchange reaction with IL ($Q^{+}X^{-}$) in the membrane to form the metal complex $Q^{+}MCl_{n+1}^{-}$.



This complex diffuses through the membrane to the membrane-stripping solution interface. At the interface between the membrane and stripping solution of low chloride concentration (usually electrolyte solution such as sodium sulphate), the reverse reactions of above equations are proceeded to release the metal complex and to form free metal ion in the stripping phase. The transport of metal ion from the feed to the stripping phase by SILM is a coupled transport.

In other cases, the metal extractants were dissolved in IL instead of conventional organic solvent, and the membrane was impregnated with IL containing the extractant as a metal carrier. Permeation mechanism of the metal ions depends on the extractant included in the membrane.

3.1. Effect of solid support and preparation method on stability of membrane

3.1.1. Supported ionic liquid membrane

The stability of SILMs is greatly affected by the type and characteristic of solid support used to immobilize the IL as well as the preparation methods of the SILMs. When the SILMs will be used to separate the metals from the metal matrix, impregnated liquid with the conventional organic solvent in membrane can be released because of two factors: evaporation of the impregnated liquid due to high vapour pressure of volatile organic solvent and dissolving impregnated liquid both in the feed solution and in the stripping solution. Use of ILs with very low vapour pressure as the impregnated liquid resolved the first problem. On the other hand, dissolution of ILs to adjacent phases remains a problem that has to be solved. The stability of SILM is mainly affected by the properties of the support membrane and IL, and preparation method [17].

Several groups have prepared SILMs using many types of solid support as well as method of preparation for metal separation. The stability of the membranes yielded was further evaluated using several techniques. de los Ríos et al. [18] used nylon, a hydrophilic polyamide membrane, as a solid support to impregnate methyltrioctylammonium chloride. This membrane was used to transport Zn(II), Cd(II), Cu(II) and Fe(III). Physical impregnation was conducted by mixing the solid support and ionic liquid in an ultrafiltration unit and applying nitrogen pressure to force the ionic liquid to enter the pores of the solid support. The membrane

resulting from this process was still stable after 456 h with the percentage of retained ionic liquid ranging from 75 to 89%, and in most membranes was higher than 80%.

Polyvinylidene fluoride (PVDF) is another solid support commonly used to immobilize IL. Baba et al. [19] used this material to impregnate 1-octyl-3-methylimidazolium bis(trifluoromethanesulphonyl)imide ([C8mim][Tf2N]) containing N-N-dioctyldiglycol amic acid (DODGAA) to separate Dy(III) and Nd(III) in magnet scrap. The SEM micrograph after immersing PVDF in IL containing DODGAA showed that the porous structure of the liquid membrane appeared was well filled with [C8mim][Tf2N]. The membrane was proved to be stable during more than 140 h of operation.

The new material, which is probably a candidate for SILM, was successfully synthesized by Qian et al. [20]. Silica gel was used as a solid support to chemically bind tropine-type ionic liquid, which contained 10% of ionic liquid. Although tropine-type ionic liquid-modified silica has not been used in membrane permeation, there is a high probability to use it as an extractant in the membrane permeation of metals because it is not only stable below 200°C, but it also has 19.36 mg/g of adsorption capacity to the Cu(II) ion.

3.1.2. Polymer inclusion membrane

The most recent type of physical impregnation, which is also the type most commonly used in metal separation, is called polymer inclusion membrane (PIM) [21]. While SILMs were commonly prepared by immersing IL to the pore of the solid support, PIMs were prepared by casting a solution containing a carrier, a plasticizer and a base polymer such as cellulose triacetate (CTA), poly(vinyl chloride) (PVC) or PVDF to form a thin, flexible and stable film. In many cases, a plasticizer or modifier is additionally incorporated into the membrane preparation in order to improve the PIM flexibility and the compatibility between the membrane components. It should be noted that an IL acts not only as a carrier but also as a plasticizer. Therefore, in the PIM using IL as a carrier, plasticizers are sometimes not needed. A PIM including ILs has a similar configuration to SILM, and it is considered to be a kind of SILM. It is found that the PIM including ILs became more stable than conventional SILM [22].

PVC is a commonly used base polymer in the preparation of PIM. Stability studies of PVC-based PIM containing Aliquat 336 as a carrier have been conducted [23]. They found that the mass loss of the membrane is due to leaching Aliquat 336 from the membrane and is suppressed in the salt solutions. They concluded that, although PIMs are capable of losing some membrane liquid phase when exposed to aqueous solutions, this loss can be minimized or even eliminated by increasing the solution concentration of the counter anion of IL. It was found that membrane of Aliquat 336 content higher than 50% was soft and sticky and mechanically too weak to be used for the metal extraction [24].

Recently, Bonggotgetsakul et al. prepared PIM containing Cyphos IL-104 as a carrier using PVC support to extract Au(III) from a hydrochloric acid solution [25]. PIMs prepared with Cyphos IL-104 alone, or with the addition of the modifier 1-dodecanol, were homogeneous, transparent and flexible. Although the permeation rate with PIM including the modifier was

faster than that with IL alone, loss of 1-dodecanol from the newly developed PIM to the aqueous solutions in contact with it was observed.

CTA is the most commonly used polymer support. Regel-Rosocka et al. [26] prepared the PIM using CTA as a support and Cyphos IL 101 as carriers to remove Zn(II) and Fe(III) from chloride solution. Although the highest Zn(II) flux was obtained for membrane without plasticizer, with the highest Cyphos IL 101 content, the membranes with *o*-nitrophenyl octyl ether as a plasticizer have been selected because of their better mechanical properties. Thus, CTA-based PIM needed plasticizer to form stable and mechanically strong membrane. Gardner et al. [27] prepared a series of new cellulose-based PIMs. The ester linkages in the cellulose backbone of the polymer are susceptible to hydrolysis under extremes of pH, especially under alkaline conditions. The durability of the newly prepared PIMs against hydrolysis under alkaline and acidic conditions was evaluated. Durability increased with replacement of acetyl substitution on the cellulose polymer with propionyl or butyryl, while they also observed that ion transport across the membrane decreased as the alkyl chain lengths increased.

Studies were carried out to compare the use of CTA and PVC as base polymer of PIM with Aliquat 336 [28] and Cyphos IL 101 and 104 [29]. Under the optimum condition, in Cr (VI) permeation with PIM including Aliquat 336, the permeation rates of CTA- and PVC-based membranes were comparative, while in Zn (II) permeation with PIM including Cyphos IL 101 or 104, transport abilities of CTA-based membranes were much better than those of PVC. The CTA-based PIM lost 42% of efficiency after 6 days [28].

PVDF is one of the most commonly used solid supports for SILM. Guo et al. [30, 31] successfully prepared new PIM including PVDF as a base polymer, 1-alkyl-3-methylimidazolium hexafluorophosphate or tetrafluoroborate as ionic liquid plasticizers and Cyphos IL 104 and modified Aliquat 336 as a carrier and used this for transport of Cr(VI). The permeation rate with PIM including modified Aliquat 336/PVDF was faster than PIMs including Cyphos IL 104/PVDF or original Aliquat 336/PVC. After nine cycles, permeation rates of PIM composed of Cyphos IL 104/PVDF decreased to 69%, while it was found that the permeation rates of similar PIM composed of original Aliquat 336/CTA and modified Aliquat 336/PVDF decreased to 33 and 59% after six cycles, respectively. More recently, Bonggotgetsakul et al. prepared new PIM containing Cyphos IL-104 as a carrier and poly(vinylidene fluoride-co-hexafluoropropene) (PVDF-HFP) as a base polymer to extract Au(III) from a hydrochloric acid solution [32]. PVDF-HFP was found to be an excellent base polymer because of its high hydrophobicity, excellent thermal and mechanical properties, higher stability in strong acids and better solubility in tetrahydrofuran used for preparing membrane casting solutions. Extraction performance of this PIM was decreased to about 70% after 2 h and until 8 h extraction performance remained at the same level.

Recently, polymer fibres using electrospinning method were successfully prepared for the metal extraction from the aqueous solutions [33–35]. Electrospinning is an innovative technique for the production of polymer fibres with diameter of less than a few micrometres, resulting in a large surface area-to-volume ratio and high porosity. A solution is first prepared by dissolving PVC and Aliquat 336 in the solvent. Then the solution is electrospun to produce the mats consisting of electrospun fibres. The role of Aliquat 336 in electrospun fibres differed from that in

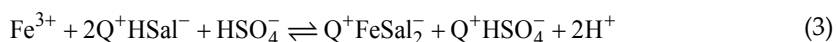
PIMs. Electrospun fibres were homogeneous and plasticized by Aliquat 336. On the other hand, PIMs composed of PVC and Aliquat 336 were visually transparent but were phase separated. Percolation threshold of electrospun fibrous mats was much lower than that of PIMs.

3.2. Effect of ionic liquid on metal separation

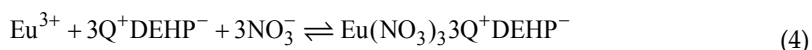
Separation of metal by ionic liquid-containing membrane is based on the chemical reaction between the ionic liquid and metal ion itself. Therefore, the efficiency and selectivity of metal separation are totally affected by the characteristic and type of ionic liquid in the membrane. This is because each ionic liquid has the specific affinity to the metallic ion as a result of the difference in functional groups bonded by an ionic liquid compound. Stojanovic et al. [36] summarized ammonium and phosphonium-based ionic liquids as shown in **Table 1** in the extraction process. This section will focus on the efficiency and selectivity of metal separation with ionic liquid itself and using supported ionic liquid membrane.

3.2.1. Quaternary ammonium salts

Quaternary ammonium salts as anion exchangers have been frequently used to extract metal ions and hence are only effective in the presence of strong anionic ligands as indicated in Eq. (1). It is known that Aliquat 336 dissolved in the organic solvent had the enhanced performance for the removal of metal ions from hydrochloric acid solutions compared to the alkyl amine extractants [37]. Sulphate [38] and thiocyanate [39] as ligands also have been used in the metal solvent extraction system using Aliquat 336. Generally, selectivity of anion exchange reactions is believed to be poor compared to that of chelating reaction. A further approach is to anchor different functional groups onto the anion [36]. By this, it is possible to combine the hydrophobicity of ammonium cation with the affinity of the functional group to desired metal ion. This enhances both efficiency and selectivity of the extractant. Aliquat 336 was modified by exchange the chloride anion of original Aliquat 336 (Q^+Cl^-) with a salicylate anion ($HSal^-$) for the extraction of Cu (II) and Fe (III) [40]. The following extraction reaction of Fe(III) was proposed.



Both extraction efficiency and selectivity of Fe (III) were enhanced compared to those of original one. And thiosalicylate-exchanged Aliquat 336 was reported to be selective to Cd (II) [41]. Aliquat 336-based ionic liquids containing bis(2-ethylhexyl)phosphate ($[DEHP]^-$) or bis(2-ethylhexyl)diglycolamate ($[DGA]^-$) anions were synthesized. The extraction of Eu (III) over Am (III) was studied, and superior extraction of Eu (III) and excellent separation factors were achieved [42]. The following extraction mechanism of Eu(III) with bis(2-ethylhexyl) phosphate-exchanged Aliquat 336 was proposed [43].



In this case, ion association mechanism was proposed instead of the anion exchange mechanism of Eq. (2) because both the Q^+ and $[DEHP]^-$ are involved in Eu(III) extraction. The molecular structures of counter-anions of Aliquat 336 described in this chapter are shown in **Figure 2**.

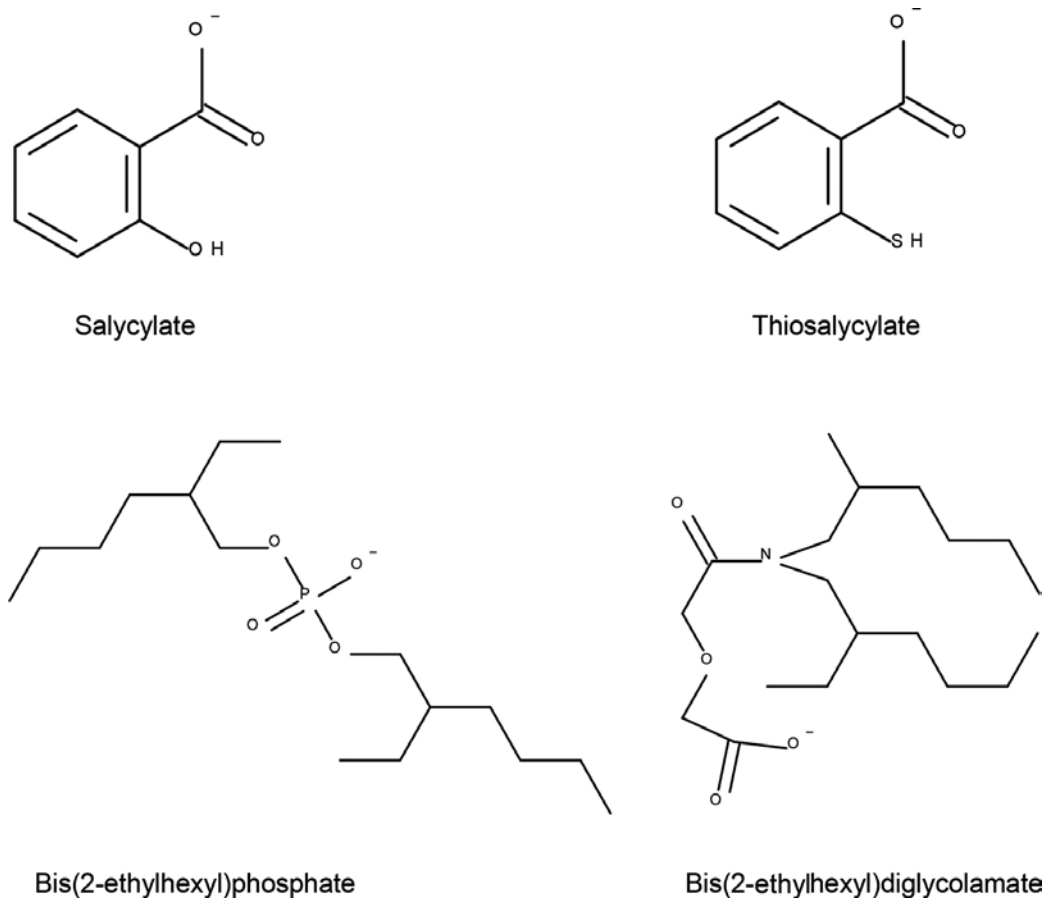


Figure 2. Molecular structures of anion part of modified Aliquat 336.

There are few examples of SILM using Aliquat 336 in the absence of diluents for metal separation. In most cases of SLM, Aliquat 336 was diluted in the organic solvent, and the membrane was impregnated with diluted Aliquat 336 solution.

de los Ríos et al. [18] studied metal separation with the SILM based on methyltrioctylammonium chloride, [MTOA⁺][Cl⁻]. In the solvent extraction, it was found that the ionic liquid [MTOA⁺][Cl⁻] allowed the almost complete removal of Zn(II), Cd(II), Fe(III) and Cu(II) from the aqueous solutions. To realize the selective permeation in SILM process, they examined the composition of the receiving solution. They found that Milli-Q water and Na₂CO₃ solution as the receiving solution allowed the recovery of Zn(II), Fe(III) while the use of NH₃ (6 M) allowed the recovery of Cd(II). These results indicate that high selectivity of metal separation can be reached by changing the receiving phase.

As described above, Aliquat 336 has been extensively applied as a carrier in PIM and used to extract different metal species (e.g. Co(II), Ni(II), Cd(II), Cu(II), Cr(VI), Au(III), As(V), Pd(II), Zn(II)) [21, 36]. Kebiche-Senhaji et al. [28] studied Cr(VI) transport from a mixture containing

Ni(II), Zn(II), Cd(II) and Cu(II) with the PIM based on Aliquat 336. Because $Q_2CrO_4^-$ complex is predominant form in the membrane, in sulphate media, Ni(II), Zn(II), Cd(II) and Cu(II) were not formed anionic species, which is exchangeable with chloride ion on Aliquat 336. Therefore, Ni(II), Zn(II), Cd(II) and Cu(II) were not transported through the PIM, while Cr(VI) is transported with high efficiency. Pont et al. [44] studied Cd(II) transport with PIM containing Aliquat 336 from the chloride solution containing Ni(II). Although the reason of this selectivity is undescribed in the original paper, this may be because of difference in the stability constants of Cd(II) and Ni(II) of Eq. (1). Similar result was obtained for Cd(II) transport with PIM containing Aliquat 336 from the chloride solution containing Cu(II) [24].

Guo et al. [31] prepared a series of PIMs composed of anion-exchanged Aliquat 336 and used them for Cr(VI) permeation in the presence of Fe(III), Co(II) Cu(II) and Zn(II). These transition metals were not transported through the PIM composed Aliquat 336 exchanged with acidic phosphorus compounds, while Cr(VI) is selectively transported. Because the optimum pHs of extractions of these transition metal cations with these modified Aliquat 336 extractants were within a range around neutrality, under the acidic conditions, the extraction reactions of these transition metal ions did not proceed.

3.2.2. Phosphonium salts

Tetraalkylphosphonium salts like Cyphos IL 101, 102 and 104 listed in **Table 1** have recently been investigated as potential new IL extractants. Cyphos IL 101 diluted in organic solvent is extensively studied to extract metal ions such as Zn(II), Fe(III), Pd(II) and U(VI) [26, 45–48]. Cyphos IL 104 and 109 ((trihexyl)tetradecylphosphonium bis(trifluoromethylsulphonyl) imide) are also used as the extractants for Zn(II), Fe(III), Cd(II), Cr(VI) and lanthanides [26, 49–51] and Au(III) [52].

Cyphos IL101 is diluted and used solely as the extractant, and many of the advantages using ILs are lost. Viscosity of pure Cyphos IL 101 is 24.69 Pa·s at 20°C, and it drops to 11.10 Pa·s by mixing with 1% water. Therefore, undiluted Cyphos IL 101 can be used as both extractant and diluents when contacting with aqueous phase [53]. Undiluted Cyphos IL 101 was used for extractions of Co(II), Fe(III) and rare earths [53–56]. Extraction mechanism of metal ions with undiluted Cyphos IL101 is same as that of Cyphos IL 101 diluted in organic solvent. Cholío-Gonzalez et al. employed Cyphos IL 101 as diluent and Cyanex 272 as extractant for separation of Co(II) and Ni(II) [57].

Unfortunately, there are no reports on metal separation with SILM with undiluted phosphonium-based ionic liquids. A number of reports on SLM described the use of diluted ionic liquids. Fe(III) and Zn(II) were transported through a PIM composed of Cyphos IL 101 and CTA or PVC [26, 58]. Sulphuric acid was found to be an effective stripping phase. Cr(VI) was removed from hydrochloric acid through a PIM composed of Cyphos IL 104 and PVDF to sodium hydroxide solution [30]. Pd(II) was permeated through a PIM composed of Cyphos IL 101, 102 or 104 and CTA [59]. The highest values of extraction efficiency were obtained for Cyphos IL 102 and 104 as IL and 3 M HCl as a receiving phase. The efficiency strongly depended on the type of carrier and the receiving phase. Separation of Cd(II) and Cu(II) from hydrochloric acid solution was conducted using PIMs composed of Cyphos IL 101 and 104,

and CTA [60]. High selectivity of Cd(II) over Cu(II) was obtained because of difference in the stability constants of Cd(II) and Cu(II) of Eq. (1). Gold (III) was successfully recovered from the hydrochloric acid solution through a PIM composed of Cyphos IL 104 and PVDF-HFP to sodium sulphite solution [32]. In the stripping process, Au(III) is reduced to Au(I), which forms a complex with the sulphite anion. Therefore, complete transport of Au(III) from the feed to the receiving solution even in the presence of other metal ions was realized.

4. Conclusion

In this chapter, we reviewed several articles discussing the effect of related parameters such as type of solid support and supporting method as well as kind of ILs on the stability of the conventional SILM and PIM, efficiency and selectivity of metal separation. Ammonium and phosphonium ILs have been used not only as the metal extractants and carriers but also as the diluents in the solvent extraction and the membrane separation processes. In gas/vapour separation, non-volatile nature of ILs should allow for significant improvement to current processes and the development of new approaches to gas/vapour separation, while in liquid separation, problems of instability of the membrane still seem to remain despite achieving considerable improvement compared with SLM using conventional organic solvent [61]. The physical dissolution of ILs to adjacent liquid phases is in principle inevitable. On this occasion, PIM will become an excellent alternative. Although it is expected to be the lower diffusivity in PIM than in SILM, this disadvantage can be easily offset by creating a much thinner membrane in comparison to its traditional SLM counterpart [62]. So far, base polymers used in PIMs were limited to CTA and PVC. Recently, new base polymers are developed for the metal separation in PIMs. Anion-exchanged ILs such as Aliquat 336 and Cyphos IL 101 had the different capacity and selectivity of metal extraction compared with the original ones. This is suggesting that design of task-specific ILs is important and possible.

Author details

Pius Dore Ola and Michiaki Matsumoto*

*Address all correspondence to: mmatsumo@mail.doshisha.ac.jp

Department of Chemical Engineering and Materials Science, Doshisha University, Kyotanabe, Kyoto, Japan

References

- [1] Fu F., Xie L., Tang B., Wang Q., Jiang S. Application of a novel strategy-advanced Fenton-chemical precipitation to the treatment of strong stability chelated heavy metal containing wastewater. *Chemical Engineering Journal*. 2012;189–190:283–287. DOI: 10.1016/j.cej.2012.02.073

- [2] Lee K.P., Arnot T.C., Mattia D. A review of reverse osmosis membrane materials for desalination: Development to date and future potential. *Journal of Membrane Science*. 2011;370:1–22. DOI: 10.1016/j.memsci.2010.12.036
- [3] Lakherwar D. Adsorption of heavy metals: A review. *International Journal of Environmental Research and Development*. 2014;4:41–48.
- [4] Nikoloski A.N., Ang K. Review of the application of ion exchange resins for the recovery of platinum-group metals from hydrochloric acid solutions. *Mineral Processing and Extractive Metallurgy Review: An International Journal*. 2014;35:369–389. DOI: 10.1080/08827508.2013.764875
- [5] Xie F., Zhang T.A., Dresinger D., Doyle F. A critical review on solvent extraction of rare earths from aqueous solutions. *Minerals Engineering*. 2014;56:10–28. DOI: 10.1016/j.mineng.2013.10.021
- [6] Kurniawan T.A., Chan G.Y.S., Loa W., Babel S. Physico-chemical treatment techniques for wastewater laden with heavy metals. *Chemical Engineering Journal*. 2006;118:83–98. DOI: 10.1016/j.cej.2006.01.015
- [7] Sun X., Ji Y., Chen J., Ma J. Solvent impregnated resin prepared using task-specific ionic liquids for rare earth separation. *Journal of Rare Earths*. 2009;27:932–936. DOI: 10.1016/S1002-0721(08)60365-8
- [8] Liu Y., Sun X., Luo F., Chen J. The preparation of sol-gel materials doped with ionic liquids and trialkyl phosphine oxides for yttrium(III) uptake. *Analytica Chimica Acta*. 2007;604:107–113. DOI: 10.1016/j.aca.2007.10.005
- [9] Guibala E., Figuerola Piñolab A., Ruizb M., Vincenta T., Jouannina C., Sastre A.M. Immobilization of cyphos ionic liquids in alginate capsules for Cd(II) sorption. *Separation Science and Technology*. 2010;45:1935–1949. DOI: 10.1080/01496395.2010.493113
- [10] Zhu L., Liu Y., Chen J. Synthesis of N-methylimidazolium functionalized strongly basic anion exchange resins for adsorption of Cr(VI). *Industrial and Engineering Chemistry Research*. 2009;48:3261–3267. DOI: 10.1021/ie801278f
- [11] Zhu L., Zhang C., Liu Y., Wang D., Chen J. Direct synthesis of ordered N-methylimidazolium functionalized mesoporous silica as highly efficient anion exchanger of Cr(VI). *Journal of Materials Chemistry*. 2010;20:1553–1559. DOI: 10.1039/B912345H
- [12] Kislik V.S. Introduction, General Description, Definitions, and Classification. Overview. In: Kislik V.S., editor. *Liquid Membranes*. 1st ed. Amsterdam: Elsevier; 2009. p. 1–15. DOI: 10.1016/B978-0-444-53218-3.00001-5
- [13] Dzygiel P., Wiczorek P.P. Supported Liquid Membranes and Their Modifications: Definition, Classification, Theory, Stability, Application and Perspectives. In: Kislik V.S., editor. *Liquid Membranes*. 1st ed. Amsterdam: Elsevier; 2009. p. 73–140. DOI: 10.1016/B978-0-444-53218-3.00003-9

- [14] Scolander P.F. Oxygen transport through hemoglobin solutions. *Science*. 1960;131:585–590. DOI: 10.1126/science.131.3400.585
- [15] Brennecke J.F., Maginn E.J. Ionic liquids: Innovative fluids for chemical processing. *AIChE Journal*. 2001;47:2384–2389. DOI: 10.1002/aic.690471102
- [16] Carlisle T.K., Bara J.E., Gabriel C.J., Noble R.D., Gin D.L. Interpretation of CO₂ solubility and selectivity in nitrile-functionalized room-temperature ionic liquids using a group contribution approach. *Industrial and Engineering Chemical Research*. 2008;47:7005–7012. DOI: 10.1021/ie8001217
- [17] Wang J., Luo J., Feng S., Li H., Wan Y., Zhang X. Recent development of ionic liquid membranes. *Green Energy and Environment*. 2016;1:43–61. DOI: 10.1016/j.gee.2016.05.002
- [18] de los Ríos A.P., Hernández-Fernández F.J., Lozano J.J., Sánchez-Segado S., Ginestá-Anzola A., Godínez C., Tomás-Alonso F., Quesada-Medina J. On the selective separation of metal ions from hydrochloride aqueous solution by pertraction through supported ionic liquid membranes. *Journal of Membrane Science*. 2013;444:469–481. DOI: 10.1016/j.memsci.2013.05.006
- [19] Baba Y., Kubota F., Kamiya N., Goto M. Selective recovery of dysprosium and neodymium ions by a supported liquid membrane based on ionic liquids. *Solvent Extraction Research and Development, Japan*. 2011;18:193–198. DOI: 10.15261/serdj.18.193
- [20] Qian G., Song H., Yao S. Immobilized chiral tropine ionic liquid on silica gel as adsorbent for separation of metal ions and racemic amino acids. *Journal of Chromatography A*. 2016;1429:127–133. DOI: 10.1016/j.chroma.2015.11.083
- [21] Almeida M.I.G.S., Cattrall R.W., Kolev S.D. Recent trends in extraction and transport of metal ions using polymer inclusion membranes (PIMs). *Journal of Membrane Science*. 2012;415–416:9–23. DOI: 10.1016/j.memsci.2012.06.006
- [22] Matsumoto M., Murakami Y., Minamidate Y., Kondo K. Separation of lactic acid through polymer inclusion membranes containing ionic liquids. *Separation Science and Technology*. 2012;47:354–359. DOI: 10.1080/01496395.2011.620582
- [23] Kagaya S., Ryokan Y., Cattrall R.W., Kolev S.D. Stability studies of poly (vinyl chloride)-based polymer inclusion membranes containing Aliquat 336 as a carrier. *Separation and Purification Technology*. 2012;101:69–75. DOI: 10.1016/j.seppur.2012.09.007
- [24] Wang L., Paimin R., Cattrall R.W., Shen W., Kolev S.D. The extraction of cadmium(II) and copper(II) from hydrochloric acid solutions using an Aliquat 336/PVC membrane. *Journal of Membrane Science*. 2000;176:105–111. DOI: 10.1016/S0376-7388(00)00436-1
- [25] Bonggotgetsakul Y.Y.N., Cattral R.W., Kolev S.D. Extraction of gold(III) from hydrochloric acid solutions with a PVC-based polymer inclusion membrane (PIM) containing Cyphos® IL 104. *Membranes*. 2015;5:903–914. DOI: 10.3390/membranes5040903

- [26] Regel-Rosocka M., Nowak Ł., Wiśniewski M. Removal of zinc(II) and iron ions from chloride solutions with phosphonium ionic liquids. *Separation and Purification Technology*. 2012;97:158–163. DOI: 10.1016/j.seppur.2012.01.035
- [27] Gardner J.S., Walker J.O., Lamb J.B. Permeability and durability effects of cellulose polymer variation in polymer inclusion membranes. *Journal of Membrane Science*. 2004;229:87–93. DOI: 10.1016/j.memsci.2003.09.017
- [28] Kebiche-Senhadjia O., Tingry S., Seta P., Benamor M. Selective extraction of Cr(VI) over metallic species by polymer inclusion membrane (PIM) using anion (Aliquat 336) as carrier. *Desalination*. 2010;258:59–65. DOI: 10.1016/j.desal.2010.03.047
- [29] Baczyńska M., Regel-Rosocka M., Nowicki M., Wiśniewski M. Effect of the structure of polymer inclusion membranes on Zn(II) transport from chloride aqueous solutions. *Journal of Applied Polymer Science*. 2015;132:42319. DOI: 10.1002/app.42319
- [30] Guo L., Liu Y., Zhang C., Chen J. Preparation of PVDF-based polymer inclusion membrane using ionic liquid plasticizer and Cyphos IL 104 carrier for Cr(VI) transport. *Journal of Membrane Science*. 2011;372:314–321. DOI: 10.1016/j.memsci.2011.02.014
- [31] Guo L., Zhang J., Zhang D., Liu Y., Deng Y., Chen J. Preparation of poly(vinylidene fluoride-co-tetrafluoroethylene)-based polymer inclusion membrane using bifunctional ionic liquid extractant for Cr(VI) transport. *Industrial and Engineering Chemistry Research*. 2012;51:2714–2722. DOI: 10.1021/ie201824s
- [32] Bonggotgetsakul Y.Y.N., Cattral R.W.L., Kolev S.D. Recovery of gold from aqua regia digested electronic scrap using a poly(vinylidene fluoride-co-hexafluoropropene) (PVDF-HFP) based polymer inclusion membrane (PIM) containing Cyphos® IL 104. *Journal of Membrane Science*. 2016;514:274–281. DOI: 10.1016/j.memsci.2016.05.002
- [33] Truong Y.H., Kyratzis I.L., Shen W. Fabrication and characterization of electrospun PVDF-aliquat 336 fibre membrane for removal of cadmium from hydrochloric acid solutions. *Journal of Materials Science*. 2009;44:1101–1106. DOI: 10.1007/s10853-008-3208-7
- [34] Wong L., Shen W., Truong Y.B. Investigation of electrospun and film-cast PVC membranes incorporated with aliquat 336 for efficient Cd extraction: A comparative study. *Journal of Applied Polymer Science*. 2011;121:327–335. DOI: 10.1002/app.33586
- [35] Abdul-Halim N.S., Whitten P.G., Nghiem L.D. Characteristics and cadmium extraction performance of PVC/Aliquat 336 electrospun fibres in comparison with polymer inclusion membranes. *Separation Science and Technology*. 2016;51:1515–1522. DOI: 10.1080/01496395.2016.1168439
- [36] Stojanovic A., Morgenbesser C., Kogelnig D., Krachler R., Keppler B.K. Quaternary Ammonium and Phosphonium Ionic Liquids in Chemical and Environmental Engineering. In: Kokorin A., editor. *Ionic Liquids: Theory, Properties, New Approaches*. Rijeka: InTech; 2011. p. 657–680.
- [37] Seeley F.G., Crouse D.J. Extraction of metals from chloride solutions and amines. *Journal of Chemical Engineering Data*. 1966;11:424–429. DOI: 10.1021/je60030a043

- [38] Nayl A.A. Extraction and separation of Co (II) and Ni (II) from acidic sulfate solutions using Aliquat 336. *Journal of Hazardous Materials*. 2010;173:223–230. DOI: 10.1016/j.jhazmat.2009.08.072
- [39] McDonald C., Alfaro-Franco C.M. Solvent extraction studies of cobalt in aqueous thiocyanate solutions using Aliquat-336. *Microchemical Journal*. 1984;30:194–200. DOI: 10.1016/0026-265X(84)90041-9
- [40] Egorov V.M., Djigailo D.I., Momotenko D.S., Chernyshov D.V., Torocheshnikova I.I., Smirnova S.V., Pletnev I.V. Task-specific ionic liquid trioctylmethylammonium salicylate as extraction solvent for transition metal ions. *Talanta*. 2010;80:1177–1182. DOI: 10.1016/j.talanta.2009.09.003
- [41] Kogelnig D., Stjanovic A., Galanski M., Grössl M., Jirsa F., Krachler R., Keppler B.K. Greener synthesis of new ammonium ionic liquids and their potential as extracting agents. *Tetrahedron Letters*. 2008;49:2782–2785. DOI: 10.1016/j.tetlet.2008.02.138
- [42] Rout A., Venkatesan K.A., Srinivasan T.G., Vasudeva Rao P.R. Ionic liquid extractants in molecular diluents: Extraction behavior of europium (III) in quaternary ammonium-based ionic liquids. *Separation and Purification Technology*. 2012;95:26–31. DOI: 10.1016/j.seppur.2012.04.020
- [43] Sun X., Ji Y., Hu F., He B., Chen J., Li D. The inner synergistic effect of bifunctional ionic liquid extractant for solvent extraction. *Talanta*. 2010;81:1877–1883. DOI: 10.1016/j.talanta.2010.03.041
- [44] Pont N., Salvadó V., Fontàs C. Selective transport and removal of Cd from chloride solutions by polymer inclusion membrane. *Journal of Membrane Science*. 2008;318:340–345. DOI:10.1016/j.memsci.2008.02.05
- [45] Regel-Rosocka M. Extractive removal of zinc(II) from chloride liquors with phosphonium ionic liquids/toluene mixtures as novel extractants. *Separation and Purification Technology*. 2009;66:19–24. DOI: 10.1016/j.seppur.2008.12.002
- [46] Kogelnig D., Stojanovic A., Jirsa F., Korner W., Krachler R., Keppler B.K. Transport and separation of iron(III) from nickel(II) with the ionic liquid trihexyl(tetradecyl)phosphonium chloride. *Separation and Purification Technology*. 2010;72:56–60. DOI: 10.1016/j.seppur.2009.12.028
- [47] Cieszynska A., Wisniewski M. Extraction of palladium(II) from chloride solutions with Cyphos®IL 101/toluene mixtures as novel extractant. *Separation and Purification Technology*. 2010;73:202–207. DOI: 10.1016/j.seppur.2010.04.001
- [48] Quinn J.E., Ogden M.D., Soldenhoff K. Solvent extraction of uranium (VI) from chloride solutions using Cyphos IL-101. *Solvent Extraction and Ion Exchange*. 2013;31:538–549. DOI: 10.1080/07366299.2013.775891
- [49] Comesaña A., Rodriguez-Monsalve J., Cerpa A., Alguacil F.J. Non-dispersive solvent extraction with strip dispersion (NDSXSD) pertraction of Cd(II) in HCl medium

- using ionic liquid CYPHOS IL101. *Chemical Engineering Journal*. 2011;175:228–232. DOI: 10.1016/j.cej.2011.09.099
- [50] Alguacil F.J., Alonso M., Lopez F.A., Lopez-Delgado A. Pseudo-emulsion membrane strip dispersion (PEMSD) pertraction of chromium(VI) using CYPHOS IL 101 ionic liquid as carrier. *Environmental Science and Technology*. 2010;44:7504–7508. DOI: 10.1021/es101302b
- [51] Kumari A., Sinha M.K., Sahu S.K., Pandey B.D. Solvent extraction and separation of tri-valent lanthanides using Cyphos IL 104, A novel phosphonium ionic liquid as extractant. *Solvent Extraction and Ion Exchange*. 2016;34:469–484. DOI: 10.1080/07366299.2016.1207459
- [52] Nguyen V.T., Lee J., Jeong J., Kim B., Cote G., Chagnes A. Extraction of gold(III) from acidic chloride media using phosphonium-based ionic liquid as an anion exchanger. *Industrial and Engineering Chemistry Research*. 2015;54:1350–1358. DOI: 10.1021/ie5045742
- [53] Cui L., Cheng F., Zhou J. Behaviors and mechanism of iron extraction from chloride solutions using undiluted Cyphos IL 101. *Industrial and Engineering Chemistry Research*. 2015;54:7534–7542. DOI: 10.1021/acs.iecr.5b01546]
- [54] Hoogerstraete T.V., Wellens S., Verachtert K., Binnemans K. Removal of transition metals from rare earths by solvent extraction with an undiluted phosphonium ionic liquid: Separations relevant to rare-earth magnet recycling. *Green Chemistry*. 2013;15:919–927. DOI: 10.1039/C3GC40198G
- [55] Wellens S., Thijs B., Binnemans K. An environmentally friendlier approach to hydrometallurgy: highly selective separation of cobalt from nickel by solvent extraction with undiluted phosphonium ionic liquids. *Green Chemistry*. 2012;14:1657–1665. DOI: 10.1039/C2GC35246J
- [56] Wellens S., Goovaerts R., Möller C., Luyten J., Thijs B., Binnemans K. A continuous ionic liquid extraction process for the separation of cobalt from nickel. *Green Chemistry*. 2013;15:3160–3164. DOI: 10.1039/C3GC41519H
- [57] Cholío-Gonzalez D., Chagnes A., Cote G., Avila-Rodriguez M. Separation of Co(II) and Ni(II) from aqueous solutions by bis(2,4,4-trimethylpentyl)phosphinic acid (Cyanex 272) using trihexyl(tetradecyl)phosphonium chloride (Cyphos IL 101) as solvent. *Journal of Molecular Liquids*. 2015;209:203–208. DOI: 10.1016/j.molliq.2015.05.048
- [58] Kogelnig D., Regelsberger A., Stojanovic A., Jirsa F., Krachler R., Keppler B.K. A polymer inclusion membrane based on the ionic liquid trihexyl(tetradecyl)phosphonium chloride and PVC for solid-liquid extraction of Zn(II) from hydrochloric acid solution. *Monatshefte für Chemie*. 2011;142:769–772. DOI: 10.1007/s00706-011-0530-6
- [59] Regel-Rosocka M., Rzelewska M., Baczynska M., Janus M., Wisniewski M. Removal of palladium (II) from aqueous solutions with Cyphos phosphonium ionic liquids as metal ion carriers for liquid-liquid extraction and transport across polymer inclusion membranes. *Physicochemical Problems of Mineral Processing*. 2015;51:621–631.

- [60] Pospiech B. Application of phosphonium ionic liquids as ion carriers in polymer inclusion membranes (PIMs) for separation of cadmium(II) and copper(II) from aqueous solutions. *Journal of Solution Chemistry*. 2015;44:2431–2447. DOI: 10.1007/s10953-015-0413-2
- [61] Matsumoto M. Ionic Liquid-Based Support Liquid Membranes. In: Mohanty K., Purkait M.K., editors. *Membrane Technologies and Applications*. Boca Raton: CRC Press; 2012. p. 305–316. DOI: 10.1201/b11416-18
- [62] Nghiem L.D., Mornane P., Potter I.D., Perera J.M., Cattrall R.W., Kolev S.D. Extraction and transport of metal ions and small organic compounds using polymer inclusion membranes (PIMs). *Journal of Membrane Science*. 2006;281:7–41. DOI: 10.1016/j.memsci.2006.03.035

Supported Ionic Liquids

Ionic Liquids Immobilized on Magnetic Nanoparticles

Masoud Mokhtary

Additional information is available at the end of the chapter

<http://dx.doi.org/10.5772/65794>

Abstract

Ionic liquids (ILs) immobilized on supports are among the most important derivatives of ILs. The immobilization process of ILs can transfer their desired properties to substrates. The combination of the advantages of ILs with those of support materials will derive new performances while retaining the properties of both moieties. As green media in organic catalytic reactions, based on utilizing the ability of ILs to stabilize the catalysts, they have many advantages over free ILs, including avoiding the leaching of ILs, reducing their amount, and improving the recoverability and reusability of both themselves and catalysts. This has critical significance from both environmental and economical points of view. Recently, ionic liquids immobilized on magnetic nanoparticles (MNPs) have drawn increasing attention in catalytic reactions and separation technologies and achieved substantial progress. The combination of MNPs and ILs gives magnetic-supported ionic liquids, which exhibit the unique properties of ILs as well as facile separation by an external magnetic field. The excellent efficiency of this kind of immobilized ionic liquids offers a great advantage compared with other sorts of magnetic supports. In this chapter, the green catalytic processes and recent advances in organic synthesis catalyzed by ionic liquids immobilized on magnetic nanoparticles are highlighted.

Keywords: ionic liquids, magnetic nanoparticles, green synthesis, retrievable catalysts

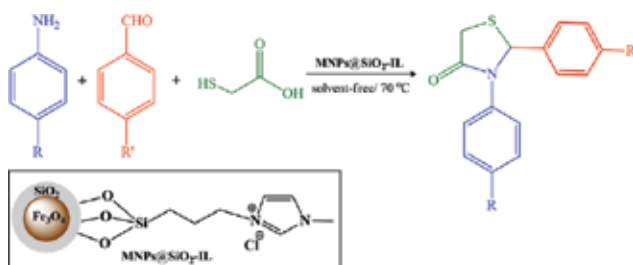
1. Introduction

Ionic liquids (ILs) are progressively being studied for targeted chemical tasks due to their unique chemical and physical properties such as nonvolatility, nonflammability, thermal stability and controlled miscibility [1]. In spite of the fact that ILs contained several advantages, but their extensive practical application was still prevented by some drawbacks like high viscosity, difficult recyclability and high cost of ILs in large-scale utilization [2]. Therefore, in

order to decrease these difficulties, immobilized IL had been prepared as a new heterogeneous catalyst with the useful features of ILs and inorganic acids for catalyzed reactions [3]. Among several usages of ILs in organic chemistry, imidazolium ionic liquid-type catalysts indicate one of the most successful developments [4]. This chapter focuses on the recent progress in organic synthesis catalyzed by ionic liquids immobilized on magnetic nanoparticles.

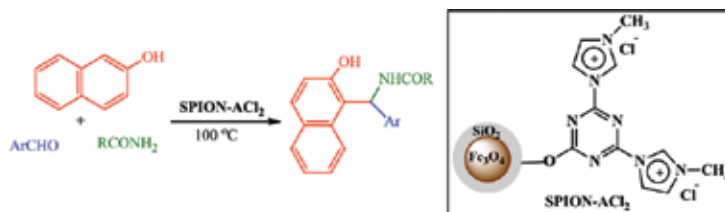
2. Ionic liquids immobilized on MNPs in multicomponent reactions

Recent studies represent that magnetic nanoparticles (MNPs) are excellent supports for ILs owing to their good stability, easily preparation and functionalization, high surface area, low toxicity and simple separation by external magnetic attractions [5]. These special features have made MNPs a convenient alternative to catalyst supports. As an example, a magnetically $\text{Fe}_3\text{O}_4@/\text{SiO}_2$ nanoparticle-immobilized ionic liquid (MNPs@ SiO_2 -IL) was prepared by Azgomi and Mokhtary [6]. The MNPs@ SiO_2 -IL was assessed as a recyclable catalyst for the one-pot synthesis of 1,3-thiazolidin-4-ones with good to great efficiency under solvent-less conditions. The catalyst could be simply recycled using a magnetic field and reused for 10 times with no considerable loss in its activity (**Scheme 1**).



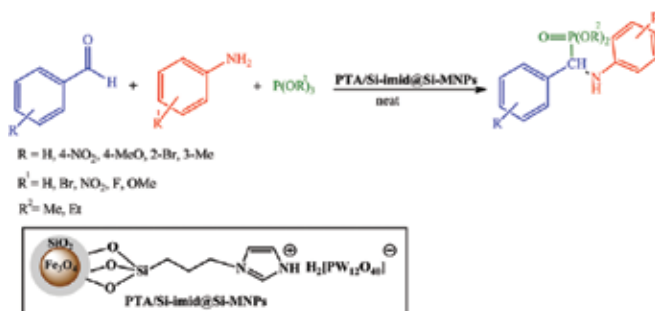
Scheme 1. One-pot synthesis of 1,3-thiazolidin-4-ones catalyzed using MNPs@ SiO_2 -IL.

A dicationic ionic liquid immobilized on superparamagnetic iron oxide nanoparticles (SPION- ACL_2) has been used as a green and powerful catalyst to effectively synthesis derivatives of β -amidoalkylnaphthol with high to excellent yields [7]. This catalyst could be recovered and reused for at least six times with no loss in catalytic activity (**Scheme 2**).



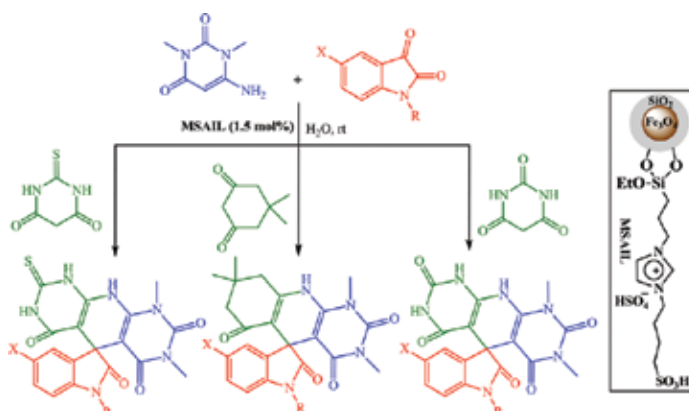
Scheme 2. Synthesis of β -amidoalkylnaphthols catalyzed by SPION- ACL_2 .

The synthesis of a magnetic nanoparticle-supported polyoxometalate has been reported, and this nanoparticle has been used as an efficient heterogeneous catalyst to prepare α -amino phosphonates under solvent-less conditions at room temperature [8]. The catalyst is easily recovered by simple magnetic separation and can be recycled several times with no considerable loss in its catalytic activity (**Scheme 3**).



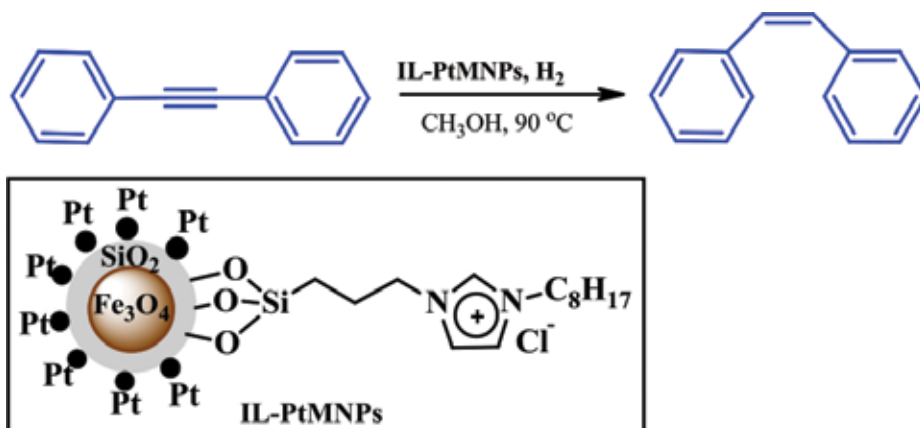
Scheme 3. PTA/Si-imid@Si-MNP's catalyzed synthesis of α -aminophosphonates.

In another research, a magnetic-supported acidic ionic liquid has been prepared and evaluated in one-pot synthesis of spirooxindoles [9]. Main properties of this approach are simplicity, low price, high efficiency, wide application scope, reusability and easy retrieval of the catalyst by an external magnet (**Scheme 4**).



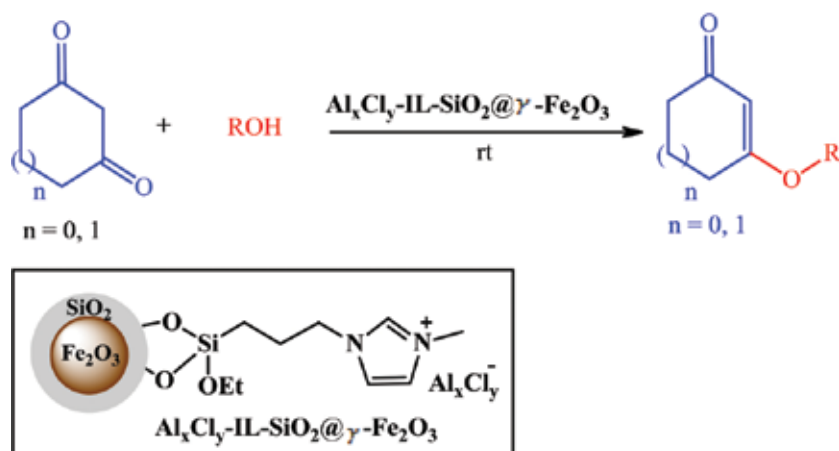
Scheme 4. Different synthesized spirooxindoles catalyzed by MSAIL.

A chemoselective hydrogenation of α,β -unsaturated aldehydes and alkynes was successfully demonstrated by Abu-Reziq et al. [10]. The Pt nanoparticles were adsorbed on the IL-functionalized MNPs via ion exchange with K_2PtCl_4 following by reduction with hydrazine. The diphenylacetylene was hydrogenated in methanol using this catalyst at 90°C under hydrogen pressure with the selective preparation of *cis*-alkenes (**Scheme 5**).



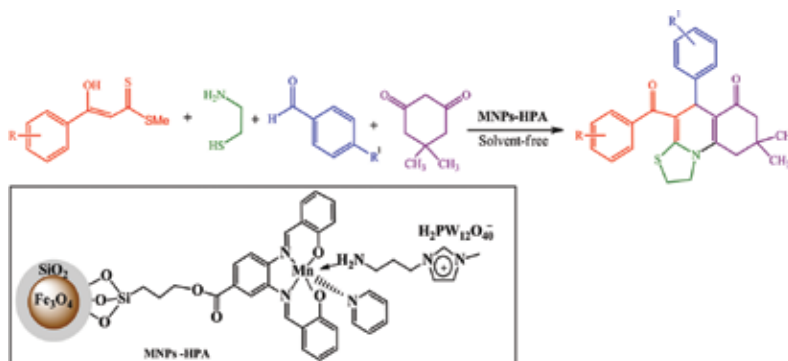
Scheme 5. Hydrogenation of diphenylacetylene in the presence of IL-PtMNPs.

Anchoring Al_xCl_y -IL onto the silica-coated $\gamma\text{-Fe}_2\text{O}_3$ particles afforded $\text{Al}_x\text{Cl}_y\text{-IL-SiO}_2@ \gamma\text{-Fe}_2\text{O}_3$ [11]. The catalyst assessment was performed to synthesis of β -ketoenol ethers (**Scheme 6**). The effectiveness of immobilized catalyst was confirmed, and the products were produced in high with excellent efficiency at ambient temperature. Furthermore, the catalyst could be simply retrieved using an external magnet and reused for six times with no considerable loss in its catalytic activity.



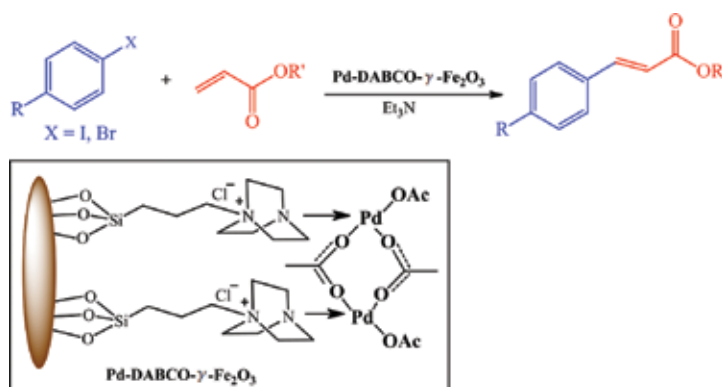
Scheme 6. Synthesis of β -keto enol ethers by $\text{Al}_x\text{Cl}_y\text{-IL-SiO}_2@ \gamma\text{-Fe}_2\text{O}_3$.

The synthesis of $\text{Fe}_3\text{O}_4@ \text{SiO}_2/\text{salen}/\text{Mn}/\text{IL}/\text{HPW}$ has been performed through attaching $\text{H}_3\text{PW}_{12}\text{O}_{40}$ on magnetite nanoparticles modified with ionic liquid [12]. The catalyst was used for one-pot synthesis of thiazoloquinolines, in good to great efficiency under solvent-less conditions (**Scheme 7**). The catalyst could be simply recovered using a magnetic field and reused ten times with no significant loss in its activity.



Scheme 7. Synthesis of thiazoloquinolines in the existence of MNPs-HPW.

Sobhani and Pakdin-Parizi have improved an efficient heterogeneous catalyst for the Mizoroki–Heck cross-coupling [13]. In this technique, γ - Fe_2O_3 magnetic nanoparticles immobilized with palladium-DABCO complex ($\text{Pd-DABCO-}\gamma\text{-Fe}_2\text{O}_3$) were prepared as a recyclable catalyst for Mizoroki–Heck cross-coupling reaction of aryl halides with olefins whose activity is not changed even after five times under solvent-less conditions (**Scheme 8**).



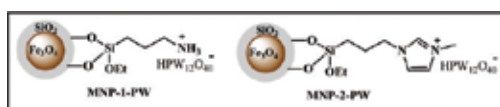
Scheme 8. Mizoroki–Heck cross-coupling reaction using $\text{Pd-DABCO-}\gamma\text{-Fe}_2\text{O}_3$.

The synthesis of hydroxyapatite-encapsulated magnetic nanoparticles immobilized with diethyl aliphatic amine basic ionic liquids ($\text{HAP-}\gamma\text{-Fe}_2\text{O}_3\text{@BILs}$) was reported, and it was applied as effective magnetic catalysts for Knoevenagel condensation reactions in aqueous medium (**Scheme 9**). The reactants were quantitatively converted under moderate conditions; the catalyst activity showed no significant loss after recovering via suitable magnetic field. The magnetic catalyst showed an excellent efficiency compared with homogeneous basic ionic liquid catalyst and the basic ionic liquid-modified polystyrene resin catalyst that was attributed to the cooperation between the base sites produced through framework HAP and the supported basic ionic liquids [14].



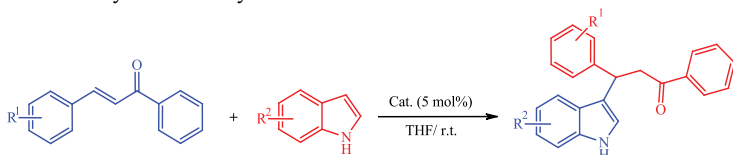
Scheme 9. A Knoevenagel condensation reaction catalyzed by HAP- γ -Fe₂O₃@BILs.

Magnetic nanoparticles supported with polyoxometalates (POMs) via ionic interaction were acquired through an easy sonication between modified magnetic nanoparticles and polyoxometalates. This material can be used as a highly active acid catalyst and as a catalyst support for chiral amines [15]. The immobilization of POM on MNPs was obtained by sonication of a mixture of MNPs (MNP-1 or MNP-2) and POM (H₃PW₁₂O₄₀) in dry THF (**Scheme 10**).



Scheme 10. Structure of MNP-1-PW and MNP-2-PW catalysts.

The Friedel-Crafts reaction of indole and chalcone was selected to examine the acidic catalytic activity and reusability of the prepared MNP-1-PW and MNP-2-PW catalysts. As observed in **Table 1**, the reactions between diverse chalcones and indoles continued efficiently to result the desired products with a high efficiency. Both magnetic POMs showed excellent activity and reusability for 12 recycles.



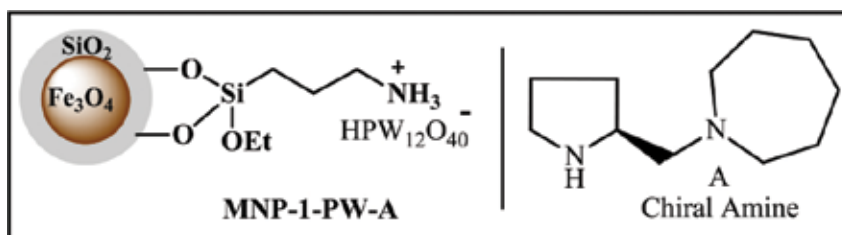
Entry	R ¹ R ²		MNP-1-PW		MNP-2-PW	
			t/h	Yield ^b (%)	t/h	Yield ^b (%)
1	H	5-MeO	20	93	20	94
2	H	5-Me	20	96	20	96
3	H	5-Br	7	98	6	97
4	H	5-Cl	7	97	6	97
5	H	5-I	7	99	6	98
6	H	6-Cl	7	98	6	98
7	4-Cl	H	12	90	12	92
8	4-Me	H	12	88	12	90

^aReaction conditions: catalyst (5 mol%), indole derivative (0.25 mmol), chalcone derivative (0.20 mmol) and THF (0.2 ml).

^bIsolated yield.

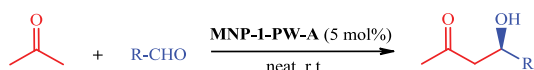
Table 1. Friedel-Crafts reactions of indoles and chalcones^a.

Also, chiral amine hybrids with magnetic POMs were easily prepared by mixing MNP-PW and chiral amine via sonication in dry THF (**Scheme 11**).



Scheme 11. Magnetic POM supported chiral amine catalyst MNP-1-PW-A.

The MNP-PW-immobilized chiral amine catalysts were next applied in typical enamine-based asymmetric direct aldol condensations. Acetone reacted with different aromatic aldehydes in the presence of 5 mol% of MNP-1-PW-A, to give the desired products with high efficiency and enantioselectivities (**Table 2**).



Entry	R	t/h	Yield ^b (%)	ee (%) ^c
1	2-NO ₂ C ₆ H ₄	12	83	89
2	3-NO ₂ C ₆ H ₄	12	87	89
3	4-CF ₃ C ₆ H ₄	30	81	90
4	2-CNC ₆ H ₄	30	80	87
5	2-ClC ₆ H ₄	48	72	87
6	2-BrC ₆ H ₄	48	77	88

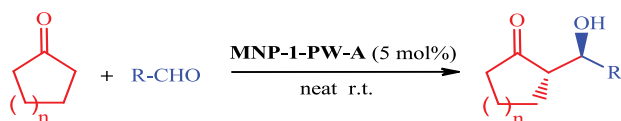
^aReaction conditions: catalyst (5 mol%), acetone (0.20 mL) and aldehyde (0.25 mmol).

^bIsolated yield.

^cDetermined by chiral HPLC.

Table 2. MNP-1-PW-A catalyzed aldol reaction of acetone^a.

Also, aldol donors such as cyclohexanone and cyclopentanone worked very well in this catalytic system (**Table 3**). Moreover, the outcomes achieved from the similar reactions with POM-chiral amine hybrid PW-A given in **Table 3** (entries 1 vs. 2). The magnetic POM-immobilized catalyst MNP-1-PW-A showed slightly higher stereoselectivity and enantioselectivity albeit with a little loss of activity. The resulted noncovalently immobilized catalyst could be reused up to 11 times with essentially no loss of activity and enantioselectivity.



Entry	N	R	t/h	Yield ^b (%)	Syn/anti ^c	ee ^d (%)
1	1	4-NO ₂ C ₆ H ₄	5	97	6:94	97
2 ^e	1	4-NO ₂ C ₆ H ₄	6	86	23:77	95
3	1	2-NO ₂ C ₆ H ₄	5	97	24:76	98
4	1	3-NO ₂ C ₆ H ₄	5	96	16:84	98
5	1	4-CF ₃ C ₆ H ₄	12	88	17:73	97
6	1	4-ClC ₆ H ₄	48	86	20:80	96
7	2	2-NO ₂ C ₆ H ₄	8	98	13:87	99
8	2	3-NO ₂ C ₆ H ₄	8	97	14:86	98
9	2	4-NO ₂ C ₆ H ₄	6	97	14:86	97
10	2	4-CF ₃ C ₆ H ₄	11	93	13:87	98
11	2	4-ClC ₆ H ₄	48	92	17:83	98

^aReaction conditions: catalyst (5 mol%), ketone (0.20 mL) and aldehyde (0.25 mmol).

^bIsolated yield.

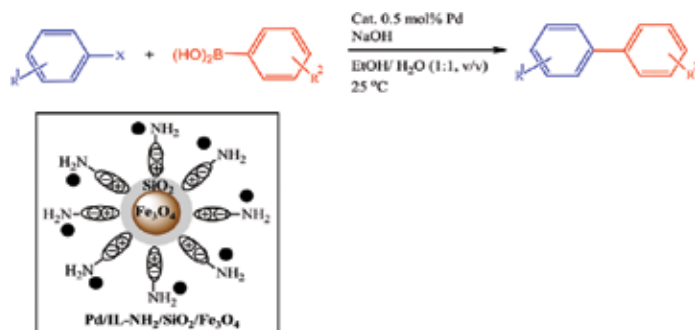
^cDetermined by chiral HPLC.

^dDetermined by chiral HPLC.

^ePW-A (1 mol%) was employed.

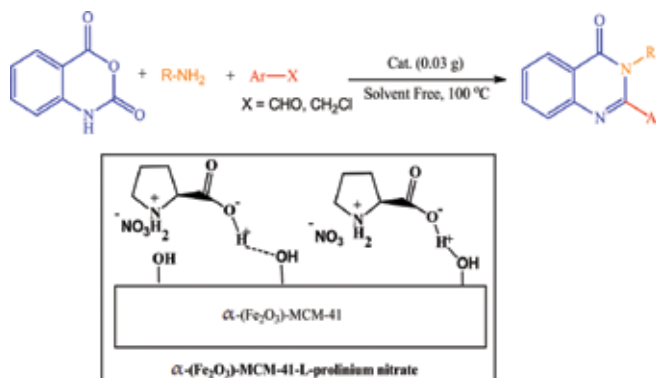
Table 3. MNP-1-PW-A catalyzed aldol reaction of different aldol donors^a.

A suitable approach has been improved for preparation of retrievable Pd catalyst using immobilization of palladium nanoparticles on magnetic nanoparticles modified with functional ionic liquid [16]. The amine functionalized ionic liquid immobilized Pd nanoparticles in the Pd/IL-NH₂/SiO₂/Fe₃O₄ catalyst demonstrates great catalytic activity for a wide diversity of aryl iodides and bromides in the Suzuki coupling reactions at ambient temperature (**Scheme 12**). Furthermore, the catalyst is able to be good distributed in the reaction media, simply retrieved from the reaction mixture by using a magnet, and reused for several times with no significant loss in activity. Because of all these advantages, this procedure is a green and appropriate for other important reactions catalyzed with metal.



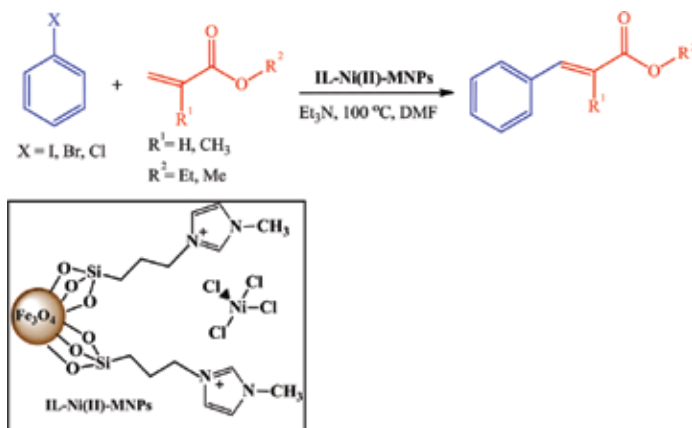
Scheme 12. The Suzuki coupling reactions of aryl iodides and bromides by Pd/IL-NH₂/SiO₂/Fe₃O₄ catalyst.

α -Fe₂O₃-MCM-41 immobilized with amino acid ionic liquid was prepared as a retrievable catalyst for synthesizing quinazolin-4(3*H*)-ones at ambient temperature in short reaction times under oxidant and solvent-less conditions (**Scheme 13**). It is supposed that the L-prolinium nitrate in the mesochannels of (α -Fe₂O₃)-MCM-41 might enhance the strength of Brønsted acid and oxidation power of catalytic system [17].



Scheme 13. (α -Fe₂O₃)-MCM-41-L-prolinium nitrate for the synthesis of quinazolin-4(3*H*)-ones.

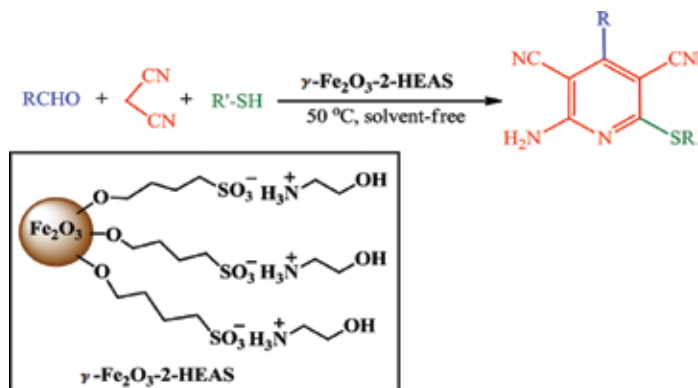
Moreover, there is a report on synthesis of magnetic nanoparticles immobilized with Ni²⁺ ion-containing 1-methyl-3-(3-trimethoxysilylpropyl) imidazolium chloride ionic liquid as a recoverable nanocatalyst for the Heck reaction at 100°C, and it can be applied after washing with no loss in activity (**Scheme 14**) [18].



Scheme 14. Heck reaction catalyzed by IL-Ni(II)-MNPs.

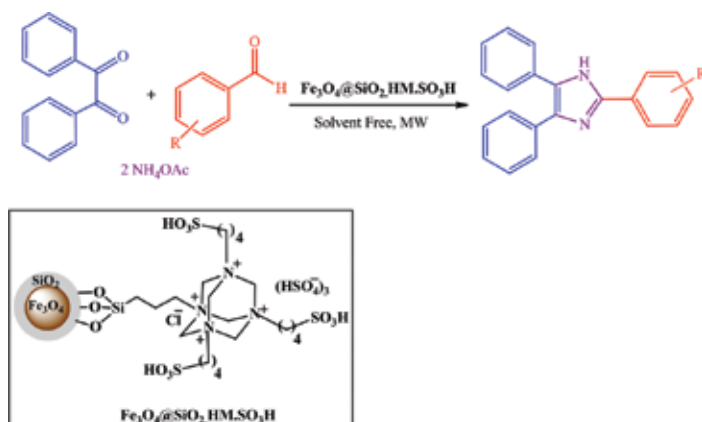
γ -Fe₂O₃ nanoparticles immobilized with 2-Hydroxyethylammonium sulphonate (γ -Fe₂O₃-2-HEAS) were prepared through the reaction of n-butylsulfonated γ -Fe₂O₃ with ethanolamine [19]. Here, the catalyst effectively increases the condensation of both aliphatic and aromatic

aldehydes and thiols with malononitrile resulting in 2-amino-3,5-dicarbonitrile-6-thio-pyridines in good to excellent efficiency under solvent-less conditions (**Scheme 15**). Separating the product and recycling the catalyst are easily performed using a suitable external magnet. The catalyst can be reused for five times with no significant loss in its catalytic activity.



Scheme 15. Synthesis of 2-amino-3,5-dicarbonitrile-6-thio-pyridines catalyzed using γ - Fe_2O_3 MNPs.

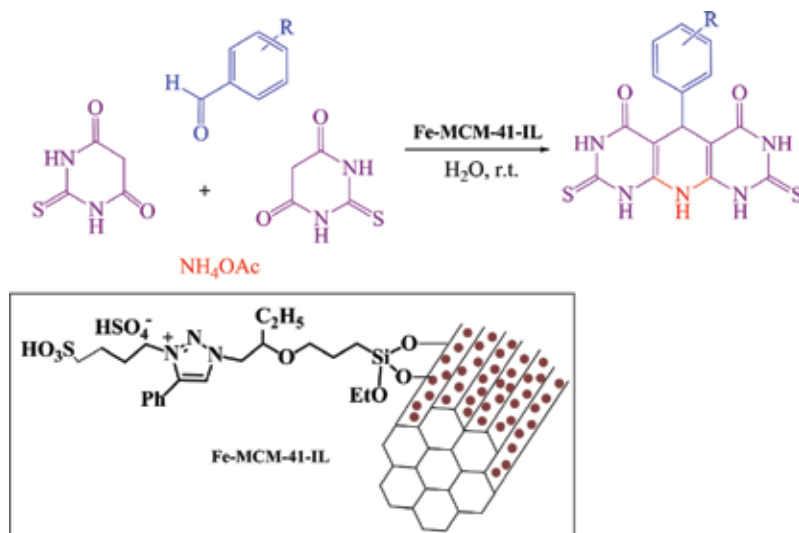
An effective synthesis of 2,4,5-trisubstituted imidazoles is achieved by silica-coated magnetite nanoparticles immobilized with multi- SO_3H functionalized acidic ionic liquid (**Scheme 16**). Because of high performance, recoverability, short reaction times, efficiency of products and operational simplicity, this process is an attractive substitute for the green synthesis of 2,4,5-trisubstituted imidazoles as biological and pharmaceutical-related substances [20].



Scheme 16. Synthesis of 2,4,5-trisubstituted imidazoles catalyzed by $\text{Fe}_3\text{O}_4@/\text{SiO}_2.\text{HM}.\text{SO}_3\text{H}$.

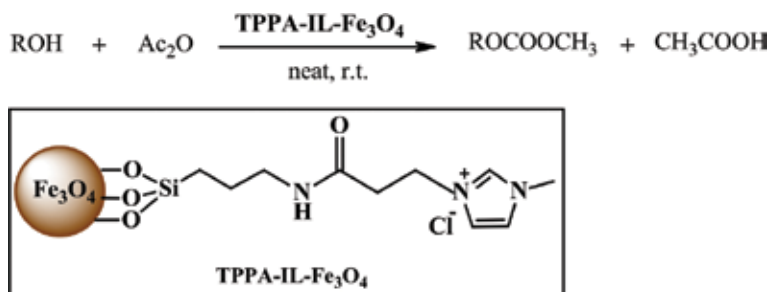
An ionic liquid stabilized iron-containing mesoporous silica nanoparticles (Fe-MCM-41-IL) was synthesized by fixing a triazolium ionic liquid on Fe-coated MCM. The pyrimidine derivatives were synthesized through one-pot method in the presence of Fe-MCM-41-IL as an

effective heterogeneous acidic IL catalyst from aldehydes, 2-thiobarbituric acid and ammonium acetate under moderate condition in excellent efficiencies (**Scheme 17**). This procedure is greener compared with other reported methods because of its moderate conditions of reaction, excellent efficiencies and simple recycling of the catalyst [21].



Scheme 17. One-pot synthesis of pyrido[2,3-d:6,5-d]dipyrimidines catalyzed by Fe-MCM-41-IL.

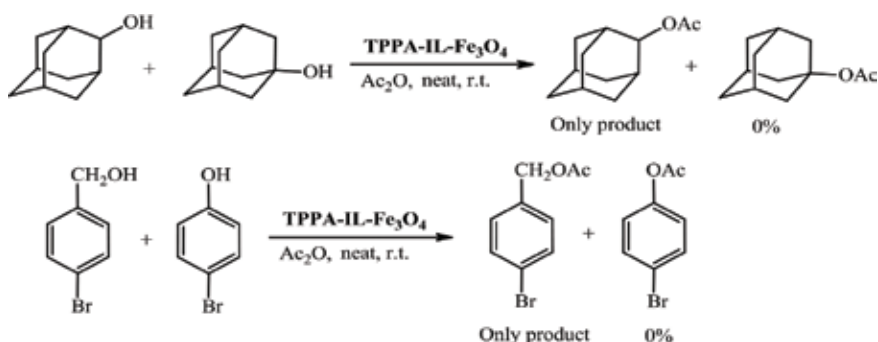
A simple and effective process has been reported for synthesizing 3-((3-(trisilyloxy)propyl)propionamide)-1-methylimidazolium chloride ionic liquid supported on magnetic nanoparticles (TPPA-IL-Fe₃O₄) [22]. The TPPA-IL-Fe₃O₄ assessed as a recoverable heterogeneous catalyst for the alcohols acetylation with acetic anhydride under moderate conditions at ambient temperature with high efficiencies (**Scheme 18**).



Scheme 18. Acetylation of alcohols catalyzed by TPPA-IL-Fe₃O₄.

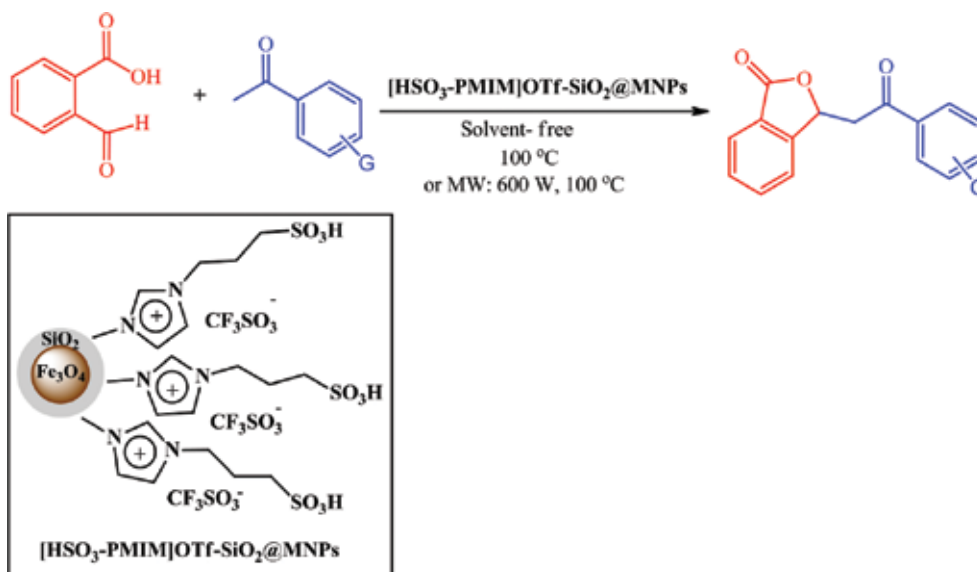
The hydroxyl groups were chemoselectively acetylated in the existence of other reactive groups by using the synthesized catalyst. The acetylation of 4-bormobenzyl alcohol did occur

selectively in the presence of 4-bromophenol, and the hydroxyl group of phenol was intact during this reaction (**Scheme 19**).



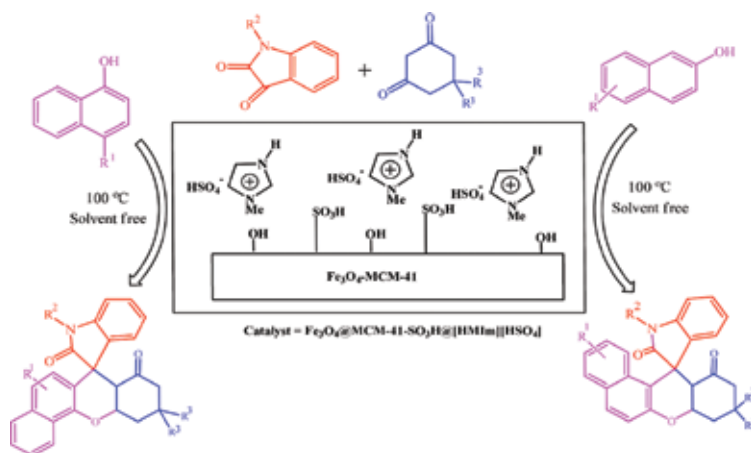
Scheme 19. Chemoselectivity of the acetylation hydroxyl groups in the presence of TPPA-IL-Fe₃O₄.

An ecologically friendly technique has been improved for preparing isobenzofuran-1(3*H*)-ones in the existence of [HSO₃PMIM]OTf-SiO₂@MNPs as a highly retrievable catalyst under solvent-free thermal conditions and MW irradiation [23]. Mono- and bis-isobenzofuran-1(3*H*)-ones were effectively synthesized in the presence of this catalyst under thermal conditions and MW irradiation. The considerable advantages of this procedure for the synthesis of isobenzofuran-1(3*H*)-ones are its simplicity, excellent yields, short times of reaction, eco-friendly and simple recycling of the catalyst (**Scheme 20**).



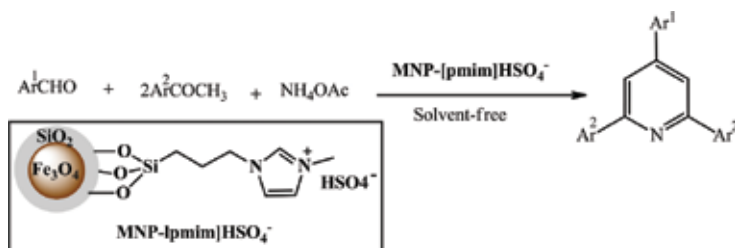
Scheme 20. Synthesis of isobenzofuran-1(3*H*)-ones catalyzed using [HSO₃PMIM]OTf-SiO₂@MNPs.

The $\text{Fe}_3\text{O}_4\text{@MCM-41-SO}_3\text{H@}[\text{HMIm}][\text{HSO}_4]$ efficiently catalyzed the one-pot three-component condensation of α or β naphthol, cyclic 1,3-diketone and isatin derivatives for the synthesis of spiro[benzoxanthene-indoline]diones (**Scheme 21**) [24]. This active catalyst was thermally stable, green, recyclable and easy to prepare. In addition, its separation of the reaction mixture is easy and it could be retrieved up to five times with no significant influence on its activity or the reaction efficiency.



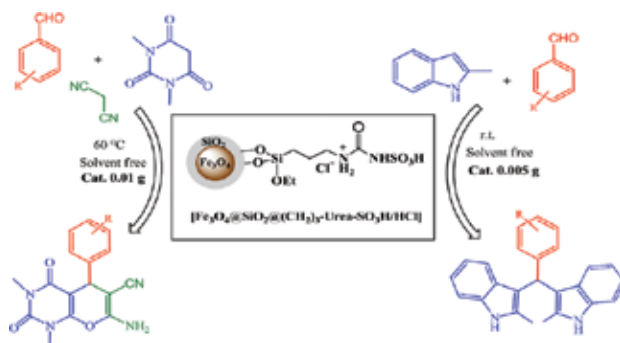
Scheme 21. Synthesis of spiro[benzoxanthene-indoline]diones catalyzed by $\text{Fe}_3\text{O}_4\text{@MCM-41-SO}_3\text{H@[HMIm][HSO}_4]$.

The silica-coated magnetic particles immobilized with 1-methyl-3-(triethoxysilylpropyl) imidazolium chloride provided the corresponding supported ionic liquid. Substituting the Cl^- anion through treatment with H_2SO_4 resulted in Bronsted ionic liquid 1-methyl-3-(triethoxysilylpropyl) imidazolium hydrogensulfate (MNP-[pmim]HSO₄) [25]. The activity of the immobilized ionic liquid was studied as a catalyst for synthesizing the polysubstituted pyridines using condensation of aromatic aldehydes with acetophenones and ammonium acetate in modest to excellent efficiency under solvent-less conditions (**Scheme 22**). The recycling of the catalyst can be simply performed using an external magnet, and it can be reapplied for at least seven times with no change in its activity.



Scheme 22. Synthesis of triarylpyridines catalyzed by MNP-[pmim]HSO_4^- .

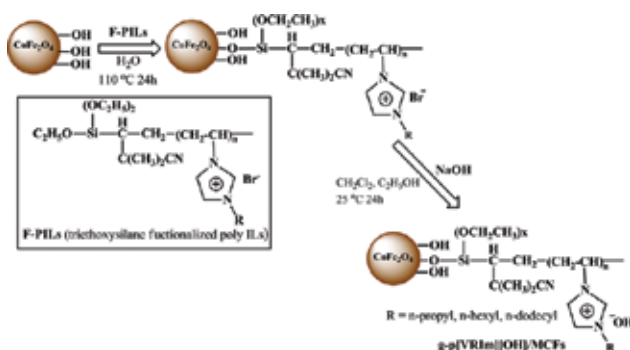
Silica-coated Fe_3O_4 magnetic nanoparticles immobilized with urea-based ionic liquid $[\text{Fe}_3\text{O}_4@\text{SiO}_2@(\text{CH}_2)_3\text{-Urea-SO}_3\text{H}/\text{HCl}]$ have been prepared [26]. The catalyst was studied for the synthesis of bis(indolyl)methane derivatives through the reaction between 2-methylindole and aldehydes at ambient temperature under solvent-free conditions. In addition, pyrano[2,3-d]pyrimidinones were synthesized in the presence of the catalyst through the one-pot condensation reaction of 1,3-dimethylbarbituric acid, aldehydes and malononitrile under solvent-less conditions at 60°C (Scheme 23).



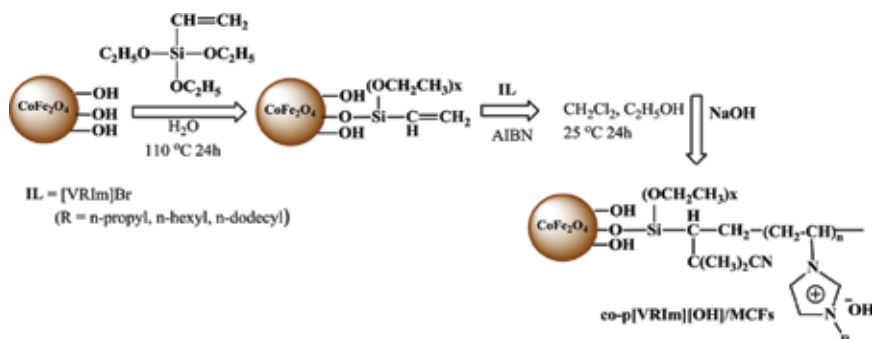
Scheme 23. Synthesis of bis(indolyl)methanes and pyrano[2,3-d]pyrimidinones catalyzed by MNPs@ILs.

3. Polymeric ionic liquids immobilized on magnetic nanoparticles

The successful synthesis of magnetic CoFe_2O_4 nanoparticles coated with basic poly(ionic liquids) was carried out, and the catalyst synthesized using the surface grafting technique (g-p[VRIm][OH]/MCFs) (Scheme 24) had a better stability, greater loading of ionic liquids and good paramagnetism compared with that synthesized through the conventional copolymerization technique (co-p[VRIm][OH]/MCFs) (Scheme 25) [27].

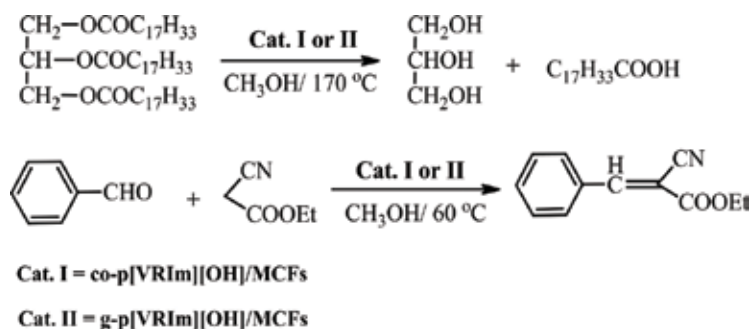


Scheme 24. The procedure for preparation of g-p[VRIm][OH]/MCFs.



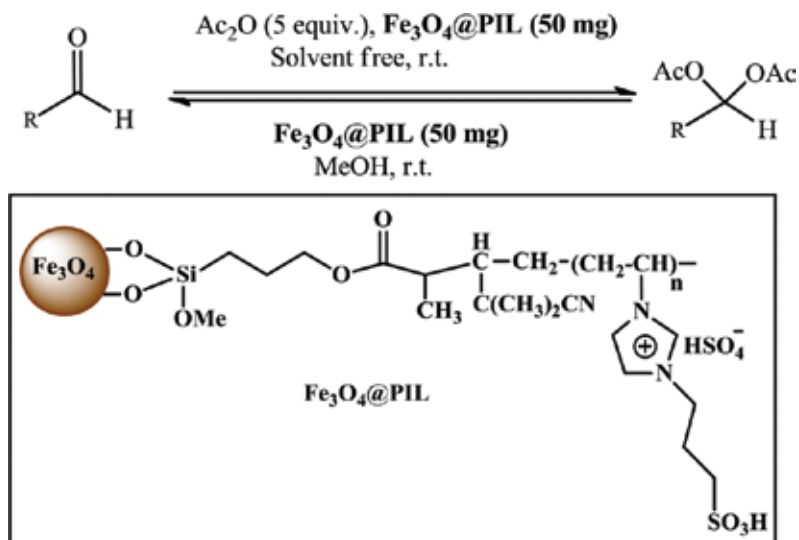
Scheme 25. The procedure for preparation of co-p[VRIm][OH]/MCFs.

The activities of the catalysts were studied for the Knoevenagel condensation reaction of benzaldehyde with ethyl cyanoacetate and for the transesterification of glycerol trioleate (TG) with methanol (**Scheme 26**). The results showed that in contrast to the sample synthesized by the copolymerization technique, the catalysts had a good catalytic efficiency.



Scheme 26. The transesterification of glycerol trioleate (TG) and the Knoevenagel condensation of benzaldehyde with ethyl cyanoacetate.

Because of the influence of steric hindrance and active sites, g-p[VDoIm][OH]/MCFs showed a higher catalytic activity than co-p[VDoIm][OH]/MCFs. The conversion of benzaldehyde was around 97% for g-p[VDoIm][OH]/MCFs higher than 72.5% for co-p[VDoIm][OH]/MCFs that was in accordance with the reaction of transesterification. Moreover, *N*-propyl-sulfonic acid bonded onto magnetic nanoparticle coated with poly(ionic liquid) (Fe₃O₄@PIL) catalyst was successfully synthesized through polymerizing functionalized vinylimidazolium in the existence of magnetic nanoparticles with modified surface [28]. The obtained catalyst is indicated to be an effective heterogeneous acidic nanocatalyst for synthesizing 1,1-diacetal from aldehydes under solvent-less conditions and ambient temperature in a good efficiency. In addition, the catalyst demonstrates an excellent activity for the deprotection reaction of acetals (**Scheme 27**). The catalyst has an excellent thermal stability and reusability because the surface of the magnetic nanoparticles is coated with polymer layers.



Scheme 27. Acetylation of aldehydes and their deprotection using $\text{Fe}_3\text{O}_4\text{@PIL}$ as catalyst.

4. Summary and outlook

According to this chapter, there are some interesting new advancements in ionic liquids supported on magnetic nanoparticles. There is a clear procedure including silica coating of magnetic nanoparticle core followed by functionalization using proper alkoxy silane derivatives. Easy modification of the magnetic iron oxide surfaces with organic ligands increases the adsorption of catalytically active metal nanoparticles, as highlighted with palladium-mediated C-C coupling and Pt-catalyzed hydrogenation reactions. The high dispersity of the MNPs in different solvents is another advantage, when it exposes the surface-bound active reaction sites for the reactants in an optimized way. This lets diffusion restriction to be dominated, which is generally found in microporous or mesoporous heterogenized solids. Clearly, the unique magnetic properties of the superparamagnetic particles lead to recyclable magnetic nanoparticles immobilized with ionic liquids for several times using a suitable magnet with no significant loss in their catalytic activity. The sustainable synthesis of magnetically retrievable ionic liquids using readily available reactants will also make this field of research green. Additional interesting improvement is the poly(ionic liquids) stabilized magnetic nanoparticles as a new group of heterogeneous catalyst that is mainly attractive in organic synthesis practiced in an ecologically friendly way. In the end, future efforts for more efficient protocols will still focus on the stability, sustainability, environmental impact and considerable cost and energy savings due to the growing needs of industry. These attempts will permit a wide diversity of industrial usages for ionic liquids immobilized on magnetic nanoparticles in the future.

Acknowledgements

Financial support by Rasht Branch, Islamic Azad University Grant No. 4.5830 is gratefully acknowledged.

Author details

Masoud Mokhtary

Address all correspondence to: mmokhtary@iaurasht.ac.ir

Department of Chemistry, Rasht Branch, Islamic Azad University, Rasht, Iran

References

- [1] Parvulescu VI, Hardacre C. Catalysis in ionic liquids. *Chemical Reviews*. 2007; 107: 2615–2665. doi:10.1021/cr050948h
- [2] Sahoo S, et al. Oxidative kinetic resolution of alcohols using chiral Mn–salen complex immobilized onto ionic liquid modified silica. *Applied Catalysis A. General*. 2009; 354: 17–25. doi:10.1016/j.apcata.2008.10.039
- [3] Miao J, Wan H, Guan G. Synthesis of immobilized Brønsted acidic ionic liquid on silica gel as heterogeneous catalyst for esterification. *Catalysis Communications*. 2011; 12: 353–356. doi:10.1016/j.catcom.2010.10.014
- [4] Zarrouk A, et al. Synthesis, characterization and comparative study of new functionalized imidazolium-based ionic liquids derivatives towards corrosion of C38 steel in molar hydrochloric acid. *International Journal of Electrochemical Science*. 2012; 7: 6998–7015.
- [5] Safari J, Zarnegar Z. Immobilized ionic liquid on superparamagnetic nanoparticles as an effective catalyst for the synthesis of tetrasubstituted imidazoles under solvent free conditions and microwave irradiation. *Comptes Rendus Chimie*. 2013; 16: 920–928. doi:10.1016/j.crci.2013.01.019
- [6] Azgomi N, Mokhtary M. Nano-Fe₃O₄@SiO₂ supported ionic liquid as an efficient catalyst for the synthesis of 1,3-thiazolidin-4-ones under solvent-free conditions. *Journal of Molecular Catalysis A: Chemical*. 2015; 398: 58–64. doi:10.1016/j.molcata.2014.11.018
- [7] Shafiee M, et al. A new green catalyst: 1,3,5-triazine-functionalized bisimidazolium dichloride tethered SPION catalyzed Betti synthesis. *Catalysis Science and Technology*. 2012; 2: 2440–2444. doi:10.1039/C2CY20187A

- [8] Hamadi H, et al. Magnetic nanoparticle supported polyoxometalate: An efficient and reusable catalyst for solvent-free synthesis of α -aminophosphonates. *Journal of Molecular Catalysis A: Chemical*. 2013; 373: 25–29. doi:10.1016/j.molcata.2013.02.018
- [9] Khalafi-Nezhad A, Mohammadi S. Magnetic, acidic, ionic liquid-catalyzed one-pot synthesis of spirooxindoles. *ACS Combinatorial Science*. 2013; 15: 512–518. doi:10.1021/co400080z
- [10] Abu-Reziq R, et al. Platinum nanoparticles supported on ionic liquid-modified magnetic nanoparticles: Selective hydrogenation catalysts. *Advanced Synthesis and Catalysis*. 2007; 349: 2145–2150. doi:10.1002/adsc.200700129
- [11] Li P-H, et al. Ionic liquid supported on magnetic nanoparticles as highly efficient and recyclable catalyst for the synthesis of β -keto enol. *Catalysis Communications*. 2014; 46: 118–122. doi:10.1016/j.catcom.2013.11.025
- [12] Sadeghzadeh S. M, A heteropolyacid-based ionic liquid immobilized onto $\text{Fe}_3\text{O}_4/\text{SiO}_2/\text{salen}/\text{Mn}$ as an environmentally friendly catalyst in a multi-component reaction. *RSC Advances*. 2015; 5: 17319–17324. doi:10.1039/c4ra16726k
- [13] Sobhani S, Pakdin-Parizi Z. Palladium-DABCO complex supported on $\gamma\text{-Fe}_2\text{O}_3$ magnetic nanoparticles: A new catalyst for C-C bond formation via Mizoroki–Heck cross-coupling reaction. *Applied Catalysis A: General*. 2014; 479: 112–120. doi:10.1016/j.apcata.2014.04.028
- [14] Zhang Y, Xia C. Magnetic hydroxyapatite-encapsulated $\gamma\text{-Fe}_2\text{O}_3$ nanoparticles functionalized with basic ionic liquids for aqueous Knoevenagel condensation. *Applied Catalysis A: General*. 2009; 366: 141–147. doi:10.1016/j.apcata.2009.06.041
- [15] Zheng X, Zhang L, Li J, Luo S, Cheng J. Magnetic nanoparticle supported polyoxometalates (POMs) via non-covalent interaction: Reusable acid catalysts and catalyst supports for chiral amines. *Chemical Communications*. 2011; 47: 12325–12327. doi:10.1039/c1cc14178c
- [16] Wang J, Xu B, Sun H, Song G. Palladium nanoparticles supported on functional ionic liquid modified magnetic nanoparticles as recyclable catalyst for room temperature Suzuki reaction. *Tetrahedron Letters*. 2013; 54: 238–241. doi:10.1016/j.tetlet.2012.11.009
- [17] Rostamizadeh S, Nojavan M, Aryan R, Isapoor E, Azad M, Amino acid-based ionic liquid immobilized on $\alpha\text{-Fe}_2\text{O}_3\text{-MCM-41}$: An efficient magnetic nanocatalyst and recyclable reaction media for the synthesis of quinazolin-4(3H)-one derivatives. *Journal of Molecular Catalysis A: Chemical*. 2013; 374–375: 102–110. doi:10.1016/j.molcata.2013.04.002
- [18] Safari J, Zarnegar Z, Ni ion-containing immobilized ionic liquid on magnetic Fe_3O_4 nanoparticles: An effective catalyst for the Heck reaction. *Comptes Rendus Chimie*. 2013; 16: 821–828. doi:10.1016/j.crci.2013.03.018
- [19] Sobhani S, Honarmand M, Ionic liquid immobilized on $\gamma\text{-Fe}_2\text{O}_3$ nanoparticles: A new magnetically recyclable heterogeneous catalyst for one-pot three-component synthesis

- of 2-amino-3, 5-dicarbonitrile-6-thio-pyridines. *Applied Catalysis A: General*. 2013; 467: 456–462. doi:10.1016/j.apcata.2013.08.006
- [20] Naeimi H, Aghaseyedkarimi D, $\text{Fe}_3\text{O}_4@\text{SiO}_2\cdot\text{HM}\cdot\text{SO}_3\text{H}$ as a recyclable heterogeneous nanocatalyst for the microwave-promoted synthesis of 2,4,5-trisubstituted imidazoles under solvent free conditions. *New Journal of Chemistry*. 2015; 39: 9415–9421. doi: 10.1039/c5nj01273b
- [21] Naeimi H, Nejadshafiee V, Islami M. R, Iron (III)-doped, ionic liquid matrix-immobilized, mesoporous silica nanoparticles: Application as recyclable catalyst for synthesis of pyrimidines in water. *Microporous and Mesoporous Materials*. 2016; 227: 23–30. doi: 10.1016/j.micromeso.2016.02.036
- [22] Ghorbani-Choghamarani A, Norouzi M, Synthesis and characterization of Ionic Liquid immobilized on magnetic nanoparticles: A recyclable heterogeneous organocatalyst for the acetylation of alcohols. *Journal of Magnetism and Magnetic Materials*. 2016; 401: 832–840. doi:10.1016/j.jmmm.2015.10.044
- [23] Rastegari F, Mohammadpoor-Baltork I, Khosropour A. R, Tangestaninejad S, Mirkhani V, Moghadam M, 1-Methyl-3-(propyl-3-sulfonic acid)imidazolium triflate supported on magnetic nanoparticles: An efficient and reusable catalyst for synthesis of mono- and bisisobenzofuran-1(3*H*)-ones under solvent-free conditions. *RSC Advances*. 2015; 5: 15274–15282. doi:10.1039/C4RA14112A
- [24] Kefayati H, Jirsaray Bazargard S, Vejdansafat P, Shariati S, Mehtar Kohankar A, $\text{Fe}_3\text{O}_4@\text{MCM-41-SO}_3\text{H}@\text{[HMIm][HSO}_4\text{]}$: An effective magnetically separable nanocatalyst for the synthesis of novel spiro[benzoxanthene-indoline]diones. *Dyes and Pigments*. 2016; 125: 309–315. doi:10.1016/j.dyepig.2015.10.034
- [25] Alinezhad H, Tajbakhsh M, Ghobadi N, Nano Fe_3O_4 -supported, hydrogensulfate ionic liquid-catalyzed, one-pot synthesis of polysubstituted pyridines. *Synthetic Communications*. 2015; 45: 1964–1976. doi:10.1080/00397911.2015.1041046
- [26] Zolfigol M. A, Ayazi-Nasrabadi R, Bagheri S, The first urea-based ionic liquid-stabilized magnetic nanoparticles: An efficient catalyst for the synthesis of bis(indolyl)methanes and pyrano[2,3-*d*]pyrimidinone derivatives. *Applied Organometallic Chemistry*. 2016; 30: 273–281. doi:10.1002/aoc.3428
- [27] Yuan H, Jiao Q, Zhang Y, Zhang J, Wu Q, Zhao Y, Neerunjun S, Li H, Magnetic CoFe_2O_4 Nanoparticles Supported Basic Poly(Ionic Liquid)s Catalysts: Preparation and Catalytic Performance Comparison in Transesterification and Knoevenagel Condensation. *Catalysis Letters*. 2016; 146: 951–959. doi:10.1007/s10562-016-1718-5
- [28] Pourjavadi A, Hosseini S. H, Doulabi M, Fakoorpoor S. M, Seidi F, Multi-layer functionalized poly(Ionic liquid) coated magnetic nanoparticles: Highly recoverable and magnetically separable Brønsted acid catalyst. *ACS Catalysis*. 2012; 2: 1259-1266. doi: 10.1021/cs300140j

Preparation of Ionic Liquids Containing Siloxane Frameworks

Yoshiro Kaneko, Akiyuki Harada, Takuya Kubo and Takuhiro Ishii

Additional information is available at the end of the chapter

<http://dx.doi.org/10.5772/65892>

Abstract

This chapter deals with our recent researches on the preparation and properties of thermally stable ionic liquids (ILs) containing siloxane frameworks. ILs containing randomly structured oligosilsesquioxanes with quaternary ammonium side-chain groups (**Am-Random-SQ-IL**) and with imidazolium side-chain groups (**Im-Random-SQ-IL**) were successfully prepared by the hydrolytic condensation of the corresponding trifunctional alkoxy silanes in aqueous bis(trifluoromethanesulfonyl)imide (HNTf₂) solution. It is also reported that ILs containing cage-like oligosilsesquioxanes (POSSs) with imidazolium side-chain groups (**Im-Cage-SQ-IL**) and with random distribution of quaternary ammonium and imidazolium side-chain groups (**Amim-Cage-SQ-IL**) were obtained, when the similar hydrolytic condensations were performed in a water/methanol (1 : 19 v/v) mixed solution of HNTf₂. In addition, we investigated the preparation of ILs containing cyclic oligosiloxanes with various imidazolium side-chain groups (**MeIm-CyS-IL-NTf₂**, **MeIm-CyS-IL-OTf**, **HIm-CyS-IL-NTf₂**, **EtIm-CyS-IL-NTf₂**, **PrIm-CyS-IL-NTf₂**, and **BuIm-CyS-IL-NTf₂**) by the hydrolytic condensation of the corresponding difunctional alkoxy silanes in the solutions of superacids, such as HNTf₂ and trifluoromethanesulfonic acid (HOTf).

Keywords: alkoxy silane, cyclic oligosiloxane, hydrolytic condensation, ionic liquid, POSS, siloxane, silsesquioxane, superacid

1. Introduction

Ionic liquids (ILs), molten salts below 100°C or 150°C, have attracted much attention because of their potential application to green solvents [1–4] and electrolyte materials [5–7]. These

compounds indicate the negligible vapor pressure, high thermal stability, and high ionic conductivity. Most ILs are regarded as organic compounds because of the presence of large amount of organic components in ILs. On the other hand, ILs with relatively more inorganic components could be applied to a wide range of materials research due to their significantly higher thermostability derived from the inorganic components.

Based on such considerations, some ILs containing inorganic frameworks, such as cage-like oligosilsesquioxanes (polyhedral oligomeric silsesquioxanes: POSSs) have been developed so far. A POSS IL (melting point (T_m) = 23°C) was first developed by Chujo et al. [8]. This POSS IL had carboxylate anionic side-chain groups and imidazolium counter cations. In other cases, a POSS IL (T_m = 18°C) containing imidazolium cationic side-chain groups and dodecyl sulfate counter anions was prepared by Feng and coworkers [9]. However, these POSS ILs had relatively lower thermal decomposition (pyrolysis) temperatures (T_d s < 250°C) because of the large proportion of organic components in their side-chains or counter ions.

In this chapter, we would like to describe our recent work on the preparation of thermally stable ILs containing siloxane frameworks, such as randomly structured oligosilsesquioxanes, POSSs, and cyclic oligosiloxanes, by the hydrolytic condensation of the corresponding tri- and di-alkoxysilanes using superacid catalysts.

2. Preparation of a quaternary ammonium-type ionic liquid containing randomly structured oligosilsesquioxane

So far, we have prepared ionic siloxane compounds with regular structures, such as POSSs [10–12], ladder-like polysilsesquioxanes [13–19], and cyclic siloxanes [20], by the hydrolytic condensation of tri- and di-alkoxysilanes containing functional organic groups, which can be converted into ionic groups during the reactions. While performing these studies on the preparation of regularly structured ionic siloxane compounds, we fortuitously found a highly thermostable IL containing randomly structured oligosilsesquioxane, which has quaternary ammonium side-chain groups. We first describe the preparation and properties of this IL.

A quaternary ammonium-type IL containing randomly structured oligosilsesquioxane (**Am-Random-SQ-IL**) was successfully prepared by the hydrolytic condensation of the quaternary ammonium salt containing organotrialkoxysilane, trimethyl[3-(triethoxysilyl)propyl] ammonium chloride (TTACl), in aqueous bis(trifluoromethanesulfonyl)imide (HNTf₂) solution under the following conditions (**Scheme 1a**) [21]: TTACl was stirred in aqueous HNTf₂ solution (0.5 mol/L) at room temperature for 2 h. Here, molar ratio of HNTf₂/TTACl (= 1.5) is the important factor. The water-insoluble viscous product was isolated, washed with water, and dried under reduced pressure. Then, the crude product was dissolved in methanol and the resulting solution was heated in an open system until the solvent completely evaporated to remove the small amount of water remaining in the product. In addition, the resulting

When the differential scanning calorimetry (DSC) measurement of **Am-Random-SQ-IL** was performed, the baseline shift assigned to the glass-transition point (T_g) was observed at 15°C (Run 1 in **Table 1**). On the other hand, the endothermic peak due to T_m could not be detected, indicating that **Am-Random-SQ-IL** is an amorphous compound. So far, ILs without T_m have been reported, e.g., 1-butyl-3-methylimidazolium tetrafluoroborate [22] and 1-ethyl-3-methylimidazolium phosphonate derivatives [23].

The flow temperature of **Am-Random-SQ-IL** was visually confirmed by the following procedure: **Am-Random-SQ-IL** was kept horizontal at 100°C for 15 min in a glass vessel, and the sample in the vessel was cooled to room temperature in the horizontal state. Then, the vessel stood at various temperatures for 15 min with tilting. Accordingly, **Am-Random-SQ-IL** showed obvious fluidity over 40°C (Run 1 in **Table 1**).

The thermal stability of **Am-Random-SQ-IL** on pyrolysis was investigated by thermogravimetric analyses (TGA). The temperatures of 3% (T_{d3}), 5% (T_{d5}), and 10% (T_{d10}) weight losses of **Am-Random-SQ-IL** (411, 417, and 425°C, respectively) (Run 1 in **Table 1**) were higher than those of *N,N,N*-trimethyl-*N*-propylammonium bis(trifluoromethanesulfonyl) imide ([TMPA][NTf₂]) (392, 400, and 411°C, respectively), which is an IL compound with the structure of the side-chains of **Am-Random-SQ-IL**. These results indicate that the thermal stability of **Am-Random-SQ-IL** was enhanced by connection to the silsesquioxane framework.

Run	IL	T_g (°C) ^a	T_m (°C) ^a	Flow temp. (°C) ^b	T_{d5} (°C) ^c
1	Am-Random-SQ-IL	15	ND ^d	~40	417
2	Am-Cage-SQ	ND ^d	172	~155	420
3	Im-Random-SQ-IL	-25	ND ^d	~0	437
4	Im-Cage-SQ-IL	-21	106	~100	436
5	Mixture of Am-Cage-SQ and Im-Cage-SQ-IL	-7	164	~120	420
6	Amim-Cage-SQ-IL	-8	ND ^d	~30	420
7	MeIm-CyS-IL-NTf₂	-43	ND ^d	~0	415
8	MeIm-CyS-IL-OTf	-14	ND ^d	~20	391
9	HIm-CyS-IL-NTf₂	-38	ND ^d	~0	-
10	EtIm-CyS-IL-NTf₂	-44	ND ^d	~0	-
11	PrIm-CyS-IL-NTf₂	-44	ND ^d	~0	-
12	Bulm-CyS-IL-NTf₂	-45	ND ^d	~0	-

^a Determined by DSC.

^b Determined by visual observation.

^c Determined by TGA.

^d Not detected.

Table 1. Properties of ILs containing siloxane frameworks.

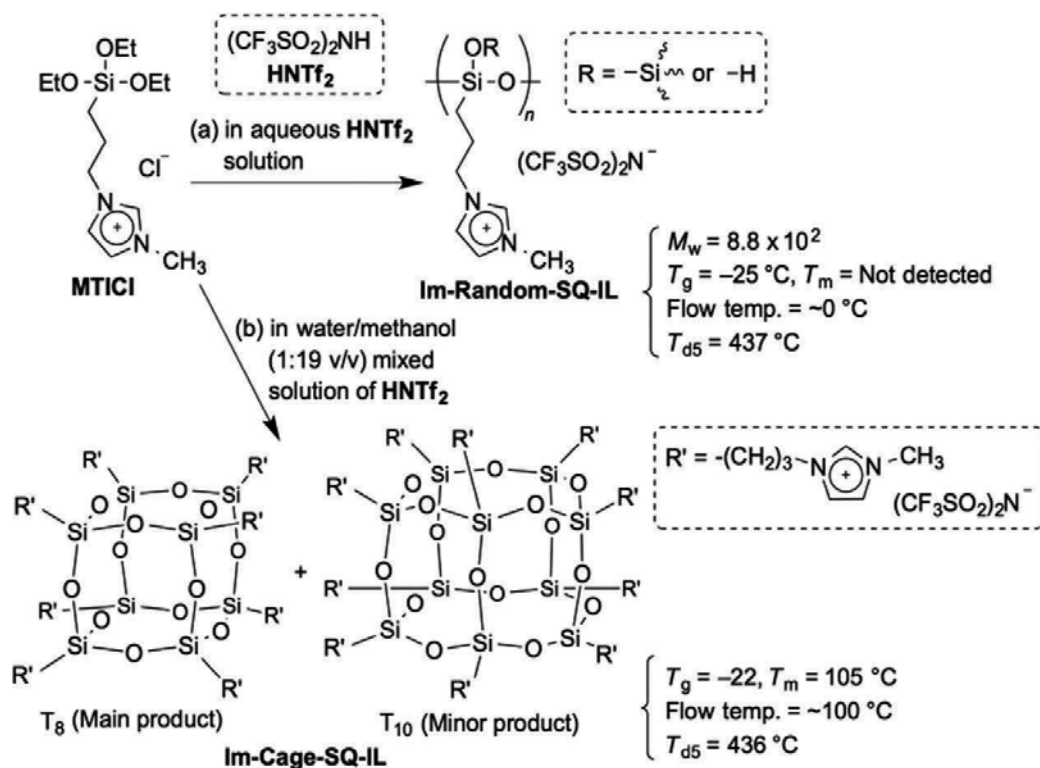
As described above, **Am-Random-SQ-IL** had an amorphous structure and displayed IL nature. Its amorphous structure is probably one of the most important factors for such IL properties. Therefore, to investigate the correlation between the IL nature and the structures of the silsesquioxanes, we investigated the preparation of a POSS compound with crystalline structure using the same reagent and superacid catalyst. When the hydrolytic condensation of TTACl was performed using HNTf_2 as a catalyst in water/methanol mixed solvent (1:19 v/v) instead of the aqueous solution as described above, a powdered POSS compound (**Am-Cage-SQ**) was prepared (**Scheme 1b**) [21]. A visual flow temperature of **Am-Cage-SQ** ($\sim 155^\circ\text{C}$) was much higher than that of **Am-Random-SQ-IL** because of the presence of higher T_m (172°C), although pyrolysis temperature was notably high ($T_{d5} = 420^\circ\text{C}$) (Run 2 in **Table 1**). Such high T_{ms} and flow temperatures of these POSS compounds are probably derived from their highly symmetrical and crystalline structures.

3. Preparation of imidazolium-type ionic liquids containing random-structured and cage-like oligosilsesquioxanes

As described in the previous section, **Am-Random-SQ-IL** had T_g of 15°C and exhibited fluidity at $\sim 40^\circ\text{C}$, i.e., it was not a room temperature IL (RT-IL). Generally, imidazolium-type ILs have relatively low T_m [24]. Therefore, to prepare a RT-IL containing a randomly structured oligosilsesquioxane framework (**Im-Random-SQ-IL**), the hydrolytic condensation of the imidazolium-group-containing organotrialkoxysilane using aqueous HNTf_2 was investigated [25]. **Im-Random-SQ-IL** could be prepared from 1-methyl-3-[3-(triethoxysilyl)propyl]imidazolium chloride (MTICl) as a starting material by the same procedure for the preparation of **Am-Random-SQ-IL** as described above (**Scheme 2a**). **Im-Random-SQ-IL** was soluble in DMSO, DMF, methanol, acetone, THF, and ethyl acetate, but insoluble in water, ethanol, 1-propanol, 2-propanol, chloroform, diethyl ether, toluene, and *n*-hexane.

The EDX pattern of **Im-Random-SQ-IL** also indicated the absence of Cl. In addition, the Si:S elemental ratio of **Im-Random-SQ-IL** was estimated to be 1:2.03, indicating that the molar ratio of imidazolium cations to NTf_2 anions was ca. 1:1. The ^{29}Si NMR spectrum of **Im-Random-SQ-IL** in $\text{DMSO-}d_6$ at 60°C exhibited two broad signals in the T^2 (-53 to -61 ppm) and T^3 (-64 to -70 ppm) regions with an integrated ratio of ca. 40:60. Similar to the aforementioned quaternary ammonium salt-type IL (**Am-Random-SQ-IL**), this compound was also stable, although it had a relatively high proportion of the silanol groups. The M_w of **Im-Random-SQ-IL** estimated by SLS data obtained in methanol was ca. 8.8×10^2 . Based on these results, it was concluded that **Im-Random-SQ-IL** was a randomly structured oligosilsesquioxane compound composed of imidazolium cations and NTf_2 anions.

The DSC analysis of **Im-Random-SQ-IL** was performed. The baseline shift assigned to T_g was observed at -25°C (Run 3 in **Table 1**). Conversely, the endothermic peak due to T_m was not detected. The amorphous structure of **Im-Random-SQ-IL** may give rise to poor packing of the ions. The flow temperature of **Im-Random-SQ-IL** was confirmed by the same procedure for **Am-Random-SQ-IL** as described above. Consequently, it showed obvious fluidity at $\sim 0^\circ\text{C}$, i.e., it is a RT-IL (Run 3 in **Table 1**).



Scheme 2. Preparation of (a) **Im-Random-SQ-IL** and (b) **Im-Cage-SQ-IL**.

We assumed that such IL properties were probably attributed to the amorphous structure. Therefore, as well as the quaternary ammonium-type ILs as described in the previous section, a POSS compound with crystalline structure was prepared. A POSS compound (**Im-Cage-SQ-IL**) was prepared by the hydrolytic condensation of MTICl using HNTf_2 as a catalyst in water/methanol (1:19, v/v) mixed solvent (Scheme 2b) [25]. **Im-Cage-SQ-IL** was soluble in DMSO, DMF, methanol, acetone, THF, and ethyl acetate, but insoluble in water, ethanol, 1-propanol, 2-propanol, chloroform, diethyl ether, toluene, and *n*-hexane. The ^1H NMR and EDX results for **Im-Cage-SQ-IL** were almost same as those for **Im-Random-SQ-IL**.

The ^{29}Si NMR spectrum of **Im-Cage-SQ-IL** in $\text{DMSO}-d_6$ at $40\text{ }^\circ\text{C}$ showed two signals assigned to the T^3 structures at -66.5 ppm (a main signal) and at -68.7 ppm (a minor signal), indicating the absence of silanol groups. These signals were derived from cage-like octasilsesquioxane (T_8) and cage-like decasilsesquioxane (T_{10}), respectively. Because the integrated ratio of these signals was estimated to be 75:25, the molar ratio of $T_8:T_{10}$ was calculated to be 79:21 (= 75/8:25/10). In addition, the MALDI-TOF MS results supported the formation of such POSS structures. Finally, the XRD pattern of **Im-Cage-SQ-IL** showed many sharp diffraction peaks, indicating the formation of a crystalline structure, unlike that of **Im-Random-SQ-IL**, which did not exhibit any diffraction peaks.

The DSC curve for **Im-Cage-SQ-IL** indicated the baseline shift due to T_g at -22°C and the endothermic peak due to T_m at 105°C (Run 4 in **Table 1**). In addition, **Im-Cage-SQ-IL** showed fluidity at $\sim 100^\circ\text{C}$ (Run 4 in **Table 1**), confirmed by the same procedure as described above for **Im-Random-SQ-IL**. This indicated that **Im-Cage-SQ-IL** was not a RT-IL. Because **Im-Cage-SQ-IL** is a crystalline compound, its flow temperature was near its T_m ($\sim 100^\circ\text{C}$). On the other hand, **Im-Random-SQ-IL** with an amorphous structure exhibited fluidity above its T_g . These results suggest that the amorphous structure of **Im-Random-SQ-IL** is essential for achieving RT-IL, in addition to the types of substituent groups in the silsesquioxanes.

The thermal stabilities of **Im-Random-SQ-IL** and **Im-Cage-SQ-IL** upon pyrolysis were investigated by TGA. The $T_{d3\%}$, $T_{d5\%}$, and $T_{d10\%}$ values for **Im-Random-SQ-IL** were 429, 437, and 447°C , respectively (Run 3 in **Table 1**), while those of **Im-Cage-SQ-IL** were 427, 436, and 446°C , respectively (Run 4 in **Table 1**). These values were higher than those of 1-methyl-3-propylimidazolium bis(trifluoromethylsulfonyl)imide ([C3mim][NTf₂]) (366 , 380 , and 399°C , respectively). This compound is an IL with the structure of the side-chains of **Im-Random-SQ-IL** and **Im-Cage-SQ-IL**. These results indicated that the thermal stabilities of **Im-Random-SQ-IL** and **Im-Cage-SQ-IL** were increased by incorporation of the silsesquioxane frameworks. Such a tendency was also observed in a quaternary ammonium-type IL, **Am-Random-SQ-IL**, as described above.

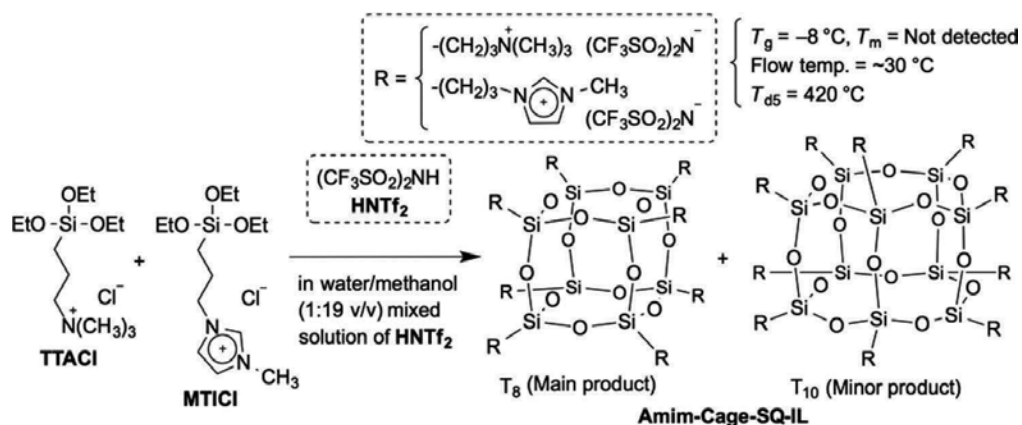
4. Preparation of ionic liquids containing cage-like oligosilsesquioxane (POSS) with the random distribution of quaternary ammonium and imidazolium side-chain groups

As described in Section 3, a highly thermostable POSS IL containing imidazolium cationic side-chains and NTf₂ anions as counter ions (**Im-Cage-SQ-IL**) could be successfully prepared by hydrolytic condensation of MTICl using superacid HNTf₂ as a catalyst. In addition, a quaternary ammonium-type POSS (**Am-Cage-SQ**) could also be prepared from TTACl as a starting material using the same procedure, as described in Section 2. However, visual flow temperatures of these compounds were relatively high ($\sim 155^\circ\text{C}$ for **Am-Cage-SQ** and $\sim 100^\circ\text{C}$ for **Im-Cage-SQ-IL**) because of their higher T_m s (172°C for **Am-Cage-SQ** and 105°C for **Im-Cage-SQ-IL**) (Run 2, 4 in **Table 1**). Such high T_m s and flow temperatures of these POSS compounds are probably derived from their highly symmetrical and crystalline structures.

The development of POSS RT-ILs with high thermal stabilities is expected for both academic and application reasons because RT-ILs are particularly useful for many applications of green solvents and electrolyte materials. Therefore, to prepare such POSS ILs, we focused on our previous studies on the preparation of low-crystalline POSS [11] and amorphous POSS-linking polymer [12]. Their synthesis was achieved by hydrolytic condensation of a mixture of two types of amino-group-containing organotrialkoxysilanes. The molecular symmetry of the resulting POSS derivatives was low because of the random distribution of the two types of side-chain groups. Consequently, their crystallization was suppressed. In this section, we describe the preparation of a thermally stable POSS RT-IL (**Amim-Cage-SQ-IL**), which contained a

random distribution of the two types of side-chain groups, by the hydrolytic condensation of a mixture of TTACl and MTICl using HNTf_2 as a catalyst in water/methanol mixed solvent [26].

Amim-Cage-SQ-IL was prepared from a mixture of TTACl and MTICl (1:1 mol/mol) by same procedures for the preparation of **Im-Cage-SQ-IL** and **Am-Cage-SQ** as described above (Scheme 3). **Amim-Cage-SQ-IL** was soluble in DMSO, acetonitrile, DMF, methanol, acetone, THF, and ethyl acetate, but insoluble in water, ethanol, 1-propanol, 2-propanol, chloroform, diethyl ether, toluene, and *n*-hexane.



Scheme 3. Preparation of **Amim-Cage-SQ-IL**.

The ^1H NMR spectrum of **Amim-Cage-SQ-IL** in $\text{DMSO-}d_6$ showed the signals attributable to the side-chain groups of both the *N,N,N*-trimethyl-*N*-propylammonium group and the 1-methyl-3-propylimidazolium group. The average compositional ratio of TTACl to MTICl components in the product was estimated to be ca. 1:1 from the ^1H NMR spectrum. The EDX pattern of **Amim-Cage-SQ-IL** did not indicate any peaks originating from Cl, and the Si:S elemental ratio was estimated to be 1.00:2.03, indicating that the molar ratio of cation species (imidazolium and ammonium) to NTf_2^- anions was ca. 1:1.

The ^{29}Si NMR spectrum of **Amim-Cage-SQ-IL** in $\text{DMSO-}d_6$ at 40°C only showed four sharp signals due to the T^3 structure at -66.8 , -67.3 , -68.8 , and -69.3 ppm, indicating the absence of silanol groups. These signals could be attributed to the MTICl and TTACl components of T_8 and the MTICl and TTACl components of T_{10} , respectively, because these chemical shifts were almost same as those of **Am-Cage-SQ** and **Im-Cage-SQ-IL** as described in the previous sections. Because the integrated ratio of $T_8:T_{10}$ signals was estimated to be 77:23, the molar ratio of $T_8:T_{10}$ was calculated to be 81:19 ($= 77/8:23/10$), indicating that T_8 was the main product. The MALDI-TOF MS analysis of **Amim-Cage-SQ-IL** also supported the ^{29}Si NMR results.

The DSC curves of **Am-Cage-SQ** and **Im-Cage-SQ-IL** (POSS compounds as described in Sections 2 and 3) indicated the endothermic peaks for T_m s at 172 and 105°C , respectively (Run 2, 4 in Table 1), i.e., **Am-Cage-SQ** and **Im-Cage-SQ-IL** are crystalline compounds.

The XRD patterns of **Am-Cage-SQ** and **Im-Cage-SQ-IL** supported that they were crystalline compounds. Therefore, **Am-Cage-SQ** and **Im-Cage-SQ-IL** showed relatively high flow temperatures (~155 and ~100°C, respectively) because of their high crystallinity (Run 2, 4 in **Table 1**). In addition, a mixture of **Am-Cage-SQ** and **Im-Cage-SQ-IL** also maintained crystalline structure, because the endothermic peak due to T_m was observed at 164°C; it showed fluidity at 120°C (Run 5 in **Table 1**).

Conversely, the DSC curve of **Amim-Cage-SQ-IL** showed a baseline shift at -8°C due to T_g , whereas an endothermic peak due to T_m was not detected (Run 6 in **Table 1**), indicating that **Amim-Cage-SQ-IL** is an amorphous compound. The XRD pattern of **Amim-Cage-SQ-IL** did not show any diffraction peaks, supporting the amorphous structure of this compound. **Amim-Cage-SQ-IL** exhibited obvious fluidity at ~30°C (Run 6 in **Table 1**). Because the molecular symmetry of the resulting POSS compound with a random distribution of the two types of side-chain groups was low, its crystallization was suppressed. Therefore, the phase transition from amorphous solid to fluid occurred above T_g . Based on these results, it was concluded that **Amim-Cage-SQ-IL** had T_g of -8°C and showed fluidity at ~30°C, i.e., it is a RT-IL.

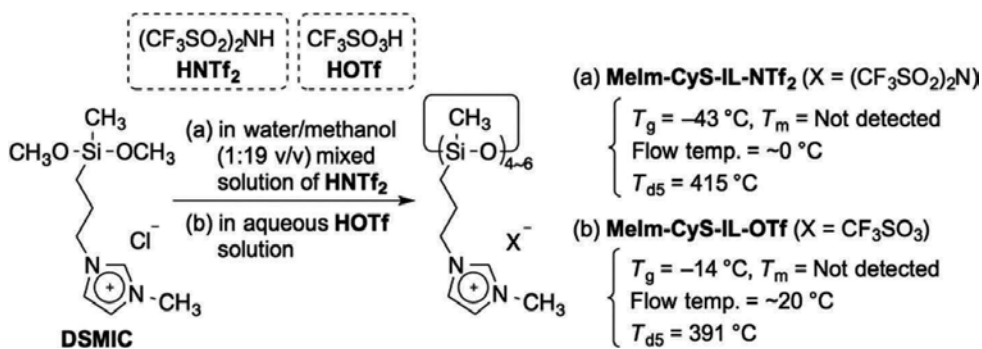
The T_{d3} , T_{d5} , and T_{d10} values estimated by TGA of **Amim-Cage-SQ-IL** were 414°C, 420°C, and 428 °C, respectively (Run 6 in **Table 1**). These values were higher than those of ILs with the side-chain structures of this IL: [TMPA][NTf₂] (392, 400, and 411°C, respectively) and [C3mim][NTf₂] (366, 380, and 399°C, respectively).

5. Preparation of ionic liquids containing cyclic oligosiloxanes

In the previous sections, we described that ILs containing silsesquioxane frameworks, such as randomly structured silsesquioxanes and POSSs, were successfully prepared. In particular, **Am-Random-SQ-IL**, **Im-Random-SQ-IL**, and **Amim-Cage-SQ-IL** had both relatively low flow temperatures (<~40°C) and high thermal stabilities ($T_{d5} > \sim 400^\circ\text{C}$). However, they also displayed high viscosities, probably because of the presence of silanol groups for randomly structured silsesquioxane ILs and relatively higher degrees of polymerization (DP) for all silsesquioxane ILs. It is assumed that siloxane-based ILs without silanol groups and with lower DP probably exhibit high thermal stability, low flow temperature, and low viscosity. In this section, therefore, we describe the preparation and properties of ILs containing cyclic oligosiloxanes as the siloxane frameworks.

To achieve the preparation of such ILs containing cyclic oligosiloxanes, we referred to our previous study for the facile preparation of cationic cyclotetrasiloxane (this is not an IL) by the hydrolytic condensation of 3-aminopropylmethyltriethoxysilane using the superacid trifluoromethanesulfonic acid (HOTf) [20]. Therefore, when the hydrolytic condensation of 1-[3-(dimethoxymethylsilyl)propyl]-3-methylimidazolium chloride (DSMIC) was performed using superacid catalysts such as HNTf₂ and HOTf, we found that imidazolium salt-type ILs containing cyclic oligosiloxane frameworks (**MeIm-CyS-IL-NTf₂** and **MeIm-CyS-IL-OTf**) were successfully prepared [27].

MeIm-CyS-IL-NTf₂ was prepared by the following procedure (**Scheme 4a**): DSMIC was stirred in a water/methanol (1:19, v/v) mixed solution of HNTf₂ at room temperature. Then, the solvent was evaporated by heating at ~50°C in an open system. The resulting crude product was further heated at 100°C for 2 h, washed with water, and then dried at 150°C for ca. 5 h to obtain **MeIm-CyS-IL-NTf₂**. On the other hand, **MeIm-CyS-IL-OTf** was prepared using almost same procedure as that of **MeIm-CyS-IL-NTf₂** but using an aqueous HOTf as a catalyst (**Scheme 4b**). The EDX results of **MeIm-CyS-IL-NTf₂** and **MeIm-CyS-IL-OTf** indicated the absence of Cl and the molar ratio of imidazolium cations to NTf₂ or OTf anions were ca. 1:1.



Scheme 4. Preparation of (a) **MeIm-CyS-IL-NTf₂** and (b) **MeIm-CyS-IL-OTf**.

In the MALDI-TOF MS analysis of **MeIm-CyS-IL-NTf₂**, several peaks assigned to cyclic siloxane tetramer (main peaks) and pentamer (minor peaks) were observed. Furthermore, the ¹H NMR spectrum exhibited multiplet signals due to methyl groups at 0.23 to -0.23 ppm. In addition, the ²⁹Si NMR spectrum of **MeIm-CyS-IL-NTf₂** in DMSO-*d*₆ at 40°C also showed two multiplet signals due to the *D*² structure (-19.2 to -19.6 ppm for cyclic tetrasiloxane (main signals) and -21.4 to -21.9 ppm for cyclic pentasiloxane (minor signals)). On the other hand, the MALDI-TOF MS results of **MeIm-CyS-IL-OTf** indicated the existence of a mixture of cyclic siloxane tetramer (main product), pentamer (main product), and hexamer (minor product). In addition, **MeIm-CyS-IL-OTf** had some stereoisomers, confirmed by the ¹H NMR spectrum with multiplet signals assigned to the methyl groups at 0.16–0.23 ppm and the ²⁹Si NMR spectrum with three multiplet signals due to the *D*² structure (-19.1 to -19.7 ppm for cyclic tetrasiloxane (main signals), -21.3 to -21.9 ppm for cyclic pentasiloxane (main signals), and -22.2 to -22.5 ppm for cyclic hexasiloxane (minor signals)). These results indicated that **MeIm-CyS-IL-NTf₂** was a mixture of cyclic tetrasiloxanes and cyclic pentasiloxanes, while **MeIm-CyS-IL-OTf** was a mixture of cyclic tetrasiloxanes, cyclic pentasiloxanes, and cyclic hexasiloxane, with some stereoisomers.

The DSC curves of the resulting products indicated the baseline shifts assigned to *T*_gs at -43°C for **MeIm-CyS-IL-NTf₂** (Run 7 in **Table 1**) and at -14°C for **MeIm-CyS-IL-OTf** (Run 8 in **Table 1**), respectively. These values were newly estimated using different DSC equipment from that in the original paper [27] and were slightly different from the values in the original paper. Conversely, the endothermic peaks due to *T*_m were not detected. In addition, **MeIm-CyS-IL-NTf₂** and **MeIm-CyS-IL-OTf** showed obvious fluidity at ~0 and ~20°C, respectively (Run 7, 8 in **Table 1**). On the basis of these results, it was concluded that **MeIm-CyS-IL-NTf₂**

and **MeIm-CyS-IL-OTf** were RT-ILs. The T_{d3} , T_{d5} , and T_{d10} values estimated by TGA were 407, 415, and 427°C for **MeIm-CyS-IL-NTf₂** (Run 7 in **Table 1**) and 380, 391, and 402°C for **MeIm-CyS-IL-OTf** (Run 8 in **Table 1**).

The viscosity of **MeIm-CyS-IL-NTf₂** was lower than that of **Im-Random-SQ-IL** containing randomly structured oligosilsesquioxane framework, as described in Section 3. Both ILs have same side-chain groups and showed low flow temperatures ($\sim 0^\circ\text{C}$), yet the siloxane frameworks differed between the ILs. **Figure 1** shows the photographs of these two samples after 0 and 10 s, with tilting at 14°C . **MeIm-CyS-IL-NTf₂** obviously flowed after 10 s, while **Im-Random-SQ-IL** did not show fluidity after 10 s. These results indicated that cyclic oligosiloxane frameworks were important factors for the lower viscosity of **MeIm-CyS-IL-NTf₂**. Further detailed studies for viscosity determination are currently in progress.

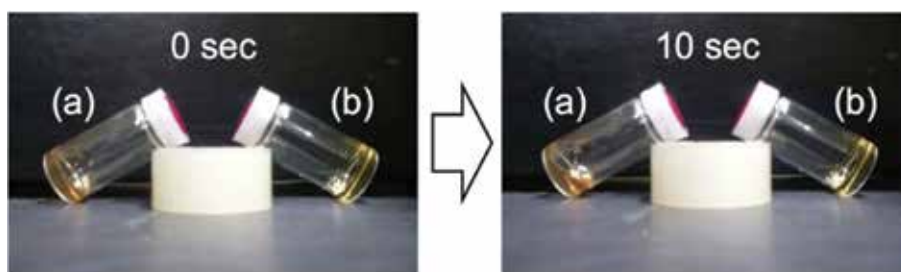
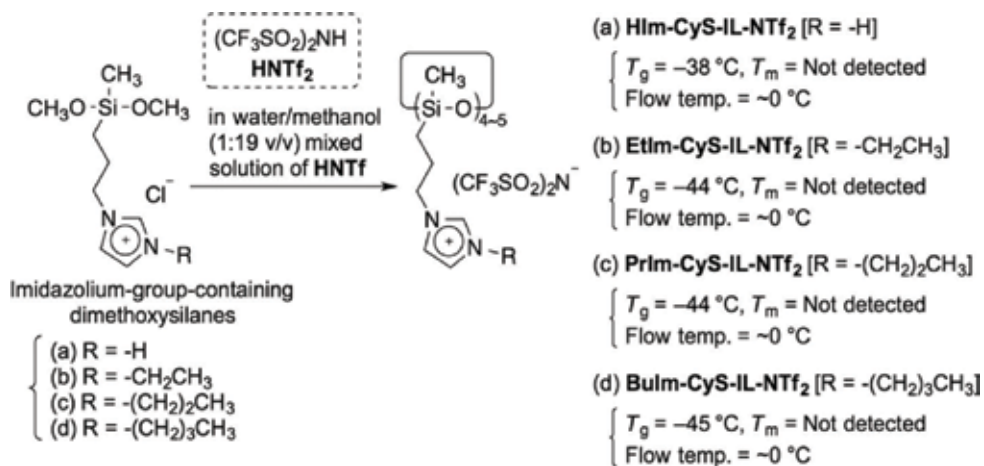


Figure 1. Photographs of (a) **MeIm-CyS-IL-NTf₂** and (b) **Im-Random-SQ-IL** after 0 and 10 s with tilting at 14°C .

For this chapter, we newly investigated the effects of the alkyl chain length in the imidazolium groups of ILs containing cyclic oligosiloxane frameworks. Therefore, imidazolium salt-type ILs containing cyclic oligosiloxane with various lengths of alkyl chains ($\text{R} = \text{H}$, CH_2CH_3 , $(\text{CH}_2)_2\text{CH}_3$, and $(\text{CH}_2)_3\text{CH}_3$) were prepared by the hydrolytic condensation of the corresponding imidazolium-group-containing dimethoxysilanes using the superacid HNTf_2 in a water/methanol (1:19, v/v) mixed solvent (**Scheme 5**). Based on the results of the ^{29}Si NMR and MALDI-TOF MS analyses, we determined that the resulting products [**HIm-CyS-IL-NTf₂** ($\text{R} = \text{H}$), **EtIm-CyS-IL-NTf₂** ($\text{R} = \text{CH}_2\text{CH}_3$), **PrIm-CyS-IL-NTf₂** ($\text{R} = (\text{CH}_2)_2\text{CH}_3$), and **BuIm-CyS-IL-NTf₂** ($\text{R} = (\text{CH}_2)_3\text{CH}_3$)] were mixtures of cyclic tetrasiloxanes (main product) and cyclic pentasiloxanes (minor product), with some stereoisomers, respectively.

The DSC curves of the resulting ILs showed the baseline shifts assigned to T_g s were observed at -38°C for **HIm-CyS-IL-NTf₂** (**Figure 2a**, Run 9 in **Table 1**), -44°C for **EtIm-CyS-IL-NTf₂** (**Figure 2b**, Run 10 in **Table 1**), -44°C for **PrIm-CyS-IL-NTf₂** (**Figure 2c**, Run 11 in **Table 1**), and -45°C for **BuIm-CyS-IL-NTf₂** (**Figure 2d**, Run 12 in **Table 1**). These values were almost same as that of **MeIm-CyS-IL-NTf₂** (-43°C) (Run 7 in **Table 1**). Conversely, the endothermic peaks due to the T_m s were not detected for all ILs. In addition, all ILs showed obvious fluidity at $\sim 0^\circ\text{C}$ (**Figure 2a–d** inset, Run 9–12 in **Table 1**). On the basis of these results, we concluded that the alkyl chain lengths in imidazolium groups of ILs containing cyclic oligosiloxane frameworks had an insignificant effect on the IL natures, such as T_g and flow temperatures.



Scheme 5. Preparation of (a) HIm-CyS-IL-NTf₂, (b) EtIm-CyS-IL-NTf₂, (c) PrIm-CyS-IL-NTf₂, and (d) BuIm-CyS-IL-NTf₂.

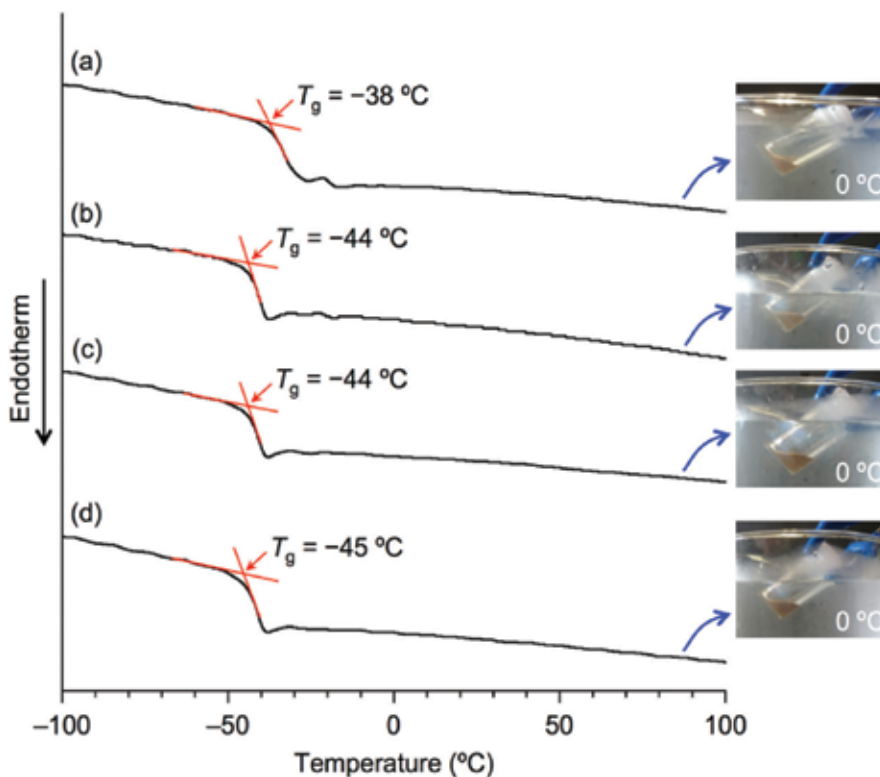


Figure 2. DSC curves and photographs of (a) HIm-CyS-IL-NTf₂, (b) EtIm-CyS-IL-NTf₂, (c) PrIm-CyS-IL-NTf₂, and (d) BuIm-CyS-IL-NTf₂.

6. Conclusions

In this chapter, we described the preparation and properties of thermally stable ILs containing siloxane frameworks, such as randomly structured oligosilsesquioxanes (**Am-Random-SQ-IL** and **Im-Random-SQ-IL**), POSSs (**Im-Cage-SQ-IL** and **Amim-Cage-SQ-IL**), and cyclic oligosiloxanes (**MeIm-CyS-IL-NTf₂**, **MeIm-CyS-IL-OTf**, **HIm-CyS-IL-NTf₂**, **EtIm-CyS-IL-NTf₂**, **PrIm-CyS-IL-NTf₂**, and **BuIm-CyS-IL-NTf₂**). We are expecting that new applications of these siloxane-based ILs are found.

The authors gratefully acknowledge Prof. J. Ohshita (Hiroshima University) and Dr. T. Mizumo (Samsung R & D Institute Japan) for their enthusiastic collaborations. The authors also gratefully give thanks for financial supports from JSPS KAKENHI (Grant-in-Aid for Challenging Exploratory Research) Number 15K13711.

Author details

Yoshiro Kaneko*, Akiyuki Harada, Takuya Kubo and Takuhiro Ishii

*Address all correspondence to: ykaneko@eng.kagoshima-u.ac.jp

Graduate School of Science and Engineering, Kagoshima University, Kagoshima, Japan

References

- [1] Welton T. Room-temperature ionic liquids. Solvents for synthesis and catalysis. *Chem. Rev.* 1999;**99**:2071–2084. DOI: 10.1021/cr980032t
- [2] Hallett JP, Welton T. Room-temperature ionic liquids: solvents for synthesis and catalysis. 2. *Chem. Rev.* 2011;**111**:3508–3576. DOI: 10.1021/cr1003248
- [3] Huddleston JG, Willauer HD, Swatloski RP, Visser AE, Rogers RD. Room temperature ionic liquids as novel media for ‘clean’ liquid–liquid extraction. *Chem. Commun.* 1998;1765–1766. DOI: 10.1039/A803999B
- [4] Dzyuba SV, Bartsch RA. Recent advances in applications of room-temperature ionic liquid/supercritical CO₂ systems. *Angew. Chem. Int. Ed.* 2003;**42**:148–150. DOI: 10.1002/anie.200390070
- [5] Armand M, Endres F, MacFarlane DR, Ohno H, Scrosati B. Ionic-liquid materials for the electrochemical challenges of the future. *Nat. Mater.* 2009;**8**:621–629. DOI: 10.1038/nmat2448
- [6] Ganapatibhotla LVNR, Zheng J, Roy D, Krishnan S. PEGylated imidazolium ionic liquid electrolytes: thermophysical and electrochemical properties. *Chem. Mater.* 2010;**22**:6347–6360. DOI: 10.1021/cm102263s

- [7] Tsurumaki A, Kagimoto J, Ohno H. Properties of polymer electrolytes composed of poly(ethylene oxide) and ionic liquids according to hard and soft acids and bases theory. *Polym. Adv. Technol.* 2011;**22**:1223–1228. DOI: 10.1002/pat.1931
- [8] Tanaka K, Ishiguro F, Chujo Y. POSS ionic liquid. *J. Am. Chem. Soc.* 2010;**132**:17649–17651. DOI: 10.1021/ja105631j
- [9] Tan J, Ma D, Sun X, Feng S, Zhang C. Synthesis and characterization of an octaimidazolium-based polyhedral oligomeric silsesquioxanes ionic liquid by an ion-exchange reaction. *Dalton Trans.* 2013;**42**:4337–4339. DOI: 10.1039/C2DT32645K
- [10] Kaneko Y, Shoiriki M, Mizumo T. Preparation of cage-like octa(3-aminopropyl)silsesquioxane trifluoromethanesulfonate in higher yield with a shorter reaction time. *J. Mater. Chem.* 2012;**22**:14475–14478. DOI: 10.1039/C2JM32355A
- [11] Tokunaga T, Shoiriki M, Mizumo T, Kaneko Y. Preparation of low-crystalline POSS containing two types of alkylammonium groups and its optically transparent film. *J. Mater. Chem. C* 2014;**2**:2496–2501. DOI: 10.1039/C3TC32292K
- [12] Tokunaga T, Koge S, Mizumo T, Ohshita J, Kaneko Y. Facile preparation of a soluble polymer containing polyhedral oligomeric silsesquioxane units in its main chain. *Polym. Chem.* 2015;**6**:3039–3045. DOI: 10.1039/C5PY00192G
- [13] Kaneko Y, Iyi N, Kurashima K, Matsumoto T, Fujita T, Kitamura K. Hexagonal-structured polysiloxane material prepared by sol–gel reaction of aminoalkyltrialkoxysilane without using surfactants. *Chem. Mater.* 2004;**16**:3417–3423.
- [14] Kaneko Y, Iyi N, Matsumoto T, Kitamura K. Synthesis of rodlike polysiloxane with hexagonal phase by sol–gel reaction of organotrialkoxysilane monomer containing two amino groups. *Polymer* 2005;**46**:1828–1833. DOI: 10.1016/j.polymer.2004.12.038
- [15] Kaneko Y, Iyi N. Sol–gel synthesis of rodlike polysilsesquioxanes forming regular higher-ordered nanostructure. *Z. Kristallogr.* 2007;**222**:656–662. DOI: 10.1524/zkri.2007.222.11.656
- [16] Kaneko Y, Toyodome H, Shoiriki M, Iyi N. Preparation of ionic silsesquioxanes with regular structures and their hybridization. *Int. J. Polym. Sci.* 2012;Article ID 684278. DOI: 10.1155/2012/684278
- [17] Toyodome H, Kaneko Y, Shikinaka K, Iyi N. Preparation of carboxylate group-containing rod-like polysilsesquioxane with hexagonally stacked structure by sol–gel reaction of 2-cyanoethyltriethoxysilane. *Polymer.* 2012;**53**:6021–6026. DOI: 10.1016/j.polymer.2012.10.052
- [18] Kaneko Y. Preparation of ionic silsesquioxanes with controlled structures and their functionalizations. *Kobunshi Ronbunshu* 2014;**71**:443–456. DOI: 10.1295/koron.71.443
- [19] Kaneko Y, Toyodome H, Mizumo T, Shikinaka K, Iyi N. Preparation of a sulfo-group-containing rod-like polysilsesquioxane with a hexagonally stacked structure and its proton conductivity. *Chem. Eur. J.* 2014;**20**:9394–9399. DOI: 10.1002/chem.201402011

- [20] Kinoshita S, Watase S, Matsukawa K, Kaneko Y. Selective synthesis of *cis-trans-cis* cyclic tetrasiloxanes and the formation of their two-dimensional layered aggregates. *J. Am. Chem. Soc.* 2015;**137**:5061–5065. DOI: 10.1021/jacs.5b00319
- [21] Ishii T, Mizumo T, Kaneko Y. Facile preparation of ionic liquid containing silsesquioxane framework. *Bull. Chem. Soc. Jpn.* 2014;**87**:155–159. DOI: 10.1246/bcsj.20130246
- [22] Nishida T, Tashiro Y, Yamamoto M. Physical and electrochemical properties of 1-alkyl-3-methylimidazolium tetrafluoroborate for electrolyte. *J. Fluorine Chem.* 2003;**120**:135–141. DOI: 10.1016/S0022-1139(02)00322-6
- [23] Fukaya Y, Hayashi K, Wada M, Ohno H. Cellulose dissolution with polar ionic liquids under mild conditions: required factors for anions. *Green Chem.* 2008;**10**:44–46. DOI: 10.1039/B713289A
- [24] Galinski M, Lewandowski A, Stepniak I. Ionic liquids as electrolytes. *Electrochim. Acta.* 2006;**51**:5567–5580. DOI: 10.1016/j.electacta.2006.03.016
- [25] Ishii T, Enoki T, Mizumo T, Ohshita J, Kaneko Y. Preparation of imidazolium-type ionic liquids containing silsesquioxane frameworks and their thermal and ion-conductive properties. *RSC Adv.* 2015;**6**:15226–15232. DOI: 10.1039/C4RA17113F
- [26] Harada A, Koge S, Ohshita J, Kaneko Y. Preparation of a thermally stable room temperature ionic liquid containing cage-like oligosilsesquioxane with two types of side-chain groups. *Bull. Chem. Soc. Jpn.* 2016;**89**:1129–1135. DOI: 10.1246/bcsj.20160170
- [27] Kubo T, Koge S, Ohshita J, Kaneko Y. Preparation of imidazolium salt type ionic liquids containing cyclic siloxane frameworks. *Chem. Lett.* 2015;**44**:1362–1364. DOI: 10.1246/cl.150598



Edited by Scott Handy

Ionic liquids, including the newer subcategory of deep eutectic solvents, continue to attract a great deal of research attention in an even increasing number of areas, including traditional areas such as synthesis (organic and materials), electrochemistry, and physical property studies and predictions, as well as less obvious areas such as lubrication and enzymatic transformations. In this volume, recent advances in a number of these different areas are reported and reviewed, thus granting some appreciation for the future that ionic liquid research holds and affording inspiration for those who have not previously considered the application of ionic liquids in their area of interest.

Photo by igorr1 / iStock

IntechOpen

